V. Bindhu
João Manuel R. S. Tavares
Chandrasekar Vuppalapati   *Editors*

Proceedings of Fourth International Conference on Communication, Computing and Electronics Systems

ICCCES 2022

Springer

Lecture Notes in Electrical Engineering

Volume 977

The book series *Lecture Notes in Electrical Engineering* (LNEE) publishes the latest developments in Electrical Engineering—quickly, informally and in high quality. While original research reported in proceedings and monographs has traditionally formed the core of LNEE, we also encourage authors to submit books devoted to supporting student education and professional training in the various fields and applications areas of electrical engineering. The series cover classical and emerging topics concerning:

- Communication Engineering, Information Theory and Networks
- Electronics Engineering and Microelectronics
- Signal, Image and Speech Processing
- Wireless and Mobile Communication
- Circuits and Systems
- Energy Systems, Power Electronics and Electrical Machines
- Electro-optical Engineering
- Instrumentation Engineering
- Avionics Engineering
- Control Systems
- Internet-of-Things and Cybersecurity
- Biomedical Devices, MEMS and NEMS

For general information about this book series, comments or suggestions, please contact leontina.dicecco@springer.com.

To submit a proposal or request further information, please contact the Publishing Editor in your country:

China

Jasmine Dou, Editor (jasmine.dou@springer.com)

India, Japan, Rest of Asia

Swati Meherishi, Editorial Director (Swati.Meherishi@springer.com)

Southeast Asia, Australia, New Zealand

Ramesh Nath Premnath, Editor (ramesh.premnath@springernature.com)

USA, Canada

Michael Luby, Senior Editor (michael.luby@springer.com)

All other Countries

Leontina Di Cecco, Senior Editor (leontina.dicecco@springer.com)

** This series is indexed by EI Compendex and Scopus databases. **

V. Bindhu · João Manuel R. S. Tavares ·
Chandrasekar Vuppalapati
Editors

Proceedings of Fourth International Conference on Communication, Computing and Electronics Systems

ICCCES 2022

Editors
V. Bindhu
Department of Electronics
and Communication Engineering
PPG Institute of Technology
Coimbatore, Tamil Nadu, India

João Manuel R. S. Tavares
Departamento de Engenharia Mecánica,
Faculdade de Engenharia
Universidade do Porto
Porto, Portugal

Chandrasekar Vuppalapati
San Jose State University
San Jose, CA, USA

We are honored to dedicate the proceedings of ICCCES 2022 to all the participants, organizers and editors of ICCCES 2022.

Preface

This Conference Proceedings volume contains the written versions of most of the contributions presented during the ICCCES 2022 conference. The conference has provided a platform to share and exchange the recent developments in a wide range of topics including computational intelligence, machine learning, signal and image processing, electronic devices and systems, antenna and wave propagation, wireless communication networks and so on. The conference has been a good opportunity for participants coming from various destinations to present and discuss the state-of-the-art topics in their respective research areas.

ICCCES 2022 Conference tends to collect the latest research results and applications on computing, communication and electronics. It includes a selection of 80 papers from 290 papers submitted to the conference from various universities and industries present across the globe. All the accepted papers were subjected to double-blinded peer-reviewing process by 2–4 expert referees. The papers are selected for its high quality and the relevance to the conference.

ICCCES 2022 would like to express our gratitude and appreciation to all the authors for their valuable research contributions to this book. We would like to extend our thanks to Keynote Speakers and Guest Editors Dr. João Manuel R. S. Tavares, Universidade do Porto (FEUP), Porto, Portugal, Prof. Chandrasekar Vuppalapati, Computer Engineering, San Jose State University, USA, and all the referees for expressing their constructive comments on all the research papers. In particular, we would like to thank the organizing committee for their tireless hard work. Finally, we would like to thank the Springer publications for producing this volume.

Coimbatore, India   Dr. V. Bindhu
                                                                                                Conference Chair

Contents

About the Editors

Dr. V. Bindhu received the B.E. degree in Electronics and Communication Engineering from Bharathiar University, Coimbatore, in 2002, M.E. Degree in Applied Electronics from Anna University, Chennai, in 2007 and Ph.D. Degree from Anna University, Chennai, in 2014. She has 11 years of teaching experience and 6 years of research experience. Currently, she is a professor at PPG Institute of Technology, Coimbatore. Her area of interest includes signal processing and VLSI design.

João Manuel R. S. Tavares graduated in Mechanical Engineering at the Universidade do Porto, Portugal in 1992. He also earned his M.Sc. degree and Ph.D. degree in Electrical and Computer Engineering from the Universidade do Porto in 1995 and 2001 and attained his Habilitation in Mechanical Engineering in 2015. He is a senior researcher at the Instituto de Ciência e Inovação em Engenharia Mecânica e Engenharia Industrial (INEGI) and an associate professor at the Department of Mechanical Engineering (DEMec) of the Faculdade de Engenharia da Universidade do Porto (FEUP).

Dr. Chandrasekar Vuppalapati is a software IT executive with diverse experience in software technologies, enterprise software architectures, cloud computing, big data business analytics, Internet of things (IoT), and software product and program management. Chandra held engineering and product leadership roles at GE Healthcare, Cisco Systems, Samsung, Deloitte, St. Jude Medical, and Lucent Technologies, Bell Laboratories Company. Chandra teaches software engineering, mobile computing, cloud technologies, and web and data mining for Master's program in San Jose State University. Additionally, Chandra held market research, strategy and technology architecture advisory roles in Cisco Systems, Lam Research, and performed a principal investigator role for Valley School of Nursing where he connected nursing educators and students with virtual reality technologies. Chandra has functioned as a chair in numerous technology and advanced computing conferences such as: IEEE

Oxford, UK, IEEE Big Data Services 2017, San Francisco, USA, and Future of Information and Communication Conference 2018, Singapore. Chandra graduated from San Jose State University Master's Program, specializing in software engineering, and completed his Master of Business Administration from Santa Clara University, Santa Clara, California, USA.

Study of Different Control Strategies Applied to a Second-Order Nonlinear Tank Process

S. Nagammai, S. Latha, D. Pradeepkannan, A. Umarani, and S. Balamurugan

Abstract Conical tank process (CTP) is used in most of the industries, namely food processing, chemical, beer production, pharmaceutical, and waste treatment plants. This unit is widely used because of its accurate and thorough mixing capability. Efficient operation of these industries would require control of enormous process variables within their specified bounds. Today, control of large continuous interconnected plant is a challenging task and needs complex control hardware. Although the conventional PID control algorithms are widely used, modern control method such as adaptive control can provide noteworthy improvement. CTP has nonlinear characteristics due to its variable area and control of level has become an exigent task. Most of the industrial process loops are interacting in nature and require enormous control effort to achieve desired level. In order to accommodate changes in process parameters, gain-scheduled PI controller (GSPI) is designed. A major implementation issue of GSPI is design of the switching function to have a smooth changeover in process variable according to the operating point variations. A fuzzy logic system is used to overcome this difficulty. In fuzzy gain-scheduled PI (FGSPI) controller, based on expertise of human operator fuzzy rules are framed, and with the associated reasoning mechanism, the controller parameters are determined. In this paper, the elucidation of proposed FGSPI controller is simulated on a interacting conical tank process (ICTP). A simulated result shows the effectiveness of FGSPI controller in terms of setpoint tracking, disturbance rejection and process parameter variations.

Keywords Interacting conical tank process · Gain-scheduled PI controller · Fuzzy GSPI · Robustness

S. Nagammai (✉) · D. Pradeepkannan · A. Umarani · S. Balamurugan
Department of Electronics and Instrumentation Engineering, K.L.N. College of Engineering, Pottapalayam 630612, India
e-mail: nagammai.s@klnce.edu

S. Latha
Department of Electrical and Electronics Engineering, Thiyagarajar. College of Engineering, Madurai 625015, India

1 Introduction

Industrial processes such as fluidized catalytic cracking unit, boiler drum, distillation process and evaporators require control of process fluid in the vessel at a desired value. Industries make use of conical process tanks (CPT) for thorough mixing and well safe storage of chemicals, because of advantages of CTP over standard vertical storage tanks. For the storage of fertilizers in chemical industries and molasses in sugar industries and in water treatment plants, the use of CPT has become a leading choice, wherein the control of liquid level in the tank is a crucial problem. The proportional plus integral plus derivative controller is used extensively in industries because of its easy implementation. Many researchers have proved that conventional feedback controller is well suited for linear system. But design of conventional controllers for nonlinear systems and higher-order systems is not straight forward. If dynamics of the process is fixed, then the controller with fixed gains will provide satisfactory performance. However, when the parameter variations become predominant, the fixed gain controller cannot give satisfactory results, and under this circumstance, adaptive control scheme will show potential approach to control conical tank process (CTP) effectively. Fuzzy logic control has become an efficient technique and used in many of the industrial applications for the past two decades. Mamdani is the pioneer in developing fuzzy logic controller (FLC) for engineering applications.

Nagammai et al. experimentally validated fuzzy integral sliding mode controller for the single capacity conical tank process, and performance comparison has been made with classical PID controller [1]. Zhen et al. and Yao et al. made a performance comparison of fuzzy gain scheduling of PID controllers with ZN controller [2, 3]. Madhubala et al. developed an optimized fuzzy controller using genetic algorithm for a variable area tank process [4]. A globally linearized controller for a nonlinear process has been designed and validated experimentally in [5]. Nithya et al. presented a real-time performance comparison of Mamdani-FL and TS-FL for controlling liquid levels in conical tank process [6]. Nagammai et al. designed a fuzzy gain-scheduled PI controller for a nonlinear tank process and validated through simulation results [7]. Motamed et al. used fuzzy gain scheduling approach to control level of a tank in real time [8]. A fuzzy logic-based gain scheduling PI control for load frequency control in two-area power systems is presented in [9, 10]. Maruthi et al. proposed experimental validation of multi-model control schemes using gap metric-based weighting approach for control of level in process tanks [11]. Vavilala et al. studied the performance of fractional-order internal model controller with optimized parameters for level control in single capacity CTP [12]. Claudio et al. applied various control strategies with load disturbance for level control in CTP under simulation [13]. Gulzar et al. presented a simulation study of AMPC and fractional-order PID controller [14]. Bhuvaneswarri et al. simulated various conventional tuning methods for level control in interacting conical tank process [15]. The tuning of traditional PID controller for nonlinear process is still an emerging research area. Hence a controller which can accommodate system nonlinearity, parameter variations and uncertainties needs to be designed. In this research paper, gain-scheduled PI control algorithm is

Table 1 Part name and specifications of experimental setup

Part name	Specifications	Make
Conical tank	Capacity 50 L	SS316 Stainless steel
Differential pressure transmitter (DPT)	Output: 4–20 mA	Yokogawa make
Rota meter 1/4"	Range: 200–2000 Lph	Telelin make
Control valve	Single-seated globe valve	RK make
I/P converter	Output: 3–15 psig	ABB make
NI USB 6008—data acquisition card	Analog output: 1–5 V	National instruments make
Air compressor	0–5 kg/cm^2	LG make

designed based on Takagi Sugeno (TS) fuzzy logic for a nonlinear interacting tank process and validated using MATLAB.

The remaining part of this paper is structured as follows: Sect. 2 gives process description, and mathematical modeling of nonlinear interacting conical tank process is given in Sect. 3. Section 4 presents the design aspects of GSPI controller. Section 5 explains design aspects of FGSPI controller for the nonlinear tank process. The simulated results are presented in Sect. 6. The concluding remarks are given in Sect. 7.

2 Process Description

A bench mark process, namely a conical tank process, is considered as an illustrative example and whose parameters, namely process gain and time constant, change with respect to change in level. A change in process parameters occurs, when the operating point (namely tank level) moves to the top of the tank. The equipment associated with the laboratory scale setup is given in Table 1.

3 Mathematical Modelıng

The Piping and Instrumentation (P&I) diagram of interacting conical tank process available at process control laboratory, Department of Electronics and Instrumentation Engineering, KLN College of Engineering, Sivagangai, is shown in Fig. 1 and consists of two identical conical tanks interconnected with a manual valve (HV4). The objective is control of water level in tank 2, namely $h_2(t)$, at its nominal value by manipulating the inlet water flow, namely $q_1(t)$ to tank 1.
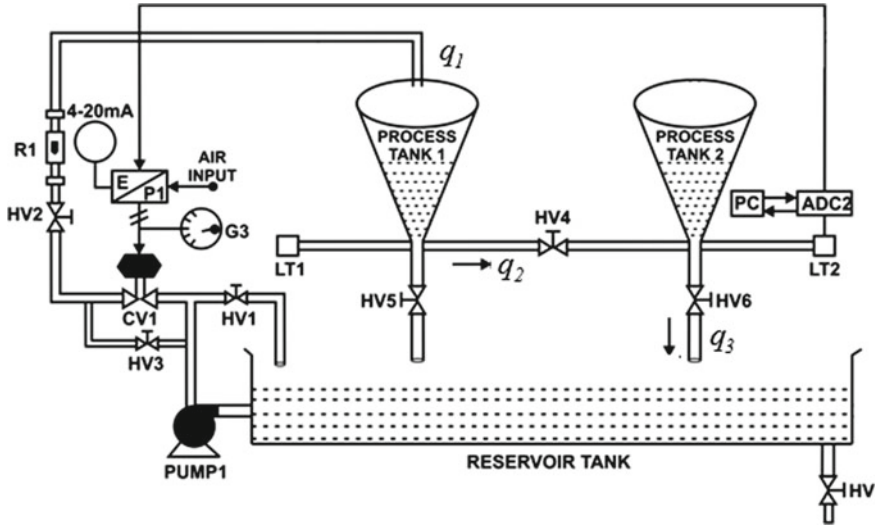
Fig. 1 P&I diagram of a ICTP

The mass balance equation around each tank is,

$$q_1 - q_2 = A_1 \frac{dh_1}{dt} = A(h_1)\frac{dh_1}{dt} = \pi r_1^2 \frac{dh_1}{dt} = \pi \left(\frac{R}{H}\right)^2 h_1^2 \frac{dh_1}{dt}$$

$$q_2 - q_3 = A_2 \frac{dh_2}{dt} = A(h_2)\frac{dh_2}{dt} = \pi r_2^2 \frac{dh_2}{dt} = \pi \left(\frac{R}{H}\right)^2 h_2^2 \frac{dh_2}{dt}$$

$$(1)$$

Also

$$q_2 = C_{12}\sqrt{h_1 - h_2}$$

$$q_3 = C_2\sqrt{h_2}$$

where
  q_1—Inflow rate to tank 1 in cm^3/s
  q_2—Outflow rate of tank 1 in cm^3/s
  q_3—Outflow rate of tank 2 in cm^3/s
  C_2—Discharge coefficient of drain valve of tank 2
  C_{12}—Discharge coefficient of drain valve between two tanks
  r_1—Radius at any height h_1 (in cm)
  r_2—Radius at any height h_2 (in cm).
  The mass balance equation around tank 1 is,

$$q_1 - C_{12}\sqrt{h_1 - h_2} = A(h_1)\frac{dh_1}{dt}$$

$$\overset{\bullet}{h}_1 = \frac{1}{A(h_1)}\left[q_1 - C_{12}\sqrt{h_1 - h_2}\right] \tag{2}$$

The mass balance equation around tank 2 is,

$$C_{12}\sqrt{h_1 - h_2} - C_2\sqrt{h_2} = A(h_2)\frac{dh_2}{dt}$$

$$\overset{\bullet}{h}_2 = \frac{1}{A(h_2)}\left[C_{12}\sqrt{h_1 - h_2} - C_2\sqrt{h_2}\right] \tag{3}$$

The linearized equations in 'S' domain are,

$$SH_1(S) = \frac{1}{A(h_1)}\left[Q_1(S) - \frac{C_{12}}{2\sqrt{h_{1s} - h_{2s}}}(H_1(S) - H_2(S))\right]$$

$$SH_2(S) = \frac{1}{A(h_2)}\left[\frac{C_{12}}{2\sqrt{h_{1s} - h_{2s}}}(H_1(S) - H_2(S)) - \frac{C_2}{2\sqrt{h_{2s}}}H_2(S)\right]$$

Let $\alpha_1 = \frac{C_{12}}{2\sqrt{h_{1s} - h_{2s}}}$ and $\alpha_2 = \frac{C_2}{2\sqrt{h_{2s}}}$
The state space representation is,

$$\begin{bmatrix} \dot{h}_1 \\ \dot{h}_2 \end{bmatrix} = \begin{bmatrix} -\frac{\alpha_1}{A(h_1)} & \frac{\alpha_1}{A(h_1)} \\ \frac{\alpha_1}{A(h_2)} & -\left(\frac{\alpha_1}{A(h_1)} + \frac{\alpha_2}{A(h_2)}\right) \end{bmatrix}\begin{bmatrix} h_1 \\ h_2 \end{bmatrix} + \begin{bmatrix} \frac{1}{A(h_1)} \\ 0 \end{bmatrix}q_1$$

$$[y] = \begin{bmatrix} 0 & 1 \end{bmatrix}\begin{bmatrix} h_1 \\ h_2 \end{bmatrix}$$

The plant transfer function relating level in tank 2 to inflow rate of tank 1 is,

$$G_p(s) = \frac{\frac{\alpha_1}{A(h_1)A(h_2)}}{S^2 + S\left(\frac{\alpha_1}{A(h_1)} + \frac{\alpha_1 + \alpha_2}{A(h_1)A(h_2)}\right) + \frac{\alpha_1\alpha_2}{A(h_1)A(h_2)}} = \frac{b_1}{S^2 + aS + b} \tag{4}$$

here, $b_1 = \frac{\alpha_1}{A(h_1)A(h_2)}$ $\qquad a = \frac{\alpha_1}{A(h_1)} + \frac{\alpha_1 + \alpha_2}{A(h_1)A(h_2)}$ $\qquad b = \frac{\alpha_1\alpha_2}{A(h_1)A(h_2)}$

3.1 Determination of Valve Discharge Coefficients

The valve discharge coefficients are determined experimentally for a certain inflow rate. The inflow rate to the tank 1 is set at 125 cm³/s, and liquid level of tank is allowed to reach steady-state value. A differential pressure transmitter is used to measure the variations of liquid level. The steady-state liquid level of tank 1 and tank

Table 2 Process parameters of the setup

Variable	Description	Value
R	Top radius of the tank	22.5 cm
H	Total height of the tank	60 cm
h_{1s}	Steady-state water level of tank 1	27.5 cm
h_{2s}	Steady-state water level of tank 2	6.5 cm
q_{1s}	Steady inflow to tank1	125 cm^3/s

2 is observed as 27.5 cm and 6.5 cm, respectively. At steady state, the inflow rate is equal to outflow rate. The process parameters used are given in Table 2. These experimental data are used to determine the valve discharge coefficient as described below.

Under steady-state condition, the mass balance equation becomes,

$$q_{1s} - q_{2s} = 0 \Rightarrow q_{1s} = C_{12}\sqrt{h_{1s} - h_{2s}}$$
$$\Rightarrow C_{12} = 27.3 \text{ cm}^2/\text{s}$$

$$q_{3s} = C_2\sqrt{h_{2s}}$$
$$\Rightarrow C_2 = 49 \text{ cm}^2/\text{s}$$

4   Design of Gain-Scheduled PI Controller

Gain scheduling is a powerful method used to control nonlinear process through set of local linear controllers and is designed to provide control over the entire operating range of the process variable. The controller parameter changes according to the value of a scheduling variable, which is a measurement that changes as the process operating point changes.

The closed-loop transfer function of the system with proportional plus integral controller is,

$$\frac{C(s)}{R(s)} = \frac{G_p(S)\left(K_p + \frac{K_i}{S}\right)}{1 + G_p(S)\left(K_p + \frac{K_i}{S}\right)} = \frac{\frac{b_1}{S^2+aS+b}\left(\frac{SK_p+K_i}{S}\right)}{1 + \frac{b_1}{S^2+aS+b}\left(\frac{SK_p+K_i}{S}\right)}$$

$$\frac{C(s)}{R(s)} = \frac{b_1\left(SK_p + K_i\right)}{S^3 + aS^2 + S\left(b + K_p b_1\right) + K_i b_1}$$

where
  K_P—Proportional gain
  K_i—Integral gain

a, b and b_1—Parameter-related process

The characteristic equation of the system under consideration is,

$$S^3 + aS^2 + S(b + K_p b_1) + K_i b_1 = 0 \tag{5}$$

The general third-order characteristic equation of the system is,

$$(S^2 + 2\zeta \omega_n S + \omega_n^2)(S + m) = 0 \tag{6}$$

It is desired to have overshoot of 5% and settling time of 200 s, which corresponds to $\zeta \omega_n = 0.02$.

And 'm' is chosen to be 10 times that of the real part of the dominant pole. Comparing Eqs. (5) and (6), we get,

$$b + K_p b_1 = 2\zeta \omega_n m + \omega_n^2$$

$$K_i b_1 = \omega_n^2 m$$

The scheduler is simplified to

$$K_{ph} = \frac{2\zeta \omega_n m + \omega_n^2 - b}{b_1} \approx \frac{\omega_n^2 - b}{b_1}$$
$$K_{ph} \approx \frac{\omega_n^2 A(h_1) A(h_2) - \alpha_1}{\alpha_1 \alpha_2} \tag{7}$$

$$K_{ih} = \frac{\omega_n^2 m}{b_1}$$
$$K_{ih} = \frac{m \omega_n^2 \times A(h_1) A(h_2)}{\alpha_1} \tag{8}$$

The control law is expressed as,

$$U(t) = K_{ph} e(t) + K_{ih} \int e(t)\, dt + u_0$$

Simulink diagram of gain-scheduled PI (GSPI) controller is shown in Fig. 2. Initial control input of 125 cm^3/s as bias is given to the plant. The PI controller gains at a steady-state operating level of 27.5 and 6.5 cm, respectively, are $K_p = 5\ and\ K_i = 0.01$.
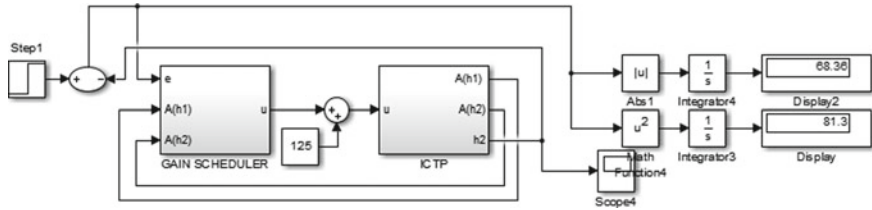
Fig. 2 Simulink diagram of gain-scheduled PI (GSPI) controller

5 Design of Fuzzy Gain-Scheduled PI Controller

In general, PI controllers are easy to design and suitable for any given linear system and gains must be updated on a regular basis to cope up with the change in process variable. In order to cope up the nonlinearities of the process, an efficient controller needs to be designed. In gain scheduling controller, an auxiliary variable that relates the process variable must be chosen properly. It is difficult to choose proper auxiliary variable for complex and nonlinear system. In many industrial processes, FLC is used to replace the human inference. A Sugeno fuzzy inference system is an efficient gain scheduler. Because each rule is linearly dependent on the input variables, the Sugeno method is ideal and acts as an interpolator of multiple local linear controllers that are combined to represent entire dynamic range of nonlinear system.

Design of FLC includes assigning membership function and framing rules based on a priori knowledge of the process. In order to develop FGSPI controller, linearized models for five different inflow rates are obtained using linear analysis of control tool box. The PI controller gains are tuned using auto tuner for each flow condition. The linear transfer function model thus obtained for each operating point and the controller gains are presented in Table 3. Based on the variation of level in tank 2 and controller gains, fuzzy rules are framed.

In TS-FLC design, the input variable is level whereas output crisp variables are PI controller gains. The linguistic variables assigned for level are, namely, very low (Vl), low (*l*), medium (*M*), high (*H*) and very high (VH). The level input range

Table 3 Process transfer function and controller parameters

Inflow rate (cm^3/s)	Process transfer function	Steady-state level of tank 1	Steady-state level of tank 2	K_p	K_i
75	$\frac{0.013}{S^2+1.14S+0.076}$	11.5	2.8	0.394	0.03
100	$\frac{0.001}{S^2+0.276S+0.0046}$	16.5	4	0.288	0.05
125	$\frac{0.138\times10^{-3}}{S^2+0.09S+0.0005}$	27.5	6.5	0.232	0.013
150	$\frac{0.18\times10^{-4}}{S^2+0.036S+0.0001}$	37	9	0.197	0.004
175	$\frac{0.67\times10^{-5}}{S^2+0.014S+5\times10^{-6}}$	45.5	11	0.171	0.002

is considered from 0 to 40 and output variable ranges from 0 to 1. The type of the membership function used is 'z' membership function for Vlow (VL), triangular membership function for low (l), medium (M), high (H) and 's' membership function for very high (VH) and the plot of membership function is shown in Fig. 3. The TS-FL outputs are proportional gain K_p and integral gain K_i and consist of five singleton membership functions, namely very small (VS), small (S), medium (M), high (H) and very large (VL).

The five rules that are framed for this level control application are as follows:

Rule 1: If level is Vhigh, then K_p is Vsmall and K_i is Vsmall
Rule 2: If level is high, then K_p is small and K_i is small
Rule 3: If level is M, then K_p is M and K_i is M
Rule 4: If level is low, then K_p is high and K_i is high
Rule 5: If level is Vlow, then K_p is Vhigh and K_i is Vhigh.

Simulink diagram of fuzzy gain-scheduled PI (FGSPI) controller is shown in Fig. 4.
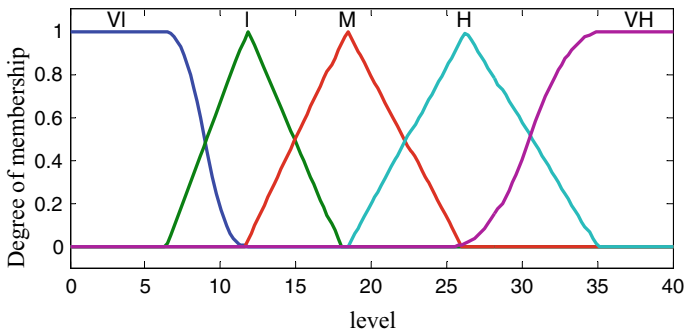
Fig. 3 Plot of membership function for level
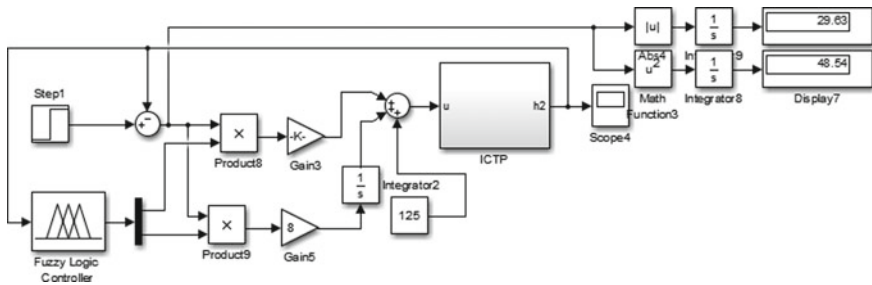
Fig. 4 Simulink diagram of fuzzy gain-scheduled PI (FGSPI) controller

6   Simulation Results

The effectiveness of the controllers proposed is examined by simulation using MATLAB. The response of each controller is shown in Fig. 5 for step change in level. It is evident that the PI controller exhibits offset and the response of GSPI controller is oscillatory.

The disturbance rejection capability is also examined and is shown in Fig. 6. It evident that FGSPI controller offers better servo and regulatory response than other two controllers.

The robustness analysis is made by increasing the valve discharge coefficient by 10% from its value of 29.5 and depicted in Fig. 7. It is evident that FGSPI is more robust than other controllers.

The variation of controller gains against level is shown in Fig. 8a and b, which shows the parameter convergence though there is change in operating point.
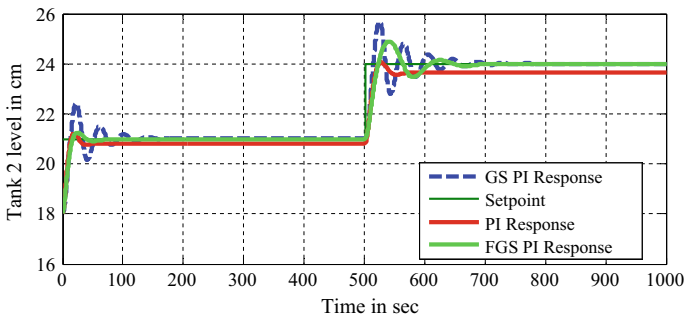
Fig. 5 Servo response of proposed controllers
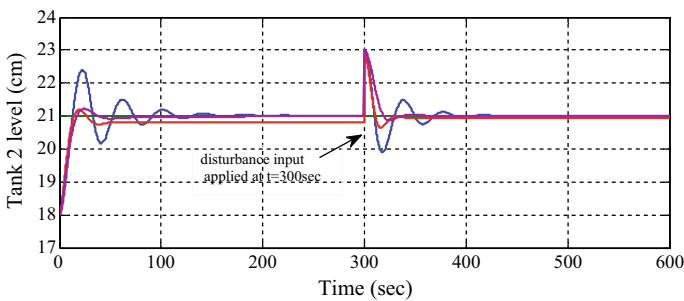
Fig.6 Servo and regulatory response of proposed controllers
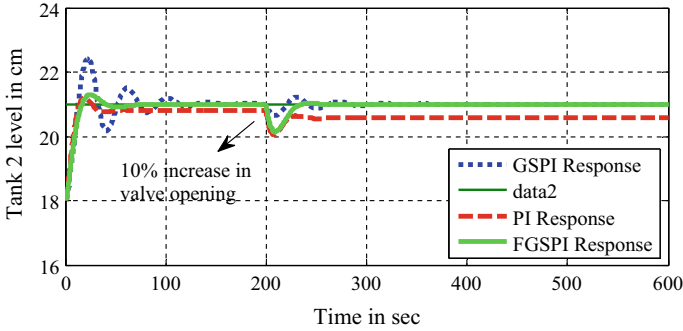
Fig.7 Robustness analysis of proposed controllers
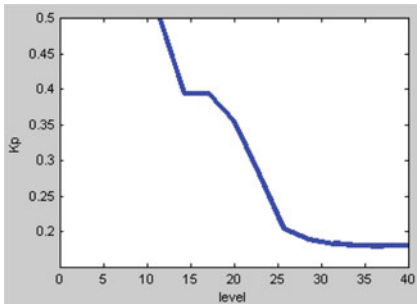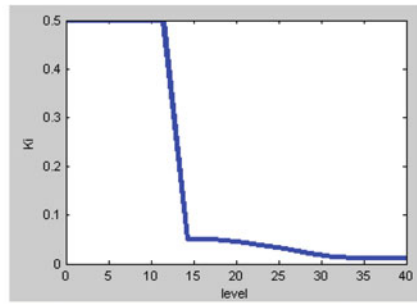
(a) Variation of Kp in FGSPI controller   (b) Variation of Ki in FGSPI Controller

Fig. 8 a Variation of K_p in FGSPI controller **b** variation of K_i in FGSPI controller

7   Conclusions

The efficacy of proposed control schemes, namely GSPI and FGSPI control algorithms, is demonstrated for a nonlinear interacting conical tank process and performance comparison is made with conventional PI controller. The time response shows that the value of settling time and overshoot are better for the FGSPI controller compared to other controllers. The response of FGSPI in region 2 (level change from 21 to 24 cm) is slightly oscillatory due to increase in nonlinearity near the top of the tank. The performance summary given in Table 4 specifies that the FGSPI controller offers less error indices, namely ISE and IAE value. It is evident that the proposed FGSPI control strategy is best suited for nonlinear tank process utilized in food processing, pharmaceutical, chemical and fertilizer industries. The future focus of the research will be adaptive fuzzy controller to meet the desired specifications.

Table 4 Time response specifications

Parameter	Conventional PI controller	Gain-scheduled PI controller	Fuzzy gain-scheduled PI controller
Settling time (in s)	58	85	46
% overshoot	1.75	6.7	1.02
ISE	60.25	81	48.54
IAE	124	68	29.63

References

1. Nagammai S, Latha S, Varatharajan M (2020) Soft computing based fuzzy integral sliding mode control: a real time investigation on a conical tank process. J Soft Comput 24(17):13135–13146
2. Zhao Z-Y, Tomizuka M, Isaka S (1993) Fuzzy gain Scheduling of PID controllers. IEEE transactions on Systems, Man and Cybernetics, pp 1392–1398
3. Yao L, Lin C-C (2007) 'Design of gain scheduled fuzzy PID controller world academy of science. Eng Technol 1:714–718
4. Madhubala TK, Boopathy M, Sarat Chandra Babu J, Radhakrishnan TK (2004) Development and tuning of fuzzy controller for a conical level system. In: Proceedings of international conference intelligent sensing and information processing, pp 450–455
5. Anandanatarajan R, Chidambaram M (2005) Experimental evaluation of a controller using variable transformation on a hemi-spherical tank level process. In: Proceedings of national conference NCPICD, pp 195–200
6. Nithya S, Sivakumaran N, Radhakrishnan TK, Anantharaman N (2010) Soft computing based controllers implementation for nonlinear process in real time. In: Proceedings of the world congress on engineering and computer science
7. Nagammai S, Swathi Lakshmi G, MahaLakshmi A (2016) Design of fuzzy gain scheduled PI controller for a nonlinear SISO process. GRD J. pp 470–478
8. Motamed A, Gogani MB, Pourgholi M (2015) Fuzzy gain scheduling of PID controller implemented on real time level control. In: 4th Iranian joint congress on fuzzy and intelligent systems
9. Hussein T, Shamekh A (2019) Design of PI fuzzy logic gain scheduling load frequency control in two-area power systems. Designs 3(2)
10. Cam E, Kocaarslan I (2005) A fuzzy gain scheduling PI controller application for an interconnected electrical power system. Electric Power Syst Res 73(3):267–274
11. Prasad GM, Rao AS (2019) Evaluation of gap-metric based multi-model control schemes for nonlinear systems: an experimental study. ISA Trans 94:246–254
12. Vavilala SK, Vinopraba T, Chandrasekaran K (2020) Level control of a conical tank using the fractional order controller. Comput Electr Eng 87
13. Urrea C, Felipe P (2021) Design and comparison of strategies for level control in a nonlinear tank. Processes 1–17

14. Gulzar MM, Munawar M, Dewan Z, Salman M, Iqbal S (2020) Level control of coupled conical
    tank system using adaptive model predictive controller. In: IEEE 17th International conference
    on smart communities: improving quality of life using ICT, IoT and AI, pp 236–240
15. Bhuvaneswarri E, Madhubala V, Savithri G, Girirajkumar SM (2019) Comparison of tuning
    methods of PID controllers of two conical tank system of interacting type. J Contr Instrument
    5(3):8–14

A Review of Direction of Arrival Estimation Techniques in Massive MIMO 5G Wireless Communication Systems

S. Aquino and G. Vairavel

Abstract Direction of arrival (DOA) estimation plays a critical function for beam forming in the massive multiple-input multiple-output (mMIMO) 5G wireless systems to increase the coverage, capacity and throughput. Accurate direction of arrival estimation of the received signals from large number of user equipment is a major issue in millimeter wave (mmWave) wireless systems due to multipath signal propagation with reflections. In this paper, we review the conventional and the state-of-the-art deep learning-based direction of arrival estimation techniques and compare with conventional techniques in the context of high resolution and accuracy.

Keywords Beamforming · Direction of arrival · Massive multiple input multiple output (mMIMO) · Millimeter wave (mmWave) · 5G

1   Introduction

The cellular network generation has evolved from 1 to 4G and the modern network has its beginnings with fifth generation (5G) [1]. The 5G aims to provide enhanced mobile broadband (eMBB) services such as high mobile data volume per area, higher user data rates of 10 Gbps and above, increase in spectral efficiency and downscale end-to-end latency of about 1 ms. The 5G services can also be broadened to ultra-reliable low-latency communications (URLLC) with high reliability, low latency and massive machine-type communications (mMTC) in cellular IOT technologies for home automation and machine monitoring systems with low data rates [2] and are shown in Fig. 1. Here, we focus on eMBB services which might expand the mobile ecosystem into a new domain which can enhance broadband access in densely

S. Aquino (✉) · G. Vairavel
Department of ECE, SRMIST, Kattankulathur, Chengalpattu 603203, India
e-mail: as5150@srmist.edu.in

G. Vairavel
e-mail: vairaveg@srmist.edu.in
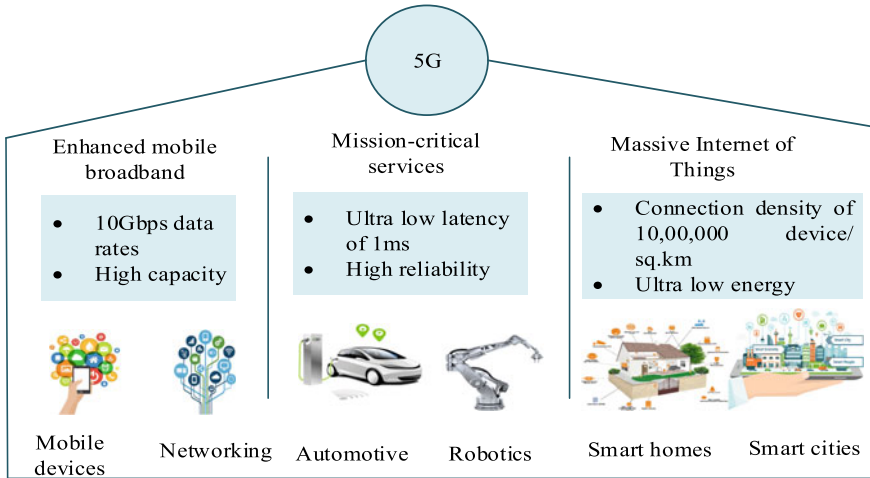
Fig. 1 5G scenario

populated areas and uplifts indoor and outdoor coverage in multistory buildings, crowded city centers, enhanced multimedia, etc.

The key enabling technology to achieve these objectives of eMBB is to deploy mmWave massive multiple-input multiple-output (mMIMO) technology [3]. The mmWave communication is the game changer for 5G which supports high data rates with the available large bandwidth for wireless systems. The multiple antenna transmission enhances the dense network coverage and also improves the spectral efficiency. The peak data rate supported by eMBB is above 10Gbps with spectral efficiency of 30 bps/Hz for downlink and 15 bps/Hz for uplink. The 5G spectrum operates in two bands named as sub-6 GHz (FR-1) and FR-2 bands which operate in mmWave spectrum [4]. The mmWave bestows a new chance for future mobile communications to use the spectrum at 28 GHz, 38 GHz and 70–80 GHz which lies at FR-2.

The mmWave signal processing is also converged with challenges such as critical ISI owing to multipath channels which bring about the successive symbols to overlap and interfere with each other. The spatial variations of omnidirectional antennas may influence tens or hundreds of nanoseconds of delay [5]. These challenges are overcome by using directional beam steering with large antenna arrays which are used to bring down the RMS delay spread experienced by the device. The physical layer (PHY) frame in a wireless communication system includes a preamble to aid beam forming with the help of DOA estimation and is shown in Fig. 2. The below figure represents the beamforming of signals from e-Node B to stream the video, VoIP and data streams to their corresponding user equipment. This beamforming is done precisely with the aid of the information given by the direction of arrival estimation to steer the signals in that particular direction of the user equipment [6]. The beamforming in massive MIMO permits the high-speed coverage to rural areas
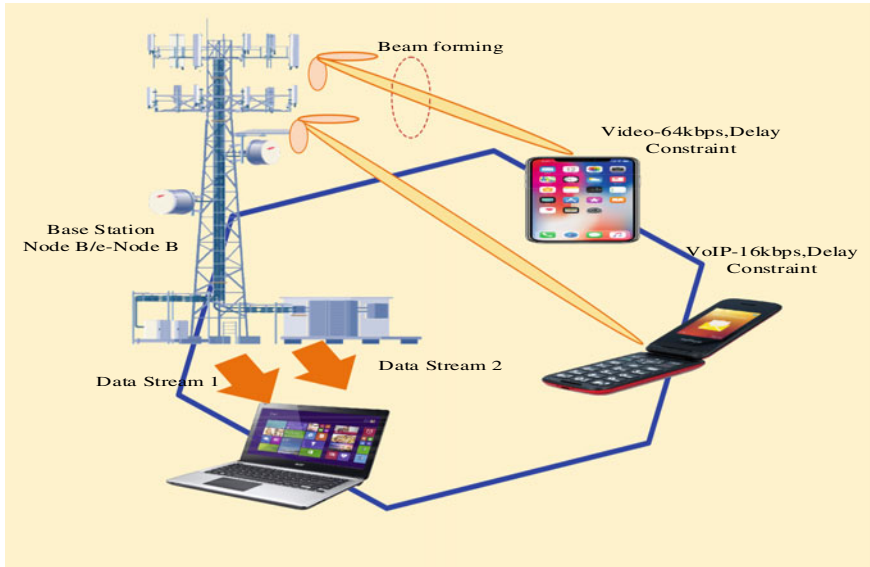
Fig. 2 mmWave mMIMO beamforming

as line of sight (LOS) performs well with millimeter wave frequencies. The different types of DOA estimation are organized as conventional DOA estimation, compressive sensing techniques and deep learning techniques.

1.1 Applications and Challenges

The direction of arrival (DOA) algorithms to determine the direction of an incoming wave are of paramount importance to steer the beam in beamforming algorithms for mmWave mMIMO applications [6]. However, the restricted form factor of wireless gadgets brings about a constraint on the large number of antennas, and in order to overcome this, the higher frequency region of electromagnetic spectrum millimeter wave spectrum is utilized. The mmWave spectrum allows more number of antennas to be integrated in any device due to its short wavelength [7]. The beamforming with DOA allows spectrally efficient communication in the required direction to a UE from a Next Generation Node Base (gNB) by focusing a signal in the required direction to improve the network service [8] and is shown in Fig. 3.

The DOA estimation is influenced by various parameters such as signal-to-noise ratio, snapshots, and antennas [9]. The SNR plays a vital role which directly alters the performance of the DOA estimation. The performance is evaluated by using root mean squared error (RMSE) which implies that as the signal SNR increases, the performance of DOA estimation is enhanced and is shown in Table 1.
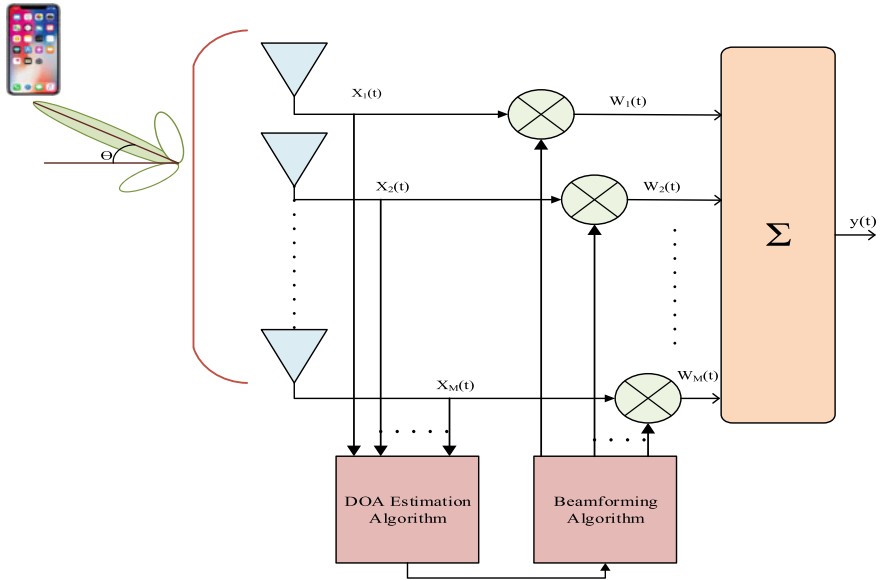
Fig. 3 DOA estimation for beamforming

Table 1 Impact of SNR on DOA estimation

References	SNR[dB]	RMSE (°)
[10]	− 10	0.02
	20	0.001
[11]	− 5	0.1
	20	0.08

The number of snapshots is defined as the number of samples taken for observation in the time domain. It is evident that from Table 2, if the number of snapshots increases from 100 to 200 in [12], the RMSE drops from 0.009 to 0.005. Thus, the DOA estimation enhances as the number of snapshots increases.

The number of antennas in the array affects the DOA estimation of the signal. Table 3 shows that as the number of antenna increases from 40 to 70, the RMSE

Table 2 Impact of snapshots on DOA estimation

References	Number of snapshots	RMSE (°)
[12]	100	0.009
	200	0.005
[13]	2	0.2
	100	0.05

Table 3 Impact of antennas on DOA estimation

References	Number of antennas	RMSE (°)
[13]	40	0.09
	70	0.02
[11]	30	0.01
	50	0.005

drops from 0.09 to 0.02 in [13]. Thus, it is relevant that the higher the number of antennas, the better the DOA estimation. The smart antenna integrates the antenna array and the sharp signal processing potential in order to transmit and receive in an adaptable way. They are useful in calculating the direction of arrival (DOA) and utilize this to estimate the beamforming vectors to recognize the beam.

1.2 Review Methodology

In this work, twenty most relevant papers related to the topic have been selected based on the challenges in massive MIMO and mmWave spectrum of cellular communication. The proposed Systematic Literature Review (SLR) [14–17] as shown in Fig. 4 focuses to research how DOA estimation can be implemented to give 100% accuracy to perform a flawless beamforming based on the DOA estimate done by various techniques from the literature (conventional techniques) to the state of the art (deep learning). The study is identified into groups such as DOA estimation, 5G and mMIMO at mmWave spectrum for inclusion criteria, and the search platform used is Google Scholar. This portal has an extensive literature making it simple to search for planning phase of SLR. Given the large number of papers nearly 2624, the duplicated papers and the papers that are insignificant such as radar, microphones and UAV were deleted with a total of 2604; the remaining 20 appropriate papers related to DOA estimation were chosen for the conducting phase of SLR. The appropriate papers are numerically analyzed according to the performances in contemplation of answering the formulated research questions for reporting phase of SLR. The proposed SLR is carried out based on the key aspects of research questions such as:

- What are the different techniques of DOA estimation in cellular communication?
- What are the factors that affect DOA estimation?
- Which technique improves the evaluation criteria of DOA estimation?

1.3 Organization

Figure 5 provides an overview of the content of this paper. The applications and challenges of mMIMO DOA estimation in cellular communications are defined in Sect. 1

| • | The research questions for DOA estimation were formulated. | • | Selection of papers related to search strings in DOA estimation. |
| • | Define the review scope and search strings such as mMIMO, DOA and 5G | • | Screen for inclusion criteria among the selected papers in DOA estimation |

Planning   Conducting

| • | Evaluate and synthesize the numerical results of DOA estimation |
| • | Final report of systematic literature review |

Reporting

Fig. 4 Systematic literature review

which serve as motivation for this paper. Section 2 describes the basic knowledge required for DOA estimation which comprises of the antenna array structures and the signal model. Sections 3, 4 and 5 discuss the different types of DOA estimation techniques from the literature till the current state-of-the-art techniques. Section 6 outlines the open issues and future directions for performing an accurate DOA estimation. Finally, we conclude this paper in Sect. 7.

2 DOA Signal Model

The system consists of N receivers and K single transmitter UEs such that $N > K$ with L number of multipaths, and the antenna array considered here is Uniform Linear Array (ULA) with distance d between each receiver. The baseband transmitted signal y at the kth element can be represented as,

$$y_k[n] = \sum_{l=0}^{L-1} s_l[n]a[\theta_l]$$
$$x_n = y_n + n_n x_n = \big[a(\theta_0)a(\theta_1)\ldots a(\theta_{L-1})\big]s_n + n_n \tag{1}$$

where $a(\theta)$ is the response vector or array steering vector, x, is the received complex signal from the UE and n is the Gaussian noise [18]. Hence, the signal vector from k user equipment brings about the matrix–vector product of channel matrix and the signal vector, which is shown in the below equation,

$$x_n = As_n + n_n$$
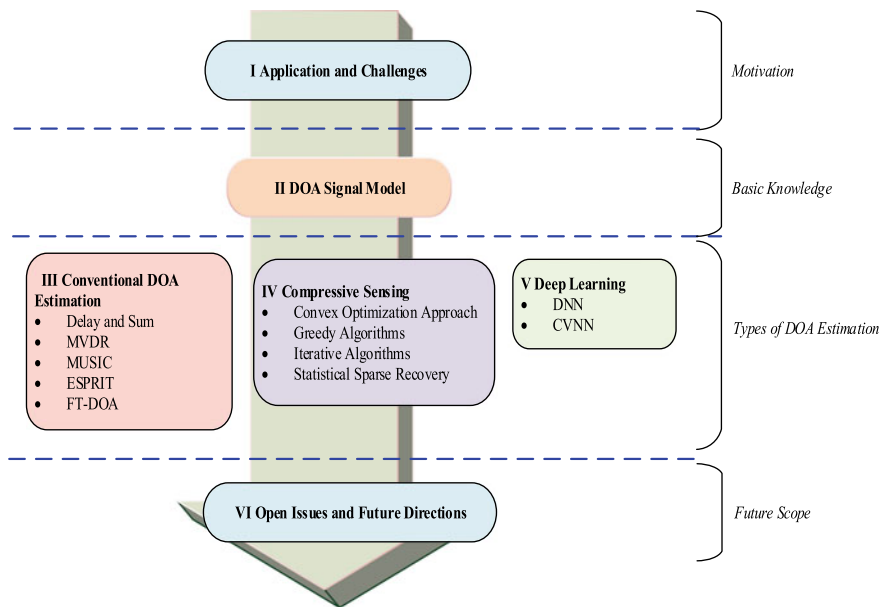
Fig. 5 Organization of this paper

$$\therefore A = [a(\theta_0)a(\theta_1)\ldots a(L-1)] \tag{2}$$

Many adaptive beamforming techniques require correlation matrix of X_n and the correlation matrix used as input for DOA estimation from conventional methods to state-of-the-art deep learning techniques is expressed as,

$$
\begin{aligned}
R = E\big[x_n x_n^H\big] &= E\big[(As_n + n_n)(As_n + n_n)^H\big] \\
&= AE\big[s_n s_n^H\big]A^H + E\big[n_n n_n^H\big] \\
&= AR_{ss}A^H + \sigma^2 I_{M \times M}
\end{aligned}
\tag{3}
$$

3 Conventional DOA Estimation

DOA estimation techniques are divided into two types: spectral estimation techniques (beam scan) and subspace techniques. Some of the beamscan techniques are delay and sum method and MVDR. The subspace techniques comprise of MUSIC and ESPRIT-based DOA estimation techniques.

3.1 Delay and Sum Method

The direction of arrival is estimated by computing the received signal strength and the occurrences of peak powers are selected as the arrival angles [8]. Thus, the highest power represents the estimated angle of arrival. The mean output power in this method is given as:

$$
\begin{aligned}
P_{DS}(\theta_0) &= E\left[\left|w^H x(n)\right|^2\right] \\
&= \left(\left|w^H a(\theta_0)\right|^2 (\sigma_s^2 + \sigma_n^2)\right)
\end{aligned}
\tag{4}
$$

where w represents the weight vectors, $n(n)$ is the noise vector, $\sigma_s{}^2$ and $\sigma_n{}^2$ are the corresponding signal and noise power. The performance analysis is done by calculating the Mean Squared Error (MSE) with respect to the low and medium SNR which ranges from -20 to 5 dB. In low SNR regime, the MSE evaluated is 6.66×10^{-6} degrees, and in high SNR regime, the MSE obtained is 4.72×10^{-12} [18].

3.2 Minimum Variance Distortion Less Response (MVDR) Method

In MVDR, the filter weights are adaptively calculated based on the environment so as to put out the unwanted signal, leaving the signal of interest undistorted [19]. The beamformer gain is kept high in the required direction such that the power contribution of signals arriving from all other directions is minimized [20]. This constrained minimization problem is used for optimization, and the idea is that for each possible angle, the power in the cost function must be minimized w.r.t. "w" the filter weights subject to a single constraint. Thus, the received output power of MVDR is the inverse of correlation matrix multiplied with the array responses of the steering vector. The extra computation done here is the inverse matrix calculation in which some performance degradation occurs due to correlation between the required signal and interferences. The MSE obtained at low SNR is 12.63×10^{-6} degrees and at high SNR is 9.52×10^{-9} degrees for a single source and 256 antenna elements. Thus, the performance of MVDR [18] is better when compared to DS method of DOA estimation.

3.3 Multiple Signal Classifier (MUSIC)

The array response or steering vector which corresponds to the incoming signal forms the signal subspace, and in order to cancel out the noise vector, the signal subspace should be orthogonal to the noise subspace [21–23]. The orthogonality property is

satisfied by $a(\theta)^H \; Q_n = 0$, where Q_n is the noise projection vectors. Hence, the pseudo-spectrum provided by the MUSIC is given by

$$P_{\text{MUSIC}}(\theta) = \frac{1}{a^H(\theta)Q_n Q_n^H a(\theta)} \tag{5}$$

The MSE of MUSIC in high SNR regime is 0.75×10^{-12} degrees and low SNR regime is 6.51×10^{-6} degrees. Thus, the performance of MUSIC outperforms in high SNR regime than the low SNR regime [18].

A variant of MUSIC called Root MUSIC method has been proposed by Barabell [24] to improve the performance, and it represents the DOA estimation by search of zeros of a polynomial, which reciprocates the maxima search in MUSIC method. Thus, the basic principle is to form a polynomial $G(z)$ and extract the roots at lth pole of $G(z)$ at z_l. Then, by solving the roots of the polynomial close to the unit circle and then the angles are determined by using the below equation,

$$\theta_l = \arcsin\left(\frac{\lambda.\arg(z_l)}{2\pi d}\right) \tag{6}$$

The MSE performance of R-MUSIC at low SNR of -20 db is 6.63×10^{-6} degrees and at high SNR of 5 dB is 16×10^{-9} degrees. Thus, it is observed that in high SNR regime the mean squared error decreases [18].

3.4 Estimation of Signal Parameters via Rotational Invariance (ESPRIT)

This refers to parameter estimation technique, where the signal of one element has a constant phase shift from the previous element of the steering vector [25]. The parameters of the signal are acquired as eigenvalues of nonlinear function that maps from a set of vectors E_1 into another set of vectors E_2. The eigen decomposition is done for the two subarrays which estimate the basis for the signal subspace, and finally, the DOA is estimated by evaluating eigenvalues of ϕ and is written as,

$$\theta_l = \arcsin\left(\frac{\lambda.\arg(\phi_l)}{2\pi \Delta}\right) \tag{7}$$

The MSE figure of merit obtained at low SNR is 2180×10^{-6} degrees and at high SNR is 878×10^{-9} degrees. The computational complexity is significantly greater than that of MUSIC, since we perform two eigen decompositions of the autocorrelation matrix [18].

Unitary ESPRIT is a modified version of ESPRIT [26], and the accuracy of DOA estimation from the standard ESPRIT is achieved by replacing the measurement

matrix and the structure of the total least squares (TLS) problem. Then, the eigen value decomposition is performed in which all the eigenvalues are real valued and the direction of arrival is estimated from,

$$\mu_k = 2 \arctan \omega_k \qquad (8)$$

where ω represents the eigen values which result from decomposition. The MSE obtained at low SNR is 1234×10^{-6} degrees and at high SNR is 899×10^{-9} degrees. Thus, the high resolution is achieved in MUSIC and ESPRIT, while the complexities are much higher in MUSIC and Unitary ESPRIT [18].

3.5 FT-DOA

The spectrum analysis of the k signals impinging on an antenna array is analyzed by using Fourier transform (FT) for the estimation of DOA of uncorrelated sources [27]. Thus, the spatial spectrum of the sampled data can be obtained and the precision of spectrum can be improved by padding zeros to $X(i)$ and further averaging can be done with the sampled data. Hence, the lth angle can be written as,

$$\theta_l = \arcsin\left(\frac{\lambda.u_l}{d}\right) \qquad (9)$$

where l is the serial number of the sample point u. Thus, the Mean Squared Error (MSE) in low SNR is 278.35×10^{-6} and at high SNR is 55.6×10^{-6} and the complexity is much smaller than the other estimation techniques [18].

3.6 Performance Analysis

In terms of MSE, the more accurate estimates are obtained with MUSIC, DS and MVDR. The mean squared error (MSE) is evaluated at high SNR regime of 5 dB with an antenna array of 256 antennas with one source and is shown in Table 4. The MUSIC technique comes up with accurate DOA estimation at high SNR regime, but at the cost of high computational intricacy. The ESPRIT comes up with reduced amount of computation time, which also provides accurate DOA estimation [18].

Thus, the above conventional algorithms obtain the source signals at the Nyquist rate, and hence, higher number of samples are obtained for DOA estimation. Hence, the computational complexity in subspace methods is high due to eigenvalue decomposition when large-scale antenna arrays are used. Instead in the case of large-scale antenna array, the property of sparsity of signal vector can be used to find the DOA estimate of the required signal [28–33]. This compressive sensing can be utilized to determine the DOA estimates in which a sparse number of samples are used for DOA

Table 4 Numerical analysis in terms of MSE

DOA estimation	MSE (°)
MUSIC	0.75×10^{-12}
DS	472×10^{-12}
MVDR	9.52×10^{-9}
R-MUSIC	16×10^{-9}
ESPRIT	878×10^{-9}
U-ESPRIT	899×10^{-9}
FT-DOA	55.6×10^{-6}

estimation where sparse refers that the signals are interpreted using a relatively few nonzero coefficients.

4 Compressive Sensing for DOA Estimation

The compressive sensing techniques estimate the DOA by reconstructing sparse signals from linear measurements. The received signal at the kth sampling time from a D uncorrelated narrowband sources on a massive array can be modeled as [34]:

$$x(t) = \sum_{d=1}^{D} a(\theta_d)s_d(t) + n(t) = A(\theta)s(t) + n(t) \qquad (10)$$

The compressive sensing matrix can be written as $\phi = [\phi_1^T, \phi_2^T, \ldots, \phi_M^T]^T \in C^{M \times N}$ ($M \ll N$) and it consists of M row sensing kernels which are orthonormal. When the compressive matrix ϕ is applied to the antenna array, the received signal vector $x(t)$ can be compressed and can be shown as,

$$y(t) = \phi x(t) = \phi A(\theta)s(t) + \phi n(t) \qquad (11)$$

The major approaches in the compressive sensing-based wireless communication are the grouping of the wireless communication problem into a suitable sparse recovery algorithm. They are grouped as l_1—norm minimization (convex optimization approach), iterative algorithm, greedy techniques, and statistical sparse recovery technique [34].

4.1 Convex Optimization Approach (l_1—Norm Minimization)

The main intention is to realize a sparse vector s such that As is certainly or nearly equal to y and this is mentioned as sparse regression. Thus, the most possible way

of recovering sparse vectors is given as,

$$\hat{s}_0 = \arg\min\|s\|_0 \, s.t. \, y = As \tag{12}$$

The main difficulty of this problem is that the objective function $\|s\|_0$ is non-convex, and hence, the researchers have delved into the prospect of l_1—norm minimization. The l_1—minimization is represented as

$$\hat{s}_1 = \arg\min\|s\|_1 \, s.t. \, y = As \tag{13}$$

In Basis Pursuit Denoising (BPDN), case y is measured with noise and is given as $y = Ax + n$ with noise power bounded to ϵ; l_1—minimization problem with the idea of regularization can perhaps be introduced for this type of sparse regression and can be written as

$$\hat{s} = \arg\min_{s}\|y - As\|_2 + \lambda\|s\|_1 \tag{14}$$

where $\lambda > 0$ is an adjustable variable and the main drawback of the approach is that regularization parameter has to be selected appropriately based on the noise [34]. It is inferred that the BPDN [13] outperforms the subspace estimation techniques in the large-scale antenna arrays, but the computational complexity of BPDN is more or less similar to that of subspace methods.

4.2 Greedy Algorithm

The l_1—norm minimization is very successful in regeneration of the desired signal; still, there exists some trade-off as the computation complexity is high. Hence, the greedy algorithms come up with an alternative solution for major engineering applications like wireless communications. The main principle behind greedy algorithm is to determine the basis matrix initially and then find the best estimate of the vector s, by trying to minimize the least squares norm. The iteration goes on until the residues stop decreasing in further iterations and is less than the stopping criteria $\in$ [13].

Some of the greedy algorithms for DOA estimation are Simultaneous Orthogonal Matching Pursuit (SOMP) [11] and Gradient Orthogonal Matching Pursuit (GOMP) [10]. The set of DOAs is obtained by plotting the angle spectrum and the peaks from the plot correspond to their respective DOAs and it implies that increase in number of antennas and at high SNR regime, the performance increases with decrease in MSE.

4.3 Iterative Algorithm

In iterative algorithm, the constraint insures that the estimate $\hat{s}$ is K-sparse such that the objective restricts it to be consistent with the measurement matrix y to solve the optimization problem [34]:

$$\hat{s} = \arg\min_{\tilde{s}} \|A\tilde{s} - x\|_2^2 s.t. \|\tilde{s}\|_0 \leq K \tag{15}$$

Each iteration consists of two steps which comprise of a hard thresholding and gradient descent steps. Here, $\hat{s}^{(i)}$ is the estimate of signal s at ith iteration and $T(.)$ is the thresholding operator. Few algorithms which belong to this category are Iterative Hard Thresholding (IHT) [13] and fast iterative shrinkage-thresholding algorithm (FISTA) [11]. The RMSE of BPDN is the smallest in the case of large antenna arrays with small number of snapshots and the performance of BPDN and IHT [13] increases with increasing number of antenna elements. Thus, the performance of IHT is suitable for massive MIMO systems.

4.4 Statistical Sparse Recovery

The Bayesian frame of reference is utilized for statistical sparse recovery which approaches the signal vector in a probabilistic manner. In Maximum-a-Posteriori (MAP) procedure, the estimate s is given as [34]:

$$\hat{s} = \arg\max_{s} \ln f(s|y) = \arg\max_{s} \ln f(y|s) + \ln f(s) \tag{16}$$

where $f(s)$ is the prior distribution of s and it is modeled such that the $f(s)$ reduces with magnitude of s. Some of the examples of prior distribution are the Gaussian prior model which leads to regularized least squares problem and the Laplacian prior model which leads to BPDN. Bayesian Compressed Sensing (BCS) and Sparse Bayesian Learning (SBL) belong to Gaussian prior model which is modeled as Gaussian with the variance parametrized by a hyper-parameter and y can be estimated from data by using expectation maximization (EM) algorithm or maximum likelihood estimation.

4.5 Performance Analysis

The performance of BPDN, OMP and SBL is analyzed by varying the sparsity level k and the SNR regime. At high SNR regime, the OMP algorithm outperforms the BPDN and SBL. When the variance of noise is at midlevel, i.e., at mid-SNR regime,

Table 5 Performance comparison of CS techniques at varying noise levels

DOA estimation	MSE (°)		
	$\sigma = 0.001$	$\sigma = 0.01$	$\sigma = 0.1$
BPDN	0.008	0.01	0.02
OMP	0.0008	0.01	0.15
SBL	0.0009	0.02	0.15

the performance of all the above-mentioned algorithms is more or less similar and is shown in Table 5.

At low SNR region, the BPDN performs significantly better [34] with mMIMO of 256 antennas and the sparsity levels of 15. Thus, the compressive sensing techniques need an accurate evaluation of the sparsity to adapt to different wireless environments. Even though the higher variance of noise levels gives better results, at times it also brings about spurious or false peaks such that the strongest peaks are split into two peaks and represent errors in the estimation [12, 35–37]. Hence, we go for deep learning which is a part of machine learning techniques to improve the accuracy at low SNR regime and reduce the computational cost.

5   Deep Learning

The network architectures mainly used in DOA estimation are Convolutional Neural Networks (CNN) and Deep Neural Networks (DNN). The CNN uses fully connected layers accompanying with convolution layers, whereas the DNN is formed by piling up of fully connected layers of neuron and is shown in Fig. 6.
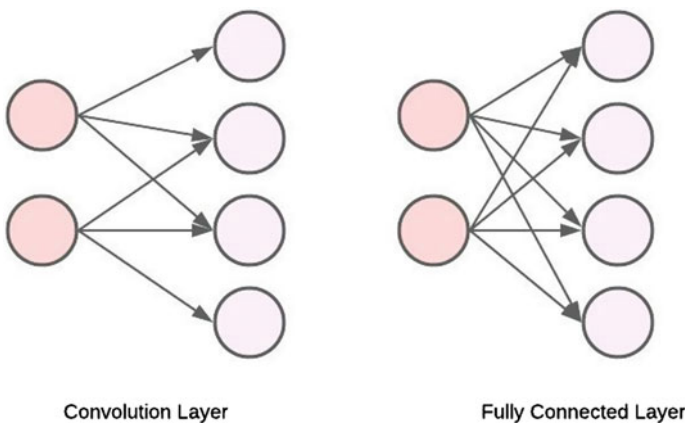
Fig. 6 Connections in convolution layer and fully connected layer

5.1 Deep Neural Network (DNN)

The DNN comprises of an input layer, output layer, and few hidden layers between them depending on the application. The DNN predicts the output of DOA estimate which deviates from the true value and this deviation is resolved by using the loss function based on classification or regression. The activation functions mainly used are hyperbolic tangent function, Rectified Linear Unit (ReLU), and sigmoid function. The objective of training a DNN is to minimize the loss function by changing the weights and biases. Three hyperparameters to be chosen for training are learning rate, batch size, and epoch which minimize the loss function [38].

In Hongji Huang et al. [39], a DNN schematic is integrated into mMIMO systems through mapping and training by using fully connected dense layers with either linear or nonlinear activation function for multilayers in the network. This framework consists of input layer, hidden layer, dropout layer, noise layer, and output layer [40]. The input layer consists of training sequence and the hidden layers are depicted to learn the features of output of the input layer. In order to avoid over-fitting, the dropout layer is employed, and then, the noise layer is designed to process the signal falsified with AWGN. The last hidden layer acts as the decoder followed by the layer which is processed by the sigmoid function. Thus, the MSE of DOA estimation becomes stable enough when the number of bits in the input layer increases and the large learning rate also makes the curve steeper than the other conventional techniques.

Ismayil Siyad et al. [41] use a DNN schematic and train the network until the accuracy becomes 100. The optimal performance is done by using different optimizers such as SGD and RMS prop optimizer. The performances are also analyzed with different learning rates and batch size. Thus, the DNN model has the potential to impart high resolution and is better than conventional subspace and sparsity techniques as they are free from complex matrix calculations [42–46]. This DNN model gives accurate resolution in general assumptions such as random SNR, random signal number, and small angular distances. Thus, the smaller the number of signal sources and the greater the number of antennas, the DOA estimate obtained is of high resolution, which is required in the massive MIMO systems in 5G.

In Yashuai Cao et al. [47], the Complex Valued Neural Network (CVNN) is proposed to perform complex arithmetic in DNN. This model can be applied to random antenna size without modifying the network for changes in antenna size. The architecture consists of affine layer, convolution layer and pooling layer. The affine layer performs the complex valued arithmetic operations, and one-dimensional filters are applied to convolution layer for feature analysis and max pooling layers are applied to the real and imaginary parts [9, 48–51]. The activation function used here is $C \tan h(c)$ as it is bounded in the complex domain and the backpropagation is performed for optimization.

5.2 Performance Analysis

The performance analysis is done for different deep learning models such as DNN and CVNN which comprises of fully connected layers in DNN. The DNN provides approximation of a function during training phase and hence produces accurate outputs by not occupying too much space in computation time rather than using conventional DOA estimation techniques. The main challenge relies on selecting a good architecture of deep learning and training data which is of good quality. Thus, the overall summary of the DOA techniques is given in Table 6 which states that the MSE decreases at high SNR regime subject to large number of antenna arrays in conventional techniques and it directly states that the deep learning techniques DNN has the potential to sort out the angles at low signal-to-noise ratio and decrease estimation error.

6 Open Issues and Future Directions

Despite the discussions mentioned above, the research gap can further be implicated on future research as:

- Small cells which operate on the licensed and unlicensed spectrum are an intrinsic element of 5G. It can be scrutinized, how this evolution process affects the direction of arrival estimation.
- The optimal selection of antenna arrays also needs to be examined to estimate the angles with accurate precision and to reduce the computational load.
- Mobility management can also be realized in the case of handover which requires accurate localization information [16].
- The convolutional neural network (CNN) can be analyzed for DOA estimation with more number of antennas in the array [52].
- The signals at low SNR region can estimated with the help of stacked auto encoders or restricted Boltzmann machines [53–56].

7 Conclusion

Numerous techniques and methods are present to estimate the DOA, but there is a trade-off between the computation time and resolution. The two conventional methods, namely MUSIC and ESPRIT, provide high resolution which requires high complex mathematical computations, especially at high SNR. The compressive sensing techniques also provide high resolution at high SNR and also provide spurious peaks or false peaks at low SNR regime. However, the deep learning which is a subset of machine learning learns the transform among the received signal and the channel by replacing the heavy computations by training the neural network,

Table 6 Overall summary of DOA techniques

DOA estimation technique	SNR(dB)		Number of antennas	MSE (°)
	Low regime	High regime		
MUSIC [18]		5	256	0.75×10^{-12}
DS [18]		5	256	472×10^{-12}
MVDR [18]		5	256	9.52×10^{-9}
R-MUSIC [18]		5	256	16×10^{-9}
ESPRIT [18]		5	256	878×10^{-9}
U-ESPRIT [18]		5	256	899×10^{-9}
FT-DOA [18]		5	256	55.6×10^{-6}
MUSIC [18]	-20		256	6.51×10^{-6}
DS [18]	-20		256	6.66×10^{-6}
ESPRIT [18]	-20		256	2180×10^{-6}
FT-DOA [18]	-20		256	278.35×10^{-6}
MVDR [18]	-20		256	12.63×10^{-6}
R-MUSIC [18]	-20		256	6.63×10^{-6}
U-ESPRIT [18]	-20		256	1234×10^{-6}
BPDN [13]		10	64	0.06
GOMP [10]		20	64	0.001
GOMP [10]	-10		64	0.02
SOMP [11]		20	50	0.08
SOMP [11]]	-5		50	0.1
IHT [13]		10	64	0.009
FISTA [11]		20	50	0.5
FISTA [11]	-5		50	2
OGSBI [11]		20	50	0.07
OGSBI [11]	-5		50	0.5
CS-MVDR [12]		20	50	0.009
CS-MVDR [12]	-20		50	10
DNN [41]		25	128	0.002
DNN [41]	0		128	0.004
CVNN [47]		10	257	0.04
CVNN [47]	-10		257	0.4
DNN [39]		25	128	0.001
DNN [39]	0		128	0.004

making it a feasible solution. In low SNR regime, the resolution can be improved by using different deep learning models, and thus, the deep learning will spare the usage of matrix inversions and decompositions which also potentially deliver a high resolution for mmWave mMIMO systems in 5G.

References

1. Chataut R, Akl R (2004) Massive MIMO systems for 5G and beyond networks—overview, recent trends, challenges, and future research direction. Sensors 2020(20):2753.https://doi.org/10.3390/s20102753Godara, L.C.: Smart Antennas, 1 edn. CRC Press, Boca Raton-FL
2. Delson TR, Jose I (2019) A survey on 5G standards, specifications and massive MIMO testbed including transceiver design models using QAM modulation schemes. In: 2019 International conference on data science and communication (IconDSC), 2019, pp 1–7. https://doi.org/10.1109/IconDSC.2019.8816942
3. Buzzi S, D'Andrea C (2017) Massive MIMO 5G cellular networks: mm-wave vs.\mu-wave frequencies. arXiv preprint arXiv:1702.07187
4. Busari SA, Mumtaz S, Al-Rubaye S, Rodriguez J (2018) 5G millimeter-wave mobile broadband: performance and challenges. IEEE Commun Mag 56(6):137–143.https://doi.org/10.1109/MCOM.2018.1700878
5. Lee J, Han M, Rim M, Kang CG (2021) 5G K-SimSys for open/modular/flexible system-level simulation: overview and its application to evaluation of 5G massive MIMO. IEEE Access 9:94017–94032. https://doi.org/10.1109/ACCESS.2021.3093460
6. Moerman A et al (2022) Beyond 5G without obstacles: mmWave-over-fiber distributed antenna systems. IEEE Commun Mag 60(1):27–33. https://doi.org/10.1109/MCOM.001.2100550
7. Nalband AH, Sarvagya M, Ahmed MR (2020) Power saving and optimal hybrid precoding in millimeter wave massive MIMO systems for 5G. Telkomnika 18(6):2842–2851
8. Godara LC (1997) Application of antenna arrays to mobile communications, part II: beamforming and direction-of-arrival considerations. Proc IEEE 85(8):1195–1245
9. Ge S, Li K, Rum SNBM (2021) Deep learning approach in DOA estimation: a systematic literature review. Mobile Inf Syst 2021:14. Article ID 6392875. https://doi.org/10.1155/2021/6392875
10. Ardah K, Haardt M (2021) Compressed sensing constant modulus constrained projection matrix design and high-resolution DoA estimation methods. arXiv preprint arXiv:2110.03385
11. Liu L, Zhang X, Chen P (2019) Compressed sensing-based DOA estimation with antenna phase errors. Electronics 8(3):294
12. Gu Y, Zhang YD (2019) Compressive sampling optimization for user signal parameter estimation in massive MIMO systems. Digit Signal Process 94:105–113
13. Stoeckle C, Munir J, Mezghani A, Nossek JA (2015) DoA estimation performance and computational complexity of subspace- and compressed sensing-based methods. In: WSA 2015; 19th international ITG workshop on smart antennas, 2015, pp 1–6
14. Kitchenham B, Charters S (2007) Guidelines for performing systematic literature reviews in software engineering version 2.3. Engineering 45:1051
15. Wang F, Bialkowski M (2011) Beam selection and antenna selection: a hybrid transmission scheme over MIMO systems operating with vary antenna arrays. Int J Commun Netw Syst Sci 4(10):638–647. https://doi.org/10.4236/ijcns.2011.410078
16. Callebaut G, Gunnarsson S, Guevara AP, Johansson AJ, Van der Perre L, Tufvesson F (2021) Experimental exploration of unlicensed Sub-GHz massive MIMO for massive Internet-of-Things. https://doi.org/10.48550/arXiv.2105.12402
17. Ai B et al (2014) Challenges toward wireless communications for high-speed railway. IEEE Trans Intell Transp Syst 15(5):2143–2158. https://doi.org/10.1109/TITS.2014.2310771

18. Gentilho E, Scalassara PR, Abrão T (2020) Direction-of-arrival estimation methods: a performance-complexity trade-off perspective. J Sig Process Syst 92(2):239–256
19. Vaidhyanathan C, Buckley KM (1995) Performance analysis of MVDR spatial spectrum estimator, IEEE Trans Sig Process
20. Trench WF (1989) Numerical Solution of the eigenvalue problem for hermitian toeplitz matrices. SIAM J Matrix Analy Appl 10(2):135–146
21. Schmidt RO (1986) Multiple emitter location and signal parameter estimation. IEEE Trans Antennas Propag 34(3):276–280
22. Hunger R (2007) Floating point operations in matrix-vector calculus. Technical report, Munich
23. Cybenko G (1980) The numerical stability of the Levinson-Durbin algorithm for Toeplitz systems of equations. SIAM J Sci Comput 1(3):303–331
24. Barabell AJ (1983) Improving the resolution performance of eigenstructure-based direction-finding algorithms. In: ICASSP '83 IEEE international conference on acoustics, speech, and signal processing 8:8–11
25. Roy R, Kailath T (1989) ESPRIT—estimation of signal parameters via rotational invariance techniques. IEEE Trans Acoust Speech Signal Process 37(7):984–995
26. Haardt M, Nossek JA (1995) Unitary ESPRIT: How to obtain increased estimation accuracy with a reduced computational burden. IEEE Trans Signal Process 43(5):1232–1242
27. Zhang K, Ma P, Zhang JY (2011) DOA estimation algorithm based on FFT in switch antenna array. In: Proceedings of 2011 IEEE CIE international conference on radar 2(4):1425–1428
28. Haykin S (1996) Adaptive filter theory, 3rd edn. Prentice Hall, New York, NY
29. Meng H, Zheng Z, Yang Y, Liu K, Ge Y (2016) A low-complexity 2-D DOA estimation algorithm for massive MIMO systems. In: 2016 IEEE/CIC international conference on communications in China (ICCC), Chengdu, IEEE, pp 1–5
30. Haardt M (1997) Efficient One-, Two-, and multidimensional high-resolution array signal processing, 1st edn. Shaker Verlag, Munich
31. Haardt M, Pesavento M, Roemer F, Nabil El Korso M (2014) Subspace methods and exploitation of special array structures. In: Academic press library in signal processing, vol 3; array and statistical signal processing, 3rd edn. Academic Press, Oxford, pp 651–717
32. Allen B, Ghavami M (2005) Adaptive array systems: fundamentals and applications. John, West Sussex
33. Yazdani H, Vosoughi A, Rahnavard N (2017) Compressive sensing based direction-of-arrival estimation using reweighted greedy block coordinate descent algorithm for ESPAR antennas. In: MILCOM 2017—2017 IEEE military communications conference (MILCOM), 2017, pp 169–173. https://doi.org/10.1109/MILCOM.2017.8170862
34. Choi JW, Shim B, Ding Y, Rao B, Kim DI (2017) Compressed sensing for wireless communications: useful tips and tricks. IEEE Commun Surv Tutorials 19(3):1527–1550. (Thirdquarter, 2017). https://doi.org/10.1109/COMST.2017.2664421
35. Nannuru S, Gemba K, Gerstoft P, Hodgkiss W, Mecklenbräuker C (2017) Multi-frequency sparse Bayesian learning with uncertainty models
36. Wu L, Liu Z, Huang Z (2019) Deep convolution network for direction of arrival estimation with sparse prior. IEEE Signal Process Lett 26(11):1688–1692. https://doi.org/10.1109/LSP.2019.2945115
37. Papageorgiou G, Sellathurai M, Eldar Y (2020) Deep networks for Direction-of-Arrival estimation in low SNR
38. Liu Z, Zhang C, Yu PS (2018) Direction-of-Arrival estimation based on deep neural networks with robustness to array imperfections. IEEE Trans Antennas Propag 66(12):7315–7327. https://doi.org/10.1109/TAP.2018.2874430
39. Huang H, Yang J, Huang H, Song Y, Gui G (2018) Deep learning for super-resolution channel estimation and DOA estimation based massive MIMO system. IEEE Trans Veh Technol 67(9):8549–8560. https://doi.org/10.1109/TVT.2018.2851783
40. Liu W (2020) Super resolution DOA estimation based on deep neural network. Sci Rep.https://doi.org/10.1038/s41598-020-76608-y

41. Tamilselvan S, Sneha VV (2020) Frequency domain learning scheme for massive MIMO using deep neural network. In: 2020 4th International conference on intelligent computing and control systems (ICICCS). IEEE
42. Ahmed T, Zhang X, Hassan WU (2019) A higher-order propagator method for 2D-DOA estimation in massive MIMO systems. IEEE Commun Lett 24(3):543–547
43. Shen Q, Liu W, Cui W, Siliang W (2016) Underdetermined DOA estimation under the compressive sensing framework: a review. IEEE Access 4:8865–8878
44. Hu A (2016) DOA-based beamforming for multi-cell massive MIMO systems. J Commun Netw 18(5):735–743
45. Yang Y, Dang S, Wen M, Mumtaz S, Guizani N (2019) Mobile millimeter wave channel tracking: a bayesian beamforming framework against DOA uncertainty. In: 2019 IEEE global communications conference (GLOBECOM). IEEE, pp 1–6
46. Zhang W, Liu K, Zhang W, Zhang Y, Jason G (2016) Deep neural networks for wireless localization in indoor and outdoor environments. Neurocomputing 194:279–287
47. Cao Y et al (2020) Complex ResNet aided DoA estimation for near-field MIMO systems. IEEE Trans Veh Technol 69(10):11139–11151
48. Chen K-T, Ma W-H, Hwang Y-T, Chang K-Y (2020) A low complexity, high throughput DoA estimation chip design for adaptive beamforming. Electronics 9(4):641
49. Zhuang Z, Ling X, Li J, Jinsong H, Sun L, Shu F, Wang J (2020) Machine-learning-based high-resolution DOA measurement and robust directional modulation for hybrid analog-digital massive MIMO transceiver. Science China Inf Sci 63(8):1–18
50. Qiu L, Lan T, Wang Y (2019) A sparse perspective for direction-of-arrival estimation under strong near-field interference environment. Sensors 20(163). https://doi.org/10.3390/s20010163
51. Li S, Wu H, Jin L (2019) Codebook-Aided DOA estimation algorithms for massive MIMO system. Electronics 8(26). https://doi.org/10.3390/electronics8010026
52. Bengio Y, Courville A, Vincent P (2013) Representation learning: a review and new perspectives. IEEE Trans Pattern Anal Mach Intell 35:8
53. Bashar A (2020) Artificial intelligence based LTE MIMO antenna for 5th generation mobile networks. J Artif Intell 2(03):155–162
54. Chen J-Z (2019) The evaluation of performance for a mass-MIMO system with the stsk scheme over 3-D α-λ-μ fading channel. IRO J Sustain Wireless Syst 1(1):1–19
55. Goodfellow I, Bengio Y, Courville A (2016) Deep learning 499–507. MIT Press, Cambridge
56. Xiao X, Zhao S, Zhong X, Jones DL, Chng ES, Li H (2015) A learning-based approach to direction of arrival estimation in noisy and reverberant environments. In: Proceedings of the ICASSP, pp. 2814–2818, IEEE, Brisbane, Australia, Apr 2015

Generation of Counters and Compressors Using Sorting Network

Kolaganti Anil Kumar and J. P. Anita

Abstract In digital signal processing applications, the critical route includes the parallel summation of multiple operands. High compression ratio counters and compressors are required to speed up the summing operation. In the proposed work, (15,4) counters and (7,3) counters are designed, while the counters are sorted using the proposed sorting network. The counter's inputs are split asymmetrically into two groups and fed into sorting networks to produce reordered sequences that can only be represented by one-hot code sequences. The counters are constructed in Xilinx using Verilog and obtained the results of time and delay. This is then applied to the sorting network and checked the sorting network for counters (7,3) and (15,4). In addition to this, sorting network was made effective in sorting the larger numbers either in the ascending or in the descending order.

Keywords Counter · (15,4) Counters · (7,3) Counters · Compressors · One-hot code · Sorting network

1 Introduction

Wallace tree operand is one of the famous methods for the multiple operands summation and upgraded method because of its reduced Wallace tree. So these are the methods that use the (3,2) counters instead of full adders to make the summation fast which results in consuming the logarithmic time. Carry slave structure is one of the similar structures. There are many papers in literature that discuss the construction of a more time-efficient structure to accelerate the summation. The main requirement is to construct a high compression ratio counter than the (3,2) counter. So the proposed work aims to construct the (15,4) and (7,3) counters which are efficient than the (3,2) counter. The compressors use the technique of compressing 'n' rows to 2 rows by making the carry bits between the side by side columns. The counter's role is to

K. Anil Kumar · J. P. Anita (✉)

Department of Electronics and Communication Engineering, Amrita School of Engineering, Amrita Vishwa Vidyapeetham, Coimbatore, India

e-mail: jp_anita@cb.amrita.edu

count the number of ones, once the ones have been sorted down with the help of the sorting method. İn this, group of inputs is divided into two groups where every two networks compare and the highest value gets on the top and likewise all the ones goes to top and zeros at the bottom. After the sorting network completes, the ones are counted using counters and then the number of ones got counted and the output will be compressed and got output in fewer bits.

The counters of (15,4) and (7,3) are planned to be designed as saturated counters with better efficiency. The logic simplification is used to optimize the new design and the main thing for compression is to compress the counters. The (4,2) compressors are also compressed using the sorting network, and in this proposed paper, the 4SN and 3SN sorting networks were used. SN means sorting network where 4SN is the method with four values sorted. Using this method, every 2 bits are compared and the highest value goes up and least value at the bottom. The counter at last counts the sorted one if it is the case of one bit and if the input values are higher values they will be sorted with highest or lower based on the ascending or descending order.

2 Literature Survey

The most well-known approach is the Wallace tree [1] approach to the summation of multiple operands, and its improved version [2] reduced the Wallace tree. To speed up the summing, these approaches use full adders as (3,2) counters, resulting in the consumption of logarithmic time. A carry-save structure is another name for this type of structure. Many publications have since examined ways to build a more time-efficient framework to speed up the summing, including [3, 4]. The fundamental idea is to use maintain the same weight with the usage of more bits or compressor with a (3,2) counter having the higher compression ratio. Compressors that compress into two rows or 4,5,6,7 rows have been discussed in certain articles. Some articles have examined counters such as (4,3), (5,3), and (6,3) [5], as well as (7,3) [6] and (15,4) [4]. All of the designs make excessive use of "XOR" gates [5] and are unsaturated. The focus of this article is on saturated counters. The (7,3) counter is saturated since a 3-bit number may just correctly represent 0–7. Fritz and Fam [6] presented a (6,3) counter with an asymmetric stacking structure.

In paper [2], it was proposed a modified Wallace tree reduction which was more effective than the conventional Wallace method. When compared to the traditional with the Wallace reduction, the number of half adders required lowered by at least 80%, while the number of full adders increases very slightly. The paper [3] developed six new architectures for the Counter-Based Wallace (CBW) multiplier in this research and compared their performance to that of the classic Wallace multiplier. A new 5:2 compressor architecture based on modifying internal equations is proposed in this research [7, 8]. A high-speed compressor is also considered when using an efficient full-adder (FA) block. In the paper [8], proposed design uses fewer transistors than the best available 5:2 compressor topologies [9]. Wallace tree multipliers are a

low-power, high-speed multiplication technique [5]. In the Wallace tree reduction, using high-speed 7:3 counters can boost the multiplier speed even more [5].

In paper [6], it was revealed that the same method of counting may be used to make 6:3 and 7:3 counters that can be used to add partial products in any binary multiplier circuit. The crucial data channel contains just 10 gates, four of which are exclusive-OR gates, and is designed as a (15,4) parallel counter circuit [4]. In terms of latency, area, and power consumption, the implementation of the proposed concept outperforms in [4] either the combined method of (7,3) and (3,2) counters [10–17].

3   Proposed Work

The research motivation for the project is to design the (15,4) and (7,3) counter with the best possible sorting network with the higher number, so came up with the most understandable sorting network like ascending and descending sorting network were used. The ascending and descending sorting networks are nothing but sorting the values in the ascending and descending order with higher numbers. Generally, only single bits are sorted in the proposed methodology where zeros and ones are sorted in such a way the higher values floats on top and lower values which are zeros will be extracted down. Figure 1 shows the sorting networks. The proposed paper developed the (15,4) and (7,3) counters in the proposed study utilizing the sorting network in Xilinx using the Verilog language. The two counters' designs were written and evaluated in the Verilog testbench. The design will dump into the FPGA once the code has been designed, and a schematic will be generated for the generated schematic. Power dissipation, time, and delay will be logged, and the waveform will be generated after the design has been implemented. The sorting network works in such a way they split into two groups and in which the sorting is done by comparing the 2 paths and sorting with largest or shortest values as shown in Fig. 1, where two groups of 4SN and 3SN were divided and sorting network have done. For example, in (15,4), we have 15 inputs and 4 outputs, and the sorting network must first sort all of the ones before counting how many were present and reflecting that count in the output. As illustrated in Fig. 2, the inputs are sorted using the sorting network operating principle, which is similar to the 3-way and 4-way sorting networks are common. Each vertical line represents a sorter with two one-bit data inputs and outputs. The sorter prioritizes the larger input, then the smaller one. Here is an example of a larger input: The four-way sorting network's (4 SN) input is sequence [0, 1, 1, 1], and the sequence is shown in Fig. 2. The 3-way sorting network input is [0, 1, 1]. (3 SN). After three levels of the sorter, the input sequences for both 4 SN and 3 SN are the sorter reorders two inputs according to numerical magnitudes, with the greater number at the top and the smaller number at the bottom. The logical circuit shown can easily sort two 1-bit datasets. Three layers of two-input basic logic gates are used in 3-way and 4-way sorting networks, whereas one layer of two-input basic logic gates is used in a sorter. The ones in the bitstream were sorted once the sorting network finished, and the ones were counted and generated in the output.
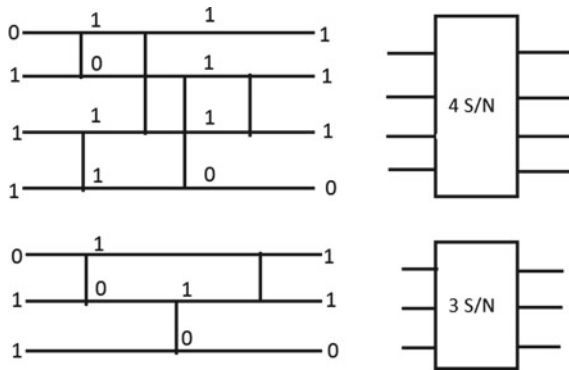
Fig. 1 Sorting network block diagram
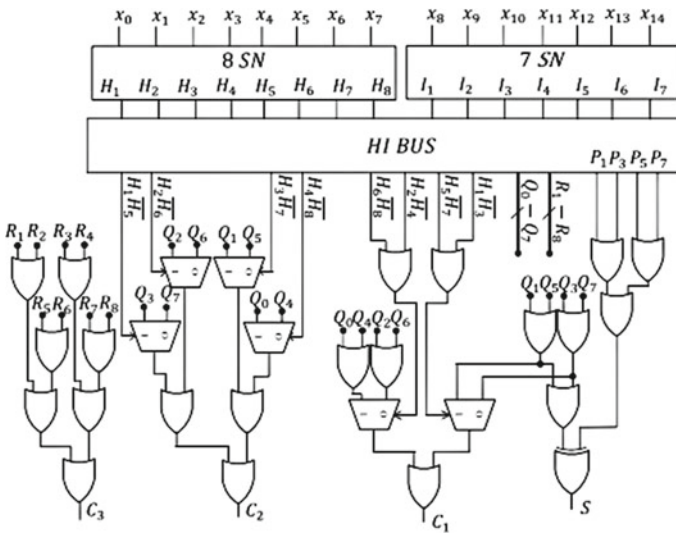
Fig. 2 Block diagram of (15,4) counter[12]

Here, the above diagram shows the block diagram for the (15,4) counter, and in this, we have given 15 inputs and 4 outputs for which the sorting has been done in such a way that all the 15 inputs were partitioned into 7-way sorting network and 8-way sorting like the sorting way block diagram which was shown in the above Fig. 1, and after the sorting mechanism was completed, the upper bits which means the ones are sorted, so now, all the ones are sorted and the counter counts the number of ones which were sorted.

Figure 3 is the schematic that got generated from the Verilog code which was dumped to FPGA, and the Xilinx tool generates the schematic for the Verilog design. The design of the counter has been written in Verilog and the Verilog design will be
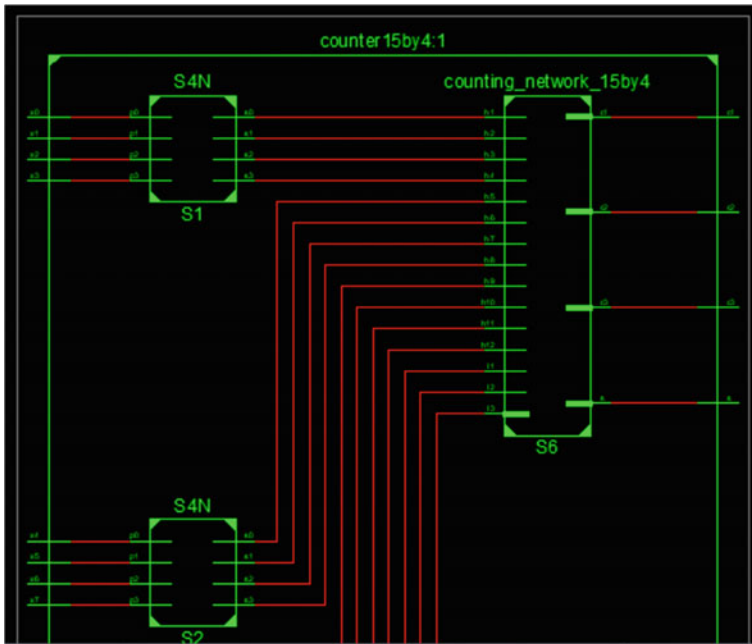
Fig. 3 Schematic of (15,4) counter using sorting method

dumped to FPGA for which Xilinx tool will generate the schematic with respect to the design in the form of Verilog code.

4 Results

Figure 4 shows the waveform of the (15,4) counter which illustrates the compressed value of the counter after the sorting network has been done; here, the number of ones in the input which is 11 so the compressed value got in the output was [1 0 1 1] this is how the counter is compressed using the sorting network.

Table 1 gives the table of the summary report which consists of the area that has been used in the designed circuit in the form of LUTs, where 24 LUTs were used in the design and the result explains that several slices with unrelated logic 0%.

Figure 5 shows the time delay and total time to simulate the design which was noticed as a total time delay of 14.736 ns and a total time taken was 5.14 s. The delay was extracted from the simulation of schematic which was generated by the tool from the Verilog design.

Figure 6 shows the waveform for making the sorting network more efficient by making it accessible in ascending order and also for higher values where few inputs were given and output was sorted in ascending order. Here, the d_in signal is the
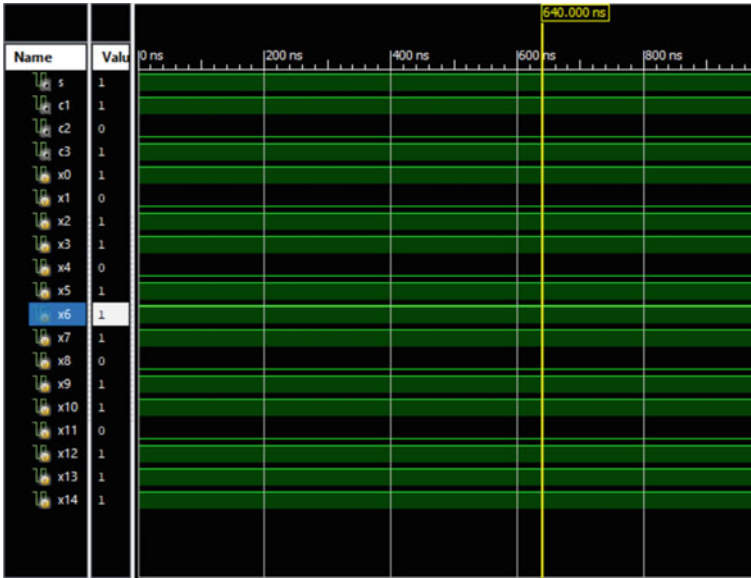
Fig. 4 Simulation of (15,4) counter using the sorting network

Table 1 Synthesis report of the (15,4) counter

Logic utilization	Used	Available	Utilization (%)
Number of 4 input LUT's	24	9312	1
Number of occupied slices	13	4656	1
Number of slices containing related logic	13	13	100
Number of slices containing unrelated logic	0	13	0
Total number of 4 input LUTs	24	9312	1
Number of bonded IOBs	19	232	8
Average fanout of non-clock nets	2.39		

random input which are to be sorted in the ascending order so the sorted values are reflected in the d_out which is shown in Fig. 6.

Table 2 gives the value of power which is dissipated during the simulation for the schematic which was generated in the tool. The total power leakage identified is 0.081 mW. After the schematic has been extracted from the Verilog design, the power dissipation from the schematic simulation is given in Table 2.

Table 3 gives the change in the size when the sorting network has been upgraded for ascending and descending orders with higher numbers; here, the number of LUTs used was 1096 in number but the usage of unrelated logic remains zero.

```
Cell:in->out      fanout  Delay   Delay   Logical Name (Net Name)
------------------------------------------    -------------
  IBUF:I->O          4     1.106   0.651   x12_IBUF (x12_IBUF)
  LUT4:I0->O         2     0.612   0.532   S6/Madd__old_ones_5_Madd_lut<0>1 (S6/Madd__old_ones_5_Madd_lut<0>)
  LUT3:I0->O         2     0.612   0.532   S6/Madd__old_ones_7_Madd_lut<0>1 (S6/Madd__old_ones_7_Madd_lut<0>)
  LUT3:I0->O         2     0.612   0.532   S6/Madd__old_ones_9_Madd_lut<0>1 (S6/Madd__old_ones_9_Madd_lut<0>)
  LUT3:I0->O         2     0.612   0.532   S6/Madd__old_ones_11_Madd_lut<0>1 (S6/Madd__old_ones_11_Madd_lut<0>)
  LUT3:I0->O         2     0.612   0.532   S6/Madd__old_ones_13_Madd_lut<0>1 (S6/Madd__old_ones_13_Madd_lut<0>)
  LUT3:I0->O         2     0.612   0.449   S6/Madd__old_ones_15_Madd_lut<0>1 (S6/Madd__old_ones_15_Madd_lut<0>)
  LUT4:I1->O         2     0.612   0.410   S6/Madd__old_ones_15_Madd_cy<1>11 (S6/Madd__old_ones_15_Madd_cy<1>)
  LUT3:I2->O         1     0.612   0.426   S6/Madd__old_ones_15_Madd_xor<2>1_SW1 (N11)
  LUT4:I1->O         1     0.612   0.357   S6/Madd__old_ones_15_Madd_xor<2>1 (c2_OBUF)
  OBUF:I->O                3.169           c2_OBUF (c2)
------------------------------------------
  Total                   14.736ns (9.783ns logic, 4.953ns route)
                                  (66.4% logic, 33.6% route)
=========================================================

Total REAL time to Xst completion: 5.00 secs
Total CPU time to Xst completion: 5.14 secs

-->

Total memory usage is 4494840 kilobytes
```

Fig. 5 Report of CPU time and delay time
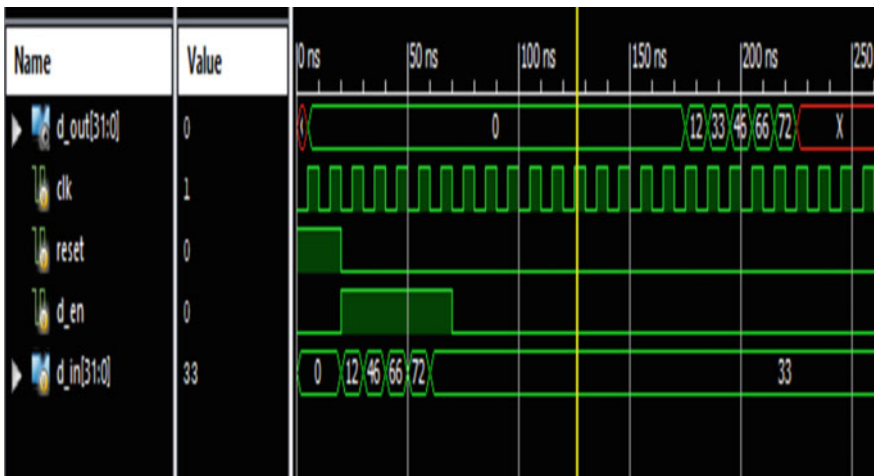
Fig. 6 Simulation of sorting network with ascending order

Table 2 Power dissipation table

On-chip	Power	Used	Available	Utilization
Clocks	0.000	1	–	–
Logic	0.000	1096	9312	12
Signals	0.000	1310	–	–
IOs	0.000	67	232	29
Leakage	0.081	–	–	–

Table 3 Synthesis report for ascending sorting network

Logic utilization	Used	Available	Utilization (%)
Number of slice Flipflops	655	9312	7
Number of 4input LUTs	1096	9312	11
Number of occupied slices	695	4656	14
Number of slices containing related logic	695	695	100
Number of slices containing unrelated logic	0	695	0
Number of 4 input LUTs	1096	9312	11
Number of bonded IOBs	67	232	28
Number of BUFGMUXs	1	24	4
Average fanout of non-clock nets	3.51		
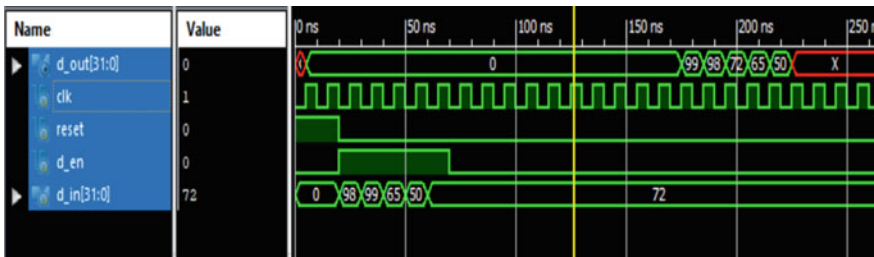
Fig. 7 Simulation of sorting network with descending order

Figure 7 shows the waveform for making the sorting network more efficient by making it accessible in descending order and also for higher values, where few inputs were given and output was sorted in descending order.

5 Discussion

Here, in the waveform, the inputs were given in form 1's to 0's, and here operation that needs to be done was to sort the ones in the background and the number of ones to be counted. In this waveform, if we see the $\times 0$ to $\times 14$ are the inputs where the inputs are given and the number of ones is 11 in number so we have to get the 11 as output in 4-bit output and we got output as 1011 as output which represents 11 in binary, and the table gives the power dissipation of the schematic above which was generated for the design which was done in Verilog where 0.081 MW of power dissipation has taken place. And the above schematics were generated for the RTL design in Verilog which was converted to schematic by the tool. The performance metrics measured for model efficiency are area, power and delay. Area includes the

number of slice flipflops used as 655 and number of 4 input LUT's used as 1096, and power leakage of 0.081mW and total time delay of 14.736 ns.

6 Conclusion and Future Scope

The (15,4) and (7,3) counters have been designed, implemented and then dumped to FPGA. The schematic has been generated using the design and power dissipation for the schematic has been extracted. The sorting network has been implemented and the output has been analyzed using the simulation waveforms. The proposed work can be extended to a different type of sorting network where higher numbers can be sorted and also particular bits can be selected to get sorted.

References

1. Wallace CS (1964) A suggestion for a fast multiplier. IEEE Trans Electron Comput EC-13(1):14–17. https://doi.org/10.1109/PGEC.1964.263830
2. Najafi A, Trimarchi S, Najafi A (2014) High-speed energy-efficient 5:2 compressor. In: Proceedings of 37th international convention on information communication technology electronics microelectronics. (MIPRO), Opatija, Croatia, pp 80–84, May 2014. https://doi.org/10.1109/MIPRO.2014.6859537
3. Fritz C, Fam AT (2017) Fast binary counters based on symmetric stacking. IEEE Trans Very Large Scale Integr (VLSI) Syst 25(10):2971–2975. https://doi.org/10.1109/TVLSI.2017.2723475
4. Asif S, Kong Y (2015) Analysis of different architectures of counter-based Wallace multipliers. In: Proceedings of 10th international conference on computer engineering systems (ICCES), Cairo, Egypt, pp 139–144, Dec 2015. https://doi.org/10.1109/ICCES.2015.7393034
5. Waters RS, Swartzlander EE (2010) A reduced complexity Wallace multiplier reduction. IEEE Trans Comput 59(8):1134–1137. https://doi.org/10.1109/TC.2010.103
6. Montgomery PL (2005) Five, six, and seven-term karatsuba-like formulae. IEEE Trans Comput 54(3):362–369. https://doi.org/10.1109/TC.2005.49
7. Jiang Q, Li S (2017) A design of manually optimized (15,4) parallel counter. In: Proceedings of international conference on electron devices solidstate circuits (EDSSC), Hsinchu, Taiwan, pp 1–2, Oct 2017. https://doi.org/10.1109/EDSSC.2017.8126527
8. Fathi A, Mashoufi B, Azizian S (2020) Very fast, high-performance 5–2 and 7–2 compressors in CMOS process for rapid parallel accumulations. IEEE Trans Very Large Scale Integr (VLSI) Syst 28(6):1403–1412. https://doi.org/10.1109/TVLSI.2020. 2983458
9. Asif A, Kong Y (2015) Design of an algorithmic Wallace multiplier using high-speed counters. In: Proceedings of 10th international conference on computer engineering and systems (ICCES), Cairo, Egypt, pp 133–138, Dec 2015. https://doi.org/10.1109/ICCES.2015.7393033
10. Najafi A, Mazloom-nezhad B, Najafi A (2013) Low-power and highspeed 4–2 compressor. In: Proceedings of 36th international convention on information and communication technology electronics and microelectronics (MIPRO), Opatija, Croatia, pp 66–69
11. Sajeeva Rao B, Ramkumar A (2017) FPGA implementation of algorithmic counter based wallace tree. Int J Electron Commun Technol 8(3)
12. Guo W, Li S (2021) Fast binary counters and compressors generated by sorting network. (99):1–11. https://doi.org/10.1109/TVLSI.2021.3067010

13. Devika C, Anita JP (2022) Design of a high speed binary counter using a stacking circuit. Lect Notes Netw Syst 311:135–143
14. Hemamithra KG, Lakshmi Priya S, Lakshmirajan K, Mohanraj R, Ramesh SR (2018) FPGA implementation of power efficient approximate multipliers. In: International conference on recent trends in electronics, information and communication technology, pp 1281–1285
15. Bhargav TAS, Prabhu E (2018) Power and area efficient FSM with comparison-free sorting algorithm for write-evaluate phase and read-sort phase. Commun Comput Inf Sci 968:433–442
16. Neethu BN, Anita JP (2022) Design of multistage counters using linear feedback shift register. Lect Notes Netw Syst 311:161–173
17. Sathesh A (2019) Energy efficient routing in clustered IoT wireless sensors networks for Qos enhancements. J IoT Soc Mobile Anal Cloud 1(1):1–11

Gujarati Language Automatic Speech Recognition Using Integrated Feature Extraction and Hybrid Acoustic Model

Mohit Dua and Akanksha

Abstract In the case of low resource language, there is still the requirement for developing more efficient Automatic Speech Recognition (ASR) systems. In the proposed work, the ASR system is developed for the Gujarati language publicly available dataset. The approach in this paper applies the combination of Mel-frequency Cepstral Coefficients (MFCC) with Constant Q Cepstral Coefficients (CQCC)-based integrated front-end feature extraction techniques. To implement the backend part of the system, hybrid acoustic model is applied. Two-dimensional Convolutional Neural Network (Conv2D) with Bi-directional Gated Recurrent Units-based (BiGRU) backend model is used as the model. To build the ASR system, Connectionist Temporal Classification (CTC) loss function, CTC and prefix-based greedy decoder are also used with the acoustic model. The proposed work shows that the joint MFCC and CQCC feature extraction techniques show the 10–19% improvement in Word Error Rate (WER) as compared to isolated delta-delta features with the available integrated model.

Keywords Gujarati ASR · MFCC · CQCC · CNN · BiGRU

1 Introduction

Speech is recognized as the most valuable, preferred and effective mode of communication for the humans. Nevertheless, the human communication is not limited to people only but it also involves machines. For instance, speech-based virtual assistants like Alexa, Apple Siri and Google Assistant are extremely well liked and offer a variety of services like monitoring gadgets and doing different tasks via voice commands [1, 2]. An ASR system mainly works in two parts, i.e., Frontend and

M. Dua (✉) · Akanksha
Department of Computer Engineering, National Institue of Technology, Kurukshetra, Haryana, India
e-mail: er.mohitdua@nitkkr.ac.in

Akanksha
e-mail: akanksha_32013102@nitkkr.ac.in

backend. At the frontend part, we apply the feature extraction techniques. These feature extraction techniques help in collecting the information about the speech signal's uniqueness and speaker authenticity. Later, we apply the extracted features to the backend model [3]. In the domain of ASR systems, numerous feature extraction techniques are frequently used, including: Mel-frequency Cepstral Coefficients (MFCC), Gammatone Cepstral Coefficients (GFCC), perceptual Linear Predictive (PLP) and Linear Frequency Cepstral Coefficients (LFCC). At the backend part of the ASR system, we process the applied feature vectors. The language model and acoustic model work as the main component here. The main task of acoustic model is to be capture the relation between the linguistic and speech vectors. The different backend acoustic models used are Gaussian Mixture Model (GMM), Hidden Markov Model (HMM), Long Short-Term Memory (LSTM) model, Convolutional Neural Network (CNN), etc., and the language models are Mono-gram, bi-gram, tri-gram and n-gram. These language models try to find out the likelihood of spoken words based on the model applied. The decoder also works at the backend part to decode the speech signal in to the required text form. Then most widely used decoders are greedy and prefix-based decoder. For ASR systems to be effective, a large training dataset is required. Only a handful of languages like English, Chinese, Spanish, etc., have such huge dataset. Whereas small regional languages like Tamil, Gujarati, Bangla, etc., do not possess such large dataset and only a handful of scholars are working on it [4, 5]. Moreover, it is predicted that only ~ 1% of the world's languages have the essential voice corpus needed to train an ASR system [6].

Dave et al., in 2015, were one of the first researchers to present HMM and ANN approach for recognizing isolated Gujarati words. They also employed Genetic algorithm (GA) to reduce Word Error Rate (WER) from 29.43% to 20.86%. In 2016, Jinal et al. [7] presented HMM approach and fed small dataset of Gujarati language to it. The WER of 5.85% was observed with this approach. Valaki et al. [8] presented HMM/ANN hybrid model and compared it with HMM model. 10 Gujarati words were used for testing and the prediction of models were recorded against actual values. It was observed that proposed HMM/ANN model performed better than base HMM model. In year 2019, Madhavaraj et al. [9] experimented with two approaches for training ASR. It was compared against baseline approach and the proposed model improved WER by 5.1% and 5.7% for Gujarati language, respectively.

Raval et al. [10], in year 2021, presented end-to-end ASR approach for recognizing Gujarati language. They employed BERT-based spelling corrector model to enhance the system's performance. This approach resulted in reducing WER by 5.87%. They also showed that performance of system can be improved even with limited dataset as in case with low resource languages like Gujarati. Constant Q Cepstral Coefficients (CQCC) [11] is one of the most popular feature extraction techniques in the area of Automatic Spoof Verification (ASV) systems. In year 2022, Chaudhari et al. [12] explore the combination of CQCC feature extraction technique with the MFCC [13]-based technique for the replay attack detection. They observe the improvement in the performance of the ASV system.

In the proposed work, the required feature vectors are extracted using the integrated CQCC and MFCC based feature extraction techniques. At the backend, the Two-dimensional Convolutional Neural Network (Conv2D) + Bi-directional Gated Recurrent Units-based (BiGRU) hybrid acoustic model is applied. Whereas for the decoding purpose, greedy and prefix-based decoder are applied to generate the output text. The ASR system is evaluated and trained on Crowdsourced High-Quality Gujarati Multi-Speaker Speech Dataset. A commonly used evaluation statistic, WER is used for assessing how effectively speech processing systems like ASR operate. The remainder of the work is organized as follows: Sect. 2 discusses about the dataset, and then Sect. 3 illustrates proposed ASR system's architecture; Sect. 4 describes the experimental details and the performance analysis, leaded by Sect. 5, which provides the conclusion to the whole research.

2 Preliminaries

This section describes about the required fundamentals used to implement the proposed ASR system are discussed in this section.

2.1 Mel-Frequency Cepstral Coefficients (MFCC)

For implementing the ASR systems, Mel-frequency Cepstral Coefficients (MFCC) is the most widely used Cepstral analysis-based feature extraction technique. The reason behind is that MFCC has the capability to capture the phonetically important features from the speech. The step-wise approach to extract the MFCC features is given below:

- Initially, we perform the pre-emphasis operation on the recorded speech signal $S(n)$. As a result, we get the pre-emphasized signal containing higher frequencies.
- Then we slice the input $S(n)$ into the smaller frames and then apply framing and windowing $W(n)$ to remove edge discontinuities.
- After windowing operation, to separate the energy contained within every frequency spectrum, Discrete Fourier Transform (DFT) is applied. The equation to represent the speech signal into frequency range having power spectrum is:

$$|F(j)|^2 = \Big| \sum_{j=1}^{P} f(j).e^{(-k2\pi jl/P-1)} \tag{1}$$

where $1 \leq l \leq P - 1$, and $|F(j)|^2 =$ Power Spectrum

- Diverse band pass filters are used to filter the spectrum produced by the DFT, and each frequency band's power is enumerated. And on the produced signal, we apply the log method with Mel-filter bank to achieve the spectrogram.
- The Mel coefficients are transformed back into the time domain using the discrete cosine transform (DCT). And later, 13-MFCC feature coefficients are produced for each frame from the DCT results.

The following is a representation of the filter bank's output equation when used to the energy spectrum:

Let $\propto_i (j) =$ filter response

$$e(i) = \sum_{j=1}^{P/2} |F(j)|^2 . \propto_i (j) \tag{2}$$

We can represent the obtained MFCC features as:

$$M(f) = \sqrt{2/X} \sum_{j=0}^{X-1} \log[e(j+1)]. \cos[\propto .(2k-1/2).\pi/X] \tag{3}$$

2.2 Constant Q Cepstral Coefficients (CQCC)

During the implementation of an Automatic Speaker Verification (ASV) system, Constant Q Cepstral Coefficients (CQCC) feature extraction is utilized to extract meaningful information from the captured speech signal. In recent time, this method has recently been shown to be the most feasible for the creation of reliable and accurate ASV systems [11, 12].

The Constant Q Transform (CQT) is used in the CQCC feature extraction procedure, which then takes the log of the powered spectrum. It also uses resampling before computing the DCT. It returns CQCC features after setting the number of feature coefficients. The following is a mathematical depiction of the CQCC feature extraction approach:

$$C_{PQR}(s) = CQT(p(t)) \tag{4}$$

$$C_{CQCC}(i) = \sum_{s=0}^{I} \log |C_{PQR}(s)|^2 \cos\{i(s-0.5)\pi |I\} \tag{5}$$

In this case, Eq. (4) determines the Constant Q Transform (CQT) of the input speech signal $p(t)$ in $C_{PQR}(s)$, and Eq. (5) determines i, total number of number of

Table 1 Characteristics of required Gujarati Speech dataset

Speaker	Count	Duration (h)	Sentences	Phonemes
Male	18	Total: 3.59	Male	18
Female	18	Total: 4.30	Female	18

CQCC parameters in CCQCC(j), where I is the number of linearly spaced bins and e denotes the number of bins to index into.

2.3 Crowdsourced High-Quality Gujarati Multi-Speaker Speech Dataset

To collect the dataset, the Gujarati speakers participated. The gathered dataset is of high quality and was captured in a clean environment. The audio files are in.wav format and designed for speech recognition purpose (Table 1).

3 Proposed Automatic Speech Recognition (ASR) System

Figure 1 illustrates the proposed ASR system's architecture. The architecture of the proposed Automatic Speech Recognition (ASR) system is majorly divided in the two parts, i.e., front endand backend. Figure 1 represents the architecture of proposed ASR system. Joint MFCC + CQCC feature extraction is employed at frontend, whereas two-dimensional Convolutional Neural Network (2D-CNN) and Bidirectional Gated Recurrent Units (BiGRU)-based hybrid model are used at backend. To build the proposed system, Crowdsourced high-quality Gujarati multi-speaker speech dataset is utilized. To extract the combine MFCC + CQCC features, voice signals are applied as an input to achieve in total of 66 feature vectors.

3.1 Combined MFCC + CQCC-Based Feature Extraction Technique

In order to extract the first 13 MFCC feature vectors, the auditory signals are first applied as an input to the MFCC technique and then those 13 features expended to get the 39 delta-delta $(\Delta - \Delta)$ features.

Similarly, the 20 CQCC features are extracted from the applied input voice signals and expended to 60 delta-delta features by applying the second order derivative function. Later, we combine these Δ features to produce the combine 99 feature vectors. Figure 2 describes the step to extract the required feature vectors.
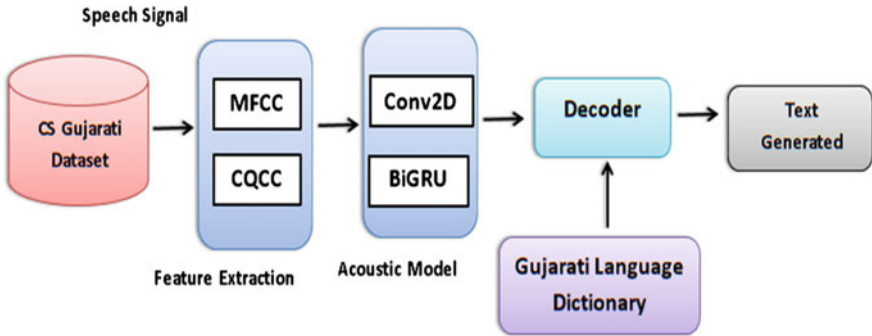
Fig. 1 Proposed automatic speech recognition (ASR) system architecture
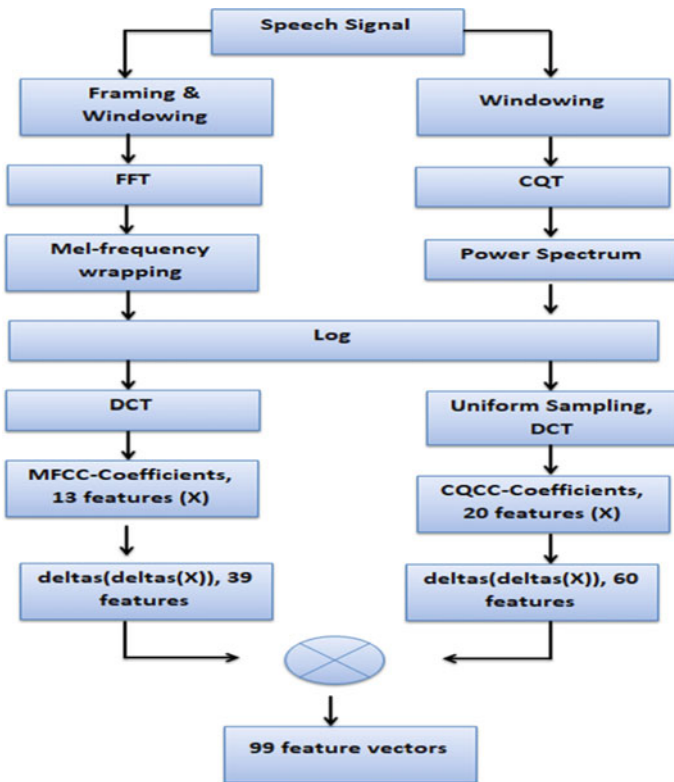
Fig. 2 Steps to apply frontend techniques

3.2 Two-Dimensional Convolutional Neural Network (Conv2D) + Bi-Directional Gated Recurrent Units-Based (BiGRU) Backend Model

Generally, a Two-dimensional Convolutional Neural Network (Conv2D) is utilized with the visual information. The model is two-dimensional as its kernel moves along 2D on the data. The proposed Conv2D model is made up of so many different layers, such as: Pooling, Dense, Flatten and Convolutional. The activation function used is soft-max and the dropout is 20%.

Recurrent Neural Networks (RNN) are kind of Neural Network that consist internal memory which makes them robust and powerful. Gated Recurrent Units (GRU) are enhanced RNN networks with less complex and strong modeling capabilities. BiGRU compromises two GRU for processing the information in backward and forward direction. The proposed BiGRU model has four BiGRU layers which consists of 512 units each with 50% of dropout.

Figure 3 explains the general architecture of the proposed backend model.

4 Experimental Setup

Initially, 13 MFCC feature vectors are extracted using the MFCC feature extraction technique and then those features are expended to 39 MFCC feature coefficients using the delta-delta function. Similarly, 20 CQCC feature vectors are expended to 60 CQCC ($\Delta - \Delta$) features. Later, we combine these features to get the in total of 99 features coefficients. To extract these features, MATLAB tool is used. For the
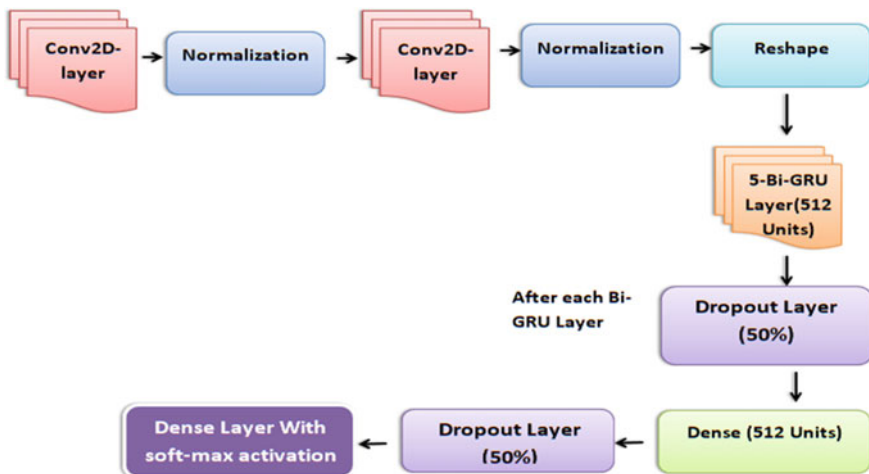
Fig. 3 Architecture of backend model

Table 2 Summarizes the WER on proposed model

Frontend	Feature vectors	WER (%)
MFCC	39	20.04
CQCC	60	8.75
MFCC + CQCC	99	1.02

implementation of backend model, Python libraries are used. To compile the model, "ADAM" optimizer is used, and for the training, connectionist temporal classification (CTC) loss function is applied and Gujarati language-based dictionary is applied at the backend. For decoding, greedy and prefix-based decoder are used. To the train and test the system, Crowdsourced (CS) high-quality Gujarati multi-speaker speech dataset is used. Word Error Rate (WER) metric is used to measure the efficiency of the system.

5 Performance Analysis

The proposed system is trained and tested on the CS high-quality Gujarati multi-speaker speech dataset. At the frontend, MFCC + CQCC-based approach is applied, whereas at the backend, Conv2D + BiGRU-based model is used.

5.1 Results

To observe the performance of the system firstly, we evaluate the model on dynamic features of each (i.e., MFCC, CQCC) as well as on integrated front-end approach. Table 2 summarizes the results achieved on the applied feature vectors.

By observing Table 2, we can understand that the combination of MFCC with CQCC enhance the systems' performance as compared to their $(\Delta - \Delta)$ features.

5.2 Comparative Analysis with Existing Approaches

In this section, we contrast the suggested strategy with some of the current strategy. In year 2021, Raval et al. [14] propose a novel approach to build an E2E ASR system. They observe that the propose approach decreases the WER by 5.87% as compared to the base model. The authors use the different type of language model, i.e., character-level and word-level. To generate the text, prefix decoding is applied at the end. Recently, in year 2022, Tailor et al. [15] presented a CNN-based approach with MFCC feature reduction for Gujarati words. An accuracy of 98.7% was achieved using these techniques. The whole experiment is carried out in three parts with the

Table 3 Comparison with existing techniques

Authors	Frontend	Backend	Dataset	WER (%)
Raval et al. [14], 2021	MFCC	CNN + Bi-directional Long Short-Term Memory (Bi-LSTM)	Microsoft Gujarati Corpus	64.78
Tailor et al. [15], 2022	MFCC	CNN	Gujarati Spoken Digits	1.3
Proposed System	Dynamic MFCC, CQCC and joint MFCC + CQCC	Conv 2D + BiGRU	CS high-quality Gujarati multi-speaker speech dataset	1.02

distinct data sizes of 2400, 1800 and 1200. Table 3 compares the already existing techniques with our proposed system.

6 Conclusion

In this paper, we have implemented the Mel-frequency-based coefficients with the Constant Q Cepstral Coefficients (CQCC) feature extraction technique, which is one of the most widely used frontend techniques in ASV systems. The CQCC technique enhances the system's performance as compared to MFCC features as they provide more equivalent time–frequency region to human understanding. At the backend part, hybrid conv2D and BiGRU-based model with CTC loss decoder is applied to implement the state of art for ASR system in Gujarati language. It is observed that the joint features show the relative improvement of 10—19% in WER as compared to alone $(\Delta - \Delta)$ features. We can further extend this work by utilizing these features on any noisy dataset with the help of an efficient backend model.

References

1. Dua M, Kadyan V, Banthia N, Bansal A, Agarwal T (2022) Spectral warping and data augmentation for low resource language ASR system under mismatched conditions. Appl Acoust 190
2. Pittala RB, Tejopriya BR, Pala E (2022) Study of speech recognition using CNN. In: International conference on artificial intelligence and smart energy (ICAIS), vol 2, pp 150–155
3. Neumann V, Kinoshita T, Drude K, Boeddeker L, Delcroix C, Nakatani M, Haeb-Umbach T (2020) End-to-end training of time domain audio separation and recognition. In: IEEE international conference on acoustics, speech and signal processing (ICASSP), pp 7004–7008
4. Wang D, Wang X, Lv S (2019) An overview of end-to-end automatic speech recognition. Symmetry 11(8):1018
5. Jain A, Singh VP, Rath SP (2019) A multi-accent acoustic model using mixture of experts for speech recognition. Interspeech 779–783

6. Scharenborg O, Ciannella F, Palaskar S, Black A, Metze F, Ondel L, Hasegawa-Johnson M (2017) Building an ASR system for a low-research language through the adaptation of a high-resource language ASR system: preliminary results. In: International conference on natural language, signal and speech processing (ICNLSSP), pp 26–30
7. Tailor JH, Shah DB (2016) Speech recognition system architecture for Gujarati language. Int J Comput Appl 138(12)
8. Valaki S, Jethva H (2017) A hybrid HMM/ANN approach for automatic Gujarati speech recognition. In: International conference on innovations in information, embedded and communication systems (ICIIECS), pp 1–5
9. Madhavaraj A, Ramakrishnan AG (2019) Data-pooling and multi-task learning for enhanced performance of speech recognition systems in multiple low resourced languages. In: National conference on communications (NCC), pp 1–5
10. Raval D, Pathak V, Patel M, Bhatt B (2020) End-to-End automatic speech recognition for Gujarati. In: International conference on natural language processing (ICON), pp 409–419
11. Mittal A, Dua M (2022) Static–dynamic features and hybrid deep learning models based spoof detection system for ASV. Complex Intell Syst 8(2):1153–1166
12. Chaudhari A, Shedge DK (2022) Integration of CQCC and MFCC based features for replay attack detection. In: International conference on emerging smart computing and informatics (ESCI), pp 1–5
13. Han W, Chan CF, Choy CS, Pun KP (2006) An efficient MFCC extraction method in speech recognition. In: IEEE international symposium on circuits and systems (ISCAS), pp 4–10
14. Raval D, Pathak V, Patel M, Bhatt B (2021) Improving deep learning based automatic speech recognition for Gujarati. Trans Asian Low-Resour Lang Inf Process 21(3):1–18
15. Tailor JH, Rakholia R, Saini JR, Kotecha K (2022) Deep learning approach for spoken digit recognition in Gujarati language. Int J Adv Comput Sci Appl 13(4)

Graphene and Fullerene in Energy Storage Devices: A Comprehensive Review

B. Yogeswari, M. Varatharaj, S. Deivanayaki, T. Malini, P. Anbarasu, and D. Prakash

Abstract Right from the discovery of electricity, human fraternity is searching for efficient techniques to store that energy in order to meet the future energy demands. Recently, the energy storage engineering is evolving by adapting innovative technologies and trying to meet out the varying energy requirements. Hence, identifying suitable, sustainable, environmental-friendly and competent energy storage devices and materials has become the most important need of the hour. Nanotechnology and nanomaterials have extremely decisive responsibility in the present energy storage sector. Nanomaterials are considered to be the "wonder" materials with their remarkable characteristics such as fast ion diffusion, high particle volume, better electronic

B. Yogeswari (✉)
Department of Physics, Sri Eshwar College of Engineering (Autonomous), Coimbatore, Tamil Nadu 641202, India
e-mail: yogeshwari.b@sece.ac.in

M. Varatharaj
Department of Electrical and Electronics Engineering, V.S.B College of Engineering Technical Campus, Coimbatore, Tamil Nadu 642109, India
e-mail: eee@vsbcetc.com

S. Deivanayaki
Department of Physics, Sri Ramakrishna Engineering College (Autonomous), Coimbatore, Tamil Nadu 641022, India
e-mail: deivanayaki.subbaiyan@srec.ac.in

T. Malini
Department of Electrical and Electronics Engineering, Sri Krishna College of Engineering and Technology (Autonomous), Coimbatore, Tamil Nadu 641008, India
e-mail: malinit@skcet.ac.in

P. Anbarasu
Department of Electrical and Electronics Engineering, Sri Eshwar College of Engineering (Autonomous), Coimbatore, Tamil Nadu 641202, India
e-mail: anbarasu.p@sece.ac.in

D. Prakash
Department of Physics, Hindustan Institute of Technology (Autonomous), Coimbatore, Tamil Nadu 641028, India
e-mail: dr.prakash@hit.edu.in

55

conductivity make them as competent nominee for energy storage. The surprising properties of carbon-based nanomaterials and their tunable surface chemistry permit them as the support for high-power energy storage devices. This article traces the role of few carbon-based nanomaterials, for instance, graphene and fullerenes in practically influencing and improving the ability and dependability of devices used for energy storage like batteries, supercapacitors and fuel cells.

1 Introduction

By considering the growing interest of portable electronic devices, there is an increasing awareness about the growth of sustainable energy storage devices. Energy storage device characteristics can be improved by carefully engineering electrode materials, device design and system performance optimization. Extensive efforts from the researchers have bestowed a collection of nanomaterials used for energy storage applications. Carbon materials are primarily enclosing carbon atoms, only one type of component, but they have widely varied structures and properties. Carbon, believed to be one of the chief elements, possesses distinctive characteristics which facilitated them to find applications in various fields including energy production and storage.

Manifestation of carbon materials as electrodes, conductive agents, etc., in energy storage has made them to be unavoidable representatives in this field. Carbon nanomaterials have a variety of chemical compositions and forms since they can form strong bonds than any other materials. This includes zero-dimensional (0D), 1D, 2D and 3D nanomaterials intended for energy generation, conversion, transmission and storage. Carbon nanomaterials consisting of fullerene, carbon nanotubes and graphene possess exclusive morphologies, exceptional structures and show potential physical, chemical and electrical properties. These chemically diverse nanoscale materials are being employed to make energy storage way out that are not possible with traditional materials. This article places emphasis on the role of two most outstanding carbon-based nanomaterials, i.e., (i) graphene and (ii) fullerenes, in enhancing the performance of four energy storage devices, i.e., lithium-ion, lithium-sulfur batteries, supercapacitors and fuel cells.

2 Role of Graphene in Energy Storage

Andre Geim and Konstantin Novoselov uncovered graphene in 2004 and received the 2010 Nobel Prize in physics. Hence, it is believed that the initial examination of graphene is actually dramatic [1] compared to several other scientific breakthroughs. Graphene is a two-dimensional nanomaterial known as an "Amazing Material" of

twenty-first century. It features a hexagonal lattice structure made of a sheet of carbon atoms [2]. Apart from two dimension, graphene in zero dimensions as Graphene Quantum Dots (GQDs) (with their outstanding physiochemical properties such as extremely tiny dimension with high surface-to-volume ratio) gains growing attention toward novel applications in energy storage.

Graphene possesses exclusive morphology and multifaceted characteristics [3] and are observed to be stronger than steel, stretchable and almost transparent. With many suitable and beneficial electrical, optical, thermal and mechanical properties including its improved chemical stability, excellent mechanical flexibility, high electrical and thermal conductivity, graphene is at the hub of most energy storage issues and can be used to enhance the usefulness, stability along with functionality of energy storage systems [4]. Mobility explains how fast a carrier moves in a material with an external electric field. Because of the inbuilt atomic thickness and sheet-like structure associated with its electronic, physical and chemical properties, graphene holds high carrier mobility (15,000 $cm^2 \cdot V^{-1} \cdot s^{-1}$) which has gained an enormous research interest in energy harvesting and storage. In addition to high mobility, graphene possesses high conductivity (low resistance). Electron cloud is found to be present above and below each carbon ring in graphene. This generates a continuous π orbital crossways the whole graphene layer. This free movement of electrons through the whole graphene layer makes graphene highly conductive.

2.1 Graphene in Enhancing Performance of Energy Storage Devices

2.1.1 Graphene @ Lithium-Ion (Li-Ion) Batteries

A Li-ion battery is an advanced rechargeable energy storage device. It is made up of cells where lithium ions travel from the cathode to anode in electrolyte for the period of charging as well as discharging. Because of its greater electrical conductivity and larger surface area of 2600 m^2/G, graphene is employed in Li-ion batteries to get better rate performance and stability [5, 6], and it has been seen as a game changer for boosting their performance [7]. In addition, it is interesting to note that graphene has a honeycomb structure and can create a three-dimensional conductive network. This successfully increases the transportation of electron and ion in the electrode. This phenomenon exhibited by graphene is exploited in Li-ion batteries to offer high chemical stability and better electrical conductivity [8].

Lu et al. [9] explored the usage of 3D porous and elastic binder-free Li-ion battery electrodes made of graphene complexes as a trial to overcome the predictable electrode swell and to avoid cyclic stability degradation. The electronic conductivity should be high for a better battery performance. The low Coulombic efficiency of pure graphene limits its use as a direct substitute for lithium-ion battery electrodes. To facilitate this complexity, electron conducting additives are often added to them

to get composite electrode materials so as to develop their electrochemical properties [10]. Zhu et al. [8] highlighted various graphene composites such as lithium metal oxide ($LiMn_2O_4$)-graphene [11], $LiFePO_4$-graphene [12] and $Li_3V_2 (PO_4)_3$-graphene in their review work and they achieved better operating capability with Li-ion batteries. Matching up to $LiFePO_4$, $Li_3V_2 (PO_4)_3$ was identified to be a smart cathode substance for Li-ion batteries [8].

2.1.2   Graphene @ Lithium-Sulfur (Li-Sulfur) Batteries

The Li-sulfur batteries are rechargeable energy storage devices and are famous for their lightweight and elevated specific energy. Even though Li-sulfur batteries are famous for their improved theoretical energy density and cost-effectiveness, they face some issues like short life and poor flexibility. In order to overcome these issues, graphene-based materials came into picture. Graphene, with good conductivity and flexibility, is widely used in Li-sulfur batteries as electrode and inter-layers and accomplished fine flexibility, energy density and higher cycling stability [13] and environmental friendliness. Fang et al. [14] made an extremely porous graphene to host the sulfur and exceedingly conductive graphene to collect the current in Li-sulfur batteries. This cathode yields an elevated opening gravimetric specific capacity of 1500 m Ah g^{-1} and areal specific capacity of 7.5 m Ah cm^{-2}. They identified that this porous graphene has great scope as cathode in more steadfast Li-sulfur batteries.

A completely packed Li-sulfur battery is anticipated to bring a specific energy of 400–600 Wh/kg. This is double times greater than that of Li-ion batteries [15]. Recently, in Chalmers University, a lighter and high-performance Li-sulfur battery with graphene aerogel was designed and the researchers predicted that theoretical energy density of Li-sulfur battery was around 1000–1500 Wh/kg. This is found to be approximately five times higher compared to Li-ion batteries [16]. Tao and his co-workers [17] used facile method to synthesize a cathode by using graphene-sulfur composite material. Here, the graphene showed anchoring effect on sulfur and reduced its loss. They added that as formed graphene conductive network for sulfur-ion batteries really enhanced the battery's Coulombic efficiency in addition to their cycling performance with a discharge capacity of 501 m Ah g^{-1}.

2.1.3   Graphene @ Supercapacitors

Supercapacitors are high-capacity capacitors that can store large quantity of energy. They overpass the crevice among electrolytic capacitors and rechargeable batteries and have a substantially larger capacitance than ordinary capacitors. In 2008, Stoller and group [18] have identified a new carbon-based material known as chemically modified graphene and demonstrated the same in a supercapacitor and reached high electrical conductivity with a better consistent performance. They have obtained the specific capacitance of 2585 F g^{-1} and almost 100% capacitance retention after

20,000 cycles. From the time when Stoller illustrated the first graphene supercapacitor, many researchers have devoted their time to find new graphene-based electrodes for supercapacitors [19].

The role of binders in supercapacitors is crucial since they act as conductive agent and strengthen during the electrode formation. It is worthy to note that different binders can lead to the different characteristics of supercapacitors and it was well supported by a study of Abbas et al. [20]. In an another notable research work, Saeed and his co-workers [21] synthesized a new three-dimensional graphene and molybdenum trioxide in a hybrid film structure. They used this novel material with exclusive structure as a binder-free electrode material for supercapacitors. They were successful in obtaining a significant improvement in specific capacitance ($1503 \, F \, g^{-1}$) along with 96.5% capacitance retention. In view of the fact that the size and structure of a material definitely influence its physiochemical properties, and graphene has been investigated in zero, one, two and three dimensional even as four-dimensional self folding structures as a component for supercapacitors [22]. Among them, three-dimensional graphene-based structures are preferred for their interconnected pore configuration desired for better performance of supercapacitors.

2.1.4 Graphene @ Fuel Cells

A fuel cell is an electrochemical unit which converts the chemical energy of a fuel into electricity as long as fuels are supplied. Even though fuel cells work similar to batteries, they need not be recharged. Fuel cells are accepted as an alluring sustainable and green energy technology to deal with universal energy and environmental issues. Currently, graphene has attracted attention as different components in fuel cells such as in electrodes, electrolytes, fillers, catalysts and conductive materials [23].

Due to the above said versatile and novel characteristics, graphene-based hybrid structures are being used in a broad range of competent and resilient fuel cell energy systems as electrode additive, catalyst and electrolyte membranes [24]. Huang et al. [25] have prepared nitrogen and sulfur doped graphene nanosheets as cathode in fuel cells. Due to their distinguishing structural advantages, the obtained nitrogen and sulfur graphene sheets showed high round-trip efficiencies. Additionally, Huang's research group incorporated platinum nanoparticles with the already prepared nitrogen and sulfur graphene sheets and identified better activity with very good poison tolerance in fuel cells. Microbial fuel cells combine wastewater treatment and chemical conversion directly into electrical energy. Even though, they are considered as one of the vital energy storage applications, they are not produced much because of their high cost. Graphene is projected to assist to overcome the above confrontation by incorporating by means of biocatalysts to build of graphene supported microbial fuel cells. Graphene can either be used as an anode or be used as a cathode to efficiently improve the oxygen reduction reaction [26–28] within fuel cells.

3   Role of Fullerene in Energy Storage

A fullerene is the third major allotrope of carbon. In fullerene, carbon atoms are connected by single and double bonds. They can adapt different shapes and sizes including sphere, tubes and, or many other. After the synthesis of fullerenes in large scale, their outstanding properties like lightweight, conductivity, good tensile strength, high chemical and thermal stability, etc., came into picture [29]. Fullerenes have been made of carbon bunches where 12 pentagons shape their surface [30].

Among other structures, carbon 60 (C60) is recognized as a largely available type of fullerene. This molecule consists of 60 carbon atoms and forms a structure that looks like a soccer ball named as "buckminsterfullerene" and "buckyball" by R. Buckminster Fuller in 1967. Discovery of fullerene was considered to be a milestone in the field of chemistry and fetched the Nobel Prize in 1996 for Curl and his co-workers. Fullerenes possess many useful properties that are suitable for energy storage applications including their exclusive electronic structures and associated electrochemical properties such as high electrical conductivity, good solubility and high electron affinity. The rich redox chemistry of fullerenes helps them to be useful for battery recycling process. In addition, fullerenes have excellent oxidation reaction in energy storage devices. With all these notable qualities, fullerenes have unlocked the gate to useful applications in energy storage devices [31].

3.1   Fullerene in Enhancing Performance of Energy Storage Devices

3.1.1   Fullerene @ Li-Ion Batteries

Fullerene C60 has derivatization that can be controlled easily. It has superior solubility and affluent redox chemistry which makes the fullerene C60 beneficial in the field of rechargeable batteries [32]. Shan et al. [33] explored four C60 molecules with pristine, carboxyl, ester and piperazine C60 functional groups as anode in Li-ion batteries. They observed that carboxyl C60 demonstrated an elevated capacity at a speedy discharge–charge rate of 370 m Ah g^{-1} because of their enhanced lithium-binding ability. Shan and his co-workers have identified that by having the basic C60 electronic and geometric characteristics with proper choice of functional groups can help us to attain extraordinarily improved capacity and rate performance in Li-ion batteries. This is well supported by Ayesha Kausar [34]. She explored that incorporation of suitable functional polymers in fullerene nanocomposites offers mechanical and other superior physical features to them and makes them suitable for energy storage applications including Li-ion batteries.

Fullerenes can be chemically hydrogenated and dehydrogenated reversibly due to their stable molecular structure. In search of better performing, stable anode elements in Li-ion batteries, Loutfy and Katagiri [35] tried several new and better performing

modified fullerene anode materials including hydrogenated fullerenes. They found that the hydrogenated fullerenes are the best choice as anodes for Li-ion batteries showed better performance with the capacity of 2062 mAh g^{-1}. Teprovich et al. [36] also tried hydrogenated fullerenes as anode material in Li-ion batteries by limiting the amount of hydrogen in the active material. The hydrogenated C60 has been identified to possess a steady theoretical capacity of 588 mAh g^{-1}.

3.1.2 Fullerene @ Li-Sulfur Batteries

Since Li-sulfur batteries have high theoretical specific energy and environmental friendliness, they are considered to be one of the most capable power sources. But Li-sulfur batteries face a downside known as polysulfide shuttle effect. The shuttle effect refers to the back and forth diffusion of polysulfide between the anode and cathode, which can result in poor cycling stability and severe anode corrosion in Li-sulfur batteries. Yongling et al. [37] prepared fullerene C60 nanorods and used it as an interlayer material for Li-sulfur batteries, and they were capable of reducing the polysulfide shuttle effect and achieved theoretical capacity of 725 mAh g^{-1} and maximum Coulombic efficiency. Recently, Ramezanitaghartapeh et al. [38] also tried to suppress the unwanted polysulfide shuttle effect and simultaneously to retain the conductivity of the sulfur cathode by using some adsorbents like cyanide as a conductive material. They used B3LYP density functional method to study this fullerene (C60)-cyanide composite as a cathode material for lithium-sulfur batteries, and they found that C60 fullerene has the potential to be a promising carbon-based material for the creation of a cathode for Li-sulfur batteries.

In order to improve the utilization of sulfur in Li-sulfur batteries and lesson the polysulfide shuttle effect, Xiang et al. [39] built fullerene C60-S supra molecular complex as the cathode material for Li-sulfur batteries. Here, almost all of the C60 molecules in the complex offered active sites for the lithium polysulfide adsorption and facilitate their conversion. This also promoted the internal ion transport within the composite cathode.

3.1.3 Fullerene @ Supercapacitors

As we are all aware, supercapacitors combine the properties of capacitors and batteries into a single unit and are deliberately constructed to have an extremely large capacitance. Supercapacitors are preferred in applications that require rapid break open of energy to be released from the storage device. They are also used for rapid charging needs and unlimited, frequent energy storage and discharging applications. Due to their longer lifetime and preferable power qualities, supercapacitors are widely used for portable electronic devices. It is reiterated that being an allotrope of carbon, with several striking qualities, fullerene C60 is considered to be a suitable candidate for energy storage applications including supercapacitors.

Several researches are going on to improve the usage of carbon-based nanomaterials like fullerene in enhancing the energy storage capabilities of supercapacitors. Khan et al. [40] prepared nanoporous C60 fullerene microparticles on carbon cloth and used it as the electrode for supercapacitors. They could find remarkable flexible characteristics and record an outstanding capacitance of 440 F/g and 10,000 cycles of firm life. Khan and his co-workers were able to manage the low energy density hindrance produced in supercapacitors with their as prepared cathode material. Piotrowski et al. [41] synthesized graphene-fullerene hybrid nanomaterials and used them as energy storage materials particularly in supercapacitors. They observed that graphene enclosed with bis-naphthalene C70 fullerene malonate showed 15% higher capacitance than the unmodified graphene.

Bairi et al. [42] fabricated a new nanostructured carbon framework with pores and tried it as an electrode material for the supercapacitors. They can reach good electrochemical capacitance of 286 F g^{-1} and brilliant cyclic stability with almost zero loss of specific capacitance. Fullerene whiskers are thin rods made up of fullerene molecules like C60, C70 or combinations of these molecules. Wang and his group [43] synthesized fullerene C60 whisker with polyaniline emeraldine composite as electrode material for supercapacitors. They observed that as prepared fullerene novel composite effortlessly improved electron transfer efficiency which is considered to be an important requirement for a material to be used in supercapacitors.

3.1.4 Fullerene @ Fuel Cells

Fuel cells, being cost-effective and eco-friendly energy storage devices, are being widely used in many commercial divisions particularly in car industry [44]. Fullerenes find application in fuel cells as an electro-catalyst; they support fuel oxidation at the anode and also used at the cathode for oxygen reduction [45]. They also boost the conductivity and water ingestion in proton conducting membranes of fuel cells. Gao and his colleagues [46] investigated the use of nitrogen-doped C60 fullerene as a cathode catalyst in hydrogen fuel cell and tried to trigger the electro catalytic reactions. They concluded that nitrogen-doped C60 fullerene could serve as an able cathode catalyst for hydrogen fuel cells. In 2017, Noh et al. [47] also used nitrogen-doped fullerenes catalysts in fuel cells and noted an improved catalytic activity.

Benzigar et al. [48] designed a porous, firm and conducting polymerized C60 network with rod-shaped morphology as energy storage materials for fuel cells. They showed notable supercapacitive characteristics. Bhavani et al. [49] prepared bimetallic palladium-tungsten nanoparticles with fullerene-C60 catalyst for high-performance direct alcohol fuel cells. The catalyst showed enlarged electrochemical active surface area, great electrocatalytic activity and elevated poison tolerance limit.

4 Conclusion

As traditional fuel sources become less available, rising energy demand will continue to put a pressure on our ecosystem. In an attempt to reduce our dependence on these sources, we ought to search for alternative energy sources with improved effectiveness and therefore cost-effective energy sources. At the same time, the demand for a more environmentally friendly alternative to fossil fuels has never been more important. This has ignited the minds of present day researchers to go for a huge progress in how to harness and store the energy with the help of smart nanomaterials.

In spite of its many hopeful properties, the major limitation of graphene-based storage devices is that in addition to their high cost, the thickness of graphene-based materials is usually limited to micrometers, which restricts the overall storage capacity of energy storage devices considerably. Apart from high cost and limited solubility, fullerenes cannot be used as an anode material in energy storage applications in their pure form. Additional modifications such as doping and chemical modifications are needed to achieve high-performance fullerene-based anode materials in energy storage devices. Regardless of the above shortcomings, efficiency, versatility and flexibility of carbon, the powerful, environment friendly and largely available element on globe with multifunctional capabilities grabbed unbelievable attention in different energy storage devices such as batteries, solar cells, fuel cells and supercapacitors, etc. Engineering the carbon-based nanomaterials such as graphene, graphene oxide, reduced graphene oxide, carbon nanotubes, carbon-based quantum dots, fullerenes, etc., appropriately for sustainable energy storage and remarkable conversion ability embraces the promise of creating new path for their future development.

This review gives a comprehensive summary on the role of most resourceful carbon nanomaterials; graphene and fullerenes in efficiently increasing the competence and dependability of four energy storage devices: lithium-ion, lithium-sulfur batteries, supercapacitirs and fuel cells. This study highlights the characteristics and adaptability of these carbon-based nanomaterials which can be used as a potential and promising future materials in different dimensions such as electrodes, catalysts and electrolytes in energy storage devices.

References

1. Zhen Z, Zhu H (2018) Structure and properties of graphene. In: Graphene fabrication, characterizations, properties and applications. Academic Press, pp 1–18
2. Tiamduangtawan P, Saenboonruang P (2019) Environmental-friendly synthesis of reduced graphene oxide (rGO) using gamma irradiation. J Phys Conf Ser 1285:012034. https://doi.org/10.1088/1742-6596/1285/1/012034
3. Rao N, Singh R, Bashambu L (2021) Carbon-based nanomaterials: synthesis and prospective applications. Mater Today Proc 44:608–614
4. Taylor-Smith K (2021) A review of graphene in energy storage devices. Azonano Online Publications. https://www.azonano.com/article.aspx?ArticleID=5791

5. Chen X, Tian Y (2021) Review of Graphene in cathode materials for lithium-ion batteries. Energy Fuels 35:3572–3580
6. Luo R, Lv W, Wen K, He W (2016) Overview of Graphene as anode in lithium-ion batteries. J Electron Sci Technol 16:57–68
7. Chang H-H, Ho T-H, Yu-Sheng Su (2021) Graphene-Enhanced battery components in rechargeable lithium-Ion and lithium metal batteries. J Carbon Res 7:65
8. Zhu J, Duan R, Zhang S, Jiang N, Zhang Y, Zhu J (2014) The application of graphene in lithium ion battery electrode materials. Springer Plus, vol 3, p 585. https://doi.org/10.1186/2193-1801-3-585
9. Lu XY, Jin XH, Sun J (2015) Advances of graphene application in electrode materials for lithium ion batteries. Sci China Technol Sci 58:1829–1840
10. Mazar Atabaki M, Kovacevic R (2013) Graphene composites as anode materials in lithium-ion batteries. Electron Mater Lett 9:133–153
11. Zhao X, Haynera CM, Kung HH (2011) Self-assembled lithium manganese oxide nanoparticles on carbon nanotube or graphene as high-performance cathode material for lithium-ion batteries. J Mater Chem 21:17297–17303
12. Kobayashi G, Nishimura S-I, Park M-S, Kanno R, Yashima M, Ida T, Yamada A (2009) Isolation of solid solution phases in size-controlled $LixFePO_4$ at room temperature. Adv Func Mater 19:395–403
13. Yang T, Xia J, Piao Z, Yang L, Zhang S, Xing Y, Zhou G (2021) Graphene-Based materials for flexible lithium-sulfur batteries. ACS Nano 15:13901–13923
14. Fang R, Zhao S, Pei S, Qian X, Hou P-X, Cheng H-M, Liu C, Li F (2016) Toward more reliable lithium-sulfur batteries: an all-graphene cathode structure. ACS Nano 10:8676–8682
15. Lin D, Liu Y, Cui Y (2017) Reviving the lithium metal anode for high-energy batteries. Nat Nanotechnol 12:194–206
16. Clemens K (2019) Graphene could improve lithium sulfur batteries. Continuing Education Center (CEC). https://www.designnews.com/electronics-test/graphene-could-improve-lithium-sulfur-batteries
17. Tao Z, Xiao J, Yang Z, Wang W (2019) Graphene/Sulfur@Graphene composite structure material for a lithium-sulfur battery cathode. J Nanomaterials 2019. Article ID 6480236. https://doi.org/10.1155/2019/6480236
18. Stoller MD, Park S, Zhu Y, An J, Ruoff RS (2008) Graphene-Based ultracapacitors. Nano Lett 8:3498–3502
19. Velasco A, Ryu YK, Boscá A, Ladrón-de-Guevara A, Hunt E, Zuo J, Pedrós J, Calle F, Martinez J (2021) Recent trends in graphene supercapacitors: from large area to microsupercapacitors. Sustain Energy Fuels 5:1235–1254
20. Abbas Q, Pajak D, Frąckowiak E, Béguin F (2014) Effect of binder on the performance of carbon/carbon symmetric capacitors in salt aqueous electrolyte. Electrochima Acta 140:132–138
21. Saeed G, Kumar S, Kim NH, Lee JH (2018) Fabrication of 3D graphene-CNTs/α-MoO3 hybrid film as an advance electrode material for asymmetric supercapacitor with excellent energy density and cycling life. Chem Eng J 352:268–276
22. El-Kady MF, Shao Y, Kaner RB (2016) Graphene for batteries, supercapacitors and beyond. Nat Rev Mater 1:16033. https://doi.org/10.1038/natrevmats.2016.33
23. Su H, Hu YH (2020) Recent advances in graphene-based materials for fuel cell applications. In: Energy science and engineering. Wiley Online Library. https://doi.org/10.1002/ese3.833
24. Iqbal MZ, Siddique S, Khan A, Haider SS, Khalid M (2020) Recent developments in graphene based novel structures for efficient and durable fuel cells. Mater Res Bull 122:110674. https://doi.org/10.1016/j.materresbull.2019.110674
25. Huang H, Zhu J, Zhang W, Tiwary CS, Zhang J, Zhang X, Jiang O, He H, Wu Y, Huang W, Ajayan PM, Yan Q (2016) Controllable codoping of nitrogen and sulfur in graphene for highly efficient li-oxygen batteries and direct methanol fuel cells. Chem Mater 28:1737–1745
26. ElMekawy A, Hegab HM, Losic D, Saint CP, Pant D (2017) Applications of graphene in microbial fuel cells: the gap between promise and reality. Renew Sustain Energy Rev 72:1389–1403

27. Sathesh A (2020) Assessment of environmental and energy performance criteria for street lighting tenders using decision support system. J Electron Inf 02:72–79
28. Bal G, Eyimaya SE (2019) Design of wind turbine system integrated with battery energy storage system. J Electr Eng Autom (EEA) 02:72–82
29. Rondags A, Yuen Y, Jonkman MF, Horváth B (2016) Fullerene C60 with cytoprotective and cytotoxic potential: prospects as a novel treatment agent in Dermatology? Experimental Dermotology. Wiley Online Library. https://doi.org/10.1111/exd.13172
30. Mishra R, Militky J (2019) 3—Carbon-based nanomaterials. Nanotechnology in textiles: theory and application. In: The textile institute book series. Woodhead Publishing, pp 163–179. https://doi.org/10.1016/B978-0-08-102609-0.00003-1
31. Fang Y, Bi C, Wang D, Huang J (2017) The functions of fullerenes in hybrid perovskite solar cells. ACS Energy Lett 2:782–794
32. Jiang Z, Zhao Y, Lu X, Xie J (2021) Fullerenes for rechargeable battery applications: Recent developments and future perspectives. J Energy Chem 55:70–79
33. Shan CS, Yen HJ, Wu K, Lin Q, Zhou M, Guo X, Wu D, Zhang H, Wu G, Wang HL Functionalized fullerenes for highly efficient lithium ion storage: structure-property-performance correlation with energy implications. Nano Energy 40:327–335
34. Kausar A (2022) Fullerene reinforced polymeric nanocomposites for energy storage-status and prognoses. Front Mater. https://doi.org/10.3389/fmats.2022.874169
35. Loutfy RO, Katagiri S (2002) Fullerene materials for lithium-ion battery applications. In: Perspectives of fullerene nanotechnology. Springer, Dordrecht, pp 357–367. https://doi.org/10.1007/0-306-47621-5_32
36. Teprovich JA, Weeks JA, Ward PA, Tinkey SC, Huang C, Zhou J, Zidan R, Jena P (2019) Hydrogenated C60 as high-capacity stable anode materials for Li ion batteries. ACS Appl Energy Mater 2:6453–6460
37. An Y, Tian Y, Fei H, Zeng G, Duan H, Zhang S, Zhou P, Ci L, Feng J (2018) Facile preparation of fullerene nanorods for high-performance lithium-sulfur batteries. Mater Lett 228:175–178
38. Ramezanitaghartapeh M, Achazi AJ, Soltani A, Miró P, Mahon PJ, Hollenkamp AF, Musameh M (2022) Sustainable cyanide-C60 fullerene cathode to suppress the lithium polysulfides in a lithium-sulfur battery. Sustain Mater Technol 32:e00403. https://doi.org/10.1016/j.susmat.2022.e00403
39. Xiang J, Shen W, Guo Z, Meng J, Yuan L, Zhang Y, Cheng Z, Shen Y, Xing Lu, Yunhui Huang (2021) A supramolecular complex of C60–S with high-density active sites as a cathode for lithium–sulfur batteries. Angewandte Chemie 60:14313–14318
40. Khan AJ, Hanif M, Javed MS, Hussain S, Liu Z (2019) Synthesis, characterization and charge storage properties of C60-fullerene microparticles as a flexible negative electrode for supercapacitors. J Mater Sci Mater Electron 30:8568–8576
41. Piotrowski P, Fedorczyk A, Grebowski J, Krogul-Sobczak A (2022) Functionalization of graphene by π−π stacking with C60/C70/Sc3N@C80 fullerene derivatives for supercapacitor electrode materials. J Carbon Res 8:1–15
42. Bairi P, Maji S, Hill JP, Kim JH, Ariga K, Shrestha LK (2019) Mesoporous carbon cubes derived from fullerene crystals as a high rate performance electrode material for supercapacitors. J Mater Chem A 7:12654–12660
43. Wang H, Yan X, Piao G (2017) A high-performance supercapacitor based on fullerene C60 whisker and polyaniline emeraldine base composite. Electrochim Acta 231:264–271
44. Chen TW, Kalimuthu P, Veerakumar P, Lin KC, Chen SM, Ramachandran R, Mariyappan V, Chitra S (2022) Recent developments in carbon-based nanocomposites for fuel cell applications: a review. Molecules 27:761. https://doi.org/10.3390/molecules27030761
45. Coro J, Suárez M, Silva LSR, Eguiluz KIB, Salazar-Banda GR (2016) Fullerene applications in fuel cells: a review. Int J Hydrogen Energy 41:17944–17959
46. Gao F, Zhao G-L, Yang S, Spivey JJ (2013) Nitrogen-Doped fullerene as a potential catalyst for hydrogen fuel cells. J Am Chem Soc 135:3315–3318
47. Noh SH, Kwon C, Hwang J, Ohsaka T, Kim BJ, Kim TY, Yoon YG, Chen Z, Seo MH, Han B (2017) Self-assembled nitrogen-doped fullerenes and their catalysis for fuel cell and rechargeable metal–air battery applications. Nanoscale 9:7373–7379

48. Benzigar MR, Joseph S, Ilbeygi H, Park D-H, Sarkar S, Chandra G, Umapathy S, Srinivasan S, Talapaneni SN, Vinu A (2017) Highly crystalline mesoporous C60 with ordered pores: a class of nanomaterials for energy applications. Angew Chem 57:569–573

49. Bhavani KS, Anusha T, Kumar JVS, Brahman PK (2020) Enhanced electrocatalytic activity of methanol and ethanol oxidation in alkaline medium at bimetallic nanoparticles electrochemically decorated fullerene-C60 nanocomposite electrocatalyst: an efficient anode material for alcohol fuel cell applications. Electroanalysis. 33:97–110

A Robust Ensemble Learning Model for Fine-Grained Detection of Cyber Harassment

S. Abarna, J. I. Sheeba, S. Jayasrilakshmi, and S. Pradeep Devaneyan

Abstract Due to innovative growth in cyberspace and portable penetration, kids in India are at risk of cyber harassment. A review of 174 central graders in Delhi exposed that a total of 8% pandered in cyber harassment and 17% described being offended by such acts. However, the occurrence of in-person harassment, hostility, and discrimination is also happening. Amid all the digital platforms, Instagram positions developed with extreme cyber harassment. Over the preceding span, it brought substantial developments in the grounds of machine learning (ML) which have been efficaciously functional in fields associated with cyber harassment findings, such as buzz recognition, sentimentality study, and forged broadcast discovery. In machine learning, methods are provided for detective work and the classification of online harassment. Researchers have conducted experiments using comparable datasets. To build an ensemble learning model for detecting and classification different categories of online harassment from social media platforms. In our proposed work, a robust method of detecting online harassment (cyberbullying) on the Instagram dataset is used. The attributes of abusive words are initially analyzed from feature selection and pre-trained word embedding language models like BERT and ELMO. The harassment words are detected using unsupervised machine learning techniques such as association rule classifier, latent semantic analysis (LSA), and clustering technique. Then, a novel ensemble typical model is planned for categorizing the different types

S. Abarna (✉) · J. I. Sheeba · S. Jayasrilakshmi
Department of Computer Science and Engineering, Puducherry Technological University, Puducherry, India
e-mail: abarna@pec.edu

J. I. Sheeba
e-mail: sheeba@pec.edu

S. Jayasrilakshmi
e-mail: jayasrilakshmis97@pec.edu

S. Pradeep Devaneyan
Department of Mechanical Engineering, Sri Venkateshwaraa College of Engineering and Technology, Puducherry, India

of online harassment using extreme gradient boosting (XGBoost) learning method. Hence, our robust method of ensemble model for detecting and classification of online harassment provides much better results with high accuracy and lesser loss function.

Keywords Cyberbullying · Bidirectional encoder representations from transformers · Ensemble learning · Extreme gradient boosting · Word2vec · Natural language processing · Embeddings from language model · Frequent pattern growth · Insulting vocabulary · Latent semantic analysis

1 Introduction

The US Nationwide Crime Deterrence Convention explains cyberbullying as "harassment through digital devices such as tablets, computers, smartphones, and laptops and can occur over gaming platforms, chat rooms, and social media" [1]. Affording to the law, cyber harassment has 3 foremost mechanisms: The practice of severe confrontations, the purpose to humiliate, pursue, and offense the object, bears the overhead via data and statement knowledge and/or digital communication technology. The furthermost public causes of cyber harassment in digital platform sites such as Instagram, Snapchart, Facebook and Twitter are facing very high risk. Instantaneous messaging amenities such as WhatsApp, SMS, and Email. Cyberbullying takes various procedures concluded period. Here are approximately public forms of cyberbullying [2, 3]:

1. Exclusion: Deliberately excluding a specific from a group in addition to posting malicious comments/communications about her.
2. Harassment: Sending threatening, abusive, or disrespectful messages.
3. Impersonation/masquerading: Creating a fictitious identity in order to harm someone's reputation by publicly revealing true or false information about them.
4. Cyberstalking: Following a person online and transferring electronic messages or emails in an attempt to terrify, maltreat, or bully him.
5. Flaming: Using nasty language against someone in emails, text messages, or chat rooms.
6. Trolling: Intentionally injuring someone by making derogatory or offensive comments.
7. Framing: Using a person's social media accounts to post inappropriate stuff in order to harm her reputation.

India's cyberbullying: [4] Among the top world countries, India stands at the 3rd position in the cyber harassment ill-treatment, which is not astonishing given the increasing quantity of users, most of them are treated with vast consequences. Children Rights and You (CRY) has made a poll which is a non-profit organization that shows 9.5% of adolescents in the Delhi region are intimidated by digital platforms, and among those children, more than half the population are not reporting the incident to the close relations even o their friends. Symantec made a survey among

8 out of 10 people who are affected by the victims of various sorts of cyberbullying. In [5], approximately 63% of these people have experienced online abuse or harassment, and 59 percent have had their reputations ruined by phony gossip and rumors. People in India are frequently subjected to cyberbullying, which includes: individuals on the Internet calling them terrible names, propagating false rumors, and receiving filthy images. People threaten them physically; people harass or message them unnecessarily; Commenting means things about someone's pictures or posts. Cyber harassment can have a wide range of negative consequences for a child. Some of them are:

- Lowering self-esteem.
- The proclivity to withdraw from others and spend time alone.
- Reluctance to provide parents or family members access to their phones or computers.
- Alterations in eating and sleeping habits.
- Fear of being revealed and humiliated.
- Making up excuses to avoid going to school.
- Skin injuries indicate self-harm; attempting to conceal the injuries by wearing clothing that covers the entire body.
- Sudden weight loss or changes in physical appearance
- Personality changes, including increased outbursts of rage, melancholy, and weeping spells.
- Drop in academic, athletic, and extracurricular activity performance.

Over the past period of time, researchers have developed many verdict strategies for cyberbullying. Even while those methods offer a respectable detection rate for cyberbullying, there are still some issues. We can identify linguistic forms castoff by intimidators and their sufferers using machine learning, and application rules to automatically distinguish cyberbullying content. Some novel techniques for identifying cyberbullying have emerged as a result of recent rapid breakthroughs in machine learning and natural language processing (NLP). It is a theory-based computing technique that emphasizes on the automatic analysis and expression of human languages and is used in a wide range of applications, including sequence generation, machine translation, and recommendation systems [6]. Supervised and unsupervised learning are the most commonly utilized strategies. To study text and subsequently classify emotion, supervised approaches mostly use machine learning technologies such as support vector machine (SVM), Naive Bayes method, and maximum entropy method. The unsupervised method focuses on analyzing emotional words, grammar, and semantics in the text, and then extracting statistical features from the text to achieve emotion categorization. One of the most significant aspects of natural language processing is the ability to accurately translate words into computer-readable languages. Traditional word embedding algorithms like Word2Wec and GloVe store various semantics meanings of the same word embedding vector when handing out polysemous words, construction it unbearable to reliably get the evidence provided by the word when performing text tasks. The goal of machine learning (ML) is to train classifiers so that they can automatically predict the category of future

texts. There are two widely used groups of conversation plotting to find numerical vector representations of documents: traditional word2vec, Bag of Words (BOW) methods, doc2vec, GloVe, and fast text. For this purpose, NLP cyberbullying detection researchers looked into analytical assets part-speech data, n-grams, and sentimentality data created on profane lexicons (with and without TF-IDF weighting). To summarize, global vectors for word representation (GloVe), Word2Vec, and term frequency-inverse document frequency (TF-IDF) are some of the common word representation strategies utilized and proved to increase classification accuracy. Figure 1 shows the different word embedding techniques used in machine learning classifiers. There are many methods for detecting online harassment using machine learning techniques but with certain limitations: Use of a single classifier may have its limitations which results in low performance, imbalance of dataset, detection of variants of harassment words are not considered, buzzwords are increasing. Hence, the collection of new abusive words should be increased.

The proposed approach uses an ensemble strategy for detecting and classifying cyber harassment in the Instagram text comments dataset in this research. Instagram is a social media platform in which users can share images followed by their corresponding comments either publicly or privately. The foremost goal line of the proposed work is to build an ensemble model for detecting and classification of different categories of cyber harassment by making use of machine learning classifiers. Deep word embedding techniques will be used to preprocess the raw data and extract the features. The following is the format of this paper: The background and interrelated works are discussed in Sect. 2, the suggested context is deliberated in Sect. 3, the results of the survey are discussed in Sect. 4, and the conclusion part in Sect. 5.
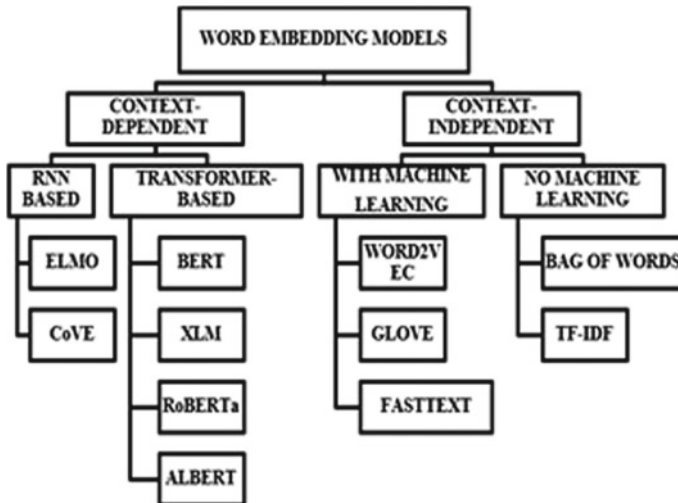
Fig. 1 Taxonomy of word embedding methods

2   Background and Related Work

Many research studies have been conducted over the last decade on cyber harassment detection in order to control or reduce abuse in the social network community. With the rapid growth in the research field of cyber harassment, many machine learning techniques for identifying harassment on social network platforms have been proposed.

2.1   Text Representation Word Embedding Models

To assess the morphology of the cyberbullying text, a pre-trained language model called the fast text with word similarity (FTSW) [6] framework is used. To determine how similar words and associated vocabularies are the Word2vec model and cosine similarity is used. The fast text approach then examines the relationship between contextual texts to determine whether there are any hidden bullying phrases in the text. The static embedding model, similar to the skip-gram model, is improved using GCN to add context syntactic information. The BERT, contextualized embedding model, is used which includes features other than syntactic and surface. The BERT [7] is an encoder with a manifold bidirectional transformer. Thus, on a variety of tasks, Skip-gram embeddings with BERT outperform embeddings with GCN enhancements. For Chinese text, the analysis of sentiment in the model is based on Elmo and a recurrent neural network (Elmo-RNN) is used to solve the problem of textual polysemous words combined with context. The model's time cost increases due to the complication of the neural network model. Elmo in addition to BERT are language models that have been pre-trained. The BERT model is described in detail in order to prepare the various multi-task learning scenarios using context-related datasets. Embeddings from language model (Elmo) investigates the syntax and semantics of words as well as their variation across linguistic cases. There is no sentence structure or lettering agreement in control supply-related text, and sentiment-related data is scattered throughout the text, according to a multi-label text cataloging typical created on Elmo and the attention mechanism for the sentimentality organization task on Kaggle's toxic reference organization dataset. Despite recent developments in contextualized linguistic model-based embeddings, still word embeddings remain a key initial idea in BioNLP study and application, particularly in low-resource frameworks and verbal semantics studies.

2.2 Machine Learning Methodologies in Cyber Harassment Detection

Cyberbullying has been identified using machine learning approaches. For detecting cases of cyberbullying, popular classification techniques such as KNN, random forest, logistic regression, Naive Bayes, linear support vector classifier, and decision tree have been proposed using Twitter datasets. This research is limited to tweets and data in the English language. Using fuzzy logic and a genetic algorithm, an effective detection approach can recognize the flaming, terrorism, harassment, and racism as examples of cyberbullying terms that can be seen in social media [1]. The form spring dataset cannot be utilized on any other social media network because it is used. A technique for unsupervised cyberbullying detection is developed to alleviate the limitations of time-expensive data labeling [8]. It is made up of two primary components: (a) Gaussian mixture model-based multi-task learning network and (b) learning network. The analysis of the temporal characteristics of cyberbullying behaviors is not considered. The data on social media is frequently skewed. To balance the dataset, Gaussian mixture model (GMM) and a multi-class sentiment classification were utilized as super-sampling approaches. For Memotion analysis, a convolutional neural network model was castoff to determine the intrinsic properties of the visual data. Due to the memory constraints, this model only uses photos with a resolution of 128×128 pixels. The introduction of social media blogging has resulted in an increase in web data. Singular value decomposition (SVD) is used to activate latent semantic analysis (LSA). In a separate experiment, the topic modeling with latent Dirichlet allocation (LDA) is used. Gaussian mixture model (GMM), k-nearest neighbors (KNN), and support vector machine (SVM) were adjusted and examined for their capacity to forecast successful transfer of embryo using cross validation. Random forests (RF), k-nearest neighbor (KNN), J48 (Java version of C4.5 algorithm, support vector machine (SVM), neural networks (NN), and Naïve Bayes (NB) are the most frequently used ML algorithms in the cyberbullying domain [3]. Around 43% of students in the United States were bullied on social media. The research [9] uses a convolutional neural network (CNN) and Naïve Bayes (NB) classifier to detect cyberbully terms. The accuracy is calculated by classifying the output from the Instagram dataset into cyberbully and non-cyberbully words.

2.3 Ensemble Model for Cyber Harassment Detection

Boosting is an ensemble technique where the training dataset for each classifier model increasingly focuses on the misclassified by previously generated classifiers. To detect offensive or non-offensive texts from a Twitter dataset, researchers used two-ensemble-based voting models. On a dataset taken from Twitter, three ensemble models and four machine learning classifiers were used along with two different feature extraction approaches and multiple n-gram analyses. An ensemble method

of these machine learning algorithms is employed to improve the accuracy alongside other performance measures. The model has categorized the data into two groups only hence multi-class classification is not done. When compared to keyword-based, rule-based approaches, using data mining (DM) and data retrieval (DR) for hate speech recognition is substantially more effective [10]. The problem benefits from the use of various complex and unpredictable because of the use of latent semantic analysis (LSA) to reduce dimensionality. Almost all cyberbullying detection models on social media platforms are only detection-based with no recourse to preventive actions. From the above survey, Sect. 2.1 explains various text representation models including the conventional method of representing the given text in a machine understandable vector format. Section 2.2 explains machine learning methodologies for harassment detection including all the supervised machine learning techniques. But the social media platform includes many natural language comments which lack annotated data samples. Section 2.3 explains the ensemble model for cyber harassment detection including multi-label classification with separate binary classified results. Comparing all the classification algorithms, the support vector machine works well to give higher accuracy. But it can predict only the categories mentioned in the training dataset, whereas other new types cannot be classified [11].

3 Proposed Work

In our proposed framework, the text data is collected and preprocessed. The features are extracted by various mechanisms suitable for the model. The extracted features are detected and classified using unsupervised machine learning techniques. The results from the different classifiers are ensembled to build a strong model. Finally, the model is evaluated by various performance metrics.

3.1 Exploration About the Dataset

In this proposal work, we plan to use one of the crucial social network platforms called Instagram where the harassment had increased.

Instagram: It is a public mass media platform that permits handlers to share, like, and comment on images. In [12], using a snowball sampling method, they have identified 25 K Instagram user ids with public profiles. These user profiles comprise our complete set of typical Instagram handlers' text information. For each and every public Instagram user, the collected profile data includes only their last 150 associated comments. Among the five social media networks with the maximum proportion of users reporting online abuse is Instagram.
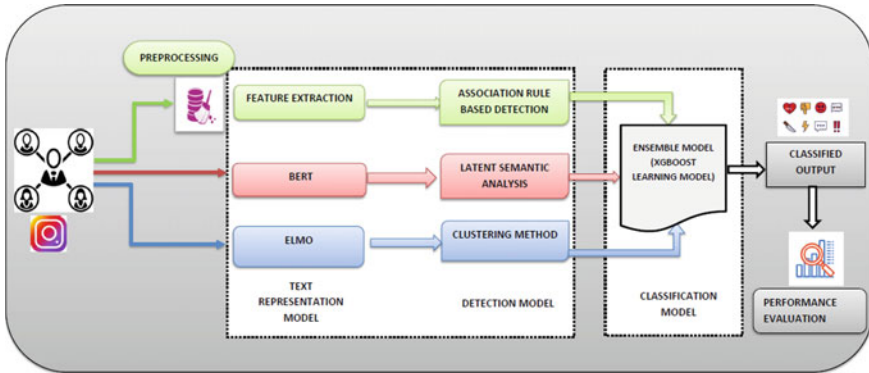
Fig. 2 Architecture of an ensemble model for detecting and classification of online harassment

3.2 Architecture Diagram

In the above Fig. 2, the text comments from Instagram social media platform are collected. And it is preprocessed by various mechanisms. Word embedding techniques are used for representing all the words in vector space. These vectors are used to create dense word embeddings, where the corpus is given without any label information using word2vec. Hence, a type of Bag of words (BOW) method called the skip-gram model is used to analyze the collection of words in a training corpus, to find the cosine similarity of the extracted features above the threshold value. To find the position and order of the given text, bidirectional encoder representations from transformers (BERT) word embedding technique is applied to the input data. The embedding language model (ELMO) is used to encompass the contextual features (semantic) and polysemy of the input text. The features extracted from conventional methods and pre-trained language models are detected using unsupervised machine learning algorithms such as association rule classifier, latent semantic analysis (LSA), and clustering method. The results from all the unsupervised algorithms are ensembled using the XGBoost learning model. This boosting model will neglect the limitations of each detector and build a strong classifier. The harassment words are classified into different categories. Finally, the ensemble model is evaluated by various performance metrics.

3.3 Modules of the Proposed Framework

Our proposed framework is divided into four modules. They are Detection using conventional embedding(M1), detection using transformer encoder(M2), detection using contextual language embedding(M3), and integration module using ensemble learning.
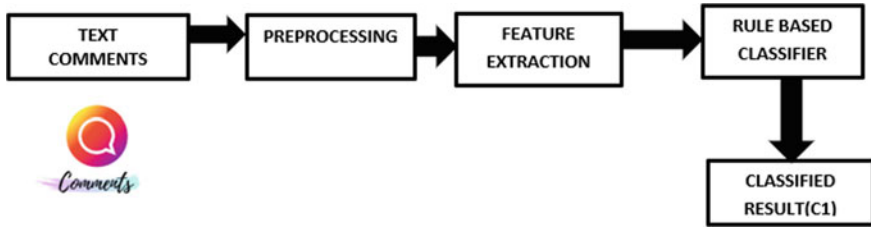
Fig. 3 Detection using the convolutional embedding

Module 1: Detection using the conventional embedding

In this module, Fig. 3, the raw text comments are given as input. It is preprocessed using tokenization and relationship extraction. The stop words are removed. The features are extracted by finding the similarity between words, concordance, and intent detection mechanism. The extracted features are detected using rule-based association techniques to detect the harassment words.

Module 2: Detection using transformer encode

In this module, Fig. 4, the raw data is directly given to the pre-trained language model called bidirectional encoder representations from transformers (BERT) to represent the given words in a way that preserves their semantic relationships and word order in the text. The vector representation of the given feature is detected using latent semantic analysis. Latent semantic analysis (LSA) is used for mining and representing the contextual-usage sense of words in a large corpus of text for acquiring knowledge. It has the ability to extract and represent meaning. Only raw text is used as input, which is then parsed into words that are identified by distinctive character strings and divided into meaningful passages or samples like sentences or paragraphs.

Module 3: Detection using contextual language embedding

In this module, Fig. 5, the preprocessed data is given to pre-trained language embedding called Embeddings from language models (ELMO) to represent the contextual features of the input text. The word vectors are detected using clustering techniques.
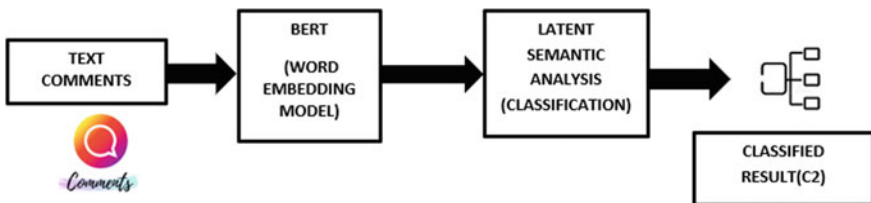
Fig. 4 Detection using transformer encode
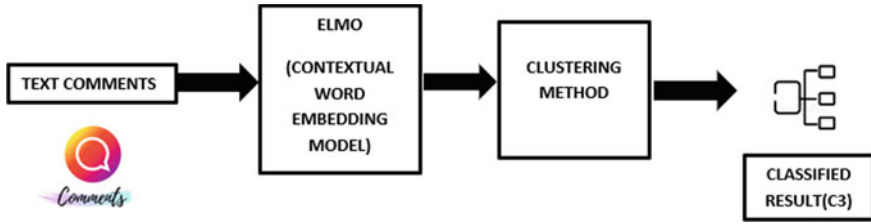
Fig. 5 Detection using contextual language embedding
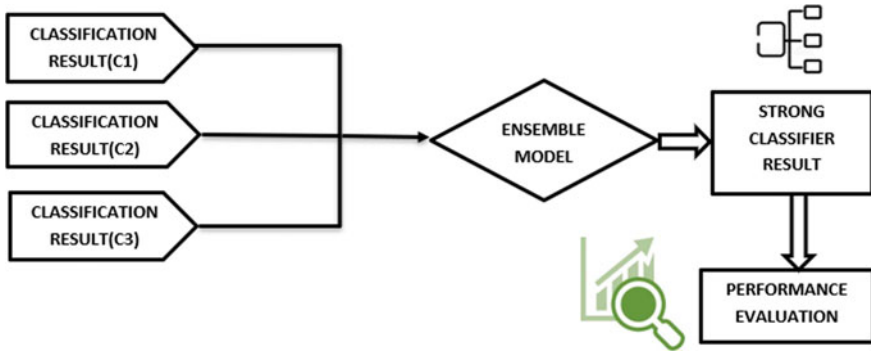
Fig. 6 Ensemble the results from all the classification models

In this clustering technique, to find all kinds of abusive words, Gaussian mixture model is used.

Module 4: Integration module using ensemble learning

In this module, Fig. 6, the results from all the detection models are combined using extreme gradient boosting (XGBoost) model to build a strong ensemble model. XGBoost is developed with efficiency, adaptability, and mobility in mind. Additionally, it speeds up memory use and reduces processing times. The learning function enables softening of final weight gains and avoids over-fitting. During each stage in an ensemble, weights are assigned for each classifier and the results are added sequentially that correct the predictions made by previous model outputs. Different categories of online harassment are classified.

3.3.1 Performance Evaluation

The efficacy of a proposed model can be investigated in this study by employing a variety of evaluation measures to determine how well the model distinguishes cyberbullying and non-cyberbullying. The metrics used in the proposed work are as follows:

Accuracy is measured as the proportion of actual detected cases to total cases and it has been used to evaluate cyberbullying prediction models.

$$Accuracy = \frac{(X1 + Y1)}{(X1 + A2 + Y1 + B2)} \tag{1}$$

From Eq. (1), it states that *X1* means true positive class, *A2* denotes false positive, *Y1* is a true negative class, and *B2* is a false negative. From Eq. (2), **Precision** determines the percentage of relevant comments among true positive (*X1*) and false positive (*A2*) comments that belong to a specific group.

$$Precision = \frac{X1}{(X1 + A2)} \tag{2}$$

From Eq. (3), The ratio of retrieved relevant comments to the total number of relevant comments is calculated by **Recall**.

$$Recall = \frac{X1}{(X1 + B2)} \tag{3}$$

From Eq. (4), **the F_1 measure** enables the combination of precision and recall into a single measure that captures both the properties.

$$F_1 = \frac{(2 * Precision * Recall)}{(Precision + Recall)} \tag{4}$$

The **Receiver Operating Characteristic curve (ROC curve)** is a chart that shows the performance measure and capability of a clustering model at all clustering thresholds. This curve represents the relationship between two parameters: (1) The synonym for the recall is true positive rate (TPR) and is defined as TPR $= X1/X1 + B2$. (2) False positive rate (FPR) is defined as FPR $= A2/A2 + Y1$. TPR is also called **sensitivity**, while TNR is called **specificity**. FPR value is calculated via the relation FPR $= 1 -$ specificity.

Area Under the ROC Curve (AUC) is a measurement of the entire two-dimensional area beneath the ROC curve. It provides an overall performance value across all possible clustering thresholds. It is defined as the likelihood that the random positive example is higher than a random negative example in a rank model.

4 Survey Results

Figure 7. shows the most recent online environment where people experience cyber harassment by percentage. Social media (75%) remains the furthermost usually cited online site where harassment takes place. By contrast, a much smaller percentage

THE MOST RECENT ONLINE ENVIRONMENTS WHERE PEOPLE EXPERIENCE CYBER HARASSMENT
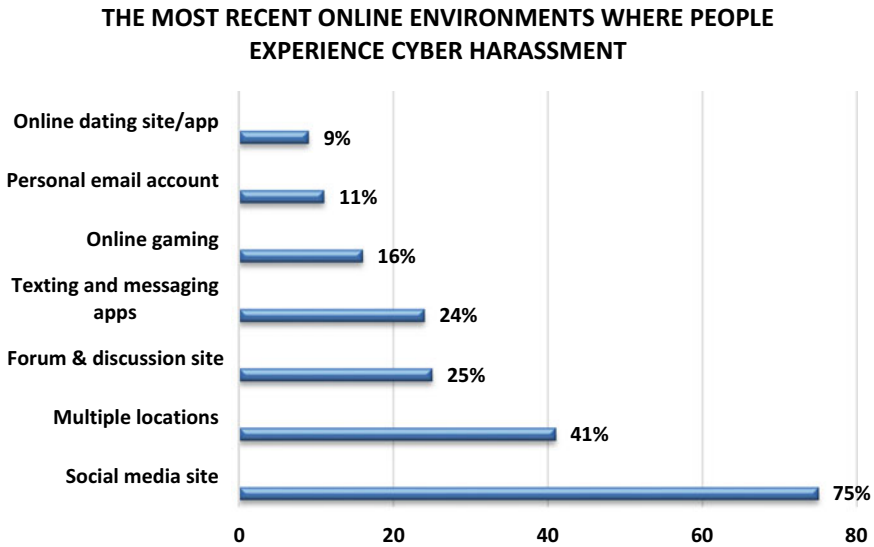
Fig. 7 Most recent online environments where people experience cyber harassment

mentioned texting or messaging apps (24%) or online forums or discussion sites (25%) as the site where their most recent involvement occurred. In total, 41% of targets of online harassment experience more than one online environment.

Figure 8 shows the main reasons for people being cyberbullied. The bully harasses the victim much on their appearance such as dark and white people with 61%, based on their academic achievements, it is with 17%, based on race and sexuality rate of 15% remains the same. Apart from this, there are also other hidden reasons for threatening the people which contribute 12%.

Figure 9 shows the different age groups of people experiencing various forms of online harassment. Among all, offensive name-calling remains at the top with 51% below 30 age group. People with age groups above 50 are affected with a lesser percentage of sexual harassment. The middle age group people between 31 and 40 are affected with half-percentage more than 30%. Thus, younger age people are affected by different types of online harassment [5].

5 Conclusion

In this work, we directed a standardized works survey on automatic online harassment recognition. The provocation of this area of study is to aid in the prevention of cyber harassment and its adverse significance which can include low self-respect, depression, and even self-destruction. Hence, we have proposed an ensemble model for classifying different categories of online harassment using different unsupervised

MAIN REASONS FOR PEOPLE BEING AFFECTED BY CYBERHARASSMENT
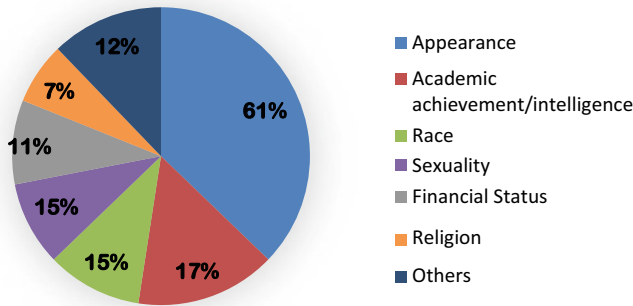
Fig. 8 Real causes of cyber harassment faced by victims

DIFFERENT AGE GROUP PEOPLE EXPERIENCING ANY FORM OF HARASSMENT ONLINE
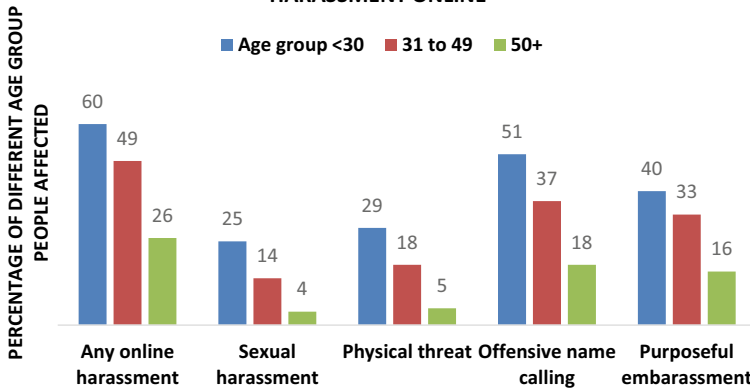
Fig. 9 Different age groups of people experiencing various forms of online harassment

machine learning techniques. It includes many preprocessing and feature extraction methods for extracting abusive words. The pre-trained word embeddings language models are used for comparing it with the conventional method. Different machine learning algorithms are used to detect and classify harassment. These outcomes can help to prevent the issues in online environments with the intention described in the survey results.

References s

1. Maheshwari R (2020) IndiaSpend.com, 'cybercrimes cases in India. https://scroll.in/author/18581
2. Parent Circle team (2020) Cyberbullying: Laws and Policies in India.https://www.parentcircle.com/cyberbullying-laws-and-policies-in-india/article
3. Elsafoury F, Katsigianni S, Pervez Z, Ramzan N (2021) When the timeline meets the pipeline: a survey on automated cyberbullying detection. IEEE Access. https://doi.org/10.1109/ACCESS.2021.3098979,July
4. Unique law (2021) Cyber-bullying in India and applicable laws.
5. Baig E (2021) Pew report: 40% of Americans have experienced online harassment and it is getting more severe. In: Magid L (ed) Connect safely, Jan 2021
6. Wang K, Cui Y, Hu J, Zhang Y, Zhao W, Feng L (2020) Cyberbullying detection, based on the fasttext and word similarity schemes. In: ACM transactions on Asian and low-resource language information processing, vol 20, no 1, Article 6,15 p. https://doi.org/10.1145/3398191
7. Kuyumcu B, Aksakalli C (2019) An automated new approach in fast text classification (fastText): a case study for Turkish text classification without pre-processing. In: Researchgate. https://doi.org/10.1145/3342827.3342828
8. Liu W, Wen B, Gao S, Zheng J, Zheng Y (2020) A multi-label text classification model based on Elmo and attention. In: CSCNS MATEC Web of conferences, vol 309, p 03015.https://doi.org/10.1051/matecconf/202030903015
9. Kennedy C (2019) Expectation maximisation on unsupervised web mined data using probabilistic latent semantic analysis (PLSA) algorithm. IEEE 978-l-5386-9236-3/19
10. Drishya SV, Saranya S, Sheeba JI, Pradeep Devaneyan S (2019) Cyberbully image and text detection using convolutional neural networks. CiiT Int J Fuzzy Syst 11(2). FS022019001. Apr–June 2019
11. Manoharan S (2020) Geospatial and social media analytics for emotion analysis of theme park visitors using text mining and GIS. J Inf Technol 2(02):100–107.4
12. Hosseinmardi H, Mattson SA (2015) Detection of Cyberbullying Incidents on the Instagram social network. Assoc Adv Artif Intell. arXiv:1503.03909v1 [cs.SI]

IoT-Based E-Parking System for Multiplexes and Shopping Malls

M. Nikhar and Surekha Kamath

Abstract This paper helps in automating process of car parking in shopping malls. It helps in making parking more efficient by burning of less fuel. This system is useful for places with large number of people considering less people-to-people contact considering Covid Pandemic and making a safe system for minimal infection transmission from people to people. This paper aims at developing a IoT-based E-parking system. This project uses Micro-controller (ATtiny85) for controlling of sensors. Set of multiple ultrasonic sensors are put on ceilings per floor with multiple slots for detection of vehicles in parked spaces with threshold set for cars. Multiple Wi-Fi modules are used for wirelessly uploading the values of vehicles parked in different floors to cloud from where the Wi-Fi module at entrance extracts data and displays on central display at entrance for assigning empty parking slots to new vehicles on arrival. Entrance display displays number of empty slots on every floor to new customer entering mall parking system. This project achieved objective of making a system which can be used in times of Covid-19 for better safety of people. This paper has been able to achieve its main objectives of making a safe, affordable, scalable parking system which can be used in shopping malls and multiplexes. It can be scaled to large usable parking systems using better sensors and better computing devices. It can provide means of work or business to youth of city for building and selling smart vehicle parking systems and deploy them to multiple malls and multiplexes using help from staff and sell at affordable rates. It can also help make more customizable and modular smart parking systems tailored to use of system in any buildings. Arduino IDE has been used for uploading code to cloud modules in project.

Keywords Internet of Things · Smart city · Parking management system · Embedded system

M. Nikhar (✉) · S. Kamath
ICE Department, MIT, Manipal, India
e-mail: nikharrm@gmail.com

S. Kamath
e-mail: surekha.kamath@manipal.edu

1   Introduction

This project aims to make a smart car parking system which will be useful in such times of Covid-19 where social distancing is necessary between parking staff and people visiting mall. It helps in automating process of car parking in shopping malls and making parking more efficient by burning of less fuel in finding parking spot. This system will be useful for places with large number of people considering less people-to-people contact. It will help in scaling solution to multiple places in every city for realizing dream of smart cities using emerging technologies such as cloud. Presently, manual car parking systems are prevalent which increase risk of virus transmission from car parking staff to customer visiting shopping mall or multiplex. So, Covid-19 has forced mall and multiplex owners to opt for a better system considering safety of customers and employees. Previous works used hardware/software which are costly to buy and maintain. It also does not let user get his/her car using automatic valet using mobile if it is out of battery. It will help create an affordable, safe, scalable parking system to be used in shopping malls, multiplexes and other crowded places.

It is an affordable system, not requires the usage of mobile and uses sensors to sense and upload data to cloud using modules, thereby making a central database and frequently updating it with update about empty and occupied slots using series of ultrasonic sensors [1]. This project achieved objective of making a system which can be used in times of Covid-19 for better safety of people. It was made using locally sourced components so that it can be made and sold at a better rate than expensive automatic systems and scaled to multiple shopping malls and multiplexes at a better rate through use of local manpower and locally sourced components [2]. This project has its main objectives of making a safe, affordable, scalable parking system which can be used in shopping malls and multiplexes. It should be scalable to large usable parking systems using better sensors and better computing devices.

This project achieved objective of making a system which can be used in times of Covid-19 for better safety of people. It was made using locally sourced components so that it can be made and sold at a better rate than expensive automatic systems and scaled to multiple shopping malls and multiplexes at a better rate through use of local manpower and locally sourced components.

2   Literature Review

Following papers presented a well-set review on the automated car parking system. Azshwanth et al. [1] explains various methods that are used for automatic car parking system. In this paper, author tried to develop an automatic car parking system without human interference. With this project, author tried to develop a system that is having minimum human interaction by incorporating sensors at various places.

Lookmuang et al. [2] tried to build a system for real smart parking by using IoT and mobile applications. They have used vision-based detection system to find vehicle plate number, to monitor vehicles in the parking area for enhancing security and also to facilitate the user to trace his/her car when he/she forgets where the car is parked.

Hilmani et al. [3] developed a system that utilizes an adaptable and hybrid self-organization algorithm for wireless sensor networks that is used to car parking system in the city. This system also offers innovative services.

Gumasing et al. [4] presented a guidance system used for parking that is based on intelligent technique for shopping centers. The responses of shopping mall owners through questionnaire were used to develop the system. An analysis based on regression analysis was employed to find very important factors affecting the service quality satisfaction.

Kanteti et al. [5] developed an improved algorithm for parking slot management using Raspberry Pi for commercial areas.

Nyambal and Klein [6] discussed on the application of CNN for a real-time parking space classification and presented a system for a real-time parking space classification system for commercial system using Caffe and Nvidia DiGITS framework.

Sadhukhan [7] designed a prototype of IoT-based parking system. The system also utilizes an integrated component called parking meter to address the disadvantages of real-time detection of improper parking.

Alsafery et al. [8] presented a car parking system which is smart and will assist the customers to solve the issue of recognizing a parking space to reduce the time spent in searching the feasible parking space.

Singh et al. [9] presented a paper on different kinds of car parking system based on intelligent system which addresses issue of parking space and vacancy issues together with the safety of cars.

Huang et al. [10] in his paper explains on secure automated valet parking which is used for privacy reservation scheme for autonomous vehicles. The scheme proposed does not preserve the user's identity privacy and location privacy.

Chaniotakis et al. [11] discussed on drivers' parking location choice under uncertain parking availability and search times. The method explains various results from a stated preference experiment on the choice behavior of drivers, in light of these uncertainties.

Khanna and Anand [12] presented a parking system which is smart and utilizes Internet of Things. The developed system utilizes the on-site deployment of an IoT module utilized to inspect and diagnose the state of availability of each single parking space.

Pham et al. [13] discussed on various algorithms that increase the efficiency of the current cloud-based smart parking system and developed a network architecture based on IoT.

Orrie et al. [14] presented a wireless system to explore parking spots remotely via a smartphone and a wireless sensor node which determines if parking spots are vacant or not.

Hassoune et al. [15] had done a survey on various smart parking systems and found various problems faced by drivers to park their vehicles during peak hours. In

the survey, they gave an overview about the concept of smart parking system. Then, they presented the latest developments in parking infrastructures.

Kamel et al. [16] discuss on tenancy status of the parking slots and found the reason behind it. They found that it is mainly due to the results of irregular parking regulation/management. By using mobile net classifiers, it is possible to identify the available parking slots based on the image mined from the live camera that feeds the status of parking lot continuously.

Vivekanadam [17] discussed on smart parking system that is based on blockchain exhibiting qualities of privacy protection, reliability and fairness. In the paper, author explained about how to protect the privacy of users and how vector-based encryption, bloom filters and group signatures can be used.

From the literature review, we found that there is need of smart parking system for multiplexes and shopping malls. The literature review shown above indicates the previous significant results obtained by various people in the field of smart car parking systems and their drawbacks which can be improved in future systems. There are various solutions proposed by various researchers in various research papers for smart car parking systems although they have limitations such as use of software/hardware which is expensive, security issues related to data, system fail due to noise in data and mobile battery issues in case of mobile issued pass for vehicle. There are certain limitations of smart car parking systems implemented until now which need to be considered in future systems as significant points of development in making a more secure, scalable, Covid safe, affordable system which can be realized using local manpower and local parts and can be sold and scaled to many places in smart cities.

3   Methodology

Figure 1 shows the detailed methodology of the proposed work. A prototype is developed for making the car parking better, efficient and secured. For this, we have developed a framework that is shown in Fig. 1.

The proposed architecture mainly uses 3 components—8-bit AVR Microcontroller (ATtiny85) for controlling of sensors, set of multiple ultrasonic sensors per floor for detection of vehicles in parked spaces and ESP8266 Wi-Fi modules for wirelessly transmitting the values of vehicles parked in different floors to central display at entrance for assigning empty parking slots to new vehicles on arrival. Ultrasonic sensors are put on ceilings per slot which detect cars in every parking spaces and transmit data to nearby display which further send data through Wi-Fi module to cloud. Data is stored by cloud and is received by display at entrance using Wi-Fi module. Entrance display displays number of empty slots on every floor to new customer entering mall parking system. It helps in saving fuel of customer and decreasing pollution caused by vehicle by pre-allotting parking slots to vehicles and thereby reducing movement and traffic problems in parking of vehicles.

Fig. 1 Detailed methodology of proposed work
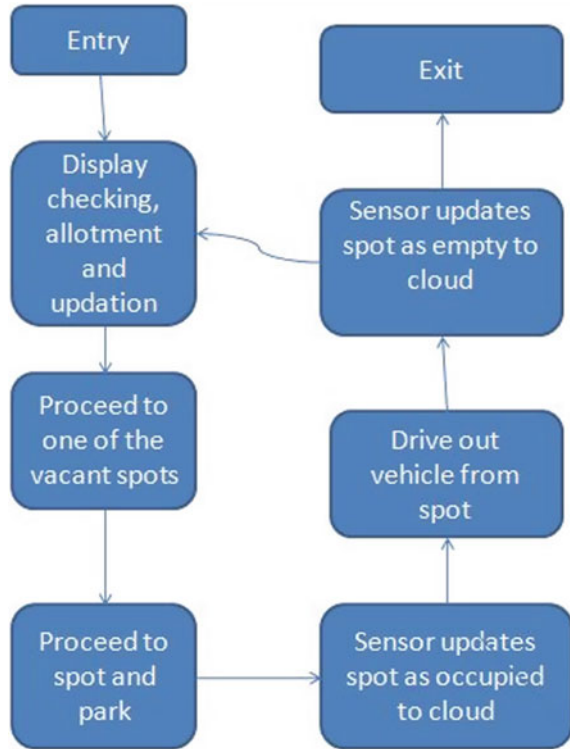
1. The output of Arduino is sent to the Wi-Fi module which sends an output signal to Blynk app. In Blynk app, the availability of parking slots is monitored, and also, the LCD will display the number of vacant slots and occupied slots.
2. The Arduino is used for connecting multiple IR sensors where each IR signal corresponds to their respective parking slot. A serial type communication between Arduino and Wi-Fi ESP8266 is represented as the Wi-Fi module.
3. After each vehicle is parked, allotment is required for next vehicle so this can be done prior to next parking.
4. The IR sensors which are used in this project are used for vehicle detection. With the help of Wi-Fi module, the vacancy of the car parking slots can be monitored within a specific range from the parking area.

Assumptions made

Threshold range for cars have been set in sensors and other vehicles have been excluded from detection, thereby reducing false positives due to other vehicles coming very rarely for only deliveries in malls.

Figure 2 depicts the arrangements of different sensors and modules that had used in our work.
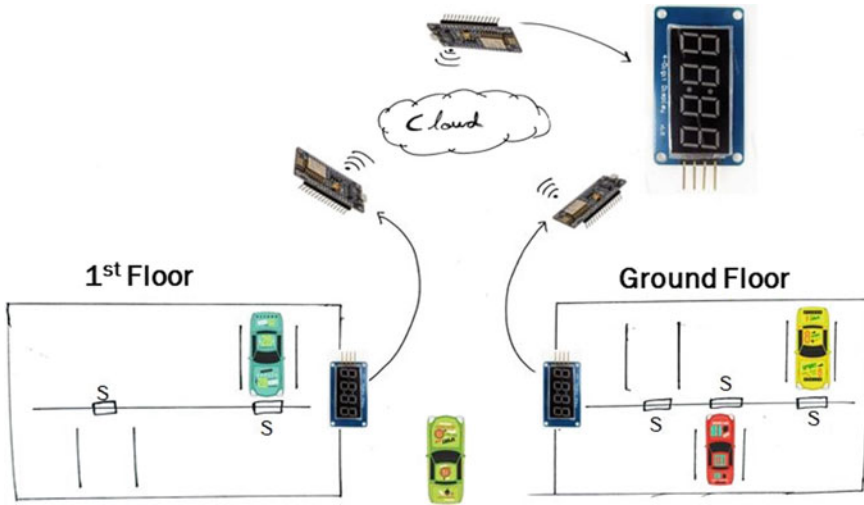
Fig. 2 Arrangement of different sensors and modules in project
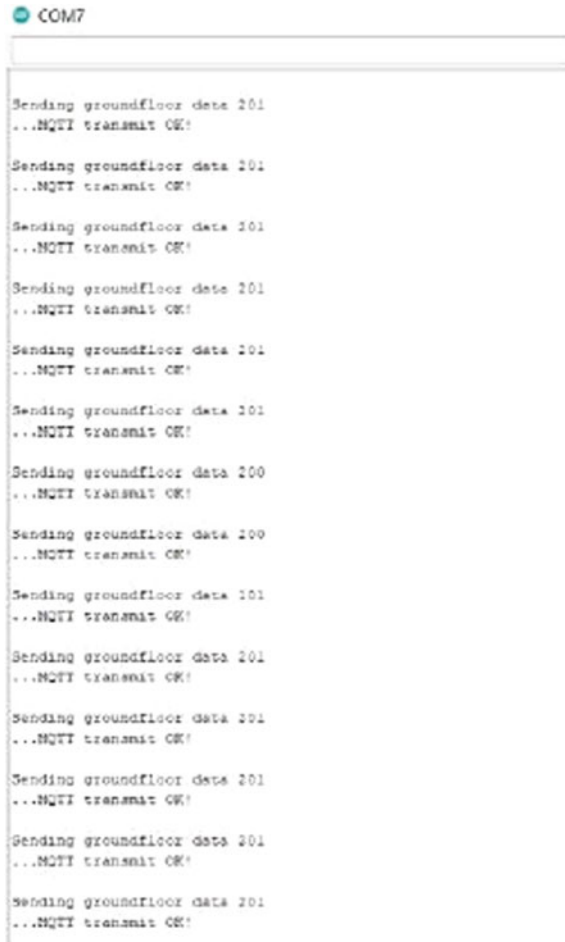
4   Results and Discussion

This section discusses on the results obtained from this project. For each signal from the microcontroller, the sensor reacts and sends signal to the Wi-Fi modules for communication. Figures 3 and 4 show the data received displays data received by Arduino IDE from ground floor and first floor NodeMCU's which refreshes data at regular intervals on cloud. Figure 5 displays the ground floor display where the 2-digit number on the left side of the colon symbol shows the vacancy on the left lane of the ground floor parking area and the 2-digit number on the right side of the colon symbol shows the vacancy on the right lane of the ground floor parking area. Results are as expected and reaffirm the project aim to build an affordable, scalable, safe smart parking system using locally available components.

5   Conclusion and Future Scope

This project helps in automating process of car parking in shopping malls. It helps in making parking more efficient by burning of less fuel. This system is useful for places with large number of people considering less people-to-people contact considering Covid Pandemic and making a safe system for minimal infection transmission from people to people. It is an affordable system which does not need mobile use for allotting parking and instead uses sensors to sense and upload data to cloud using modules, thereby making a central database and frequently updating it with update about empty and occupied slots using a series of ultrasonic sensors per floor and

Fig. 3 Receiving data from ground floor in Arduino IDE


```
COM7

Sending groundfloor data 201
...MQTT transmit OK!

Sending groundfloor data 201
...MQTT transmit OK!

Sending groundfloor data 201
...MQTT transmit OK!

Sending groundfloor data 201
...MQTT transmit OK!

Sending groundfloor data 201
...MQTT transmit OK!

Sending groundfloor data 201
...MQTT transmit OK!

Sending groundfloor data 200
...MQTT transmit OK!

Sending groundfloor data 200
...MQTT transmit OK!

Sending groundfloor data 101
...MQTT transmit OK!

Sending groundfloor data 201
...MQTT transmit OK!

Sending groundfloor data 201
...MQTT transmit OK!

Sending groundfloor data 201
...MQTT transmit OK!

Sending groundfloor data 201
...MQTT transmit OK!

Sending groundfloor data 201
...MQTT transmit OK!
```

displaying vacancies per floor and at the main entrance for both the floors. Smart parking system achieves the project aim to build an affordable, scalable, safe smart parking system using locally available components for use in crowded places like shopping malls, multiplexes, cinemas, etc. The results obtained in the project help in building up the path to build a robust, safe, scalable, affordable smart parking system for shopping malls, multiplexes, cinemas, etc., using locally available components and manpower, thereby increasing reliance on local businesses and providing employment and realizing dream of Atmanirbhar Bharat.

Future scope of the work mainly includes the following: It can focus on testing system with more sensors conducting large trials in real situations. It can help in making system more near to real-world situation where many cars are parked per floor which will help in making system more efficient in handling large traffic. It can also focus on making system more modular which will make system more easy to
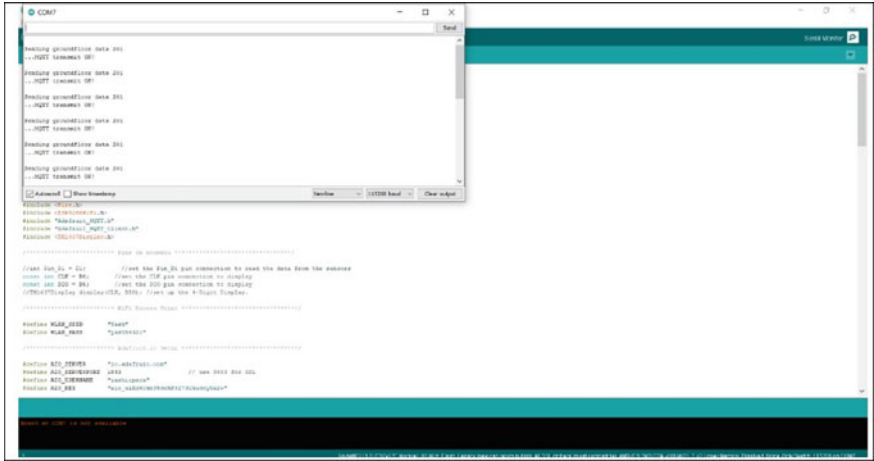
Fig. 4 Receiving data from first floor in Arduino IDE

Fig. 5 Display at ground
floor

configure and install in cities where there is less trained manpower. It can help us
make smart cities a reality with more digital and automatic systems. It can focus on
testing and finding more efficient positioning of sensors on ceiling or side or front
walls for more better detection. It can help in decreasing false positives and lead to
more better results of system and more efficient system.

References

1. Azshwanth D, Koshy MT, Balachander MT (2019) Automated car parking system. In:
   International conference on physics and photonics process in nano sciences, 01 Nov 2019

2. Lookmuang R, Nambut K, Usanavasin S (2018) Smart parking using IoT technology. In: 2018 5th International conference on business and industrial research (ICBIR), Bangkok, 2018, pp 1–6

3. Hilmani A, Maizate A, Hassouni L (2018) Designing and managing a smart parking system using wireless sensor networks. J Sens Actuator Netw 7(2):24

4. Gumasing MJJ, Atienza CAV (2018) A design of automated parking system for shopping centers in Metro Manila. In: 2018 5th International conference on industrial engineering and applications (ICIEA). https://doi.org/10.1109/iea.2018.8387136

5. Kanteti D, Srikar DVS, Ramesh TK (2017) Smart parking system for commercial stretch in cities. In: 2017 International conference on communication and signal processing (ICCSP). https://doi.org/10.1109/iccsp.2017.8286588

6. Nyambal J, Klein R (2017) Automated parking space detection using convolutional neural networks. In: 2017 Pattern recognition association of South Africa and robotics and mechatronics (PRASA-RobMech). https://doi.org/10.1109/robomech.2017.8261114

7. Sadhukhan P (2017) An IoT-based E-parking system for smart cities. In: 2017 International conference on advances in computing, communications and informatics (ICACCI). https://doi.org/10.1109/icacci.2017.8125982

8. Alsafery W, Alturki B, Reiff-Marganiec S, Jambi K (2018) Smart Car parking system solution for the Internet of Things in smart cities. In: 2018 1st International conference on computer applications & information security (ICCAIS). https://doi.org/10.1109/cais.2018.8442004

9. Singh A, Shawl MS, Bathla S, Gaur N, Mehra A (2018) Rfid and Hdl based pre-paid car parking system. In: 2018 Second international conference on electronics, communication and aerospace technology (ICECA). https://doi.org/10.1109/iceca.2018.8474606

10. Huang C, Lu R, Lin X, Shen X (2018) Secure automated valet parking: a privacy-preserving reservation scheme for autonomous vehicles. IEEE Trans Veh Technol 67(11):11169–11180. https://doi.org/10.1109/tvt.2018.2870167

11. Chaniotakis E, Pel AJ (2015) Drivers' parking location choice under uncertain parking availability and search times: a stated preference experiment. Transp Res Part A: Policy Pract 82:228–239. https://doi.org/10.1016/j.tra.2015.10.004

12. Khanna A, Anand R (2016) IoT based smart parking system. In: 2016 International conference on internet of things and applications (IOTA). https://doi.org/10.1109/iota.2016.7562735

13. Pham TN, Tsai M-F, Nguyen DB, Dow C-R, Deng D-J (2015) A cloud-based smart-parking system based on Internet-of-Things technologies. IEEE Access 3:1581–1591. https://doi.org/10.1109/access.2015.2477299

14. Orrie O, Silva B, Hancke GP (2015) A wireless smart parking system. In: IECON 2015—41st annual conference of the IEEE industrial electronics society. https://doi.org/10.1109/iecon.2015.7392741

15. Hassoune K, Dachry W, Moutaouakkil F, Medromi H (2016) Smart parking systems: a survey. In: 2016 11th International conference on intelligent systems: theories and applications (SITA). https://doi.org/10.1109/sita.2016.7772297

16. Kamel K, Smys S, Bashar A (2020) Tenancy status identification of parking slots using mobile net binary classifier. J Artif Intell 2(03):146–154

17. Vivekanadam B (2021) Smart parking with fair selection and imposing higher privacy constraints in parking owner and driver information. IRO J Sustain Wirel Syst 3(1):11–20

Enhancing S-Box Nonlinearity in AES for Improved Security Using Key-Dependent Dynamic S-Box

Prajwal Patil, Akash Karoshi, Abhinandan Marje, and Veena Desai

Abstract The Advanced Encryption Standard (AES) is the most widely used symmetric and secure encryption algorithm for commercial and research purposes. The core of AES is its substitution box (S-box), which primarily provides nonlinearity, confusion, and diffusion. The improvements to nonlinearity in S-box is one of the methods used by researchers to enhance security in AES. In this paper, to increase the nonlinearity of the S-box, AES using a key-dependent dynamic S-box is implemented and compared with the AES using a static S-box. The algorithm proposed in this paper draws observation from results of security parameters like hamming distance, strict avalanche criteria (SAC), and balanced output while comparing key-dependent S-box and static AES S-box. Among 40 experimental results, the key-dependent dynamic S-box performs 22.5% times better for hamming distance observation drawn is that the hamming distance is more in the dynamic AES than static AES. The average bit difference of 10 rounds of dynamic AES is around 65%, which is a good avalanche criterion.

Keywords Cybersecurity · Cryptography · AES · Bit difference · Dynamic S-Box · Strict avalanche criterion (SAC) · Hamming distance · Balanced output

P. Patil (✉) · A. Karoshi · A. Marje · V. Desai
Gogte Institute of Technology Belagavi, Belagavi, Karnataka, India
e-mail: prajwalpatil3764@gmail.com

A. Karoshi
e-mail: akashmkaroshi@gmail.com

A. Marje
e-mail: abhimarje5910@gmail.com

V. Desai
e-mail: veenades@gmail.com

1   Introduction

In today's world, tremendous amount of sensitive data is stored online and managed on connected servers or cloud computing devices. Protection of this data is paramount and encryption aims to protect data against attacks. Cybersecurity employs encryption to protect against cyber-attacks. Most commonly used encryption techniques are symmetric and asymmetric. Asymmetric encryption is computationally expensive and has key management issues, hence symmetric key encryption is used widely for various applications of which, AES is the current standard. Many modifications to the original AES given by National Institute of Standards and Technology (NIST) have been implemented by researchers [1]. This research work proposes a modification to the S-box of the original AES.

Asymmetric encryption operates with two keys each for decryption and encryption. For the decryption of data private key is used and is not shared. A public key is shared with everyone and is used to encrypt the data [2]. In symmetric encryption, the key is similar for encryption and decryption, and it is moderately inexpensive to produce a strong key for ciphertext [3]. Hence, improving the security of symmetric ciphers is a challenge in today's era with an increase in number of cybercriminals.

2   Background of Static S-Box in AES

AES standard is used to encrypt data in hardware and software using the standard specification of Rijndael's key size and block sizes. The specification mentions that the key and block size should be multiple of 32 bits, both with a minimum of 128 bits and 256 bits [4].

In every round of AES encryption, there are four steps:

- **Transformation of Substitution Bytes**: Every byte of the input state array is substituted with another byte of a nonlinear substitution table (S-Box).
- **Shifting of Rows**: This transformation provides the intra-column diffusion of the input state matrix [4].
- **Mixing of Columns**: Columns in the state array are multiplied by a fixed matrix, and the multiplication is performed over Galois Field GF (28) [5].
- **AddRoundKey**: 128 bits of the State are XORed bitwise with the key of that particular round. AddRoundKey proceeds one column at a time.

According to Claude Shannon, for any encryption algorithm to perform optimally and ideally from a security perspective, it should have confusion and diffusion properties for secure cipher [6, 7]. Confusion is used to obscure the relationship between the ciphertext and secret key and if a single bit in the key is modified then more than half bits in the ciphertext will be changed. Substitution techniques achieve confusion. Diffusion is used to increase the randomness of the plain text by spreading out the message across rows and columns. Diffusion's goal is to obscure the relationship

between ciphertext and plain text. In confusion, the relationship between the cipher-text and the value of the key is made difficult by using transformation techniques [8, 9].

3 AES Using Dynamic S-Box

A few properties are used to compare the security of dynamic S-box and static S-box. The most commonly used are SAC, hamming distance, and balanced output.

3.1 Strict Avalanche Criterion (SAC)

SAC is an important feature of cryptography. According to SAC, a 1-bit change in plaintext affects more than half of the bits in the ciphertext. If you modify one bit of the key, it should affect more than half of the bits in the ciphertext. This is known as the avalanche effect [10, 11].

3.2 Hamming Distance (Bit Difference)

The hamming distance between two equal length strings is the number of positions where the corresponding bits differ [12].

3.3 Balanced Output

The balanced output is the output which has the number of 1's and 0's should be matched approximately [13].

4 Proposed Algorithm

This section details the algorithm proposed for increasing the nonlinearity of S-box using key-dependent dynamic property.

4.1 Dynamic S-Box in AES

In Rijndael AES, the static S-box is generated from the plain text and lookup table, and the static S-box will remain static in all ten rounds of the AES encryption and decryption process. To enhance the randomness of the static S-box, this study proposes to introduce a key-dependent dynamic S-box in which for all ten rounds of AES the key is changed based on the key expansion algorithm that, in turn, changes the S-box and its security [14]. Figure 1 shows the location of the dynamic S-box in the encryption and decryption process of AES.
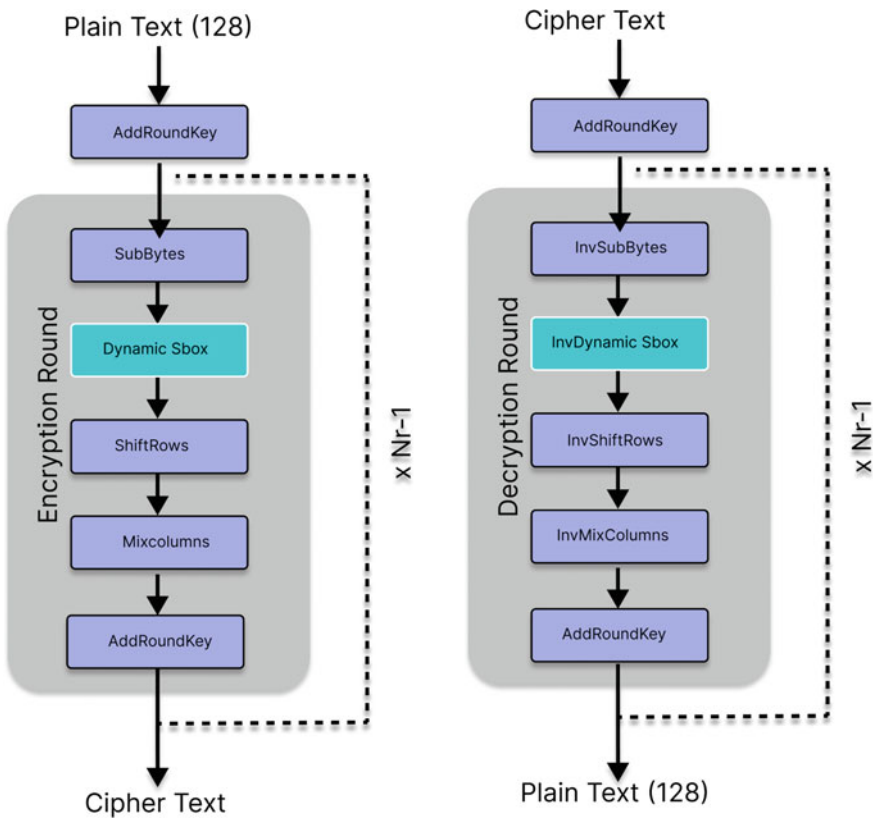
Fig. 1 Encryption and decryption using dynamic S-box

4.2 Steps to Generate Dynamic S-Box

In this paper, the key-dependent dynamic S-box replaces the static S-box using the flow as in Fig. 2

A plain text (Plain Text1) and round keys for sample experiments are shown in Figs. 3 and 4. The corresponding matrix values for 1st round static S-box and 1st round dynamic S-box are shown in Figs. 5 and 6.

Generation of dynamic S-box using an example with matrix values as in Figs. 3, 4, 5 and 6 is as shown below.

1st Step: The first byte of the key matrix is XORed with the first byte of the static S-box matrix.
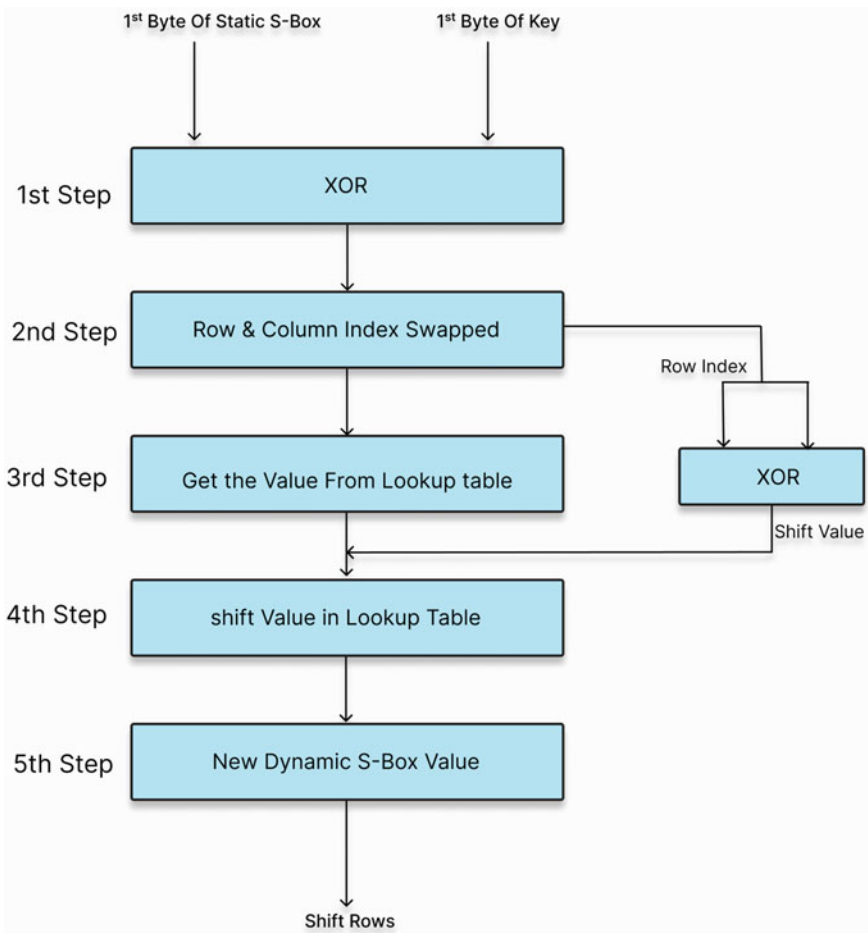
Fig. 2 Structure of dynamic S-box

Fig. 3 Matrix formed by plain text 1

Plain Text1:26bf40cbd0ce36bd8a046baf34d9f3d7

26	d0	8a	34
bf	ce	04	d9
40	36	6b	f3
cb	bd	af	d7

Fig. 4 Matrix formed by 1st round key

1st Round key: 445934f6e9d2bdc1be532cf0502a65a2

44	e9	be	50
59	d2	53	2a
34	bd	2c	65
f6	c1	f0	a2

Fig. 5 Matrix formed by 1st round of static S-box

1st round Static S-box:

03c192bfff6e087ec1972d0b57e0f497

03	ff	c1	57
c1	6e	97	e0
92	08	2d	f4
bf	7e	0b	97

Fig. 6 Matrix formed by 1st round of dynamic S-box

1st Round Dynamic S-Box:

a3b3aaeaeab865b8b315171e15eb6315

a3	ea	b3	15
b3	ba	15	eb
aa	65	17	83
ea	ba	1e	15

$$03 \text{ XOR } 44 = 47$$

2nd Step: Row index 04 and column index 07 are swapped. The new indices of the S-box is 74.

3rd Step: Row 07 and column 04, extracting this value from the lookup table gives the value 92.

4th Step: The row index and column index are XORed, and this is the shift value.

$$04 \text{ XOR } 07 = 3$$

5th Step: The value 92 from the lookup table is shifted according to this shift value (3) generated in Step 4, which will give the value a3 is the new dynamic value.

The steps 1–5 are repeated for all bytes in the key matrix and static S-box matrix. The remaining steps of AES, i.e., shift rows, mix columns, and add round key remain the same [15]. The difference is that in place of a static S-box the proposed algorithm uses the key-dependent dynamic S-box.

5   Experimental Results

The properties of the S-box used for security analysis in this paper are strict avalanche criterion, hamming distance, and balanced output are compared between the conventional AES algorithm and the proposed dynamic S-box algorithm for security analysis.

5.1   Hamming Distance and SAC in Ciphertext

To analyze the avalanche criteria with respect to key and plain text. On flipping a single bit in the key or plain text, at least half or more than half of the number of bits should be changed in ciphertext [16]. In this paper, comparison of the avalanche criteria in both plain text and key for static S-box AES and key-dependent dynamic S-box AES is made. Experimentation is formed to calculate the bit difference in both static AES and dynamic AES to analyze the diffusion and confusion properties of S-box.

Plaintext1: 26bf40cbd0ce36bd8a046baf34d9f3d7
SecretKey1: f362343fad8b893757819131ee794952
SecretKey2: f362343fad8b893757819131ee794953
Ciphertext1: Ciphertext when key is secret key 1
Ciphertext2: Ciphertext when key is secret key 2.

Table 1 gives the results of 10 rounds of AES considering Plaintext1 and Secretkey1 generating ciphertext1 using static S-box. Changing one last bit or LSB

of the Secretkey1, the Secretkey2 is generated and its corresponding ciphertext2 is generated and tabulated. The hamming distance between ciphertext 1 and ciphertext 2 is tabulated, and their average is found to be 56.4.

Continuing with same the Plaintext1, Secretkey1, and Secretkey2, the results for ciphertext 3 and ciphertext 4 for proposed algorithm using dynamic S-box are tabulated in Table 2 and the average hamming distance is found to be 63.5.

Ciphertext 3: Ciphertext when key is secret key 1.
Ciphertext 4: Ciphertext when key is secret key 2.

The average hamming distance 63.5 of the dynamic S-box as compared to 56.4 of the static S-box shows that the ciphertext for the key-dependent dynamic S-box is more balanced as compared to static S-box.

The above experiment was only for the last bit of key change. Exhaustive experimentation was carried out by changing the first bit of the key, the last bit of the key, the first bit of plain text, and the last bit of plain text.

Complementing the LSB in key, more than half of the bits in the cipher are flipped (meaning changing from 0 to 1 or 1 to 0) in all rounds, which indicates strict avalanche criterion is obeyed in the dynamic S-box AES.

Formula to calculate the avalanche effect from bit difference and the total number of bits in the ciphertext [17].

$$\text{Avalanche effect} = \frac{\text{No. of flipped bits in ciphertext}}{\text{Total No. bits in cipher text}} \tag{1}$$

To analyze the effect of position of the changed bit, the avalanche effect is calculated using Eq. (1). The results of this experimentation are given in Table 3 with reference to the avalanche effect.

The last bit of the plain text is flipped keeping the key constant and the average change in the bits of ten rounds of ciphertext is calculated to compare with both methods. The average bit difference is more in the dynamic AES than in the static AES.

The first bit of the key is changed keeping the plain text constant and in the next iteration, the first bit of plain text is changed while the key is constant. The avalanche effect in ciphertext between static AES and dynamic AES is calculated.

5.2   Balanced Output of Ciphertext

The number of 0's and 1's in ciphertext of conventional AES and dynamic AES are calculated for balanced output analyses. With 128-bit ciphertext, the number of 0's and 1's should be equal, i.e., 64 to have a strong cipher.

Plaintext 2: 26bf40cbd0ce36bd8a046baf34d9f3d7.
Secretkey 2: f362343fad8b893757819131ee794952.

Table 1 Comparison of hamming distance in ciphertext of static AES

Rounds	Ciphertext 1	Ciphertext 2	Hamming distance
1	0bc30471f5a0fcdde09ab02b5f7fe84	4a66a185e5a0fcddf09ab026a5f7fe84	18
2	6689f188563e7ee2b668b146200a78d0	97740cc91c351d96bc5e476cbae3b6fe	68
3	27040acab09de32a96c87fca10214508	95848e80369e8a800de609d394fb0ebb	56
4	46a2088357d819f4842777dbdf8ff2a39	7738fec65e79dc5e5157c1a8a29787fc	61
5	728e688cc32cbf7719aacf8f6f93d683	e2c675345f4fb1a75900e0c6a6dce70a	54
6	37b52f2d505a31451f295287752e70c6	eac8df72dd865f972c585cd29d7f980e	69
7	bd52683255604445ededec4169b1735	55033e243dd6801b74d2b40c66980001	54
8	c0bc6fc14d6b42ee1079fe58bd2c2c62	5583d596685f433365f60cf21ec99a98c	70
9	8e42d7a03e8098ad00b4a555b5a3ad02	a2b67ea3322df23e32eb05343aa3f796	55
10	89971ee309282ad044f89c3c5ad38044	ae3677f198f8d7cf00f861ee0fb14f55	59
Average hamming distance			56.4

Table 2 Comparison of hamming distance in ciphertext of dynamic AES

Rounds	Ciphertext 3	Ciphertext 4	Hamming distance
1	c58b39ec13dc0f2c4720b8e45969b49e	c8bd3e8d905da15df770e814cff32b77	57
2	9bff470d3230f46361536040bd20733d	45cfdabc159d64121a8e27e08655ee82	72
3	59e699f284e72f98d295b00f4d3fc2c2	a07f45c405ad2e93d0e2061f01a22b5d	60
4	d9e8da33097e4f39490924e305bf6a67	efc9124bfe4e89835d517603fc40d5cb	67
5	887e946d99c594530106ee57c4346a57	c551f0a406912e93d6d8fcae573903f9	68
6	178202fa45aa3bf6baea45ad9995a59f	5f82fdf0845387b13ffab8c9d8972dc4	54
7	42bf5f03d2f30cc4399cdb535fafbeae	01340e511154d02db61179307ef5a95a	63
8	128defd543fd813fcaeea9714ee4f7ca	dfc7401add5d61ce502e8b133a39eb5d	64
9	0cde1ef4501828f75be503a845f5793c	30b5fef55c89e180d91d5ad989bcfc8a	58
10	8dfc4ef663b2e7e9afc1016da7992dca	f72da4cd3c72545655704bfb4c89a33b	72
Average hamming distance			63.5

Table 3 Avg. of avalanche effect between static and dynamic S-box

S. No.	Change	Static AES	Dynamic AES	Avalanche effect	
				Static AES	Dynamic AES
1	First bit of key	58.5	64.1	0.457	0.500
2	Last bit of key	59.6	62.8	0.465	0.491
3	First bit of plain text	60.3	60.6	0.470	0.474
4	Last bit of plain text	58.1	59.6	0.454	0.466

Table 4 gives the result of the number 1's and number 0's in ciphertext using static S-box AES. The standard deviation is calculated and is found to be 8.485.

Table 4 Balanced output of ciphertext in static AES

Ciphertext	No. of 1's	No. of 0's
0bc30471f5a0fcdde09ab026b5f7fe84	66	62
6689f188563e7ee2b668b146200a78d0	58	70
27040acab09de32a96c87fca10214508	52	76
46a2088357d819f484277dbdf8ff2a39	65	63
728e688cc32cbf7719aacf8f6f93d683	70	58
37b52f2d505a31451f295287752e70c6	62	66
bd526832556044455ededec4169b1735	62	66
c0bc6fc14d6b42ee1079fe58bd2c2c62	64	64
8e42d7a03e8098ad00b4a555b5a3ad02	55	73
89971ee309282ad044f89c3c5ad38044	54	74
Standard deviation	8.485	8.485

Table 5 Balanced output of ciphertext in dynamic AES

Ciphertext	No. of 1's	No. of 0's
c58b39ec13dc0f2c4720b8e45969b49e	62	66
9bff470d3230f46361536040bd20733d	61	67
59e699f284e72f98d295b00f4d3fc2c2	65	63
d9e8da33097e4f39490924e305bf6a67	65	63
887e946d99c594530106ee57c4346a57	60	68
178202fa45aa3bf6baea45ad9995a59f	67	61
42bf5f03d2f30cc4399cdb535fafbeae	73	55
128defd543fd813fcaeea9714ee4f7ca	73	55
0cde1ef4501828f75be503a845f5793c	63	65
8dfc4ef663b2e7e9afc1016da7992dca	71	57
Standard deviation	6.363	6.363

Table 5 gives the result of the number 1's and number 0's in ciphertext using key-dependent dynamic S-box AES. The standard deviation is calculated and is found to be 6.363.

The standard deviation 6.363 from the dynamic S-box as compared to 8.485 of the static S-box shows that the ciphertext of key-dependent dynamic S-box is more balanced as compared to static S-box.

6 Conclusion

In this paper, a key-dependent dynamic S-box for AES is proposed and strict avalanche criteria, hamming distance, and balanced output are the parameters used to compare with the static S-box. On performing 40 experimentations, the observation is that the key-dependent dynamic S-box performs 22.5% times better than the static AES S-box. With hamming distance as the criteria, the dynamic S-box AES has an improved average of 63.5 against 56.4 for static S-box AES. The ciphertext is assumed to be more secure if the standard deviation approaches zero. In this paper, the standard deviation in dynamic S-box AES is less than static AES. Hence, overall the dynamic S-box performs better for SAC, hamming distance, and balanced output as compared to the static S-box AES.

Further extensive experimentation would yield better credibility to the results presented in this paper and would be part of future work.

References

1. National Institute of Standards and Technology http://www.nist.gov.lindex.html
2. Manjula G, Mohan HS (2016) Constructing key dependent dynamic S-Box for AES block cipher system. In: 2016 2nd International conference on applied and theoretical computing and communication technology (iCATccT). IEEE
3. Kak A (2021) Computer and Network Security. https://engineering.purdue.edu/kak/compsec/NewLectures/Lecture8.pdf
4. Nadaf R, Desai V (2012) Hardware implementation of modified AES with key dependent dynamic S-box. IEEE ICARET 576–580
5. Mahrousa Z et al (2020) A novel method to increase diffusion and confusion in AES algorithm. Int J Comput Appl 177(36):39–47. https://doi.org/10.5120/ijca2020919872
6. Joe CV, Raj JS (2021) Deniable authentication encryption for privacy protection using blockchain. J Artif Intell Capsule Netw 3(3):259–271
7. Nissar G, Garg DK, Khan BUI (2019) Implementation of security enhancement in AES by inducting dynamicity in AES s-box. Int J Innov Technol Explor Eng 8(10):1–9
8. Forouzan BA, Mukhopadhyay D (2015) Cryptography and network security. Mc Graw Hill Education (India) Private Limited
9. Hosseinkhani R, Javadi HHS (2012) Using cipher key to generate dynamic S-box in AES cipher system. Int J Comput Sci Secur (IJCSS) 6(1):19–28
10. Maram B, Gnanasekar JM (2018) A block cipher algorithm to enhance the avalanche effect using dynamic key-dependent S-box and genetic operations. Int J Pure Appl Math 119(10):399–418
11. Chatterjee R, Chakraborty R, Mondal JK (2019) Design of lightweight cryptographic model for end-to-end encryption in IoT domain. IRO J Sustain Wirel Syst 1(4):215–224
12. Hussain S et al (2020) A power associative loop structure for the construction of non-linear components of block cipher. IEEE Access 8:123492–123506
13. Lo O, Buchanan WJ, Carson D (2017) Power analysis attacks on the AES-128 S-box using differential power analysis (DPA) and correlation power analysis (CPA). J Cyber Secur Technol 1(2):88–107
14. Ejaz A et al (2021) A secure key dependent dynamic substitution method for symmetric cryptosystems. PeerJ Comput Sci 7:e587
15. Mizuki T, Hayashi Y (2014) AES cipher keys suitable for efficient side-channel vulnerability evaluation. Cryptology ePrint Archive
16. Su N, Zhang Y, Li M (2019) Research on data encryption standard based on aes algorithm in internet of things environment. In: 2019 IEEE 3rd information technology, networking, electronic and automation control conference (ITNEC). IEEE
17. Yan J, Chen F (2016) An improved AES key expansion algorithm. In: International conference on electrical, mechanical and industrial engineering

Estimated Computing for Effective Configurable Adder

Vishnumolakala Raghavendra Rao and B. Bala Tripura Sundari

Abstract Effective configurable adder is a traditional method used for obtaining high accuracy. In day-to-day life, everyone's goal is to reduce delay and increase speed. The proposed study is mainly focused on these parameters for obtaining high accuracy, less power, and speed operation. The proposed adder includes an effective configurable adder with high-speed error detectable model with easy testability. By incorporating the process of traditional carry look-ahead adder, the proposed adder utilizes the propagation with carry masking method. Then, the accuracy has been tested to remain configurable at run-time. The results from the proposed study indicate that the implementation of proposed design on a Spartan3E FPGA utilizes 62% fewer slice registers and 47% fewer slice LUTs when compared with the standard configurable adder design.

Keywords Configurable adder · Gracefully degrading adder (GDA) · Carry look-ahead adder · Carry maskable half adder · Verilog

1 Introduction

While considering the recently developed technologies, (such as image identification, battery-powered wearable devices, and computationally intensive digital signal processing) along with its various advantages, it also leads to many challenges in terms of power consumption and utilization. The advanced level also has some basic digital blocks, i.e., an adder for performing arithmetic functions [1, 2]. Most of these programs include a built-in tolerance for minor inaccuracies. The computing analysis should be used to achieve an understanding balance between two parameters:

V. Raghavendra Rao (✉) · B. Bala Tripura Sundari
Department of Electronics and Communication Engineering Amrita School of Engineering,
Amrita Vishwa Vidyapeetham, Coimbatore, India
e-mail: raghavendrarao916@gmail.com

B. Bala Tripura Sundari
e-mail: b_bala@cb.amrita.edu

One is accuracy, and another one is the utilization of inherent tolerance characteristics. In such application domains, this trade-off plays a substantial role [3]. Due to the increasing computational quality, the run-time may change drastically. Hence, the quality configurable systems that can round off between computation quality analysis on computation and computing effort based on current trends to the current requirements should be in a constant stage [4]. The previous configurable suggestions have come at the cost of more power [5] or delay [6]. A high-speed and low-power configurable approximation is essential to prove such application.

Configurable adder leverages less power dissipation and delay. Also, the area parameters should be very relative. Further, in the proposed adder, delay is very low when compared to power consumption, and this research work utilizes ripple carry adder and look-ahead adder with carrying analysis including ten in Verilog language and simulated in Xilinx ISE tool and to ease the testability, an error detectable carry select adder has been additionally included.

At the transistor level, researchers [7] have described different ways to reduce the hardness of a traditional mirror-related model. Furthermore, a research discussion [8] has begun on the lower-part-OR adder, which uses lower-bit addition with OR gates, and precision adders for r higher bit should be used. In [9], the authors have recommended that an analogous circuit, which is not timed has determined the quality of the approximation.

The accuracy configurable adder (ACA) given by Kahng and Kang [4] is related to a pipeline construction, where the ACA modification process takes place from stage 1 to stage 4 and continues further, and if the most important sections that should follow for observing the correct things, the design availability should be analyzed. In response to the foregoing, the researchers have [5] suggested to select sub-adders, and hence, the degrading adder is preferred. Similarly, in this analysis, the adder analysis method has not considered the pipeline structure method. Multiplexers and other logic blocks are necessary to provide outputs with varying degrees of different circuits, which have high accuracy, and further, the reconfigured analysis should be utilized for performing the analysis. On the other side, the remaining logic blocks consume greater space.

Furthermore, when the outputs of these blocks are underutilized, the total power will be wasted. Yang et al. [10] To address this challenge, a less power-adjustable OR gate is proposed. The OR gates are then utilized to generate an approximation sum. Although [10] is the only technique to acquire user-based consumption, it results in a lengthy delay. As a result, the less power-adjustable OR gate does not satisfy the speed requirements of an application.

2 Proposed

CLA: 1st part consists of half adders with a separation for propagation (P) and carry generation (G), and in the second part, the carry look-ahead value is used for carrying generation and carrying past containing XOR gate for generating the sum value. For

G and H, w concentrates on the half adders mainly, and for getting all data, we suggest several bits that should be denoted as a letter as 'n' for that CLA should be notified and get the output termed as P, and it will be notified by applying the input to carry maskable half adder, then it will indicate to carry look-ahead adder in that we can skip the carry for saving the memory.

When the inputs A_i and B_i both are equals to 1, and $M\ X_i$ is equals to 1, the correct sum S_i and carry C_i will be 0 and 1 (C_i, $S_i = 1, 0$); when $M\ X_0$, $M\ X_1$, $M\ X_2$, ..., $M\ X_i$ are all 0, $S_i = P_i\ (= A_i$ XOR $B_i = 0$) as an approximate total, and C_i will be 0 (C_i, $S_i = 0, 0$), as stated above. [11] This signifies that there is a 2-point gap between the exact and approximate sums. When $M\ X = 0$ sum. [12] As per the result, the difference should be reduced to only one. A two-input XOR gate may be made with two-input logic gates, which are used as basic gates. Figure 2 depicts the analogous circuit of a standard half adder.

[13] CMHA which is the dashed frame depicts a 2-input XOR gate consisting of inputs and two-input circuits ($M\ X = 1$). [14] The information will be obtained when $M\ X = 1$, P equals A XOR B, and G equals A AND B; when $M\ X$ is equal to 0, P equals B, and G equals 0. As a result, $M\ X$ will be a maskable carry, given Figs. 1 and 2 taken from [10] reference is the base paper.

Figure 4 shows the internal connections of the schematic diagram here, which contains 4-bit four half adders.

Fig. 1   Half adder with carrying
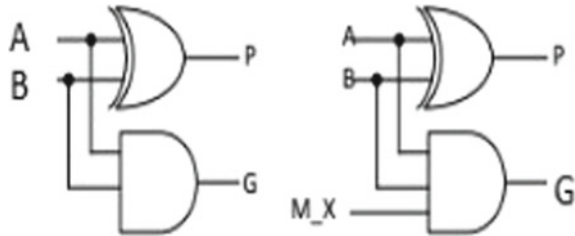
Fig. 2   Maskable half adder along with carrying
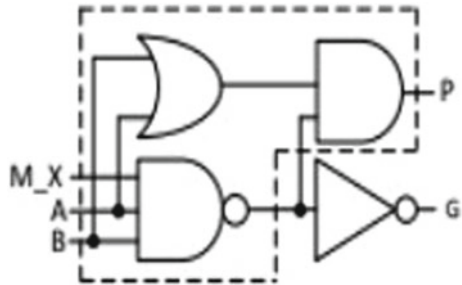
Table 1 Synthesis report of high-speed configurable adder

Logic utilization	Used	Available	Utilization (%)
Number of 4 input LUTs	180	9312	1
Number of occupied slices	101	4656	2
Number of slices containing related logic	13	101	100
Number of slices containing unrelated logic	0	101	0
Total number of 4 input LUTs	180	9312	1
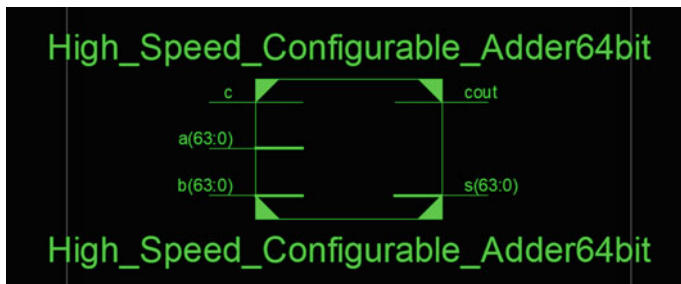
Fig. 3 Schematic RTL diagram for high-speed configurable adder

3 Results

Configurable adder analysis has been implemented in the tool by applying the stimuli to programming language as Verilog and analyze the waveform that generated by tool, and the report has been observed and identified shown in Table 1, there we can identify the different logic gates that are used in the paper for performing the analysis. It has been observed that a smaller number of LUTs are used, and when the carry select adder operates as carry skipper, the area will reduce, and further, the number of LUTs are also reduced when compared to the available count in the project. Schematic RTL diagram for high-speed configurable adder is shown in Fig. 3.

4 Discussion

Today, almost all data processing systems now proposed the carry select adder (CSA) to execute the fastest arithmetic operations. The proposed method is carry select adder (CSA), which results in high speed than the conventional select adder (CSA) with carrying, but it has a smaller area and less power. So, if speed and power are the key restrictions, the conventional carry chooses the proposed select adder consisting of carrying can substitute adder. The proposed structure shows to be a more straightforward approach to increasing the speed of the carry choose adder. The traditional
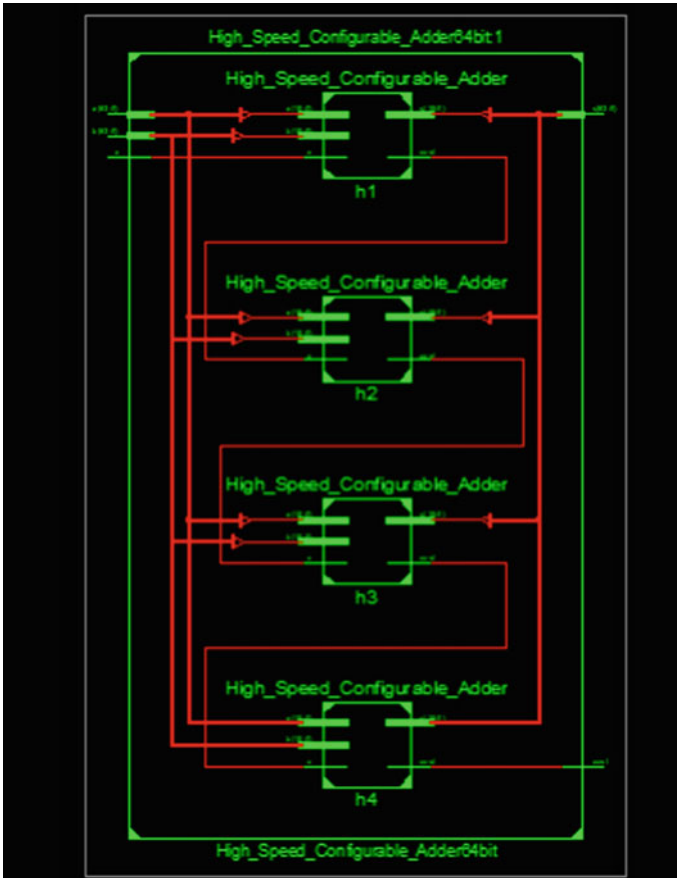
Fig. 4 Internal connections of schematic diagram

CSA has a limitation of using up more chip space, which has been solved with the suggested incremented unit. In addition, the suggested unit is proven to consume less energy. The proposed carry select adder can deliver speedy operation not only in parallel multiplier circuits but also in other architectures that employ a schematic adder. The waveform of a configurable adder with high speed and accuracy is shown in Fig. 5.

Synthesis report containing calculation of time taken and observed time delay is shown in Fig. 6.

Figure 7 is generated by the Xilinx tool after applying the proposed adder with the modification in the program code for leveraging easy testability.
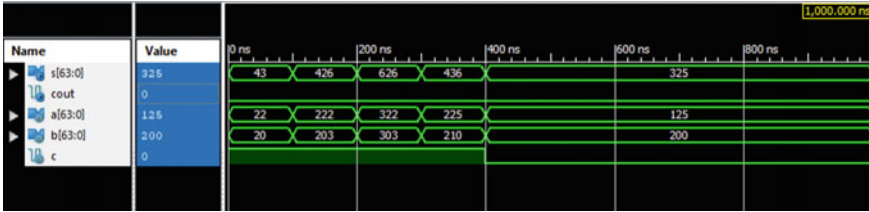
Fig. 5 Waveform of a configurable adder with high speed and accuracy
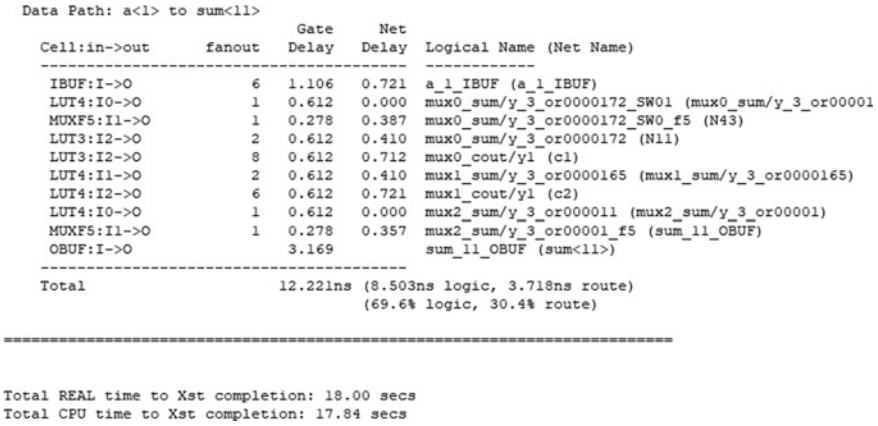
Fig. 6 Synthesis report containing calculation of time taken and observed time delay
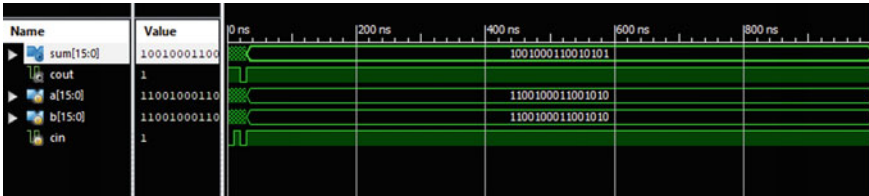
Fig. 7 Waveform for proposed configurable adder with error detectable easy testability

5 Literature Review

According to the previous analysis on different maskable adders, we obtain knowledge on how carry should be generated, as well as information about carry masking in the analysis, and the proposed adder [10] achieves the original goal of delivering an unbiased and optimized result between power and delay without compromising the accuracy.

6 Conclusion

This paper concludes that the logic level must be reduced, resulting in the development of carrying with high speed while reducing the structural complexity of the adder. Following that, the experimental findings show that, when compared to previously investigated customized adders, the proposed method provides an error detectable carry select adder with easier testability, decreased power consumption, and an optimized area.

7 Future Directions

The proposed method clearly shows that there is a reduction in power and delay when compared to the configurable adder to carry select adder, and experimental results show that the proposed method achieves high accuracy. Also, in the proposed adder, there is clearly less area, which leads to faster operation in the process. In future, this technology can be applied to generate more sophisticated solutions that will result in super-fast computers and develop the Synopsys tool for calculating minute values.

References

1. Cotofana S, Lageweg C, Vassiliadis S (2005) Addition related arithmetic operations via controlled transport of charge. IEEE Trans Comput 54(3):243–256
2. Beiu V, Aunet S, Nyathi J, Rydberg RR, Ibrahim W (2007) Serial addition: locally connected architectures. IEEE Trans Circuits Syst I Regul Pap 54(11):2564–2579
3. Venkataramani S, VK Chippa, Chakradhar ST, Roy K, Raghunathan A (2013) Quality programmable vector processors for approximate computing. In: 2013 46th Annual IEEE/ACM international symposium on microarchitecture (MICRO). IEEE, pp 1–12
4. Kahng AB, Kang S (2012) Accuracy-configurable adder for approximate arithmetic designs. In: Proceedings of the 49th annual design automation conference, pp 820–825
5. Ye R, Wang T, Yuan F, Kumar R, Xu Q (2013) On reconfiguration-oriented approximate adder design and its application. In: 2013 IEEE/ACM international conference on computer-aided design (ICCAD). IEEE, pp 48–54
6. Lau MS, Ling K-V, The Chu Y-C (2009) Energy-aware probabilistic multiplier: design and analysis. In: Proceedings of the 2009 international conference on compilers, architecture, and synthesis for embedded systems, pp 281–290
7. Gupta V, Mohapatra D, Raghunathan A, Roy K (2012) Low-power digital signal processing using approximate adders. IEEE Trans Comput Aided Des Integr Circuits Syst 32(1):124–137
8. Mahdiani HR, Ahmadi A, Fakhraie SM, Lucas C (2009) Bio-inspired imprecise computational blocks for efficient VLSI implementation of soft-computing applications. IEEE Trans Circ Syst I: Regul Pap 57(4):850–862
9. Venkatesan R, Agarwal A, Roy K, Raghunathan A (2011) Macaco: modeling and analysis of circuits for approximate computing. In: 2011 IEEE/ACM international conference on computer-aided design (ICCAD). IEEE, pp 667–673

10. Yang T, Ukezono T, Sato T (2018) A low-power configurable adder for approximate applications. In: 2018 19th International symposium on quality electronic design (ISQED). IEEE, pp 347–352
11. Devika C, Anita J (2022) Design of a high-speed binary counter using a stacking circuit. In: Inventive communication and computational technologies. Springer, pp 135–143
12. Hemamithra K, Priya SL, Lakshmirajan K, Mohanrai R, Ramesh S (2018) Fpga implementation of power efficient approximate multipliers. In: 2018 3rd IEEE international conference on recent trends in electronics, information & communication technology (RTEICT). IEEE, 2018, pp 1281–1285
13. Bhargav T, Prabhu E (2018) Power and area efficient FSM with comparison-free sorting algorithm for write-evaluate phase and read-sort phase. In: International symposium on signal processing and intelligent recognition systems. Springer, pp 433–442
14. Nair NB, Anita J (2022) Design of multistage counters using linear feedback shift register. In: Inventive communication and computational technologies. Springer, pp 161–173

E-Waste Is Becoming a Predominant Pollutant in Future India—An IoT Based Proposal to Monitor and Report the Air Quality Index

S. Siva Rama Krishnan, Kaliyaperumal Surendheran, Velayutham Vivek, M. Iyapparaja, and S. Sankaran

Abstract Since the start of the industrial revolution from the fifteenth century man-made machines and the usage of fossil fuel paves the way for today's air pollution. Air pollution leads to the death of nearly seven million people all-round the world. Air pollution means the release of carbon dioxide, sulphur dioxide, nitrogen dioxide, methane and particulate matter which includes $PM_{2.5}$ and PM_{10} in the atmosphere which are the major metrics for measuring the air quality index (AQI). In addition to these pollutants, due to the increased production and improper disposal of electronic goods, several other poisonous air pollutants such as chromium dioxide impact the quality of breathable air severely. This article addresses the issues caused by improper handling of the e-waste and also proposes a new way to monitor and instantly report the air quality around the e-waste dump yards with the help of IoT in the Vellore region.

Keywords E-Waste · Air quality index · Air pollutants · Internet of Things · Remote monitoring

S. Siva Rama Krishnan (✉) · K. Surendheran · V. Vivek · M. Iyapparaja
Vellore Institute of Technology, Vellore, India
e-mail: siva.s@vit.ac.in

K. Surendheran
e-mail: surendheran.k@vit.ac.in

V. Vivek
e-mail: vivek.velayutham@vit.ac.in

M. Iyapparaja
e-mail: iyapparaja.m@vit.ac.in

S. Sankaran
CSIR, Hyderabad, India

1 Introduction

Due to the increase in electronic gadgets, the electronic waste dump would increase causing emission of poisonous gases which becomes the most significant cause of air pollution. Most of the carbon deposits in the atmosphere [1, 2] increase the heat levels; this effect is majorly due to the release of greenhouse gases. Various types of greenhouses gases are as follows,

Carbon dioxide (CO_2): Major contribution of carbon dioxide in the air is due to burning of fossil fuel, solid waste and ecological substances. This can be avoided by implementing the Sankalptaru scheme [3] by Govt. of India.

Methane (CH_4): This gas is released due to the process of unearthing natural gas, coal and burying of organic and inorganic waste. But, this methane gas can be effectively used as a major source of bio-energy.

Fluorinated Gases and Nitrous Oxide (N_2O): These gases are produced by various industrial activities and due to the huge densities of transport vehicles. These gases are the major cause of global warming. Greenhouse gas concentration in various parts of India is shown in the Fig. 1.

Particulate matter (PM) is a pollution occurring in air due to the aggregation of solid and liquid particles. This aggregation contains organic and inorganic particles in various sizes, and this may be due to burning of fossil fuels and dust contained
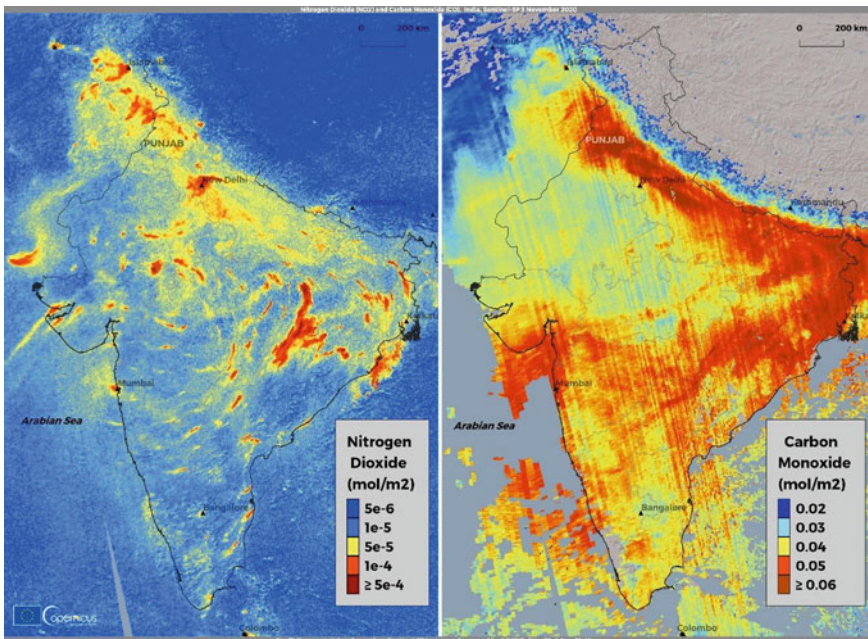
Fig. 1 Greenhouse gas concentration in various parts of India [4]

AQI	Remark	Colour Code	Possible Health Impacts
0-50	Good		Minimal Impact
51-100	Satisfactory		Minor breathing discomfort to sensitive people
101-200	Moderate		Breathing discomfort to the people with lungs, asthma and heart diseases
201-300	Poor		Breathing discomfort to most people on prolonged exposure
301-400	Very Poor		Respiratory illness on prolonged exposure
401-500	Severe		Affects healthy people and seriously impacts those with existing diseases

Fig. 2 AQI values and its health effects [6]

in the air. The threshold set for these fine particles is 2.5 which is termed as $PM_{2.5}$ [5]. Air quality index (AQI) value is required for measuring the air pollution content and to classify the health parameters of the air we breathe. AQI values and its health effects as in the Fig. 2.

Currently, health issues are increasing due to the level of exposure to polluted air, tiny particles like smoke, dust, soil, chemicals, allergen mixed in form of gas and solids carried away in air [7]. Major factors causing air pollution are from factories, power plants, burning of petroleum products, coal and natural gases. Hazardous air pollutions like dioxins, benzene, mercury, lead may lead to cancer, brain ailments, problems in central nervous system dysfunction and kidneys as well.

Internet of Things is a framework consisting of sensors and microprocessors which is used to collect data and send it to cloud/servers for further processing. This is used in various domains for creating smarter devices thereby improvising usage of data effectively. There are various use cases where IoT is used; for example, IoT is embedded in vehicles for automating different tasks that eases the driver to have better control. Medical domain is another scenario where body-aware sensors are deployed for continuous health monitoring of the patients. IoT network is also deployed to monitor environmental pollution wherein the sensors can collect the pollutant data and send it to the processing system for measuring the air/water quality. This system would help in formulating better policies for managing environment pollution.

1.1 Background

Urbanization and development of smart cities have led to over utilization of natural resources affecting the flora and fauna. This has subsequently caused degradation in the atmosphere which has stimulated to the following environmental effects:

Acid Rain: The rain traversing from the atmosphere contains huge quantities of nitric and sulphuric acids. This is due to the water which combines with CO_2 and NO_2 present in the atmosphere. The major components contained in acid rain are sulphuric acid (H_2SO_4), nitric acid (HNO_3) and carbonic acid (H_2CO_3). This acid

rain leads to an increase in the pH content contaminating the ecology of the earth [8].

Eutrophication: Vehicle emission and smoke released containing NO_x from industries leads to eutrophication. Though eutrophication is a natural process, which accelerates the production of nutrients in aquatic bodies, acid rain could restrict this process [9].

Haze: Haze occurs due to the PM combined with sunlight causing disturbance in the visibility. This is due to the burning of biomass material and industrial emissions increasing the chloride content and is typically seen in Delhi [10].

Ozone Depletion: Ozone is a layer in the atmosphere which protects the sun's UV rays from entering the earth's surface. The pollutants in the air deplete this ozone layer causing major health effects such as skin cancer.

As of December 2021, there are 261 air quality monitoring centres in 134 major cities in India [11]. These centres provide real-time AQI data via a web base portal which is managed by Central Pollution Control Board (CPCB). The National Clean Air programme launched by Government of India strategizes the pollution monitoring by majorly reducing the PM concentration in air. In connection with the above scheme, the Government deployed an app called SAMEER which renders real-time air quality data to the public. The Ministry of Environmental and Forest (MoEF) implemented an educational awareness programme to create awareness of the consequences of air pollution to the public. Similarly National Green Corps (NGC) established various eco-clubs in schools encouraging the students to actively participate in environmental conservation activities which address various challenges related to air pollution.

Current AQI in Vellore is 55 and $PM_{2.5}$ is 26(ug-m^3), this value is great then is set norms by WHO which is 25(ug-m^3). It is observed that air quality worsens during winter than the other sessions. This air pollution is due to solid liquid particles called aerosols and vehicle emissions, burning of fossil fuels by the industries and factories in Vellore region [12].

1.2 Analysing Pollutants Using IoT

Most cities throughout India have deployed Internet of Things (IoT) frameworks which consist of various gas sensors, microprocessors and Wi-Fi modules to monitor real-time air pollution data. The various gas sensors used in this IoT framework are as follows.

- Carbon dioxide sensor

    It is an air quality sensor that performs with low power consumption.

- Carbon monoxide detector

    It is a device to prevent carbon monoxide poison.

- Catalytic bead sensor

     This type of sensor has the ability to detect most combustible gasses.

- Hydrogen sensor

     It helps to detect the presence of hydrogen.

- Nitrogen oxide sensor

     It is used in diesel vehicles that helps to measure the engine-out NO_x gas concentration.

- Oxygen sensor

     This type of sensor measures respiration or production of oxygen

- Ozone monitor

     It helps to monitor in Ozone Generator Rooms

- Electrochemical gas sensor

     It helps to stop the diffuse of gasses in environment

- Gas detector

     It helps to detect combustible, flammable and toxic gasses and oxygen depletion.

- Hygrometer

     It is an instrument used to measure the amount of water vapour in air, in soil or in confined spaces.

These sensors are used to detect the presence of smoke, gases and flames in and around the location of the IoT setup.

1.3   Contributions of This Study

- Surveying various air pollution effects and methods.
- Effectively analyse the pollution levels in various strategic locations in Vellore with the help of IoT network.
- Summarize the existing methods which deal with mitigation of air pollution with the help of various research studies.

1.4   Organization of the Work

The rest of the paper is organized as follows: Sect. 1 introduces the causes of air pollution and its effects and also discusses various Govt. schemes available to curtail air pollution. Section 2 surveys the various methods involved in measuring the air pollution and different IT strategies to control air pollution. Section 3 discusses industrial scenarios in reducing air pollution. Section 4 deals with current methods deployed for air pollution monitoring in Vellore. Section 5 concludes the work discussed and provides future directions.

2   Literature Survey

2.1   Existing Methods for Monitoring Air Pollution

One of the major causes of air pollution is urbanization. The increase in the industries and motor vehicles add to the rise in the toxic gases. Badami and Madhav [13] address some of the measures in addressing the control of motor vehicle pollution. Emission standards were implemented in major cities to control the air pollution levels. The adulteration in the fuel quality is one of the major challenges in India. Methyl Tertiary Butyl Ether (MTBE) has been added to fuel to decrease the Benzene content to curb the pollutants [14]. Vehicle maintenance also affects the emission control. This would be due to the expensive spare parts or heavy taxes levied on the users. Brauer et al. [15] also discusses a relation between the population density and pollution. Further, the authors compare the pollution monitoring mechanisms with other populated countries like China and the statistics shows that in 2016 the pollution monitoring density was 0.14 monitors/million persons which is less than other populated countries. To address this issue, the authors suggest deploying monitoring stations at various places which will be integrated to a high-end monitoring base by which pollution levels can be easily measured and further actions could be taken. One of the metrics in measuring air pollution is the ambient particulate matter ($PM_{2.5}$). Balakrishnan et al. [16] discuss the statistical data correlating the population with respect to the $PM_{2.5}$ which was 89·9 $\mu g/m^3$. The author's findings state that Delhi topped the $PM_{2.5}$ value followed by Haryana and other northern cities. The direct health effect of such level of pollution leads to many chronic diseases such as ischaemic heart diseases, stroke, chronic obstructive pulmonary disease and lung cancer. As conclusive remarks, the authors suggest that there is a dire need to implement mitigation strategies to curb the effects of air pollution in order to reduce the mortality rate. In a similar research, Rao et al. [17] discuss about $PM_{2.5}$ contributing from household activities such as biomass cook stoves especially used by poor people who are prone to higher health risks. The authors also suggest that clean cooking fuels would decrease the health issues caused by air pollution. Khilnani et al. [18] discusses a report in 2015 that discloses the direct effect of premature deaths to

atmospheric air pollution due to $PM_{2.5}$. Achieving the air quality standards set by WHO can decrease the morbidity and mortality because of air pollution in India. Weather conditions in some cities of India are extreme especially during winter with fog adding to the pollution. This affects the visibility of the drivers in the road as well as the delay in flights. Guttikunda et al. [19] analysed the air pollution levels using the Lagrangian model also known as Atmospheric Transport Modelling System to study the climate and pollution effects in Delhi. The authors observed that tracer density is higher in the winter season with respect to the average density annually. This opens up further research on relation between climatic conditions and pollution levels [20].

Air quality directly affects human health due to the presence of poisonous gases. Implementing various statistical methods can lead to determining the pollutant levels in air by analysing the real-time data. This can help in building a prediction model for efficient air pollution management. Ravindra et al. [21] discusses the air quality in India with respect to particulate matter. The study done by the authors can facilitate monitoring of pollution levels accurately for alerting the health and the government officials to implement policies which can reduce the air pollution. These policy decisions can be deployed with the help of the knowledge gained from the big data analysis and thus providing a bridge between science and the policy decisions. The Govt. of India along with the Central Pollution Control Board (CPCB) updates the policies to control and mitigate air pollution every 3 years. It is not possible to completely eradicate the air pollution but effective measures could be taken to control it. This is due to the development in various industries and the consumer growth. The industries as well as the vehicles release various toxic gases such as sulphur oxides (SO_x), nitrous oxides (NO_x), carbon monoxide (CO) and other volatile organic compounds (CH) such as methane, benzene, toluene and xylene. These gases are carcinogenic and prolonged exposure leads to chronic diseases such as leukaemia and other respiratory disorders [18, 22]. High levels of air pollution can completely disturb the natural bio-network as well as the environment. Ashfaq et al. [23] discusses various impacts caused by air pollution. Global warming is one of the major effects which may lead to melting of snow caps and thus increasing the sea levels. Another major effect is the acid rain which increases the pH levels of the water source affecting the human and the aquatic life. The authors also discuss the various policies such as emission standards in India (Bharat stages) and the United Nations Conference on Environment and Development (UNCED) designed Kyoto Protocol to reduce the greenhouse gas emissions.

2.2 Monitoring Air Pollution Using IoT

Internet of Things (IoT) is an amalgamation of devices, sensors and microprocessors which have the capability of communicating with other devices. The data collected and processed from these IoT devices are used to render real time solutions for various domains. Some of the age old systems deployed to monitor air pollution lack

accuracy and also need complex lab analysis. Dhingra et al. [24] proposes an air pollution monitoring system which consists of gas sensors, Arduino microprocessor, and Wi-Fi module. This kit can be deployed in various locations and data collected is stored in the cloud. The authors also implemented an App called the IoT-Mobair, which provides the users with real time air quality data. Traditional air quality monitoring techniques are ineffective to render enough amounts of spatial and temporal resolutions of the air quality data. It is also not feasible for current scenarios as these incur in delay in producing real time air quality information. Senthilkumar et al. [25] deployed a novel framework which embeds fog computing with IoT for recording air quality information. The sensors send the data to the fog nodes which processes this data in a virtualized environment. This framework reduces the time in storing and processing the data in the cloud and thus gives efficient data in a timely manner.

Data collected from sensors need to be processed in an effective way for gaining its usefulness. Ayele et al. [26] proposed an IoT-based prediction system for air pollution in a specific region. The data from the sensors are fed into a recurrent neural network for accurate prediction of air pollution levels. In a similar work, an IoT-based air quality monitoring is proposed for smart cities [27]. The data collected in real time is analysed by the smart devices and notifies the public about the impact of air pollution. One of the major causes of air pollution in the cities is due to the increase of vehicles on the road. There should be a system to control the pollution from vehicle emissions. Though we have Bharat emission standards, pollution levels are on the rise. Pal et al. [28] developed an IoT system for measuring the pollution from the vehicles. The system gives the air pollution levels generated by each vehicle. This system, if deployed in major cities, can curb the pollution levels as it creates awareness among the people about the effects of pollution generated. In a similar research, Marques et al. [29] proposed an air quality monitoring system using IoT for enhanced living. This system considers the spatial–temporal information for measuring air quality and also implements a cyber-physical system for data aggregation. The authors also suggest that this system can be deployed in vehicles for effective air quality monitoring while on the go. Indoor air quality has been taken seriously to enhance the living standards and health. There have been various air purifiers in the market which claim to reduce indoor air pollution. One such air purifier which has the largest selling base is Amway's Atmosphere Mini [30] and claims to capture particles as small as 0.0024 micron. Saini et al. [31] reviews various IoT methods for monitoring indoor air quality. Air conditioners, cylinders used for cooking, and other home appliances could be a major cause of increase in CO_2 and PM levels. Significant existing works in air pollution is tabulated in Table 1.

3 Industrial Scenarios for Reducing Air Pollution

It's a sad truth that industries do not concentrate as much on bringing technological innovations into pollution control as they do with their production. The primary way to mitigate air pollution from the industry is, try to adopt the culture of minimizing

Table 1 Significant existing works in air pollution

Ref. No.	Methods	Evaluation metrics	Research challenges
[17]	Indoor pollution by biofuel	$PM_{2.5}$	Lack of awareness in the people about the ill-effects incurred by burning the biomass
[18]	Ambient air pollution	AQI	Policies for reducing the air pollution and methods to improve air quality needs to be implemented
[24]	IoT for mobile air pollution monitoring	Gas sensors data	Data collected in real time and stored in cloud has a delay and sensors data need to be accurate
[28]	IoT deployed in vehicles	CO_2, SO_2, AQI	Congestion of data may cause delay in display accurate data in the mobile

the energy usages of production equipment. It leads to usage of natural resources for their manufacturing. In general, industries are emitting their pollutants in two modes: stationary-based emission and mobile-based emission. Using some static erected sources, they are emitting poisonous gases in every minute through air. In mobile emission, the dangerous nitrogen dioxide gases are emitted by their garbage transports. The only way to avoid these kinds of air pollution is to implement a green environment in industry philosophy [32]. With the steady development of industrial growth in terms of production and market reach, they never have more significant time to truly take their part in curbing the air contamination [33]. Here, we are pointing out a few effective practices that could be followed by industries to mitigate the air pollution as much as possible. The industries can decrease air contamination by switching out lights, PCs, forced air systems and different machines when not being used. In a organisations, during brainstorming sessions, the experts can suggest the employees to use public transport for commuting purposes to reduce the carbon emissions. Recommendations can be put forth to the organizations for purchasing Electrical vehicles to reduce the emissions [32].

By implementing these kinds of practices in real time, the industries can avoid or at least mitigate the probability of polluting air, which will lead to a green industry environment with a reduced amount of air pollution.

4 Case Study of Air Pollution in Vellore

4.1 Necessity of Choosing Vellore

Vellore is one of the busiest towns in the state of Tamil Nadu and surrounded by a lot of industries, tanneries and cement factories. In fact, Vellore city is called the

leather hub of India as this city plays a significant role in leather production and management.

Generally, the literature indicates that the environmental and socio-economic aspects of industrial effluents have not been studied as extensively as domestic sewage. In developing countries like India, industrial waste, chemical effluents from Effluent Treatment Plants (ETPs) and medical waste are being dumped in open lands. With time, all these will ultimately impact the air quality as well as surface/ground water. All along the Palar River that runs across the city Vellore, a number of leather and chemical industries are spread right from Gudiyatham in the upstream to Vellore in the downstream. The potential soil zone spread in these valley fill areas have been polluted and unfit for agriculture.

4.2 Proposed and Significance of the Work

In recent years, almost every job demands the use of computer intervention. Due to the rapid innovations in the IT sector, people are in a race to acquire better computer equipment to meet the day-to-day computing needs. In the process, a lot of used/damaged IT components are discarded and are not properly disposed. The government is also struggling to enforce stringent regulations in disposing of e-waste.

As a result, e-waste dump yards are rapidly growing in size and are posing a threat to become the most dominant air pollutant in the near future. As we have discussed in the previous sections, the need to control the increase in air pollutants due to e-waste is at all-time high. To tackle the collection of e-waste pollutant data, this article proposes a way employing remote controlled drones. The following Fig. 3 explains the proposed framework architecture.

The authorities who monitor the AQI may use high-powered drones such as "DJI Phantom Pro 4" fitted with gas detection sensors. The drones are mere carriers of the IoT module along with its sensors, attached to its belly. This type of drones flies comparatively farther from the person who controls it increasing the safety for the humans. Also, the AQI measuring drones make it convenient to the authorities to measure the quality of air at different altitudes which opens up more possibilities for efficient mitigation methods. The drones can be used as many times as possible otherwise would become tedious, if done on foot. In this method, the cost of measuring the AQI over the e-waste dump yard also becomes cheaper and faster. The drone's IoT module may also be fitted with a SIM module capable of 4G communication. The measured AQI may be immediately sent to a centralized server which records the air quality straight from the drone. If needed, the data being sent shall be secured using any network encryption algorithm to increase the security. Weekly reports of this AQI measurements shall be shared with the authorities for their perusal. The collected data for the last 3 months will be readily available from the server and the data older than this period shall be archived in any other external backup medium.
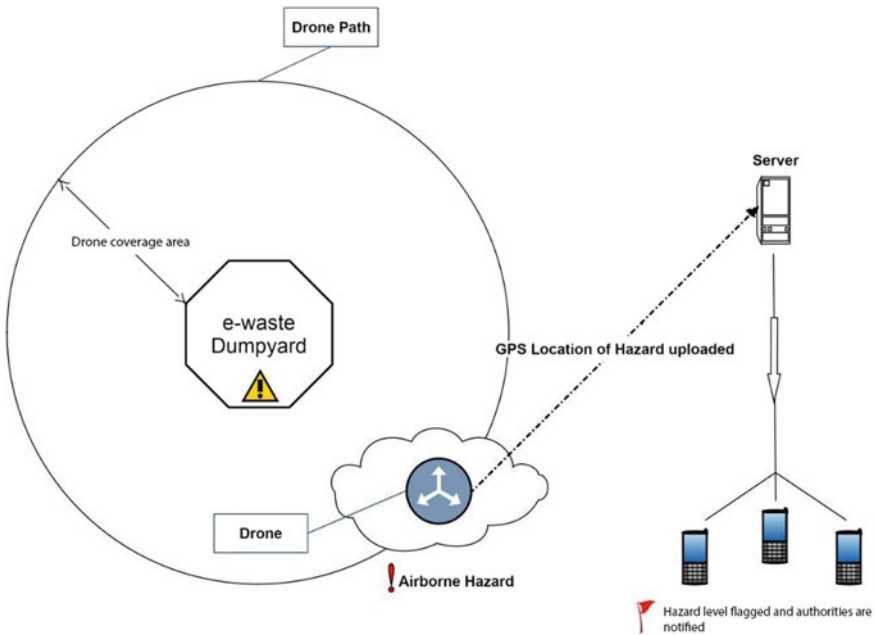
Fig. 3 Proposed architecture for monitoring pollutants from e-waste

4.3 Limitations

The limitations of the current proposed model is that it has been designed to explore only the airborne pollutants caused by the e-waste dumpyard but did not take the pollutants that are injected into the soil. The drones with IoT modules would swiftly patrol the airspace around the dumpyard but to consider the soil pollution, other stationary sensors need to be erected which will be an extension of this study. However, the pollutants that are released into the air pose immediate threat as the breathable air is becoming toxic.

5 Conclusion and Future Work

This case study surveyed different air pollution monitoring strategies deployed in various parts of India and also discussed the severity of air quality affected by the disposal of e-waste. This study took the Vellore region of Tamil Nadu as the case to propose a new way of monitoring and reporting the severity of air quality index with the help of IoT. The proposed framework will allow the authorities of corporations and municipalities to monitor the quality of air safely (remotely) and report the anomalies swiftly to the concerned authorities on-the-fly.

The future of this study shall be the implementation of the proposed model and also an addition of a module that would monitor and report the amount of pollutants being released by the e-wastes into the soil.

References

1. https://www.nrdc.org/stories/air-pollution-everything-you-need-know
2. https://www.epa.gov/ghgemissions/overview-greenhouse-gases
3. https://sankalptaru.org/
4. https://www.copernicus.eu/en/media/image-day-gallery/nitrogen-dioxide-and-carbon-mon oxide-levels-over-india
5. https://www.greenfacts.org/en/particulate-matter-pm/level-2/01-presentation.html
6. https://app.cpcbccr.com/AQI_India/
7. https://www.frontiersin.org/articles/10.3389/fpubh.2020.00014/full
8. https://www.epa.gov/acidrain
9. https://oceanservice.noaa.gov/facts/eutrophication.html
10. https://cen.acs.org/environment/atmospheric-chemistry/New-Delhis-haze-surprising-culprit/ 99/web/2021/02
11. https://cpcb.nic.in/displaypdf.php?id=bmF0aW9uYWwtYWlyLXF1YWxpdHktaW5kZXgv TmF0aW9uYWxfTmV0d29yay5wZGY=
12. https://www.aqi.in/dashboard/india/tamil-nadu/vellore
13. Badami MG (2005) Transport and urban air pollution in India. Environ Manage 36(2):195–204
14. https://www.bis.gov.in/
15. Brauer M, Guttikunda SK, Nishad KA, Dey S, Tripathi SN, Weagle C, Martin RV (2019) Examination of monitoring approaches for ambient air pollution: a case study for India. Atmos Environ 216:116940
16. Balakrishnan K, Dey S, Gupta T, Dhaliwal RS, Brauer M, Cohen AJ, Dandona L (2019) The impact of air pollution on deaths, disease burden, and life expectancy across the states of India: the global burden of disease study 2017. Lancet Planet Health 3(1):e26–e39
17. Rao ND, Kiesewetter G, Min J, Pachauri S, Wagner F (2021) Household contributions to and impacts from air pollution in India. Nat Sustain 4(10):859–867
18. Khilnani GC, Tiwari P (2018) Air pollution in India and related adverse respiratory health effects: past, present, and future directions. Curr Opin Pulm Med 24(2):108–116
19. Guttikunda SK, Gurjar BR (2012) Role of meteorology in seasonality of air pollution in megacity Delhi India. Environ Monit Assess 184(5):3199–3211
20. Mishra M (2019) Poison in the air: declining air quality in India Lung. India Official Organ Indian Chest Soc 36(2):160
21. Ravindra K, Sidhu MK, Mor S, John S, Pyne S (2016) Air pollution in India: bridging the gap between science and policy. J Hazard Toxic Radioactive Waste 20(4):A4015003
22. Choudhary, M.P., Garg, V.: Causes, consequences and control of air pollution. In: All India seminar on methodologies for air pollution control, Jaipur, Rajasthan (2013)
23. Ashfaq A, Sharma P (2012) Environmental effects of air pollution and application of engineered methods to combat the problem. I Control Pollut 29(1) (2012)
24. Dhingra S, Madda RB, Gandomi AH, Patan R, Daneshmand M (2019) Internet of Things mobile–air pollution monitoring system (IoT-Mobair). IEEE Internet Things J 6(3):5577–5584
25. Senthilkumar R, Venkatakrishnan P, Balaji N (2020) Intelligent based novel embedded system based IoT enabled air pollution monitoring system. Microprocess Microsyst 77:103172
26. Ayele TW, Mehta R (2018) Air pollution monitoring and prediction using IoT. In: 2018 second international conference on inventive communication and computational technologies (ICICCT). IEEE, pp 1741–1745

27. Gupta H, Bhardwaj D, Agrawal H, Tikkiwal VA, Kumar A (2019) An IoT based air pollution monitoring system for smart cities. In: 2019 IEEE international conference on sustainable energy technologies and systems (ICSETS). IEEE, pp 173–177
28. Pal S, Ghosh A, Sethi V (2018) Vehicle air pollution monitoring using IoTs. In Proceedings of the 16th ACM conference on embedded networked sensor systems, pp 400–401
29. Marques G, Miranda N, Kumar Bhoi A, Garcia-Zapirain B, Hamrioui S, de la Torre Díez I (2020) Internet of Things and enhanced living environments: measuring and mapping air quality using cyber-physical systems and mobile computing technologies. Sensors 20(3):720
30. https://www.amway.in/atmosphere-mini-air-purifier-1-replacement-filter/p/123328ID
31. Saini J, Dutta M, Marques G (2020) Indoor air quality monitoring systems based on Internet of things: a systematic review. Int J Environ Res Public Health 17(14):4942
32. https://www.ppsthane.com/blog/reduce-air-pollution-industries#:~:text=We%20can%20reduce%20air%20pollution,and%20opting%20for%20natural%20gas.&text=Any%20type%20of%20air%20pollution,known%20as%20Industrial%20air%20pollution
33. https://www.altenergymag.com/article/2020/04/readers-choice-2020-how-to-prevent-industrial-air-pollution-in-manufacturing/33006

Continuous Passenger Monitoring and Accident Detection (CPMAD) System

S. K. Akash Krishnaa, T. Pavan Reddy, S. P. Aakash, G. L. V. N. S. Vamsikrishna, and M. E. Harikumar

Abstract Unnatural fatalities are rising in our contemporary period, but road accidents account for a significant portion of these deaths. This work mostly deals with road accident detection and methods to reduce the time period between the victim and the emergency service area. According to the statistics, some accidents have occurred due to some momentary health issues like low/high BP, heart rate abnormality, lack of intaking oxygen-increased breathing rate, and also due to drunk and driving, these kinds of stuff are incredibly hazardous, resulting in automobile collisions and traffic injuries. So, continuous passenger and driver monitoring was also introduced for the utmost safety. Besides of preventative actions implemented, like seizure of vehicle permits, fines, penalties, and seizure of licenses. Despite the numerous prolepses taken, the number of accidents caused by drunk driving and sudden heart attacks is on the rise. This module is suggested to prevent individuals from dying needlessly as a result of intoxicated driving incidents, momentary health issues with the help of continuous monitoring, and to detect the occurrence of accident and also sends location coordinates to nearby hospitals/toll plazas/police stations and passenger's trustworthy relatives for their navigation purpose. This module consists of Raspberry Pi 0, Arduino UNO, alcohol detection sensor (MQ-2), MEMS Accelerometer Sensor, ECG, GPS module, pulse oximeter, digital vibration sensor, LCD displays, ADC, PHP server, and relay to control the vehicle.

Keywords Micro electro mechanical system (MEMS) · Beats per minute (BPM) · Electrocardiogram (ECG) · Application programmable interface (API) · Hypertext preprocessor (PHP)

S. K. Akash Krishnaa · T. Pavan Reddy · S. P. Aakash · G. L. V. N. S. Vamsikrishna · M. E. Harikumar (✉)
Department of Electronics and Communication Engineering, Amrita School of Engineering, Amrita Vishwa Vidyapeetham, Coimbatore, India
e-mail: me_harikumar@cb.amrita.edu

1 Introduction

Human civilization's ascent over all other creatures on the earth has been fueled by the development of transportation systems. Automobiles are essential in our everyday lives. We employ it to go to work, interact with family members and friends, and send and receive things. However, accidents are capable of injuring us and even killing us. One of the most important factors in driving is speed. It has an impact not just on the severity of an accident, but also on the likelihood of being engaged in one. Increasing automobile demand has resulted in increased road traffic and road accidents. People's lives are in grave danger. This is due to the lack of high-quality emergency services in our nation. Despite the numerous measures taken by the government and non-government groups throughout the world to make people aware of reckless driving via various programs, incidents continue to happen on a daily basis. Many lives may have been saved if emergency responders had gotten the crash report sooner. As per statistics 4.6% of accident deaths can be prevented if emergency responders had arrived at the time of the crash on time at every incident [1, 2]. As a consequence, intelligent system accident detection with immediate reporting of the accident site to emergency personnel is crucial to preserving human lives.

In this work, an IoT system has been implemented that could help the community reduce the number of people killed in car accidents [3, 4]. The approach had a number of benefits, reducing the contact between wounded passengers, providing basic health information to rescue workers, recognizing exact and accurate accident sites, and making the routing process simpler [5–7]. Our product will monitor the passenger's health by measurement of ECG signals, check for accident occurrence, and also check whether the driver has drunk. The vehicle enters into a stop state when the passenger ECG fluctuates more or when the driver has drunk [8, 9]. When the passengers fluctuate more or any accident is detected, an alert message is generated with a location link (Google maps) and sent to the nearest hospital/Toll plaza and also to the passenger's family members. An ambulance from the hospital will arrive at the accident location using the location link [10–13]. The proposed system will continuously monitor passengers and also monitor whether the accident occurred or not, thus many accidents can be prevented. These existing systems has some limitations: (a) Existing system has not dealt with GPS and accident detection combinedly, we have included both of these so we can get accurate location (b) Existing systems have used GSM-based connectivity which has a disadvantage of high cost of implementation. (c) Existing systems only concentrated on accident detection and not included the monitoring of the passenger and immediate alerting system. (d) No database is maintained for the accident-prone area.

2 Design and Working

The proposed system should detect the occurrence of accident and passenger's momentary health issues in a significantly shorter time and communicates in a couple of seconds, essential information such as geographic coordinates, time, and angle of an automobile accident is sent to the first aid center. This emergency notification is sent to the rescue team in a timely way, saving lives. When an accident occurs, an automated alert is issued to the rescue crew and the police station. The message is sent through the PHP server, and the location of the accident is established using a GPS module. By implementing the PHP server (web-based application with data storage), the overall, system behaves like a CLIENT–SERVER architecture. The collision may be detected accurately using both MEMS sensors and digital vibration sensors, and the passengers and driver are continually monitored using an alcohol detection sensor (just for the driver), an ECG sensor, and a pulse oximeter. The information from the MEMS sensor can also provide the inclination details regarding the car's rollover incident. This program intends to give the best possible answer to substandard emergency services supplied to road traffic incidents. Overall, the proposed System is a Client–Server based network architecture. On the Client End, Master(Raspberry Pi)—Slave(Arduino) [14] with sensor setup and the Server end is powered by PHP Server.

The vehicle gets input from various sensor outlets, then the core processors compute for any abnormality as an accident occurs, heart and breathing rate fluctuates more, and detects the consumption of alcohol. If any above-mentioned abnormality has been detected then the vehicle immediately enters into a stop state and gets GPS coordinates—latitude and longitude. Upload the GPS location to the cloud—PHP server, from the PHP server—the alert message will be sent to nearby emergency service providers like Hospital/Police Station/Toll Plaza and an alert message also sent to the passenger's registered relatives as illustrated in Fig. 1.

From Fig. 2, Arduino is the Passenger—End controller used to measure the passenger's saturation. If any abnormality is detected then Arduino will send the toggle signal to the Raspberry Pi—Central Processor. Arduino is used to perform Passenger End computation and also used to extract ECG signals and also to monitor the bpm. Interface: it will connect to pulse oximeter and ECG sensor. If any abnormality is absorbed then it will send a signal to Raspberry Pi, the main purpose of using this is to reduce the computation of Raspberry Pi if the number of passengers increases—it will be difficult for the Raspberry Pi to perform all tasks. Pulse-Oximeter—MAX30100, ECG-AD8232, and Normal 16*2 LCD are connected with Arduino via a wired medium.

Raspberry Pi is a central processor, with a GPS module, accelerometer, alcohol sensor, and vibration sensor, these are connected to Raspberry Pi via the wired medium. In this work, Raspberry Pi 0w is introduced which is used a central computation unit as it has better processing ability when compared to Arduino. Hence, Raspberry acts as master and Arduino acts as slave. Specifications of Raspberry Pi are: 802.11 b/g/n wireless LAN, Bluetooth 4.1, Bluetooth Low Energy (BLE),
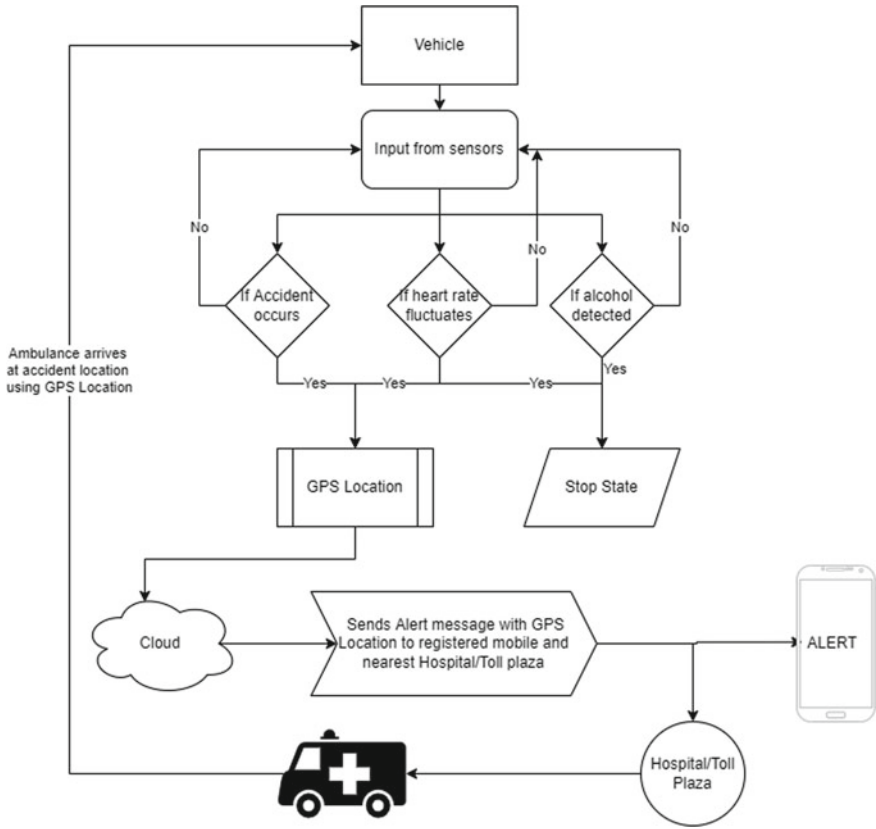
Fig. 1 Proposed flowchart
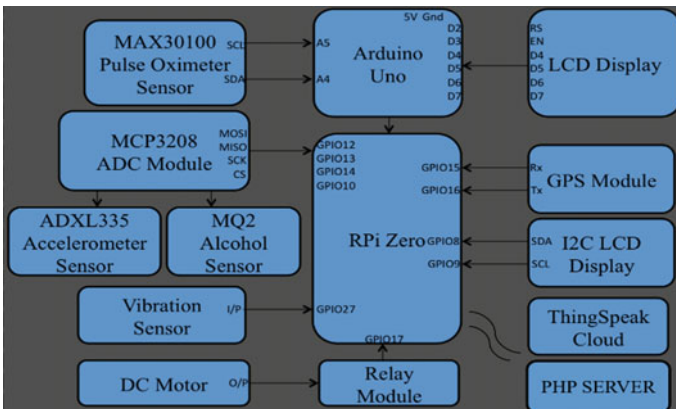
Fig. 2 Block diagram of the system

1 GHz, single-core CPU, 512 MB RAM, Mini HDMI port and micro-USB On-The-Go (OTG) port, Micro USB power, HAT-compatible 40-pin header, Composite video, and reset headers. It is easily can be fit in to our prototype. PHP server and Thingspeak are connected Wireless by integrating the API and API-Key in Raspberry Pi [4, 15].

2.1 ADXL335

By sensing the mounting angle, the sensor can help compensate for the device's mounting angle, allowing for the employment of ACCELEROMETER FACTSHEET MEMS 3-AXIS ACCELEROMETER typical SMD technology in high-density boards as well as precise inclination angle detection [16]. If an accident occurred on the front side of the vehicle, then the center of mass of the vehicle will shift toward the impact location, so we can observe some upward jerk in the vehicle's backside. To find out vehicle orientation like accident is detected on the front, back, left, and right, we kept ADXL in respective positions several times to find out the threshold. By repeating for various orientations, a threshold for operation is fixed.

2.2 MQ2

Gas sensors come in a variety of configurations based on sensitivity levels, gas type, physical dimensions, and a variety of other considerations. Gas is ionized and then adsorbed by the detecting element when it comes into contact with this sensor. This adsorption causes a potential difference in the element, which is sent as current to the processing unit through output pins. According to tests conducted by us using sanitizer—the sensor value is always greater than 2000. In a normal state, it's varying around some 200. Hence, after observing these values, we have fixed a threshold value as 2000 (for alcohol) which is detected from the MQ2 sensor. When threshold value crosses 2000, a signal is sent to the Raspberry Pi, stopping the motor driver which eventually moves vehicle to stop state. For alcohol-based hand sanitizers, a concentration of 60–95% ethanol, so we have fixed a threshold as 2000.

2.3 SW420

The SW420 Vibration Sensor Module is based on the SW-420 vibration sensor, which works on the basis of the circuit being briefly severed and the output low when movement or vibration occurs. As a result, the sensor's regular condition is closed. An inbuilt potentiometer and an LM393 Comparator IC may regulate the sensitivity of the SW420 Sensor. Collisions, burglary protection alarm systems, vibration alert

systems, and other applications benefit greatly from this. Accidents will be confirmed with help of the accelerometer and vibration sensor, If an accident occurred then the vehicle will undergo some severe vibrations and change in vehicle orientation and position. The effect of accident was introduced in this model by hit and tap, where the prototype take a hit in the front is reflect as accident from the front. When the vibration is been detected, then resistance of potentiometer is increases abruptly (tends to infinite) so there is no current flow, since a current flow in a low resistance path therefore there will not be any potential-drop, so the output voltage will be same as input voltage (high state).

2.4 MAX30100

The MAX30100 is a pulse oximeter and a heart rate monitor in one device. It detects pulse oximetry and heart rate signals using two LEDs, a photodetector, improved optics, and low-noise analog signal processing. It works with 1.8 and 3.3 V power sources and can be software-shut down with an extremely low standby current, allowing the power supply to remain connected at all times. According to studies, the normal saturation value range for human body is, for spo2—90–99% and for BPM-less than 120 and greater than 60 beats per minute which mean 60–120—R peaks per minute [17]. If any above-mentioned threshold crosses, then we can say that a particular person is on edge of saturation—immediate medication is required. By continuously collecting the heart rate and oxygen level (SPO2) of the passengers using this sensor which is compared with the medical standards, and sudden abnormality is identified and sends the alert signal to the possible rescue teams.

2.5 SIM28M

A global positioning system (GPS) device estimates the current location of the user, speed, and elevation via trilateration, a mathematical technique. A GPS system can compute the exact distance or range of any satellite being monitored by continuously collecting and analyzing radio signals from several GPS satellites and using the geometries of circles, spheres, and triangles. GPS receiver will get data from different providers like GPS, GNSS-GNRMC, GLONASS, etc., but for accuracy in this system GNSS has used—approximately GNSS will be using more than 66 satellites [3, 10, 12]. The first step is to filter the GNSS from received data from the GPS receiver module. Under hardware requirements and its overview section, given the general format of GPS modules receiving data from satellites. By using string and format comparison, we can easily get the required data.

2.6 MCP3208

The MCP3208 12-bit ADC is good for applications controlled by embedded devices because it combines better performance and less power consumption. The MCP3208 provides 12-bit ADC capabilities to any PICmicro controller using a sequential approximation register (SAR) architecture and an industry-standard SPITM serial interface. The MCP3208 uses a sampling rate of 100k samples per second, eight input channels, less power (5 nA normal standby, 400 A maximum active), and a 16-pin PDIP and SOIC design.

2.7 LCD Display

A liquid–crystal display (LCD) is a flat-panel display or another electronically manipulated optical device that uses liquid crystals and polarizers to modulate light. LCD is used to print the SPO2 and BPM, by using standard normal parallel communication.

2.8 I2C LCD Display

It is used to reduce pin use, since it uses serial communication and to print alcohol value in 1st line and state of the vehicle in 2nd line like normal state, accident detected in front, accident detected in back, accident detected in left and accident detected right. If vibration is detected or alcohol consumption is detected, it will print in the 2nd line.

Software specifications:

Python 3: Coding in Raspberry Pi and calculating RR interval
Arduino ide: Coding for Arduino uno
Noobs os: Creating a user-interface for Raspberry Pi 0
html and php used for web application development. HTML is for front-end and PHP for back-end.

3 Results and Discussion

If an accident occurs at any side of the vehicle. Then the motor enters into stop state, in LCD it displays as an accident occurred at the corresponding sides of the vehicle.

Figure 3a corresponds to a normal state, Fig. 3d corresponds to when the accident happened on the right side, and Fig. 3g corresponds to when an accident occurred on the front side. Similarly, the sensor will detect the accident that occurred on the back and left sides.
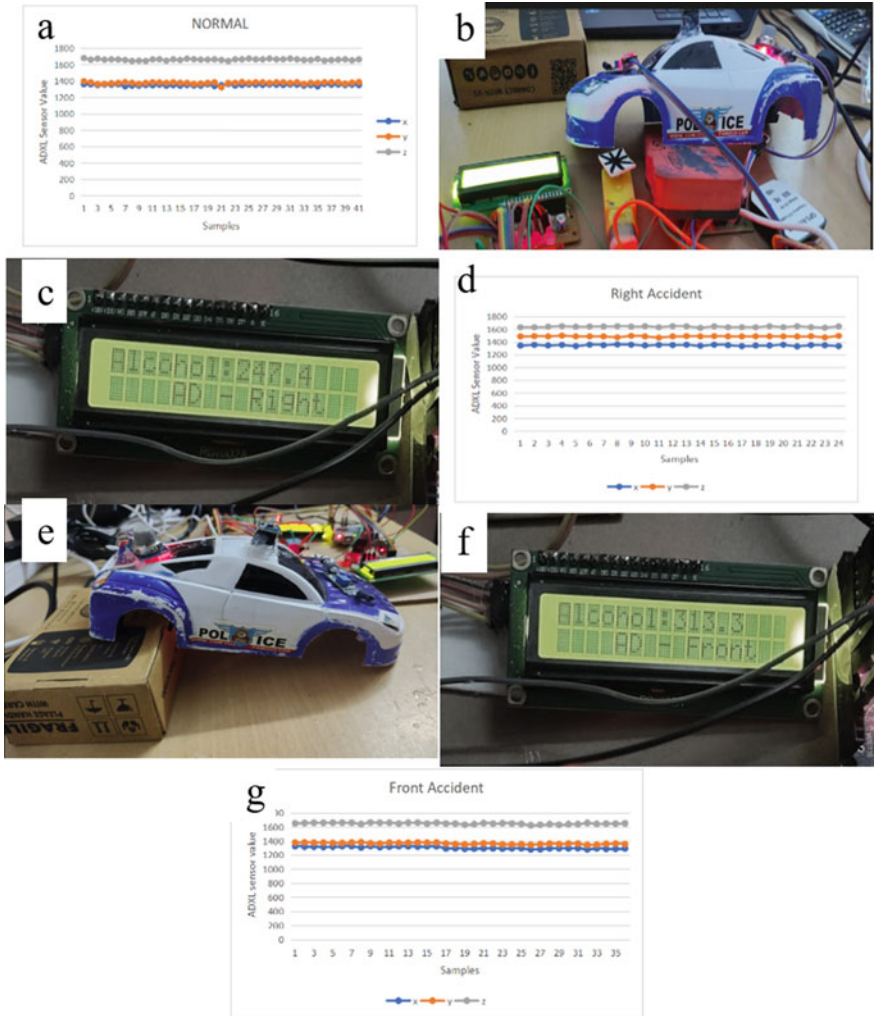
Fig. 3 **a** Normal state, **b** the car tilted toward the right, **c** LCD displaying an accident that occurred on the right, **d** accident occurred at right side, **e** car tilted frontwards, **f** LCD displaying an accident that occurred, **g** the accident occurred at the front

When alcohol is detected by an alcohol sensor then it displays on LCD—alcohol is detected and it will make the vehicle enter into a stop state. A sanitizer bottle cap is used for testing purposes, Fig. 4.

When the accident occurs along with the accelerometer sensor, the vibration sensor will sense the crash—the impact of collision that is when the accident occurred then huge vibration will be experienced by the car. SW420—crash sensor used in Fig. 5.

Spo2 and BPM of a person will be monitored for each minute along with ECG to detect sudden abnormalities and displays the reading values in normal LCD display
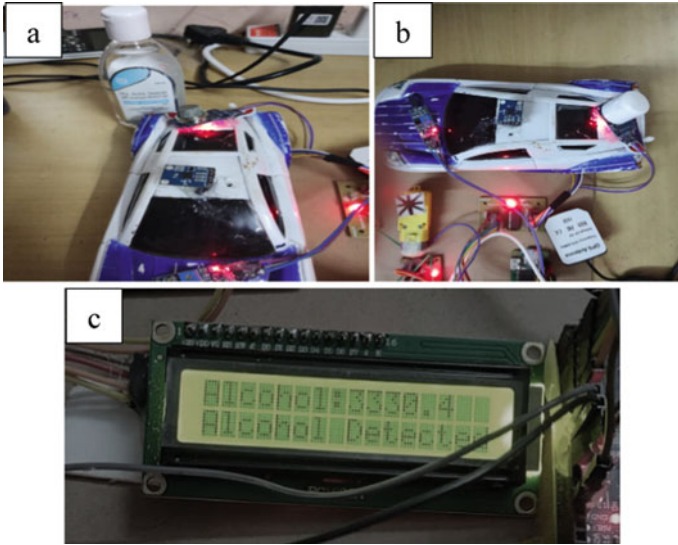
Fig. 4 Alcohol detection with help of sanitizer **a** when the bottle is capped, **b** bottle uncapped and sensed, **c** signal processed and displayed
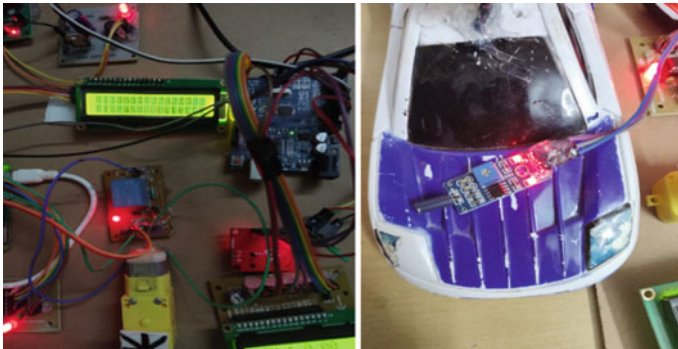
Fig. 5 Vibration detection

under Passenger's module-Arduino UNO and if any abnormality happened then immediately Arduino will send the toggle signal to Raspberry Pi 0 then Raspberry Pi displays on abnormality message on I2C-LCD, results represented in Fig. 6.

The red-colored peak value in Fig. 7 is nothing but an R peak from the "PQRST" Complex—that is equivalent to one heartbeat. The green-colored plot is the moving average, by using this R peak has been calculated. The average BPM for this particular heartbeat is 117.8. And, its standard deviation is a 30% deviation from mean value. R-R intervals are calculated with the help of the heart beat plot in Fig. 8 and interpolated for ease of frequency analysis.
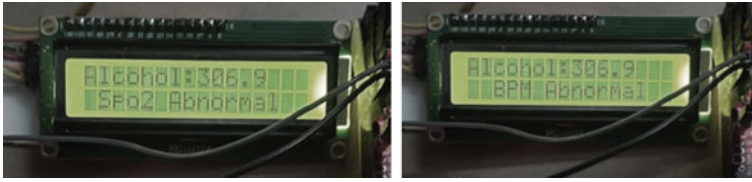
Fig. 6 BPM and SPO2 sensors
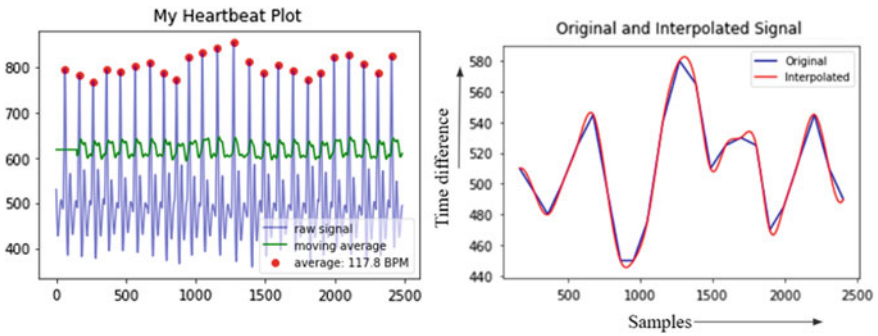
Fig. 7 Heart beat and list of RR intervals
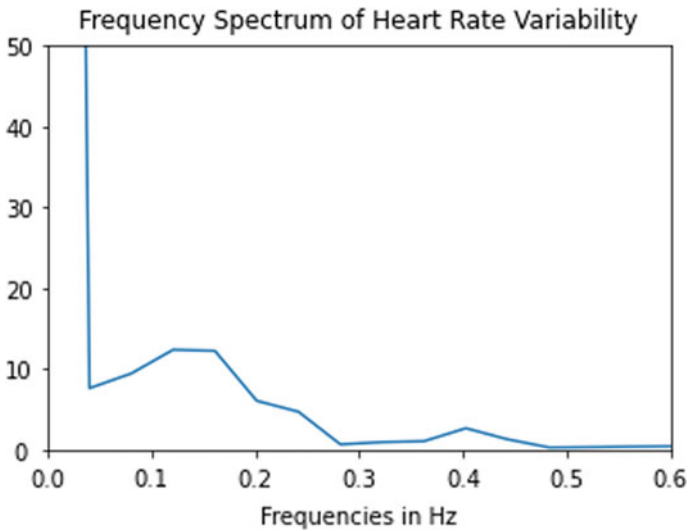
Fig. 8 List of RR intervals in the frequency spectrum

3.1 PHP Server and Webpage Interface

On the whole, the proposed system is a three-end alerting system, the 1st is sending an alert message to Nearby Hospital/Toll Plaza/Police Station, the 2nd is sending an alert message to Passenger's relatives and the third one is—our back-end team will be notified when any abnormality occurs by monitoring PHP Server index page in Fig. 9a. For the ease of use, users can easily update their Personal details in Fig. 9d. In Fig. 9b, the registration team will update the hospital/toll plaza/police station details by adding new things or editing the existing things and in Fig. 9a, having a list of emergency service providers. Also, maintaining a list of accidents occurring locations in the database to notify the user about the accident-prone area. In this work, a page has been designed that will be accessed only by the user to add his/her relative's details. If an accident or any anomaly occurs then CPMAD gets Coordinates data—Latitude and Longitude from GPS the module and sends the alert message to nearby emergency service providers like Hospital/Toll Plaza/Police Station and also to the Passengers' relatives with the help of CPMAD's PHP server by using the Webber leads. In Fig. 9d by clicking the link present in the Alert MessageGoogle Maps will be opened for ease of Navigation. Registration phase architectural diagram is shown in Fig. 10.

The web application has been developed in such a way to allow the authorized users to add more emergency service provider and also to add user's personal Information. The emergency service provider includes Hospitals, Toll Plazas, Police stations, etc. The location and contact details can be uploaded into the database and it then serves as an emergency service provider. The User's personal Information can also be added using the web application. This includes the relative's mobile number/Email. Both the emergency service provider and relative will be notified once an accident is detected.

Further this work can be improvised by implementing the following additional features: (1) Making the real-time system by implementing them in the vehicle (four-wheelers), (2) Checking for abnormality of the passengers using the ECG electrodes placed in the seat belt.

4 Conclusion

A system to detect an event of an accident can also check for heart anomalies and drunken drivers in a vehicle. The proposed system works for accident and abnormal heart detection and alerting. It reads the passenger's BPM and oxygen level using SPO2 and BPM sensors continuously for abnormality. If found, an alert will be generated and passed to the nearest emergency service (Hospital/toll plaza/police station). For the accident detection, using ADXL335 data, we are classifying whether the accident occurred as front/back/right/left. Once detected, accurate latitude and longitude coordinates of the vehicle at the time of the accident are found using a
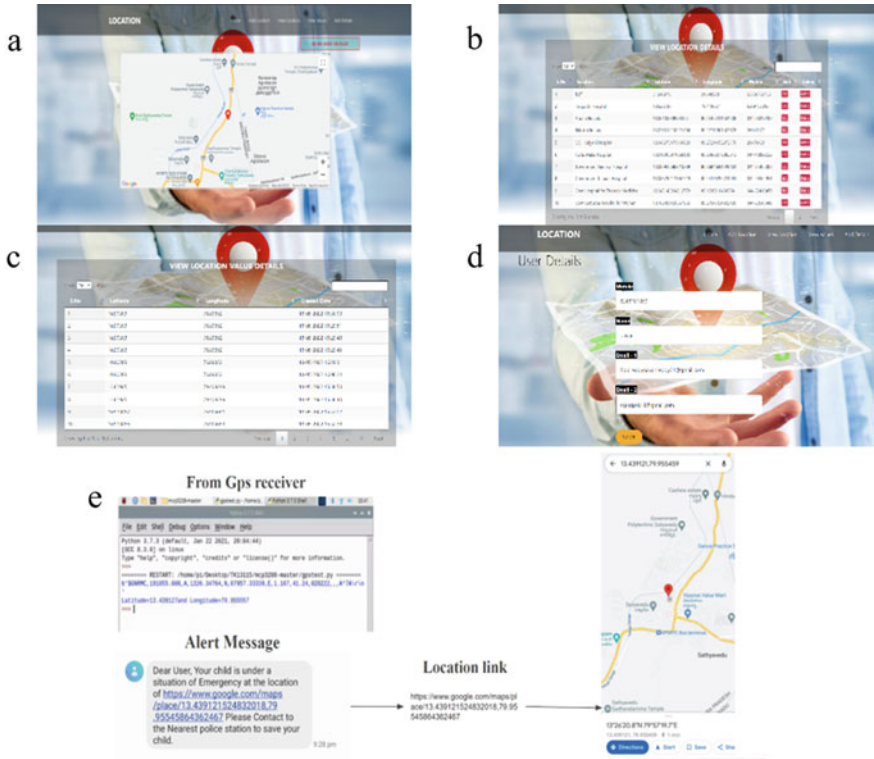
Fig. 9 **a** Accident occurred location, **b** list of emergency service providers, **c** list of accident occurred location, **d** passenger's relative details, **e** alert message sent by CPMAD to nearby emergency service providers and passenger's relatives
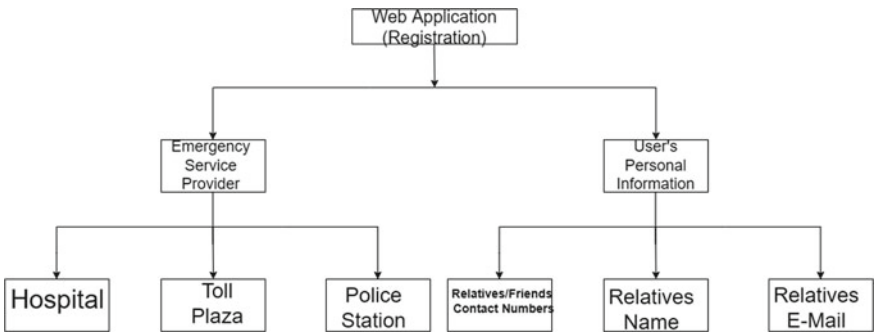
Fig. 10 Registration phase architectural diagram

GPS receiver, and an alert message along with the GPS location link is sent to the nearest hospital, from where ambulance service is sent to the accident location for support. This system also proposes accident detection with the help of an mq2 sensor (alcohol detection). It detects whether the driver has drunk or not, and stops the car's engine if the driver is drunk, the MQ2 sensor (Alcohol Detection). Gas sensors react spontaneously to the presence of alcohol in the air, keeping the system informed of any increasing concentration of molecules in the gaseous state. When the gas comes into contact with these sensors, it is first ionized and then adsorbed by the detecting element. This adsorption produces a potential difference in the element, which is sent to the processing unit as the current through output pins. It detects whether the driver has drunk or not, and stops the car's engine if he is drunk using an MQ2 sensor.

References

1. Virtanen N, Schirokoff A, Luoma J (2005) Impacts of an automatic emergency call system on accident consequences
2. Byrne JP, Mann NC, Dai M, Mason SA, Karanicolas P, Rizoli S, Nathens AB (2019) Association between emergency medical service response time and motor vehicle crash mortality in the United States. JAMA Surg 154:286. https://doi.org/10.1001/JAMASURG.2018.5097
3. Luthfi AM, Karna N, Mayasari R (2019) Google maps API implementation on IOT platform for tracking an object using GPS. In: Proceedings—2019 IEEE Asia Pacific conference on wireless and mobile, APWiMob 2019, pp 126–131. https://doi.org/10.1109/APWIMOB48441.2019.8964139
4. Bin Kamarozaman N, Awang AH (2021) IOT COVID-19 portable health monitoring system using Raspberry Pi, Node-Red and ThingSpeak. In: 2021 IEEE Symposium on Wireless Technology & Applications (ISWTA), pp 107–112. https://doi.org/10.1109/ISWTA52208.2021.9587444
5. Nasr E, Kfoury E, Khoury D (2016) An IoT approach to vehicle accident detection, reporting, and navigation. 2016 IEEE international multidisciplinary conference on engineering technology (IMCET), pp 231–236. https://doi.org/10.1109/IMCET.2016.7777457
6. Patil PJ, Zalke RV, Tumasare KR, Shiwankar BA, Singh SR, Sakhare S (2021) IoT protocol for accident spotting with medical facility. J Artif Intell Capsul Netw 3:140–150. https://doi.org/10.36548/jaicn.2021.2.006
7. Bhambri P, Bagga S, Priya D, Singh H, Dhiman HK (2020) Suspicious human activity detection system. J ISMAC 2:216–221. https://doi.org/10.36548/jismac.2020.4.005
8. Sandra KR, Anusha AS, Mohan NM, George B (2015) Simulation study of a contactless, capacitive ECG system. In: IEEE Region 10 annual international conference proceedings/TENCON. 2015-January. https://doi.org/10.1109/TENCON.2014.7022474
9. Zu Li H, Boulanger P (2020) A survey of heart anomaly detection using ambulatory electrocardiogram (ECG). Sensors 20:1461. https://doi.org/10.3390/S20051461
10. Shah D (2013) Automatic vehicle accident detection system based on ARM&GPS
11. Ramasami S, Gowri Shankar E, Moulishankar R, Sriramprasad D, Sudharsan Narayanan P (2018) Advanced ambulance emergency services using GPS navigation. Int J Eng Res Technol 6:4–8
12. Mitha MG, Mutharasu S (2008) Vehicle accident detection system by using GSM and GPS. Int Res J Eng Technol 1574. www.irjet.net
13. Goud V (2012) Vehicle accident automatic detection and remote alarm device. Int J Reconfig Embed Syst 1. https://doi.org/10.11591/ijres.v1i2.493

14. Harikumar ME, Reguram M, Nayar P, Low cost traffic control system for emergency vehicles using ZigBee. In: Proceedings of the 2018 3rd international conference on communication and electronics systems (ICCES). https://doi.org/10.1109/CESYS.2018.8724035
15. Chen X, Zhang J (2021) The applications PHP, HTML and MYSQL in development of website—query function. In: ICMLCA 2021; 2nd international conference on machine learning and computer application, pp 1–4
16. Hasibuzzaman M, Shufian A, Shefa RK, Raihan R, Ghosh J, Sarker A (2020) Vibration measurement analysis using Arduino based accelerometer. In: 2020 IEEE Region 10 symposium (TENSYMP 2020), pp 508–512. https://doi.org/10.1109/TENSYMP50017.2020.9230668
17. Raj A, Karthik AK, Sachin S, Sanchana M, Ganesan M (2019) A wearable device to detect blood volume change. In: 2019 5th international conference on advanced computing & communication systems (ICACCS), pp 379–381. https://doi.org/10.1109/ICACCS.2019.8728520

Design and Implementation of a Safety Device—Protecta Watch

V. Hindumathi, Pulavarti Vennela, R. Mahima, Devireddy Varshitha Reddy, and Heena Shahanaz

Abstract In today's world, acts of abducting and brutality against people are increasing at an alarming rate. According to World Health Organization (WHO) poll, 35% of individuals are abducted around the world. Even though smartphone technology has advanced rapidly, holding phone to make a call or send message remains inconvenient. As a result, Protecta watch was created, which helps to prevent danger. It is an IoT device that transforms smartwatch with a safety device. It generates a live location sharing, an alert message, and an emergency call dial that the victim starts with a click of a button. It uploads data of mobile global positioning system (GPS) to the cloud every 5 min using Blynk server. The circuitry is designed on a printed circuit board (PCB) for a form factor. This device is both affordable and revolutionary in terms of protection strategy due to the convergence of all three functional areas.

Keywords Location sharing · Alert message · Emergency call · Mobile GPS · Blynk server · Gadget

1 Introduction

In worldwide, missing persons cases have become one of the most serious issues as shown in Fig. 1. With a survey [1] of missing persons, an average of 174 cases of missing persons are reported daily, with 50% of the missing persons remaining untraceable. In 2019, National Crime Records Bureau (NCRB) data revealed that 422,439 women and 270,433 men were reported missing in India. People, especially women, are not secure in any place, especially while travelling alone on isolated roads, desolate areas [2], and in public venues such as railways, bus stops, and pathways [3]. A sufficient effort is needed to make the world a safer place. Atrocities

V. Hindumathi · P. Vennela (✉) · R. Mahima · D. Varshitha Reddy · H. Shahanaz
Department of Electronics and Communication Engineering, BVRIT HYDERABAD College of
Engineering for Women, Hyderabad, India
e-mail: vennelapulavarti@gmail.com

V. Hindumathi
e-mail: hindumathi.v@bvrithyderabad.edu.in

Fig. 1 Rate of kidnapping
and abduction cases [4]
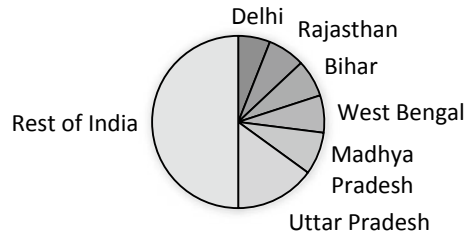
against people in the current scenario, and concerns about missing victims and threats
against them, led to the development of a GPS-based watch that may provide a
valuable solution. A watch can track individual's location by utilizing a Subscriber
Identification Module (SIM) 800L module and an ESP8266 microprocessor with
built-in Wi-Fi. All of these factors contribute to the device's low cost and ease of
use. Furthermore, this device supports both Wi-Fi and mobile data connections. This
watch will act as an equipment that continuously broadcasts location data to the
cloud, allowing anyone to track a person's last known location if they go missing
without requiring much interaction in extreme situations. Any such information will
be essential in resolving the case of a missing individual. As a result, the safety of a
person in danger will be secured to some extent.

It is planned to execute with 2 GPS setting

- Getting mobile GPS directly
- Using GSM module.

During an emergency, a person's location can be communicated with individuals
on the "emergency list" through short message service (SMS). A person can also
dial 100 or any other government-issued emergency number that has been added to
their watch's emergency number list. As a result, assistance can be provided as soon
as feasible. The Protecta watch also has a smart display that shows the date, time,
battery percentage, message notifications, and Internet connectivity, among other
things. As a result, it is exceptionally comfortable to wear as a regular watch.

2 Literature Review

Several authors from around the world provided a wide range of technical approaches
to minimizing vulnerabilities [5]. One-touch alarm system for women's safety using
GSM is a PIC micro-controller device that alerts friends and family in the event of an
emergency with just a push of a button, sends an automatic call, and transfers location
of the victim to a neighbouring police station and stored numbers. Global System
for Mobile Communication (GSM) module is connected to the microcontroller via
serial communication port RS232 using the IC MAX 232.

The device [6, 7] FEMME, an ARM-based safety device, and it is a type of security equipment made exclusively for women. By connecting the device through Bluetooth with the phone and triggering an instant location, emergency message, and video and audio of entire occurrence to the registered contacts. It also contains a concealed camera detection module that uses a RF receiver to detect EM waves that are emitted by camera. Similarly, [8, 9] are apps that are made specifically for women's use.

Personal monitoring devices, such as smartwatches, wristbands, monitoring patches, and smart textiles, are increasingly being employed outside of clinical settings as complicated physiological observation systems get minute, economic, and handy. Pantelopoulos and Bourbakis created a gadget [10] with medical sensors that can measure several parameters like pulse rate, rate of breathing, wearer's temperature, and glucose levels.

A Real-time Location Tracker for Critically ill Patients [11] is an IoT gadget built with sensors such as GPS Neo 6m, Arduino, and GSM Sim800L which send the precise GPS coordinates of patient to the server. Physicians and hospital staff may also track the patient's actual location using the server's web interface and Google Maps, and treat him accordingly.

Reference [12] outlines a GPS and GSM-based vehicle monitoring and women employee security system that uses a GPS gadget and specialized software to track the vehicle's location, send warnings and messages, and activate an emergency button. Google Maps can display the device's information about the vehicle's location.

The astute device "Smart Foot Device for Women Safety", according to Viswanath et al [13] is fitted within client's footwear. When one foot after another is repeatedly tapped, an alarm is sent via Bluetooth communication to an application on the victim's phone. It is set to generate an SMS requesting assistance with the device's related territory.

SMARISA [14] is a personal safety gadget for women. Hardware components like buzzer, Raspberry Pi and switch are used to activate the services provided by the gadget. The device can be activated by the person by clicking the switch. The camera captures the attacker's image with a click, which is subsequently sent to the police and programmed emergency contact numbers through victim's smartphone.

According to Muhamad [15], a Smart Bike Monitoring System for Riders by IoT helps in analysing cyclists' health and performance. Sensors such as a heart rate sensor, a pulse oximetry sensor, and a GPS module are linked to a microcontroller and a Wi-Fi module via an IoT platform, a Blynk application. Cyclists' data can be tracked by both the rider and coach.

The user and their smartphone can effortlessly communicate with the help of the wristwatch application [16]. Apps offer a wide range of smartwatch modification applications. A wearable device has a significant potential for guidance and assistance.

3 System Design

Figure 2 shows the schematic of PCB for the watch. The schematic consists of ESP12, SIM800L, organic light emitting diode (OLED) display, universal serial bus (USB) to transistor–transistor logic (TTL) converter, battery charger, battery protection, voltage regulator, USB, buttons, and uploader.

The Protecta watch is composed of several parts that work together to do various tasks [17]. Here, ESP12F is used as a microcontroller. The main criterion to select ESP12F as microcontroller is it a WIFI-module based on ESP8266, with built-in 32 M bit Flash, in the small SMD22 package. There are also onboard PCB antenna and metal shield. The ESP12F microcontroller controls the watch's numerous functions and operations. For example, it utilizes the I2C (inter-integrated circuit) protocol to communicate with the screen and the Universal Asynchronous Receiver–Transmitter (UART) communication protocol to communicate with the SIM800L [18]. The SIM800L module has three main functions: making an emergency call and sending an SMS to pre-saved phone numbers [19], sharing the victim's location with the emergency list via SMS, and locating the victim in the absence of WI-FI using a technique called mobile positioning, which detects the nearest cell tower.

The home screen of the watch, a 128 * 64 OLED display, displays Wi-Fi, network availability, time, date, and battery charge percentage. A TP4056 IC lithium-ion battery powers the watch, while the DW01 IC acts as the battery protection circuit,
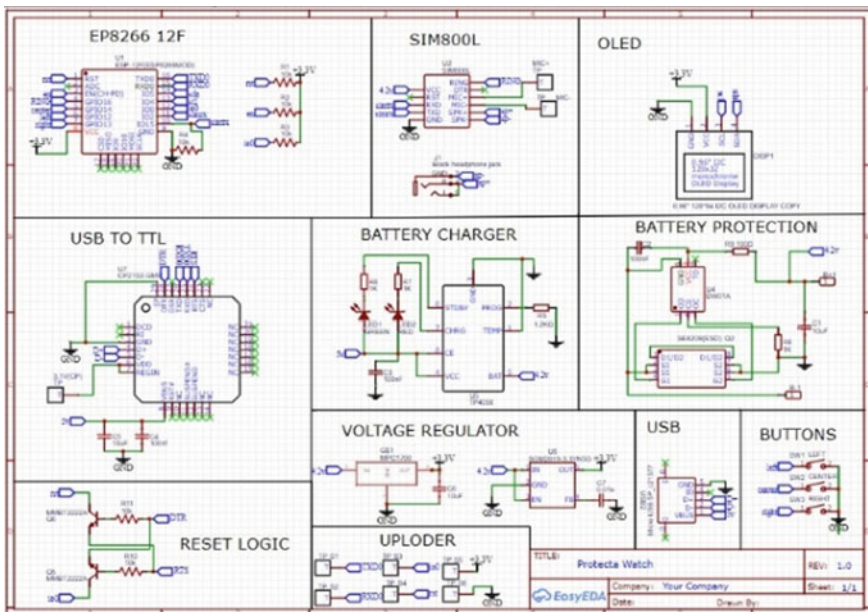
Fig. 2 Schematic of PCB for Protecta watch

protecting the battery from overcharging and discharge. The TLV702 IC controls the voltage supply to all of the watch's modules following their voltage needs.

USB to TTL converter creates a communication channel between the PC & the microcontroller via UART serial port. USB-To-TTL converter module is used because we cannot just hook the RX/TX pins to the D+/D− pins of a USB port. The USB to TTL converter translates data from USB pins to TTL format, which is the microcontroller's preferred format. Its main purpose is to transfer code to the microcontroller. The USB to TTL converter is supported by reset logic. The Protecta watch's USB connector is of the Micro-B variety. It serves two functions. The first step is to upload code to the ESP12F, followed by charging the watch.

All communications between the smartphone and hardware are handled by the Blynk server. You can host your private Blynk server locally or utilize Blynk cloud.

In order for us to access the person's position through mobile devices as well, the location that was gathered above through SIM800L is transferred to the Blynk cloud.

4 Result

This section presents the output of the gadget with the proposed hardware design and the mobile application.

4.1 Initialization

Here, booting of microcontroller takes place and the device gets connected to Wi-Fi.

When the device is switched ON, initial page is displayed as in Fig. 3. The device then searches for available Wi-Fi as in Fig. 4 and connects to it. After connecting to Wi-Fi, home page is displayed. The time, day, date, Wi-Fi connectivity, signal and battery percentage are displayed on the home page as in Fig. 5. Several other options are also available to navigate through using buttons like calling, sending message, and sending device location.

4.2 GPS Screen

On selecting GPS option as in Fig. 6, location is displayed which consists of latitude number and longitude number, and altitude is displayed as in Fig. 7.

Fig. 3 Initial page

Fig. 4 Connects to Wi-Fi

Fig. 5 Home page

Fig. 6 Satellite logo

Fig. 7 Location display

4.3 Call Screen

On selecting phone option as in Fig. 8, saved contacts are displayed as in Fig. 9. On selecting the required contact, the call is initiated as shown in Fig. 10.

After initiating the call with specified contact, it gets connected as shown in Fig. 11. Wired earphones can be connected to the device for communicating with the contact. The call can be ended by the user by clicking right button and can be seen as in Fig. 12. After ending the call, phone logo is displayed again.

Fig. 8 Phone logo

Fig. 9 Contacts display

Fig. 10 Call display

Fig. 11 Connected

Fig. 12 Call end

4.4 Message Screen

On selecting message option as in Fig. 13, contacts are displayed as shown in Fig. 14. On selecting the required contact and the message as shown in Fig. 15, the message together with the device location is sent, and the screen as shown in Fig. 16 is displayed as soon as the message is delivered to the person.

4.5 Battery Screen

On selecting battery option as shown in Fig. 17, the level of the LiPo battery connected to the device is displayed as shown in Fig. 18 in terms of percentage.

Fig. 13 Message logo

Fig. 14 Contacts list

Fig. 15 Message list

Fig. 16 Message sent
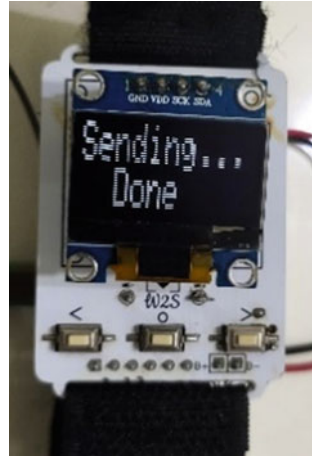
Fig. 17 Battery logo

4.6 Emergency Situation

In case the user is stuck in any emergency situation where he wants to reach for any help, then by clicking the centre button of the device continuously for three times, emergency mode can be activated. After entering the emergency mode, alert message which includes location of device is sent to the first three saved contacts as shown in Fig. 19, and a call is initiated to emergency helpline number as shown in Fig. 20.

Fig. 18 Battery status
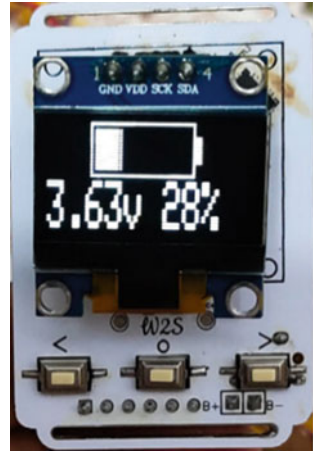
Fig. 19 Alert message

4.7 Wi-Fi Unavailability

The device is always connected to available Wi-Fi, and when Wi-Fi is not available, it can be seen as in Fig. 21 and then starts searching for Wi-Fi as shown in Fig. 22, and if it is not available, the device switches on its mobile data and again displays home page again as in Fig. 23. From the device configuration, it can access data of 2G speed.

Fig. 20 Emergency call

Fig. 21 Wi-Fi unavailable
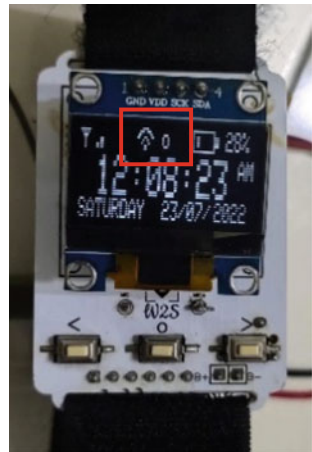
4.8 BLYNK App

The device also gets connected to Blynk application which is an IoT platform that can be used to control ESP 12F, the microcontroller used in this device. In Blynk application, two devices are created to interface with Protecta watch as shown in Fig. 24. The Blynk app displays the information stored in the cloud about position coordinates. Additionally, the level of the battery in the device is also shown in terms of the percentage.

Fig. 22 Searching for data

Fig. 23 Switched to mobile data

5 Conclusion

The device "Protecta watch" has been successfully designed and tested. This device assists in finding the quickest route to safety. The proposed design addresses the victim's unsafe conditions and will aid in resolving them. The intention behind this device is to develop a smart, low-cost device that will help in building a safe environment that will bring succour to sufferers of rape, harassment, child trafficking, and other hazardous situations. The calibre of this work is to not only provide safety but also to serve as an efficient smartwatch. With furthermore analysis, this device will enable protection in every facet of security and surveillance all around the globe.

Fig. 24 Blynk display
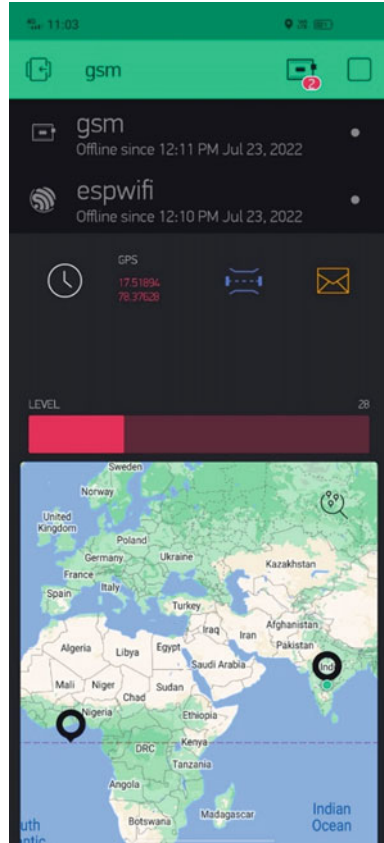
6   Future Scope

This device extends the potential to design a system that stands as a forewarning for all the offenders, which will help evict crime rates. Notifications can be received on watch for SMS along with call purpose and including a pedometer, pulsometer, and temperature sensor could help in evaluating heart rate, step count, and temperature correspondingly.

References

1. Sai PDNH, Kiran VVS, Rohith K, Rajeswara Rao D (2022) Identification of missing person using convolutional neural networks. In: 2022 international conference on sustainable computing and data communication systems (ICSCDS), 2022, pp 485–489. https://doi.org/10.1109/ICSCDS53736.2022.9760777

2. Akram W, Jain M, Hemalatha CS (2019) Design of a smart safety device for women using IoT. Procedia Comput Sci 165:656–662

3. Mishra V, Shivankar N, Gadpayle S, Shinde S, Khan MA, Zunke S (2020) Women's safety system by voice recognition. In: 2020 IEEE international students' conference on electrical, electronics and computer science (SCEECS), 2020, pp. 1–5. https://doi.org/10.1109/SCEECS48394.2020.3

4. Singh SK (2016) Heinous crimes against women in India. J Soc Polit Econ Stud 41(3):51

5. Premkumar P, CibiChakkaravarthi R, Keerthana M, Ravivarma R, Sharmila T (2015) One touch alarm system for women's safety using GSM. Int J Sci Technol Manag 04(01)

6. Monisha DG, Monisha M, Pavithra G, Subhashini R (2016) Women safety device and application-FEMME. Indian J Sci Technol 9(10):1–6

7. Chaware M, Itankar D, Dharale D, Borkar D, Kumar Pendyala S, Nimbarte M (2020) Smart safety gadgets for women: a survey

8. Yarrabothu RS, Thota B (2015) Abhaya: an Android app for the safety of women. In: 2015 annual IEEE India conference (INDICON), pp 1–4. https://doi.org/10.1109/INDICON.2015.7443652

9. Bhardwaj N, Aggarwal N (2014) Design and development of "Suraksha"—a women safety device. Int J Inf Comput Technol 4(8):787–792

10. Pantelopoulos A, Bourbakis NG (2010) A survey on wearable sensor-based systems for health monitoring and prognosis. IEEE Trans Syst Man Cybern Part C (Appl Rev) 40(1):1–12. https://doi.org/10.1109/TSMCC.2009.2032660

11. Kanani P, Padole M (2020) Real-time location tracker for critical health patient using Arduino, GPS Neo6m and GSM Sim800L in health care. In: 2020 4th international conference on intelligent computing and control systems (ICICCS), pp 242–249. https://doi.org/10.1109/ICICCS48265.2020.9121128

12. Bhilare P, Mohite A, Kamble D, Makode S, Kahane R (2015) Women employee security system using GPS and GSM based vehicle tracking. Int J Res Emerg Sci Technol 2(1)

13. Viswanath N, Pakyala NV, Muneeswari G (2016) Smart foot device for women safety. In: 2016 IEEE region 10 symposium (TENSYMP), pp 130–134. https://doi.org/10.1109/TENCONSpring.2016.7519391

14. Sogi NR, Chatterjee P, Nethra U, Suma V (2018) SMARISA: A raspberry pi based smart ring for women safety using IoT. In: 2018 international conference on inventive research in computing applications (ICIRCA), pp 451–454. https://doi.org/10.1109/ICIRCA.2018.8597424

15. Muhamad WNW, Razali SAB, Wahab NA, Azreen MM, Sarnin SS, Naim NF (2020) Smart bike monitoring system for cyclist via Internet of Things (IoT). In: 2020 IEEE 5th international symposium on telecommunication technologies (ISTT), pp 168–173

16. Chauhan J, Seneviratne S, Kaafar MA, Mahanti A, Seneviratne A (2016) Characterization of early smartwatch apps. In: 2016 IEEE international conference on pervasive computing and communication workshops (PerCom workshops). IEEE, pp 1–6

17. Panda PK, Mehtre B, Sunil DM, Devanathan M, Subhash BK, Panda SK (2020) A compact safety system for women security using IoT. In: 2020 IEEE international conference on technology, engineering, management for societal impact using marketing, entrepreneurship and talent (TEMSMET), pp 1–6. https://doi.org/10.1109/TEMSMET51618.2020.9557450

18. Hanif MI, Ahmed S, Akanda W, Barman S (2020) Anti-molestation: an IoT based device for women's self-security system to avoid unlawful activities. Int J Adv Comput Sci Appl 11(11)

19. Mela JL, Herrera EC, Mendoza GB (2019) Design and implementation of security device with dual wireless communication interface for cloud-based framework

A Survey on Energy Management Evolution and Techniques for Green IoT Environment

I. Shanmugapriya

Abstract The introduction of Internet of Things (IoT) has benefitted smart cities, healthcare, and transportation applications for enabling smart connections and analyzing the performance. As the number of IoT devices and potential connectivity increases, the distance between smart hubs, smartphone software complexity, and people behaviors changes rapidly resulting in a power utilization challenge. Energy efficiency and power dissipation are two of the most significant challenges in green IoT-enabled technologies. Based on a systematic literature review, this study presents the power management possibilities in the Internet of Things (IoT) domain. The main purpose of this study is to develop energy-efficient approaches for WSNs that enable IoT. The "Green IoT" concept aims to reduce the energy consumption of IoT devices while maintaining sustainability conditions. In this study, which is driven by establishing a viable IoT environment for the future phase and moving the globe toward the formation of Green IoT, a review of Green IoT (GIoT) is first provided, and then the challenges and potential possibilities for GIoT are studied.

Keywords Cloud computing · Green Internet of Things (IoT) ·
Machine-to-machine (M2M) · Near-field communication (NFC) · Radio-frequency identification (RFID) · Wireless sensor networks (WSNs)

1 Introduction

Internet of Things (IoT) is gaining an increasing research interest among Information and Communication Technology (ICT) researchers. The term Internet of Things (IoT) is described as a network of billions of things/people connected to one another [1]. The communication between IoT devices can be established at any point of time and any place by employing different services via any link. IoT is a heterogeneous environment, which includes a number of nodes, such as sensors, RFID tags, RFID readers, and mobile devices [2]. Internet of Things (IoT) is more than simply

I. Shanmugapriya (✉)
Department of Computer Science, PSG College of Arts & Science, Coimbatore, Tamil Nadu, India
e-mail: drshanmugapriya2@gmail.com; shanmugapriyai@psgcas.ac.in

a network for transferring data; it is a system that uses big data processing, events, and protocols. The advancement of IoT technology provides opportunities but also challenges. Many problems exist in the IoT research subjects including data analysis and storing, transportation, digital transfer, safety, communications, and power administration, which remain as the different aspects of information analysis and storing [3].

For a daily routine, IoT technologies are playing a significant role in human lives. It is also known that IoT will emerge as a revolutionary technology, capable of transforming the world into a digital space [4, 5]. Internet of Things (IoT) has the potential to connect thousands of digital objects. It is frequently considered as an advanced version of machine-to-machine (M2M) communication, where each machine or digital entity interacts with each other without any human involvement [6]. IoT and similar innovations cover a wide range of devices, including actuators, sensors, access points, and portable gadgets, which remain connected to the web and capable of detecting their surroundings, transferring data, and establishing communication in different ways [7]. IoT devices utilize energy to function and run, just like any other device. However, in a few cases, these devices consume much more energy than is required, resulting in energy wastage through the formation of unwanted heat. This wastage of energy and unnecessary temperature must be reduced to benefit the economy and ensure environmental safety. The quantity of energy required to operate a gadget has increased due to the recent technological developments and the continuous growth of functional IoT devices. This has paved way for the growth of GIoT or low-power IoT [8]. According to reports, the Internet of Things (IoT) will be instrumental in preventing future natural calamities by adopting low-energy consumption practices [9].

The increasing number of energy-consuming digital devices and wide variety of digital domains, the energy consumption rates have increased unprecedently [10]. The utilization of connected IoT gadgets is growing at an exponential rate, as well as the amount of data produced and moved throughout the IoT model has prompted the researcher to predict the high data rate and large content size, which leads to an unavoidable carbon cost [9]. According to recent research reports, the increased amount of carbon dioxide generated by mobile systems are predicted to reach 345 million tons by 2020 [11]. Pure or green technology are developing as an important study area due to the increasing large carbon dioxide outputs as well as the ecological and medical issues. However, there are a number of issues with the GIoT ecosystem as a whole, including the issues with security and service quality, as well as the complexity of using a global framework, heterogeneous devices, etc. As a result, researchers are working to create new alternatives such as unique GIoT solutions and the incorporation of supportive technologies such as cloud computing, fog computing, and other similar technologies to address these issues. The primary goal of this research work is to make the readers have a short outline on GIoT and usage of GIoT methods to develop an eco-friendly sustainable world.

2 Green Internet of Things

This section provides a taxonomy to emphasize the technical aspects of energy management and green computing technologies in any IoT environment. Figure 1 shows a novel taxonomy for enabling energy management in Internet of Things (IoT) systems. Six categories can be used to categorize the study on energy management and power consumption solutions in I/O settings: Smart technologies include, smart grids, smart energy collection, smart cities, smart industries, and smart building and environments.

With the IoT experiencing several challenges like security and privacy, and interoperability [12], the most important challenge faced during the implementation of IoT is energy consumption. The power consumption will increase as there are more Internet-connected IoT devices including RFIDs, sensors, actuators, and mobile devices [13]. A high amount of energy is required on a daily basis if billions of IoT devices are operating continuously, and also a huge amount of data will be produced. Additionally, the energy required to transfer and store the large-scale data increases exponentially. As a result of this excessive energy consumption, an increasing amount of carbon dioxide (CO_2) will be discharged into the atmosphere without any limitations. GIoT is presented as a solution to these challenges [14].
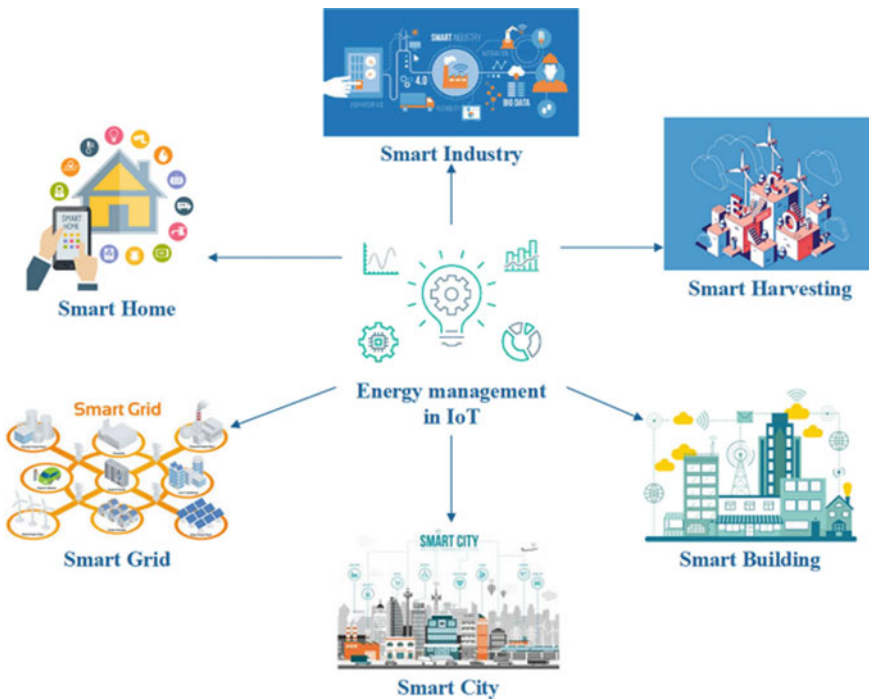
Fig. 1 Proposed taxonomy for energy management solutions in IoT environments

3   Literature Survey

This section provides a comprehensive literature review of all the recent concepts for energy-efficient IoT deployment. Due to the rapid depletion of traditional energy resources and the exponentially increase in energy consumption, green IoT has gained potential research interest in the ICT industry.

Miorandi et al. [15] explained about various methods and technologies helpful in attaining energy efficiency in the IoT, however there was no discussion on system models that are precisely developed for Green IoT. Baliga et al. [16] compared the energy usage of cloud computing and PC computing in various circumstances and it was concluded that selecting the models based on scenarios would be the best option. Additionally, these estimates do not include Quality of Service (QoS) issues, which may enhance energy consumption in certain instances. Green technologies for the implementation of IoT by considering the QoS across different domains were studied in [17]. It is directly aimed at generating solutions for Green IoT. The background of an IoT network, the information center and cloud computing, as well as its green solutions, were not highlighted.

Akkaya et al. [18] described various mechanisms for saving energy in smart buildings. This is accomplished by using the data gathered through IoT, and it was discovered from the respective systems that in case of heating, when proper ventilation and air conditioning systems are in place, huge amounts of energy can be saved. Despite all of the existing research works, the comparison of energy preservation concepts has not been examined.

Wireless sensor networks (WSN) is considered as an important element in the implementation of IoT. Shaikh and Zeadally [19] discussed about the taxonomy of the methods employed for harvesting energy in WSN by applying various environmental resources in detail. However, instead of batteries, another media for energy storage could result in high energy effectiveness; therefore, this field requires extensive research.

An energy evaluation approach for smart homes based on the MQTT communications protocol in an IoT environment and Big Data was developed and tested by Al-Ali [20]. The proposed energy management system makes use of analytics, and business intelligence. The proposed approach uses benchmarking to perform data mining and also uses a business intelligence platform to instantly produce graphs, charts, and reports. Further, the suggested solution enables users to operate and monitor the equipment remotely, create online invoices by using a user-friendly mobile application, and provide novel techniques for enabling smart energy management based on IoT and Big Data. The proposed method highly emphasizes on speed and security parameters to enable efficient energy management systems in wireless sensor networks (WSN). A number of parameters were developed to assess the system performance, including storage, database speed measurement, and scalability in MQTT servers.

Cho et al. [21] proposed an IoT-based technique for limiting the energy consumption in household appliances. The proposed algorithm is divided into three modules:

first is the heterogeneous network end device module, which is a framework that translates the processing of various devices into recognized standards for other devices, as well as the administration systems; second is the electric appliance-oriented interoperability module, which includes a sub-module; third is the electric appliance-oriented interoperability module, which is considered as the most important module in the proposed algorithm. The technology is then tested on home appliances present in a smart house for a particular period of time. This method can be implemented with the use of local and worldwide Internet connection techniques such as Bluetooth, ZigBee, and others. Finally, the power precision and recollection metrics were assessed. The potential challenge observed here is smart management, which is defined as the precise identification of the efficiency and energy distribution of all devices at the same time period. Upcoming research must concentrate on predicting the user behaviors and employing a recognition model with hybrid data like image and position.

Li et al. [22] have reviewed the procedures for designing an IoT-based Self Learning Home Management System (SHMS) based on machine learning. Features like power alert, price clustering, and price estimate, for which machine learning technology has been extremely useful in the implementation and development, are among the recommended strategies. In the suggested method, a smart home was used to simulate the system design. A smart plugin has been considered to track the amount of power used, and data analysis was also used to optimize power dissipation based on the product utilization. The authors provided a suitable method for monitoring the amount of electricity consumed, after which the smart home model will get optimized by reducing the additional demand for power supply and the cost associated with its utilization.

An Internet of Things (IoT) based smart home management system was created by Naik and Patel [23]. JSON is the algorithm used in their proposed model. The filtering will only be applied in this technique once when the data is submitted to the server, and later the retrieved information will get stored. For connecting and managing microprocessors, sensors, and Internet-enabled devices via web servers, smartphone apps or databases are utilized. Xenserver and a microcontroller board are used in this project. After completing the development of proposed system, the authors have experimented it for several months. The outcomes of their work are compared to other contemporary technologies in terms of price and performance metrics, such as reliability and energy consumption to know about the effectiveness of the proposed technology. The proposed technique has the advantage of being able to check the regional climate and dynamically modify the room temperature; nevertheless, the system security has not been ensured in this research.

In the domain of home power administration, Park et al. [24] have explored numerous varieties of predicted risks and elements that impact the risk factor of IoT. The demographic variables have also been explored. There have been discoveries of security, privacy, financial, electromagnetic radiation (EMR), and other risks. The observed EMR is the most effective value. The writers have specifically considered the individual's choice, which includes sensitivity to changes in electricity consumption, ecological degradation, and so on. Also, two vital factors include the changes in

electricity cost and adoption of novel technology. Possibly, the users concern about EMR even though the researchers have perceived cyber security threats as the drawback of ICT services. However, the exploration on the relevance of demographic variables along with perception of risk has gained more research attention and it is important to carry out extended research works.

Kamienski et al. [25] introduced a system, where the system operation is carried out through traceable graphical contexts to manage data based on the scalable IoT systems in smart cities. The developed representations form the elementary principles are far behind the illustration of the technique used in this system. An application has been introduced to realize the context principles and designs. This article attempts to provide an environment in which these user-designed contexts require tracking, and this system should also ensure data security. The approach has been further examined from various perspectives, including error detection, modification, and platform effectiveness. This approach has a restricted scope of the context awareness framework, and it requires new techniques to improve it.

Designing a deep reinforcement learning (DRL)-based IoT fog node design focused on power efficiency applications has been developed by Liu et al. [26]. This research work provides information on enabling energy administration in smart cities. Edge computation is used to introduce the software foundation of an IoT-based environment. Since the IoT system is employed in smart cities, the smart environment faces numerous challenges in detecting and conducting strong control actions in compliance. As a result, the evolving DRL is a potential technology comprised of the deep neural networks (DNN).

Sodhro et al. [27] proposed two algorithms, HABPA and DSA to achieve the goal of developing green and robust smart communities. The smart city applications have been extended to several sectors of society, including health care, industry, and media streaming. IOT connects the devices connect with one another, but a substantial amount of energy is consumed by them, therefore the algorithms (HABPA and DSA) are implemented to establish a balance between energy resources and system requirements by maintaining the efficiency of the smart city and prevention of data loss. Attempts have been made to make the best use of recyclable green energy sources rather than the simulated ones. It can be inferred from the results that both the algorithms are very efficient though there are few challenges to be addressed, they are: buffer area and the amount of increase in energy consumption. It is expected that developed technologies will be expanded into health care system in the near future.

Terroso-Saenz et al. [28] have presented the IoT Energy Platform (IoTEP) to find a solution for the energy operational issues, which include a large amount of energy consumption and wastage. It is found that the existing techniques are insufficient to solve the current problems, for example, the sensing system used in apartments do not have the ability to deal with the energy loss. Hence, IoTEP technique is proposed to optimize the ways in which the energy is balanced in buildings by using data probing, energy savings can estimate the energy requirements. IoTEP will not only reduce the energy loss but also yield the advantages of personated energy criticism for incorporating more enhancements. In the near future, other approaches can be

synchronized with the proposed technique. It is also expected that these hybrid forms would yield improved results in this field.

Pawar and Tarun Kumar [29] presented an IoT-based intelligent energy administration platform with no constraints or limits for the utilization of renewable energy resources. The suggested method was designed and constructed to represent the assessment of different architectures.

Tom et al. [30] introduced an IoT-based technique for measuring and regulating the energy depreciation with the goal of increasing the use of eco-friendly and green energy. Since IoT-enabled homes and devices are connected to the internet, the data consumption levels, occupants' demands, high-consumption devices, peak hours, and the expenses incurred by each model may be collected. As a result of these assessments, the power utilization framework for smart homes is found to be likely to result in predicting the estimated power consumption, peak periods, and participatory requirements for the next three days, and the results are communicated to customers via demand response (DR) scheme. The main purpose of this research work is to balance the energy usage during peak hours while decreasing the consumption and resultant cost. If the residence permits it, the utility may be authorized to regulate and use the auto-control equipment.

Salman et al. have proposed a novel energy management system for smart homes. This technology was designed specifically for sensors and cameras as it was determined to be unsuitable for the heterogeneous nature of IoT environment. Furthermore, it does not have the ability to adapt to the systems capable of transmitting large amounts of data, such as IoT environment [31].

Ku et al. have developed a smart energy service for Internet of Things (IoT) applications. The collection of energy data is required for this service. The major drawback in this service is that it does not address the problem of fault tolerance, as well as the lack of trials that involve IoT infrastructure [32].

Choi et al. [33] have developed a power monitoring system for a particular type of public environment, this technique is characterized as a special purpose system. Furthermore, the research studies are not exclusively designed to provide reliable outcomes that satisfy the emerging research requirements.

Prathik et al. [34] developed a system for scaling the energy consumed by IoT technology (i.e., the IoT technology is utilized in the form of a tool in this technical work). There is no solution proposed in this research for dealing with the energy utilization challenges in IoT.

In order to adopt IoT-based energy approaches with smart plugs, Srinivasan et al. [35] have developed a smart strategy, but it was not energy critical at the same levels of IoT energy-based nodes. Also, the implementation part has not considered the unique characteristics of Internet of Things (IoT).

Kumar et al. [36] proposed an IoT-based energy harvesting system. This system has not considered the issue of IoT power utilization, especially for non-renewable energy nodes.

Chaouch et al. [37] considered a machine-to-machine statement to develop an energy management approach with an intent to monitor and reduce the energy

dissipation. Due to its architecture, this system is considered as a special purpose system.

Panahi et al. [38] investigated a smart mechanism that can be used to charge the mobile sensors wirelessly by using the IoT technologies. This intelligent method's modeled testing ground is inadequate to show the IoT environment because it focuses solely on the WSN ecosystem, ignoring RFID and other energy-based nodes.

Only a real-time surveillance method for energy levels identified in the IoT systems is suggested by Alaudin et al. [39].

A hardware design that can change the rate of energy consumption was studied by Tcarenko et al. [40].

Suresh et al. [41] proposed a theoretical technique to reduce the sensor node energy dissipation in the IoT environment.

Using IoT technologies, Yaghmaee et al. [42] have developed a smart power measuring device by including a cloud server, smart plugs, and a gateway. When combined with a defect in the IoT standards, the results of this system has become incorrect and inadequate.

In the IoT environment, Pan et al. [43] suggested an energy surveillance mechanism and lower power usage rates. This system is also built by considering a specific goal. Furthermore, its deployment testing strategy does not reflect the characteristics of IoT.

Ding and Wu [44] proposed a schedule method for minimizing the energy loss. Because this model was evaluated in a WSN rather than an IoT situation, the findings could then be utilized in IoT.

Ejaz et al. [45] have involved in developing an optimal and planned energy-efficient model for smart cities, as well as the energy collection to extend the life of low-power products. The efficacy evaluation of this system is poor due to its dependency on four devices. It has failed to consider the enormous amount of data that could be exchanged in a smart city or over the Internet of Things.

4 Inference from Existing Work

GIoT can enhance people's lives and the environment by strengthening the eco-friendliness of the technologies and the associated infrastructure. Recently, GIoT research is focused on developing energy-efficient models and scheduling, energy-efficient RFIDs, green IoT systems and solutions, and GIoT device localization [46]. Furthermore, the majority of IoT devices are expected to be designed to be recyclable as many times as possible, thereby lowering the number of toxic and dangerous materials discharged into the environment. Furthermore, it is expected that the GIoT systems would progressively combine the supportive technologies such as cloud computing [47], fog computing, edge computing, and blockchain, since these techniques may improve the basic IoT environment's sustainability, security, and efficiency [48–50].

5 Conclusion

This paper explores the sustainable strategy of IoT. The most recent efforts in the green IoT domain as well as the potential sectors requiring attention in the future for green IoT are reviewed. There is a collection of IoT technologies that can positively impact the environment and conserve energy. This study investigates the key enablers of green IoT, and examines how they make the best use of diverse techniques to improve energy efficiency. To offer a sensitive connection across diverse domains of green IoT, including heterogeneous combinations, sensor cloud integration, proper service administration, and adverse physical environments, the standardized frameworks are necessary. Several global initiatives have been proposed to promote and accommodate the green environment. Further, the recent research initiatives and standardization efforts are reviewed, and their future perspectives are also highlighted. From the proposed review, It is envisioned that the increased industrial focus on green IoT will boost its future prospects, and that researchers and industrialists will be fully involved in implementing the goal of green IoT.

References

1. Wu J, Dong M, Ota K, Li J, Yang W, Wang M (2019) Fog-computing-enabled cognitive network function virtualization for an information-centric future Internet. IEEE Commun Mag 57(7):48–54
2. Lin X, Li J, Wu J, Liang H, Yang W (2019) Making knowledge tradable in edge-AI enabled IoT: a consortium blockchain-based efficient and incentive approach. IEEE Trans Ind Inform 15(12):6367–6378
3. Zhou Z, Feng J, Gu B, Ai B, Mumtaz S, Rodriguez J, Guizani M (2018) When mobile crowd sensing meets UAV: energy-efficient task assignment and route planning. IEEE Trans Commun 66(11):5526–5538
4. Kagita MK, Thilakarathne N, Rajput D, Lanka DS (2020) A detail study of security and privacy issues of Internet of Things. arXiv preprint arXiv:2009.06341
5. Al-Turjman F, Kamal A, Husain Rehmani M, Radwan A, Khan Pathan AS (2019) The green internet of things (G-IoT). Wirel Commun Mob Comput
6. Prasad SS, Kumar C (2013) A green and reliable internet of things. Commun Netw 5(1):44–48
7. Huang J, Meng Y, Gong X, Liu Y, Duan Q (2014) A novel deployment scheme for green internet of things. IEEE Internet Things J 1(2):196–205
8. Shaikh FK, Zeadally S, Exposito E (2015) Enabling technologies for green internet of things. IEEE Systems J 11(2):983–994
9. Green IoT. https://www.telekom.com/en/company/topic-specials/internet-of-things/greeniot
10. Varjovi AE, Babaie S (2020) Green Internet of Things (GIoT): vision, applications and research challenges. Sustain Comput: Inform Syst 28
11. Green Power for Mobile, The Global Telecom Tower ESCO Market, Technical Report (2015)
12. Thilakarathne NN (2020) Security and privacy issues in IoT environment. Int J Eng Manag Res 10
13. Alsamhi SH, Ma O, Ansari M, Meng Q (2019) Greening internet of things for greener and smarter cities: a survey and future prospects. Telecommun Syst 72(4):609–632
14. Arshad R, Zahoor S, Shah MA, Wahid A, Yu H (2017) Green IoT: an investigation on energy saving practices for 2020 and beyond. IEEE Access 5:15667–15681

15. Miorandi D, Sicari S, De Pellegrini F, Chlamtac I (2012) Internet of things: vision, applications and research challenges. Ad Hoc Netw 10(7):1497–1516

16. Baliga J, Ayre RW, Hinton K, Tucker RS (2010) Green cloud computing: Balancing energy in processing, storage, and transport. Proc IEEE 99(1):149–167

17. Kiourti A, Lee C, Volakis JL (2015) Fabrication of textile antennas and circuits with 0.1 mm precision. IEEE Antennas Wirel Propag Lett 15:151–153

18. Akkaya K, Guvenc I, Aygun R, Pala N, Kadri A (2015) IoT-based occupancy monitoring techniques for energy-efficient smart buildings. In: IEEE wireless communications and networking conference workshops (WCNCW), pp 58–63

19. Shaikh FK, Zeadally S (2016) Energy harvesting in wireless sensor networks: a comprehensive review. Renew Sustain Energy Rev 55:1041–1054

20. Al-Ali AR, Zualkernan IA, Rashid M, Gupta R, AliKarar M (2017) A smart home energy management system using IoT and big data analytics approach. IEEE Trans Consum Electron 63(4):426–434

21. Cho WT, Lai YX, Lai CF, Huang YM (2013) Appliance-aware activity recognition mechanism for IoT energy management system. Comput J 56(8):1020–1033

22. Li W, Logenthiran T, Phan VT, Woo WL (2018) Implemented IoT-based self-learning home management system (SHMS) for Singapore. IEEE Internet Things J 5(3):2212–2219

23. Naik K, Patel S (2018) An open source smart home management system based on IOT. Wirel Netw 1–7

24. Park C, Kim Y, Jeong M (2018) Influencing factors on risk perception of IoT-based home energy management services. Telematics Informatics 35(8):2355–2365

25. Kamienski CA, Borelli FF, Biondi GO, Pinheiro I, Zyrianoff ID, Jentsch M (2017) Context design and tracking for IoT-based energy management in smart cities. IEEE Internet Things J 5(2):687–695

26. Liu Y, Yang C, Jiang L, Xie S, Zhang Y (2019) Intelligent edge computing for IoT-based energy management in smart cities. IEEE Netw 33(2):111–117

27. Sodhro AH, Pirbhulal S, Luo Z, De Albuquerque VHC (2019) Towards an optimal resource management for IoT based Green and sustainable smart cities. J Clean Prod 220:1167–1179

28. Terroso-Saenz F, González-Vidal A, Ramallo-González AP, Skarmeta AF (2019) An open IoT platform for the management and analysis of energy data. Futur Gener Comput Syst 92:1066–1079

29. Pawar P, Tarun Kumar M (2020) An IoT based Intelligent Smart Energy Management System with accurate forecasting and load strategy for renewable generation. Measurement 152

30. Tom RJ, Sankaranarayanan S, Rodrigues JJPC (2019) Smart energy management and demand reduction by consumers and utilities in an IoT-Fog-based power distribution system. IEEE Internet Things J 6(5):7386–7394

31. Salman L, Salman S, Jahangirian S, Abraham M, German F, Blair C, Krenz P (2016) Energy efficient IoT-based smart home. In: IEEE 3rd world forum on Internet of Things (WF-IoT), pp 526–529

32. Ku TY, Park WK, Choi H (2017) IoT energy management platform for microgrid. In: IEEE 7th international conference on power and energy systems (ICPES), pp 106–110

33. Choi CS, Jeong JD, Lee IW, Park WK (2018) LoRa based renewable energy monitoring system with open IoT platform, In international conference on Electronics, Information, and Communication (ICEIC), pp 1–2

34. Prathik M, Anitha K, Anitha V (2018) Smart energy meter surveillance using IoT. In: International conference on power, energy, control and transmission systems (ICPECTS), pp 186–189

35. Srinivasan A, Baskaran K, Yann G (2019) IoT based smart plug-load energy conservation and management system. In: IEEE 2nd international conference on power and energy applications (ICPEA), pp 155–158

36. Kumar SS, Kaviyaraj R, Narayanan LJ (2019) Energy harvesting by piezoelectric sensor array in road using Internet of Things. In: 5th international conference on advanced computing & communication systems (ICACCS), pp 482–484

37. Chaouch H, Bayraktar AS, Çeken C (2018) Energy management in smart buildings by using M2M communication. In: 7th international Istanbul smart grids and cities congress and fair (ICSG), pp 31–35
38. Panahi FH, Moshirvaziri S, Mihemmedi Y, Panahi FH, Ohtsuki T (2018) Smart energy harvesting for Internet of Things. In: Proceedings of the smart grid conference (SGC), pp 1–5
39. Bin Alaudin AH, Zan MMM, Mahmud AR, Yahaya CKHCK, Yusof MI, Yussoff YM (2018) Real-time residential energy monitoring device using Internet of Things. In: IEEE 8th international conference on system engineering and technology (ICSET), pp 97–101
40. Tcarenko I, Huan Y, Juhasz D, Rahmani AM, Zou Z, Westerlund T, Tenhunen H (2017) Smart energy efficient gateway for Internet of mobile things. In: 14th IEEE annual consumer communications & networking conference (CCNC), pp 1016–1017
41. Suresh K, RajasekharaBabu M, Patan R (2016) EEIoT: energy efficient mechanism to leverage the Internet of Things (IoT). In: International conference on emerging technological trends (ICETT), pp 1–4
42. Yaghmaee MH, Hejazi H (2018) Design and implementation of an Internet of Things based smart energy metering. In: IEEE international conference on smart energy grid engineering (SEGE), pp 191–194
43. Pan J, Jain R, Paul S, Vu T, Saifullah A, Sha M (2015) An internet of things framework for smart energy in buildings: designs, prototype, and experiments. IEEE Internet Things J 2(6):527–537
44. Ding X, Wu J (2019) Study on energy consumption optimization scheduling for internet of things. IEEE Access 7:70574–70583
45. Ejaz W, Naeem M, Shahid A, Anpalagan A, Jo M (2017) Efficient energy management for the internet of things in smart cities. IEEE Commun Mag 55(1):84–91
46. Albreem MA, El-Saleh AA, Isa M, Salah W, Jusoh M, Azizan MM, Ali A (2017) Green internet of things (IoT): an overview. In: IEEE 4th international conference on smart instrumentation, measurement and application (ICSIMA), pp 1–6
47. Thilakarathne NN, Wickramaaarachchi D (2020) Improved hierarchical role based access control model for cloud computing. arXiv preprint arXiv:2011.07764
48. Sharma PK, Kumar N, Park JH (2020) Blockchain technology toward green IoT: opportunities and challenges. IEEE Netw 34(4):263–269
49. Chen, JI-Z, Yeh L-T (2020) Greenhouse protection against frost conditions in smart farming using IoT enabled artificial neural networks. J Electron 2(04):228–232
50. Bashar DA (2020) Review on sustainable green Internet of Things and its application. J Sustain Wirel Syst 1(4):256–264

Ayurvedic Medicinal Plant Identification System Using Embedded Image Processing Techniques

Arnab Das, B. Siva Sai Kumar, S. Shiva Shankar Reddy, S Naveen Reddy, and K. P. Peeyush

Abstract Plants can be classified based on various classification methods such as cell, genetic and serum etc. It's difficult for an individual to explore the various classification methods and it's practically not feasible as it demands good knowledge in plant taxonomy and long-term time investment. Due to the shortage of experienced and qualified taxonomists in identification and classification of medicinal plants, with the help of different image processing algorithms and computer vision, the above difference can be bridged. The main objective is to develop a Deep Learning and Machine Learning based model to identify and classify plants based on various features, which is done with the help of Gabor filter and Gray Level Co-occurrence Matrices (GLCM) and using classifiers such as Random Forest (RF), and Light Gradient Boosting Machine (LGBM), and made a comparative analysis which resulted an accuracy of 95.5% with LGBM and GLCM filter and used to develop a standalone device that clicks a picture and identifies the medicinal plant.

Keywords Feature extraction · Segmentation · Classification · Machine learning · Convolutional neural network · Light gradient boosting machine · Random forest classifier · Gabor filter · Gray level co-occurrence matrix · Shannon entropy · Medicinal plants · Image processing

1 Introduction

Plants are vital to the survival for life and biodiversity on earth by allowing the air, water flow for all existence. The most significant classes of the flora are medicinal herbs that are used to treat various diseases. The knowledge [1] of medicinal plants that has been passed down through the years ought to be conserved as well as guarded. Vision systems, specific pattern classification, different methods for imagery analysis are a promise to identifying and then categorizing medicinal uses of flora. One [2–4]

A. Das · B. Siva Sai Kumar · S. Shiva Shankar Reddy · S. Naveen Reddy · K. P. Peeyush (✉)
Department of Electronics and Communication Engineering, Amrita School of Engineering,
Amrita Vishwa Vidyapeetham, Coimbatore, India
e-mail: kp_peeyush@cb.amrita.edu

of the most difficult jobs is identifying a medical plant with the needed therapeutic properties. Even if herbal therapy has no negative effects, a patient's life might be lost if a medicinal plant is misidentified. As a result, at this point in time, a completely automated method to accurately recognize medicinal plants is inevitable.

For production of ayurvedic medications [5], the identification and categorization of medicinal plants is critical. Appropriate classification of medicinal plants benefits horticulturists, botanists, ayurvedic medical therapists, forest service authorities, as well as those engaged in the making of ayurvedic pharmaceuticals. However, a critical shortage of skilled taxonomists exists in this field. There is a growing segment of the population who prefers ayurvedic medicine over other medications. Taxonomists employ leaf, flower, trunk, and branch characteristics to classify based on their respective features. The leaves are the greatest choice for plant categorization.

A handy device has been pitched in this paper to perform the above-mentioned action as there will be network issues deep inside the forest. For the hardware implementation of this project, Raspberry Pi 3 Model B+ was used which is one of the cheapest mini-computers we can find in market. A webcam of 720p video recording was attached to this board. Since real-life images include many noise and other disruptions in the image, image pre-processing like noise reduction and histogram equalization was used.

2   Literature Survey

A plant leaf identification system based on morphological characteristics and adaptive boosting methods is provided in this study [6]. They employed k-NN, decision trees, and multilayer perceptrons, among other categorization algorithms. The accuracy rate has been improved with AdaBoost approach compared to conventional approach.

For recognizing contoured borders of overlapped leaves from a complicated backdrop, the working procedures outlined in this study [7] are used. The proposed approach divides the primary picture into leaf regions by segmenting the specified contour areas. The model attained a segmentation rate of 90.46% overall, with segmentation rates of 95.34% for single leaves and 86.73% for overlapping leaves, respectively, according to the experimental data.

The key processes in identifying the leaf are feature extraction and classification. The author [8] utilized histogram and texture to extract features and a support vector machine to classify them. They employed five distinct classes, each including four different leaf sizes. Following the categorization, the output forecasts which class the leaf corresponds to.

Deep learning relates to neural network structure, according to the findings of the research [9], it can learn characteristics from huge data automatically and train and categorize plant leaf samples through the use of a neural network model using a back propagation method. Leaf form, color, and texture are the most important factors in

plant categorization. Leaf texture veins have more consistent properties than color and form.

Ayurleaf [1], a CNN-based methodology for classifying medicinal plants, has been presented. Neural network with deep learning based on Alexnet is used for the employment to extract the features of the flora. To classify the data, SVM classifiers and SoftMax were utilized.

The author compared well-known models VGG16 and VGG19 and presented a complete analysis of deep learning-based convolution neural networks. They created [2] their own dataset, which includes 64 medicinal plant species and 1000 samples from each.

The CNN [10] is a form of neural network that is extensively employed in image processing. Convolution, Max-pool, and fully linked layers combine to form CNN. The author uses CNN to construct a hardware device that can distinguish between plastic and non-plastic with a 97.8% accuracy.

According to CNN, a machine [11] has been created that can determine if a plant leaf is healthy or unhealthy. For processing, the author employed a Linux-based machine with a CUDA-enabled GPU, darknet for image processing and recognition, and Python to interface the program with the darknet [12].

The database is the most significant element of image processing in general. The author [13] analyses three distinct methods of feature extractions, including Wavelet transformations with an accuracy of 56.5%, Gray Level Co-occurrence matrix (GLCM) with an accuracy of 36.66%, and Gray Level Difference method (GLDM) with an accuracy of 52.5%, using varied training and validation percentages. The classifier utilized is k-NN. Finally, they came to the conclusion that Wavelet transformations had the highest accuracy. In this paper, a conflicting result has been observed. GLCM feature extractor has been used with LBGM as the classifier has given the best result with 95.5% accuracy.

3   Methodology

Feature extraction is the most important aspect of classification/identification. Image processing, picture feature extraction, and image classification are the three phases that make up the recognition process as shown in Fig. 1.

Image pre-processing and segmentation techniques are the two key processes in the image recognition process. Image restoration and transformation are two of the

Fig. 1 Classification process
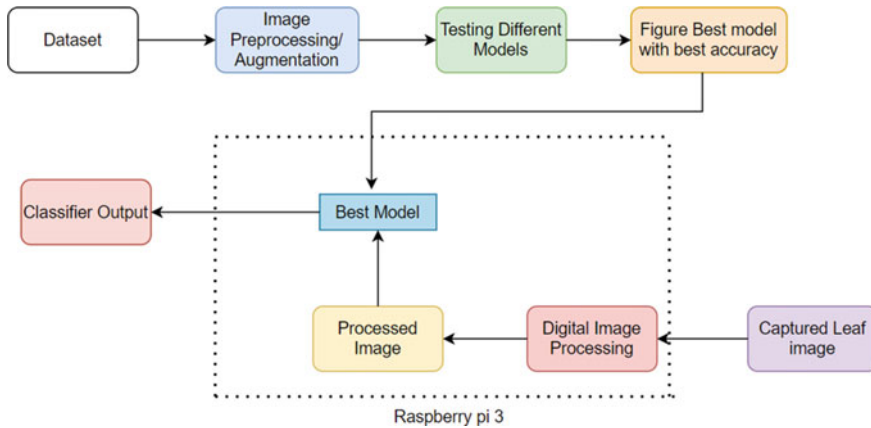
Fig. 2 Methodology

most used image pre-processing techniques. Its major goal is to reduce picture inter-
ference and noise, increase image usable information, and improve object detec-
tion. This paper does not describe about image restoration techniques, but have
implemented image segmentation for image transformation like Contrast Limited
Adaptive Histogram Equalization (CLAHE) and few noise removal filters for image
pre-processing. The purpose of segmentation is to divide a recognized image into
subregion. Pre-processing is done when image is captured lively for hardware imple-
mentation but Kaggle dataset which is used for training is already segmented and
pre-processed. The proposed model methodology is shown in Fig. 2.

3.1 Dataset

When it comes to object categorization, the dataset is crucial. Segmented leaves
dataset is obtained from Kaggle which consists of leaves of 30 classes of which each
class has an average of 60 images of size 1600×1200.

Data augmentation is a strategy for extending the quantity of data available by
generating new data from current data. It allows us to improve the dataset's size and
variety without having to acquire fresh information.

The following data enhancements were performed: Rotation of the images and
horizontal flip. For data augmentation, Gaussian noise is injected into the picture.
The process of blurring a picture entails averaging nearby pixels. This blurs the image
and lowers the amount of information. The dataset size grows larger, and the model's
training improves. To enhance the precision of a deep learning-based model, data
augmentation technique is applied. The training and testing dataset are randomly
split from the dataset. The train set is liable for 80% of the data source, whilst the
testing set is liable for 20%. From the information provided by the original owner of

the dataset which was posted in Kaggle, it was found out that the dataset was created by scanning a single leaf using a scanner with white background behind, as like a segmented leaf image.

3.2   Image Pre-processing

The initial step in the pre-processing of the image is noise reduction. Block Matching and 3D filtering (BM3D) are used to eliminate noise. The BM3D collaborative filtering approach. Using this filter, a group of similar blocks from the image are extracted. If a block's dissimilarity to a reference fragment is less than a predetermined threshold, it is grouped using a procedure known as block matching. In order to construct three-dimensional cylinder formations, the group's blocks are then piled on top of one another. After that, each block is put through screening. The Weiner filtering is followed by the linear transform, which recreates all of the filtered blocks. Finally, the image is changed to its 2D format.

For enhancing the visibility of the image during pre-processing, Contrast limited adaptive histogram equalization (CLAHE) is used to improve visibility. In general, the histogram equalization increases a picture's contrast by dispersing the pixel histogram values. Adaptive histogram equalization breaks the image into small pieces. There is an equalized histogram for each block. To stop the amplification of noise, contrast limiting is applied.

3.3   Image Segmentation

Because leaves are most typically observed in groups with natural backgrounds, leaf identification and segmentation are challenging tasks. Because of their similar colors, the edges of leaves are difficult to see from the photograph. It's also more difficult to separate each individual leaf, especially overlapping ones, because leaves are almost identical in color, texture, and shape.

Leaf segmentation entails two steps: (1) separating the main leaf region from the natural backdrop, and (2) extracting individual leaves and covered or overlapped (i.e., objects on object) leaves from the picture. A contour selection-based leaf segmentation technique is used for segmentation. The segmentation flow is shown in Fig. 3.

Input image is read in blue, green, and red format instead of red, green, and blue format as we are using OpenCV Library for model development and we need to segment foreground image from the background. We must first determine the contours of each leaf before segmenting the connected regions inside them, as our goal is to identify the contour or edges of each leaf. Internal texture is smoothed and boundary edges are preserved using the Edge Preserving Filter.

Fig. 3 Segmentation flow
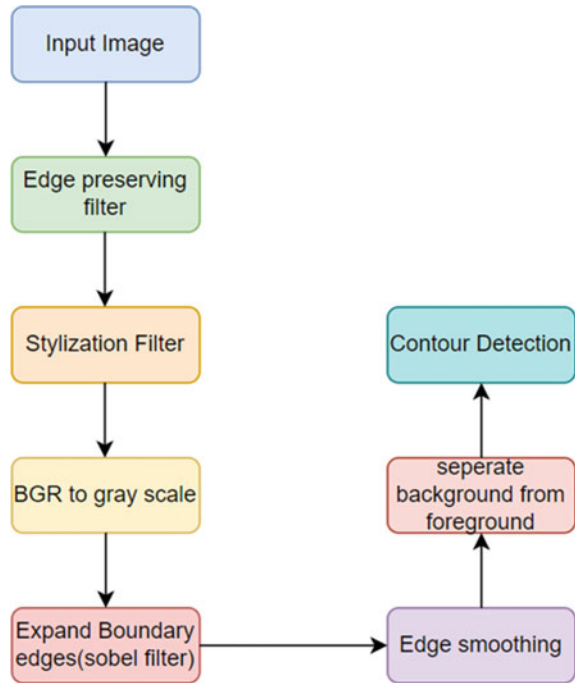
To make every item's edge, shape, or contour sleek and crisp at the same time, we employ a stylization filter, it uses the Normalized Conv (NC) filter to increase accuracy and speed. Internal texture has no effect on it as it hardens all boundary edges over time. Next, the data in BGR format (3 channels) is then processed to a gray level (1 channel), which greatly minimizes the amount of computation and memory usage. Followed by expanding boundary edges, this process enlarges the outline borders of leaves by expanding the areas of bright regions. This processing phase also aids in the separation of overlapping edges. This is done using a Sobel filter.

When the dilatation procedure expands the bright borders, this may enlarge remaining portions of the leaf's internal texture edges. To solve the issue, we perform a smoothing operation after dilatation. We use a single intensity to differentiate the pixels in the foreground first from pixels in the backdrop. By recognizing the contours of the connected regions, we are able to identify them. The OpenCV Library has a function which is used to detect contours.

3.4 Deep Learning Model (CNN)

A CNN sequential model is implemented by considering VGG16 and Alexnet as reference. A combination of VGG16, Alexnet with some modifications was done to this combination to create a new model as in Fig. 4. Alexnet was chosen because it uses ReLu activation function which does not allow much loss of features and also prevents the negative output of summation of gradients. VGG16 is one the most popular architectures in deep learning. The input layer is the initial layer, and it defines the size of the input pictures. The convolution layer uses 32 (3 × 3) filters with a stride size of one followed by a ReLU activation layer, which is accompanied by the max-pooling layer by a 2 × 2 filter. The previous layer precisely halves the exact size of its return. A secondary convolution layer follows this max pooling layer in which a 32 kernel is performed with a dimension of 3 × 3. ReLU layered will be followed, accompanied with the layer of max pool with 2 × 2 of size of the filter by a stride value of 1. Now the next two layers are back-to-back convolution layers with following configurations. Both of them employ 3 × 3 kernels by a stride value of 1, with 64 and 250 kernels in each. Following these layers, a ReLU layer is added. The next layer is a convolution layer having 128 (3 × 3) kernels, after that a ReLU activation, an averaging pool layer by a value of (2, 2) size. The next levels follow a similar pattern, with 64 (3 × 3) filters, after that a ReLU activation function, then averaging pool layers by a value of (2, 2) size.

Last convolution layer is of size 256 (2 × 2) and followed by activation of the ReLU function and max pool layers with a value of (2 × 2) size. Final value of the last max-pool layers is transferred to fully connected layers which have 6400-neurons. And, it is again processed through another fully connected layer of size 30 as our dataset consists of 30 classes. Final classification of the model is done with the help of SoftMax which is used for multi-classification purposes.

In this paper, AdaMax optimizer has been used which is an Adam version of gradient descent that approach to infinity norm(max).

Fig. 4 Implemented CNN model

3.5 Machine Learning Model

3.5.1 Gabor Filter Bank

Gabor is just a convolutional filter that comprises a Gaussian and sinusoidal term together. The weights are given by the Gaussian component, whereas the directionality is given by the sine component.

Gabor is used to provide texture and edge features. Gabor kernel actually mimics the visual cortex meaning, the way we recognize textures with our eyes can be simulated using Gabor kernel.

$$g(x, y; \lambda, \theta, \psi, \sigma, \gamma) = \exp\left(-\frac{x'^2 + \gamma^2 y'^2}{2\sigma^2}\right)\exp\left(i\left(2\pi\frac{x'}{\lambda} + \psi\right)\right)$$

Λ—Wavelength of the sine component
θ—Orientation of filter
ψ—Phase offset
σ—Std. dev. of the Gaussian envelop
γ—Spatial aspect ratio.
Where

$$X' = x\cos + y\sin \quad \text{and} \quad Y' = -x\sin + y\cos.$$

For example, if there is any change in the parameters like lambda, theta, and phase offset of the standard deviation of the Gaussian, then it would generate an ideally infinite number of filters.

By observing Fig. 5, one can infer that by changing the parameters of the filter it generates filters with various orientations through which we can extract features from the original image. Usually, one filter is not enough, so nearly 12 Gabor filters, were generated and convoluted with the image and then fed to implemented ML model.
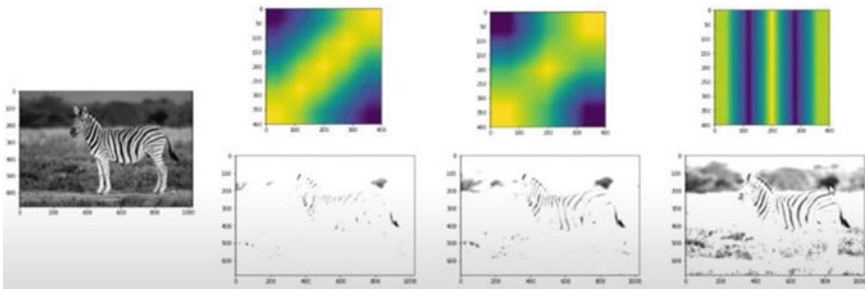
Fig. 5 Different orientations of Gabor filter

3.5.2 GLCM—Gray Level Co-occurrence Matrices

Features like aspect ratio, roundness, perimeter, area, length, and breadth [6] give better results, but in most of the cases, these features are not enough or efficient enough to classify the leaves. There are chances that two different leaves might have the same length and breadth. But to an extent it's sure that the texture of two different kinds of leaves will be different. The textures determine the patterns that appear repeatedly and are regarded as local changes in picture intensity. In this paper, a statistical approach like the use of GLCM is being suggested [8]. GLCM uses second order statistics for features that can be used to infer the degree of correlation between pairs of pixels. Uses pairs of pixels where the user can define the distance and angle between the pixels. It is recommended to extract GLCM for multiple distances and angles between pixels. First gray-level co-occurrence matrix needs to be calculated and then from that matrix, many texture properties can be calculated. Some texture properties are mentioned below.

- Contrast

$$\sum_{i,j=0}^{levels-1} P_{i,j}(i-j)^2$$

- Dissimilarity

$$\sum_{i,j=0}^{levels-1} P_{i,j}|i-j|^2$$

- Homogeneity

$$\sum_{i,j=0}^{levels-1} \frac{P_{i,j}}{1+(i-j)^2}$$

- ASM

$$\sum_{i,j=0}^{levels-1} P_{i,j}^2$$

- Energy

$$\sqrt{ASM}$$

- Correlation

$$\sum_{i,j=0}^{\text{levels}-1} P_{i,j} \left[\frac{(i - \mu_i)(j - \mu_j)}{\sqrt{\sigma_i^2 \sigma_j^2}} \right]$$

3.5.3 RFC—Random Forest Classifier

Random forest classifiers and SVMs are the mostly used traditional ML models. As the name says, random forest means it has a number of decision trees. Random forest classifier randomly picks the attributes or features that are generated previously, the Gabor filter banks among a selection or sub selection of all the attributes or features. RFC uses Gini impurity to pick a node to split that yields maximum information gain. This is used to take the decision of the tree.

A random forest is made up of a huge set of discrete trees that work together as a unit. Each tree offers a forecast, and the model's prediction is the group with the most votes.

This classifier has been chosen since it helps to minimize overfitting (works great on training data but not on new data). Bootstrap/bagging in random forest allows each tree to randomly sample from the dataset. Feature randomness is introduced by only allowing a subset of available features at each node.

In the implemented model, we have used 40 n_estimators (decision trees) and the image size which is given to our model is 256×256 which is resized from our original image which is of size 1600×1200. Features such as Gabor filter banks, original pixel values, and Sobel filter to train our model. In the model, bootstrapping of samples technique is also implemented to minimize overfitting.

3.5.4 LGBM—Light Gradient Boosting Machine

In this paper, LBGM is also used as classifier which works great with the GLCM feature extractor. It's a fast, distributed, low memory usage, high-performance gradient boosting framework based on a decision tree algorithm. It splits the tree leaf wise, unlike other models do it tree wise or level wise. Accuracy of the model depends on the provided parameters. Main parameters on which model depends are,

- Max depth: describes maximum depth of a tree
- Min data in leaf: describes about minimum number of the records a leaf may have
- Bagging fraction: used to speed up the training and avoid overfitting
- Lambda: specifies regularization.
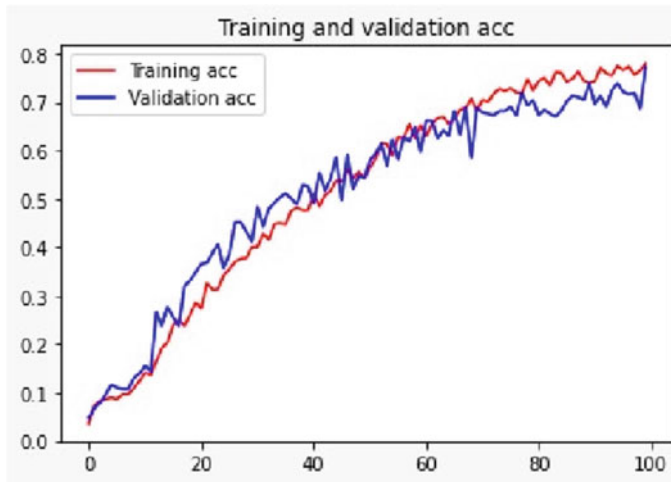
Fig. 6 Training and validation accuracy

4 Results

4.1 Deep Learning (CNN) Results

For the implemented CNN-based model which is constructed taking VGG16 and Alexnet as reference consists of 15 layers with various functions. Validation and training accuracy of the model are around 77% and 78%, respectively.

By observing above graphs of training and testing accuracy as well as the loss of the implemented sequential models in Figs. 6 and 7. From Fig. 7 as the number of epochs increases validation loss deviates more than expected from training loss. As the expected accuracy is not achieved, so machine learning based models were used which produced good results compared to deep learning based model. When an image is provided as an input to predict, implemented model have achieved an accuracy of 75%.

4.2 Machine Learning Model Results

For the RFC-based ML model due to memory constraints, model has been trained with only nine classes which consist of data from following classes Basella Alba (Basale), Carissa Carandas (Karanda), Ficus Religiosa (Peepal Tree), Jasminum (Jasmine), Mangifera Indica (Mango), Mentha (Mint), Moringa Oleifera (Drumstick), Ocimum Tenuiflorum (Tulsi), and Psidium Guajava (Guava). In this paper
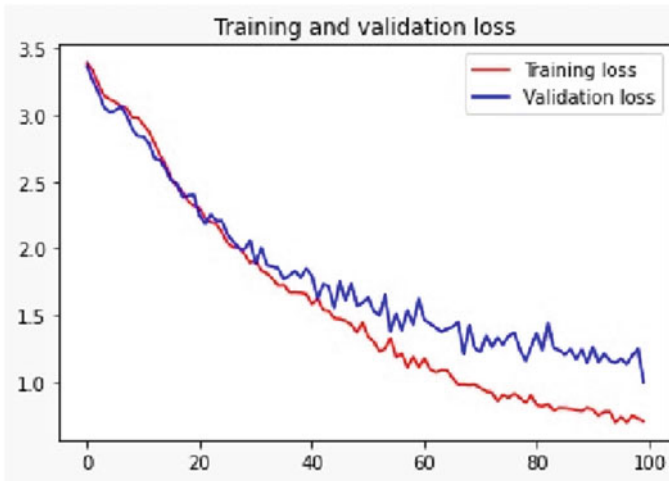
Fig.7 Training and validation loss

with accuracy as major metric a comparison has been made different feature extractors and different classifiers with accuracy as our major metric. In the testing phase around 25 images of each leaf class were used to calculate the accuracy of our model. As said above, nine leaf classes are used to compare different models and feature extractors. Gabor filter bank with random forest classifier achieves the highest accuracy of 96%. Next, LBGM classifier with GLCM and Shannon entropy as feature extractor were used and achieved an accuracy of 95.5% also random forest classifier with GLCM and Shannon entropy extractors achieves an accuracy of same 95.5% max. Table 1 gives the details of accuracy after changing various parameters of the classifiers and feature extractors.

Gabor filter banks were used to extract the features of leaves which is the most widely used filter and which depends on various parameters like theta, sigma, lambda, and gamma, etc. It generates filters of various orientations which makes it easier for models to train. 12 Gabor filters were generated with varying parameters of which gamma and lambda values are constant 0.5 and 0.7853 respectively. Whereas sigma is incremented from 1 to 5 in steps of 2 in an iterative loop. The final parameter theta which signifies the orientation of the generated filters holds different values in steps of 0.78 for every third iteration cycle.

The accuracy of each class we trained is shown below, respectively, and overall accuracy is around 95.5%.

When testing dataset images are given to test the implemented model, Table 2 describes how many images of each class the model is correctly predicting out of the images given as input. For example, if testing dataset of a class consists of 10 images and nine were correctly predicted then accuracy will be 0.9. Confusion matrix is plotted Fig. 8 which describes the validation accuracy of each class from Table 2.

Table 1 Accuracy comparison of different classifiers and feature extractors

Classifier	Features	Accuracy					
RF	Gabor, pixel and Sobel	n_estimator = 40					
		Max feature	Accuracy				
		0.2	0.96				
		0.3	0.96				
		0.5	0.96				
		0.6	0.955				
	GLCM and Shannon entropy	n_estimator = 40		n_estimator = 50		n_estimator = 70	
		Max_feature	Accuracy	Max_feature	Accuracy	Max_feature	Accuracy
		0.3	0.933	0.3	0.944	0.3	0.955
		0.4	0.922	0.4	0.922	0.4	0.933
		0.8	0.933	0.8	0.933	0.9	0.922
		n_estimator = 90		n_estimator = 110		n_estimator = 140	
		Max_feature	Accuracy	Max_feature	Accuracy	Max_feature	Accuracy
		0.3	0.944	0.6	0.944	0.3	0.944
		0.4	0.933	0.8	0.933	0.4	0.933
		0.6	0.922	0.9	0.933	0.6	0.944
LGBM	GLCM and Shannon entropy	Learningrate	Accuracy				
		0.04	0.911				
		0.06	0.933				
		0.08	0.944				
		0.2	0.955				
		0.5	0.944				

Table 2 Implemented classes and model accuracy

Class	Class name	Accuracy
1	Basella Alba (Basale)	0.9
2	Carissa Carandas (Karanda)	1.0
3	Ficus Religiosa (Peepal Tree)	1.0
4	Jasminum (Jasmine)	0.9
5	Magnifera Indica (Mango)	1.0
6	Mentha (Mint)	0.9
7	Moringa Oleifera (Drumstick)	1.0
8	Ocimum Tenuiflorum (Tulsi)	0.8
9	Psidium Guajava (Guava)	1.0
	Overall accuracy	0.955

Fig. 8 Confusion matrix of implemented model
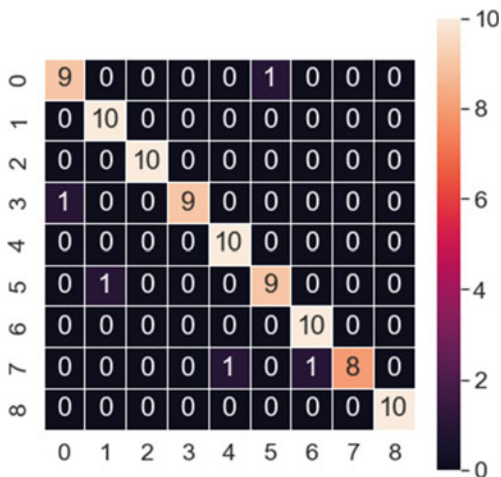
4.3 Segmentation Results

When an image consisting of multiple leaf images of the same class is given as input our task is to segregate or find contours from the image and give it as an input to implemented models to classify it as in Fig. 9.

When an image (a) consisting of multiple leaves of same class is given as input to segment foreground image from background first we will be performing edge preserving (b) followed by stylization filter whose output is shown in image (c). In order to decrease the complexity and increase the computation speed we will be converting BGR to gray scale whose output is depicted in image (d). After applying Sobel filter to expand the boundaries of gray scale image output will be like image (e). Output after performing smoothing of edges is viewed in image, (f) and final output contour detection is showed in image (g).

4.4 Hardware Output

For the hardware implementation of this project, Raspberry Pi 3 Model B V1.2 has been chosen which is one of the cheapest mini computers which you can buy in the market. It's so small, that its size is comparable to a credit card. In this project, one of the USB ports of Rpi 3 will be connected webcam which has a specification of 0.9MP with 720p video quality. The GLCM feature extractor with LGBM classifier model was used to predict the real-life segmented leaf images.

From the webcam real-time data, that is live fed can be seen on the screen of the system (PC) to capture the object. Here, the webcam is placed above the leaf and is focused to capture a clear image of the leaf for further process. In order to capture the image from live feed we need to press 'q' to capture the image and save it in
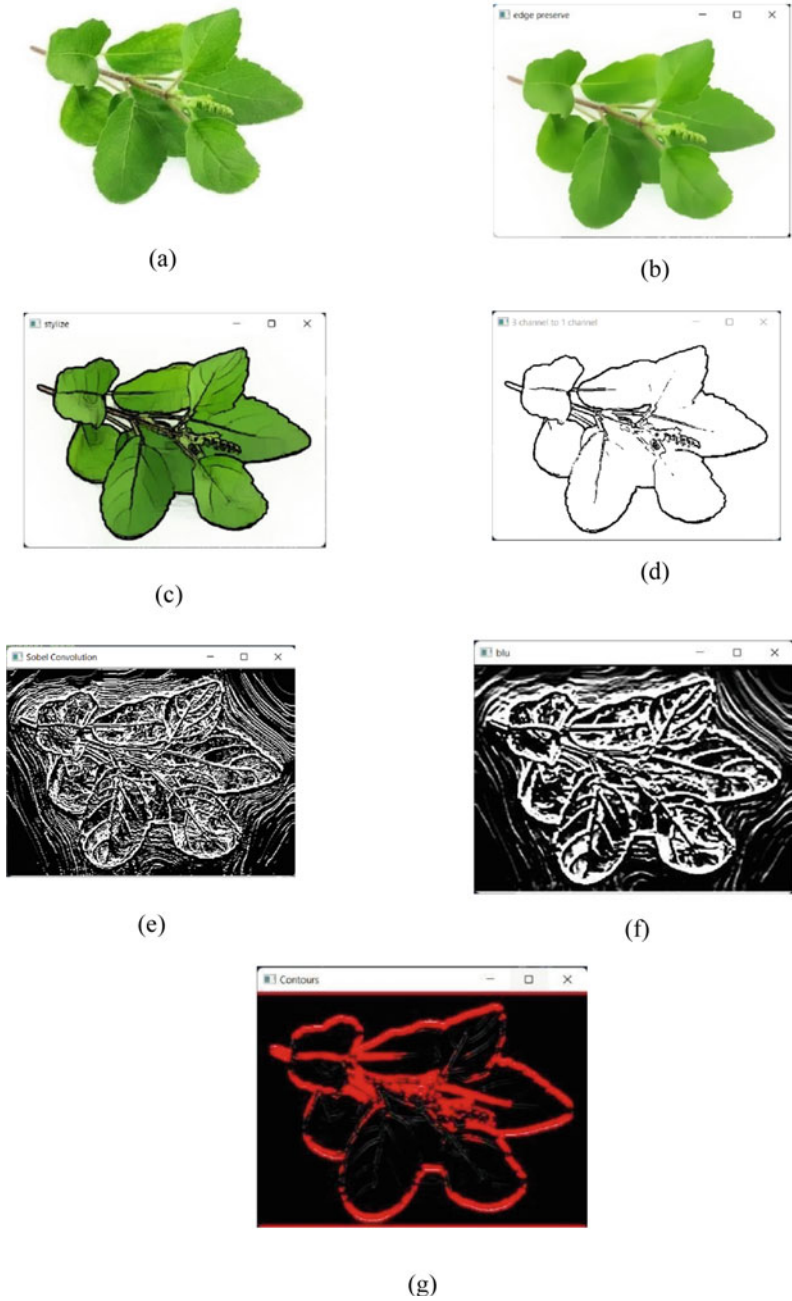
Fig. 9   Segmentation results

the system in order to further process the captured image to predict. The hardware implementation and its corresponding output are shown in Figs. 10 and 11.

A simple User Interface is designed which will help the user to navigate and use program/model with ease. This UI has been designed in Python language with

Fig. 10 Hardware Implementation and capturing image using webcam
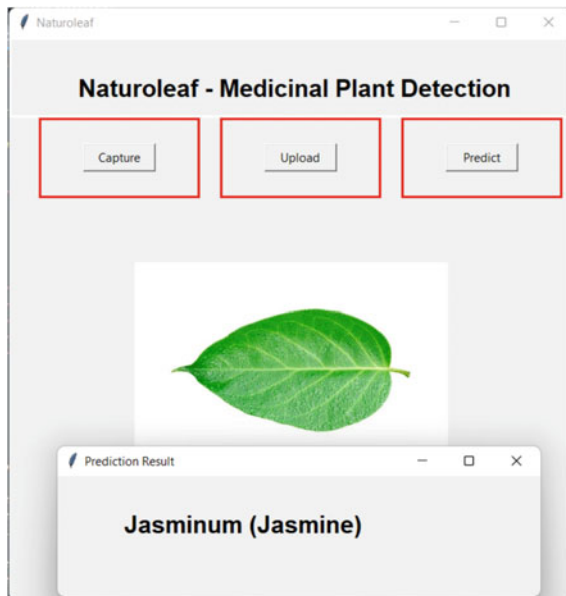
Fig. 11 UI output from implemented ML model

the help of Tkinter library. Tkinter is Python's one of the standard Graphical User Interface (GUI) library. Python with Tkinter make it simple and quick to design graphical user interfaces. Tkinter gives the Tk GUI toolkit a robust object-oriented interface.

5 Conclusion and Future Work

Achieved an accuracy of 95.5% with implemented model which has LGBM classifier and GLCM as feature extractor, which is also used for implementation of standalone device for identification of ayurvedic medicinal plants. A comparative analysis is made to choose the best model based on parameters such as accuracy, and computation memory size.

Segmentation of disease leaves from good ones could be considered as future work as disease leaves cannot add its value to ayurvedic medicinal preparation and due to dataset constraints, we propose this as future work.

Due to memory constrains, we are working with nine classes as of now, in our future scope we try to implement with all the classes in the dataset. And, implementation of android application and integrate it with hardware for better results and app will be handy most of the times in real-world applications. And improvement of the dataset with segmented and non-segmented leaves as it improves the model accuracy and classification.

References

1. Dileep MR, Pournami PN (2019) AyurLeaf: a deep learning approach for classification of medicinal plants. In: TENCON 2019—2019 IEEE Region 10, conference (TENCON), Kochi, India. https://doi.org/10.1109/TENCON.2019.8929394
2. Paulson A, Ravishankar S (2020) AI based indigenous medicinal plant identification, In: 2020 advanced computing and communication technologies for high performance applications (ACCTHPA), Cochin, India. https://doi.org/10.1109/ACCTHPA49271.2020.9213224
3. Gao L, Lin X (2019) Fully automatic segmentation method for medicinal plant leaf images in complex background. Comput Electron Agric 164:104924
4. Dyrmann M, Karstoft H, Midtiby HS (2016) Plant species classification using deep convolutional neural network. Biosyst Eng 151:72–80
5. Amuthalingeswaran C, Sivakumar M, Renuga P, Alexpandi S, Elamathi J, Santhana Hari S (2019) Identification of medicinal plant's and their usage by using deep learning. In: 2019 3rd international conference on trends in electronics and informatics (ICOEI), Tirunelveli, India, 23–25 April 2019. https://doi.org/10.1109/ICOEI.2019.8862765
6. Kumar M, Gupta S, Gao X-Z, Singh A (2019) Plant species recognition using morphological features and adaptive boosting methodology. IEEE Access 7. https://doi.org/10.1109/ACCESS.2019.2952176
7. Khan R, Debnath R (2019) Segmentation of single and overlapping leaves by extracting appropriate contours. https://doi.org/10.5121/csit.2019.91323

8. Pushpa BR, Megha N, Amaljith KB (2020) Comparison and classification of medicinal plant leaf based on texture feature. In: 2020 international conference for emerging technology (INCET), 2020, pp 1–5. https://doi.org/10.1109/INCET49848.2020.9154155
9. Huixian J (2020) The analysis of plants image recognition based on deep learning and artificial neural network. IEEE (Data Min Internet Things). https://doi.org/10.1109/ACCESS.2020.2986946
10. Kesava PSA, Peeyush KP (2019) Autonomous robot to detect diseased leaves in plants using convolutional neural networks. In: 2019 3rd international conference on trends in electronics and informatics (ICOEI), 2019, pp 806–809. https://doi.org/10.1109/ICOEI.2019.8862737
11. Venkataraman D, Mangayarkarasi N (2017) Support vector machine based classification of medicinal plants using leaf features. In: 2017 international conference on advances in computing, communications and informatics (ICACCI), 2017, pp 793–798. https://doi.org/10.1109/ICACCI.2017.8125939
12. Sivaganesan D (2021) Performance estimation of sustainable smart farming with blockchain technology. IRO J Sustain Wirel Syst 3(2):97–106
13. Palani U, Vasanthi D, Rabiya Begam S (2020) Enhancement of medical image fusion using image processing. J Innov Image Process (JIIP) 2(04):165–174

FIR and IIR Filter Design Using Modified Dadda Multiplier

K. S. Yadeeswaran, D. Prakalya, N. Mithun Mithra, Charan Athukuri, and Navya Mohan

Abstract Filters are an integral part of Digital Signal Processors (DSPs), which are necessary for signal processing in digital devices. DSPs are required to process sound signals to provide meaningful data and they are also required to process images captured by digital cameras. Multipliers and adders together form most parts of a filter. Existing filter architectures utilize various multipliers like Array multiplier, Wallace multiplier, Vedic multiplier, etc. These multipliers have a high delay resulting in performance degradation of the filters. Thus, an improvement in the architecture of the multiplier results in the betterment of the overall performance of the filters. The multipliers in turn can be improved by making changes in the algorithm used for the reduction of partial products and also by making changes to the architecture of the adder. For this purpose, a modified Dadda multiplier in which the final addition is done using the Kogge-Stone adder is being proposed in this work. The designed multiplier is an 8-bit multiplier that takes in 9-bit signed magnitude values as input and gives out 23-bit outputs which are then added together for the output to be produced. The FIR and IIR systems have been designed using VHDL and implemented in Vivado 2017.4 to obtain results.

Keywords Dadda multiplier · Parallel prefix adders · Kogge-Stone adder · Finite impulse response filter · Infinite impulse response filter

K. S. Yadeeswaran · D. Prakalya · N. Mithun Mithra · C. Athukuri · N. Mohan (✉)
Department of Electronics and Communication Engineering, Amrita School of Engineering,
Amrita Vishwa Vidyapeetham, Coimbatore, India
e-mail: m_navya@cb.amrita.edu

K. S. Yadeeswaran
e-mail: cb.en.u4ece18266@cb.students.amrita.edu

D. Prakalya
e-mail: cb.en.u4ece18238@cb.students.amrita.edu

N. Mithun Mithra
e-mail: cb.en.u4ece18230@cb.students.amrita.edu

C. Athukuri
e-mail: cb.en.u4ece18210@cb.students.amrita.edu

1   Introduction

The objective of our project is to design FIR and IIR filters with lower delay so that the processing of real-time information can be done at a faster pace. Multipliers and adders constitute most of the components of filters. The multipliers in turn consist of adders again primarily. A change in the architecture of the adder used will result in changes in every critical parameter in a filter. An FIR filter has three main components. They are delay-inducing elements, multipliers and adders. The delay-inducing elements form the first part of the filter, while the multipliers come together to form the second stage. The final stage is addition, the products from the multipliers are added together to produce the output. The adders that are used commonly are Ripple carry adder, Carry look ahead adder, Carry save adder, etc. These conventional adders are slow due to the carry propagation. The increase in width of the inputs also increases the length of the carry chain. It is possible to improve the performance of the adder by accelerating the process of carry calculation. Thus, improving the carry propagation mechanism results in the overall improvement of performance of adders.

Parallel prefix adders are a class of adders that look to reduce the time taken to calculate the carry components. There are multiple architectures in Parallel prefix adders. Some of them are the Kogge-Stone adder (KSA), Brent-Kung (BK) adder, Sklansky-adder, etc. Out of these architectures, the Kogge-Stone adder is a form of carry look ahead that calculates multiple carry components parallelly. The lower depth and fan-out results in faster performance but at the cost of higher area. It is generally considered the fastest adder. The BK adder reduces the area and power while sacrificing on the overall number of stages. The increase in the number of stages makes the Brent-Kung adder slower while comparing it to its sibling, the KSA.

The multipliers used in the filter are the most important components as most of the calculations required are done in the multipliers. There are multiple architectures of multipliers like Array multiplier, Booth multiplier, Wallace multiplier and Vedic multiplier. Wallace multipliers are one of the most efficient adders in all the parameters like area, delay and power. There are multiple variants in the Wallace multiplier optimizing it according to the requirements of the user. One such multiplier is the Dadda multiplier which reduces both the area and the critical path delay characteristics of the Wallace multiplier. The multipliers can further be optimized by using an efficient adder for the final addition. Thus, considering all the factors mentioned, we have made some architectural changes to the Dadda multiplier resulting in lower hardware usage which in turn reduces the power consumption as well. The Kogge-Stone adder is used for the addition performed in the multiplier, resulting in low delay as well. The first phase of our project deals with the changes made in the architecture of the multiplier and optimizing it for low delay. The second phase of our project will deal with using the multiplier blocks in the filter and optimizing the overall design for low delay.

2 Literature Survey

Mittal et al. [1] have tried to implement 16-order FIR filter using different multiplier designs. The multipliers they have used are Vedic multiplier, shift-and-add methods, Wallace tree multiplier. They have also used various adders with various architectures forming multiple combinations. The authors have stated that the FIR filter designed using the Wallace multiplier has an advantage in the performance front while comparing with the other architectures that they simulated.

Ykuntam et al. [2] have compared Kogge-Stone adder, Sklansky adder, Brent-Kung adder, Ladner-Fischer adder and Han-Carlson adder when being used in the design of proposed Wallace tree multiplier. It has been shown that Kogge-Stone adders are the fastest while they also utilize the most area. The traditional Wallace tree multiplier with Ripple carry adder is the slowest and occupies the least area.

Raju et al. [3] have compared different types of Parallel prefix adders. These include the Kogge-Stone (KS) adder, Sparse Kogge-Stone adder, Brent-Kung (BK) adder, Sklansky adder, Ladner-Fischer adder and Han-Carlson adder. All the adders are implemented in very high-speed integrated circuit Hardware Description Language (VHDL) using the Xilinx ISE 9.2i Design suite. 4-, 8-, 16- and 32-bit adders had been implemented. Parameters like delay, cell usage and device utilization have been compared. In conclusion, they have stated that none of the adder architectures are good for all kinds of applications. The paper offers insights on which adder would be the better choice on basic of the application.

Prasath et al. [4] have implemented an FIR filter system using Parallel prefix adder in place of normal serial adder. They have used Sklansky adders and Kogge-Stone adders and then have compared the results of the same. The number of LUTs utilized by the KSA adder is more than what the Sklansky adder uses which means that the KSA utilizes more area for the same operation. Also, due to higher hardware utilization, the power utilization is higher in the filter with Kogge-Stone adder.

Aboagye [5] details about the various structures of implementation of the IIR filter. The article also details about multiple techniques to avoid overflow. The paper deals with different scaling techniques and their comparison. The paper talks about when the different methods would be useful and about the structures in which the techniques would be most effective.

Sayed et al. [6] have used Vedic multiplier and hybrid adder instead of the conventional adder circuits that is usually used. The adders are modeled using transmission gates instead of conventional CMOS gates resulting in reduction of power utilization. Also, the utilization of direct form implementation instead of transposed form results in lower hardware utilization which in turn reduces the area occupied. The results also show that the direct form utilizes lower power.

AlJuffri et al. [7] have used Wallace tree and Vedic multipliers to implement FIR filters. The circuits are realized using 150 nm technology based on LFoundry standard-cells. There are 4 different architectures that is being implemented and the results are being compared. The Wallace multiplier has been implemented using Carry skip adder (CSA) and Ripple carry adder (RCA) while the Vedic multiplier is

implemented with RC adder and KS adder. The results show that Wallace multiplier with Carry skip adder has the lowest delay among all combinations while Wallace multiplier with Ripple carry adder has the lowest power utilization. Wallace multiplier with Ripple carry adder also has the lowest area utilization among all the architectures that has been implemented. The overall results point to the conclusion that Wallace multipliers are efficient in all parameters when compared with Vedic multipliers.

Gaur et al. [8] have implemented FIR filter using Vedic multiplier and inbuilt addition technique in VHDL and the filter coefficients are chosen as per requirements and D-flip flop is used as delay-inducing element. The results show that this paper's design consumes less components when compared to conventional designs.

Malviya and Nandi [9] have designed an IIR filter using the Wallace tree multiplier. The adders that are being used are RC adder and the BK adder. Butterworth method is used for calculating the filter coefficients of low pass IIR filter. The results have shown that the proposed filter with WTM and RCA has a lower power delay product while comparing with Vedic multiplier.

Thakur and Tiwari [10] have implemented fir filter with a complex multiplier which in turn contains 4 Vedic multiplier, adder and subtractor, and the adder used in the filter is CBL (Common Boolean Logic) adder where higher bit length uses Vedic multiplication and lower bit length uses ordinary multiplication. Parameters like delay, LUT utilization and number of IO banks used are compared between the multiplier using RCA and CBL where CBL showed better performance when compared to RCA.

Maurya et al. [11] have implemented different 32-bit adders like CINA (Carry increment adder), CBYA (Carry bypass adder) and RCA (Ripple carry adder). Three different architectures of full adders designed using multiplexers which consumes less area, power and delay depending on the architecture are used in the proposed adders and the results are compared.

Devika and Anita [12] have introduced a novel design for 7:3-bit counter. The design has been done by using 5-bit and 2-bit stacking circuits. Since the design does not have any XOR gates or multiplexers in the critical path, the circuit is very efficient.

Ghayathri et al. [13] have tried to optimize full adders by simulating and comparing various EOR and ENOR circuits. Appropriate transistor sizing is used in order to improve the results. Artificial Bee colony algorithm has been implemented using Python 3.7 to get the correct transistor sizes.

Mohan et al. [14] have proposed a possible for reducing the power dissipation during testing and a new reseeding technique. Reduction in power dissipation is obtained by implementing properties of AND and OR operations. Results show up to 20% reduction in power consumption while comparing to traditional single Linear Feedback Shift Register (LFSR).

Reddy and Ramesh [15] have proposed using Quantum Dot Automata (QCA) for combinational circuits like full adder, full subtractor and comparator. QCA 2.0.3 has been used from implementation, simulation and verification. The authors have concluded that the proposed design has lower delay and utilizes lesser number of cells as well.

Karuppusamy [16] has compared various multiplier architectures and has proposed a new multiplier architecture based on the Baugh Wooley algorithm. Domino logic has been utilized to design the adder for final addition. The usage of Domino logic in the multiplier has resulted in lower delay and power values while comparing with the existing designs.

3 Methodology

An FIR and IIR filter is shown in Fig. 1. The input is represented using $x[n]$ while the coefficients are represented using b_i, a_i and the outputs are represented by $y[n]$. The number of taps represent the number of data, coefficient pairs that are required for computation of the results. As seen from Fig. 1, multipliers, adders and delay elements are the components used to construct FIR filters. An improvement in the multiplier architecture results in improvement of the performance of the filter.

Among the available multiplier architectures, Dadda multipliers have been proven to strike a balance in the critical parameters like delay, area and power consumption. A new architecture has been proposed for Dadda multiplier so as to reduce the size of the adder used for final addition in the multiplier without increasing the number of stages required for the reduction of partial products. Five half adders have been utilized in excess to the conventional Dadda multiplier. The 1st extra half adder has been added in the 2nd stage of reduction. Another adder has been utilized in the 3rd stage. In the next stage, 2 more adders are being used and the last extra half adder is used in the last stage. The extra adders result in the reduction of final adder width. 5-bits in the LSB are directly taken for the output and a 10-bit adder is required for the final addition. Without the modification, the final adder width was 14-bit. The final addition is done using a 10-bit Kogge-Stone adder.

Figure 2 shows the schematic of the implemented multiplier. The schematic was obtained from Quartus Prime software and functional verification of the same is also done. Figure 3 shows the architecture of the designed multiplier. The diagonal lines
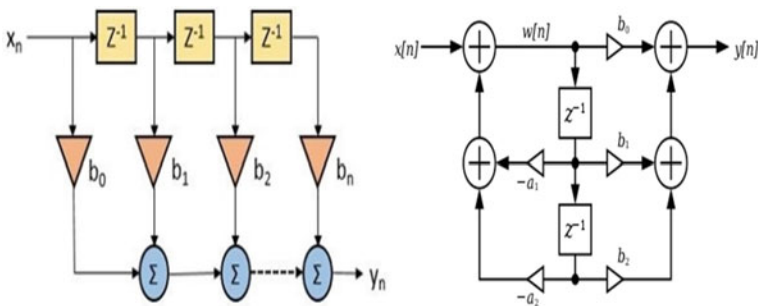
Fig. 1 FIR and IIR filter

represent full adders while the crossed lines represent half adders. The output of the designed multiplier is 16 bits long. Since FIR and IIR filters require signed inputs, the multiplier takes in signed values and outputs the appropriate product. The inputs are 9-bits long in which the leading bit is assigned as the sign bit. Signed magnitude representation is used in the inputs of the multiplier. Five half adders have been utilized in excess to the conventional Dadda multiplier. The 1st extra half adder has been added in the 2nd stage of reduction. Another adder has been utilized in the 3rd stage. In the next stage, two more adders are being used and the last extra half adder is used in the last stage. The extra adders result in the reduction of final adder width. 5-bits in the LSB are directly taken for the output and a 10-bit adder is required for the final addition. Without the modification, the final adder width was 14-bit, but now only a 10-bit adder is required. The output from the multiplier is 16-bit long by default. Then the inputs to the multiplier are checked and depending on their sign, the output is represented using 2's complement notation and the output is extended to 24-bits.

FIR filter is implemented using the designed multiplier. The Kogge-Stone adders are utilized for the purpose of addition in the filter. 24-bit adders are utilized since the output of the multipliers has been made 24-bit long. D-flip flops are used in order to delay successive inputs. A 4-tap filter is realized using the proposed multiplier. The filter takes in coefficients and data as inputs and gives output. The filter can be used to filter at various frequencies by changing the coefficients.

The coefficients can be generated from MATLAB. Figure 4 shows the schematic of the FIR filter. The IIR filter also utilizes the same blocks that were designed for the FIR filter. A 2nd order IIR filter has been implemented. It is implemented using direct form two. Figure 5 shows the schematic of the IIR filter. Since IIR filters utilize feedback mechanism, the intermediate signal width will keep increasing if it's not trimmed periodically. The output signal of the multipliers is truncated to 9-bit long so that the problem of overflow can be avoided.
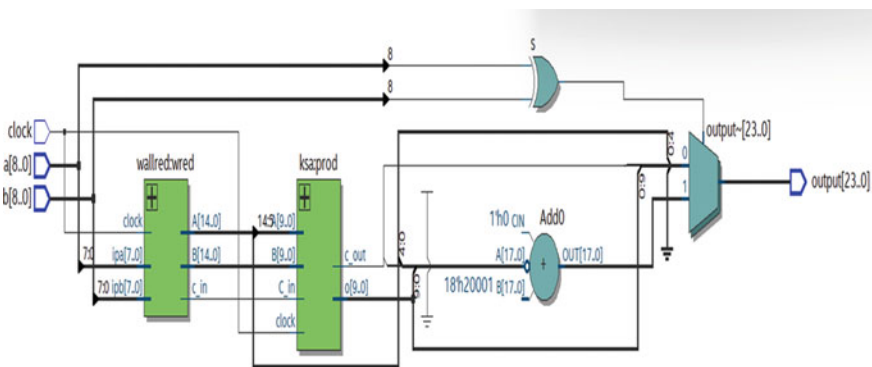
Fig. 2 Multiplier schematic
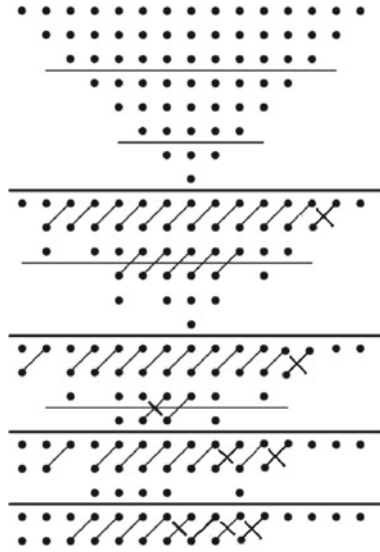
Fig. 3 Modified Dadda multiplier architecture
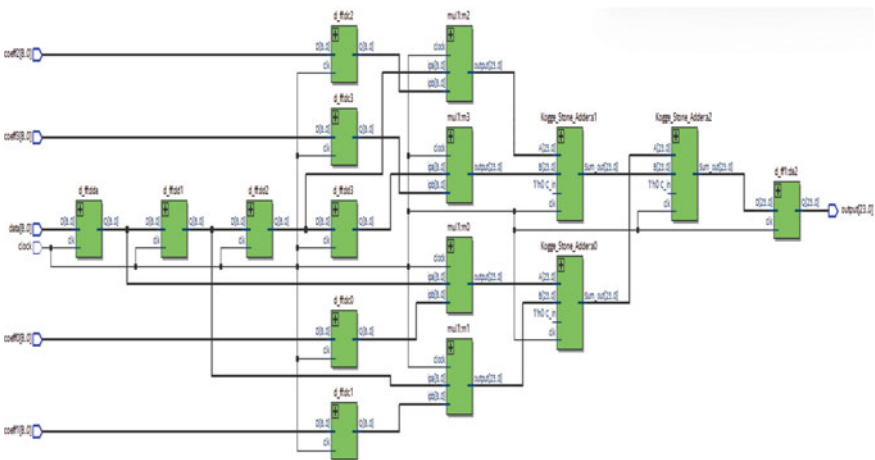
Fig. 4 FIR filter architecture

4 Results

The filters are coded using VHDL and the functionality and other results were obtained from Vivado 2017.4. The various metrics that are obtained from the tool are delay, LUT utilization, power consumption, etc. The delay refers to the critical path delay of the circuit. LUT refers to look-up table. LUTs are utilized in FPGAs
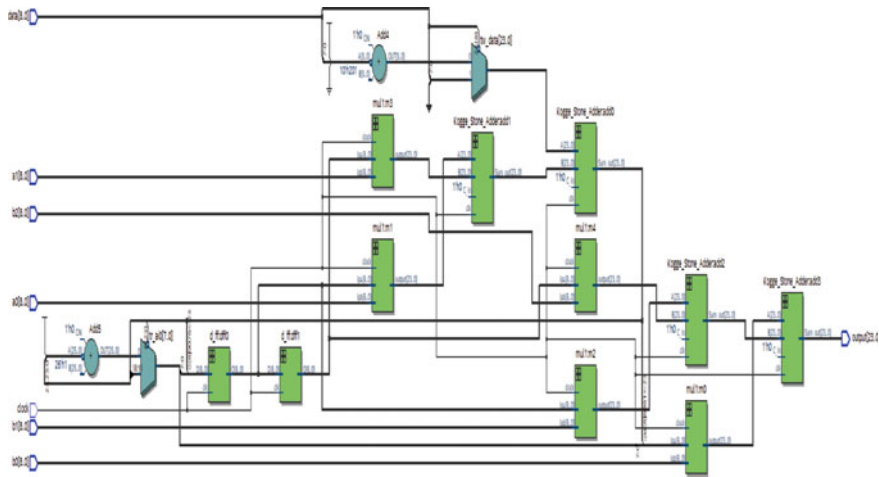
Fig. 5 IIR filter architecture

for mapping inputs to outputs. LUTs consist of SRAM cells which store the output values for each combination of input. Power consumption refers to the amount of power that will be consumed when the circuit is implemented in an FPGA.

Figure 6 shows the power utilization of the proposed multiplier. The power is divided into static power and dynamic power primarily. The dynamic power is then split into multiple facets like the power used by the internal signals, the clock, logic and by the input output signals. Table 1 gives a summary of the power results obtained from the tool. Table 2 shows the comparison of delay and the related parameters of the multipliers.
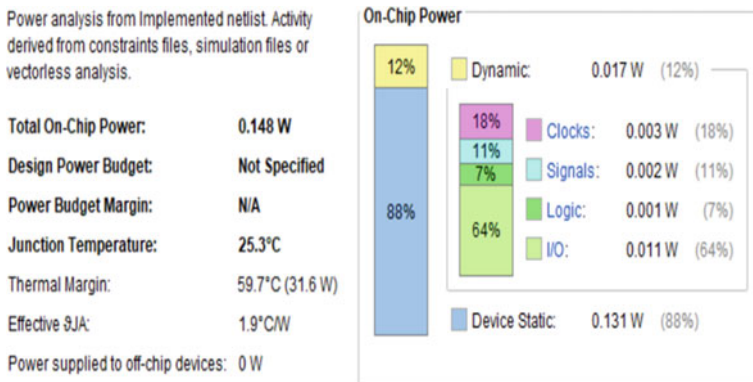
Fig. 6 Power utilization of the proposed multiplier

Table 1 Power results

Multiplier design	Static power (W)	Dynamic power (W)	Total power (W)
Proposed multiplier	0.131	0.017	0.148
Conventional Dadda multiplier	0.131	0.015	0.146
Dadda multiplier with Brent-Kung adder	0.131	0.015	0.145
Conventional Wallace multiplier	0.131	0.009	0.14

Table 2 Timing results

Multiplier design	Setup delay (ns)	Hold delay (ns)	Maximum frequency (MHz)
Proposed multiplier	2.971	0.588	334.335
Conventional Dadda multiplier	3.848	0.650	458.505
Dadda multiplier with Brent-Kung adder	3.413	0.822	279.799
Conventional Wallace multiplier	3.372	0.723	241.818

Table 3 LUT utilization

Multiplier design	LUT utilization (%)	No. of LUTs
Proposed multiplier	0.11	148
Conventional Dadda multiplier	0.11	147
Dadda multiplier with Brent-Kung adder	0.1	131
Conventional Wallace multiplier	0.11	141

Table 2 shows the comparison of different results from the timing report. The setup delay, hold delay and the maximum frequency at which the architectures can work has been mentioned in the table. Table 3 shows the comparison of LUT utilization.

5 Conclusion

From the results obtained, we can conclude that the proposed multiplier has the least delay among all the architectures. The conventional multiplier uses the least amount of power but the other metrics are not good. The Dadda multiplier using Brent-Kung adder utilizes the least area but has high delay when compared to the proposed architecture. Thus, the aim of developing a multiplier with better performance in the delay parameter has been achieved successfully. The multiplier can further be enhanced so that reduction in the other metrices is achieved as well. The multiplier

can be improved using domino logic and reversible logic for obtaining lower power and delay metrics.

Filter use only three components for the calculations, they are multipliers, adders and delay elements. The multipliers and adders are the components that cause performance bottlenecks in the filters. Thus, replacing the existing multipliers by the designed multipliers and replacing the adders by Kogge-Stone adders in the filter results in the least possible delay thus improving the filter performance but at the cost of higher power utilization.

References

1. Mittal A, Nandi A, Yadav D (2017) Comparative study of 16-order FIR filter design using different multiplication techniques. IET Circuits Devices Syst 11(3):196–200
2. Ykuntam Yd, Pavani K, Saladi K (2020) Design and analysis of High speed Wallace tree multiplier using parallel prefix adders for VLSI circuit designs. In: 2020 11th international conference on computing, communication and networking technologies (ICCCNT), pp 1–6. https://doi.org/10.1109/ICCCNT49239.2020.9225404
3. Raju A, Patnaik R, Babu RK, Mahato P (2016) Parallel prefix adders—a comparative study for fastest response. In: 2016 international conference on communication and electronics systems (ICCES), pp 1–6. https://doi.org/10.1109/CESYS.2016.7889974
4. Prasath AM, Arjun RV, Deepaknath K, Gayathree K (2020) Implementation of optimized digital filter using Sklansky adder and Kogge stone adder. In: 2020 6th international conference on advanced computing and communication systems (ICACCS), pp 661–664. https://doi.org/10.1109/ICACCS48705.2020.9074440
5. Aboagye AK. Overflow avoidance techniques in cascaded IIR filter ...—ti.com [online]. Available at: https://www.ti.com/lit/pdf/spra509
6. Sayed JF, Hasan BH, Muntasir B, Hasan M, Arifin F (2021) Design and evaluation of a FIR filter using hybrid adders and Vedic multipliers. In: 2021 2nd international conference on robotics, electrical and signal processing techniques (ICREST), pp 748–752. https://doi.org/10.1109/ICREST51555.2021.9331063
7. AlJuffri AA et al (2015) ASIC realization and performance evaluation of scalable microprogrammed FIR filters using Wallace tree and Vedic multipliers. In: 2015 IEEE 15th international conference on environment and electrical engineering (EEEIC), pp 1995–1998. https://doi.org/10.1109/EEEIC.2015.7165480
8. Gaur N, Kapur S, Mehra A (2020) Application of Vedic multiplier: design of a FIR filter. In: 2020 4th international conference on electronics, communication and aerospace technology (ICECA), pp 234–237. https://doi.org/10.1109/ICECA49313.2020.9297659
9. Malviya KK, Nandi A (2018) Design of IIR filter using Wallace tree multiplier. In: 2018 2nd international conference on power, energy and environment: towards smart technology (ICEPE), pp 1–4. https://doi.org/10.1109/EPETSG.2018.8659159
10. Thakur AS, Tiwari V (2018) Design high speed FIR filter based on complex Vedic multiplier using CBL adder. In: 2018 international conference on recent innovations in electrical, electronics & communication engineering (ICRIEECE), pp 559–563. https://doi.org/10.1109/ICRIEECE44171.2018.9008438
11. Maurya KAK, Lakshmanna YR, Sindhuri KB, Kumar NU (2017) Design and implementation of 32-bit adders using various full adders. In: 2017 innovations in power and advanced computing technologies (i-PACT), pp 1–6. https://doi.org/10.1109/IPACT.2017.8245176
12. Devika C, Anita JP (2022) Design of a high-speed binary counter using a stacking circuit. Inventive communication and computational technologies. Springer, Singapore, pp 135–143

13. Ghayathri T, Lavanya T, Srivastava Y, Anita JP (2021) Optimization of EOR and ENOR for design of full adders with efficient transistor sizing. In: 2021 5th international conference on trends in electronics and informatics (ICOEI). IEEE, pp 107–112
14. Mohan N, Aravinda Kumar M, Dhanush D, Gokul Prasath J, Kumar JS (2021) Low transition dual LFSR for low power testing. Inventive communication and computational technologies. Springer, Singapore, pp 397–406
15. Reddy BM, Ramesh SR (2021) Design of combinational arithmetic circuits using quantum dot cellular automata. In: 2021 5th international conference on trends in electronics and informatics (ICOEI). IEEE, pp 117–122
16. Karuppusamy P (2019) Design and analysis of low-power. High-speed Baugh Wooley multiplier. J Electron 1(02):60–70

High Speed and Power Efficient Multiplier and Adder Designs for Linear Convolution

S. Shrinidhi, S. Vinuja, R. Lakshmi Prasanna, B. Sumanth, and Navya Mohan

Abstract In most of the prominent areas of digital signal processing (DSP) applications, the operation of linear convolution finds a pivotal role. With the increasing demand for applying convolution to varied applications of DSP, there has also come a need to develop techniques to compute complex high-speed computations. Hence, this paper focuses on providing a linear convolution architectural model for computing the operation fast and accurately with minimal power dissipation and area. Here, the 16-bit linear convolution architecture has been designed by proposing a set of 4-bit reversible Vedic multipliers (RVMs) architecture, 8-bit and 9-bit reversible Kogge–Stone adders (KSAs). The 4-bit RVM architecture is built based on the Urdhva Triyagbhyam (UT) algorithm and the 8-bit and 9-bit KSAs employ the proposed reversible black cell (PRBC) and proposed reversible grey cell (PRGC). The performance of the proposed reversible KSA is compared with existing reversible KSA and other parallel-prefix adders (PPAs), designed using PRBC and PRGC. The PRGC and PRBC have resulted in a nearly 50% reduction in the number of clock cycles (CCs), constant inputs (CIs), and garbage outputs (GOs) compared to the existing grey and black cells. The 16-bit linear convolution system has been designed using VHDL and implemented in Vivado 2017.4 to obtain the results of power, area, and delay.

S. Shrinidhi (✉) · S. Vinuja · R. Lakshmi Prasanna · B. Sumanth · N. Mohan
Department of Electronics and Communication Engineering, Amrita School of Engineering,
Amrita Vishwa Vidyapeetham, Coimbatore, India
e-mail: cb.en.u4ece18269@cb.students.amrita.edu

S. Vinuja
e-mail: cb.en.u4ece18264@cb.students.amrita.edu

R. Lakshmi Prasanna
e-mail: cb.en.u4ece18240@cb.students.amrita.edu

B. Sumanth
e-mail: cb.en.u4ece18211@cb.students.amrita.edu

N. Mohan
e-mail: m_navya@cb.amrita.edu

1 Introduction

Linear convolution is one of the most prominent mathematical operations between the input and the impulse response of a linear time-invariant (LTI) system to compute its output. It is applied in several areas of DSP, audio processing, image processing, probability, artificial intelligence, etc. Using efficient multipliers in the design of a linear convolution system is highly essential since they are responsible for the speed of the convolution process. In this paper, we are using the concept of the Vedic multipliers (VMs) which are used for high-speed applications, majorly using the UT algorithm. Here, the multiplication operation on any two operands is performed by multiplying vertically and cross-wise and finally adding all the results. The computations performed by employing this method are easy, powerful, and rational.

The concept of reversible logic has found its use in various low-power applications since it has a tremendous ability to reduce net power dissipated during the operation of a system. Employing reversible logic in the design of circuits ensures no loss of information. The primary goals of reversible logic are to reduce quantum cost, circuit depth, and the number of garbage outputs. Hence, the reversible logic is newly invested in the proposed design to suit a particular application to obtain the desired outputs. In this paper, new reversible logic gates are also designed in such a manner that there exists a direct correlation betwixt the inputs and outputs. The proposed 16-bit convolution architecture work of this paper will be discussed in detail in the below sections.

2 Literature Review

Many types of multipliers were introduced to improve the power, area, and delay parameters. Amongst them, the high-speed VM executes better in terms of speed and area [1]. For reducing power consumption, Baugh Wooley algorithm was used in multipliers [2]. This VM uses UT algorithm to compute the multiplication result in parallel manner which leads to faster computation [3]. Though the VM is quite efficient, a major challenge involved here is internal energy dissipation. This was evident in all conventional non-reversible circuits and was proved by Landauer [4]. After this, Bennett proved and concluded from the work that reversible circuits can be used to produce zero energy loss, and in turn, the power is conserved. In [5], array multiplier is designed using reversible HA and multiplexer-based reversible FA. This reversible logic is flexible to be incorporated in any functional hardware block. The work in paper [6] incorporates the array, Vedic, Wallace and Dadda algorithms to perform comparison amongst them.

Further, different adders are used in summation of partial products of Vedic multipliers to increase the speed of operations. The proposed architecture in this paper [7] for 4-bit multiplier uses carry-save adder. In the work of paper [8], the fast-Fourier transform butterfly structure is implemented by using the VM technique. Different types of PPA's are generated depending on the number of black and grey cells used and based on the interconnections between the black and grey cells. One of the PPA's which is KSA is used in [9] to develop 8-bit RVM.

Eventually, the multipliers, adders and all the basic hardware are to build complicated applications. This paper [10] majorly focuses on designing a system to compute fast linear convolution with multipliers and adders. The detailed process of the design proposed here for high-speed 16-bit linear convolution architecture will be explained below in the section of methodology.

3 Methodology

3.1 Matrix Method of Linear Convolution

The growing demand for linear convolution of long sequences within a limited amount of time has necessitated the need for high-speed linear convolution architectures. Further, power, area and delay are required to be minimized to make the convolution process efficient. There are 2 approaches used for finding the convolution of two discrete length signals. One is the tabular method, and the other is the matrix method. The tabular method involves the traditional convolution process which is time-consuming and inefficient for implementation in hardware. The matrix method is quite simple, involving only the multiplication and addition processes. To understand the matrix method, let us consider two signals of length 4 in decimal. $X[k] = [1, 1, 1, 1]$, $H[k] = [1, 1, 1, 1]$.

This process involves 4 steps:

1. The two signals should be written in a matrix form as shown in Fig. 1, with the row having one signal ($H[k]$) and the column having the other signal ($X[k]$) in binary format.
2. Multiply each element in the row with each element in the column and enter it in the respective index. For instance, for the 1st element of the row 1(0) and

Fig. 1 Multiplication using matrix method

X[k] H[k]	1(0)	1(1)	1(2)	1(3)
1(0)	$1^{(0,0)}$	$1^{(0,1)}$	$1^{(0,2)}$	$1^{(0,3)}$
1(1)	$1^{(1,0)}$	$1^{(1,1)}$	$1^{(1,2)}$	$1^{(1,3)}$
1(2)	$1^{(2,0)}$	$1^{(2,1)}$	$1^{(2,2)}$	$1^{(2,3)}$
1(3)	$1^{(3,0)}$	$1^{(3,1)}$	$1^{(3,2)}$	$1^{(3,3)}$

column 1(0), $1 \times 1 = 1$. Hence, in the (0, 0), position 1 should be entered as shown below.

3. Now, the diagonals should be drawn as shown in Fig. 1. For this convolution, 7 diagonals should be drawn to get 7 output signals. The length of the output signal can be cross checked with the formula:

$$\text{Length (output)} = 2 * \text{length (signal)} - 1 \tag{1}$$

4. Finally, by adding the elements inside the respective diagonal, we can get the convoluted signal $g[k] = [1, 10, 11, 100, 11, 10, 1]$ as output. For instance, in value (i, j), i denotes the ith row, and j denotes the jth column. For instance, in Fig. 1, value $(0, 0) = 1$, is the first bit output. Value $(1, 0)$ + Value $(0, 1) \rightarrow 1 + 1 = 10$ is the second bit output.

As seen above, this is the simplest process to find the convolution of two signals. So, in this paper, the matrix method is taken as a base to implement convolution architecture. Matrix method of approach can be implemented efficiently in hardware with the help of VM using UT algorithm. Now, to understand the UT algorithm, consider 4×4 bit multiplication operation with inputs A = 1111 and B = 1111 as shown in Fig. 2. Here, all the products will be computed first, and then, each row of products will be added, and outputs will be calculated directly. If carry exists, then the carry will be propagated to the next. But, in the convolution operation, carry need not be propagated to the next. The sum of each row of partial products is added separately and taken as output. So, by using the same UT algorithm, except for propagating carry, multiplication is performed. Hence, the final output in convolution will have 7 bits from g[0] to g[6]. This can be implemented by adding each row of the partial products as shown in the steps below.

g[0] = A1B1 = 1
g[1] = A2B1 + A1B2 = 1 + 1 = 10
g[2] = A3B1 + A2B2 + A1B3 = 1 + 1 + 1 = 11
g[3] = A4B1 + A3B2 + A2B3 + A1B4 = 1 + 1 + 1 + 1 = 100
g[4] = A4B2 + A3B3 + A2B4 = 1 + 1 + 1 = 11
g[5] = A4B3 + A3B4 = 1 + 1   10
g[6] = A4B4 = 1.

Fig. 2 Multiplication for 4 × 4 bit inputs

```
       1 1 1 1
     x 1 1 1 1
     ──────────
       1 1 1 1
     1 1 1 1 0
   1 1 1 1 0 0
 1 1 1 1 0 0 0
 ──────────────
```

In this paper, convolution for 16-bit is proposed. So, the first step of multiplying the signals in matrix method is employed in hardware by initially giving the input signals for convolution as input to 4-bit RVM's. Then, the summation of diagonal values in matrix method is done by using 8-bit and 9-bit KSA. The KSAs are designed using PRBC and PRGC gates which are proposed in this paper. Here, for addition, the carry signals are not propagated. In the below sections, the 4-bit RVM, 8-bit and 9-bit KSA architectures and the overall architecture of 16-bit convolution will be explained in detail.

3.2   Proposed Reversible Vedic Multiplier

The existing Vedic multiplier designs compute the partial products and add them. Then, the carry is propagated to the next column. When such architecture is presented, the clock cycles are more to perform the multiplication. To overcome problems of delay, garbage outputs and clock cycles, a 4-bit RVM architecture has been proposed which can implement addition in parallel and propagates carry in just 7 clock cycles with a smaller number of gates, constant inputs and garbage outputs as shown in Fig. 5. The 4-bit RVMs constructed here are based on the UT algorithm plays the role of multiplying two signals in the matrix method. In the multiplier, initially, products are computed using PERES gate for AND operation, and then, we add each row of products as per UT algorithm using PERES gate as HA and HNG gate as FA to compute the sum. The architecture of the multiplier introduced in this paper is such that the multiplier can compute the summation in parallel. The proposed multiplier architecture is shown below in Fig. 3. The output of this 4-bit multiplier is 8 bits. The outputs of the final convoluted signal p [7:0] and p [63:56] are directly obtained from 4-bit multipliers which is shown in Fig. 6.

Other 8-bit outputs are given as inputs to the reversible KSA-8-bit adders. The summation is done using reversible KSA-8, and the outputs are 9 bits. The outputs p [16:8] and p [55:47] are directly obtained from reversible KSA-8 adders. The other 9-bit outputs will be added along with 8-bit multiplier outputs using reversible KSA-9. The output of reversible KSA-9-bit adder is 10 bits. Finally, these outputs are obtained which is p [46:17]. Here, the carry from adders will not be propagated in convolution. The sum is calculated individually and given as output. The overall architectural flow of the proposed RVM design is shown in Fig. 3.

3.3   Proposed Reversible Kogge–Stone Adder

KSA belongs to the category of PPA. PPAs are known for performing fast computation and consuming less area. The Brent–Kung adder (BKA), Sklansky adder (SA), Han-Carlson adder (HCA) and Ladner Fischer adder (LFA) are some of the
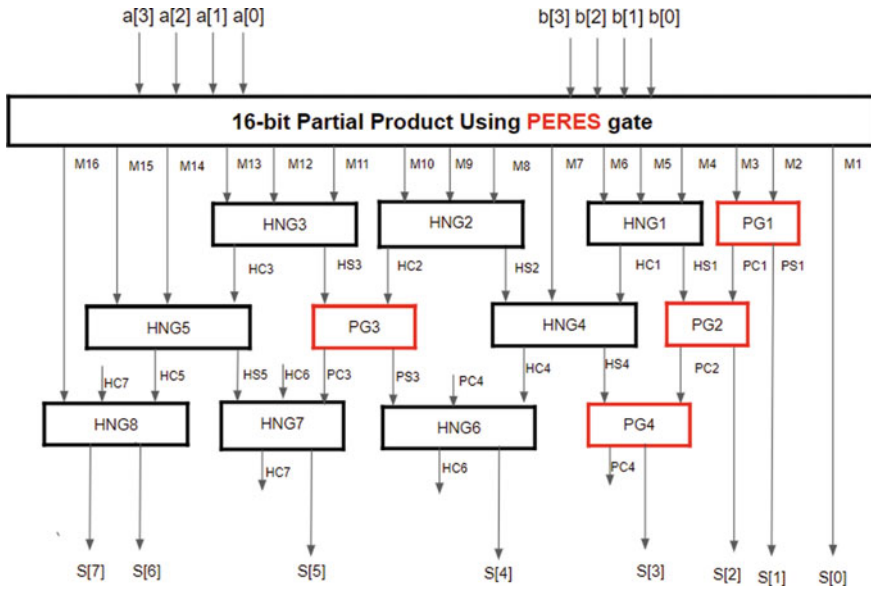
Fig. 3 Proposed reversible Vedic multiplier architecture

other PPAs. In this work, 16-bit linear convolution is implemented using the above-mentioned PPAs and compared with the proposed architecture employing reversible KSA.

In general, all reversible PPAs are constructed using black cells and grey cells. The existing reversible grey cell and black cell are designed using the Toffoli gate and UPG gate. Since these cells make use of 2 gates, the feedback of Toffoli gate is given as input to the UPG gate to generate the carry cell. Hence, the grey and black cells take 2 clock cycles to implement the carry generate and propagate signals. Further, the garbage output and constant inputs are high. So, when the reversible parameters are high, the overall efficiency of the architecture decreases in terms of area and delay. Hence, the PRGC and PRBC have been introduced in this work. All the reversible PPAs used in this work are implemented using the PRGC and PRBC. The operation of the PRGC and PRBC are showcased in Figs. 4 and 5, respectively. Here, the number of clock cycles is reduced to 1, as a single gate is used to develop both generate carry and propagate signals. The advantages of these PRBC and PRGC are shown in detail in the results section.

3.4 Proposed Fast Convolution Architecture

The design of 16-bit linear convolution is proposed in this paper using RVMs and reversible KSA with reversible technology employed in its design. The proposed
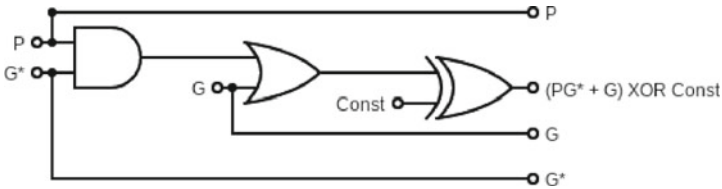
Fig. 4 Proposed reversible grey cell
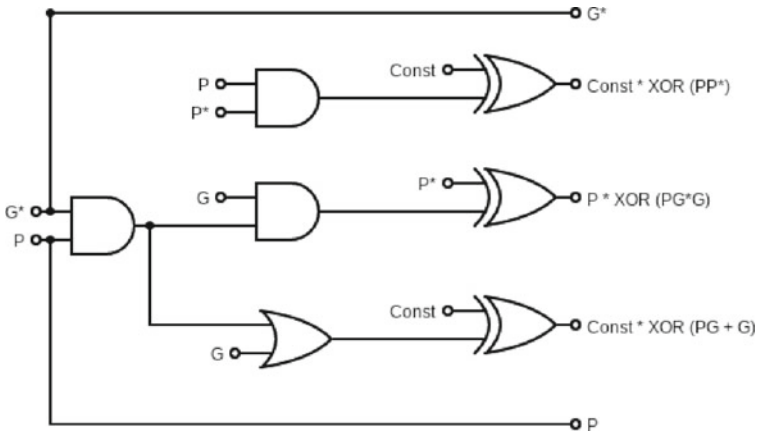
Fig. 5 Proposed reversible black cell
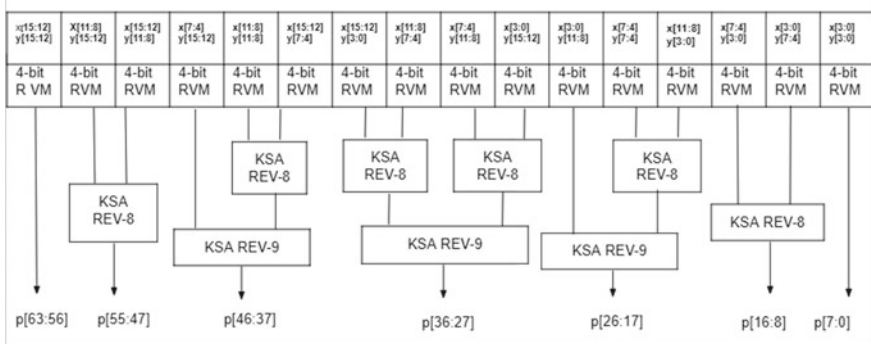
Fig. 6 Proposed architecture of high-speed 16-bit linear convolution

architecture of 16-bit linear convolution is designed to consume a total of 17 clock cycles. It consists of 16 4-bit RVM, 6 reversible 8-bit KSAs and 3 reversible 9-bit KSAs. The overall architecture has been constructed by considering the length of the linear convolution output. Here, the output length being 64-bits can be obtained from the outputs of 4-bit RVMs passed through 8-bit and 9-bit reversible KSAs,

based on the specific desired output length at each stage of operation. Initially, two 16-bit sequences are obtained as binary inputs from the user for which the maximum decimal value is 15. The outputs of the 4-bit RVMs on either side are taken directly. The subsequent outputs of the two RVMs on either side are passed as inputs into the 8-bit reversible KSAs. These inputs are then sent as bit streams into the 16 4-bit RVMs, where each generates 16 partial products and an 8-bit output. The outputs of 8-bit length of the RVMs placed at the 4,5; 7,8; 9,10; 11,12 positions from the right in Fig. 6 are then forced as inputs into the 8-bit and 9-bit reversible KSAs to further generate outputs of 10-bit length. Finally, the architecture generates two blocks of 8-bit and 9-bit outputs and three blocks of 10-bit outputs, summing to a total of 64-bits at the output.

4   Results

All the presented designs of 16-bit linear convolution and reversible multipliers have been implemented using VHDL in ModelSim and simulated for the correctness of the design. Further, the implementation and the synthesis of the design were done in the Vivado 2017.4 tool [11] using ZedBoard Zynq evaluation and development kit, and the results were tabulated and compared on various essential parameters of the design.

The PRBC and PRGC used in the PPAs to generate carry propagation and carry generation signals resulted in nearly 50% deduction in the number of CIs, GOs and CCs when compared to the conventional black and grey cells as shown in Table 1. From the above table, it is also clear that the garbage output, constant inputs and gate count of PRBC, PRGC is less when compared to the existing designs. Hence, the adder designs introduced in this paper using PRBC and PRGC will consume less area and LUT's when compared to the traditional adder designs.

The proposed RVM consumes a total of 7 clock cycles when compared to that presented in [8, 12–14]. The proposed design of the reversible 4-bit RVM has resulted in the reduced number of constant inputs of 28, number of garbage outputs of 52 and a quantum cost of 128 when compared to that presented in [8, 12–14]. Table 2 explains the comparison of the characteristics of the presented design of RVM with other similar designs demonstrated in [8, 12–14] in terms of the number of CCs, gate

Table 1 Comparison of PRBC and PRGC with conventional black and grey cells

Parameters	Black cell	PRBC	Grey cell	PRGC
CIs	3	1	2	1
GOs	6	3	4	3
CCs	2	1	2	1
Clk cycles in KSA-8	8	5	8	5
Clk cycles in KSA-9	9	6	9	6

Table 2 Comparison of proposed RVM with other existing multiplier designs

Parameters	Proposed multiplier	[12]	[13]	[14]	[8]
CCs	7	13	8	8	18
GC	28	28	29	28	44
CIs	28	44	34	32	40
GOs	52	72	58	56	41
QC	128	168	285	244	162

Table 3 Modified reversible KSA versus existing KSA

Reversible KSA adders	LUT (%)	Path delay (ns)	Worst negative slack (ns)	Worst hold slack (ns)
Conventional reversible KSA	0.12	8.024	7.219	0.144
Modified reversible KSA	0.07	7.995	7.118	0.106

count (GC), CIs, GOs and quantum cost (QC). As the gate count, constant inputs and garbage outputs are less for the proposed multiplier when compared to the exiting designs; it consumes less area, and LUT utilization will be comparatively less which is shown in Table 5.

Table 3 shows the comparison results of conventional reversible KSA and the modified reversible KSA. The modified design of reversible KSA has resulted in 71% better LUT utilization and 0.4% reduced path delay than the conventional reversible KSA. This shows that the complexity of the proposed 16-bit convolution architecture is less in terms of delay and area (LUT's). Hence, the design proves to be simple when compared to the existing designs.

Table 4 shows the results of the five reversible PPAs implemented using PRBC and PRGC. The 8-bit reversible KSA design has resulted in the least path delay of 7.995 ns compared to other 8-bit reversible PPAs thereby operating at a very high speed. The BKA has a higher delay compared to KSA but has an area lesser than the KSA. The SA and HCA are efficient in terms of power. They have the least power of all the other PPAs. The results of the presented were compared on the parameters of power (P), dynamic power (DP), static power (SP), path delay (PD), worst negative slack (WNS), number of LUTs and worst hold slack (WHS) after implementing the design in the Vivado 2017.4 tool.

The power consumption of the proposed 16-bit linear convolution is 0.128 which is the summation of static power and dynamic power. The static power depends on the processor used and is same for all the designs. The results in Table 5 depict that the proposed16-bit linear convolution with 4-bit RVM has resulted in 6.6%, 2.3%, 1.5% and 16.4% reduced power than that of the multiplier designs proposed in [8, 12–14], respectively. Critical path delay is an important parameter to determine the working speed of circuits [15]. The path delay of proposed 4-bit RVM is 11.461 ns

Table 4 Comparison of 8-bit reversible parallel-prefix adders

Parameters	KSA	BKA	SA	HCA	LFA
P (W)	0.111	0.111	0.106	0.106	0.111
DP (W)	0.006	0.006	0.002	0.002	0.006
SP (W)	0.104	0.104	0.104	0.104	0.104
PD (ns)	7.995	8.053	8.061	8.053	8.017
WNS (ns)	7.118	7.173	7.556	7.254	7.201
LUTs (%)	0.07	0.07	0.07	0.07	0.07
WHS (ns)	0.106	0.106	0.152	0.154	0.152

Table 5 Comparison of proposed convolution with other designs using Vivado 2017.4

Parameters	Proposed RVM	[12]	[13]	[14]	[8]
P (W)	0.128	0.137	0.131	0.130	0.149
DP (W)	0.023	0.032	0.026	0.026	0.044
SP (W)	0.105	0.105	0.105	0.105	0.105
PD (ns)	11.461	14.351	13.469	11.795	12.195
WNS (ns)	6.210	6.838	6.494	6.551	6.962
LUTs (%)	1.75	2.30	1.86	1.79	3.26
WHS (ns)	0.042	0.052	0.104	0.038	0.106
CCs	18	24	19	19	29

which is less when compared with other normal multipliers like Vedic, array, Booth and Wallace which is shown in paper [16]. The major difference is because of the adder which is used in the design.

5   Conclusion

In this work, a high-speed 16-bit linear convolution system has been implemented using 16 4-bit RVMs, 6 8-bit and 3 9-bit reversible KSA. The proposed reversible 4-bit RVM has resulted in a reduced delay of 11.461 ns in the overall 16-bit linear convolution process compared to the works presented in [8, 12–14].

The proposed reversible gates PRBC and PRGC can be used in other architectures in future to make the design efficient and fast. The performance of the proposed reversible KSA is improved in various aspects of the number of CCs, CIs, GOs, LUT, PD, WNS and WHS when compared the conventional KSA. The proposed reversible KSA has the least path delay in comparison to other reversible parallel-prefix adders thereby making the 16-bit linear convolution system to operate at a very high speed. The proposed convolution architecture can be further expanded to implement higher-order circular convolution, de-convolution, multi-dimensional

discrete convolution and in other processes involved in machine learning (ML) and DSP.

References

1. Bansal Y, Madhu C, Kaur P (2014) High speed Vedic multiplier designs—a review. Recent Adv Eng Comput Sci (RAECS) 2014:1–6. https://doi.org/10.1109/RAECS.2014.6799502
2. Karuppusamy P (2019) Design and analysis of low-power. High-speed Baugh Wooley multiplier. J Electron 1(02):60–70
3. Kunchigi V, Kulkarni L, Kulkarni S (2012) High speed and area efficient Vedic multiplier. In: 2012 International conference on devices, circuits and systems (ICDCS), pp 360–364. https://doi.org/10.1109/ICDCSyst.2012.6188747
4. Landauer R (1961) Irreversibility and heat generation in the computing process. IBM J Res Dev 5(3):183–191
5. Yugandhar K, Raja VG, Tejkumar M, Siva D (2018) High performance array multiplier using reversible logic structure. In: 2018 international conference on current trends towards converging technologies (ICCTCT), pp 1–5. https://doi.org/10.1109/ICCTCT.2018.8550872
6. Sivanandam K, Kumar P (2019) Design and performance analysis of reconfigurable modified Vedic multiplier with 3-1-1-2 compressor. Microprocessors Microsystems 65. https://doi.org/10.1016/j.micpro.2019.01.002
7. Ariafar Z, Mosleh M (2019) Effective designs of reversible Vedic multiplier. Int J Theor Phys 58:2556–2574
8. Nikhil GV, Vaibhav BP, Naik VG, Premananda BS (2017) Design of low power barrel shifter and Vedic multiplier with Kogge-Stone adder using reversible logic gates. In: 2017 international conference on communication and signal processing (ICCSP), pp 1690–1694. https://doi.org/10.1109/ICCSP.2017.8286680
9. Thapliyal H, Srinivas MB (2006) Novel reversible multiplier architecture using reversible TSG gate. In: IEEE international conference on computer systems and applications, 2006, pp 100–103. https://doi.org/10.1109/AICCSA.2006.205074
10. Shams M, Haghparast M, Navi K (2008) Novel reversible multiplier circuit in nanotechnology. World Appl Sci J 3:806–810
11. Reddy BM, Ramesh SR (2021) Design of combinational arithmetic circuits using quantum dot cellular automata. In: 2021 5th international conference on trends in electronics and informatics (ICOEI). IEEE, pp 117–122
12. Akhter S, Chaturvedi S (2019) Modified binary multiplier circuit based on Vedic mathematics. In: 2019 6th international conference on signal processing and integrated networks (SPIN), pp 234–237. https://doi.org/10.1109/SPIN.2019.8711583
13. Devika C, Anita JP (2022) Design of a high-speed binary counter using a stacking circuit. In: Inventive communication and computational technologies. Springer, Singapore, pp 135–143
14. Ghayathri T, Lavanya T, Srivastava Y, Anita JP (2021) Optimization of EOR and ENOR for design of full adders with efficient transistor sizing. In: 2021 5th international conference on trends in electronics and informatics (ICOEI). IEEE, pp 107–112
15. Mohan N, Aravinda Kumar M, Dhanush D, Gokul Prasath J, Kumar JS (2021) Low transition dual LFSR for low power testing. In: Inventive communication and computational technologies. Springer, Singapore, pp 397–406
16. Chandrashekara MN, Rohith S (2019) Design of 8 bit Vedic multiplier using Urdhva Tiryagbhyam sutra with modified carry save adder. In: 2019 4th international conference on recent trends on electronics, information, communication & technology (RTEICT), pp 116–120. https://doi.org/10.1109/RTEICT46194.2019.9016965

A Decision-Making System for Dynamic Scheduling and Routing of Mixed Fleets with Simultaneous Synchronization in Home Health Care

R. V. Sangeetha and A. G. Srinivasan

Abstract Globally, the growing number of elderly people, chronic disorders and the spread of COVID-19 have all contributed to a significant growth of Home Health Care (HHC) services. One of HHC's main goals is to provide a coordinated set of medical services to individuals in the comfort of their own homes. On the basis of the current demand for HHC services, this paper attempts to develop a novel and effective mathematical model and a suitable decision-making technique for reducing costs associated with HHC service delivery systems. The proposed system of decision making identifies the real needs of HHCs which incorporate dynamic, synchronized services and coordinates routes by a group of caregivers among a mixed fleet of services. Initially, this study models the optimization problem using Mixed Integer Linear Programming (MILP). The Revised Version of the Discrete Firefly Algorithm is designed to address the HHC planning decision-making problem due to its unique properties and its computational complexity. To evaluate the scalability of this proposed approach, random test instances are generated. The results of the experiments revealed that the algorithm performed well even with the different scenarios such as dynamic and synchronized visits. Furthermore, the improved version of nature-inspired solution methodology has proven to be effective and efficient. As a result, the proposed algorithm has significantly reduced costs and time efficiency.

R. V. Sangeetha (✉) · A. G. Srinivasan
Department of Mathematics, Dr. MGR Educational and Research Institute, Chennai, Tamil Nadu, India
e-mail: sangeedev@gmail.com

A. G. Srinivasan
e-mail: srinivasan.ags.math@drmgrdu.ac.in

1   Introduction

The healthcare industry has experienced unprecedented growth in the recent decades due to the growing expectation of continuity of care among patients. According to the World Health Organization (WHO), there is a continuous rise in the aging population [1] due to advancements in healthcare technologies [2, 3]. Consequently, the hospital service delivery system is faced with a number of challenges, including the difficulty of scheduling different healthcare professionals, organizing in-patients' accommodations, managing hospitalization demands, uncertainty regarding lengths of hospital stays, multiple patients arriving at the same time, etc., which can lead to stressful situations if you attempt to manage them all simultaneously. Several alternatives to hospitalization have been proposed as a way to shorten hospital stays and increase access to care as the need for hospitalizations continues to rise. One of the alternatives to overcome these challenges, it is necessary to understand the advantages of home-based health care, which is enabling the Home Health Care (HHC) system [4, 5]. In widespread pandemics like COVID-19, the access to healthcare facilities becomes a very challenging one because individuals are unable to travel. This creates a demand for the HHC system that requires a thorough, systematic and scientific investigation. Home Health Care (HHC) is a type of service delivery system that provides healthcare services from the comfort of the patient's own home, by a team of healthcare professionals.

A large number of multidimensional resources are managed by HHC since routing of these resources is one of their primary concerns. So, in this paper, a dynamic scheduling and routing problem has been discussed associated with mixed fleets of vehicles. It includes caregivers' assignments, vehicles scheduling, patients' allocation based on their preferences, caregivers' routing decisions, etc. The literature on HHC indicates that only a few heuristic and metaheuristic algorithms have been developed to address such dynamic routing and scheduling problems. Demirbilek et al. [6] modeled dynamic scheduling of patients by homogenous caregivers. They presented a heuristic that generates a number of scenarios that involve generating and scheduling random requests, assigning new patients based on a simple and quick heuristic procedure, analyzing the results and making a decision on whether or not to accept the patient. As a means of reducing the cost of the Dynamic Vehicle Routing Problem (DVRP) in HHC, [7] developed a Hypermutation Genetic Algorithm (HGA) that considers real-time requests [8]. Application of an Enhanced Ant Colony Optimization (E-ACO) to a DVRP in order to minimize costs [9]. A variant of combined mixed fleet vehicles with Elitism of ACO can be developed to balance the work load of caregivers [10]. The heuristic developed for home care is intended to integrate vehicle routing and scheduling with prioritization constraints and synchronization requirements [11]. Build a constructive heuristic using the best insertion heuristic, taking synchronization with time window constraints into account to minimize the time required [12]. An ant colony heuristic-based clustering algorithm has been used to solve the Vehicle Routing Problem with Time Windows and Synchronized Visits in Home Health Care [13]. To solve the Home Health Care problem with respect

to balancing working hours, a hybrid of memetic and ant colony optimization algorithms is proposed. The objective of the design is to minimize travel times among caregivers, patients' poor time window matching their schedules, the non-respect of synergistic visiting times and the maximum difference in time between caregivers [14]. A LINGO_11.0 solver from LINDO Systems, Inc., is used to schedule and route caregivers in HHC for synchronized visits. HHC is currently faced with challenging and complex optimization problems at various levels of decision making [15]. Since many dynamic routing models of HHCs are modeled in the literature, there is still some unmatched scenarios are present in real-time instances. To match or overcome such scenarios, we develop a novel variant of the HHC model called Dynamic Scheduling and Routing Problem for Mixed Fleet with Simultaneous Synchronization (DSRPMFSS). As a result, the HHC operations team needs a proper decision-making system to handle such real-time models.

The primary goal of this study is to identify an appropriate Nature-Inspired Optimization (NIO) technique or metaheuristic algorithm that can serve as decision-making systems to support the proposed variant DSRPMFSS of HHC [5, 15]. In order to meet multiple objectives, all test instances are focused on reducing the total transportation costs and time while increasing the number of nodes visited. There are several metaheuristic algorithms available today, but one of the most appealing and simplest metaheuristic algorithms is the Firefly Algorithm (FA). Researchers from diverse disciplines are interested in it because of its easy and uncomplicated steps. The FA mainly inspires on the way fireflies communicate with each other using flashing lights to attract mates or recognize predators. Researchers have developed Discrete Firefly Algorithms (DFAs) and Improved Firefly Algorithms (IFAs) to solve traveling salesman problems [16, 17] and capacitated vehicle routing problems (CVRPs) [18]. In this case, the Discrete Firefly Algorithm (DFA) has been revised [17, 19, 20] and used to solve DSRPMFSS by improvising the movements of fireflies (FFs) [21]. Each FF is chosen based on its weights. Using this improved move of FFs, it is able to avoid stagnation at local optima and accelerate convergence. This algorithm has been compared to one of the most powerful and successful NIO techniques known as Discrete Cuckoo Search Algorithm (DCSA) [22]. According to the experimental analysis, RVDFA outperforms DCSA for this unique model, which is more time-saving and cost-effective.

1.1 Main Contribution of Research

The following is the major contribution of this research study:

- Introduced an ideal model that is similar to real-time scenarios, such as DSRMFSS;
- Developed a NIO technique called RVDFA. It is especially designed to deal with complex issues such as DSRMFSS;

- Solving multi-objectives such as reducing the cost, time and number of resources as well as increasing the number of patient visits;
- Identified the most effective and efficient system for making decisions that save time and money.

Therefore, the paper is organized to solve the variant of DSRPMFSS as follows: In Sect. 2, a description of the model is provided. In Sect. 3, the mathematical formulation is presented. In Sect. 4, the Firefly Algorithm is described. In Sect. 5, the experimental results are discussed.

2   Model Description

Generally, HHC organizations would prefer to maximize patient visits while minimizing costs. To achieve this, it is necessary to find an optimal schedule and route to follow for each vehicle. On a given day, a team of caregivers will determine the order in which visits should be performed and the tasks to be accomplished at each location. Caregivers work for a single depot during their working hours, which means the vehicles start and end their work at the same depot. During the course of the day, set of caregivers uses mixed fleet of transportation (i.e., Small Vehicle (SV) type, Medium Vehicle (MV) type and Large Vehicle (LV) type). Large vehicles are assigned to more qualified and highly skilled caregivers than small vehicles. Due to the dynamic nature of the problem, accepting and scheduling time slots cannot be delayed. Overtime is not permitted because of increased costs. As a result, a decision must be made in response to the patient's request as soon as possible. Using a greedy algorithm, we include new patients under the feasible criteria [16]. A patient may be preferred by one or more care services at the same time depending on their requirements. Consequently, they require a simultaneous set of care services. In order to accomplish this, the mix fleet of vehicles must be synchronized simultaneously [23]. Moreover, the travel cost and fixed cost of each vehicle type vary based on the capacities of the vehicles. This proposed model is validated by developing a mathematical model of mixed integers for reducing transport costs, time and the number of vehicles involved in a routing plan as well as increasing the number of patients' nodes who are seen by a particular set of professional caregivers.

2.1   Problem Formulation

The problem can be described as a classic Dynamic Vehicle Routing Problem with Time Window (DVRPTW) along with synchronized constraints [24], which is known as the "DSRPMFSS" of HHC. Usually, breaks are not considered when routing and scheduling systems are designed. This problem includes both shift breaks and day breaks in one whole working day as shown in Table 1. As part of the dynamic

Table 1 Duration of time slots for each shift

Shifts	Time slots	Duration (min)
SHIFT-I	Slot 1 (8.00–10.30 am)	150
	Shift break (10.30–10.45 am)	15
	Slot 2 (10.45 am to 13.15 pm)	150
DAY BREAK	Day break (13.15–13.45 pm)	30
SHIFT-II	Slot 3 (13.45–16.15 pm)	150
	Shift break (16.15–16.30 pm)	15
	Slot 4 (16.30–19.00 pm)	150

routing design, allocate vehicles to the patient nodes in order to match the patient's demands with the vehicle's capacity so that services can be provided within the feasible criteria. In such cases, depending on the availability of the patients, time slots of vehicles are synchronized whenever a patient needs more than one type of service at a time. In order to accomplish this, the mix fleet of vehicles must be synchronized simultaneously. Therefore, each vehicle can visit known or dynamic patients, as well as perform synchronization [11] as often as necessary. A priority-based service is also provided, so penalty charges are incorporated, and because there is a threat to the patient's health, no delay is tolerated. Vehicles that fail to visit the scheduled patients' nodes in their route plan will be assessed penalties.

2.2 Assumptions

Our assumptions suggest that the data of all patients and caregivers are well managed by HHC. HHCs can provide patients with a wide range of healthcare services. At the depot, they have an adequate number of vehicles available to visit patients. Moreover, there is a balance between the number of resources that are available and the number of patient requests received on any given day. The speed of each vehicle is determined by the type of vehicle being used. As per patients' requests, all patients must be visited on the same day. Caregivers are prohibited from working extra hours. Once the route has been completed, all vehicles must be returned to the depot.

3   Mathematical Formulation

Based on real-world scenarios, our proposed DSRPMFSS model assumes that total time (including travel and service time) and costs are asymmetric. It means that the total time and costs between any two nodes (i, j) differ from those between nodes (j, i). This feature is rare in literature [6] related to scheduling and routing problems, which closely matches the situation in practical life. Our new variant DSRPMFSS is described as a graph $G = (P, A)$, where P is the number of patients' nodes and A is the number of arcs (i, j). Arcs have the following definition: $A = \{(i, j)/i, j \in P, i \neq j\}$. If there is one depot 0, a number of mixed fleet vehicles K with certain capacity (C) limits leave the depot and visit a set of patients $(i = 1, 2, 3, …, P)$ before returning to the depot. Three types of vehicles are mentioned in the form $C_i = [C_1, C_2, C_3]$, where C_1 refers to the capacity of vehicle I, C_2 refers to the capacity of vehicle II and C_3 refers to the capacity of vehicle III. The dynamic routing system ensures that different vehicles are allocated to different patient nodes depending upon their demand d_i and vehicle capacity C_i. In addition, make sure that all services are being provided within the caregiver's working time limit. A goal of the model is to identify and schedule routes that serve and meet all the patients' needs. As a result, our proposed model DSRPMFSS involves multiple objectives as follows:

- Minimizing the overall travel time as well as the amount of idle time spent during their route plan;
- Minimizing the total travel cost and the penalty cost associated with vehicles that have pending nodes to visit;
- Minimizing the number of vehicles utilized during their route plan;
- Maximizing patient visits within a specified time period.

3.1   Parameters and Notations

Following is a list of parameters and notations [24] that should be used to formulate in MILP:

P = The number of nodes or patients' homes = $[0, 1, 2, …, P, P + 1]$
K = Different types of healthcare vehicles = [Vehicle I-SV, Vehicle II-MV, Vehicle III-LV]
C^k = Set of multi-capacity vehicles = $[C^1, C^2, C^3]$
v = Maximum number of vehicles available for each type $k = [1, 2, 3, …, n]$
P^k = Services provided by K-type vehicles for a set of patients
w_i^k = Set of new patients arriving for each vehicle type $K = \{w_i^1, w_i^2, w_i^3\}$
ts_{ij} = Transit time taken between nodes i and j as well as service time spent at node j
d_i = The node i demands a set of services
st_i = Service time required to perform the care at the node i

qu_{P^k} = The skills of the caregivers in vehicle K should match the demand required for the allotted set of patients P^k

r = The number of routes r_i available during a shift

I^k = The amount of time spent idle during the route plan by a K-type vehicle

$[a_v^k, b_v^k]$ = Initial and final time horizons for the vth k-type vehicle, i.e., $a_v^k < b_v^k$

$[e_i, l_i]$ = Time of the earliest and latest visits to the patient node i

t_{total}^k = Maximum working time limit for k-type vehicles

S_t = Scheduling of the time slots for each day = $[S_1, S_2, S_3, S_4]$

$S_t^{kk'} = \bigcup_{i=1}^4 S_i^{kk'} \ k \neq k', \quad \forall \ kk' \in K$, describes different K-type vehicles simultaneously synchronized in a certain time frame at the respective patient's node

k_v = Set of vehicles accessible for each vehicle type

p_r = Penalty cost incurred for failing to visit the allotted patients' nodes within the assigned time slots during the planned route r_i

c_{ij} = The total cost of traveling from node i to node j as well as the service provided at node j

α = Travel cost per minute

β = Idle cost per minute.

3.2 Decision Variables

$$x_{ij}^k = \begin{cases} 1, & \text{If } k\text{-type vehicle transits from node } i \text{ to node } j \\ 0, & \text{Otherwise} \end{cases}$$

$$y_i^k = \begin{cases} 1, & \text{If the patient's demand is compatible with the vehicle's capacity,} \\ & \text{schedule the nodes based on the route plan} \\ 0, & \text{Otherwise} \end{cases}$$

$$z_{vi}^k = \begin{cases} 1, & \text{If there is an availability of } k\text{-type vehicles meet the dynamic} \\ & \text{patient } i \text{ demands, schedule them in their respective timeframes.} \\ 0, & \text{Otherwise} \end{cases}$$

$$u_r^k = \begin{cases} 1, & \text{if the vehicle type-}k \text{ assigned to the routeis based} \\ & \text{on the skills of the caregivers} \\ 0, & \text{Otherwise} \end{cases}$$

The proposed MILP model is as follows:

Objective functions are:

(1) minimize the (i) total amount of travel and penalty costs, (ii) the total amount of time the vehicles are in transit and idle and (iii) number of vehicles used for routing plan.

(2) maximize the number of patient visits in each route plan within the time horizon.

$$\text{Min}\left\{\left\{\sum_{i=0}^{P}\sum_{j=1}^{P+1}\alpha c_{ij}x_{ij}^{k}+\sum_{r=1}^{P}\beta p_{r}I^{k}\right\}+\left\{\sum_{i=0}^{P}\sum_{j=1}^{P+1}ts_{ij}x_{ij}^{k}+\sum_{i=0}^{P}I^{k}y_{i}^{k}\right\}\right.$$

$$\left.+\left\{\sum_{i=0}^{P}k_{v}u_{r}^{k}\right\}\right\}\quad \forall\, k\in K \tag{1}$$

$$\text{Max}\left\{\sum_{i=0}^{P}w_{i}^{k}z_{vi}^{k}\right\}\quad \forall\, k\in K\ \text{ and }\ v=1,2,\ldots,n \tag{2}$$

Scheduling and routing constraints are expressed in the following manner: Ensure all the vehicles (3) are required to visit the node exactly once.

$$\sum_{i=0}^{P}x_{ij}^{k}=1\quad \forall\, j=1,2,\ldots,P+1\ \text{ and }\ k\in K \tag{3}$$

All vehicles (4) must arrive and leave the node

$$\sum_{i=0}^{P}x_{ij}^{k}-\sum_{i=0}^{P}x_{ji}^{k}=0\quad \forall\, j=1,2,\ldots,P+1\ \text{ and }\ k\in K \tag{4}$$

All vehicles begin and end at the depot according to constraints (5) and (6).

$$\sum_{j=1}^{P+1}x_{0j}^{k}\leq 1\quad \forall\, i=1,2,\ldots,P\ \text{ and }\ k\in K \tag{5}$$

$$\sum_{j=1}^{P+1}x_{jn+1}^{k}\leq 1\quad \forall\, i=1,2,\ldots,P\ \text{ and }\ k\in K \tag{6}$$

Constraint (7), skills of caregivers should match the demands of assigned patients' nodes.

$$x_{ij}^{k}-M(1-st_{j}^{k})\ \leq\ qu_{Pk}\quad \forall\, i=1,2,\ldots,P;\ j=1,2,\ldots,P+1;$$
$$i\neq j;\quad \text{and}\quad k\in K \tag{7}$$

Constraint (8), the number of care services required at node j cannot exceed the capacity of k-type vehicles.

$$\sum_{j=1}^{P+1}d_{j}x_{ij}^{k}\leq 1\quad \forall\, i=1,2,\ldots,P\ \text{ and }\ k\in K \tag{8}$$

(9) and (10) correspond to a time horizon constraints.

$$e_i \sum_{i=0}^{k} x_{ij}^k \leq ts_{ij} \leq l_i \sum_{i=0}^{k} x_{ij}^k \quad \forall \, i = 1, 2, \ldots, P;$$
$$j = 1, 2, \ldots, P + 1; i \neq j; \quad \text{and} \quad k \in K \tag{9}$$

$$b_v^k - a_v^k \leq t_{\text{total}}^k \quad \forall \, v = 1, 2, \ldots, n \ \text{and} \ k \in K \tag{10}$$

The constraints (11) and (12) indicate the requirements necessary to achieve synchronization of mixed fleets

$$\sum_{i=0}^{P} st_i^k = \sum_{i=0}^{P} st_i^{k'} \quad \forall \, k, k' \in K \tag{11}$$

$$S_{r_i}^k \cap S_{r_j}^k = \phi, i \neq j \quad \forall \, k, k' \in K \ \text{and} \ r_i \in K \tag{12}$$

Constraint (13) states that each vehicle's idle time should not exceed the maximum working time.

$$b_v^k - a_v^k < t_{\text{total}}^k = I^k \quad \forall \, v = 1, 2, \ldots, n \ \text{and} \ k \in K \tag{13}$$

Constraint (14) emphasizes the elimination of all subtour.

$$x_{ij}^k \leq |M| - 1 \quad \forall \, M \subseteq \{1, 2, \ldots, P\}; \quad j = 1, \, 2, \ldots, \ P + 1 \ \text{and} \ k \in K \tag{14}$$

Lastly, the constraints (15)–(18) define several variables that will be used to make a decision.

$$x_{ij}^k \in \{0, 1\} \quad \forall i = 0, 1, 2, \ldots P; \quad j = 1, 2 \ldots, P + 1; \quad i \neq j \quad \text{and} \ k \in K \tag{15}$$

$$y_i^k \in \{0, 1\} \quad \forall i = 0, 1, 2, \ldots P \ \text{and} \ k \in K \tag{16}$$

$$z_{vi}^k \in \{0, 1\} \quad \forall i = 0, 1, 2, \ldots P; \quad v = 1, 2, \ldots n; \quad k \in K \tag{17}$$

$$u_r^k \in \{0, 1\} \quad \forall r_i \in r \ \text{and} \ k \in K \tag{18}$$

4 Proposed Methodology of the Revised Version of Discrete Firefly Algorithm

It is possible to increase transportation costs by managing the fleet of vehicles inefficiently. So, in order to minimize transportation costs as well as to make better fleet management decisions, an enhanced nature-inspired algorithm is proposed as a Revised Version of the Discrete Firefly Algorithm (RVDFA) which works well in various routing models [25]. The following sections describe how to implement this algorithm.

Initialization. In order to perform the RVDFA's overall action by initiating with the parameters, namely population size (NP), synch nodes, number of vehicles, maximum number of iterations (N_iter), etc. To ensure the effectiveness of the metaheuristic algorithm, the initial population of the algorithm should be generated on a random basis. Thus, the revised version of the metaheuristic algorithm FA generated initial population randomly. The fireflies in the modified version are constructed as follows:

(1) Each route path is defined with a start and end node depot.
(2) In order to avoid selecting random patients' nodes from the list of nodes more than once and deleting the same node from the list repeatedly.
(3) In addition to adding specific patients to a route path, it is also essential to ensure that the needs of these patients are aligned with the vehicle's capacity.
(4) Repeat the above steps until the patient's capacity equals or exceeds the vehicle's capacity.
(5) A new route has been added.
(6) It is necessary to repeat steps 1 to 5 till all of the patients' nodes have been scheduled.

Check the feasibility criteria. Test whether the current best x_{best} for the firefly and other x_i fireflies is feasible by measuring the total travel time each firefly takes provided it does not exceed the maximum time limit of the horizon.

Main concept of RVDFA. One of the primary disadvantages of the Firefly Algorithm is that it reaches convergence early and stagnates at the same point after a certain number of runs. To overcome this disadvantage, it is necessary to modify the classic FA in order to solve our new variant. In RVDFA, firefly movements have been enhanced by its use of neighborhood structures in accordance with the criterion of feasibility, which is a combination of random movement and movement toward. These modifications are mainly introduced to speed up the convergence. The firefly's objective function can then be calculated once it has been constructed. Each firefly's objective function represents the total amount of time that was spent in flight. Time taken for each route is estimated by using the Cartesian distance equation between all the patients in the route path and the depot at the starting point. A firefly with a least objective function value is the most attractive solution to DSRPMFSS, since it is a minimization problem.

The Hamming distance ($r_{i,\text{best}}$) [26] is the distance between one of the lightest fireflies and another that yields the best possible solution, which, in turn, calculates how intense each firefly's light that emits. A firefly r distance is the distance between the fireflies and the number of nodes that are not concurrent between them.

$$I_i = \text{Random}(1, r_{i,\text{best}}) \tag{19}$$

Equation (19) is used to calculate the light intensity of a firefly i (I_i) after $r_{i,\text{best}}$ has been calculated. Firefly i seems to have moved toward a brighter firefly based on observations of I_i. After calculating I_i between two fireflies x_i and x_{best}, find the brightest or most attractive firefly. Firefly's movements have been improved by adopting 2-opt inter-route neighborhood structures, which shift the nodes in-between or outside of the routes based on the weight's strategy. This implies that, in the presence of a brighter firefly, the less bright one will approach the brighter one. Otherwise, it will move in a random manner. Thus, this revised version is intended to increase the convergence speed and to escape from local minima.

Whenever a movement of the firefly occurs, the existing solution is changed immediately. This process is repeated m times by each firefly [21]. After every iteration, $(m \times n) + 1$ fireflies should have been generated, since only those fireflies with the best fitness values will be eligible to be taken into account in subsequent iterations. Based on the objective function, NP best fireflies will be selected for the next iteration. This procedure has been repeated until iterations have reached the maximum number. A comparison of the current best firefly and new fireflies is performed to select the best function.

Determine the feasibility solution. As far as feasibility considerations are concerned, the current best firefly x_i and other x_j fireflies are the most feasible solutions among the candidate solutions.

Termination criteria. After reaching the maximum number of iterations N_iter, the proposed algorithm ends. As a result, identify the optimal solution among all candidate solutions (Fig. 1).
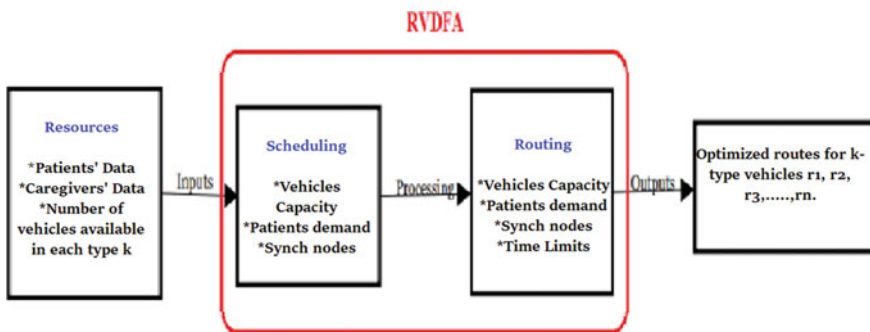
Fig. 1 Schematic diagram of RVDFA

4.1 Pseudocode of RVDFA

Begin

    Input: objective function f (x);
    Output: the best firefly best_x;
    Initialize parameters P, v, N_iter;
    t = 0;   /* t is the iteration starts */
    Firefly population N is initialized as X = $(x_1, x_2, \ldots, x_p)$;
    for i = 1 to P then   /*for each of the fireflies present in P*/
    Determine the objective function f (x_i) that corresponds to firefly x_i;
    Equation (9) determines the intensity of the light I_i at x_i;
    Current best_x should be identified;
    end
    while the termination criterion is not met then
    for i = 1 to P then   /*for each of the fireflies present in P*/
    for j = 1 to i then
    if $I_i > I_j$ then
    Move towards
    else
    Move randomly
    end
    end
    Sort the fireflies and determine which is the best out of all of them
    Check the feasibility criteria and includes new nodes using greedy algorithm
    t = t + 1;
    end
    Return global best firefly x_i
    end

5 Discussion and Computational Outcomes

The novel variant of DSRPMFSS proposed in this paper has never been considered in the literature [5] of HHC before. Here, patients are scattered geographically. Instances of mixed fleets are launched from the single depot. The working day can be divided into two shifts. At 8 a.m., the first shift will begin and last until 1.15 p.m. At 1.45 p.m., the second shift will begin and last until 7 p.m. Each shift lasts 5 h, plus a 15-min shift break. As shown in Table 1, there are four different time slots during the day (two slots during each shift), along with a day break.

In this case, the updated version of discrete firefly algorithm is applied and compared with the well-known classical DCSA [22]. This problem involves several constraints including those connected with capacity, caregiver qualifications, travel

and service time, idle time, time windows, synchronization, etc. Healthcare vehicles are classified into three categories: small, medium and large. Using a greedy algorithm, instances with dynamic patients are selected according to the feasibility criteria. In the experimental study, RVDFA proved to be more efficient than DCSA in terms of total travel time using randomly generated test instances as illustrated in Fig. 2.

Figure 2 illustrates the type of vehicle as the *x*-axis and the total travel time as the *y*-axis, while in Fig. 3, the *x*-axis as the type of vehicle and the *y*-axis as the number of patients' nodes visited. Hence, it has been proved that this revised version of proposed algorithm visited a greater number of patients than DCSA. Further, for each test instance [14], the total travel cost and penalty cost are analyzed and compared between DCSA and RVDFA in Table 2. This experiment analysis was conducted using python 3.9 and the configuration Intel(R) Core (TM) i5-1135G7 @ 2.40 GHz, 2419 MHz, 4 Core(s), 8 Logical Processor(s) on Windows 11 with 64 bits.

Here, the total travel cost includes travel cost per minute and fixed cost [26] per shift. Travel costs for small, medium and large vehicles are defined as Rs. 1, Rs. 2 and Rs. 3 per minute, respectively. Depending on the capacity of the vehicle, the fixed costs vary as Rs. 100, Rs. 200 and Rs. 300 per shift, respectively. Accordingly, if there are pending nodes available in each shift, the routing cost will include penalties for three categories of vehicles such as Rs. 75, Rs. 1.5 and Rs. 2.25 per minute associated with the idle time of each vehicle. Hence, the optimal cost for each
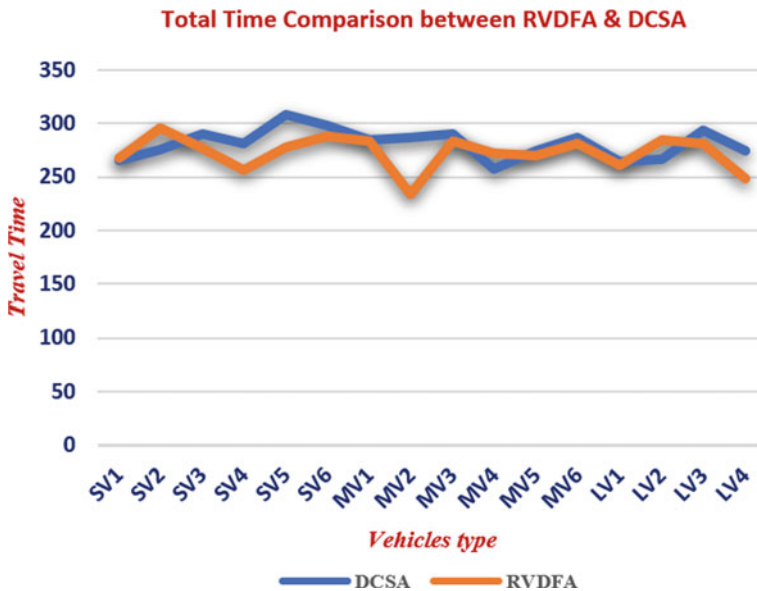
Fig. 2 Comparison of total time taken between RVDFA and DCSA
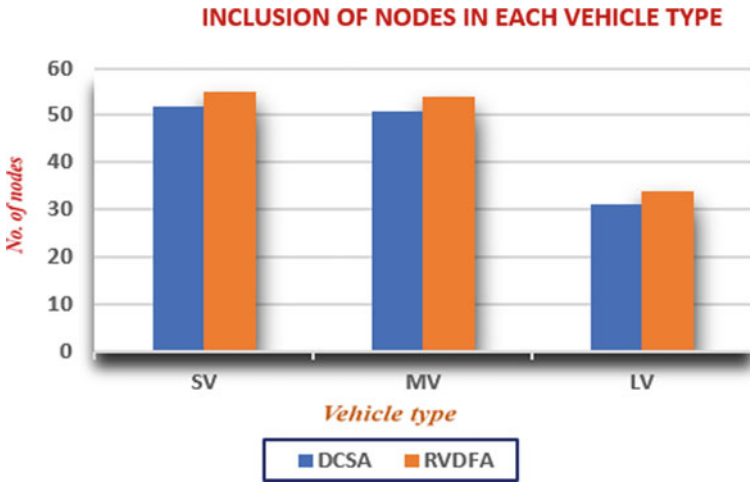
Fig. 3 Comparison of the number of patients included in both RVDFA and DCSA

Table 2 Computational results of DCSA and RVDFA for the model DSRPMFSS

Instances	DCSA				RVDFA			
	t_{ij}	Total cost	No. of nodes visited	Nodes not visited	t_{ij}	Total cost	No. of nodes visited	Nodes not visited
SV1	266	391.5	8	57, 78, 114	268	**368**	8	Nil
SV2	276	394	7		296	**396**	10	
SV3	290	397.5	10		277	**377**	10	
SV4	281	395.25	8		256	**356**	9	
SV5	308	412	9		278	**378**	8	
SV6	298	404	10		288	**388**	10	
MV1	285	792.5	10	91, 108, 92	284	**768**	10	Nil
MV2	287	793.5	9		234	**668**	8	
MV3	290	795	8		284	**768**	9	
MV4	258	779	7		272	**744**	9	
MV5	274	787	8		270	**740**	9	
MV6	287	808.5	9		281	**762**	9	
LV1	264	1173	7	112, 114	261	**1083**	8	Nil
LV2	267	1175.25	8		285	**1155**	9	
LV3	294	1195.5	10		281	**1143**	10	
LV4	274	1180.5	8		249	**1047**	7	

instance is bolded in Table 2. Furthermore, the following figures show the comparison between RVDFA and DCSA for costs associated with small, medium and large type of vehicles, including travel costs, fixed costs and penalties.

From Table 2, it exhibits that RVDFA is effective in all three instances of small, medium and large. Thus, our proposed algorithm is more cost efficient than DCSA.

5.1 Mixed-Fleet Synchronization Simultaneously

The synchronization of vehicles [23, 26] is carried out simultaneously in order to provide multiple services at the same node. Hence, after confirming the efficiency of RVDFA, we synchronized mixed fleets of vehicles simultaneously depending on the priority of patients' nodes and the feasibility criteria [23] at the respective time slots.

Table 3, it can be seen clearly that two different types of vechicles visited the synced node successfully at the same time, which are bolded. Thus, enhanced RVDFA serves as the best decision-making framework, which takes into account the requirements of HHC services that need to manage multiple schedules with existing and dynamic patients under the conditions of synchronization made possible by combining mixed fleets.

6 Conclusion

This paper seeks to develop a multi-objective optimization technique which matches practical scenarios such as simultaneous synchronization, route scheduling, balancing workloads and time window constraints. A major goal is to minimize both the total time taken and the cost of HHC services at the same time. Due to this model's uncertain nature, exact solvers cannot resolve this optimality in real-life situations involving large data scales. Therefore, the ideal model DSRPMFSS implements using an improved version of nature-inspired algorithm RVDFA. This algorithm showed the highest efficiency in all tests when compared to the powerful DCSA algorithm. RVDFA visits 11% more nodes than DCSA. Additionally, some sensitivity analyses were carried out in order to calculate the action of the operating time in different time slots and the total costs. On the basis of the experimental results, discussion and computational analysis of this research work, we conclude that the efficiency of how constraint penalties are weighted based on the HHC system's tolerance has greatly improved. Further research may focus on the following aspects: increasing the level of uncertainty and introducing long-term planning horizon in our model. Additionally, we can examine a wide range of hybrid metaheuristic algorithms to solve HHC problems by incorporating green emissions into our sustainability model.

Table 3 Simultaneous synchronized visits among mixed fleet of vehicles

SV1			MV1			LV2			SV4		
Nodes	Starting time	ts_{ij}	Nodes	Starting time	ts_{ij}	Nodes	Starting time	ts_{ij}	Nodes	Starting time	ts_{ij}
0	0	0	0	0	0	0	0	0	0	0	0
5	**0**	**26**	5	**0**	**26**	41	**0**	**27**	41	**0**	**27**
66	26	82	30	26	65	34	27	63	10	27	58
59	82	119	94	65	90	44	63	88	69	58	84
55	119	149	81	90	115	39	88	115	71	84	110
			102	115	140	36	115	140	74	110	136
Break	**150**	**165**	**Break**	**150**	**165**	**Break**	**150**	**165**	**Break**	**150**	**165**
9	**165**	**199**	9	**170**	**199**	42	**165**	**198**	42	**167**	**198**
77	199	226	17	199	229	38	198	231	53	198	226
16	226	254	95	229	257	43	231	257	49	226	259
112	**258**	**315**	84	257	289	112	**259**	**315**	73	259	287
–	–	–	98	289	314	–	–	–	–	–	–

MV3			LV3			SV5			MV5		
Nodes	Starting time	ts_{ij}	Nodes	Starting time	ts_{ij}	Nodes	Starting time	ts_{ij}	Nodes	Starting time	ts_{ij}
0	0	0	0	0	0	0	0	0	0	0	0
45	**0**	**33**	45	**0**	**33**	56	**0**	**33**	56	**0**	**36**
26	33	62	123	33	62	11	36	62	99	36	67
83	62	89	118	62	87	8	82	87	106	67	92
108	89	114	120	87	112	1	122	112	104	92	118
91	114	145	119	112	139				97	118	145

(continued)

Table 3 (continued)

MV3			LV3			SV5			MV5		
Nodes	Starting time	ts_{ij}	Nodes	Starting time	ts_{ij}	Nodes	Starting time	ts_{ij}	Nodes	Starting time	ts_{ij}
Break	**150**	**165**	**Break**	**150**	**165**	**Break**	**150**	**165**	**Break**	**150**	**165**
37	165	199	37	171	199	63	165	216	63	178	216
23	199	225	33	199	224	76	216	241	25	216	250
111	225	259	35	224	252	14	241	268	21	250	278
82	259	305	40	252	279	3	268	293	87	278	306
–	–	–	47	279	308	–	–	–	–	–	–

SV2			LV1			SV6			MV4		
Nodes	Starting time	ts_{ij}	Nodes	Starting time	ts_{ij}	Nodes	Starting time	ts_{ij}	Nodes	Starting time	ts_{ij}
0	0	0	0	0	0	0	**0**	0	0	**0**	0
2	**0**	37	2	0	37	90	0	**31**	90	0	**31**
13	37	67	122	37	71	15	31	64	29	31	73
70	67	93	46	71	99	62	64	89	18	73	100
58	93	123	124	99	138	60	89	114	20	100	129
51	123	149	–	–	–	65	114	140	–	–	–
Break	**150**	**165**	**Break**	**150**	**165**	**Break**	**150**	**165**	**Break**	**150**	**165**
4	**165**	**196**	**4**	**167**	**196**	**86**	**165**	**199**	**86**	**173**	**199**
68	196	221	113	196	233	7	199	230	92	199	229
57	221	253	117	233	262	79	230	259	19	229	256
75	253	283	125	262	296	78	259	285	22	256	288

(continued)

Table 3 (continued)

SV2			LV1			SV6			MV4		
Nodes	Starting time	ts_{ij}	Nodes	Starting time	ts_{ij}	Nodes	Starting time	ts_{ij}	Nodes	Starting time	ts_{ij}
67	283	312	–	–	312	12	285	312	31	288	314

SV3			MV2			LV4			MV6		
Nodes	Starting time	ts_{ij}	Nodes	Starting time	ts_{ij}	Nodes	Starting time	ts_{ij}	Nodes	Starting time	ts_{ij}
0	**0**	**0**	**0**	**0**	**0**	**0**	**0**	**0**	**0**	**0**	**0**
32	**0**	**25**	*32*	**0**	**25**	*107*	**0**	**39**	*107*	**0**	**39**
50	25	58	93	25	53	121	39	78	27	39	70
61	58	83	85	53	94	48	78	113	24	70	95
54	83	110	103	94	121	–	–	–	80	95	124
72	110	141	–	–	–	–	–	–	96	124	149
Break	**150**	**165**	**Break**	**150**	**165**	**Break**	**150**	**165**	**Break**	**150**	**165**
28	**165**	**199**	*28*	**173**	**199**	*110*	**178**	**206**	*110*	**165**	**206**
6	199	226	105	199	224	116	206	234	109	206	239
64	226	253	100	224	257	115	234	273	88	239	271
52	253	282	101	257	286	*114*	**273**	**314**	89	271	297
114	**284**	**315**	–	–	–	–	–	–	–	–	–

References

1. WHO (World Health Organization) (2011) Global health and ageing. WHO, US National Institute of Aging, pp 1–27
2. Andi HK (2021) Construction of business intelligence model for information technology sector with decision support system. J Inf Technol Digit World 3(4):259–268
3. Sungheetha DA (2021) COVID-19 risk minimization decision making strategy using data-driven model. J Inf Technol Digit World 3(1):57–66
4. Di Mascolo M, Espinouse M-L, el Hajri Z (2017) Planning in home health care structures: a literature review. IFAC-PapersOnLine 50:4654–4659
5. Sangeetha RV, Srinivasan AG (2020) A review of static, dynamic and stochastic vehicle routing problems in home healthcare. Eur J Mol Clin Med 7(3):5037–5046
6. Demirbilek M, Branke J, Strauss AK (2019) Dynamically accepting and scheduling patients for home healthcare. Health Care Manag Sci 22:140–155
7. Ouertani N, Nouaouri I, Ben-Romdhane H, Allaoui H, Krichen S (2020) A hypermutation genetic algorithm for the dynamic home health-care routing problem. In: IESM 2019 international conference on industrial engineering and systems management, 25–27 Sept, Shanghai, China
8. Xu H, Pu P, Duan F (2018) Dynamic vehicle routing problems with enhanced ant colony optimization. Discrete Dyn Nat Soc 2018:1–13
9. Sangeetha RV, Srinivasan AG (2020) Heterogeneous vehicle routing problem in home health-care enhanced by elitism of ACO using neighborhood structures. Int J Adv Sci Technol 29(9):2993–3008
10. Bredström D, Rönnqvist M (2008) Combined vehicle routing and scheduling with temporal precedence and synchronization constraints. Eur J Oper Res 191(1):19–31
11. En-nahli L, Afifi S, Allaoui et al (2016) Local search analysis for a vehicle routing problem with synchronization and time windows constraints in home health care services. IFAC-PapersOnLine 49(12):1210–1215
12. Euchi J, Zidi S, Laouamer L (2020) A hybrid approach to solve the vehicle routing problem with time windows and synchronized visits in-home health care. Arab J Sci Eng 45:10637–10652
13. Decerle J et al (2019) A hybrid memetic-ant colony optimization algorithm for the home health care problem with time window, synchronization and working time balancing. Swarm Evol Comput 46:171–183
14. Redjem R, Kharraja S, Xie X, Marcon E (2012) Routing and scheduling of caregivers in home health care with synchronized visits. In: 9th international conference on modeling, optimization & simulation, June 6–8, Bordeaux, France, pp 1–10
15. Nasir JA, Kuo Y-H (2020) A decision support framework for home health care transportation with simultaneous multi-vehicle routing and staff scheduling synchronization. Decis Support Syst 138:113361–113403
16. Saraei M, Analouei R, Mansouri P (2015) Solving of travelling salesman problem using firefly algorithm with greedy approach. Cumhuriyet Sci J 36(6):267–273
17. Wang M-b, Fu Q, Tong N, Li M, Zhao Y (2015) An improved firefly algorithm for traveling salesman problems. In: Proceedings of the 4th national conference on electrical, electronics and computer engineering, 12–13 Dec, Xi'an, China, pp 1085–1092
18. Asma M, Altabeeb AM, Mohsen AG (2019) An improved hybrid firefly algorithm for capacitated vehicle routing problem. Appl Soft Comput 84:105728–105737
19. Jati GK, Suyanto (2011) Evolutionary discrete firefly algorithm for travelling salesman problem. Lect Notes Comput Sci 6943:393–403
20. Dekhici L, Redjem R, Belkadi K, Mhamedi AE (2019) Discretization of the firefly algorithm for home care. Can J Electr Comput Eng 42(1):20–26
21. Zhou L, Ding L, Qiang X (2014) A multi-population discrete firefly algorithm to solve TSP. In: 9th international conference, BIC-TA 2014, 16–19 Oct, Wuhan, China, vol 472, pp 648–653
22. Ouaarab A, Ahiod B, Yang XS (2014) Discrete cuckoo search algorithm for the travelling salesman problem. Neural Comput Appl 24:1659–1669

23. Sangeetha RV, Srinivasan AG (2021) Mutated cuckoo search algorithm for dynamic vehicle routing problem and synchronization occurs within the time slots in home healthcare. Int J Syst Assur Eng Manag. https://doi.org/10.1007/s13198-021-01300-x
24. Gong I, Lee K, Kim J, Min Y, Shin K (2020) Optimizing vehicle routing for simultaneous delivery and pick-up considering reusable transporting containers: case of convenience stores. Appl Sci 10(12):4162
25. Matthopoulos P-P, Sofianopoulou S (2019) A firefly algorithm for the heterogeneous fixed fleet vehicle routing problem. Int J Ind Syst Eng 33(2):204–224
26. Osaba E, Yang XS, Diaz F et al (2017) A discrete firefly algorithm to solve a rich vehicle routing problem modelling a newspaper distribution system with recycling policy. Soft Comput 21:5295–5308

Accuracy Comparison of Neural Models for Spelling Correction in Handwriting OCR Data

Shivalila Hangaragi, Peeta Basa Pati ⓘ, and N. Neelima

Abstract In the present scenario, Handwriting Recognition (HWR) plays a very important role as due to current pandemic situations most of the exams are conducted in online mode. In HWR the device translates the user's handwritten characters or words into readable by a computer system. The problem with HWR is there are different types of handwriting and different styles of writing each character which makes it difficult to analyze each letter uniquely and correctly also the major problem with HWR is when people write there is no specific font and font sizes are taken care which also plays important role in recognizing the letters. The paper presents an accuracy comparison system of spelling correction in Handwritten OCR data using four neural models BERT, SC-LSTM, CHAR-CNN-LSTM, CHAR-LSTM-LSTM. In task, sequence matcher algorithm is used for computation of similarity score between input text data and outputs of the different neural models at each iteration. It is observed that the BERT model gives the highest accuracy of 71.4% followed by SC-LSTM with 69.12%, CHAR-CNN-LSTM with 67.80% and CHAR-LSTM-LSTM with 69.34%.

Keywords Text enhancement · Handwritten recognition inaccuracies · Optical character recognition errors · Long short-term memory · Bidirectional encoder representations from transformers

S. Hangaragi (✉) · N. Neelima
Department of Electronics and Communication Engineering, Amrita School of Engineering, Amrita Vishwa Vidyapeetham, Bengaluru, India
e-mail: bl.en.r4ece21008@bl.students.amrita.edu

N. Neelima
e-mail: n_neelima@blr.amrita.edu

P. B. Pati
Department of Computer Science and Engineering, Amrita School of Engineering, Amrita Vishwa Vidyapeetham, Bengaluru, India

1 Introduction

The handwriting recognition (HWR) system transcribes the handwritten content present in image documents into computer-readable text. The major task of the HWR system is to identify each character correctly. This is a difficult task as people write with wide variations in styles and sizes. Furthermore, the handwritten content may be categorized into constrained and unconstrained writing. In constrained writing, the writer is needed to write in prespecified boxes or each character in isolation. Cursive writing, unconstrained writing, has no such limitations. In this form of writing, the characters are connected to each other. This, in addition to the writer-specific variations, poses quite a big challenge for HWR systems. These HWR systems are alternately called Intelligent Character Recognition (ICR) engines.

The myriad complexities associated with HWR technology lead to the misrecognition of content present in input images. This leads to the generation of text with anomalies. For all downstream consumption of such contents, expect the text to be accurate, at least to the best extent possible. To enhance the accuracy of the HWR systems, researchers, as well as system builders, employ sophisticated image enhancement and recognition techniques. However, due to the limitations of the systems involved, the generated text invariably contains errors.

Besides HWR, text documents may be created by other means such as typing in the content, OCR on typewritten text, speech recognition. Depending on the mechanism of creation of the text document, the anomalies present may differ. Text documents may be created by typing in the content or through recognition technologies dealing with typewritten or handwritten documents. For example, when a document is created by typing the content, the inaccuracies present are due to (i) hitting the wrong keys on the keyboard, (ii) malfunction of the keyboard where some keys are not working leading to missing a few characters, (iii) domain knowledge of the typist (Ex: 'heat' typed as 'hit' or 'psychology' typed as 'sychology'), etc. An unskilled person while typing content may induce grammatical errors as well.

On the other hand, errors induced due to HWR are different from the ones induced by typing errors. Here the errors occur due to the following reasons: (i) structural similarity between characters leading to misrecognition, (ii) characters being joined during binarization leading to recognition as a single entity rather than multiple (Ex: 'c' and 'l' get combined as one character in the image and gets recognized as 'd'), (iii) character images are broken leading to recognition as multiple entities (Ex: 'm' gets recognized as 'r' and 'n'), and (iv) noise in the document leads to misrecognition as textual components. Moreover, most software suggest corrections while typing as well as spell correction packages may be used by typists for improving accuracy. Such features are unavailable to a system performing HWR. This leads us to believe that the number of errors present, in general, in HWR performed documents is higher than the typing errors created by typists.

Many recent research works have explored using various deep learning techniques to detect and correct the anomalies present in text documents. Most of these

works deal with inaccuracies due to typing, and very few works deal with handling inaccuracies due to limitations of recognition technologies.

While there are dissimilarities in the types of errors induced, the underlying principles for their detection and mechanisms to suggest corrections are fairly similar. Thus, it's pertinent to assume that the techniques developed for enhancing textual quality with typing anomalies may apply equally well to text documents produced by HWR from a document image. However, we found no such study that evaluates the performance of these algorithms on HWR-generated documents. We, therefore, undertake the exercise to conduct this experiment and study the performance of four existing algorithms on handling errors present in text generated from handwritten document images with the usage of an existing HWR engine. The four text modeling algorithms are: (i) BERT, (ii) SC-LSTM, (iii) CHAR-CNN-LSTM and (iv) CHAR-LSTM-LSTM.

2 Related Work

Many researchers have developed technologies for HWR. Some of the significant research contributions are reported subsequently. Pati et al. [1] conducted a survey on developments in OCRs in Indian scripts. They reported that in Indian scripts a consonant unites with another vowel or consonant to generate a distinct symbol. Analysis of various methodologies employed in pattern recognition systems is discussed.

Duth and Amulya [2] proposed text recognition using OCR and KNN algorithm and classifier. The proposed model is implemented to recognize both typewritten and Handwritten Italic text, for different styles namely Tahoma, San-Serif, Calibri and Comic Sans. The methodology was built to recognize the text, both in capital letters and small letters for the above-mentioned styles. The accuracy achieved for text recognition of styles mentioned above is 95.60%.

Rani et al. [3] proposed the recognition of degraded character images from ancient Kannada typewritten and handwritten documents. AlexNet, one of the variants of CNN is used for character image classification. They have achieved recognition accuracy of 91.3% for printed characters and 92% for handwritten text.

Anand et al. [4] proposed character recognition using CNN with LeNET architecture. Experiments were conducted on scanned passport documents and 93.4% accuracy on training is achieved while the test dataset yields an accuracy of 86.5%.

Graves et al. [5] proposed a neural network for recognizing handwritten text. Recurrent neural networks are used for sequence labeling tasks. The accuracy achieved for word recognition is 79.7% for online data and 74.1% for offline data.

Ghanim et al. [6] proposed a multistage cascading system to recognize Arabic Handwriting. Hierarchical Agglomerative Clustering (HAC) is applied to splitting the database into interrelated clusters. Cluster members are ranked using the Pyramid Histogram of Oriented Gradients (PHOG), and Kullback–Leibler (KL) methods. Divergence classification is applied for matching classes of high rank. The analogy

is done on six different deep convolutional neural networks (DCNN's) on the final recognition rates. Experiments are conducted on IFN/ENIT Arabic database.

Hamdan et al. [7] proposed a scalable technique of identifying and recognizing handwritten characters. The technique is implemented using adversarial learning to enable learning from several variations from limited resource scripts. The proposed adversarial augmentation scheme provides better performance in identifying and recognizing handwritten characters compared to different baselines.

Devlin et al. [8] proposed Bidirectional Encoder Representations from Transformers (BERT) a pre-trained model. BERT is used to pre-train deep bidirectional representations using unlabeled text by constraining both right & left content in all layers. The model is able to attain results on eleven natural language processing (NLP) tasks. The model also increases the General Language Understanding Evaluation (GLUE) benchmark score to 80.5% (absolute improvement is 7.7%) and The Multi-Genre Natural Language Inference (MultiNLI) corpus accuracy to 86.7% (absolute improvement is 4.6%).

Lu et al. [9] proposed new Long Short-Term Memory (LSTM) cell called Shared-cell LSTM (SC-LSTM). Experiments were conducted on three sequence labeling benchmarks to demonstrate the effectiveness of the SC-LSTM cell. The three benchmarks are part-of-speech (POS) tagging, named-entity recognition (NER) and text chunking.

Sooraj et al. [10] proposed a spelling correction model for Malayalam Language using deep learning algorithms. Spelling correction involves two steps namely: Detection of error and correcting the error. Detection of error is accomplished using LSTM neural network. The network is trained to identify the misspelled words with the position. F1-score is used to calculate the accuracy of error detection. The error correction of the misspelled word is done by choosing the most appropriate word from the candidate word suggestion.

Jayanthi et al. [11] have developed an open-source package, namely, NeuSpell, for spelling correction. It implements a wide range of models including BERT, SC-LSTM, CHAR-CNN-LSTM and CHAR-LSTM-LSTM. Using the NeuSpell system, they have reported an accuracy improvement of 9% on synthetic examples and 3% on richer contextual representations.

Sreevidhya and Narayanan [12] proposed effective and simple methods to assess one-word answers. Students' answers and the model answers are matched using word embedding algorithms for assessment. The marks are evaluated based on the similarity score. The method-wise analysis is conducted to compute the accuracy of the scores obtained.

Raghavendra Babu et al. [13] proposed the hybrid methodology to differentiate the positive and negative aspects of restaurant reviews using sentimental analysis. Machine learning algorithms are used to make wiser predictions and decisions. The reviews are classified as negative and positive, and the score of each sentiment is also reported. The classification accuracy for the proposed approach is 84.76%.

We select four existing and well-performing algorithms available in NeuSpell for text error correction. These algorithms are selected based on the accuracy improvement report by Jayanthi et al. and multiple other researchers. They have additionally

been tested in multiple languages. While these techniques have been evaluated independently on various data sets, we have not come across a single instance where their usage has been evaluated for error corrections to the recognized output text from a handwritten document image.

3 Data Description

Our dataset consists of handwriting-recognized text documents from input images obtained from the IAM dataset [14]. The IAM database is based on the Lancaster-Oslo/Bergen (LOB) corpus. This corpus is a collection of handwritten texts that were used to generate forms, which eventually were written by people with their handwriting. Figure 1 shows a sample document image, from this dataset, used for our work. The database includes 556 forms produced by approximately 250 different writers. The documents present in the dataset are categorized based on their domain and coded as categories A–N. For our experiments, we have picked 529 form images of A–D categories from this corpus.

Each input image consists of 4 segments separated by horizontal straight lines as shown in Fig. 1. The 2nd segment in the document contains typed text which is handwritten by the writer in the 3rd segment. We have segmented the document and have taken these 2nd and 3rd segments for our work. These segments obtained from
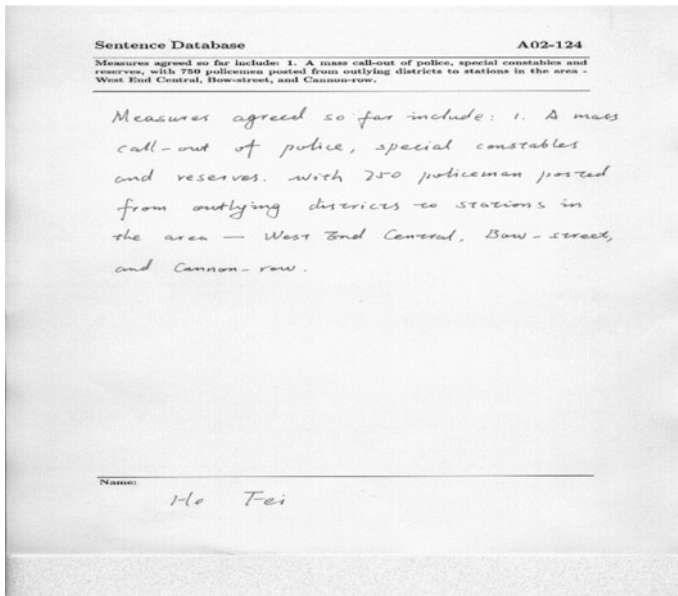
Fig. 1 Sample input form image containing handwritten text. The segmented portions of this image are run through the Google OCR engine to generate input text data and target text

Input text	Target text
A mass Measures agreed so for include call-out of police , special constables and reserves , with 250 policeman posted districes to from outlying the West and Central Bow - street , , stations in area and Cannon_row.	Measures agreed so far include 1 A mass call-out of police, special constables and reserves, with 750 policemen posted from outlying districts to stations in the area -West End Central, Bow-street, and Cannon-row.

Fig. 2 A sample input text data (left) with its corresponding target text data is present on the right. These texts were obtained from the sample image shown in Fig. 1

the input images are run through the OCR engine from Google Cloud Vision APIs, hereafter referred to as Google OCR, and their textual equivalents are obtained for our experiments.

In this paper, the text output generated by the Google OCR engine for segment 3 of the image (handwritten text) in Fig. 1, is referred to as input text data. The left side box of Fig. 2 shows this input text data for the sample image available in Fig. 1. Similarly, the text obtained for the typed segment (segment 2) of the form is called target text (refer to the right block of Fig. 2). The input text data contains misspelled words, grammatical errors, and the presence of some special characters due to misrecognition. The typed text output data (target data) consist of text with correct spelling and grammatically correct words.

4   System Description

The system used in the experiment consists of four pre-trained neural models, namely, BERT, SC-LSTM, CHAR-CNN-LSTM and CHAR-LSTM-LSTM. For the input text data, four different neural model outputs are produced which are used for accuracy comparison. The accuracy comparison is accomplished using the sequence matcher algorithm (similarity algorithm) [15]. The difflib similarity function calculates the similarity score of two text elements T1 and T2 using Eq. (1). The function compares the two text strings

$$\text{Sim(T1, T2)} = 2 * \frac{M}{T} \tag{1}$$

$$\text{Accuracy } (A) = \text{Sim(T1, T2)} * 100 \tag{2}$$

where M = number of characters matching with respect to the position in both the strings and T = maximum length of the strings to be compared.
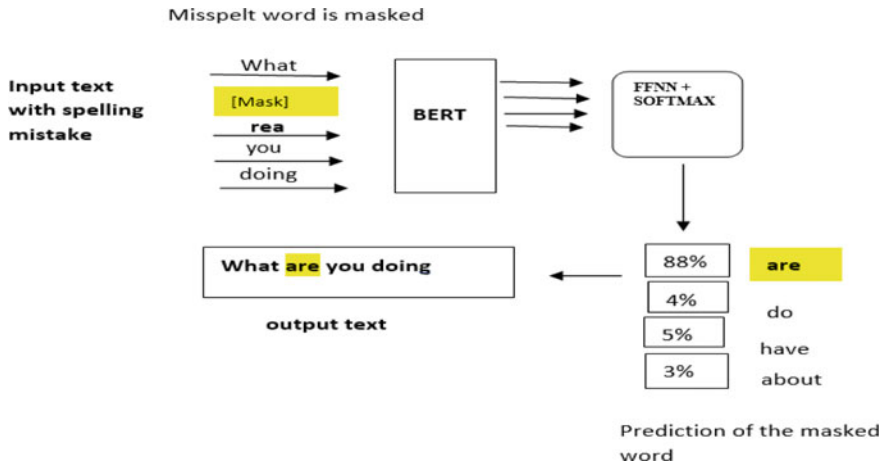
Fig. 3 Working of BERT model with example

4.1 BERT

BERT model is able to predict the correct word with the position for the misspelled word in a sentence based on the context. The text dataset from Wikipedia (2.5B words) is used to train the BERT model. The misspelled word is masked for correct word prediction and this mechanism is known as masked word prediction. BERT takes only one masked token (word) from a sentence as input at a time and predicts a list of candidate words along with the prediction probabilities. As shown in Fig. 3.

The masked misspelled word is replaced by the word with the highest probability. As shown in the above example masked misspelled word is replaced by 'are' having the highest probability of 88%.

The steps involved in predicting the correct word for a masked word are (i) classification layer is added above the encoder output (ii) output vectors are multiplied with an embedding matrix to transform them into vocabulary dimension and (iii) the probability of each word is computed in the vocabulary with SoftMax. Architecture of the BERT model is shown in Fig. 4.

4.2 SC-LSTM

SC-LSTM uses semi-character representations fed through a bi-LSTM network to correct misspelled words. The semi-character representations combine one-hot embeddings for the first, last and bag of internal characters.
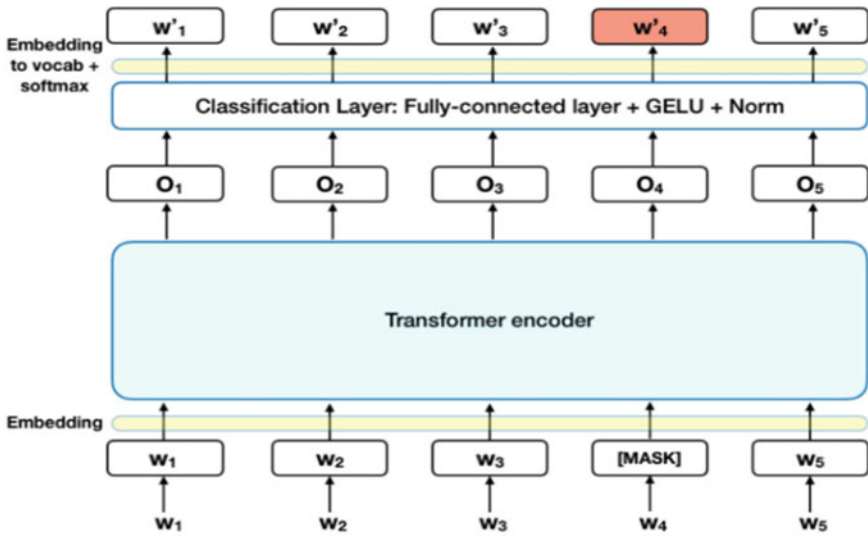
Fig. 4 Architecture of the BERT model [16]

4.3 CHAR-CNN-LSTM

CHAR-CNN-LSTM model as in Fig. 5 uses a convolutional neural network to develop word-level representations from individual characters. CNN LSTMs are used in various applications such as visual time series prediction problems and generating textual descriptions from videos. Specifically, the problems of Activity recognition, Image description and video description.

CHAR-CNN is used to leverage the subword information, the output of this is given as input to the LSTM model. An affine transformation followed by softmax is applied over hidden states of LSTM to predict the next word.
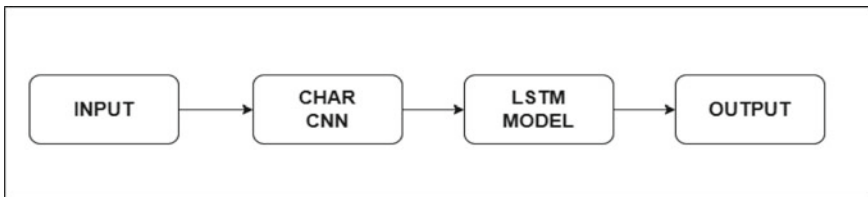
Fig. 5 The image depicting the workflow of CNN-LSTM architecture

4.4 CHAR-LSTM-LSTM

CHAR-LSTM-LSTM model passes individual characters to a bi-LSTM to develop word representations. To predict the correction these representations are further fed to another bi-LSTM trained.

5 Results and Discussion

The outputs of the respective models used in the system for the sample input text data are given in Fig. 2 and are presented in Table 1.

The accuracy measure, formulated in Eq. (2), is tabulated in Table 2 for the sample data shown in Fig. 2.

Similarly, accuracy calculations are computed for all the 529 input text data. The mean is calculated for computed accuracies, for accuracy comparison.

Table 1 Output generated, for the sample input text data shown in Fig. 2, from the four different studied models

Models	Output
BERT	"A mass measures agreed so far include call out of police, special constables and reserves, with 250 policemen posted districts to from outlying the West and Central Bow streets,, stations in area and Cannon_row"
SC-LSTM	"A mass measures agreed so for include calls out of police, special constables and reserves, with 250 policemen posted districts to form outlying the West and Central Bow street, stations in area and Cannon row"
CHAR-CNN-LSTM	"A mass measures agreed so for include call out of police, special constables and reserves, with 250 policemen posted districts to from outlying the West and Central Bow street.. stations in area and Cannon row"
CHAR-LSTM-LSTM	"A mass measures agreed so far include call out of police, special constables and reserves, with 250 policemen posted districts to from outlying the West and Central Bow street, stations in area and Cannon_row"

Table 2 Accuracy measure for the example data in Fig. 2

	INPUT TEXT	BERT	SC-LSTM	CHAR-CNN-LSTM	CHAR-LSTM-LSTM
M	110	155	128	144	141
T	431	431	427	427	426
Accuracy (A, %)	51	71.9	59.9	67.4	66

Table 3 Accuracy comparison of the models used in the experiment with improvement in accuracy and CER

Models	Average accuracy (%)	% increase in accuracy	CER%
INPUT	62.2		11.50
BERT	71.4	9.2	11.06
SC-LSTM	69.1	6.9	11.74
CHAR-CNN-LSTM	67.8	5.6	11.34
CHAR-LSTM-LSTM	69.3	7.1	11.42

5.1 *Character Error Rate (CER)*

CER is one of the metrics to evaluate the count of errors present in a text string. CER is based on the concept of Levenshtein distance. It gives the count of the minimum number of character level operations (Substitution, Insertion and Deletion) required to transform the reference text into input text. The character accuracy (CA) [17] and Character error rate (CER) [17] are given in Eqs. (3) and (4).

$$\text{Character Accuracy (CA)} = \frac{a}{n} \times 100 \tag{3}$$

$$\text{Character error rate (CER)} = 100 - \text{CA} \tag{4}$$

where $a =$ Total number of characters in the reference text document and n is the total number of characters in the input text string.

$$\text{Average Accuracy \%} = \frac{T_{\text{total}} * 100}{\text{Number of Input Text lines used in the experiment}} \tag{5}$$

T_{total} is the average sum matching between the input text and target text for 529 samples and %Increase in Accuracy is a percentage increase in the accuracy of the Input Text by implementing four different studied models.

In the experimented conducted BERT achieves the highest accuracy of 71.4% with lowest character error rate of 11.06%. The improvement in accuracy attained by using BERT is 9.2%. Similarly, CER values for all the models used in experiment, average accuracy and improvement in accuracy is depicted in Table 3.

6 Conclusion

The Accuracy comparison between different neural models was conducted on Handwritten OCR text data. The images were obtained from the IAM dataset for experiments conducted. The sequence matcher algorithm is used for the computation of the

similarity score between the two strings. The average of accuracies, obtained from the models is calculated for comparison as shown in Table 3. It is observed that BERT gives the highest accuracy of 71.4% with lowest CER of 11.06% and the SC-LSTM attains 69.12% accuracy with 11.74% CER, CHAR-CNN-LSTM attains 67.8% accuracy with 11.34% CER value and CHAR-LSTM-LSTM accuracy of 69.34% with character error rate of 11.42%.

References

1. Pati PB, Ramakrishnan AG (2005) OCR in Indian scripts: a survey. IETE Tech 23(3):217–227
2. Duth S, Amulya B (2020) Recognition of hand written and printed text of cursive writing utilizing optical character recognition. In: 2020 4th international conference on intelligent computing and control systems (ICICCS), pp 576–581
3. Shobha Rani N, Chandan N, Sajan Jain A, Kiran HR (2018) Deformed character recognition using convolutional neural networks. Int J Eng Technol 7(3):1599–1604
4. Anand R, Shanthi T, Sabeenian RS, Veni S (2020) Real time noisy dataset implementation of optical character identification using CNN. Int J Intell Enterpr 7(1/2/3):67–80
5. Graves A, Liwicki M, Fernández S, Bertolami R, Bunke H, Schmidhuber J (2008) A novel connectionist system for unconstrained handwriting recognition. IEEE Trans PAMI 31(5):855–868
6. Ghanim TM, Khalil MI, Abbas HM (2020) Comparative study on deep convolution neural networks DCNN-based offline Arabic handwriting recognition. IEEE Access 8:95465–95482
7. Hamdan YB, Sathesh A (2021) Deep learning-based handwriting recognition with adversarial feature deformation and regularization. J Innov Image Process 3(4):367–376
8. Devlin J, Chang M-W, Lee K, Toutanova K (2018) Bert: pretraining of deep bidirectional transformers for language understanding. abs/1810.04805
9. Lu P, Bai T, Langlais P (2019) SC-LSTM: learning task-specific representations in multi-task learning for sequence labelling. NAACL-HLT 2019, vol 1, pp 2396–2406
10. Sooraj S, Manjusha K, Anand Kumar M, Soman KP (2018) Deep learning-based spell checker for Malayalam language. J Intell Fuzzy Syst 34(3):1427–1434
11. Jayanthi SM, Pruthi D, Neubig G (2020) Neuspell: a neural spelling correction toolkit. In: Proceedings of the 2020 conference on empirical methods in natural language processing: system demonstrations, EMNLP 2020, pp 158–164
12. Sreevidhya V, Narayanan J (2021) Short descriptive answer evaluation using word-embedding techniques. In: 2021 12th international conference on computing communication and networking technologies (ICCCNT), pp 1–4
13. Raghavendra Babu P, Sreenivas S, Vinay Varma US, Neelima N (2021) A hybrid approach to review mining-restaurant data in depth analysis. Innovative data communication technologies and application, vol 59. Springer, Singapore, pp 831–841
14. Marti U, Bunke H (2002) The IAM-database: an English sentence database for off-line handwriting recognition. Int J Doc Anal Recognit 5:39–46
15. Makmum A, Thamrin H (1977) Performance of similarity algorithms for statement mapping in a SWAT analysis application. AIP Conf Proc 1:2018
16. Khattak FK, Jeblee S, Pou-Prom C, Abdalla M, Meaney C, Rudzicz F (2019) A survey of word embeddings for clinical text. J Biomed Inform 4:1–18
17. Vijayarani S, Sakila A (2015) Performance comparison of OCR tools. Int J UbiComp (IJU) 6(3):19–30

An Insight into EDGE-Based Solutions for Augmented Reality

Pankaj Joshi, Sanskar Jain, and Simran Vanjani

Abstract The term "augmented reality" refers to a technology that combines digital and actual experiences. It is an immersive experience of a physical environment in which actual objects are enhanced with digital visual features, sound, or other sensory stimuli. The rapid advancement of augmented reality has piqued people's interest in recent years. It is a rapidly developing area among businesses that deal with mobile computing and commercial apps. Using AR, digital information can be placed in reality to improve a human's perspective of reality. This paper begins by defining augmented reality, its history, and its challenges. The paper then discusses some essential technology, development tools, and augmented reality applications in several industries. The main focus point of the paper is centered around the discussion on EDGE Technology as a solution to the limitations of AR. We have drawn a comparison between some frameworks that have been developed over time, merging AR with EDGE. Finally, it anticipates future advancements in augmented reality technologies, such as the Mobile AR.

Keywords Augmented reality · Virtual reality · EDGE devices · Head mount display · Mobile augmented reality

P. Joshi (✉) · S. Jain · S. Vanjani
Department of Electronics Engineering, Shri Ramdeobaba College of Engineering and Management, Nagpur, Maharashtra, India
e-mail: joshipu@rknec.edu

S. Jain
e-mail: jainsr_1@rknec.edu

S. Vanjani
e-mail: vanjanisd@rknec.edu

241

1   Introduction

Augmented reality (AR) is a cutting-edge technology which enhances users' perceptions of engagement with real-world environments by including digital things, and it is the most organic way to connect with your virtual environment.

Augmented reality is a structure that:

1.   integrates actual and digital objects in an actual world;
2.   aligns actual and digital objects with one another;
3.   runs dynamically, in 3D, and on a real-time basis.

There are three parts of this definition worth mentioning.

For starters, AR is not limited to specific display technology like a head-mounted display (HMD). AR can and may extend to all aspects, including sound, contact, and odor, and the term is not restricted to the sense of vision. Finally, AR includes the removal of real items in favor of virtual ones [1].

In this paper, we discuss some potential worldwide applications of augmented reality in education where computer-generated visuals in classrooms help students; tourism where enhanced augmented guides improve a tourist's experience; e-commerce. We also discuss domestic applications of AR which include agriculture where farmers can get a 3D overview of their field which will help them make the best decisions for themselves: Smart City Planning and E-Commerce.

We then address the fact that AR devices lack the processing power needed to provide users with authentic AR experiences and address the limitations of AR. These limitations can now be overcome with the help of EDGE devices.

Edge computing refers to a set of virtualized computing solutions that provide processing, memory storage, and web server resources at the network's edge. Edge servers are machines that give services to end devices. Edge computing tackles the essential issues of AI-based systems, and edge computing and AI combined offer a potential solution. Edge intelligence, also known as mobile intelligence, is the name given to this new intelligence paradigm [2]. The paper concludes with a discussion on the EDGE solutions and the scope of AR.

1.1   Overview of Augmented Reality

Augmented reality (AR) is a form of technology that mixes virtual and actual information. It involves real-time tracking and 3D modeling, sensing, intelligent interactions, and other multimedia. Its aim is to apply machine-generated virtual data to the real world following simulation, such as information, pictures, 3D models, audio, and video. In this way, the two information sources complement one another, resulting in a better real-world experience. The most popular way for AR to be implemented is through the use of a guiding anchor in the real universe. The most common sort of anchor is a unique pattern picture, and attaching virtual items to pattern photos

makes it easy to position and connect virtual things to physical objects. A display of some form is used to allow the user to interact with the augmented reality systems.

AR development tools: In 2017, Apple announced ARKit, an AR programming tool. Engineers could use this set of techniques to make AR apps for devices with iOS like iPads and iPhones. ARKit helps engineers make AR apps that let two devices interact with the same virtual items, increasing the AR experience. Google also proposed a software foundation for creating AR applications named ARCore, which was similar to the one Apple proposed. It took the help of cloud-based software to portray physical images. The most widely used Software Development Kit is Vuforia, which is the most popular at the moment. Another one is the Wikitude SDK which can reconstruct its ideas utilizing an image recognition and tracking development framework as well as geolocation technologies [3].

AR Devices: Three types of devices are utilized in augmented reality: (i) head-worn devices also known as helmet-mounted display (HMD) devices, (ii) handheld devices that have portable displays, and (iii) spatial devices. These three devices use different methods to display information. Figure 1 shows an overview of these devices and the different displays they use [4].

The different types of displays work in the following way:

1. Video: The user experiences a complete digital view and the real and digital worlds are merged.
2. Optical: Digital objects are placed right above the real ones.
3. Retinal: Digital objects are portrayed right onto the retina with the help of a laser of low power.
4. Hologram: A photometric mixture of light patterns is used to display the digital objects.
5. Projector: A digital projector is used to portray digital objects directly.
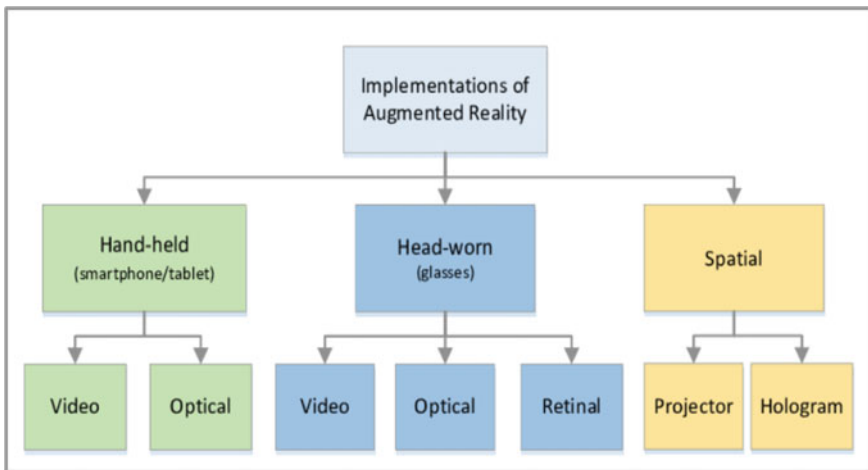
Fig. 1 Various AR devices and their displays (*Source* IEEE Access 2017, p. 3)

Each device and its display type has its benefits and drawbacks according to the needs of the applications. One such device is a head-mounted display device (HMD), it can be worn on your head or can be adjusted in your helmet, and it portrays both digital and real images to the user. HMDs have video-see-through devices inbuilt into them; this has two camera hatches to help see the augmented reality more organically. This AR is generated through a computer chip which enhances the outcome. Figure 2 shows a basic head-mounted display device that can be used for entertainment and educational purposes [5]. Image-guided surgery is shown in Fig. 3.

Smartphones with Android or iOS compatibility are now more commonly used than handheld screens, these phones can also serve as an AR display. The most powerful ones are personal computers or tablets; however, they are too expensive or too big to be used by just one hand. However, with the introduction of iPads, tablets are now a usable platform for augmented reality.

Fig. 2 Head-mounted display device (HMD) (*Source* IJITEE 2019, p.1331)
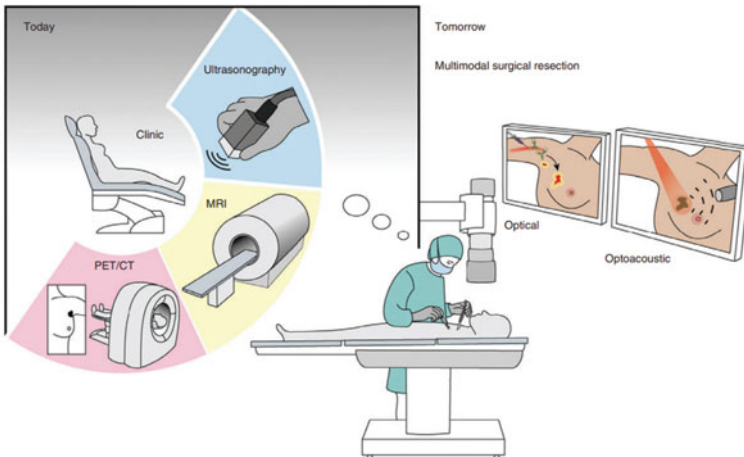
Fig. 3 Image-guided surgery (*Source* British Journal of Surgery, 2015 p58)

Visual data is displayed directly on actual objects in spatial augmented reality (SAR) without the user needing to wear or handle the device. The majority of technology is isolated from the user by spatial displays that integrate it into the environment. Such a technology can be used in image-guided surgeries where the doctors can use AR to better plan and operate on a patient [6].

Metrics used to measure performances of AR devices are:

1. Camera Position Tracking: A video-based AR system essentially has two cameras: a real one, which generates video of the real environment, and a virtual one, which generates the 3D graphics to be merged with the live video stream. Both cameras must have the same internal and external parameters in order for the real and virtual objects to be properly aligned. To achieve this, an initial calibration of the real camera and a dynamic update of its external parameters are required. There are two crucial problems of AR applications with respect to camera tracking: (1) the accurate alignment of real and virtual coordinate frames for overlay, and (2) capturing the 3D motion for each video frame of a camera including camera position. The latter is very important for interactive AR applications, where users can manipulate virtual objects in an augmented real 3D environment. This issue has never been successfully addressed using only video input measurements. The system used by Dieter Koller et al. successfully tracks in real time at approximately 10 Hz; it showed that robustness can be achieved by using a Kalman filter along with landmark detection and tracking which is model-driven instead of using a complete data-driven motion estimation. Camera parameters are evaluated using an automated camera calibration procedure using landmark detection. These parameters are of two types: intrinsic and extrinsic. Extrinsic parameters can be manipulated and built in a 3D environment which will assist in collision detection taking room boundary into consideration. If the virtual objects would be floating in front of real ones, it would result in disorientation for the user. Intrinsic parameters are taken to be independent in terms of position and orientation. These parameters are associated with the internal geometry of the camera, like focal length, pixel size, and resolution [7].

2. Latency: In augmented reality (AR) systems, registration (or alignment) of the artificial picture with the real world is essential. It is necessary to register the user's perspective of the environment both temporally and spatially with the input from user-input devices, surveillance devices, and imaging equipment. Each device experiences a delay between when it observes the world and when a change in the data first appears to have an impact on the AR display it is showing the user. The variations in latency are referred to as relative latencies. Relative delay contributes to misregistration and needs to be minimized. In a functioning AR system, we provide general techniques for managing multiple data streams with various latency values.

3. QoA: QoA or quality of augmentation consists of two major components:

    (1) Virtual Object Pose Accuracy: The virtual object's deviation from the ideal position or orientation is quantified by the pose accuracy. The actual pose is provided by initiating the handset.

(2) Virtual Object Pose Jitter and Drift: The motion of the virtual object between succeeding frames is measured by pose jitter. The pose drift estimates how much position and orientation error has accumulated with time. Low jitter and drift indicate that over time, regardless of user movement, the virtual item maintains its position with regard to the physical world.

2   A Brief History of AR

Augmented reality (AR) was first discussed in 1950s by Morton Heilg, who he film as something that will immerse the audience in the theater's screen by utilizing all of their sensations. Owing to this thought, Morton built "The Sehensorama," a pre-digital computer model in 1962, which was described by him as "The Cinema of the Future," in 1955.

The first head-mounted display was designed in 1966, and in 1968, the first AR-based system was developed; both of these designs were proposed by Ivan Sutherland. He used a head-mounted display in his designs.

A virtual environment was developed in 1975 referred to as "The Video Place"; it offered the population to interact with digital items for the very first time. This was proposed by Myron Krueger [8].

Bruce Thomas debuted ARQuake, the very first outdoor mobile-based AR game, at the International Symposium on Wearable Computers in 2000. AR technologies will become more generally available in the next four to five years, according to the Horizon Report, and camera systems that can evaluate physical situations in real-time and link locations between things and surroundings were introduced the same year, validating that prediction. This style of camera system has served as the foundation for combining virtual objects with reality in AR systems. In the years thereafter, several AR apps have been developed, primarily for mobile devices (such as Wikitude AR Travel Guide, which was released in 2008), but also for medical applications (in 2007).

With the help of recent technological advancements, an increasing number of AR systems and applications are being developed, in all possible sectors.

3   Components of AR

Augmented reality is an amalgamation of output and input components.

Output Components: These are responsible for the presentation of the virtual world and how it is perceived by the user; these components are responsible to provide the best experience possible to the user. Output components can be categorized on how they are perceived by the user; hence, they can be divided on the basis of the five human senses.

(1) Vision: Most of the information which our brain processes is owed to our vision. So an AR system must be successful in capturing the visuals by perfectly combining real and virtual environment. This can be achieved using head-mounted display (HMD). HMDs have video-see-through devices inbuilt into them; this has two camera hatches to help see the augmented reality more organically.

(2) Touch: The human touch is an extremely important perception channel; the tactile and kinesthetic senses of the human haptic system show that the ability of touch increases the sense of presence. The PHANTOM, manufactured by Sensable Technologies, looks like a robotic arm (copy figure) helps in giving the users a very real-like sense of actually interacting and touching the virtual objects.

(3) Sound: It is one of the most important senses to offer user a real-life experience. The basic steps required for successful simulation of virtual sounds are: sound generation, spatial propagation, and mapping of parameters. It is evident that combination of sound and graphic enhances the sense of presence.

(4) Smell and touch also play a crucial role in increasing the user experience and some flow delivery systems have been put into use for the same. A few examples of which are "taste interfaces" and "food simulators."

Input Components: Input components are in charge of engagement and determine how a user interacts with virtual objects. Ideally, all of these devices should come together to make user environment control as simple and natural as possible. Some of these components are:

(1) Live Input: Video Camera

   It is used to obtain continuous visual images which are further collaborated with virtual images to produce the augmented view as an end result. The resolution of the video image and the speed of transmission to the video compositor engine, so that they can be augmented and displayed to the user in real time, are two important factors to think of when selecting the camera. Along with this, camera model and calibration should also be taken into consideration.

(2) Trackers: These are devices which are used to keep track of the user's head (or wherever the camera is fixed) in order to correctly detect and calculate the position and orientation of the real-world scenario. They also track other body parts to enhance user experience. Trackers help in improving Update Rate, Latency, Accuracy, and Range. Some sensor-based trackers include Magnetic Trackers, Ultrasonic Tracker, Mechanical Tracker, and Inertial, Optical, and Vision-based Tracker [9].

4 Applications of Augmented Reality

4.1 General Application

Education: Many schools are implementing new technology to improve students' learning experiences. AR allows digital visuals to be placed on the actual environment in one's field of vision. Vector graphics, concept visualization, annotations, virtual instructions, and X-ray vision are examples of AR features that may be employed in current classroom circumstances to give an interactive and spatial learning experience. Students may undertake laboratory experiments and exercises safely and reliably with the aid of augmented reality technology. Because of interactive overlays of virtual items on the actual environment, this is feasible. AR is most commonly used in the fields of science, mathematics, and humanities. AR is effective in motivating and improving learning performance in several studies [10].

Entertainment: Advanced technologies like augmented reality (AR) are expected to have an impact on the future of entertainment. The entertainment sector has been able to revolutionize the way people connect and participate in games, athletics, tours, and concerts, among other activities, thanks to technological advancements. AR is a 3D interactive technology that merges physical and digital worlds in 3D. AR is already being utilized to improve the efficacy of multimedia presentations and films, in addition to rethinking traditional games [11]. It may, however, be applied to a far broader range of entertainment industries, such as how we listen to songs and how we travel. To develop diverse and physical interfaces, interface and visualization tech, as well as certain fundamental supporting technologies, are being included. AR can also be utilized in a group setting to provide individualized data to each user. Furthermore, by emphasizing or introducing information, it improves broadcasting during athletic events, concerts, as well as other events. As a result, AR's application in the entertainment business has advanced tremendously, as seen by the most recent well-known success, which is a location-based gaming example. Non-AR experiences restrict people to a screen, whereas AR converts books into an AR play area, urging individuals to venture outside and read more. Many AR entertainment systems contain on-device components, such as localized game control and player tracking; but, when shared resources, location-based gaming, and continuous synchronization are necessary, a server connection is used [12].

Tourism: AR plays an important role in the tourist business, and new generation smartphones and tablets, which are commonly equipped with GPS sensors and swift system connections, have made a significant contribution. These devices are equipped to assist with location-based AR administrations. A tourist experience may be enhanced by incorporating interactive media and redesigned content based on the demands of the visitors. The most common type of AR application for travel is augmented guides; an enhanced guide searches for, retrieves, and photographs data

gathered from select online sources as shown in Fig. 5. Accommodations, restaurants, and other services aimed at attracting tourists might reap significant benefits. They may evolve as places to visit rather than demands of travel. AR would also most certainly see a lot more open and direct communication between such authorities and visitors. AR used in gaming utility is shown in Fig. 4 [13].

E-commerce: The management of corporate websites or e-commerce systems can be improved by new purchasing techniques with varied properties compared to traditional online buying. E-commerce is a choice-based innovation that relies on AR cooperation to eliminate physical connection with the goods. For quite some time, the use of the Internet for purchasing has been rising rapidly. AR could be the most critical factor in changing how people shop online. The growth of new AR technology will be helpful if it can duplicate the features that have made online shopping the most popular shopping option in recent years. It is a simple method of constructing a 3D model in front of a person who may be successfully similar, resulting in a better appearance of the object by reconstructing it in reality. The use of AR purchasing

Fig. 4 AR being used as a gaming utility (*Source* MRV 2019, p. 39)

Fig. 5 An augmented reality application in tourism (*Source* IEEE Potentials 38(1):43–47, 2019 p.45)

is revolutionizing the online industry by assisting web merchants in reducing their rising profit margins and providing their customers with a more engaging and advantageous way to purchase through their devices. Clients may see their items in real time, from the luxury of their own home, thanks to imaginative AR setups. With a specialty area, it might play a big part in the industrial revolution [14, 15].

4.2 Domestic Application

Agriculture: In India, augmented agriculture is a revolutionary technological breakthrough that will advise farmers on the best pesticides and insect treatments. Additionally, this technology has the potential to reach both urban and rural populations about India's diverse flora and wildlife.

Farmers will be able to come up with enhanced and greater harvest amounts if augmented reality (AR) is used in farming. This technique may be used to judge the integrity of a site and its soils for agricultural purposes, resulting in higher crop yields in a variety of climatic circumstances. AR can analyze and identify soil quality, fertility, and nutrition, all of which are necessary for crop development to be productive. It also can forecast the weather. It will provide complete information on any plants that you choose to grow. Figure 6 shows assessment of a wind farm layout onsite by augmented reality [16].

Smart City Planning: The concept of "Smart Cities" is particularly significant in India since it attempts to enhance people's living standards by improving infrastructure, administration, irrigation, energy, water, health, education, safety, and security, among other things as shown in Fig. 7. It is critical to have a tool to communicate with all stakeholders and understand their primary problems in a nation where settlements are not structured and developed haphazardly. As a result, augmented reality emerges as a solution to all stakeholders' concerns about smart city infrastructure mobility, connection, and security. Mobility encompasses not just the ability to travel from one location to another, but also the supply of amenities that facilitate mobility, such

Fig. 6 Wind farm layout onsite by AR (*Source* Journal of Physics Conference Series, 2016 p.8)
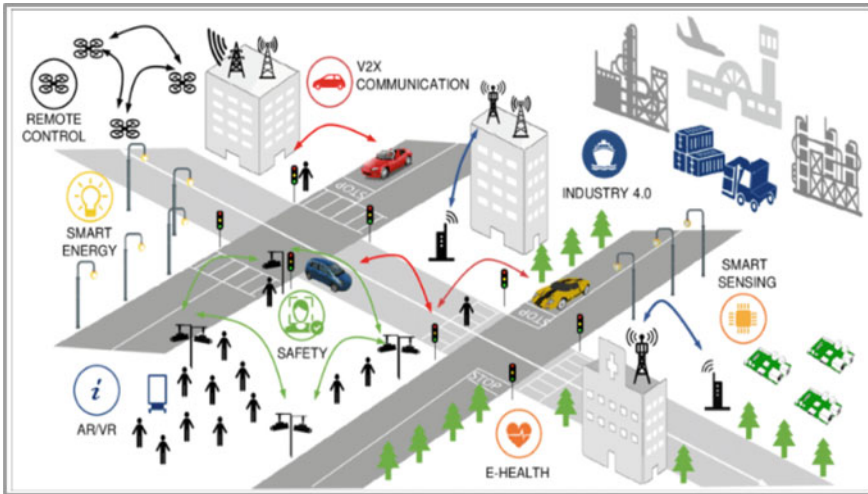
Fig. 7 IoT ecosystem assisted by AR in smart city (*Source* IEEE Communications Standards Magazine 3(2):26–34, 2019 p.27)

as educational opportunities, job training, professional progression, and company expansion. Permanent transportation systems such as roadways, railroads, and highways might be digitally connected through AR apps that give real-time information on timetables, disasters, and routes, as well as help navigation, using augmented reality applications. All the smart city technologies rely on real-time data transmission, which is only possible with a reliable connection. As a result, augmented reality aids smart networking and infrastructure management [17].

5 Limitations of AR

Augmented reality (AR) has been shown to be beneficial in various circumstances. However, current AR gear lacks the processing power needed to provide users with authentic AR experiences. Previously, devices like Google Glass introduced in 2012 executing highly demanding AR algorithms struggled from overheating and extremely limited battery life. However, even more, recent devices such as Microsoft HoloLens have limitations, such as the number of renderable polygons, and bringing AR apps into action and bringing them up to date locally on various mobile devices are quite expensive. Web AR will become one of the most important techniques for bringing AR to more people. However, even web AR suffers from certain limitations—**Computational Efficiency for CPU-Hungry Tasks on Mobile Web Browsers**: JavaScript, a popular programming language, performs poorly when dealing with sophisticated computations like matrices and floating-point calculations. To fulfill the requirement for computational efficiency, web browsers must be updated

to a more effective computation paradigm. The hardware resources of end devices can be fully utilized by browser-kernel-based extension solutions for web augmented reality implementations to improve speed. As a web AR solution, we believe this has more potential. However, as distinct web AR applications can only be utilized by their own browser, a variety of existing browser-kernel-based extension solutions have substantial compatibility issues, which significantly limits the popularity of web AR. The aforementioned compatibility issue will be one of the most important issues to be resolved in the future in order to market web AR applications on a broad scale.

Network Constraints: The latency and bandwidth of the network are crucial to MAR. Wireless networks, however, have a negative impact on how well web AR apps work. Even while the present 4G networks are capable of good performance, they cannot yet satisfy the low-latency demands of novel applications like AR and VR. New methods for optimizing wireless network resources are made possible by technologies including software-defined networking (SDN), device-to-device (D2D) communication, and mobile crowdsourcing mechanisms. However, there is still a lot of potential for optimization to boost the functionality of web AR applications [18].

5.1 State-of-the-Art Solutions

Pure front-end solutions: AR.js is a popular marker-based MAR solution for quickly executing AR applications on the web, such as identification, monitoring, and 3D object rendering, using WebRTC and WebGL on any mobile device. JSARToolKit is a JavaScript-based AR framework that allows you to generate a 3D representation of a detected marker inside a camera feed in real time by determining the distance between the camera and the physical marker. CaffeJS attempts to conduct neural-network operations (e.g., image recognition) using a modified version of ConvNetJS to convert Caffe models to a web browser, which will save some network traffic and server resources.

Browser-kernel-based extension solutions: These days, a user's first step in connecting to the Internet is through their web browser. Web AR apps may frequently achieve almost natural performance on mobile devices and, as a result, a better user experience by extending the browser kernel to accommodate AR. Browser-kernel-based extension solutions, which are a subset of web AR solutions, rely heavily on browsers to perform the functionality of AR applications. Many browser-kernel-based web AR projects are already in closed beta stages as of right now. The variety of APIs offered by various browser-kernel-based extension solutions, however, would, in contrast, impede the large-scale promotion of web AR apps before the standardization of AR-supported browsers is complete. However, some standardization has already begun. To enable developers to create AR experiences using web technologies, Google is creating the experimental iOS and Android apps WebARonARKit and WebARonARCore. The Mozilla WebXR program, which promises to make it

simple for web developers to construct web apps that adapt to the characteristics of any platform, has just been unveiled by Mozilla. A widespread online AR application deployment platform is offered by the AR-supporting web browser Argon4. The JavaScript library argon.js, which Argon implements, attempts to facilitate web AR apps in any web browser. These initiatives seek to give web AR developers a standard environment. But they have not yet been widely used in practice and are still in their infancy [19].

6 AR and EDGE

Over time, EDGE computing has been given several definitions. According to Satyanarayanan et al., "Edge computing is a new computing model that deploys computing and storage resources (such as cloudlets, micro data centers, or fog nodes, etc.) at the edge of the network closer to mobile devices or sensors" [19]. Zha et al. describe it as "Edge computing is a new computing model that unifies resources that are close to the user in geographical distance or network distance to provide computing, storage, and network for applications" [20]. However, the basic idea of EDGE remains the same throughout—to bring computing near the data source. Proximity affects factors such as latency, feasible bandwidth, and survivability.

Need for EDGE-based AR Systems: All of the previous web AR systems have limitations. Pure front-end solutions are inefficient in terms of computing, whereas browser-kernel-based extension solutions seem to be under development and are not generally used. The cloud computing paradigm substantially expands the computational capabilities of terminal devices. Although the cloud computing paradigm expands users' end-device compute and storage capabilities, it introduces substantial delay into the mobile network. MAR applications, on the other hand, need low latency [21–24]. Edge computing offers to scale back network delay by placing apps closer to consumers at the network edge, potentially improving web AR performance. We would be looking into the architecture and performance of two such EDGE-based AR solutions to overcome the current limitations.

EDGE-Based Solution

Working Principle: Qiao et al. proposed a framework consisting of three main components: Terminal, Edge Cloud Server, and Remote Cloud Server. The basic idea is to pass on computationally heavy tasks to the edge cloud for better performance [21].

Terminal Side: The terminal contains the scheduling layer which is responsible for web AR service scheduling. It also contains the processing module, for basic processing, which further contains sub-modules for capturing images, matching images, and rendering a 3D model. Due to the sub-modules using basic algorithms for matching, some images might not be sufficient for the application. This is where edge cloud services come into the picture.

Edge Cloud Side: The edge cloud server will immediately transmit any image-matching requests that it gets from the terminal side to the specific web AR application instance. All web AR applications have access to the AR cache on the edge cloud server. However, the abstract MAR service layer will forward the application deployment request to the distant cloud server if the desired web AR application has not yet been deployed. The decision regarding the deployment of the web AR application is made using the edge server's current performance, including the CPU, memory, and storage utilization. The application service provider (ASP), a remote cloud server, ultimately chooses where a certain program will be put while accounting for the entire deployment and transmission costs.

Another function of the layer is to manage the web AR application objects while the underlying layer contains modules for better working of instances present in the upper layer.

Remote Cloud Side: During deployment decision-making, the overall cost of deployment and transmission is taken into account. According to these decisions, particular web AR resources are combined into web AR applications by resource packaging service layer present in a remote cloud and deployed to an edge server. Successfully matched images are also sent to remote cloud servers from edge cloud servers as the terminal side cannot handle such images for time being.

Performance Evaluation: Theoretical results suggest that edge servers have better computational capability and decrease time requirements compared to the same algorithm being used on the terminal side and increased accuracy of the image-matching process. The algorithm used for matching is far more optimized and the server performs better due to its proximity to users. For matching multiple images, edge provides the great computational capability and shifting the web AR application from remote to edge decreased delay effectively.

Experimental analysis was done on a Samsung Note 4 smartphone, the browser being Chrome and the following results were achieved in terms of latency, fps, power consumption, and the number of matched key points. It was concluded that MEC is more efficient than its counterparts and can be the future of MAR as shown in Fig. 8.

Mobile Augmented Reality Based (MAR)

Working principle: Huang et al. proposed CLoudRid AR, a cloud-based MAR framework to deploy MAR applications. The objective of this framework is as follows:

- Provide built-in modules to give developers uniform interfaces to deploy MAR applications and to simplify work using a predefined task flow along with flexibility in changes using the dynamic registration mechanism.
- Limited battery usage and prolonging battery life by offloading computationally heavy tasks to cloud servers which also eliminates the need for severe hardware or software requirements on mobiles.
- Increase scalability on different handsets using abstract layers. The hardware abstraction layer is used to build upper modules for the diversification of platforms.
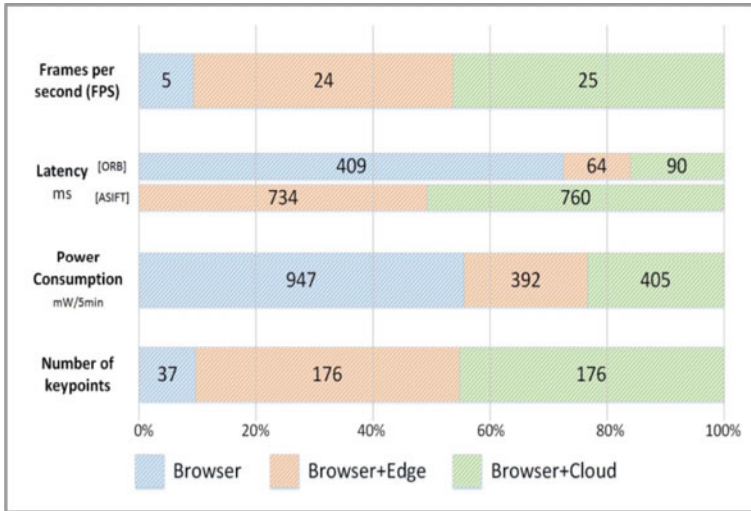
Fig. 8 Experimental results (*Source* IEEE Internet Computing, 2018 p. 53)

The workflow of the framework is predefined; however, its configuration is flexible according to user requirements. The data flow starts with initialization in which registered hardware calls its respective predefined functions to initialize their status. The decision whether to run the most computationally heavy task on the device or cloud is taken by the task allocation mechanism. Offloading tasks have to be synchronized to ensure that outsourced tasks are getting done before the next step. Real environment and rendering objects are mixed and displayed on display devices and open for users to interact with using voice, gestures, etc. [25]. Dataflow of the framework is shown in Fig. 9. The software stack of the framework is shown in Fig. 10.

Performance Evaluation: Two prototypes were successfully developed on this framework. The first one involved a virtual car on a mobile phone running on a real path. It is an immersive game in which players may create a dynamic course to influence how and where the vehicle travels. The second is a multiuser ping pong game. To strike the simulated Ping-Pong ball, participants can choose any solid flat object as a bat. The rendering process is handled on the mobile phone instead of the cloud in both prototypes since virtual content is quite basic and does not involve a lot of computation. Collision detection, as well as rigid body simulation, is conducted in the cloud in the latter prototype. As feature extraction involves significant computational overhead, it typically cannot attain real-time performance on mobile devices because they lack the processing power to complete the computation quickly. We offload the feature extraction to the cloud for processing acceleration by utilizing the cloud computing architecture. For example to direct the movement of the car, the coordinates of recognized line features are transmitted back to the phone and constructed as geometric paths. Users can have direct interactions with cars thanks to
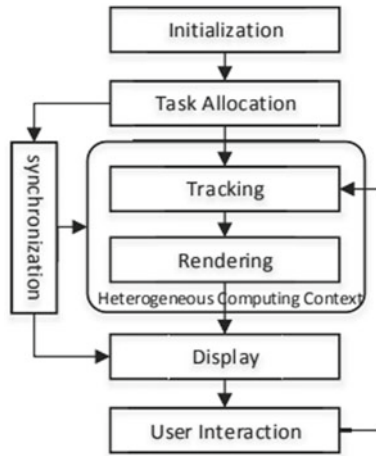
Fig. 9 Dataflow of the framework (*Source* ACM Press, 2014 p. 31)
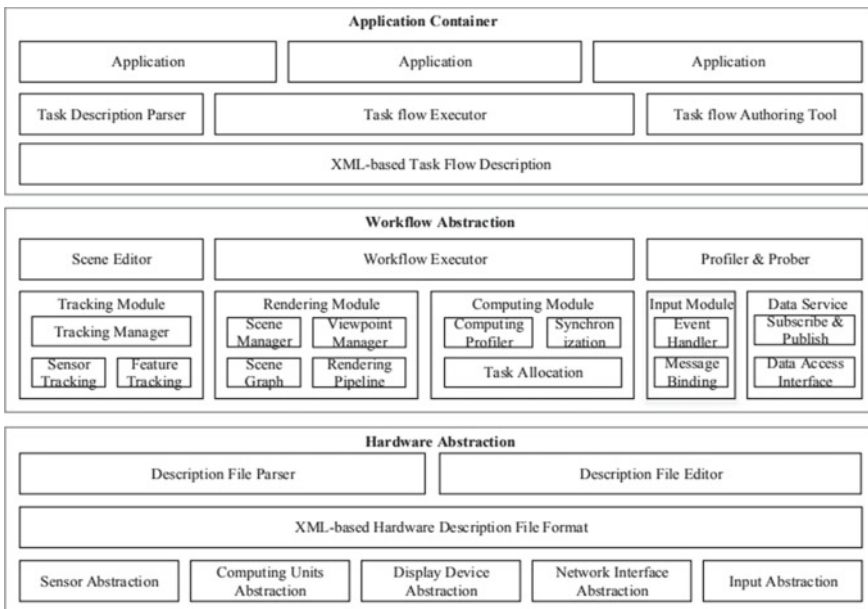
Fig. 10 Software stack of the framework (*Source* ACM Press, 2014 p. 32)

real-time feature extraction on the cloud. Consumption of higher computation power is also caused by high latency. Low latency would lead to inaccuracy. Since mobile devices have much less storage and processing power than AR-oriented devices, MAR faces unique difficulties. Additionally, MAR is projected to conserve battery

life given that mobile platforms are used for a variety of daily chores in addition to MAR (such as social network applications and web search).

Alternate Solution: To overcome this, instead of image retrieval and a convolutional neural network (CNN), as was the case in earlier MAR work, we can use visual and inertial 6-DOF localization to recognize and track objects on the screen. By synchronizing the coordinate systems of the cloud and mobile device and being able to distinguish between instances of the same type, 6-DOF locations make it easier for them to work together. By employing heavy and slow local optical flow and cloud offloading selectively while using light and quick local inertial data processing, optical flow is only locally computed when the device collects enough position changes, and pictures are only offloaded when local results need to be calibrated. Due to this, both object recognition and tracking may now be done with latency as low as 100 ms. Low latency allows for the mobile device's energy consumption (including computing and offloading overhead) to be reduced without compromising accuracy. This was proposed by Chen et al. and is known as MARVEL (MAR with Viable Energy and Latency) [26].

7 Future Prospects

Because of its lightweight and cross-platform capabilities, web AR is becoming increasingly popular. We believe that it will provide MAR with a bright future. However, more effort needs to be done to further encourage the use of online AR. On mobile web browsers, computational efficiency for CPU-intensive tasks. For sophisticated computing tasks like matrix and floating-point computation, the commonly used JavaScript performs badly. To achieve the computational efficiency criteria, web browsers will need to implement a more efficient processing paradigm. Although certain sophisticated approaches like Web Assembly and Web Workers are currently implemented in several common web browsers, there remains indeed potential for improvement in terms of end-device compute efficiency. To achieve improved performance, browser-kernel-based extension solutions may make full advantage of end devices' hardware resources. As a web AR solution, we believe it has greater promise. However, there are serious compatibility issues with several current browser-kernel-based extension solutions. Different online AR apps can only be utilized with their browser, which severely restricts the adoption of web AR.

Constrictions in the Network: The latency and bandwidth of the network are critical to MAR. Wireless networks, on the other hand, have a negative effect on the productivity of web AR apps. Despite the fact that contemporary 4G networks are capable of high performance, they are still unable to match the low-latency needs of emerging applications like AR and VR. Nevertheless, there is still a lot of opportunity for improvement in the performance of augmented reality applications which will surely enhance the experience of users in the near future.

References

1. Sharma L (2019) Recent advancements of augmented reality in real time applications. 8:537–542. https://doi.org/10.35940/ijrte.B10100.0782S719
2. Xu D, Li T, Li Y, Su X, Tarkoma S, Jiang T, Crowcroft J, Hui P (2020) Edge intelligence: architectures, challenges, and applications. arXiv: Networking Internet Architect
3. Chen Y, Wang Q, Chen H, Song X, Tang H, Tian M (2019) An overview of augmented reality technology. J Phys: Conf Ser
4. Syberfeldt A, Danielsson O, Gustavsson P (2017) Augmented reality smart glasses in the smart factory: product evaluation guidelines and review of available products. IEEE Access 1–1. https://doi.org/10.1109/ACCESS.2017.2703952
5. Singla S, Aswath SK, Bhatt VK, Sharma BK, Pal VK (2019) Virtual reality in non-communicable diseases
6. de Boer E, Harlaar NJ, Taruttis A, Nagengast WB, Rosenthal EL, Ntziachristos V, van Dam GM (2015) Optical innovations in surgery. Br J Surg 102(2):e56–e72. https://doi.org/10.1002/bjs.9713
7. Ran X, Slocum C, Gorlatova M, Chen J (2019) ShareAR: communication-efficient multi-user mobile augmented reality. In: Proceedings of the 18th ACM workshop on hot topics in networks. https://doi.org/10.1145/3365609.3365867
8. van Krevelen D, Poelman R (2010) A survey of augmented reality technologies, applications and limitations. Int J Virtual Reality 9(2):1–20. https://doi.org/10.20870/IJVR.2010.9.2.2767
9. Albasiouny E, Medhat T, Sarhan A, Eltobely T (2011) Stepping into augmented reality. Int J Networked Comput Adv Inf Manage 1:9–47. https://doi.org/10.4156/ijncm.vol1.issue1.2
10. Sarkar P, Pillai JS (2019) User expectations of augmented reality experience in Indian school education. In: Chakrabarti A (eds) Research into design for a connected world. Smart innovation, systems and technologies, vol 135. Springer, Singapore. https://doi.org/10.1007/978-981-13-5977-4_63
11. Parekh P, Patel S, Patel N, Shah M (2020) Systematic review and meta-analysis of augmented reality in medicine, retail, and games. Vis Comput Ind Biomed Art 3:21. https://doi.org/10.1186/s42492-020-00057-7
12. Riegler A, Kun A, Brewster S, Riener A, Gabbard J, Wienrich C (2019) MRV 2019: 3rd workshop on mixed reality for intelligent vehicles. 38–44. https://doi.org/10.1145/3349263.3350758
13. Akram W (2017) A study on role and applications of augmented reality in tourism: its challenges and future prospects. Int J Adv Res Comput Sci 8:168–172. https://doi.org/10.26483/ijarcs.v8i8.4633
14. Shabani N, Munir A, Hassan A (2019) E-Marketing via augmented reality: a case study in the tourism and hospitality industry. IEEE Potentials 38:43–47. https://doi.org/10.1109/MPOT.2018.2850598
15. Garg N, Pareek A, Lale A, Charya S (2021) Evolution in e-commerce with augmented reality. IOP Conf Ser: Mater Sci Eng 1012:012041. https://doi.org/10.1088/1757-899X/1012/1/012041
16. Nigam A, Kabra P, Doke P (2011) Augmented reality in agriculture. In: 2011 IEEE 7th international conference on wireless and mobile computing, networking, and communications (WiMob)—Shanghai, China (2011.10.10–2011.10.12)
17. Jha S, Joshi S (2019) Role of augmented reality applications for smart city planning. Int J Innovative Technol Exploring Eng 8:2278–3075
18. Zanzi L, Cirillo F, Sciancalepore V, Giust F, Costa-Pérez X, Mangiante S, Klas G (2019) Evolving multi-access edge computing to support enhanced IoT deployments. IEEE Commun Stan Mag 3:26–34. https://doi.org/10.1109/MCOMSTD.2019.1800009
19. Rambach J, Schneider M, Stricker D (2017) Augmented reality based on edge computing using the example of remote live support. https://doi.org/10.1109/ICIT.2017.7915547
20. Qiao X, Pei R, Dustdar S, Liu L, Ma H, Junliang C (2019) Web AR: a promising future for mobile augmented reality—state of the art, challenges, and insights. Proc IEEE 107:1–16. https://doi.org/10.1109/JPROC.2019.2895105

21. Ren P, Qiao X, Chen J, Dustdar S (2018) Mobile edge computing—a booster for the practical provisioning approach of web-based augmented reality. In: IEEE 2018 IEEE/ACM symposium on edge computing (SEC)—Seattle, WA, USA (2018.10.25–2018.10.27), pp 349–350. https://doi.org/10.1109/SEC.2018.00041
22. Satyanarayanan M (2017) The emergence of edge computing. Computer 50(1):30–39
23. Zha ZM, Liu F, Cai ZP (2018) Edge computing: platforms; applications and challenges. J Comput Res Dev 55(2):327–337
24. Shi WS, Zhang XZ, Wang YF (2019) Edge computing: state-of-the-art and future directions. J Comput Res Dev 56(1):1–21
25. Huang Z, Li W, Hui P, Peylo C (2014) CloudRidAR: a cloud-based architecture for mobile augmented reality. 29–34. https://doi.org/10.1145/2609829.2609832
26. Chen K, Li T, Kim H-S, Culler D, Katz R (2018) MARVEL: enabling mobile augmented reality with low energy and low latency. https://doi.org/10.1145/3274783.3274834

Smart Door Unlocking System

M. Bhavya Sri, D. Rama Lakshmi, Y. Pranavi, and Ch Nanda Krishna

Abstract Face recognition-based phone unlocking was first introduced by Apple on its iPhones in 2017 and has since become a disruptive breakthrough in the smartphone business. Home security, monitoring, and automation technologies, meanwhile, have recently become an important part of many people's daily lives. This Face Recognition and Voice Recognition Smart Door Unlock System aims to increase security. In this system, a camera sensor is utilised to capture the face, and an image matching algorithm is used to recognise authorised faces, as well as a voice sensor to record sound. Only the person with the matching face or voice may unlock the door. The security system is also built by including maintenance into the design.

1 Introduction

Burglary and theft are both important worries for any family. People may build Smart Home Security systems that will be accessible via a single device, allowing them to be free of constant anxiety, especially at night. For security, most individuals have cameras installed at all entrances to their houses, allowing them to see who is visiting. In some sophisticated home security systems, face recognition is also accessible. Face recognition may be done using a method that combines geometrical feature points with low-level visual information. Thieves, on the other hand, can get around this by showing a photo of the owner or a family member. The innovation comprises a home security system that combines both face and speech recognition in addition to facial verification. Every visitor to the residence will be authenticated twice via a live stream, with the input compared to the names kept in the owner's database. As a result of the increased usage of smart devices, many operations have been automated. One of the most actively developed technologies is home automation, which is extensively employed by society's upper crust. It is significantly more difficult to rely simply on

M. Bhavya Sri (✉) · D. R. Lakshmi · Y. Pranavi · C. N. Krishna
Department of Information Technology, V.R Siddhartha Engineering College, Vijayawada, India
e-mail: bhavya3004sri@gmail.com

the device's traditional and basic security capabilities. Mechanical locks [1], which have a limited number of keys and give less protection, are used on many doors in earlier technologies. Traditional locking mechanisms must be updated and made smart and automated to address the aforementioned difficulties. As a result, a two-level biometric system is proposed. The faces of the individuals are first identified. The phrase recognition is then performed for improved authentication.

2 Literature Review

2.1 Using Artificial Neural Networks Approach for Face Detection System

Face recognition using artificial neural networks was offered for comparison in this study in the context of face verification and face recognition using photometric normalisation. In both PCA and LDA, the experimental findings show that N.N. beats the Euclidean distance [2] and normalised correlation decision rules in terms of overall verification performance. The E.D. classifier, on the other hand, delivers the maximum recognition accuracy when using the original face image.

2.2 About the Study on Automatic Speech Recognition

There was a review of Automatic Speech and phrase Recognition Systems. In the first portions, they described the system and its main characteristics, as well as the general architecture of the Automatic Speech and phrase Recognition System. The 2nd portion examined the outcomes of several recent research investigations after outlining the bulk of the issues faced and the numerous solutions offered.

2.3 Automatic Speech Recognition

They addressed the different strategies of Automatic Speech [3] and phrase Recognition also called as ASR and Hidden Markov Model also called as HMM, as well as how technology has advanced in recent years. ASR entails the collaboration of speech scientists, linguists, computer scientists, mathematicians, and engineers, as well as fast computers with plenty of data capacity and memory, which is required for sophisticated recognition jobs [4–6].

2.4 Design of a Real-Time Face Detection and Evaluation of a Real-Time Face Recognition System Using CNN also Called as Convolutional Neural Networks

The use of Convolutional Neural Networks [7] in the construction and assessment of a real-time facial recognition system is presented. Tuning various CNN parameters to improve the recognition accuracy of the system created is used to evaluate the performance of the proposed system and CNN architecture [7].

2.5 Deep Learning for Face Recognition: A Critical Analysis

This provided a critical examination of contemporary face recognition [1, 8–10] techniques, advances, and problems. It also included a comparison of the existing datasets as well as relevant benchmarks. It identified flaws in current approaches and assessed actions to resolve these flaws, highlighting lingering concerns that have yet to be solved.

2.6 Speech Recognition by Machine

They have sought to offer a quick glance and evaluation of how far voice recognition technology has gone in the previous 60 years in this study.

3 Proposed Work

3.1 Design Methodology

The three primary steps in the design technique is shown in Fig. 1 and the architecture diagram is shown in Fig. 2.

3.2 Description of Algorithm

Deep face is a Python framework for facial attribute analysis and face identification (age, gender, emotion, and race). Hybrid facial recognition frameworks include VGG-Facial, Google Face Net, Open Face, Facebook Deep Face, Deep ID, Arc Face,
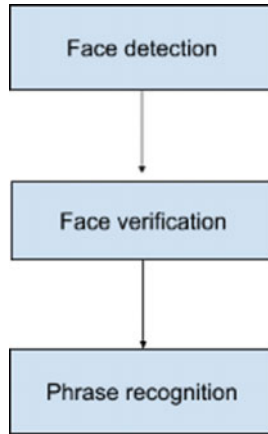
Fig. 1 The three primary steps in the design technique
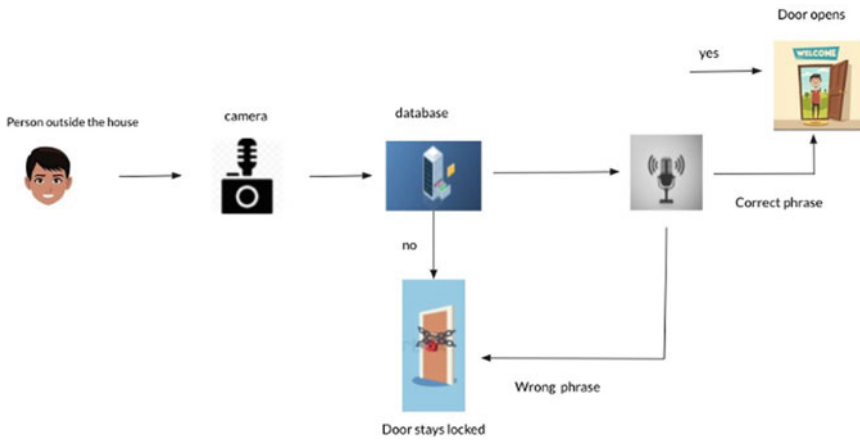
Fig. 2 The architecture diagram

and Dlib. According to research, humans have 97.53% accuracy on facial recognition tasks, whereas those models have already reached and surpassed that level of accuracy. The deepface module is shown in Fig. 3.

```
result = DeepFace.verify(img_path = "img1.jpeg", img2_path = "img2.jpeg", model_nam
#different person images
#testing using Facenet
print(result)

{'verified': False, 'distance': 0.8642480145362179, 'threshold': 0.4,
'model': 'Facenet', 'detector_backend': 'opencv', 'similarity_metric':
'cosine'}
```

Fig. 3 Using the deepface module

4 Description of Datasets and Tools Used

4.1 Datasets

The dataset consists of images of faces required to unlock the door. Link to dataset: https://drive.google.com/drive/folders/1GDVQtL8mlUo0E9Zhun8G6K8 WNxIo2aAp?usp=sharing.

4.2 Requirements

Juypter Notebook with deepface and speech recognition installed.

5 Results and Observations

5.1 Stepwise Description of Results

If image pair is the same person: Verified is true. Else if the image pair is not the same person: Verified is false. Distance shows the similarity between the images. Model shows which model is used. Deep Face verify method verifies 2 images or an image with a set of images (here the dataset). DeepFace detectFace module detects faces from an image. Captures the image of the person arrived as in Fig. 4.

Checks if the captured image is in the dataset. It gives the list of images which matched with the current image. If the number of recognised images [11] is greater than the set threshold values then the person is allowed to say the phrase to unlock the door. Else, if the recognised images are less than the threshold, the door stays locked. The function voice (Fig. 5) checks the phrase said by the person. If the phrase is the same as the set one then the door opens else it stays closed. When the database's data and the captured data does not match the recognition is shown as zero. It displays the amount of similarities [3] detected with the photographs in the database for each individual in the database. It looks for the phrase after verifying the person's face. If

```python
import cv2

cam = cv2.VideoCapture(0)

cv2.namedWindow("test")

while True:
    ret, frame = cam.read()
    if not ret:
        print("failed to grab frame")
        break
    cv2.imshow("test", frame)

    k = cv2.waitKey(1)
    if k%256 == 27:
        # ESC pressed
        print("Escape hit, closing...")
        break
    elif k%256 == 32:
        # SPACE pressed
        img_name = "image.png"
        cv2.imwrite(img_name, frame)
        print("{} written!".format(img_name))

cam.release()

cv2.destroyAllWindows()
```

```
image.png written!
Escape hit, closing...
```

Fig. 4 Captures the image of the person arrived

the incomer says the proper phrase, the door will open and he will be permitted to enter the residence. Otherwise, the door will remain shut. The Arc Face model has more accuracy than all the other models used for the construction.

Figure 6 shows the graph representation of the accuracy levels of each model. The models are:

1. VGG-Face
2. Facenet
3. Facenet512
4. Openface
5. Deepface.

ArcFace From Fig. 6, it can be concluded that the Arcface model has a higher accuracy when compared to the other algorithms.

```
def voice():
    r=sr.Recognizer()
    with sr.Microphone() as source:
        print("SAY")
        audio = r.listen(source)
        print("Thank you")
        try:
            if r.recognize_google(audio) == "hello":
                print('Door unlocked!')
            else:
                print('Door stays locked')
        except:
            pass
```

Fig. 5 Captures the image of the person arrived
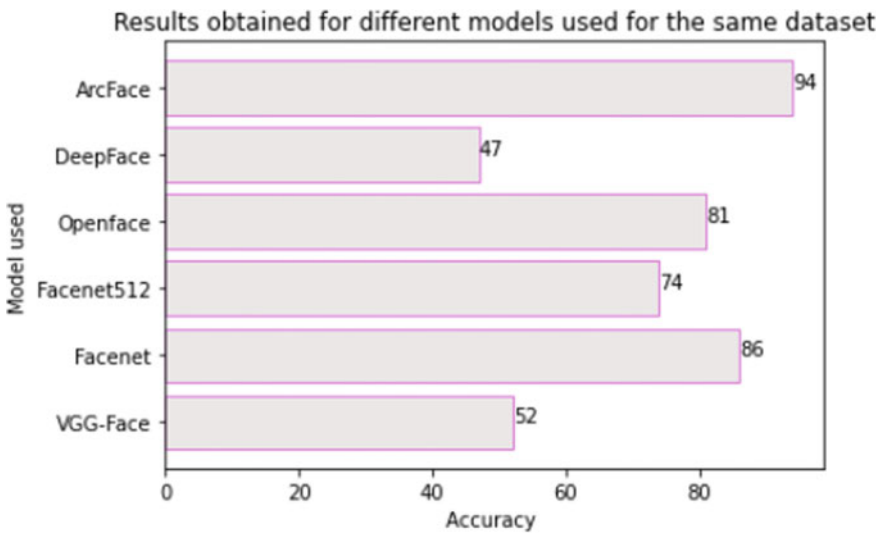
Fig. 6 Shows the accuracy of different models

The image (Fig. 7) shows the pie chart representation of the threshold values for Facenet, VGG-Face, ArcFace, Deepface, OpenFace, Facenet512. The Arcface model has a higher threshold [4] value.

Fig. 7 Threshold values of each model
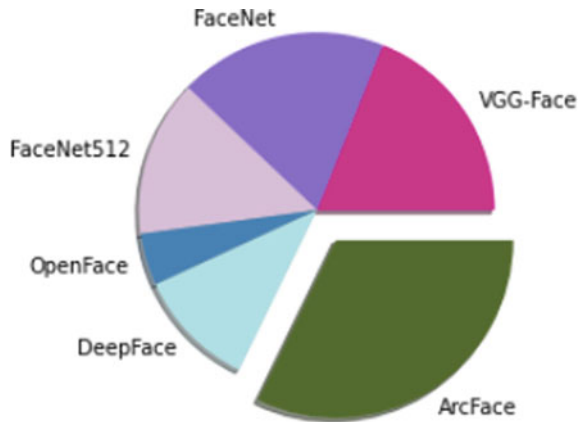
5.2 Social Benefits

Face recognition has several advantages for society, ranging from minimising needless human contact and labour to avoiding crimes and boosting safety and security. It can even aid boost medical efforts [12–14] in rare cases. Speech recognition technology can be used in various ways. Many sectors are increasingly using phrase recognition to aid in day-to-day operations. Typing takes far longer than talking [2]. A document may be dictated three times faster than it can be typed. When you combine dictation with transcription software, you may save money on transcribing and streamline your productivity. Any industry may benefit from voice recognition [15] software. Get more done throughout the day and week. As a result, combining face recognition and speech recognition [16–18] produces amazing results.

6 Conclusion and Future Work

The suggested method allows for remote door locking and unlocking without the requirement for physical user interaction. This type of lock provides more security than mechanical locks. This paper looked at existing work on smart home security and incorporated it into a streamlined [8] method to building a safe architecture that improves security. Due to the vast range of applications in the commercial and law enforcement industries, face recognition (FR) is becoming a popular study topic. Traditional FR techniques based on Visible Spectrum have challenges with object illumination, position fluctuation, attitude variations, and face disguises (VS). Unfortunately, these limitations affect the accuracy of item identification and verification. In human FR, the Infrared Spectrum (IRS) might be used to get beyond all of these limitations. As a consequence, researchers are inspired and motivated to continue their work in the subject of FR. As the demand for smart home security develops,

developers who create the products and services that keep millions of people safe, continue to experiment with new technologies that might improve overall security and safety. The quest of industry-leading protection drives SimpliSafe, an award winning home security business established in Boston, Massachusetts. The speech recognition market was worth USD10.70 billion in 2020 and is predicted to grow at a CAGR of 16.8% from 2021 to 2026, reaching USD 27.155 billion by 2026. This rise is being driven by virtual assistants in the retail, banking, and automotive industries, as well as personal home usage.

References

1. Lui YM, Bolme DS, Phillips PJ, Beveridge JR, Draper BA (2012) Preliminary studies on the good, the bad, and the ugly face recognition challenge problem. In: Computer vision and pattern recognition workshops (CVPRW), pp 9–16
2. Lilia L, Mohamed TL, Rachid B (2017) Discriminant learning for hybrid HMM/MLP speech recognition system using a fuzzy genetic clustering. In: 2017 Intelligent systems conference, pp 76–81—London, UK.
3. Ibiyemi TS, Akintola AG (2012) Speaker authentication and speech recognition enabled telephone auto-dial in Yorùbá. Int J Sci Adv Technol 12(4):88–187
4. Günther M, Haufe D, Würtz RP (2012) Face recognition with disparity corrected Gabor phase differences. In: Artificial neural networks and machine learning. Lecture notes in computer science, vol 7552, pp 411–418
5. Zhang W, Shan S, Gao W, Chen X, Zhang H (2005) Local Gabor binary pattern histogram sequence (LGBPHS): a novel non-statistical model for face representation and recognition. In: IEEE international conference on computer vision, vol 1, pp 786–791
6. Tan X, Triggs B (2010) Enhanced local texture feature sets for face recognition under difficult lighting conditions. IEEE Trans Image Process 19(6):1635–1650
7. Günther M, Würtz RP (2009) Face detection and recognition using maximum likelihood classifiers on Gabor graphs. Int J Pattern Recogn Artif Intell 23(3):433–461
8. Phillips PJ, Beveridge JR, Draper BA, Givens G, O'Toole AJ, Bolme DS, Dunlop J, Lui YM, Sahibzada H, Weimer S (2011) An introduction to the good, the bad, the ugly face recognition challenge problem. In: Automatic face gesture recognition and workshops (FG 2011), pp 346–353
9. Santosh KG, Bharti WG, Pravin Y (2010) A review on speech recognition technique. Int J Comput Appl 10(3). ISSN: 0975-8887
10. Galliano S, Geoffrois E, Mostefa D, Choukri K, Bonastre J-F, Gravier G (2005) The ESTER phase II evaluation campaign for the rich transcription of French broadcast news. In: Interspeech, pp 1149–1152
11. Ibiyemi TS, Ogunsakin J, Daramola SA (2012) Bi-Modal biometric authentication by face recognition and signature verification. Int J Comput Appl 42(20):17–21
12. Guillaume G, Gilles A, Niklas P, Matthieu C, Aude G, Olivier G (2012) The ETAPE corpus for the evaluation of speech- based TV content processing in the French language. In: Proceedings of the international conference on language resources, evaluation and corpora (LREC)
13. Stefan H, Marco D, Christian R, Fabrice L, Patrick L, Renato D, Alessandro M, Hermann N, Giuseppe R (2011) Comparing stochastic approaches to spoken language understanding in multiple languages. IEEE Trans Audio Speech Lang Process 19(6):1569–1583
14. Yuki S, Shinnosuke T (2018) Statistical parametric speech synthesis incorporating generative adversarial networks. IEEE/ACM Trans Audio Speech Lang Process 26(1)
15. Dominique F, Odile M, Irina I (2017) New paradigm in speech recognition: deep neural networks, the ContNomina project supported. French National Research Agency (ANR)

16. Toygar O, Acan A (2003) Face recognition using PCA, LDA and ICA approaches on colored images. J Electr Electron Eng 3(1):735–743
17. Wiskott L, Fellous J-M, Krüger N, Kuiger N, Von Der Malsburg C (1997) Face recognition by elastic bunch graph matching. IEEE Trans Pattern Anal Mach Intell 19(7):775–779
18. Slavković M, Jevtić D (2012) Face recognition using eigenface approach. Serb J Electr Eng 9(1):121–130

An Insight into AI and ICT Towards Sustainable Manufacturing

Omolayo M. Ikumapayi, Opeyeolu T. Laseinde, Temitayo S. Ogedengbe, Sunday A. Afolalu, Adebayo T. Ogundipe, and Esther T. Akinlabi

Abstract Artificial intelligence's value has increased in recent years. Artificial intelligence (AI) backed by big data analytics has expanded over the past few years. According to reports and reviews, artificial intelligence structured on large volumes of data analytics and information and communications technology has the potential to greatly improve supply chain performance; however, research into the reasons why companies engage in manufacturing activities and the novel artificial intelligent systems is limited. It is in this regard that this study has been carried out. To this end, several theoretical approaches have been proposed as explanations for how manufacturing businesses generate valuable resources and worker skills to impose innovation and enhance circular economy proficiency. The goal of this study is to gain approval for an intellectual concept that explains how institutional pressures on resources affect the implementation of big data in artificial intelligence, as well as its influence on sustainable manufacturing and the model of production and consumption proficiency when regulating the effects of industrial flexibility and industry effectiveness. We believe that if companies want to see a meaningful return on their AI efforts, they must fill this gap and promote AI capability. It is on this central aim that this study will expose and encourage research into this area; moreover, it hopes to create

O. M. Ikumapayi (✉) · S. A. Afolalu
Department of Mechanical and Mechatronics Engineering, Afe Babalola University, Ado-Ekiti 360101, Ekiti State, Nigeria
e-mail: ikumapayi.omolayo@abuad.edu.ng

O. M. Ikumapayi · O. T. Laseinde
Department of Mechanical and Industrial Engineering Technology, University of Johannesburg, Johannesburg, South Africa

T. S. Ogedengbe
Department of Mechanical Engineering, Nile University of Nigeria, Jabi, Abuja 900001, Nigeria

A. T. Ogundipe
Directorate of Information Communication Technology, Afe Babalola University, Ado Ekiti, Nigeria

E. T. Akinlabi
Department of Mechanical and Construction Engineering, Northumbria University Newcastle, Newcastle upon Tyne, UK

awareness among new industrial facilities of the essence of implementing AI features to boost any form of manufacturing and fabrication process.

Keywords Artificial intelligence · Information communication technology · Industry · Manufacturing

1 Introduction

The development of industrial value in modern industrialized countries is currently being modelled by the fourth phase of industrialization, often known as the evolution of industrialization. This development is in line with the third industrial revolution, which began in the early 1970s and was centred on electronics [1]. To increase the degree of automation in manufacturing, information and technology will be used. The shift to the fourth phase of industrialization is now having an impact on the manufacturing sector. The focal point is on the advancement of modern goods, intelligent enterprises, and modern services, all of which are integrated into an Internet of things and services, also known as the industrial Internet [2]. Innovative and discouraging business tactics are emerging in reaction to the current industry's components, though. This shift towards industry opens up a plethora of opportunities for entrepreneurs [1]. Although the Fourth Industrial Revolution is a driver of sustainable development, the nexus between digital transformation and sustainability has yet to be addressed. Various links between Industry 4.0 technology and actions that can be performed have been discovered in recent studies [3]. This study breaks new ground by examining how various technologies have been applied to addressing sustainable operations in a broader sense, as well as the numerous standards set forth by government-sponsored Industry 4.0 initiatives [2].

2 Literature Review

2.1 Artificial Intelligence

The potential of a computer-controlled robot to do activities that have been designed after the behaviours of humans with greater intellect is known as artificial intelligence (AI) [3]. The word is frequently used in projects aimed at giving machines human-like brain processes and traits, notably the ability to generalise, reason, find meaning, and build on prior experiences [4]. It has been known since the 1940s, when the first digital computer was developed, that computers can be taught to perform incredibly difficult tasks, like playing chess, with astonishing skill [5]. Despite recent advancements in the computational speed and storing capability of several computer systems, no computer program can compare to or equal the conceptual versatility and activity of humanity across wider areas or in tasks that need a considerable quantity of common
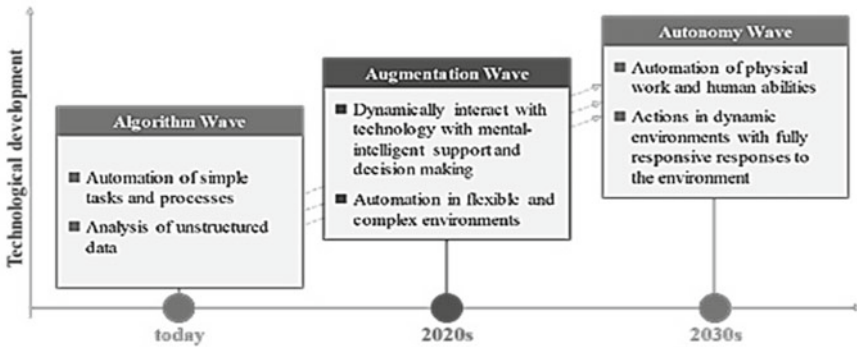
Fig. 1 Artificial intelligence [2]

knowledge. Psychologists contend that rather than being characterised by a single attribute, intelligence is perhaps best described as a combination of multiple unique talents [3]. The only objective of AI research has been to advance the following intelligence components such as reasoning, perceptions, problem analysis, learning, as well as language usage. The trends of AI up to the 2030s are depicted in Fig. 1.

2.2 Information Communication Technology (ICT)

Information and communications technology (ICT) is a term used to describe information technology (IT) that emphasizes the importance of comprehensive data exchange or connectivity using various data transfer methods, including computers and telecommunications (the use of signals and communication lines), to enable users to store, send, interpret, as well as manipulate information [4]. ICT is the merging of computer networks with telephone networks, audiovisual networks, and networks of computers with singular connection and/or single wire. With constantly evolving ideas, ICT is a broad field. This is so because it includes any device that can store, access, manipulate, transmit, or collect data in a digital format [6]. This data accessing and manipulation is made possible through the use of some basic ICT tools which can alter or organize such data for specific purposes. The utilization of communication signals, which are transferred by signal delivery, cabling, etc. with the help of an administration system to link telephone and computer networks, is the foundation of ICT. ICT still goes further than the aforementioned, embracing all forms of communication technology, including computers, mobile phones, radio, satellite systems as well as television, etc. [4]. It also includes the many services that modern technology provides to society, some of which include video conferencing and distance learning. ICT also includes analogue and digital technology [4] as in Fig. 2. Online presence is always protected using the virtual private network (VPN)
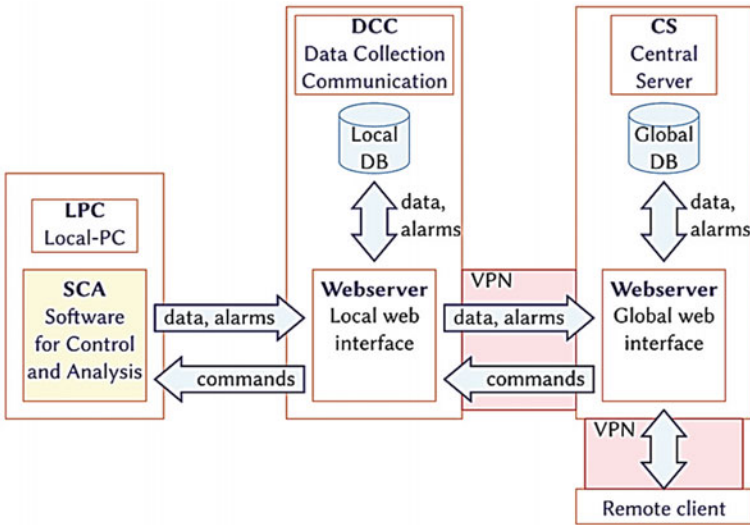
Fig. 2 Information and communication technology [4]

which actively hides the Internet protocol (IP) address of the user especially while using the Internet via a public domain.

2.3 Sustainable Manufacturing

Sustainable manufacturing as depicted in Table 1 is characterized as a synergy of systems and processes that can produce a range of goods with high quality and efficiency while also providing necessary services with more sustainable resources in place of scarce ones. A brand's ability to establish a better reputation, get access to new markets, and reduce costs is aided by sustainable production [5, 6].

The scope of attaining sustainability in manufacturing is defined in four elements, each with its unique objects and closely-related disciplines, which were utilized to identify the articles in the sample:

- Manufacturing technologies are based on process and equipment (machine-tool, facility); related disciplines such as manufacturing or production engineering, planning and layout of factories, and management of industrial processes and operations [7].
- Product lifecycles (items to be manufactured) with emphasis on the design and structuring of products and services, emphasis is also placed on the related field of engineering design [8].
- Value creation networks that centre on the arrangement and organization of industrial firms and factories in the network of a manufacturing process.

Table 1 Sustainable manufacturing in Industry 4.0

Sustainable manufacturing in Industry 4.0			
S/N	Industry 4.0 and SM	Technological pillars	Sustainability dynamics models	Scope of sustainable manufacturing
1	Value creation network	Simulation	Direct effects on the social dimension	Value creation networks
2	Organization of smart factories	The cloud	Direct effects on the environmental dimension	Manufacturing technologies
3	Business model	Big data and analysis	Direct effects on economical dimension	Global manufacturing impacts
4	Product development	Autonomous robots	Indirect effects on the social dimension	Product lifecycles
5	Equipment	Augmented reality	Indirect effects on economical dimension	
6	Sustainable manufacturing processes	Cybersecurity	Indirect effects on the environmental dimension	
7	Human factor	Horizontal and vertical system integration		
8		Additive manufacturing		
9		The Industrial IoT		

- Global manufacturing impacts are based on research on the effects of manufacturing on society, the environment, and the economy throughout the world [5].

Sustainable manufacturing strategy implementation can be aided by the development of several indicators or parameters that can assess the sustainability of a process or system, and procedures (design strategies that improve sustainability) as well as policies that can influence company cultures and produce suitable internal conditions that favour sustainability, and stakeholder engagement for sustainability and technologies. Global manufacturing specifically involves all the efforts put into the conversion of a product design to a final product [7, 9].

2.4 Industry 4.0

The phrase "Industry 4.0" refers to the technological standpoint of the Cyber Physical-System (CPS), which is integrated into many industrial processes of manufacturing or fabrication, as well as the integration of the technology of the Internet of Things (IoT) into these same factories or industrial processes. Smart factories and products are used in production processes as evidence of this inclusion. In a CPS-created social network, the resources—human, material (machines), and capital—are connected vertically while the horizontal ties span the businesses taking part in the value chain of the CPS network [8, 10].

Manufacturing technology that has been created powers this sophisticated industrial system. For this analysis, we shall take into account the following "pillars of technological development":

- Autonomous Robots—With increased autonomy, versatility, and interaction with humans and other robots, robots in production are becoming increasingly valuable [11–13].
- Simulation—This plays a major role in prototyping major products, services, and systems that cost a lot to build prototypes for testing as well as enhancing factory operations using virtual models of the factory system [14].
- Augmented Reality (AR)—This is a major aspect of the virtualization technology used in many prototyping simulations. This has played a major role in improving this technology in addition to its many other applications [15].

There are other pillars of technological development which include: Cybersecurity, Big data, and analytics [9, 16], horizontal and vertical integration, additive manufacturing (AM) as well as Internet of Things (IoT). The conversion of a manufacturing facility into a smart industry necessitates the vertical and horizontal integration of all industrial facilities, suppliers, and users. The increased transparency of the manufacturing processes and supply chain activities made possible by Industry 4.0 technologies and Information and Communication technology platforms aid in the efficient use of all the energy and resources. These interconnected activities generate massive amounts of information on every facet of manufacturing. All of these data will be turned into knowledge that can be used to construct strategies from the viewpoints of the economy, society as well as the environment [17]. Sustainable manufacturing is currently being addressed by industry and academic specialists using industry 4.0 technologies. As illustrated in Fig. 3, Industry 4.0 technologies will handle environmental issues including environmental preservation, climate change as well as resource depletion. Industry 4.0 now has a different viewpoint than before, which historically focused on digitizing processes and gaining advantages. Industry 4.0 technologies must, however, be completely coherent and converged in order for this to be implemented. The Industry 4.0 revolution's key technology enablers are depicted in Fig. 3. These technologies are anticipated to be crucial in ensuring sustainable production in the twenty-first century.

Fig. 3 Technologies of
Industry 4.0
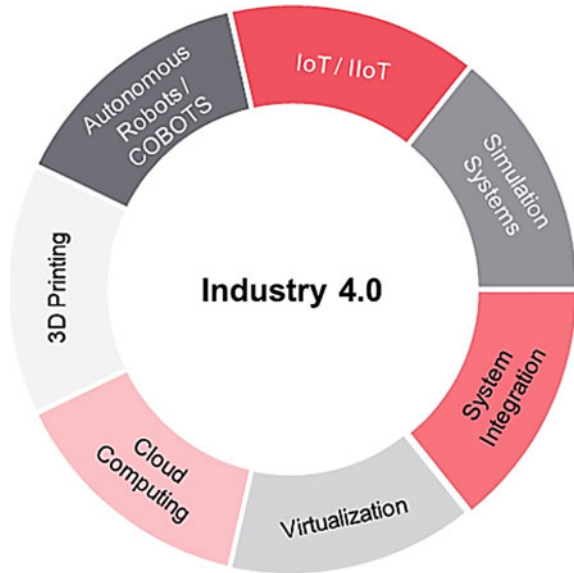
2.5 Sustainable Manufacturing (AM) and Industry 4.0

Sustainability and digitalization are two concerns that have an impact on every phase
of the manufacturing process. Every information technology possesses a cycle of life
from its creation/production to retirement/end of life, this is regarded as the life cycle
of the IT system. Life cycle management strategies including assembly and disas-
sembly, refabrication, recycling, etc., are incorporated into both systems. Industry
4.0 has value and potential to move the industry toward sustainable practices [18].
The goal of sustainable manufacturing is to create a perfect manufacturing process
whereby both raw materials and by-products are recyclable, reused, and have the
capacity to retain value [19]. In order to accomplish this, Industry 4.0 integrates the
simplicity and dependability of AI and ICT technologies to enhance the efficiency
of the machining process [20], enhance process modelling, recognise and evaluate
prospects, in addition to establish and reconfigure business concepts to yield the
best implementation results. Designing and developing manufacturing procedures
and goods with zero environmental effect and complete product recyclability are
the core goal of sustainability. While technical developments facilitate the develop-
ment of new processes and products, digital technologies must be integrated with
sustainability to achieve sustainable development. As a result, manufacturers are
concentrating on this convergence in order to reap the full benefits of Industry 4.0,
or sustainable production [21]. Depending on the goal and application, sustainable
manufacturing is viewed from a variety of angles; nevertheless, among industrial
players, the angles that are most frequently acknowledged are Technology, Society,
Performance Management, Environment as well as Economy. The three pillars of

sustainable development—Economy, Environment, as well as Society—among the
aforementioned dimensions are frequently referred to as the "Triple Bottom Line"
as shown in Fig. 4 [22].

3   Conclusion

From a business standpoint, Industry 4.0, made possible by Machine Learning
(ML), IoT, Machine Vision (MV), data analytics, as well as artificial intelligence
(AI) facilitates the generation of equipment at significantly lower prices through
the improvement of energy efficiency and resources. Manufacturers are constantly
looking for ways to lower the operational expenses associated with their manufac-
turing processes. The tactics created by the manufacturers to save costs, nevertheless,
are constantly hampered by issues like waste formation (which results from both
production and maintenance operations), productivity loss, and higher energy usage.
Manufacturers will be able to see the optimized and non-optimized processes in their
value chain with the correct Industry 4.0 technology installation. Such technologies
will give manufacturers the ability to properly size their facilities, employees, and
resources while also revealing process flaws that can be closed, lowering maintenance
costs and boosting productivity. Aside from this, measures like using 3D printing
and new, cleaner production techniques will also assist manufacturers in eliminating
waste.

In many businesses especially industry-centred businesses that focus on manufacturing or production, there has been little interest in the role that the industrial revolution of the information age can play in improving manufacturing processes towards sustainability. However, there is considerable growth in manufacturing processes that are computerized to implement ICT towards enhancing productivity. This development is unfortunately limited mainly to first and second-world countries, while so many particularly in Africa have suffered huge setbacks in this regard. It is hoped that this research will create awareness and steady the palms of those whose hands are on deck in the manufacturing industry of the essence of this industrial revolution on the improvement of manufacturing in general.

References

1. Borges AFS, Laurindo FJB, Spínola MM, Gonçalves RF, Mattos CA (2021) The strategic use of artificial intelligence in the digital era: systematic literature review and future research directions. Int J Inf Manage 57:102225. https://doi.org/10.1016/J.IJINFOMGT.2020.102225
2. Mikalef P, Fjørtoft SO, Torvatn HY (2019) Developing an artificial intelligence capability: a theoretical framework for business value. In: Lecture notes in business information processing (LNBIP), vol 373, pp 409–416. https://doi.org/10.1007/978-3-030-36691-9_34
3. Jamwal A, Agrawal R, Sharma M, Giallanza A (2021) Industry 4.0 technologies for manufacturing sustainability: a systematic review and future research directions. Appl Sci 11(12):5725. https://doi.org/10.3390/app11125725
4. Mikalef P, Pateli A (2017) Information technology-enabled dynamic capabilities and their indirect effect on competitive performance: findings from PLS-SEM and fsQCA. J Bus Res 70:1–16. https://doi.org/10.1016/J.JBUSRES.2016.09.004
5. Machado CG, Winroth MP, Ribeiro da Silva EHD (2020) Sustainable manufacturing in Industry 4.0: an emerging research agenda. Int J Prod Res 58(5):1462–1484. https://doi.org/10.1080/00207543.2019.1652777
6. Vinuesa R, Azizpour H, Leite I et al (2020) The role of artificial intelligence in achieving the sustainable development goals. Nat Commun 11:233. https://doi.org/10.1038/s41467-019-14108-y
7. Zamponi ME, Barbierato E (2022) The dual role of artificial intelligence in developing smart cities. Smart Cities 5(2):728–755. https://doi.org/10.3390/smartcities5020038
8. Slob N, Hurst W (2022) Digital twins and industry 4.0 technologies for agricultural greenhouses. Smart Cities 5(3):1179–1192. https://doi.org/10.3390/smartcities5030059
9. Bai C, Dallasega P, Orzes G, Sarkis J (2020) Industry 4.0 technologies assessment: a sustainability perspective. Int J Prod Econ 229:107776. https://doi.org/10.1016/J.IJPE.2020.107776
10. Ghasemaghaei M (2021) Understanding the impact of big data on firm performance: the necessity of conceptually differentiating among big data characteristics. Int J Inf Manage 57. https://doi.org/10.1016/j.ijinfomgt.2019.102055
11. Dwivedi YK et al (2021) Artificial intelligence (AI): multidisciplinary perspectives on emerging challenges, opportunities, and agenda for research, practice and policy. Int J Inf Manage 57. https://doi.org/10.1016/j.ijinfomgt.2019.08.002

12. Vinuesa R et al (2020) The role of artificial intelligence in achieving the sustainable development goals. Nat Commun 11(1):1–10. https://doi.org/10.1038/s41467-019-14108-y
13. Gupta M, George JF (2016) Toward the development of a big data analytics capability. Inf Manag 53(8):1049–1064. https://doi.org/10.1016/J.IM.2016.07.004
14. Bag S, Pretorius JHC, Gupta S, Dwivedi YK (2021) Role of institutional pressures and resources in the adoption of big data analytics powered artificial intelligence, sustainable manufacturing practices and circular economy capabilities. Technol Forecast Soc Change 163:120420. https://doi.org/10.1016/J.TECHFORE.2020.120420
15. Frazzon EM, Freitag M, Ivanov D (2021) Intelligent methods and systems for decision-making support: toward digital supply chain twins. Int J Inf Manage 57. https://doi.org/10.1016/j.ijinfomgt.2020.102281
16. Mikalef P, Pappas IO, Krogstie J, Giannakos M (2018) Big data analytics capabilities: a systematic literature review and research agenda. Inf Syst E-bus Manag 16(3):547–578. https://doi.org/10.1007/S10257-017-0362-Y
17. Li BH, Hou BC, Yu WT, Lu XB, Yang CW (2017) Applications of artificial intelligence in intelligent manufacturing: a review. Front Inf Technol Electron Eng 18(1):86–96. https://doi.org/10.1631/FITEE.1601885
18. Bryn Bennett The fundamental theories behind artificial intelligence. Better programming. https://betterprogramming.pub/the-fundamental-theories-behind-artificial-intelligence-b1fa9d75c552. (Accessed 13 Jan 2022)
19. Jarrahi MH (2018) Artificial intelligence and the future of work: human-AI symbiosis in organizational decision making. Bus Horiz 61(4):577–586. https://doi.org/10.1016/J.BUSHOR.2018.03.007
20. Verma S, Sharma R, Deb S, Maitra D (2021) Artificial intelligence in marketing: systematic review and future research direction. Int J Inf Manag Data Insights 1(1):100002. https://doi.org/10.1016/j.jjimei.2020.100002
21. Karuppusamy P (2021) Machine learning approach to predictive maintenance in manufacturing industry—a comparative study. J Soft Comput Paradigm 2(4):246–255
22. Bashar A (2019) Intelligent development of big data analytics for manufacturing industry in cloud computing. J Ubiquit Comput Commun Technol (UCCT) 1(01):13–22

FPGA Implementation of Efficient 32-Bit 3-Operand Addition Using Kogge–Stone (KS) Parallel Prefix Adder

Masarla Rajesh and B. Bala Tripura Sundari

Abstract For performing efficient modular arithmetic operations, several cryptographic and pseudorandom bit generator (PRBG) algorithms utilize a 3-operand binary adder as the primary functional unit. The Carry Save Adder is the most common adder used for performing the three-operand extension (CS3A). On the other hand, the ripple-carry step of CS3A results in a significant delay while transmitting the output signals. Due to the lengthy delay, it influences the performance of MDCLG architecture. For performing three-operand addition, two-operand adders, such as Kooge Stone (KSA), can be used. This will decrease the critical route latency, delay, and area compared to other parallel prefix adders. The proposed high-speed and space-efficient adder architecture for performing three-operand binary operations includes carry-prefix computation logic after performing the pre-compute bitwise addition. The proposed adder design reduces the adder latency while consuming less area and power. A Kogge–Stone parallel prefix adder has been used to develop a novel architecture for the proposed 8-bit, 16-bit, and 32-bit three-operand adders. The proposed architecture is implemented by using Verilog coding, and further, the power and delay extraction has been performed by using a Xilinx tool. The proposed architecture has been developed by using the MDCLCG method with the three-operand adder, and further, the proposed architecture is proven with respect to delay as well as area and power.

Keywords Parallel prefix adder · Kogge–Stone · Carry save two and three operands

M. Rajesh (✉) · B. Bala Tripura Sundari
Department of Electronics and Communication Engineering, Amrita School of Engineering,
Amrita Vishwa Vidyapeetham, Coimbatore, India
e-mail: rajesh.masarla@gmail.com

B. Bala Tripura Sundari
e-mail: b_bala@cb.amrita.edu

1   Introduction

The cryptographic algorithms must be developed on hardware to obtain the highest possible system efficiency while ensuring the security. Many cryptographic algorithms employ modular arithmetic operations, such as modular addition, multiplication, and exponentiation, as their arithmetic operations. As a result, the effectiveness of the approach for performing crypt analysis is dependent on the efficient execution of the congruential modular arithmetic operation. The Montgomery algorithm, the core of which relies on 3-operand binary addition, is the method that proves to be the most productive when it comes to performing the modular operations of multiplication and exponentiation. The linear congruential generator (LCG)-based pseudorandom bit generators (PRBG) [1], such as linked linear congruential generators (CLCG), modified dual-linear congruential generators (MDCLCG), and coupled variable input LCG (CVLCG), are available. The role of PRBG is that it is not feasible to produce real random numbers from the deterministic things like computers, and hence, a technology known as PRBG has been developed to generate random bits. From all of the LCG algorithms and other extended PRBG algorithms, the modified dual-CLCG, also known as MDCLCG, is considered to be the safest and most random model. If n is less than 32 bits, it is unpredictable in terms of polynomial time and security. As a result, an increase in operand size results in leveraging an improvement in the level of security offered by MDCLCG. However, due to the fact that its hardware design is comprised of two comparators, four multiplexers, and four adders with three operands and modulo $2n$, both the area and the critical path latency grow linearly. Therefore, the performance of the MDCLCG can be made better by implementing the three-operand adder in a way it remains both efficient and effective [1].

To perform 3-operand binary addition, one adder with three operands or two adders with two operands may be used. For this purpose, Carry Save Adder (CS3A) is a technique that is extensively used as it is both area-efficient and effective in performing 3-operand binary addition and in performing modular arithmetic operations and is also used in cryptography techniques and PRBG techniques. CS3A is usually a power efficient adder, and because of that, it is widely used in binary addition [2]. The operation of Carry Save Adder is performed by adding two or more bits and then obtaining sum and carry results independently. The sum bits are generated without considering the previous carry bits, and these carry bits are considered separately, and then, in the next step these independent sum and carry bits are added to get final results. On the other hand, the greater delay while propagating the carry signal through ripple-carry stages of Carry Save Adder (CS3A) has a significant impact on the operation of the MDCLCG technique. A parallel prefixed 2-operand adder like Kooge Stone (KSA) is also capable of performing three-operand binary addition, which may be utilized to reduce the latency on the critical route. Normally, parallel prefix adders have less delay due to its less waiting time of carry for next addition but area consumption is more but Kogge–Stone parallel prefix adder which performs parallel arithmetic operations [3]. It brings the critical route latency down, as well as

the area. As a result, it is essential to design an effective architecture in order to do high-speed 3-operand binary additions with the least amount of hardware resources. Therefore, in this paper, a new adder technique is proposed which is efficient in area and lesser delay. This technique uses pre-computed bitwise addition and then prefix computation of carry signal to execute the 3-operand binary additions. This technique preserves a less amount of gate area and parallelly reduces the propagation delay. In addition, the proposed adder design is realized by using Verilog Hardware Description Language [4]; after that, it is synthesized by using Xilinx FPGA for obtaining the area and power results.

The remaining parts of this article are structured as follows: The operations of a three-operand binary adder are separated and described in Sect. 2. The proposed three-operand adder design and the complexity of its hardware are discussed in Sect. 3. This part not only explains the integration result of the suggested adder architecture but also analyzes the results of other existing adder methodologies. In addition, the proposed adder is implemented in the MDCLCG application in order to assess the performance parameters described in Sect. 4, and then, the final results are compared with the simulated synthesis results depicted in Sect. 5. In addition to this, the proposed design has been prototyped on a Vertex 5 FPGA as it may be validated by using a real-time signal by utilizing the ModelSim. Finally, the proposed research work is concluded in Sect. 6.

2   The 3-Operand Binary Adder Techniques

The most commonly used technique used arithmetic operations in congruential modular structures, and PRBG techniques like CLCG, MDCLCG, and CVLCG are considered for performing the three-operand binary addition. Other LCG-based PRBG methods include CVLCG [5]. It is also possible to implement it by using either a single stage 3-operand adder or dual stage 2-operand adder. The Carry Save Adder, often known as CSA [6], is the most frequently used method to execute the 3-operand addition. The two different phases perform the computation of adding three operands together [7]. First, the individual sum and carry bits are generated for all bits, and then, the sum and carry bits are again added to get the final results.

The array of complete adders is the initial step involved in this process. Each complete adder is responsible for simultaneously computing the "carry and sum" bits by using the three binary inputs a_i, b_i, and c_i. Then, the 3-operand adder's output is further connected to the ripple-carry adder stage and it generates the final "sum signal," which has a size of n bits, and the "carry-out" signal, which has a size of one bit. In the step known as the ripple-carry, the signal "carry-out" is sent via a multiple number of complete adders. As a consequence, the delay increases at a rate proportional to the growth in bit length. Figure 1 illustrates the design of the 3-operand CSA, and a dashed line considers the important route delay. Here, the carry bit plays the vital role in generating the sum bit, and because of that delay, the addition relies on the carry propagated path. This demonstrates that the delay
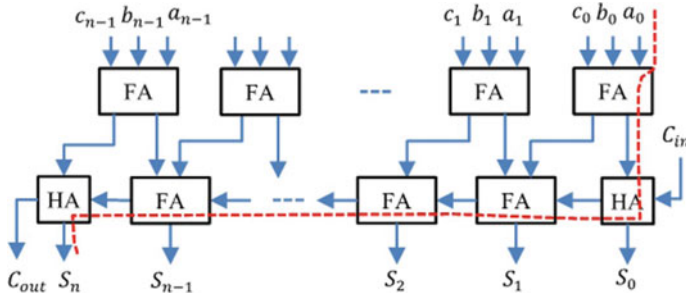
Fig. 1 3-Operand carry save adder (CS3A) [1]

across critical path is dependent on the delay along with the carry propagation of the ripple-carry stage, and the evaluation will be carried out as shown in Eq. 1

$$T_{\text{CS3A}} = (n+1)T_{\text{FA}} = 3T_{\text{X}} + 2nT_{\text{G}} \tag{1}$$

Here, T_{X} indicates the propagation delay of XOR gate and T_{G} indicates the propagation delay of two input gates like AND, OR, NOR, and NAND. One of the most significant drawbacks of the CS3A is that it has a longer critical path latency, which generates longer bit length. This essential propagation route delay has an effect on the total latency of the congruential and PRBG designs, the key component of which is the three-operand adder. As a result, dual stage parallel prefix 2-operand adder is also used in order to reduce the latency along the crucial route. According to the research availability, the fastest two-operand adding algorithms are logarithmic prefix and parallel prefix adders [8]. Six distinct structures are available for these adder approaches; they are Brent–Kung (BK), Sklansky, Ladner–Fischer (LF), Kogge–Stone (KS), and Han–Carlson (HC). Kogge–Stone adder is one of the fastest adders that consume less power when compared to other prefix adders. The hybrid Kogge–Stone adder is extremely appealing for high-speed applications since it requires less space and power than conventional adders. The architecture of Kogge–Stone has a latency expressed as $\log_2 n$, and there are $[n(\log_2 n) - n + 1]$ computation nodes. A regular architecture and a regulated fan-out are also considered as features of this adder. The 16-bit KS parallel prefix adder architecture is shown in Fig. 2.

3   The Proposed 3-Operand Adder Architecture

The fundamental operational unit for performing fast modular arithmetic operations in many algorithms is the 3-operand binary addition. The 3-operand extension is most often implemented by using the Carry Save Adder (CS3A). The RCA stage of the CS3A causes a substantial delay in the output signal transmission (n). As an alternative, a two-operand adder, such as the Kooge–Stone adder (KSA), may be used
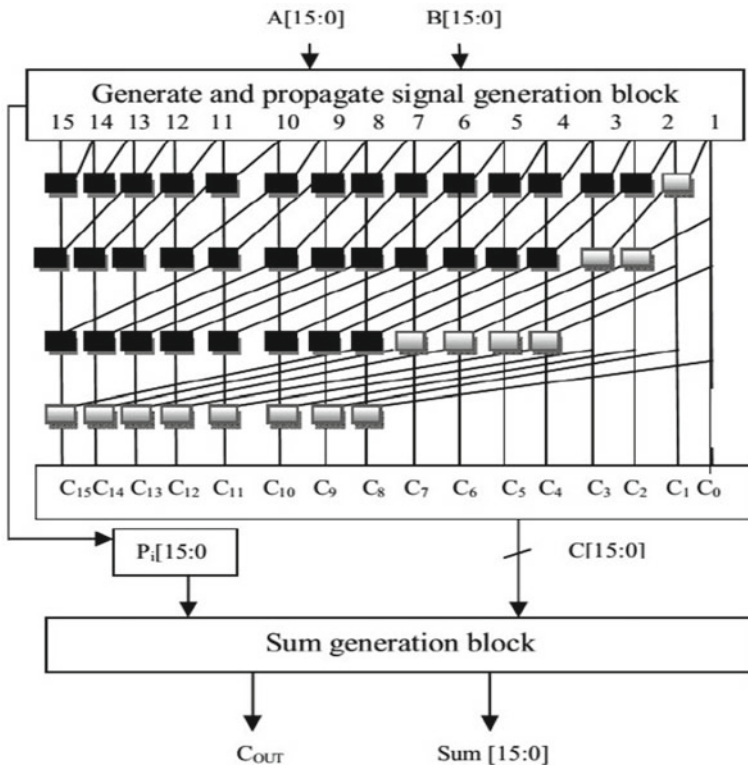
Fig. 2 Structure of 16-bit Kogge–Stone adder (KSA)

instead of other parallel prefix adders to reduce the critical route latency, delay, and area. Basically, the Kogge–Stone parallel approach gives a way for fast carry generation to intermediate stages [9]. In this approach, after executing a bitwise addition, the new high-speed and compact adder uses a carry-prefix calculation mechanism to achieve 3-operand binary addition. The carry-prefix computation logic is used to accomplish three-operand addition, which uses much less gate space while reducing the propagation time. Due to this, the adder latency may be reduced by an order of magnitude while using less space and power with the proposed adder architecture [10]. The proposed architecture for a three-operand adder at 8 bits, 16 bits, and 32 bits will be developed by using a Kogge–Stone parallel prefix adder. In order to achieve a 3-operand addition, a novel adder mechanism and its VLSI design are going to be presented in this section. The considered adder method is known as a parallel prefix adder. For calculating the three-input binary addition, 4-stage structures are used rather than 3-stage structures in the prefix adder. These structures include a logic for performing addition of bits, generation of base logic, logic to propagate and generate (PG), and finally a logic for sum generation. In addition, it contains a sum logic.

The following is a definition of the logical expression of each of these four steps in order:

Stage-1: Logic for addition of bits:

$$S_i' = a_i \oplus b_i \oplus c_i, \tag{2}$$

$$cy_i' = a_i \cdot b_i + b_i \cdot c_i + a_i \cdot c_i \tag{3}$$

Stage-2: Base logic:

$$G_{i:i} = G_i = S_i' \cdot cy_{i-1} \tag{4}$$

$$P_{i:i} = P_i = S_i' \oplus cy_{i-1} \tag{5}$$

Stage-3: PG (propagate and generate) logic:

$$G_{i:i} = G_i = G_{i:k} + P_{i:k} \cdot G_{k-1:j} \tag{6}$$

Stage-4: Sum logic:

$$P_{i:i} = P_i = P_{i:k} \cdot P_{k-1:j} \tag{7}$$

$$S_i = (P_i \oplus G_{i-1:0}) \tag{8}$$

Here, G_i denotes generate signal and P_i denotes the propagate signal. The 3-operand binary adder's proposed VLSI design and its components are shown in Fig. 3. A total of three binary inputs which are having n bits are summed up using the innovative adder method, which is carried out in four distinct steps. The bit addition of these three operands is carried out by using a set of full adders during the first stage (bit-addition logic), and the "carry (cy_i) and sum (S_i)" signals are generated by each full adder, as shown in the highlighted portion of Fig. 3. In Stage-1, the logical blocks for generating the carry (cy_i) and the sum (S_i) signals are developed. Figure 4 depicts the internal logic structure for the bit-addition logic, base logic, and sum logic [1].
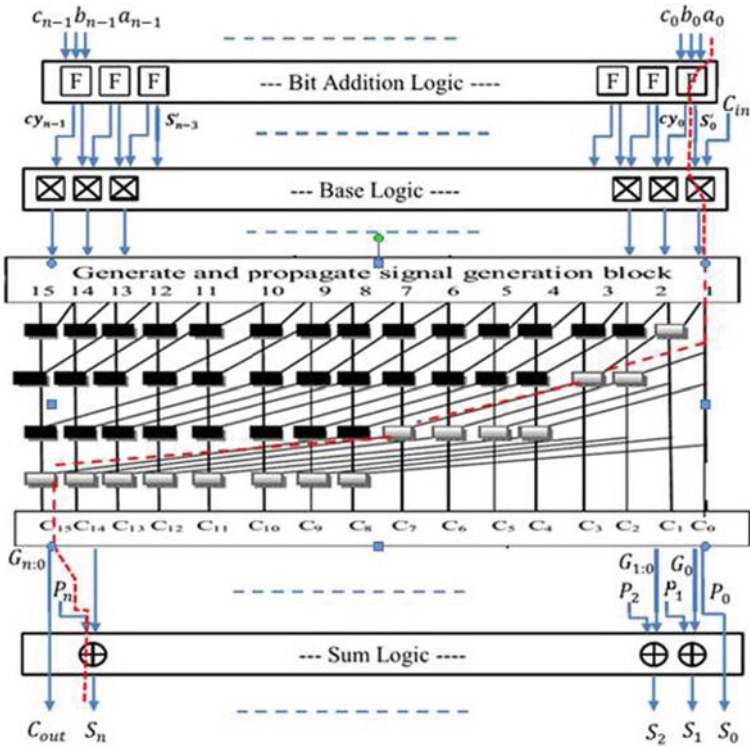
Fig. 3 Proposed three-operand adder using Kooge–Stone prefix adder
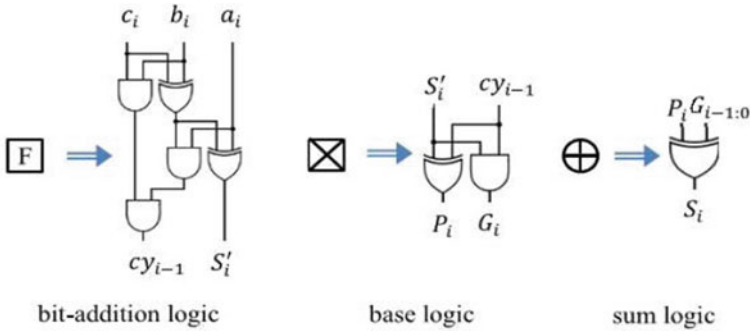
Fig. 4 Architecture of bit-addition logic, base logic, and sum logic [1]

Fig. 5 Architecture of black cell and gray cell for PG logic [1]
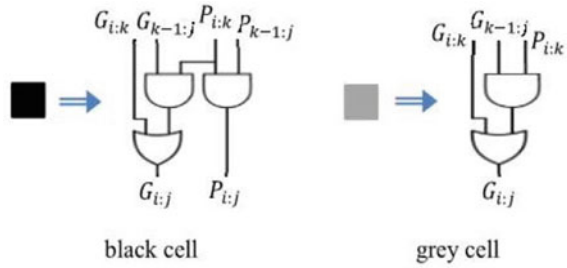
These logics are utilized in the first stage to calculate the propagate (P_i) and generate (G_i) signals for the next stage shown in Fig. 5. Therefore, the suggested adder has multiple number of stages for prefix computation and this carry propagation chain is mostly responsible for proposed adder's critical path delay. The end stage of this architecture is sum logic, where the "sum (S_i)" is calculated by using a log ic $S_i = (P_i \, G_i)$ in which P_i is the carry propagate bits and G_i is the carry generate bit. This expression is derived from the carry propagate P_i bits. The carry-out signal, often known as C_{out}, may be derived in a straightforward manner from the carry generate bit $G_{n:0}$.

4 The Effectiveness of the MDCLCG Architecture When Combined with the Proposed Adder Architecture Performance

The generation of encrypted and decrypted data for avoiding hardware Trojan attacks in digital circuits uses cryptography by involving stream cipher technique [11]. The seed generator for those techniques is known as the pseudorandom bit generator (PRBG). The modified dual-CLCG, also known as MDCLCG, is one of the effective PRBG algorithms currently available, which is considered as an excellent choice for enabling stream cipher-based hardware security. It is also known as MDCLCG. On the other hand, the security level provided by the MDCLCG approach is proportional in a linear fashion to the congruential modulus bit size [12]. The dual-CLCG approach is more secure and effective than LCG-based PRBGs since it requires the dual coupling of four LCGs rather than two LCGs and it generates random bits for every uniform clock cycle. As shown in Fig. 6, the design architecture of MDCLCG technique is involved with LCG. The fundamental computational arithmetic block in LCG is a three-operand modulo-$2n$ adder, which is also the case with the MDLCG method [9]. The MDCLCG architecture described in Fig. 6 is constructed by using four 3-operand modulo-$2n$ CSA, two magnitude comparators, and four multiplexers and registers in addition to these elements. This architecture defines a hardware random number generator, which produces a random number as an output from two comparators [13, 14]. The increased bit size has a negative impact on the performance
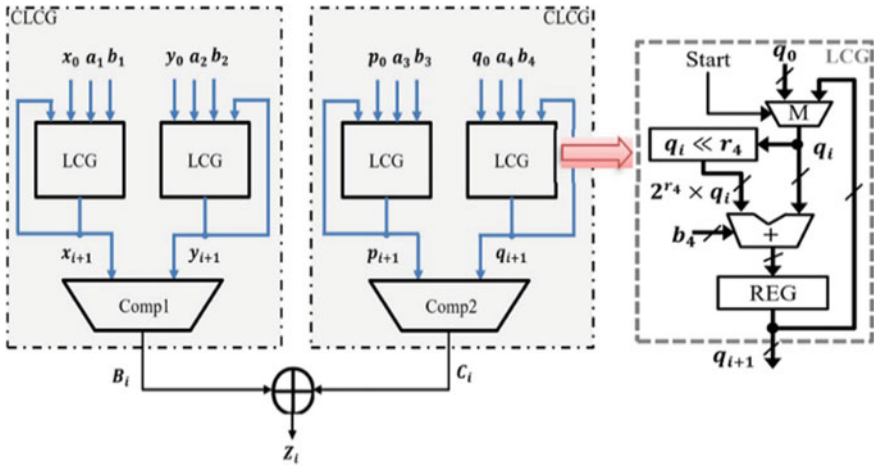
Fig. 6 Architecture of MDCLCG method [1]

of MDCLCG architecture due to its increased propagation delay while computing carry in the CS3A adder. Therefore, the CS3A adder will be replaced with the KS3A and the proposed adder topologies assess the performance metrics of MDCLCG. Likewise, for enabling a fair assessment, the KS3A adder was further modified to produce an architecture for the 32-bit MD.

CLCG, and the design was implemented by using Verilog HDL. The performance metrics have also found to be efficient [15]. In a similar fashion, CS3A and KS3A are involved in the architecture design of the 32-bit MDCLCG with the same coding language Verilog HDL. In addition, each of these designs is synthesized by using the Xilinx environment.

5 Results and Implementations

The proposed three-operand adder was functionally verified on Xilinx FPGA by making use of the Kooge–Stone parallel prefix adder and the MDCLCG method. The 3-operand adder architecture may be developed in 8-bit, 16-bit, and 32-bit architectures, respectively. Figure 7 shows the results of running a simulation using a 32-bit three-operand adder. The RTL schematic of a 32-bit three-operand adder is depicted in Fig. 8. Then, the synthesized results of the 32-bit 3-operand adder are seen in Fig. 9. After that, both Figs. 10 and 11 illustrate the power and delay results of a three-operand binary adder. These are the results which are obtained for the proposed Kogge–Stone 3-operand adder which was implemented using Verilog HDL and synthesized using Xilinx.
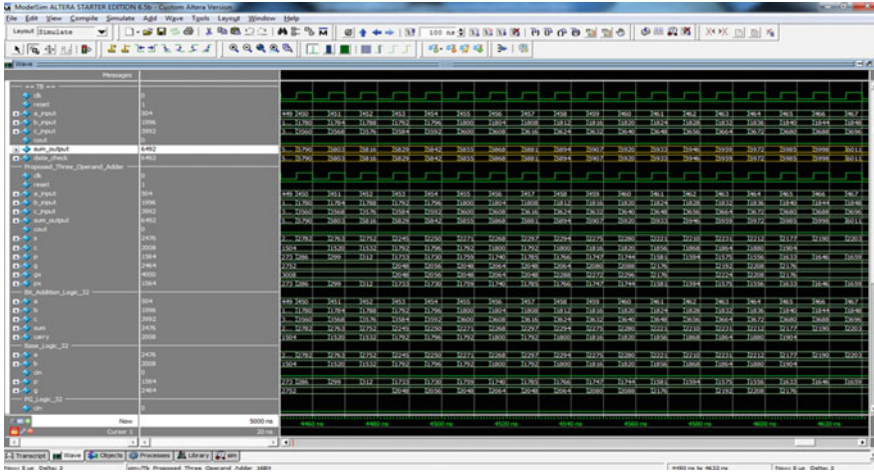
Fig. 7 Simulation results of 32-bit three-operand KSA
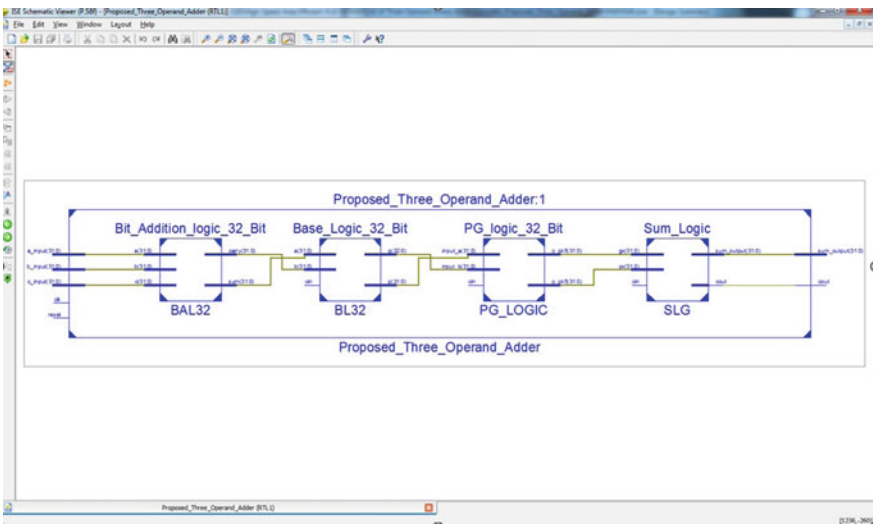
Fig. 8 RTL schematic of 32-bit three-operand KSA

6 Conclusion

For the efficient calculation of modular arithmetic, an area-efficient and high-speed adder mechanism and its associated VLSI design have been developed in this study to execute three-operand binary addition. It is a parallel prefix adder with a four-level structure to add three input operands simultaneously. As a result, the proposed architecture shows reduced delay along critical path, less Area Delay Product (ADP), and
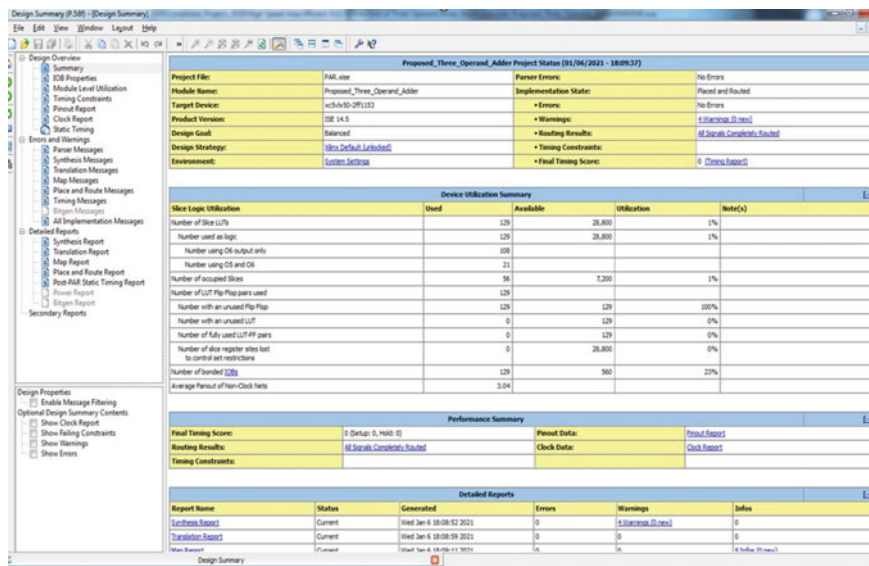
Fig. 9 Synthesize results of 32-bit three-operand KSA
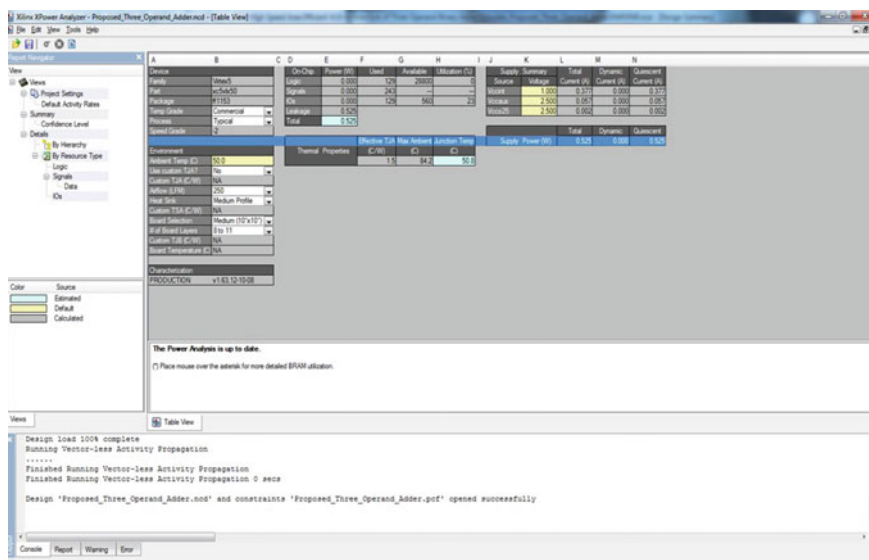
Fig. 10 Power result of 32-bit three-operand KSA
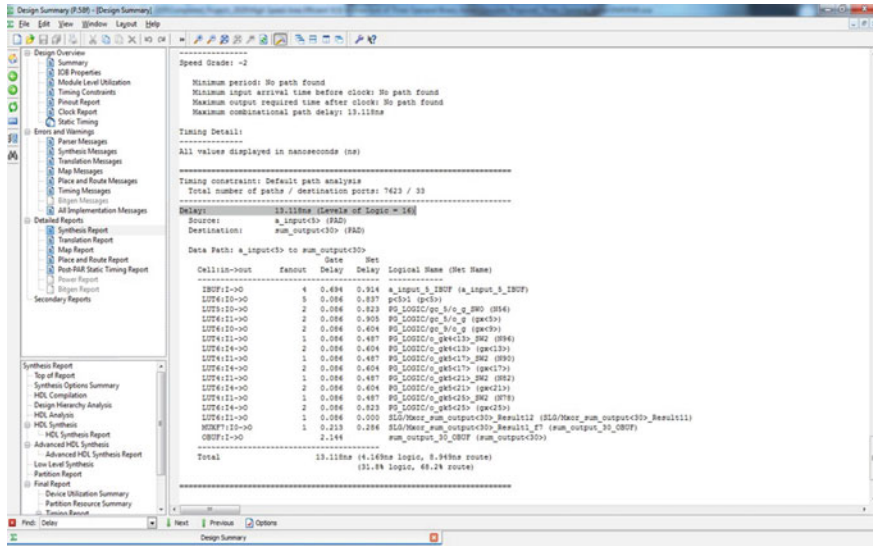
Fig. 11 Delay report of 32-bit three-operand KSA

also less Power Delay Product (PDP). The hybrid Kooge–Stone 2-operand adder (KS2A) idea is expanded to implement a hybrid Kooge–Stone 3-operand adder (KS3A) architecture for comparative purposes. Verilog HDL is used to implement the KS3A and CS3A by using same coding language as the proposed adder design. The reason behind implementing both KS3A and CS3A is to differentiate that the KS3A delivers better performance in terms of area, speed, and power. In addition, Xilinx FPGA is used to generate all of these designs in order to determine their area, timing, and power for various word sizes. In addition, the proposed adder that uses less area has a shorter timing route and dissipates less power than the C3A adder. Furthermore, the proposed adder has much lower product of area delay and power delay than previous 3-operand adder approaches. For further validation, the proposed 32-bit MDCLCG architecture was provided with a proposed adder by substituting its CS3A architecture, and the design was dumped on a FPGA device. For designing a faster data transmission, the proposed adder-based MDCLCG has been used.

References

1. Panda AK, Palisetty R, Ray KC (2020) High-speed area-efficient VLSI architecture of three-operand binary adder. IEEE Trans Circ Syst I Regul Pap 67(11):3944–3953. https://doi.org/10.1109/TCSI.2020.3016275
2. Mahalakshmi R, Sasilatha T (2013) A power efficient carry save adder and modified carry save adder using CMOS technology. In: 2013 IEEE international conference on computational intelligence and computing research, pp 1–5. https://doi.org/10.1109/ICCIC.2013.6724189

3. Daphni S, Vijula Grace KS (2021) Design an area efficient Kogge stone adder using pass transistor logic. In: 2021 Third international conference on intelligent communication technologies and virtual mobile networks (ICICV), pp 614–618. https://doi.org/10.1109/ICICV50876.2021.9388489

4. Padmanabhan TR, Bala Tripura Sundari B (2004) Introduction to Verilog. In: Design through Verilog HDL. IEEE, pp 11–29. https://doi.org/10.1002/0471723002.ch2

5. Panda AK, Ray KC (2020) A coupled variable input LCG method and its VLSI architecture for pseudorandom bit generation. In: IEEE transactions on instrumentation and measurement, vol 69, no 4, pp 1011–1019. https://doi.org/10.1109/TIM.2019.2909248

6. Simson A, Deepak S (2021) Design and implementation of high speed hybrid carry select adder. In: 2021 International conference on advances in electrical, computing, communication and sustainable technologies (ICAECT), pp 1–6. https://doi.org/10.1109/ICAECT49130.2021.9392452

7. Koyada B, Meghana N, Jaleel MO, Jeripotula PR (2017) A comparative study on adders. In: 2017 international conference on wireless communications, signal processing and networking (WiSPNET), pp 2226–2230. https://doi.org/10.1109/WiSPNET.2017.8300155

8. Han T, Carlson DA (1987) Fast area-efficient VLSI adders. In: 1987 IEEE 8th symposium on computer arithmetic (ARITH), pp 49–56. https://doi.org/10.1109/ARITH.1987.6158699

9. Tapasvi B, Sinduri KB, Lakshmi BGSSB, Kumar NU (2015) Implementation of 64-bit Kogge Stone carry select adder with ZFC for efficient area. In: 2015 IEEE international conference on electrical, computer and communication technologies (ICECCT), pp 1–6. https://doi.org/10.1109/ICECCT.2015.7226154

10. Abhiram T, Ashwin T, Sivaprasad B, Aakash S, Anita JP (2017) Modified carry select adder for power and area reduction. In: 2017 International conference on circuit, power and computing technologies (ICCPCT), pp 1–8. https://doi.org/10.1109/ICCPCT.2017.8074371

11. Anahita G, Krishnapriya KPM, Shiva R, Mohan N (2018) HD-sign: hardware based digital signature generation using true random number generator. Int J Eng Technol 7:147. https://doi.org/10.14419/ijet.v7i3.8.16850

12. Ramapragada KST, Netla AKR, Chattada PK, Manickam B (2021) Design and FPGA implementation of high-speed area and power efficient 64-bit modified dual CLCG based pseudo random bit generator. In: 2021 IEEE international symposium on smart electronic systems (iSES), pp 93–98. https://doi.org/10.1109/iSES52644.2021.00032

13. Mohan K, Devi A, Nirmala Sethumadhavan M, Santhya R (2018) A selective generation of hybrid random numbers via Android smart phones. Int J Pure Appl Math 118:311–316

14. Katti RS, Srinivasan SK (2009) Efficient hardware implementation of a new pseudo-random bit sequence generator. In: 2009 IEEE international symposium on circuits and systems, pp 1393–1396. https://doi.org/10.1109/ISCAS.2009.5118025

15. Karuppusamy P (2019) Design and analysis of low-power. High-speed Baugh Wooley multiplier. J Electron 1(02):60–70

Automatic Mulching Machine

C. B. Yughander, G. Raghul, S. Seralathan, and K. P. Peeyush

Abstract Mulching is a long-standing agricultural practice that entails spreading a layer of organic matter around plants to shield their roots from heat, cold, or drought, as well as to keep the crop clean. Mulching provides its own set of benefits like retention of soil water content, protecting the soil from erosion, harsh winds, hot sunshine, and overall damage due to other environmental and external factors. In recent decade, the demand for mulch laying machine has been drastically increased with the abovementioned benefits. However, it is a very labour-intensive process if done manually, thus the need for an automatic one. In this project, we have prototyped an automatic mulching machine. Initially, a software model was designed using Autodesk Fusion 360. The hardware modelling was done with the help of an Arduino, a Bluetooth module, slider-crank mechanism, and the interface of hardware with software was done using a mobile app.

Keywords Embedded systems · Internet of things · Mulching machine · Slider-crank mechanism · Arduino · Bluetooth module

1   Introduction

Agriculture, together with its linked sectors, is indisputably India's largest source of income, as well as one of the largest job-creating sectors, particularly in our nation's vast and widespread village areas. It also makes a substantial contribution to the income and trade of our country and its GDP. But in recent decades, India has been gradually declining in being an effective producer of food and raw materials. We, as a country, have struggled in coming up with effective solutions in combating the

C. B. Yughander (✉) · G. Raghul · S. Seralathan · K. P. Peeyush
Department of Electronics and Communication Engineering, Amrita School of Engineering, Amrita Vishwa Vidyapeetham, Coimbatore, India
e-mail: cbyughander@gmail.com

K. P. Peeyush
e-mail: kp_peeyush@cb.amrita.edu

various issues surrounding agriculture, leading to inflation and more sensitive consequences like farmers' suicide. In terms of food security, rural job opportunities, and environmentally sustainable innovations such as soil protection and natural resource management, the protection of biodiversity and eco-friendly agricultural activities are extremely important for substantial rural development.

To accelerate food and other agricultural production, there is an immediate need to introduce innovative ideas using technology, such as modern irrigation methods and automated machineries. New methods are required to push pre-existing efficient farming methods even further, more efficiently utilize inputs, and diversify cropping patterns towards a more sustainable and higher-value cropping methods. These are all knowledge-filled changes and ideas that necessitate not only an extensive research and extension system and experienced farmers, but also a revised interface where the focus is on mutual data exchange, bringing benefits to everyone. Agriculture extension, in conjunction with adequate infrastructure, is critical to agricultural growth. And these are just few of the many techniques that can be employed as technologies on an actual agricultural field. Mulching is one such technique, which has been extensively used by several farmers in the recent years to combat the challenges faced on field.

Traditionally, mulching has been a very labour-intensive process if done manually, as it requires a lot of huge machineries that need to be operated by the farmers using either heavy-duty motors or cattle. In this project, we aim to make this process less labour-intensive by prototyping an automated mulching machine. We combine the fields of Embedded Systems and Internet of Things by using Arduino IDE, a mobile application and Bluetooth module to interconnect the machine with the user mobile to provide an innovative solution for the problem at hand.

2   Literature Review

A line-follower bot is proposed in [1] for agricultural application, which could be used for irrigation as an effective solution, both in terms of reducing cost and minimizing water loss. This agricultural bot is easily operable and is linked with a microcontroller, along with water tank and pump. The field to be watered by the bot can be of any dimension or size with all the vegetation placed in a predetermined path. In the work done [2], an integrated antenna scheme is capable of parallel operation of near-field communication (NFC) and dual-band ultra-high frequency (UHF, 920–925 MHz)/2.45 GHz radio frequency identification (RFID) functions, whereby the NFC and UHF RFID modules read the universal identification (UID) of NFC and UHF RFID tags. The data is then sent to a cloud server and can be viewed on smartphones via the Blynk phone app with the help of Internet of Things.

The works in [3] and [4] have both proposed IoT-based solutions in their research papers. In [4], an Internet of Things-based hospital management system for the people affected with COVID 19, for handling their services, monitoring, and treatment workflow. In this case, shared access will help in the monitoring of a patient's

health by making it visible to several doctors, researchers, and the government simultaneously. Moving on, the main components used in the research cited in [3] are the pressure sensor (MPX5700AP), a microcontroller (Wemos D1 mini), a notification system (Blynk), and a monitoring system (ThingSpeak). When the air pressure sensed does not meet the desired standard, the Blynk app notifies the user via the Android smartphone.

The main goal of [5] was to create a working hardware model for an Internet of Things-based open precision farming solution, which increases the efficiency of farming by minimizing the wastage of water and also keeping an eye on the fertility of the soil. When the user receives a Twitter notification, he can control the flow of water by operating the solenoid valve using Blynk application. The paper [6] presented the design of a drive bot that helps in sowing of seeds in vegetative fields without manual intervention of humans by following a predetermined path using the field area and dimensions like length, breadth, and seed spacing intervals as the inputs from the user. The seed sowing mechanism had also performed admirably by a factor of two.

The authors in [7] presented a working model, which is basically a management system for agricultural fields that can be controlled using an application on a mobile. The survey by in [8] gave us an insight on how Internet of Things can impact the development in agriculture and irrigation. Similarly, [9] provided us with some additional information on how embedded systems can be used in automatic agricultural machines. In [10], the authors have designed an automatic path finding bot for hospital environment. The bot detects the objects in its surroundings and finds an optimal route to the destination from the starting point. Similarly in [11], the authors have built a pole climbing bot with the help of an Android-based app called as MIT app inventor. They have used a Bluetooth module to interface the Arduino and the applications in the mobile phone. In [12], a software simulation of a smart glove using flex sensors integrated with Arduino has been presented.

The goal of the work cited in [13] is to create a robotic dolphin with a new mechatronic configuration based on the slider-crank technique, which pledges a considerably large manoeuvrability, efficiency, fast swimming, and low power consumption when compared to other similar mechanisms. The developed mechanism's motion control has been established on an ARM-based embedded system using DC and servo motors. The design of a cost-efficient agricultural bot for seed sowing is described in [14]. When the DC motor is turned on, it rotates the crank, which pushes the injection pole connected to the slider down towards the ground, implanting the seeds.

3 Methodology

The aim of our project is to design and implement a machine that will lay mulch sheet over the furrow for certain distance, specified by the user. Following the machine's movement, the mulching sheet is dragged along and laid on the surface of the field. The aluminium arms push soil onto the sides of the mulching sheet to hold it in place.

There is a crank and slider mechanism to punch hole into the mulch sheet after it is laid on the field. To transform rotational motion into reciprocating linear motion and/or vice versa, a slider-crank mechanism can be used. This mechanism is made up of three major components: A crank—rotating disc, the slider—which moves in a fixed plane, and the connecting rod—which links the crank and the slider. This mechanism is a four-bar chain kinematic inversion with one sliding pair and three turning pairs. The path length is the total distance travelled by the slider between its two farthest positions. When the axes of the crank and slider are parallel, this distance is equal to twice the span of the crank. The process and the brief of methodology involved in achieving the objective are shown in Fig. 1.

Fig. 1 Methodology flowchart
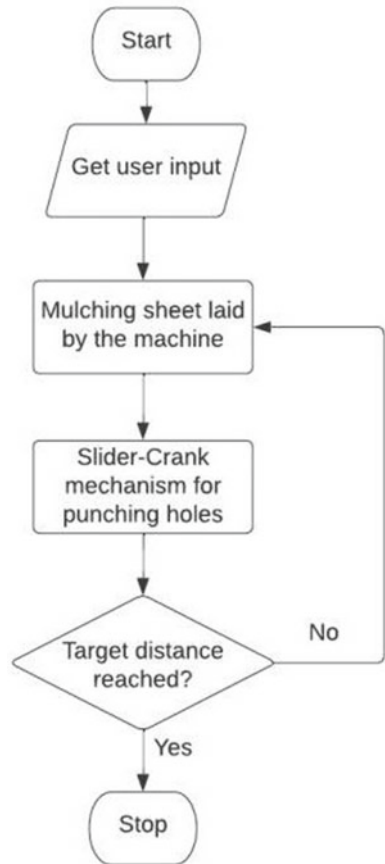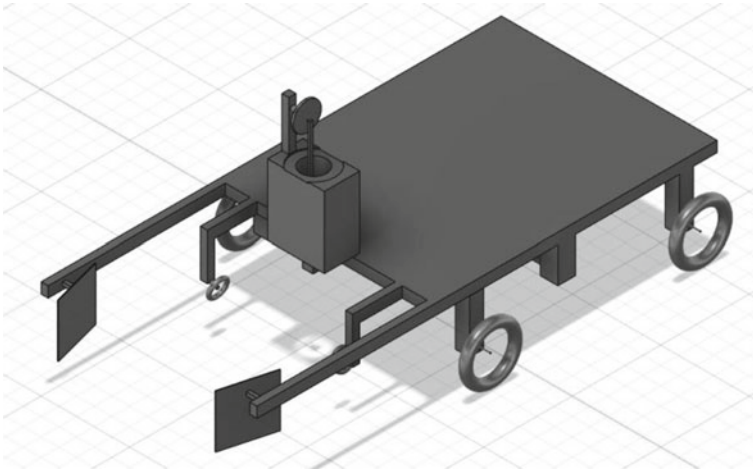
Fig. 2 Fusion 360 software—3D model

3.1 Software Modelling

In our project, we have used several tools available in Fusion 360 to make a simple design of the vehicle chassis of our automatic mulching machine as shown in Fig. 2. We also used Bluetooth RC controller application to control the automatic mulching machine after interfacing the hardware and hardware, details of which are given in subsequent chapters.

3.2 Hardware Modelling

Several components were used to build the hardware prototype of our model for automatic mulching machine, which include: Arduino UNO, HC-05 Bluetooth module, L298N H-bridge motor driver, 12 V DC battery, 12 V DC 100 RPM side shaft motor, 12 V DC 60 RPM motor, crank and slider, roller wheels of diameter 2 inches, chassis wheels of diameter 4 inches and miscellaneous. Figures 3 and 4 show the final hardware assembly and circuitry of our model. Figure 5 shows the slider-crank mechanism implemented for the hole punching mechanism.

3.3 Software Interface

We can use the formula given below to find the amount of time the machine has to run before it halts after travelling the desired distance.
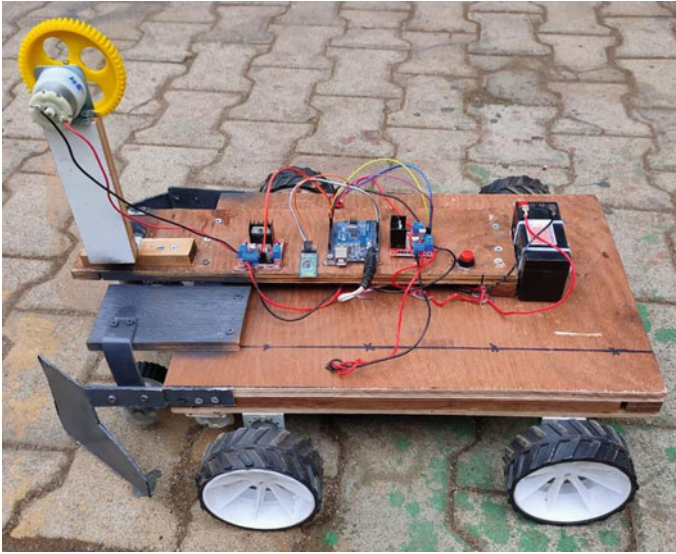
Fig. 3 Automatic mulching machine—hardware model
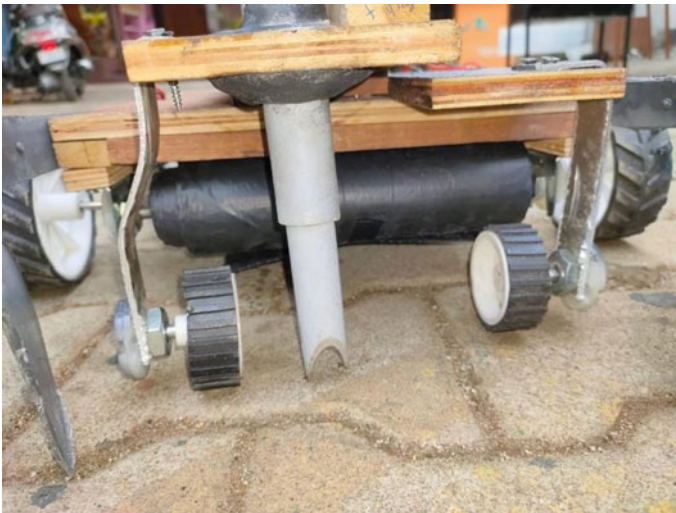
Fig. 4 View of the mulching sheet, hole punching mechanism, and roller wheels

$$S = \frac{2\pi r \times N}{60} \tag{1}$$

where S is the speed of the vehicle in m/s, N is rotational speed of motor in RPM, and r is the radius of the wheel. We also know that the time, distance, and speed

Fig. 5 Slider-crank mechanism—hardware model

relation is given by the formula as in (2).

$$t = \frac{d}{S} \tag{2}$$

where t is the time in seconds, d in the distance in metres, and S is the speed in metres per second. Combining both the Eqs. (1) and (2), we can get the formula for calculating the time taken as given in (3), for our machine to travel the desired distance, which can be entered in the Arduino IDE source code and uploaded to the microcontroller before starting the operation.

$$t = \frac{d \times 60}{2\pi r \times N} \tag{3}$$

Since we know that the motor RPM is 100 and the radius of the wheel is 0.0508 m (4 inches diameter), we can substitute those constant values in the formula in (3) to simplify it to the form in (4).

$$t = \frac{d \times 60}{31.9185}$$

$$t = 1.88d \tag{4}$$
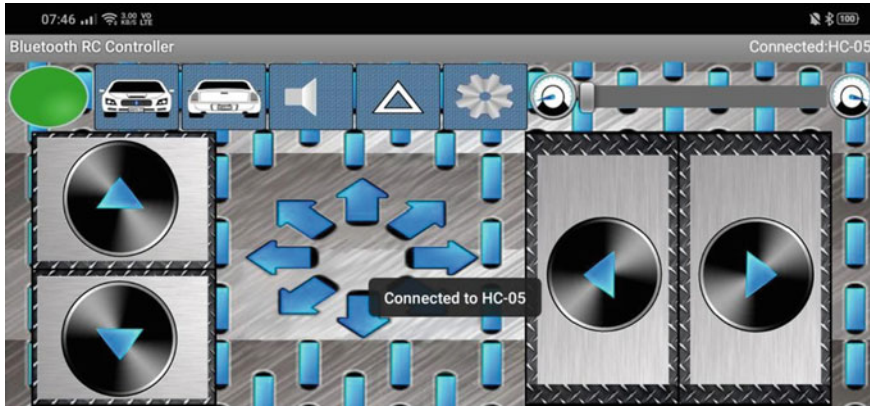
Fig. 6 User interface of Bluetooth RC controller mobile application

where *t* is the time of operation in seconds and *d* is the distance to be travelled by the automatic mulching machine in metres. Thus, by simply substituting the value of distance to be travelled by the machine in metres in the formula, we can get the time of operation in seconds. The user interface of the Bluetooth RC controller app for controlling the mulching machine via HC-05 Bluetooth module is shown in Fig. 6.

4 Conclusion

We were able to interface the model successfully with the HC-05 Bluetooth module via the Bluetooth RC controller mobile app. The Arduino code was uploaded to the microcontroller successfully, and the commands from the user were obtained. The automatic mulching machine was able to run on a field. As the machine moves, the mulching sheet was laid and the hole punching mechanism worked as expected.

4.1 Limitations and Future Scope

In the current user interface model of our project, the input distance provided by the user is to be entered directly in the Arduino code. This can be modified so as to get these inputs via a mobile app to make it more user-friendly. The code can be improved to accommodate the stop–start movement of the automatic mulching machine, in such a way that the hole punching mechanism works only when the machine has stopped. After punching a hole, the machine again starts and moves to a point where the next hole has to be punched and halts again. This cycle is repeated until the length of the furrow has been completely traversed by the machine. By doing so, we can integrate the hole punching mechanism safely without any risk of

damage to the hardware model. A seed sowing mechanism can also be integrated along with the punching mechanism to model a multi-purpose automatic mulching machine along with seed sowing. The machine can also be made to turn left and right automatically after it has finished mulching a particular furrow to move on to the next one. This method can be used to lay multiple furrows without human intervention. For larger prototypes based of this model, we cannot use HC-05 Bluetooth module as it has a range of only 10 m. We can use Wi-Fi modules and cloud-based apps instead to control and store information and commands related to such models.

References

1. Rafi RH, Das S, Ahmed N, Hossain I, Reza SMT (2017) Design and implementation of a line following robot for irrigation based application. In: 19th International conference on computer and information technology, ICCIT 2016, pp 480–483
2. Romputtal A, Phongcharoenpanich C (2019) IoT-linked integrated NFC and dual band UHF/2.45 GHz RFID reader antenna scheme. IEEE Access 7:177832–177843
3. Waworundeng JMS, Fernando Tiwow D, Tulangi LM (2019) Air pressure detection system on motorized vehicle tires based on IoT platform. In: 2019 1st International conference on cybernetics and intelligent system, ICORIS, August, pp 251–256
4. More SJ, Patil PS, More JM, Patil PS, Marathe SS (2020) IoT based patient health care for COVID 19 centre. Int J Recent Technol Eng (IJRTE) 9(3):258–263
5. Kumar CK, Ibrahim MM, Srikanth NM, Aswin S, Peeyush KP (2017) Internet of things based approach for open precision farming. In: 2017 International conference on advances in computing, communications and informatics (ICACCI), pp 2225–2230
6. Jayakrishna PVS, Reddy MS, Sai NJ, Susheel N, Peeyush KP (2018) Autonomous seed sowing agricultural robot. In: 2018 International conference on advances in computing, communications and informatics, ICACCI, pp 2332–2336
7. Pavithra DS, Srinath MS (2014) GSM based automatic irrigation control system for efficient use of resources and crop planning by using an Android mobile. IOSR J Mech Civ Eng 11(4):49–55
8. Kour VP, Arora S (2020) Recent developments of the internet of things in agriculture: a survey. IEEE Access 8:129924–129957
9. Dong Z, Wang H, Tang Y, Wang M, Zhao J (2019) Research on automatic driving system of agricultural machinery based on embedded. In: Proceedings of 2019 IEEE 3rd information technology, networking, electronic and automation control conference, ITNEC, pp 1940–1943
10. Navya P, Ranjith R (2021) Analysis of path planning algorithms for service robots in hospital environment. In: 2021 12th International conference on computing communication and networking technologies, ICCCNT, pp 4–9
11. Megalingam RK, Reddy SV, Sriharsha G, Teja PS, Kumar KS, Gopal P (2016) Study and development of Android controlled wireless pole climbing robot. In: 2015 IEEE international WIE conference on electrical and computer engineering, WIECON-ECE, pp 439–442
12. Muralidharan NT, Rahul Ram S, Rohidh MR, Senthil Nathan M, Harikumar ME (2022) Modelling of sign language smart glove based on bit equivalent implementation using flex sensor. In: International conference on wireless communications signal processing and networking (WiSPNET), pp 99–104. https://doi.org/10.1109/WiSPNET54241.2022.9767137
13. Wei C, Yu J (2012) Mechanical design of a slider-crank centered robotic dolphin. In: Proceedings of the world congress on intelligent control and automation (WCICA), pp 3741–3746
14. Azmi HN, Hajjaj SSH, Gsangaya KR, Sultan MTH, Mail MF, Hua LS (2021) Design and fabrication of an agricultural robot for crop seeding. Mater Today: Proc

Multi-user Hybrid Beamforming for mmWave Systems Using Learning-Aided Link Adaptation

Kakitala Hemanth Reddy, Kottam Akshay Reddy, and P. Sudheesh

Abstract The mmWave technology is employed because it has a big bandwidth and is designed with hybrid beamforming using a huge antenna array. The amount of BF gain required for effective transmission is determined on how far away the user is from the base station. The user's distance affects the beamforming (BF) gain. The amount of antenna elements affects BF gain. So, hybrid beamforming (HBF) design user needs are met. Because certain groups of users are supplied by particular groups of RF chains, RF chains are grouped. Using link adaptation techniques, the data rate may also be boosted. Simultaneously, the required bit error rate (BER) is obtained. As the channel has nonlinear features, it is dependent on specified signal-to-noise ratio (SNR) threshold values, which affects the system's performance. As a result, we use link adaptation approaches in two stages. In diverse places, data streams are represented utilizing wireless sensor nodes. During the beginning phase of the link adaptation process, the digital precoder and combiner are switched between modes according to the characteristics of the channel. A machine learning (ML)-aided link adaptation is applied in second step. The base station (BS) receiver anticipates whether it should request spatial multiplexing or diversity-aided transmission for each additional channel realization. Both the precoder and the combiner are unnecessary for a single dominating route. Most notably, learning-aided adaptation produces more data than conventional link adaptation.

Keywords Hybrid beamforming · Link adaptation · Precoder · Combiner · mmWave

1 Introduction

Mobile consumer's data rate needs in the sub-6 GHz spectrum have risen as time has passed. As a result, we use millimeter wave frequencies, which have a wide

K. H. Reddy · K. A. Reddy · P. Sudheesh (✉)
Department of Electronics and Communication Engineering, Amrita School of Engineering, Amrita Vishwa Vidyapeetham, Coimbatore, India
e-mail: p_sudheesh@cb.amrita.edu

bandwidth and can handle enormous data rates. Due to their sensitivity to climate, millimeter wave frequencies have a substantial propagation loss. Attenuation is due to air absorption, foliage density, and fading caused by rain. We employ directional transmission to prevent this propagation loss.

Traditionally, we transmit signals directionally, which performed by using DSP components for each of the RF chains, which depend on ADCs/DACs. However, since enormous antenna arrays are required at millimeter wave frequencies to achieve high beamforming gain, which is done by allocating ADC/DAC to every individual RF chain would be prohibitively expensive, complicated, and power-intensive[1, 2]. To avoid heavy power consumption and complexity, an HBF architecture is proposed, in which signals created by DSP in the baseband, and depends on a few RF chains. Before being broadcast from the antennas, analog phase shifters in the RF stage are fed [3–5].

The design of transceivers for multi-user millimeter wave (MU) systems is the subject of a significant amount of research and published material. In reference paper [6], there is a transmitter design, where they use of beam space MIMO, and it allows data to be multiplexed across orthogonal spatial beams. Liang et al. developed a zero-forcing (ZF) precoding architecture, that is equivalent to a low-complexity hybrid precoder tailored for multi-user multiple input multiple output (MIMO) systems. Bogale counted the amount of RF chains required at the BS to meet the needs of the full-RF digital BF solution for downlink multi-user millimeter wave communications, which might be outrageously costly [7–9]. For downlink communications, Han et al. recommended employing a beam domain reference signal to optimize beam-forming gain in the desired direction. This was done in order to facilitate maximum data transfer. **Antenna beamforming techniques can be used with systems like MIMO as more adaptive systems and more processing power become available. To increase the signal intensity and deliver higher bitrates to a single user, MIMO uses beamforming. Additionally, beamforming facilitates multi-user MIMO, or MU-MIMO, which enables simultaneous communication between several users using multiple antennas on the spectrum.**

Link adaptation is utilized to optimize data rate while fulfilling BER standards to manage escalating data rate demands [10]. A cutoff is used to change the connection based on pre-defined transmission modes, for each of the legal transmission modes, a look-up table for BER versus rate is created. **Transmit beamforming aims to increase capacity by maximizing received signal strength for each user while reducing interference signal power from other users. This can be accomplished by sending the same signal using various transmitter amplitudes and phases.** As a result, the particular mode that has the maximum throughput as well a BER objective is engaged after post-processing of SNR data. Link adaptation research prior to [11–13] is based on average SNR threshold values. On the other hand, in [12, 14] they use adaptation relies on rapidly changing time-variant channels. Traditional adaptation, on the other hand, doesn't work as well because the wireless channel is always changing and the amplifiers don't work in a straight line [12]. This is because the scheme of transmission is activated on the basis of skewed threshold values, which are caused by the fact that the channel changes over time and the amplifiers

aren't perfectly linear. Training dataset used for observation, link adaptation, ML learning methods may be applied, even if there are problems at different stages of processing [15]. To put it another way, no threshold values are utilized to determine which transmission technique should be employed. Instead, a choice that is more certain of itself is arrived at by using the model that was acquired throughout the stage of training.

Within the realm of adaptive modulation and coding, research published in academic journals has focused on studying algorithms that are helped by machine learning (AMC). In [12], there is thought of a structure to overcome the limitations of MIMO-OFDM with AMC based on supervised learning algorithms like the KNN [16], in order to improve the precision of link adaptation. This was done in order to raise the accuracy of link adaptation [10] KNN. Again, using the KNN algorithm, the research paper referred to above proposes link adaptation as a method for single carrier frequency domain equalization. In more recent times, a wider category of ML techniques, including approaches to deep learning, has been used in both indoor and outdoor locations and detection.

If millimeter wave HBF literature is discussed, analog BF and digital BF are always merged together, regardless of the kind of channel being discussed. In this study, we show that when there is only one dominant route accessible over the channel, it is unnecessary to activate both a digital precoder and combiner, contrary to popular belief. By turning off the digital precoder and digital combiner and activating the analog-only BF, the most efficient use of energy is obtained.

2   Related Works

We provide a transmitter idea that can be employed in MU-MIMO mmWave systems, in which users may be geographically separated, both in terms of distance and the beam direction they want to broadcast in. Instead, we suggest allocating transmit AEs on a per-user basis, with each user's necessary BF gain included into the number of active AEs. Our goal is to create this design by making use of a portion of the total number of phase shifters that are available, we want to do this by turning on a subset of those phase shifters. Consequently, our approach is more energy-efficient than traditional multi-user mmWave since not all phase shifters are engaged at the same time, unlike conventional systems. After grouping the RF chains, we now concentrate on the design of the per-user link. Analog-only BF may be used in a circumstance where there is just one dominant propagation route, making the need for any digital precoder or combiner redundant.

Based on the practically immediate post-processed SNR, we describe a learning-assisted adaptive transceiver design for each user connection, where the adaptation changes among multiplexing and diversity-oriented modes of transmission and accurately tunes the modulation used to provide both high-reliability and high-rate operation. This design is based on the fact that the adaptation shifts among transmission modes based on multiplexing and diversity. An immediate post-processed SNR is

used in conjunction with supervised learning and feedback information from the BS in order to determine the multiplexing or diversity-aided transmission mode of the transmitter and to choose the precise modulation scheme. For example, in this study, we use the KNN classification method to make decisions at the receiver.

Simulations show that learning-assisted adaptation achieves a much quicker rate with an SNR increase of around 4.99 dB at a target BER of 10-3, while still preserving the needed goal BER. This is in contrast to the usual link adaptation method, which is performed using hard cutoff values. Furthermore, we demonstrate via simulations that the performance of the HBF-based system is superior and the performance of the system that relies on analog-only BF is comparable in a situation where there is just one dominant communication channel.

There will be a presentation of a quantitative analysis on the difficulty of the KNN algorithm.

3   Proposed Work

A communication system consists of a base station that is connecting to K users that each have Nu antennas RF links. Geographical barriers have been erected between users. The BS is arranged with Nt antennas in addition to available RF chains. Baseband is processed with the help of Nt RF chains, and then Nt phase shifters are used in the RF stage to adjust the phase of the signal before it is sent from antennas. Because BF gain is also dependent on distance, it varies the number of active phase shifters.

In this Fig. 1, user 1 is closer to the BS, the propagation loss1 experienced by the user 1 is lower than that of user 2, which is farther from the BS. As a result, the BF gain required to compensate for the loss is higher for user 2 than that of user 1. This philosophy makes our design more energy-efficient than the conventional design where all the phase shifters remain active at a given time. As BF1 gain is greater than BF2 gain, we may infer that $d1$ is greater than $d2$. In this work, in order to facilitate the computation process, we will be employing free space loss. The design is superior in terms of energy efficiency than a traditional method since each of the phase shifters is not active at the same moment in time. The beam that user1 is receiving is stronger than the beam that user2 is receiving due to the huge number of phase shifters. There are additional degrees of freedom provided by angular arrangement of RF chains when they're grouped. There is a limit on the total number of RF chains that may be employed by a single group. Illustration of active phase shifters is shown in Fig. 2.

3.1   HBF

When designing the matrices F_{RF}^k and F_{BB}^k, we make sure to use as much of the hybrid precoder's capability as possible. To be more specific, the formulation of the
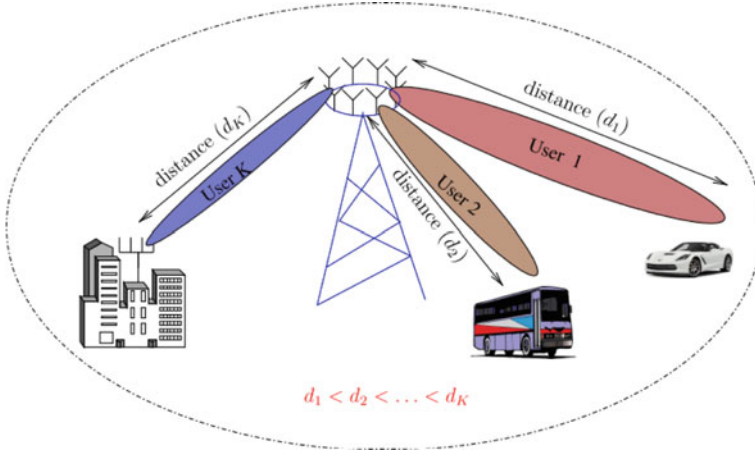
Fig. 1 System model
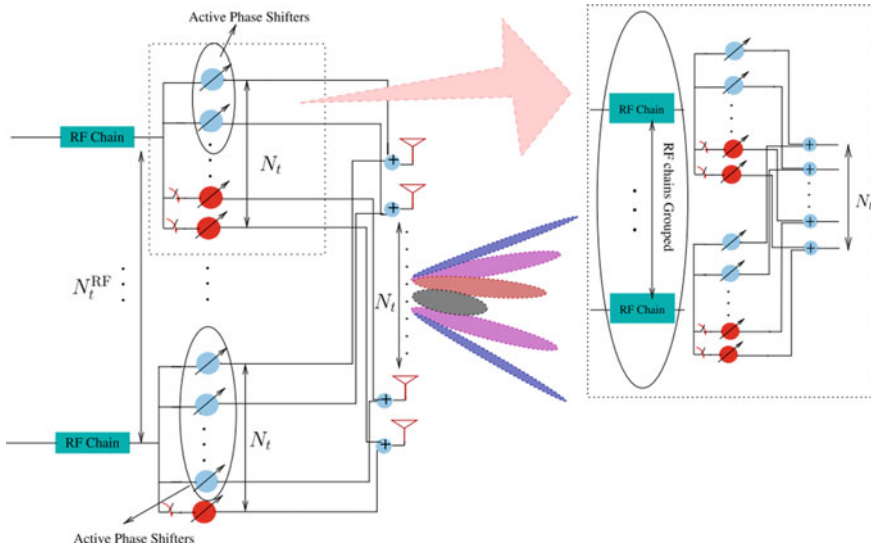
Fig. 2 Illustration of active phase shifters

objective function leads to the reduction of Frobenius norm between optimal matrices F_{RF}^k and F_{BB}^k which may be written as

$$\min_{F_{RF}^k,\ F_{BB}^k} \left\| F_{opt}^k - F_{RF}^k F_{BB}^k \right\| F, \tag{1}$$

$$s.t. \left\| F_{RF}^k F_{BB}^k \right\|_F^2 = N_s, \tag{2}$$

$$\left| F_{\mathrm{RF}}^{k}(m,\, n) \right| = 1 \tag{3}$$

As shown in the system model (2), the best precoder is determined by performing a singular value decomposition (SVD) on the channel matrices $H_{\mathrm{k}} = U_{\mathrm{k}} \sum k V_{k}^{H}$ and V_{k}. The F_{opt}^{k} matrix for the precoder (3) is obtained from the first N_{s} columns of V_{k} right singular matrices.

Ghauch et al. [15] provided the near-optimal solution to Eq. (1) under the condition in which the records of F_{opt}^{k} are the H_{k} channel matrices right singular vectors. On the other hand, while we opted to apply the approach described in [16] to decompose the optimal digital precoder matrix F_{opt}^{k} into its hybrid product. In similar way, the solutions for W_{RF}^{k} and W_{BB}^{k} may be derived through bisecting H_{k}'s left-singular vectors, as shown (1).

The link adaptation procedure has always been based on approximated threshold values. The receiver will compute post-processing SNR as soon as the signal arrives. Using this value, the receiver will determine transmission mode that will provide the best results making a comparison to the estimated SNR threshold values that have been pre-defined [13].

In a given channel realization H_{k} and noise variance σ_{n}^{2}, the overall post-processing SNR (4) is calculated after matrix W_{k}. When it comes to user k, it is represented as:

$$\mathrm{SNR} = \frac{\mathrm{tr}\left(\left(W^{k^{H}} H_{\mathrm{k}} F^{k} \right) W^{k^{H}} H_{\mathrm{k}} F^{k} \right)}{\mathrm{tr}\left(W^{k} W^{k^{H}} \sigma_{\mathrm{n}}^{2} \right)} \tag{4}$$

where $W_{\mathrm{k}} = W_{\mathrm{RF}}^{k} W_{\mathrm{BB}}^{k}$ and $F^{\mathrm{k}} = F_{\mathrm{RF}}^{k} F_{\mathrm{BB}}^{k}$.

Remark 1: In a situation in which the beams of different users are very near to one another, it is necessary to take into consideration the interference that might be caused by leakage through one beam into the other (2). Non-orthogonal multiple access (NOMA) systems follow a similar principle. The matrices $W_{\mathrm{BB}}^{k^{H}} W_{\mathrm{RF}}^{k^{H}}$ may be built to reduce interference in this situation, as explained in [16], while designing the matrices F_{RF}^{k} and F_{BB}^{k} is explored in the upcoming sections.

3.2 Improved Energy-Efficient HBF

The previous section's HBF does not account for the channel's characteristics. As it is essential to note if there is just a single dominant route across the channel, using F_{BB} and W_{BB} is unnecessary, as we shall demonstrate in the latter part of this work. This is something that has to be emphasized. This is because analog BF with phase shifters reliably catches the signal whenever the channel has just one dominant route. This is comparable to establishing the columns of the F_{BB} and W_{BB} matrices from the Identity I.

Similarly, displays the system's feasible rate. It is clear from looking at the chart that the rate of the system with no digital processing is the same as the rate of the system with digital processing combined. Additionally, the RF's analog phase shifters steer and combine effectively with regard to BS and receiver response vectors. The conventional and suggested link adaptations are discussed in the next section.

Remark 2: It's worth noting that the system under consideration is not dissimilar to the case of unknown interferences. By utilizing the SINR instead of the SNR, the suggested design may easily be expanded to situations if there is interference from unwanted transmitters. If this is the case, the modified text's denominator would include an additional word, namely "interference." Furthermore, during the time of huge number interferences, the interventions induced are described by extra Gaussian noise using the central limit theorem. Except for greater noise variation, would stay the same in this instance. **Instantaneous post-processed SNR at the receiver gives an idea about type of transmission and type of modulation scheme by comparing with pre-defined threshold values. There are training phase and the testing phase. In the training phase, both the BER and the instantaneous post-processing SNR are calculated for each channel realization and stored in memory. Then, equipped with the post-processed SNR and the required BER as the parameters, the K-nearest neighbors are chosen from the set _C_. Finally, the specific class which has more points in the neighborhood is selected. The selection of the class from set _C_ based on the average threshold values would result in low rates because of the wide-ranging scattering of the instantaneous post-processing SNR values. During the testing phase, upon estimating the channel state information, the receiver calculates the post-processing SNR assuming that spatial multiplexing is used relying and then finds the 7Div denotes diversity, while Mux denotes multiplexing. K-nearest neighbors with the aid of the post-processed SNR calculated and the required BER, followed by selecting the class through majority voting.**

3.3 *Conventional Adaptation*

The adaptation is carried out after deciding whether or not to turn off the digital precoder and combiner based on the channel circumstances. In traditional adaptation, the receiver makes a choice based on post-processed SNR values that satisfy pre-defined threshold values for a certain BER. The BER objective of 10-3 is achieved by using particular threshold values defined for each scheme. After calculating post-processed SNR values, the receiver compares these to specified threshold values to determine the transmission method and modulation mode. Because the channel doesn't allow for multiplexing or diversity, the digital BF is turned off, and when there is only one dominant way, adaptation is done only among the modulation schemes.

3.4 Learning-Assisted Adaptation

The adaptation is carried out after deciding whether or not to turn off the digital precoder and combiner based on the channel circumstances. In traditional adaptation, the receiver makes a choice based on post-processed SNR values that satisfy pre-defined threshold values for a certain BER. The BER objective of 10-3 is achieved by using particular threshold values defined for each scheme. After calculating post-processed SNR values, the receiver compares these to specified threshold values to determine the transmission method and modulation mode. Because the channel doesn't allow for multiplexing or diversity, the digital BF is turned off, and when there is only one dominant way, adaptation is done only among the modulation schemes.

The receiver in the proposed architecture makes decisions based on learning, dividing pre-defined threshold values. As a result, we'll need a categorization method. Most classification techniques need a functional mapping between features and classifiers. The SNR and BER are among the features of the study, while the classifiers include 37 spatial multiplexing with modulation techniques and spatial diversity with various modulations. As a result, we used a nonparametric KNN classification technique that does not need any functional mapping information. The KNN classification method is the best option since it is independent of assumptions and prior knowledge. The feature set known as F, which is utilized for link adaptation, comprises of {SNR, BER}. C = {SNR, BER} is used for link adaptation and C = {DivBPSK, DivQPSK, MuxQPSK, Mux16QAM} to non-line of sight channels, although C = {QPSK, 16QAM} for channels with just a single dominant route and no multiplexing/diversity gain. When there is just one dominant route, second-stage adaptation merely modifies the strategy of modulation.

We know that, suggested learning adaptation is divided into stages: training and testing. For each channel realization, the BER and immediate post-processed SNR values get computed and kept in memory during the training phase. The testing step comes after the data from the training phase has been gathered. The post-processed SNR is determined each time a new data point arrives. From this set C, the SNR post-processed and the needed BER are selected. Finally, the particular class with the most points in the area is chosen.

Using a class from set C based on weighted threshold values would result in low rates as a consequence of the wide-ranging dispersion of the instantaneous post-processing SNR values. During the phase of testing, the receiver makes an estimation of the channel state information, determining the post-processing SNR under the assumption that spatial multiplexing is used, finds the K-nearest neighbors based on the post-processing SNR and the needed BER, and then chooses the class by using a majority vote. All of these steps take place simultaneously.

4 Results

From Figs. 3, 4, 5, 6, 7 and 8, different users from different locations, these graphs are the representation of data stream over a geographical area. Different wireless sensor nodes are transmitting data to base station.

From Figs. 9, 10, 11, 12, 13, 14 and 15, we can say that learning-assisted adaptation is better than conventional adaptation, which has better throughput and SNR. Desired BER was achieved through learning-assisted adaptation. **While the Mux QPSK mode begins to share the possibility of being activated with the Div QPSK mode, the probability of the class Div BPSK gradually decreases as the SNR grows, where calculating the relative likelihood yields the probabilities how often each class will utilize the suggested learning assistance based on link adaptation of the post-processing SNR and toward the BER aim. Similarly, at high SNRs, the MuxQPSK mode gets stronger.**

Squares and circles in Fig. 14 differentiate the training data of two classifiers. Because it is a K-NN method (identifying the closest neighbor), the graph shows an uneven border rather than a straight line or curve. In a testing area, when a data

Fig. 3 Channel realization 1
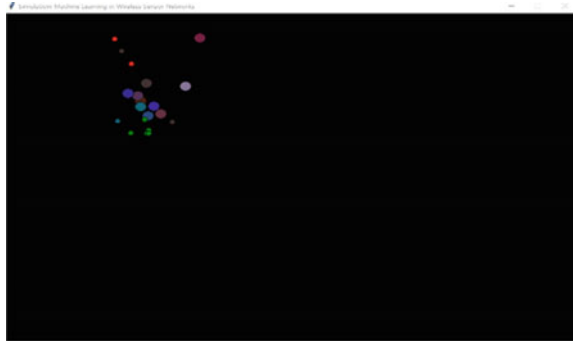
Fig. 4 Channel realization 2

Fig. 5 Channel realization 3
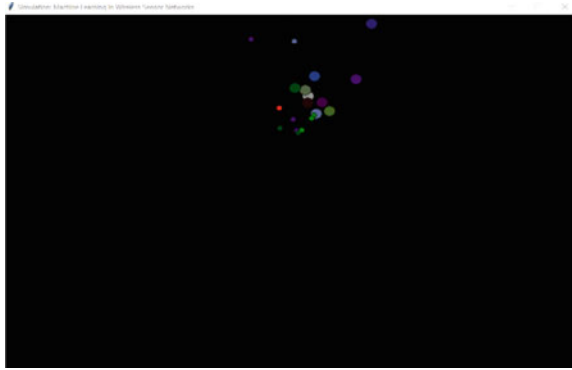
Fig. 6 Channel realization 4

Fig. 7 Channel realization 5

point is provided, a circle is created around it, centering the tested data. Then, using majority voting, the class with the most nodes in the circle or center will be picked. In the scenario when the total number of points gained in each category equals, then class with the highest throughput is chosen. Each object casts a vote for their class,
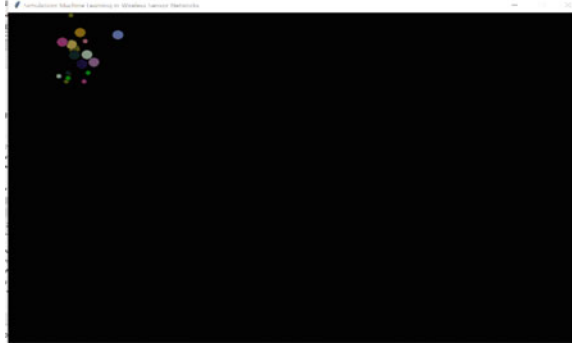
Fig. 8 Channel realization 6
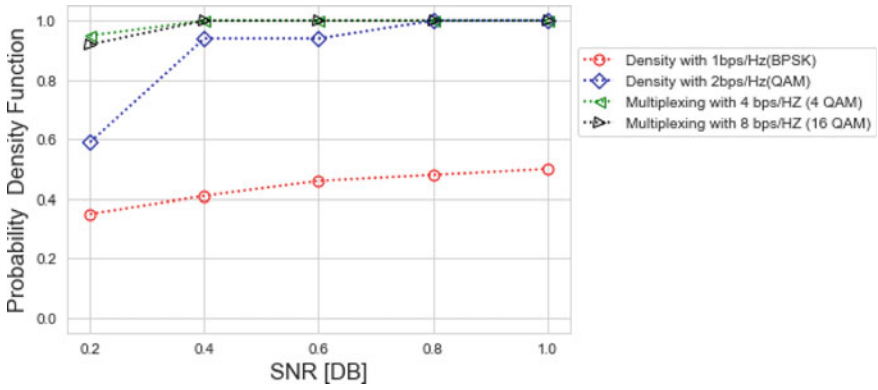
Fig. 9 SNR versus P.D.F
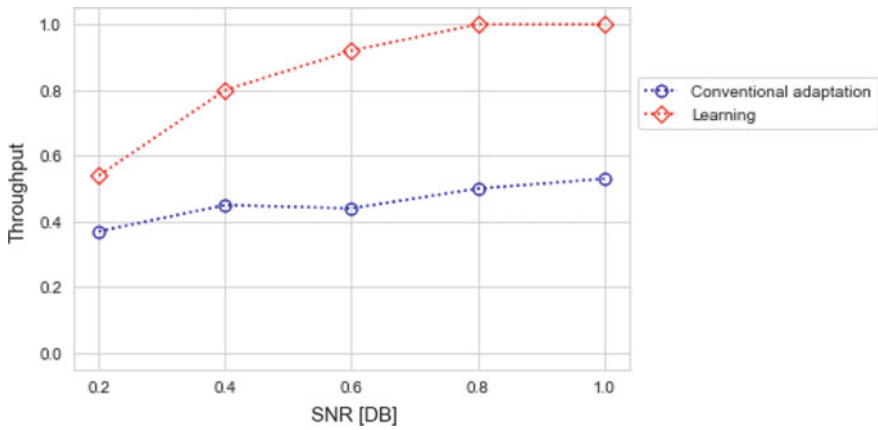
Fig. 10 SNR versus throughput
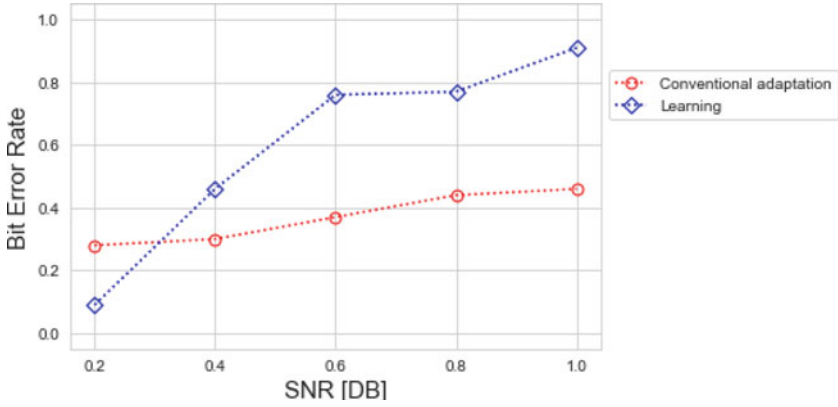
Fig. 11 SNR versus BER
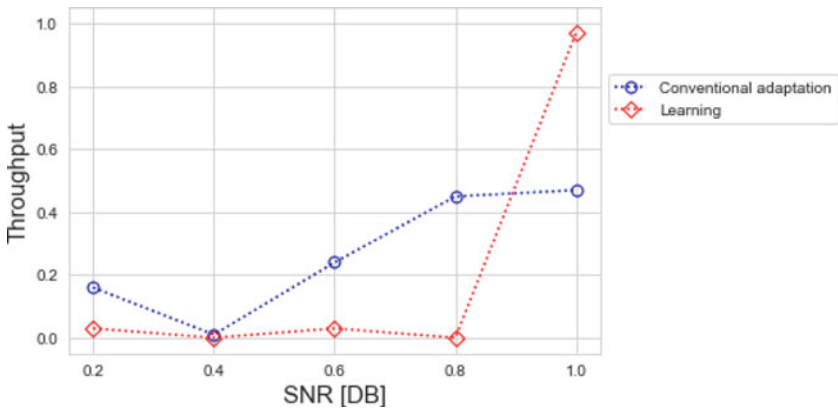
Fig. 12 SNR versus throughput

and the class with the most nodes is taken for prediction. The Euclidian, Hamming, and Manhattan distances are used. Datasets versus time is shown in Fig. 15.

5 Conclusion

For multi-user mmWave systems, we presented a transmitter architecture in which BF gain determines the phase shifters, that is necessary to compensate for each user's propagation loss. We activate the exact count of phase shifters required for this model. Following this, we suggested organizing the RF chains at the BS according to user channel to assist every user. After this, we offered ML-aided link adaptation strategy that was created for mmWave systems. In this scheme, the receiver determines the
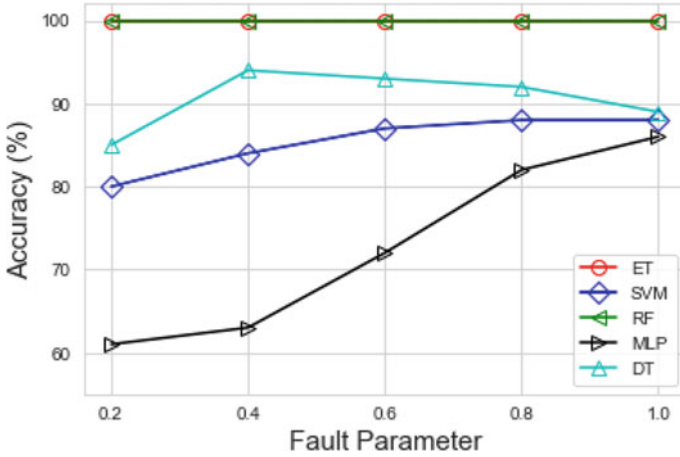
Fig. 13 Fault versus accuracy
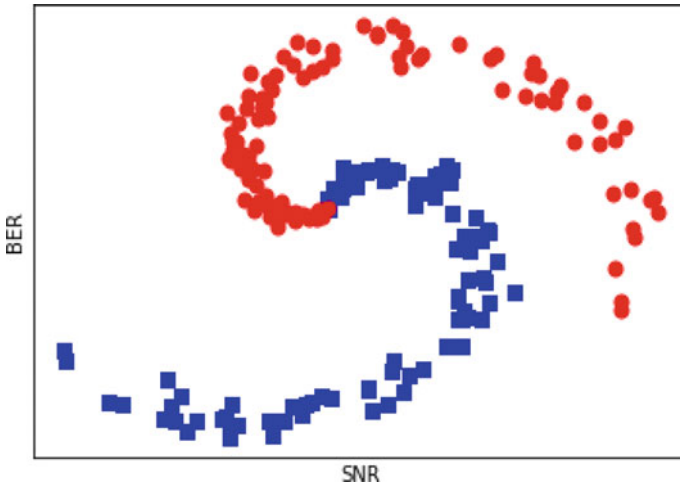
Fig. 14 SNR versus BER

suitable kind of spatial multiplexing transmission and modulation method for each channel realization. This allows the receiver to adjust to new channel realizations. We also considered to stop using the digital precoder after communication has been successfully created and the channel has only a unique dominant route. We were able to demonstrate that it easily satisfies the intended BER while delivering a substantially greater data rate than typical link adaption based on SNR threshold values after performing learning-aided adaptation simulation.
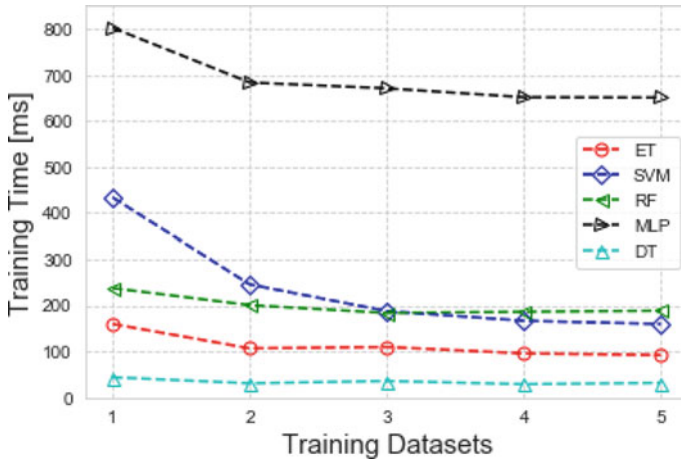
Fig. 15 Datasets versus time

References

1. Hemadeh IA, Satyanarayana K, El-Hajjar M, Hanzo L (2018) Millimeter-wave communications: physical channel models, design considerations, antenna constructions, and link-budget. IEEE Commun Surv Tutorials 20(2):870–913 (2nd Quart.)
2. Maccartney GR Jr, Samimi MK, Rappaport TS (2015) Exploiting directionality for millimeter-wave wireless system improvement. In: Proceedings of the 2015 IEEE international conference on communications (ICC), June 2015, pp 2416–2422
3. Megha SK, Ramanathan R (2017) Impact of anchor position errors on WSN localization using mobile anchor positioning algorithm. In: International conference on wireless communications, signal processing and networking
4. Satyanarayana K, El-Hajjar M, Kuo P, Mourad A, Hanzo L (2018) Dualfunction hybrid beamforming and transmit diversity aided millimeter wave architecture. IEEE Trans Veh Technol 67(3):2798–2803
5. Satyanarayana K, El-Hajjar M, Kuo P, Mourad A, Hanzo L (2017) Millimeter wave hybrid beamforming with DFT-MUB aided precoder codebook design. In: Proceedings of the 2017 IEEE 86th vehicular technology conference (VTC-Fall), Sep 2017, pp 1–5
6. Narayanam S, Bandaru P, Kirthiga S (2018) Two-staged precoder for massive MIMO millimeter wave systems. In: 2018 International conference on advances in computing and informatics (ICACCI)
7. Liang L, Xu W, Dong X (2014) Low-complexity hybrid precoding in massive multiuser MIMO systems. IEEE Wireless Commun Lett 3(6):653–656
8. Bogale TE, Le LB, Haghighat A, Vandendorpe L (2016) On the number of RF chains and phase shifters, and scheduling design with hybrid analog digital beamforming. IEEE Trans Wireless Commun 15(5):3311–3326
9. Gutta V, Padmanabam S (2015) Low complexity channel estimation using fuzzy Kalman Filter for fast time varying MIMO-OFDM systems. In: 2015 International conference on advanced computing and communications
10. Jensen TL, Kant S, Wehinger J, Fleury BH (2010) Fast link adaptation for MIMO OFDM. IEEE Trans Veh Technol 59(8):3766–3778
11. Peng F, Zhang J, Ryan WE (2007) Adaptive modulation and coding for IEEE 802.11n. In: Proceedings of the 2007 IEEE Wireless communications and networking conference, WCNC, Mar 2007, pp 656–661

12. Satyanarayana K, El-Hajjar M, Kuo P, Mourad AM, Hanzo L (2018) Adaptive transceiver design for C-RAN in mmwave communications. IEEE Access 6:16770–16782
13. Daniels RC, Caramanis CM, Heath RW Jr (2010) Adaptation in convolutionally coded MIMO-OFDM wireless systems through supervised learning and SNR ordering. IEEE Trans Veh Technol 59(1):114–126
14. Duda RO, Hart PE, Stork DG (2000) Pattern classification, 2nd edn. Wiley, Hoboken, NJ, USA
15. Ghauch H, Kim T, Bengtsson M, Skoglund M (2016) Subspace estimation and decomposition for large millimeter-wave MIMO systems. IEEE J Sel Top Sig Process 10(3):528–542
16. Satyanarayana K, El-Hajjar M, Kuo P, Mourad A, Hanzo L (2019) Hybrid beamforming design for full-duplex millimeter wave communication. IEEE Trans Veh Technol 68(2):1394–1404

Prediction of Disease Using Retinal Image in Deep Learning

R. Sivakani and **M. Syed Masood**

Abstract Alzheimer's disease is an elderly chronic disease, which affects the people with age more than 60. In India more than 5 million people are affected by the Alzheimer's disease (AD), it may be increased to 7.6 million by 2030. 6.2 million US people are living with AD and may be increased by 8.6 million by 2030. As per a report of Alzheimer's Association in worldwide every 10 of 100,000 people are developing AD each year. As per the report of world health organization nearly 55 million people are living with AD in worldwide and for every year 10 million new cases are developed. By 2022 the cases may be increased to triple the count of now. This is the 7th leading death causes disease in world. If a person is affected by AD then they cannot able to do any activity by their own because of the memory loss. The caretakers will guide them to their day-to-day activity. There are no medicines for the AD so we are in the situation of protecting the people from this disease. In this paper the early prediction has been focused. Early prediction of AD and the diabetics has been done with the retinal fundus image. The nerves in the brain resembles in the retina image. The image preprocessing is done and the image is segmented. The segmented image is given to the deep learning model for the prediction of the disease. The accuracy of this model is 90%.

Keywords Alzheimer's disease · Diabetes · Retinal images · Segmentation · Convolutional neural network · Recurrent neural network

1 Introduction

AD will damage the nerve in the brain and because of this the memory loss will occur. The nerves are damaged because of the deposition of the protein in the brain. The retina is the extension of the brain. So the protein will be deposited in the eyes also. The damaged nerve in the eyes shows the early symptoms that the person can have a chance of brain nerve damage and which leads to the AD. 21st September is

R. Sivakani (✉) · M. S. Masood
B.S. Abdur Rahman Crescent Institute of Science and Technology, Chennai, India
e-mail: sivakani13@gmail.com

the world Alzheimer's day and 14th November is the world Diabetes day. A person with diabetes has a more chance for getting the AD [1]. Type 2 diabetes has more influences than the other diabetes in the AD patients [2]. AD and Type 2 diabetes are the elderly disease. Diabetes is a chronic disease which caused due to the increase of glucose in the blood due to the problem in insulin secretion in pancreas. The increased glucose will damage the eyes, nerves, kidney etc., [3]. As per the report of the World Health Organization (WHO), in worldwide nearly 1.5 million deaths has been occurred due to the diabetes. More than 537 million people are living with diabetes and this may increase by 643 in 2045. In India nearly 74 million people are living with diabetes disease [4].

AD and type 2 diabetes can be predicted earlier using the retinal fundus images. The retinal diseases will damage any part of the retina. Retina has millions of light-sensitive cells and nerve cells that are responsible for receiving the visual information and organizing it. The retina sends the received information to the brain through the optic nerve enabling and responding to the information [5]. An image of the eyes will represent the future risk of the neuro disease. Predicting the early sign of the disease will give more life to the patients. Researchers are developing blood tests and retinal screening for the prediction of AD [6].

Figure 1 shows the people affected with AD and diabetes in India and worldwide. The count is represented in million. In India the people living with AD and diabetes are 5 million and 74 million. In worldwide the people living with AD and diabetes are 55 million and 537 million. Both diseases are leading death cause diseases.

The main contribution of this paper is to predict AD and diabetes using the fundus images.

- Fundus dataset
- Preprocessing
- DL model construction
- Prediction of disease.

The paper has the introduction part followed by literature review, proposed model, results and discussion finally the conclusion.

Fig. 1 AD and diabetes affected people
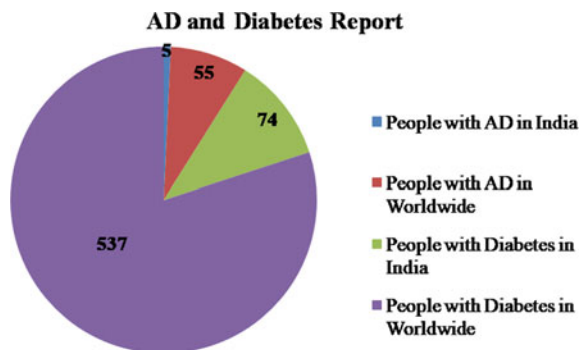
2   Literature Review

A review has been done to predict the dementia using the fundus camera image of retinal. Using the fundus images the subtypes of the dementia can be categorized. In future the focus will be done on the refine and standardized method for the prediction [7]. A comparison has been done with the retinal macula and the nerves in the eyes for the prediction of the Alzheimer's disease. Also the OCTA angiograms of AD, POAG and HC patients are compared and the result says that the AD and the POAG are associated with the retinal. The future work will be focused on the diagnosing method for the neurodegenerative disease [8]. A review has been done to predict the Alzheimer's disease using the visual abnormalities [9]. A review has been done for the prediction of Alzheimer's disease with the retinal biomarker. Based on the review the future research recommendation has been done [10]. A new method has been proposed for the early prediction of the AD. The fundus retinal image has been segmented using the wavelet network method and the prediction has been done. The prediction has been done using two steps; the network weight has been generated using the orthogonal least square algorithm and next the optimization has been done [11]. A machine learning technique has been used for the prediction of AD using the retinal images. The classification accuracy of 82.44% [12]. Alzheimer's disease has been predicted using the retinal images. The amyloid deposition shows the AD; the deposition was higher in AD than the NC [13].

A Convolutional neural network model has been developed for the object detection and the image classification using the eye fundus images. The validation has been done using four public datasets [14]. Retinal image classification has been done using the convolutional neural networks. Blood vessel extraction has been done; optic disc and lesions techniques also applied to detect the retinal images [15]. A framework has been developed for the retinal image classification. To improve the quality of the image fuzzy preprocessing techniques are used. Convolutional neural network algorithm has been used for the classification of disease [16].

A deep learning model has been developed for the prediction of the type 2 diabetes and the kidney disease using the fundus images and the clinical metadata [17]. A deep learning convolutional neural network model has been created using the MatConvNet for the detection of retinal diseases. The validation of the model has been done using the STARE database. Also, the transfer learning techniques has been applied for the performance improvement of the model [18]. A deep learning model has been developed for the classification of disease using the Age-related macular degeneration data. The algorithm has been validated using the fundus images [19]. A fast region-based convolutional neural network algorithm has been developed with the fuzzy k-means clustering method for the segmentation of the images and the prediction of the disease. The validation of the algorithm has been done using various dataset [20]. A study has been done for the prediction of Alzheimer's disease by finding the thickness of the retinal nerve fiber layer of the mild Alzheimer's disease patients [21].

A study has been done for the prediction of Alzheimer's disease by analyzing the deposition of the protein in the retinal [22]. A study has been done for the prediction of the Alzheimer's disease by analyzing the thickness of the macular area in the retina [23]. Several diseases have been labeled using the deep learning model. A transfer learning technique has been proposed for labeling the fundus images. The images used are 250 and the accuracy of the proposed method is 96.2% [24]. A convolutional neural network has been constructed for the prediction of the diabetic retinopathy in the early stage. 92% accuracy has been predicted by this model [25]. A deep learning model has been proposed for the segmentation of the lung CT images. The result has been compared for various datasets and proved that the proposed model is better [26].

From the literature, it is analyzed that the retinal image has been used for the prediction of various diseases with the CNN deep learning model. The contribution of the paper is a combination of RNN and the CNN deep learning model. The input is in image format; to increase the accuracy of the prediction the deep learning model has been constructed.

3   Proposed Model

The proposed block diagram has the dataset and is preprocessed; then the preprocessed data is given to deep learning model and the prediction of disease has been done. Figure 2 shows the block diagram of the proposed model.

3.1   Dataset

The data has been taken from the kaggle repository. The data stored in the kaggle repository has been collected from the Joint Shantou International Eye Center, China. In that dataset, there are 39 classes and 209,494 fundus images. From that for this paper only 5 classes has been considered for processing. Totally 1750 fundus images are considered for the prediction of the disease. The features considered for the prediction are DR1, DR2, DR3, possible glaucoma, optic atrophy, sever hypertensive,
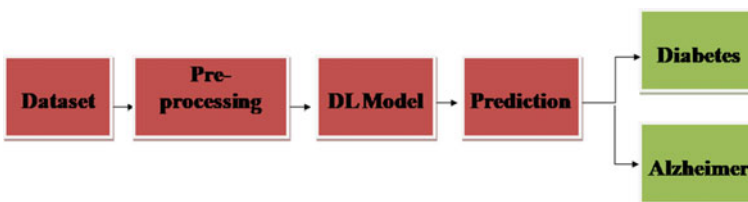
Fig. 2 Proposed block diagram
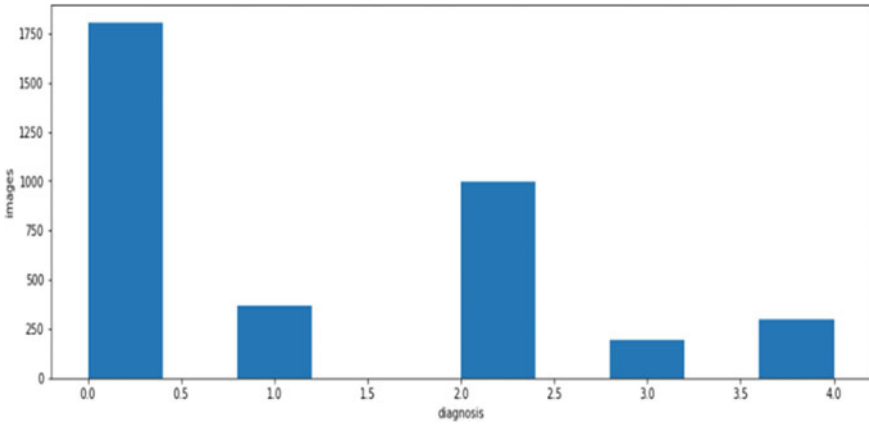
Fig. 3 Distribution of data

myelinater nerve fiber, massive hard excudates, yellow-white spots, cotton-wool spots, vessel tortuosity, chorioretinal atrophy, preretinal hemorrhage, fibrosis, laser spots and silicon oil in eye. The split ratio for the testing and training dataset is 75–25%.

Figure 3 represents the different classes in the dataset. The classes are specified as:

0—Normal, 1—Mild diabetes disease, 2—Mild Alzheimer's disease, 3—Severe Alzheimer's disease, 4—Severe diabetes disease.

3.2 Preprocessing

Preprocessing is to be done for the quality prediction of a model. Preprocessing is an important task for the correct prediction. In the preprocessing the image will be formatted as required for prediction. The noise in the image can be removed using the autoencoding technique. Figure 4 shows the steps taken place in the deep learning model.

Fig. 4 Preprocessing steps

The preprocessing steps are resize, orientation, gray scale and segmentation.

Resize

All the images are to be in same dimension for the processing, so all the images are to be converted same size. The image is converted to 256 * 256 using the resize function in python. The equation of the resize method is given in Eqs. 1 and 2.

$$x = {}^a/_{\text{width}} \tag{1}$$

$$y = {}^b/_{\text{height}} \tag{2}$$

where x and y are the scale of x and y value; a and b are the new width and new height.

Orientation

Orientation is a kind of image transformation. This is done to using the rotation function [27]. The equation for the transformation to the origin is given in Eqs. 3 and 4.

$$x_2 = \cos(\theta) * (x_1) + \sin(\theta) * (y_1) \tag{3}$$

$$y_2 = -\sin(\theta) * (x_1) + \cos(\theta) * (y_1) \tag{4}$$

Gray Scale

The images which are using for the process should be in high quality. The disease to be predicted correctly so, the gray scale conversion is done. If the RGB image is processed the prediction will not be perfect. So, the image is converted to gray scale [28].

Image Segmentation

The complexity of the images should be reduced for good prediction. In segmentation the subgroups are created and the labels will be assigned to the pixels. The threshold value is fixed and segmentation has been done. Otsu method is used for the automatic threshold fixing in the image preprocessing [29]. The pixel can be calculated using the Eq. 5.

$$N = \sum_{k=0}^{L-1} n_k = n_0 + n_1 + \ldots + n_{L-1} \tag{5}$$
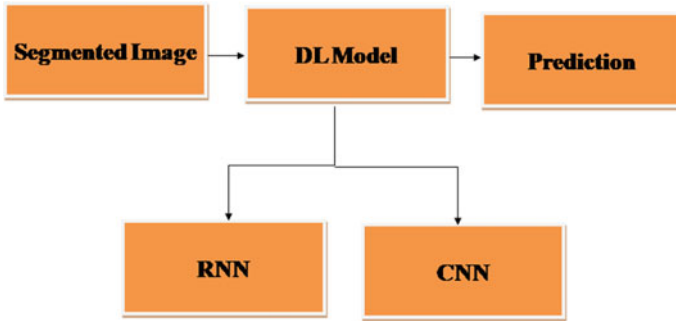
Fig. 5 Deep learning model

Deep Learning Model

The deep learning model RNN and CNN classifiers are used for the prediction. Figure 5 shows the deep learning model and in which the segmented image has been given and using the RNN and CNN the prediction has been done.

RNN

RNN is a neural network classification. It has a memory unit for storing the previous input data. It has three layers for the prediction.

Input Layer

Input layer receives the input images and give the input to the hidden layer. It has two input data to predict the output; they are current input data and the previous data.

Hidden Layer

Hidden layer is present in between the input layer and the output layer. In a prediction model, it has more than hidden layer.

Output Layer

Output layer receives the input from the hidden layer and generate the output.

CNN

CNN is a type of neural network used for the prediction with the help of visuals. It has three layers for prediction.

Convolution Layer

Convolution layer receives the segmented image and extract the feature for the prediction with the help of the convolutional filter.

Pooling Layer

Pooling layer receives the features from the convolution layer and the size of the input will be reduced to increase the computational speed of the model. To increase the performance of the model the max pooling parameter is used.

Fully Connected Layer

This layer receives the input from the pooling layer and applies the linear combination for generating the output. The CNN layers can be generated using the Eq. 6.

$$y_i^{l+1}, \ j^{l+1}, \ d = \sum_{i=0}^{H} \sum_{j=0}^{W} \sum_{d^l=0}^{D^l} f_{i, \, j, \, d^l, \, d} \ X x_{i^{l+1}+i, \, j^{l+1}+ \, j, \, d^l}^{1} \tag{6}$$

4 Result and Discussion

The input retinal image has been subjected to preprocessing and then given to deep learning model for the processing and the output is predicted as normal or diseased. In the preprocessing, the input image has been resized, oriented, grayscale conversion has been done and then it is segmented. The segmented image has been given to the deep learning model; in the deep learning model, first RNN model has been used and then CNN model has been used. The prediction of AD and the diabetes has been done using the DL model and the result has been noted. In the RNN model the segmented image has been processed and the accuracy for this model is 72%. Then the same segmented images have been given to the CNN model and 2 convolutional layers have been generated and the max-pooling technique has been applied. The accuracy of this model is 90%.

When comparing both the results the CNN algorithm gives the best result. Figure 6, shows the sample segmented images and then based on the segmentation the prediction has been done using the DL model. After segmenting the labeling has been done the categorizing of the disease using the DL model. The result comparison is shown in Fig. 7. It shows the accuracy of the RNN model and the CNN model. The CNN model gives a better result than the RNN model for this data set. Also the RSME and the MAE has been calculated to find the error rate of the prediction; it is shown in the Eqs. (7) and (8). The RNN model has the error rate of 28% and the CNN model has the error rate of 10%.

$$\text{MAE} = \sum_{i=1}^{n} \frac{|y_i - x_i|}{n} \tag{7}$$

$$\text{RSME} = \sqrt{\sum_{i=1}^{n} \frac{(y_i - x_i)^2}{n}} \tag{8}$$
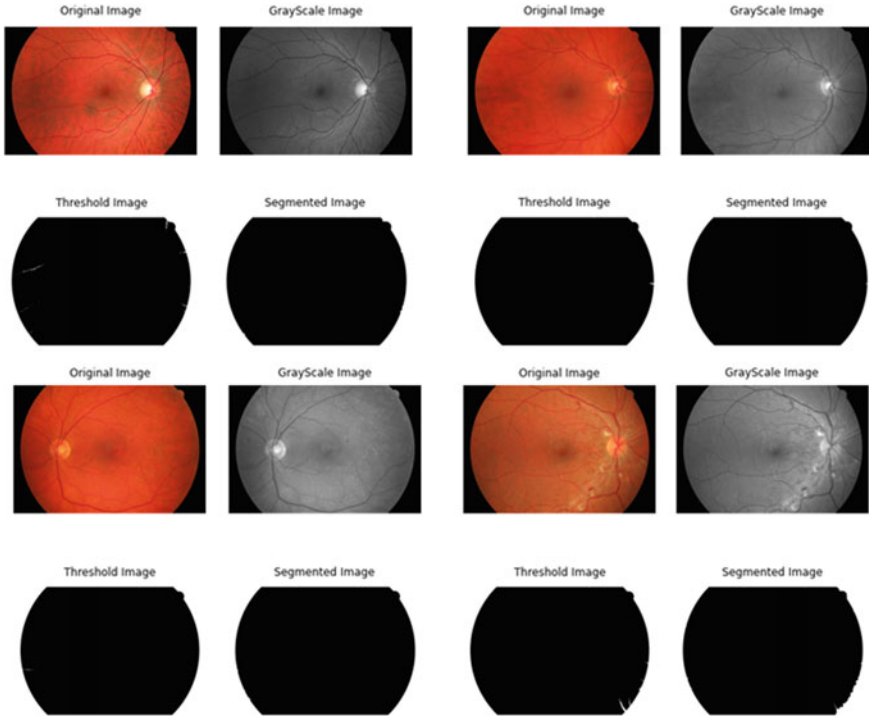
Fig. 6 Sample preprocessed images

Fig. 7 Result predicted
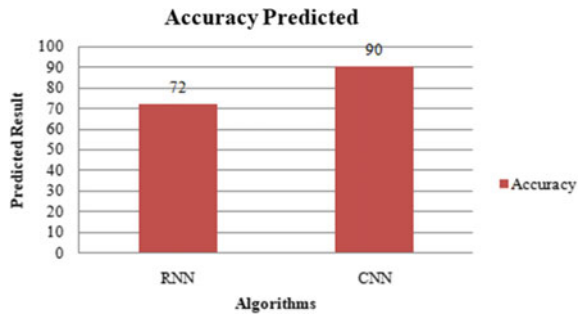
5 Conclusion and Future Enhancement

AD and the diabetes are the elderly disease. Previously it affected the aged but nowadays it affects the younger generation also, so it is to be identified in the early stage and should be cured. The deep learning model uses the retinal images for the prediction of the disease. The retinal resembles the brain neuron connection so using that the early prediction can be possible. The deep learning model has the RNN and CNN classifier. The accuracy of the RNN and the CNN are 72 and 90%. When comparing both the accuracy the CNN model has the good prediction. So it is concluded that the CNN model is best than the RNN model. In the future the early prediction of both the disease will be done using other deep learning model.

References

1. Barbagallo M, Dominguez LJ (2014) Type 2 diabetes mellitus and Alzheimer's disease. World J Diab
2. Chatterjee S, Mudher A (2018) Alzheimer's disease and type 2 diabetes: a critical assessment of the shared pathological traits. Front Neurosci
3. https://www.niddk.nih.gov/health-information/diabetes/overview/what-is-diabetes
4. https://www.who.int/news-room/fact-sheets/detail/diabetes
5. https://www.mayoclinic.org/diseases-conditions/retinal-diseases/symptoms-causes/syc-203 55825
6. https://www.washingtonpost.com/health/retiina-changes-in-early-alzheimers
7. McGrory S, Cameron JR, Pellegrini E, Warren C, Doubal FN, Deary IJ, Dhillon B, Wardlaw JM, Trucco E, MacGillivray TJ (2016) The application of retinal fundus camera imaging in dementia: a systematic review. Alzheimer Dement: Diagn Assess Dis Monit (Elsevier)
8. Zabel P, Kaluzny JJ, Wilkosc Debczynska M et al (2019) Comparison of retinal microvasculature in patients with Alzheimer's disease and primary open-angle glaucoma by optical coherence tomography angiography. Invest Ophthalmol Vis Sci
9. Colligris P, Perez de Lara MJ, Colligris B, Pintor J (2018) Ocular manifestations of Alzheimer's and other neurodegenerative diseases: the prospect of the eye as a tool for the early diagnosis of Alzheimer's disease. J Ophthalmol (Hindawi)
10. Alber J, Goldfarb D, Thompson LI, Arthur E, Hernandez K, Cheng D, DeBuc DC, Francesca C, Provetti-Cunha L, den Haan J, Van Stavern GP, Salloway SP, Sinoff S, Snyder PJ (2020) Developing retinal biomarkers for the earliest stages of Alzheimer's disease: what we know, what we don't, and how to move forward. Alzheimer's Demen (Wiley Publication)
11. Sandeep CS, Sukesh Kumar A (2018) WN segmentation of retina images for the early diagnosis of Alzheimer's disease (AD). J Anal Pharm Res
12. Tian J, Smith G, Guo H, Liu B, Pan Z, Wang Z, Xiong S, Fang R (2021) Modular machine learning for Alzheimer's disease classification from retinal vasculature. Sci Rep
13. Tadokoro K, Yamashita T, Kimura S, Nomura E, Ohta Y, Omote Y, Takemoto M, Hishikawa N, Morihara R, Morizane Y, Abe K (2021) Retinal amyloid imaging for screening Alzheimer's disease. IOS Press
14. Maninis K-K, Pont-Tuset J, Arbeláez P, Van Gool L (2016) Deep retinal image understanding. Springer International Publishing
15. Rajan K, Sreejith C (2019) Retinal image processing and classification using convolutional neural networks. Springer Nature Switzerland AG

16. El-Hag NA, Sedik A, El-Shafai W, El-Hoseny HM, Khalaf AAM, El-Fishawy AS, Al-Nuaimy W, Abd El-Samie FE, El-Banby GM (2020) Classification of retinal images based on convolutional neural network. Microsc Res Tech (Wiley Publication)
17. Zhang K et al (2021) Deep-learning models for the detection and incidence prediction of chronic kidney disease and type 2 diabetes from retinal fundus images. Nat Biomed Eng
18. Choi JY, Yoo TK, Seo JG, Kwak J, Um TT, Rim TH (2017) Multi-categorical deep learning neural network to classify retinal images: a pilot study employing small database. PLOS ONE
19. Grassmann F et al (2018) A deep learning algorithm for prediction of age-related eye disease study severity scale for age-related macular degeneration from color fundus photograph. Ophthalmology (American Academy)
20. Nazir T, Irtaza A, Javed A, Malik H, Hussain D, Naqvi RA (2020) Retinal image analysis for diabetes-based eye disease detection using deep learning. Appl Sci (MDPI)
21. Salobrar-Garcia E et al (2015) Analysis of retinal peripapillary segmentation in early Alzheimer's disease patients. BioMed Res Int (Hindawi Publication)
22. Sharafi SM et al (2019) Vascular retinal biomarkers improves the detection of the likely cerebral amyloid status from hyperspectral retinal images. Alzheimer's Dement: Transl Res Clin Interv (Elsevier Publication)
23. Garcia-Martin ES et al (2014) Macular thickness as a potential biomarker of mild Alzheimer's disease. Ophthalmology
24. Guo C, Yu M, Li J (2021) Prediction of different eye diseases based on fundus photography via deep transfer learning. J Clin Med
25. Parthasharathi GU, Vasanthakumar K, Premnivas R, Jasmine K (2022) Diabetic retinopathy detection using machine learning. J Innovative Image Process
26. Sungheetha A, Rajesh SR (2020) Comparative study: statistical approach and deep learning method for automatic segmentation methods for lung CT image segmentation. J Innovative Image Process
27. Gaster BR, Schaa D (2013) Heterogeneous computing with OpenCL. Elseiver
28. Jana S, Sarkar B (2021) A semi-supervised approach for automatic detection and segmentation of optic disc from retinal fundus image. In: Handbook of computational intelligence in biomedical engineering and healthcare
29. Huang C, Li X, Wen Y (2021) AN OTSU image segmentation based on fruitfly optimization algorithm. Elseiver

Plant Health Analyzer Using Convolutional Neural Networks

M. Bhavani, K. P. Peeyush, and R. Jayabarathi

Abstract Plant diseases could lead to huge production loss for the cultivators. These diseases are typically in the form of visible symptoms like color changes on the surface of the leaves, different colored spots, or streaks. This region of interest is extracted using image processing, and the area of the disease-affected part of the leaf is calculated. This system is proposed to support agriculturists to identify plant diseases efficiently and constantly monitor the health conditions of the plants. A convolutional neural network is used to identify common diseases of a few types of fruit leaves. The overall accuracy of this system is found to be 90% with a loss of 2.8%. Determining the disease and the leaf's disease-affected area will help in maintaining a better quality of the crop by taking the required actions.

Keywords Plant disease identification · Convolutional neural network · Image processing

1 Introduction

Agriculture is the backbone of our country. They are a major contribution to the economy, and if plants are affected by diseases, it can cause major production loss, leading to economic loss. The pathogens present in plants may cause distress to humans if they are not cultivated with utmost care. Recognition and identification of such plant diseases are vital to maintain food safety and also to improve the quality of agricultural produce. Plants are useful for food and also other basic necessity like clothing, food, etc. Plants play a very crucial role in every human's life either directly or indirectly.

M. Bhavani · R. Jayabarathi (✉)
Department of Electrical and Electronics Engineering, Amrita School of Engineering, Amrita Vishwa Vidyapeetham, Coimbatore, India
e-mail: r_jayabarathi@cb.amrita.edu

K. P. Peeyush
Department of Electronics and Communication Engineering, Amrita School of Engineering, Amrita Vishwa Vidyapeetham, Coimbatore, India

By using image-based automatic disease identification systems and machine learning, the early detection of diseases is done which helps farmers and laboratory technicians [1]. The efficiency of the system depends on the feature extraction from the unhealthy region of plant images and healthy area calculation. Further machine learning classification like convolutional neural networks (CNN) can be applied to the training set to classify diseased plants apart from healthy ones. Leaf diseases can be diagnosed using a few chemical methods also, but it is damaging and also requires a wide range of experimental analyses which may not be able to produce a real-time diagnosis of the disease. Thus, using image processing technology in the field of agriculture can be deployed. By this, results can be obtained faster and without the involvement of chemical processes. With the help of machine learning classification, a large number of leaves can be classified increasing the scope of the usefulness of the work [2].

In order to enhance the accuracy of the plant disease recognition and timeliness of the prediction, this work uses datasets of various plants to be a common platform for the diagnosis of plant diseases. Identifying the disease and giving preventive measures will further help in maintaining the crop. The organization of the content of this paper is as follows: The introduction is in Sect. 1. A detailed literature survey is covered in Sect. 2. The proposed system overview has been detailed in Sect. 3. Section 4 has the implementation and results of this system. It is concluded in Sect. 5, and it is followed by the reference details.

2 Literature Review

The literature survey for this project identifies various datasets used and the various work done on finding the best segmentation technique and also a suitable deep learning algorithm (like CNN) for classification and identification techniques that are to be applied to the datasets.

In this paper, a multi-disease identification system has been offered. The algorithm was used in validating three common diseases of the wheat crop which are the Septoria, rust, and the tan spot on the leaf images [3]. The same has been deployed as an application on a smartphone and tested under real-time conditions.

The basis of this paper is to use the color information of a diseased leaf for image-based disease recognition. To bring this into usage, a three-channel convolutional neural networks (TCCNN) model is developed by the combination of the three-color elements used for disease identification [4]. As an enhanced version of the above-mentioned work, principal component analysis is used to select R, G, and B components and also the H, S, and V components. After this, K-means segmentation is implemented for the segmentation of the images. This algorithm has advantages such as the usage of an adaptive channel, computing the adaptive weight of the channel, and fewer iterations [5]. The algorithm in this work can increase both the size and diversity of the image datasets suggestively as natural changeability is considered. This solution leads to a more dependable result by considering the

context of limitations in the data availability. It also has a few limitations as the dataset is unique [6].

The use of a combination of convolutional neural networks (CNN) and robotics is found to be a useful method to deal with plant disease identification in a simplified manner using an Arduino-based robot and image processing [7]. This work aims to deliver advanced deep neural network classifiers and provide enhanced results. It will also find the percentage of the disease-affected area of the plant for better clarity of the results [8]. This paper converses the techniques required for the discovery of plant diseases by utilizing leaf images. A computer vision-based disease discovery system to evaluate the illness of maize plants is projected here [9]. This paper has developed a faster and lite CNN for refining the correctness from 85.7 to 93.75%. The proposed model here also needs a small storage capacity, and it is quicker in terms of inference time [10].

In this paper, an algorithm for the extraction spots disease of cucumber plant's leaves against a complex background is presented [11]. The algorithm familiarizes regional grayscale information and then overcomes the under-usage of the spatial information of the image pixels in the system. It also advances the noise-filtering capacity and can be achieved in very few iterations, in reduced run time, and also in improving system efficiency. An innovative hybrid model was proposed which was intended for disease detection of the plants. It was built on the convolutional autoencoder network (CAE) and the deep learning technique—convolutional neural network (CNN). For the trial, this model was applied to peach plants for detecting bacterial spots on the leaves. The model attained an accuracy of 99.35% during training, and the testing accuracy was found to be 98.38%. Using 9914 training parameters, which is a small amount, the projected hybrid model suggestively reduced the total time required, which included training the model and identifying the disease [12]. The proposed system trails the influential factors for the growth of grapes within vineyards and offers this data using the Internet and a few sensors. It aids in grape disease stoppage through a perceptive model and procures signals to the cultivators from the winegrower field [13].

After referring to various works in this field, the idea of proposing this work is to identify the disease-affected area of the plant with the help of image processing techniques, identify a few common diseases of a few fruit plants using neural networks, and also calculate the area of the affected leaf for the effectiveness of the result in taking necessary actions.

3 Proposed System

3.1 Dataset

The leaf images used are obtained from an online source named the PlantVillage dataset from Kaggle.com. For the implementation of the plant disease detection system, the total number of leaf images used is 31,520. It is split into training and validation data in the ratio of 75:25. Common diseases of six (6) types of fruit leaves (summing up to 24 classes) are being fed to the neural network. Leaves of apple, blueberry, cherry, peach, grapes, and tomato are considered.

All the images are captured using a camera and saved into folders in JPG format. The size of all the images is fixed at 256 * 256, and it is in RGB format. These images are extracted using a simple load function in the Python code of the system.

3.2 Block Diagram of the System

The system overview for this proposed work is shown in Fig. 1.

After fetching the dataset, the flow of this system includes preprocessing the images and to find the region of interest. Then the classification is done by applying deep learning to these leaf images to know if they are diseased leaves or healthy ones. If it is a diseased leaf, the type of disease is also predicted by the help of convolutional neural networks. Then, using this extracted region of interest of the image, the area of the affected leaf is computed and the percentage of the same is produced. Once the model is trained with these images from the dataset, the deep learning model is saved in the system and it is also stored in the Raspberry Pi microcontroller [14].
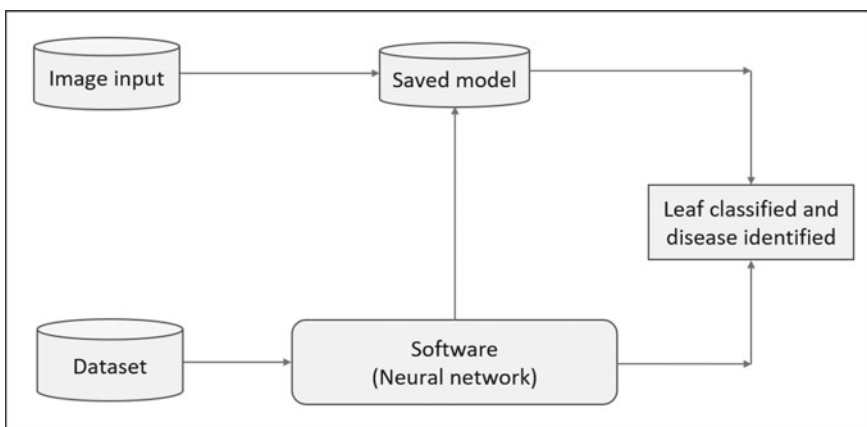
Fig. 1 Block diagram of plant health analyzer

All of this is performed using the software platform—Jupyter notebook in Python language.

Whenever the leaf image, which is to be tested, is given as input, the health, type of disease, and area of the leaf affected by the disease are predicted via this saved model.

4 Implementation and Results

4.1 Preprocessing

The dataset is loaded into the system, and all the images in the dataset are scaled to 256 * 256 and fed. This reduces the extra step of resizing the image.

In preprocessing, the RGB image is converted to an HSV image, to retain the color information. As the color gives most of the information, if the leaf is healthy, it will usually be in green shades. And the shade will be yellow to brown or black when it is affected by some disease [15]. Then the images are converted into numerical formats for ease of computation. Binarizer is used to discretize these numerical values and then fed to the CNN. Label binarizer function is used for this data labeling process.

Masks of green, brown, and yellow are applied to the input leaf, and the leaf is extracted from the background;

4.2 Convolutional Neural Networks (CNN)

The overall architecture of convolutional neural networks (CNN) comprises an input layer, output layer, pooling layers, convolutional layers, and fully connected layers (FC). The pooling and convolutional layers perform as feature signifiers, and the fully connected (output layers) perform as classifiers/identifiers. The selection of these CNN model layers is purely based on experimental analysis done while designing the neural network and also by referring to similar models, because there is no method to calculate these layers as they are data specific and can be done only by analytical ways.

Convolutional layer: This layer extracts the significant features from the layer of input images. Here, the convolution operation is performed among the input image and a pre-defined sized filter $(M \times N)$. By sliding this distinct filter all over the surface of the input image, the dot product is computed by sliding the pre-defined filter over the entire image. In this model, five Conv2D layers are being used.

Pooling layer: The pooling layer aims to lessen the size of a convoluted feature map to decrease the effort and costs of computation.

- In the MaxPooling layer, the largest element from the feature map is considered.

- However, in AveragePooling, the average of the elements from the feature map of a pre-defined size is considered.

  In this model, the usage of three MaxPooling2D layers is done.

Fully connected layer: The fully connected (FC) layer can be used to change the dimensions of the vector and to connect neurons from two different layers. This layer comprises the weights and biases of the neurons. The placement of this layer is generally before the final output layer. A dense layer is also a regular type of densely connected neural network layer.

This model has two (2) dense layers; the final dense layer has the sum of neurons equal to the sum of types (24 classes) of the plants which are to be classified according to their health.

After the images are trained with the CNN, at the end of Epoch 18, an accuracy of 91% is achieved for training data, and an accuracy of 89.5% is achieved for validation data. Accuracy here constitutes the number of images that are classified correctly out of the total number of images that are fed to the network.

The loss is to determine the deviation of predicted images compared to the actual images from the training dataset.

For Fig. 2a and b, the *x*-axis corresponds to the 'Number of Epochs' and the *y*-axis corresponds to the 'Accuracy'.

Figure 2a also shows the graph of training and validation accuracy and Fig. 2b shows the graph of training and validation loss, respectively.

The resulting example of identifying the disease and classification is obtained, and two leaves are displayed below as examples. The image is displayed with the name of the plant which is also the type of disease if the leaf is affected by a disease; if the leaf is healthy, it is displayed as healthy.

In Fig. 3a, the apple leaf with cedar rust disease is uploaded to the system. The pre-trained model is used for prediction, and the output shows the correct prediction of the disease. In Fig. 3b, an example of the healthy leaf of a strawberry plant is used, and the output gives the correct prediction of the healthy leaf as well.
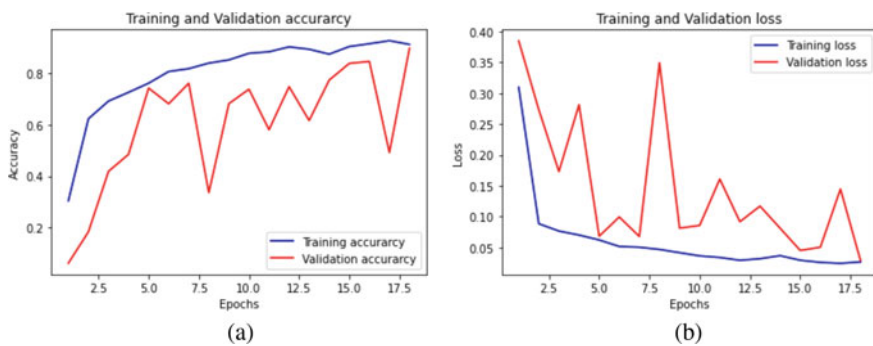
Fig. 2 Graphs of training vs validation accuracy and training versus validation loss
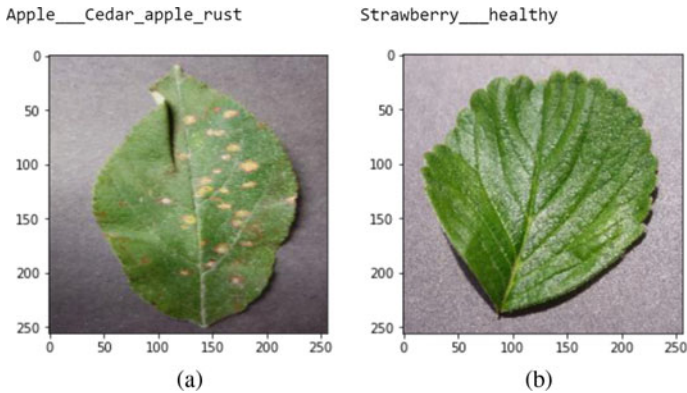
Fig. 3 Prediction of the leaves as healthy or diseased—output

4.3 Area Calculation of Diseased Leaves

The area calculation is done with the help of the OpenCV library in Python. Filtering is done by applying a green and brown color extraction mask, and the leaf outline is obtained. The green mask will extract the leaf portion, and the brown mask will extract the diseased portion of the leaf. Then both masks are combined to eliminate the background, and this helps in classifying the leaf better. In the below equation, the 'total ratio' is the total number of leaf pixels in the given image, 'ratio green' corresponds to the green pixels of the leaf, and 'ratio disease' corresponds to the diseased pixels of the leaf in the given image.

$$\text{total ratio} = \text{ratio green} + \text{ratio disease}$$

The healthy area is computed by using a simple ratio of the green pixel area to the total pixel area of the leaf. The final area of the healthy percentage of the leaf is 'Percent Healthy', and it could be obtained by simply multiplying by 100. The same is given in the form of a simple equation below:

$$\text{Percent Healthy} = \left(\text{ratio\_green} / \text{total\_ratio}\right) * 100$$

Figure 4 shows a grape healthy leaf which on computation shows 93.81% is the healthiness of the leaf. This can indicate that the leaf can be retained in the plant as it is healthy.

Figure 5 shows a mildly affected apple leaf with scab disease, on calculating the healthy area, it is found to be that the leaf is 87.87% healthy. This indicated that the disease is in the initial phase and it has to be monitored and checked so that the disease does not spread further.

Figure 6 is a case of an extremely affected grape leaf by the blight disease. The healthy area of this leaf is found to be only 12.04%, which means more than 87% of
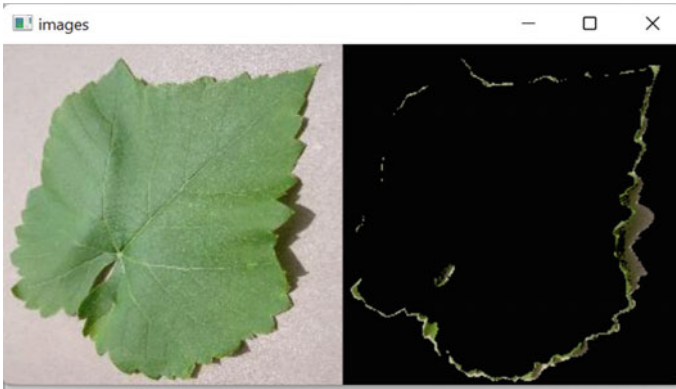
Fig. 4 Grape healthy leaf—healthy area prediction

Fig. 5 Apple leaf scab disease leaf—healthy area prediction

the leaf is affected by the disease. Such highly affected leaves can be discarded from the crops.

Table 1 shows the green pixel percentage, disease pixel percentage, and the healthy area of the above example leaves in percentage.

5   Conclusion

The scope of this system is to support agriculturists and crop cultivators. It monitors the health condition of plants by identifying the disease and also finds the total diseased area of the affected leaf. This system provides a common platform to find out healthy or diseased leaves for various kinds of plants. A convolutional neural network is used for identifying common diseases of a few types of fruit plant leaves.
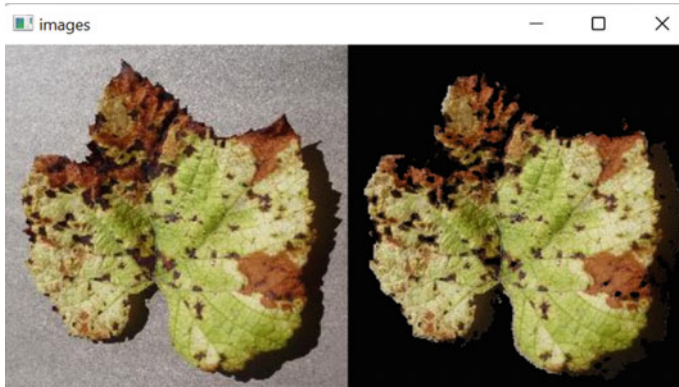
Fig. 6 Grape blight disease leaf—healthy area prediction

Table 1 Green pixel %, disease pixel %, and healthy area information of the leaves

Leaf name and type	Green pixel (%)	Disease pixel (%)	Healthy area of the leaf (%)
Grape—healthy (Fig. 4)	20.15	1.33	93.81
Apple—scab disease (Fig. 5)	18.76	2.59	87.87
Grape—blight disease (Fig. 6)	0.4	17.27	12.04

Determining the area of a leaf affected by the disease will help to maintain a better quality of the crop. By analyzing these results, a possible solution could be suggested that helps in preserving the plants. Further, by saving the trained deep learning model, this system is used to find the health of plants as and when the new input image of the leaf is uploaded.

The future enhancements of this system are that it could be made portable by implementing it on a microcontroller (like Raspberry Pi). This also helps to find the health of the plant leaves spontaneously when the input image of the leaf is uploaded.

References

1. Pooja V, Das R, Kanchana V (2017) Identification of plant leaf diseases using image processing techniques. In: IEEE technological innovations in ICT for agriculture and rural development (TIAR), pp 130–133
2. Supriya P, Jayabarathi R, Jeyanth C, Yogeshwar B, Sarvesh A, Shurfudeen M (2020) Preliminary investigation for Tamil cine music deployment for mood music recommender system. In: 6th International conference on advanced computing and communication systems (ICACCS), pp 1111–1115
3. Johannes A, Picon A, Alvarez-Gila A, Echazarra J, Rodriguez-Vaamonde S, Navajas AD, Ortiz-Barredo A (2017) Automatic plant disease diagnosis using mobile capture devices, applied on

a wheat use case. Comput Electron Agric 138:200–209

4. Zhang S, Wang H (2017) Plant diseased leaf segmentation and recognition by fusion of superpixel, K-means and PHOG. Cogn Syst Res Optik 866–872

5. Hu Q-X, Tian J, He D-J (2017) Wheat leaf lesion color image segmentation with improved multichannel selection based on the Chan–Vese model. J Comput Electron Agric 260–268

6. Elangovan K, Nalini S (2017) Plant disease classification using image segmentation and SVM techniques. Int J Comput Intell Res 13:1821–1828

7. Kesava PSA, Peeyush KP (2019) Autonomous robot to detect diseased leaves in plants using convolutional neural networks. In: 3rd International conference on trends in electronics and informatics (ICOEI), pp 806–809

8. Nage A, Raut VR (2019) Detection and identification of plant leaf diseases based on Python. Int J Eng Res Technol 8:296–300

9. Prashanthi V, Srinivas K (2020) Plant disease detection using convolutional neural networks. Int J Adv Trends Comput Sci Eng 9:2632–2637

10. Li Y, Nie J, Chao X (2020) Do we really need deep CNN for plant diseases identification. J Comput Electron Agric 1–7

11. Agarwal M, Gupta S, Biswas KK (2021) A new Conv2D model with modified ReLU activation function for identification of disease type and severity in cucumber plant. J Sustain Comput Inf Syst 1–17

12. Bedi P, Gole P (2021) Plant disease detection using hybrid model based on convolutional autoencoder and convolutional neural network. Artif Intell Agric 5:90–101

13. Sanghavi K, Sanghavi M, Rajurkar AM (2021) Early stage detection of Downey and Powdery Mildew grape disease using atmospheric parameters through sensor nodes. Artif Intell Agric 5:223–232

14. Aasha Nandhini S, Hemalatha R, Radha S, Indumathi K (2018) Web enabled plant disease detection system for agricultural applications using WMSN. Wireless Pers Commun 725–740

15. Giriraja CV, Siddharth CM, Saketa C, Sai Kiran M (2017) Plant health analyser. In: International conference on advances in computing, communications and informatics (ICACCI). IEEE, pp 1821–1825

Behaviors of Modern Game Non-playable Characters

S. Saranya Rubini, R. Vishnu Ram, C. V. Narasiman, J. Mohammed Umar, and S. Naveen

Abstract The recent trends in the gaming world have been more inclined to shooter games which covers a wide range of audiences including streamers and many more people. People expect the games to be closer to reality for a lively experience. Behaviors of non-playable characters (NPC) in various games like Grand Theft Auto are studied and various methods of defining behaviors to non-playable characters like behavior trees and Q-Learning behavior tree are compared for performance and activities. The comparisons of the resultant agents are made using certain performance criteria like the closeness of AI behavior to the humans, latency to respond to events etc.,

Keywords Shooter games · Non-playable character behavior · Non-playable character · Behavior trees · Quality-learning

1 Introduction

Shooter video games, sometimes known as shooters, are a subset of action videogames in which the player's primary goal is to defeat the character's adversaries with the weapons available to them. These weapons are primarily rifles or other long-range weapons that can be used in conjunction with other items such as bombs for indirect offensive, armor for additional defense, or accessories such as magnifying sights also known as aim down sights to alter the weapon's functionality. The first-person shooter (FPS) is a thread of shooter video games concentrating on gun and other weapon-based warfare in a first-person viewpoint, with the user directing the player character in three-dimensional space and witnessing the event through the main character. There are a lot of games that involve not only the one character but infinitely many characters to suffice multiple needs like improving the competitiveness of the game, improving the quality of the game such that it is more

S. Saranya Rubini (✉) · R. V. Ram · C. V. Narasiman · J. M. Umar · S. Naveen
Department of Computer Science and Engineering, Coimbatore Institute of Technology, Coimbatore, Tamil Nadu, India
e-mail: ssaranya@cit.edu.in

closely related to reality etc., The multiplayer games satisfy these requirements very well because the opposite agents are controlled by humans who have a unique way of thinking. Other games that involve non-playable characters find it difficult to satisfy the need of deploying an environment that is much closer to reality because they have fixed behaviors and their modeling architecture which is likely to be a finite state machine. The reason for their very limited behavior is the smaller number of states or actions defined for each one of the characters. It is also highly likely that the NPC could not be able to perform a certain type of action such as react to a death of another character as those states that trigger these reactions might not be accessible by the NPC at that instant because the game is played in real time. These limitations of the non-playable character make the games less interesting and more artificial to play.

2 Objectives of Games

There are two types of shooter games based on the environment played upon. Open world games and closed world games are the two major types. The closed world games provide a smaller map and a shorter game time for a particular match. Among those are the famous games like Counter Strike Global Offensive and Valorant. These games are played in a smaller map with five people on a team [1]. A team which is attacking will be considered as a winner if all the members have been eliminated or whether they have planted the bomb in the respective sites and guard it, till it detonates. Counter Strike Global Offensive also works upon similar action-based team gameplay which made it a well-known popular game for around 19 years [2]. They have the high streaming rates in today's online community for gamers like twitch and YouTube.

The open world games on the other hand provide a much larger game map with free roam features so that the character can move anywhere to the map irrespective of the instance the game is in. The main objectives in these types of games follow story mode completion which is enacted using missions involving the main character, i.e., the protagonist of the game. The most popular open world game is Rockstar game's Grand Theft Auto: San Andreas which involves the main objective as completion of the main character CJ's story [3]. Both these types of games can be played either in online mode which involves meeting many real players around the globe or offline mode where all the people other than the player are the Non playable characters.

3 Massive Multiplayer Online Game [MMOG]

To face the challenges in designing a modern Massive Multiplayer Online Game, the MMOG [4] presents a new and exciting domain in service-oriented computing, multi-agent systems (MAS), agent organization, and electronic institution. The MMOG

Layer is a sophisticated subsystem that implements all the game logic and mechanics and must solve them at runtime. The MMOG Layer is an open, dedicated MAS that runs the game. This MAS models some game mechanics using agent technologies such as agent services, electronic institutions, and agent organizations, and converts common MMOG issues and situations into problems that can be solved using classic software agent features such as agent interactions, agent communication protocols, service-oriented computing, event-driven behaviors, role models, and so on. For example, instead of a single central unit for storing the details like health, power, ammo, etc., for each agent, the MAS distributes the logic for each and every individual agent reducing the complexity of the system to a great extent and thereby increasing performance. These features give the players a smooth experience and make them to strive for expertise in their gaming skills. The players who want to get better at a MMOG often use third party applications like aim lab for shooter games in addition to inner game resources available and redeemable [5].

In case of open world games like Grand Theft Auto or Watch dogs, the user can choose to play as protagonist or one of the pedestrians imparting more lively features to the game. There are also other type of games falling under the category of Battle Royale like PUBG and Fortnite where each character is highly likely to be a real player. This makes each game different that is no two separate games can be a replica of one another.

4 Fairness and Strategies in Game

The game must be balanced by rules and fairness between the two teams that play. There must be an equal chance of attacking and defending team winning. There are also roles assigned to players and they play accordingly. The tendency to participate, behave, and relate with others in a specific way was termed as 'Team Role'. According to the 'Team Role Balance Hypothesis,' there should be a mixture of team roles, each performed out by a skilled individual, for optimal team performance. Each person has a primary and secondary function as mentioned in Table 1, which helps them with finest performance [6].

Apart from these the game maps are also designed in such a way that it is balanced and winnable for both attacking and defending sides to take control. Usually, there will be two or more sites to plant the bomb and the sites will be ease of access to the defending sides. This may first appear as a disadvantage to the attacking side, but it is

Table 1 Roles in Valorant

Role	Description
Duelist controller sentinels initiator	Entry fragger second entry fragger
	Support and in game leader recon and crowd control

not. The players get to choose a site and push in with all members of a team whereas the defending team would be split up into two between each site. This makes the play of the game more interesting. The map creators keep in mind a lot of factors while designing a map. Some of them are the balance between cover and visible sight, camping hotspots reductions, distance to cover from spawn, and distance between spawn points [7]. With all these considerations and keeping in mind the esthetic value of environment, the game environment and the maps are made for the players to enjoy and play. In open world games cheaters or hackers can be detected with the help of other players in the game. Malicious activities can be easily identified by other players than the server itself as hackers tweak existing function only. So, if a player is reported by many other players in the same server the anti-cheat force for that game reviews the player and bans the gamer from that server to maintain the ethics of the game.

5   NPC Behavior in Games

In the known games, the finite state machine (FSM) model is the main method of behavior modeling [8]. FSM is concept friendly and the structure of which is clear. Fixed rules give the agent a drab appearance, which is unsatisfactory. The behavior tree model [9] is created to address FSM's deficiency, which considerably improves development productivity, it is not without flaws. But, it is still a decision-making model with fixed rules. A behavior tree is a directed tree, which is composed of nodes and edges [10]. Nodes are divided into leaf nodes and non-leaf nodes. Each node has only one parent node except root node. Parent nodes generally have many children nodes each corresponding to a specific task of a desired event. There are three main types of nodes in the behavior tree as mentioned in Table 2. They are the sequence node, selector node, and parallel node. The sequence node as shown in Fig. 1 is considered to be executed successfully if all the children under that node successfully executes. If one of the nodes fails, the whole sequence node fails. The selector node on the other hand is said to be successful if any one of its children can be executed successfully and if no child can execute, it is considered to be a failure. The parallel node is a special kind of node where if at least N nodes succeed, it is successful [11].

In order to diversify the NPC behavior and make the game more random and unpredictable, games like GTA have made the behavior tree model complex for each and every NPC. There are up to 300 different NPC's and 60,000 different

Table 2 Node types and behavior

Node type	Conditions for success
Selector sequence parallel	If one child succeeds if all children succeed
	If at least N children succeeds

Fig. 1 Sample behavior tree with a sequence node
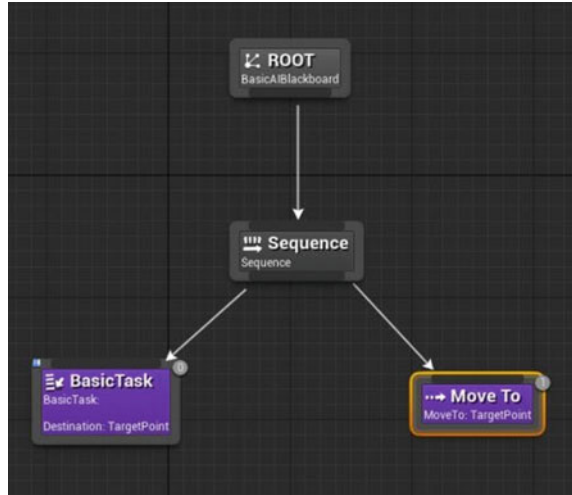
communication line and many more behavior traits so that no player can be able to remember or notify every one of them. It is highly unlikely that an in-game player could have heard the whole game audio. Apart from these specialized NPC like policemen, firemen, paramedics, and many more types have been included in game to provide a close to reality experience for the gamer.

6 Case Study of Some Behaviors in NPC's of Grand Theft Auto

Grand Theft Auto is a popular game where NPC behaviors can be uniquely identified and can be considered as benchmark for other open world games that are similar to it. The characters in those environments can adapt and learn in real time as the environment changes dynamically like finding alternate ways to move around a blocked path as shown in Fig. 2.

The NPC's are designed in such a way that they can read and react to certain events in the gaming environment. The NPC's in game can also develop human feelings and emotions like fear as shown in Fig. 3, irritation, and hospitability. These kinds of behaviors can also be developed using the behavior tree.

Differences between the NPC behaviors can also be observed. Different NPC's behave differently in the case of similar events. For example, on seeing a dead body some NPC's get curious about it and gather around the dead body as shown in Fig. 4., whereas some characters just walk away in a pacey way from the dead body in fear of being framed for the killing or murder.

Casual behaviors of NPC are also defined. These behaviors play a crucial part in making the game lively. For example, NPC's in GTA take pictures around super cars

Fig. 2 NPC walking around a blocked sidewalk

Fig. 3 NPC runs due to fear when the player uses guns toward them

Fig. 4 Shows NPC's surrounding a dead body

or luxury cars as shown in Fig. 5 just like people do in the real world. If the car is normal, they just do not bother it.

There are a lot of other actions in NPC behavior. Some get annoyed on honking horns for a long time and move away. When fights happen, some NPCs join them or watch them whilst some just run away. They can also sense a vehicle coming to dash them and jump out the path immediately. There are also specific voice lines to express certain feelings and much more to the game. For example, a policeman who is clearly a non-Playable character can be triggered when the player talks abusively to the non-playable character. The NPC can also arrest the player for the same showing that the NPC can understand and process the language in which people communicate and respond or react accordingly.

Fig. 5 An NPC taking photos of a super car

Every NPC has been designed very closely to practice daily routines as normal humans do including visiting an ATM or participating in parties or even watching and admiring street performances. The player character PC also utters dialogs to express how the character is feeling in a certain state [12]. For example, after a collision with a NPC the player character speaks dialogs like "Look out!" and "Hey, Sorry!" [16] for which the NPC would automatically respond. Considering all these a NPC in game is highly similar to the behavior of a real life person. These features make the advertisements for the game and people do enjoy being a virtual character in an environment which is highly like the real world today. Other similar games like Cyberpunk, Assassin's creed and even in older versions of the game, the non-playable character is not able to display such diverse characteristics thus making the game less associated to reality as shown in Figs. 6 and 7.

Fig. 6 NPC not reacting to events like deaths of other NPC's in cyberpunk

Fig. 7 NPC cannot find an alternate path and it just tries to walk forward

7 Behavior-Based Learning for NPC

Q-Learning is a reinforcement learning method that establishes and manages a table of values that estimates the utility of performing a task in a given condition. A function is given to the NPC that links states to a specified reward. This specified function allows the agent to choose either of two decisions-exploit or explore. The exploit action reviews all the specific actions and their respective rewards that can be attained from a certain state and performs the action. The explore decision on the other hand tells the agent to perform a random action from the current state. The idea of exploration is that to uncover new series of states that cannot be found by exploitation. This allows the NPC to act more dynamically rather than exploiting the only way to get maximum reward. The system then feeds incentives that is obtained by performing a certain action from a state back into state-action pairings, resulting in reward states that improve utility estimations over time [13]. These improvements make the in-game NPC think rationally and take optimal decisions as the game progresses. In a behavior tree the nodes are executed from left to right generally. For applying the learning algorithms, the low-level behaviors are split into small actions and hierarchical reinforcement learning algorithms are applied [14]. Integrating the behavior tree and Q-learning methodology, the node with highest optimum value is selected as the left most node and this Q-values change as the environment of the character continuously changes.

The Q-values are updated at the end of an episode which may mean in many ways including the completion of the game, completing a certain objective or any terminal point. Successive episodes leads to convergence of the Q-values and thus the agent has learned by quality. Q-Learning is an epsilon greedy approach-based algorithm [15]. Epsilon greedy method chooses the best optimum value and increases

new node explorations with a small probability. Each scenario is characterized with a state '*s*' and each state has a specific action '*a*' to be performed. The program will analyze the condition of agents at the selector node, which can be done by discretizing various agent indicators. The state and child nodes of the switcher will produce a state-action pair (state '*s*', action '*a*') in this way. [11] The model will reward the character when it fulfills a requirement, such as hitting an enemy, killing an opponent, or obtaining a supply. When the learning-selector is enabled, it will first assess the character's present condition. Then it will rank the state-action pair within a given state according to $Q(s, a)$, tick the children in this order with likelihood, and update the Q value. Mathematically, this can be formulated as,

$$Q(s, a) = Q(s, a) + \alpha \cdot \left(r + \gamma \, Q(s', a') - Q(s, a)\right) \tag{1}$$

The α in the Eq. 1 denotes the learning rate, r denotes the current reward for performing action a from state s and the γ denotes the discount factor. The discount factor is always kept between 0 and 1 as to reduce the value of future rewards that are obtained by choosing the future action a' from the next state s' because the current reward must be valued more. This updating of values as shown in Eq. 1 continues till the agent reaches the convergence point and the state of the behavior tree changes at every instance. This combination of behavior tree and reinforcement learning can be used as the framework for adaptive behavior modeling in a gaming environment. Many more complex character structures in games can be made using the method of behavior tree with reinforcement learning algorithms. This affects the liveliness of the gameplay and thus the people playing and streaming the game.

8   Conclusion

People like games that simulates events like reality. The environment can be made effectively, but the people or the non-playable characters must be programmed to behave like people which is a hard task. FSM were used, but they tend to follow a certain behavior and couldn't react to even happening real-time. Figures 6 and 7 illustrate this concept very clearly as the NPC follows undefined behavior rather than adapting to the current environment. This is a very big limitation in the world of story games where most of the characters are computer controlled. A data structure called behavior tree is introduced that made imparting behaviors to the NPC easier and efficient. Combining hierarchal reinforcement learning algorithms like Q-learning which associates every action with a reward like Markov Decision process and chooses the action with highest reward was proposed and used for modeling those characters. Usage of this data structure in modeling a non-playable character resulted in positive outcomes. A study was also made on NPC in the game of Grand Theft auto: *V* in which the NPC is modeled using behavior trees and it is noticed that the characters in game could respond and react to dynamic events that is happening

real time. This has proven that Q-learning behavior trees are highly rewarding and is a promising area to work on for future research purposes.

References

1. https://playvalorant.com/en-us/
2. https://store.steampowered.com/app/730/CounterStrike_Global_Offensive/
3. Annandale D (2006) The subversive carnival of grand theft auto: San Andreas. In: The meaning and culture of grand theft auto: critical essays, pp 88–103
4. Aranda G, Botti V, Carrascosa C (2009) Mmog based on mas: the mmog layer. In: Proceedings of the 8th international conference on autonomous agents and multiagent systems, vol 2
5. Voulgari I, Komis V (2011) On studying collaborative learning interactions in massively multi-player online games. In: 2011 Third international conference on games and virtual worlds for serious applications. IEEE
6. Buchan A, Taylor J (2016) A qualitative exploration of factors affecting group cohesion and team play in multiplayer online battle arenas (mobas). Comput Games J 5(1):65–89
7. Kruse J, Connor AM, Marks S (2021) An interactive multi-agent system for game design. Comput Games J 10(1):41–63
8. Dawe M et al (2013) Behavior selection algorithms. In: Game AI pro: collected wisdom of game AI professionals 47
9. Isla D (2005) Handling complexity in the Halo 2 AI. In: Game developers conference, vol 12
10. Ogren P (2012) Increasing modularity of UAV control systems using computer game behavior trees. In: AIAA guidance, navigation, and control conference 2012
11. Fu Y, Qin L, Yin Q (2016) A reinforcement learning behavior tree framework for game AI. In: 2016 International conference on economics, social science, arts, education and management engineering. Atlantis Press
12. Dahlan F (2013) The study of slang in pedestrian dialogue of GTA San Andreas video game. Abstract of Undergraduate Research, Faculty of Humanities, Bung Hatta University 3(2)
13. Dey R, Child C (2013) Ql-bt: enhancing behaviour tree design and implementation with q-learning. In: 2013 IEEE conference on computational intelligence in games (CIG). IEEE
14. Du X, Li Q, Han J (2009) Applying hierarchical reinforcement learning to computer games. In: 2009 IEEE international conference on automation and logistics. IEEE
15. Sutton RS (1998) Introduction to reinforcement learning. MIT Press, Cambridge, Mass

Low-Noise Amplifier with Co-designed Microstrip Antenna for 60 GHz Wireless Communications

Garre Pranay Phaneendra, Gokada Sri Lekha, Kariveda Manvitha, Nalla Sowmya Sri, and Karthigha Balamurgan

Abstract Significant gains in semiconductor technology devices have enabled high-data-rate communications at 60 GHz which stimulates short-range multigigabits-per-second transmission for multimedia applications. This work focusses on the design of the first block of the receiver and the low-noise amplifier with integrated antenna which is considered to be the most challenging task. Over the desired frequency of 60 GHz, microstrip antenna and low-noise amplifier have been designed and integrated with co-design approach. Using inductive source degeneration technique, two-stage common source low-noise amplifier in a 65-nm CMOS technology has been designed and found to produce gain of 12.557 dB and noise figure of 3.626 dB. Antenna efficiency is the amount of RF power delivered to the antenna (from radio) which is actually transmitted into the air.

Keywords Microstrip antenna · Antenna co-design · Input–output matching · Inductive source degeneration · Two-stage common source · HFSS · Advance design system (ADS)

1 Introduction

There is an ever-increasing supply and demand for broadband multimedia applications, mandating increased wireless network capacity equipped with highly integrated silicon receiver. Several applications such as gigabit WLAN, WPAN, fiber to the home, unlicensed point-to-point networks, etc. are termed as high-volume applications which require high data rates in terms of Giga bits/s over a short range. The apparent solution for addressing this need is to use unlicensed spectrum of nearly 7 GHz available at 60 GHz band [1]. The 57–64 GHz band has been recognized

G. P. Phaneendra (✉) · G. S. Lekha · K. Manvitha · N. Sowmya Sri · K. Balamurgan
Department of Electronics and Communication Engineering, Amrita School of Engineering, Amrita Vishwa Vidyapeetham, Coimbatore, India
e-mail: pranayphaneendra1819@gmail.com

K. Balamurgan
e-mail: b_karthigha@cb.amrita.edu

as the biggest unlicensed band by the Federal Communications Commission, and its frequency is suitable for short-range and high-speed wireless communication. In comparison to lower frequencies, O_2 absorption is very high at 60 GHz. Because of this, signals get attenuate over time, preventing them from traveling much beyond their intended target [2]. Due to its channel characteristics, 60 GHz has extended its hand to support wireless data transmission in the industrial, scientific, and medical (ISM) band.

The success of wireless communication systems lies in the design of high-performance receivers. The crucial components that decide the noise figure (NF) of receiver, sensitivity, and its dynamic range are the low-noise amplifier (LNA) and mixer blocks [3]. Challenges faced in designing these sub-blocks are noticed as follows: limited f_T of the device, distributed effects present at GHz frequencies, noise, power, topology selection, integration of antenna, lossy substrate, power, cost, etc. CMOS-based millimeter-wave integrated circuit has ignited the researchers due to low-cost integration possibilities, low power, scaling, moderate noise margins, etc. A typical 65-nm submicron CMOS device has reached its f_T (transit frequency) and f_{max} (unity power gain) frequencies greater than 200 GHz.

The objective of this paper is to design a microstrip patch antenna and LNA suitable for 60 GHz receiver and to integrate both by co-design approach with minimal degradation. The paper is organized as follows: Sect. 2 describes the technical challenges of antenna and provides the details of the intended design; Sect. 3 presents the selection of MOSFET device and discusses the LNA topology and impedance matching of the proposed work; Sect. 4 discusses the results of antenna, LNA, and their co-designed integration outputs; and Sect. 5 concludes the work with glimpse of future scope.

2 Antenna Design and Challenges

Designing a giga Hz antenna with small size, high directivity, wide bandwidth, high data rate, and low fabrication cost that encourages mass production is a challenging task. At 60 GHz, signal attenuation is more due to oxygen absorption and heavy rain fall. Most of GHz antenna suffers from electromagnetic losses and low precision errors [4]. In spite, several research works have been done [4–8] by considering few or all mentioned factors.

Horn antennas, metallic antennas, dielectric type, and PCB antennas are available at the frequency of interests [5]. But they are affected by design complexity and high cost. Nowadays microstrip patch antenna at GHz is preferred due to high gain, less bulky, low cost, compact size, and ease of fabrication and that supports multichannel requirements even though it is limited to narrow bandwidth and possesses lower power efficiency [5]. Moreover, it supports multidirectional polarization methods.

In literature paper [6], authors have proposed a compact, single-feed, dual-band, circularly polarized annular ring patch antenna coupled to a cross-slot. The antenna consists of two annular rings configured by two small strips which is coupled to a

cross-slot in the ground plane for gain enhancement. Circular polarization in both the bands is produced by introducing perturbations in the outer annular ring and by placing two orthogonal strips in the center space of the inner annular ring. Basically small perturbations create arbitrary shape in microstrip patch antenna. This arbitrary shape is used to generate perturbated and unpertuburated electromagnetic waves. So in order to strengthen or to enhance electromagnetic field, circular polarization is to be formed on circumference of antenna. For achieving this, small perturbations have been created (sm where either perimeter or annular ring surface). The gain has been observed as 3.68 dB at 1176.45 MHz frequency.

In paper [7], authors have proposed a microstrip patch antenna using stripline direct feeding technique and Duroid 5870 substrate with the following dimensions: length of patch $= 1.59$ mm, width of patch $= 1.91$ mm, width of stripline $= 0.05$ mm, and length of stripline is 1.2 mm. Their return loss is of -24.77 dB and gain of 7.4 dB at 60 GHz have been achieved which is enough to use for defense applications. The feedline is kept slightly offset from the middle of width for better impedance matching and improved radiation pattern.

In paper [8], the proposed antenna has two symmetrical rectangular slots on the patch edges with a metal cladding strip of length 'L/3' reserved at the center of patch. This design is similar to a group of two extra-wide microstrip patch elements that are fed together on a line. The design details are as follows: substrate thickness $(h) = 0.127$ mm, $L = 4.4$ mm, and $W = 5.54$ mm. This gave results of return loss (S_{11}) as -9.92 dB with gain of 13.5 dB at 60 GHz.

The major advantage of implementing a rectangular patch is that it provides the highest impedance over the bandwidth for any patch shape. A patch antenna designed on a Duroid substrate excels than on a liquid crystal polymer (LCP) or FR4 EPOXY substrates in terms of electrical performance. Duroid offers benefits such as low dielectric constant, low loss tangent, and low cost over other materials [7]. The lowered substrate thickness helps to reduce surface wave propagation. The focus of this research is to demonstrate the microstrip design approach that considerably improves the gain and bandwidth at GHz frequencies while still allowing the antenna to be fabricated using the traditional etching method which is cost-effective. The direct feeding technique is simpler because of its planar structure that increases the surface waves and radiation along with the thickness of the dielectric substrate. It provides proper output impedance for matching with LNA when compared to inset feeding technique that suffers from return loss and limited bandwidth. The antenna performance parameters that are focused in this work are return loss, input impedance, bandwidth, gain, directivity, radiation pattern, HPBW (half-power beamwidth), and surface charge density.

In this work, a rectangular microstrip patch antenna is designed on RT/Duroid5880 bearing a dielectric constant (ε_r) of 2.2 with a thickness (h) of 0.5 mm over resonance frequency (f_r) of 60 GHz using direct feeding approach. The design parameters are computed using the transmission line model equations [5].

Table 1 Design parameters

Parameter symbol	Parameter name	Value (mm)
W	Width of antenna	1.976
L	Length of antenna	1.3244
H	Thickness of antenna	0.5

$$W = \frac{c}{2f_r}\sqrt{\frac{2}{\varepsilon_r + 1}} \tag{1}$$

Effective relative permittivity is given by

$$\varepsilon_{\text{reff}} = \frac{\varepsilon_r + 1}{2} + \frac{\varepsilon_r - 1}{2} * \left[1 + 12\frac{h}{W}\right]^{-12} \text{ for } \frac{W}{h} > 1 \tag{2}$$

$$\Delta L = 0.412h\left(\frac{(\varepsilon_{\text{reff}} + 0.3)\left(\frac{W}{h} + 0.264\right)}{(\varepsilon_{\text{reff}} - 0.258)\left(\frac{W}{h} + 0.8\right)}\right) \tag{3}$$

$$L = \frac{c}{2f_r\sqrt{\varepsilon_{\text{reff}}}} - 2\Delta L \tag{4}$$

w—width of patch, L—Length of patch, h—thickness of substrate, ε_r—dielectric constant, f_r—resonance frequency, c—velocity of light, $\varepsilon_{\text{reff}}$—effective dielectric constant, and ΔL—extended length (due to fringing fields patch antenna electrically seen to be bit larger than usual design) (Table 1).

3 LNA Design and Challenges

The primary function of LNA is to amplify extremely low signals without adding noise on its own, while maintaining the constant signal-to-noise ratio throughout the receiver. There is always a trade-off among LNA parameters such as gain, noise figure, input–output impedance, bandwidth, stability, power, linearity, and output swing [3].

For LNA implementations, common source (CS) and common gate (CG) designs are mostly used. The CS LNA features a high-gain and low-noise figure but bandwidth is limited due to Miller capacitance [9]. In the case of CG, wider bandwidth is achieved but with poor noise performance especially at high frequencies. In most of the cases, inductive load has been used in place of resistive load because it offers less NF. Some strategies have been proposed to increase noise performance such as capacitive cross-coupling [9], gm boosting, current reuse, etc. For narrowband applications, CS with inductive source degeneration (ISD) configuration is commonly used. But the degenerated inductor affects the gain, NF, and stability of the LNA

circuit. However, using proper matching network that encourages multistage design can be used to alleviate the mentioned drawbacks to some extent.

Cascode configuration [10] offers superior isolation, improved bandwidth, and higher gain but the drain capacitance present at the junction of cascode devices causes severe noise problems. In order to avoid these problems, literature [10] uses a middle inductor in a two-stage ISD architecture. This strategy enhances the stability and expands the linearity. It has been implemented using 65-nm CMOS technology which provides NF of 1.54, gain of 24.5 dB, input return loss of -9.1 dB, and static power dissipation of 6.63 mW at 60 GHz. Equivalently, multistage designs, like in literature [11], use double transformers as current reused elements in a three-stage CS LNA. The circuit has a reflection coefficient of -10 dB, a gain of 31.5 dB, and an NF of 1.9 dB observed at 60 GHz [12–15].

This work uses two-stage CS topology with ISD at each stage. It provides inherent resistance of 50 Ω which is used for input impedance matching, thus reducing the return loss and improvising gain. Before going to the actual design of LNA, the device parameters like bias point, transconductance gain, transit frequency (f_T), and unity power gain frequency (f_{max}) have to be extracted. These parameters depend on the width of device, number of fingers, supply voltage, and input and output impedances [15–19].

This work uses 65-nm CMOS technology that operates at 1.1 V. Using BSIM4 NMOS model, our device is prepared to work at 60 GHz by selecting optimal width, number of fingers, and bias current that guarantee higher gain and minimal NF. The circuit is shown in Fig. 1 and its details are given as follows: width = 65 um, number of fingers = 4, drain current, $I_D = 28.1$ mA, $V_{GS} = 606$ mV, $V_{TH} = 299$ mV, $V_{OV} = 307$ mV, $V_{D(Sat)} = 177$ mV, and gm = 99.4 mS. Figures 2 and 3 show the f_T and f_{max} curves observed over the mentioned bias point. The values are found to be 180 GHz and 161 GHz, respectively. From this, it can be inferred that the device has been prepared and found to be suitable for 60 GHz LNA applications. The input matching is done using the source inductance, L_2, and gate inductance, L_1, in order to cancel the pure capacitive input, C_{gs}, of M_1. The resistive part, $\omega_T L_2$, is inherently generated which is matched with $Z_{in} = 50$ Ω Here, $\omega_T = g_m/C_{gs}$ is the transit frequency of device. Since no physical resistor is involved, the NF is lower in this configuration.

Figure 4 shows the two-stage CS with ISD configuration formed by M_1 and M_2 as the first and second stages. V_1 and V_2 are the biasing voltages of M_1 and M_2 which has L_3 and L_6 as the inductive loads. L_1, L_2, L_4, and L_5 are used for matching the impedance in the first and second stage in which L_2 and L_5 form the ISD inductors. The capacitance C_1 along with the drain capacitance of M_1 and C_{gs2} of M_2 form the intermediate matching network. The optimal width of M_1 and M_2 have been selected based on maximum available gain from f_{max} curve which is presented in Fig. 3. This guarantees that the LNA achieves simultaneous input matching and minimum NF [12].

In Fig. 4, the first stage operates at required bias point and is observed to produce gain of 6.1 dB and NF of 3.7 dB. In order to improve the performance, second stage has been designed in this work. For this requirement, impedance matching has been done using single time constant networks at input and output ports. Before matching

Fig. 1 Biasing circuit of MOS device
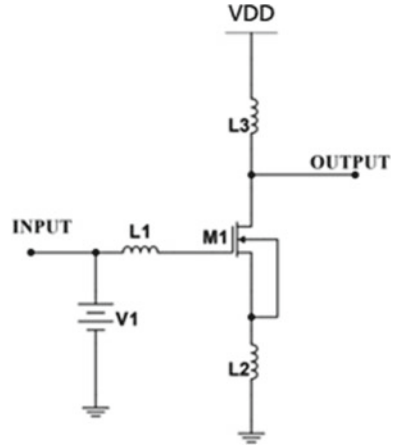
Fig. 2 f_T of CMOS model
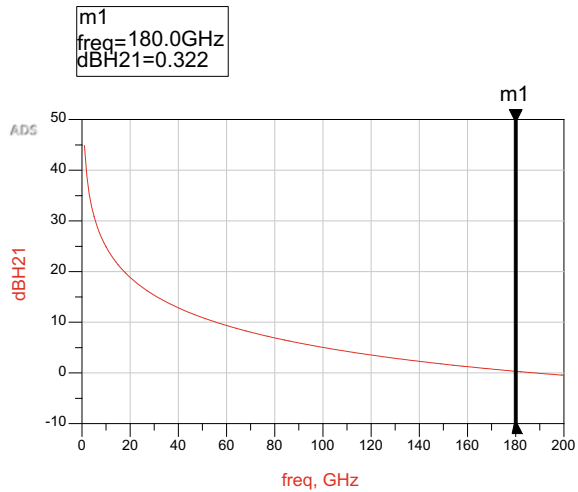
network, adding the second stage in Fig. 4 shows the input and output return loss, S_{11} and S_{22}, as $0.180\angle160.056$ and $0.128\angle-178.404$, respectively, at 60 GHz in Fig. 5. After designing proper input and output matching networks, the improved S_{11} and S_{22} are observed in Fig. 6. The values noticed are $0.069\angle68.875$ and $0.111\angle-81.859$, respectively, at 60 GHz.

4 Results and Discussion

The proposed work described in Sects. 2 and 3 have been implemented and integrated using co-design approach by considering impedance parameter. The results

Fig. 3 f_{max} of CMOS model

m2
freq=161.0GHz
MAG=0.359

Fig. 4 Two-stage CS with ISD

m1
freq=60.00GHz
S(2,2)=0.128 / -178.404
impedance = Z0 * (0.773 - j0.006)

m2
freq=60.00GHz
S(1,1)=0.180 / 160.056
impedance = Z0 * (0.706 + j0.090)

freq (1.000GHz to 100.0GHz)

S(1,1)
S(2,2)
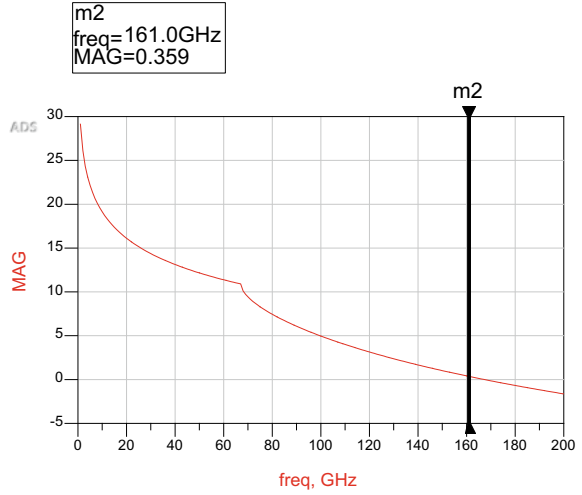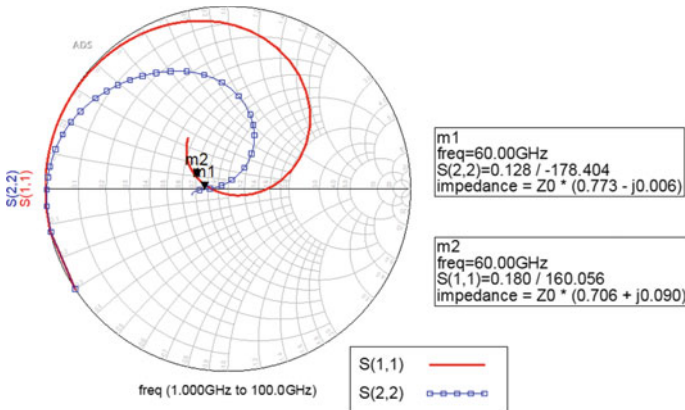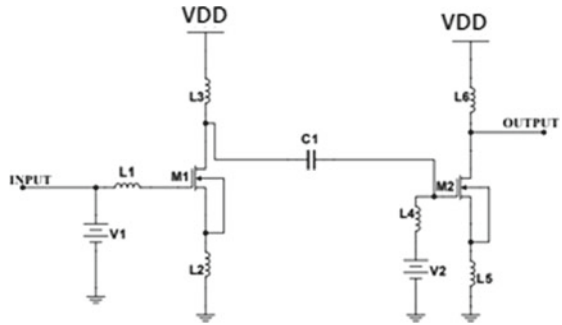
Fig. 5 S chart representation of S_{11} and S_{22} without impedance matching networks
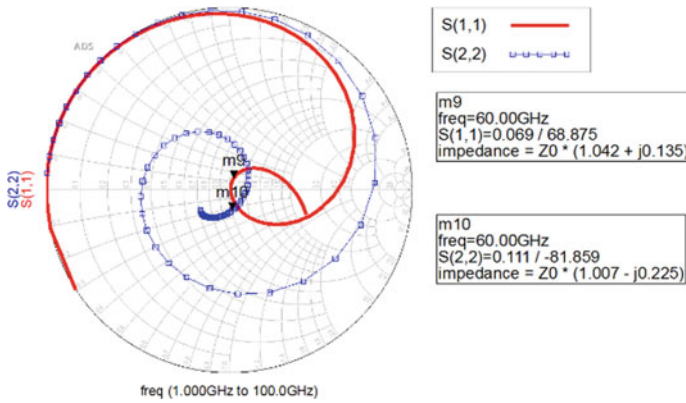
Fig. 6 Smith chart representation of S_{11} and S_{22} with impedance matching networks

are presented in the following three sub-sections namely antenna, LNA outputs, and integration of LNA with antenna using co-design method.

4.1 Antenna Results

Based on design methodology presented in Sect. 2, return loss, gain, E-plane and H-plane radiation patterns, 3D-polar plot, and surface current density have been observed over the frequency range of 40–80 GHz for the microstrip patch antenna. Figure 7 shows S_{11} versus frequency (also known as return loss) which demonstrates that the rectangular patch antenna resonates at 59.8 GHz with a return loss of -24.8687 dB and a -10 dB bandwidth of 4.9 GHz. This shows that the impedance is perfect at the resonance frequency. From Fig. 8, the overall gain of the antenna is noticed as 4.54 dB at 60 GHz. It is known that gain (G) is directly proportional to directivity (D). This result shows that the designed antenna has sufficient directivity in spite of oxygen attenuation that limits the link distances.

$$G = \varepsilon_r D \tag{5}$$

Figure 9 shows the far-field amplitude patterns along the E-plane (i.e., $E\varphi$ when $\varphi = 0°$) with the observed 3-dB beamwidth of 76.8781. Similarly, Fig. 10 shows the far-field amplitude patterns along the H-plane (i.e., $E\varphi$ when $\varphi = 90°$) with a 3-dB beamwidth of 104.42. The beamwidth is the angular distance between the half-power points while the half-power beamwidth is sometimes referred to as 3-dB beamwidth. This is because half the power is represented in decibels as -3 dB. Figure 11 illustrates a 3D visualization of the antenna's far field that indicates a more accurate representation of the radiation pattern in space. When designing these antennas, it is frequently believed that the microstrip components are positioned on infinitely large
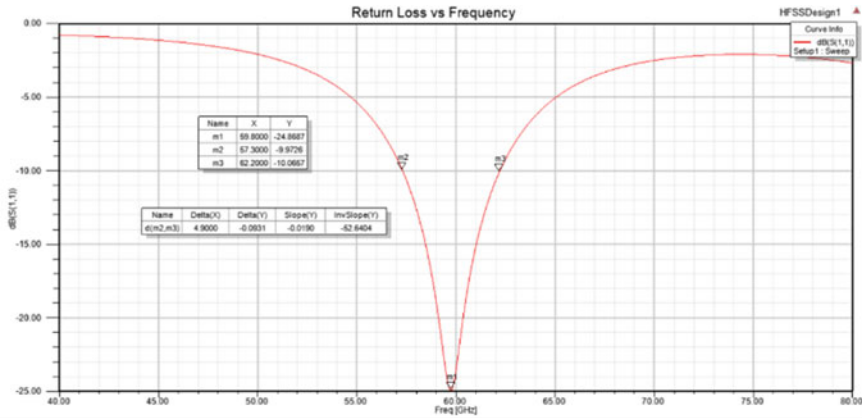
Fig. 7 Return loss
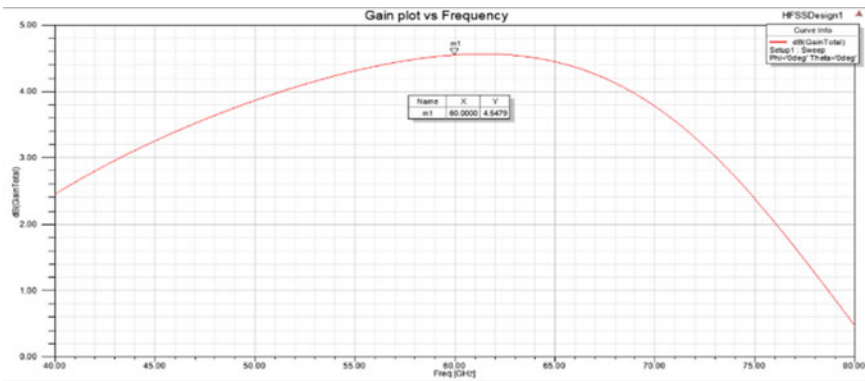
Fig. 8 Gain of the antenna

ground planes, hence ignoring diffraction from the ground plane's edges. However, in real applications, diffraction from these edges can have a substantial impact on the radiation pattern. It would be ideal to have an analytical model that can be utilized to determine the magnitude of this effect. Treatment of these edges may be required to regulate their influence on the radiation pattern, which is frequently performed by inserting lossy materials near the edges to reduce the fields that diffract off them.

Figure 12 illustrates the surface current density along the antenna patch. It describes the total amount of charge per unit area. The results presented from Figs. 7, 8, 9, 10, 11 and 12 depict the validity of designed antenna that could meet the requirements of LNA at 60 GHz.

Figure 13 illustrates input impedance of microstrip patch antenna. Impedance (Z_{11}) is $55.77 + j * 3.98 \, \Omega$ at 60 GHz. Figure 14 illustrates the VSWR of microstrip patch antenna. VSWR is 1.14 at 60 GHz.
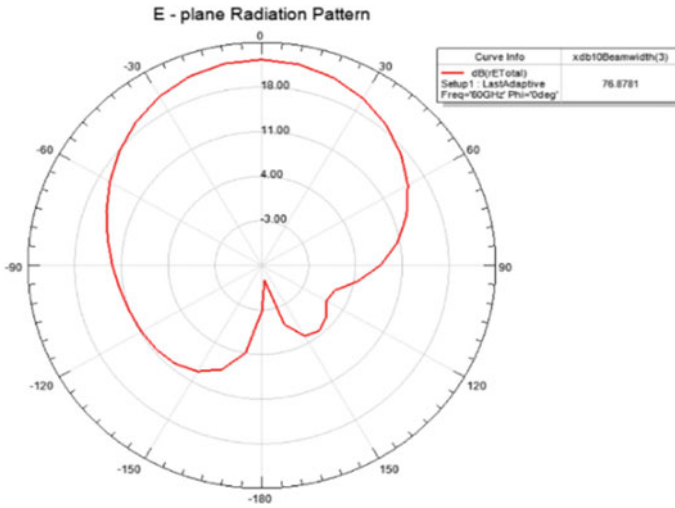
Fig. 9 E-plane radiation pattern
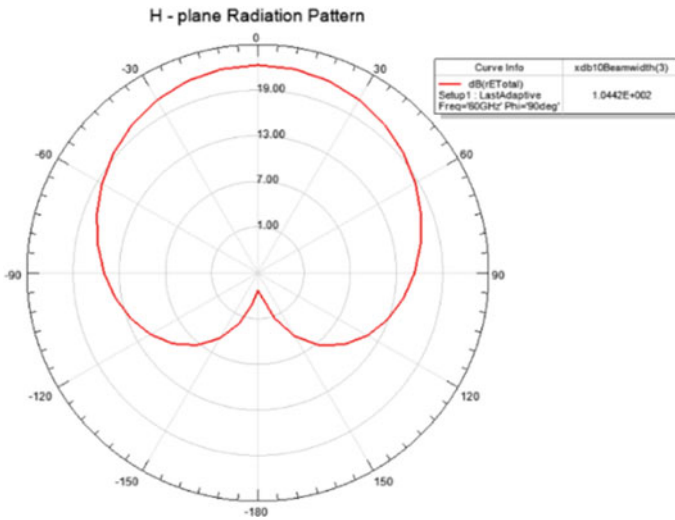
Fig. 10 H-plane radiation pattern

4.2 LNA Results

Table 2 shows the comparison between the results of single-stage and two-stage LNA after designing proper matching networks at input and output side as per the circuit given in Fig. 4.

Fig. 11 3D-polar plot of radiation pattern
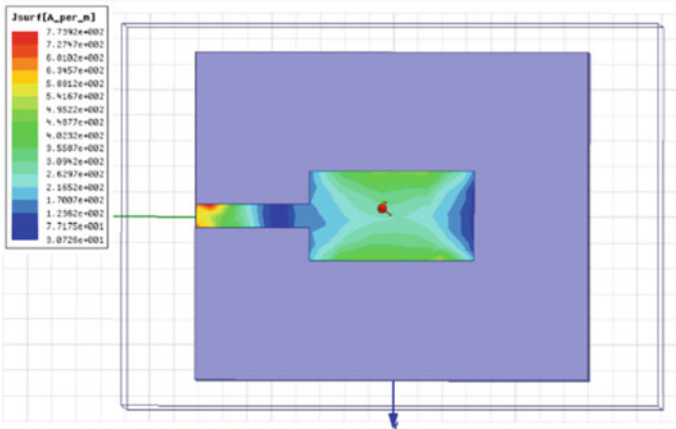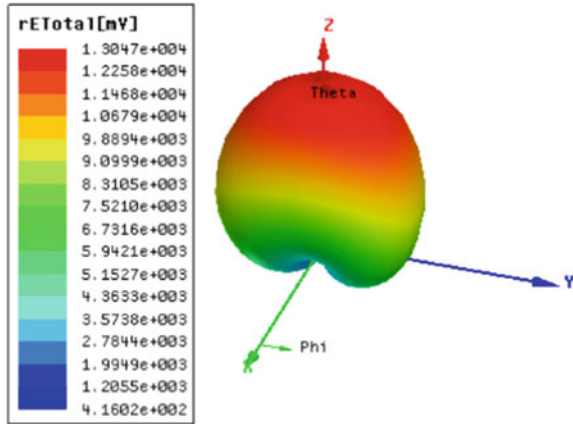
Fig. 12 Surface current density of antenna

In two-stage LNA, it has been observed that the input return loss, S_{11}, is -23.028 dB and NF is 3.626 dB which have been improved by 99.89% and 2.158%, respectively. Similarly, the forward transmission gain, S_{21}, is 12.557 dB and reverse transmission gain, S_{12}, is -28.993 dB which have been improved by 105.68% and 97.63%, respectively. While S_{22} has been degraded in two-stage LNA which is due to the distributed parasitic at output side, LNA has been created in ADS software and PTM (Predictive Technology Model) used for 65-nm technology and run the simulation. Figure 15 shows the consolidated S-parameters of two-stage CS LNA which are observed from 0 to 100 GHz frequencies. In this connection, Fig. 16 shows the corresponding NF which is observed to be 3.626 dB at 60 GHz. It is to be noted that the specification of maximum NF of a good receiver block is 8 dB, while in our case, for a NF of 3.626 dB obtained, the allowable NF of the remaining
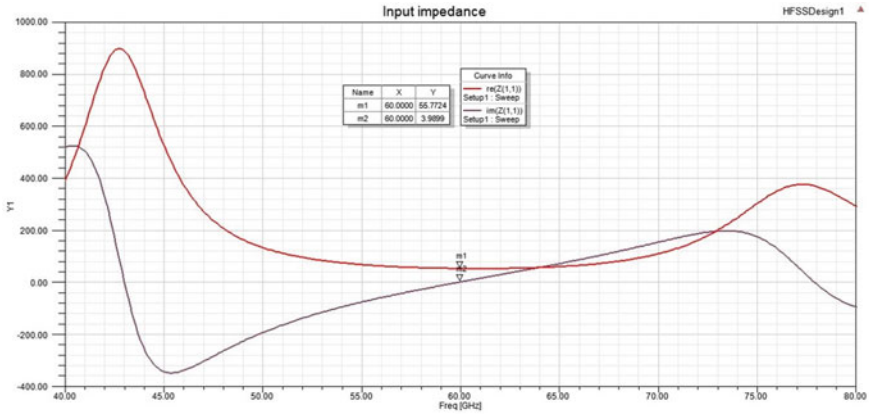
Fig. 13 Input impedance of antenna
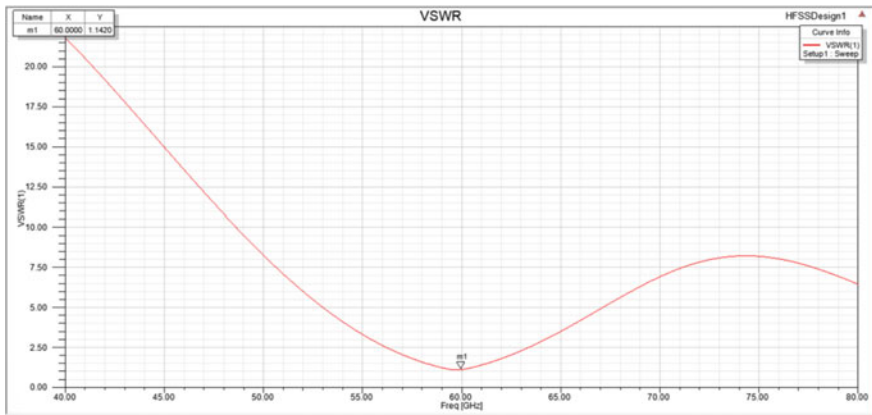
Fig. 14 VSWR of antenna

Table 2 Comparison between single-stage and two-stage CS LNA

Single-stage LNA		Two-stage LNA	
S_{11}	−11.52 dB	S_{11}	−23.028 dB
S_{12}	−14.67 dB	S_{12}	−28.993 dB
S_{21}	6.105 dB	S_{21}	12.557 dB
S_{22}	−24.64 dB	S_{22}	−19.044 dB
NF	3.706 dB	NF	3.626 dB

Fig. 15 Consolidated
S-parameters of two-stage
CS LNA
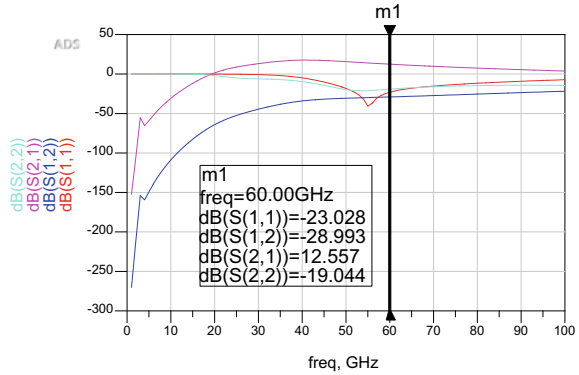
Fig. 16 NF of two-stage CS
LNA
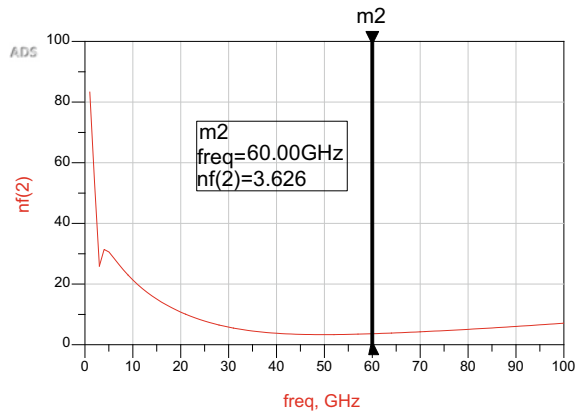
blocks has to be within 4.374 dB. This is observed to be more than sufficient for implementation of remaining blocks.

For a 2 * 2 matrix *S*-parameters, the following equation calculates the stability factor (k) using the determinant, Δ.

$$k = \frac{1 - |S_{11}|^2 - |S_{22}|^2 + |\Delta|^2}{2|S_{12} * S_{21}|} \tag{6}$$

$$|\Delta| = |S_{11} * S_{22} - S_{12} * S_{21}| \tag{7}$$

k—stability factor, Δ—Determinant of *S*-parameter matrix.

It is noted that 'k' should be greater than unity and Δ should be greater than zero for unconditional stability to exist. In our case, 'k' has been found to be 3.336 and Δ is 0.153 at 60 GHz.

We also measured *'Muprime'*, a single parameter, that ensures necessary and sufficient conditions of stability. It measures the distance between the Smith chart's

center and the closest unstable-input (source) stability circle. The value of *Muprime* should be greater than one for a 2-port network representation which is given by

$$Muprime = \frac{1 - |S_{22}|^2}{|S_{11} - \text{Conj}(S_{22}) * \Delta| + |S_{21} * S_{12}|} \tag{8}$$

It gives that the *Muprime* is 4.464 at 60 GHz for our two-stage CS LNA design.

Gain compression happens when an amplifier's input power (Pin) is raised to a point resulting in a nonlinear rise in the output power. In our work, we have measured 1-dB compression point and third order intercept point, IP_3. In this, 1-dB compression point is defined as the input signal level that causes the gain to drop by 1-dB. It has been observed as -4 dBm for our two-stage CS LNA.

IM refers to intermodulation interference that occurs when two tone frequencies are combined in a nonlinear system. Figure 17 shows that our two-stage LNA circuit exhibits IP_3, the intersection of first and third order harmonics when Pin equals to 5 dBm. To support this, we have measured the output spectrum which consists of third order IM products which are presented in Fig. 18. IM products are represented by the marker heads in Fig. 18 as follows: $m5$—$2W_1$−W_2 is -2.109 dBm, $m7$—$W_1 = 8.739$ dBm, $m4$—$W_2 = 9.352$ dBm, and $m6$—$2W_2$−$W_1 = -4.023$ dBm. In this, the third order IM products, say, $m5$ and $m6$ hold less significant values when compared to $m4$ and $m7$.

Table 3 shows the comparison of our work with other reported results noted at 60 GHz using 65-nm CMOS technology. Figure of merit, FOM, has been calculated using the formula given as

$$\text{FOM} = \frac{\text{Gain(abs)} * f_c(\text{GHz})}{(\text{NF} - 1)(\text{abs}) * P_{\text{DC}}(\text{mW})} \tag{9}$$

FOM—Figure of merit, NF—Noise Figure, P_{DC}—DC Power, f_c—Operating frequency.

FOM of our design observed to be 6.31. The presented results from Figs. 15, 16, 17 and 18 along with Tables 1 and 2 show that our two-stage CS LNA design would

Fig. 17 IP_3
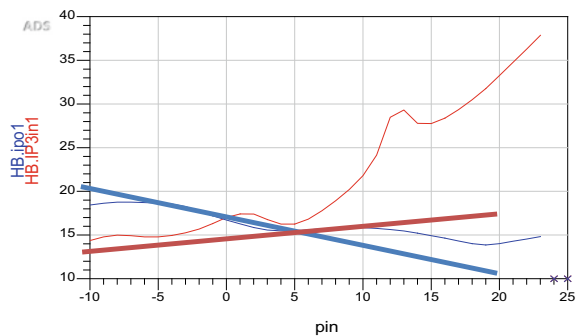
Fig. 18 The output spectrum containing IM$_3$
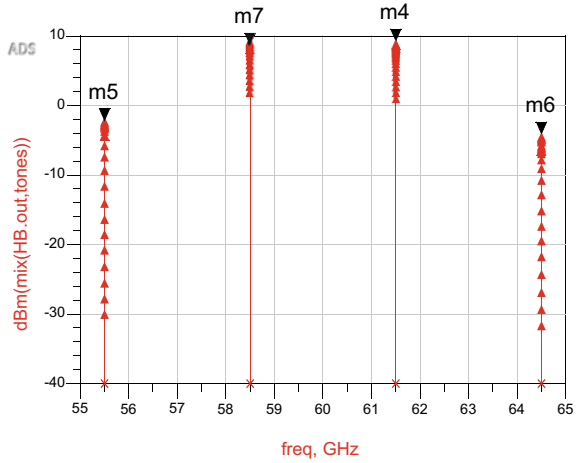
Table 3 Comparison of our work with reported results

Refs.	Freq (GHz)	Gain (dB)	P_{diss}/V_{dd} (mW, V)	NF$_{min}$ (dB)	$P_{1\text{-}dB}$ (dBm)	FOM
[16]	59	22.5	9.11/1.5	1.5	–	7.5
[17]	50–61	10.969	4.64/1.1	1.099	−2	7.593
This work	60	12.557	30.91/1.1	3.626	−4	6.31

be a proficient design that could meet the demands of the application mentioned in Sect. 1.

4.3 Co-design of Antenna with LNA

Microstrip patch antenna has been designed in HFSS which is then converted to a s1p file containing the antenna's *S*-matrix. This is imported and integrated properly with the designed two-stage CS LNA as shown in Fig. 19 using co-design approach. The output impedance of the antenna and the input impedance of the LNA should be the same but practically due to mismatches and insertion loss, integration results with degradation of LNA parameters. So, in this work, antenna impedance is co-designed by including it as a part of input matching network of LNA along with source impedance, R_S. Few trials of matching impedance have been tried to properly integrate antenna with LNA.

From Table 4, it can be seen that the LNA performances have been little degraded due to impedances mismatch. We could reduce this mismatch by extracting RC parasitic by using layout parameters. The total NF is increased because of the insertion loss of the antenna.
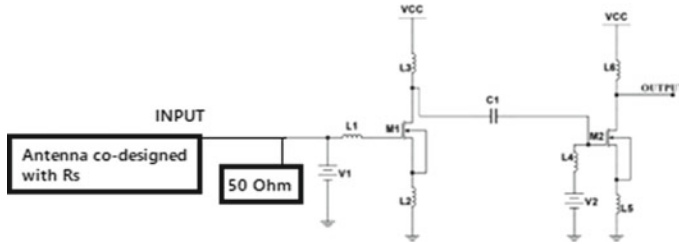
Fig. 19 Schematic of co-designed antenna with LNA

Table 4 *S*-parameters with and without integration

S. No.	S-parameters	Before integration	After integration	Percentage decrease (%)
1	S_{11}	−24.8	−7.83	68.4
2	S_{12}	−29.04	−32.02	10.2
3	S_{21}	12.84	9.527	25.8
4	S_{22}	−20.74	−17.041	17.8
5	NF	3.6	6.8	88 increased

5 Conclusion

In this work, antenna is integrated with LNA by co-designing its impedance along with source resistance at 60 GHz. A microstrip patch antenna with a gain of 4.54 dB and a bandwidth of 4.9 GHz has been designed and observed to be suitable for 60 GHz applications. With the ISD, LNA produced gain of 12.55 dB and an NF of 3.6 dB with the input and output reflection coefficients lesser than −19 dB. After co-design process, the integrated LNA has tolerable performance degradation with observed total gain of 9.5 dB and NF of 6.8 dB. The performances can be further increased by including the insertion loss and by using custom-designed high-Q inductors for ISD purposes.

References

1. Saini J, Agarwal SK (2017) Design a single band microstrip patch antenna at 60 GHz millimeter wave for 5G application. In: 2017 International conference on computer, communications and electronics (Comptelix), pp 227–230. https://doi.org/10.1109/COMPTELIX.2017.8003969
2. Adhikari P (2008) Understanding millimeter wave wireless communication. Loea Corporation, San Diego
3. Razavi B (1998) RF microelectronics. Prentice Hall Press, Upper Saddle River, New Jersey, USA
4. Suraj K, Ammal MN (2018) Design and development of microstrip patch antenna at 2.4 GHz for wireless applications. Indian J Sci Technol 1–5. https://doi.org/10.17485/ijst/2018/v11i23/125651

5. Balanis CA (ed) Antenna theory analysis and design, 2nd edn. Wiley
6. Sahana C, Nirmala Devi M, Jayakumar M Dual-band circularly polarized annular ring patch antenna for GPS Aided GEO augmented navigation receivers. IEEE Antennas Wireless Propag. https://doi.org/10.1109/LAWP.2022.3178980
7. Negi D (2017) Designing of microstrip patch antenna at 60 GHz using strip line feeding for defense applications. Int J Control Theory Appl
8. Rabbani MS, Ghafouri-Shiraz H (2016) Improvement of microstrip patch antenna gain and bandwidth at 60 GHz and X bands for wireless applications. IET Microwaves Antennas Propag
9. Bierbuesse D, Bousseaud P, Negra R (2015) Inductorless and cross-coupled wideband LNA with high linearity. In: 2015 Nordic circuits and systems conference (NORCAS): NORCHIP and international symposium on system-on-chip (SoC), pp 1–4. https://doi.org/10.1109/NORCHIP.2015.7364391
10. Pournamy S, Kumar N (2017) Design of 60 GHz broadband LNA for 5G cellular using 65 nm CMOS technology. In: 2017 7th International conference on communication systems and network technologies (CSNT), pp 320–324. https://doi.org/10.1109/CSNT.2017.8418559
11. Kong S, Lee HD, Lee M, Park B (2016) A V-band current-reused LNA with a double-transformer-coupling technique. IEEE Microwave Wirel Compon Lett 26(11):942–944. https://doi.org/10.1109/LMWC.2016.2615017
12. Lee TH (2004) The design Of CMOS radio frequency integrated circuits, 2nd edn. Cambridge University Press
13. El Oualkadi A, Faitah K, Ouahman AA (2009) mm-Wave CMOS mixer design in 65 nm technology for 60 GHz wireless communications. In: 2009 Mediterrannean microwave symposium (MMS), pp 1–4. https://doi.org/10.1109/MMS.2009.5409796
14. Emami S, Doan CH, Niknejad AM, Brodersen RW (2005) A 60-GHz down-converting CMOS single-gate mixer. In: 2005 IEEE radio frequency integrated circuits (RFIC) symposium—digest of papers, pp 163–166. https://doi.org/10.1109/RFIC.2005.1489619
15. Sahana C, Jayakumar M, Kumar VS (2018) High performance dual circularly polarized microstrip patch antenna for satellite communication. In: 2018 International conference on advances in computing, communications and informatics (ICACCI), pp 1608–1611. https://doi.org/10.1109/ICACCI.2018.8554817
16. Pournamy S, Kumar N, Maran P (2021) A linear high frequency gm boosting wideband LNA in 130 nm SiGe HBT with minimum NF of 4.3 dB for WiGig application. J Circuits Syst Comput 31(1). World Scientific Publishing Company. https://doi.org/10.1142/S0218126622500013
17. Roopika N, Moheth M, Vinod S, Sanjana PM, Balamurugan K (2021) CMOS based variable gain LNA at V-band. In: 2021 International conference on advances in computing and communications (ICACC), pp 1–7. https://doi.org/10.1109/ICACC-202152719.2021.9708219
18. Prakasam V, Sandeep P Dual edge-fed left hand and right hand circularly polarized rectangular micro-strip patch antenna for wireless communication applications. IRO J Sustain Wireless Syst 2(3):107–117
19. Christina G (2021) A Review on microstrip patch antenna performance improvement techniques on various applications. J Trends Comput Sci Smart Technol 3(03):175–189

Impact of High Dimensionality Reduction in Financial Datasets of SMEs with Feature Pre-processing in Data Mining

R. Mahalingam and K. Jayanthi

Abstract High Data Dimensionality Reduction (HDDR) removes the irrelevant features in a complex dataset and incorporates various techniques that could be used to foretell the research outcomes in a predictive model. The major objective of the paper is to analyse and survey the various models on the basis of HDDR and its feature pre-processing methods applied in financial dataset predictions. Numerous techniques of data mining and its strategies were discussed and assessed to ascertain the importance of augmenting the performance of the financial dataset with classifiers. The pre-processing techniques applied in various research works and their outcomes are highlighted. The HDDR methods used in financial prediction of Small Medium Enterprises (SMEs) are studied for existing frameworks and models by different authors. The paper encapsulates the gist of the models, frameworks and algorithms involved in effective elimination of irrelevant features and extraction of best features for best prediction of financial datasets.

1 Introduction

Though Data Dimensionality is one of the prominent areas in data world that huge data with tuple could be handled [1], the high dimensionality couldn't be handled. Data Dimensionality denotes the quantity of features or columns or values in a dataset used in the evaluation of data using algorithms. It is evident that dataset

R. Mahalingam (✉)
Department of Computer and Information Science, Annamalai University, Chidambaram, Tamil Nadu, India
e-mail: r.mahalingamphd@gmail.com

K. Jayanthi
Department of Computer Application, Government Arts College, Chidambaram, Tamil Nadu, India
e-mail: jayanthirab@gmail.com

with high dimension is very complex to handle using available resources. High Data Dimensionality (HDD) indicates the high quantity of features used in predicting the outcomes of an experiment [2] that exceeds more than 100s or even 1000s of features. Heavy features would slow down the process of prediction and may also produce irrelevant or less accuracy outputs. High Data Dimensionality Reduction (HDDR) is important in such huge feature [3] set to detect and remove the irrelevant features of the dataset. This reduces the input variables and ultimately might lead to the enhancement of the results. However, this High Data Dimensionality Reduction is considered as a curse of dimensionality of datasets by many predictive engines and also makes the model more complex. The major objective of this research paper is to conduct a profound and extensive review on various High Data Dimensionality Reduction techniques and its impact on Financial Data Analysis (FDA) to predict crisis, bankruptcy, and financial gain in Small Medium Enterprises (SMEs). Nevertheless, numerous algorithms in data mining plays a significant role in testing the success of HDDR and visualise the high dimensionality statistics, analytics, and models. The increase in the features results in increase of complexity and leads to poor performance with the algorithm. Also, high infrastructure is required for experimentation and evaluation. The input variables contained in features are used to predict the target feature in the dataset with the answer collected from trusted sources. This mapping becomes complex when the number of features is very high. The dataset contained in the spreadsheet could be represented as rows with samples and columns as features with n-dimension, respectively. This representation is known as geometric construal of the dataset. If this geometric construal is high [2, 3], it is also known as HDD. For example, if the dataset comprised of 150 features and 1200 samples, the total dimension will be 180,000(150 * 1200) records. This is very high and it increases the operational time and space with reduction in accuracy. The outcomes attained from HDD also means that the volume of the dataset is huge and would be non-represented samples of the dataset. The ordinant solution to this problem especially in financial predictions of SMEs can be handled with HDDR because less and reliable inputs could always bring solutions with less degrees of freedom. Any model in data mining could be easily used to bring solution to the problem with less Data Dimensionality with less space and time complexities. High degrees of freedom may result in overfitting and could not deliver best results in new data on the whole. Models could be made simple when the input features are less especially among linear models in data mining. Thus, HDDR is highly important and relevant in handling complex dataset like financial data from SMEs. The scope of the review is to find the high dimensional financial data predictions in earlier methods where dimensionality played a significant role in prediction with good accuracy. This paper analysed various papers published to handle FDD among different financial organisations in recent times with a surge to outperform the HDD problem with knowledge incorporated from data mining models and techniques.

2   Related Works on High Dimensionality Reduction

HDDR is a technique in data mining during the data preparation stage accomplished before data modelling, data cleaning and scaling process. This assists training the predictive model and providing the best features for effective prediction. HDDR was more easy and portable and compressed data features for better outcomes in research. Thus, HDDR codes for predictive modelling which forecast outcomes based on statistics and probability using the best predictors. The features must be selected with high predictive possibilities that can be tested, validated and involved in highly accurate predictions in any area of research.

2.1   *High Data Dimensionality Reduction Methods*

Feature reduction is highly recommended in classification-based problems since too many factors results in complex analytics. It also makes the visualisation of the training set and the outcomes much impossible. The dimensionality can be identified in many ways. There may be redundant features or irrelevant features that increases the dimensionality of the dataset. The features might also be correlated with each other directly or indirectly coding for same features to be used in prediction. Thus, HDDR is highly essential and significant in reducing the unwanted features thereby finding the best features for prediction of outcomes. This also has high possibilities for finding the outcomes with high accuracy. Various methods are used to find the best features through feature selection and feature extraction techniques and algorithms. To solve the problem of HDDR, the feature extraction and feature section process has various components. In feature selection, the overall set of features are assessed and condensed to a set of small subsets and the problem is modelled to bring solution to the problem. It can be done through filtering or wrapper or embedded methods. Same way, the irrelevant features in the dataset can be reduced or removed thereby reducing the dimensionality of the dataset.

HDDR is performed in datasets based on various methods. The methods are Principal Component Analysis (PCA), Linear Discriminant Analysis (LDA) and Generalised Discriminant Analysis (GDA). They are classified under linear and non-linear methods. The HDDR assists in data compression, reduces computation time, clears redundant features and ultimately provides a better way in prediction of any complex problems in research. However, sometimes it might result in extreme data loss due to the fact that many features were removed automatically without the intervention of the user. Various authors studied the importance of high dimensionality reduction in terms of various parameters. Ayesha et al. [4] collected various dimensionality reduction techniques that were found, state-of-the-art methods to handle various types of data in different areas like medical and financial predictions. It was found that dimensionality reduction is one of the complex problems to be solved for effective functioning of the dataset in terms of throughput and output.

A similar review was conducted by Xu et al. [5] to understand the dimensionality reduction and various feature selection methods through data processing machine learning algorithms. Various algorithms like random forest, clustering, heuristic and deep learning models were tested. A new framework was analysed in the paper that combined selection and high dimensionality reduction at the same phase. The discussion was carried out in a sequential and simultaneous manner. The author concluded that machine learning, data mining and deep learning algorithms could be used for processing large data and their dimensionality.

Espadoto et al. [6] analysed and reviewed various projection techniques through various quantitative metrics offered for managing high dimensionality reduction techniques in complex datasets. The author concluded that researchers are capable of handling complex data with the help of effective HDR techniques. It has scope to handle complex financial datasets too and could make a standard prediction method for future datasets in different disciplines as well.

A novel method to handle the challenges of HDD problem was proposed by Chormunge and Jena [7] through integration of features using clustering method and testing correlation to remove irrelevant features of the dataset. The evaluation of the quality of solution obtained from microarray and the text-based datasets were performed using Naïve Bayesian Classifier. The outcomes suggested that HDD can be reduced using feature selection methods.

Solorio-Fernández et al. [8] developed a nomenclature of various methods and listed merits and demerits of each method used in the reduction of High Data Dimensionality Reduction process. The major concepts of dimensionality reduction with its merits and demerits were analysed and tested experimentally. The outcomes are also compared with the existing models. Few futuristic challenges were discussed in the proposed approach. It was identified that High Data Dimensionality Reduction is highly essential for the enhancement of prediction of complex data.

Nguyen et al. [9] embarked a wide survey on the various methods in swarm intelligence to perform feature selection methods at the best level possible using search methods at the state-of-the-art models. The author also identified various merits and demerits of the model. It was found that the model is highly effective to remove inapposite features at the pre-processing level itself. However, the cost and time are high for small problems. Hence various guidelines and methods with appropriate regulations are proposed in this work.

Nilashi et al. [10] put forth an opinion on various problems like scalability, sparsity and other problems to be reduced using ontology and dimensionality reduction techniques. The ontology at the initial stage would improve on the accuracy of the prediction whereas the dimensionality reduction technique called Singular Value Decomposition method is used to remove irrelevant features and enhance the scalability aspects of the dataset. The evaluation of the model was carried out under two real-world datasets to test and evaluate the efficiency and also its reduced sparsity and scalability problems. This model was sufficient to show that HDDR is required for better prediction of complex and real-world datasets.

A similar analysis was aimed by Thudumu et al. [11] under three areas including the high dimensionality reduction, algorithms and techniques used in prediction and

the various tools involved in the removal of irrelevant features. The purpose was to find the existence of anomalies in the complex dataset due to the presence of enormous features. The dataset usually forms the subset and can be used for the prediction at the better space and time complexities. The review was focused on the impact of traditional models and its future implications in the field of big data.

Pes [12] studied various selection algorithms under different categories like embedded, filter, univariate and multivariate methods under 18 classification techniques, respectively. The process identified variations among heterogeneous features belonging to various relationships from mapping cardinalities and ensemble models. The relationship was found to be binary and had high impact in classifying the similar and dissimilar features of the dataset.

Liu et al. [13] designed a new supervised model called structured optimal graph-based sparse feature extraction (SOGSFE) to handle the learning of structures, label propagation and the Data Dimensionality reduction methods. The author used calculative iteration methods to obtain the similarity and projection matrix to find the irrelevant feature in public image datasets. The proposed model showed good results in identifying unwanted features and removing them to reduce the complexity of the dataset.

These methods of HDDR showed that HDDR can be performed during the pre-processing stage of data mining and has high impact on the enriched performance of prediction of complex datasets.

3 Review on Assessing Financial Datasets in Small Major Enterprises

As reviewed in the earlier papers, high dimensionality has been recognised as one of the renowned problems especially in complex datasets. It is customary that these complex datasets with huge features comprise a mixture of relevant, irrelevant and partially associated, completely not associated, features. These enormous features make it complicated for users to identify associated and wrong credibility of the data that can be used for prediction. The occurrence of completely unassociated or errored features may result in wrong outputs or wrong predictions.

The context of this part of the paper is to analyse the effects of huge features resulting in error or poor outcomes of the research. The case study was conducted on the financial crisis or bankruptcy or financial problem analysis in Small Major Enterprises (SMEs) from various scientific research in the existing stage.

Nkwabi and Mboya [14] conducted research on the growth of SMEs by analysing the various factors or features like business training, capital problems, non-availability of finance and infrastructure, corruption in various sectors and competency-based problems from various human activities etc. After analysing various literatures, descriptive statistics and content analysis in Tanzania, it was found that frequency of unwanted features or factors in a financial dataset of SMEs would

increase the error rate and decrease the reliability and accuracy of prediction. Finally, the best features among the 21 features examined were found to be capital problems, financial problems and lack of technology. Other features had very minimal on the overall outcome of the prediction. Thus, extraction of the best features is one of the major significances of better prediction. Rao et al. [15] studied the various factors that affect the capital of SMEs in India based on 174 non-financial institutions. A novel method called Generalised Method of Moments (GMM) is experimented with numerous test cases based on the decision-making parameters such as age, size, tangibility, etc. This paper professes if we focus on enhancing the model with numerous features to cater the demands of the present system, it will have severe impact on financial predictions of SMEs.

To counteract the research conducted on SMEs in India, foreign market analysis considering various factors like innovation, features of product and intensity of export has been identified as best factors by Lin and Ho [16]. The challenge of financial analysis in markets can be resolved optimally by reducing the dimensionality and extraction of features.

Nasution et al. [17] studied and analysed 21 owners of SMEs using basic statistical methods like Structural Equation Model Part Least Square (SEM-PLS) to find the threats and low outcomes of financial status of the year. The analysis was based on the revolution 4.0 concepts and various factors were analysed. Only few factors were finalised and proved that the reduction of inapposite features in a financial statement would eventually bring best solution for the enhanced prediction of the financial statements. It improved the performance of the business model as well.

Papadopoulos et al. [18] noticed various ways to enhance the performance and productivity of SMEs based on the digital technologies in extreme situations like COVID-19. The major factors studied were on research avenues and managerial implications of digital technologies for securing continuous business. This research proved that dimensionality reduction would assist in forecasting of financial crisis and the extraction of best features for handling tough financial situations.

Hanggraeni et al. [19] conducted research to study the internal and external factors that affect the Micro Small Medium Enterprises (MSMEs)' performance of 1401 data from 14 Indonesian cities in terms of business. The work identified the risk management factors of the MSMEs to coordinate and manage the marketing and financial resources of an organisation. The Enterprise Resource Management process of MSMEs is also tested with questionnaires to find the risk involved in the financial management during extreme conditions. This method proved that complex datasets are hard to be predicted with excess features.

The relationship between knowledge and innovation is examined by Abbas et al. [20] using stratified random sampling method based on the analysis of business data in Lahore and Gujranwala. The outcomes suggested a significant change in results due to the reduction of inappropriate features or factors in the dataset. So as per Jaffer Abbas study by reducing the high dimensionality of the dataset, the accuracy and efficiency of prediction can be improved. Malakauskas and Lakštutienė [21] acknowledged financial distress as a major challenge in the financial predictions of SMEs based on the 12 samples tested using binomial classifiers. The techniques

used are the logistic regression, random forest and neural networks methods. The results showed that the financial crisis in SMEs is hard to be predicted when the number of factors or features exceeds a limit of 100 and more features. Among the techniques tested, Random Forest Tree model predicted highest accuracy and as the result, number of inappropirate features got reduced.

Many authors analysed and reviewed various techniques used in effective financial prediction of SMEs. A comprehensive review was conducted by Ciampi et al. [22] during the COVID-19 situation where the financial crisis prediction during 2007–2009 was compared with the 2020 situation using 100 peer reviewed journals from 1986 to 2020. The research outcomes were analysed based on how it overcame challenges to assist researchers in bringing new solutions to problems. The outcomes showed that in new techniques like machine learning, artificial intelligence can be used to provide best results to complex problems in financial predictions.

Kou et al. [23] showed the use of accounting and financial ratios from statistical methods in prediction of bankruptcy for SMEs. The research used variables under financial and payment basis. The author proposed a two-stage multi-objective model for classifying data and enhancing the relationship of the data in the complex SMEs dataset. The result showed that better performance was achieved in reduced dataset than the actual dataset with all the features. The optimal subset formation had been achieved for financial bankruptcy prediction.

Similar research was conducted by Sun et al. [24] to concentrate on the financial distress on a binary basis. The research tested with support vector machine (SVM) based on fusion and decomposition methods. Four states were tested for finding efficiency viz financial soundness, financial pseudo soundness, serious and moderate financial distress, respectively. Various SMEs companies from different countries participated in the prediction models. The outcomes suggested that huge data can be handled by simple algorithms when the features are reduced to the maximum level resulting in high dimensionality reduction.

The financial distress reviewed that all these models based on SMEs showed the significance of the prediction in the financial world based on simple algorithms. This effective prediction is possible only by reducing irrelevant features thereby performing High Data Dimensionality Reduction (HDDR) at the pre-processing level.

4 Materials and Methods in Data Mining

Based on the reviews on High Data Dimensionality Reduction and its impact on financial crisis predictions in SMEs, it is important that methodology and the strategy applied in performing HDDR are essential for the successful outcome. Hence a substantial review was conducted on the various materials and methods that can be employed in finding the best and optimal solution for the problem. Data mining is a research area which has various stages including the pre-processing stage. It was in this stage the High Data Dimensionality Reduction process was carried out to reduce

the irrelevant features of the dataset. Many research works were completed in course of time on the reduction of dimension and outlier analysis in complex datasets by various researchers. Various fields like medical diagnosis, business intelligence and analytics have used these methods for identifying better features with optimal best cost results. The data mining methods always extract the supervised and unsupervised data in terms of predictable and unpredictable hidden patterns of financial datasets.

Sankhwar et al. [25] developed an optimised framework for predicting the optimal features using grey wolf optimisation and fuzzy neural classifier models. The algorithms were tested on two complex datasets Australian credit and German dataset to determine the best models. They were able to predict the optimal features with enhanced accuracy after removal of certain features.

Dimensionality reduction in data mining can also be applied through big data, IoT and cloud computing methods. It was proved by Shang et al. [26] using financial indicators at the multiple levels to determine the fuzzy cluster methods using rules and parallel mining algorithm. The listed rules were able to identify the risks involved in financial predictions at the maximum level possible. The ardent prediction was conducted by Uthayakumar et al. [27] by classifying models and applying ant colony optimisation (ACO)-based financial crisis prediction (FCP) model on financial crisis prediction. The validation of the outcomes is performed on five benchmark datasets under financial crisis datasets to identify the best features with optimal cost. Also, genetic algorithm was used in feature selection process and a comparative result is obtained. It was found that the five datasets showed enhanced outcomes after removing irrelevant features of the dataset. The models were found very competent with the existing models at that stage based on dimensionality reduction.

Subasi et al. [28] used a new method called Synthetic Minority Over-Sampling Technique (SMOTE) to handle imbalanced datasets using Random Forest algorithm. The outcome suggested best performance by accurate performance of 89.01% and also with low error rates, respectively. This model was used in predicting the early loss of finance and also to predict the loss of credit card over a period of time. This assisted in common people to assess financial loss of data. The AUC (0.947) and F-Measure (0.89) also showed considerable results that was far better than other classifiers tested in the experiment. Laborda and Olmo [29] applied dimensionality reduction techniques in network models to identify the crisis associated with banking, finance and technologies. Also, the author formed a hybrid of techniques with another existing model and proved that it can be used for predicting crisis during adverse situations like COVID-19. The volatility levels were able to be predicted by the spill overs of the existing models. This algorithm and models assisted various economic sectors to predict financial crisis at the earliest stage possible to avoid loss of money.

Similar research was conducted by Jabeur et al. [30] to predict the financial crisis in global credit rating and bonding by determining the best features. The high dimensionality was applied in the earlier stage and then accompanied by the selection of best features through ranking algorithm. Also, the statistical methods were studied with algorithms like support vector machines, neural networks and decision tree algorithm that were sensitive to cost predictions. The classifiers were tested with logistic and discriminant methods to enhance the output and results. Kim et al. [31]

predicted the price drop and raise of US stock values using regression algorithms in data mining like multilayer perceptron, logistic regression, RFT, XGBoost, etc. Among the models, multilayer perceptron showed good results with the assistance from HDDR process. The reduction in features enabled the ease of prediction at the maximum level possible in comparison to the dataset without feature removal.

Cheng et al. [32] used classification models like decision tree and Apriori models to determine the nature of investors in financial predictions through the reduction of irrelevant features of the dataset. The model was designed based on three ideas viz design of systematic model using decision tree and Apriori algorithm, creating a decision model and also to predict the financial crisis based on the association rules designed for prediction. Jan [33] used deep learning models with neural networks and statistical chi-square automatic interaction detector for predicting the financial distress of the organisation. The research was conducted with 86 companies and 344 companies. The accuracy was obtained as 94.23% with 258 financial distress organisations predicted after feature removal. The error rates Type-I (0.96%) and Type-II (4.81%) are found to be very less thus confirming that with reduction in irrelevant features, the accuracy and performance gets increased.

Moradi and Rafiei [34] analysed and developed a novel model to predict the political and economic factors in comparison with the real-life problems. The model predicted the financial crisis and differentiated the bad customers from the good customers for enhancing the financial position of SMEs. However, the model was considered static and needed refinement for further process. Van Nguyen et al. [35] used data mining techniques to predict the robustness and accuracy of remanufactured products. Also, the non-linear market analysis was performed to identify the customer needs. The experiment was tested with Amazon dataset collected from real-time primary sources using data mining and machine learning techniques. The research identified market factors that could foresee the financial crisis of an organisation. This was possible using the removal of irrelevant features of the real-time dataset. The overall analysis of the materials and methods used in data mining to predict financial crisis in SMEs and other financial organisations is summarised in Table 1.

4.1 Algorithms in the Financial Predictions for SMEs

The financial distress predictions in Small Major Enterprises have been possible based on the impact of various algorithms used in the predictions. The algorithms depict the methods and techniques that could be employed on the datasets to achieve the best outcome.

The data mining algorithms used in the financial predictions of SMEs are given in Table 2.

Table 1 Methodologies and techniques used in HDDR on SMEs with outcomes

Ref. No.	Methodology	Techniques used	Outcomes achieved
[25]	Optimal model designed for reducing Australian and German financial distress datasets	Grey wolf optimisation and fuzzy neural classifier models	The efficiency was good with optimisation models
[26]	Multilevel financial predictions using data mining and big data techniques	Fuzzy clusters and parallel mining algorithm	The dataset reduced in terms of features and values showed good results
[27]	Ant Colony optimisation (ACO) based financial crisis prediction (FCP) model on financial crisis prediction	Ant colony optimisation technique	Irrelevant features reduced from all 5 datasets
[28]	Feature reduction process carried out in imbalanced datasets	Synthetic minority over-sampling technique (SMOTE), Random Forest algorithm	Accuracy: 89.01% AUC (0.947) and F-measure (0.89)
[29]	Analysis of volatility levels using spill over models to identify the crisis associated with banking, finance and technologies	Dimensionality reduction techniques in network models	Predicted financial crisis during adverse situations like COVID-19
[30]	Predict the financial crisis in global credit rating and bonding by determining the best features	High dimensionality reduction using ranking techniques, SVM, neural networks and decision tree	The testing shows sensitiveness to cost predictions
[31]	Foretells the price drop and raise of US stock values using regression algorithms in data mining	Multilayer perceptron, logistic regression, RFT and XGBoost	Multilayer perceptron shows good results compared to other models
[32]	Classification models used to determine the nature of investors in financial predictions by reducing inapposite features of the dataset	Decision tree, Apriori models	Decision model created to predict the financial crisis based on the association rules
[33]	Predict the financial distress of the organisation by reducing the irrelevant features	Deep learning models with neural networks and statistical chi-square automatic interaction detector	Accuracy: 94.23% Type-I (0.96%) and Type-II (4.81%)

Table 2 The existing frameworks for performing dimensionality reduction to enhance prediction

Ref. No.	Purpose of the study	Algorithms used	Performance
[36]	To reduce the error in the dataset by at least 5–10% and enhance forecasting of results	Grey correlation analysis Artificial neural network (ANN)	Eliminated repeated features with low correlation
[37]	Comparing the three-dimensionality reduction technique with SVM model	Principal component analysis (PCA), Locally linear embedding (LLE), Isometric mapping (Isomap)	Existing models were outperformed by nonlinear global dimension models
[38]	Developed spatial-spectral manifold reconstruction preserving embedding (SSMRPE) for HSI classification	Unsupervised dimensionality reduction algorithm	Found the irrelevant features and amended classification performance
[39]	Created a model for predicting the dataset values for single-cell gene expression data	Probabilistic parametric mapping function	The outcomes were augmented after feature reduction
[40]	categorise features that have the same characteristics in one cluster, so that redundancy in microarray data is removed	Random Forest algorithm	Accuracy colon—85.87%; lung cancer—98.9%; prostate tumour—89%
[41]	Intrusion detection was performed using data mining to predict anomalies	C4.5, Bayesian networks (BN) based classifier, Firefly algorithm	Feature extraction of best 10 features predicted with enhanced accuracy

5 Frameworks in Existence to Perform HDR in Financial Datasets

The dimensionality reduction techniques were proposed as frameworks in different models and examined with the financial datasets to predict the financial crisis in SMEs. Zhang et al. [42] utilised deep learning framework on an unsupervised environment to design a novel hybrid framework with stacked contractive auto encoder (SCAE) and LDFA for enhancing the prediction through feature reduction. The dimensionality reduction applied with deep learning was successful in augmenting the performance of results with complex financial datasets. Also, Abdulhammed et al. [43] performed feature dimensionality reduction technique using auto encoder and PCA algorithm. The result was tested with other models like RFT, Bayesian network, linear discriminant analysis (LDA), etc. using performance measures including *F*-score, accuracy and false detection rate. The outcomes after feature elimination

showed 99.6% of accuracy. The author combined the models to form a hybrid to enhance the performance and was successful.

Becht et al. [44] developed a uniform manifold approximation and projection (UMAP) framework to reduce the unwanted and redundant features in a biological dataset to enhance the performance of the prediction. Various tools were used to form the clusters and enhance the performance of the data. In the similar manner, Salo et al. [45] also removed irrelevant and repeated features to detect anomalies in the network. To perform this experiment, various models like information gain (IG) and principal component analysis (PCA) with an ensemble classifier based on support vector machine (SVM), instance-based learning algorithms (IBK) and multilayer perceptron (MLP) were used as hybrid model for designing a novel framework. The proposed framework IG-PCA-ensemble method provided maximum results with good accuracy, F-score, etc. Townes et al. [46] created a novel framework comprising of multinomial models for restricting irrelevant features in gene expressions. The gene datasets are complex to analyse and find the best features. Hence generalised principal component analysis (GLM-PCA) is used to identify the best features and involve them in prediction thereby enhancing the results.

Ali et al. [47] designed a new framework to reduce irrelevant features and monitor the health care of patients using data mining techniques. The dataset is usually very complex as it gets consistent updates from online sources. Various data like blood pressure, diabetes and other web-related values are monitored. Hence a dimensionality reduction method was proposed to remove unwanted features and data to predict the anomaly at the best accuracy level possible. The outcome showed substantial improvement in accuracy after feature extraction and removal process. To tackle the need for designing a framework for dimensionality reduction techniques, Elezaj et al. [48] studied various problems associated with SMEs and designed a hybrid anomaly detection framework to reduce irrelevant features and improve the training models. The prediction was tested with intrusion detection datasets as well. The results indicated considerable improvement in the prediction accuracy with reduced feature subsets.

Stjepić et al. [49] analysed SMEs using logistic regression using 100 SMEs data from Croatia. The irrelevant features were identified and removed using Technology, Organization and Environment (TOE) framework. The outcomes suggested that prediction levels have improved with the reduction of features. The research was able to predict the outcomes with less space and time complexity after reducing the dimension of the dataset. Gao et al. [50] manipulated 123 SMEs related to various banks from China during the period from 2016 to 2020 using a hybrid credit risk evaluation model. The model used various algorithms like logistic regression, RFT, graded boost, etc. The outcomes of the framework model suggested that complex bank data can be used for prediction of risk after removing the features of the dataset that are uncommon for banks.

6 Research Gaps in the Methods

HDDR is one of the blends of conventional and contemporary process that involves combinations of various techniques and methods used in predictions. Hence to propose a novel model, the research gaps have to be assessed. There are few major problems identified at the end of the survey.

The major problem found in all these models was the underfitting of data that lead to the presence of irrelevant data in the dataset. If that happens in a complex dataset like financial datasets of SMEs, it down-performs the accuracy and other performance measures of the algorithm in predictions. It is important to identify the right framework model and the algorithms to enhance the performance of prediction. This underfitting can be solved using High Data Dimensionality Reduction methods. Also, noisy data and irrelevant data can be removed.

Another major issue identified is the reverse problem of underfitting. When the dataset comprises of huge number of features it may lead to overfitting with the algorithms to be tested. This overfitting may be caused during entry of irrelevant and redundant data from the user during the input. The overfitting of data might lead to predictions with less accuracy. Hence the model has to identify and extract relevant features into the subset of the data and then predict the outcome of the research. The high variance that occurs from high features can be reduced to find the perfect fit for the algorithm. The high variance indicated as $\theta_0 + \theta_{1\times} + \theta_{2\times2} + \ldots$ can be reduced using High Data Dimensionality Reduction techniques and formed as a subset of predictable and non-predictable data. To attain appropriate fitting of data, the training data can be improved with reduction in complexity of the model. Also lasso regularisation and ridge regularisation can be promoted in the proposed model. The dropouts can also be used in neural networks.

The problem with identifying the best and the worst features identification is of high priority that has to be addressed in the oncoming research with complex financial datasets. The model must have at least three layers of the pre-processing units and must remove all kinds of errors like noisy data, repeated data and unrelated data in the dataset.

The limitations of handling complex unsupervised dataset has to be handled with the use of neural networks as one of the testing mechanisms to identify and remove irrelevant features, extract best features using best cost ranking mode. The ranked data could be formed as subset and tested for further predictions. The concept of dimensionality reduction could solve all these research gaps to provide the best dataset for evaluation and training. If the trained data is highly efficient, obviously, the outcome of the prediction is also expected to have the optimal outcomes. The impact of big data on the financial predictions [51] and industrial revolutions [52] have impact on the current research scenario. However, improvisation in the models, frameworks and algorithms of the data mining could outperform the use of Bigdata in minimum financial predictions. This could reduce the cost of the predictions especially the Small Medium Enterprises.

The research gaps could be solved in the proposed model based on the following recommendations:

- The reduction in the dimension of data can be made possible for both supervised and unsupervised models,
- The problem of overfitting and underfitting can be solved by forming a hybrid framework comprising of feature elimination and feature extraction at the same space,
- Data visualisation can be endorsed during pre-processing of data to identify the relationship between the components of data using PCS Model,
- The regression and multicollinearity problems could be handled using dimensionality reduction models,
- The factor analysis considering the latent variables should be assessed in the proposed model for identifying the relationship between the variables and rank the variables,
- The pre-processing must be capable of handling three layers that might include filtering of noise, removing repeated features and outlier detections to make the dataset free from errors.

The High Data Dimensionality Reduction had been used predominantly in image and video processing methods. The proposed model must support HDDR in numeric dataset for both linear and non-linear data. The proposed framework could be used to handle complex linear and non-linear data in any field especially in Small Major Enterprises.

7 Conclusion

The concept of High Data Dimensionality Reduction had been studied and analysed in the context of bringing a highly enhanced prediction model for financial distress in Small Major Enterprises. Various existing models were analysed based on HDDR and financial predictions of SMEs. Also, the novel frameworks and algorithms used in dimensionality reduction for SMEs are analysed and discussed in this paper. The significant purpose of the work is to identify the research gaps in the financial distress predictions for SMEs based on reducing the irrelevant features and remove noisy data thereby increasing the accuracy of the prediction. The research work concluded with the recommendations for future proposed work and the impact of effective pre-processing in ranking features to eliminate irrelevant features as well as to select best features for prediction at the final stage. The research survey has given the substantial evidence that reduction in features could enhance the outcome of the prediction for financial datasets.

References

1. Chhikara P, Jain N, Tekchandani R, Kumar N (2022) Data dimensionality reduction techniques for Industry 4.0: Research results, challenges, and future research directions. Soft Pract Experience 52(3):658–688
2. Ray P, Reddy SS, Banerjee T (2021) Various dimension reduction techniques for high dimensional data analysis: a review. Artif Intell Rev 54(5):3473–3515
3. Thrun MC, Ultsch A (2021) Using projection-based clustering to find distance-and density-based clusters in high-dimensional data. J Classif 38(2):280–312
4. Ayesha S, Hanif MK, Talib R (2020) Overview and comparative study of dimensionality reduction techniques for high dimensional data. Inf Fusion 59:44–58. https://doi.org/10.1016/j.inffus.2020.01.005
5. Xu X, Liang T, Zhu J, Zheng D, Sun T (2019) Review of classical dimensionality reduction and sample selection methods for large-scale data processing. Neurocomputing 328:5–15. https://doi.org/10.1016/j.neucom.2018.02.100
6. Espadoto M, Martins RM, Kerren A, Hirata NS, Telea AC (2019) Toward a quantitative survey of dimension reduction techniques. IEEE Trans Visual Comput Graphics 27(3):2153–2173. https://doi.org/10.1109/TVCG.2019.2944182
7. Chormunge S, Jena S (2018) Correlation based feature selection with clustering for high dimensional data. J Electr Syst Inf Technol 5(3):542–549. https://doi.org/10.1016/j.jesit.2017.06.004
8. Solorio-Fernández S, Carrasco-Ochoa JA, Martínez-Trinidad JF (2020) A review of unsupervised feature selection methods. Artif Intell Rev 53(2):907–948. https://doi.org/10.1007/s10462-019-09682-y
9. Nguyen BH, Xue B, Zhang M (2020) A survey on swarm intelligence approaches to feature selection in data mining. Swarm Evol Comput 54:100663. https://doi.org/10.1016/j.swevo.2020.100663
10. Nilashi M, Ibrahim O, Bagherifard K (2018) A recommender system based on collaborative filtering using ontology and dimensionality reduction techniques. Expert Syst Appl 92:507–520. https://doi.org/10.1016/j.eswa.2017.09.058
11. Thudumu S, Branch P, Jin J, Singh JJ (2020) A comprehensive survey of anomaly detection techniques for high dimensional big data. J Big Data 7(1):1–30. https://doi.org/10.1186/s40537-020-00320-x
12. Pes B (2020) Ensemble feature selection for high-dimensional data: a stability analysis across multiple domains. Neural Comput Appl 32(10):5951–5973. https://doi.org/10.1007/s00521-019-04082-3
13. Liu Z, Lai Z, Ou W, Zhang K, Zheng R (2020) Structured optimal graph based sparse feature extraction for semi-supervised learning. Signal Process 170:107456. https://doi.org/10.1016/j.sigpro.2020.107456
14. Nkwabi J, Mboya L (2019) A review of factors affecting the growth of small and medium enterprises (SMEs) in Tanzania. Eur J Bus Manage 11(33):1–8. https://doi.org/10.7176/EJBM/11-33-01
15. Rao P, Kumar S, Madhavan V (2019) A study on factors driving the capital structure decisions of small and medium enterprises (SMEs) in India. IIMB Manage Rev 31(1):37–50. https://doi.org/10.1016/j.iimb.2018.08.010
16. Lin FJ, Ho CW (2019) The knowledge of entry mode decision for small and medium enterprises. J Innov Knowl 4(1):32–37. https://doi.org/10.1016/j.jik.2018.02.001
17. Nasution MI, Fahmi M, Prayogi MA (2020) The quality of small and medium enterprises performance using the structural equation model-part least square (SEM-PLS). J Phys: Conf Ser 1477(5):052052. IOP Publishing
18. Papadopoulos T, Baltas KN, Balta ME (2020) The use of digital technologies by small and medium enterprises during COVID-19: implications for theory and practice. Int J Inf Manage 55:102192. https://doi.org/10.1016/j.ijinfomgt.2020.102192

19. Hanggraeni D, Ślusarczyk B, Sulung LAK, Subroto A (2019) The impact of internal, external and enterprise risk management on the performance of micro, small and medium enterprises. Sustainability 11(7):2172. https://doi.org/10.3390/su11072172

20. Abbas J, Zhang Q, Hussain I, Akram S, Afaq A, Shad MA (2020) Sustainable innovation in small medium enterprises: the impact of knowledge management on organizational innovation through a mediation analysis by using SEM approach. Sustainability 12(6):2407. https://doi.org/10.3390/su12062407

21. Malakauskas A, Lakštutienė A (2021) Financial distress prediction for small and medium enterprises using machine learning techniques. Eng Econ 32(1):4–14. https://doi.org/10.5755/j01.ee.32.1.27382

22. Ciampi F, Giannozzi A, Marzi G, Altman EI (2021) Rethinking SME default prediction: a systematic literature review and future perspectives. Scientometrics 126(3):2141–2188. https://doi.org/10.1007/s11192-020-03856-0

23. Kou G, Xu Y, Peng Y, Shen F, Chen Y, Chang K, Kou S (2021) Bankruptcy prediction for SMEs using transactional data and two-stage multiobjective feature selection. Decis Support Syst 140:113429. https://doi.org/10.1016/j.dss.2020.113429

24. Sun J, Fujita H, Zheng Y, Ai W (2021) Multi-class financial distress prediction based on support vector machines integrated with the decomposition and fusion methods. Inf Sci 559:153–170. https://doi.org/10.1016/j.ins.2021.01.059

25. Sankhwar S, Gupta D, Ramya KC, Sheeba Rani S, Shankar K, Lakshmanaprabu SK (2020) Improved grey wolf optimization-based feature subset selection with fuzzy neural classifier for financial crisis prediction. Soft Comput 24(1):101–110. https://doi.org/10.1007/s00500-019-04323-6

26. Shang H, Lu D, Zhou Q (2021) Early warning of enterprise finance risk of big data mining in internet of things based on fuzzy association rules. Neural Comput Appl 33(9):3901–3909. https://doi.org/10.1007/s00521-020-05510-5

27. Uthayakumar J, Metawa N, Shankar K, Lakshmanaprabu SK (2020) Financial crisis prediction model using ant colony optimization. Int J Inf Manage 50:538–556. https://doi.org/10.1016/j.ijinfomgt.2018.12.001

28. Subasi A, Cankurt S (2019) Prediction of default payment of credit card clients using data mining techniques. In: 2019 International engineering conference (IEC), pp 115–120. IEEE. https://doi.org/10.1109/IEC47844.2019.8950597

29. Laborda R, Olmo J (2021) Volatility spillover between economic sectors in financial crisis prediction: evidence spanning the great financial crisis and covid-19 pandemic. Res Int Bus Financ 57:101402. https://doi.org/10.1016/j.ribaf.2021.101402

30. Jabeur SB, Sadaaoui A, Sghaier A, Aloui R (2020) Machine learning models and cost-sensitive decision trees for bond rating prediction. J Oper Res Soc 71(8):1161–1179. https://doi.org/10.1080/01605682.2019.1581405

31. Kim S, Ku S, Chang W, Song JW (2020) Predicting the direction of US stock prices using effective transfer entropy and machine learning techniques. IEEE Access 8:111660–111682. https://doi.org/10.1109/ACCESS.2020.3002174

32. Cheng KC, Huang MJ, Fu CK, Wang KH, Wang HM, Lin LH (2021) Establishing a multiple-criteria decision-making model for stock investment decisions using data mining techniques. Sustainability 13(6):3100. https://doi.org/10.3390/su13063100

33. Jan CL (2021) Financial information asymmetry: using deep learning algorithms to predict financial distress. Symmetry 13(3):443. https://doi.org/10.3390/sym13030443

34. Moradi S, Rafiei FM (2019) A dynamic credit risk assessment model with data mining techniques: evidence from Iranian banks. Financ Innov 5(1):1–27. https://doi.org/10.1186/s40854-019-0121-9

35. Van Nguyen T, Zhou L, Chong AYL, Li B, Pu X (2020) Predicting customer demand for remanufactured products: a data-mining approach. Eur J Oper Res 281(3):543–558. https://doi.org/10.1016/j.ejor.2019.08.015

36. Jahangir H, Tayarani H, Baghali S, Ahmadian A, Elkamel A, Golkar MA, Castilla M (2019) A novel electricity price forecasting approach based on dimension reduction strategy and rough

artificial neural networks. IEEE Trans Industr Inf 16(4):2369–2381. https://doi.org/10.1109/TII.2019.2933009

37. Bai Y, Sun Z, Zeng B, Long J, Li L, de Oliveira JV, Li C (2019) A comparison of dimension reduction techniques for support vector machine modeling of multi-parameter manufacturing quality prediction. J Intell Manuf 30(5):2245–2256. https://doi.org/10.1007/s10845-017-1388-1

38. Huang H, Shi G, He H, Duan Y, Luo F (2019) Dimensionality reduction of hyperspectral imagery based on spatial–spectral manifold learning. IEEE Trans Cybern 50(6):2604–2616. https://doi.org/10.1109/TCYB.2019.2905793

39. Ding J, Condon A, Shah SP (2018) Interpretable dimensionality reduction of single cell transcriptome data with deep generative models. Nat Commun 9(1):1–13. https://doi.org/10.1038/s41467-018-04368-5

40. Aydadenta H, Adiwijaya A (2018) A clustering approach for feature selection in microarray data classification using random forest. J Inf Process Syst 14(5):1167–1175. https://doi.org/10.3745/JIPS.04.0087

41. Selvakumar B, Muneeswaran K (2019) Firefly algorithm-based feature selection for network intrusion detection. Comput Secur 81:148–155. https://doi.org/10.1016/j.cose.2018.11.005

42. Zhang J, Yu J, Tao D (2018) Local deep-feature alignment for unsupervised dimension reduction. IEEE Trans Image Process 27(5):2420–2432. https://doi.org/10.1109/TIP.2018.2804218

43. Abdulhammed R, Musafer H, Alessa A, Faezipour M, Abuzneid A (2019) Features dimensionality reduction approaches for machine learning based network intrusion detection. Electronics 8(3):322. https://doi.org/10.3390/electronics8030322

44. Becht E, McInnes L, Healy J, Dutertre CA, Kwok IW, Ng LG, Ginhoux F, Newell EW (2019) Dimensionality reduction for visualizing single-cell data using UMAP. Nat Biotechnol 37(1):38–44. https://doi.org/10.1038/nbt.4314

45. Salo F, Nassif AB, Essex A (2019) Dimensionality reduction with IG-PCA and ensemble classifier for network intrusion detection. Comput Netw 148:164–175. https://doi.org/10.1016/j.comnet.2018.11.010

46. Townes FW, Hicks SC, Aryee MJ, Irizarry RA (2019) Feature selection and dimension reduction for single-cell RNA-Seq based on a multinomial model. Genome Biol 20(1):1–16. https://doi.org/10.1186/s13059-019-1861-6

47. Ali F, El-Sappagh S, Islam SR, Ali A, Attique M, Imran M, Kwak KS (2021) An intelligent healthcare monitoring framework using wearable sensors and social networking data. Futur Gener Comput Syst 114:23–43. https://doi.org/10.1016/j.future.2020.07.047

48. Elezaj O, Yayilgan SY, Abomhara M, Yeng P, Ahmed J (2019) Data-driven intrusion detection system for small and medium enterprises. In: 2019 IEEE 24th international workshop on computer aided modeling and design of communication links and networks (CAMAD), pp 1–7. IEEE. https://doi.org/10.1109/CAMAD.2019.8858166

49. Stjepić AM, Pejić Bach M, Bosilj Vukšić V (2021) Exploring risks in the adoption of business intelligence in SMEs using the TOE framework. J Risk Financ Manage 14(2):58. https://doi.org/10.3390/jrfm14020058

50. Gao G, Wang H, Gao P (2021) Establishing a credit risk evaluation system for SMEs using the soft voting fusion model. Risks 9(11):202. https://doi.org/10.3390/risks9110202

51. Shakya S, Smys S (2021) Big data analytics for improved risk management and customer segregation in banking applications. J ISMAC 3(03):235–249. https://doi.org/10.36548/jismac.2021.3.005

52. Suma V (2019) Towards sustainable industrialization using big data and internet of things. J ISMAC 1(01):24–37. https://doi.org/10.36548/jismac.2019.1.003

Deep Learning-Based Triphase Community Detection for Multimedia Data

D. Sowmyadevi and S. Srividhya

Abstract Network analysis plays a significant role in business which is achieved through community detection. The relationship between the nodes is mined by community detection, which facilitates the analysis of complicated networks. In the current era, social media is the commonest mode of communication that leads to complex online social networks, from which useful information can be retrieved. Not only textual data is shared in social media, in addition multimedia data plays a significant role in content sharing in social network. This research work proposes a community detection method based on deep learning algorithm to detect communities for both textual content and multimedia content. The proposed method triphase–deep learning community detection (TriDL-CD) method illustrates the relationship of data in a graphical way in the first step. Second step converts the graph into user relationship table using similarity weightage analysis from which the communities are formed using convolution neural network. The proposed method proved to be efficient in detecting high quality communities for multimedia content compared with Louvain community detection algorithm, Leiden community detection, and surprise community detection algorithms. Experimental results show the efficacy of deep learning in the concept of community detection.

Keywords Deep learning · Community detection · Multimedia · Social network analysis

D. Sowmyadevi (✉)
Department of Computer Science, PSG College of Arts and Science, Coimbatore, India
e-mail: sowmyadevidpr@gmail.com

S. Srividhya
Department of Computer Science, KPR College of Arts Science and Research, Coimbatore, India
e-mail: srividhya.s@kprcas.ac.in

1 Introduction

With the advent of Internet and smart devices, data is emerging at an enormous rate in recent years. Social media being the powerful mode of communication has helped businesses in many ways. In addition to the textual content, video, and images are also shared among people in social media. Social media network is a complex network to represent real world. The massive amount of data in social networks and the availability of data in social networks have turned the attention of researchers toward social media analytics. Community detection and sentiment analysis are the two main hot topics with data in social networks. Community detection plays a vital role in detecting similar groups of people sharing common interest. Communities can be groups of research papers sharing same topic [1]. Communities in social networks groups people having similar interest or in same profession [2–4]. Sentiment analysis or opinion mining determines the opinions of the users based on the topic they have created [5]. The main criteria of community detection are to know the quality of the communities formed. The most common metric used to check the quality and wellness of formed communities are modularity metric [6]. Newman and Girvan's [7] proposed modularity measures the difference between the fraction of edges within communities and the expected value in a network with random edges. Figure 1 shows the sample community structure in a network referred from [8].

The concept of graph partitioning and hierarchical clustering takes up the role in detecting communities. In graph partitioning method, the entire structure of the network and the number of subgroups to be divided should be known in advance. Hierarchical partitioning is a clustering method where the nodes in the network are divided into several subgroups which is not known in advance. Similar nodes are grouped into same community where the relationship between nodes is measured by vertex similarity [9] or edge betweenness [10]. Community detection is mainly classified into four approaches, namely 1. Node centric, 2. Group centric, 3. Network centric, and 4. Hierarchical centric.

Existing state-of-the-art techniques like spectral clustering [11, 12] are implemented in small networks which are not feasible and effective for social media

Fig. 1 Community structure in a network
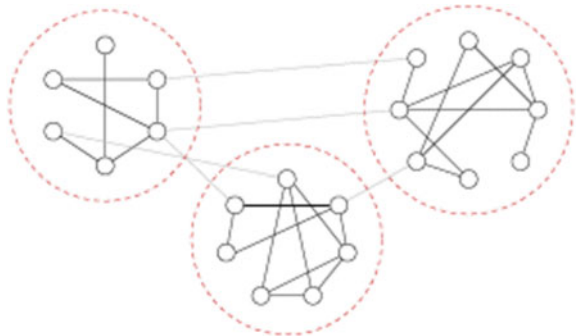
networks. The complex network topology of social media networks made the traditional methods less applicable to detect communities. The advanced features of deep learning provide good response to detect communities in social networks. They are flexible to non-linear network properties. The low-dimensional network embedding property preserves the complex network. Growth and usage of multimedia data multimedia social networks (MSNs) is phenomenal. Growth and usage of multimedia system in social networks resulted in MSNs. Social media users publish textual content, audio, video, and image content in social networks for marketing, political, or personal purposes. This discovers affinities between a user to user or between a user to a multimedia content. Similarity between the objects can also create links or similarities between the social media users. Due to the growth of MSNs, identifying communities tend to be complicated considering the network interactions and user information. Due the hierarchical structure, heterogeneous network, dynamic network, community embedding, and signed information on edges recent approaches to detect communities then dealt with deep learning models tend to have some disadvantages. To overcome the above issues, the current work proposes an approach to detect communities for multimedia data. The relationship among the users based on the similar interest is grouped to extract useful information [13, 14]. The proposed work is a triphase methodology that creates a directed acyclic graph which is then converted to user relationship table using similarity weightage analysis. Similarity weightage analysis finds and assigns weight to the users with similar interest. Finally, communities are detected using convolution neural network. The paper is organized in the following manner. Section 2 discusses the related work. Section 3 presents the proposed methodology for multimedia social networks. Section 4 illustrates the experimental analysis for social media datasets. Section 5 concludes the work with future enhancements. Many methods for detecting communities have been proposed.

2 Literature Survey

Researchers have come out with many attempts to detect communities using divisive methods [3, 15], networks dynamics [16, 17], and local expansion methods [18, 19]. This section reviews some of the existing community detection methods.

Zhang et al. [20] suggested a community detection method drew on the similarity of behavior in IP node communication. Communities are formed with highest similarity nodes based on frequency of interactions. The proposed method is used to analyze complex public network datasets as well as real-world IP datasets. In terms of modularity and normalized mutual information indicators, the proposed method outperformed existing state-of-the-art methods. Avrachenkov et al. [21] detected communities in a network using game theory concept. This method not only highlights link density but also considers cluster formation. The proposed methods use two approaches, namely Myerson value and hedonic games. The intuitive part in hedonic games is tuning of resolution parameter. The method also incorporated with Gibbs sampling.

Blondel et al. [22] evolved Louvain community detection based on the structure of network measurement. This algorithm uses two phases, namely local movement of nodes and aggregation of network. In the first phase, each node is assigned to a different community, it then finds the neighbors of each node and calculates the modularity gain by removing a node from current community and placing in neighbors' community if the gain is maximized or positive. If the gain is not positive or maximized, then the node remains in the same. The first phase of the algorithm is come to an end when the modularity reaches the maximum value. Second phase terminates by building a network from the detected communities. First and second phase are repeated up to the status of network is stable and when the modularity stretch-out to the maximum.

Zhang et al. [23] developed fast Louvain algorithm for community detection. This algorithm successfully detects the community for large networks. Fast Louvain algorithm uses dynamic iteration instead of cyclic iteration that will increase the convergence speed and also splits the network. The results from the implementation prove that it reduces the computation, and excellence of community detection is improved. Also proved that the proposed fast Louvain algorithm is better than conventional Louvain algorithm in terms of partition result and operation competence.

Mourchid et al. [24] applied community detection algorithms for image segmentation. In addition to it, authors also proposed a study on five community detection methods for a complex network. Finally, communities are detected with highest modularity. Experiments proved that the proposed methods are superior for Berkeley database with rand index PRI of 0.81.

Ding et al. [25] proposed divisive algorithm to identify external links, to eliminate external links, and to terminate the algorithm without predefined parameters and community definitions. The proposed algorithm uses link break strategy to detach numerous links at each and every iteration. Weak link notion was initiated to come of the challenges faced. Proposed algorithm proved to be better in terms of accuracy-efficiency trade-off than some of the latest divisive algorithms. Tryouts are accomplished for artificial and actual networks.

Surprisingly, there is a statistical measure for community detection. The main drawback seems to be the resolution limit its hardness to optimize due to non-linearity. Considering this, Tang et al. [26] propose a more effective algorithm for surprise optimization. The three approaches included are a topological structure pre-processing based on local random walks, a community partition pre-processing, and a community partition post-processing. The proposed method is implied in biological networks like disease network and protein network. A set of notable disease-gene modules was identified for each disease, and the operational improvement of the genes was investigated. The observation of these modules can provide useful information for disease-gene spotting as well as illumination for the study of disease molecular mechanisms. The proposed method has no effect on the time complexity. The proposed algorithm has been found to be very effective for network analysis in computational biology.

Zhou et al. [27] proposed an algorithm for detecting overlapping communities based on cooperative game theory. Shapley value and coalition of node are calculated using edge weight computation. Choosing coalitions will improve characteristic function to avoid small coalitions. The number and size of communities are not required, and the algorithm results in a stable overlapping community structure. Experiments are carried out on both artificial and real networks through which the proposed method is proved to be effective and detects overlapping communities very accurately.

Deitrick and Hu [28] use sentiment classification for community detection enhancement and community partitions for analyzing sentiment data. These two methods analyze four networks from Twitter online social networks. The network used for the work has 60,000 users and had 2 million tweets. Community detection has been enhanced with mentions, hashtags, replies, retweets, and sentiment classifications. Combining sentiment classifications and grouping communities analyze sentiment data. This novel approach of combining community detection and sentiment analysis proved to be mutually informative.

Balaji et al. [29] applied RSA algorithm to compute ciphertext and plaintext from multimedia inputs using public key pair for secure data transmission. Due to this secure data transmission, the throughput can be increased which improves the quality of data delivery in MANNET.

Chen and Smys [30] presented software defined networks (SDNs) platform for secure point-to-point delivery in social network platform. Proposed method also includes support vector machine and restricted Blotzmann machine approach to detect the suspicious flow detection in social communication to enhance the power and efficacy of the system. Performance of the system is analyzed by detecting malicious events like confidential data collection, profile cloning, and identify theft.

3 Proposed Methodology

This section discusses the proposed (TriDL-CD) triphase deep learning-based community detection approach to discover the communities among the users in multimedia social network. TriDL-CD analyzes the social media networks with multimedia content that gives a good impact on the growth and development of various businesses. Related communities are detected based on deep learning model to handle complex relationships. Social media has become most prevalent among people to communicate and to share data with each other. In addition to the textual data, multimedia data is often shared in social media. In the proposed TriDL-CD, every user in a network can have a relationship with another user, or there can also be a relationship among the user and a multimedia entity.

Relationships can be in two ways between one user to another user or between a user and a multimedia content. Users interact with another user in the first case, and a user can post any multimedia content in their social media sites in the form of text, image, or video. With such interactions, strength between the users and

Fig. 2 Phases of proposed
CD-DL model
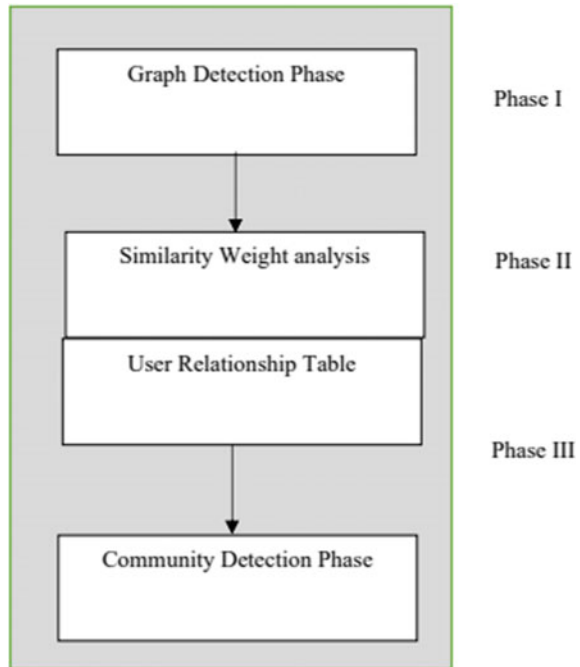
between a user and the multimedia content can be calculated. In such cases, links strength will be maximum when two users interact with the same image or video. This is also true when two users interact with similar types of images or videos. The proposed model works in three phases where the first graph generation phase involves in depicting the graphical representation of entities. Entities are users and any of the multimedia object. Secondly, similarity weightage analysis phase deals with finding the weightage of the similarity among the users and objects from which user object relationship table is generated. This user object relationship table depicts the user-to-content and similarity relationships. Finally, the community detection phase identifies the communities with the link strength using convolution neural network. Phases of the proposed model are depicted in Fig. 2.

3.1 Graph Detection Phase

The proposed model represents the interaction between the users and the multimedia objects taking into account the social networking sites like Twitter, Facebook, LinkedIn, Instagram, YouTube, Flickr, etc.… The multiple one to one, one to many, many to one, and many to many can be easily implemented. A social network with multimedia data is a directed acyclic graph (DAG) with V as the vertex and E as the edges, represented by.

DAG $= (V, E)$ with weight as wt.
where $e_i = e_1, e_2 \ldots.. e_n \in E$.

$$V = V_1 \cup V_2, \ V_1 = Ve_i^+ \text{ and } V_2 = Ve_i^-$$

A set of vertices in the graph $V = \{U, I\}$, U represents the users and I represent multimedia images.

wt $\rightarrow [0,1]$.

wt is a function that assigns a weight to every arc (e_i) in the DAG that falls in a range between 0 and 1.

Each arc on DAG is defined as $e_i = \{e_i^+, e_i^-\}$ with $e_i^+ = (Ve_i^+, i)$ and $e_i^- = (Ve_i^-, i)$ where Ve_i^+ is one end of the edge and Ve_i^- is the other end. $d(e_i)$ is the degree of the arc which is the number of vertices that have incident arcs. $d(v)$ is the number of hyperarcs that are incident to vertex v. Two main associations are taken into consideration, namely user to user and user to multimedia objects.

User-to-user association is defined as $e_i = (Ve_i^+, i); (Ve_i^-, i)$.

User to multimedia object has a weight wt (e_i) assigned to each arc in the DAG. It is represented mathematically as $e_i = \{(Ve_i^+, i); (Ve_i^-, i)\}$ in which $Ve_i^+ = U_n$ with $U_n \subset U$ and $Ve_i^- = I_n$ where $I_n \subset I$. Initially, the weight of the DAG arc is set as 1. Figure 3 is depicted as a multimedia network model which has 5 users and 5 multimedia objects which represents how the users are related to the multimedia objects. From Fig. 3, the model can extract the different path connecting two users through various multimedia objects. The connecting path between the users is the consecutive arcs in the DAG that connects the two users through a multimedia object.
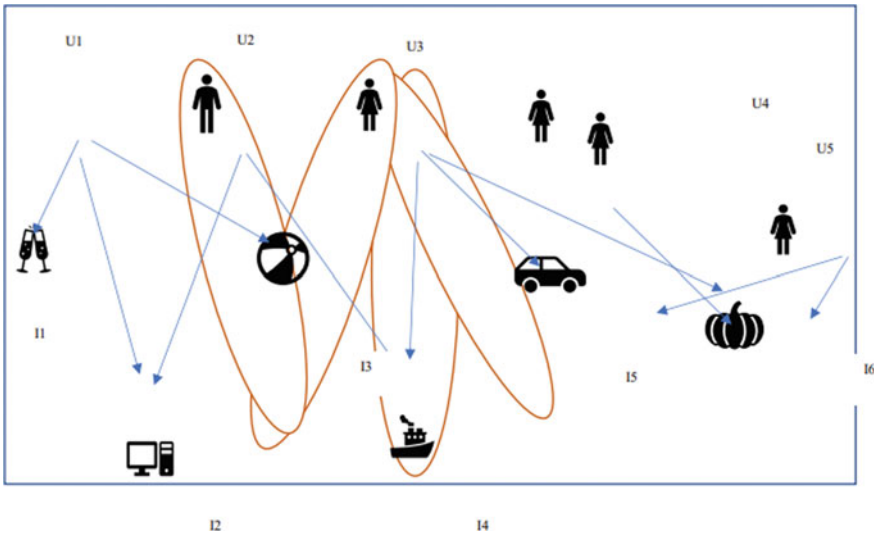
Fig. 3 User to object interactions

3.2 Similarity Weightage Analysis

There exists a path between the users based on the user's common interest. The proportion of the number of paths in the arc between the users represents the similarity weightage of the link between the two users. Similarly, the similarity weightage is calculated for all the users and the objects to which they are related to either directly or indirectly. Figure 4 illustrates the interaction path between the users. When two objects or two users are having similar relations, then they are defined as connection between two users = user + the relationship between two users which is then represented mathematically as below.

edge$_i$ = U_i + r_i (where U is the user and r is the relationship).

U + edge$_i$ = {e_k} and U-edge$_i$ = {v_j} with $k \neq j$.

The weight of each relationship is based on the measure and the type of the user considered. When the multimedia object is considered, the weight will be calculated as to low- and high-level component feature. When the relationship is between user to user, then the relative weight is taken into consideration with the proportion to the user relationships. In case of user to object relationship, the weight will be calculated based on the content published between the user and the object.

The interaction path results in a user relationship table with the relevant weight between the users based on the number of interaction paths. Figure 5 shows the user relationship table for the multimedia network shown above in Fig. 3. Table 1 exactly shows how the users are interlinked.
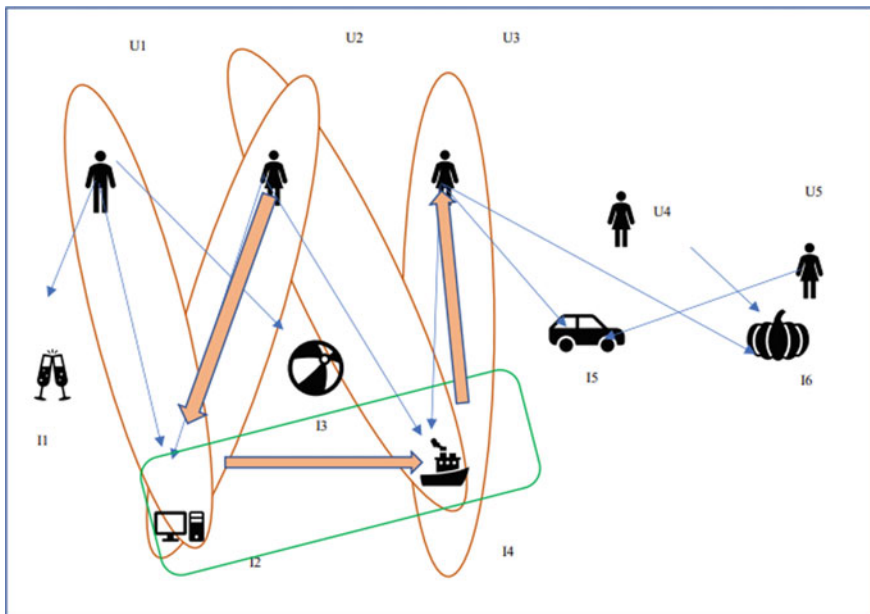
Fig. 4 Interaction path between users
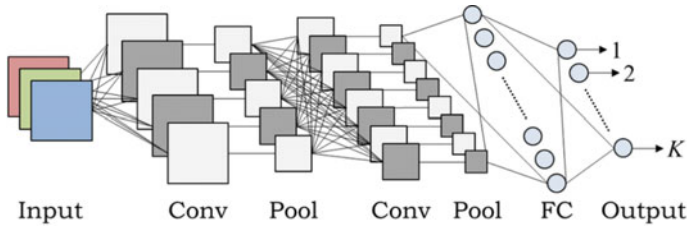
Fig. 5 Architecture of convolution neural network

Table 1 User relationship table

U/I	U1	U2	U3	U4	U5
I1	1	0	0	0	0
I2	1	1	0	0	0
I3	1	0	1	0	0
I4	0	1	1	0	0
I5	0	0	1	0	1
I6	0	0	0	1	0

This user relationship table shows the strength of the relationships between the users with the same likings. The element (i, j) shows the probability of connection calculated from the number of relationships and the weight associated between the user and the objects.

3.3 Community Detection Using Convolution Neural Network

Convolution neural network (CNN) architecture is used to handle high sparsity data and to generate communities among users and between users and multimedia objects. The proposed convolution neural network (CNN) uses the user relationship table as an input and identify the communities with the topological content. CNN's four layers such as convolution layer, ReLU layer, pooling layer, and fully connected layer will extract information from images. Each and every image is considered as a matrix. The extracted features are then moved to ReLU layer. Element wise operation is done here in this layer, and a graph is generated using ReLU function. The features are found by scanning the original image using convolutions and ReLU layers. The third pooling layer down samples by reducing the features and generated pooled feature map. The next flattening process converts the output from the pooled layer into single layered vector list which is then fed as an input to the fully connected layer.

3.3.1 Convolution with ReLU Layer

The vector of features is n, which denotes the number of users in the network. The user relationship table displays how users are associated to network objects in relation to other nodes in the network. This was created with a non-proportional function to the distance between the nodes. The major features are extracted using a collection of filters in the convolution layer, which creates a feature map as an output. The elements of the feature map are calculated using the formula below. [29].

$$v_{ij}^n = \text{relu}\left(b_w + \sum_{i=0}^{w'-1}\sum_{j=0}^{h'-1} w_{ij} X p_{(x+i)(y+j)}^n\right) \tag{1}$$

$p_{(x+i)(y+j)}^n$ is the value at position $x + i$, $y + j$, w_{ij} is the weight, and b_w represents the bias value. The result of the convolution layer is asset of feature maps.

3.3.2 Pooling Layer

The output of the previous layer is taken as an input to this pooling layer which subsamples the feature map by reducing the number of features. Pooling operation is done on feature map with $f_1 \times f_2$ dimension with cardinality of $m_1 \times m_2$ which gives an output of matrix $f_1 m_1 \times f_2 m_2$.

3.3.3 Fully Connected Layer

This is the network's final layer, with k neurons, where k equals the number of communities. Each neuron in the network is linked to the community by setting the relative neuron's output to 1 and the rest to 0. All of the values on feature maps are linked to all of the neurons in the fully connected layer. The proposed system's accuracy is improved by optimizing the parameters.

Back propagation method is adopted here. The input image is now converted to the required format, and now, the image is flattened into a column vector. For every iteration, the flattened output is fed into back propagation method. This model uses softmax classification technique to differentiate low-level features in images.

4 Experimental Analysis

This segment assesses the effectiveness of the proposed for BlogCatalog3 and Yahoo Flickr Creative Commons 100 M and artificial datasets. The way that has been proposed is tested based on the following criteria.

- Execution time
- Performance analysis.

The performance analysis is tested based on macro-$F1$ [30] and micro-$F1$ [31] using the following formula:

$$\text{Macro} - F1 = \frac{\sum_{X \in C} F1 - \text{measure}(x)}{|C|} \tag{2}$$

$$\text{Micro} - F1 = \frac{2 \times \text{Precision} \times \text{Recall}}{\text{Precision} + \text{Recall}} \tag{3}$$

The result was depicted with number of nodes varying with 10,000, 50,000, 100,000, 150,000 nodes.

From Fig. 6, it is clear that the proposed TriDL-CD appears to become more efficient as the number of nodes increases. It is also clear that the execution time is proportional to the number of nodes, and it is based on the adopted workstation. A result was also generated with the 75,000 nodes and with 10^{-8} and 10^{-3} matrix sparsity. The result from Fig. 7 proved that the proposed method depends on dense matrix but not based on sparse matrix, till the sparsity value is between 10^{-4} and 10^{-3}. The degree of sparsity in social networks is 10^{-6} and 10^{-8}.

The execution time of the suggested method is compared with traditional Deep-Walk [32], LINE [33], and CANE [34]. Table 2 shows the execution time of TriDL-CD compared with DeepWalk, LINE, and CANE for two datasets, namely BlogCatalog and Flickr.
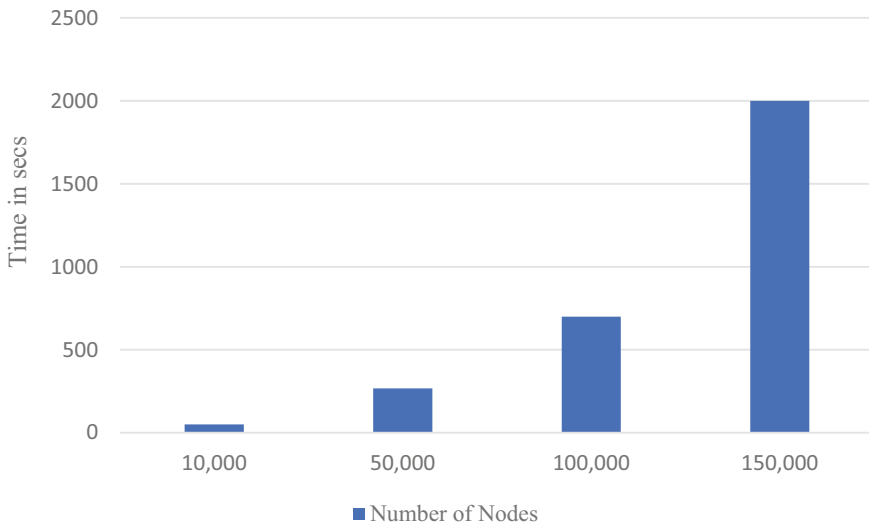
Fig. 6 Execution time with varying number of nodes
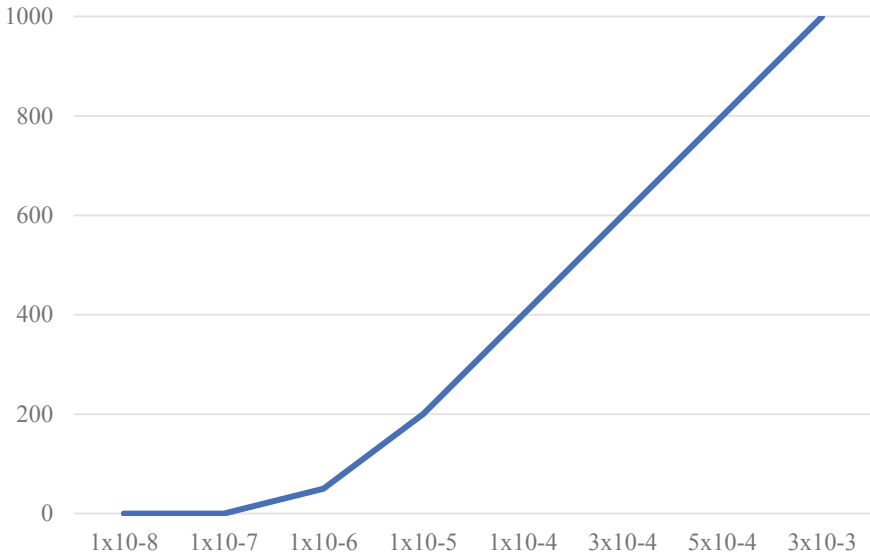
Fig. 7 Execution time with varying sparse matrix and constant number of nodes

Table 2 Execution time of TriDL-CD, DeepWalkm LINE, and CANE for two datasets

Method/dataset	BlogCatalog (min)	Flickr (min)
DeepWalk	57	156
LINE	54	145
CANE	60	164
TriDL-CD	42	134

It is evident from the table that the execution time of the proposed TriDL-CD is less compared to other state-of-the-art methods. TriDL-CD method takes only 42 min for BlogCatalog dataset and 134 min for Flickr dataset which is lesser than other methods like DeepWalk, CANE, and LINE.

The accuracy for the proposed TriDL-CD method with respect to two datasets is shown in Fig. 8. It is proved from the result that as the percentage of deleted edges increases, the accuracy drops down. When the percentage of deleted edges is 10%, then the accuracy is 90% for BlogCatalog and 92% for Flickr. For 50% of deleted edges, accuracy dropped to 61% for BlogCatalog and 70% for Flickr. For 70% of deleted edges, the accuracy dropped to 32% and 55% for BlogCatalog and Flickr, respectively. Increase in hops did not show a promising result in accuracy. The performance of the proposed approach TriDL-CD compared to DeepWalk, LINE, and CANE with respect to micro-$F1$ and macro-$F1$ is shown in Fig. 8. Efficiency of the two datasets is shown with varying number of nodes in Figs. 9 and 10, and Table 3.
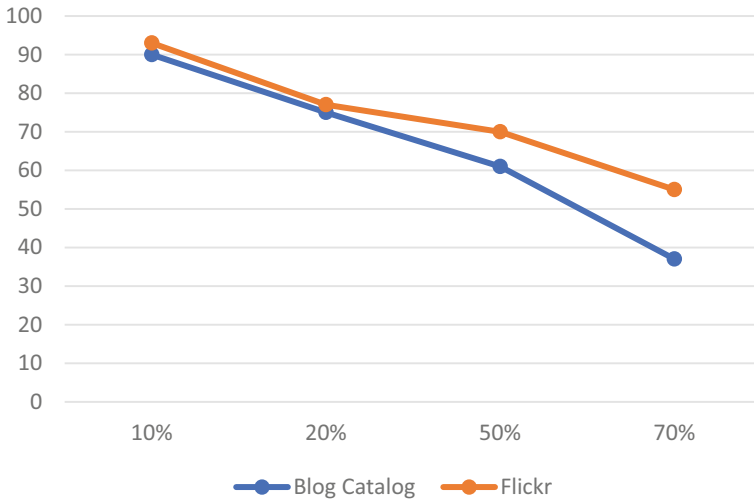
Fig. 8 Accuracy based on deleted edges
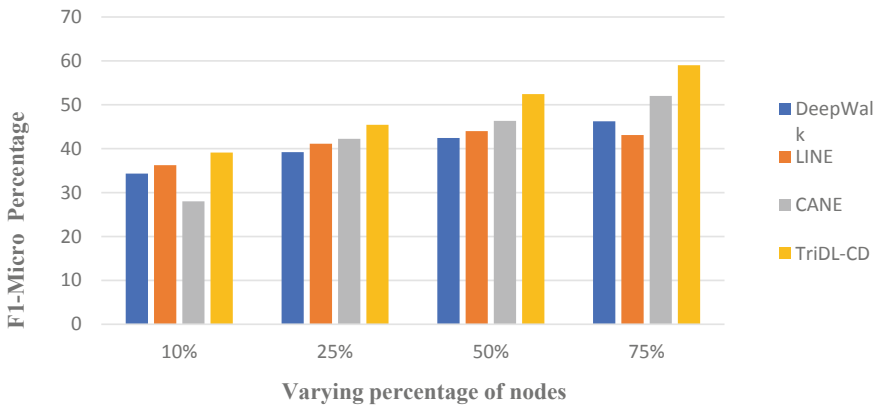
Fig. 9 Micro-$F1$ measure for TriDL-CD and other state-of-the-art methods for BlogCatalog

The suggested approach TriDL-CD performs better than the state-of-the-art methods for varied percentages of nodes, as seen in the Figs. 9 and 10 and Table 3.

5 Conclusion

The generation and availability of data have turned the attention of researchers to mine useful information out of it. One of the domains where a huge amount of
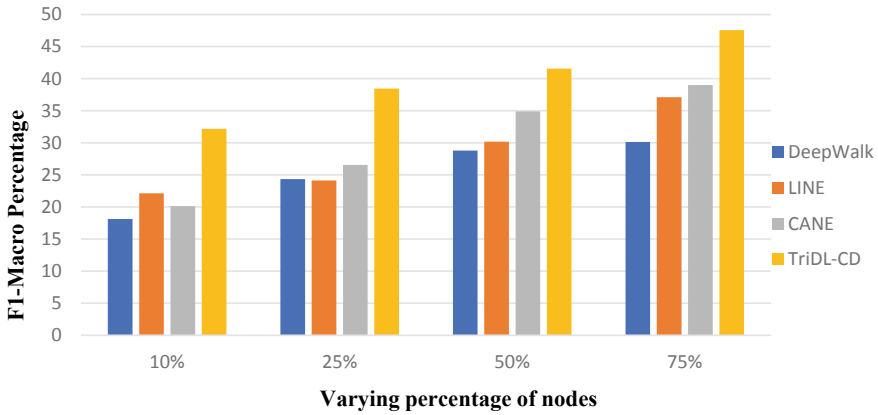
Fig. 10 Macro-$F1$ measure for TriDL-CD and other state-of-the-art methods for BlogCatalog dataset

Table 3 Micro-$F1$ and macro-$F1$ measure for TriDL-CD and other state-of-the-art methods for Flickr dataset

Metrics	Methods/% of labelled nodes (%)	5	7	9	10
Micro-$F1$ (%)	DeepWalk	25.43	29.45	34.65	45.12
	LINE	30.12	32.34	37.89	43.34
	CANE	23.56	27.89	32.21	40.23
	TriDL-CD	27.54	34.56	43.56	48.98
Macro-$F1$ (%)	DeepWalk	14.45	19.45	23.56	30.21
	LINE	16.45	18.76	19.87	22.45
	CANE	15.33	18.34	21.56	22.45
	TriDL-CD	13.45	19.56	24.67	28.44

heterogeneous unstructured data generated is social media. Human relationships and their common interests can be analyzed from social media network which promotes business in different domains. Moreover, enormous multimedia data is being shared in social media for effective communication. This research work aims to detect similar communities in multimedia social network by using directed acyclic graph. The interaction between the users is found out and depicted in a table to find the user–user relationship. Finally, deep learning-based CNN is used to detect communities to identify the user of common interests. Our future work can be extended with other social media networks. It can also be further extended by considering video and animated data. The proposed method is proved to be feasible and effective for community detection in multimedia data.

References

1. Chen P, Redner S (2010) Community structure of the physical review citation network. J Informetr 4(3):278–290
2. Nunes R, Amaral LA, Amaral LAN (2005) Functional cartography of complex metabolic networks. Nature 433(7028):895
3. Girvan M, Newman MEJ (2002) Community structure in social and biological networks. Proc Natl Acad Sci 99(12):7821–7826
4. Wang C, Tang W, Sun B, Fang J, Wang Y (2015) Review on community detection algorithms in social networks. In: 2015 IEEE international conference on progress in informatics and computing (PIC), pp 551–555
5. Liu K, Li W, Guo M (2012) Emoticon smoothed language models for twitter sentiment analysis. In: Proceedings of the 26th AAAI conference on artificial intelligence, pp 1678. Toronto, 22–26 July 2012
6. Amini AA, Chen A, Bickel PJ, Levina E et al (2013) Pseudo-likelihood methods for community detection in large sparse networks. Ann Stat 41(4):2097–2122
7. Newman, MEJ, Girvan M (2004) Finding and evaluating community structure in networks. Phys Rev E 69(2). Article ID: 026113. https://doi.org/10.1103/PhysRevE.69.026113
8. Alamsyah A (2014) Community detection methods in social network analysis—scientific figure. ResearchGate, https://www.researchgate.net/figure/Illustration-of-community-structure-inside-a-network-taken-from-Newman-4_fig1_257890111. Accessed 10 Jul 2022
9. Fortunato S (2010) Community detection in graph. Phys Rep 486:75–174
10. Newman MEJ (2004) Fast algorithm for detecting community structures in networks. Phys Rev E 69:066133
11. de Lange S, de Reus M, Van Den Heuvel M (2014) The Laplacian spectrum of neural networks. Front Comput Neurosci 7:189
12. Schaeffer SE (2007) Graph clustering. Comput Sci Rev 1(1):27–64. https://doi.org/10.1016/j.cosrev.2007.05.001
13. Tang J, Qu M, Wang M, Zhang M, Yan J, Mei Q (2015) Line: large-scale information network embedding. In: Proceedings of the 24th international conference on world wide web, Florence, pp 1067–1077. Italy, 18–22 May 2015
14. Wang J, Cao J, Li W, Wang S (2021) CANE: community-aware network embedding via adversarial training. Knowl Inf Syst 63:411–438
15. Radicchi F, Castellano C, Cecconi F, Loreto V, Parisi D (2004) Defining and identifying communities in networks. Proc Natl Acad Sci USA 101(9):2658–2663
16. Arenas A, Diaz-Guilera A, Pérez-Vicente CJ (2006) Synchronization reveals topological scales in complex networks. Phys Rev Lett 96(11):114102
17. Assenza S, Gutiérrez R, Gómez-Gardenes J, Latora V, Boccaletti S (2011) Emergence of structural patterns out of synchronization in networks with competitive interactions. Sci Rep 1
18. Jiang F, Jin S, Wu Y, Xu J (2014) A uniform framework for community detection via influence maximization in social networks. In: 2014 IEEE/ACM international conference on advances in social networks analysis and mining (ASONAM). IEEE, pp 27–32
19. Kloumann IM, Kleinberg JM (2014) Community membership identification from small seed sets. In: Proceedings of the 20th ACM SIGKDD international conference on knowledge discovery and data mining. ACM, pp 1366–1375
20. Zhang S, Zhang Y, Zhou M, Peng L (2020) Community detection based on similarities of communication behavior in IP networks. J Ambient Intell Humanized Comput
21. Avrachenkov KE, Kondratev AY, Mazalov VV, Rubanov DG (2018) Network partitioning algorithms as cooperative games. Comput Soc Netw 5:11. https://doi.org/10.1186/s40649-018-0059-5
22. Blondel VD, Guillaume JL, Lambiotte R, Lefebvre E (2008) Fast unfolding of communities in large networks. J Stat Mech P10008:12
23. Zhang J, Fei J, Song X, Feng J (2021) An improved louvain algorithm for community detection. Hindawi Math Prob Eng 2021:14. Article ID: 1485592.https://doi.org/10.1155/2021/1485592

24. Mourchid Y, El Hassouni M, Cherifi H (2016) Image segmentation based on community detection approach. Int J Comput Inf Syst Ind Manage Appl 8:195–204. ISSN: 2150-7988

25. Ding X, Zhang J, Yang J, Shen Y (2018) An autonomous divisive algorithm for community detection based on weak link and link-break strategy. Hindawi Math Prob Eng 2018:12. Article ID: 2942054. https://doi.org/10.1155/2018/2942054

26. Tang YN, Xiang J, Gao YY, Wang ZZ, Li HJ, Chen S, Zhang Y, Li JM, Tang YH, Chen YJ (2019) An effective algorithm for optimizing surprise in network community detection. IEEE Access. https://doi.org/10.1109/ACCESS.2019.2946080

27. Zhou X, Cheng S, Liu Y (2020) A cooperative game theory-based algorithm for overlapping community detection. IEEE Access 8:68417–68425. https://doi.org/10.1109/ACCESS.2020.2985397

28. Deitrick W, Hu W (2013) Mutually enhancing community detection and sentiment analysis on twitter networks. J Data Anal Inf Process1:19–2

29. Balaji S, Harold Robinson Y, Golden Julie E (2019) Secure multimedia data transmission in mobile AD-HOC Networks. IRO J Sustain Wirel Syst 1(1):62–68

30. Chen JIZ, Smys S (2020) Social multimedia security and suspicious activity detection in SDN using hybrid deep learning technique. J Inf Technol 2(02):108–115

31. Ferraro A, Moscato V, Sperlí G (2021) Deep learning-based community detection approach on multimedia social networks. Appl Sci 11:11447. https://doi.org/10.3390/app112311447

32. Wang D, Cui P, Zhu W (2016) Structural deep network embedding. In: Proceedings of the 22nd ACM SIGKDD international conference on knowledge discovery and data mining, pp 1225–1234. San Francisco, 13–17 Aug 2016

33. Tang L, Liu H (2009) Relational learning via latent social dimensions. In: Proceedings of the 15th ACM SIGKDD international conference on knowledge discovery and data mining, pp 817–826. Paris, 28 June–1 July 2009

34. Perozzi B, Al-Rfou R, Skiena S (2014) DeepWalk: online learning of social representations. In: Proceedings of the 20th ACM SIGKDD international conference on knowledge discovery and data mining, pp 701–710. Association for Computing Machinery, New York, 24–27 Aug 2014

Design of a High-Speed and Low-Power AES Architecture

Talluri Venkata Sai, Karthi Balasubramanian, and B. Yamuna

Abstract Data security is becoming a major concern in recent years due to the proliferation of interconnected devices. With the number of devices connected to the Internet of things (IoT) growing at a very rapid pace, design of speed and power efficient crypto systems is very essential. This paper explores the design of a high-speed and low-power advanced encryption standard (AES) architecture to be used as a hardware accelerator in various cryptographic systems. The use of Rijndael S-Box for byte substitution, merging of ShiftRows operation with the State Register updation, implementation of MixColumns transformation through substructure sharing, and clock gating methods are investigated in this work for obtaining a high-speed device with low-power consumption. The proposed design is designed using Verilog and co-simulated in MATLAB and implemented as an ASIC using 90 nm GPDK technology. It is seen that the proposed design has 83% increase in speed, 39% decrease in area, and 82% reduction in power dissipation as compared to a standard AES design implementation.

1 Introduction

The IoT is a network of interrelated computing devices, digital and mechanical machines, and objects, each with unique identifiers and ability to transfer data over a network without human intervention. With the number of connected devices increasing exponentially, there is always a looming cyber threat in the system [1–3]. This creates an urgent need to provide security to the information being exchanged

T. V. Sai · K. Balasubramanian (✉) · B. Yamuna
Department of Electronics and Communication Engineering, Amrita School of Engineering, Amrita Vishwa Vidyapeetham, Coimbatore, India
e-mail: b_karthi@cb.amrita.edu

between the devices. But this is not an easy task since the tiny nodes at the end generally lack resources required for creating a secure environment. This necessitates the design of high-speed security architectures that are both cost and power efficient.

Cryptography is a process where the data to be sent is added with a secret key in order to communicate the information safely to the target. There are two types of cryptography: symmetric key cryptography and asymmetric key cryptography [4–6]. Cryptographic algorithms are employed in varied applications including wireless sensor networks, cloud computing, blockchain, wireless local area networks, IoT, and smart cards [7–14]. One of the secure symmetric cryptographic algorithms is advanced encryption standard (AES), which is widely used in various applications. The main reason of selecting AES is its large key size. The time required to break any encryption algorithm is based on the size of the key given to the algorithm. According to the length of the key used in the algorithm, different security levels are provided. AES algorithm with a 256-bit key provides an efficient and high level of security of different levels as required by IoT platforms [15]. AES was preceded by data encryption standard (DES) algorithm which had a small key size. With a rapid increase in processing power, it became very vulnerable to being decoded easily and hence triple DES, with an enhanced key size was introduced but it turned out to be sluggish and slow [16] and has been completely replaced with AES. AES is now the de facto algorithm for most of the standard cryptographic applications.

AES algorithm involves various steps including byte substitution (SubBytes), row shifting (ShiftRows), mixing of columns (MixColumns), and AddRoundKey. With the goal of implementing AES algorithm with low-area and low-power dissipation, various approaches have been tried by researchers [17]. One of the key components in AES is the S-Box that conceals the relationship between the key and the cipher text, ensuring Shannon's property of confusion. The byte substitution operation in the AES is performed by Rijndael S-Box block. Design of the S-Box is a widely concentrated area of research in cryptography [18]. Studies have shown that the combinational logic based S-Box that replaces lookup table-based I/O tasks are more efficient and result in low area and power designs [19–21]. Implementing the AES algorithm in software results in high latency for data processing and transmission [18]. Hence, hardware implementation approaches are preferred especially for applications requiring high speed, low power, and area. Shahbazi and Ko. in [22] propose a low-power and low-areas 8-bit lightweight datapath accelerator for AES architecture—nano-AES—intended for mobile SoCs and devices with resource constraints. Our research work builds upon this architecture and is aimed toward a high-speed realization of the same by efficient design of the MixColumns operation of the AES algorithm as proposed in [23].

The paper is organized as follows. Section 2 reviews the basic structure of the AES algorithm. Section 3 describes the proposed architecture based on the nano-AES presented in [22]. Section 4 deals with results and analysis and the paper concludes in Sect. 5.

2 AES Algorithm

AES algorithm is a symmetric block cipher algorithm consisting of four main functions: SubBytes, MixColumns, AddRoundKey, and ShiftRows. The encryption and decryption process occur in blocks of 128, 192, or 256 bits using keys of the same length. The four main functions occur over several rounds, with the number of rounds being 10, 12, and 14 for key sizes of 128, 192, and 256, respectively. All four functions are executed during all the rounds with the exception of MixColumns that is omitted from the last round. The original input and the results obtained during the intermediate rounds are known as states and are represented as four rows of 16 bytes each. SubBytes operation takes place over each byte of the state, and it involves a nonlinear transformation of multiplicative inverse succeeded by affine transformation. Multiplying the columns of the state with a predefined matrix constitutes the MixColumns operation. ShiftRows operation is intended to provide a diffusion property by cyclically shifting left state in a row. Shifting is avoided for the first row, while left-shift of 1, 2, and 3 is performed for rows 2–4, respectively. A bitwise XOR of the input and the keys constitute the AddRoundKey operation. For executing the functions in each round, an initial key with the same size as of the state is used and for the following rounds, and the initial key is extended and utilized. Key expansion module involves operations involving shifting of the key's last column, byte substitution, and XORing a round constant (RCON) with the result of the first two operations.

Figure 1 shows the block diagram representation of the encryption process. For a complete description of the AES standard, readers are referred to the original document by the National Institute of Standards and Technology (NIST) [24].

3 Proposed Architecture

A high-speed, low-power, and area architecture for AES encryption is proposed in this study incorporating a harmonious blend of ideas presented in [22, 23]. The key features of this architecture include the following:

- A reduction in the amount of logic used is achieved by embedding the ShiftRows operations inside the State Register.
- Using Rijndael S-Box for SubBytes and sharing the same for both encryption as well as in key expansion logic.
- Design of a 'XTime' block for the MixColumn logic and using substructure sharing for both the stand alone byte computation and for the four byte computations required in a column of the state.
- Clock gating for low-power consumption.

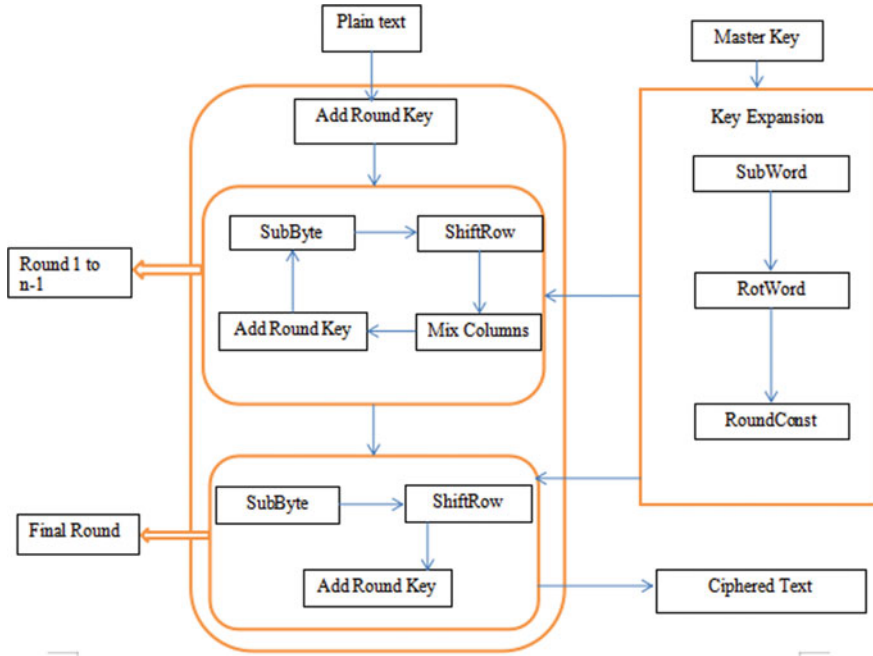Figure 2 shows the block diagram representation of the proposed architecture.

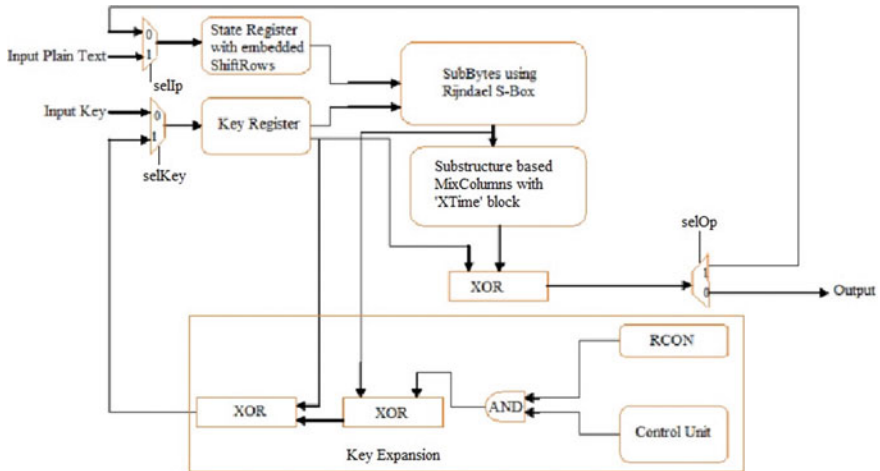**Fig. 1** Block diagram representation of the AES algorithm

Fig. 2 Block diagram of the proposed high-speed and low-power AES architecture

The architecture consists of one SubBytes block (Rijndael S-Box), one 8-bit high-speed MixColumns block, a Key Register (for key storage), a State Register (for plain text storage and for ShiftRow operation), and a key expansion logic (that uses the data from key register and SubBytes) containing RCON and control blocks. The two multiplexers and the demultiplexer are controlled by select lines selIp, selKey, and selOp, respectively, that are dependent on the rounds of operation. For the multiplexers, in the first round, input plain text and the input key are selected, while the feedback data is used for the remaining rounds.

In the case of the demultiplexer, data is sent to the output after the last round and is fed back during the intermediate rounds.

State Register

Sixteen eight-bit registers with eight flip flops each make up the State Register where one byte is input into the design, and one byte is stored during each clock cycle. Each register can be loaded with either the input plain text or the internal feedback data, and the choice is made with the help of a control signal 'selIp'. One of the main operations performed by the State Register is the ShiftRow operation. Since ShiftRow operation is also executed byte wise, it can be done with data in the same State Register block, thus saving precious silicon area. The data from the register is read out after the ShiftRow operation.

SubBytes

The SubBytes block is used for both the substitution logic and for key expansion. Instead of using an area-expensive lookup table methodology for substitution, a composite field arithmetic using affine transformation as proposed in [23] is used. The SubBytes operation is performed using Rijndael S-Box with a size 8 bits. Sixteen S-Boxes are used, thus making the entire size as 128 bits. The SubBytes are calculated by a multiplicative inverse followed by the affine transformation [20]. The key expansion logic uses the last column of the Shift Register and the values from RCON block to generate the expanded key.

High-speed MixColumn Block

Different architectures have been proposed in literature for the implementation of MixColumn operation [25–27]. A high-speed design of the MixColumn operation, as proposed by Zhang *et. al.* in [23], is implemented in this work. The use of a 'XTime' block to compute multiplicative constants leads to a high-speed computation of the MixColumns transformation. For computing the constants for the 8 bits, the 'XTime' block performs left-shift operation of bits 0, 2, 5, 6, 7, while simple XoR operation is sufficient for the remaining three bits [28]. A substructure sharing architecture for byte computation is the key aspect of this block.

Clock gating for Low-power Design

Clock gating is a powerful technique for power reduction in synchronous circuits and is used in various applications. It prevents the clock signal from triggering the circuit and disables the flip flops from switching between states, when the circuit

is not in use. Hence, the switching power is greatly reduced, and power dissipation is only due to the leakage power. It prunes the clock tree, thus saving power, but at the cost of increased logic and area occupied [29–31]. Clock gating is independently applied on MixColumn internal registers, State Register, Key Register, and RCON to decrease the dynamic power consumption. The key expansion logic is where the maximum power saving can be achieved by disabling the clock of State Register and MixColumn. This is made possible since key expansion phase does not involve any computation in these blocks.

4   Implementation Results and Analysis

The proposed architecture was coded in Verilog and co-simulated in MATLAB R2014a with ModelSim 6.4a for RTL simulation. For functional verification, test data in the form of text and images was provided. This was taken through the encryption process, and the cipher text was passed through a decrypter to obtain back the original image. The decryption follows the same process as the encryption, with the exception of performing inverse SubBytes and inverse MixColumns instead of the original operations. For verifying text data, the data was given directly as a test input to the Verilog file, and the obtained output was compared with the expected output. For working with images, gray scale images were read in MATLAB, and the pixel values were given as input to the Verilog files. The Verilog output was again read by MATLAB to produce back the original image. The entire co-simulation of MATLAB with Verilog has been automated, thus creating an environment for rapid verification of the encryption and the decryption process. Figure 3 shows the top level design flow approach.

Figure 4 shows an example of an image being encrypted and decrypted back to obtain the original image successfully.
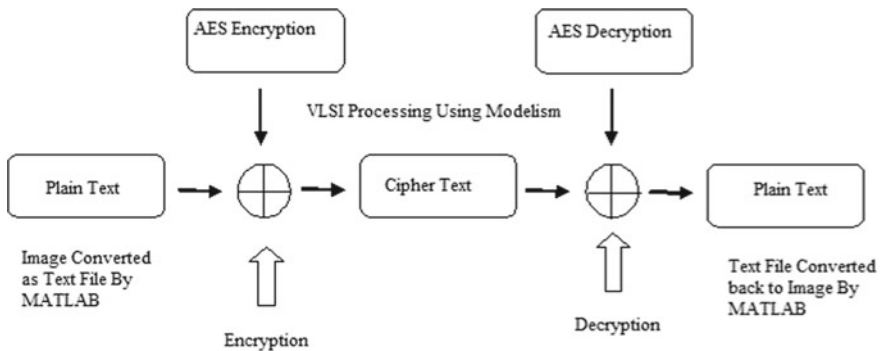
Fig. 3 Top level design flow
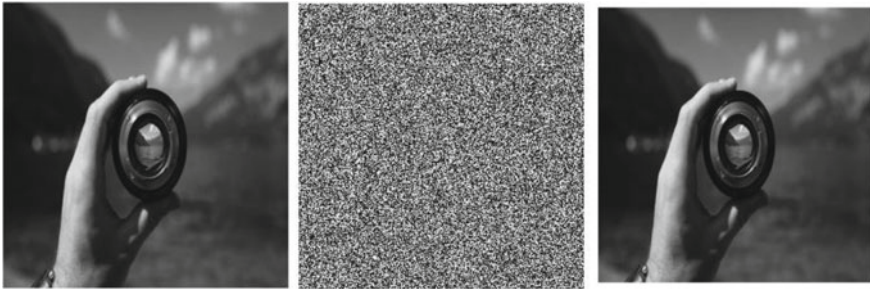
Fig. 4 Verification flow showing the input test image, the encrypted image, and the decrypted image

Table 1 Comparative analysis of area, power, and delay for the standard, nano, and the proposed AES designs

S. No.	Method name	Area (μm^2)	Power (mW)	Delay (ns)
1	Standard AES design	386,371.68	15.32	56.86
2	Nano-AES design	273,907.64	2.73	23.50
3	Proposed AES design	235,824.36	2.73	9.72

Having verified the functionality, the design was implemented as an ASIC in 90 nm GPDK technology using Synopsys Design compiler. The standard AES design, the nano-AES as proposed in [22], and the proposed AES were synthesized, and the implementation results are shown in Table 1.

The proposed design occupies 39% less area, dissipates 82% less power and is 83% faster than the standard AES design. It shows an improvement in area and speed by 14 and 58% when compared to that of nano-AES design with the power dissipation being the same.

5 Conclusion

With the number of interconnected tiny devices connected to the IoT rising at an exponential rate, it becomes imperative to design high-speed cryptographic devices dissipating low power and occupying minimum area. In this work, an AES module suitable for IoT applications has been designed and implemented as an ASIC in 90 nm technology. To reduce the area, the ShiftRows was merged with the State Register, and SubBytes is shared with both the encryption and the key expansion modules. The use of clock gating resulted in appreciable power reduction. A substructure sharing approach for the MixColumns was used that made it possible for the design of area

and power efficient AES architecture with very high speed operation. It is envisaged that the proposed architecture will be useful for designing secure and efficient IoT devices.

References

1. Tsiknas K, Taketzis D, Demertzis K, Skianis C (2021) Cyber threats to industrial IoT: a survey on attacks and countermeasures. IoT 2(1):163–186
2. Pallavi S, Narayanan VA (2019) An overview of practical attacks on BLE based IoT devices and their security. In: 2019 5th International conference on advanced computing and communication systems (ICACCS). IEEE, pp 694–698
3. Kandasamy K, Srinivas S, Achuthan K, Rangan VP (2020) IoT cyber risk: a holistic analysis of cyber risk assessment frameworks, risk vectors, and risk ranking process. EURASIP J Inf Secur 2020(1):1–18
4. Equihua C, Anides E, García JL, Vázquez E, Sánchez G, Avalos J-G, Sánchez G (2021) A low-cost and highly compact FPGA-based encryption/decryption architecture for AES algorithm. IEEE Lat Am Trans 19(9):1443–1450
5. Bharathi P, Annam G, Kandi JB, Duggana VK, Anjali T (2021) Secure file storage using hybrid cryptography. In: 2021 6th International conference on communication and electronics systems (ICCES). IEEE, pp 1–6
6. Chatterjee R, Chakraborty R, Mondal J (2019) Design of lightweight cryptographic model for end-to-end encryption in IoT domain. IRO J Sustain Wirel Syst 1(4):215–224
7. Desai SS, Nene MJ (2019) Node-level trust evaluation in wireless sensor networks. IEEE Trans Inf Forensics Secur 14(8):2139–2152
8. Muhammad K, Hamza R, Ahmad J, Lloret J, Wang H, Baik SW (2018) Secure surveillance framework for IoT systems using probabilistic image encryption. IEEE Trans Industr Inf 14(8):3679–3689
9. Saha A, Srinivasan C (2019) White-box cryptography based data encryption- decryption scheme for IoT environment. In: 2019 5th International conference on advanced computing and communication systems (ICACCS). IEEE, pp 637–641
10. Zhai S, Yang Y, Li J, Qiu C, Zhao J (2019) Research on the application of cryptography on the blockchain. J Phys Conf Ser 1168(3):032077. IOP Publishing
11. Sreevidya B, Rajesh M (2018) False data injection prevention in wireless sensor networks using node-level trust value computation. In: 2018 International conference on advances in computing, communications and informatics (ICACCI). IEEE, pp 2107–2112
12. Nair GC, Yamuna B, Balasubramanian K, Mishra D (2021) Hardware design of a turbo product code decoder. In: Proceedings of international conference on communication, circuits, and systems. Springer, pp 249–255
13. Khavya S, Balasubramanian K, Yamuna B, Mishra D (2021) Design and analysis of a secure coded communication system using chaotic encryption and turbo product code decoder. In: Advances in computing and network communications. Springer, pp 657–666
14. Joe CV, Raj JS (2021) Deniable authentication encryption for privacy protection using blockchain. J Artif Intell Capsule Netw 3(3):259–271
15. Liu Z, Choo K-KR, Grossschadl J (2018) Securing edge devices in the post-quantum internet of things using lattice-based cryptography. IEEE Commun Mag 56(2):158–162
16. Mitchell CJ (2016) On the security of 2-key triple des. IEEE Trans Inf Theory 62(11):6260–6267
17. Reyhani-Masoleh A, Taha M, Ashmawy D (2019) New low-area designs for the aes forward, inverse and combined s-boxes. IEEE Trans Comput 69(12):1757–1773

18. Bui DH, Puschini D, Bacles-Min S, Beigné E, Tran XT (2017) AES datapath optimization strategies for low-power low-energy multisecurity-level internet-of-things applications. IEEE Trans Very Large Scale Integr (VLSI) Syst 25(12):3281–3290
19. Ahmad N, Hasan R, Jubadi WM (2010) Design of AES S-box using combinational logic optimization. In: 2010 IEEE symposium on industrial electronics and applications (ISIEA). IEEE, pp 696–699
20. Mui EN, Custom R, Engineer D (2007) Practical implementation of Rijndael S-box using combinational logic. Custom R&D Engineer Texco Enterprise Pvt. Ltd.
21. Boyar J, Peralta R (2010) A new combinational logic minimization technique with applications to cryptology. In: International symposium on experimental algorithms. Springer, pp 178–189
22. Shahbazi K, Ko SB (2020) Area-efficient nano-AES implementation for internet-of-things devices. IEEE Trans Very Large Scale Integr (VLSI) Syst 29(1):136–148
23. Zhang X, Parhi KK (2004) High-speed VLSI architectures for the AES algorithm. IEEE Trans Very Large Scale Integr (VLSI) Syst 12(9):957–967
24. Wright MA (2001) The advanced encryption standard. Netw Secur 2001(10):11–13
25. Kuo H, Verbauwhede I (2001) Architectural optimization for a 1.82 Gbits/sec VLSI implementation of the AES Rijndael algorithm. In: International workshop on cryptographic hardware and embedded systems. Springer, pp 51–64
26. Satoh A, Morioka S, Takano K, Munetoh S (2001) A compact Rijndael hardware architecture with S-box optimization. In: International conference on the theory and application of cryptology and information security. Springer, pp 239–254
27. Zhang X, Parhi KK (2002) Implementation approaches for the advanced encryption standard algorithm. IEEE Circuits Syst Mag 2(4):24–46
28. Standaert FX, Rouvroy G, Quisquater JJ, Legat JD (2003) Efficient implementation of Rijndael encryption in reconfigurable hardware: improvements and design tradeoffs. In: International workshop on cryptographic hardware and embedded systems. Springer, pp 334–350
29. Wu Q, Pedram M, Wu X (2000) Clock-gating and its application to low power design of sequential circuits. IEEE Trans Circuits Syst I: Fundam Theory Appl 47(3):415–420
30. Kathuria J, Ayoubkhan M, Noor A (2011) A review of clock gating techniques. MIT Int J Electron Commun Eng 1(2):106–114
31. Shinde J, Salankar S (2011) Clock gating—a power optimizing technique for VLSI circuits. In: 2011 Annual IEEE India conference. IEEE, pp 1–4

Improving Sleep Apnea Screening with Variational Mode Decomposition and Deep Learning Techniques

C. Sai Manasa, K. T. Sreekumar, G. B. Mrudula, and C. Santhosh Kumar

Abstract Obstructive sleep apnea (OSA), a sleep condition, is characterized by recurrent bouts of irregular breathing. This study uses deep learning (DL) and variational mode decomposition (VMD) techniques to develop a classification system for sleep apnea. VMD is an adaptive signal decomposition technique to simplify complicated signals into a finite number of decomposed intrinsic mode functions (IMF). The baseline systems consist of support vector machine (SVM)-classifiers constructed using statistical features. Each of the ECG recordings is segmented; into one-minute segments. VMD is then performed on each of the one-minute long ECG segments. Statistical features derived from the derived IMFs, time, and frequency domain (TD and FD) segments are used to train SVM classifiers. We then developed convolutional neural networks (CNNs) and evaluated the performance. The CNN models trained with first, second, and third IMFs were the best performing systems. Subsequently, we added the first, second, and third IMFs to reconstruct a denoised ECG signal. CNN model trained with this regenerated ECG signal showed an accuracy, sensitivity, and specificity of 88.187%, 93.128%, and 80.339%, respectively. Subsequently, we extracted bottleneck features (BNF) from the bottleneck layer of the CNN. We trained a smaller dense neural network using the BNFs. When compared to the CNN model, the dense neural network trained with BNF extracted from the regenerated ECG signal (resulting from summing first, second, and third IMFs) gave the best performance with 4.24% 6.84%, and 2.55% improvements in accuracy, specificity, and sensitivity, respectively; with an area under the ROC curve 0.914.

Keywords Variational mode decomposition · Convolutional neural networks · Intrinsic mode functions · Bottleneck features · Obstructive sleep apnea · Electrocardiogram · Support vector machine

C. S. Manasa · K. T. Sreekumar · G. B. Mrudula · C. S. Kumar (✉)
Machine Intelligence Research Laboratory, Department of Electronics and Communication Engineering, Amrita School of Engineering, Coimbatore, Amrita Vishwa Vidyapeetham, Coimbatore, India
e-mail: cs_kumar@cb.amrita.edu

1   Introduction

Sleep is an important biological function essential for life. Humans suffer from various sleep disorders. OSA arises because of the recurring upper-airway collapse during sleep. OSA reduces oxygen saturation and disrupts sleep. OSA is linked to daytime drowsiness and has a large global impact. Each night, apnea episodes can happen many times, and they are characterized by changes in heart rate, a reduction in oxygen saturation, and loud breath noises. It has important effects on physical and mental health, including cardiovascular health, insulin-resistant diabetes, and accidents caused by lack of sleep. Plysomnography (PSG) is the standard reference technique to diagnose OSA. It is usually conducted in a sleep laboratory. But not everyone has access to PSG equipment. PSG is also expensive, time consuming, and labor intensive. Hence, an alternate cheap and automated way to diagnosing OSA in a more efficient and patient-friendly manner [1, 2]. Approximately, one billion of the world's adult population are estimated to have OSA, and its prevalence is rising globally. Undiagnosed and untreated OSA will likely lead to comorbidities and mortality, indicating tremendous risk to individual and global well-being. As the ubiquity of unpredictable lifestyles among populations and obesity increases, susceptibility to OSA increases. A better understanding of the pathophysiology is essential to facilitate the management of this chronic disease. Early diagnosis of OSA can be done using long-term electrocardiogram (ECG) recordings. An ECG signal records the electrical activity of the heart. People with sleep disorders show unusual heart rates. Characteristics and features of electrocardiographic signals can be used to screen sleep disorders [3]. Significant research has been going on in the field of sleep disorders. Mrudula G.B, et al. described a sleep apnea screening system using covariance normalization and bottleneck features of single-lead ECG signal [4]. In order to increase sleep duration and reduce stress in accordance with the measured sleep quality, Pandian proposed a sleep pattern analysis utilizing artificial intelligence and music therapy [5]. Sheta et al. investigated a machine learning-based sleep apnea screening system that was proposed by extracting features from denoised ECG signals. The ECG signals were denoised using a notch filter. In their experimental results, the deep learning-based approach achieved the best validation accuracy of 86.25% [6]. Qatmh et al. proposed a system consisting of artificial neural networks trained with features extracted from decomposed ECG signals. The ECG signals were decomposed using wavelet transform [7]. Pathinarupothi et al. developed an LSTM-RNN-based sleep apnea screening system using instantaneous heart rates [8]. Tripathy et al. deployed the time, frequency, and time–frequency domain features extracted from a computed cardiopulmonary activity, which are then fed into support vector machines and random forest classifiers. The cardiopulmonary activity is computed using heart and respiration rate signals extracted from ECG [9]. ECG signal analysis can be used to understand abnormal breathing patterns and hence, as a method for early detection of OSA. This work develops an OSA screening system based on convolutional neural networks (CNN) and variational mode decomposition (VMD) on ECG signals.

2   System Description

2.1   *Database*

This work uses the apnea-ECG dataset from the PhysioNet repository [10, 11]. The apnea-ECG dataset contains seventy annotated nighttime ECG recordings. The annotations were based on visual scoring of disoriented sleep breathing patterns. The recordings may be ranging from nearly seven to ten hours each. Each recording contains a sampled ECG signal with an annotation file. All ECG signals are sampled at 100 Hz. The annotation file contains the annotation for each one minute indicating the absence or presence of apnea at that time.

2.2   *Variational Mode Decomposition (VMD)*

A typical signal decomposition technique is empirical mode decomposition (EMD). Before breaking the input signal down from high to low frequency, EMD adjusts the multi-scale and adaptive time-scale characteristics. However, the model aliasing in the decomposition process renders the EMD approach useless if any typical event is present in the defective signal. A fully intrinsic and adaptable method of signal decomposition is called VMD. A signal is broken down by VMD into a set number of intrinsic mode functions (IMF). Variational mode decomposition (VMD), which iteratively screens the best variational model solution, regulates the bandwidth and center frequency of each IMF. IMFs are amplitude-modulated–frequency-modulated (AM-FM) signals. IMF can be expressed as

$$x_k(t) = Y_k(t) \cos(\phi_k(t)) \tag{1}$$

where Y_k is the amplitude, $\phi_k(t)$ is a non-decreasing function. Each IMF is band-limited and is compact around a central frequency. VMD can be used to address the presence of noise in a signal. Each IMF will have a cosine function which are slowly changing positive envelopes. VMD technique consists of Wiener filtering, Hilbert transform, frequency mixing, and heterodyne demodulation. Due to Wiener filtering, the technique is robust to noise and sampling. Hence, it can be used as a means to denoise a signal [12–15]. In VMD, alternate direction method multipliers (ADMM) are used to solve the constrained variational optimization problem which results in K number of decomposed IMFs. Here, K is a pre-defined mode number, which is the decomposition level of the signal. The VMD method is succinctly presented below

1. Initialize mode number K, center frequency u_k, and tolerance parameter α. Let the decomposed IMFs be represented as $x_k(t)$.
2. Construct single side band analytic signal from the signal's Hilbert transform.

3. Shift the frequency spectrum of each IMF by multiplying it with complex exponential term $e^{i\omega}mt$.
4. Solve the constrained variational optimization problem by finding an optimal solution for u_k.

$$L(\{u_k\}, \{\omega_k\}, \lambda) = \alpha \sum_k \left\| \partial_t \left[\left(\delta(t) + \frac{i}{\pi t} \right) \right] e^{i\omega_k t} \right\|_2^2$$
$$+ \left\| x_t - \sum_k u_k(t) \right\|_2^2$$
$$+ \left\langle \lambda(t), x(t) - \sum_k u_k(t) \right\rangle \tag{2}$$

where ∂_t is the partial derivative with respect to time, $\delta(t)$ is the Dirac distribution, and * is the convolution operator. Equation (2) can be solved iteratively by ADMM which results in K IMFs in frequency domain for each iteration n. The saddle point of the augmented Lagrangian $L(u_k, k,)$ is determined by ADMM algorithm.

$$u_k^{n+1}(\omega) = \frac{x(\omega) - \sum_{i<k} u^{n+1}(\omega) - \sum_{i>k} u^n(\omega) + \left(\lambda^n(\omega) / 2 \right)}{1 + 2\alpha \left(\omega - \omega_k^n \right)^2} \tag{3}$$

The IMFs in Eq. (3) updated by Wiener filtering. The center frequencies are updated iteratively as shown in Eqs. (3) and (4) are iteratively solved until the convergence criteria are reached. The convergence criteria are shown in Eq. (5).

$$\omega_k^{n+1} = \frac{\int_0^\infty \omega \left| u_k^{n+1}(\omega) \right|^2 d\omega}{\int_0^\infty \left| u_k^{n+1}(\omega) \right|^2 d\omega} \tag{4}$$

$$\sum_{k=1}^k \left\| u_k^{n+1} - u_k^n \right\|_2^2 \Big/ \left\| u_k^n \right\|_2^2 < \varepsilon \tag{5}$$

In this work, VMD is used to decompose the ECG segments into number of IMFs. We decomposed the ECG segments with various modes ($K = 3$ through 10) and evaluated the performance to identify the best decomposition level. Empirically, it has been observed that setting the number of decomposition levels, K as 5 gives the best performance. Additionally, it has been found that some IMFs carry more relevant information about the presence or absence of apnea. Subsequently, VMD has also been used as a means to denoise the ECG segments. Upon evaluation of the individual IMFs, the best performing IMFs are used to regenerate denoised and clean ECG segments. VMD representation for a portion of an ECG segment is shown in Fig. 1.
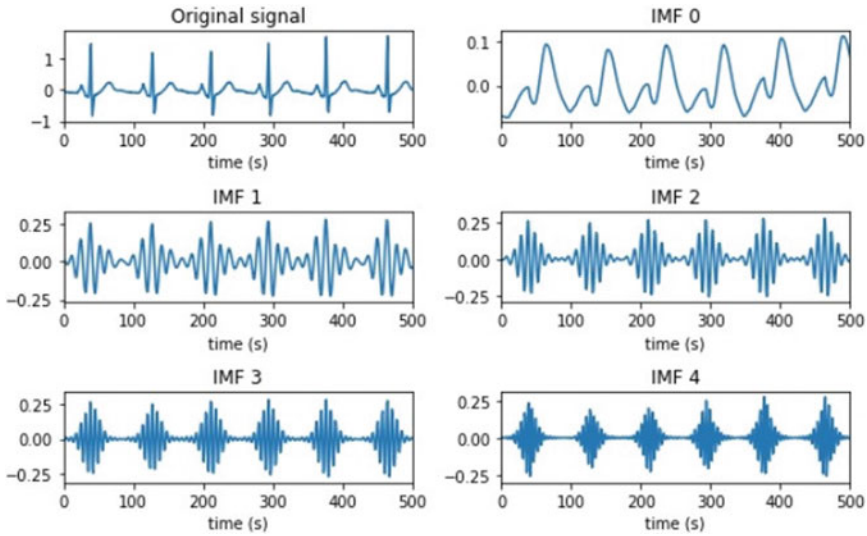
Fig. 1 VMD representation

2.3 Feature Extraction

Statistical Features: In this work, statistical features are concatenated to form a feature set. Statistical features were computed from time domain and frequency domain as well as individual IMF signals and were used to train SVM classifiers. Prior to feature extraction, each of the ECG recording was segmented into one-minute long segments. After segmentation, a total of 32,845 one-minute long segments were obtained. Each of these segments annotated that specifying the presence of apnea (A) or absence of apnea (N). The feature extraction procedure is shown in Fig. 2. The statistical features extracted include mean, standard deviation, variance, kurtosis, first moment, second moment, third moment, minimum value, maximum value, range, median, and skewness. The statistical features are summarized in Table 1.

2.4 Support Vector Machine (SVM)

Algorithms for supervised machine learning include SVMs. The aim of SVM in binary classification is to build a hyperplane that clearly classifies all the data points. SVMs optimize the width between the two classes by mapping the training data to points in space. The baseline system consists of support vector machine (SVM) classifiers that are trained with statistical features. Baseline system was trained using statistical feature set obtained from the individual IMFs post VMD, time domain, frequency domain segments. SVM classification was performed with an
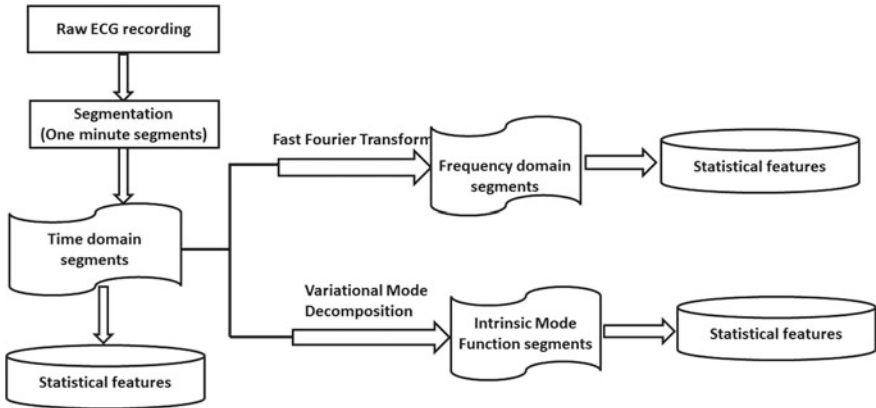
Fig. 2 Feature extraction

Table 1 Statistical features

Feature	Description
Mean (μ)	$\frac{1}{n}\sum_{i=i}^{n} x_i$
Standard deviation (σ)	$\sqrt{\frac{1}{N-1}\sum_{i=1}^{N}(x_i-\overline{x})^2}$
Variance (S)	$\frac{\sum(x_i-\overline{x})^2}{N-1}$
Kurtosis (κ)	$\frac{\sum(x_i-\overline{x})^4}{n\sigma^4}$
kth moment (M_1)	$\frac{1}{n}\sum_{i=i}^{n}(x_i-\overline{x})$
Second moment (M_2)	$\frac{1}{n}\sum_{i=i}^{n}(x_i-\overline{x})^2$
Third moment (M_3)	$\frac{1}{n}\sum_{i=i}^{n}(x_i-\overline{x})^3$
Minimum value (Max)	$\min\{x\}$
Maximum value (Min)	$\max\{x\}$
Range (R)	Max–Min
Median (M_m)	$x\left[\frac{n}{2}\right]$ if n is even
	$\frac{\left(x\left[\frac{n-1}{2}\right]+x\left[\frac{n+1}{2}\right]\right)}{2}$ if n is odd
Skewness (γ)	$\frac{3(\mu-M_m)}{\sigma}$

80–20 split between training and testing data using three kernels linear, radial basis function (RBF), and sigmoid. Upon evaluation, the best performing IMFs were used to construct regenerated ECG segments. SVM classification was performed using the statistical features extracted from the regenerated ECG segments. Machine learning-based estimators like SVMs generally assume the data to be normally distributed with zero mean and uniform variance. Before fitting the data in the SVM classifier, the feature set has been standardized by removing the mean and scaling it unit variance. Class weights have been used to deal with class imbalance in the dataset. Class apnea (A) has been given a weight of 0.55, and class non-apnea (N) has been given a weight of 0.45. These weights were experimentally derived and were found to relatively give the best performance [16, 17]. The baseline system is depicted in Fig. 2.

2.5   Convolutional Neural Networks (CNNs)

A CNN is a deep learning architecture that learns from raw signals unlike machine learning algorithms like SVMs that require manual feature extraction. CNNs have a wide range of applications. In this work, CNNs have been employed for binary classification task—the model should be able to predict whether an ECG segment has apnea or not. In a CNN, the convolutional layer is the main element. It puts the data through a series of convolutional filters that activates certain features. A CNN can have multiple convolutional layers with each layer identifying different set of features. After the CNN has learnt the features through various convolutional layers, the architecture now shifts to classification. The last few set of layers are the dense layers which feeds all of the outputs from the previous layers to all its neurons. The final layer uses a classification layer which outputs a vector of N dimensions. N is the number of classes the CNN should be able to predict. The final output of the CNN is a vector that contains N prediction probabilities for each class.

In this work, a CNN model was constructed using five convolutional layers and five dense layers. The convolutional layers have 128, 256, 512, 256, and 128 layers, respectively, with ReLU activation. $L2$ class layer weight regularizers have been used in all the convolutional layers with a weight of 1e-6. Regularization applies layer penalties and updates the cost function adding an additional regularization term. This helps to reduce over-fitting of the model. Dense layers receive the flattened output of the convolutional layer. Before going on to thick layers, an applied dropout of 0.8 has been made. There are 512, 256, 128, and 512 hidden neurons in each of the five thick layers, respectively. Last layer of the CNN model is another dense layer with softmax activation and 2 neurons that classifies an ECG segment as apneic or non-apneic. The model has been compiled with categorical cross-entropy loss function
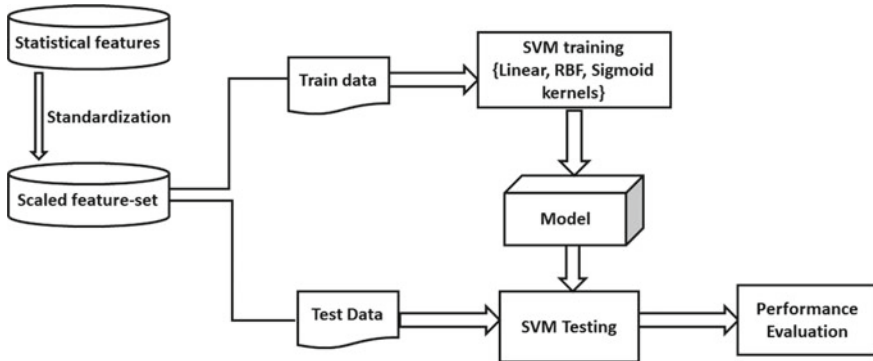
Fig. 3 Baseline system

and Adam optimizer. The model has been trained with 50 epochs using a batch size of 256, and a train–test split of 80–20. In each epoch, 20% of the training data has been used for validation. Early stopping has been employed to restrain the model from over-fitting. As mentioned in the case of baseline system, class weights were employed for CNN models also. Apneic and non-apneic classes were given weights of 0.55 and 0.45, respectively. The CNN architecture is shown in Fig. 3. Initially, the CNN models were trained with raw ECG segments in time domain and frequency domain. Subsequently, each of the individual IMFs post VMD were used to train the CNN models. Upon evaluation, the best performing IMFs were used to construct regenerated ECG segments. CNN classification was performed using the regenerated ECG segments in time and frequency domain [18, 19].

Bottleneck features (BNFs) The bottleneck layer in a neural network is a dense layer with fewer of neurons than the layer above or below it. A bottleneck layer compresses the salient feature representations of the target variable to best fit in the available space. Hence, a bottleneck layer enables the extraction of lower dimensional features by compressing the neural network. In this work, the BNFs were extracted from the dense layer containing 128 neurons which is the bottleneck layer, as shown in Fig. 4. For each ECG segment given as input to the model, the bottleneck layer outputs a feature vector of dimension 128. The bottleneck features have been extracted from the raw ECG segments in the time and frequency domain, the individual IMFs post VMD, and the regenerated signal constructed using best performing IMFs. The BNFs were given to a dense neural network consisting of five layers with 250, 500, 750, 500, and 250 neurons respectively, each with ReLU activation. The final layer is a dense layer with softmax activation and outputs the classification probabilities each class.
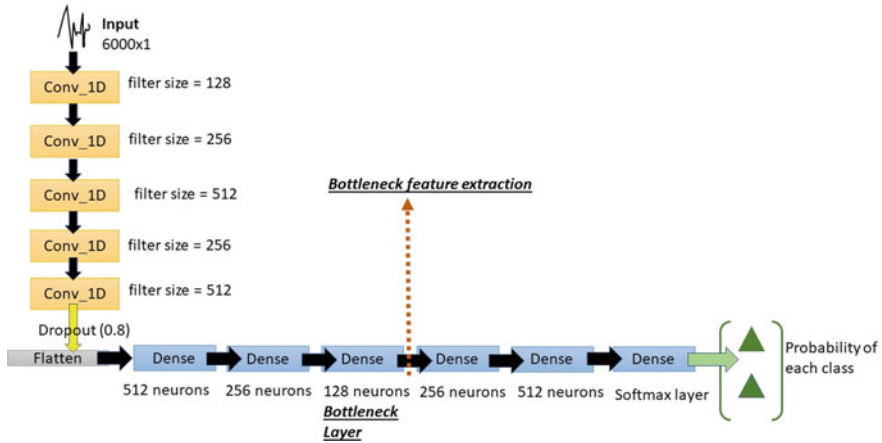
Fig. 4 CNN architecture with BNF extraction

3 Results and Discussion

3.1 Baseline System

The results from baseline system comprising of SVM classifiers are summarized in Table 2. The SVM classifiers were trained with statistical features extracted from TD, FD, and VMD ECG segments. When the SVMs from individual IMFs were evaluated, it was noted that IMFs 1, 2, and 3 perform relatively better. The corresponding SVMs showed better ROC-AUC values. Hence, these IMFs were added to generate reconstructed denoised ECG segments. Statistical features were extracted from these reconstructed segments and given to SVM classifiers. It has been observed that, among all the baseline SVM classifiers, RBF kernel SVM trained with statistical features from regenerated segments performed better with ROC-AUC score of 0.59.

3.2 CNN and BNF Models

CNN models were trained with TD and FD raw segments as well as IMF segments post VMD. The CNN models from IMFs 1, 2, and 3 showed ROC-AUC scores of 0.78, 0.77, and 0.79, respectively. As in the case of baseline system, these IMF segments were used to construct a denoised and clean regenerated ECG signal. CNN model trained with regenerated ECG segments showed an improvement in accuracy by 7%. Performance metrics for classification problems at different threshold levels are represented by AUC-ROC curves. ROC is a probability curve, and AUC represents for the level or measurement of separability. It demonstrates how effectively the model can distinguish between classes. Higher AUC-ROC values indicate better

Table 2 Baseline system results

KERNEL

Input	RBF				Sigmoid				Linear		
	Accuracy	Sensitivity	Specificity	ROC-AUC score	Accuracy	Sensitivity	Specificity	ROC-AUC score	Sensitivity	Specificity	ROC-AUC score
Raw ECG-TD	65.657	92.02	23.678	0.578	51.773	60.099	38.516	0.493	42.429	66.496	0.545
Raw ECG-FD	63.815	97.992	7.683	0.528	50.891	59.025	37.53	0.483	44.795	67.619	0.562
IMF 0	61.638	99.425	2.916	0.512	50.845	61.696	33.981	0.478	29.747	74.533	0.5076
IMF 1	64.363	92.836	19.053	0.556	51.454	61.319	35.449	0.484	59.99	44.95	0.525
IMF 2	66.388	89.985	29.077	0.595	52.169	60.512	38.978	0.497	47.192	60.55	0.539
IMF 3	63.434	94.223	15.002	0.546	53.189	61.23	40.541	0.509	48.83	59.42	0.541
IMF 4	62.414	96.36	10.097	0.532	48.318	59.212	31.528	0.454	97.841	4.836	0.513
Regenerated signal	64.804	85.868	32.34	0.591	50.099	56.074	40.89	0.485	90.889	19.497	0.551

categorization ability. The results from CNN models are shown in Table 3, and the area under the curve for receiver operating characteristics (AUC-ROC) curves are shown in Fig. 5. For the CNN models trained with individual IMFs and regenerated ECG segments, BNFs were extracted. These BNFs were used to train dense neural networks. BNF dense neural networks showed a performance improvement in all the IMFs. In the case of CNN model performance, IMFs 1, 2, and 3 performed better compared to other IMF's. BNF was extracted from the reconstructed signal obtained from IMFs 1, 2, and 3. The dense neural network model with BNF extracted from the reconstructed signal performed better compared to the dense neural network model with BNF extracted from the best IMF with a performance improvement of 4.58% in accuracy, 1.56% in sensitivity, 9.24% in specificity, and 5.26% in precision. This is the best performing model with an ROC-AUC score of 0.914. When compared with the CNN models that were trained with the ECG segments only, this model showed an improvement of 4.24%, 2.55%, and 6.84% in accuracy, sensitivity, and specificity, respectively. The results from BNF models are shown in Table 4, and the AUC-ROC curves are depicted in Fig. 6.

Table 3 CNN model results

Input	Accuracy	Sensitivity	Specificity	ROC-AUC score
Raw ECG-TD	75.308	90.149	51.903	0.71
IMF 0	76.343	84.891	62.829	0.734
IMF 1	80.926	91.302	64.519	0.779
IMF 2	80.012	91.542	61.828	0.767
IMF 3	81.824	90.814	67.572	0.792
IMF 4	69.143	91.301	34.376	0.628
Regenerated signal	**88.187**	**93.128**	**80.339**	**0.867**

Bold value represents the performance metrics of the best performing model
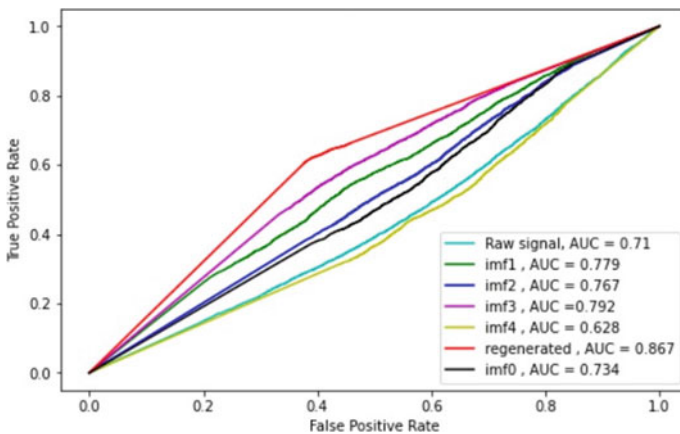
Fig. 5 AUC-ROC for CNN models

Table 4 BNF model results

Input	Accuracy	Sensitivity	Specificity	ROC-AUC score
IMF 0	83.346	90.438	71.811	0.811
IMF 1	85.142	92.304	74.341	0.833
IMF 2	82.798	86.886	76.292	0.816
IMF 3	87.852	94.131	77.943	0.86
IMF 4	75.598	82.366	65.185	0.734
Regenerated signal	**92.434**	**95.685**	**87.187**	**0.914**

Bold value represents the performance metrics of the best performing model
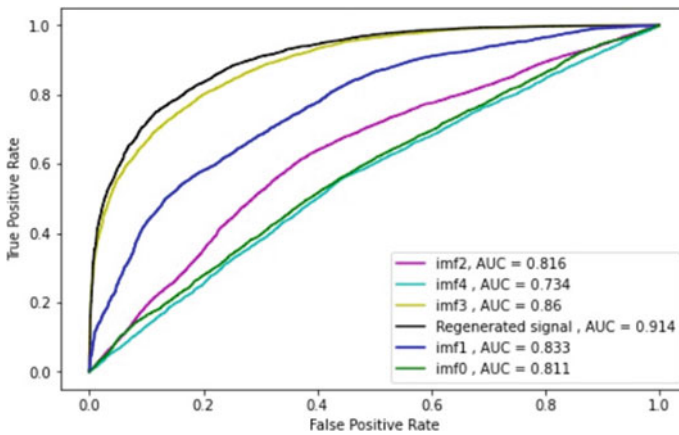
Fig. 6 AUC-ROC for BNF models

4 Conclusion

Sleep apnea is a dangerous sleep condition. People who have OSA run the major danger of acquiring respiratory and cardiovascular illnesses. It will take less time to solve this issue if sleep apnea is diagnosed early and in a patient-friendly manner. In this study, we created a CNN and BNF model-based automated OSA screening method. The use of VMD to glean relevant information from ECG segments was a major goal of this research. ECG segments were denoised using the VMD approach. In addition to denoising ECG segments, the VMD approach was examined to determine which IMFs offer more pertinent information about OSA. The baseline system was constructed using statistical features derived from raw ECG segments in time and frequency domain as well as from IMFs post VMD. The baseline systems were developed for the purpose of reference. Through, the investigation of baseline systems was observed that IMFs 1, 2, and 3 perform slightly better than the other IMFs. The SVMs with statistical features from IMFs perform better than the SVMs with statistical features from raw ECG segments in frequency and time domain. The better

performing IMFs were again used to reconstruct clean ECG segments. The statistical features derived from these clean ECG segments were fed into SVM classifiers. Subsequently, a similar outline of experimental approach was followed for CNN and BNF models. The BNFs were used to train a neural network consisting of only dense layers. The BNF models outperformed all the classifiers including CNN models. The best performing BNF model had a AUC-ROC value of 0.914 compared to the best performing CNN model with AUC-ROC value of 0.867. The best performing classifier is the BNF model trained with BNF derived from clean ECG signal reconstructed from IMFs 1, 2, and 3. This model performed with an accuracy of 92.434%, sensitivity of 95.685%, and specificity of 87.187%. An improvement of 4.24, 2.55, and 6.84% was observed in the respective values when compared to the best performing CNN model.

References

1. Slowik JM, Collen JF (2022) Obstructive sleep apnea. In: StatPearls [Internet]. StatPearls Publishing, Treasure Island (FL)
2. Chokroverty S, Bhatt M, Goldhammer T (2005) Polysomnographic recording technique. In: Chokroverty S, Bhatt M, Thomas RJ (eds) Atlas of sleep medicine. Butterworth- Heinemann, pp 1–28, ISBN: 9780750673983. Lyons MM, Bhatt NY, Pack AI, Magalang UJ (2020) Global burden of sleep-disordered breathing and its implications. Respirology 25:690–702. https://doi.org/10.1111/resp.13838
3. Guilleminault C, Connolly S, Winkle R, Melvin K, Tilkian A (1984) Cyclical variation of the heart rate in sleep apnoea syndrome. Mechanisms, and usefulness of 24 h electrocardiography as a screening technique. Lancet 1(8369):126–131. PMID: 6140442. https://doi.org/10.1016/s0140-6736(84)90062-x
4. Mrudula GB, Kumar C (2021) Covariance normalization and bottleneck features for improving the performance of sleep apnea screening system, pp 286–291. https://doi.org/10.1109/DISCOVER52564.2021.9663594
5. Pandian MD (2019) Sleep pattern analysis and improvement using artificial intelligence and music therapy. J Artif Intell 1(02):54–62
6. Sheta A, Turabieh H, Thaher T, Too J, Mafarja M, Hossain M, Surani S, Ho K, Hu YH (2021) Diagnosis of obstructive sleep apnea from ECG signals using machine learning and deep learning classifiers. https://doi.org/10.3390/app11146622
7. Qatmh M et al. (2022) Sleep apnea detection based on ECG signals using discrete wavelet transform and artificial neural network. In: 2022 Advances in science and engineering technology international conferences (ASET), pp 1–5. https://doi.org/10.1109/ASET53988.2022.9735064
8. Pathinarupothi RK, Vinaykumar R, Rangan E, Gopalakrishnan E, Soman K (2017) Instantaneous heart rate as a robust feature for sleep apnea severity detection using deep learning. In: 2017 IEEE EMBS international conference on biomedical and health informatics (BHI). IEEE, pp 293–296

9. Tripathy R, Gajbhiye P, Acharya UR (2020) Automated sleep apnea detection from cardio-pulmonary signal using bivariate fast and adaptive EMD coupled with cross time–frequency analysis. Comput Biol Med 120:103769–103795

10. Goldberger AL, Amaral LA, Glass L, Hausdorff JM, Ivanov PC, Mark RG, Mietus JE, Moody GB, Peng CK, Stanley HE (2000) PhysioBank, PhysioToolkit, and PhysioNet: components of a new research resource for complex physiologic signals. Circulation 101(23):e125–e2220

11. Penzel T, Moody GB, Mark RG, Goldberger AL, Peter JH (2000) The apnea-ECG database. In: Computers in cardiology, vol 27. IEEE, pp 255–258

12. Dragomiretskiy K, Zosso D (2014) Variational mode decomposition. IEEE Trans Signal Process 62(3):531–544. https://doi.org/10.1109/TSP.2013.2288675

13. Isham MF, Leong MS, Lim MH, Ahmad ZA (2018) Variational mode decomposition: mode determination method for rotating machinery diagnosis. J Vibroeng 20(7):2604–2621

14. Sreekumar KT, George KK, Kumar CS, Ramachandran KI (2019) Performance enhancement of the machine-fault diagnosis system using feature mapping, normalisation and decision fusion. IET Sci Meas Technol 13(9):1287–1298

15. Carvalho VR, Moraes MFD, Braga AP, Mendes EMAM (2020) Evaluating five different adaptive decomposition methods for EEG signal seizure detection and classification. Biomed Signal Process Control 62:102073. ISSN: 1746-8094

16. Pedregosa F et al. (2011) Scikit-learn: machine learning in python. J Mach Learn Res 12:2825–2830

17. Ma B et al. (2019) A SVM-based algorithm to diagnose sleep apnea. In: 2019 IEEE international conference on bioinformatics and biomedicine (BIBM), pp 1556–1560. https://doi.org/10.1109/BIBM47256.2019.8983201

18. Chollet F et al. (2015) Keras. Retrieved from https://github.com/fchollet/keras

19. Krishnan KK, Soman K (2021) CNN based classification of motor imaginary using variational mode decomposed EEG-spectrum image. Biomed Eng Lett 1–13

Effect of Selectively-Filled-Ethanol on Dispersion Characteristics of Circular Shaped Hollow Core Photonic Crystal Fiber

Vishal Chaudhary and Sonal Singh

Abstract In this work, a circular shaped ethanol-filled hollow core photonic crystal fiber (PCF) is proposed. The optical properties, like dispersion, effective area, confinement loss, and nonlinear coefficient of the proposed hollow core PCF, have been studied for the wavelength range from 800 to 1600 nm. The main focus of this research work is to achieve nearly zero dispersion wavelength (ZDW) by using finite element method. When air is poured into the entire hole ring, ethanol is poured into the middle hole ring, and ethanol is poured into the entire hole ring, then the ZDW of 880 nm, 1220 nm, and 1250 nm is achieved, respectively. This kind of PCF is useful in sensing applications, nonlinear applications, laser technologies, and telecommunication.

Keywords Circular photonic crystal fiber · Dispersion · Ethanol · Effective mode area · Nonlinear coefficient · Confinement loss

1 Introduction

In recent years, photonic crystal fibers (PCF) are garnered a lot of attention due to their unusual and remarkable features and properties [1]. PCF also known as Holey fibers or micro-structured fibers represents one of the major applications of the photonic crystals [2, 3]. PCFs have the capability to control the light that enters the fiber, which was previously unfeasible due to their conventional design issues. By adjusting the number of liquid-filled holes, pitch distance, and air hole size of the PCF, the structural cross section may exhibit unique properties such as controlled effective area, low confinement loss, dispersion control, and higher nonlinearity [4]. However, some researchers have used the air holes filled PCF to regulate the

V. Chaudhary · S. Singh (✉)
Department of Electronics and Communication Engineering, Delhi Technological University, Delhi 110042, India
e-mail: sonalsingh@dtu.ac.in

V. Chaudhary
e-mail: vishalchaudhary_2k21phdec14@dtu.ac.in

optical and transmission characteristics of the PCF by filling them with other types of liquids like as water [5], ethanol [6], liquid crystals [7, 8] and polymers [9–11]. By suitably tailoring their optical characteristics, liquid-filled PCFs are employed for various sensing parameters such as temperature, magnetic field, refractive index (RI), and many other applications [12–15]. Using an asymmetric circular dual core-PCF, Md. Mahbub Hossain et al. demonstrated a PCF Chloroform infiltration temperature sensor in 2018 [16]. Shi et al. also demonstrated stress and temperature sensors with alcohol filled holes in their experiments [17]. Furthermore, theoretical PCF structures for water-ethanol [18], ethanol, benzyne, and water [19] solutions are proposed. The researcher recently presented a liquid-filled PCFs-based tunable multiband pass filter [20].

Thus, the intention of this work is to design a selectively-filled-ethanol circular shaped hollow core PCF for the zero dispersion wavelength. The proposed PCF configuration is designed using the COMSOL software, which uses the full-vector finite element method (FV-FEM). For geometry statistics 38 domains, 152 boundaries, 152 vertices and for mesh statistics 14,172 triangular elements, 1224 edge elements, 152 vertex elements are analyzed. This kind of PCF is useful in nonlinear applications, sensing applications, laser technologies, and telecommunications.

2 PCF Design

The proposed circular shaped hollow core PCF geometry is shown in Fig. 1. In this design, a diameter, d of 0.22 µm and a pitch length, Λ of 1.5 µm are chosen for circular holes with silica as the PCF background material. The RI of ethanol (n_{etha} = 1.352) and air (n_{air} = 1) is considered. Equation (1) gives the RI of silica (n_{silica}) which is called Sellmeier equation.

$$n_{\text{silica}}^2(\lambda) = 1 + \frac{A_1\lambda^2}{\lambda^2 - B_1} + \frac{A_2\lambda^2}{\lambda^2 - B_2} + \frac{A_3\lambda^2}{\lambda^2 - B_3} \tag{1}$$

The operational wavelength in µm is denoted by λ, and the Sellmeier coefficients are $A_1 = 0.696166300$, $A_2 = 0.407942600$, $A_3 = 0.897479400$, $B_1 = 4.67914826 \times 10^{-3}$ µm², $B_2 = 1.35120631 \times 10^{-2}$ µm², and $B_3 = 97.9340025$ µm², respectively [12].

The PCF effective mode area is an important characteristic that attracts a lot of attention in a vast area of applications. A PCF having a large effective mode area is highly useful in field of lasers and telecommunication devices, whereas a PCF having a small effective area is considered suitable for nonlinear effects. The effective area, A_{eff} of the PCF is determined using the below equation

$$A_{\text{eff}} = \frac{\left(\int \int |E|^2 \mathrm{d}x\mathrm{d}y\right)^2}{\int \int |E|^4 \mathrm{d}x\mathrm{d}y} \tag{2}$$
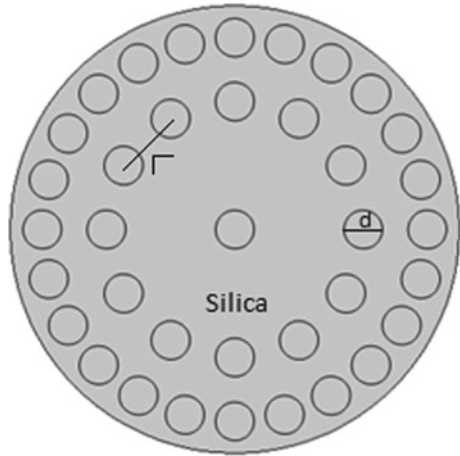
where 'E' represents the fundamental modes of PCF transverse electric field [21, 23].

The effective area of the fiber is intimately linked to nonlinearity. The nonlinear coefficient can be determined using the below equation

$$\gamma = \left(\frac{2\pi}{\lambda}\right)\left(\frac{n_2}{A_{\text{eff}}}\right) \tag{3}$$

where n_2 denotes the nonlinear refractive index of PCF, λ denotes the wavelength, and A_{eff} denotes the effective area of PCF. For silica material, ($n_2 = 3.2 \times 10^{-20}$ m^2/W) is considered [21, 22].

Confinement loss (L_c) is the term for the attenuation caused on by the waveguide geometry. This is an new type of loss that occurs in single material fibers especially in PCFs because they are generally made of silica and can be determined using the below equation

$$L_c = -20\log_{10}\varepsilon^{-k\text{Im}[n_{\text{eff}}]} = 8.686k\text{Im}[n_{\text{eff}}] \tag{4}$$

where k_0 represents the propagation constant $\left(k = \frac{2\pi}{\lambda}\right)$ in free space and Im[n_{eff}] denotes the imaginary part of the complex effective index [3].

The dispersion parameter D of PCF is calculated by using Eq. (5)

$$D = -\frac{\lambda}{c}\frac{d^2\text{Re}[n_{\text{eff}}]}{d\lambda^2} \tag{5}$$

where c denotes light velocity in vacuum and Re[n_{eff}] represents the real part of effective refractive index [4].

3   Results and Discussion

Figure 2 shows the basic mode's electric field profile of PCF with and without ethanol filling the holes. The FV-FEM mode solver is used to compute the effective refractive indices (n_{eff}) of the proposed PCF basic guided modes. At transmission wavelength of 1500 nm, n_{eff} becomes 1.379906281, 1.333575804, and 1.417018929 when air is poured into the entire hole ring, ethanol is poured into the middle hole ring, and ethanol is poured into the entire hole ring, respectively. The variation of n_{eff} with wavelengths is shown in Fig. 3. According to the figure as wavelength increases, the n_{eff} of the proposed PCFs decreases.

After obtaining the effective refractive indices for various modes of the PCF, the effective area is calculated using Eq. (2). At transmission wavelength of 1500 nm, the effective area of the proposed PCF comes out to be 4.36 μm^2, 4.91 μm^2, and 6.39 μm^2 when air is poured into the entire hole ring, ethanol is poured into the middle hole ring, and ethanol is poured into the entire hole ring, respectively. The effective mode area variation with wavelengths is shown in Fig. 4. According to the graph, the A_{eff} of the proposed PCF increases as the wavelength increases, and it can also
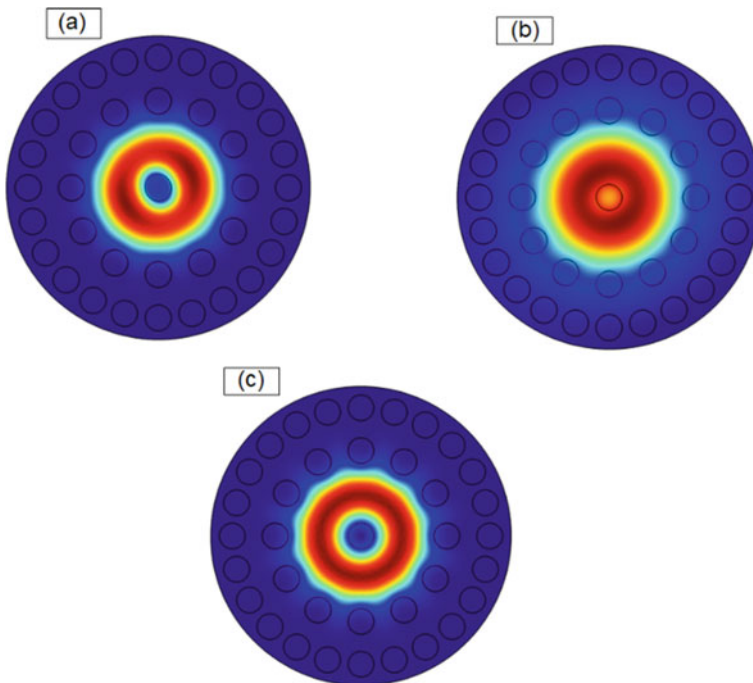
Fig. 2 Electric field profile for the basic modes of PCF when **a** air is poured into the entire hole ring, **b** ethanol is poured into the middle hole ring, **c** ethanol is poured into the entire hole ring, at λ = 1500 nm
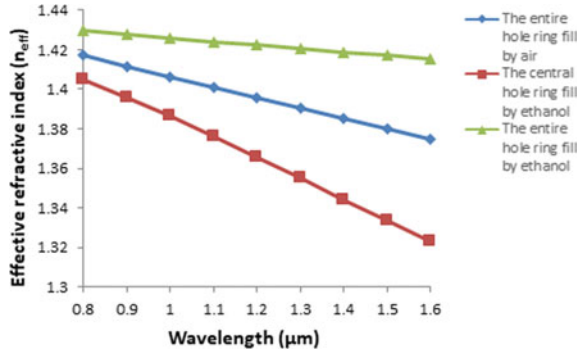
be shown that pouring ethanol into the hole ring increases the effective mode area compared to pouring air into the hole ring.

The existence of ethanol in the cladding section increases the n_{eff} of the cladding section of the PCF because ethanol has a higher refractive index than air. As a result, when compared to air-filled holes, the difference in RI between cladding and core region is smaller. When light passes through the ethanol-filled fiber's core, some
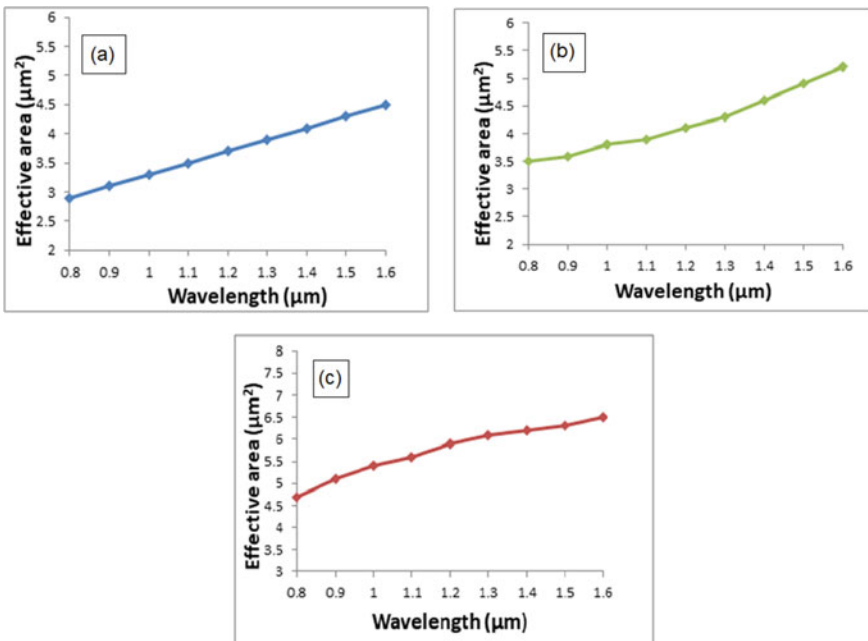
Fig. 4 Effective area variation with wavelength when **a** air is poured into the entire hole ring, **b** ethanol is poured into the middle hole ring, **c** ethanol is poured into the entire hole ring

of it leaks into the cladding region, increasing the effective area. As a result, the ethanol-filled PCF's effective mode area is larger than the air-filled PCF.

After obtaining the A_{eff} of the PCF, the nonlinear coefficient is calculated using Eq. (3). At transmission wavelength of 1500 nm, the nonlinear coefficient of the proposed PCF comes out to be 31.17, 27.36, and 21.28 when air is poured into the entire hole ring, ethanol is poured into the middle hole ring, and ethanol is poured into the entire hole ring, respectively. Figure 5 represents the variation of nonlinear coefficient with respect to wavelength of the proposed PCF. It can be seen that nonlinearity of the proposed PCF decreases as the wavelength increases.

The confinement loss of the proposed PCF is calculated using Eq. (4). At transmission wavelength of 1500 nm, the confinement loss of the proposed PCF comes out to be 1.03878×10^{-9} dB/m, 9.18252×10^{-6} dB/m and 2.63927×10^{-9} dB/m when air is poured into the entire hole ring, ethanol is poured into the middle hole ring, and ethanol is poured into the entire hole ring, respectively.

Figure 6 represents the variation of dispersion parameter with respect to wavelength of the proposed circular shaped hollow core PCF as calculated from Eq. (5). The ZDW is determined to be 880 nm, 1220 nm, and 1250 nm when air is poured into the entire hole ring, ethanol is poured into the middle hole ring, and ethanol is poured into the entire hole ring, respectively. As indicated from the graph, when the
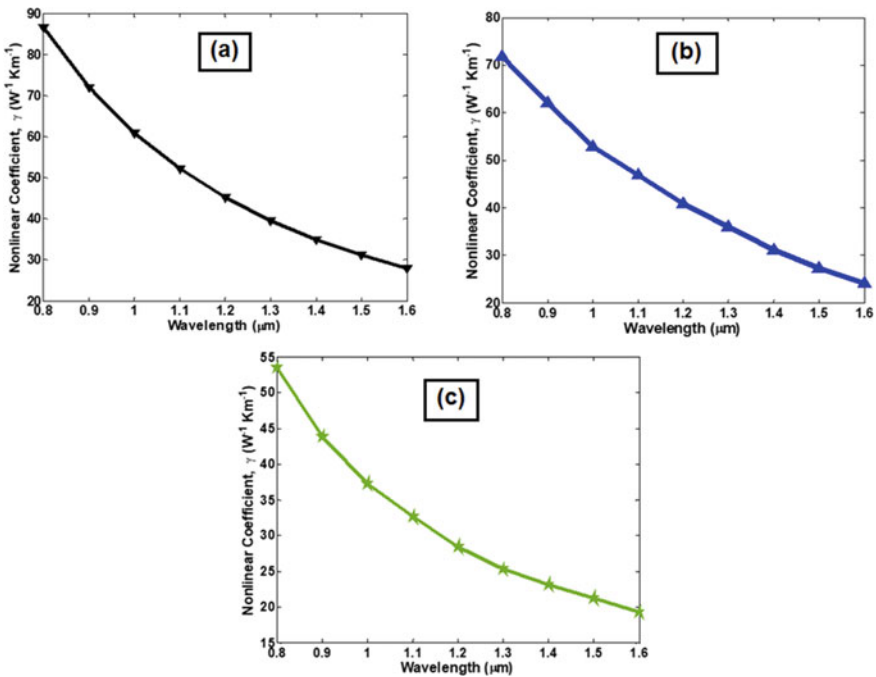
Fig. 5 Nonlinear coefficient variation with wavelength when **a** air is poured into the entire hole ring, **b** ethanol is poured into the middle hole ring, **c** ethanol is poured into the entire hole ring

number of hole rings filled with ethanol increases, a shift in zero dispersion toward higher wavelength is observed, as compare to hole rings filled with air. As the value of dispersion is extremely sensitive to the fiber parameters and the doping level of the materials, like the difference between the refractive indices and core radius, dispersion can be changed by doping the silica with different materials and changing the n_{eff} values of the guided mode. Additionally, a rise in effective refractive indices can lead to an increase in dispersion. Since, the ZDW values achieved in our case are almost close and equal to the values of pump wavelength as required by the fiber laser devices, this kind of PCF is found useful in the area of laser technology as well, other than their already proven utilizations in the field of sensing, telecommunication, and nonlinear applications.

Based on our research work, a comparison of optical parameters of PCF with and without ethanol filling the holes is presented in Table 1. Highest effective area is achieved when ethanol is filled into the entire hole ring. ZDW is attained for all proposed PCFs with maximum wavelength reaching in PCF entirely filled with ethanol.

Fig. 6 Dispersion graph of the circular shaped hollow core PCF when **a** air is poured into the entire hole ring, **b** ethanol is poured into the middle hole ring, **c** ethanol is poured into the entire hole ring

Table 1 Comparison of changes in parameters with and without ethanol filling the holes

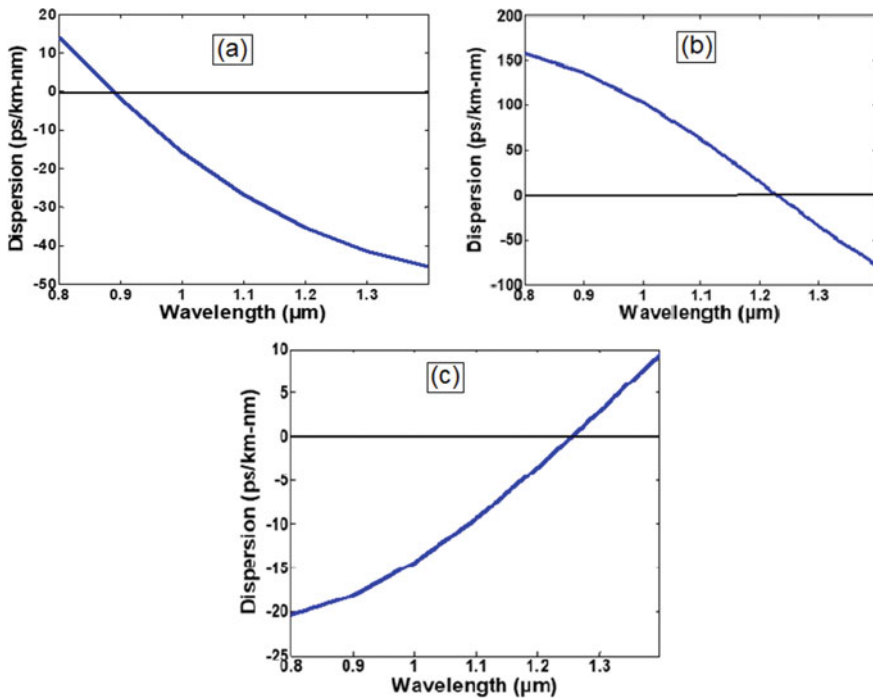| Optical parameters	Air is poured into the entire hole ring	Ethanol is poured into the middle hole ring	Ethanol is poured into the entire hole ring
Effective mode area at $\lambda = 1500$ nm (μm^2)	4.36	4.91	6.39
Zero dispersion wavelength (nm)	880	1220	1250

4 Conclusion

This research work proposes a circular shaped hollow core PCF designed by COMSOL software using finite element method. By regulating the number of hole rings poured with ethanol, the optical characteristics of the proposed PCF, such as effective area, confinement loss, dispersion, and nonlinear coefficient have been investigated. This study clearly indicates that when the number of ethanol-filled hole rings increases, zero dispersion can easily be shifted from 880 to 1250 nm, i.e., from near-infrared to mid-infrared region. We may conclude from this research that ethanol has a considerable impact on the effective area and dispersion parameter. This kind of proposed PCF is very useful in nonlinear applications, sensing applications, laser technology, and telecommunication.

References

1. Ozbay E, Bulu I, Aydin K, Caglayan H, Guven K (2004) Physics and applications of photonic crystals. Photonics Nanostruct Fundam Appl 2:87–95
2. Broeng J, Mogilevstev D, Barkou SE, Bjarklev A (1999) Photonic crystal fibers: a new class of optical waveguides. Opt Fiber Technol 5:305–330
3. Russell PSJ (2006) Photonic-crystal fibers. J Light Technol 24:4729–4749
4. Sinha RK, Varshney SK (2003) Dispersion properties of photonic crystal fibers. Microw Opt Technol Lett 37:129–132
5. Martelli C, Canning J, Lyytikainen K, Groothoff N (2005) Water-core Fresnel fiber. Opt Express 13:3890
6. Yiou S, Delaye P, Rouvie A, Chinaud J, Frey R, Roosen G, Viale P, Février S, Roy P, Auguste J-L, Blondy J-M (2005) Stimulated Raman scattering in an ethanol core microstructured optical fiber. Opt Express 13:4786
7. Zhang C, Kai G, Wang Z, Sun T, Wang C, Liu Y, Zhang W, Liu J, Yuan S, Dong X (2005) Transformation of a transmission mechanism by filling the holes of normal silica-guiding microstructure fibers with nematic liquid crystal. Opt Lett 30:2372
8. Alkeskjold TT, Lægsgaard J, Bjarklev A, Hermann DS, Broeng J, Li J, Gauza S, Wu ST (2006) Highly tunable large-core single-mode liquid-crystal photonic bandgap fiber. Appl Opt 45:2261–2264

9. Eggleton B, Kerbage C, Westbrook P, Windeler R, Hale A (2001) Microstructured optical fiber devices. Opt Express 9:698
10. Kerbage C, Steinvurzel P, Reyes P, Westbrook PS, Windeler RS, Hale A, Eggleton BJ (2002) Highly tunable birefringent microstructured optical fiber. Opt Lett 27:842
11. Cox FM, Argyros A, Large MCJ (2006) Liquid-filled hollow core microstructured polymer optical fiber. Opt Express 14:4135
12. Gangwar RK, Singh VK (2017) Highly sensitive surface plasmon resonance based D-shaped photonic crystal fiber refractive index sensor. Plasmonics 12:1367–1372
13. Gangwar RK, Singh VK (2015) Refractive index sensor based on selectively liquid infiltrated dual core photonic crystal fibers. Photonics Nanostruct Fundam Appl 15:46–52
14. Lee KJ, Liu X, Vuillemin N, Lwin R, Leon-Saval SG, Argyros A, Kuhlmey BT (2014) Refractive index sensor based on a polymer fiber directional coupler for low index sensing. Opt Express 22:17497
15. Gangwar RK, Bhardwaj V, Singh VK (2016) Magnetic field sensor based on selectively magnetic fluid infiltrated dual-core photonic crystal fiber. Opt Eng 55:026111
16. Hossain MM, Mandal R, Amin MZ, Mondal HS, Rahaman ME (2018) Chloroform infiltrate temperature sensor using asymmetric circular dual-core photonic crystal fiber. J Biomed Photonics Eng 4:030302
17. Shi FQ, Luo YY, Chen DR, Chen JJ, Ren ZJ, Peng BJ (2018) A dual-parameter sensor based on the asymmetry of alcohol filling the photonic crystal fiber in sagnac loop. IEEE Sens J 18:6188–6195
18. Zhou C, Zhang HK, Song P, Wang J, Zhu CG, Wang PP, Peng F (2018) Geometrically structural parameters insensitive fiber sensor for detection of ethanol concentration. IEEE Photonics Technol Lett 30:2037–2039
19. Suganthy M, Paul BK, Ahmed K, Islam MI, Jabin MA, Bahar AN, Mani Rajan MS (2019) Analysis of optical sensitivity of analytes in aqua solutions. Optik (Stuttg) 178:970–977
20. Liu Y, Wang Y, Sun B, Liao C, Song J, Yang K, Wang G, Wang Q, Yin G, Zhou J (2014) Compact tunable multibandpass filters based on liquid-filled photonic crystal fibers. Opt Lett 39:2148
21. Benhaddad M, Kerrour F, Benabbes O (2018) Design and analysis of non-linear properties of photonic crystal fiber with various doping concentration. J Phys Conf Ser 987
22. Shakya S (2019) Machine learning based nonlinearity determination for optical fiber communication—review. J Ubiquit Comput Commun Technol 2019:121–127
23. Karuppusamy P (2019) Mimo based high speed optical fiber communication system. J Electron Inf 107–116

A Demand Management Planning System for a Meat Factory Based on the Predicted Market Price Under Indian Market Scenario

R. R. Lekshmi and C. Bansi

Abstract Indian electricity industry is under transition from vertical to restructured structure. In a 24 h electricity market, the operator performs auction for each hour in a day. Each time slot corresponds to different market clearing price. Energy consumption cost of intensive users can be reduced through demand response programs that involve planning of various processes stages in industries. This requires prediction of market price. This research work presents demand management planning model based on predicted price for a 24 h day ahead Indian electricity market. The proposed system is employed on the cooling production and distribution segment in a meat industry to control the chillers and dryers. The system employs autoregressive integrated moving average model to predict the Indian market price using real-time data. The ARIMA (2, 1, 5) appears to be an adequate model. The proposed model provides an evidence of significant saving in consumption cost in a day.

Keywords Autoregressive integrated moving average · Demand management · Forecasting · Indian energy exchange · Mean absolute percentage error · Market clearing price

1 Introduction

Traditional Indian electricity industry has been under the process of restructuring. The newly created structure involves various independent entities that include generation companies (GENCOs), distribution companies (DISCOs), transmission companies (TRANSCOs), retail energy service companies (RESCOs), and independent system operator (ISO) [1]. The restructured power industry incorporates a power trading platform—market that takes various models like single buyer, bilateral, or Poolco. The power trading in a bilateral market is based on agreements that can be short term or long term. Under Poolco and single buyer electricity market, the power trade is

R. R. Lekshmi (✉) · C. Bansi
Department of Electrical and Electronics Engineering, Amrita School of Engineering,
Coimbatore, Amrita Vishwa Vidyapeetham, Coimbatore, India
e-mail: rr_lekshmi@cb.amrita.edu

performed based on auction mechanism. In an auction based market, the operations are administered by the system operator to clear the market and decide the winning players, market power (MP), and market clearing price (MCP). The type of auction market decides the time slot for which auction is performed. This paper considers a 24 h day ahead market where the auction is performed one day before, for each hour of the day. Thus, auction is performed for 24 time slots. Hence, the MCP and MP may be different for each time slot in a day, unlike in vertical system where price is based on peak/off peak period [2]. Prediction of MCP is essential when comes to energy saving and consumption cost minimization. Reduction in energy consumption can be done through demand response (DR) program [3]. DR programs can be executed when the cost of electricity in the area is high.

Unlike residential or commercial users, industrial plants such as aluminum, steel, cement, and food are intensive consumers of electricity. Thus, industries can be expected to be the substantial participators in DR programs. DR programs ensure industries to have enormous potential to deliver large-scale energy flexibility. These programs allow industries to plan the sequence of operation of various process stages and the corresponding duration. However, planning under deregulated environment requires prediction of MCP [4–7]. Many research works are performed in the area of prediction [8–14]. The accuracy of ARIMA model in predicting time series data has been proved by many researchers [15–21] and hence employed in this paper.

This paper considers Indian electricity market price prediction using time series method. The method employs autoregressive integrated moving average (ARIMA) model to predict future MCP in Indian electricity market. Unlike existing research works, the model employs real-time dataset available in Indian Energy Exchange (IEX) Website. The model accuracy is evaluated using accuracy measure index–mean absolute percentage error (MAPE). The price prediction model is then incorporated in the demand management system, to control the chillers and dryers in the drying unit of meat industry. The effective and efficient performance of demand management planning system incorporating the ARIMA model is finally tested and validated.

The paper is organized as follows:

Section 2 briefly presents the structure of deregulated power system with the auction mechanism in a Poolco market. The methodology for MCP prediction and operation of demand management system based on the forecasted MCP is illustrated in Sect. 3. Section 4 includes the performance evaluation and validation of ARIMA model and proposed demand management system based on the predicted price. This section is followed by conclusion (Sect. 5).

2 Deregulated Electricity Industry

The reformed system provides customers with options to choose the suppliers and retailers, enabling competition that leads to lower prices in the market. Deregulated electricity industry is composed of various components that include GENCOs,

Fig. 1 Schematic of deregulated electricity system
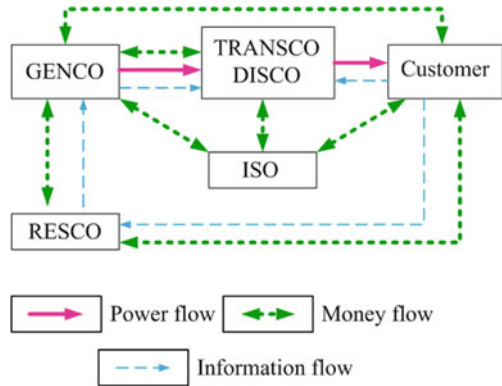
RESCOs, DISCOs, TRANSCOs, and ISO. Each entity operates independently as shown in Fig. 1.

GENCOs that own generating units produce and sell power independently. This creates competition among the GENCOs in wholesale level. The TRANSCOs and DISCOs are responsible for transmission and distribution of the generated power. RESCO buys power in bulk from the GENCOs and sells to the end customer. RESCOs are intended to provide better service and uninterrupted power to the customers. This creates competition among the RESCOs in retail level. The security and stability of the entire system are tracked by the ISO.

The competition is encouraged by creating a market platform in the system. Under bilateral market, the buyers and seller enter into negotiations to agree for a quantity of power and price corresponding to a time slot. Single buyer market involves single sided auction, performed by the system operator. The operator collects offers from the sellers and clears market against predicted demand for a time slot. Poolco market involves two sided auction that involves both buyers and seller. The auction is conducted by the operator to clear the market and determine the players, MP, and MCP. The auction procedure [22, 23] is depicted in Fig. 2.

Fig. 2 MCP from Supply-demand curves
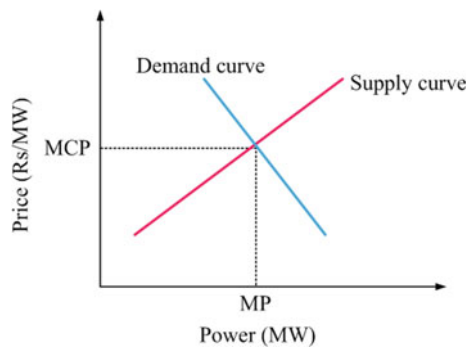
As seen from Fig. 2, the system operator plots demand and supply curves in the decreasing and increasing order of price, respectively. The operator then finds the point of intersection between the curves. This point is extrapolated to meet y and x axis to get the MCP and MP, respectively. For a 24 h market, the mechanism explained above is performed for each hour in a day. Thus, the operator performs 24 auctions for a day.

3 Methodology

Section 3 presents the hourly variation of MCP and MP in a 24 h electricity market. DR programs play a vital role in reduction of energy consumption of intensive electricity consumers. DR programs can be employed to plan various processes stages in industry based on the hourly MCP. This requires prediction of MCP.

This paper focuses on time series model to forecast MCP for a 24 h day ahead Indian electricity market. The prediction system employs ARIMA model to predict future MCP values. The model developed in Python uses the dataset available in IEX Website that includes date, time, and corresponding hourly MCP values from 01, January 2020 to 31, December 2020. The available input is split into train and test data in the ratio 80:20. The dataset is then subjected to pre-processing, resampling, decomposition, and stationarity check before applying suitable time series model as shown in Fig. 3.

3.1 Pre-processing

The real-time dataset is collected from IEX Website [24] which is composed of date, hour, and corresponding MCP values. Pre-processing involves representing dataset in specific format that allows easy data processing. The date is represented in the format YYYY-MM-DD, and the time is represented in the format HH:MM:SS. A date_time column is then created which is set as the dataset index.

Fig. 3 Block diagram representation of forecast process

3.2 Resampling

The paper considers 24 h Indian electricity market, thus hourly MCP is required. The data must be made available for a fixed time frame. Resampling is performed on the MCP data available for a day to obtain hourly MCP against date-time stamping. Resampling allows the data to be available at equal intervals and also improves the predictive accuracy of forecasting.

3.3 Decomposition

Time series data consists of components like trend, seasonality, cycles, and noise. Trend parameter represents the increasing or decreasing nature of data. Seasonality represents the short-time cyclic variation in the data, while cycle represents the variation in data over long term. The noise parameter is the random variation present within the data. Decomposition involves a statistical way to represent the data into each of these components. Decomposition is performed on the time series dataset as it is a useful conceptual model for best understanding the problem during time series analysis and forecasting.

3.4 Autoregressive Integrated Moving Average Model

ARIMA pioneered by Box and Jenkins [25] is the most general and famous statistical model employed to forecast a stationary time series model. The dataset is said to be stationary if the statistical properties does not vary over time. ARIMA model is efficient to filter the noise in the data and allows accurate prediction of future values. ARIMA combines autoregressive (AR) and moving average (MA) models. AR (p) and MA (q) along with the degree of differentiation (d) form the three parameters for ARIMA model and are represented as per Eq. (1).

$$y'(t) = c + \emptyset_1 y'(t-1) + \ldots + \emptyset_p y'(t-p) + \theta_1 \varepsilon(t-1) + \ldots + \theta_q \varepsilon(t-q) + \varepsilon_t \tag{1}$$

where

$\emptyset_1$ is the coefficient of the first AR term.

θ_1 is the coefficient of the first MA term.

p is the order of the AR term.

q is the order of the MA term.

ε_t is the error.

3.5 Mean Absolute Percentage Error

MAPE, due to its advantages of interpretability and scale-independency, is one of the most widely used accuracy measures. The accuracy measure represents the average of absolute percentage errors. The error is obtained from the difference between the predicted and actual values. Thus, MAPE is obtained while considering the test dataset. MAPE value is determined using the Eq. (2).

$$\text{MAPE} = \frac{1}{N} \sum \frac{\text{actual} - \text{predicted}}{\text{actual}} \times 100 \tag{2}$$

From Eq. (2), it is clear that the MAPE value is expressed as the percentage of the error.

3.6 Demand Management System Under Deregulated Environment

Demand management is a group of planned actions that are implemented to manage and optimize the electricity consumptions by a facility to save costs. It is one of the major program where customers are given a significant role to reduce their electricity consumption when the MCP is high, to maintain the reliability of the grid. The system also provides the flexibility in load management by allowing customers to shift or drop loads during the peak or high MCP period. The schematic of the proposed demand management system based on the predicted price is shown in the Fig. 4.

The proposed system depicted in Fig. 4 decides the status of DR program based on the predicted and reference prices. The systems observe the predicted values closely and activate the demand management program by turning off the loads, while the predicted price exceeds the critical value.
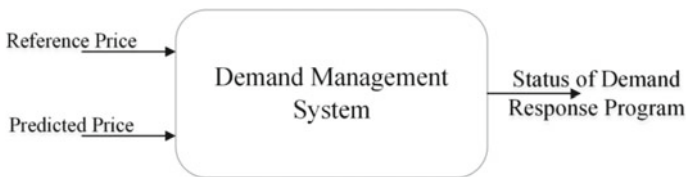
Fig. 4 Schematic of the proposed demand management system based on predicted price

4 Results and Discussion

This section presents the experimental results of MCP prediction model and evaluates the performance of proposed demand management planning system based on predicted MCP. The first stage of this paper involves selection of suitable ARIMA model based on the available dataset.

The real-time dataset available in IEX Website [24] for the period from 01, January 2020 to 31, December 2020 is employed. This dataset is divided into train and test data based on 80:20 ratio. The development of prediction model involves training process using the pre-processed dataset. The pre-processing stage creates a data time index against each MCP as shown in Fig. 5.

Resampling is required to make data available at equal intervals. In a 24 h market, the price changes for every hour of the day. Thus, the resampling frequency of the data is set to 1 h. The data after resampling is shown in Fig. 6.

The ARIMA model has the integration ability to make the sequence stationary and hence is applied on non-stationary time series data. It is important to check the stationarity in time series forecasting. Stationarity of time series indicates that the statistical properties like mean and variance of the series do not change with time. Augmented Dickey-Fuller (ADF) test is a common statistical test employed to test the stationarity. The ADF test conducted for the Indian MCP is found to be 0.0007 which is less than the critical value of 0.05. Thus, the time series data is stationary.

Fig. 5 Pre-processed dataset

date_time	Date	Hour	MCP
2020-01-01 00:00:00	2020-01-01	00:00:00	2024.25
2020-01-01 01:00:00	2020-01-01	01:00:00	1986.57
2020-01-01 02:00:00	2020-01-01	02:00:00	1935.58
2020-01-01 03:00:00	2020-01-01	03:00:00	1918.93
2020-01-01 04:00:00	2020-01-01	04:00:00	1968.74
...	...	...	...
2020-12-31 19:00:00	2020-12-31	19:00:00	4015.24
2020-12-31 20:00:00	2020-12-31	20:00:00	2778.67
2020-12-31 21:00:00	2020-12-31	21:00:00	2444.55
2020-12-31 22:00:00	2020-12-31	22:00:00	2101.65
2020-12-31 23:00:00	2020-12-31	23:00:00	2007.56

8784 rows × 3 columns

```
date_time
2020-10-19 19:00:00     4732.953343
2020-10-19 20:00:00     3817.281408
2020-10-19 21:00:00     2826.184636
2020-10-19 22:00:00     2855.574134
2020-10-19 23:00:00     2790.975395
                              ...
2020-12-31 19:00:00     4498.467928
2020-12-31 20:00:00     3564.436061
2020-12-31 21:00:00     2432.836415
2020-12-31 22:00:00     2374.861930
2020-12-31 23:00:00     2193.311320
Freq: H, Name: predicted_mean, Length: 1757, dtype: float64
```

Fig. 6 Resampled dataset

The resampled MCP data is split into test and train set in the ratio 80:20. The model is trained using the training set, while testing is done using the testing set. Training helps to select the suitable hyper parameters for fitting the ARIMA model. The optimal parameters for the ARIMA model are obtained through Akaike information criterion (AIC) test. AIC is an estimate of predicted error, which indicates that the model with least AIC is associated with least error. The p, d, and q values corresponding to the least AIC values are found to be 2, 1, 5. It is now required to test the accuracy of selected ARIMA model using the test data. The predicted and actual values for the period from 24, December 2020 to 31, December 2020 are presented in Fig. 7.

The accuracy of ARIMA (2, 1, 5) model is tested using the performance measure, MAPE. The MAPE value is calculated using Eq. (2) and is found to be 11.65%.

Finally, the chosen ARIMA (2, 1, 5) model is incorporated with the demand management planning system with the aim to provide flexibility.

The demand management system is considered for the cooling production and distribution system in a meat factory [26] where the operations of chillers and dryers that supplies services to the drying rooms are controlled.
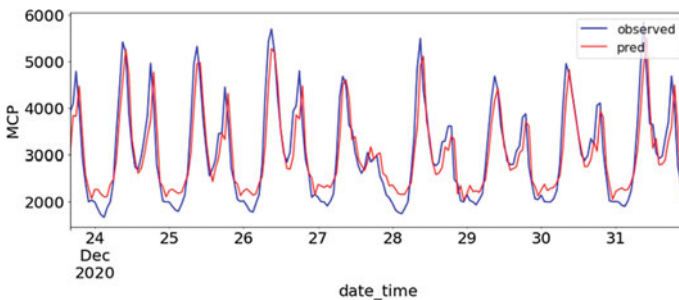
Fig. 7 ARIMA (2, 1, 5) MCP price prediction

These devices have an installed power of 66.5 kW. The proposed system accepts the reference price set by the user and turns on the demand management program when the predicted price is greater than the reference price. This paper considers the reference price of 4.6 Rs/KWh. The hourly price predicted by the ARIMA (2, 1, 5) model for the day 01-01-2021 is shown in Fig. 8.

From Fig. 8, it is clear that the predicted price is greater than the reference from 9:00 am to 10:00 am. Thus, the proposed demand management system turns on DR program during the considered period. The hourly status of chillers and dryers is depicted in Fig. 9.
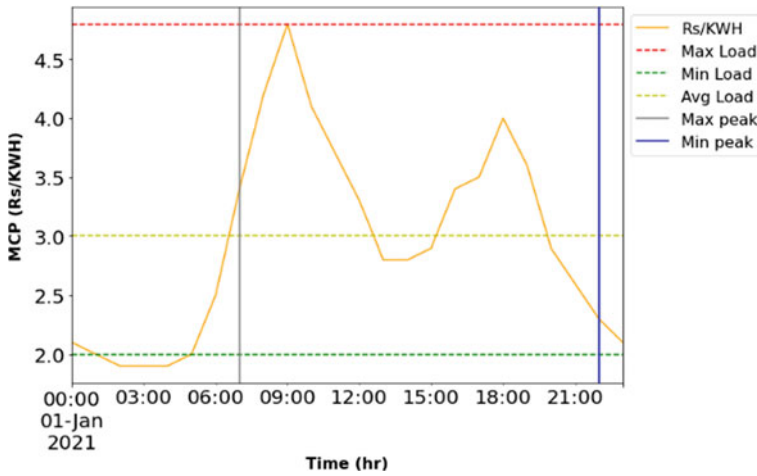
Fig. 8 Predicted price for the day 01-01-2021
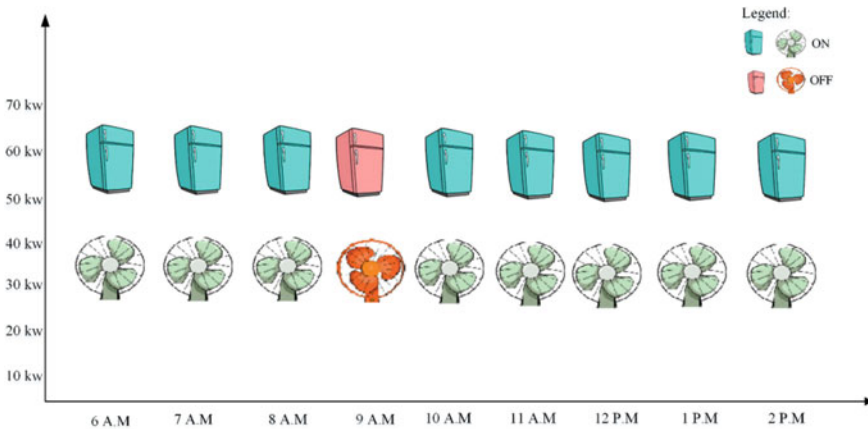
Fig. 9 Hourly consumption status of chillers and dryers for the day 01-01-2021

As pointed out in the case study by Alcázar-Ortega et. al. [26], an interruption of 1 h results in temperature and humidity variation lower than 8% which is acceptable to the factory's quality technicians. The total consumption cost with the interruption is found to drop by 6.78%. The reduction in the consumption cost proves the effectiveness of the proposed demand management planning system.

5   Conclusion

The reformation of Indian electricity market has created competition among the business players in wholesale and retail level. A market platform allows these players to perform power trading. The power trading can be through bilateral contract or auction mechanism. The auction process, conducted by the system operator, calls for submission of offers and bids. The system operator then clears the market and announces the players, market power, and market clearing price. This paper considers short-term market model. In the 24 h Indian electricity market, the auction is performed for each hour in a day. Thus, the market power and clearing price corresponding to each hour may vary. Prediction of market conditions plays an important role during planning, scheduling, flexibility, and budgeting.

The first stage of paper focuses on the market price prediction that is performed using time series method that employs ARIMA model. The model investigates real-time market price available in Indian Energy Exchange Website during the period from January to December, 2020. The dataset is divided into train and test based on 80:20 ratio. The test data is employed by the forecast model to choose the suitable ARIMA model that predicts Indian market price under day ahead market. The performance accuracy is validated using the mean absolute percentage error and is found to be 11.65%. The result shows the satisfactory performance of ARIMA (2, 1, 5) model.

In the second stage of the paper, the predicted price is used to plan demand management. Flexibility plays an important role for the better use of energy. The demand management program is employed in the cooling production and distribution section that interrupts the supply during the high predicted price period. The result shows the effective operation of the proposed demand management planning system. The system effectively interrupts the load between 9:00 am and 10:00 am. Thus, it provides a significant reduction in the consumption cost by 6.78%. The paper provides evidence on the effective use of demand management system in a promising sector such as meat industry.

References

1. Lai LL (2001) Power system restructuring and deregulation—trading, performance and information technology. Wiley
2. Balamurugan S, Shanthini BM, Lekshmi RR, Vijaya Chandrakala KRM (2014) Fuzzy Based Tariff. J Electr Syst 10:465–471
3. Paterakis NG, Erdinç O, Catalão JPS (2017) An overview of demand response: key-elements and international experience. Renew Sustain Energy Rev 69:871–891
4. Uritskaya OY, Uritsky VM (2015) Predictability of price movements in deregulated electricity markets. Energy Econ 49:72–81
5. Brusaferri A, Matteucci M, Portolani P, Vitali A (2019) Bayesian deep learning based method for probabilistic forecast of day-ahead electricity prices. Appl Energy 250:1158–1175
6. Sharma V, Srinivasan D (2013) A hybrid intelligent model based on recurrent neural networks and excitable dynamics for price prediction in deregulated electricity market. Eng Appl Artif Intell 26:1562–1574
7. Anamika, Kumar N (2016) Market clearing price prediction using ANN in Indian electricity markets. In: IEEE international conference on energy efficient technologies for sustainability. Nagercoil, India, pp 454–458
8. Wilson ID, Paris SD, Ware JA, Jenkins DH (2002) Residential property price time series forecasting with neural networks. Knowl-Based Syst 15:335–341
9. Jiang W (2021) Applications of deep learning in stock market prediction: recent progress. Expert Syst Appl 184:1–22
10. Jiang W (2022) Cellular traffic prediction with machine learning: a survey. Expert Syst Appl 201:1–19
11. Xiao ZM, Higgins S (2018) The power of noise and the art of prediction. Int J Educ Res 87:36–46
12. Wang J, Xu W, Zhang Y, Dong J (2022) A novel air quality prediction and early warning system based on combined model of optimal feature extraction and intelligent optimization. Chaos, Solitons Fractals 158:1–23
13. Al-Shargabi AA, Ibrahima DM, Chiclana F (2022) Buildings' energy consumption prediction models based on buildings' characteristics: research trends, taxonomy, and performance measures. J Build Eng 54:1–34
14. Wang H, Xiong M, Chen H, Liu S (2022) Multi-step ahead wind speed prediction based on a two-step decomposition technique and prediction model parameter optimization. Energy Rep 8:6086–6100
15. Matyjaszek M, Fernández PR, Krzemień A, Wodarski K, Valverde GF (2019) Forecasting coking coal prices by means of ARIMA models and neural networks, considering the transgenic time series theory. Resour Policy 61:283–292
16. Phan TTH, Nguyen XH (2020) Combining statistical machine learning models with ARIMA for water level forecasting: the case of the Red river. Adv Water Resour 142:1–35
17. Liu X, Lin Z, Feng Z (2021) Short-term offshore wind speed forecast by seasonal ARIMA—a comparison against GRU and LSTM. Energy 227:1–23
18. Gellert A, Fiore U, Florea A, Chis R, Palmieri F (2022) Forecasting electricity consumption and production in smart homes through statistical methods. Sustain Cities Soc 76:1–16
19. Sun F, Jin T (2022) A hybrid approach to multi-step, short-term wind speed forecasting using correlated features. Renew Energy 186:742–754
20. Bagavathi Sivakumar P, Mohandas VP (2010) Performance analysis of hybrid forecasting models with traditional ARIMA models—a case study on financial time series data. Int J Comput Inf Syst Ind Manage Appli 2:187–211
21. Ashok A, Prathibhamol CP (2021) Improved analysis of stock market prediction (ARIMA-LSTM-SMP). In: IEEE international conference on nascent technologies in engineering, NaviMumbai, India

22. Lekshmi RR, Swathy S, Lakshmi B, Vamsi Sai N, Suraj Vijaykumar V (2018) Market clearing mechanism considering congestion under deregulated power system. Procedia Comput Sci 143:686–693
23. Lekshmi RR, Balamurugan S (2017) Area and economic participation factor calculation of GENCOs in a multi area competitive power system. In: IEEE international conference on circuit, power and computing technologies, Kollam, India, pp 1–8
24. Indian Energy Exchange Limited, http://www.iexindia.com
25. Box GEP, Jenkins G (1970) Time series analysis, forecasting and control. Holden-Day, San Francisco
26. Alcázar-Ortega M, Álvarez-Bel C, Escrivá-Escrivá G, Domijan A (2012) Evaluation and assessment of demand response potential applied to the meat industry. Appl Energy 92:84–91

Performance Comparison of MCML, PFSCL, and Dynamic CML Gates with Parametric Analysis in 45 nm CMOS Technology

M. Sivasakthi and P. Radhika ⓘ

Abstract In this survey, the comparison results of current mode logic styles such as MOS Current Mode Logic (MCML), Dynamic Current Mode Logic (DyCML), and Positive Feedback Source Coupled Logic (PFSCL) gate structures are analyzed. In this, MCML and PFSCL are static logic circuits. The dynamic logic uses a clock signal as one of the inputs. The simulation results are performed at a voltage of 1 V and a temperature of 27 °C. The values of power, propagation delay, and power delay product are obtained and analyzed using the Cadence Virtuoso tool. The power and the delay values are verified with Monte Carlo simulations using a histogram plot of 200 samples. The process variations for different corners are simulated and the parametric analysis with different temperatures are compared for the different topologies of current mode logic gates. From the comparison, it is clear that Dynamic CML provides high performance and operates in a low-power environment.

Keywords Current mode logic (CML) · MOS current mode logic (MCML) · Inverters · Dynamic current mode logic (DyCML) · Positive feedback source coupled logic (PFSCL)

1 Introduction

Rapid technological improvement depends mainly on low-power and high-speed hardware devices. Recent progress in the fields of optical communication and signal processing has led to improvement in the field of mixed-signal circuit design. In this, analog circuit determination is restricted by the switching noise that is produced because of fabricating mixed-signal circuits on the same chip [1]. As for higher switching noise in CMOS circuits, it is not chosen nowadays in circuit design.

M. Sivasakthi · P. Radhika (✉)
Department of Electronics and Communication Engineering, SRM Institute of Science and Technology, Kattankulathur, Chennai 603203, India
e-mail: radhikap@srmist.edu.in

M. Sivasakthi
e-mail: sm3131@srmist.edu.in

Along with this, CMOS has more power consumption and hence it cannot be preferred for high-speed applications [2, 3].

Hence, a new logic style called current mode logic is preferred because of its low-power consumption and low noise [4]. Three different types of current mode logic styles are MCML [5, 6], Dynamic CML [7, 8], and PFSCL [9, 10].

The MCML circuit has 2 differential inputs and 2 differential outputs. PFSCL has one input and produces one output, along with positive feedback in the circuit. Hence, in Dynamic CML, instead of a constant current source in MCML and PFSCL, a dynamic current source is used, and hence it achieves low-power consumption. It operates in the precharge and evaluation mode and has true and complementary input and output similar to MCML with less propagation delay.

In this survey, the performance comparison of three different topologies of current mode logic circuits are analyzed and compared using power, delay, and PDP. It is simulated using Cadence Virtuoso 45 nm technology with a temperature of 27 °C and a voltage of 1 V. The results are also verified with Monte Carlo simulation using a histogram plot of 200 samples. From the comparison result, it proves that dynamic topology achieves higher performance compared to others.

The following section is arranged as: Sect. 2 represents the conventional architecture of different CML topologies. Section 3 discusses the comparison of different simulation results and their performance, and finally, Sect. 4 describes the conclusion.

2 Different CML Topologies

Current Mode Logic (CML) circuits are generally designed around differential amplifiers with a pair of source coupled transistors acting as pulldown networks. According to the fundamental idea of CML, current from a constant current generator is switched between two different routes based on logical values. CML circuits operate quickly primarily because of lower swing voltage.

2.1 MOS Current Mode Logic (MCML) Gates

The traditional MCML structure is shown in Fig. 1 [11]. Transistors M_2 and M_3 act as a pulldown network, a constant source current is applied via V_{bias} through transistor M_1 and the load circuit M_4 and M_5. The logic function is performed by the transistors M_2 and M_3. The inputs for M_2 and M_3 are differential, so the system requires both the logical input and its inverse. The pulldown network, which is made up of NMOS transistors (M_2 and M_3), carries out the Boolean function of the gate. Depending on the logical operation carried out, this network directs more current to one or the other of the two output branches, resulting in a lower voltage on one side than the other. Although in reality, this source is an NMOS transistor that is functioning in
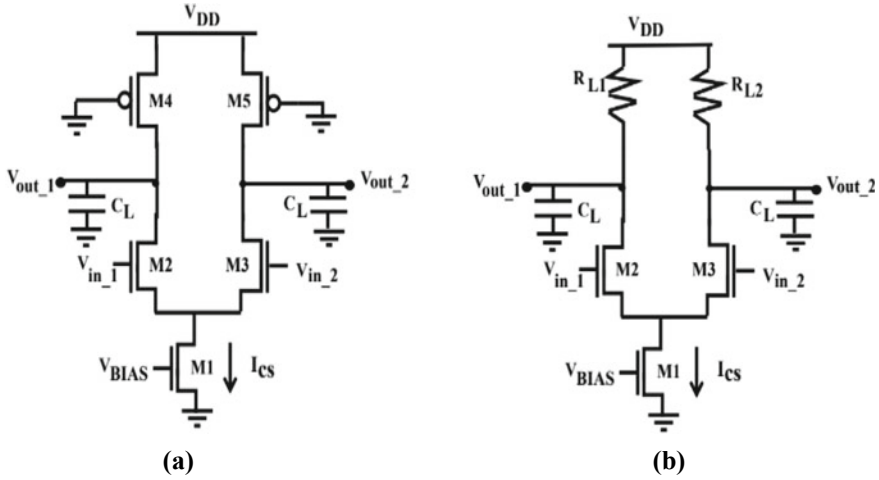
Fig. 1 MCML inverter logic [11]: **a** traditional MCML logic gate, **b** MCML gate with PMOS load

the saturation region, the current source for an ideal gate will be considered as ideal. This source offers a bias current, I_B, that is constant.

Load resistance R_L determines swing voltage. Since the current is present in both paths of the device, each resistance should be adjusted to provide an equal voltage swing on either side of the device. The load resistance and the biasing current source are the only factors that affect the swing voltage, which is often hundreds of millivolts lower than V_{dd}. The load resistors are frequently implemented as active devices in the form of PMOS transistors that operate in the linear region, providing a voltage-controlled resistance.

The voltage swing is determined by the load circuit, R_L, and current source I_{ss}. The MCML relies on current steering to function. The overall swing voltage [12] is,

$$V_{swing} = R_L \times I_{ss} \tag{1}$$

The voltage gain A_v is calculated as

$$A_v = g_{m1} R_L \tag{2}$$

where g_{m1} is the transconductance of transistor M_2 and R_L is the load resistance.

In Fig. 1b, the load resistors are replaced by PMOS load. As compared to the passive resistance R_L, the PMOS consumes minimum area but it varies from the linear characteristics at higher speeds [13].

According to the BSIM3v3 model, the PMOS resistance R_p is,

$$R_P = \frac{R_{int}}{1 - \frac{R_{DS}}{R_{int}}} \tag{3}$$

$$R_{\text{int}} = \left[\mu_{\text{eff,p}} C_{\text{ox}} \frac{w_p}{L_p} \left(V_{\text{DD}} - \left| V_{\text{T,P}} \right| \right) \right]^{-1} \tag{4}$$

Because of the constant current source used in MCML circuits, static power dissipation may be high. Therefore, to minimize that, DyCML circuits are preferred.

2.2 Dynamic Current Mode Logic (DyCML) Gates

The DyCML uses the CLK signal to reduce static dissipation and other drawbacks. Dynamic CML has a high switching speed because of capacitance arrangement. For this, a CLK signal with full swing is employed. The circuit must exhibit a precharge phase for low CLK signal values, which means the load capacitance must be precharged to V_{DD} and gate inputs must not have changed the voltage level at the output node. As an alternative, with high CLK values, the gate is evaluated according to the inputs while the output capacitance is disconnected from the power supply. To achieve this, the PMOS load transistors (M_1, M_2), which are now referred to as precharge transistors, are driven by CLK.

The load resistors in MCML are replaced by the active loads to minimize dissipation of power. Figure 2 depicts the structure of Dynamic CML. Figure 2c consists of an MCML block, a precharge circuit, a dynamic current source, and latches. For evaluating logic functions, the MCML block is used, and the transistors M_5, M_6, and M_2 act as a pre charge circuit.

During the low clock phase, the precharge transistors become ON and M_1 becomes OFF, and the output nodes are charged to V_{dd} by the transistors M_5, M_6, and M_2 discharge C_1 to the ground. When CLK is high, transistors M_5, M_6, and M_2 becomes
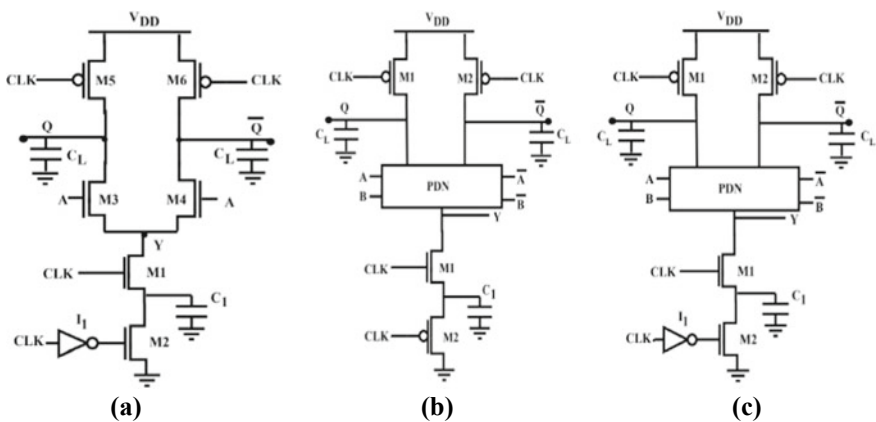
Fig. 2 Dynamic CML logic gate [11]: **a** DyCML-NN gate, **b** DyCML-NP gate, **c** dynamic CML inverter

OFF and M_1 becomes ON which forms the current route between precharged output nodes and the capacitor C_1. At the time of evaluation, if any one of the outputs becomes lower than $V_{dd} - |V_{tp}|$, it will turn on the transistor that is connected at that node, and hence it charges another node to V_{dd} again.

As a result of the construction between C_L and C_1 based on the inputs, the logic function is assessed during the evaluation phase. The output node potential decreases because of charge transfer from C_L to C_1. The charge transfer continues until the potential of both capacitors is equal. Therefore, it is important to make sure that charge transfer only stops when V_{swing} reduces the output node's potential. This can be achieved by sizing capacitor C_1 appropriately. With the usage of the charge conservation principle [14],

$$V_{DD}C_{OUT} = (C_1 + C_{out})(V_{DD} - V_{swing}) \tag{5}$$

where C_{out} is the sum of load capacitance C_L. C_1 can be written as,

$$C_1 = \frac{V_{swing}C_{out}}{V_{DD} - V_{swing}} \tag{6}$$

In Dynamic CML inverter, the transistor pairings M_1 and M_2 never switch ON simultaneously, because a direct link between the source and ground is not established. This is due to differential signal driving these transistors. As a result, the static power is quite small, but because these gates include capacitors, they need dynamic power. The power consumption of Dynamic CML inverter is given as,

$$P_{dyn} = C_{out}V_{DD}V_{swing}f_{clk} + P_{CMOS\_inv} \tag{7}$$

where f_{clk} is the clock frequency and P_{CMOS_inv} is the CMOS inverter power consumption [15].

2.3 Positive Feedback Source Coupled Logic (PFSCL) Gates

The PFSCL inverter structure is shown in Fig. 3. Transistor M_1 for biasing and transistors M_2 and M_3 form a pair of nMOS transistors. Positive feedback is applied from the output terminal to the M_3 gate terminal. The operation of the PFSCL is similar to that of the MCML with the same swing voltage and the linear resistance R_p as in Eqs. (1) and (2). Because of the feedback, the mid-swing voltage gain [12] is,

$$A_v = \frac{g_{m1}R_p/2}{1 - g_{m1}R_p/2} \tag{8}$$

Noise margin NM is,
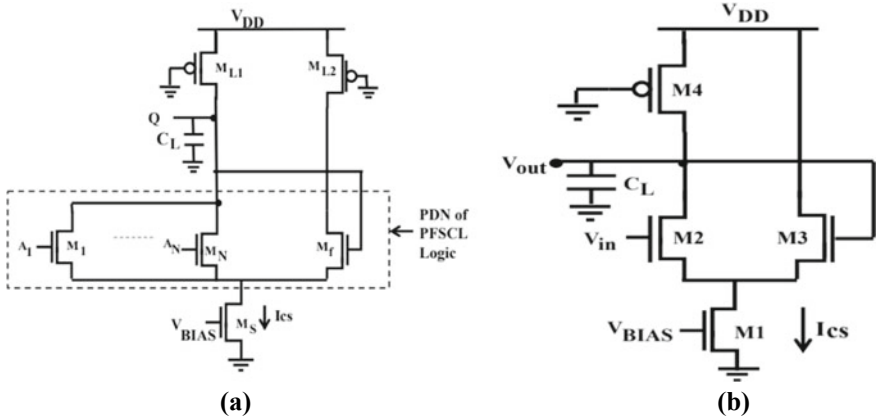
Fig. 3 PFSCL logic gate [11]: **a** *N*-input PFSCL gate, **b** PFSCL inverter

$$NM = \frac{V_{swing}}{2}\left(1 - \frac{1}{A_v}\right) \tag{9}$$

Signal lines in digital multiplexers are used in order to direct the data. Demultiplexers work in conjunction with multiplexers to improve the communication of concurrent data. This can be utilized in the multimedia streams and wireless communication [16].

3 Simulation Results of MCML, Dynamic CML, and PFSCL Gates

The performance of MCML, Dynamic CML, and PFSCL inverters are verified using the simulation environment as mentioned in Table 1.

Table 1 Simulation environment

CMOS technology	45 nm
Supply voltage	1 V
Process corner	TT, FF, SS, SF, FS
Load capacitance	10 fF
Source current	100 μA
Temperature	27 °C
Operating frequency	50 Hz
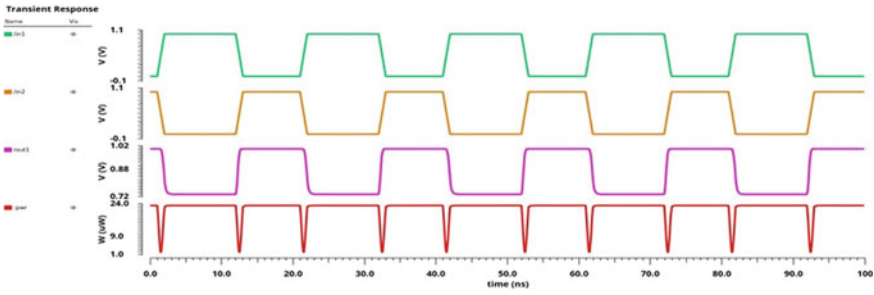
Fig. 4 Simulation waveform of MCML inverter logic
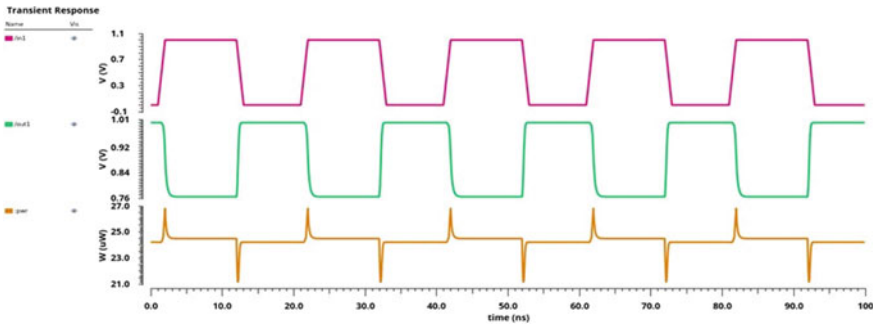
Fig. 5 Simulation waveform of PFSCL inverter logic

3.1 Output Waveform of MCML, PFSCL, and Dynamic CML

The output waveform for the MCML inverter topology using Cadence Virtuoso is shown in Fig. 4. The differential inputs applied in the pulldown network performs the Boolean function. Depending on the logical operation, it produces the output. One end of the transistor produces inverted output and its differential end produces buffer output. The average power consumed by the MCML circuit is 21.75 μW, PFSCL is 24.35 μW and for Dynamic CML is 0.054 μW.

The output waveforms of PFSCL and Dynamic CML is shown in Figs. 5 and 6, respectively, along with the average power values.

Table 2 compares the power, propagation delay, and power delay product values for the MCML, PFSCL, and Dynamic CML for different process corners.

3.2 Monte Carlo Analysis

In Monte Carlo, 200 samples of random statistical variations are analyzed. The histogram plot in Fig. 7 reveals that the average power value, which is mentioned
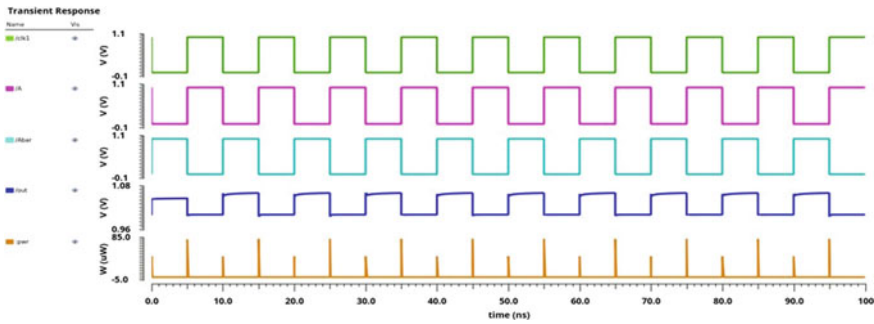
Fig. 6 Simulation waveform of dynamic CML inverter logic

Table 2 Comparison of Simulation results with different process corners

Parameter	Different topology of CML	Different process corners				
		TT	FF	SS	FS	SF
Power (μW)	MCML	21.75	29.1	14.68	23.7	17.93
	PFSCL	24.35	32.72	16.47	26.79	20.52
	DyCML	0.054	0.059	0.049	0.055	0.053
Propagation delay (ps)	MCML	360.7	281.7	407.9	357.9	380.9
	PFSCL	446.5	385.6	530.1	421.3	487.6
	DyCML	20.4	1.75	45.36	10.81	30.8
Power delay product (fJ)	MCML	7.85	8.19	5.98	8.48	6.82
	PFSCL	10.87	12.61	8.73	11.28	10.1
	DyCML	1.10	0.10	2.22	0.59	1.63

in Table. 2, is nearer to the mean value. The histogram plot represents the average values of power and propagation delay.

3.3 Parametric Analysis

The parametric analysis with different temperatures is analyzed using the Cadence Virtuoso tool and the corresponding average delay values for different topologies are compared in Table 3.

3.3.1 Simulation Results Using Parametric Analysis with Temperature

The parametric analysis is performed with different temperatures as shown in Fig. 8. The simulation results of input voltage with 1 V and its corresponding output results
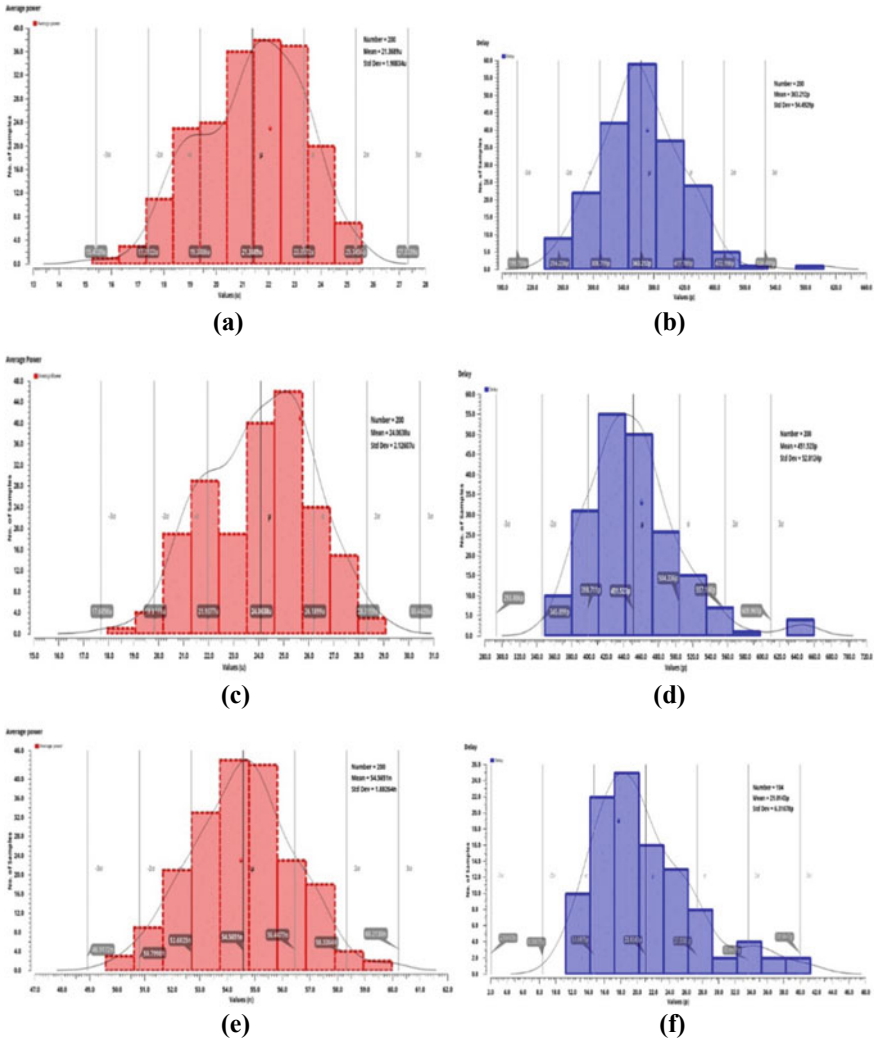
Fig. 7 Histogram plot of Monte Carlo simulation for the inverter logic: **a** MCML power, **b** MCML propagation delay, **c** PFSCL power, **d** PFSCL propagation delay, **e** dynamic CML power, **f** dynamic CML propagation delay

with different temperatures as mentioned in Table 3, along with the propagation delay and average power waveform for MCML, PFSCL, and Dynamic CML, respectively. These results reveal that CML topology can be performed in various temperatures with less propagation delay.

Table 3 Comparison of propagation delay with different temperatures

S. No.	Temperature (°C)	Propagation delay (ps)		
		MCML	PFSCL	Dynamic CML
1	0	353	437	1.4
2	25	358	445	20.8
3	50	363	454	47.4
4	75	372	462	74.6
5	100	378	468	97.8

3.4 Overall Performance Comparison of MCML, DyCML, and PFSCL

The overall performance comparison of different CML topologies are verified with different process corners. Figure 9 shows the overall comparison of various process corners Vs power, propagation delay, and power delay product.

This graph is plotted based on the values in Table 2. In this, the power values of MCML, PFSCL, and Dynamic CML are measured in μW, propagation delay in ps, and power delay product in fJ. Among these, the comparison graph shows clearly the dynamic CML can achieve more performance with reduced power and delay values as compared to the other topologies.

4 Conclusion

In this survey, the performance comparison of different CML topologies, namely MCML, PFSCL, and DyCML, have been analyzed using the Cadence Virtuoso tool. The simulation results are achieved with different process corners. The results of power and propagation delay are verified with Monte Carlo simulations using a histogram plot of 200 samples. The parametric analysis has been performed with different temperatures, and the corresponding delay values are analyzed. The simulation results reveal that Dynamic CML achieves greater performance in terms of power and delay than MCML and PFSCL, but it is quite complex to design. In future, current mode logic can be used to achieve better performance in high-speed applications. It is also used to achieve less switching noise in mixed-signal circuit design such as optical communication and signal processing.

(a)

(b)

(c)
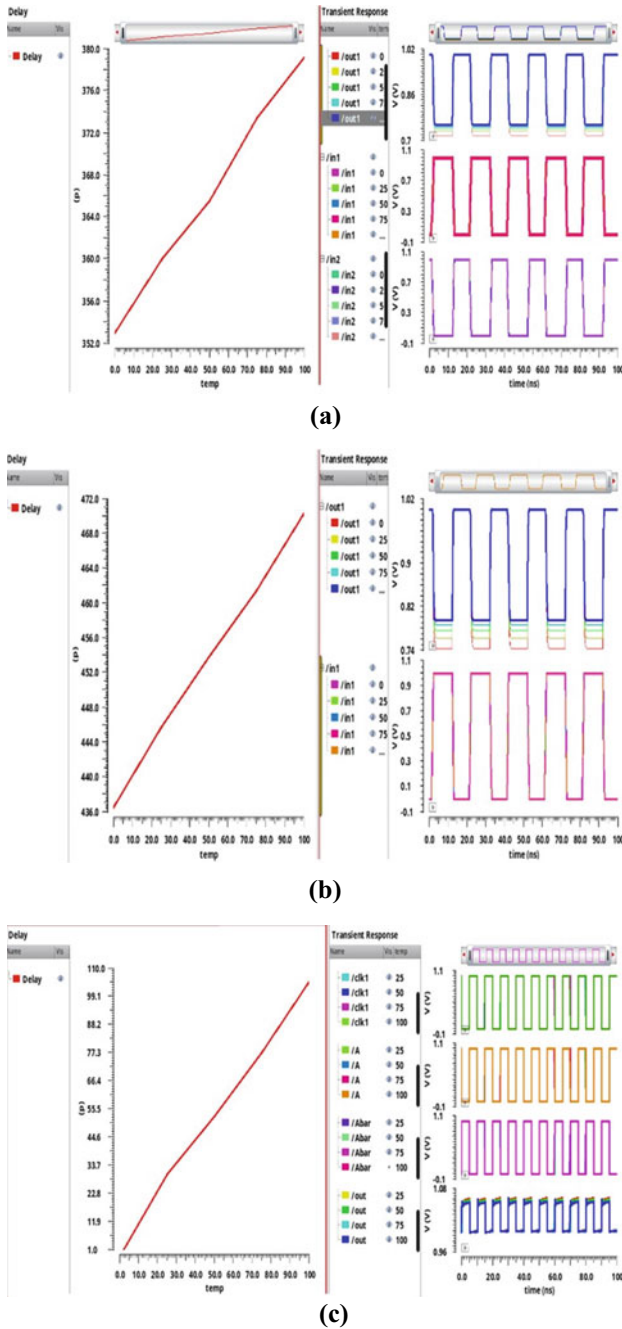
Fig. 8 Parametric analysis of temperature with delay and power waveforms: **a** MCML temperature versus delay, **b** PFSCL temperature versus delay, **c** DyCML temperature versus delay
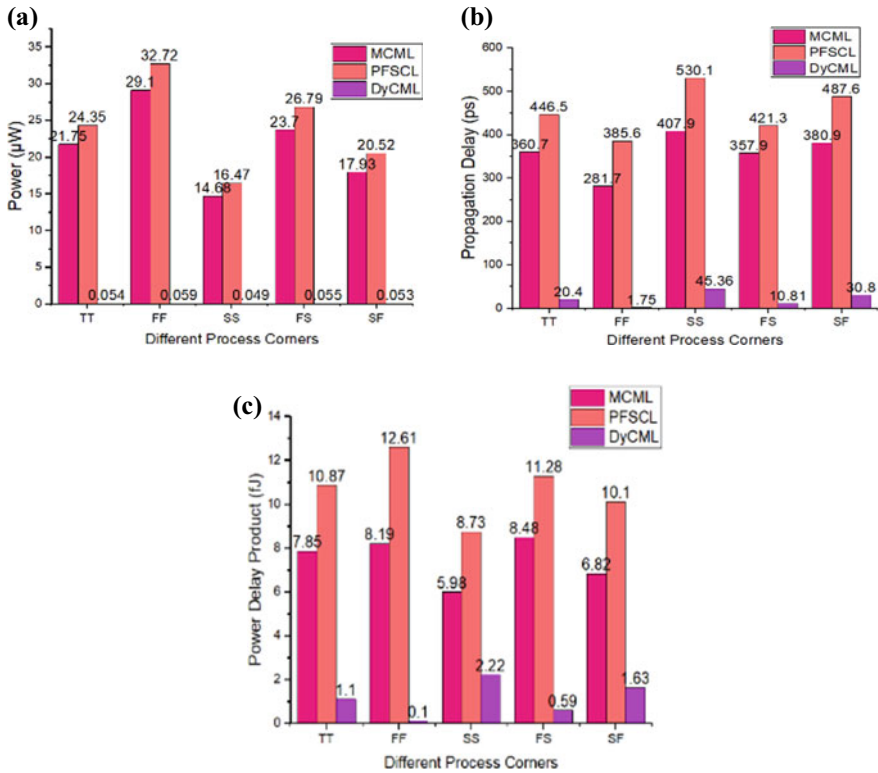
Fig. 9 Overall performance comparison with different process corners versus **a** power, **b** propagation delay, **c** power delay product

References

1. Allstot DSC, Kiaei S, Shristawa M (1993) Folded source-coupled logic vs. CMOS static logic for low-noise mixed-signal ICs. IEEE Trans Circuits Sys 40:553–563. https://doi.org/10.1109/81.244904
2. Kup BMJ, Dijkmans EC, Naus PJA, Sneep J (1991) A bit-stream digital-to-analog converter with 18-b resolution. IEEE J Solid-State Circuits 26(12):1757–1763. https://doi.org/10.1109/4.104166
3. Yu J, Dai FF (2010) A 3-dimensional Vernier ring time-to-digital converter in 0.13μm CMOS. In: IEEE custom integrated circuits conference 2010, pp 1–4. https://doi.org/10.1109/CICC.2010.561743
4. Kiaei S, Chee SH, Allstot D (1990) CMOS source-coupled logic for mixed-mode VLSI. In: IEEE International symposium on circuits and systems, vol 2, pp 1608–1611. https://doi.org/10.1109/ISCAS.1990.112444
5. Caruso G, Macchiarella A (2008) Optimum design of two-level MCML gates. In: 2008 15th IEEE international conference on electronics, circuits and systems, pp 141–144. https://doi.org/10.1109/ICECS.2008.4674811
6. Musicer JM, Rabaey J (2000) MOS current mode logic for low power, low noise, CORDIC

computation in mixed-signal environments. In: Proceedings of the 2000 international symposium of low power electronics and design, pp 102–107. https://doi.org/10.1145/344166.344532

7. Allam MW, Elmasry MI (2000) Dynamic current mode logic (DyCML), a new low-power high-performance logic family. In: Proceedings of the IEEE 2000 custom integrated circuits conference (Cat. No. 00CH37044), pp 421–424. https://doi.org/10.1109/CICC.2000.852699

8. Allam MW, Elmasry MI (2001) Dynamic current mode logic (DyCML): a new low-power high-performance logic style. IEEE J Solid-State Circuits 36(3):550–558. https://doi.org/10.1109/4.910495

9. Alioto M, Pancioni L, Rocchi S, Vignoli V (2004) Modeling and evaluation of positive-feedback source-coupled logic. IEEE Trans Circuits Syst I Regul Pap 51(12):2345–2355. https://doi.org/10.1109/TCSI.2004.838149

10. Alioto M, Pancioni L, Rocchi S, Vignoli V (2007) Power–delay–area–noise margin tradeoffs in positive-feedback MOS current-mode logic. IEEE Trans Circuits Syst I Regul Pap 54(9):1916–1928. https://doi.org/10.1109/TCSI.2007.904685

11. Gupta K, Pandey N, Gupta M (2020) Model and design of improved current mode logic gates. Springer, Singapore. https://doi.org/10.1007/978-981-15-0982-7

12. Gupta K, Sridhar R, Chaudhary J, Pandey N, Gupta M (2011) Performance comparison of MCML and PFSCL gates in 0.18 µm CMOS technology. In: 2nd International conference on computer and communication technology (ICCCT-2011), pp 230–233. https://doi.org/10.1109/ICCCT.2011.6075165

13. Hassan H, Anis M, Elmasry M (2005) MOS current-mode circuits: analysis, design, and variability. IEEE Trans Very Large Scale Integr (VLSI) Syst 13(8):885–898. https://doi.org/10.1109/TVLSI.2005.853609

14. Alioto M, Palumbo G (2005) Model and design of bipolar and MOS current-mode logic: CML, ECL and SCL digital circuits. Kluwer Academic Publications

15. Rabaey JM, Chandrakasan A, Nikolic B (2003) Digital integrated circuits, 2nd edn. Pearson Education

16. Bansal M, Singh H, Sharma G (2021) A taxonomical review of multiplexer designs for electronic circuits and devices. J Electron Inf 02:77–88

VANET Authentication with Privacy-Preserving Schemes—A Survey

M. Prakash and K. Saranya

Abstract Intelligent transportation has provided tremendous convenience to drivers as they have gained interest in Vehicle Ad Hoc Networks (VANETs). The messages can be broadcasted by any user on the open communication network. In some cases, the user can misbehave by sending wrong messages, malicious and bogus messages that disrupt the system's normal operation. As a result, we required to verify the message sender's identity. Due to its greater security over single-component user authentication, multi-component user authentication is becoming increasingly popular. Existing security and privacy authentication schemes, on the other hand, necessitate repeated interactions between users and various authentication components when sensing many components, resulting in additional costs and poor user experiences. Most of the existing schemes is not efficient to perform the certification validation due to the transmission overhead. As a result, these techniques are not suitable to implement real-life problems. Different types of authentication schemes are analyzed to perform the comparison between the varieties of components to improve the security requirements and efficiency in this paper.

Keywords Vehicle ad hoc networks · Security · Privacy · Authentication · Identity · Components

1 Introduction

A Wireless Ad Hoc Network (WANET) is a form of Wi-Fi community that is decentralized. Because there may be no predating infrastructure, the community is advert hoc. In stressed networks, routers are used, while in controlled Wi-Fi networks, get right of entry to factors are used. Instead, every node participates in routing through

M. Prakash
Information Technology, Karpagam College of Engineering, Coimbatore, India

K. Saranya (✉)
Information Technology, Dr. Mahalingam College of Engineering and Technology, Pollachi, Coimbatore, Tamil Nadu, India
e-mail: saranyak@drmcet.ac.in

sending information to different nodes, and the nodes that ahead information are decided dynamically primarily based totally on community connectivity. Ad hoc networks can make use of flooding to ahead information similarly to conventional routing.

VANETs (Vehicular Ad hoc Networks) are a sort of Wi-Fi community wherein motors speak with each other at the road. In VANETs, conventional routing protocols for Mobile Ad hoc Networks carry out badly because conversation hyperlinks in VANETs fail extra regularly than in MANETs, the routing dependability of such especially dynamic networks calls for unique consideration. In the difficulty of clever towns and clever transportation systems, educational and commercial researchers have targeted on heading off visitors congestion and automobile collisions which will offer a more secure using experience.

In each three hundred milliseconds, site visitor-associated messages may be communicated among the automobiles in VANET. There are type of privateness and safety dangers due to the inherited nature of the open and unsecured Wi-Fi nodes' interplay channels, in addition to the short mobility of the automobiles.

As depicted in Fig. 1, trusted authority (TA), roadside units (RSUs), and onboard units (OBUs) are the components odf architecture of a VANET. The trusted authority is a fully trusted entity with much more processing and communication capacity than the rest of the system. Management and communication to vehicles within their coverage area are used as the dedicated short-range communications (DSRC) standard to deliver services when RSUs are infrastructure devices positioned near intersections. Each car has an OBU that uses vehicle-to-vehicle (V2V) and vehicle-to-infrastructure (V2I) modes to communicate information about the driving conditions with other vehicles or surrounding RSU. Using these communication channels, each car provides information about the road condition to surrounding vehicles via DSRC. By transmitting messages to a vehicle within its coverage area, RSUs help to improve traffic control.

The safety and privateness problems that V2V and V2I communications gift with inside the VANET must be very well investigated. Vehicles in a VANET context are uncovered to safety and privateness threats due to the fact of the open nature of the network. As a result, they should be addressed so as for VANET customers to keep away from the aforementioned problems. Authentication has been the difficulty of a notable deal of have a look at in VANET. The current solutions, however, have some drawbacks. Furthermore, the bulk of those techniques have an extensive overhead in phrases of processing complexity while achieved consecutively. The major aim of this study is to adopt a crucial examination of identity-primarily based totally safety and privateness schemes in phrases of safety, privateness, and assessment metrics.

The remainder of this research is summarized as follows: The ideas of VANET security and privacy requirements are discussed in Sect. 2. Section 3 explains a pertinent survey on the current work. Section 4 examines existing schemes and provides a critical assessment of related research. The paper's conclusions are presented in Sect. 5.
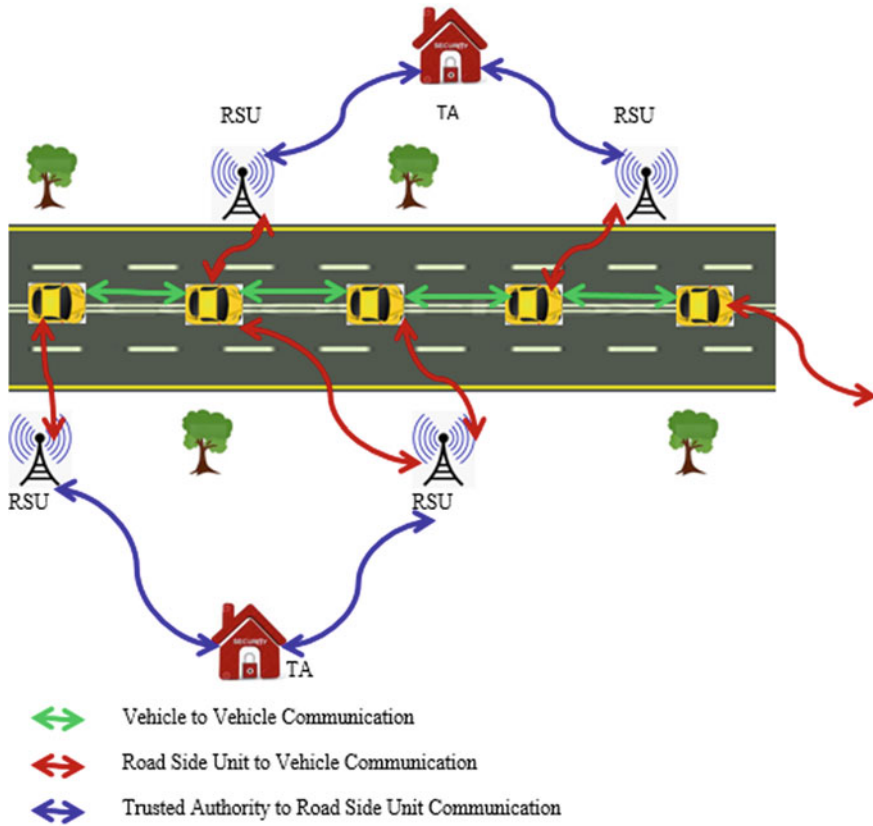
Fig. 1 Architecture of vehicular Ad Hoc network

2 Requirements of Security and Privacy

The security and privacy requirements of VANET are discussed in this section.

2.1 Security Requirements

It is vulnerable to different security attacks because of the inherent characteristics of VANETs. The control of the communication channel can be easily attacked by the malicious user [1, 2]. By confirming the signer's validity, the receiver can decide whether or not the obtained message is legitimate. Verifying the supply of dispatched messages in VANET is a fundamental requirement for stable communications. Message authentication guarantees that no adverse individual can ship messages below a bogus identity. When messages are frequently exchanged over

VANETs, the content material of the real message need to be checked to assure that it became broadcast without corruption.

The sender of messages should not be able to dispute that messages have been aired. Non-repudiation refers to the message sender's inability to refute the communication's transmission. Because erroneous messages in VANET frequently deceive car users, each user must be accountable for the messages they send.

Authentication: The receiver can evaluate the legitimacy of the received message by validating the signer. Verifying the origin of delivered messages in VANET is a critical need for secure communications. Message authentication guarantees that no hostile party may send messages under a false name.

Integrity: When messages are exchanged on a regular basis on VANETs, the content of the authentic message should be verified to guarantee that it was broadcast without corruption. Message integrity: During broadcasting or transmission, messages were not tampered with. Integrity safeguards message authenticity and reliability while also boosting system security.

Non-repudiation: The sender of communications should be unable to deny sending messages. The message sender cannot deny the message it transmitted, according to non-repudiation. Because false communications on the VANET regularly confuse automobile users, each user must assume accountability for the message delivered. Non-repudiation can successfully thwart forgery attacks by stopping any hostile user from inserting bogus data into the VANET.

Traceability: The genuine identity of the vehicle may be retrieved by authorized entity trusted authority in order to audit the vehicle and check for harmful activity. Traceability implies that trusted authority can determine the true identification of a vehicle in the aftermath of a traffic collision and examine legal liability. The trusted authority is in charge of monitoring the safety and identity of cars in VANETs.

Mutual authentication: TA and cars may validate communications from other entities, preventing forging attacks.

Data confidentiality: By using encryption techniques, it makes sure that data is sent safely between vehicles and distant stations. The mail should not be given to anyone attempting to learn more about the drivers. Confidentiality is required to provide secure communications using encryption methods, any vehicle statistics, such as speed, journey time, and total distance traveled.

2.2 Privacy Requirements

Privacy worries have end up as important. During the conversation, the attacker can use the gathered messages to find out the car's actual identification or maybe its tour courses, and use the captured messages to cross-suit several broadcasted

indicators from the equal source. This sort of assault exposes the driver's private and car information, and it may be used to release diverse kinds of attacks.

Identity privacy protection is a critical privacy necessity. In a VANET, it provides privacy protection, which implies that personal information about the driver and cars, such as identity, should be safely communicated.

Unlinkability: The attacker cannot tell whether a single source signed multiple messages or not.

Unobservability: During service consumption, VANET registered nodes can sign and verify communications without the attacker being aware of it.

2.3 Attack Model

Internal and outside attackers are styles of attackers in VANETs. External attackers, in contrast to internal attackers, are not able to advantageously get entry to the system; as a result, they may be deemed to be surprisingly resilient attackers. Internal attackers are VANET entities which have been compromised. Internal attackers may use touchy data due to the fact they may be part of the system.

Repetition of attacks: It is a widespread security flaw in VANETs. Another term for it is a playback attack. A replay attacker is more likely to be present in the network if a legitimate message is purposefully replayed, producing a delay in its impact.

Modification attacks: Changing or modifying the intercepted message is a common attack in these two communication modes. The attacker might purposely send a fake message to the system, causing confusion among automobiles and potentially significant safety consequences. To prevent being a victim of a modification attack, the recipient should double-check all messages received from other nodes.

Impersonation attacks: Each node in a VANET has a unique identification ID, which is used to identify automobiles in need of assistance, especially in the case of an emergency or accident. Nonetheless, during an impersonation attack, an attacker may disguise himself as the original sender of the communication.

MITM (Man-in-the-Middle) attacks: The communication between registered nodes in a VANET is compromised by this vulnerability by changing the messages sent between them. A well-known and incredibly damaging cyberattack against VANET transmission is the MITM attack, especially when the message contains crucial road and other status information. The attacker assumes two possibilities before launching the MITM attack: (i) the adversary receives a message on VANET containing crucial information, and (ii) the adversary is capable of deciphering the message's contents.

2.4 Challenges

The research team and the company must address many issues. Some of them, specifically:

Time restrictions: Security messages must be transmitted within the time limit since VANET is time sensitive. To meet the ongoing need, rapid cryptographic computing should be used. It would be difficult to validate transportation and communications [3, 4]. For instance, this is used to send information in all emergency service applications. The consumer receives the warning notice with plenty of time to respond. The results may be disastrous if the arrival time is met.

The scale of the network: VANET is the world's most sophisticated and specifically created system. The number of nodes in the system is rapidly expanding. If there is no solid private method capable of distributing cryptographic keys to such a vast number of nodes, this may have an influence on their capabilities. As a result, before supplying VANETs, an examined framework should be established to assure scalability in the event of changes in vehicular communication.

The high mobility of nodes: VANET nodes frequently change topology rapidly. As a result, projecting a car's location and protecting vehicle privacy has become substantially more difficult. Because of the increased mobility of automobiles, traditional vehicle and information verification approaches are difficult to employ.

Network volatility: Due to the rapid mobility of cars in the network, the link between two vehicles may be ephemeral. As a result, connections will be dropped often. Furthermore, the linked cars may go in different directions. Applying security measures that rely on identity verification is difficult.

3 Related Works

Zhang et al. furnished the identity-primarily based totally signature machine with inside the IEEE P1363 standard [5] and their implementation can keep the personal key from being disclosed on the identical time because the set of rules is walking in an untrustworthy surroundings. The scenario with VANET, then again, is slightly particular for the purpose that Wi-Fi conversation is the number one form of conversation and the cars pressure at a quicker tempo. Authentication is a vital device [4, 6–9] for ensuring the protection of information during transmission, and it's been extensively applied in VANET.

Lu et al. [10] proposed the concept of conditional privateness safety to protect OBU privacy from attackers on the identical time as moreover preventing unfavorable OBUs from interfering with normal using communique. The well-known public can't hint an OBU, but a TA can determine the genuine identity of an uncovered OBU. With inside the same year, Zhang et al. [11] created an identity-primarily based totally

authentication method with conditional privacy that doesn't require a certificate in RSU and automobiles.

Shim [12] and Lee et al. [13], on the alternative hand, every diagnosed weaknesses with inside the protocol in [11], which encompass vulnerability to replay assault and absence of nonrepudiation [12, 13]. The protocol in [12] can handiest deliver a decrease stage of safety than advertised, in keeping with Liu et al. [14]. Furthermore, Zhang et al. [15] decided that the protocol in [13] turned into prone to forging and tracking attacks. He et al. [16] endorsed an identity-based totally authentication technique for VANET that doesn't need bilinear pairing, which reduces processing costs.

Later, primarily based totally mostly on He et al. method's [16], extra modifications [17, 18] were proposed to decorate performance even further. Lo and Tsai [19] mounted an authentication approach without pairing in 2016 to maintain computational complexity. In 2017, Wang and Yao [20] brought an identification-primarily based totally authentication scheme with contemporary certificate change, albeit they suggested that precise RSU hold close keys be communicated to the cars. Islam et al. [21] proposed a brand new VANET authentication method primarily based totally on password and company key agreement.

Based on [22], Cui et al. [23] proposed an additional inexperienced method. However, each automobile with inside the protocols, [21, 23], has a hard and fast random huge range this is included in every authentication section. The changeless random amount may be used as a mark of the car, despite the fact that the pseudo identification is altered in every session, which violates the unlinkablity requirement.

In retaining with [22], the institution key generated in trusted authority may be introduced without delay to the auto, making the message dispatched from the car to the RSU superfluous in the authentication system. Finally, proving that the group key need to be modified while the car exits the RSU's vicinity is hard. If the OBU in an unmarried car fails all of sudden, it's going to possibly be now no longer capable of speak the departure statistics. The group key will thereafter be not able to be up to date effectively. As a quit result, the protocols in [21, 23] might not be appropriate for the actual situation [24].

The researchers have advanced numerous privacy-maintaining protocols primarily based totally on public key cryptographic techniques to make sure the protection of VANETs: In 2005, Raya and Hubaux [25] recommended a VANET privacy-retaining approach primarily based totally on traditional PKI generation that preserves OBU's real identification via updating certificate on a regular foundation. TA friends anonymous certificate with authentic OBU for traceability by means of manner of last a maintained table. Lin et al. [22] had been the primary to include business enterprise signature with inside the VANET privacy-retaining technique, which eliminated the want for OBU to hold a huge variety of pseudonym keys and certificate. At INFOCOM'08, Lu et al. [10] established a brand new comfortable method based totally on business enterprise signature generation. The common motive is to limit RSU's jurisdiction through implementing "on-the-fly" brief-time period institution-member certifications.

Even as addressing the problem of key escrowing, the technique improves device efficiency. In 2010, Wu et al. [26] proposed a brand new tool for V2V communications, which contained a criterion to ensure message trustworthiness and a privacy-defensive method that preserved every a priori and a posteriori facts. In 2013, Horng et al. [27] recommended a privacy-retaining technique that offers message integrity and authentication while simultaneously defensive closer to collusion assaults. Liu et al. [28] devised an allocated computing-primarily based totally and agent-primarily based totally absolutely authentication mechanism that lets in the proxy server to have a look at many messages proper away. In 2018, Li et al. [29] created a nameless certificate-much less public key cryptography authentication mechanism.

Moreover, the scheme mitigates replication assaults and consists of a malicious-node detection technique. We can reputation on growing lightweight authentication and revocation protocols with verifiable calculations in moderate of the contributions supplied by means of manner of the foregoing strategies to the protection paradigm of VANETs [30]. In the identical 12 months, hash features are used to suggest diverse conditional privacy-keeping authentication systems [31]. Our observe will deliver more green algorithms by means of outsourcing computations and gift a better safety shape and protocol than earlier artwork on VANET privacy maintenance.

4 Review of the Existing Schemes Based on Lightweight Privacy Preserving Schemes

In this subsection, we describe the review of the existing privacy and security scheme and their methods as follows,

In Li et al.: [32], the 4 steps of an authentication machine mentioned are initialization, RSU registration, automobile registration, and message authentication. During Initialization, the truthful authority selects a hash feature and a mystery key. The relied on authority selects RSU's identifier and a shared mystery among the relied on authority and RSU, following which the document is saved with inside the TA's database and securely transmitted to RSU.

The relied on authority chooses an identification for an automobile and shops it with inside the database. The relied on authority then chooses a pseudo identification and calculates the 2 hash features the usage of the automobile identification and the automobile's pseudo identification and sends it to the automobile in a steady manner, which includes the vehicle identification, hash feature fee 1(HF1), hash feature fee 2(HF2), and automobile's pseudo identification. The acquired facts is stored at the automobile's evidence tamper OBU. Hash function is a technique that encodes communications right into a virtual signature of predefined numbers, making it not possible to infer the unique message from the encoded digits.

During the message authentication, 4 steps are followed, In Step 1, the automobile sends a message to the RSU, when automobile input into the variety of RSU, it selects a random variety and receives a timestamp. Based on that, it calculates the

hash feature. In Step 2, the RSU ship a message to the relied on authority with timestamp and hash feature. In Step 3, the relied on authority sends a message to the RSU through checking the timestamp and hash features calculated in preceding step. Trusted authority selects a brand new pseudo identification and receives the timestamp. Based on that relied on authority calculates new consultation key and new hash features and ships a message to the RSU with hash features. In Step 4, RSU sends a message to the automobile through checking the time freshness and consultation key. When getting a message from RSU, the automobile tests the freshness of the message and consultation key. Session keys for automobile and RSU are used as consultation keys, respectively, after the mutual authentication. For a period, the 2 entities can maintain their personal keys till the opposite is not detectable. If automobiles are with inside the equal RSU's detecting region, they could engage with every different through with the assist of the RSU. This protocol accomplishes some of protection objectives.

Alshudukhi et al.: [1] the usage of lightweight authentication for VANETs privacy. Once the automobile arrived on the insurance place of RSU, the automobile must input the RSU area to get the RSU's temporal key. A pseudonym ID is created with the aid of using the onboard unit with the aid of using automobile's unique identification and depended on authority's preliminary settings. The onboard unit authenticates itself with the machine at the same time as supporting RSU with depended on authority's mystery key. After presenting the name of the game key, the RSU might also additionally securely connect to the onboard tool the usage of its temporal key. The pseudonym ID and related personal key created with the aid of using the onboard unit are legitimate until the C programming language expires. This pseudonym ID and its corresponding personal key are utilized by OBU to signal the traffic-associated messages that need to be created. The 4 levels that comply with are covered with inside the proposed scheme: initialization of the machine, mutual authentication, signing message, and verifying messages as proven in Fig. 2.

During the initialization phase, the trustworthy authority selects a random integer for its secret key and computes its suitable public key. The trustworthy authority then selects the symmetric function's encryption and decryption, as well as three

Fig. 2 Privacy preserving scheme
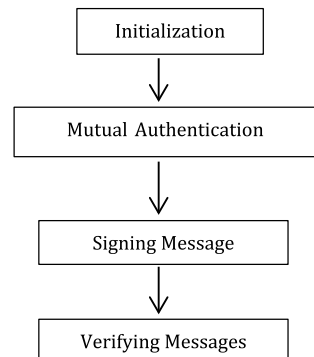
one-way has functions. All RSUs and OBUs will then have their settings preloaded. The trusted authority produces a secret key for each RSU, which is subsequently saved on the TPD of each RSU together with the secret key of the trusted authority.

When a vehicle reaches each RSU's coverage domain during the Mutual Authentication phase, the OBU must approve itself with the system in order to get each RSU's secret temporal key. Follow the procedures below to finish the process of OBU joining the RSU domain. OBU chooses a random value and computes its pseudonym ID before transmitting to RSU. This pseudonym ID is generated from the vehicle's original identifier and the trustworthy authority's public key. RSU utilizes the trusted authority's secret key, which is kept in its TPD, after obtaining the pseudonym ID from OBU, to expose the vehicle's genuine identity.

The RSU then checks to verify if the OID is contained in the CRL, which is issued by a trusted authority to guarantee that the vehicle is not revoked. If the vehicle is authenticated, the RSU computes a symmetric secret key. RSU creates a new temporal key (refresh in TS) in the same way that it generates a new secret key, which is kept in its TPD. RSU then generates the appropriate public key. It then sends its public key, together with its TS, to its covered domain on a regular basis.

The OBU uses symmetric secret key to decrypt the function in order to obtain RSU's private key, RSU encrypts RSU's private key with the symmetric secret key, which RSU uses to encrypt the symmetric function of RSU's private key. In mutual authentication process, the RSU and OBU share the symmetric secret key. Then the encrypted RSU private key is sent to OBU. When it arrives, OBU decrypts it to retrieve the temporal key TS.

- OBU initially chooses a random value and calculates its pseudonym ID and private key.
- OBU calculates the message's signature
- OBU broadcasts the beacon to recipients.

After receiving the signal, the receiver checks to see if the message mi is valid.

In Wei et al.: [2], an identification-primarily-based signature is proposed primarily based on the belief of simple RSA. Without the use of a random oracle, this signature technique can be verified to be unforgeable toward selected-message attacks. The safety of this outsourcing method, which also consists of a verification mechanism, is decided with the aid of the intractability of integer factorization.

We broaden and implement a proxy re-signature for authentications in a privateness-keeping VANET protocol using outsourced computations and the afore-mentioned IBS roadside unit employs a proxy re-signature technique to convert onboard unit's signature into depended on authority's signature, so concealing onboard unit's actual identification. Depended on authority appoints roadside unit as an agent and employs a proxy re-signature set of rules to turn onboard unit's signature into depended on authority's signature, effectively overlaying onboard unit's real identification. While malicious communications are detected, trusted authority can utilize its secret key to quick and accurately determine the true identification

of the onboard unit. The proposed solution then incorporates anonymity, trace-ability, and privacy into the equation. The privacy-keeping protocol of the VANET is primarily based on the safety of the IBS. Moreover, our approach does now not want pairing operations, and the aforementioned outsourcing techniques save you every participant from doing huge exponential operations.

The VANET era can substantially reduce calculating loads. The following contri-butions had been made in overall: If we provide an identification-primarily-based signature, we provide unforgeability in opposition to selected-message assaults without using a random oracle. The use of the aforementioned safety architecture and outsourcing strategies in VANETs, we can propose a completely unique and green privateness-preserving protocol for VANETs.

In Alfadhli et al.: [33], the vehicle setup, message authentication, beacon exchange, vehicle retraction, and key update are the five phases that make up VANETs. The vehicle sends a configuration request to the trusted authority along with its vehicle identifying number during the setup process. When the trusted authority receives the request, it produces a random challenge C and delivers it to the vehicle for later authentication. When the vehicle receives the challenge C, it calculates the P physical unclonable function and sends it to the trusted authority. The trusted authority then generates a secret key that will be used as the vehicle's first authentication component as well as a one-time authentication pseudo identity. Ksys is the system key, which it keeps and delivers to the vehicle TPD.

Before entering the VANET or meeting a new domain, a vehicle must first authen-ticate itself to show its eligibility in the two-component mutual authentication phase. The following techniques are illustrated in detail in the following examples:

Event 1 (Send a request to join): The vehicle TPD creates a random number and then uses the vehicle secret key and random number to compute a new random number. The joining request message is then written and sent to the trusted authority via the RSU closest to them.

Event 2 (Verification and Response): The trusted authority searches its databases for the API and retrieves the required data after receiving the message. After that, the trustworthy authority creates a nonce NCA with the previous NCA and the vehicle secret key, extracts the vehicle random number with the vehicle secret key and the new random number, and computes a new challenge with the old challenge and the vehicle secret key. Finally, using a random number generated by the vehicle during mutual authentication, a new number of trusted authorities, and a new challenge, it calculates the signature and transmits the answer message to the car through RSU.

Event 3 (Trusted Authority Authentication) The vehicle examines the signature as soon as it receives the message in Event 3. If the communication is incorrect, the car will disregard it. Otherwise, the vehicle validates the trusted authority, extracts the challenge, and computes the outcome of the public unclonable function. It also uses the fuzzy generator to identify the number of trustworthy authorities, as well as the secret key-member and helper data. After that, the car computes new assistance data,

a new challenge, and the vehicle's secret key. Finally, it uses the RSU to communicate with the trusted authority.

Event 4 (Vehicle authentication): Once the trustworthy authority gets the message, by using the fuzzy reconstruction process, it first extracts the helper data and the secret key-member. The trustworthy authority then computes a new hash function to validate the existing hash function. If it is validated, the trusted authority will do the following: (a) It links assistance data with vehicle verification data. b) It retrieves the updated answer. (c) It brings the new challenge up to date. (d) It changes the pseudo-identity for one-time authentication. (e) It updates the car's private key. Now, the V2I verification data on both sides of the vehicle and trusted authority are updated for the next encounter.

Event 5 (Trusted Authority Authentication): When the message is received, the vehicle retrieves the regional key agent and the updated verifier key. It then checks to see if the hash function is valid before accepting the message. As a result, the V2I mutual authentication is completed. The car may now exchange messages with other vehicles as well as RSUs after calculating the regional key.

Exchange of Beacons Phase

The steps for maintaining the V2V interface and updating the regional key are outlined in this section.

(1) **Signature of a Beacon**

The vehicle can interact with the nearby nodes after successfully completing mutual authentication with the trusted authority. The car transmits a traffic-related communication to its vehicle temporary proof device to generate a beacon. The temporary proof gadget does the following tasks:

- It creates a broadcasting pseudo identity at first. Second, it calculates the hash signature of the message.
- As a message, the vehicle transmits the beacon.

(2) **Verification of Beacons**

It examines the message's freshness against time, when the message is received by the surrounding node, it checks the signature's validity, if it is fresh and the node considers the message, if the signature is valid; it rejects it, otherwise.

(3) **Vehicle Revocation Phase**

If a vehicle is reported to the trustworthy authority as malicious or misbehaving, the trusted authority will examine the vehicle's database after it gets the car's dynamic broadcasting pseudo identity. The trustworthy authority then extracts the vehicle's true identification and marks it as a revoked node. The CA then broadcasts a revocation message to all cars through the reporter RSU, using an efficient lightweight symmetric technique. When the reported vehicle's Tamper Proof Device receives the message, it confirms it; if this is true, the TPD eliminates all of the secret materials

Table 1 Security and privacy requirements achieved by existing schemes

	[32]	[32]	[32]	[32]
Key security	Yes	No	No	No
Non-forgery	Yes	No	No	No
Privacy	Yes	No	No	Yes
Anti-replay attack	Yes	Yes	Yes	Yes
Message integrity and authentication	No	Yes	Yes	Yes
Identity privacy-preservation	No	Yes	No	No
Unlinkability	No	Yes	Yes	Yes
Traceability and revocation	No	Yes	Yes	Yes
Resistance to impersonation attacks	No	Yes	No	No
Resistance to modification attacks	No	Yes	Yes	No
Resistance to man-in-the-middle attacks	No	Yes	No	No
Vehicle anonymity	No	No	Yes	No
Resistance to forgery attack	No	No	Yes	No
Non-repudiation	No	No	No	Yes
Practical vehicle authentication	No	No	No	Yes
Practical TPD	No	No	No	Yes
Practical system key dependency	No	No	No	Yes
Practical revocation	No	No	No	Yes

that were preloaded during the configuration step. Table 1 summarizes the security and privacy requirements achieved by privacy preserving schemes, and Table 2 provides the comparison of existing systems.

5 Conclusion

A vehicle is significant since it not only carries passengers from one point to another, but it also assures their safety. As a result, various studies have been carried out. The VANET was offered as a way to increase and improve traffic and road administration. The attacker, on the other hand, can remove, edit, and replace data on the driving simulator, as well as replay and modify the exchange message. In this setting, V2V and V2I communication systems are disturbed. As a result, a group of academics proposed a security system, as well as a privacy approach [34–36], to solve the aforementioned issues. In this work, several strategies for identity-based security and privacy needs are categorized as Lightweight Authentication with Privacy-Preserving Scheme [37]. The security requirements, privacy requirements, cyber-attack resistance, and assessment criteria are evaluated and contrasted for each class. The purpose of this paper is

Table 2 Comparison of existing schemes

Existing paper	Attributes		
	Techniques used	Advantages	Formal security analysis
[32]	Proxy re-signature scheme	The VANET system's calculation loads can be greatly decreased	The calculation burdens for the VANET system can be significantly reduced
[1]	Elliptic curve cryptography	In terms of calculation and transmission costs, it is less expensive than other existing methods	A game among an attacker A and the challenger C
[2]	Hash functions and exclusive-OR operations	The protocol is strong enough to withstand typical assaults while keeping communication data private	Burrows–Abadi–Needham (BAN) logic
[33]	A combination of PUF and one-time dynamic pseudo identities	Efficient, with lower communication and computation costs and features than previous methods	Burrows–Abadi–Needham (BAN) logic

to assist researchers and developers in defining and grasping the major requirements for security, privacy, and evaluation metrics in VANET V2V and V2I communication.

References

1. Alshudukhi JS et al. (2021) Lightweight Authentication with Privacy-Preserving Scheme for VANETs based on elliptic curve cryptography. IEEE Access 9:15633–15642
2. Li et al. (2020) Lightweight privacy-preserving authentication protocol for VANETs, 1937-9234 © 2020 IEEE
3. Raya M, Hubaux J-P (2007) Securing vehicular ad hoc networks. J Comput Secur 15(1):39–68
4. Li X, Niu J-W, Ma J, Wang W-D, Liu C-L (2011) Cryptanalysis and improvement of a biometrics-based remote user authentication scheme using smart cards. J Netw Comput Appl 34(1):73–79
5. Zhang Y, He D, Huang X, Wang D, Choo K-KR, Wang J (2019) White-box implementation of the identity-based signature scheme in the IEEE P1363 standard for public key cryptography. IEICE Trans Inf Syst 1(99):1–8
6. Li X, Niu J, Khan MK, Liao J (2013) An enhanced smart card based remote user password authentication scheme. J Netw Comput Appl 36(5):1365–1371
7. Li X, Ma J, Wang W, Xiong Y, Zhang J (2013) A novel smart card and dynamic id based remote user authentication scheme for multi-server environments. Math Comput Model 58(1/2):85–95
8. Wang D, Li W, Wang P (2018) Measuring two-factor authentication schemes for real-time data access in industrial wireless sensor networks. IEEE Trans Ind Inf 14(9):4081–4092
9. Wang D, Wang P (2018) Two birds with one stone: Two-factor authentication with security beyond conventional bound. IEEE Trans Dependable Secure Comput 15(4):708–722

10. Lu R, Lin X, Zhu H, Ho PH, Shen X (2008) ECPP: efficient conditional privacy preservation protocol for secure vehicular communications. In: Proceedings of the IEEE 27th conference on computer communications, pp 1229–1237
11. Zhang C, Lu R, Lin X, Ho PH, Shen X (2008) An efficient identity-based batch verification scheme for vehicular sensor networks. In: Proceedings of the IEEE 27th conference on computer communications, pp 246–250
12. Shim K-A (2012) CPAS: an efficient conditional privacy-preserving authentication scheme for vehicular sensor networks. IEEE Trans Veh Technol 61(4):1874–1883
13. Lee C-C, Lai Y-M (2013) Toward a secure batch verification with group testing for VANET. Wireless Netw 19(6):1441–1449
14. Liu JK, Yuen TH, Au MH, Susilo W (2014) Improvements on an authentication scheme for vehicular sensor networks. Expert Syst Appl 41(5):2559–2564
15. Zhang J, Xu M, Liu L (2014) On the security of a secure batch verification with group testing for VANET. Int J Netw Secur 16(5):351–358
16. He D, Zeadally S, Xu B, Huang X (2015) An efficient identity-based conditional privacy-preserving authentication scheme for vehicular ad hoc networks. IEEE Trans Inf Forensics Secur 10(12):2681–2691
17. Zhong H, Wen J, Cui J, Zhang S (2016) Efficient conditional privacy-preserving and authentication scheme for secure service provision in VANET. Tsinghua Sci Technol 21(6):620–629
18. Gayathri N, Thumbur G, Reddy PV, Muhammad ZUR (2018) Efficient pairing-free certificate-less authentication scheme with batch verification for vehicular ad-hoc networks. IEEE Access 6:31808–31819
19. Lo N-W, Tsai J-L (2016) An efficient conditional privacy-preserving authentication scheme for vehicular sensor networks without pairings. IEEE Trans Intell Transp Syst 17(5):1319–1328
20. Wang S, Yao N (2017) LIAP: a local identity-based anonymous message authentication protocol in VANETs. Comput Commun 112:154–164
21. Islam SH, Obaidat MS, Vijayakumar P, Abdulhay E, Li F, Reddy MKC (2018) A robust and efficient password-based conditional privacy preserving authentication and group-key agreement protocol for VANETs. Future Gener Comput Syst 84:216–227
22. Lin X, Sun X, Ho P-H, Shen X (2007) GSIS: a secure and privacy preserving protocol for vehicular communications. IEEE Trans Veh Technol 56(6):3442–3456
23. Cui J, Tao X, Zhang J, Xu Y, Zhong H (2018) HCPA-GKA: a hash function-based conditional privacy-preserving authentication and group key agreement scheme for VANETs. Veh Commun 14:15–25
24. Puspitorini O, Siswandari N, Wijayanti A, Mahmudah H (2017) Measurement of inter-connecting network for roadside unit placement on cellular network to support intelligent transportation system. Asian J Appl Sci 5(2):247–258
25. Raya M, Hubaux JP (2005) The security of vehicular ad hoc networks. In: Proceedings of the 3rd ACM workshop on security of ad hoc and sensor networks (SASN), pp 11–21
26. Wu Q, Domingo-Ferrer J, Gonzalez-Nicolas Ú (2010) Balanced trustworthiness, safety, and privacy in vehicle-to-vehicle communications. IEEE Trans Veh Technol 59(2):559–573
27. Horng S-J et al (2013) B-SPECSC: batch verification for secure pseudonymous authentication in VANET. IEEE Trans Inf Forensics Secur 8(11):1860–1875
28. Liu Y, Wang L, Chen H-H (2015) Message authentication using proxy vehicles in vehicular ad hoc networks. IEEE Trans Veh Technol 64(8):3697–3710
29. Li C, Zhang X, Wang H, Li D (2018) An enhanced secure identity based certificate less public key authentication scheme for vehicular sensor networks. Sensors 18(1):194
30. Li J, Li J, Chen X, Jia C, Lou W (2015) Identity-based encryption with outsourced revocation in cloud computing. IEEE Trans Comput 64(2):425–437
31. Li J et al (2018) EPA-CPPA: an efficient, provably-secure and anonymous conditional privacy-preserving authentication scheme for vehicular ad hoc networks. Veh Commun 13:104–113
32. Wei Z et al. (2019) Lightweight privacy-preserving protocol for VANETs based on secure outsourcing computing. IEEE Access 7:62785–62793

33. Alfadhli SA et al (2020) MFSPV: a multi-factor secured and lightweight privacy-preserving authentication scheme for VANETs. IEEE Access. https://doi.org/10.1109/ACCESS.2020.3014038

34. Alazzawi MA, Lu H, Yassin AA, Chen K (2019) Efficient conditional anonymity with message integrity and authentication in a vehicular ad-hoc network. IEEE Access 7:71424–71435

35. Engoulou RG, Bellaïche M, Pierre S, Quintero A (2014) VANET security surveys. Comput Commun 44:1–13

36. Kenney JB (2011) Dedicated short-range communications (DSRC) standards in the United States. Proc IEEE 99(7):1162–1182

37. Alfadhli SA, Alresheedi S, Lu S, Fatani A, Ince M (2019) ELCPH: an efficient lightweight conditional privacy-preserving authentication scheme based on hash function and local group secrete key for VANET. In: Proceedings of the 2019 the world symposium on software engineering, pp 32–36

An Effective Protection Approach for Deceive Attacker in AES Attack

R. Shashank and E. Prabhu

Abstract Nowadays, data security has gained much importance. Encryption has evolved as a solution and is now a necessary component of every information security system. A variety of processes are necessary to protect the shared data. The present research focuses on employing encryption to protect data as it travels across the internet. This paper proposes that the data being sent from sender to receiver in the network must be encrypted using the AES-128 encryption approach. Decryption techniques allow the recipient to access the original data. This study examines the methods for manipulating messages and data. Most of the time, these attacks substitute encrypted data with corrupted data, resulting in unwanted data. These data are included by attackers throughout RTL design, physical design layout level, and maybe manufacture levels. Hardware Trojans are the term for them. However, there is a countermeasure for every assault, and therefore in this work, a deception of attacker approach is proposed to enable data transaction.

Keywords Advanced encryption standard (AES) · Finite state machine · Hardware trojan · Verilog hardware description language · QuestaSim 10.4e

1 Introduction

In today's fast-paced technological world, sending a message from one device to another has never been easier or faster. This transmitting and receiving can be in the form of an image message, sensitive data in the form of words or bits, or both. At the same time, the same technology is being utilized to steal or corrupt those messages. As a result, message encryption is employed, which generates a message that is incoherent or altogether different from the original message. Even if an attacker gains access to the system, decrypting the encryption data makes it harder for them to steal data [1]. Only one key is needed to encrypt, and decrypt data is done with symmetric

R. Shashank · E. Prabhu (✉)

Department of Electronics and Communication Engineering, Amrita School of Engineering, Coimbatore, Amrita Vishwa Vidyapeetham, Coimbatore, India

e-mail: e_prabhu@cb.amrita.edu

keys encryption, also known as secret key encryption. Cryptography methods such as DES and AES provide several examples of strong and weak keys. DES technique uses a single key which is of 64 bit whereas, AES supports wide varieties of keys such as 128, 192, and 256-bit keys.

To tackle the problem of key distribution, asymmetric key encryption, also known as public key encryption, is employed. In asymmetric keys, there are two sorts of keys: public and private keys. A public key is used for encryption data, and a private key is being used to decrypt it (e.g., RSA and Digital Signatures). The public key is visible to the public and the private key is only visible to the user [2]. It is not authorized to issue them before sending them out. Public key encryption, on the other hand, is based on mathematical functions, which is computationally intensive and inefficient for small mobile devices.

To encrypt and decode electronic data in cryptography, a symmetrical key is used. It implies that you must encrypt and decode data using the same key. This is because data is changed to a type using symmetric encryption techniques, which only a secret key can decipher. As a result, the symmetrical technique has a high level of security. Symmetric key algorithms are usually very safe. Asymmetric key algorithms are generally believed to be less safe. It is thought that some symmetric key algorithms are virtually indestructible. Furthermore, symmetric key approaches are quite fast. Therefore, they are typically employed when a large amount of data needs to be encrypted.

Coming to assault techniques, AES-128 was the target of a known-key attack in 2009. A known key was utilized to decipher the encryption's structure. However, the attack only targeted an eight-round variant of AES-128, as opposed to the usual 10-round variant, rendering the danger very low. Side-channel attacks pose a significant danger to AES encryption. Side-channel attacks entail gathering knowledge about how a computer performs cryptographic operations in order to reverse-engineer its cryptographic system [3]. Side-channel attacks can be defended against by avoiding data leakage. In addition, randomization approaches can assist in preventing any correlation between cipher-protected data and any leaked data that could be gathered via side-channel assault.

The encryption and decryption implemented here is in Verilog [4]. Synthesis programs employ Verilog as an input to build a gate-level description (a netlist) for the circuit. There are some Verilog constructs that cannot be synthesized. The size and speed of the synthesized circuit are also influenced by the way the code is written. Non-synthesizable structures should only be used for test benches because most readers will wish to synthesis their circuits. These are program modules that create I/O for the rest of the design simulation.

Everything is integrated on a single chip in a System-On-Chip (SOC), resulting in significant space and cost savings. However, a third-party vendor may be involved in the design of a chip at times. As a result, there's a good probability that an attacker might sneak their IP/block into the process when designing various phases. As a result, it's difficult to track down the attacker's block, which could potentially alter data in our situation. The attackers might place the block anywhere in the process, causing data corruption. Instead of detecting the blockage, a protection block is

added before decryption, which initiates a comparison that informs the system that an attacker is there, and a deception process is initiated, as indicated.

The entirety of the paper is structured as follows: Sect. 2 introduces the AES-128 encryption and decryption, Sect. 3 outlines the Trojan attack on encryption mechanism, Sect. 4 discusses the proposed protection model, Sect. 5 illustrates the results and implementations, and Sect. 6 covers the conclusion.

2 AES-128 Encryption and Decryption

The Advanced Encryption Standard (AES) algorithm is known for its high speed as well as its security. The implementation of both hardware and software is even quicker. NIST recommends that DES be replaced with a new encryption standard. It can be used on a variety of platforms, including mobile phones and tablets. For many security applications, it has been thoroughly tested. To calculate all the round keys from a key, a key schedule algorithm is utilized. Thus, the initial key is utilized to generate a large number of round keys that will be employed in each round of encryption. The AES-128 encryption goes through a series of stages naming: 1. substitution box, 2. shift rows, 3. mix columns, and 4. add round key which is depicted as shown in the Fig. 1 [5].

1. Substitution box: S-box is another name for the substitution box. This is a fixed table that will replace the plain text provided. This AES employs the Rijndael S-box. There are 16 columns and 16 rows in the Rijndael S-box. The column is chosen by the least significant nibble, whereas the row is defined by the most significant nibble. A four-row, four-column matrix is the outcome.
2. Shift rows: In a circular pattern, the matrix's four rows are being shifted to the left. The first row doesn't shift. By one position, the second row shifts to the left. The third row advances two spaces to the left, whereas the fourth row moves three spaces.
3. Mix columns: A specific math function occurs in this block, in which the first row of a fixed matrix is multiplied by the current state matrix. These data are then XORed to produce a new state matrix.
4. Add round key: To generate the AES-128 bit key for each round, add round key place key function. The total number of rounds in 128 bit is ten, from round one to round ten. The user specifies the default key value for Round0. To get the new state matrix, the state and round0 matrices are XORed. Crypt text is produced in the final round. The 128 bits are then translated into 16 bytes and the procedure is repeated.

The same four blocks are used in AES decryption, but in reverse order [6]. (a) Inverse shift rows, (b) inverse replace bytes, (c) add round key, and (d) inverse mix columns are used in decryption to inverse all the processes that were accomplished during encryption. In the third step, the outcome of the first two phases is XORed
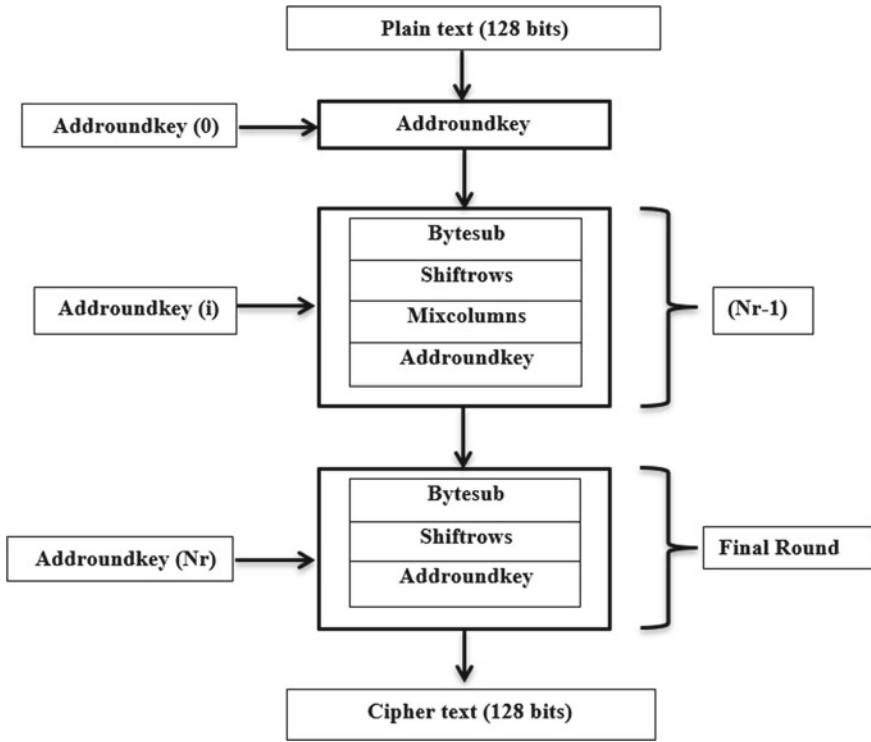
Fig. 1 Block diagram AES 128-bit encryption

with four words from the key schedule. In the last phase of decryption, the "inverse mix columns" step is bypassed. Despite the fact that it is similar to AES encryption, it should be implemented separately and then executed at the same time.

3 Trojan Attack on the 128-Bit AES Encryption

Hardware Trojans [7] are malicious software that alters a hardware circuit's intended operation. These changes are unwanted and unknown to the hardware designer, and they can have devastating effects on the electrical grid. Malicious purpose, evasion of detection, and rarity of activation are three fundamental characteristics of Trojans. A Trojan's goal is always the same: to perform an unanticipated action that compromises the underlying hardware's confidentiality, integrity, or authentication [8].

The Trojan can be a software or code which doesn't disturb the code unless it gets triggered. Trojans are initiated by a trigger and perform a specific function known as a payload [9]. In a multi-million transistor Soc design, they can vary greatly in

size from some transistors to thousands of gates, based on their size relative to the remainder of the circuit. Trojans come in a variety of shapes and sizes.

Sequential or combinational digital circuitry is frequently used to energize them (or a hybrid of the two), although they can also be triggered by analog stimuli [10]. It's feasible that the payload is digital or analog, and each is carefully designed to dispatch malevolent outcomes when activated. This Trojan could be programmed to corrupt, damage, or steal data, or to perform malicious actions on the system or network. These Trojans can be accessed via a backdoor, which is achieved by installing third-party software or by granting access directly [11]. The Denial-of-Service Trojan is a type of malware in which a hacker remotely controls a signal that is accessed through a link. There is a ransomware malware that prevents data access and pressures users to pay a ransom. If they do not comply, they will corrupt or sell the data to competitors.

The goal of this hardware Trojan attack is to tamper with data and make the output useless to consumers [12]. When the attackers do not want the information shared with the recipients, these types of attacks are imposed, and are most common in military and corporate settings. In this approach, they suffer significant losses in terms of money, national security, and individuals. The attacker uses a block with a trigger and payload, as well as corrupted data in memory, as in the Fig. 2. The trigger block contains Finite State Machines (FSM) [13], which extracts four different bits from the AES-encrypted bits. The FSMs are necessary for comprehending the logic of decision-making and controlling digital systems. In the FSM, the outputs are the current state and the input function, as well as the subsequent state. This implies that the selection of the subsequent state is primarily determined by the input value and power, resulting in a more complex system's performance.

In a system where specific inputs result in specific state transitions, finite state machines may be used to represent the system. These bits travel through an XNOR process, causing the FSM to select the incorrect data via MUX. This corrupted data is sent to be decrypted later.
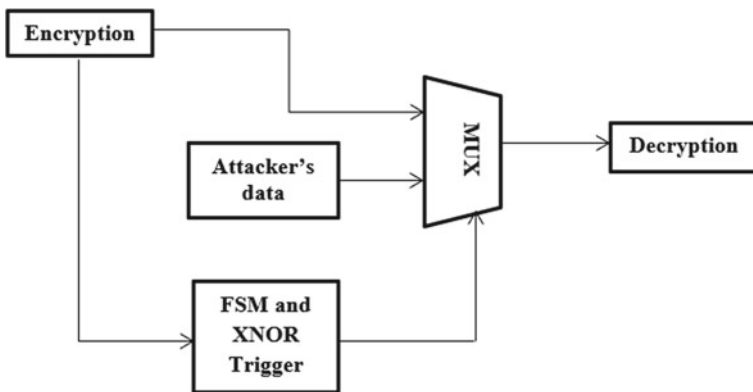

Fig. 2 Hardware trojan block diagram

4   Proposed Protection Model

Deception takes strategic weaknesses to manipulate people's perceptions, which has a direct impact on their perceptions, decisions, and deeds. It could be valuable for both hackers and cyber-defenders. In this paper, a deception approach [14] is used as a cyber defender, in which the attacker is deceived into believing that the system bits have been corrupted with his data, despite the fact that those are the required encrypted bits in mapped bits form.

The attacker intends to communicate the decrypted data to the attacker. Instead of detecting and fixing the block, a "Tester" protection block [16] is inserted in front of the decryption as shown in Fig. 4. A comparator, a mapping block, and a remapping block are all included in this block. The comparator block compares the incoming data for decryption to the encrypted data' golden reference [15]. If the data matches the golden reference, it is passed to the decryption block directly. If a difference is discovered, it can be assumed that a Trojan is running in the background. The golden reference encrypted is directed to map ping as shown in Fig. 3.

There are three sets in this mapping block. Each set has its own mapping, which uses the set to replace the encrypted bits. If the mapper selects set-1, for example, encrypted bits are replaced according to the set. If in the mapping block "5" is mapped to "0", "a" is mapped to "4", and "f" is mapped to "b", then the identical elements 5, a, f present in the encrypted bits are replaced by 0, 4, b, respectively. This set selection is entirely at random. The attacker could be fooled if he just saw the mapped output.

To decrypt the data, the mapped bits must first be remapped to the encrypted bits. To begin, the set's selection should be updated in the remapping block. Then the bits around are swapped until the result is the same as the encrypted bits.

The encrypted bits are sent to the decryption block, which will decrypt the original bits. Once enabled, this remapping is done behind the scenes; otherwise, the attacker would only be able to view the mapped bits, presuming the data is corrupted. As a result, the bits are protected from attackers.
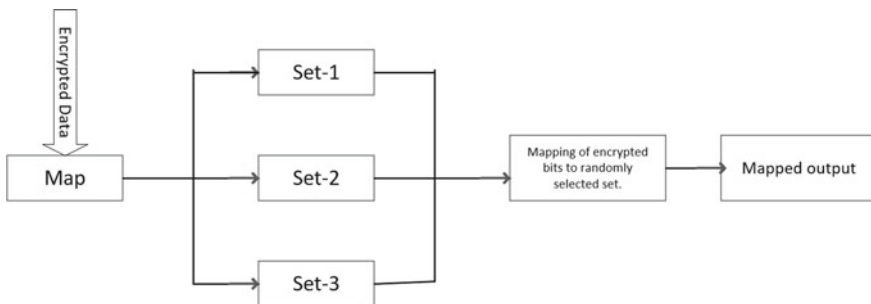

Fig. 3 Block diagram of mapping

Fig. 4 Block diagram of proposed protection scheme

5 Results and Discussions

The data and the key in AES are provided. The symmetric AES algorithm is utilized here, which means that the same key is used for encryption and decryption. The output, i.e., the original given data, is not noticed if the key defers at any point. The "BLOCK" is where the input data is delivered and the key is used in the encryption process, as shown in the Fig. 5. The "encrypted output" illustrates that the data and key are encrypted, and that even if the same key is used, and data for each run, the encrypted output will be different. The "result" is the output of a decrypted block using encrypted output, and key is the input. If the output matches the input, the system is free of Trojans and deflections.

If an attacker block is present, it passes the tainted data to the decryption block, causing a delay in output. When the Trojan is activated by the FSM, which has the inputs from the encrypted bits, the corrupted data stored in a memory register is delivered, as seen in Fig. 6. The tester block is placed to help detect as well as confuse the attacker in order to secure the data from the attacker, presuming the attacker's block is unknown.

The findings show that the "Result" is not the same as the input, implying that the system is compromised or that a Trojan is present. However, the encrypted bits are mapped to specific bits from other sets as shown in Fig. 7. This way, the attacker

Fig. 5 Simulation result for AES-128 encryption without trojan insertion

Fig. 6 Simulation result for AES-128 encryption with trojan insertion

Fig. 7 Simulation result for proposed mapping technique

Fig. 8 Remapping and decryption of the data

could be tricked, and to recover the encrypted data, the remapping block should be activated to obtain the encrypted bits, which are then delivered to the decryption block at the receiver's end to recover the original input data, that is observed in Fig. 8.

6 Conclusion

In today's technology, data security is a bit dangerous. The attackers are continually attempting to corrupt or steal data. This research demonstrates a root to safeguard data from deception by attackers. The results are tested on a simulator to provide insight into how to trick the attackers. The Questasim10.4e simulator has been designed to be a user-friendly simulator that displays the results prominently. Verilog is the hardware description language that is employed for developing this methodology. A hardware Trojan is introduced and activated before protection in order to illustrate the attack and its countermeasure. Even if the Trojan is activated, the comparator may detect the difference and attempt to modify the mapping block. As a result, the attacker is deceived.

References

1. Thambiraja E, Ramesh G, Umarani R (2012) A survey on various most common encryption techniques. Int J Adv Res Comput Sci Softw Eng 2:226–233
2. Mahajan P, Sachdeva A (2013) A study of encryption algorithms AES, DES and RSA for security. Global J Comput SciTechnol
3. Sivaganesan D (2021) A data driven trust mechanism based on blockchain in IoT sensor networks for detection and mitigation of attacks. J Trends Comput Sci Smart Technol (TCSST) 3(01):59–69
4. Thomas D, Moorby P (2008) The Verilog® hardware description language. Springer Science Business Media
5. Borhan R, Fuad Tangka Aziz RM (2012) Successful implementation of AES algorithm in hardware. In: 2012 IEEE international conference on electronics design, systems and applications (ICEDSA), pp 27–32. https://doi.org/10.1109/ICEDSA.2012.6507810
6. Wang W, Chen J, Xu F (2012) An implementation of AES algorithm based on FPGA. In: 2012 9th International conference on fuzzy systems and knowledge discovery, pp 1615–1617. https://doi.org/10.1109/FSKD.2012.6233811
7. Krishna AV, Prabhu E (2022) Hardware trojan detection at behavioral level using inline assertions and verification using UVM. In: Smys S, Balas VE, Palanisamy R (eds) Inventive computation and information technologies, Lecture notes in networks and systems, vol 336. Springer, Singapore
8. Gowtham M, Harsha KS, Nikhil J, Eswar MS, Ramesh SR (2021) Hardware trojan detection using supervised machine learning. In: 2021 6th International conference on communication and electronics systems (ICCES), pp 1451–1456
9. Deepthi S, Ramesh SR, Nirmala Devi M (2021) Hardware trojan detection using ring oscillator. In: 2021 6th International conference on communication and electronics systems (ICCES), pp 362–368. https://doi.org/10.1109/ICCES51350.2021.9488935
10. Vinta M, Sivanantham S (2020) Modeling and test generation for combinational hardware Trojans. In: 2020 IEEE international test conference India, pp 1–4. https://doi.org/10.1109/ITCIndia49857.2020.9171791
11. Jin Y, Kupp N, Makris Y (2009) Experiences in hardware trojan design and implementation. In: 2009 IEEE international workshop on hardware-oriented security and trust, pp 50–57
12. Hemachand M, Prabhu E (2020) Secured netlist generation using obfuscation technique. J Crit Rev 7(4):878–881
13. Wang TH, Edsall T (1998) Practical FSM analysis for Verilog. In: Proceedings international verilog HDL conference and VHDL international users forum, pp 52–58. https://doi.org/10.1109/IVC.1998.660680
14. Karuna P et al. (2018) Enhancing cohesion and coherence of fake text to improve believability for deceiving cyber attackers. https://aclanthology.org/W18-4104
15. Bhunia S, Hsiao MS, Banga M, Narasimhan S (2014) Hardware trojan attacks: threat analysis and countermeasures. Proc IEEE 102(8):1229–1247. https://doi.org/10.1109/JPROC.2014.2334493
16. Chakraborty RS et al. (2013) Hardware trojan insertion by direct modification of FPGA configuration bitstream. IEEE Des Test 30(2):45–54

Effective EMI Reductıon in Medical Devices and Automotive Power Converters

S. Sasipriya, D. Ruth Anita Shirley, A. R. Rincy, S. Sruthi, and K. Yazhini

Abstract Advanced automotive electronic-control technology has led to added electronic equipment in the vehicle. Frequencies and power have gradually increased in the vehicle, creating a denser atmosphere of electromagnetic waves. The automotive components tend to produce Electromagnetic Interference (EMI). This will greatly contribute to EMI in the vehicle, thus disturbing electrical/electronic equipment and possibly damaging electrical/electronic components. Implantable Cardioverter Defibrillator (ICD) monitor your heart rate with a battery-powered device placed under the skin. ICD is connected to heart using thin wires. An electric shock will be delivered if it detects an abnormal heart rhythm if your heart is wildly beating and too fast. These medical devices tend to malfunction when they are exposed to high levels of EMI radiation. Electromagnetic compatibility (EMC) regulations must be met by the automotive industry and individual vehicle manufacturers. Regulatory compliance to EMC standards and CISPR 25 for automotive application circuits must be met which are not achieved under certain circumstances. For medical devices like ICDS CISPR 22 standards must be met. The radiation from EMI is capable of causing pacemaker or ICD malfunctions, ICDs to send shocks that aren't needed, and EMI can interfere with PA sensor readings. Here, two types of filtering techniques have been designed in order to mitigate the CM noise which affects performance of Electromagnetic Compatibility (EMC). The results were compared, and the effective filtering solution is identified to reduce the conducted emission due to common-mode noise

S. Sasipriya · D. Ruth Anita Shirley · A. R. Rincy · S. Sruthi (✉) · K. Yazhini
Department of ECE, Sri Krishna College of Engineering and Technology, Coimbatore, India
e-mail: 18euec159@skcet.ac.in

S. Sasipriya
e-mail: sasipriyas@skcet.ac.in

D. Ruth Anita Shirley
e-mail: ruthanitad@skcet.ac.in

A. R. Rincy
e-mail: 18euec140@skcet.ac.in

K. Yazhini
e-mail: 18euec183@skcet.ac.in

491

for the range of frequency from 150 kHz to 18 GHz according to the standard. As per EMC standard CISPR 22, the RF inductor is depicted and investigated within 150 kHz–30 MHz frequency range. The capacitive and parasitic impedance are calculated and used in the simulation process. This allows us to reduce the noise by as much as 30 dB which is an efficient noise reduction.

1 Introduction

In automotive and medical circumstances, linear regulators are replaced by switching regulators in areas where low heat dissipation and efficiency are rated. A switching regulator employs a switching element to convert the incoming power source into a pulsed voltage, which is subsequently smoothed by capacitors, inductors, and other components. To transmit energy along with input to output, switching regulator circuits makes use of an inductor, a power switch, and a diode. Upon rearranging the fundamental components of the switching circuit, a step-up (boost) converter, an inverter (flyback) or a step-down (buck) converter can be fabricated.

The possible issue when numerous DC/DC switch mode regulators have been paralleled for current sharing and increased output power, interference and noise can be generated. In the presence of multiple regulators operating at similar frequency in a circuit, then the combined energy that is being generated can be intensified at one frequency. In addition, this energy can be a trouble if other PC boards that contains ICs or boards on other systems are closer together and this radiation may affect those who are suspectable. Specifically, it could be problematic in systems that are automotive which are frequently in near proximity to the RF, audio, radar, and Controller Area Network bus systems. Furthermore, the foremost active component on the input power line is switching regulator. On that account, it has a serious impact on the EMI performance of the complete converter circuit. As a result of the switching, other parts of the circuit experience voltage and current overshoot, which results in input and output voltage ripple and current ripple, and transient energy spikes at the switching frequency.

The consequences of system interference can be terrible in automotives. It has been reported that airbags are spontaneously deployed, due to transmissions and engine management systems from emergency service vehicles, and the cruise control systems which are forcing 'full throttle' upon the exposure of electromagnetic waves [1]. On top of that, it has also been reported that "When certain types of cell phones are held close to the steering, the RF fields propagating can ignite the explosives that detonate the airbag around 1.8 GHz and over 100 V/m, while automotive EMC testing is only required for 1 GHz and 24 V/m".

In ICD's, one possible complication due to EMI is the triggering of arrhythmic events. The frequency ranges from 10 to 60 Hz in EMI signals can affect the devices used for heart negatively. The electromagnetic interference (EMI) in the implantable medical device can be produced by various external sources like mobile phones, radio frequency identification (RFID) based systems, and microwaves. Also, EMI is a critical concern in medical equipment's leading to electronic system malfunctions under varying levels of EMI. The electromagnetic compatibility (EMC) are important to sustain the stable and normal function in implantable medical devices as humans are always surrounded by electrical equipment's.

CISPR 25 Standard has been followed to reduce the EMI emissions in automotive environments. CISPR 25 is concerned with "radio disturbance characteristics for the protection of on-board vehicle receivers."

CISPR 22, which is often used in all European EMC standards, covers measuring methodologies, measurement equipment, limit lines interpretation, and limit line application for medical devices. Thus, the RF inductor is designed and investigated for automotive power converters as per EMC standard CISPR 25 within the frequency range of 150 kHz–18 GHz and for medical devices as per EMC standard CISPR 22 within the frequency range of 150 kHz–30 MHz.

2 Literature Survey

EMI occurs in different ways and occurs due to various sources. But it is still to be caused by unwanted currents or by unwanted voltages which are present, that affects the electronic system's performance or an electrical device's performance negatively. When we manage the EMI, it gives a huge number of various solutions at emitter as well as victim devices. From time to time it is as simple as that of fixing as devices that are moving so there can be much gap between source and the victim and also could rotate single device which can perform the needed trick. The fixes that are done as mentioned above will get those things to be done and the solution which is better for this kind of case will include all the equipment's appropriate design for reducing the discharge or by manufacturing less vulnerable external disturbance to equipment.

Paul and Hardin [2] have described a systematic method for diagnosis and to reduce the conducted noise emissions. Majority of emission problems in equipment are caused by common mode currents as found by EUT test [3]. For predicting the conducted EMI from a boost converter (DC-DC) a terminal modeling technique was proposed in [4] and there was a good agreement by predicting these conducted emissions up to 50 MHz as proposed by Laour et. al. [5]. The results demonstrated by employing a filtering technique shows that both the emission levels (conducted and radiated) can be lowered to 30 dB.

The EMI produced by the buck converter (DC-DC) has an impact on the integrated circuit's performance when it receives the power from the buck converter [6]. To counter this problem, the PCB design is modified for including definite planes for

both input and output and also for switching and ground ports [7]. The noise level of a DC-DC buck converter was discussed using an example of filter design in compliance with the standard CISPR25 [8]. Power sources have become a major contribution to the degradation of the electromagnetic environment. Nagrial and Hellany [9] seeks to explore the topic of EMI in SMPS in general, incorporating basic ideas and EMC categories.

A number of approaches are used to identify the root cause of the EMI [10]. To decrease CM noise, EMI filters are utilized, however their efficiency is highly influenced by the parasitic effects of the grounding pathways [11]. Electrical modules and electronic control units with a high density are now widely incorporated into current car systems. [12]. Automotive electronics, such as any high-speed, sophisticated digital electronic system, may be a source and highly susceptible to EMI, and failure can be lethal [1]. There were instances of airbags voluntarily positioning, when exposed to EMI. The emergency service vehicle RF transmissions and engine management, as well as cruise control systems, demand "full throttle.". The interactions between parasitic parameters in EMI filters and transformed impedances by power interconnects are thoroughly investigated [13]. It has been discovered that interactions can decrease the CISPR 22's norms for measuring the CM conducted voltage emissions on vulnerable twisted pair cables and specifies the use of Impedance Stabilization Network (ISN) [14].

In implantable cardioverter defibrillators the EMI might result in oversensing and, as a result, improper ICD therapy. The present prevalence and clinical significance of EMI-related oversensing was investigated in [15]. Noise qualification tests for electromagnetic compatibility (EMC) are typically performed after a prototype has been developed, constructed, and tested, and the procedure was repeated if non-compliance occurs [16]. It is consequently desirable to be able to evaluate compliance with EMI standards at the designing stage [17]. The major cause of the EMI in power static converters was semiconductor devices switching.

In some cases, like fast power device which emit significant amounts of radiation as common mode (CM) and differential mode (DM) currents in high frequency mode a two-wire unshielded and shielded energy cables was described in [18]. In [19] a distributed parameter model that accounts for skin and proximity effects, as well as dielectric losses was discussed. The radiations can interfere with the operation of other devices in some situations, which is known as electromagnetic interference (EMI). Understanding the reception route of the EMI or noise is required to make a system more immune [20]. The DC-DC converter's performance was significantly improved along with a reduction in conducted emissions and radiated emissions as per the EMC standard [21]. Different algorithms involved in constructing the electrical impedance tomography for medical imaging applications was discussed [22]. A rechargeable battery embedded with an implantable medical device was proposed [23] to support uninterrupted monitoring of the vital signs such as blood pressure, pulse rate, body temperature and respiration rate.

In [24] an EMI filter was proposed to minimize interference the common mode and difference mode signals.

The current focus of the research is to minimize the conducted and radiated emissions through a proper filter design and physical modelling through the PCB layout and implementation. The DC-DC converters designed to minimize the EMI should provide a constant output suitable for medical and automotive applications. An RF inductor filter is proposed in this paper to improve the performance of ICD and automotive power converters by reducing the EMI.

3   Methods to Mitigate EMI

EMI emissions are of two types

(1) Conducted EMI is basically coupled through the cables and physical conductors such as power connections, parasitic impedances and ground connections. Requirements of conductive emissions can be met relatively early in the design process, because the noise is confined to a specific connector or terminal.

(2) Radiated EMI is coupled through radio transmission sources through the air due to magnetic fields (magnetic coupling) or electric fields (capacitive coupling). An electromagnetic field is radiated by the board that carries current. On the board, each trace plays the role of an antenna whereas every copper plane plays the role of a resonator. The noise is produced throughout the spectrum when any other signal other than the sine wave or DC voltage is passed. It is not possible to perform formal radiated emissions testing until the design is practically completed.

A common-mode choke is used to minimize the common-mode currents that occur due to the conducted and radiated EMI. A non-zero potential difference between different ground regions is another cause of the common-mode currents and is minimized by connecting all grounds to the same potential.

The electromagnetic compatibility (EMC) of a system in an environment is determined by the below three criteria.

- It doesn't induce interference with systems nearby.
- It is unaffected by the emissions from other systems.
- It doesn't produce interference by itself.

The following are the three different methods used to eliminate EMI:

- Shielding,
- Filtering and
- Grounding.

Filtering is a direct way to remove the unwanted signals. Nowadays, passive filters are used to eradicate EMI in equipment's. For example, in the product line of magnetic components, the EMI is reduced by inductive filters in which the common-mode

choke obstructs undesired noise thus, allowing only the required signals to move through.

The different types of filters are:

- DC filters
- Common mode filters
- Difference mode filters
- EMI filters
- RF inductor filters.

DC filters: The high-frequency currents are occluded by means of passing DC and low-frequency currents. A differential mode rejection in low frequency is added to this filter which diverts the needless noise and allows the device to work precisely.

Common mode filters: Generally, common-mode filters play as an inductor for common-mode noise as well as transmission line for differential mode signals. The filters that act as inductor for common-mode noise will have an impedance known as "Common-mode impedance". For a common-mode rejection process, an impedance value of 100 MHz is used as a standard indicator.

Differential mode filters: An outgoing signal current travels through one wire, then returns along the other differential mode. In the core, the magnetic fluxes oppose each other, aborting each other out to allow the signal to pass through.

EMI filters: Electromagnetic interference (EMI) filters are one of the constructive ways to protect against the harmful impacts of electromagnetic interference. It is also known as radio-frequency interference (RFI) filters.

RF inductor filters: RF Inductor filter design not only effectively shields but also decouples the signals which might agitate the functionality of an electronic component. In order to eliminate the noise, the selected signals are passed through accordingly.

Grounding: It can be defined as a formation of conductive electric path between the reference ground plane and electronic/electrical element of a system. It can also refer as a connection made to the earth electrically.

The following methods should be practiced in order to attain the finest possible ground:

- Ensure that the internal circuits and components are lead free to reduce the inductance.
- On a large ground, use multiple ground points for desirable outcome.
- Isolate circuits from ground when the loop voltages are uncontrollable.
- It is advisable to separate analogue and digital grounds which can be combined later.

Shielding is where the circuit is enclosed in a completely sealed environment, like a metallic box to contain the radiation in source or casualty devices. An enclosure that has shielding is essential for reflecting electromagnetic waves into it and absorbing waves that are not reflected. On the whole, radiation eventually penetrates the shield

if the shield is not thick enough. Any common metals like steel, copper, aluminum etc., can be used for shielding.

An RF-inductor filtering technique is being proposed for suppression of EMI in medical devices and automotive power converters as per the EMC Standard.

4 Existing and Proposed System

In present-day electronic systems, it is difficult to reduce the high-frequency common-mode electromagnetic interference (EMI). Moreover, there will be a notable difference in the filter efficacy when there are two filters with identical topologies and different layouts [13]. Generally, to suppress CM noise, EMI filters are utilized which is depicted in Fig. 1. But parasitic effects due to the grounding path affects the performance of the filter immensely.

Moreover, in automotives transportation systems like ships, electric vehicles, and aircrafts are becoming increasingly excited where numerous power converters are closely packed in a space to execute missions. In this closely networked architecture, a significant increase in the overall CM EMI is emitted to the shared ground, exhibiting a nonlinear variation resulting in a very noise environment [25] When designing a power network, a Wide Bandgap (WB) power switch has a severe effect. CM EMI analysis of a power converter is the state of the art. Nevertheless, limited research has been done on the CM EMI network constructed with numerous power converters. Power electronic network architecture designers will have an add on degree of freedom by using the existing CM EMI filter in wide power circuit systems without any trade-offs.

The proposed design uses an RF–inductor filtering method to extinguish EMI in automotive power converting systems. In this technique, a ground inductor is inserted (earthed through an RF inductor). At high frequencies, the RF inductor avoids the return current of common mode (CM) noise. It has been inserted between the earth ground and the chassis ground of the converter. Hence, it isolates the converter chassis from the power line ground. Besides, it maintains electrical safety grounding with
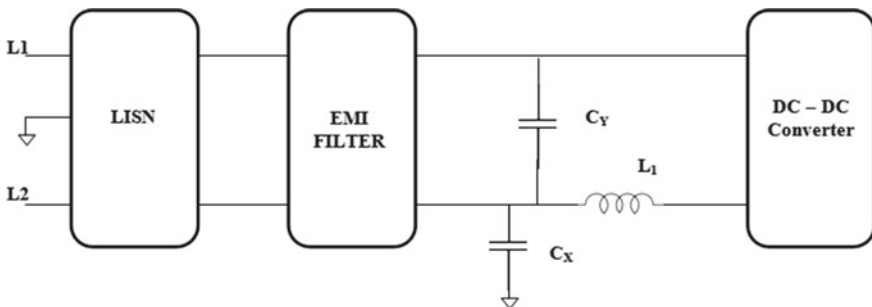

Fig. 1 Block diagram of EMI filter in DC-DC convertor

low impedance to ground at power frequencies. Combination of measurements and simulations for fast testing is used to demonstrate the effectiveness of the proposed method. A specific standard is used to compare the level of CM current. This exhibits a result of reducing EMI emission to as much as 30 dB. Furthermore, the proposed method can also be practically implemented with ease, and the ground inductor is sized primarily with accordance to the CM current, that is much lower than the supply current.

The source of radiated EMI is identified and minimized through the software that integrates with the physical layout of PCB design and analysis. A simple and most effective model of common mode current has been developed and simulated based on a single measurement of CM voltage without using any EMI filter at the terminal of the line impedance network stabilizer (LISN).

5   Results and Discussions

Buck converters are designed as fixed frequency, current control circuits which operate from 3 to 20 V. Using the proposed circuit, it is possible to reduce the output to 0.8 V and operates at a fixed frequency of 700 kHz. The circuit produces a stable and continuous current, improving its transient performance. Figure 2a–c depicts the PCB layout, implementation and experimental setup of the proposed model.

The ADP2303 step down converter down converts the input 12 V DC voltage to 6 V as in Fig. 3. for a peak current of 3 mA. The corresponding current waveforms is observed as in Fig. 4.

The MATLAB simulation output of noise in time domain with and without filter is shown in Fig. 5. It is observed that the noise of the proposed RF filter falls between − 1.5 and + 1.5 V compared to the EMI filter which lies between − 2.4 and + 2.4 V.

Table 1 depicts the noise voltage with and without filters. It is proved that the RF Filter is an effective solution to reduce EMI in power convertors.

6   Conclusion

The purpose of this work is to minimize the conducted emissions existing in automotive power converters and medical devices that might cause malfunctions of the electronic systems. In this proposed work, we have introduced a constructive solution to minimize and suppress the common-mode noise in the automotive and medical environment by means of RF inductor filtering technique. MATLAB software is used for simulation, and LISN is used for testing based on the CISPR-22 and CISPR-25 standards. The results of the filters designed is compared and the best optimal solution is derived. A tangible reduction in a noise voltage of up to 30 dB is achieved with the proposed filter as compared to the other DC-DC converter's. The work
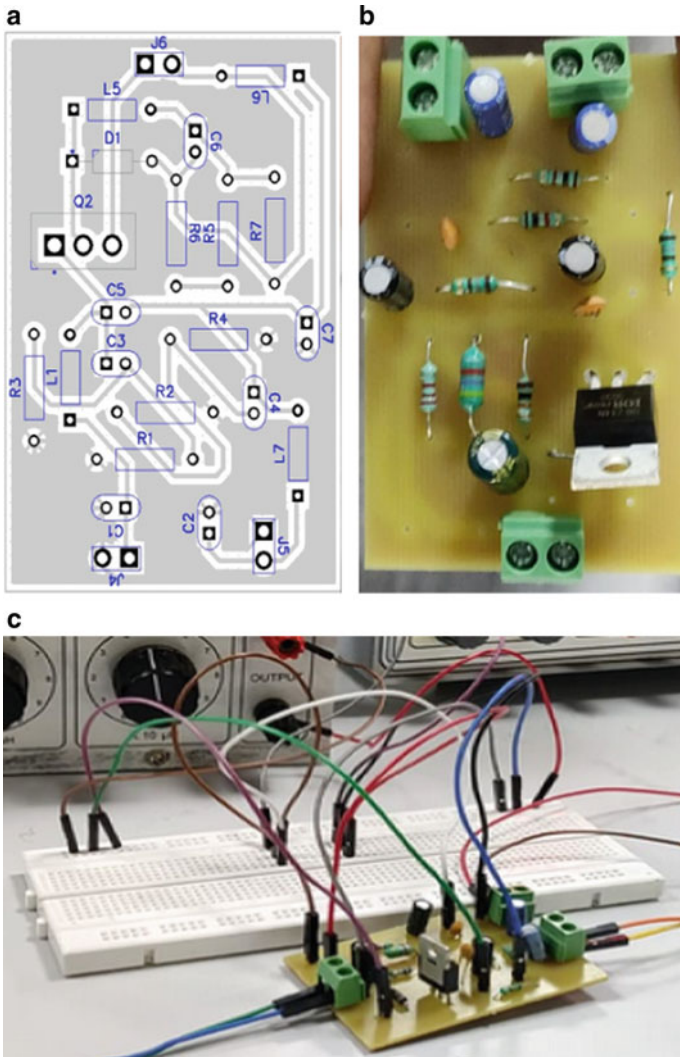
Fig. 2 **a** and **b** PCB layout and implementation, **c** experimental setup

can be extended to analyze the EMI issues using FFT analysis and spread spectrum frequency modulation.
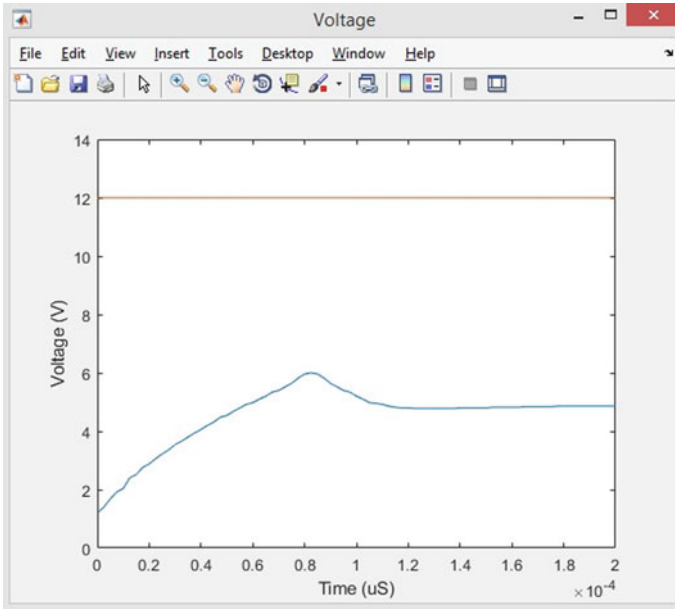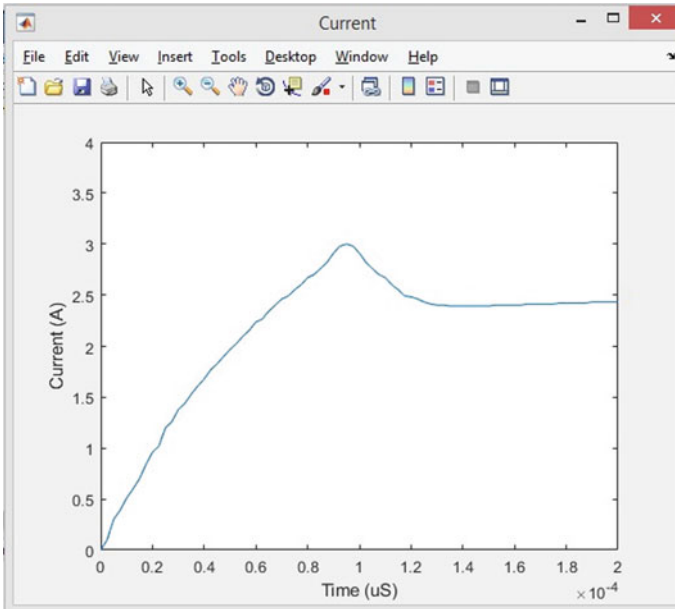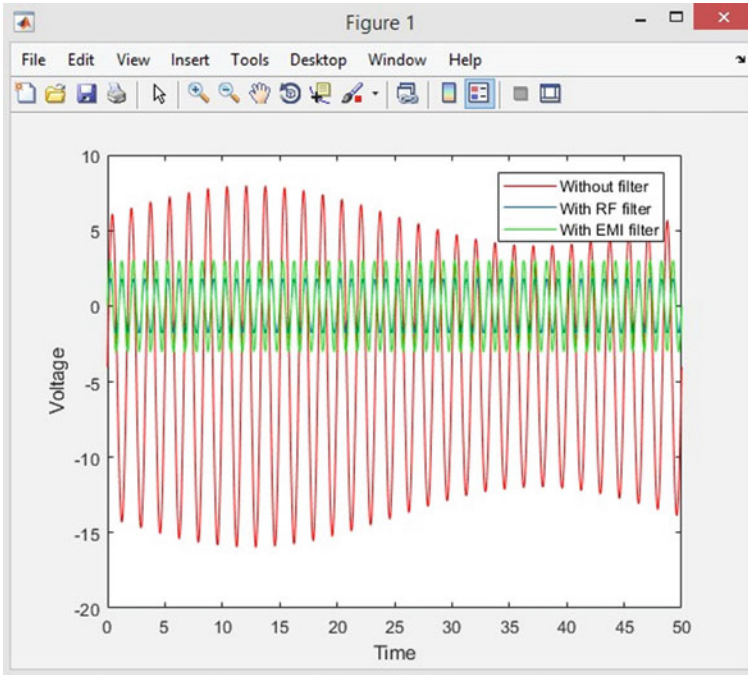
Fig. 3 Voltage waveform

Fig. 4 Current waveform

Fig. 5 Simulation output of noise in time domain with and without filter

Table 1 Comparison of noise voltages

Filter types	Noise voltage (Vp-p)
Without filter	21
With EMI filter	4.8
With RF filter	3

References

1. Bajwa A (2020) EMC/EMI challenges for the connected car. Automotive design, telecom, article
2. Paul CR, Hardin KB (1988) Diagnosis and reduction of conducted noise emissions. IEEE Trans Electromagn Compat 30:19–23. https://doi.org/10.1109/ISEMC.1988.14080
3. Kaires RG (2000) The correlation between common mode currents and radiated emissions. In: IEEE international symposium on electromagnetic compatibility, symposium record (Cat. No. 00CH37016), vol 1, pp 141–146. https://doi.org/10.1109/ISEMC.2000.875552
4. Bishnoi H, Baisden AC, Mattavelli P et al. (2012) Analysis of EMI terminal modeling of switched power converters. IEEE Trans Power Electron 27(9):3924–3933
5. Laour M, Tahmi R, Vollaire C (2017) Modeling and analysis of conducted and radiated emissions due to common mode current of a buck converter. IEEE Trans Electromagn Compat 59(4):1260–1267. https://doi.org/10.1109/TEMC.2017.2651984

6. Park SH, Huynh HA, Kim S (2015) Analysis of EMI reduction methods of DC-DC buck converter. In: 10th International workshop on the electromagnetic compatibility of integrated circuits (EMC Compo), pp 92–96. https://doi.org/10.1109/EMCCompo.2015.7358337

7. Makarenko VV, Pilinsky VV, Gurin VK (2022) The DC-DC converters EMI filters calculation method using LTspice. Tekhnichna Elektrodynamika 35–42. https://doi.org/10.15407/techned2022.02.035

8. Abinaya AB, Magdaline SA (2017) Design and analysis of line impedance stabilization network using RLC components for ITE. In: 2017 International conference on innovations in information, embedded and communication systems (ICIIECS), pp 1–5. https://doi.org/10.1109/ICIIECS.2017.8275974

9. Nagrial M, Hellany A (1999) EMI/EMC issues in switch mode power supplies (SMPS). In: EMC York 99 international conference and exhibition, pp 180–185. https://doi.org/10.1049/cp:19990266

10. Kam KW, Pommerenke D, Lam CW, Steinfeld R (2008) EMI analysis methods for synchronous buck converter EMI root cause analysis. In: 2008 IEEE international symposium on electromagnetic compatibility, pp 1–7. https://doi.org/10.1109/ISEMC.2008.4652125

11. Wang S, Maillet YY, Wang F, Lai R, Luo F, Boroyevich D (2010) Parasitic effects of grounding paths on common-mode EMI filter's performance in power electronics systems. IEEE Trans Ind Electron 57(9):3050–3059. https://doi.org/10.1109/TIE.2009.2037643

12. Jia J (2015) Current scan methods to predict radiated emissions of automotive components according to CISPR 25. https://doi.org/10.17877/DE290R-7441

13. Wang S, Wyk J, Lee FCY (2008) Effects of interactions between filter parasitics and power interconnects on EMI filter performance. IEEE Trans Ind Electron 54:3344–3352. https://doi.org/10.1109/TIE.2007.906126

14. Harlacher BL, Tran M, Stewart RW (2002) CISPR 22 conducted common mode emissions: a discussion on the effect of Balun quality on the calibration of impedance stabilization networks (ISNs). Pain Manage Nurs 1:12–15. https://doi.org/10.1109/ISEMC.2002.1032439

15. Von Olshausen G, Rondak IC, Lennerz C, Semmler V, Grebmer C, Reents T, Ammar-Busch S, Buiatti A, Bourier F, Deisenhofer I, Kolb C (2016) Electromagnetic interference in implantable cardioverter defibrillators: present but rare. Clin Res Cardiol 105(8):657–665. https://doi.org/10.1007/s00392-016-0965-1

16. Grobler I, Gitau MN (2015) Conducted EMC modeling for accreditation in DC-DC converters. In: IEEE IECON. IEEE Industrial Electronics Society, Yokohama, 9–12 Nov 2015, pp 2329–2335

17. Weens Y, Idhir N, Bausiere R, Franchaud JJ (2006) Modeling and simulation of unshielded and shielded energy cables in frequency and time domains. IEEE Trans Magn 42(7):1876–1882

18. Zhou Y, Zhu Y, Song Q, Jin Z, Yang D, Yu X (2011) Prediction and reduction of electromagnetic conducted emission in active clamp forward converter. In: 2011 IEEE international symposium on electromagnetic compatibility. Long Beach, USA, 14–19 Aug 2011, pp 729–733

19. Keiser B (1987) Principles of electromagnetic compatibility. Artech House

20. Stephens L (2009) Understanding EMI reduction techniques, vol 53, pp 18–19

21. Shirley DRA, Sasipriya S (2022) Design and analysis of a RF inductor filter for EMI suppression in an implantable cardioverter defibrillator (ICD). IEEE Trans Power Electron

22. Adam EEE, Babikir E (2021) Survey on medical imaging of electrical impedance tomography (EIT) by variable current pattern methods. J ISMAC 3(02):82–95

23. Smys S, Wang H (2019) Enhanced wireless power transfer system for implantable medical devices. J Electr Eng Autom 1(1):41–49

24. Shirley DRA, Sasipriya S, Sibi T, Ragul B, Praveen S (2022) Reduction of electromagnetic interference using EMI filter in a buck converter. In: Proceedings of international conference on electronic circuits and signalling technologies (ICECST 2022)

25. Amin A, Mannan TI, Choi S (2021) Common mode EMI analysis in power electronics enabled power system. In: IEEE Energy Conversion Congress and Exposition (ECCE), pp 3537–3544. https://doi.org/10.1109/ECCE47101.2021.9595537

Conformal Antenna with Bow and Arrow Shaped Radiator for Wireless Capsule Endoscopy

Pradyut Mohapatra and Sumit Kumar Khandelwal

Abstract This paper presents two conformal antennas for wireless capsule endoscopic systems for robust biotelemetry communications, one of them covers 865 MHz band and the other one covers both 865 MHz and 2.4 GHz ISM bands. Biotelemetry is one of the applications of these bands. Two planar antennas are designed first and then they are conformed around a cylindrical capsule. The simulation is performed in ANSYS Electronics Desktop simulation software and it is observed that the antennas have wider bandwidth at respective bands. The peak realized gain for both antennas at 865 MHz are -18.1 dBi while antenna with bow and arrow shaped radiator has peak gain of -13.3 dBi at 2.4 GHz. Since the capsule needs to be ingested by the patient for endoscopy, biocompatibility has been ensured. The maximum specific SAR value is obtained for both the antennas and is considered safe in accordance with the IEEE standard safety guidelines. The recommended antennas' conformal design idea, omnidirectional radiations, and multiband capability with wider bandwidth in the ISM band(s) will improve the scope for capsule endoscopy and would provide valuable contribution in the domain of biotelemetry.

Keywords Wireless capsule endoscopy (WCE) · Conformal antenna · Industrial, scientific, and medical (ISM) band · Wideband

1 Introduction

Capsule endoscopy is a process that involves using a small wireless camera to examine one's digestive tract. The camera, enclosed within a pill, captures multiple images as it goes through one's digestive tract. Capsule endoscopy, as opposed to

P. Mohapatra (✉) · S. K. Khandelwal
Delhi Technological University, Delhi, India
e-mail: pradyut10@yahoo.com

S. K. Khandelwal
e-mail: sumit.khandelwal@dtu.ac.in

traditional wired cable-connected endoscopies, provides better diagnosis and treatment with less pain and discomfort for patients [1]. Capsule endoscopy can detect and identify anatomical changes in the small intestine like ulcers, Crohn's disease, Celiac disease, Gastrointestinal cancer, and other gastrointestinal illnesses.

Capsule endoscopy has several advantages over conventional endoscopic techniques. This procedure can investigate the small intestine, which can be difficult to reach during an upper endoscopy or colonoscopy. In classic endoscopic treatments, a flexible tube with a video camera passes through one's digestive tract which can be painful. In contrast, capsule endoscopy is as simple as swallowing a tablet. The disposable capsule travels through the rest of the gastrointestinal tract before being excreted from the body naturally and painlessly. It can also identify intestinal issues that are not obvious on imaging tests such as X-rays or CT scans. Capsule endoscopy provides the added benefit of requiring minimal preparation and no anesthetic. So, in this paper we have designed an antenna which will be useful in WCE and also have ensured that it is biocompatible so that the antenna does not harm the patient. Usually, capsule endoscopy is a painless and risk-free process. It does, however, have a few flaws. The capsule has a very modest probability of becoming stuck in the patient's small intestine and causing a blockage.

Two types of antennas are considered for capsule endoscopy. Embedded antennas are placed inside the capsule cavity. While the conformal structure only uses the capsule module's surface, leaving the interior free for other equipment, allowing the capsule's surface area to be used as efficiently as possible. Since there are various industrial, scientific, and medical (ISM) bands available, choosing the right operating frequency is critical. The 433 MHz ISM band, for example, has small bandwidth; the 2.4 GHz ISM band, on the other hand, has a larger bandwidth but higher path loss. Wireless systems such as Zigbee and Bluetooth can cause significant interference as they operate in the same ISM band [2]. As a result, the 865 MHz ISM band is preferred. The antenna which passes through interior of the patient's body will be able to communicate with the medical practitioners by transmitting the images to an external receiving antenna operating in the same bands as the transmitter, thereby allowing them to monitor the patient.

Two conformal antennas for wireless telemetry [3] have been proposed for the applications of wireless capsule endoscopy (WCE). A helical and a meander line antenna have been simulated, built, and measured in a human body tissue environment. Capsule system dimensions are 30 mm × 10 mm on the outside, and 8.6 mm on the inside. For helical and a meander line antenna, fractional bandwidths of 51.3% and 20.8%, respectively, were found, with maximum gains of −28.3 dB and −41.3 dB. A conformal ultrawideband (UWB) meandering loop antenna has been proposed for WCE applications [4]. The antenna has a height of 14 mm and diameter of 10 mm. In planar form, the antenna is 28 mm in length and 14 mm in width. A 254 μm thick polytetrafluoroethylene (PTFE) substrate was used to develop and fabricate the antenna. The antenna's bandwidth is 164% of the fractional bandwidth, ranging from 200 MHz to 2.05 GHz. It emits omnidirectional radiation with a maximum gain of −31.5 dBi.

A small antenna with WCE that operates in the 433 MHz ISM band is described in the study [5]. A printed monopole with a partial ground plane acts as a receiving antenna which is placed on the body of patient, while the in-body transmitting capsule is a UWB loop antenna conformed around it. The in-body antenna is composed of Preperm 255, and is attached to the capsule's exterior wall. The capsule has a wall thickness of 0.5 mm, a diameter of 11 mm, and a length of 27 mm, respectively. With a max achieved gain of -23 dBi, the fractional bandwidth is found to be 112.5%. A loop antenna with a meander design is proposed for a UWB endoscope system built on the capsule's exterior surface [6]. The interior and exterior radius of the capsule are 5 mm and 5.5 mm, respectively. The proposed antenna is built of a flexible PCB with a 25.4 μm thick polyamide layer. Fractional bandwidth of 52% is obtained. A conformal, implantable and UWB antenna is designed to be used for WCE in this study [7]. The antenna can be attached to the capsule surface to make the most of the space available. The results obtained from simulation show that this antenna performs well with a wider bandwidth of 541 MHz. At 403 MHz, the maximum achieved gain is 31.5 dBi.

In this paper, two cases are considered for conformal antenna. In case 1, the antenna radiator is a simple T-shaped structure which operates only at the 865 MHz band. For case 2, the structure of the radiator is modified and the antenna now resonates in the both 865 MHz and 2.4 GHz bands. Wider bandwidth is observed for both the cases. Also, the SAR value observed is considered safe. The planar antennas are wound around the cylindrical capsule structure which is placed in a box that depicts the human body environment. One of the limitations of this work is the availability of the biocompatible materials in the market. The antenna is modeled and simulated on ANSYS Electronics Desktop (AEDT) simulation software which is illustrated in Sect. 2. Experimental results obtained from simulation and effects on frequency band of the antenna by changing battery length are discussed in Sect. 3. This paper is then concluded in Sect. 4 followed by references.

2 Antenna Design

For WCE, outer wall antennas are proposed, as they save space inside the capsule while providing greater performance than an antenna inside the capsule. Since the size of capsule is so small electrically in comparison to the frequency range, the antenna design has a significant impact on the quality, energy efficiency, and form factor of the capsule [8]. Furthermore, capsule antenna must have wider bandwidth. As the capsule moves through the digestive tract, the body tissue around it changes and so does the dielectric properties of tissues. So, the capsule antenna goes through large impedance variations, which could significantly alter the antenna's properties, therefore antennas with narrow bandwidth can get detuned as the capsule moves through the GI tract. Thus, the use of ultra-wide bandwidth can serve to minimise detuning effects [4].

Fig. 1 Dimensions of capsule
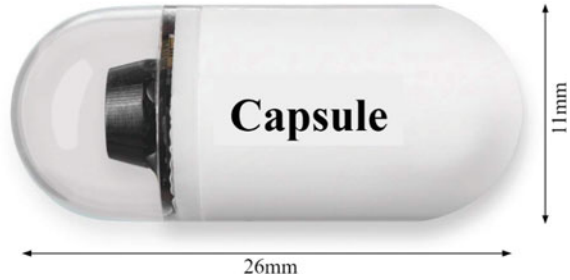
The dimensions of the capsule, as displayed in Fig. 1, are 26 mm × 11 mm. The antenna is designed to conform to the surface of capsule, which has a cylindrical shape (radius of 5.5 mm and height of 15 mm) and a Teflon substrate ($\varepsilon_r = 2.1$, tan $\delta = 0.001$) of height 0.8 mm, to maximise the usage of space inside the capsule. To maintain biocompatibility ULTEM ($\varepsilon_r = 3.05$, tan $\delta = 0.006$) is used to make the 0.5 mm thick capsule [9, 10]. The capsule cylinder is considered to be hollow. Blood, muscle, bone, and fat are dielectric and conductivity materials with varying dielectric and conductivity properties inside the human body. This results in a very complex electromagnetic structure to model and design, as well as a significant computational load, which lengthens simulation time. Thereby, in this paper we have used a homogeneous human body phantom ($\varepsilon_r = 56$ and $\sigma = 0.8$ S/m) to replicate the environment inside the human body [7, 11]. The antenna presented in this paper for WCE is designed in the HFSS Design window of the AEDT simulation software. All the results are obtained with the help of this software. Using this software, we were able to operate the antenna at the desired frequencies.

2.1 Case-1

A simple T-shaped structure is taken as the radiator as shown in Fig. 2. For any application, microstrip patch antenna is considered [12]. In our work, we want the antenna to operate at lower frequency bands but the dimensions of the patch antenna increase as the frequency of operation decreases. Since, capsule requires smaller antenna to conform around it, patch antenna will not help our cause. By gaining information from numerous literatures, it is deduced that by increasing the path length, the antenna resonates at lower frequencies. So, in our design we consider several striplines and increase the current path to attain resonance at 865 MHz. Then the antenna is conformed around the exterior of the capsule (see Fig. 4a). The dimensions of the antenna are discussed in Table 1. The radiator is metal and it is harmful to the body upon exposure, so zirconia can be used for bio-encapsulation.
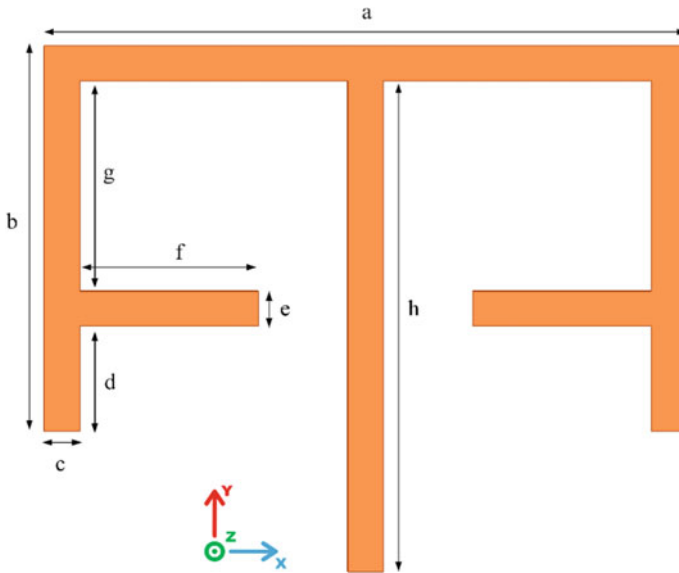
Fig. 2 Planar design and of antenna

Table 1 Dimensions of planar antenna

S. No.	Parameters	Value (mm)
1	a	18
2	b	11
3	c	1
4	d	3
5	e	1
6	f	5
7	g	6
8	h	14

2.2 Case-2

Here the structure of the radiator is modified and is made into bow and arrow shape as illustrated in Fig. 3. Similarly, the antenna is conformed around the exterior of the capsule (see Fig. 4b). The dimensions of the antenna are discussed in Table 2.
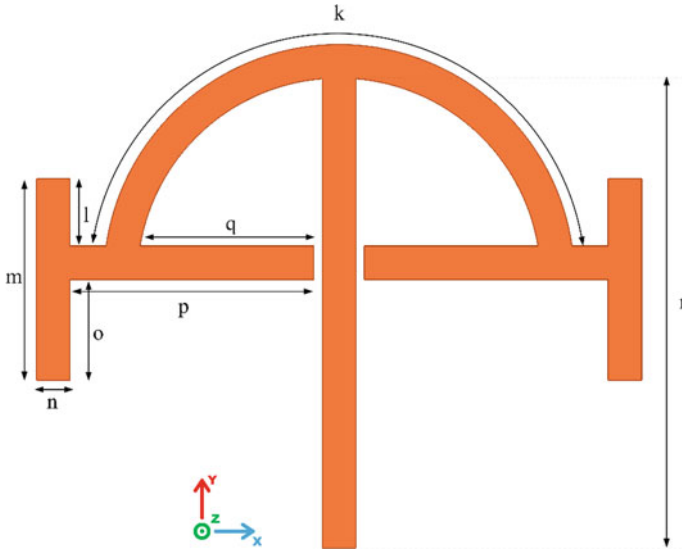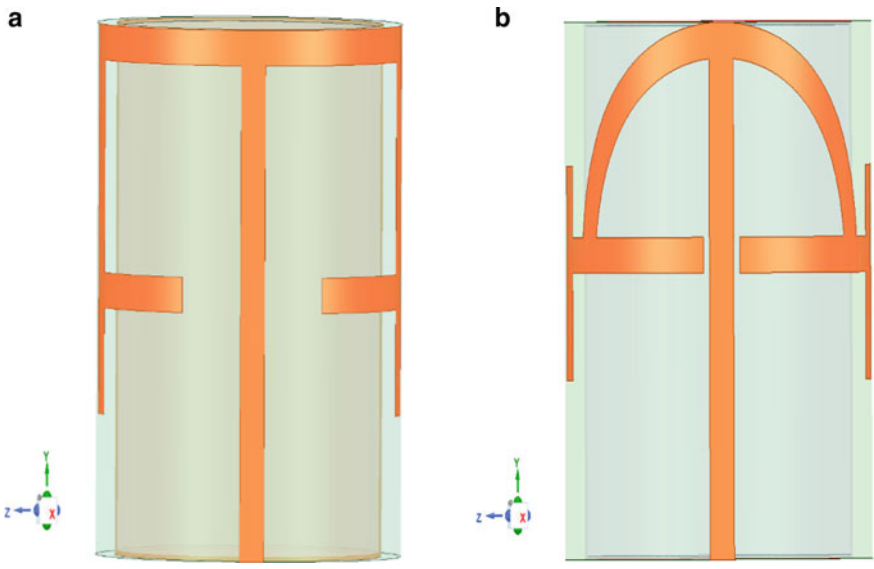
Fig. 3 Planar design of antenna

Fig. 4 Conformal design of antenna, **a** case-1 and **b** case-2

Table 2 Dimensions of planar antenna

S. No.	Parameters	Value (mm)
1	k	19.98
2	l	2
3	m	6
4	n	1
5	o	3
6	p	7.25
7	q	5.17
8	r	13.98

3 Results

The antenna performances, such as gain, return loss, SAR and radiation patterns, are evaluated using simulations. Wide bandwidth has been observed for both the antenna cases. For 1 g human tissue the average SAR must be less than 1.6 W/kg as given in IEEE C95.1-1999 guidelines [7].

3.1 Case-1

The results are obtained from the simulation software. From Fig. 5, it is observed that the antenna operates from 833.5 to 1110.7 MHz (28.51%). The peak realized gain of the antenna is found out to be −18.1 dBi and the SAR value is 1.5933 W/kg when input power is 2.7 mW at 865 MHz (see Fig. 6). 2D Radiation patterns are also observed in Fig. 7.

3.2 Case-2

The results are obtained from the Results tab of the simulation software. Here, two frequencies i.e., 865 MHz and 2.4 GHz are taken as solution frequencies and the frequency range is from 100 MHz to 3 GHz. From Fig. 8, it is observed that the antenna operates from 858.2 to 1132.1 MHz (27.52%) and beyond 2.1648 GHz (wide band). The additional resonant frequency is obtained as a result of curvature of T-shape path. The gain of the antenna is found out to be −18.1 dBi and the SAR value is 1.5859 W/kg when input power is 2.5 mW at 865 MHz (see Fig. 9) while at 2.4 GHz, peak gain of the antenna is found out to be −13.3 dBi and the SAR value is 1.5859 W/kg when input power is 7.4 mW (see Fig. 11). 2D Radiation patterns at 865 MHz and 2.4 GHz are observed in Figs. 10 and 12 respectively.

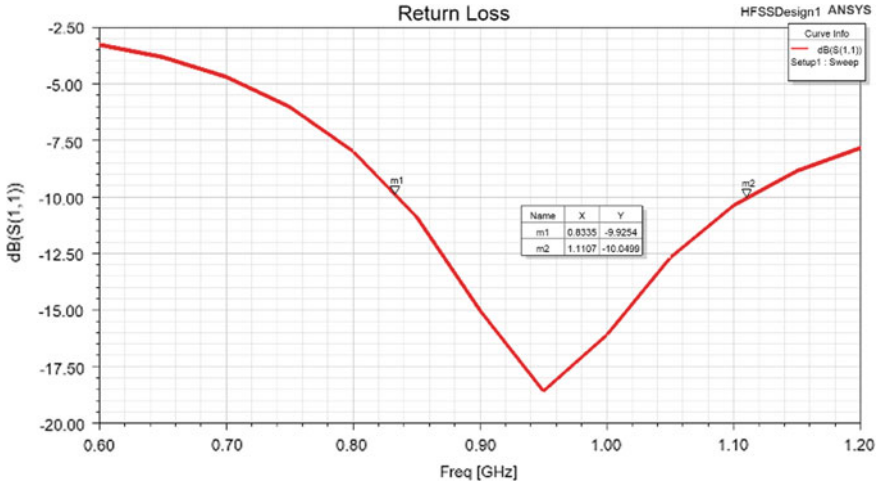Fig. 5   Return loss versus frequency plot
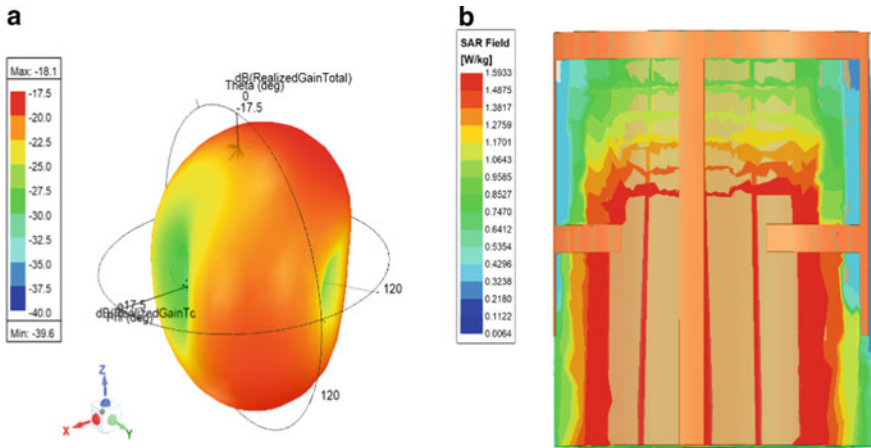
Fig. 6   a 3D radiation pattern and b SAR pattern

3.3   Changing Battery Length

Since batteries are larger components inside the capsule, their impact on bandwidth needs to be explored. The length of the battery was modified to 0 mm, 5 mm, and 10 mm in three instances. It is observed that varying the lengths of battery does not affect the bandwidth (see Fig. 13).
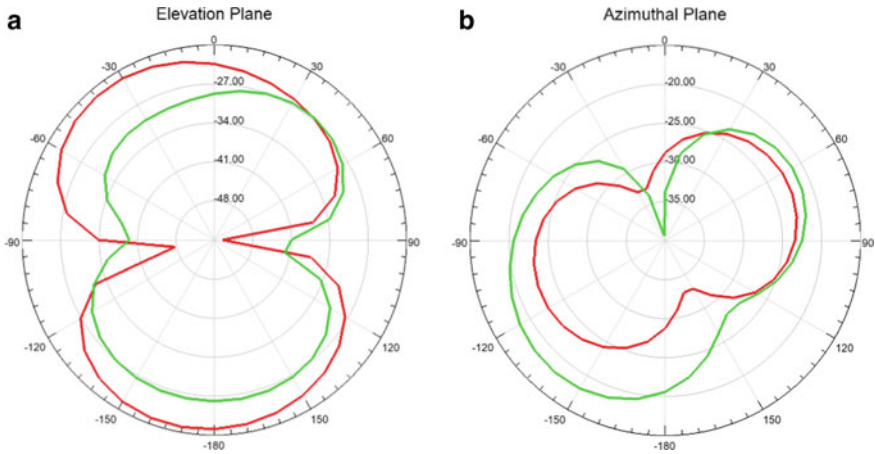
Fig. 7 **a** Elevation plane and **b** azimuthal plane
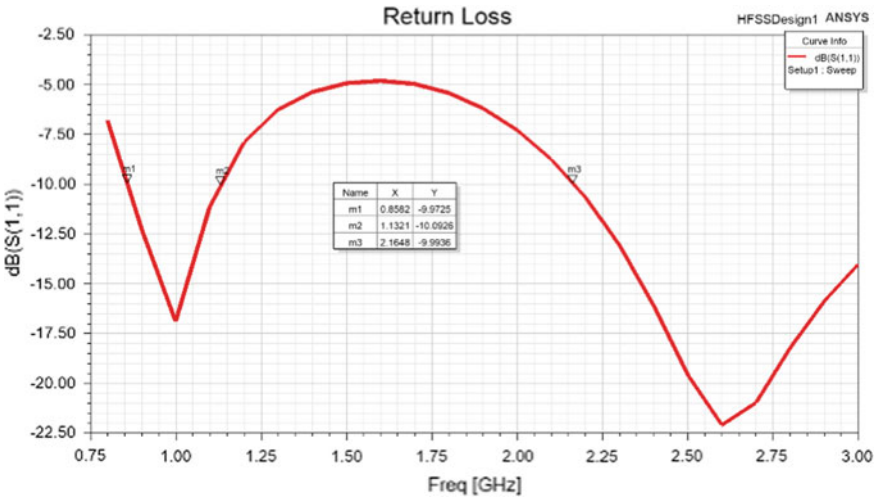
Fig. 8 Return loss versus frequency plot

4　Conclusion

For wireless capsule endoscopy, two conformal wideband antennas are designed. Both the antennas operate in the 865 MHz band while one of them also operates in 2.4 GHz band. First two planar antennas are designed, then they are conformed around a cylindrical capsule. The simulation is performed in AEDT simulation software and it is observed that the antennas have wider bandwidth at respective bands. The peak realized gain for both antennas at 865 MHz are −18.1 dBi while antenna with bow and
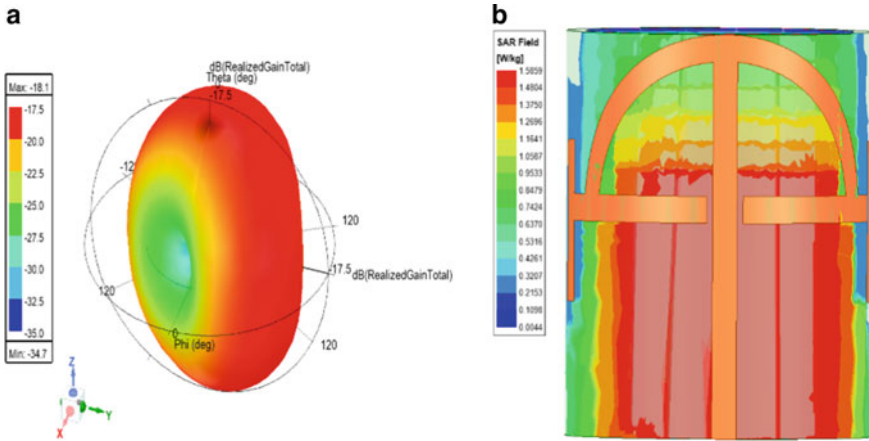
Fig. 9 **a** 3D radiation pattern and **b** SAR pattern
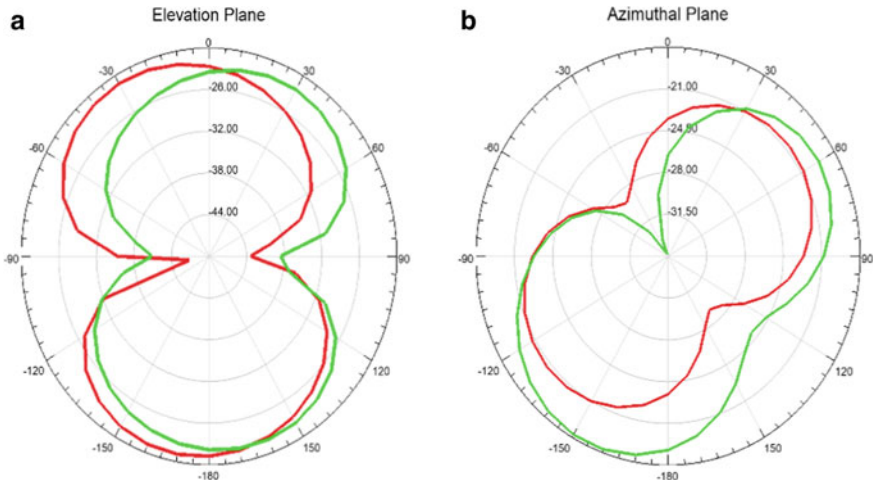
Fig. 10 **a** Elevation plane and **b** azimuthal plane

arrow shaped radiator has peak realized gain of −13.3 dBi at 2.4 GHz. At 865 MHz with input power < 2.5 mW and at 2.4 GHz with input power < 7.4 mW, satisfactory SAR values are obtained for bow and arrow shaped radiator. The antennas have been designed to be biocompatible since the capsule gets ingested by the patient. The antennas can be fabricated in the future and the results obtained upon testing can be compared with simulated results.
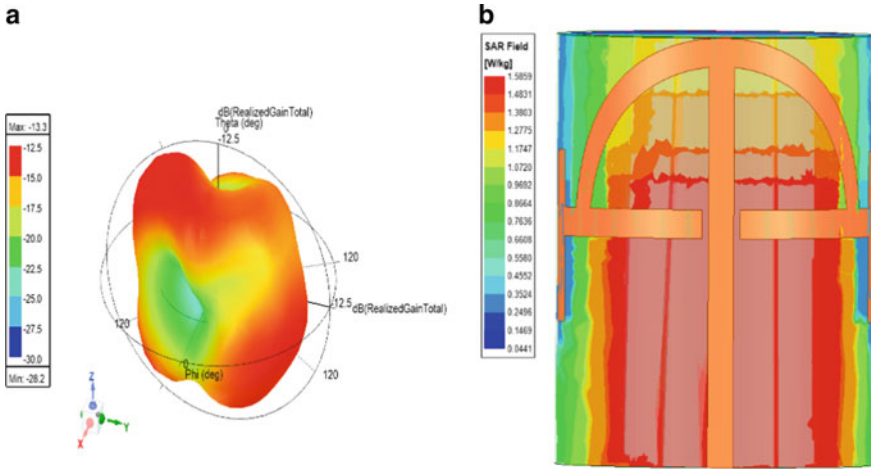
Fig. 11 a 3D radiation pattern and **b** SAR pattern
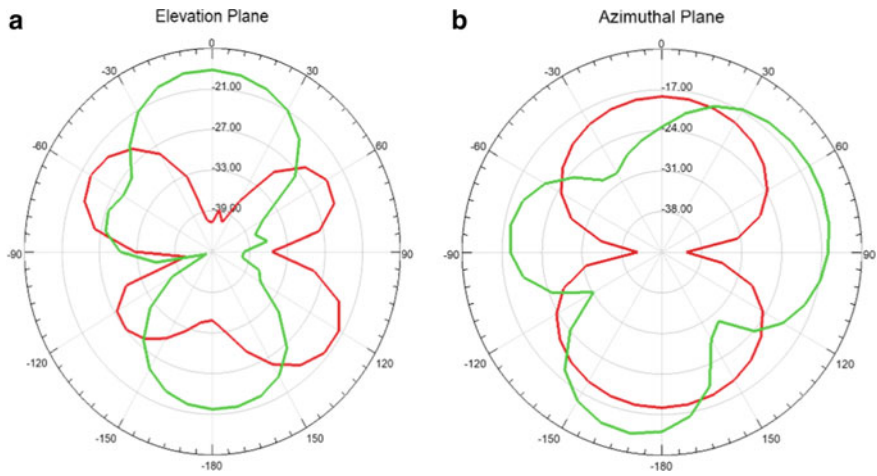
Fig. 12 a Elevation plane and **b** azimuthal plane
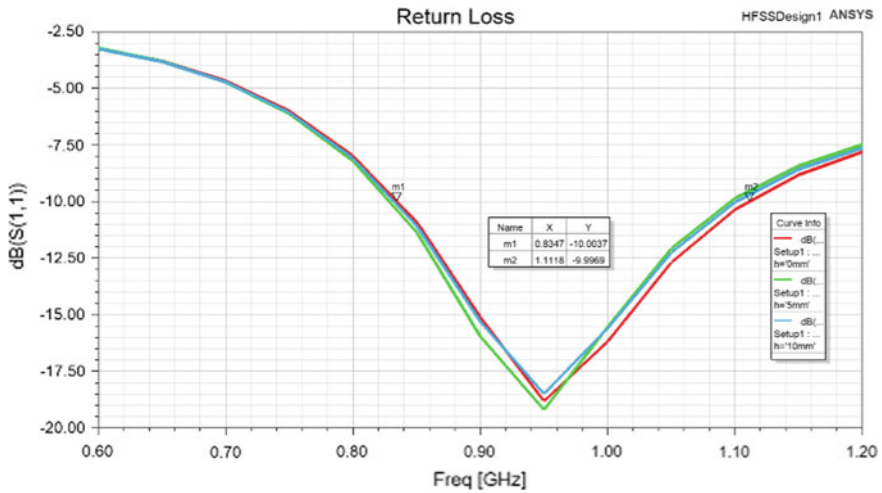
Fig. 13 Return loss versus frequency plot

References

1. Capsule endoscopy: preparation, pros, cons. Lubbock Gastro. https://lubbockgastro.com/ser vices/capsule-endoscopy/
2. Biswas B, Karmakar A, Chandra V (2020) Miniaturised wideband ingestible antenna for wireless capsule endoscopy. IET Microwaves Antennas Propag 14:293–301
3. Faerber J, Cummins G, Desmulliez M (2016) Design of conformal wideband antennas for capsule endoscopy within a body tissue environment. In: 2016 46th European microwave conference (EuMC)
4. Kim S, Shin H (2019) An ultra-wideband conformal meandered loop antenna for wireless capsule endoscopy. J Electromagnet Eng Sci 19:101–106
5. Miah M, Khan A, Icheln C, Haneda K, Takizawa K (2018) Antenna systems for wireless capsule endoscope: design, analysis and experimental validation. IEEE Trans Antennas Propag 1–11
6. Yun S, Kim K, Nam S (2010) Outer-wall loop antenna for ultrawideband capsule endoscope system. IEEE Antennas Wirel Propag Lett 9:1135–1138
7. Wang J, Leach M, Lim E, Wang Z, Pei R, Huang Y (2018) An implantable and conformal antenna for wireless capsule endoscopy. IEEE Antennas Wirel Propag Lett 17:1153–1157
8. Kumar D, Kalaipriyan T, Raghav RS (2019) A study of research notions in wireless body sensor network (WBSN). IRO J Sustain Wirel Syst 2:77–86
9. Malik N, Sant P, Ajmal T, Ur-Rehman M (2021) Implantable antennas for bio-medical applications. IEEE J Electromagnet RF Microwaves Med Biol 5:84–96
10. Lee S, Lee J, Yoon Y, Park S, Cheon C, Kim K, Nam S (2011) A wideband spiral antenna for ingestible capsule endoscope systems: experimental results in a human phantom and a pig. IEEE Trans Biomed Eng 58:1734–1741
11. Alemaryeen A (2021) Compact wideband antenna for wireless capsule endoscopy system. Appl Phys A 127:271
12. Christina G (2021) A review on microstrip patch antenna performance improvement techniques on various applications. J Trends Comput Sci Smart Technol 3:175–189

Dense Video Captioning Using Video-Audio Features and Topic Modeling Based on Caption

Lakshmi Harika Palivela, S. Swetha, M. Nithish Guhan, and M. Prasanna Venkatesh

Abstract Videos are composed of multiple tasks. Dense video captioning entails captioning of different events in the video. A textual description is generated based on visual, speech and audio cues from a video and then topic modeling is performed on the generated caption. Uncertainty modeling technique is applied for finding temporal event proposals where timestamps for each event in the video are produced and also uses Transformer which inputs multi-modal features to identify captions effectively and to make it more precise. Topic modeling tasks include highlighted keywords in the captions generated and topic generation i.e., category under which the whole caption belongs to. The proposed model generates a textual description based on the dynamic and static visual features and audio cues from a video and then topic modeling is performed on the generated caption.

Keywords Video captioning · Event proposals · Topic modeling · Feature extraction

1 Introduction

Videos have a big influence on our life. Every day, a sizable amount of video data is tracked and processed. Videos are used everywhere nowadays for various purposes [1]. There is great improvement in visual innovations, which has wide applications. Videos are essential in almost all industries such as surveillance cameras, social network, e-learning, advertisements, medical, etc. Thus, video data processing becomes a tedious problem. Automatic video content analysis has recently seen a rise in popularity as video data volumes increase. The video captioning content analysis generates a computational linguistics sentence that describes the content of the input clip.

Multimedia statistics analysis plays a crucial role, in order to generate a meaningful description of the overall action event, it is critical to consider the sequence

L. H. Palivela (✉) · S. Swetha · M. Nithish Guhan · M. Prasanna Venkatesh
Madras Institute of Technology, Anna University, Chennai, Tamil Nadu, India
e-mail: lakshmiharika@mitindia.edu

of actions in a video [2]. When annotating videos as opposed to images, the scene is much more dynamic and has more details. Therefore, video caption requires more feature extraction for the creation of written description, making it more important than image caption. Applications like video object detection, video retrieval, and video summarizing can all benefit from dense video captioning methods. Audio and speech are also essential clues that help a human observer comprehend their surroundings [3]. The value of a captioning system resides in its capacity to increase accessibility to video in several ways. The goal is to perform topic modeling on the generated captions and automatically describe a video's content using natural language based on visual and auditory modalities.

2   Literature Review

Many Video Captioning methods are present with various pros and cons and even incorporating temporal event segments along with captioning techniques. Buch et al. [4], put forth a recurrent model architecture that delivers temporal action proposals quickly and with a high level of temporal overlap with the ground truth action intervals. However, compared to BI-SST, Single Stream Temporal performs poorly since it is single directional whereas BI-SST works on both forwards and backwards. Rahman et al. [5] suggested a multimodal that takes both audio and video into account. It will be cued using visual features incorporating fusion techniques after audio features have been extracted. Then temporal segments are created using an attention feature fusion process, and the caption generator uses these along with encoded features to create captions [6]. However, it is unable to determine when the event started and simply creates two event captions.

Li et al. [7] have put up a method for detecting events with the straightforward goal of binary classification, modeling phrase production with LSTM, and improving the temporal event proposal. Additionally, by using semantic characteristics and reinforcement learning to enhance LSTM with non-differentiable metrics, the sentence production module is given a boost. Even if it makes use of more category names, it falls short when measured against other cutting-edge research. Zhao et al. [8] presented the tube feature, an object-aware feature for video captioning. The authors used Faster-RCNN to abstract object regions in frames and built an encoder-decoder architecture for video caption creation where the encoder is a bi-directional based LSTM, which collects the dynamic information of each tube, and the decoder is one attention based LSTM which permits to attend to the most of the tubes which are correlated adaptively [9]. However, this method is unable to identify smaller objects, which causes errors in the caption's keywords.

Deng et al. [10] discussed the technique known as SGR, or Sketch, ground and refine, which creates a story at the level of a video and grounds it to video segments for future improvement. They implemented a refining stage to make use of the event-level data and added more precise information to the event captions. The event portions can be more accurate based on the improved subtitles. A special LSTM cell

developed by the authors of paper Carreira et al. [11] can identify breaks in segments to modify the temporal relations in the encoding layers in response. However, it performs comparably poorly compared to other cutting-edge techniques and cannot be used for videos with no clear framework.

By combining self-supervised hierarchical representation learning with auxiliary tasks, the authors of paper Gao et al. [12] suggested a unique end-to-end framework called HRNAT to overcome the aforementioned difficulties. However, the suggested method is unable to caption the repeated motions in the video and it is unable to identify if the individual is a male or a woman. Zhou et al. [13] suggested a back-to-back transformer model. As soon as the encoder part transforms the given input into the correct representations, the proposal decoder model decodes it by using a variety of anchors to produce video event proposals. A self-attention method is used by the captioning decoder to enable the employment of effective non-recurrent structure during encoding. The masking network is used to limit the captioning decoder's attention rather than the encoding features. Since the transformer, is more effective decoder than RNN, is used in this model, it functions well with ground truth proposals [14]. Their findings regarding learnt proposals, however, are less successful. Donahue et al. [15], presented a back-to-back trainable model that can be used to visually recognize the image and produce a suitable description. It uses a CNN to process the variable-length visual input, and then feeds the outputs to a stack of repetitive sequences, which ultimately yields a varying prediction [16]. The suggested model does not take audio or speech into account as a parameter, but it does recognize and offer proper description as an output.

In this study, various video captioning methods are discussed. The existing approaches have some cons which include unidentified smaller objects, imprecise subtitles, unable to capture the repeatable motions and improper event generation [17]. To overcome the disadvantages, we adopt dense video captioning using multi-modal features which are audio, video and speech and perform topic modeling tasks.

3 Dense Video Captioning and Topic Modelling (DVCTM)

In this section, we outline the dense video captioning task along with topic modeling (DVCTM) in Fig. 1. The events in the video are first localised, and then a computational linguistics sentence is generated. Three stages are performed to achieve the task. The dataset includes videos and annotations from ActivityNet [18] and Thumos. The annotation contains timestamps and captions for each segment.
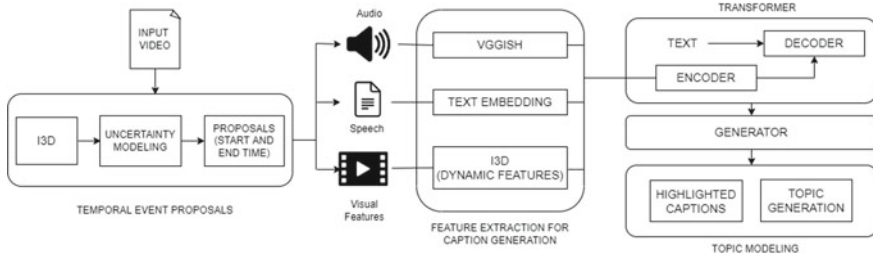
Fig. 1 DVCTM-system architecture

3.1 Temporal Event Proposals

In the event proposal module, the videos are preprocessed using I3D where segments of RGB and flow are extracted from the features. We must distinguish between the action and background frames in order to determine the temporal intervals. By using uncertainty modeling as proposed in [19], it is possible to separate the action and background frames in a video. Based on the features, Segment level scores are predicted by the Action classifier and the top k scores are aggregated using the softmax function.

Due to the inconsistency in the background frames, uncertainty modeling loss and background entropy loss are predicted. Pseudo action and pseudo background segments are selected depending on the magnitudes of the features [20]. The feature magnitudes of the pseudo action frames are increased and those of the background segments are decreased in uncertainty modeling loss. With the help of background entropy loss, the background segments have a uniform action probability distribution. In light of this, time segments are suggested, each with a start and end time.

3.2 Feature Extraction for Caption Generation

For the video captioning task, three input modalities—visual, audio, and speech are used. Each modality's features are retrieved separately. VGGish, which was initially trained on AudioSet, is used to extract the features for auditory cues [21]. A periodic Hann window and the Short_time Fourier Transform are used to transform a mono audio file into a log mel-scaled spectrogram, which is the input for the VGGish model. The classification layer of VGGish outputs each spectrogram as a 128-d embedding which is saved and used in numpy file format.

Using Inflated 3D, a pre-trained model on Kinetics 400, the visual features are retrieved with both RGB and flow streams, Optical flow features are extracted using Recurrent All-Pairs Field Transforms (RAFT) type, where frames are extracted for each subsequent pair of frames in a video [22]. RGB data includes the color, texture and shape of the object and optical flow to have information about motion of the

objects across frames. Optical flow is extracted using Raft type. The frames are resized and cropped at center and are passed to I3D. The resulting feature vectors are saved as numpy file.

Text segments that have been assigned a specific time serve as the input for speech modality. The input for speech modality is the subtitle file with appropriate start and end timestamps along with the corresponding text for that interval. Using the YouTube Transcript API, which offers the SRT file, the text (or subtitles) for the video is accessed. For Youtube videos, the subtitles are generated by specifying the video id and the API produces it for that specific video. The SRT file has text and timestamps spaced out at regular intervals. Google's speech recognition algorithm is used for videos that are not present in YouTube. The Speech module includes the subtitles file for the video.

3.3 Caption Generation

The video captioning approach uses a Transformer mechanism similar to other event proposals [23]. The features are combined using an encoder model and a decoder model for each modality. The codec receives a set of extracted features that chronologically match a proposal and transforms them into a number of internal representations. The generator uses the decoder to model an allocation across a dictionary for the next word based on the encoder output and the embedding of the words in the caption. The following word is selected based on the highest probability [24]. The multi-headed attention is extremely important for the encoder and decoder blocks. A crucial aspect of the multi-head attention theory is dot-product attention. The generator blends the outputs of all modalities and produces the subsequent text. The generator applies softmax function and produces the distribution over vocabulary of words and thus the word with highest probability is selected. The Adam optimizer is used in both speech and visual modalities.

Kullback–Leibler divergence loss is used to train the captioning which averages the attributes for each word in batches while neglecting the masked tokens [25]. The gap between the actual and anticipated distributions is measured by this loss. In order to lessen the certainty of the model's predictions, we employ label smoothing, utilizing the smoothing parameter on the ground truth labels.

3.4 Topic Modeling

The captions generated undergo topic modeling tasks. The keywords in the captions are found using KeyBERT algorithm and those keywords alone are highlighted in the results [26]. KeyBERT is a keyword extraction algorithm that employs SBERT embeddings to produce more closely related keywords and key phrases from a page. It is used to predict the most closely related words to the given text. KeyBERT uses

sentence BERT for document embedding first and the word embeddings for N-gram sentences are extracted. The similarity of each sub phrase is measured using cosine similarity.

The most comparable terms can then be determined to be the keywords that best describe the entire document. Thus, the most similar words are considered as keywords and they are highlighted. The relevant topic category to the input text is found using IBM Natural Language Understanding, it analyses and maps the input with the appropriate output it belongs to. When input text is given, it classifies and gives all the classification output that matches with the text corpus in the backend. The relevant categories are produced and the percentage for each topic category is displayed. Based on the scores, the most relevant topics are depicted in the form of a bar graph. Thus the top 3 scores are selected and plotted as bar graph. Thus, for a given video, the results are captions with highlighted keywords for each event proposal generated and the overall category of the video.

3.5 DVCTM Algorithm

Input: Video
Output: Captions with highlighted keywords and topic related to the caption.
Step 1: Input video is separated into visual and audio modalities.
Step 2: Audio is separated from video and vggish approach is applied.

2.1 Convert waveform to array.
2.2 Periodic Hann window is calculated.

$$\text{result1} = 0.5 - (0.5 * \text{npy.cos}(2 * \text{npy.pi/win\_Length} \\ * \text{np.arange(win\_Length)}))//\text{npy-numpy, win-window}$$

2.3 Short Time Fourier Transform frequency is calculated.
2.4 Frequencies are converted to mel scale spectrogram.

$$\text{result2} = \_\text{Mel\_High\_Freq.\_Q} * \text{npy.log}(1.0 \\ + (\text{frequencies\_hertz/\_Mel\_Break\_Freq.\_Hertz}))$$

2.5 128-d feature vector is obtained.
2.6 Saved as numpy file.

Step 3: Visual features extracted using Inflated 3D network.

3.1 Input requires RGB streams and Flow streams.
3.2 Optical flow is extracted by using Raft feature type.
3.3 1024-d feature vector is obtained for each stream.
3.4 Saved as numpy file.

Step 4: Speech modality input (subtitles)

For youtube videos:

4.1 SRT files are extracted using Youtube Transcript API

For other videos:

4.2 Subtitles from Google speech recognition.

Step 5: Temporal event proposals for video

5.1 Feature extraction using Inflated 3D approach.
5.2 Segment level class scores are calculated.

$$A_n = \text{classifier}(F_n; \varphi\text{cls}) // F_n\text{-features}, \varphi\text{cls-parameters}$$

5.3 Uncertainty modeling loss to enlarge feature magnitude for action segments.

$$\text{un} = 1/N \sum (n = 1 \text{ to } N) \left(\max\left(0, m - ||f^{\text{act}}(_n)||\right) + ||f^{\text{bkg}}(_n)|| \right)^2$$

5.4 Background entropy loss function to maximize the entropy of action probability from background segments.
5.5 Top scores are obtained from segments for each class.

Step 6: For each time segment, video features are split.

6.1 Features are fed into transformer.
6.2 Encoder inputs a set of extracted features $v_i = (v1, v2, \ldots, vT_i)$
6.3 Produces an internal representation z.
6.4 Decoder inputs encoder output and word embeddings and produce an internal representation.
6.5 Generator uses decoder output and softmax function is applied.
6.6 Word with high probability is selected.

Step 7: Captions generated with timestamps for each event.
Step 8: Keywords extraction using KeyBERT

8.1 Embeddings are generated using Sentence BERT for n-grams.
8.2 Cosine similarity is applied to check similarity for key phrases.
8.3 Similar words are considered as keywords and top n words are selected and highlighted.

Step 9: Topic generation using IBM Natural language understanding.

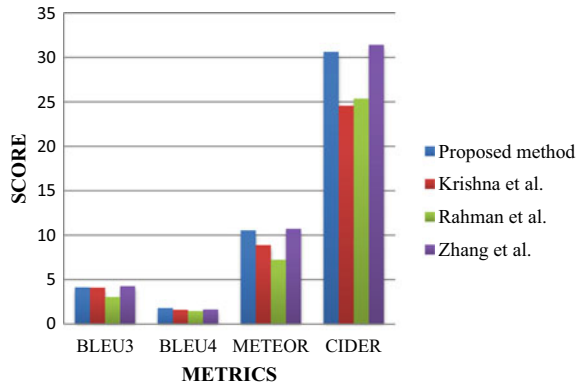9.1 Matches with the text corpus in the backend of IBM NLU.
9.2 Classifies output with high scores.
9.3 Topic generated with their scores.

Table 1 Comparative analysis

Approach	BLEU3	BLEU4	Meteor	Cider
Proposed method	4.13	1.80	10.54	30.62
Krishna et al. [27]	4.09	1.60	8.88	24.56
Rahman et al. [5]	3.04	1.46	7.23	25.36
Zhang et al. [28]	4.26	1.64	10.71	31.41

Fig. 2 Comparison graph

4 Results

We employ on ActivityNet dataset [18], the videos and annotations are used for this approach. The generated captions are compared across the reference ground truth captions using various metrics. Bleu, Meteor and Cider metrics are used for evaluation purposes in Table 1 and in Fig. 2.

The Dense Video Captioning method is tested using real videos taken in mobile camera. The captions are generated with highlighted keywords and the category is visualized in the form of bar graph. A snippet of the real traffic video captured in Fig. 3 and the results are given below in Figs. 4 and 5. The video revolves around the event where a person is driving a bike and talking to a camera. The captions for the video are generated along with each event start and end timestamps in Fig. 4. The topic related to the video captured is displayed in Fig. 5 where it points to automotive and vehicles.

5 Conclusion

Today, the usage of videos has increased abruptly and according to the survey videos uploaded to the web in a month is more than the videos created for television in the last thirty years. The proposed method creates event captions for videos and also

Fig. 3 Sample traffic video captured

```
Start: 8.4 End: 9.5
A man in a black shirt is talking to the camera
Start: 0.3 End: 2.0
A person is seen sitting on a bike and riding down on a hill
Start: 0.0 End: 9.9
A person is seen sitting on a bike and leads into them walking down a hill
Start: 6.7 End: 9.7
A man in a red shirt is standing on a bike
Start: 8.5 End: 8.7
A man in a black shirt is talking to the camera
Start: 3.6 End: 5.1
A man in a black jacket walking in the street
Start: 8.9 End: 9.2
A man in a black shirt is standing on a bike
```

Fig. 4 Sample traffic video caption results

highlights the keywords of the generated caption to make the video accessible in numerous ways. The relevant category is identified based on the captions generated and top three categories are selected based on the probability that is visualized in the form bar graph. The proposed work can be further improved by collecting a huge dataset and also improving the accuracy of the captions. For certain scenarios the generated captions contain simple and basic mistakes. With large dataset covering these scenarios, the accuracy of the generated captions can be improved.
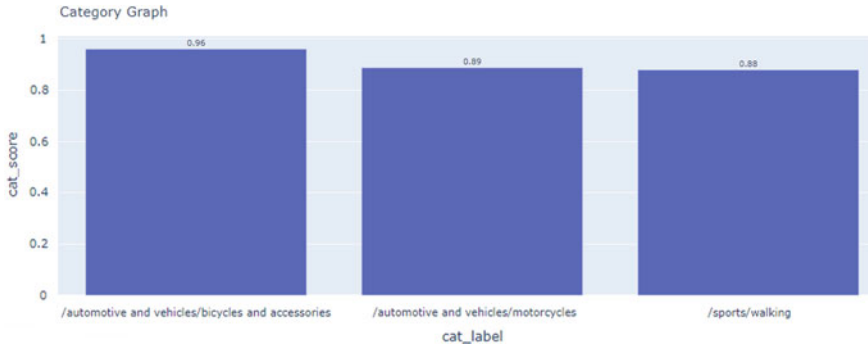
Fig. 5 Sample video category generation

References

1. Xiong Y, Dai B, Lin D (2018) Move forward and tell: a progressive generator of video descriptions. In: Proceedings of the European conference on computer vision, pp 468–483
2. Chadha A, Arora G, Kaloty N (2022) iPerceive: applying common-sense reasoning to multi-modal dense video captioning and video question answering, pp 1–13
3. Hao W, Zhang Z, Guan H (2018) Integrating both visual and audio cues for enhanced video caption. In: Proceedings of the AAAI conference on artificial intelligence, vol 32, no 1
4. Buch S, Escorcia V, Shen C, Ghanem B, Niebles J (2017) SST: single-stream temporal action proposals. In: IEEE conference on computer vision and pattern recognition (CVPR), pp 6373–6382
5. Rahman T, Xu B, Sigal L (2019) Watch, listen and tell: multi-modal weakly supervised dense event captioning. In: IEEE/CVF international conference on computer vision (ICCV), pp 8907–8916
6. Hori C, Hori T, Lee T, Zhang Z, Harsham B, Hershey J, Marks T, Sumi K (2017) Attention-based multimodal fusion for video description. In: Proceedings of the IEEE international conference on computer vision, pp 4193–4202
7. Li Y, Yao T, Pan Y, Chao H, Mei T (2018) Jointly localizing and describing events for dense video captioning. In: IEEE/CVF conference on computer vision and pattern recognition, pp 7492–7500
8. Zhao B, Li X, Lu X (2018) Video captioning with tube features. In: Proceedings of the 27th international joint conference on artificial intelligence (IJCAI'18). AAAI Press, pp 1177–1183
9. Baraldi L, Grana C, Cucchiara R (2017) Hierarchical boundary-aware neural encoder for video captioning. In: IEEE conference on computer vision and pattern recognition (CVPR), pp 3185–3194
10. Deng C, Chen S, Chen D, He Y, Wu Q (2021) Sketch, ground, and refine: top-down dense video captioning. In: IEEE/CVF conference on computer vision and pattern recognition (CVPR), pp 234–243
11. Carreira J, Zisserman A (2017) Quo vadis, action recognition? A new model and the kinetics dataset. In: Proceedings of the IEEE conference on computer vision and pattern recognition, pp 6299–6308
12. Gao L, Lei Y, Zeng P, Song J, Wang M, Shen H (2022) Hierarchical representation network with auxiliary tasks for video captioning and video question answering. IEEE Trans Image Process 31:202–215
13. Zhou L, Zhou Y, Corso J, Socher R, Xiong C (2018) End-to-end dense video captioning with masked transformer. In: Proceedings of IEEE conference on computer vision and pattern recognition, pp 8739–8748

14. Venugopalan S, Xu H, Donahue J, Rohrbach M, Mooney R, Saenko K (2015) Translating videos to natural language using deep recurrent neural networks. In: Proceedings of the 2015 conference of the North American chapter of the association for computational linguistics: human language technologies, pp 1494–1504
15. Donahue J, Hendricks L, Rohrbach M, Venugopalan S, Guadarrama S, Saenko K, Darrell T (2015) Long-term recurrent convolutional networks for visual recognition and description, pp 2625–2634
16. Hershey S, Chaudhuri S, Ellis D, Gemmeke J, Jansen A, Moore C, Plakal M, Platt D, Saurous R, Seybold B (2017) CNN architectures for large-scale audio classification. In: 2017 IEEE international conference on acoustics, speech and signal process, pp 131–135
17. Lee S, Kim I (2018) Multimodal feature learning for video captioning. Math Probl Eng 1–8
18. ActivityNet dataset: http://activity-net.org/
19. Lee P, Wang J, Lu Y, Byun H (2021) Weakly-supervised temporal action localization by uncertainty modeling. In: The thirty-fifth AAAI conference on artificial intelligence, pp 1854–1862
20. Sumalatha MR, Lakshmi Harika P, Aravind J, Dhaarani S, Rajavi P (2018) Detection of static and dynamic abnormal activities in crowded areas using hybrid clustering. In: International conference on ISMAC in computational vision and bio-engineering, pp 815–824
21. Simonyan K, Zisserman A (2014) Very deep convolutional networks for large-scale image recognition. arXiv preprint arXiv:1409.1556
22. Koshti D, Kamoji S, Kalnad N, Sreekumar S, Bhujbal S (2020) Video anomaly detection using inflated 3D convolution network. In: International conference on inventive computation technologies (ICICT), pp 729–733
23. Iashin V, Rahtu E (2020) Multi-modal dense video captioning. In: IEEE/CVF conference on computer vision and pattern recognition (2020)
24. Pennington J, Socher R, Manning C (2014) Glove: global vectors for word representation. In: Proceedings of the 2014 conference on empirical methods in natural language process (EMNLP), pp 1532–1543
25. Hinton G, Vinyals O, Dean J (2015) Distilling the knowledge in a neural network, vol 2, no 7. arXiv preprint arXiv:1503.02531
26. Grootendorst M (2020) Keybert: minimal keyword extraction with bert
27. Krishna R, Hata K, Ren F, Fei-Fei L, Niebles J (2017) Dense-captioning events in videos. In: 2017 IEEE international conference on computer vision (ICCV), pp 706–715
28. Zhang Z, Xu D, Ouyang W, Tan C (2020) Show, tell and summarize: dense video captioning using visual cue aided sentence summarization. IEEE Trans Circuits Syst Video Technol 30(9):3130–3139

Impact of Autonomous Vehicles Accidents on the Public Attitude Towards This Emerging Technology

Kareem Othman

Abstract Over the last few years, autonomous vehicles (AVs) have attracted researchers from different disciplines. Despite the effort put into the understanding and development of AVs, little is known about the factors that affect the public attitude towards this emerging technology. On the other side, public attitude is the main factor for the success of emerging technologies. Additionally, over the last few years, AVs were involved in multiple accidents that negatively affect the public attitude towards AVs. This paper focuses on investigating the impact of AVs' accidents on the public attitude towards AVs for different groups with different demographic characteristics (age, gender, educational level, household, and income) in the USA by analyzing the opinions of 5880 respondents who participated in the online questionnaire survey. The results show that people become less positive towards AVs after accidents but with different magnitudes for respondents with different demographic characteristics. Additionally, the results shed light on the importance of educating the public about the benefits and state of technology of AVs.

Keywords Accident · Autonomous vehicles · Crashes · Public acceptance · Demographic characteristics

1 Introduction

Vehicle automation has always been one of the main areas that attracted researchers from different disciplines. In the 20s, the focus was on the use of radio waves in order to establish the vehicle-to-vehicle communication [1]. In the 40s, the focus was on the invention of the electromagnetic guidance system [2]. This was followed by the cooperation between the Bundeswehr University in Munich and Mercedes-Benz that resulted in the invention of the first system for autonomous vehicles (AVs) [3].

K. Othman (✉)

Civil Engineering Department, University of Toronto, Toronto, Canada
e-mail: kareem.othman@mail.utoronto.ca; karemmohamed1993@cu.edu.eg

Public Works Department, Faculty of Engineering, Cairo University, Giza, Egypt

This invention was one of the biggest milestones that have attracted researchers and manufacturers from all over the world to introduce AVs [4]. In general, the National Highway and Transportation Safety Administration has classified AVs functionalities into 5 levels starting with level 0, that refers to the case of no automation at all, to level 5 that refers to full automation. Level 0 automation means no automation at all that the driver is responsible for performing all the driving tasks. Level 1 automation refers to the driver assistance system feature that assists the driver in some functions. Level 2 refers to partial automation as some functions are automated, but the driver must keep control of the vehicle and be alerted to the surrounding environment. Level 3 refers to conditional automation which requires the driver to be alerted to take control of the vehicle at all times with notice. Level 4 refers to high automation which indicates that the vehicle is able to operate autonomously but the vehicle can also be manually controlled. Level 5 refers to full automation which means that the vehicle is able to operate or navigate in all environmental conditions safely [5].

Over the last few years, the development of AVs has witnessed tremendous focus from researchers and manufacturers at a multidisciplinary level that the traditional vehicle manufacturers are not taking the lead in this area [6]. For example, Google has launched its AVs program in 2009 to develop its first self-driving car by 2020 [7]. Uber is one of the leading companies, in the area of vehicle automation, that partnered with Volvo in 2014 to introduce the third generation of their AVs that was anticipated to be to be tested by 2020 [8]. Similarly, Apple has launched the "Titan" project that focuses on developing AVs in 2014 with the vision of introducing AVs by 2023 to 2025 [9]. Additionally, AVs have attracted startup companies and a large number of companies are established with the goal of developing AVs such as Zoox [10]. From the perspective of cities, multiple cities started legalizing AVs as a quick reaction to this rapid development in the technology [11, 12]. In general, previous studies have shown that AVs have the potential to offer multiple benefits (improve the level of mobility, comfort, and productivity) [13–16] and risks (increase the vehicle travel distance, and in turn increase the level of congestion and emissions) [17]. While the implications of AVs have been investigated in a large number of studies, the public attitude has been rarely investigated in the literature. However, the main issues facing new technologies are non-technological and AVs are not an exception. For example, the IEEE has reported that the public attitude and acceptance of AVs will be the main barrier to the adoption of AVs [18].

Over the last few years, multiple studies have investigated the public attitude towards AVs, such as the studies by Othman [19], Jing et al. [20], Hilgarter and Granig [21], Wang et al. [22], Butler et al. [23], and Ahmed et al. [24]. Previous studies mainly focus on investigating the public acceptance of AVs for different groups with different demographics such as the gender, age, and education. On the other side, these studies show different levels of acceptance of AVs at different countries and at different years. While the public attitude has been investigated in the literature, the factors affecting the public attitude towards AVs have been rarely discussed. For example, Šinko et al. [25] study showed that while the level of awareness of AVs increases over time, the public became more negative towards AVs as the level of interest in AVs was dropping from 40% in 2014 (as shown in the study by Schoettle and Sivak

[26]) to 10% in 2017. Similarly, the study by Panagiotopoulos and Dimitrakopoulos [27] shows similar results as people become more negative towards AVs. The only difference between the early studies that showed high levels of interest in AVs and the more recent studies that show lower levels of interest towards AVs is the incidents involving AVs. In 2022, Othman [28] managed to explain this decline in the level of interest and they concluded that these two surveys by Schoettle and Sivak [26] and Panagiotopoulos and Dimitrakopoulos [27] were accompanied by the first fatal accident involving an AV in July 2016 that contributed to this negative switch in the public attitude towards AVs. Thus, accidents involving AVs have a major effect on the public perception of this emerging technology. Additionally, the study by Othman [19] studied the relation between the public attitude towards AVs and the number of fatal accidents involving AVs over the years using the data between 2016 and 2019 in the USA. The analysis shows a clear relation between the number of fatal accidents involving AVs and the percentage of respondents worried about AVs as this percentage increases with the increase in the number of accidents as shown in Fig. 1. As a result, it is crucial to investigate the relation between accidents of AVs and the public attitude towards this emerging technology. While the public acceptance of AVs has been investigated in multiple studies in the literature, the impact of accidents involving AVs on the public attitude has never been investigated in detail. Thus, the main objective of this study is to understand and quantify the impact of accidents involving AVs on the level of trust, interest, and concern of the public towards AVs. Additionally, a detailed analysis was conducted for different groups with different demographics (such as the age, gender, education, income, and previous knowledge about the technology) in order to understand how the opinions of these groups are affected by these accidents.
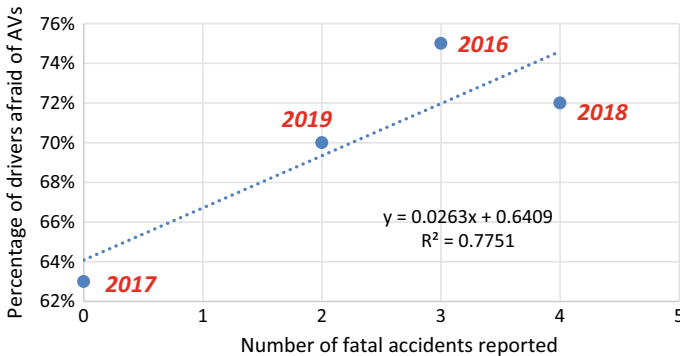
Fig. 1 The relation between the number of fatal accidents involving AVs and the percentage of people afraid of AVs in the USA. Adopted from [19]

2   Literature Review

In general, the studies that focus on analyzing the impacts of AVs' accidents are rare and these studies mainly analyze social media data in order to understand the public attitude towards AVs before and after an accident that involved an AV. Starting with the first study by Jefferson and McDonald [29] that used sentiment analysis of Twitter in order to understand how the public attitude towards AVs changes as a result of an AV accident. The study focused on analyzing tweets before and after the 10th of February 2019 accident that involved an AV. The authors collected and analyzed tweets three days before the accident, the day of the accident, and three days after the accident [30]. The analysis shows a major shift in the public attitude towards AVs. For example, the word "crash" did not appear prior to the accident; however, it became one of the most common words used on the day of the accident and three days prior. Additionally, the most common words prior to the accident were mainly about Amazon, startups, and investments. On the other side, the words "crash," "autopilot," and "vehicle" become the most common words used on the day of the accident and three days after the accident. Additionally, a sentiment analysis was conducted to measure the positivity and negativity of the tweets in order to understand the public attitude towards AVs. The sentiment analysis of the tweets shows a significant drop in the positive sentiment to almost half after the accident.

Penmetsa et al. [30] investigated the influence of two fatal accidents that occurred in March 2018. The first accident occurred on 18 March 2018 and it involved an Uber-operated Volvo vehicle with a self-driving system that collided with and killed a pedestrian who was crossing the street in Arizona [31, 32]. This accident was the first fatal accident involving a pedestrian. The second accident occurred on 23 March 2018, and it involved a Tesla Model X vehicle that speeded up and steered into a concrete barrier while it was operating on the autopilot mode [33, 34]. Penmetsa et al. [30] conducted a before-and-after sentiment analysis using the data collected 15 days before and 15 days after every incident. The analysis shows a significant change in the public attitude towards AVs. For example, the results show that the negative tweets about AVs or self-driving cars increased by 32%, jumping from 14 to 46%. Additionally, the average compound sentiment score witnessed a major decrease for the tweets involving Uber (-6%), Tesla (-6%), or self-driving cars (-11%). Thus, these results show a major impact of these two accidents on the public trust in AVs.

Finally, the study by Jing et al. [35] explored the impact of the NIO crash in August 2021 on the public attitude towards AVs in China. Unlike the previous two studies, this study collected and analyzed comments from Chinese mainstream social media platforms (Sina Weibo and TikTok) seven days before and seven days after the accident. In general, Sina Weibo and TikTok are the leading social media platforms in China that the report by Sina [36] revealed that Weibo had 530 million monthly active users, which represents one-third of the Chinese population. Similarly, TikTok has more than 680 million daily active users [37]. Results of the sentiment analysis show major changes in the positive and negative emotions before and after the accident as the negative sentiments witnessed 18% increase (from 29 to 47%), while the

positive sentiments witnessed 10% decrease (from 40 to 30%). Additionally, a day-by-day analysis of the comments shows that negative sentiment remains consistently negative at the same level for the entire seven days after the crash. Additionally, one of the key points highlighted by this study is that the sentiment score of the different brands of AVs is negatively affected by any accident involving an AVs in general even from a totally different brand. For example, in this study, the accident involved a NIO car; however, the sentiment analysis of Tesla shows a negative trend after the accident as the negative sentiment towards Tesla increased by 5% (from 43 to 43%), while the positive sentiment decreased by 9% (from 32 to 23%).

3   Research Gap and Study Objectives

Analyzing social media data is beneficial as it offers a large amount of data that helps in building conclusions. For example, Twitter holds over 300 million active accounts with more than 45%, and 30% of adults aged 18–24 years and 25–49 years use Twitter [29]. Thus, analyzing social media data provide a lot of insights about the impact of AVs accidents on the public attitude towards AVs. However, this analysis is subjected to multiple limitations and cannot really provide a detailed analysis for the different groups with different demographics. For example, the sentiment gathered from social media platforms might not accurately represent the general public. For example, more than one-third of Twitter users in the USA have a college degree and earn more than 75.000$ a year, which indicates that the US-based Twitter users have more education and higher income than the general average population in the USA [38]. Additionally, the 2021 report by Twitter shows that 62% of Twitter users are males [39]. Similarly, for the most leading social media platforms in China, around 80% of the users of both Sina Weibo and TikTok are adults who have an age of 30–40 years [37]. Thus, the results of analyzing social media data might be biased towards a specific group with specific demographics, which necessitates the need for a study that balance these demographics in the samples in order to have results that can generalize.

Secondly, the previous studies that used sentiment analysis concluded that there are several deficiencies in the application of topic modeling and sentiment analysis in the AV crash domain [29, 30]. First, the analysis shows that there is a mismatch between the sentiment assigned to words in a traditional sentiment dictionary and the likely sentiment of words in the AV domain [30], which necessitate the need to develop a domain-specific sentiment dictionary for AV domain. Second, the study by Jefferson and McDonald [29] mentioned that a notable number of tweets adopted the concept of blaming the vehicle and that the vehicle got confused. This frequent repetition of the words "blame" and "confused" suggests that Twitter users may be drawn to discussions of crashes involving compelling and concise narratives. The emergence of these terms highlighted a limitation in the keyword search, which suggests the need for a more advanced search method. Finally, the analysis shows

that most of the tweets are linked a website from newspapers [40], which is hard to analyze and include in the sentiment analysis.

Thus, this paper mainly focuses on investigating the change in the public attitude as a result of AVs' accidents in detail for different groups with different demographics in the USA. The main objectives of this study are:

- Understand the impact of AVs' accidents on the public trust, interest, and concern towards AVs.
- Understand how these accidents change the opinions of people in different age groups.
- Understand how these accidents change the opinions of males and females towards AVs.
- Understand how the opinions of people with different educational levels change after the accidents.
- Understand how these accidents affect the opinions of the people with different levels of income.

4 Methodology

This public survey was designed in order to assess the public attitude, trust, interest, and concern towards AVs before and after accidents that involve AVs. Before sending the main survey to the public, a pilot survey was conducted in order to make sure that the questions included in the survey are fair, accurate, descriptive, comprehensive, and understandable to the public. Thus, the survey was initially sent to five professors (from multiple universities across Canada and the USA) who mainly lead research in the domain of public surveys, and 20 participants from the general public in the USA. The assessment of the survey shows a great level of satisfaction from both the professors and the public participants as all the 25 respondents declared that they had no difficulty reading or understanding the questions. The survey consisted of three sections. The first section of the survey was an introductory page that provide the respondents with a brief overview about AVs and the purpose of the survey. The second section focuses on collecting the general opinion about AVs. In this section, the respondents were asked to rank their level of interest, trust, and concern about AVs on a Likert scale from 1 to 5. At beginning of the third section of the survey, nine different accidents with different levels of severity (minor, major, fatal) were introduced to the respondents with some images that visually shows the impact of the accident as summarized in Fig. 2. The main idea for choosing these different accidents was to introduce the different malfunctions that might occur and cause accidents from AVs starting from issues in the vision, issues in controlling speed (the vehicle speed up instead of slowing down in some cases causing an accident), and directions, to issues with the batteries that might cause explosion of the vehicle. The main objective of introducing these accidents is to try to put all the presidents on the same level of information regarding AVs accidents and the possible issues. After introducing these accidents, the respondents were asked to rank their level of interest,

Fig. 2 Details about the accidents introduced to the respondents during the survey (red text for fatal accidents and orange text for minor injury accidents)

trust, and concern regarding AVs once again on a Likert scale from 1 to 5. Finally, the last section of the survey focuses on collecting the demographic information of the respondents.

The survey was then posted online on SurveyMonkey platform between February to June 2022 and a total of 5880 responses were collected from respondents from the USA. The demographic characteristics of the sample used in this paper are summarized in Table 1. The table shows a good representation of the different groups in the sample, which is essential for this study to understand the impact of accidents of AVs on the different age groups. The gender ratio was balanced as 48% of the respondents were males and the remaining 52% were females. Similarly, the different age groups are well represented in the survey sample as the different groups are almost equally represented in the sample. For the educational levels attained, most of the respondents either have a high school degree or lower, or have a bachelor's degree, while 22% of the respondents have a master's degree or a higher. While the sample seems to underrepresent respondents with higher degrees of education, it is actually very representative of the educational attainment data published by the United States Census Bureau in February 2022 [41]. The Census Bureau report shows that 36.8% of the US population has a high school degree or less, compared to 32.8% of the respondents who highlighted that they have a high school degree or lower. Similarly, the Census Bureau report shows that 48.9% of the US population have bachelor's degrees, and 14.4% have master's degrees, compared to 45% and 16% of the survey respondents. A similar trend can be observed for the yearly household income, the different percentages are very similar to the real income distribution in the USA as shown in the Census Bureau report in 2021 [42]. The Census Bureau report shows that 18.1%, 19.7%, 28.7%, and 23.3% of the US population has a yearly annual

**Table 1** Demographic information of the respondents participated in the survey

Demographic characteristics		Frequency (N)	Percentage (%)
Gender	Male	2805	47.70
	Female	3075	52.30
Age	18–29	1315	22.36
	30–44	1814	30.85
	45–60	1345	22.87
	>60	1406	23.91
Education	High school or lower	1930	32.82
	Bachelor	2648	45.03
	Master's degree	943	16.04
	Higher than master's degree	359	6.11
Household income ($/year)	<25,000	1204	20.48
	25,000–50,000	1237	21.04
	50,000–100,000	2067	35.15
	100,000–200,000	1186	20.17
	>200,000	186	3.16

household income of 25K$, 25–50K$, 50–100K$, and 100–200K$, compared to 20.48%, 21.04%, 35.15%, and 20.17% from the survey respondents.

5 Results

5.1 Impact of AVs' Accidents on the Public Attitude Towards AVs

This part focuses on understanding how the public attitude towards AVs changes for all respondents after introducing the accidents. Figures 3, 4, and 5 show the average level of interest, trust, and concern about AVs before and after introducing the accidents. The results show major changes in the public attitude towards the negative direction after introducing the accidents. The general opinion about AVs became more negative towards AVs after introducing the accidents. On a scale from 1 to 5 where 1 indicates that the respondent has a very negative opinion about AVs and 5 indicates that the respondent has a very positive opinion about AVs, the average opinion of all respondents moves in the negative direction after the accident jumping from 3.2 before introducing the accidents to 2.9 after the accidents as shown in Fig. 3. Additionally, there is a major reduction in the level of trust in AVs as the level of trust decreases from an average value of 3.22–2.86 after introduction the accidents as shown in Fig. 4. Finally, the level of concern regarding AVs increased
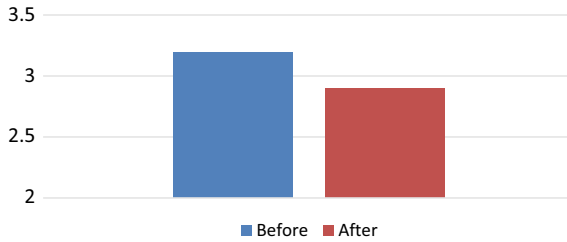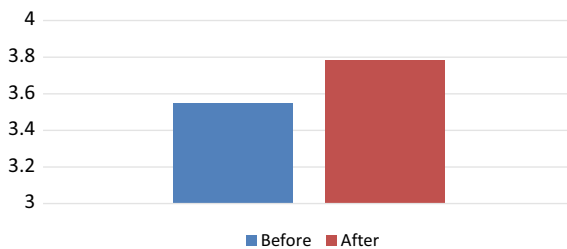
Fig. 3 Average level of interest for all respondents before and after introducing the accidents (where 5 indicates "very positive opinion" and 1 indicates "very negative opinion"). Before = before introducing the accidents, After = after introducing the accidents

after introducing the accidents from an average value of 3.55–3.78 as shown in Fig. 5. The results presented in this subsection are consistent with the results introduced in previous studies that analyzed social media data [29–33] as all these studies concluded that the public attitude becomes more pessimistic towards AVs after an accident.
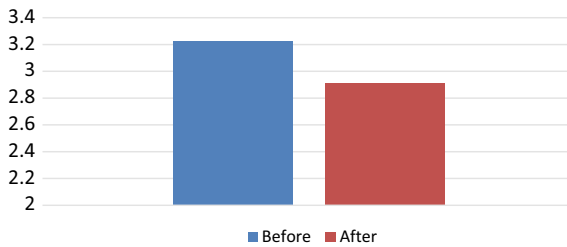
Fig. 4 Average level of trust for all respondents in AVs before and after introducing the accidents (where 5 indicates "strongly agree" and 1 indicates "strongly disagree"). Before = before introducing the accidents, After = after introducing the accidents


Fig. 5 Average level of concern for all respondents about AVs before and after introducing the accidents (where 5 indicates "highly concerned" and 1 indicates "not concerned at all"). Before = before introducing the accidents, After = after introducing the accidents
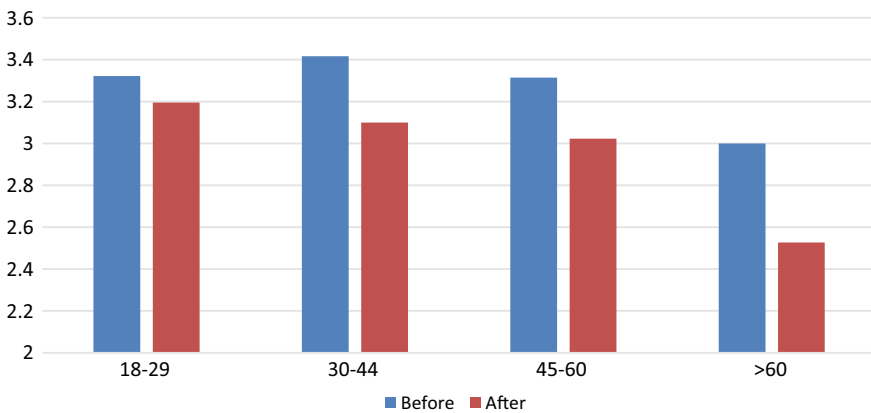
5.2 Perception of AVs for Different Age Groups Before and After AVs Accidents

Previous studies that investigated the public attitude towards AVs highlighted that the public acceptance of AVs changes according to the age of the respondents. In general, a large number of studies concluded that there is an inverse relationship between the age of the respondent and the level of interest in AVs [43–47]. In this subsection, the public attitude of the different age groups will be investigated before and after introducing the accidents. Figures 6, 7, and 8 show the opinion, level of trust, and concern of the different age groups in AVs. In general, the public attitude towards AVs became more negative after introducing the accidents for the different age groups. Before introducing the accidents, the general opinion about AVs for the respondents who have 18–29 years old was at an average value of 3.43 and increased to 3.5 for respondents who have 30–44, then, it declined to 3 and 2.75 for respondents at the 45–60 and > 60 age groups as shown in Fig. 6. On the other side, after introducing the accidents, the general opinion had a different pattern as respondents became more pessimistic towards AVs with the increase in the age. Figure 6 shows that, after introducing the accidents, the general opinions have an average value of 3.28, 3.1, 2.87, and 2.39 for respondents in the 18–29, 30–44, 45–60, and > 60 age groups. For the level of trust in AVs, the before and after cases have two different patterns very similar to the two patterns observed in the general opinion about AVs. Before introducing the accidents, the level of trust for the 18–29 years group was at an average value of 3.32 and increased to 3.42 for the 30–40 years group and then declined to 3.31 and 3 for the 45–60 and > 60 groups as shown in Fig. 7. On the other side, after introducing the accidents, the level of trust in AVs has an inverse relation with the age as the average level of trust is 3.2, 3.1, 3.02, and 2.53 for respondents in the 18–29, 30–44, 45–60, and > 60 age groups. Additionally, it can be seen that the elder group (>60) is not only the group with the lowest level of interest in AVs before introducing the accidents, but also the group with the most significant decrease in the level of interest and trust after introducing the accidents as their average opinion moves from 2.75 to 2.36 (15% decrease) and the average level of trust moves from 3 to 2.53 (16% decrease).

For the level of concern about AVs, the results show that there is a direct relationship between the age of the respondents and the level of concern towards AVs for the two cases before and after the accidents as shown in Fig. 8. Before introducing the accidents, the average levels of concerns were 3.2, 3.54, 3.53, and 3.86 for respondents in the 18–29, 30–44, 45–60, and > 60 age groups. On the other side, the levels of concerns increase after introducing the accidents to 3.45, 3.74, 3.74, and 4.17 for respondents in the 18–29, 30–44, 45–60, and > 60 age groups. Additionally, the elder group does not (>60) only has the highest level of concerns regarding AVs before and after introducing the accidents, but also has the highest increase in the level of concerns from 3.86 to 4.17 (8% increase).
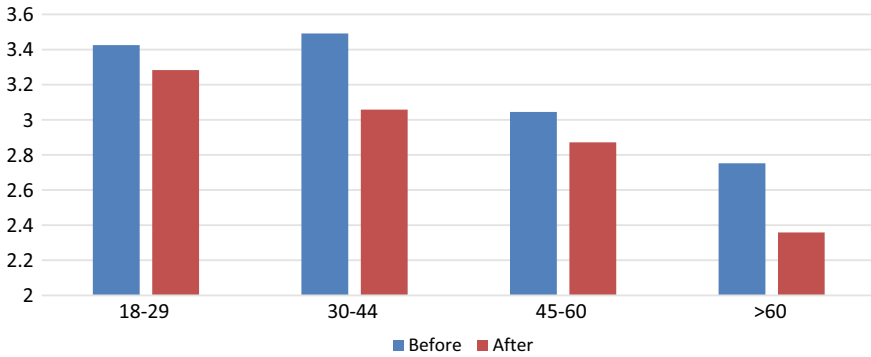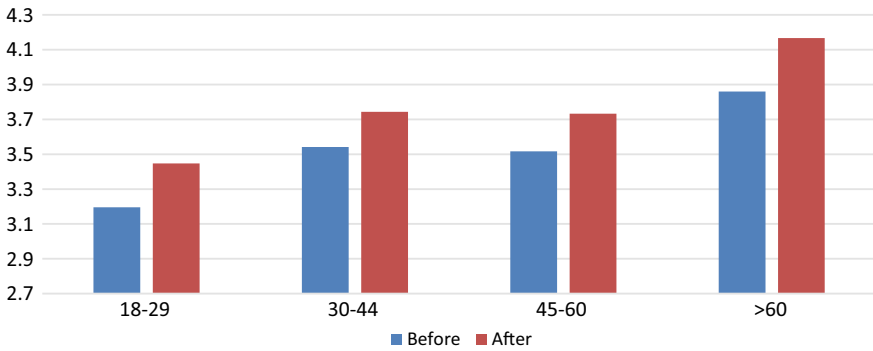
Fig. 6 Average level of interest for the different age groups before and after introducing the accidents (where 5 indicates "very positive opinion" and 1 indicates "very negative opinion"). Before = before introducing the accidents, After = after introducing the accidents

Fig. 7 Average level of trust in AVs for the different age groups before and after introducing the accidents (where 5 indicates "strongly agree" and 1 indicates "strongly disagree"). Before = before introducing the accidents, After = after introducing the accidents

5.3 *Impact of AVs' Accidents on the Public Attitude of Males and Females*

In general, previous studies that investigated the public attitude towards AVs highlighted that the public attitude towards AVs changes according to the gender of the respondents. In general, males are more optimistic towards AVs than females as concluded in a large number of studies [43–45, 47–51]. This subsection focuses on quantifying the impact of AVs' accidents on the opinion, level of trust, and concerns of males and females towards AVs. Figures 9, 10, and 11 summarize the opinion,

Fig. 8 Average level of concern about AVs for the different age groups before and after introducing the accidents (where 5 indicates "highly concerned" and 1 indicates "not concerned at all"). Before = before introducing the accidents, After = after introducing the accidents

level of trust, and concern of male and female respondents before and after introducing the accidents. Additionally, introducing the accidents had a significant impact on the attitude of female respondents when compared to the change in the attitude of male respondents. In general, male respondents are more optimistic towards AVs than female respondents before and after introducing the accidents. Before introducing the accidents, male respondents had an average positive opinion of 3.39 which is higher than the 3.23 for the average aver opinion of female responses as shown in Fig. 9. Then, after introducing the accidents, the opinions of male and female respondents reached an average value of 3.23 and 2.7. For the level of trust, male respondents had an average level of trust of 3.48 before introducing the accidents and female respondents had an average level of trust of 3 as shown in Fig. 10. Then, this level of trust declined, after introducing the accidents, to 3.19 and 2.67 for male and female respondents. Finally, the level of concern increased for both male and female respondents after the accidents moving from 3.33 to 3.58 for male respondents and from 3.76 to 4.06 for female respondents as shown in Fig. 11. While the previous results show that female respondents are always less optimistic towards AVs than male respondents, it also shows that the impact of these accidents on the opinion of female respondents is more significant than on the opinions of male respondents. The positive opinion of female respondents moves from 3.03 before introducing the accidents to 2.7 after introducing the accidents (11% decrease), while the female respondents' level of trust moves from 3 to 2.67 (11% decrease). Similarly, the level of concerns about AVs moved from 3.75 to 4.06 (8.5% increase) for female respondents.
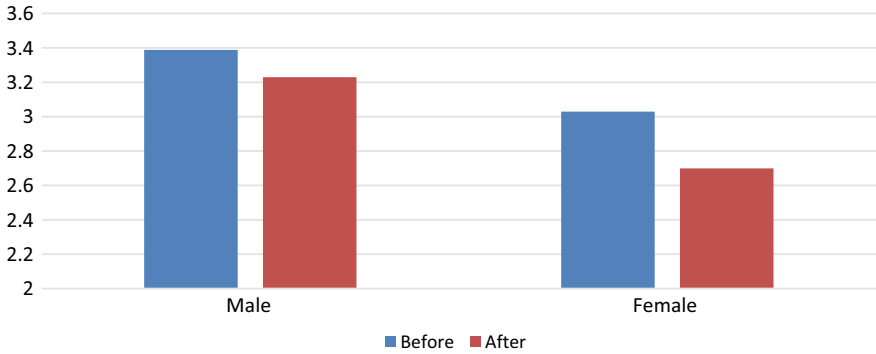
Fig. 9 Average level of interest for males and females before and after introducing the accidents (where 5 indicates "very positive opinion" and 1 indicates "very negative opinion"). Before = before introducing the accidents, After = after introducing the accidents
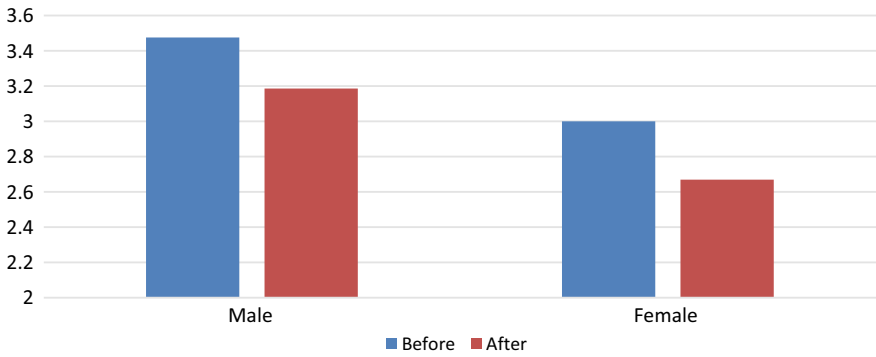
Fig. 10 Average level of trust in AVs for males and females before and after introducing the accidents (where 5 indicates "strongly agree" and 1 indicates "strongly disagree"). Before = before introducing the accidents, After = after introducing the accidents
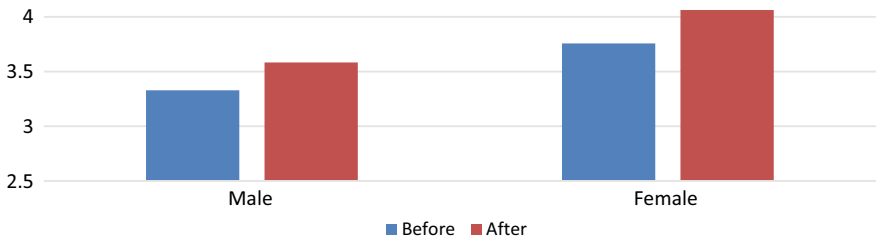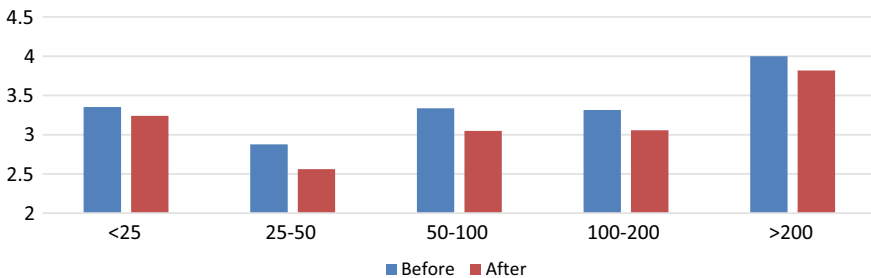

Fig. 11 Average level of concern about AVs for males and females before and after introducing the accidents (where 5 indicates "highly concerned" and 1 indicates "not concerned at all"). Before = before introducing the accidents, After = after introducing the accidents

5.4 Impact of AVs' Accidents on Respondents with Different Household Incomes

Analyzing the level of acceptance of AVs technology based on the level of income has been rarely discussed in the literature. However, plenty of studies managed to analyze the public acceptance of AVs for respondents with different household income levels in different countries [52, 53]. Thus, in this subsection, the public attitude towards AVs before and after introducing the accidents for respondents with different household income levels was investigated. Figures 12, 13, and 14 show the opinion, level of trust, and concerns towards AVs for respondents within a specific household income level. The figures show that the level of interest and trust in AVs decreased after introducing the accident for the different respondents within the different household income levels. Additionally, both the general opinion and level of trust in AVs have the same pattern before and after introducing the accidents and in general respondents within the 25–50K$ are the least optimistic and have the lowest level of trust in AVs before and after introducing the accidents. On the other side, respondents who have a household income of more than 200K$ are the most optimistic towards AVs and show the highest level of trust towards AVs before and after introducing the accidents. Comparing these results with the results of the survey by Lee et al. [54] in the USA shows a high level of consistency in the results of the two surveys as the results of the two surveys have similar patterns. Lee et al. [54] study shows that the level of interest in AVs has a parabolic with the different household income levels, which is consistent with the results presented in Figs. 12 and 13.

For the level of concern regarding AVs, respondents show similar results as the relation between the level of concern and household income takes an inverse parabolic shape before and after introducing the accidents which is the opposite of the relations shown in Figs. 12 and 13 for the level of trust and interest in AVs. Additionally, respondents within the 25–50K$ household income have the highest level of concerns regarding AVs (peak point) before and after introducing the accidents with an average

Fig. 12 Average level of interest for respondents with different household income before and after introducing the accidents (where 5 indicates "very positive opinion" and 1 indicates "very negative opinion"). Before = before introducing the accidents, After = after introducing the accidents
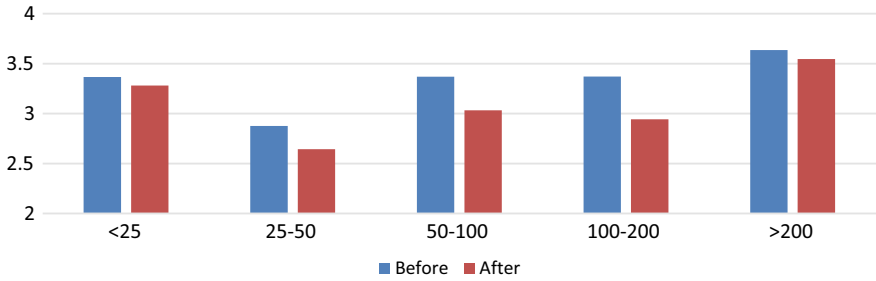
Fig. 13 Average level of trust in AVs for respondents with different household income before and after introducing the accidents (where 5 indicates "strongly agree" and 1 indicates "strongly disagree"). Before = before introducing the accidents, After = after introducing the accidents
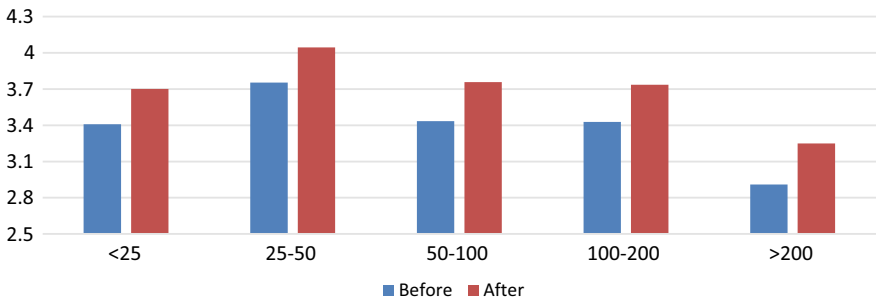
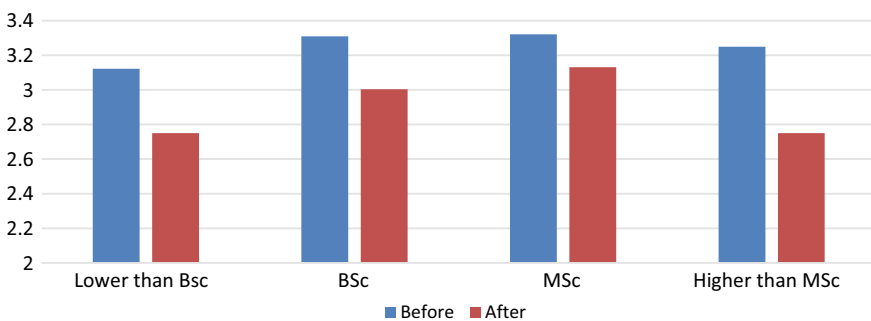**Fig. 14** Average level of concern about AVs for respondents with different household income before and after introducing the accidents (where 5 indicates "highly concerned" and 1 indicates "not concerned at all"). Before = before introducing the accidents, After = after introducing the accidents

concern level of 3.75 and 4.04 before and after introducing the accidents. On the other hand, respondents with the highest level of household income, which is > 200K$, are the least concerned about AVs before and after introducing the accidents with an average level of concern of 2.9 and 3.25 before and after introducing the accidents. Additionally, Fig. 14 shows that the level of concern regarding AVs increases for the different levels of household incomes after introducing the accidents.

## 5.5   Impact of AVs' Accidents on Respondents with Different Educational Levels

Over the last few years, multiple studies investigated the attitude of people with different education levels towards AVs. In general, the results of previous studies show that people with different educational levels perceive the benefits and drawbacks of AVs differently [43, 50, 55]. The general trend observed is that people with higher

educational levels are more optimistic towards AVs, which was concluded in the studies by Piao et al. [43] and Lee et al. [54]. Thus, this subsection focuses on investigating the public attitude of the respondents within the different educational levels before and after introducing the accidents. Figures 15, 16, and 17 show the opinion, level of trust, and concern about AVs of the respondents with different educational levels before and after introducing the accidents. For the general opinion towards AVs before introducing the accidents, respondents with higher educational levels show higher positive opinion, except for respondents with an educational level that is higher than a master's degree who show a minor lower level of positive opinion towards AVs than respondents as shown in Fig. 15. After introducing the accidents, the general opinion towards AVs became less positive for the four groups; however, the positive opinion towards AVs had the same pattern as before introducing the accidents as respondents with higher educational levels showed higher positive attitude towards AVs, except for respondents with an educational level that is higher than a master's degree who showed a major decrease in their positive opinion towards AVs from 3.25 before the accidents to 2.75 after introducing the accidents (15.4% decrease) to make their opinion towards AVs similar to the opinion of the respondents with an educational level that is lower than a bachelor's degree after introducing the accident. For the level of trust of AVs before introducing the accidents, Fig. 16 shows that respondents with higher educational levels have higher levels of trust towards AVs, except for respondents who have an educational level that is higher than a master's degree. On the other side, after introducing the accidents, the different respondents with different educational levels show similar levels of trust towards AVs ranging from a maximum value of 2.94 for respondents with a master's degree to a minimum value of 2.8 for respondents with a bachelor's degree. Comparing these results with the results of the study by Lee et al. [54] in the USA shows that the two studies show a high level of agreement as the two studies show similar patterns for the relations between the educational levels and the level of interest towards AVs.

Fig. 15 Average level of interest for respondents with different educational levels before and after introducing the accidents (where 5 indicates "very positive opinion" and 1 indicates "very negative opinion"). Before = before introducing the accidents, After = after introducing the accidents
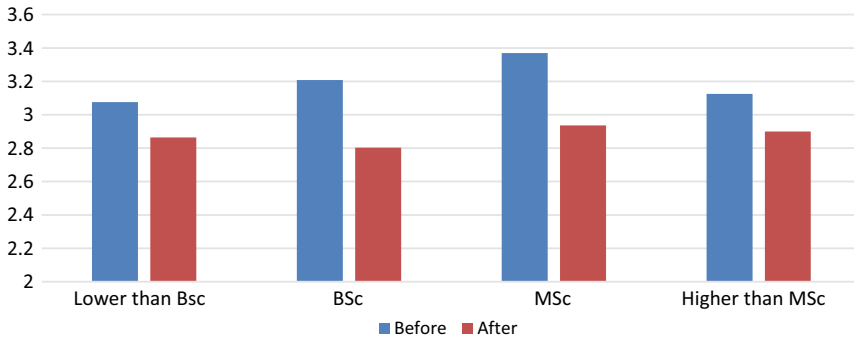
Fig. 16 Average level of trust in AVs for respondents with different educational levels before and after introducing the accidents (where 5 indicates "strongly agree" and 1 indicates "strongly disagree"). Before = before introducing the accidents, After = after introducing the accidents
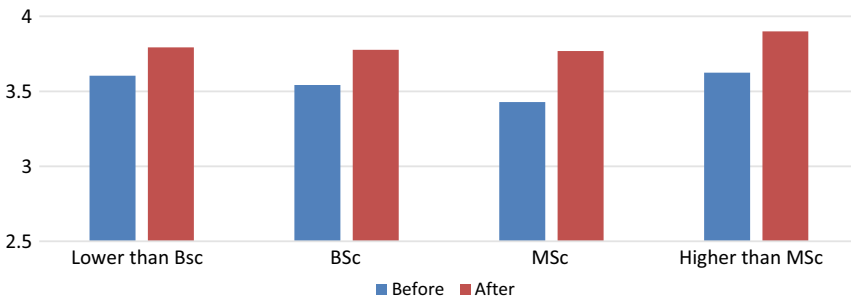
Fig. 17 Average level of concern about AVs for respondents with different educational levels before and after introducing the accidents (where 5 indicates "highly concerned" and 1 indicates "not concerned at all"). Before = before introducing the accidents, After = after introducing the accidents

Finally, for the levels of concern towards AVs before introducing the accidents, the results show that respondents with higher educational levels have lower levels of concern towards AVs except for the respondents with a degree higher than a master's degree who showed a higher level of concern that is similar to the respondents with a degree lower than a bachelor's degree as shown in Fig. 17. On the other hand, after introducing the accidents to the respondents, the levels of concern increased for all respondents across the different educational levels that the respondents with different educational levels showed similar levels of concern, except for respondents with a degree higher than a master's degree who had higher levels of concern. Specifically, the average levels of concern regarding AVs after introducing the accidents were 3.79, 3.78, 3.3.77, and 3.9 for respondents with a degree lower than a bachelor's degree, respondents with bachelor's degrees, respondents with master's degrees, and respondents with a degree higher than a master's degree.

6 Conclusion

This study focuses on investigating the impact of accidents involving AVs on the public attitude towards this emerging technology for the different groups with different demographic characteristics. Thus, a questionnaire survey was conducted, and a total of 5880 complete responses were collected from respondents with different demographic characteristics in the USA. During the survey, the respondents were asked to rank their interest, level of trust, and concern about AVs on a Likert scale from 1 to 5; then, multiple accidents that involved AVs were introduced to the respondent and they were asked to rank their level of interest, trust, and concern about AVs once again. Then, the responses were analyzed based on the different demographic characteristics of the survey respondents (age, gender, educational level, household income, prior knowledge about AVs, and prior knowledge about AVs' accidents) before and after the accidents. This study offers multiple insights about the impact of AVs' accidents on the public attitude towards this emerging technology as follows:

- In general, the public attitude towards AVs became more negative after introducing the accidents as the respondents showed lower levels of interest and trust in AVs with higher levels of concern about the technology after introducing the accidents.
- Analyzing the responses based on the age of the respondents showed that younger respondents are more optimistic towards AVs before and after introducing the accidents. In other words, there are inverse relations between the age of the respondents from the one side and the level of interest and trust in AVs from the other side. On the other side, there is a direct relation between the level of concern about AVs and the age of the responses for the two cases before and after introducing the accidents. Additionally, the negative shift in the respondents' opinion increases with the increase in the age of the respondents.
- Analyzing the responses based on the gender shows that male respondents are more optimistic towards AVs than female respondents before and after introducing the accidents. Additionally, after introducing the accidents, the negative shift in the opinion of female respondents was much larger than the negative shift in the opinion of male respondents.
- Analyzing the responses based on the household income of the respondents shows that the relations between the level of interest, trust, and concern and the household income take a parabolic shape before and after introducing the accidents. The results show that respondents who have a household income of 25–50K$ are the most pessimistic towards AVs, while respondents with a household income > 200K$ have the highest level of interest towards AVs. Additionally, the negative shift in the opinion of the respondents in the 25–50K$ household income group is the largest when compared with the other groups.
- Analyzing the data based on the educational levels shows that respondents with higher educational levels are more in AVs technology before introducing the accidents, except for respondents who hold a degree higher than a master's degree. On the other side, after introducing the accidents, a similar pattern can be observed for the general opinion of the responses with different educational levels, but the

levels of trust and concern towards AVs became similar for the different groups except for the respondents with a degree higher than a master's degree who showed slightly higher levels of concern regarding the technology.

- The results show that respondents with prior knowledge about AVs are more optimistic about this emerging technology for both cases before and after introducing the accidents. Additionally, after introducing the accidents, the negative shift in the attitude decreases with the increase in the level of prior knowledge of the respondents about AVs. This analysis sheds light on the importance of educating the public about AVs and their benefits in order to achieve the highest level of acceptance of this emerging technology.

7 Limitations and Recommendations for Future Studies

While this study gives insights into the impact of accidents of AVs on the public attitude, this study has its limitations. This study focuses on the opinion of respondents from the USA, so further studies are needed to understand the impact of AVs accidents using the same approach in other countries. Additionally, the public awareness about AVs and in turn the public attitude are expected to change over time. Thus, it is recommended to replicate the survey regularly in order to understand how the change in the level of awareness is correlated with the public attitude.

References

1. The Milwaukee Sentinel. Phantom auto' will tour city, 8 Dec 1926
2. The Victoria Advocate. Power companies build for your new electric living, 24 Mar 1957
3. Davidson P, Spinoulas A (2015) Autonomous vehicles—what could this mean for the future of transport? In: AITPM 2015 national conference, Sydney
4. Berrada J, Leurent F (2017) Modeling transportation systems involving autonomous vehicles: a state of the art. In: Transportation research procedia. 20th EURO working group on transportation meeting, EWGT 2017, Budapest, Hungary, 4–6 Sept 2017
5. Greenblatt JB, Shaheen S (2015) Automated vehicles, on-demand mobility, and environmental impacts. Curr Sustain Renew Energy Rep 2:74–81. https://doi.org/10.1007/s40518-015-0038-5
6. Mallozzi P, Pelliccione P, Knauss A, Berger C, Mohammadiha N (2019) Autonomous vehicles: state of the art, future trends, and challenges. In: Dajsuren Y, van den Brand M (eds) Automotive systems and software engineering. Springer, Berlin. http://doi.org/10.1007/978-3-030-12157-0_16
7. Hartmans A (2016) How Google's self-driving car project rose from a crazy idea to a top contender in the race toward a driverless future. https://www.businessinsider.com/google-driverless-car-history-photos-2016-10
8. O'Kane S (2019) Uber debuts a new self-driving car with more fail-safes. https://www.theverge.com/2019/6/12/18662626/uber-volvo-self-driving-car-safety-autonomous-factory-level
9. Staff M (2019) Apple's vehicle project, focused on building an autonomous driving system. https://www.macrumors.com/roundup/apple-car/#release_date
10. Taylo T (2018) Top 8 self-driving startups to watch in 2018 and 2019. http://techgenix.com/self-driving-startups/

11. National Conference of State Legislatures (2020) Autonomous vehicles|self-driving vehicles enacted legislation. https://www.ncsl.org/research/transportation/autonomous-vehicles-self-driving-vehicles-enacted-legislation.aspx

12. Laukkonen J (2020) Are self-driving cars legal in your state? https://www.lifewire.com/are-self-driving-cars-legal-4587765

13. Othman K (2021) Impact of autonomous vehicles on the physical infrastructure: changes and challenges. Designs 5(3):40

14. Mugunthan SR (2020) Concept of Li-Fi on smart communication between vehicles and traffic signals. J Ubiquitous Comput Commun Technol 2:59–69

15. Othman K (2022) Cities in the era of autonomous vehicles: a comparison between conventional vehicles and autonomous vehicles. In: Resilient and responsible smart cities. Springer, Cham, pp 95–108

16. Bindhu V (2020) An enhanced safety system for auto mode E-vehicles through mind wave feedback. J Inf Technol 2(03):144–150

17. Othman K (2022) Multidimension analysis of autonomous vehicles: the future of mobility. Civ Eng J 7:71–93

18. Newcomb (2012) You won't need a driver's license by 2040. Cable News Network, 18 Sept 2012. Web, 19 Nov 2012. http://www.cnn.com/2012/09/18/tech/innovation/ieee-2040-cars/index.html

19. Othman K (2021) Public acceptance and perception of autonomous vehicles: a comprehensive review. AI Ethics 1:355–387. https://doi.org/10.1007/s43681-021-00041-8

20. Jing P, Xu G, Chen Y, Shi Y, Zhan F (2020) The determinants behind the acceptance of autonomous vehicles: a systematic review. Sustainability 12(5):1719

21. Hilgarter K, Granig P (2020) Public perception of autonomous vehicles: a qualitative study based on interviews after riding an autonomous shuttle. Transp Res F Traffic Psychol Behav 72:226–243

22. Wang S, Jiang Z, Noland RB, Mondschein AS (2020) Attitudes towards privately-owned and shared autonomous vehicles. Transp Res F Traffic Psychol Behav 72:297–306

23. Butler L, Yigitcanlar T, Paz A (2021) Factors influencing public awareness of autonomous vehicles: empirical evidence from Brisbane. Transp Res F Traffic Psychol Behav 82:256–267

24. Ahmed ML, Iqbal R, Karyotis C, Palade V, Amin SA (2021) Predicting the public adoption of connected and autonomous vehicles. IEEE Trans Intell Transp Syst 23(2):1680–1688

25. Šinko S, Knez M, Obrecht M (2017) Analysis of public opinion on autonomous vehicles. In: Challenges of Europe: international conference proceedings. Sveuciliste u Splitu, pp 219–230

26. Schoettle B, Sivak M (2014) A survey of public opinion about autonomous and self-driving vehicles in the US, the UK, and Australia. University of Michigan, Ann Arbor, Transportation Research Institute

27. Panagiotopoulos I, Dimitrakopoulos G (2018) Consumers' perceptions towards autonomous and connected vehicles: a focus-group survey on university population. In: Proceedings of the 6th humanist conference, The Hague, Netherlands

28. Othman K (2022) Exploring the implications of autonomous vehicles: a comprehensive review. Innov Infrastruct Solutions 7(2):1–32

29. Jefferson J, McDonald AD (2019) The autonomous vehicle social network: analyzing tweets after a recent tesla autopilot crash. In: Proceedings of the human factors and ergonomics society annual meeting, vol 63, no 1. SAGE Publications, Los Angeles, pp 2071–2075

30. Penmetsa P, Sheinidashtegol P, Musaev A, Adanu EK, Hudnall M (2021) Effects of the autonomous vehicle crashes on public perception of the technology. IATSS Research

31. Levin S (2018) Tesla fatal crash: 'autopilot' mode sped up car before driver killed, report finds. The Guardian. https://www.theguardian.com/technology/2018/jun/07/tesla-fatal-crash-silicon-valley-autopilot-mode-report

32. Levin S, Carrie J (2018) Self-driving Uber kills Arizona woman in first fatal crash involving pedestrian. The Guardian. https://www.theguardian.com/technology/2018/mar/19/uber-self-driving-car-kills-woman-arizona-tempe

33. Levin S, Woolf N (2016) Tesla driver killed while using autopilot was watching Harry Potter, witness says. The Guardian. https://www.theguardian.com/technology/2016/jul/01/tesla-driver-killed-autopilot-self-driving-car-harry-potter
34. Guardian staff. Tesla car that crashed and killed driver was running on Autopilot, firm says. The Guardian. https://www.theguardian.com/technology/2018/mar/31/tesla-car-crash-autopilot-mountain-view
35. Jing P, Cai Y, Wang B, Wang B, Huang J, Jiang C, Yang C. Listen to social media users: mining Chinese public perception of autonomous vehicles after crashes. Available at SSRN 4011917
36. Sina (2020) Weibo monthly active users reach 523 million, user portraits and behavior analysis 9 of China's mobile social industry in 2020
37. CaiLian Press (2021) Tik Tok aims to have 680 million daily active users this year. https://3g.163.com/tech/article_cambrian/G7MVS9LP00097U7R.html
38. Alambeigi H, Smith A, Wei R, McDonald A, Arachie C, Huang B (2021) A novel approach to social media guideline design and its application to automated vehicle events. In: Proceedings of the human factors and ergonomics society annual meeting, vol 65, no 1. SAGE Publications, Los Angeles, pp 1510–1514
39. Luo S, He SY (2021) Understanding gender difference in perceptions toward transit services across space and time: a social media mining approach. Transp Policy 111:63–73
40. McDonald T, Huang B, Wei R, Alambeigi H, Arachie C, Smith A, Jefferson J, Safety through Disruption (2021) Data mining Twitter to improve automated vehicle safety (No. 04-098). Safety through Disruption (Safe-D), University Transportation Center (UTC)
41. United States Census Bureau (2022) Census Bureau releases new educational attainment data. https://www.census.gov/newsroom/press-releases/2022/educational-attainment.html
42. Shrider EA, Kollar M, Chen F, Semega J (2021) Income and poverty in the United States: 2020. US Census Bureau, current population reports (P60-273)
43. Piao J, McDonald M, Hounsell N, Graindorge M, Graindorge T, Malhene N (2016) Public views towards implementation of automated vehicles in urban areas. Transp Res Procedia 14:2168–2177
44. Richardson E, Davies P (2018) The changing public's perception of self-driving cars
45. Abraham H et al (2017) Autonomous vehicles and alternatives to driving: trust, preferences, and effects of age. In: Transportation Research Board 96th annual meeting
46. Lee C, Ward C, Raue M, D'Ambrosio L, Coughlin JF (2017) Age differences in acceptance of self-driving cars: a survey of perceptions and attitudes. In: international conference on human aspects of IT for the aged population. Springer, Cham, pp 3–13
47. Park J, Hong E, Le HT (2021) Adopting autonomous vehicles: the moderating effects of demographic variables. J Retail Consum Serv 63:102687
48. Polydoropoulou A, Tsouros I, Thomopoulos N, Pronello C, Elvarsson A, Sigþórsson H, Dadashzadeh N, Stojmenova K, Sodnik J, Neophytou S, Esztergár-Kiss D (2021) Who is willing to share their AV? Insights about gender differences among seven countries. Sustainability 13(9):4769
49. Pigeon C, Alauzet A, Paire-Ficout L (2021) Factors of acceptability, acceptance and usage for non-rail autonomous public transport vehicles: a systematic literature review. Transpo Res F Traffic Psychol Behav 81:251–270
50. Rezaei A, Caulfield B (2020) Examining public acceptance of autonomous mobility. Trav Behav Soc 21:235–246
51. Schoettle B, Sivak M (2014) A survey of public opinion about autonomous and self-driving vehicles in the U.S., the U.K., and Australia
52. Yuen KF, Wong YD, Ma F, Wang X (2020) The determinants of public acceptance of autonomous vehicles: an innovation diffusion perspective. J Clean Prod 270:121904
53. Yuen KF, Chua G, Wang X, Ma F, Li KX (2020) Understanding public acceptance of autonomous vehicles using the theory of planned behaviour. Int J Environ Res Public Health 17(12):4419
54. Lee C, Seppelt B, Reimer B, Mehler B, Coughlin JF (2019) Acceptance of vehicle automation: effects of demographic traits, technology experience and media exposure. In: Proceedings of

the Human Factors and Ergonomics Society annual meeting, vol 63, no 1. SAGE Publications, Los Angeles, pp 2066–2070

55. Zhang Q, Yang XJ, Robert LP Jr (2022) Individual differences and expectations of automated vehicles. Int J Human-Comput Inter 38(9):825–836

Increasing Efficiency in the Correlation Processing of Information Signals for Radar

Juliy Boiko and **Lesya Karpova**

Abstract This chapter investigates mathematical models of radar echo signals. The correlation properties of these signals were evaluated. A method of increasing the radar resolution based on the autocorrelation estimation algorithm is proposed. Potential possibilities of the method are investigated. The main contribution of this chapter is the consideration of the signal detection algorithm in accordance with the signal database. The main goal is to increase the degree of their resolution and increase noise immunity during coherent processing. A model of the radar echo signal is presented, taking into account the variety of possible probing factors. The experimental results made it possible to estimate the potential gain in terms of signal/noise when using the method. The resulting increase in resolution reached several times at a fixed signal/noise level. The findings will be useful in improving radar signal processing algorithms taking into account fluctuation components in their complex envelope.

Keywords Electromagnetic · Signal processing · Radar · Autocorrelation estimation · Signal-to-noise ratio · Probing · Antenna

1 Introduction

The algorithm for processing radar signals is the first and most important component of the triad: algorithms, processor architecture—the element base, which is the basis of digital processing. A special element of such a scheme is the correlator or matched filter. It determines the efficiency of detection and discrimination of signals by a radar tool. In this case, the potential capabilities of probing signals (active, semi-active radars) are taken into account, as well as the computing power of the elements for implementing the processing method [1].

A number of works have been devoted to improving the resolution of active and semi-active radar systems [2–4].

J. Boiko (✉) · L. Karpova
Khmelnytskyi National University, 11, Instytuts'ka str., Khmelnytskyi 29016, Ukraine
e-mail: boiko_julius@ukr.net

At present, two clear trends can be identified [5–7] to create a model of the echo signals in the active radar channel. The first is to create a generalized model for the echo signal which has a fairly common property. Second, in creating a model of the echo signal [8] for the particular type of radar and radar observation conditions. There are models that result from methodological differences in the solution of Maxwell's equations [6]. Theoretically, accurate models are mainly intended for solving problems of field scattering on bodies of the simplest shape. The analysis of fields of objects of complex shape is associated with the use of various simplified equations when solving. The combination of these approximations and the physical meaning of electromagnetic processes determines the group of physical models.

The approach to constructing the internal structure of echo-signal models is determined by the classification of radar models and objects [9, 10]. Select point or distributed, concentrated or extended, linear or surface objects.

Existing echo modeling techniques can be divided into deterministic method and a statistical method. For deterministic models characterized by the presence of the specified current position of the observed objects and their dependencies known reflective characteristics. Statistical modeling is used when the reflective properties of radar objects are random. It is used when there are interfering components in the echo signal [11].

The formation of a real echo signal is influenced by the parameters of the radar, the radar track, the radar object, and its reflection properties. Existing approaches to modeling the echo signal differ in the adequacy of taking into account real physical processes. The modeling of echo signals is based on models and methods for representing the scattering properties of objects [12, 13]. The greatest difficulties arise when imitating the radar parameters of an object observed on the surface of its placement.

Fields of complex-shaped objects, which include marine objects in the centimeter range, can be analyzed using methods of geometric optics or methods of physical theory of diffraction [14–17]. These allow you to get results with a high degree of accuracy. However, they are accompanied by a significant number of calculations and require an analytical description of the object surface. Repetitions are required for each new view of the full computational object.

One of the first approaches to calculating the radar cross section (RCS) of complex-shaped objects is the minimax method. This method occupies a transitional position between the classical methods of scattering theory and methods that allow calculating probabilistic characteristics. These methods allow one to estimate only the boundaries (top and bottom) of random changes in the RCS.

Analytical methods for calculating the probabilistic characteristics of the reflected field are also used. These are methods of random fields (analog model) and local sources (phenomenological-based on Huygens-Fresnel methods). The model of random fields is formulated in the works of [15, 16]. In the modern interpretation [18, 19], the model of random fields represents an object with a set of independent point reflectors distributed on the "illuminated" part of this object.

The method of local sources is promising. It is based on the model of local sources. Used experimental data on the local nature of the reflection of radio waves from ships, aircraft, and ground objects [20, 21].

Another direction determination pattern is an imitation of the environment, for example—the sea surface. The Kirchhoff method is used to build surface scattering models (physical optics) [13]. The method of geometric optics, the method of small perturbations, and the facet method are applied. Models based on the families of K-distributions and the Weibull distribution show the best agreement with the results of experimental studies.

The next direction is determining the adequacy of the model in connection with the simulation of the attenuating effect of radar path [21] on the echo signal. Such an effect is determined by a decrease in the power of the probing radio pulse in the presence of meteorological influences on the radar path [22]. If there is a distribution of rain, hail, or snow on the radar path, the echo may be subject not only to attenuation, but also to contain random fluctuations [23, 24].

A simulation model of a radar echo signal can be represented as a combination of the following elements: modeling the current position of an object in space, modeling reflecting the properties of the observed object, taking into account the stochastic conditions for the formation of an echo signal (interference from the sea surface), meteorological influences, and the random nature of the object's movement.

Within the framework of the echo-signal model proposed in the chapter, an attempt was made to combine them into a complex model of local sources and random fields. This echo-signal model is limited to simulating ordinary navigation conditions, making it possible to develop it for extreme situations.

In the proposed chapter, additionally, the proposed mathematical model of the probing radio signal, taking into account the non-deterministic fluctuation components in the complex envelope. A method is proposed for increasing the degree of difference between echo signals based on an algorithm for the correlation assessment of the complex envelope of their mixture. The developed method allows realizing the potential capabilities of signals even taking into account their non-deterministic properties. Such properties arise when exposed to various fluctuation processes in the transmitter, antenna-feeder path and when signals are reflected from targets.

2 Improved Mathematical Model of Probing Signals Taking into Account Amplitude and Angular Fluctuations

2.1 Correlation Functions of Radio Signals

The use of incoherent sources of probing signals, due to the imperfection of microwave generators, leads to a limitation of the potential capabilities of active radar stations. This is due to the non-optimal correlation properties of the probing signal model, which is embedded in the signal processing algorithms in the receiver.

This model has the form of a radio signal without internal angular modulation with a rectangular amplitude. This is due to the non-optimal correlation properties of the probing signal model, which is embedded in the signal processing algorithms in the receiver. This model has the form of a radio signal without internal angular modulation with a rectangular amplitude. However, if in the first case the shape of distortions can still be predicted, in the second case it is practically impossible. A statistical evaluation of fluctuations is required to form an improved model of the radar signal. The analytical dependences of their distribution are determined. This procedure is suggested in the article.

The content of the improved model is based on the expression of a pulsed probing radio signal:

$$\dot{u}(t) = \dot{U}(t) \exp j(\omega_0 t) \tag{1}$$

where $\dot{U}(t) = U(t) \exp j(\phi(t) + \phi_0)$ is the complex envelope; $U(t)$ is the shape of the amplitude modulating signal; $\phi(t)$ is the angular modulating shape.

The shape of the complex envelope model and its correlation properties are determined by the shape of the amplitude modulating pulse:

$$B(\tau) = \begin{cases} U_0^2(\tau_i - |\tau|), & |\tau| \le \tau_i \\ 0, & |\tau| > \tau_i \end{cases} \tag{2}$$

This form of the complex envelope is the basis for the synthesis of a coherent processing algorithm. As a result of a number of destabilizing factors in the complex envelope of the transmitter, the probe signal comprises a number of fluctuation components [24, 25]. Properties and shape are determined by the design features of the transmitter and can be approximated by certain distribution laws. Different combinations of distribution laws with different parameters can give different potential gains in the correlation estimation of the complex signal envelope.

In pulsed radar systems, the receiver's frequency band is reserved, and the shape of the probe signal acquires certain transformations during its formation and emission. Thus, the potential correlation properties of radar signals can be significantly higher than anticipated. Next, we checked the assumption that we proposed. An improved mathematical model of a radar probing signal is proposed, in which possible random distortions and fluctuations are taken into account in the form of amplitude and angular components. These components were presented in the form of narrow-band, slowly oscillating functions of time with certain distribution laws:

$$\dot{u}(t) = \dot{U}(t) U_\xi(t) \exp j(\omega_0 t) \exp j\phi_\xi(t) \tag{3}$$

where $U_\xi(t) = \zeta_U(k_1 t)$ is the amplitude fluctuation component (random process with parameter k_1); $\phi_\xi(t) = \zeta_\phi(k_2 t)$ is the angular fluctuation component (random process with parameter k_2).

The generalized signal model can be written as:

$$\dot{u}(t) = U(t)\xi_u(k_1 t) \exp j(\omega_0 t + \phi(t) + \phi_0) \exp j\xi_\phi(k_2 t) \tag{4}$$

The specific gravity of the fluctuation components is insignificant. It is incorrect to define them as additional internal modulation due to non-determinism. However, their presence introduces a certain broadband into the signal by expanding the receiver bandwidth to reduce power losses. An analysis of their possible distributions was carried out depending on the operating mode of the transmitter and the type of microwave generator.

Regardless of the type of generator, distortion of the complex envelope will occur with both amplitude and angular components. Thus, the complex envelope of the probing radio signal (4) generally takes the form of the equation:

$$\dot{U}(t) = U(t)\xi_u(k_1 t) \exp j\xi_\phi(k_2 t) \tag{5}$$

and in the case of impulse probing signals:

$$\dot{U}(t) = \begin{cases} \xi_u(k_1 t) \exp j\xi_\phi(k_2 t), & t \le |\tau_i| \\ 0, & t > |\tau_i| \end{cases} \tag{6}$$

Determining the analytical form of the components $\xi_u(k_1 t)$ and $\xi_\phi(k_2 t)$ and their parameters is a difficult tas. Their form was established empirically—experimentally, for various generators and microwave amplifiers under the same operating conditions. We determined the shape of the amplitude envelope and the dynamics of the frequency change in the middle of the probing radio pulse.

A statistical apparatus was applied (Pearson's test of consistency). The results of experimental studies were approximated in the analytical expressions that are given in Table 1.

For generator magnetron type:

- complex envelope is determined from the formula

Table 1 Analytical expressions for fluctuation modulation components of a signal

Generator type	$\xi_u(k_1 t)$	$\xi_\phi(k_2 t)$	k_1	k_2
Idealized	1	0	–	–
Magnetron	$k_1 \exp(-\pi k_1^2 t^2)$	$k_2 t$	$\frac{1}{\sqrt{2\pi}\sigma}$	$-\beta t$
Zener diode	$k_1 \exp(-\pi k_1^2 t^2)$	$k_2 t$	$\frac{1}{\sqrt{2\pi}\sigma}$	$-(0.1\ldots0.05)\beta t$
Amplifier with crossed fields	1	$k_2 t$	–	$\triangle \phi_{max} \sin\left(\frac{2\pi t}{\tau_i}\right)/t$
Klystron generator	$\exp(k_1 t)$	$k_2 t$	$(0.3\ldots0.4)\tau_i$	ct^2
Traveling-wave tube	$k_1 \exp(-\pi k_1^2 (t-0.3\tau_i)^2)$	0	$\frac{1}{\sqrt{2\pi}\sigma}$	–

$$\dot{U}(t) = k_1 \exp(-\pi k_1^2 t^2) \exp(j\beta t^2)$$

$$= \frac{1}{\sqrt{2\pi}\sigma} \exp\left(-\frac{t^2}{2\sigma^2}\right) \exp(j\beta t^2) \tag{7}$$

- time delay correlation function

$$B(\tau) = \exp\left[-\frac{1}{2}\left(\frac{\tau^2}{2\pi\sigma^2} + \beta^2\tau^2\sigma^2 2\pi\right)\right] \tag{8}$$

- frequency offset correlation function

$$B(\tau) = \exp\left[-\frac{1}{2}\left(\frac{\tau^2}{2\pi\sigma^2} + \beta^2\tau^2\sigma^2 2\pi\right)\right] \tag{9}$$

For klystron-based transmitter:

- complex envelope is determined from the expression

$$\dot{U}(t) = \exp\left(\frac{\tau_i}{3}t\right)\exp(jct^3) \tag{10}$$

- time delay correlation function

$$B(\tau) = \sqrt{\frac{1}{2c\tau}\left[(C_1 + C_2)^2 + (S_1 + S_2)^2\right]} \tag{11}$$

where C_1, C_2, S_1, S_2 is the Fresnel integrals by arguments $c\bar{\tau}(\tau_i - |\tau|)$.

$$B(F) = \frac{\sin(\pi\tau_i F)}{\pi\tau_i F} \tag{12}$$

The simulation of the expressions obtained in this way showed that the correlation properties of signals with such complex envelopes depend not only on the amplitude of fluctuations, but also on their combination.

Figure 1 shows the simulation results in the form of one-way correlation functions of signals. Various distributions and parameter values of fluctuation components are taken into account using the example of a magnetron-type generator—Gaussian amplitude and linear frequency modulation (chirp) [19].

Figures 2 and 3 show one-way correlation functions of radio signals with a rectangular, Gaussian amplitude envelope (formulas for a klystron).

As can be seen from these graphs, the correlation of the signal as a whole depends significantly on the distribution parameters. It was found that this dependence is not linear and not monotonic but has local extrema.

The expression for the correlation function of the complex envelope for the magnetron is as follows:
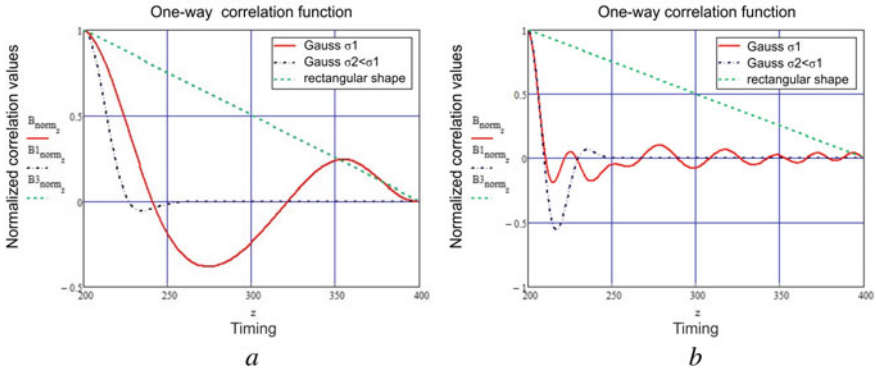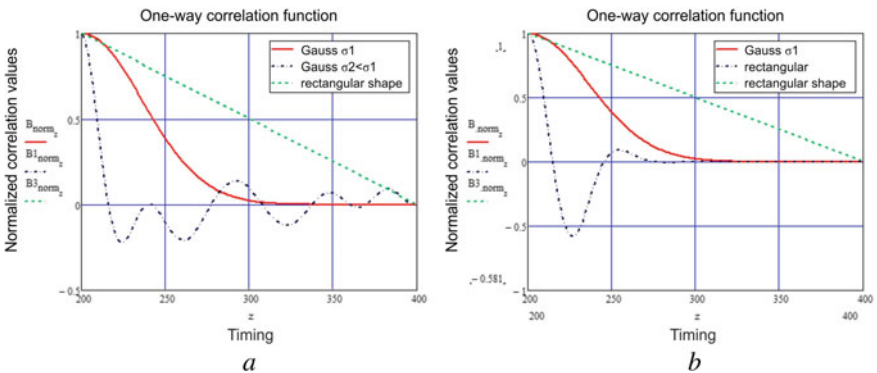
Fig. 1 One-way correlation functions of radio signals: **a** with Gaussian amplitude modulation and monotonic frequency filling; **b** with Gaussian amplitude modulation and chirp
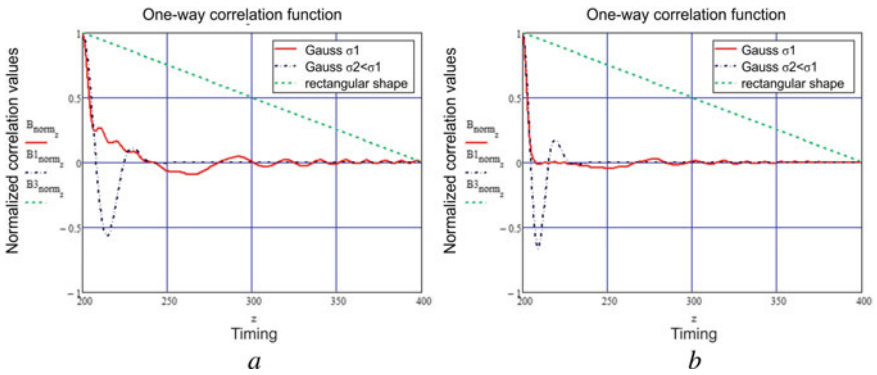
Fig. 2 One-way correlation functions of radio signals: **a** with Gaussian amplitude modulation and chirp; **b** with Gaussian amplitude modulation and parabolic FM

Fig. 3 One-way correlation functions of radio signals: **a** with Gaussian amplitude modulation and chirp; **b** with Gaussian amplitude modulation and rectangular envelope
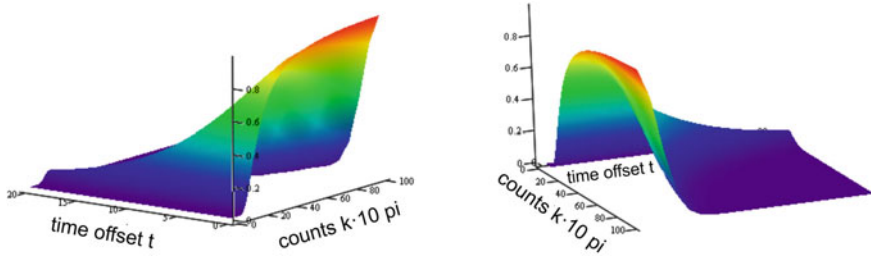
Fig. 4 Dependence of the correlation coefficient on time shift and coefficient values k_1

$$B(\tau) = \exp\left(-\frac{1}{2}\tau^2\left(k_1^2 + \frac{\beta^2}{k_1^2}\right)\right) \tag{13}$$

where is $k_1 = \frac{1}{\sqrt{2\pi}\sigma}$.

An extreme value of σ was established, at which the level of correlation remains in a fairly wide range of values of τ (see Fig. 4).

In the transmitter, it is necessary to correct fluctuations so that they correspond to the optimal value.

The improved mathematical model made it possible to confirm the hypothesis of increasing the capabilities of the radar resolution probing signal. However, the non-determinism of these fluctuations requires the use of additional measures for their application. It is necessary to develop a method for processing echoes that allows you to realize possible radar resolution at the receiver signal stage.

2.2 Formulation General Principles Simulation Radar Echo-Signal Active Radiolocation

The simulation model of the radar echo signal is presented on the following principles. As a radar model of the object, a complex model is adopted, which includes an analog model of random fields, for example, a sea vessel. The echo signal is formed by distributed sources located on the "illuminated" part of the side surface of the object body. The composition includes a phenomenological model of local sources using the Huygens–Fresnel principle (to represent the structures of the body object). Stochastic conditions for the formation of an echo signal are represented by modeling the reflectivity of sea waves. The attenuation of the echo signal during its propagation, thermal noise of the receiving path, the random nature of the movement is represented by lateral transverse rotational vibrations of the object relative to the equilibrium position.

The power of the echo signal from some nth element with RCS s_n, which is remote from the antenna at a distance R_n, at the input of the radar receiving path can be determined based on the basic radar equation [19]. For free space, taking into

account the attenuation δ of electromagnetic energy in the atmosphere, we can write the equation:

$$P_{\text{es},n} = \frac{P_i(\eta\lambda G)^2 s_n}{(4\pi)^3 R_n^4} e^{-0.46\delta R_n} \tag{14}$$

where P_i is the pulse power of the transmitter; η is the efficiency coefficient of the antenna-feeder path [26, 27]; λ is the carrier wavelength of radio emission.

Observations of objects at sea is carried out in the first interference lobe of the antenna [28]. The antenna gain G can be represented [24] as a function of the angular deviation $\phi D_n = \phi_n - \phi_c$ of the nth element from the center line ϕ_c of the antenna visibility zone:

$$G(\phi D_n) = \frac{6}{\pi\phi_A} G_0 e^{-2.78(\phi D_n/\phi_A)^2} \tag{15}$$

where G_0 is the antenna gain value on the radiation axis.

Taking into account expressions (14) and (15), the power $P_{\text{es},n}$ of the echo signal at the antenna output has the form:

$$P_{\text{es},n} = \left(\frac{3}{4\phi_A}\right)^2 \frac{P_i(\eta\lambda G)^2 s_\varsigma}{\pi^5 R_n^4} e^{-0.46\delta R_n - 5.56(\phi D_n/\phi_A)^2} \tag{16}$$

Assuming in this case the conditions $R_n = R_0$, where $R_0 = c\tau/2$, we transform the power $P_{\text{es},n}$ (16), taking into account the attenuation K_r of the power due to meteorological influences and the attenuation of electromagnetic energy in the atmosphere, into the corresponding amplitude echo voltage at the output of the receiving path:

$$U_{\text{es},n} = K_{\text{pr}} \frac{3\eta\lambda G_0\sqrt{K_R P_i R_A s_n/\pi}}{\phi_A(2\pi R_0)^2} e^{-2.78(\phi D_n/\phi_A)^2} \tag{17}$$

where R_A is the antenna resistance; $K_{\text{pr}} = \frac{\phi_A(\pi c\tau)^2}{3\eta\lambda G_0\sqrt{P_i R_A/\pi}}$ is the coefficient instant amplification of the receiving path; c is the radio propagation speed; τ is the propagation time of a probing radio pulse.

The instantaneous value of the echo-signal voltage at the output of the receiving path of the radar is represented by the formula. An expression is obtained for a certain angular position F of its antenna in the form of a sum of complex vectors:

$$u_{\text{es},F} = \sqrt{K_R}\left[U_{\text{ds},F}e^{j\phi_{\text{ds}},F} + U_{\text{ls},F}e^{j\phi_{\text{ls}},F} + U_{s\omega,F}e^{j\phi_{s\omega},F}\right]e^{-j\omega\tau} \tag{18}$$

where ω is the frequency of the carrier wave generated by the probing radio pulse; $U_{\text{ds},F}$ and $\phi_{\text{ds},F}$, $U_{\text{ls},F}$ and $\phi_{\text{ls},F}$, $U_{s\omega,F}$ and $\phi_{s\omega,F}$ is the total amplitudes and phases

of the voltage components of the echo signal from distributed local sources and sea waves.

Considering $U_{\text{es},n} \sim \sqrt{s_n}$ (17), components of the echo-signal coherence and omitting the factor $e^{-2.78(\phi D_n/\phi_A)^2}$, expression for the amplitude of the voltage of the echo signal (18) at the output of the receiving path as the sum of its quadrature components:

$$U_{\text{es},F} = \sqrt{K_R} \left(\left(\sqrt{S_{\text{ds},F}} \cos \phi_{\text{ds},F} + \sqrt{S_{\text{ls},F}} \cos \phi_{\text{ls},F} + \sqrt{S_{s\omega,F}} \cos \phi_{s\omega,F} \right)^2 \right.$$
$$\left. + \left(\sqrt{S_{\text{ds},F}} \cos \phi_{\text{ds},F} + \sqrt{S_{\text{ls},F}} \cos \phi_{\text{ls},F} + \sqrt{S_{s\omega,F}} \cos \phi_{s\omega,F} \right)^2 \right)^{1/2} \quad (19)$$

where $S_{\text{sd},F}$, $S_{\text{ls},F}$, $S_{s\omega,F}$ is the RCS distributed local sources and sea waves in the resolution zone for a given angular position F of the antenna.

3 Radar Echo Model with Multiple Possible Probing Factors

3.1 Mathematical Modeling of Radar Signals

Suppose that the object has a lateral reflective surface of the body, the linear dimensions of which significantly exceed the wavelength. The radar model of such a surface in non-specular directions is a set of reflective points (distributed sources) located continuously "practically at its edges," that is, along the generatrix of the elliptical contour of the object. Reflections from these points have a small amplitude and a random phase [25], uniformly distributed over the interval $(0, 2\pi)$.

The measurement of the antenna rotation angle is carried out simultaneously with the emission of the next probing radio pulse. This allows the antenna rotation to be considered as quasi-discrete with an angular step $\Delta\theta = 2\pi T_{\text{imp}}/T_A$, where T_{imp} is transmission period of probing radio pulses; T_A is antenna rotation period. At the next angular step of the antenna, a new section of the elliptic contour of the object with the nth group of distributed sources continuously located along it falls into its visibility zone. The number of groups of distributed sources in the visible area of the antenna $N_{\text{ds}} = \phi_A^*/\Delta\theta$, where ϕ_A^* is part of the radiation pattern width, "illuminates" the elliptical contour of the object for a given angular position of the antenna.

Let us denote the RCS of the nth group of distributed sources by a random variable $S_{sd,n}$. Distributed sources are characterized by the additivity of the average values of their RCS, then the average RCS of the nth group will be:

$$\overline{S_{\text{sd},n}} = \int\limits_{l_n}^{l_n+1} \frac{\partial \overline{S_{\text{sd}}}}{\partial l} dl \quad (20)$$

where $(l_n,\ l_n + 1)$ is the integration interval along the elliptical contour of the projection on a horizontal axis normal to the sector to determine the position of distributed sources nth group.

The ratio between the mean RCS $\overline{S_{\text{ob}}}$ of the object and the mean RCS $\overline{S_{\text{ob,ds}}}$ of distributed sources is represented by the formula:

$$\overline{S_{\text{ob,ds}}} = \upsilon_{\text{ds}} \overline{S_{\text{ob}}} \tag{21}$$

where υ_{ds} is the total weight average RCS distributed sources in general average RCS object.

The linear density of the average values of the RCS distributed sources can be determined from the expression:

$$\frac{\partial \overline{S_{\text{ob}}}}{\partial l} = \frac{\upsilon_{\text{ds}} \overline{S_{\text{ob}}}}{l_{\text{el}}} \tag{22}$$

where l_{el} is the length elliptic generatrix object outline.

We take into account the expression $U_{\text{es},n} \sim \sqrt{s_n}$ (17). Represent the instantaneous voltage of the echo signal from the nth group of distributed sources:

$$u_{\text{ds},n} = \sqrt{S_{\text{ds},n}}\, e^{j\phi_{\text{ds},n}} e^{-j\omega\tau}$$

The total amplitude of the echo voltage from all groups for a given antenna angle F can be determined by the expression:

$$U_{\text{ds},F} = \sqrt{K_R} \sqrt{\left(\sum_{n=1}^{N_{\text{ds}}} \sqrt{S_{\text{ds},n}}\cos\phi_{\text{ds},n}\right)^2 + \left(\sum_{n=1}^{N_{\text{ds}}} \sqrt{S_{\text{ds},n}}\sin\phi_{\text{ds},n}\right)^2} \tag{23}$$

RCS of distributed sources in the antenna visibility range will be:

$$S_{\text{ds},F} = \left(\sum_{n=1}^{N_{\text{ds}}} \sqrt{S_{\text{ds},n}}\cos\phi_{\text{ds},n}\right)^2 + \left(\sum_{n=1}^{N_{\text{ds}}} \sqrt{S_{\text{ds},n}}\sin\phi_{\text{ds},n}\right)^2 \tag{24}$$

where $\phi_{\text{ds},n} = 2k\lambda R_{\text{ds},n} + \phi_{\text{rnd,ds},n}$; $2k\lambda R_{\text{ds},n}$ is a regular component of the wave phase the nth group of distributed sources; $k\lambda$ is a wave number; $R_{\text{ds},n}$ is a distance from the antenna to the nth group of distributed sources; $\phi_{\text{rnd,ds},n}$ is the random phase component of the voltage of the echo signal from the nth group of distributed sources which are uniformly distributed on the interval $(0, 2\pi)$.

The RCS value of the n-group of distributed sources $R_{\text{ds},n}$ (24) obeys the exponential distribution law:

$$f_{\text{ds}}\left(S_{\text{ds},n}\right) = \frac{1}{\overline{S_{\text{ds},n}}} e^{-\left(S_{\text{ds},n}/\overline{S_{\text{ds},n}}\right)} \tag{25}$$

with an average value $\overline{S_{\mathrm{ds},n}}$, which is determined by the expression (21).

The radar model of local sources of an object [20] is represented by a certain distribution of isotropic reflectors along its diametral plane:

$$\phi_{\mathrm{ds},F} = \arctan\left[\frac{\sum_{n=1}^{N_{\mathrm{ds}}} \sqrt{S_{\mathrm{ds},n}} \sin\phi_{\mathrm{ds},n}}{\sum_{n=1}^{N_{\mathrm{ds}}} \sqrt{S_{\mathrm{ds},n}} \cos\phi_{\mathrm{ds},n}}\right] \tag{26}$$

Experimental studies show that the distribution function of the RCS of local sources S_{ls} of objects is close to the lognormal law:

$$l_{\mathrm{ls}}(S_{\mathrm{ls}}) = \frac{1}{S_{\mathrm{ls}}\sigma_{\ell n}\sqrt{2\pi}} e - \frac{(\ln S_{\mathrm{ls}} - \mu_{\ell n})^2}{2\sigma_{\ell n}^2}, \quad S_{\mathrm{ls}} > 0 \tag{27}$$

In this case, the mean value $\overline{S_{\mathrm{ls}}}$ and variance $\sigma_{\ell s}^2$ of the random variable S_{ls} are associated with the parameters of the lognormal distribution and $\sigma_{\ell n}^2$ by the relations [20]:

$$\overline{S_{\mathrm{ls}}} = \mathrm{e}^{\mu_{\ell n} + 0.5\sigma_{\ell n}^2} \text{ and } \sigma_{\mathrm{ls}}^2 = \mathrm{e}^{2\mu_{\ell n} + \sigma_{\ell n}^2} - \mathrm{e}^{2\mu_{\ell n} + \sigma_{\ell n}^2} \tag{28}$$

In practice [12], not all local sources are considered, but only the strongest ones, the RCS of which will be denoted by the variable $S_{B,\mathrm{ls}}$. The strongest local sources form the main part (up to 90%) of the reflected field [18]. This allows us to write a truncated lognormal distribution for the RCS of the strongest local sources:

$$f_{B,\mathrm{ls}}(S_{B,\mathrm{ls}}) = \frac{1}{S_{B,\mathrm{ls}}\sigma_{B,\ell n}\sqrt{2\pi}} \mathrm{e}^{-\frac{(\ln S_{B,\mathrm{ls}} - \mu_{B,\ell n})^2}{2\sigma_{B,\ell n}^2}}, \quad \mathrm{SB}, \mathrm{ls}_{\mathrm{ls,min}} \tag{29}$$

In this case, the parameters $\mu_{B,\ell n}$ and $\sigma_{B,\ell n}^2$ of the truncated lognormal distribution are determined similarly to (28) from the system of equations:

$$\begin{cases} \overline{S_{\sum,\mathrm{ls}}} = \mathrm{e}^{\mu_{B,\ell n} + 0.5\sigma_{B,\ell n}^2} \\ \sigma_{\sum,\mathrm{ls}}^2 = \mathrm{e}^{2\mu_{B,\ell n} + 2\sigma_{B,\ell n}^2} - \mathrm{e}^{2\mu_{B,\ell n} + 2\sigma_{B,\ell n}^2} \end{cases} \tag{30}$$

where $\overline{S_{\sum,\mathrm{ls}}} = \nu_{S_{B,\mathrm{ls}}}^{-1} \overline{S_{B,\mathrm{ls}}}$ and $\sigma_{\sum,\mathrm{ls}}^2 = \alpha(\overline{S_{\sum,\mathrm{ls}}})^2$ is the RCS and dispersion generalized local source (without the separation in the most strong and weak sources); $\nu_{S_{B,\mathrm{ls}}}$ is specific weight average RCS value of the strongest source local average value of the RCS generalized local source; $\alpha_{\mathrm{ls}} > 1$ is dispersion coefficient of RCS of local sources, the numerical value of which is determined by the beating features of local sources in each specific case.

Number strongest local sources in general for an object may create value $N_{\mathrm{ob}} = 2n_{\phi_A}\alpha/\phi_A R_0^*$, where n_{ϕ_A} is the number of the strongest local sources (from 3 to 5 [21]) in the visible area of the antenna ϕ_A for the location normal to the object's motion vector at a given distance R_0^*. The total average RCS of all the strongest local

sources of the object, taking into account (21), is determined by the expression:

$$\overline{S_{B,\mathrm{ls,ob}}} = (1 - \nu_{\mathrm{ds}})\overline{S_{\mathrm{ob}}} \tag{31}$$

Then considering additivity, the average RCS local sources, the average RCS strongest local source is:

$$\overline{S_{B,\mathrm{ls}}} = \frac{\overline{S_{B,\mathrm{ls,ob}}}}{N_{\mathrm{ob}}} \tag{32}$$

The lower bound $S_{\mathrm{ls,min}}$ in expression (29) is determined from the equation for the initial moment of the first order $S_{B,\mathrm{ls}}$:

$$\overline{S_{B,\mathrm{ls}}} = \int\limits_{S_{\mathrm{ls,min}}}^{\infty} \frac{1}{\sigma_{B,\ell n}\sqrt{2\pi}} e^{-\frac{(\ln S_{B,\mathrm{ls}} - \mu_{B,\ell n})^2}{2\sigma_{B,\ell n}^2}} \, dS_{B,\mathrm{ls}} \tag{33}$$

Let's take into account the random nature of the placement of the reflecting surfaces. We take in the rectangular coordinate system $O'x'y'z'$ the distribution of coordinates N_{ob} of local sources in the form of independent uniform distributions within the space bounded by the inequalities $-a \le x_i' \le a, -b \le y_i' \le b, 0 \le z_i' \le h$.

Then the total amplitude of the voltage of echo signals from all N_F strongest local sources located in the zone of difference between the antenna can be determined by the expression:

$$U_{B,\mathrm{ls},F} = \sqrt{K_R} \sqrt{\left(\sum_{i=1}^{N_F} \sqrt{S_{B,\mathrm{ls},i}} \cos\phi_{B,\mathrm{ls},i}\right)^2 + \left(\sum_{i=1}^{N_F} \sqrt{S_{B,\mathrm{ls},i}} \sin\phi_{B,\mathrm{ls},i}\right)^2} \tag{34}$$

The total RCS of the strongest local sources for a given angular position of the antenna F, taking into account the phase $\phi_{B,\mathrm{ls},i}$ of the echo-signal voltage from the ith source, can be represented by the sum:

$$U_{B,\mathrm{ls},F} = \left(\sum_{i=1}^{N_F} \sqrt{S_{B,\mathrm{ls},i}} \cos\phi_{B,\mathrm{ls},i}\right)^2 + \left(\sum_{i=1}^{N_F} \sqrt{S_{B,\mathrm{ls},i}} \sin\phi_{B,\mathrm{ls},i}\right)^2 \tag{35}$$

where $N_F \ge n\phi_A$; $\phi_{B,\mathrm{ls},i} = 2k_\lambda R_{\mathrm{ls},i}$.

$$R_{\mathrm{ls},i} = \sqrt{(x_{0E} + x_{\vartheta,i})^2 + (y_{0E} + y_{\vartheta,i})^2 + (h_A - z_{\vartheta,i} - h_b)^2}$$

$$x_{\vartheta,i} \approx x_i' \cos(F - K)\big[y_i' \cos\vartheta - z_i' \sin\vartheta\big] \sin(F - K)$$

$$y_{\vartheta,i} \approx x_i' \cos(F - K)\left[y_i' \cos\vartheta - z_i' \sin\vartheta\right]\cos(F - K)$$

$$z_{\vartheta,i} \approx y_i' \sin\vartheta + z_i' \cos\vartheta$$

$x_{0,E}$, $y_{0,E}$ are the coordinates the start position coordinates $O'x'y'z'$ system $Oxyz$.

The angle of transverse rotational vibrations θ of an object according to its equilibrium position can be represented by a Gaussian centered random variable [24].

The phase of the total voltage of the echo signal from the local sources is placed on the differences in the antenna zone, defined as the ratio of the quadrature components:

$$\phi_{B,\mathrm{ls},F} = \arctan\left[\frac{\sum_{i=1}^{N_F} \sqrt{S_{B,\mathrm{ls},i}}\,\sin\phi_{B,\mathrm{ls},i}}{\sum_{i=1}^{N_F} \sqrt{S_{B,\mathrm{ls},i}}\,\cos\phi_{B,\mathrm{ls},i}}\right] \tag{36}$$

At the same time, $N_{s\omega}$ of the reflecting sections of the disturbed sea surface falls into the zone of difference between the antenna of length d_A and width ϕ_A. RCS which is a sum:

$$S_{s\omega,F} = \left(\sum_{k=1}^{N_{s\omega}} \sqrt{S_{s\omega,k}}\,\cos\phi_{s\omega,k}\right)^2 + \left(\sum_{k=1}^{N_{s\omega}} \sqrt{S_{s\omega,k}}\,\sin\phi_{s\omega,k}\right)^2 \tag{37}$$

Experimental studies of the total echo-signal $u_{s\omega,F} = \sqrt{S_{s\omega,F}}\mathrm{e}^{j\phi_{s\omega,F}}\mathrm{e}^{-j\omega\tau}$ located in the zone of difference of the antenna showed that its amplitude $U_{s\omega,F}$ is described by the Weibull [27] distribution:

$$f_{s\omega}\left(S_{s\omega,F}\right) = \frac{b'(\ln 2)U_{s\omega,F}^{b'-1}}{G_{s\omega}^{b'}}\mathrm{e}^{\ln 2(U_{s\omega,F}/G_{s\omega})^{b'}} \tag{38}$$

where $G_{s\omega}$ is the value of the median of the distribution due to the intensity of the waves; $c' = 1/b'$ is a form parameter.

Given equiprobability phase center reflected differences in the antenna zone, the distribution phase $\phi_{s\omega,F'}$ is received at a uniform interval $(0, 2\pi)$.

The attenuation of the power of the sounding radio pulse is due to the fading (14) of electromagnetic energy in the atmosphere: $Y_\delta = \mathrm{e}^{-0.46\delta R_0}$. We take into account the influence of radar reflectors in the form of fog, rain, hail, snow. They which can form a regular or random propagation medium of the probing radio pulse K_R of the echo-signal voltage (18):

$$K_R = Y_\delta \mathrm{e}^{-(\rho_{\mathrm{det}}+\rho_{\mathrm{rnd}})R_0} \tag{39}$$

where ρ_{det} is the reflection coefficient from meteorological scatterers, the spatial and temporal properties of which are constant during the location; ρ_{rnd} is the coefficient of reflection from random meteorological reflectors (random variable of Weibull) [27],

median distribution $G_{\omega c, \text{rnd}}$ is determined by the intensity of random meteorological formations).

As the noise in the echo-signal voltage also includes thermal noise u_{hn}. They were modeled by a Gaussian centered quantity, the power, and variance σ_{hn}^2, which at the input of the receiving path is determined by the expression [14]:

$$P_{\text{hn}} = F_K k_b T_0 B_K \qquad (40)$$

where F_K is the noise ratio of the receive path; k_b is the Boltzmann constant; T_0 is the stationary temperature; B_K is the receive channel bandwidth.

Taking into account the components of the model (25), (26), (36), (38)–(40), the amplitude of the echo-signal voltage (19) at the output of the amplifier of the receiving path can be represented by the expression:

$$
\begin{aligned}
U_{\text{es},F} = \sqrt{K_R} \Big(\Big(& \sqrt{S_{\text{ds},F}} \cos \phi_{\text{ds},F} + \sqrt{S_{B,\text{ls},F}} \cos \phi_{B,\text{ls},F} \\
& + U_{s\omega,F} \cos \phi_{s\omega,F} \Big)^2 + \Big(\sqrt{S_{\text{ds},F}} \sin \phi_{\text{ds},F} + \sqrt{S_{B,\text{ls},F}} \sin \phi_{B,\text{ls},F} \\
& + U_{s\omega,F} \sin \phi_{s\omega,F} \Big)^2 \Big)^{1/2} + K_{\text{TG}} u_{\text{hn}}
\end{aligned}
\qquad (41)
$$

3.2 Radar Resolution Enhancement Method Based on Autocorrelation Estimation Algorithm

The paper proposes a method based on the use of autocorrelation properties of the signal. The method takes into account the assessment of deterministic and non-deterministic signal components. The main idea of the method is based on the presence of a correlation [29] between deterministic and non-deterministic components of the echo signal during active and semi-active radar [28].

The mathematical model of a group echo signal—a mixture of echo signals from n-targets is presented in the following form:

$$
\begin{aligned}
u_{\text{rp}}(t) = \text{Re} \Big\{ \sum_{n=1}^{M} & A_n U(t - \tau_n) \xi_u(t - \tau_n) \exp j \\
& \times \big(\omega_0 t + \omega_n (t - \tau_n) + \phi_0 + \phi_n + \xi_\phi (t - \tau_n) \big) \Big\}
\end{aligned}
\qquad (42)
$$

where $\omega_n = 4\pi \vartheta_{rn}/\lambda$ is the Doppler frequency shift [30, 31]; $\phi_n = 2\omega_0 D_n/c$ is the phase shift of the echo signal; ϑ_{rn} is the range rate of the nth target (target element); D_n is the distance to nth target (target element).

To assess the potential for distinguishing echo signals in such a mixture, we analyze its correlation function [29], which was expressed through a complex envelope. We represent the complex envelope of the mixture of echo signal (42) by the equation:

$$
\dot{U}_{\mathrm{rp}}(t) = \sum_{n=1}^{M} A_n U(t - \tau_n) \xi_u(t - \tau_n) \exp j
$$
$$
\times \left[\omega_n(t - \tau_n) + \xi_\phi(t - \tau_n) \right] \exp j\phi_n \tag{43}
$$

We presented the complex envelope correlation function (43) as the sum of auto- and inter-correlation functions of the complex envelopes of individual echo signal:

$$
B(\tau) = \sum_{n=1}^{M} \sum_{n=1}^{M} B_{n,m}(\tau) \tag{44}
$$

or in matrix form:

$$
B_{n,m}(\tau) = \begin{pmatrix} B_{1,1}(\tau) & \dots & B_{1,M}(\tau) \\ \dots & \dots & \dots \\ B_{M,1}(\tau) & \dots & B_{M,M}(\tau) \end{pmatrix} \tag{45}
$$

The autocorrelation estimation algorithm is implemented in the form of an additional channel for processing echo signals. It will be effective only in the presence of significant additional modulation [19, 32], regardless of its determinism.

The receiver model for the implementation of the method based on the autocorrelation estimation algorithm is shown in Fig. 5.

According to the diagram in Fig. 5, echo-signal processing is done in two steps. At the first, the receiver signal is detected in the main channel (establishing the presence
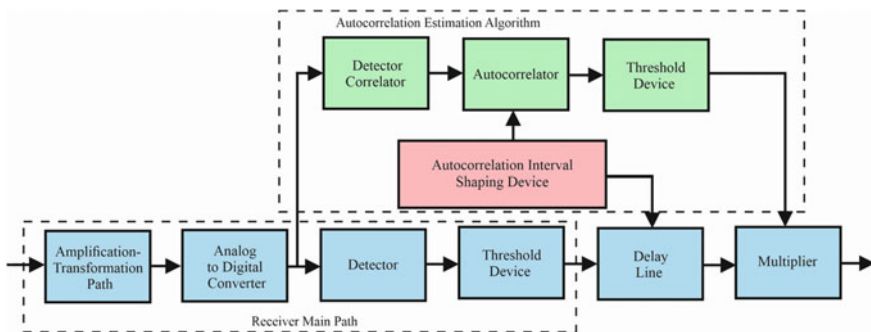
Fig. 5 Scheme radar receiver realizing the method of increasing resolution echo signals
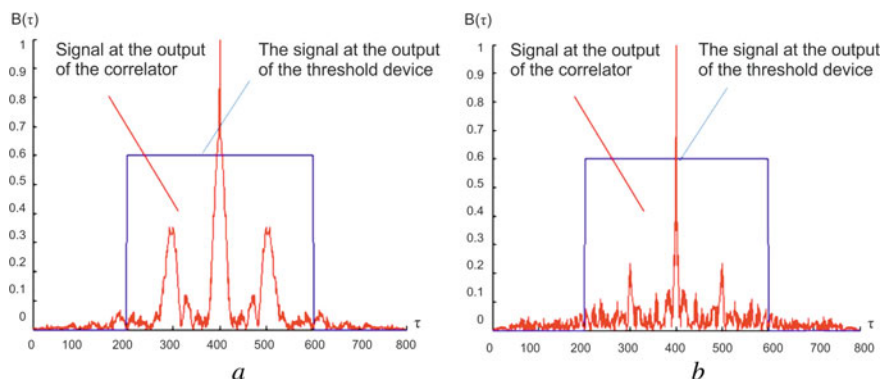
Fig. 6 The autocorrelation of the complex envelope of the echo signals mixture (at the signal-to-noise ratio at the output of the complex envelope detector: **a** +10 dB; **b** 0 dB)

of a useful signal) [33, 34]. At the second stage, the number of echo signals in the mixture is estimated for its correlation properties.

Figure 6a, b shows the shape of the autocorrelation function of two echo signals with a rectangular envelope and linear frequency modulation (LFM) at different frequency deviations. In fact, this corresponds to a different bandwidth of the receiver to a different signal-to-noise ratio at the output of the complex envelope detector.

In Fig. 7, graphs of the complex envelopes of the probing signal (mixture of two echoes and noise). In Fig. 7b, c are the same graphs (the range of the frequency instability of the probing signal is changed).

The efficiency of autocorrelation estimation of a mixture of echo signals at a higher noise level is shown in Fig. 8. There is a tendency to a sharp decrease in the effectiveness of the proposed method depending on the noise level.

In Fig. 9 dependence of autocorrelation components in the form of a mixture of two echo signals at different values of the frequency instability of the microwave generator.

The limitations of the method are as follows: An increase in the difference between echo signals is possible only under the condition of their stable reception and detection of their complex envelope with a signal-to-noise ratio of no worse than 0 dB. This is confirmed by the graphs in Fig. 9.

From the graphs we establish—only at the level of 0.5 dB a sharp surge is observed in all cases, regardless of the correlation of the complex envelope of the probing signal itself. When the signal-to-noise ratio is above 1 dB, the gain from the application of the method depends on the shape of the complex envelope of the probing signal, regardless of its determinism.

Experimental studies have shown a gain in resolution several times. The value depends on the type of microwave generator, the method of construction of the modulator of its mode of operation, and the bandwidth of the receiver.
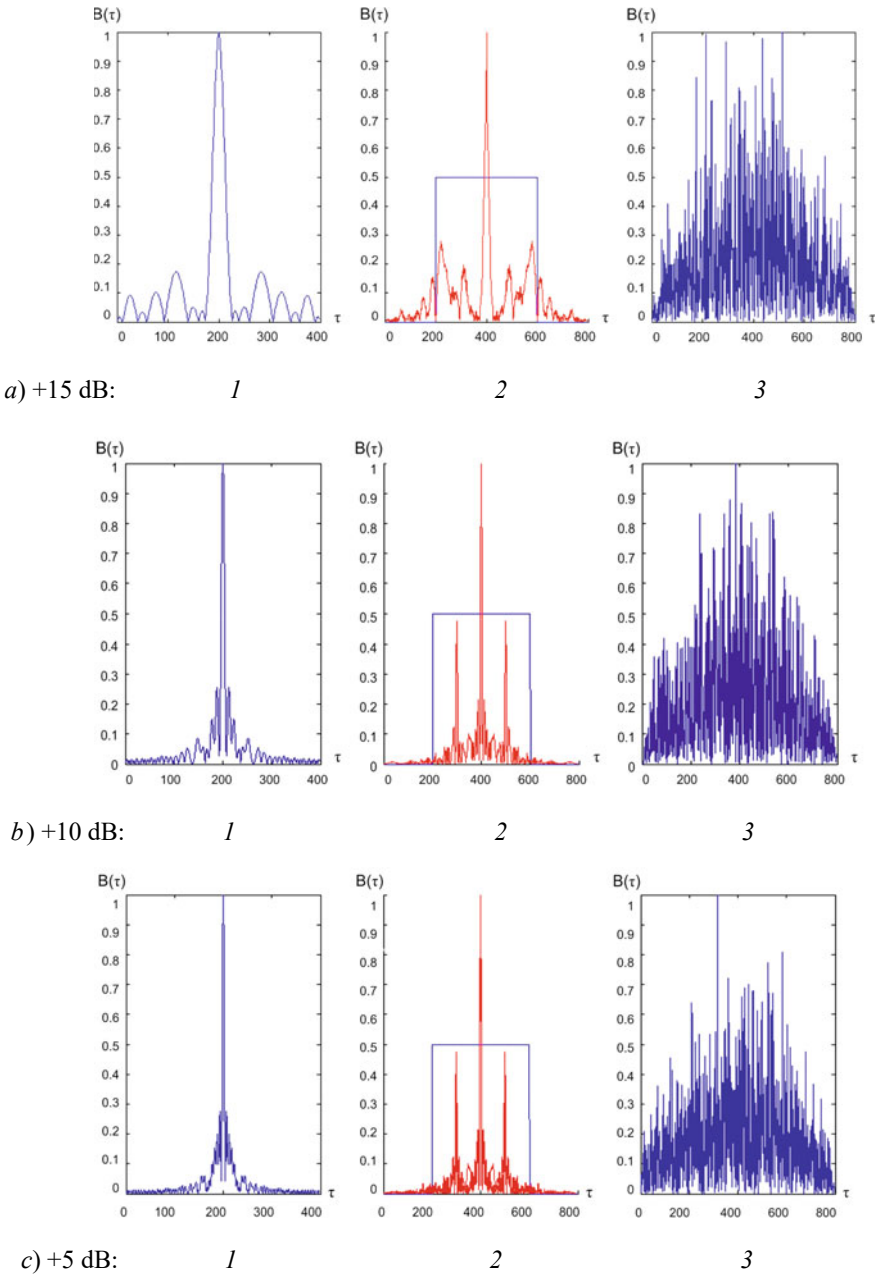
Fig. 7 Autocorrelation of complex envelope: *1* is the probing signal; *2* is a mixture of two echo signals at a signal-to-noise ratio at the output of a complex envelope detector; *3* is a noise
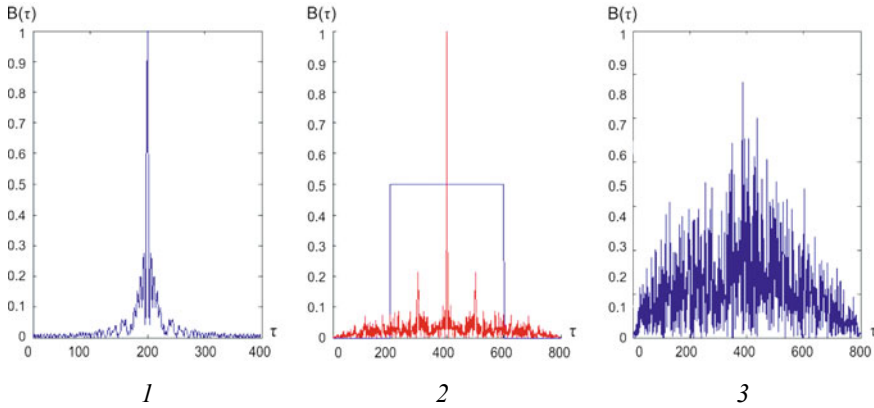
Fig. 8 Autocorrelation of complex envelope: *1* is the probing signal; *2* is a mixture of two echo signals at a signal-to-noise ratio at the output of a complex envelope detector 0 dB; *3* is a noise
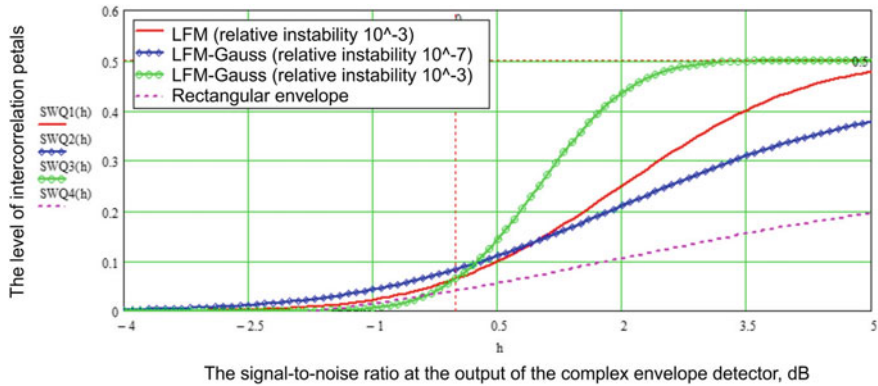
Fig. 9 Graphs of the normalized level of cross-correlation terms from the signal-to-noise ratio at the output of the complex envelope detector

4 Conclusions

The chapter presents the development of a method for increasing the resolution of echo signals based on the algorithm for correlation estimation of the complex envelope and their mixture. The novelty of the method lies in the use of an additional channel for correlation estimation of the mixture of echo signals. The assessment was carried out in the interval of the radar system difference element in range.

The developed method allows realizing the potential capabilities of signals, taking into account their non-deterministic properties. Such properties occur under the influence of various fluctuation processes in the transmitter, antenna-feeder path, when signals are reflected from targets.

We used statistical analysis and analyzed a model of a radar signal that is reflected by a target with a complex surface.

Evaluation of the algorithm's efficiency based on spectral analysis showed that a change in the shape of the pulse edges can affect its productivity. The maximum efficiency of the method is achieved with a Gaussian pulse shape and with an exponential shape of the edges, and the minimum with a rectangular one.

As a result of experimental studies, a gain in resolution has been obtained up to several times. The result is influenced by the choice of the type of microwave generator, the method of constructing the modulator, its operating mode, and the bandwidth of the receiver.

References

1. Dürr A et al (2019) High-resolution 160-GHz imaging MIMO radar using MMICs with on-chip frequency synthesizers. IEEE Trans Microw Theor Tech 67(9):3897–3907
2. Cerutti-Maori D, Sikaneta I, Klare J, Gierull CH (2014) MIMO SAR processing for multi-channel high-resolution wide-swath radars. IEEE Trans Geosci Remote Sens 52(8):5034–5055
3. Ma C et al (2020) Microwave photonic imaging radar with a sub-centimeter-level resolution. J Lightwave Technol 38(18):4948–4954
4. Alotaibi M (2021) Correction to: low noise moving target detection in high resolution radar using binary codes. EURASIP J Adv Signal Process 2021:12
5. JieLa Q, Wang H, Hu S et al (2020) Echo simulation of dual polarization Doppler weather radar based on the physical model. J Wirel Com Netw 2020:196
6. Sun B, Cao Y, Chen J et al (2014) Compressive sensing imaging for general synthetic aperture radar echo model based on Maxwell's equations. EURASIP J Adv Signal Process 2014:153
7. Kaydok U (2018) Baseband signal modelling of chaff echoes for coherent pulsed radars. In: 2018 IEEE radar conference (RadarConf18). IEEE Press, Oklahoma City, pp 0642–0646
8. Donets IV, Reizenkind YA, Shevchenko VN (2018) Experimental testing of the variational procedure for constructing multidimensional radio images of echo signals in non-emitting radars. Optoelectron Instrum Proc 54:162–167
9. Yu A, Idubore O, Dimian M (2016) Radar cross section calculation for subsurface objects. In: 2016 IEEE radar conference (RadarConf). IEEE Press, Philadelphia, pp 1–5
10. Lee J, Bang H (2018) Radial basis function network-based available measurement classification of interferometric radar altimeter for terrain-aided navigation. IET Radar Sonar Navig 12(9):920–930
11. Ji S, Zhang Z, Yan H et al (2016) Application of fractal algorithms of coastline echo's generation on marine radar simulator. Vis Eng 4:8
12. Bychkov VE, Mrachkovsky OD, Pravda VI (2014) About results of simulation of multi-channel radar detector. Radioelectron Commun Syst 57:306–310
13. Virkki A, Muinonen K (2015) Radar scattering by boulders studied using geometric optics. Planet Space Sci 118:277–284
14. Johansen PM (1999) Time-domain version of the physical theory of diffraction. IEEE Trans Antennas Propag 47(2):261–270
15. Hristopulos DT (2020) Random fields for spatial data modeling. Springer, Netherlands
16. Jiang Z (1987) On Markov models of random fields. Acta Math Applicatae Sinic 3:328–341
17. Schmidt V (2014) Stochastic geometry, spatial statistics and random fields. Springer, Berlin
18. Lombardini F, Gini F (2005) Model order selection in multi-baseline interferometric radar systems. EURASIP J Adv Signal Process 108784

19. Boiko J, Karpova L, Eromenko O, Havrylko Y (2020) Evaluation of phase-frequency instability when processing complex radar signals. Int J Elec Comp Eng 10(4):4226–4236
20. Daim TJ, Lee RMA (2019) A weighted least squares consideration for IR-UWB radar-based device-free object positioning estimation for indoor environment. Indonesian J Elec Eng Comp Sci 15(2):894–901
21. Nieh J, Romero RA (2018) Comparison of ambiguity function of eigenwave form to wideband and pulsed radar waveforms: a comprehensive tutorial. J Eng 2018(4):203–221
22. Zeyang Z, Huang J (2021) Mixed design of radar/infrared stealth for advanced fighter intake and exhaust system. Aerosp Sci Technol 110:106490
23. Xu-Dong H et al (2017) Research on multi-target resolution process with the same beam of monopulse radar. In: 2017 IEEE 17th international conference on communication technology (ICCT). IEEE Press, Chengdu, pp 1102–1105
24. Khudov HS et al (2019) The proposals for synchronization positions of MIMO radar system on the basis of surveillance radars. In: 2019 IEEE international scientific-practical conference problems of infocommunications, science and technology (PIC S&T). IEEE Press, Kyiv, pp 547–551
25. Palm S, Sommer R, Stilla U (2018) Mobile radar mapping—subcentimeter SAR imaging of roads. IEEE Trans Geosci Remote Sens 56(11):6734–6746
26. Li HY, Li Q, Xue K et al (2013) Research into influence of Gaussian beam on terahertz radar cross section of a conducting cylinder. J Infrared Milli Terahz Waves 34:289–298
27. Lai CD, Murthy DN, Xie M (2006) Weibull distributions and their applications. In: Springer handbooks, pp 63–78
28. Lee BS, Winder WF, Smith D (1994) Design of an antenna subsystem for a semi active radar target. In: Proceedings of MELECON '94. Mediterranean electrotechnical conference. IEEE Press, Antalya, pp 1158–1161
29. Manziuk EA et al (2020) Approach to creating an ensemble on a hierarchy of clusters using model decisions correlation. Przegl elektrotechniczny 1(9):110–115
30. Zeng R et al (2017) Joint estimation of frequency offset and Doppler shift in high mobility environments based on orthogonal angle domain subspace projection. IEEE Trans Veh Technol 67(3):2254–2266
31. Galiuk SD, Kushnir MY, Politanskyi RL (2011) Communication with use of symbolic dynamics of chaotic systems. In: 21st IEEE international Crimean conference microwave & telecommunication technology. IEEE Press, Sevastopol, pp 423–424
32. Schvartzman D, Curtis CD (2019) Signal processing and radar characteristics (SPARC) simulator: a Flexible dual-polarization weather-radar signal simulation framework based on preexisting radar-variable data. IEEE J Sel Top Appl Earth Observations Remote Sens 12(1):135–150
33. Parkhomey I, Boiko J, Tsopa N, Zeniv I, Eromenko O (2020) Assessment of quality indicators of the automatic control system influence of accident interference. TELKOMNIKA Telecommun Comput El Control 18(4):2070–2079
34. Bestak R (2020) Interference reduction using principles and application of cognitive radar in pulse jammer suppression. IRO J Sustain Wirel Syst 2(1):33–41

Sketching How Synthetic Cells Can Function as a Platform to Investigate Chemical AI and Information Theories in the Wetware Domain

Pasquale Stano

Abstract Recent advancements in synthetic cell construction have made possible the begin of a research program whereby these man-made systems, which resemble biological cells at a minimal complexity level, can be conceived as tools for investigating information and communication theories in the "wetware" domain. In this paper, we will firstly present the field of synthetic biology and the features of synthetic cells (in particular, synthetic cells built from scratch). In the practical field, their potential role as "smart" drug delivery agents is probably one of the most ambitious goals, which needs a well-conceived SC design and advanced features. The latter includes sensing and perception, information transduction, control and programmability. These considerations elicit, at the same time, more general and theoretical questions, here presented as a sort of programmatic discussion. We ask whether and at what extent synthetic cells can be considered a valuable platform for investigating AI, cognition, communication, evolutionary optimization in novel versions: the chemical ones. We will not deal on what AI offers to synthetic biology, but on what synthetic biology offers to AI. By depicting some research paths, here, we intend to stimulate the bottom-up synthetic cells community to look toward such themes, to develop chemical AI in basic and applied sciences.

Keywords Artificial intelligence · Biological cell-synthetic cell interaction · Cognitive science · Smart drug delivery · Synthetic biology · Synthetic cells

P. Stano (✉)
Department of Biological and Environmental Sciences and Technologies (DiSTeBA), University of Salento, Lecce, Italy
e-mail: pasquale.stano@unisalento.it

1 Synthetic Cell Research: A Brief Introduction

1.1 Synthetic Biology

Synthetic biology is a new scientific discipline, born at the beginning of the 2000s mainly in US bio-engineering Departments, and aims at applying an engineering approach to biology [3, 10]. It targets the construction of engineered biological systems with medical, environmental, industrial utility. A possible definition of synthetic biology refers to bio-engineering procedures and reads: "synthetic biology consists in the design and construction of new biological parts, devices and systems, and in redesigning existing natural biological systems, in order to make them useful for some purpose" [10].

Curiously, the very term "synthetic biology" is not a modern one. It was coined more than a hundred years ago by the French chemist Stéphan Leduc, who, in a historical and scientific context completely different from the current one, called *biologie synthétique* his research devoted to "synthesize" a sort of proto-biological systems starting from mixtures of simple chemicals [22]. Such a vein is still present in modern synthetic biology, but of course reexamined in a different way. In particular, we refer to the construction of simplified cellular models to understand molecular and cellular mechanisms, often from a *systemic viewpoint*, with relevance to contemporary cells or to primitive organisms (protocells) that could have had a role in the origin and development of life on earth [43]. Synthetic biology is then a frontier research, deriving from the fusion of chemistry, biology, and (bio)physics that uses rational principles to create models, systems, machines in the (bio)chemical domain. The main target of synthetic biology is the construction of *synthetic (or artificial) cells* (SCs), for different purposes.

It should be firstly noted that the very terms "synthetic cells" and "artificial cells" are used to indicate different systems, having different complexity, different properties, and serve for different scopes (see Table 1). Among the several approaches, the first one refers to the artificial synthesis of a whole bacterial genome that, when transplanted in a cell deprived of its own genome, takes its control [15, 33]. The genome design includes concepts related to the essential genes for life and the limits of minimization. Until now, this approach is reserved to only few laboratories in the world because of its cost and complexity.

A second approach consists in the addition, elimination, modification, substitution, link, control, etc., of genes and/or metabolic pathways by traditional and innovative bio-engineering techniques. The idea is that the resulting cell is "rewired" in order modify its behavior. Part of the metabolism and/or the genetic expression pattern is channeled in a desired way for useful goals (the production of biofuels, pharmaceuticals, fine chemicals; functioning like colored or fluorescent biosensors, or being able to metabolize pollutants). These are the premises (and promises) of the bio-economy, whereby organisms (generally micro-organisms) are used for bio-production thanks to their astonishing capacities of catalysis, chemical transformations, as if they were microscopic chemical factories.

Table 1 Comparison between three different "synthetic cells" approaches

Type	Approach and notes	Main aims
1st	A full genome, designed and constructed artificially by a combination of chemical and biotechnological methods, is inserted in a living cell deprived of its own genome. The synthetic genome contains the minimal number of genes to sustain target functions or life itself. The design and the construction of a full artificial genome is not trivial	Experimental verification of the minimal genome; ab initio design and construction of living cells; starting a new era in biology and biotechnology: from understanding to constructing
2nd	Addition, subtraction, modification, silencing, exchange of genes aiming at "rewiring" living cells, via several technologies. The resulting cells are alive but their functioning has been partially modified at various degrees. Somehow, this approach extends traditional bio-engineering practices (genetic engineering, metabolic engineering) to a new (more complex) systemic level, making use of systemic design (systems biology) in order to optimize the desired output	Mainly for practical purposes such as bio-production, biosensors, etc. E.g., construction of efficient cellular systems for practical purposes, such as production of biofuel, chemicals, pharmaceutics; for their use as colored/fluorescent/luminescent biosensors, for bioremediation, etc.
3rd	Construction of cell-like structure from scratch, by employing self- and guided-assembling methods. The starting materials are known mixtures of defined (bio)chemicals. Cell extracts can be also used, as well as organellae or other cellular parts. In addition to biochemical molecules, cell-like structures can be obtained when artificial compounds are used (e.g., polymers, alternative forms of nucleic acids, catalysts of various types, etc.). To date, the resulting structures are quite simple when compared to biological cells and are not alive	Investigating basic physico-chemical requirements for life; emergence and origins of life; inventing alternative cellular forms; construction of non-living cell-like systems for biotechnological applications, potential use as "smart" drug delivery agents

Alongside top-down synthetic biology (this is the term, partially equivocal, generally reserved for the two approaches above), there is another way, called bottom-up synthetic biology, that somehow resembles Leduc's studies of about one century ago. The scientific understanding of what cells are and how they function is much progressed, of course, and the contemporary attempts are instead quite sophisticated. It is possible, indeed, to construct cytomimetic systems that display some cellular features. As it will be explained in details in Sect. 2, the relevance of bottom-up SCs are not only related to basic science, but can converge toward the applicative field, in particular in nanomedicine (e.g., to fight tumors [20]).

In this contribution, however, we will focus on how, and at what extent, bottom-up SCs might constitute an experimental platform for exploring and developing theoretical aspects of artificiality in the chemical domain [6, 7].

1.2 What Are Bottom-Up Synthetic Cells?

Bottom-up SCs are artificial structures created in the laboratory based on the encapsulation of functional molecules inside some sort of micro-compartments, see Fig. 1a. This operation is made by exploiting molecular self-assembly and various forms of guided-assembly to produce cell-like particles whose size varies depending on the preparation method. If properly built, SCs display some cellular processes of interest in a minimal and simplified manner. Because of the latter feature, SCs are sometimes called minimal SCs (or semi-synthetic cells) [24, 25] because the function of interest is achieved with the minimal number of components.

The bottom-up approach is quite versatile, and it has been put forward because of several motivations. Firstly, it can be realized with a wide range of materials. If interested in modeling primitive cells, allegedly, primitive molecules should be used (e.g., short peptides and nucleotides, fatty acids, etc.); if interested in modeling modern cells, one should use modern molecules such as phospholipids, enzymes, RNAs, etc.; finally, completely artificial systems can be built by employing compounds of non-biological origin (polymers, ad hoc designed molecules, complex catalysts, etc.), see Fig. 1b. Hybrid systems also attract the attention because of the unique blend of properties deriving from the coexistence of materials of diverse nature, or by the advantage of using both isolated molecules and prefabricated modules (e.g., biological organellae inserted inside SCs [2]). A second motivation lies in the fact that minimal synthetic cells, built from allegedly primitive molecules, are models of primitive cells (protocells) and can help understanding the origins of life on earth. Third, using the reliable and known mechanisms of molecular biology, building bottom-up SCs is equivalent to build a sort of molecular robot whose behavior can be programmed by a proper design of its internal biochemical mechanisms. Fourth, as it will be introduced in Sect. 2, non-living bottom-up SCs can be potentially developed as advanced drug delivery systems or as biotechnological tools (for assays, as biosensors, to test drugs for membrane proteins, to reconstruct and study biochemical pathways, and so on).

The experimental strategies for building bottom-up SCs are also numerous and interesting, but not in-topic for this article. It is enough to mention that the current strategies are based on: (1) liposome technology and in general "micro-compartment" technology; (2) microfluidics; (3) cell-free systems (in the particular gene expression in vitro); (4) numerical modeling and simulations. Liposome technology allows the formation of conventional ($< 1\,\mu m$) and giant ($> 1\,\mu m$) phospholipid vesicles in a solution containing the molecule(s) of interest. As a result, some molecules will be encapsulated inside the vesicles; others will remain free, in the solution outside the vesicles. The latter molecules are removed or inhibited, so that only intra-vesicle
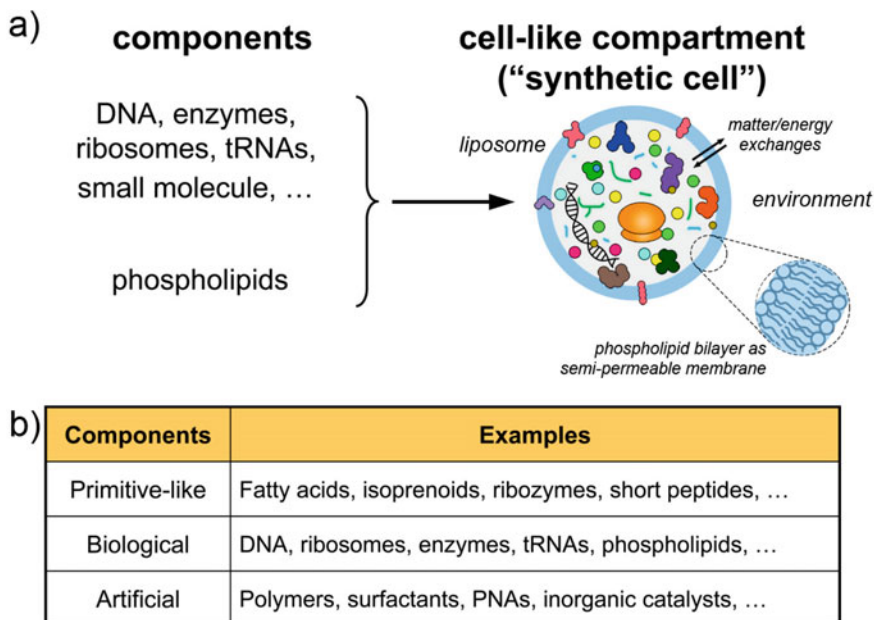
Fig. 1 Synthetic cells made by the encapsulation of chemicals inside artificial compartments. **a** The case of semi-synthetic cells from biochemical components and liposomes. **b** Different types of synthetic cells can be envisaged, depending on the experimental scope. Hybrid systems are also possible. Reproduced from [41], according to the terms and conditions of the Creative Commons Attribution (CC-BY) license

molecules react and display the dynamics of interest. In order to achieve significant SC functionalization, enzymes are (i) encapsulated inside lipid vesicles or (ii) produced in situ, by means of gene expression [40]. In the latter case, not the enzyme itself, but the corresponding gene is co-encapsulated inside vesicles together with the many other macromolecules and small molecules required for completing the set of reactions called transcription-translation (TX-TL). In such a manner, the behavior of a cell is closely reproduced because genetic information is transferred from the DNA sequence to the three-dimensional structure of a protein (e.g., an enzyme), and the latter then operates according to its catalytic capacity. Instead of an enzyme, other types of proteins can be produced (sensors, regulators, cytoskeletal elements, transcription factors, etc.) increasing in significant manner the range of functions available in SCs. In other words, thanks to TX-TL reactions, SC internal mechanism closely simulate cells with respect to the generation and control of functions, and at the same time allow a design based on easy-to-manipulate genes. As we will see in the next paragraph, if the product of TX-TL reactions is a toxin, SCs can be employed as advanced drug delivery systems to produce and deliver a drug (e.g., the toxin) near a target (biological) cell—in the body of a patient.

2 Synthetic Cells as "Smart" Drug Delivery Agents

The idea of using small smart particles as drug delivery agents—and in general to heal (or kill) sick cells—is quite old. The Nobel Prize winner Paul Ehrlich, for example, maintained that efficient medicine would have needed "silver bullets" in order to deliver the active ingredient of drugs exactly to the target tissue/location. Such a vision guided the development of drug delivery systems, in the sense that the physical association of a drug to a certain nanosized *vehicle* can alter the clearance rate and the bio-distribution of the drug in the body. Higher performances are linked to additional concepts such as biospecific targeting and controlled release (academic and industrial research is active in this field). Drug delivery systems generally consist of small particles (typical size below 200 nm) which bind or contain the active ingredient(s). Lipid vesicles are among the most well known drug delivery systems, approved by FDA and other regulatory agencies for some diseases (e.g., AmBisome against systemic infections, Doxil against tumors). The recent anti-SARS-CoV-2 vaccines (e.g., from BioNTech) are also based on lipid-RNA nanoparticles [46].

It was recognized, even before the development of modern SC technology, that complex vehicles such as semipermeable cellulose nitrate nanocapsules containing enzymes could serve as innovative agents that perform metabolic reactions in the blood in order to complement or substitute a missing or malfunctioning biological function [4, 5], for a kind of therapy based on enzyme delivery [9]. Such an approach can be considered anticipatory of the idea discussed in this section. SCs, then, can play a central role in future nanomedicine as "smart" and/or "programmable" drug delivery agents. SCs represent a possible evolution of drug delivery based on simple particles because SC function is not limited to passive transport and diffusion (as it happens in simple liposome-based drug delivery systems or in the enzyme-filled nanocapsules proposed in the 1950s), but can include sophisticated behavior such as motion, sensorial capacities, autonomous production of drug, controlled release, recognition of the environment, and self-destruction. These advanced features could be achieved by a proper design of corresponding "modules," in the same way it is currently done for other scopes (e.g., reconstruction of a flagellum for motility, reconstruction of a membrane pore for releasing a drug, and so on). P. LeDuc and collaborators called "nanofactories" such kind of systems [21].

Recent studies, moreover, showed that programmable genetic/metabolic circuits, which function in vitro [32], can be inserted in SCs. These circuits, for example, could guarantee a production of therapeutic molecules controlled by external stimuli: the SC can be constructed with a pro-drug cargo and activate the pro-drug to drug transformation via enzyme reaction, release the drug only after a membrane pore is assembled, etc., and perform all these operations only when a chemical signal has been received *by the target tissue*. As mentioned, a SC with an internal "enzymatic assembly line" would operate as a nanofactory [21]. Even if these systems are not available yet, because of their complexity, other results show the interest in developing this direction in SC research. For example, a recent report by Avi Schroeder and collaborators (2018) marks a new step along this path. The "agent" is a SC

that synthesizes a protein with therapeutic purpose (a toxin) directly in the patient's body (a mouse was used) [20]. The molecular machinery used for protein synthesis, extracted from *E. coli* cells, was encapsulated inside vesicles to perform TX-TL reactions, generating the therapeutic toxin starting from the DNA genetic information. The resulting system, however, did not display any sort of control (the toxin was produced continuously, without a switch).

2.1 Chemical Communications Between Biological Cells and Synthetic Cells

The abovementioned scenario clearly recalls the need of developing SCs endowed with control functions, by exploiting molecular sensors and actuators. Such an advanced system could perceive the environment—a (bio)chemical one—and behave correspondingly. It is then not surprising, then, that several experimental efforts have been started in order to endow SCs with such features. Already in 2012, it was made clear that these new requirements had to be conceptualized and realized under the guidance of theoretical frameworks related to SC-biological cell communication, interpreted as an example of bio-chem Information and Communication Technologies (bio-chemICTs) [42]: according to the "wetware" approaches to artificial systems and to the—at the time—newborn field of "molecular communication" [30]. Reviews of experimental results are available [16, 18, 34, 37]. Among them, it must be mentioned a relevant investigation dealing with *bidirectional* chemical communication between SCs and bacteria, utilizing quorum-sensing signaling [23].

Intriguingly, the improvement of SC sensori-responsive abilities nicely complements TX-TL and metabolic functions, which have been introduced from the beginning of SC research. These considerations bring us straight to the next discussions (Sects. 3 and 4), where we assess the current research arena and depict new technical-theoretical horizons about it. It is specifically in this latter respect that this paper intends to contribute to ICCCES 2022, providing an overview and a perspective about frontier goals in artificial computation and communication in the wetware domain.

3 Where Do These Recent Research Directions Bring the Field?

In the previous sections, we have made a survey on the recent SC research developments, discovering that the most relevant ones point to an emergent field. We intend the use of SCs as experimental platform, in the wetware domain, for new forms of artifacts that can be programmed (i.e., genetic circuits), are responsive (i.e., stimulus-response, signal transduction), and can be interfaced with biological

counterparts (i.e., SC-biological cell communication, smart drug delivery). As a due consideration, a second element to include is a comparison between synthetic biology approaches and two other (more established) research areas in the sciences of artificial, namely, robotics and artificial intelligence. Both deal with the reconstruction of organism-like behavior by means of artifacts, which take the form of hardware and software artifacts, respectively. Synthetic biology complements these important sci-tech fields because it provides a new path to artifacts based on bio/chemical materials.

The motivations behind this article, therefore, refer to the necessity—originated by the abovementioned progress and by imminent directions that research can undertake—of inquiring how classical questions that have been faced traditionally by hardware and software approaches can be now faced by wetware approaches. We believe, indeed, that SCs can represent a quite valuable tool for starting this new path, which is completely unexplored and challenging, yet fascinating. SC technology recently emerged as a technology not resembling anything already existing, and therefore very amenable to creative ideas, innovations, discoveries. It can become the substrate, the strategy, and the framework to develop new forms of information and communication technologies, based on (bio)chemistry. We will briefly introduce and comment aspects of this new enterprise, aiming at stimulating the discussion between experts and newcomers. Will it be possible to develop novel ways to face classical questions related to communication, information, computation theories by means of synthetic biology?

4   Synthetic Cells as a Platform to Investigate Chemical AI and Information Theories in the Wetware Domain.

In order to keep the discussion relevant to the ICCCES, we will focus on keywords related to the conference themes: Artificial Intelligence (AI), Cognitive Sciences, Human–Computer Interaction (here translated into biological cell-SC interaction), Evolutionary Optimization.

4.1   AI in the Chemical Domain

Approaches to computation in the biochemical domain typically make use of genetic circuits, which are well known and can be build both in vivo and in vitro (although examples of genetic circuits inside SCs are rare). In the simplest realization, a genetic device could consist in just one gene, expressed thanks a TX-TL machinery, according to an input, which can be physical or chemical. For example, TX-TL reactions are negligible at low temperature (e.g., in ice), but take place at significant rate at 25–37 °C. Therefore, temperature functions as a simple switch in such a complex reaction

network. More sophisticated and interesting examples have been reported, thanks to the presence of transcription regulators (and/or small molecules that they bind). Gene expression patterns develop accordingly, and their computational "result" can be measured by quantifying the concentration of mRNAs or proteins. When a threshold is applied to convert the intrinsic continuous concentration values into binary output, a genetic circuit can admit a symbolic representation of its operations (OFF/ON). Thanks to this analog-to-digital conversion genetic circuits and alike are generally treated with the symbolism of logic gates.

An intriguing new direction has been recently sketched, mentioning the possibility of endowing SCs with *chemical neural networks*. In neural networks, information is not manipulated/transduced in linear manner, but it is submitted to a sort of parallel distributed processing which makes the procedure more "systemic," and somehow point to the ultimate goal of a "whole-SC computing" (currently out of experimental reach). Several chemical neural networks have been studied in the past years, mainly via computational investigation, while only few experiments have been reported (reviewed in [38]). We recently proposed that an around-the-corner scenario would be the construction of chemical neural network based on the so-called "two-component signaling systems." These are bacterial signaling networks that rely on phosphorylation reactions [14]. It is possible to imagine the construction of this sort of "phospho-neural networks" [17] inside SCs by the incorporation of proper membrane proteins (the sensors, which constitute the input layer of the neural network) and of their cognate soluble proteins (the response regulators, which constitute the hidden layer of the neural network). The latter directly affects gene expression (genes, mRNA, or proteins can be considered the output layer of the neural network). The question about what kind of behavior can be originated, and what is the corresponding network topology, the number of "neurons" in each layer, their connectivity (weights, biases) and activation function (isothermal binding, Michaelis-Menten profiles) is still open. Numerical models will help to determine the best design. Because the embodied chemical nature of such phospho-neural networks, we have suggested that fuzzy logic approaches provide more accurate results [14, 39].

Recent considerations, based on the inferential nature of mind [11, 12] (and on the mind-like character of autonomous SCs, when they will become available [44]), suggest that another intriguing target for future research would be the realization of chemical Bayesian mechanisms or Bayesian chemical networks. The challenging task refers to the implementation of Bayesian conditional probabilities [26] via (bio)chemical reactions. It would be interesting, for example, to show whether a chemical network inside SCs can compute the probability that its environment is in a state x, given a received set of perturbations π, i.e., $p(x|\pi)$ (we acknowledge J. C. Letelier, University of Chile, who presented these inspiring insights at the ALIFE 2022 Virtual Conference, 18–22 July 2022).

4.2   Cognition and Its Roots in Organization

SC research actually originated as an approach to model primitive cells, searching for answers in the field of origins of life. In modern scientific terms, investigating the origin of life means exploring the conditions that could have lead to the emergence of early living systems (protocells). Practitioners soon realize, however, that a related question must be answered first, namely, "what is life?" Several theories can be deployed. Among the most popular ones, autopoiesis [27, 45] and chemoton [13] must be cited. Here, we will refer to the first one. Autopoiesis is a systemic theory of living beings introduced by H. Maturana and F. Varela in 1972. They put forward that living systems are a special class of machines endowed with the fundamental property of being autopoietic (self-producing), i.e., are made of a set of chemicals that establish an *organizationally closed* dynamical reaction network. The network is defined by a set of processes and relations between processes, whose products are the very elements and processes of the network and constitute in the physical space a *topologically closed* system, which can be distinguished from the surroundings. The result of autopoietic dynamics is the autopoietic system itself. Organization is conserved despite the material elements are continuously renewed. The abovementioned closures should not be confused with a related terms used in thermodynamics. Autopoietic systems are indeed thermodynamically open and function out of equilibrium.

According to Maturana and Varela, autopoietic systems are also cognitive systems by definition. Thus, the theory of autopoiesis replies to both questions: "what is life?" and "what is cognition?" Because of the indissoluble link between living systems and their environment, it is a self-evident fact that living systems recognize and have the capacity of including in their organization only those stimuli that do not destroy their autopoietic organization. The set of allowed perturbations has been generated in co-constructive, dialectic manner (action-perception loops) during the evolutionary history of the organism/environment super-system. In autopoiesis, that very living process is a cognitive one, and "life = cognition."

Can SCs display cognitive behavior? Cognition is rooted in the organization (chemical network) that constitutes the autopoietic system in its development. But, current SCs are not alive, have no evolutionary history, are not autopoietic, and a fortiori not cognitive. However, having realized that such properties are all related to organization we could attempt to construct minimal (or better, partial) forms of cognitive systems by focusing on intra-SC sub-systems endowed with the desired organizational features. Although authors like Maturana and Varela remarked that autopoiesis is an all-or-none property, empirical experimental research can take the liberty of waiving to these strict theoretical requirements if the achieved results are somehow useful (to progress knowledge, to demonstrate a principle, as case study, as inspiration for other research). Approaches based on self-regulatory sub-systems embedded inside SCs, for example, are good candidates for exploring minimal cognition, even if the whole system (the SC) remains not cognitive. By means of experimental or numerical models, future targets can include forms of partial plasticity, possibly in response to external stimuli, closed causal loops (e.g., production of proteins that regulate their own production), bistable circuits.

4.3   Biological Cell-Synthetic Cell Interaction

Section 2.1 includes a discussion on this topic. It is now possible to devise SCs whose internal mechanisms are capable of synthesizing (i) signal molecules via enzymatic reactions, (ii) proteins that make a pore in the membrane facilitating the import/export processes [1], (iii) enzymes (via TX-TL) that participate to the signal molecule production [35]. Lipid vesicles have been also endowed with connexin-4x3 gap junctions, allowing a physical connection (via a transmembrane pore) between two adjacent vesicles [28, 36].

4.4   Evolutionary Optimization Relies on the Embodiment of "Meaning" in Forms of Organization

Current SCs are not yet able to undertake an evolutionary path. Indeed they do not have the sufficient complexity and potentiality to change their internal organization (plasticity) as an adaptive response. Therefore, considerations about evolutionary optimization can be done only in related theoretical modeling work. We suggest that a clue about how SCs can undergo an adapting behavior to their environment and possibly observe such a dynamics in computer simulations, comes from recent studies the "semantic" information that SCs extract from the environment. Following a paper on agents' autonomy, authored by A. Kolchinsky and D. Wolpert [19], it is possible to compute what is the "best" environmental pattern E_{opt}, intended as spatio-temporal distribution of signals, nutrients, etc., that fits with SC organization Ω_i (the set of intra-SC reactions, physical constants, reaction rates, etc.). But, this is tantamount to say that the reverse is also true (although can be more difficult to compute): i.e., given a certain environmental pattern E_i, it will exists an optimal SC internal organization Ω_{opt} (or a set of organizations) that allow SCs to perform optimally therein. By performance here, we mean a measurable quantity related to SC existence, viability, or successful task completion.

In our opinion, this suggests that the set of chemical reactions which constitute a SC organization Ω (types, topology, kinetic and thermodynamic parameters) ultimately is a sort of semantic map referred to a certain environmental patter E, to which that specific SC is adapted (and it can be computed despite the absence of a real historical adaptation dynamics). It seems to us that such a concept (the semantic map) founds an echo in D. Nauta cyber-semiotic theory [31], and although intuitive reasoning suggests that the principles here described constitute a promising vein, implementations and examples are open to future investigations and criticisms. This article, therefore, intends to call into action all scholars with the due expertise, who can contribute in the clarification of these still unexplored concepts.

5   Conclusions and Outlooks

Synthetic biology (Sect. 1.1) represents a new research area located at the interface of biology and engineering and offers opportunities for theoretical insights and application studies. The top-down approach (Sect. 1.2) permits the construction of cell-like systems of minimal complexity, which generate in an organizational-relevant manner some aspects of cellular behavior [8]. SCs, often made of lipid vesicles that encapsulate biochemical macromolecules, can be considered as a (bio)technological tool for reaching these goals.

In this paper, we have highlight how, driven by their potential application as smart drug delivery systems (Sect. 2), SC research started to encompass approaches, patterns, behaviors that can trigger the interest of theoreticians because themes as computation, communication, information can be now investigated and developed in a new domain: the chemical (wetware) one (Sect. 4). These development should, in our opinion, parallel what has been done in the past years in the hardware and software domains—think, for instance, to the progress in robotics and AI. In order to give the readers a flavor of what we are referring to, we have shortly discussed some selected key themes. While AI methods are being used more and more frequently in biological research [29], here, we have proposed that biology can provide concepts, materials, and opportunities to develop chemical AI.

References

1. Adamala KP, Martin-Alarcon DA, Guthrie-Honea KR, Boyden ES (2017) Engineering genetic circuit interactions within and between synthetic minimal cells. Nat Chem 9(5):431–439. https://doi.org/10.1038/nchem.2644
2. Altamura E, Albanese P, Marotta R, Milano F, Fiore M, Trotta M, Stano P, Mavelli F (2021) Chromatophores efficiently promote light-driven ATP synthesis and DNA transcription inside hybrid multicompartment artificial cells. Proc Natl Acad Sci U S A 118(7):e2012170118. https://doi.org/10.1073/pnas.2012170118
3. Andrianantoandro E, Basu S, Karig DK, Weiss R (2006) Synthetic biology: new engineering rules for an emerging discipline. Mol Syst Biol 2(2006):0028. https://doi.org/10.1038/msb4100073
4. Chang TMS (1972) Artificial cells. Charles C. Thomas, Springfield, IL
5. Chang TMS (2019) Artificial cell evolves into nanomedicine, biotherapeutics, blood substitutes, drug delivery, enzyme/gene therapy, cancer therapy, cell/stem cell therapy, nanoparticles, liposomes, bioencapsulation, replicating synthetic cells, cell encapsulation/scaffold, biosorbent/immunosorbent haemoperfusion/plasmapheresis, regenerative medicine, encapsulated microbe, nanobiotechnology, nanotechnology. Artif Cells Nanomedicine Biotechnol 47(1):997–1013
6. Damiano L, Hiolle A, Caãmero L (2011) Grounding synthetic knowledge. In: Lenaerts T, Giacobini M, Bersini H, Bourgine P, Dorigo M, Doursat R (eds) Advances in artificial life, ECAL 2011. MIT Press, pp 200–207

7. Damiano L, Stano P (2018) Synthetic biology and artificial intelligence. Grounding a cross-disciplinary approach to the synthetic exploration of (embodied) cognition. Complex Syst 27:199–228. https://doi.org/10.25088/ComplexSystems.27.3.199

8. Damiano L, Stano P (2020) On the "life-likeness" of synthetic cells. Front Bioeng Biotechnol 8:953. https://doi.org/10.3389/fbioe.2020.00953

9. Dean SN, Turner KB, Medintz IL, Walper SA (2017) Targeting and delivery of therapeutic enzymes. Ther Deliv 8(7):577–595. https://doi.org/10.4155/tde-2017-0020

10. Endy D (2005) Foundations for engineering biology. Nature 438(7067):449–453. https://doi.org/10.1038/nature04342

11. Feldman Barrett L (2020) Seven and half lessons about the brain. Picador (Pan Macmillan), London

12. Friston K, Kilner J, Harrison L (2006) A free energy principle for the brain. J Physiol-Paris 100(1):70–87. https://doi.org/10.1016/j.jphysparis.2006.10.001

13. Gánti T (1975) Organization of chemical reactions into dividing and metabolizing units: the chemotons. Biosystems 7(1):15–21. https://doi.org/10.1016/0303-2647(75)90038-6

14. Gentili PL, Stano P (2022) Chemical neural networks inside synthetic cells? A proposal for their realization and modeling. Front Bioeng Biotechnol 10:927110

15. Gibson DG, Glass JI, Lartigue C, Noskov VN, Chuang RY, Algire MA, Benders GA, Montague MG, Ma L, Moodie MM, Merryman C, Vashee S, Krishnakumar R, Assad-Garcia N, Andrews-Pfannkoch C, Denisova EA, Young L, Qi ZQ, Segall-Shapiro TH, Calvey CH, Parmar PP, Hutchison CA 3rd, Smith HO, Venter JC (2010) Creation of a bacterial cell controlled by a chemically synthesized genome. Science 329(5987):52–56. https://doi.org/10.1126/science.1190719

16. Grimes PJ, Galanti A, Gobbo P (2021) Bioinspired networks of communicating synthetic protocells. Front Mol Biosci 8

17. Hellingwerf KJ, Postma PW, Tommassen J, Westerhoff HV (1995) Signal transduction in bacteria: phospho-neural network(s) in *Escherichia coli*? FEMS Microbiol Rev 16(4):309–321. https://doi.org/10.1111/j.1574-6976.1995.tb00178.x

18. Karoui H, Patwal PS, Pavan Kumar BVVS, Martin N (2022) Chemical communication in artificial cells: basic concepts, design and challenges. Front Mol Biosci 9

19. Kolchinsky A, Wolpert DH (2018) Semantic information, autonomous agency and non-equilibrium statistical physics. Interface Focus 8:20180041. https://doi.org/10.1098/rsfs.2018.0041

20. Krinsky N, Kaduri M, Zinger A, Shainsky-Roitman J, Goldfeder M, Benhar I, Hershkovitz D, Schroeder A (2018) Synthetic cells synthesize therapeutic proteins inside tumors. Adv Healthc Mater 7(9):e1701163. https://doi.org/10.1002/adhm.201701163

21. Leduc PR, Wong MS, Ferreira PM, Groff RE, Haslinger K, Koonce MP, Lee WY, Love JC, McCammon JA, Monteiro-Riviere NA, Rotello VM, Rubloff GW, Westervelt R, Yoda M (2007) Towards an in vivo biologically inspired nanofactory. Nat Nanotechnol 2(1):3–7. https://doi.org/10.1038/nnano.2006.180

22. Leduc S (1912) La Biologie Synthétique. Etudes de Biophysique, 1st edn. A. Poinat, Paris. http://www.peiresc.org/bstitre.htm

23. Lentini R, Martín NY, Forlin M, Belmonte L, Fontana J, Cornella M, Martini L, Tamburini S, Bentley WE, Jousson O, Mansy SS (2017) Two-way chemical communication between artificial and natural cells. ACS Central Sci 3(2):117–123. https://doi.org/10.1021/acscentsci.6b00330

24. Luisi PL (2002) Toward the engineering of minimal living cells. Anat Rec 268(3):208–214. https://doi.org/10.1002/ar.10155

25. Luisi PL, Ferri F, Stano P (2006) Approaches to semi-synthetic minimal cells: a review. Die Naturwissenschaften 93(1):1–13. https://doi.org/10.1007/s00114-005-0056-z

26. MacKay DM (1969) Information, mechanism and meaning. MIT Press, Cambridge, MA

27. Maturana HR, Varela FJ (1980) Autopoiesis and cognition: the realization of the living, 1st edn. D. Reidel Publishing Company

28. Moritani Y, Nomura SIM, Morita I, Akiyoshi K (2010) Direct integration of cell-free-synthesized connexin-43 into liposomes and hemichannel formation. FEBS J 277(16):3343–3352. https://doi.org/10.1111/j.1742-4658.2010.07736.x
29. Muthumanjula M, Bhoopalan R (2022) Detection of white blood cell cancer using deep learning using Cmyk-Moment localisation for information retrieval. J IoT Soc Mob Anal Cloud 4(1):54–72. https://irojournals.com/iroismac/article/pdf/4/1/6
30. Nakano T, Eckford AW, Haraguchi T (2013) Molecular communications. Cambridge University Press, Cambridge, UK
31. Nauta D (1972) The meaning of information. Approaches to semiotics [AS]. Mouton (De Grutyer), The Hague
32. Noireaux V, Bar-Ziv R, Libchaber A (2003) Principles of cell-free genetic circuit assembly. Proc Natl Acad Sci USA 100(22):12672–12677. https://doi.org/10.1073/pnas.2135496100
33. Pelletier JF, Sun L, Wise KS, Assad-Garcia N, Karas BJ, Deerinck TJ, Ellisman MH, Mershin A, Gershenfeld N, Chuang RY, Glass JI, Strychalski EA (2021) Genetic requirements for cell division in a genomically minimal cell. Cell 184(9):2430-2440.e16. https://doi.org/10.1016/j.cell.2021.03.008
34. Rampioni G, D'Angelo F, Leoni L, Stano P (2019) Gene-expressing liposomes as synthetic cells for molecular communication studies. Front Bioeng Biotechnol 7:1. https://doi.org/10.3389/fbioe.2019.00001
35. Rampioni G, D'Angelo F, Messina M, Zennaro A, Kuruma Y, Tofani D, Leoni L, Stano P (2018) Synthetic cells produce a quorum sensing chemical signal perceived by *Pseudomonas aeruginosa*. Chem Commun 54:2090–2093. https://doi.org/10.1039/C7CC09678J
36. Ramundo-Orlando A, Serafino A, Schiavo R, Liberti M, d'Inzeo G (2005) Permeability changes of connexin32 hemi channels reconstituted in liposomes induced by extremely low frequency, low amplitude magnetic fields. Biochim Biophys Acta 1668(1):33–40. https://doi.org/10.1016/j.bbamem.2004.11.003
37. Smith JM, Chowdhry R, Booth MJ (2022) Controlling synthetic cell–cell communication. Front Mol Biosci 8
38. Stano P (2022) Chemical neural networks and synthetic cell biotechnology: preludes to chemical AI. In: Proceedings of CIBB 2021—computational intelligence methods for bioinformatics and biostatistics. Lecture notes in bioinformatics. Springer, in press
39. Stano P, Rampioni G, Roli A, Gentili PL, Damiano L (2022) En route for implanting a minimal chemical perceptron into artificial cells. In: Holler S, Löffler R, Bartlett S (eds) Proceedings of the ALIFE 2022: the 2022 conference on artificial life, 18–22 July 2022. MIT Press, Cambridge, MA, pp 465–467 (online)
40. Stano P (2019) Gene expression inside liposomes: from early studies to current protocols. Chemistry 25(33). https://doi.org/10.1002/chem.201806445
41. Stano P (2019) Is research on "synthetic cells" moving to the next level? Life 9(1):3. https://doi.org/10.3390/life9010003
42. Stano P, Rampioni G, Carrara P, Damiano L, Leoni L, Luisi PL (2012) Semi-synthetic minimal cells as a tool for biochemical ICT. BioSystems 109(1):24–34. https://doi.org/10.1016/j.biosystems.2012.01.002
43. Szostak JW, Bartel DP, Luisi PL (2001) Synthesizing life. Nature 409(6818):387–390. https://doi.org/10.1038/35053176
44. Varela FJ (1979) Principles of biological autonomy. The North-Holland series in general systems research. Elsevier North-Holland Inc, New York
45. Varela F, Maturana H, Uribe R (1974) Autopoiesis: the organization of living systems, its characterization and a model. Biosystems 5(4):187–196. https://doi.org/10.1016/0303-2647(74)90031-8
46. Walde P, Ichikawa S (2021) Lipid vesicles and other polymolecular aggregates-from basic studies of polar lipids to innovative applications. Appl Sci 11(21):10345. https://doi.org/10.3390/app112110345

Investigation of Effectiveness of Deep Learning on OFDM and NOMA Systems

Bircan Çalışır

Abstract Research on deep learning (DL) to do detection of non-orthogonal multiple access (NOMA) and OFDM is presented in this paper. The successive interference cancelation (SIC) is generally fulfilled at the receiver in NOMA systems that decode multiple users in a successively. The detection accuracy is mostly based on the true detection of previous users due to the effects of error propagation. The NOMA receiver based on DL is described with deep neural network (DNN), which implements an estimation of channel and detection of signal together. The receiver has robust characteristics on the power allocation of the user is explicit from the simulation results. DNN is suitable for both linear channels and nonlinear channels, also the receiver is getting well on detection while the number of users is increasing. DL approximation obtains better achievement than a ML detection that ignores interference effects when the interference of the inter-symbol is intense.

Keywords Deep learning · Deep neural network · Orthogonal frequency division modulation

1 Introduction

System throughput and rate of information transmission are getting higher both with the improvement of communication technology and the operation of information transfer necessity. Widely used in 5G, NOMA improves the spectral effectiveness of the communication system [1–3]. While multiple users in NOMA utilize the same frequency and time domain but different power is allocated to each user. NOMA bases to utilize coding of superposition at the transmitter side to transmit data by multiple users simultaneously and to utilize SIC at the receiver side to detect operation [4]. As the basic method of 4G, OFDM improves the spectrum via used the orthogonality between subcarriers. Also, OFDM adds cyclic prefix (CP) to mitigate inter-symbol interference (ISI) and inter-subcarrier interference (ICI) reasoned by

B. Çalışır (✉)
Electrical and Electronical Engineering, Firat University, Elazig, Turkey
e-mail: bkamislioglu@firat.edu.tr

multipath spreading. Recently, it has been interesting for researchers designing of the continuously optimized receiver detector for the NOMA-OFDM signal. SIC wants to predict the channel firstly as a detector based on the channel model, but during the duration of data transmission, the pilots encounter interference signals from different users, the conclusion in the unsuccess to get full CSI. Also, when users are decoded SIC one by one, time delay will be produced [5, 6]. Based on deep learning (DL), the NOMA receiver is shown by a DNN, which utilizes one full link layer and detects whole users at the same time. While the detection impact of DL is strong, the trained data is big, which decreases the detection proficiency [7]. The general disadvantage of the all mentioned detection ways is that there is a dependence between users of decode correctness. To resolve all of the available questions, this study utilizes the fully mentioned info on deep learning [8] to advance the detector in [7]. The proposed receiver is based on DNN, utilizes the classification capability of DNN, accepts the consecutive training method [9], and joins with the smooth interference removal algorithm [10]. The design comprises two parts stage that DNN classification and decision soft. The detector output utilizes the distribution of probability to estimate the label of the transmitter. The performance verifying of the developed receiver is mainly represented with bit error rate (BER). Simultaneously, the success of the developed receiver in linear and nonlinear channels and the states in different user numbers are confirmed.

2 System Model

2.1 OFDM Structure

OFDM system signal flow is depicted in Fig. 1 Transmitted symbols convert to parallel signals which are BPSK modulated signals. The modulated signals are then transformed into the frequency domain utilizing an FFT block. Adding cyclic prefix to the signals decreases the impacts of ISI and ICC. Then the signals are transformed into serial signals and are transmitting operation is realized. Rayleigh channel is considered the best near-to real-life channel and due to its facilitation of the formation, the Rayleigh channel is preferred in this work. This channel can be modeled by adding Additive White Gaussian Noise (AWGN) to the signal.

$$y(n) = x(n) \otimes h(n) + w(n) \tag{1}$$

In Eq. 1, the received signal is y, h is a gain matrix of the channel, the modulated signal is x and w is the AWGN noise. Transforming operation from serial to the parallel of the received signal is realized and the cyclic prefix is extracted on the receiver side. Then the signal is transformed from frequency domain to time domain utilizing the IFFT process. In literature, generally Least Square estimator (LSE) and Minimum Mean Square Error (MMSE) estimator is used for channel estimation.
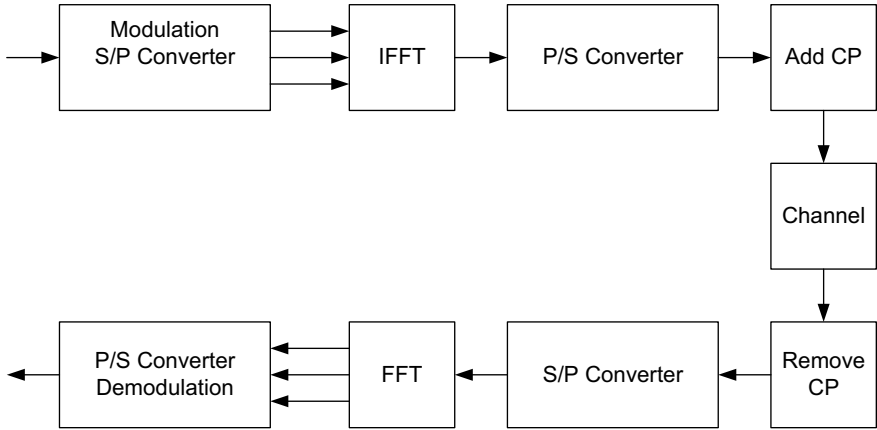
Fig. 1 OFDM block diagram

LS estimation channel response is given with Eq. 2 where $x_{p1}, x_{p2} \ldots x_{pn}$ are OFDM pilot symbols and $y_{p1}, y_{p2} \ldots y_{pn}$ are received pilot symbols.

$$h_{LS}^{\wedge} = [y_{p1}/x_{p1}, y_{p2}/x_{p2} \ldots y_{pn}/x_{pn}] \tag{2}$$

Using MMSE estimation channel response is written as Eq. 3.

$$h_{MMSE}^{\wedge} = R_{hh}[R_{hh} + \sigma_n^2 (xx^H)^{-1}]^{-1} h_{LS}^{\wedge} \tag{3}$$

When considering Eq. 3, R_{hh} matrix corresponds to the autocovariance of gain of channel, σ_n^2 represents the noise variance, $h_{LS}^{\wedge}$ is channel response using LS estimation.

Components of the channel matrix between the estimates are figured out by varied interpolation methods. Both these estimator methods do not outcome in excellent detection of signal because these methods cannot estimate the channel completely [11].

2.2 NOMA-OFDM

NOMA is a strong transmission technology that is preferred in 5G. In the wireless channels, users utilize NOMA technology for transmission and this saves frequency sources greatly [12]. In NOMA, data are sent at the same time by utilizing the same frequency resources. The total of data symbols and channel interference corruption are received by the base station as seen in Fig. 2.
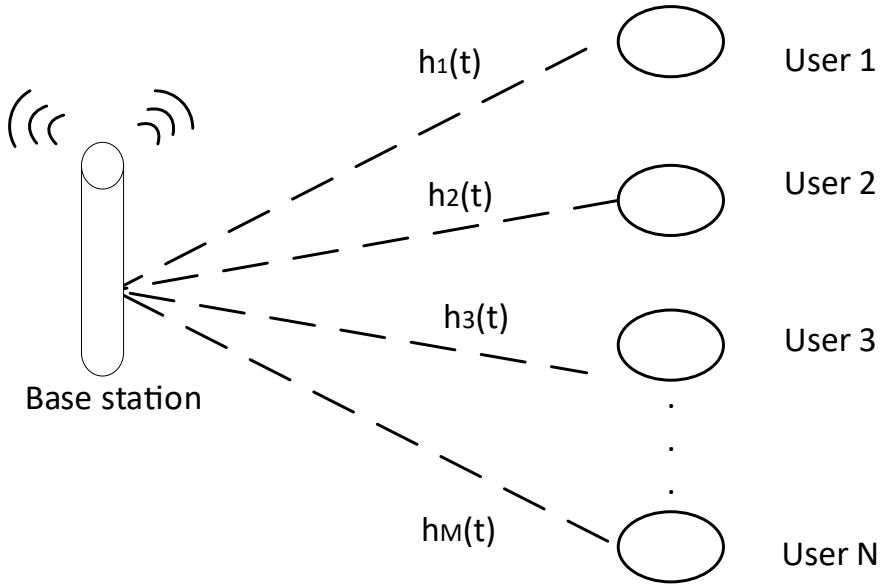
Fig. 2 NOMA system model

3 Deep Neural Network

In this work, the back-propagation algorithm has been proposed to detect received signals corrupted by the AWG and Rayleigh channels.

In Fig. 3, utilizing a trained neural network, the process of data rescue is made after parallel to serial conversion of FFT applied signals. Training of the back-propagation neural network is realized using BPSK-operated OFDM signals corrupted by AWGN and Rayleigh channel. Deep learning layers are shown in Fig. 4.

When the FFT applied OFDM symbols are the input vector, the layers of the neural network outputs are as Eq. 4:

$$V_1 = B_{\tanh h}(Z_1 * W_1)$$
$$V_2 = B_{\tanh h}(V_1 * W_2)$$
$$V_3 = B_{\tanh h}(V_2 * W_3)$$
$$V_4 = \text{softmax}(V_3 * W_4) \tag{4}$$

Z_1 corresponds to the input, W_1, W_2, W_3, and W_4 symbolize the weights united, V_1, V_2, and V_3 define the hidden layers output and V_4 represents the output of the neural network. The output layer comprises two nodes, each for the followed constellation points of BPSK.

Btanh (bounded-tanh) process represents the activation function for the primary three layers and is given by Eq. 5.
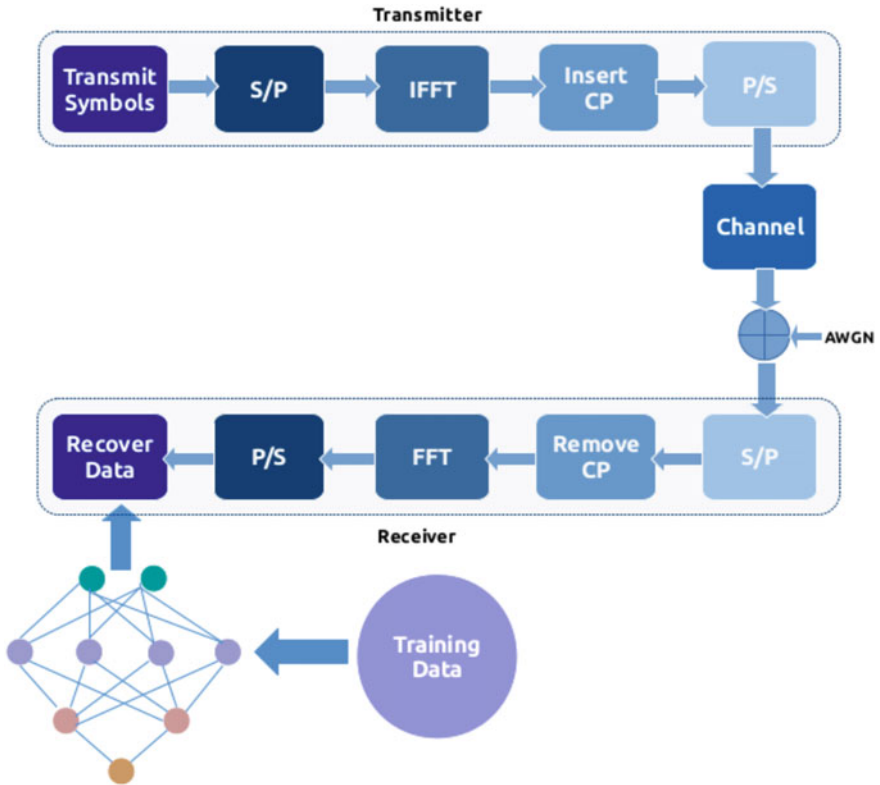
Fig. 3 Model of purposed system
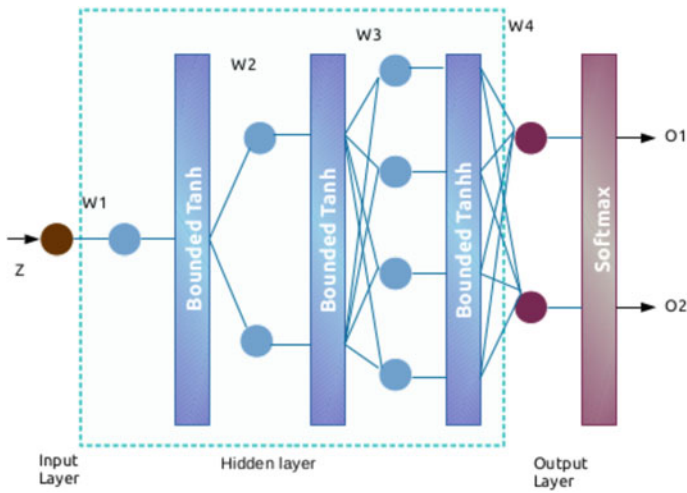
Fig. 4 Deep learning layers

$$y = \frac{1}{2}\left(1 + \tanh\left(\frac{x}{2}\right)\right) \tag{5}$$

Softmax function is utilized as an activation function of the output layer and gets an input x with N-dimensional, y output is an N-dimensional vector that is between 0 and 1. It describes as Eq. 6.

$$y_i = \frac{e^{x_i}}{\sum_{k=1}^{N} e^{x_k}} \tag{6}$$

4 Simulations Results

The OFDM symbol that does not have ISI has the given parameters in Table 1. It is considered that equal channel conditions are utilized in the DNN training and testing stages. With respect to the uplink power assignment guideline, power allocating in User 1 is more than power allocating in User 2. The proposed SNR has the same value for two users. After simulation, the DNN training progress is shown in Fig. 5 in terms of accuracy and loss curves. The BER performance of each receiver is given in Figs. 6 and 7 for 64 and 16 subcarriers, respectively. The change graph of accuracy and loss entropy is given in Fig. 3 the duration of data repetitive appropriating when the DNN model is training.

Decreases or rises are seen in the curve of the graph rapidly, which indicates that there is a significant impact on some neurons have on the weight change in the duration of model training, and it is arrived finally converge in the curve.

The sum time to train model is 9 min and 33 s which is illustrated in Fig. 5. The simulation throughputs demonstrate that the purposed receiver has both short training time, and well performance. The developed receiver performance of offline training in Fig. 5 is tested in Figs. 6 and 7. The evolved receiver is compared Maximum likelihood (ML) and DL detectors, least square (LS) [13] and minimum mean square error (MMSE) [14, 15]. Number of subcarriers of applied simulations is 64, pilot length is 64, multipath channel is 20, CP length is 20, users number is 2 are given in Table 1. Again in Table 1, as a DNN parameters, DNN layers is 1, batch size is

Table 1 The parameters of simulations	Parameters	Value	Parameters	Value
	Number of subcarriers	64	DNN layers	1
	Pilot length	64	Batch size	4000
	Multipath channel	20	Epoches	50
	CP length	20	Learning rate	0.01
	Users number	2	Training data	5000
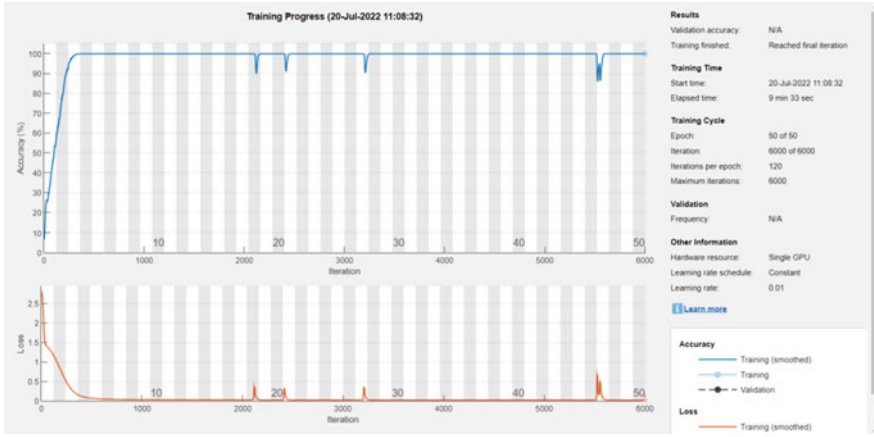
Fig. 5 Training progress of DNN
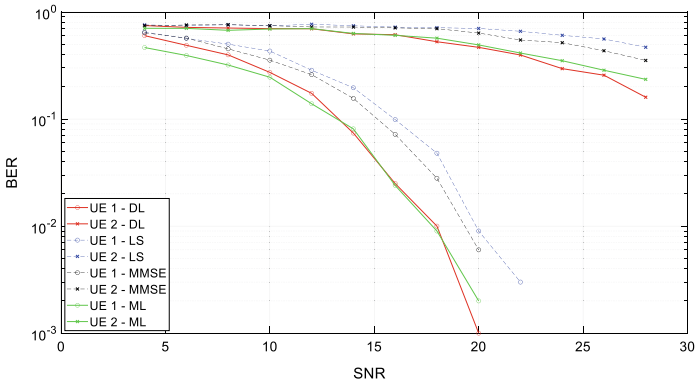
Fig. 6 BER to SNR for User 1 and User 2 including DL, LS, and MMSE for 64 subcarriers
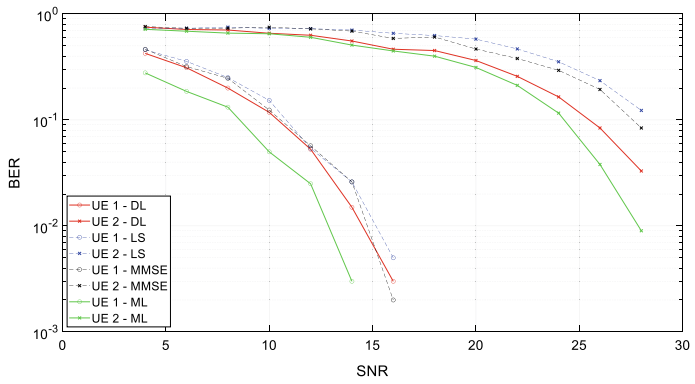
Fig. 7 BER to SNR for User 1 and User 2 including DL, LS, and MMSE for 16 subcarriers

4000, epoches is 50, learning rate that can be seen in Fig. 5 is 0.01 and training data is 5000.

For User 1 and User 2, and 64 subcarriers BER to SNR curve is illustrated in Fig. 6, and for User 1 and User 2, and 16 subcarriers BER to SNR curve is illustrated in Fig. 7.

The achievement of LS and MMSE channel estimators is related to pilot symbols, which are acknowledged by the receiver and utilized to rescue the response of the channel. For the impact of the number of pilot symbols researched for the DL receiver, 64 or 16 pilot symbols in each pilot sequence are used in the simulation.

From Fig. 6, when using 64 pilot symbols, each LS and MMSE method for User 1 and User 2 provides confident predicts. However, it is seen that the DL receiver obtains better success from Fig. 6. As for 16 pilot symbols, it is obviously shown the correctness of LS and MMSE estimators are reduced remarkably at a higher SNR for User 1 and User 2.

Nevertheless, the performance of the DL receiver is still comparable to the 64 pilot symbol conditions, which demonstrates that the DNN has a robust feature to the pilot symbols number and may provide more superior success with utilizing fewer pilots.

Figures 8 and 9 illustrate frequency-domain channel gains compared with the actual channel, LS, and MMSE for User1 and User 2. Compared with User 1, for User 2, channel gain is less. When compared LS, MMSE is more near to actual channel for both users.

Generally, to prevent ISI and provide the orthogonality of subcarriers a finite-length CP adding is done between consecutive symbols. Figures 10 and 11 indicate the BER curves for two different lengths CP 12 and 20, respectively.

When the CP has no shorter length than the impulse response of channel (CP Length is 20), the DL receiver has better performance than LS or MMSE estimation. Furthermore, for User 2 known as the weaker user in Fig. 4, the DL receiver provides a larger BER difference from other receivers and obtains a similar BER to User 1,
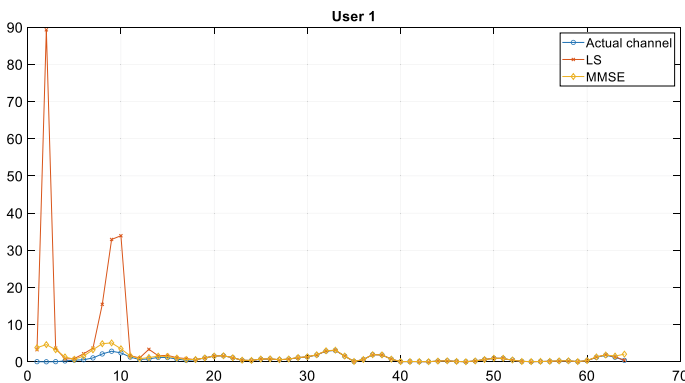
Fig. 8 Channel gains compared with the actual channel, LS, and MMSE for User 1
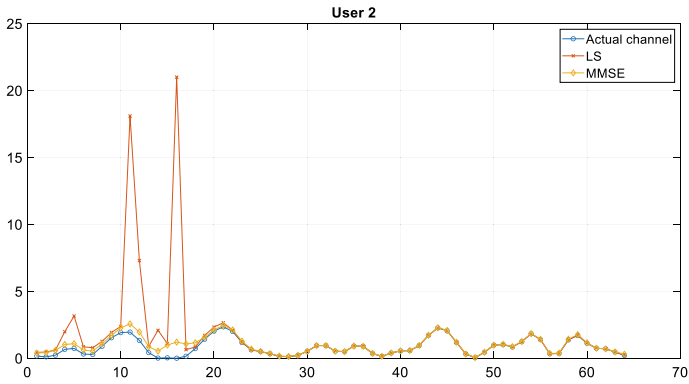
Fig. 9 Channel gains compared with the actual channel, LS, and MMSE for User 2
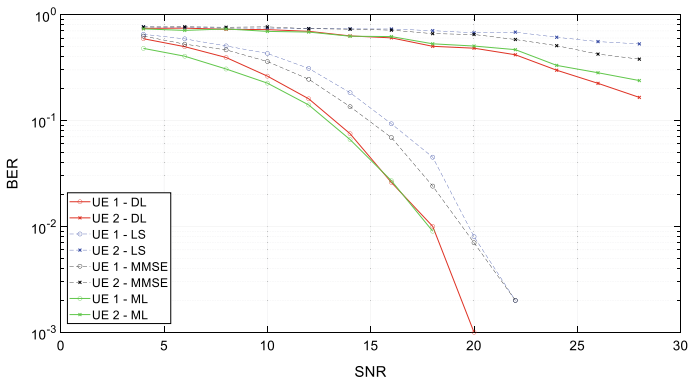
Fig. 10 BER to SNR for CP number is 12
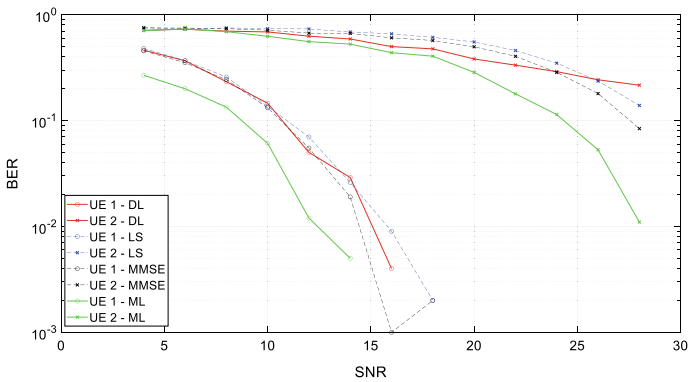
Fig. 11 BER to SNR for CP number is 20

and this situation presents DNN has robust structure for the signal power and can reduce the impacts of error propagation of detection.

Once CP is much shorter than the channel (CP Length = 12), the channel estimation cannot be done effectively neither LS nor MMSE. Because of heavy impacts of ISI, the optimal solution can no longer obtain even in case of perfect CSI. However, the DL receiver still has better performance than others and can also carry out better than the other receiver for both users. It is seen from this conclusions demonstrates that the DNN has more robust structure to distortion of the signal caused by ISI and can understand characteristics of channel considering the trained data. Software requirements of the proposed system include MATLAB Environment and used MATLAB 2017.b version for simulating system.

5 Conclusion

This work demonstrates an examination of DL for channel estimation and signals detection in a two-user OFDM-NOMA system. The obtained results from the simulation indicate that the DL approximation is better than the conventional channel estimation methods such as LS and MMSE receivers are more strong to the restricted radio sources, such as the power of signal, pilot symbols, and cyclic prefix. The offline training time, percentage of accuracy, entropy curve, and BER curve show us the superiority of the developed receiver that is wanted less training data, short time for training, higher accuracy, and no limitation to decode between users. As a future study, further searches and tests will be done for more complicated communication technology, such as MIMO applications.

References

1. Wang Y, Ren B, Sun S, Kang S, Yue X (2016) Analysis of nonorthogonal multiple access for 5G. China Commun 13(2):52–66
2. Dai L, Wang B, Yuan Y, Han S, Chih-lin I, Wang Z (2015) Non-orthogonal multiple access for 5G: solutions challenges opportunities and future research trends. IEEE Commun Mag 53(9):74–81
3. Ding Z, Yang Z, Fan P, Poor HV (2014) On the performance of non-orthogonal multiple access in 5G systems with randomly deployed users. IEEE Signal Process Lett 21(12):1501–1505
4. Islam SMR, Avazov N, Dobre OA, Kwak K (2017) Power-domain non-orthogonal multiple access (NOMA) in 5G systems: potentials and challenges. IEEE Commun Surv Tutorials 19(2):721–742
5. Higuchi K, Benjebbour A (2015) Non-orthogonal multiple access (NOMA) with successive interference cancellation for future radio access. IEICE Trans Commun E-98(3)
6. Chen M, Yang et al (2020) Iterative interference cancellation for nonorthogonal multiple access system. Chin J Electron 29(03):148–154
7. Narengerile TJ (2019) Deep learning for signal detection in non-orthogonal multiple access wireless systems. In: 2019 UK/China emerging technologies (UCET)
8. Hao X, Zhang G, Ma S (2016) Deep learning. Int J Semant Comput 10(03):417–439

9. Shlezinger N, Fu R, Eldar YC (2020) DeepSIC: deep soft interference cancellation for multiuser MIMO detection
10. Andrews G (2005) Interference cancellation for cellular systems: a contemporary overview. Wirel Commun IEEE 12(2):19–29
11. Tan Y, Zhou J, Qin J (2016) Novel channel estimation for nonorthogonal multiple access systems. IEEE Signal Process Lett 23(12):1781–1785
12. Balogun MB, Takawira F, Oyerinde OO (2019) Weighted least square based iterative channel estimation for uplink NOMA-OFDM systems. In: 2019 13th international conference on signal processing and communication systems (ICSPCS)
13. Ye H, Li GY, Juang B (2018) Power of deep learning for channel estimation and signal detection in OFDM systems. IEEE Wirel Commun Lett 7(1):114–117
14. Yan L (2017) Linear mmse interference cancellation detection for MIMO-OFDM system. In: International conference on measuring technology & mechatronics automation
15. Wang H (2021) Optimal compression of remote sensing images using deep learning during transmission of data. J Innov Image Process (4):357–366

Diagnostic System and Classification of Diabetic Retinopathy Using Convolutional Neural Network

Abdelhafid Errabih, Abdessamad Benbah, Benayad Nsiri, Abdelalim Sadiq, My Hachem El Yousfi Alaoui, Rachid Oulad Haj Tham, and Brahim Benaji

Abstract Early detection of the progress of Diabetic Retinopathy (DR) in people with diabetes is essential to prevent vision loss. Our project is based on the diagnosis of DR which relies on the prediction of disease stage in the patient via the fundus image taken by a retinal camera. As symptoms, we took blood vessels and exudates as the segmentation target. For classification, we used the deep learning approach to train our model. Toward the end implement a user interface to facilitate the diagnosis of retinal images. The results of the DR stage classification distinguish between six stages: no DR, moderate, severe, and very severe non-proliferative diabetic retinopathy (NPDR), and then moderate and severe proliferative diabetic retinopathy (PDR). The evaluation of the proposed methods is performed by calculating the following parameters: sensitivity, specificity, and accuracy rates.

A. Errabih · A. Sadiq
Laboratory of Information Modelling and Communication Systems, Ibn Tofail University, Kenitra, Morocco

A. Benbah · B. Nsiri (✉) · M. H. El Yousfi Alaoui · B. Benaji
Biomedical Engineering Department, National School of Arts and Crafts of Rabat (ENSAM), Mohammed V University, Rabat, Morocco
e-mail: benayad.nsiri@ensam.um5.ac.ma

R. Oulad Haj Tham
ADMIR Lab, National School of Computer Science and Systems Analysis, ENSIAS, Mohammed V University, Rabat, Morocco

1   Introduction

The eye is an important part of the human body that acts as an organ that reacts to light and helps to observe everything around us. It turns light energy into vision and transmits it to the brain via the optic nerve. If the retina is damaged, it can affect all or part of vision [1].

Some diseases can be diagnosed by symptoms appearing on retinal images, such as diabetic retinopathy, glaucoma, hypertension disease, and macular edema [1]. In this work, we are interested in the lesions caused by diabetes, which damages the blood vessels of the retina, and which can either leak fluid or cause bleeding. This is the leading cause of diabetic retinopathy (DR), one of the most serious consequences of diabetes and the leading cause of blindness in persons aged 20–74 years [1].

Abnormal symptoms that may appear during the development of DR are exudates, hemorrhages, microaneurysms, and cotton wool spots [1]. To be able to detect the early symptoms of these diseases, patients should opt for periodic retinal imaging to provide early diagnosis. The number of images collected can be very large, which makes the visual diagnosis to a specialist a lot of time and effort. The application of a DR detection system on retinal images will help a lot in the early detection of this anomaly, saving time and reducing the burden, prioritizing the diagnosis and treatment of the disease that requires early treatment.

The ambition of this project will be to provide the segmentation technique to detect some clinical signs related to this pathology and to classify its pathological stage, with the aim of establishing an accurate diagnosis and improving the treatment of retinal diseases. The first phase segments the blood vessels, the retinal mask, the optic disc, and the exudates in order to facilitate their visualization during the diagnosis. The second phase is dedicated to the classification of DR stages, using deep CNNs, such as AlexNet, ResNet-50, and Inception-V3. The last phase consists in developing a graphical user interface.

2   Materials and Methods

2.1   Dataset

DRIVE Image Dataset. Include 40 fundus images and segmentation of the vascular network of each fondus image. This was used as a basis for evaluating the segmentation of retinal vessels [2].

E-OPHTA Exudates Image Dataset. Contain 47 photos with exudates and 35 without lesions. Each record represents a patient visit and includes one or more color fundus photos as well as binary lesion masks. This database was used to evaluate the segmentation of retinal exudates [3].
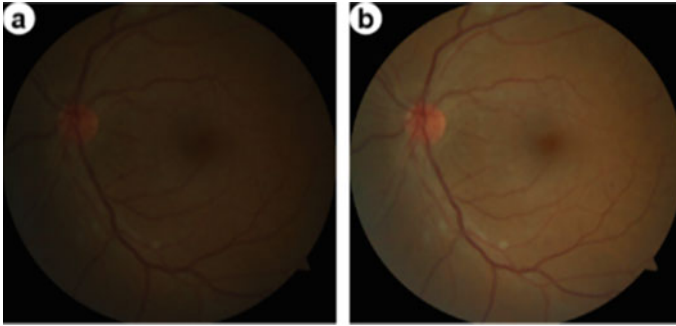
Fig. 1 Image enhancement **a** before and **b** after

Veronica et al. Dataset. This database contains 1437 fundus images that were acquired with the Zeiss Visucam 524 retinal angiograph. Expert ophthalmologists classified the dataset into 7 categories: No signs of DR (711 images), mild NPDR (6 images), moderate NPDR (110 images), severe NPDR (210 images), very severe NPDR (139 images), PDR (116 images), and advanced PDR (145 images) [4]. We used this dataset to train our prediction model. Firstly, we used 6 classes of which we merged classes 2 and 3 into a single "moderate" class. Secondly, some images have light artifacts, and some are very blurry, because of bad shooting, so we removed them. Thirdly, several images are very dark, but we have remedied this by increasing the exposure (+2) and contrast (+10) of each image as in Fig. 1.

2.2 Segmentation of Fundus Images

The retinal image is made up of three channels: green, red, and blue. Because of the significant contrast between the blood vessels and the background, the green channel was chosen among these three channels for the detection of vascular and retinal lesion abnormalities, as well as the clear representation of brightly colored lesions.

Segmentation of Blood Vessels. The retinal masking step plays an important role in removing noise details that do not belong to the retina [5], serves to distinguish the retinal image area from the outer black border. After that, CLAHE filter is applied, which makes the retinal image significantly more detailed, followed by the median filter for noise cancelation, with the pixels located at the edge put in zero. For the mean-C thresholding, give a different threshold for each pixel [5]. We chose $N = 13$ and $C = 0.035$. After separating the blood vessels, small objects are removed, and a retina mask is applied to remove the surrounding circular border. Steps to separate the retinal vessels are shown in Fig. 2 and related images in Fig. 3.
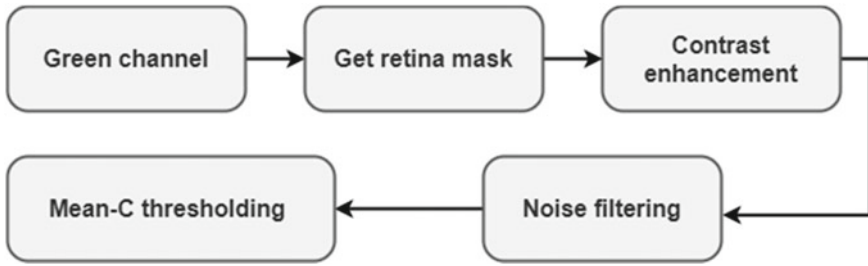
Fig. 2 Steps to separate the retinal vessels
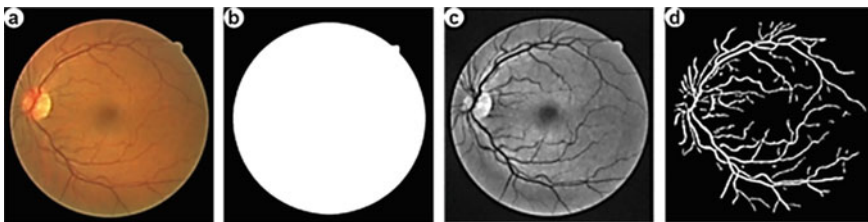
Fig. 3 Blood vessels segmentation **a** input image, **b** retina mask, **c** CLAHE filter, **d** blood vessels mask

Optical Disc Segmentation. For optical disc segmentation, we start with median filtering of the green channel image, then enhance the image contrast by the CLAHE filter [5]. Then apply an intensity-based thresholding. The resulting image will be processed by a morphological treatment presented by erosion, closure, space filling, new closure, and expansion [6]. We select the elements that have the most common points with the blood vessels and finally make an erosion of the resulting optic disc. Steps to separate the optical disc are shown in Fig. 4 and related images in Fig. 5.

Segmentation of Exudates. In this part, there are several constraints for the segmentation of the exudates, such as erroneous detection of part of the optic disc area or healthy natural light areas along the blood vessels. Therefore, to solve these problems,
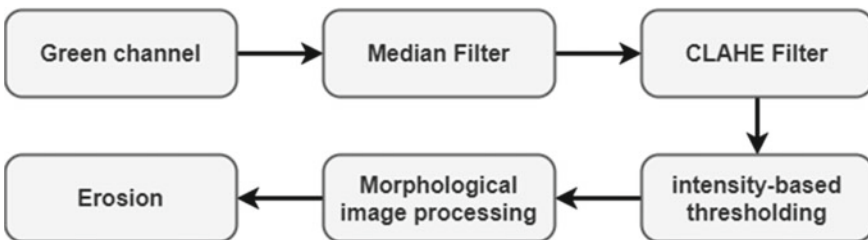
Fig. 4 Steps to separate the optical disc
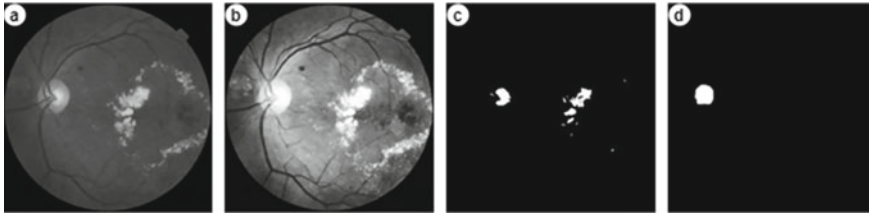
Fig. 5 **a** Green channel of the image, **b** CLAHE filter, **c** performed sharpening operations, **d** final result of optical disc segmentation

we have a combination between the median filter and the Kirsch filter by applying the steps shown in Fig. 6.

The monochrome image reconstruction method allows us to select the marked objects of the marker image among the existing objects in the masked image [7]. Which is very useful for image filtering and segmentation tasks.

We get a filtered background by applying median filter to the retinal image, then enhanced by a monochrome reconstruction. The result of the single-color initialization will be a well-detailed background estimation image that captures more detail than the simple estimation using the median filter [8]. Then remove from the original image the filtered background, followed by thresholding to obtain the bright lesion mask [9].

In the second part, the Kirsch filter is able to emphasize the locations of the bright edges of the lesions that show strong and sharp changes in gray level [10]. The result
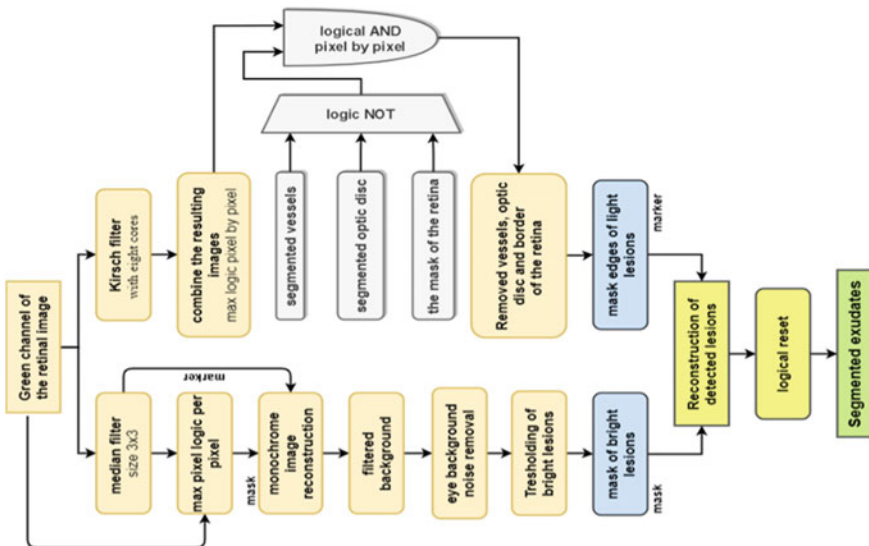
Fig. 6 Diagram of exudates segmentation steps
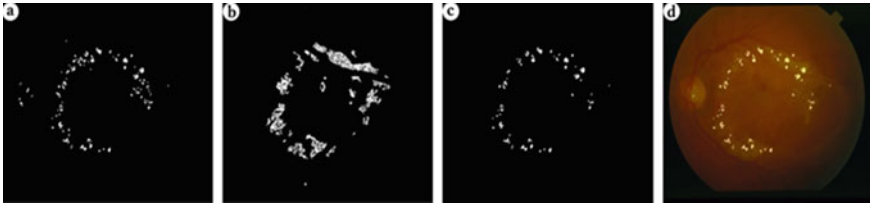
Fig. 7 **a** Candidate of the bright lesion, **b** edge of the light lesions, **c** result of the detected lesion reconstruction, **d** exudates on the original retinal image

of this filter is followed by a thresholding of value 5. Next, we expand and exclude the vascular mask and optic disc as well as used the retinal mask to remove the edge from the image. The resulting image contains candidates for light lesion edges [11].

The two resulting images have gaps. They also contain uninjured light objects such as a healthy light area or prominent edges that may not be bright lesions. The goal of our method is to select the marked objects in the marker image as the light lesion edge image from the existing objects in the masked bright lesion candidate image, by applying a monochrome image initialization is shown in Fig. 7 [7].

2.3 Classification of the Stage of Diabetic Retinopathy

The Deep Network Designer application was used to adapt pre-trained deep neural networks to the classification of our image collection. This process, called transfer learning, is generally faster and easier than training a new network.

This tool helps us to manage many deep learning experiments, to follow the training parameters, and to analyze the results. The architectures discussed in this chapter correspond to the Convolutional Neural Network (CNN).

AlexNet Model. This model has 8 layers of depth. The network has an input image size of 227 by 227. The applied AlexNet architecture consists of 25 cascaded layers: one input and one output layer, 5 convolution layers (conv), 5 pooling layers, 5 ReLU correction layers, 2 normalization layers, 2 dropout layers, a softmax layer and 3 fully connected layers (fc) [10].

Resnet-50 Model. This model has a depth of 50 layers. The input image size for the network is 224 by 224. This architecture is divided into four stages of initial convolution and max-pooling; each ResNet design employs 77 and 33 kernels, respectively. The first phase of the network begins, with three residual blocks each containing three layers. The kernels used to execute the convolution operation in the three layers of the stage 1 block are 64, 64, and 128 in size. The identity link is represented by the curved arrows. The dashed connected arrow indicates that the convolution operation in the residual block is performed using step 2, which reduces the size of the input

while doubling the channel width. While we go through the steps, the channel width doubles and the input size is decreased [11].

Inception-V3 Model. This model is 48 layers deep. The network has an image input size of 299 by 299. The architecture of this model can be considered as a microgrid inside another network. It has 192 input channels. It has only 128 filters of size 3×3 and 32 filters of size 5×5. The computational order of the 5×5 filters is $25 \times 32 \times 192$, which can increase as the network is deepened, when the width of the network and the number of 5×5 filters increase. To prevent this, the authoring module first applies larger kernels to minimize the size of the input channels before applying 1×1 convolutions. Finally, following the last convolutional layer, we find a simple global average pool that means the channel values throughout the 2D feature map. This greatly decreases the number of parameters while maintaining accuracy [12].

3 Results and Discussion

3.1 Segmentation of Fundus Images

Blood Vessel Segmentation. The test of our vessel segmentation algorithm is done on the DRIVE database. Our retinal vessel segmentation showed good performance measures. Table 1 shows the comparison between its performance and other methods of the same subject. With a sensitivity of 72%, it means that there still exit parts of minimal vessels not was detected, but with an accuracy of 95.82%, we are sure that the segmented vessels are detected correctly.

Exudate Segmentation. Testing of our algorithm is done on the E-OPHTA-EX database. Our exudate segmentation showed good performance measures. Table 2 shows the comparison between its performance and other methods of the same subject. The only concern about our method is the low sensitivity of 24.16% which means that there are several undetected exudate areas, but with the accuracy of 99.72%, we are sure that the segmented exudates are detected correctly.

Table 1 Performance of blood vessels segmentation method

	Sensitivity	Specificity	Accuracy (%)
Our method	72.00%	98.09%	95.82
Amin and Yan [13]	–	–	92
Safarzadeh et al. [14]	–	–	93
Vlachos and Dermatas [15]	–	–	94
Xiao et al. [16]	–	–	96

Table 2 Performance of exudates segmentation method

	Sensitivity (%)	Specificity (%)	Accuracy (%)
Our method	24.16	99.98	99.72
Benzamin and Chakraborty [17]	41.4	98.3	96.6
Xue et al. [18]	77.9	99.6	99.2

3.2 Stage Classification of Diabetic Retinopathy

Database Pre-processing

Wavelet thresholding for image denoising: This is a technique that we used to improve the sharpness of images. It consists in doing a wavelet conversion to the images and then we apply a hard thresholding in the wavelet domain. The thresholding depends on some parameters of the wavelet coefficients. It allows us to get rid of noise by eliminating the coefficients that are not important compared to a certain threshold [19, 20]

Data augmentation: The option of increasing the data has been applied, since the model will be trained from different orientations and angles, with a random reflection along the *X* and *Y* axis, as well as a random rotation with a degree of 0.5°.

Data distribution: We divided the dataset into 80% for training and 20% for validation. We note that each class contains 334 images (jpg), with a total of 2004 images. So, each class uses 267 images for training and 67 images for validation.

AlexNet Model: After several training experiments with this model, we tested several parameters to arrive at a validation accuracy of 99.49%. Before reaching this value, the first accuracy achieved was 79.5% with the parameters shown in Table 3. This first model performed better when wavelet denoising was applied to the processed baseline images to reach an accuracy of 88.57%. Subsequently, we further improved the dark images of the given base by increasing the contrast and exposure, and then eliminated the images with lighting artifacts or poorly taken, in order to achieve this last accuracy.

To compare this model, we performed further training by two other CNN architectures using the latest parameters assigned to the AlexNet model.

Model Resnet-50: The training of this model arrives at a validation accuracy of 98%. Applied parameters on the training of Resnet-50 model is shown in Table 4.

Inception-V3 Model: The training of this model arrives at a validation accuracy of 99.5%. Applied parameters on the training of Inception-V3 model is shown in Table 5.

The proposed classification's performance is a measure of sensitivity, specificity, and accuracy. While sensitivity is the rate of a positive test, conditioned on truly being positive. Specificity is the rate of a negative test, conditioned on truly being negative. The accuracy rate is the total number of correctly identified photos divided

Table 3 Applied parameters on each training of AlexNet model and their performance

Experience number	1	2	3	4	5
Parameter change	• Solver = sgdm • Initial learn rate = 0.0001 • Max epochs = 20 • Mini batch size = 80 • Sequence length = longest • Shuffle = every epoch • Learn rate drop factor = 0.1 • Learn rate drop period = 10 • Batch normalization statistics = population • Fc-weight learn rate factor = 20 • Fc-bias learn rate factor = 20	• Update dataset (augment contrast of images) • max epochs = 25 • Mini batch size = 75 • The other parameters remain constant	• Max epochs = 20 • Mini batch size = 50 • The other parameters remain constant	• Update dataset (apply wavelet denoising) • max epochs = 40 • Mini batch size = 50 • The other parameters remain constant	• Update dataset (delete photos with artifacts and augment exposure of dark images) • Apply data augmentation • max epochs = 50 • mini batch size = 50 • The other parameters remain constant
Validation accuracy	79.5%	82.4%	85.24%	88.57	99.49%

Table 4 Applied parameters on the training of Resnet-50 model

• Apply data augmentation	• Shuffle = every epoch
• Solver = sgdm	• Learn rate drop factor = 0.1
• Initial learn rate = 0.0001	• Learn rate drop period = 10
• Max epochs = 20	• Batch normalization statistics = population
• Mini batch size = 50	• Fc-weight learn rate factor = 20
• Sequence length = longest	• Fc-bias learn rate factor = 20

Table 5 Applied parameters on the training of Inception-V3 model

• Apply data augmentation	• Shuffle = every epoch
• Solver = sgdm	• Learn rate drop factor = 0.1
• Initial learn rate = 0.0001	• Learn rate drop period = 10
• Max epochs = 30	• Batch normalization statistics = population
• Mini batch size = 50	• Fc-weight learn rate factor = 20
• Sequence length = longest	• Fc-bias learn rate factor = 20

by the total number of pictures. The performance measurements are calculated using the following equations:

$$\text{Sensitivity} = \frac{\text{TP}}{\text{TP} + \text{FN}} \tag{1}$$

$$\text{Specificity} = \frac{\text{NT}}{\text{NT} + \text{FP}} \tag{2}$$

$$\text{Accuracy} = \frac{\text{TP} + \text{TN}}{\text{TP} + \text{TN} + \text{FP} + \text{FN}} \tag{3}$$

True negatives (TN) are test findings that accurately indicate a condition's absence. True positive (TP) is a test result that correctly reveals the presence of a condition. False positives (FP) are a test result that incorrectly suggests the presence of a certain condition or attribute, while false negatives (FN) are a test result that incorrectly indicates the absence of a specific condition.

Table 6 shows the results of the performance measures for each model processed. The sensitivity, specificity, and accuracy for each category are above 99%, demonstrating the effectiveness of the 3 proposed models. So, in order to distinguish between the three models, we used the activation map to explain the network predictions and verify that our network focuses on the correct parts of an image. The resulted outputs are shown in Figs. 8, 9, 10 and 11.

Figure 12 shows retinal images each belonging to a class with the activation mapping for each prediction according to the CNN model used and its accuracy. The first thing to observe is that each model focuses on different parts of the retina for the same picture, so we find the Inception-V3 model focuses much more on large areas of the retina for each class especially the optic disc, macula, and different symptoms. Followed by the AlexNet model which focuses more on the most apparent anomalies,

Table 6 Results of the performance measurements

	Sensitivity (%)	Specificity (%)	Accuracy (%)
AlexNet	99.00	99.80	99.68
ResNet-50	99.00	99.80	99.72
Inception-V3	99.50	99.90	99.84
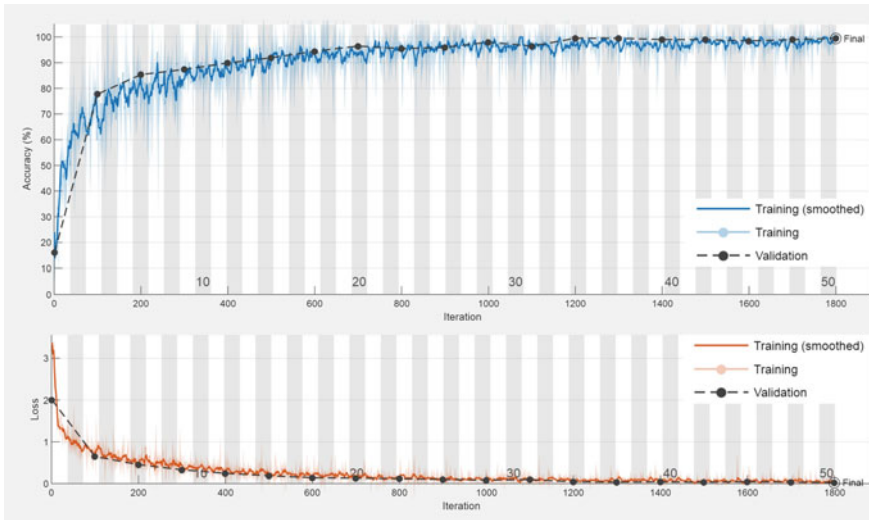
Fig. 8 AlexNet training process. Upper graph: accuracy of training, lower graph: loss of training
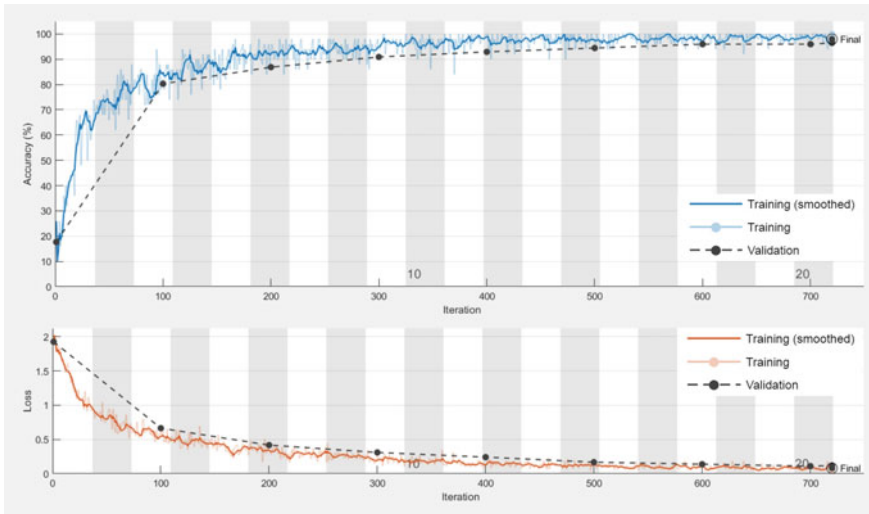
Fig. 9 ResNet-50 training process. Upper graph: accuracy of training, lower graph: loss of training
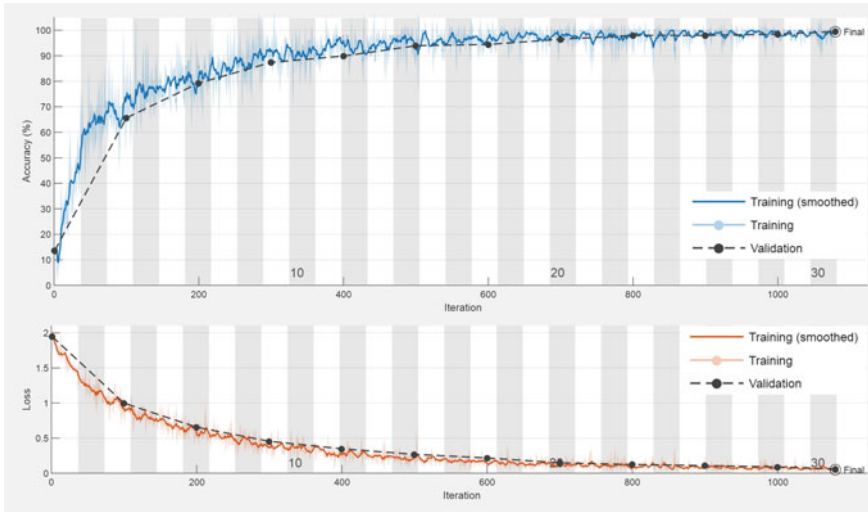
Fig. 10 Inception-V3 training process. Upper graph: accuracy of training, lower graph: loss of training
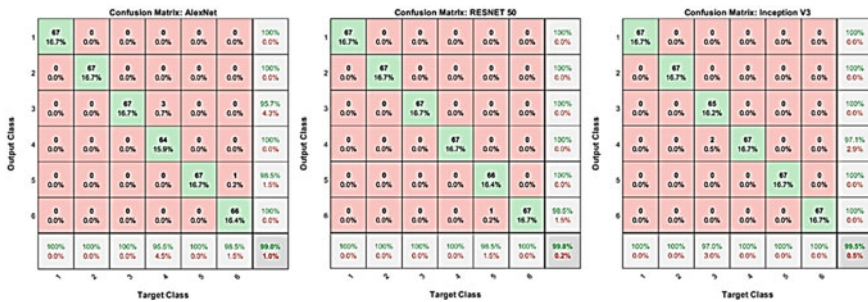
Fig. 11 Confusion matrix of classification results of each model. Respectively from the left, we have AlexNet, ResNet-50, and Inception-V3. The rows reflect real class instances, while the columns represent predicted class instances

the ResNet-50 model sometimes lacks this focus on the defect area and gives more interest to the optic disc and macula.

3.3 User Interface

For the user interface, we used MathWorks App Designer to make our system developed as an application with a user interface to facilitate its use during the diagnosis of retinal images as in Fig. 13: First section for the segmentation process; secondly,
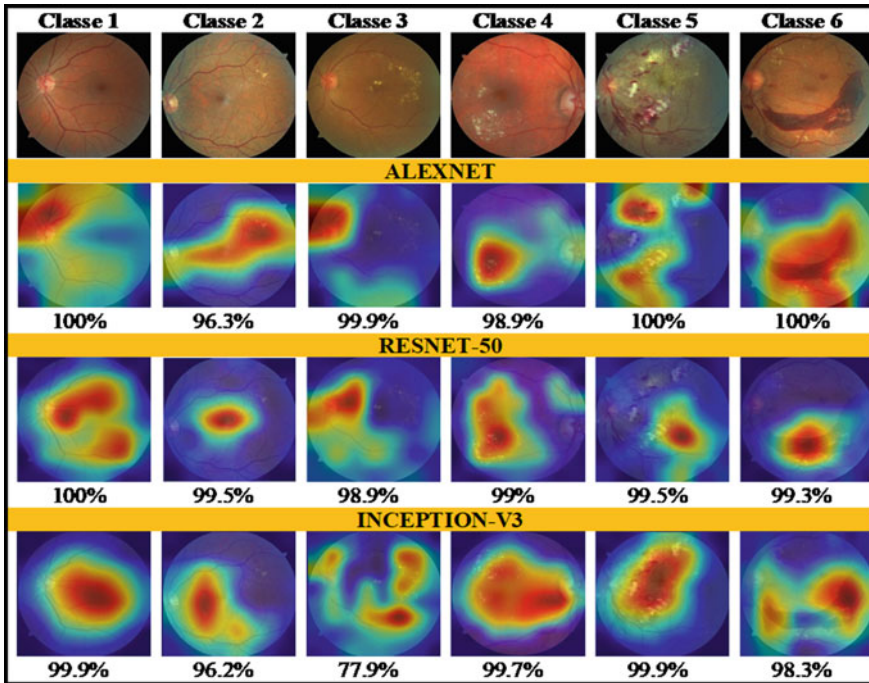
Fig. 12 Activation map of the prediction of the tree models proposed with the accuracy of every prediction

there is a part dedicated to the image characteristics, which gives information, such as contrast, homogeneity, correlation, vessel surface, and exudate surface. Another section is dedicated to the classification, to give the prediction result and its accuracy, with a graph of the probabilities of each class in a descending order.

4 Conclusion

In this project, an automatic method for segmentation of retinal vessels and exudates has been proposed. It is based on a combination of several image processing techniques, including CLAHE, thresholding, median, and kirsch filtering. This segmentation showed good performance measures. In addition, a DR stage classification method was proposed. This method is based on deep learning of three deep neural network architecture models trained on our image collection consisting of six DR stages. The proposed classification showed good performance measures for AlexNet, ResNet-50, and Inception-V3 models. Then to facilitate the use of our DR diagnostic
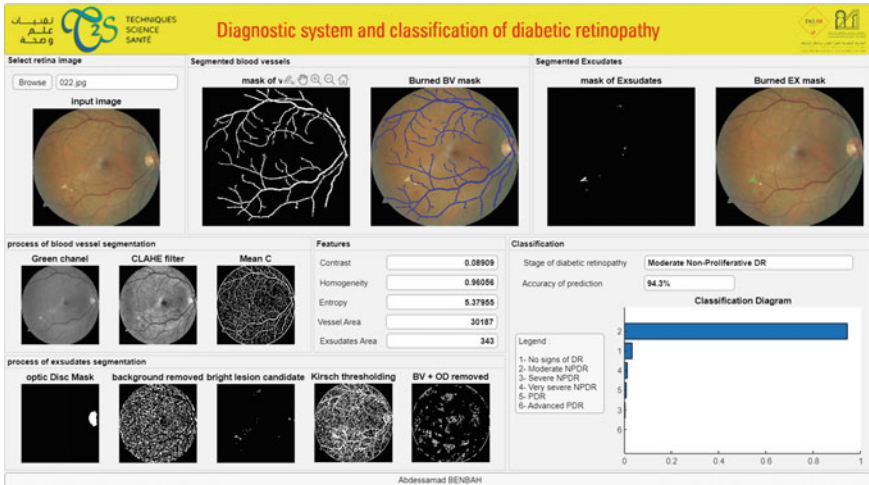
Fig. 13 User interface of the proposed diagnostic system with result of its application

system a user interface in the form of an application has been proposed. This interface allows to visualize the segmentation process and give the prediction result and its accuracy, with a graph of the probabilities of each class in a descending order.

References

1. Joussen AM, Gardner TW, Kirchhof B, Ryan SJ (eds) (2007) Retinal vascular disease, vol 75. Springer, Berlin
2. Staal JJ, Abramoff MD, Niemeijer M, Viergever MA, van Ginneken B (2004) DRIVE digital retinal images for vessel extraction. IEEE Trans Med Imaging 23:501–509
3. Decenciere E, Cazuguel G, Zhang X, Thibault G, Klein JC, Meyer F, Chabouis A (2013) TeleOphta: machine learning and image processing methods for teleophthalmology. Irbm 34(2):196–203
4. Castillo Benítez VE, Castro Matto I, Mello Román JC, Vázquez Noguera JL, García-Torres M, Ayala J, Pinto-Roa DP, Gardel-Sotomayor PE, Facon J, Grillo SA (2021) Dataset from fundus images for the study of diabetic retinopathy. Data Brief 36:107068
5. Dash J, Bhoi N (2017) A thresholding-based technique to extract retinal blood vessels from fundus images. Future Comput Inf J 2(2):103–109
6. Giancardo L (2011) Automated fundus images analysis techniques to screen retinal diseases in diabetic patients. Doctoral dissertation, Université de Bourgogne
7. Vincent L (1993) Morphological grayscale reconstruction in image analysis: applications and efficient algorithms. IEEE Trans Image Process 2(2):176–201
8. Gandhi M, Dhanasekaran R (2013) Diagnosis of diabetic retinopathy using morphological process and SVM classifier. In: 2013 international conference on communication and signal processing. IEEE, pp 873–877
9. Kirsch RA (1971) Computer determination of the constituent structure of biological images. Comput Biomed Res 4(3):315–328
10. Saxena S (2021) Introduction to the architecture of Alexnet. Analytics Vidhya

11. He K, Zhang X, Ren S, Sun J (2016) Deep residual learning for image recognition. In: Proceedings of the IEEE conference on computer vision and pattern recognition, pp 770–778
12. Szegedy C, Vanhoucke V, Ioffe S, Shlens J, Wojna Z (2016) Rethinking the inception architecture for computer vision. In: Proceedings of the IEEE conference on computer vision and pattern recognition, pp 2818–2826
13. Amin MA, Yan H (2011) High speed detection of retinal blood vessels in fundus image using phase congruency. Soft Comput 15(6):1217–1230
14. Saffarzadeh VM, Osareh A, Shadgar B (2014) Vessel segmentation in retinal images using multi-scale line operator and K-means clustering. J Med Sig Sens 4(2):122
15. Vlachos M, Dermatas E (2010) Multi-scale retinal vessel segmentation using line tracking. Comput Med Imaging Graph 34(3):213–227
16. Xiao Z, Zhang X, Geng L, Zhang F, Wu J, Tong J et al (2017) Automatic non-proliferative diabetic retinopathy screening system based on color fundus image. Biomed Eng Online 16(1):1–19
17. Benzamin A, Chakraborty C (2018) Detection of hard exudates in retinal fundus images using deep learning. In: 2018 joint 7th international conference on informatics, electronics and vision (ICIEV) and 2018 2nd international conference on imaging, vision and pattern recognition (icIVPR). IEEE, pp 465–469
18. Xue J, Yan S, Qu J, Qi F, Qiu C, Zhang H et al (2019) Deep membrane systems for multitask segmentation in diabetic retinopathy. Knowl Based Syst 183:104887
19. Jasoriya S (2016) Image denoising using wavelet thresholding techniques. University of Wisconsin, Madison
20. Parthasharathi GU, Premnivas R, Jasmine K (2022) Diabetic retinopathy detection using machine learning. J Innov Image Process 4(1):26–33

Design and Implementation of an FPGA-Based Digital Twin for an Electric Motor

Mehmet Riza Sarac and **Omur Aydogmus**

Abstract This paper presented a development of a system that can emulate a real electric motor in real time. This system, called digital twin or real-time digital simulator (RTDS), has critical value for many applications. The digital twin was developed in the field-programmable gate array (FPGA) structure, which is a high-speed digital system for real-time operation. The motor model was rearranged so that it can be run in real time on the FPGA. The developed digital twin was operated together with the real motor under the same conditions. Both the armature currents and motor speeds of the two motors were examined instantaneously on the same scope screen. Digital twin motor results were achieved to be nearly identical to real motor results. Especially, the digital twin showed dynamics similar to real motor dynamics with high accuracy as expected for reference signals with very fast transitions. The latency of the developed system was measured as about $10\,\mu s$. It can be said that this latency is quite enough to emulate electric motors.

Keywords FPGA · Digital twin · Real-time simulator

1 Introduction

The concept of digital twin can be considered as a new technology. The first use of the "digital twin" terminology is based on a 1997 paper by Hernàndez and Hernàndez [1]. In addition, Dr. Grieves at the University of Michigan was first introduced as digital equivalent to a physical product in 2003 [2]. However, NASA contributed to the spread of this concept by using the terms "Digital Twin" in its 2010 Technology Area 12 report [3, 4]. The studies presented under this concept have increased rapidly after 2011. According to the research conducted by the Gartner consulting company, the

M. R. Sarac (✉) · O. Aydogmus
Department of Mechatronics Engineering, Faculty of Technology, Firat University,
23200 Elazig, Turkey
e-mail: mrsarac@firat.edu.tr
URL: http://mekatronik.tf.firat.edu.tr/en

digital twin concept is seen as one of the top ten strategic technologies in the industrial field. It is estimated that the DT market will reach approximately 16 billion dollar by 2023, with an annual growth rate of more than 35% [5–7]. Although this concept is considered as new, it was actually evaluated under different name as a real-time digital simulator (RTDS) in some application areas long ago [8]. RTDSs are widely used in some applications such as power systems [9], microgrids [10], fault detection [11], developing of control algorithms [12], and simulation of electric motors [13], etc. It is very critical to test especially high-cost and dangerous system scenarios with RTDSs. Generally, it is necessary to consider situations in terms of time, cost, and danger when working with real electric motors in practical applications. An electric motor model can be described as a hybrid formation of both an electrical and mechanical system. Therefore, a fast digital system is needed to simulate an electric motor in real time. Field-programmable gate array (FPGA) is one of the most preferred approaches for obtaining high-speed requirement. FPGAs are widely used in many applications such as image and audio processing, digital modulation and demodulation, data processing, automation systems, communication systems, memory and peripheral interfacing, robotics, defense, aerospace, medical [14].

In the last decade, some applications have been presented about FPGA based RTDS in the literature. [15] presents a frequency-dependent phase domain transmission line model with an FPGA for an electromagnetic transient type real-time digital simulator. In another study, a co-simulation platform using FPGA has been proposed for the simulation of large power systems [16]. In [17], an electro-mechanical transient simulation system has been implemented with a FPGA-based digital solver. It is possible to say that FPGA is the best solution for RTDS as presented in the literature.

In this study, a digital twin of a brushed DC motor (Maxon F2140-934) was developed using DE10-Nano Terasic FPGA development kit (including Intel Cyclone V SE 5CSEBA6U23I7). First, the motor model was obtained in accordance with the FPGA. The digital twin of the motor was obtained by synthesizing the obtained model with FPGA. The real motor and the digital twin of the motor were operated together for different voltage references, and the angular velocity and armature currents were displayed on a scope screen in real time. Then, the necessary analyzes and explanations were discussed in the results section of the paper.

2   Motor Modeling for FPGA

Classical motor model that includes additional torque input as seen in Fig. 1 is used as a starting point to model a permanent magnet brushed DC motor. This additional torque input T_i can model additional load torque or the torque applied as an input when using motor as a generator.

Simulation of a system requires both input signal $X(s)$ and transfer function of the system $G(s)$. Output signal of a system is defined as $Y(s) = X(s) G(s)$ in the laplace domain. For real-time digital simulators however, the input signal is sampled

form of input signal seen as consecutive step functions with the amplitude value of sampled input signal. Between sampling times previous calculated values are saved for the next calculation as boundary values. These boundary input values of i and ω saved from previous calculations for model is illustrated with Fig. 2.

One approach is to calculate the system response to these consecutive step functions by solving $y(t) = \mathcal{L}^{-1}\{\frac{a}{s}\cdot G(s)\}$ where "a" is the amplitude of step function. But this approach needs the solution for different ζ values which will chance with system parameters. Our approach is to embed the time domain system model into FPGA. Model seen in the s domain needs proper replacement with time domain modules. Any block that has a polynomial expression of complex variable s needs to be replaced with time domain equivalent modules to be used in RDTSs as shown in Fig. 3.

After modules of s domain are replaced with time domain equivalents the produced model seen as in Fig. 4 can be implemented with an RTDS.

By the model shown by Fig. 4. we can establish the required equations to be used in RTDS. Our model has two inputs, applied voltage $V_s(t)$ and input torque as $T_i(t)$. The system outputs are armature current $i_a(t)$ and rotor angular velocity $\omega_m(t)$. These output signals, respectively, have equations given in Eqs. 1 and 2.

$$i(t) = i(t - \Delta t) + \Delta t \left\{ \left[i(t - \Delta t) + \frac{1}{L}\left(V_s(t) - K_b\omega(t)\right) \right] - \frac{R}{L}i(t) \right\} \quad (1)$$

$$\omega(t) = \omega(t - \Delta t) + \Delta t \left\{ \left[\omega(t - \Delta t) + \frac{1}{J}\left(T_i(t) + K_m i(t)\right) \right] - \frac{B}{J}\omega(t) \right\} \quad (2)$$
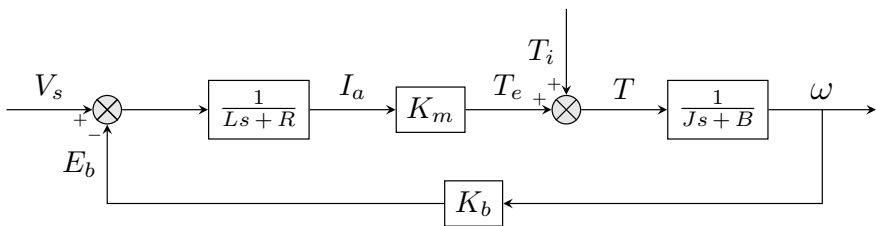
Fig. 1 Motor model including torque input used for system
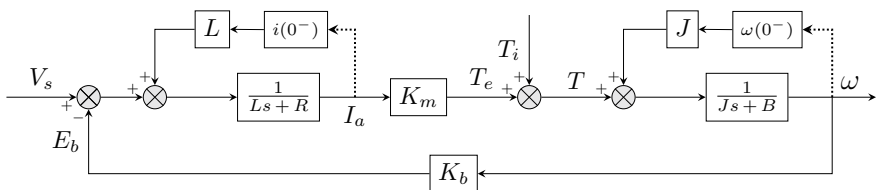
Fig. 2 Motor model including boundary values of system variables
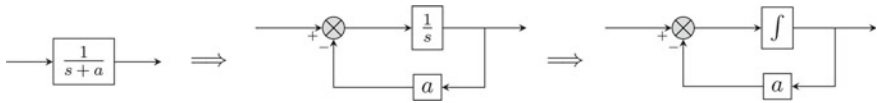
Fig. 3 Block replacement
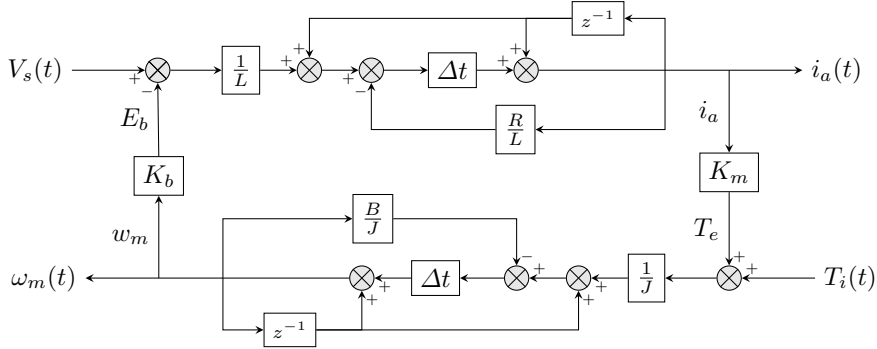
Fig. 4 Motor model to be used in RTDS

Equations 3 and 4 are driven from Eqs. 1 and 2.

$$i(t) = \frac{(1 + \frac{B\Delta t}{J})\frac{\Delta t}{L}V(t) - \frac{\Delta t^2 K_b}{JL}T_i(t)}{(1 + \Delta t \frac{R}{L})(1 + \Delta t \frac{B}{J}) + \Delta t^2 \frac{K_m K_b}{JL}} + \frac{(1 + \Delta t)[(1 + \Delta t \frac{B}{J})i(t - \Delta t) - \frac{\Delta t K_b}{L}\omega(t - \Delta t)]}{(1 + \Delta t \frac{R}{L})(1 + \Delta t \frac{B}{J}) + \Delta t^2 \frac{K_m K_b}{JL}} \tag{3}$$

$$\omega(t) = \frac{(1 + \frac{R\Delta t}{L})\frac{\Delta t}{J}T_i(t) + \frac{\Delta t^2 K_m}{JL}V(t)}{(1 + \Delta t \frac{R}{L})(1 + \Delta t \frac{B}{J}) + \Delta t^2 \frac{K_m K_b}{JL}} + \frac{(1 + \Delta t)[(1 + \Delta t \frac{R}{L})\omega(t - \Delta t) + \frac{\Delta t K_m}{J}i(t - \Delta t)]}{(1 + \Delta t \frac{R}{L})(1 + \Delta t \frac{B}{J}) + \Delta t^2 \frac{K_m K_b}{JL}} \tag{4}$$

Both Eqs. 3 and 4 have Eq. 5 as denominator.

$$G = \left(1 + \Delta t \frac{R}{L}\right)\left(1 + \Delta t \frac{B}{J}\right) + \Delta t^2 \frac{K_m K_b}{JL} \tag{5}$$

State-space representation of model can be seen by Eq. 6.

$$\begin{bmatrix} i(t) \\ \omega(t) \end{bmatrix} = \frac{1}{G} \begin{bmatrix} (1 + B\frac{\Delta t}{J})\frac{\Delta t}{L} & K_b \frac{\Delta t^2}{JL} \\ K_m \frac{\Delta t^2}{JL} & (1 + R\frac{\Delta t}{L})\frac{\Delta t}{J} \end{bmatrix} \begin{bmatrix} V_s(t) \\ T_i(t) \end{bmatrix}$$
$$+ \frac{1 + \Delta t}{G} \begin{bmatrix} 1 + B\frac{\Delta t}{J} & -K_b \frac{\Delta t}{L} \\ K_m \frac{\Delta t}{J} & 1 + R\frac{\Delta t}{L} \end{bmatrix} \begin{bmatrix} i(t - \Delta t) \\ \omega(t - \Delta t) \end{bmatrix} \tag{6}$$

3 Developing of FPGA-Based Digital Twin

Development board contains 50 MHz clock generator, USB Blaster II on board programmer. 2 push buttons, 4 slide switches, 8 LEDs, two 40 pins expansion headers and A/D converter IC (LTC2308) with 8 channels input.

A/D converter uses SPI interface. LTC2308 has 8-channel. 12 bits ADC with 500 ksps speed. Our SPI interface runs at maximum allowed speed for ADC. SPI interface has primary and secondary channels in reading sequence. For motor model, we have two primary channels $V_s(t)$ and $T_i(t)$ and these channels are been read in every read cycle of ADC. In a read cycle, only one of secondary channel is read to maximize primary channels sampling speed. ADC can read a channel in $2\,\mu s$, with two primary and one secondary channel reading the sampling rate will be $3 * 2\,\mu s = 6\,\mu s$. Remaining secondary channels are fully read with every 6 consecutive ADC read operations.

As shown in Fig. 5, primary ADC channels also have offset and gain adjustments to work with both positive and negative signals. $V_s(t)$ signal is being produced by Analog Discovery 2 then send to AB type power amplifier to drive DC motor, a shunt resistance is used to read armature current. Voltage applied to motor is also read by a buffer to eliminate voltage difference applied to physical motor and the RTDS. $T_i(t)$ input is used to simulate load torque or supply torque if the motor is tested as a generator. Secondary ADC inputs are R, L, B, J, K_m, and K_b. RTDS has also embedded values for unloaded Maxon F2140-934 motor parameters, system can operate with embedded values or measured parameters or arithmetic sum of same parameters of embedded and measured values.

Both parameter calculation and simulator modules use 50 MHz clock to operate. As seen in Fig. 6, the parameter calculation module gets parameters of secondary channel readings and produces required multipliers for the simulator module. Both modules use single precision floating point arithmetic modules. Double precision requires much more resources that can exceed the available resources of used FPGA. Intel floating-point intellectual property (IP) cores used in this simulator system are being controlled by global control units by using clock enable inputs of IP module instances according to latency of each module described by the user guide [18]. Module instances are also vertically aligned according to their calculation sequences both in Fig. 7 and in Fig. 8.

The simulator module shown in Fig. 7 gets values of primary channels directly and uses previous calculated multiplier values to calculate $i_a(t)$ and $\omega_m(t)$, and store
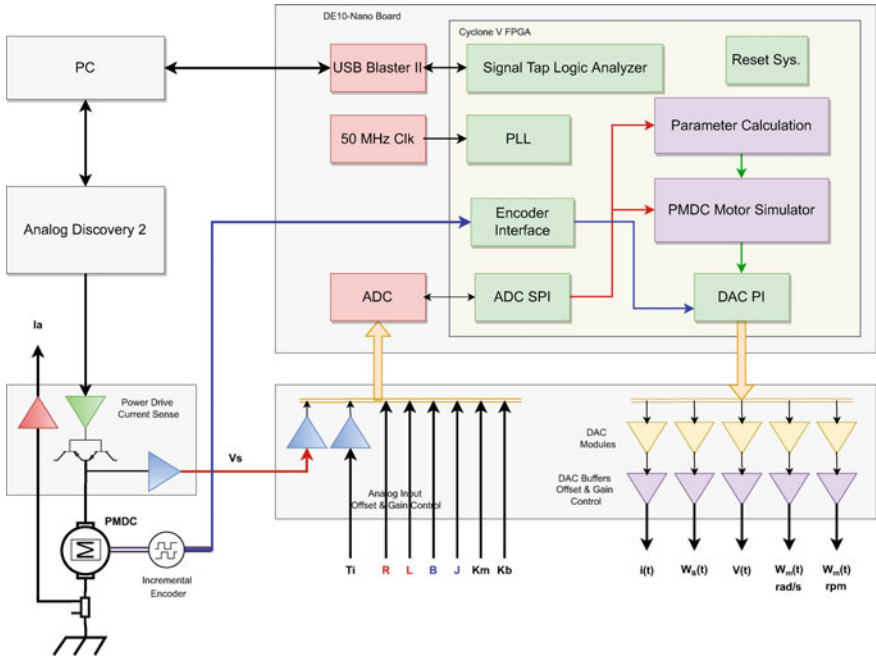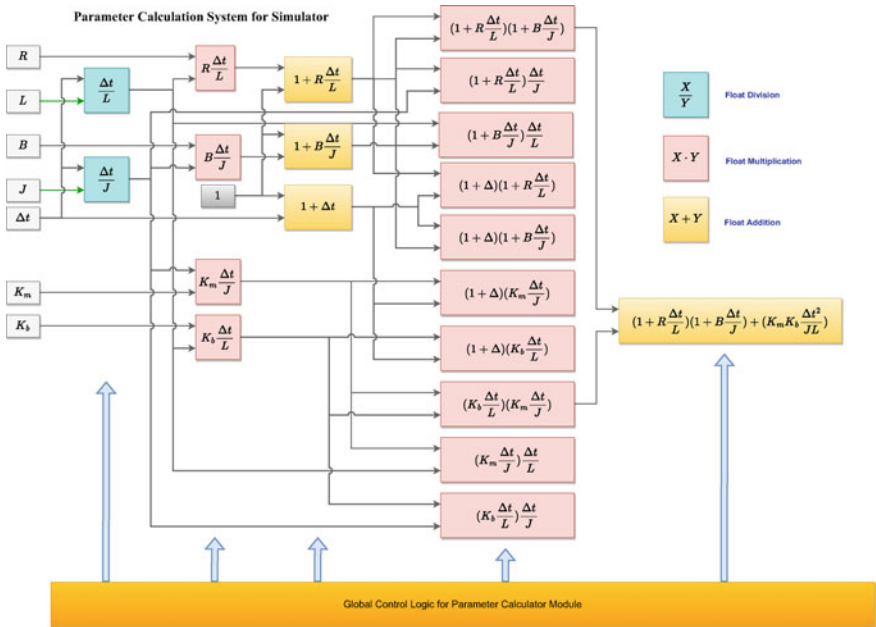
Fig. 5 RTDS system and peripherals
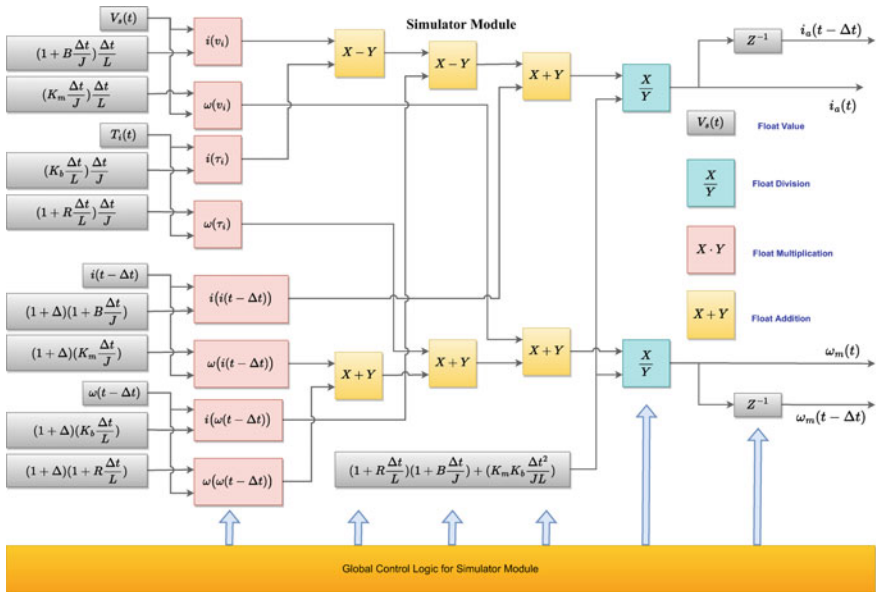

Fig. 6 Parameter calculation system

**Fig. 7** Main simulator system

Table 1 Utilization of synthesis

Resources name	Used	FPGA resource	Percentage (%)
ALMs	10,496	41,910	25
Block mem	29,464	5,662,720	0.52
M10Ks	138	553	25
DSP blocks	53	112	47
PLL	1	6	25

calculated value for next calculation step. Simulator module has its own global control unit.

Compilation report of Intel Quartus Prime software shows the utilization percentage of proposed RTDS in Table 1.

4 System Design and Results

The designed system consists of a brushed permanent magnet DC motor, an FPGA, a digital–analog converter (DAC) and calibration board, power circuit, and measurement devices. A view of the designed system is given in Fig. 9. The parameters of the PMDC motor are given in Table 2. The Analog Discovery 2 was used as a signal
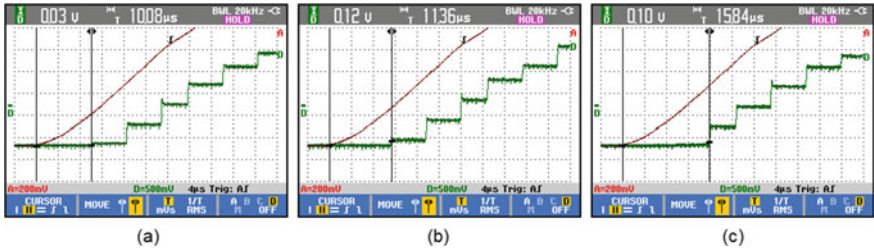
Fig. 8 Latency of real-time simulator; **a** minimum latency, **b** intermediate latency, **c** maximum latency
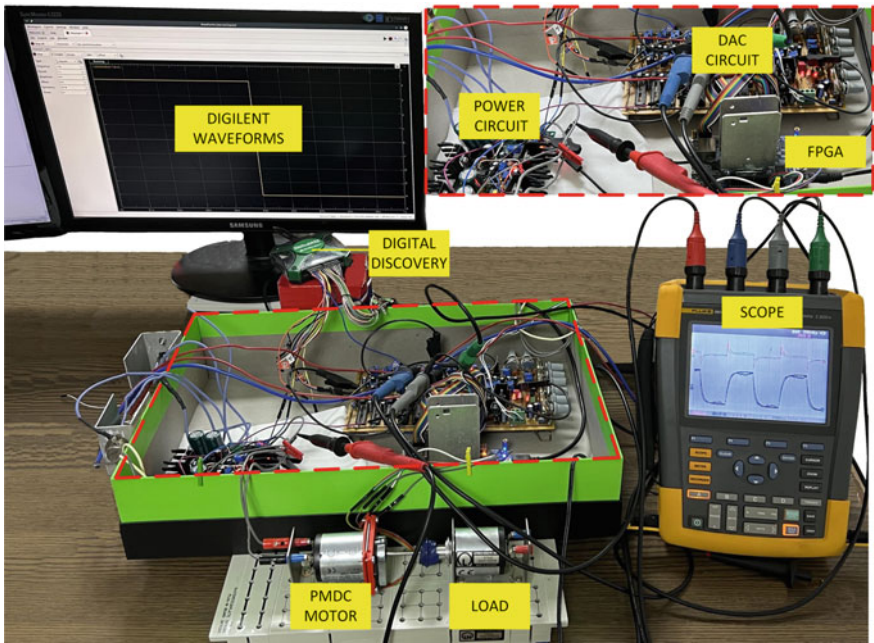
Fig. 9 A view of experimental setup

generator to create voltage reference signals for real power circuit and the digital twin system. The generated reference signal was amplified by using a standard transistor-based amplifier circuit. Also, the signal was connected to the analog–digital converter (ADC) of the FPGA board for using the voltage input of the digital twin motor created in the FPGA. The DAC board was used to simulate the armature current and the motor speed. The DAC board was connected to FPGA by using serial peripheral interface (SPI) communication protocol. All results of both the real motor and the digital motor were measured by using 200 MHz scope which was connected to the DAC board.

Table 2 Maxon F2140-934 motor data at nominal voltage

Electrical parameters	Values	Mechanical parameters	Values
Nominal voltage (V)	12	Torque constant (mNm/A)	27.8
No load speed (rpm)	4090	Speed constant (rpm/V)	344
No load current (mA)	12.3	Mech. time constant (ms)	31.9
Nominal speed (rpm)	2430	Rotor inertia (g cm^2)	25.3
Nominal torque (cont.) (mNm)	13.9		
Nominal current (cont.) (A)	0.508		
Stall torque (mNm)	34.2		
Starting current (A)	1.23		
Efficiency (max.) %	82		
Thermal resistance (Ω)	9.73		
Thermal inductance (mH)	1.27		

The real motor and digital twin motor were operated by using various reference voltage signals as given in Fig. 10. Channel-A (*red*) shows the real motor armature current, Channel-D (*green*) measures the digital motor armature current, Channel-B (*blue*) shows the real motor speed, and Channel-C (*black*) measures the digital motor speed. First, the motors were operated with a square wave which had peak to peak 8 V with 1 Hz as shown in Fig. 10a. Second, 1 Hz sine wave was used as shown in Fig. 10b. As a last work, randomly generated reference signal patterns were used as illustrated in Fig. 10c. All results showed that the developed digital twin motor achieved to give the same responses as the real motor. The signals look almost the same when analyzed the results. Therefore, the difference between results of the real motor and the digital motor cannot be observed clearly. For this reason, Fig. 10c is presented again in Fig. 11 in detail for a better view of the details. The reference signal was generated by using Analog Discovery 2 device. Figure 11a shows the armature currents of the real motor and digital twin motor. In addition, at the same conditions the speeds of the motors are given in Fig. 11b. Figure 11c, d shows the details of the signals between 3 and 4 s. Both real motor signals and digital twin motor signals were obtained almost equally. It is possible to say that they are quite satisfactory, when the results are examined. Latency of RTDS can be seen from Fig. 8, because of required clock domain crossing procedures the latency of system varies between minimum 10 μs and less than 16 μs.

5 Conclusions

In this paper, a study was carried out on the recently popular digital twin concept. This study focuses on a permanent magnet brushed dc motor, which continues to be preferred in medical, robotic, automotive, and defense industry devices. A highly
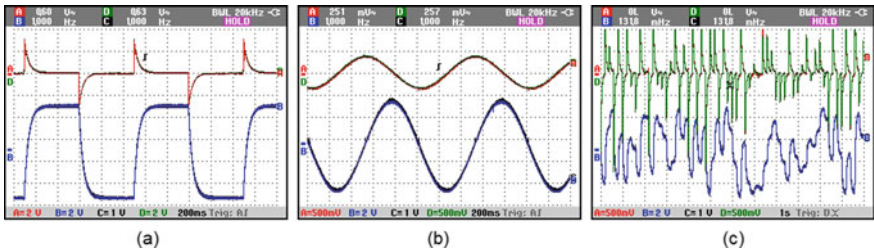
Fig. 10 Armature currents and motor speeds of real motor and RTDS for various voltage references; **a** 1 Hz square wave , **b** 1 Hz sine wave, **c** randomly generated reference signal. Channel-A: real motor current, Channel-D: digital motor current, Channel-B: real motor speed, Channel-C: digital motor speed
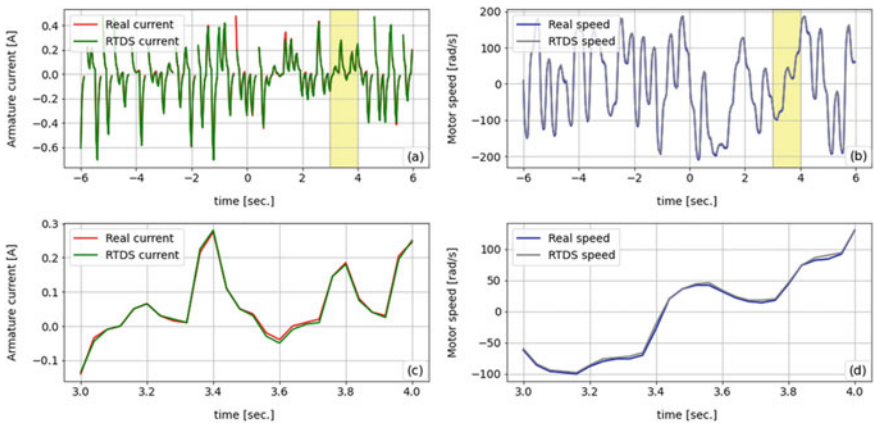
Fig. 11 Performance signals of real motor and RTDS under randomly generated reference voltage signal; **a** armature currents, **b** motor speed, **c** details of currents between 3 and 4 s, **c** details of speeds between 3 and 4 s

accurate digital twin of a commercially available electric motor has been developed. The developed digital twin system was composed of three main components: FPGA, power circuit board, and ADC/DAC board. First, the motor model consists of two different sub-components as electrical and mechanical. The motor model was rearranged in accordance with FPGA structure. Second, this model was synthesized for FPGA in order to obtain a real-time simulation. The latency of the system was measured as about $10-15\,\mu s$. This latency was changing instantaneously in the system. It can be said that a latency of $10\,\mu s$ is an acceptable value, especially for modeling systems such as motor. Finally, the real motor and the developed digital motor were tested together under the same conditions. The digital twin was able to successfully emulate the dynamics of the real motor under all conditions. In this way, it was proven that it can respond close to reality when working with a digital twin electric motor. In the future study, it will be investigated whether the control parameters obtained

by controlling the motor with a closed-loop control system can be used in the real system.

References

1. Hernández LA, Hernández S (1997) Application of digital 3D models on urban planning and highway design. WIT Trans Built Environ 33
2. Michael G (2014) Digital twin: manufacturing excellence through virtual factory replication. White paper 1, pp 1–7
3. Shafto M, Conroy M, Doyle R, Gleassgen E, Kemp C, LeMoigne J, Wang L (2010) Draft modelling, simulation, information technology and processing roadmap. Technol Area 11
4. Lo CK, Chen CH, Zhong RY (2021) A review of digital twin in product design and development. Adv Eng Inform 48:101297
5. El Saddik A (2018) Digital twins: the convergence of multimedia technologies. IEEE Multimedia 25(2):87–92
6. Lu Y, Liu C, Kevin I, Wang K, Huang H, Xu X (2020) Digital twin-driven smart manufacturing: connotation, reference model, applications and research issues. Robot Comput Integr Manuf 61:101837
7. Qi Q, Tao F, Zuo Y, Zhao D (2018) Digital twin service towards smart manufacturing. Procedia CIRP 72:237–242
8. McLaren PG, Kuffel R, Wierckx R, Giesbrecht J, Arendt L (1992) A real time digital simulator for testing relays. IEEE Trans Power Delivery 7(1):207–213
9. Kawal K, Hong Q, Paladhi S, Liu D, Papadopoulos PN, Blair S, Booth C (2022) Vulnerability assessment of line current differential protection in converter-dominated power systems. In: IET 16th international conference on developments in power system protection, pp 1–6
10. Avendaño A (2022) Microgrid controller evaluation using real-time digital simulation. In: 2022 IEEE power and energy society innovative smart grid technologies conference (ISGT). IEEE, pp 1–5
11. Afshar M, Majidi M, Gashteroodkhani OA, Amoli ME (2022) High impedance fault detection in a practical platform using a real-time-digital simulator. In: 2022 IEEE Texas power and energy conference (TPEC). IEEE, pp 1–6
12. Li H, Meng K, Peng Y, Li X (2022) Control strategy for seamless switching of virtual synchronous generators based on secondary frequency and voltage regulation. Alexandria Eng J 61(12):10477–10484
13. Dehkordi AB, Maguire TL (2021) A multi-star synchronous machine model for real-time digital simulation and its applications. Electr Power Syst Res 197:107312
14. Aydogmus O, Boztas G (2019) Implementation of an FPGA-based motor control with low resource utilization. In: 2019 4th international conference on power electronics and their applications (ICPEA), pp 1–5
15. Liu J, Chen Y, Ding H, Zhang Y (2021) Development of phase domain frequency-dependent transmission line model on fpga for real-time digital simulator. Electr Power Sys Res 197:107305
16. Yang C, Xue Y, Zhang XP, Zhang Y, Chen Y (2018) Real-time fpga-rtds co-simulator for power systems. IEEE Access 6:44917–44926
17. Zhang B, Wang Y, Tu S, Jin Z (2018) Fpga-based realtime digital solver for electro-mechanical transient simulation. Energies 11(10):2650
18. Intel. Floating-Point IP Cores User Guide. intel, September 2021. UG01058

Novel Approach Implementation of AES Algorithm Based on Radiation-Tolerant FPGA for Secure Mission in Satellite Remote Sensing: LST-SW Case

Assaad El Makhloufi, Samir El Adib, and Naoufal Raissouni

Abstract Security applications in remote sensing missions have grown in the recent decade since the confidentiality of data carried from satellite to ground station can be hacked, and the space environment can damage satellite hardware. This study provides a unique architecture for secure Land Surface Temperature via radiation FPGA based on the AES algorithm. The T-Box method was used for the implementation of the AES algorithm. The testing results demonstrate that the suggested implementation achieved a throughput of 524.26 Mbps using Xilinx Virtex-4QV FPGA, at a maximum clock frequency of 208.453. Furthermore, the proposed solution occupies 8% of the slice in terms of area consumption. Moroever, an evaluation of the suggested method for prior implementation reveals that the presented approach has the best trade-off between area utilization, frequency, and throughput. Therefore, The suggested approach offers excellent performance, making it appropriate for future satellite remote sensing missions that utilize radiation-tolerant LST-SW computations.

Keywords Security · Land surface temperature · Field programmable gate arrays · Advanced encryption standard · T-Box

1 Introduction

Security of data has become increasingly critical in various application of embedded system [1], particularly in remote sensing satellites, which may carry sensitive information. As a result of the rising number of operational remote sensing missions, the necessity for protecting the sending of images captured from satellites has expanded significantly [2].

A. El Makhloufi (✉) · S. El Adib · N. Raissouni
Remote Sensing, Systems and Telecommunications (RST), University Abdelmalek Essaadi, Tétouan, Morocco
e-mail: assaadelmakhloufi@gmail.com

Land Surface Temperature (LST) is a critical metric for surface energy and water balance at the local and global levels [3]. Recovering the LST-SW algorithm from remote sensing satellites is very challenging due to its biophysical nature and the large data size and bandwidth issue. Therefore, onboard computed LST-SW is a powerful solution, in addition, it's essential to secure this algorithm from any attack that can happen during transmission to the ground station.

Therefore, efficient encryption of AES algorithm [4, 5] and its implementation on FPGAs [6] can minimize any risk to data transferred to the ground station, in addition, radiation FPGA can reduce the threat affected to the hardware satellite by the space environment [7].

AES algorithm is a block encryption method that uses a secret key. It is the replacement for the now-vulnerable DES (Data Encryption Standard). AES's use of basic binary operations like permutations and substitutions justified its efficiency and cheap memory cost. This enables the technique to be used in applications that handle huge data, like satellite images. The AES algorithm employs an enormous number of rounds involving pair combinations (key lengths, block length) [8].

The main block in AES is the S-box. In the literature to implement it, numerous different approaches have been described. The authors in [9–11] concentrated on on their BRAM and LUT implementations, which are utilized to reserve all preset 256 8-bit values. This results to reduced area utilization, however, this technique conducts to a decrease in throughput. Nevertheless, if we apply the iterative looping, loop unrolled, and pipeline techniques, we can get better performance in throughput metrics. The next method, S-box is implemented based on computational resources without using any BRAMs. This result protects data against the SEE in the space environment, however, this technique conducts to a decrease in throughput. In the letereture two previous paper was focuses on securing the LST-SW algorithm with AES algorithm. The authors in [12] is focusing on implementing the LST-SW algorithm using only logical ressource approach. This last has the advantage of the none use of BRAMs, however, this technique consume more ressources. The authors in [13] present a secure implementation using iterative architecture. This method achieve high throupghut, however consume more ressources belong with BRAMs.

In general, one of the most essential issues in the study phase is the design of S-box substitute with fast speed and low area, given that it is the only non-linear transformation among the four AES arithmetic transformations and is crucial for increasing throughput and minimizing resource use. The encryption technique for a space mission is chosen based on: Security efficiency, attack resiliency, hardware and software compatibility, very low ressource and memory requirements, and computing power. As on October 1, 2015, AES is used in the United States for all sensitive material up to the TOP SECRET level. In fact, increasing the resources utilized to make encryption highly effective will have the unintended consequence of making the process less efficient. As a result, the best potential compromise between these three criteria must be found as a function of the desired space mission.

Space radiation can affect the confidentiel information transfered to the ground station, therefore, the need for a solution is important to decrease this problem. As a solution, Virtex-4QV [14] is radiation-tolerant FPGA type which can resist the rspace radiation, and has ability to operate in a severe radiation environment.

FPGAs have many advantages in developing the cryptography algorithm:

- Algorithm Agility, Upload, and modification
- Architecture Efficiency
- Resource Efficiency
- Cost Efficiency.

In this research article, we presented a novel approach based on The T-Box for securing the LST-SW algorithm. The proposed system was developed using VHDL language and simulated in the Xilinx VIVADO 14.7 tool. The accomplishment in this article is to achieve a trade-off between the resources, frequency, and throughput for a satellite remote sensing mission.

2 AES Algorithm

AES is a symmetric block cipher algorithm intended to supersede DES which has become too weak in view of current attacks. Historically, the development of AES was instigated by the National Institute of Standards and Technology (NIST). It is also authorized by the National Security Agency (NSA) for the encryption of so-called very sensitive information. AES algorithm offers block and key sizes that are multiples of 32 (between 128 and 256 bits). These various actions are done numerous times to form a "round". Each round, a unique key is calculated from the encryption key and incorporated into the calculations as describe in Eq. (1) [15]. The algorithm is fed a 128-bit block as input (16 bytes), the key is therefore between 128, 192 or, 256 bits. As a result, AES replaces the DES algorithm which used only 56-bit keys. The AES steps are shown in Fig. 1.

The processes performed to encrypt data with the AES algorithm are depicted in Fig. 1. These stages begin with the "AddRoundKey" operation, which involves multiplying each 128-bit block of the image by a modulo 2 and comparing it to its counterpart in the encryption key matrix. This matrix will be employed as input data for the following stage. The functioning of the rounds follows, which is dependent on the size of the key utilized. Each routine patrol operation consists of four phases. The first stage is called "SubByte," and it involves by replacing a different value from an "S-box" for every byte in the block, which is a matrix that embodies Shannon's confusion principle. The second stage is "ShiftRow," in which the rows are shifted cyclically with varied "offsets". The ShiftRows operation is describing in Fig. 2. The first row doesn't change. for the second row, if we take the first row represented by a (1,3), this last is shifted by 1 position to the left. The third row is shifted by 2 positions and the last one by 4 positions.
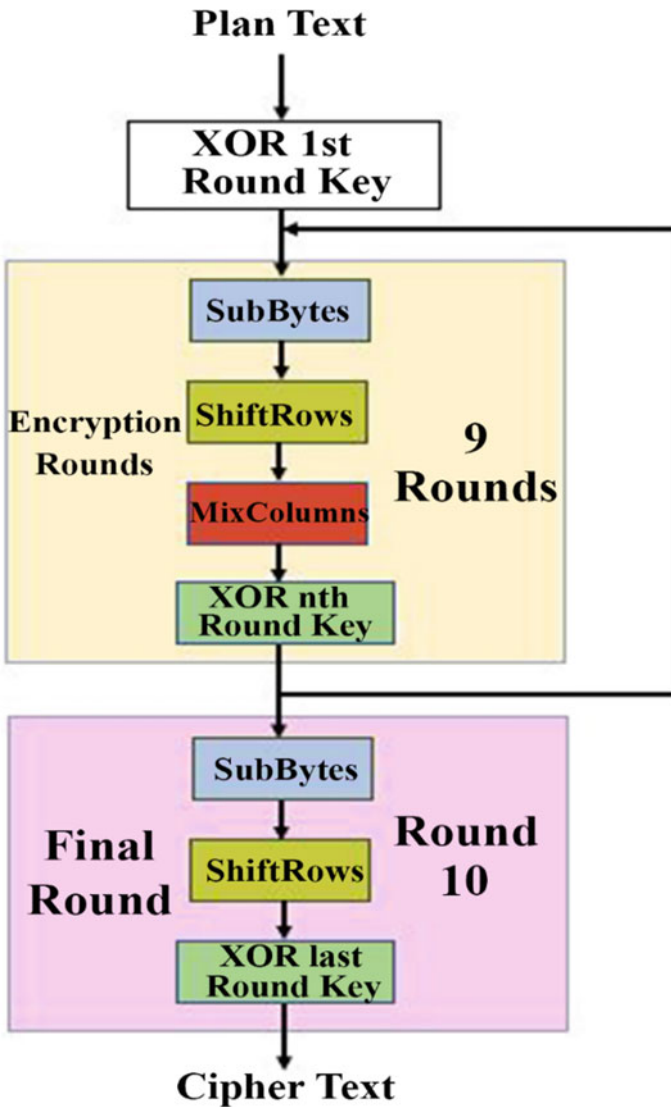
Fig. 1 Rijndael encryption process

Each column is regarded as a polynomial in the third stage, "MixColumn," and multiplied on GF(28) (Galois Field) by a constant matrix that also obeys Shannon's diffusion principle. The final step of a round is the step designated "AddRoundKey," which is a simple "exclusive or" between the current data and the current round's subkey. This stage consists in producing a key matrix at each iteration, which will be utilized in the following iteration and allows the assaults associated with the key to be eliminated by the loss of symmetry. For each AddRoundKey operation, Round
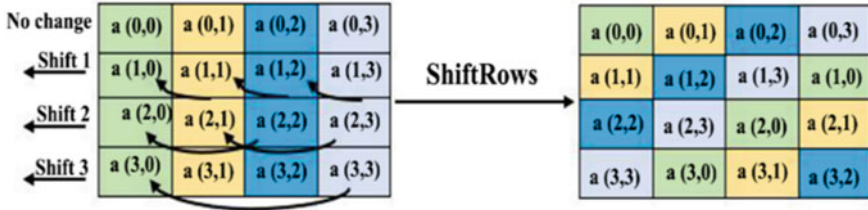
Fig. 2 ShiftRows operation

Keys are generated using the key schedule. The initial encryption key is the first (rk^0) used in the additional AddRoundKey at the start of the first round in AES128. In fact, The preceding rk^{i-1} is used to calculate rk^i, where $0 < i \leq 10$. Let $q(j)$ ($0 \leq j \leq 3$) represent the column j of the rk^{i-1} and $w(j)$ represent the column j of the rk^i. The new rk^i is then computed as follows:

$$
\begin{aligned}
w(0) &= q(0) \oplus (\mathrm{Rot}(\mathrm{SB}(q(3)))) \oplus \mathrm{rcon}^i \\
w(1) &= q(1) \oplus w(0) \\
w(2) &= q(2) \oplus w(1) \\
w(3) &= q(3) \oplus w(2)
\end{aligned}
\tag{1}
$$

3 Proposed T-Box Approach for the Secure LST-SW Algrithm

T-box-based technique for implementing AES was initially presented in [16] for a software implementation employing 32-bit microprocessors. This method was extended for hardware implementations in [17]. The proposed FPGA hardware is focused on implementing the secure LST-SW algorithm based on Look-ups Table's approach, this last consists of merging the MixColumn and SubByte transformation into a single table consisting of 256 1-bytes columns. In the LUT-based design technique, this last is used to implement the Rijndael algorithm's complex and slow operations. Logic may be used to carry out these operations, which include multiplicative inverse operations, multiplication, and addition in GF(28). The method shown here, however, precomputes these operations for all potential inputs and stores the results in LUTs. Using the LUT, fast designs may be produced. However, the LUT approach results in great area utilisation. In contrary, the proposed implementation in this research is based on the merging the MixColumn and SubByte transformation into a single table consisting of 256 1-bytes columns. This technique gives the best trade-off between the metrics: consume less resources and achieving high throughput
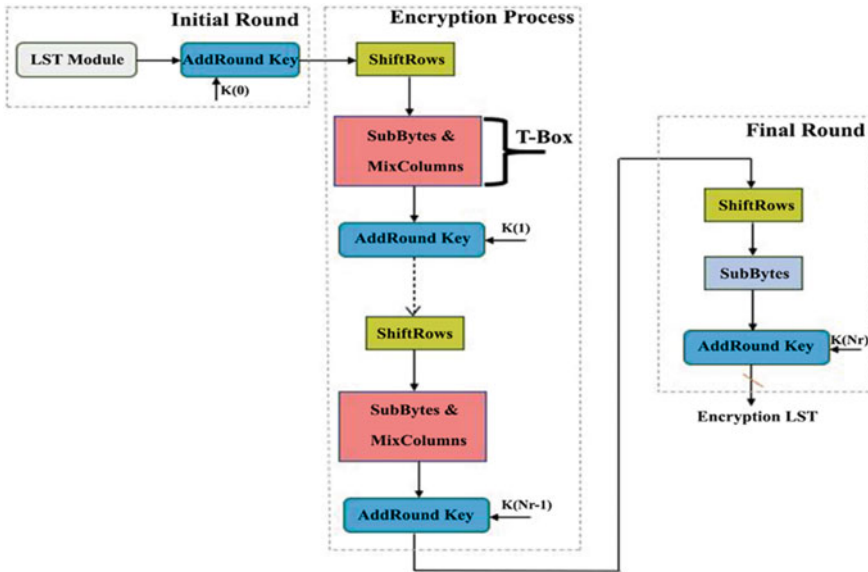
Fig. 3 Proposed secure LST-SW algorithm using T-Box approach

adequate for satellite remote sensing. The LST algorithm has already been implemented in a previous paper [18]. Figure 3 depicts the operation architecture of T-Box approach.

Using look-up tables and XOR operations, the technique can compute the complete AES iteration. These pre-computed look-up tables are the result of the SubBytes and MixColumns transformations working together. The combined application of the SubBytes and MixColumns transformations is represented by the precomputed tables, and can be defined as in (2):

$$R = \mathrm{MC}(\mathrm{SB}(\mathrm{SR}(\mathrm{state}))) = A(x) \oplus \mathrm{SB}(\mathrm{SR}(\mathrm{state})) \tag{2}$$

where $A(x)$ is the matrix of multiplicative vectors as in (3)

$$R = \mathrm{MC}(\mathrm{SB}(\mathrm{SR}(\mathrm{state}))) = \begin{pmatrix} \text{'02'} & \text{'03'} & \text{'01'} & \text{'01'} \\ \text{'01'} & \text{'02'} & \text{'03'} & \text{'01'} \\ \text{'01'} & \text{'01'} & \text{'02'} & \text{'03'} \\ \text{'03'} & \text{'01'} & \text{'01'} & \text{'02'} \end{pmatrix}$$

$$\oplus \begin{pmatrix} \mathrm{SB}(d15) & \mathrm{SB}(d11) & \mathrm{SB}(d7) & \mathrm{SB}(d3) \\ \mathrm{SB}(d10) & \mathrm{SB}(d6) & \mathrm{SB}(d2) & \mathrm{SB}(d14) \\ \mathrm{SB}(d5) & \mathrm{SB}(d1) & \mathrm{SB}(d13) & \mathrm{SB}(d9) \\ \mathrm{SB}(d0) & \mathrm{SB}(d12) & \mathrm{SB}(d8) & \mathrm{SB}(d4) \end{pmatrix} \tag{3}$$

While the ShiftRow transformation is defined as follows (4):

$$SR(\text{State}) = \begin{pmatrix} SR(d15) & SR(d11) & SR(d7) & SR(d3) \\ SR(d10) & SR(d6) & SR(d2) & SR(d14) \\ SR(d5) & SR(d1) & SR(d13) & SR(d9) \\ SR(d0) & SR(d12) & SR(d8) & SR(d4) \end{pmatrix} \tag{4}$$

And the subbytes transformation is represented as follows (5):

$$SB(SR(\text{State})) = \begin{pmatrix} SB(d15) & SB(d11) & SB(d7) & SB(d3) \\ SB(d14) & SB(d10) & SB(d6) & SB(d2) \\ SB(d13) & SB(d9) & SB(d5) & SB(d1) \\ SB(d12) & SB(d8) & SB(d4) & SB(d0) \end{pmatrix} \tag{5}$$

And the state represented as:

$$\text{State} = \begin{pmatrix} d15 & d11 & d7 & d3 \\ d14 & d10 & d6 & d2 \\ d13 & d9 & d5 & d1 \\ d12 & d8 & d4 & d0 \end{pmatrix} \tag{6}$$

For the first quarter of the round can be expressed in (7), as R15...12:

$$\begin{pmatrix} R15 \\ R14 \\ R13 \\ R12 \end{pmatrix} = \begin{pmatrix} `02` & `03` & `01` & `01` \\ `01` & `02` & `03` & `01` \\ `01` & `01` & `02` & `03` \\ `03` & `01` & `01` & `02` \end{pmatrix} \oplus \begin{pmatrix} SB(d15) \\ SB(d10) \\ SB(d5) \\ SB(d0) \end{pmatrix} \tag{7}$$

which is also equivalent in (8) to:

$$\begin{pmatrix} `02` \\ `01` \\ `01` \\ `03` \end{pmatrix} \oplus (SB(d15)) \oplus \begin{pmatrix} `03` \\ `02` \\ `01` \\ `01` \end{pmatrix} \oplus (SB(d10)) \oplus \begin{pmatrix} `01` \\ `03` \\ `02` \\ `01` \end{pmatrix}$$

$$\oplus (SB(d5)) \oplus \begin{pmatrix} `01` \\ `01` \\ `03` \\ `02` \end{pmatrix} \oplus (SB(d0)) \tag{8}$$

The aforementioned multiplication may be done with a logarithm and anti-logarithm table.

Table 1 Virtex-4QV resources utilization for the T-Box technique implementation

Device	Virtex- 4QV		
Device utilization	Used	Total	%
Slice registers	1972	24,576	8
Slice LUTs	3484	49,152	7
Block RAM/FIFO	4	60	1
DSP48Es	20	512	4
Maximum frequency	208.453 MHz		

4 Hardware Results and Simulation

4.1 Hardware Results

The suggested hardware design, which is based on the T-Box technique, was developed using the VHDL language. The Virtex-4QV XQR4VSX55 FPGA is used to implement the secure LST-SW algorithm. The resources used for the suggested approach-based T-Box are shown in Table 1.

4.2 Simulation Results

To verify the functioning of the presented implementation, we developed a testbench to be used to verify the effectiveness by using text format files with pixel values written with the Textio package in VHDL, with the help of XILINX VIVADO 14.7 Tools. As a result, in the suggested method, we employed four files holding 16-bit pixel values that represent the inputs T4, T5, and Epsilon. The simulation of the suggested system is illustrated in Fig. 4. This suggested approach is handled by the following variables: CLK, rest, read en l, and write en l. Furthermore, the simulation displays all of the system's inputs as well as the AES-LST output.

5 Performance Comparison with Existing Implementation

Table 2 indicates the resources used for the proposed approach and for existing implementation with different techniques for the secure LST-SW algorithm design

The number of slice registers used by the proposed technique and by existing work is shown in Fig. 5a. The proposed T-Box approach consumes less slice register with 4 BRAMs compared to [12, 13]. In addition, the S-Box based BRAMs implementation approach, need a fewer LUTs than techniques that use combinational blocks for their
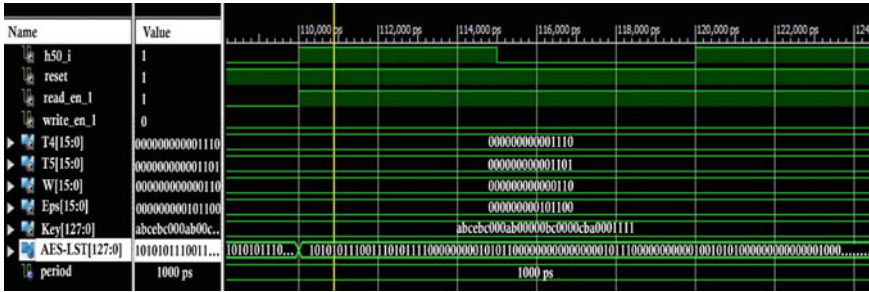
Fig. 4 Simulation results for the T-Box encryption technique

Table 2 Interpretation results between the presented and existing implementation

Design	Device	Device utilization			fmax (MHz)	Throughput (Mbps)	TPS (Mbps/slices)
		Slices	LUTs	BRAM			
[13]	Virtex-5 LX50T	3564 (12%)	3352 (11%)	1 (1%)	268.196	1634.71	0.45
[12]	Virtex-5 LX50T	3306 (11%)	11,402 (23%)	–	295.253	328.629	0.09
Proposed	Virtex-4QV	1972 (8%)	3484 (7%)	4 (1%)	208.453	524.26	0.26

S-box implementation as shown in Fig. 5b. Therefore, as illustrate in Fig. 5a, the suggested T-Box method and the implementation in [13] consume less LUTs.

In Reference [12] there isn't any stage of pipelined or sub-pipelined, but the implementation of S-box using logical resources (Slices and LUTs) leads to a higher frequency although it needs a greater number of slices LUTs as compared to the proposed implementation using T-Box, this last has a good frequency and fewer slices LUT as shown in Fig. 5c. Furthermore, we have computed the throughput, and the TPS metrics of each method, and the results are presented in Fig. 5d. It can be seen that the implementation using iterative looping architecture [13] leads to better throughput, hence, The selected design has ten rounds, each of which is executed in a single clock cycle, for a total of ten clock cycles, which implies higher throughput. Therefore, the proposed implementation has the best trade-off compared to others works.

6   Conclusion

In this article, we handled the requirement for onboard protection for earth observation satellite algorithm. The T-Box architecture was selected for the suggested implementation. The authors presented a method for a secure FPGA implementation
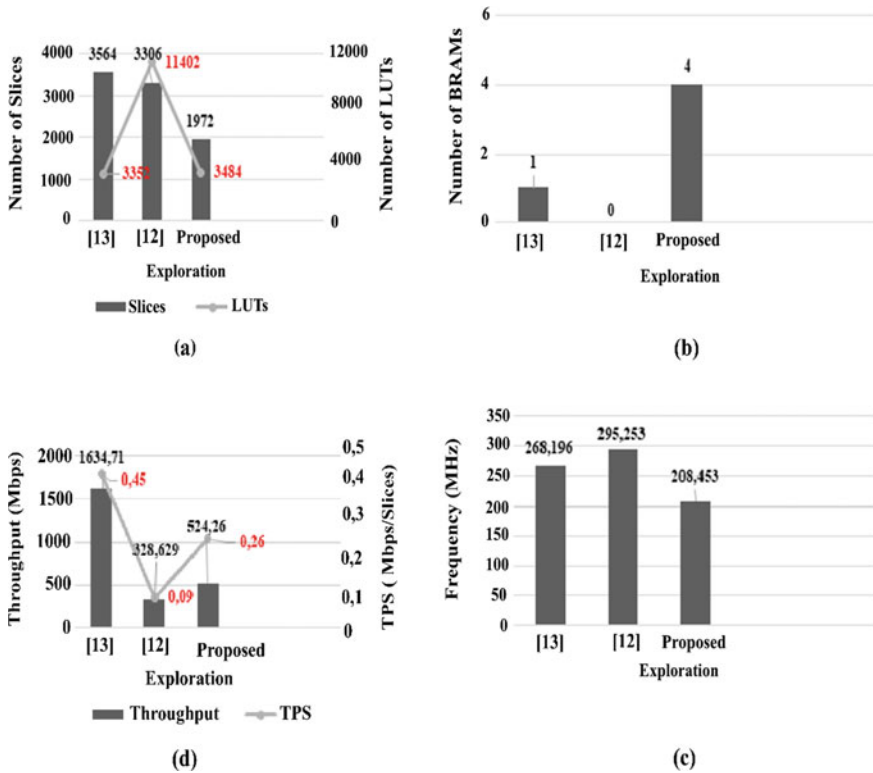
Fig. 5 a Number of slices and LUTs used, **b** number of BRAMs used, **c** frequency, and **d** throughput/TPS metrics for each design

of the LST-SW algorithm based on the AES algorithm. The observed results demonstrated that the proposed implementation achieved a throughput of 524.26 Mbps using Xilinx Virtex-4QV FPGA, at a maximum clock frequency of 208.453. Furthermore, the proposed solution occupies 8% of the slice in terms of area consumption. Furthermore, a comparison of the suggested implementation to prior work reveals that the proposed approach has the best trade-off between area utilization, frequency, and throughput. Therefore, The suggested approach offers excellent performance, making it appropriate for future satellite remote sensing missions that utilize radiation-tolerant LST-SW computations.

References

1. Wang W, Zhang X, Hao Q, Zhang Z, Xu B, Dong H, Xia T, Wang X (2019) Hardware-enhanced protection for the runtime data security in embedded systems. Electronics 8:52. https://doi.org/10.3390/electronics8010052

2. Joseph SIT (2021) Accurate segmentation for low resolution satellite images by discriminative generative adversarial network for ıdentifying agriculture fields. J Innovative Image Process 3:298–310. https://doi.org/10.36548/jiip.2021.4.002

3. Benmecheta A, Abdellaoui A, Hamou A (2013) A comparative study of land surface temperature retrieval methods from remote sensing data. Can J Remote Sens 39:59–73. https://doi.org/10.5589/m13-008

4. Borkar AM, Kshirsagar RV, Vyawahare MV (2011) FPGA implementation of AES algorithm. In: 2011 3rd ınternational conference on electronics computer technology. pp 401–405. https://doi.org/10.1109/ICECTECH.2011.5941780

5. Zodpe H, Sapkal A (2020) An efficient AES implementation using FPGA with enhanced security features. J King Saud Univ—Eng Sci 32:115–122. https://doi.org/10.1016/j.jksues.2018.07.002

6. Priya SSS, Karthigai Kumar P, SivaMangai NM, Rejula V (2015) FPGA implementation of efficient AES encryption. In: International conference on ınnovations in ınformation, embedded and communication systems (ICIIECS). pp 1–4. https://doi.org/10.1109/ICIIECS.2015.7193081

7. Quinn H (2017) Radiation effects in reconfigurable FPGAs. Semicond Sci Technol 32:044001. https://doi.org/10.1088/1361-6641/aa57f6

8. Daemen J, Rijmen V (2000) The block cipher Rijndael. In: Quisquater J-J, Schneier B (eds) Smart card research and applications. Springer, Berlin, Heidelberg, pp 277–284. https://doi.org/10.1007/10721064_26

9. Rais MH, Qasim SM (2009) FPGA implementation of Rijndael algorithm using reduced residue of prime numbers. In: 4th ınternational design and test workshop (IDT). pp 1–4. https://doi.org/10.1109/IDT.2009.5404130

10. Gielata A, Russek P, Wiatr K (2008) AES hardware implementation in FPGA for algorithm acceleration purpose. In: International conference on signals and electronic systems. pp 137–140. https://doi.org/10.1109/ICSES.2008.4673377

11. Granado-Criado JM, Vega-Rodríguez MA, Sánchez-Pérez JM, Gómez-Pulido JA (2010) A new methodology to implement the AES algorithm using partial and dynamic reconfiguration. Integration 43:72–80. https://doi.org/10.1016/j.vlsi.2009.05.003

12. El Makhloufi A, Chekroun N, Tagmouti N, El Adib S, Sobrino JA, Raissouni N (2020) FPGA/LST-SW encryption module ımplementation for satellite remote sensing secure systems. In: Fourth ınternational conference on ıntelligent computing in data sciences (ICDS). pp 1–7. https://doi.org/10.1109/ICDS50568.2020.9268739

13. El Makhloufi A, Chekroun N, Tagmouti N, El Adib S, Sobrino JA, Raissouni N (2020) AES/FPGA encryption module ıntegration for satellite remote sensing systems: LST-SW case. In: 3rd ınternational conference on advanced communication technologies and networking (CommNet). pp 1–7. https://doi.org/10.1109/CommNet49926.2020.9199644

14. (2014) Space-grade Virtex-4QV family overview (DS653). 8

15. Daemen J, Rijmen V (2002) The design of Rijndael: AES—the advanced encryption standard. Springer-Verlag, Berlin Heidelberg. https://doi.org/10.1007/978-3-662-04722-4

16. Daemen J, Rijmen V (1999) AES proposal: Rijndael

17. Fischer V, Drutarovský M (2001) Two methods of Rijndael ımplementation in reconfigurable hardware. In: Koç ÇK, Naccache D, Paar C (eds) Cryptographic hardware and embedded systems—CHES. Springer, Berlin, Heidelberg, pp 77–92. https://doi.org/10.1007/3-540-447 09-1_8

18. El Makhloufi A, Chekroun N, Tagmouti N, El Adib S, Raissouni N (2021) Improvements in space radiation-tolerant FPGA implementation of land surface temperature-split window algorithm. Int J Electr Comput Eng (IJECE) 11:3844–3854. https://doi.org/10.11591/ijece. v11i5.pp3844-3854

Detecting Intrusion in WiFi Network Using Graph Neural Networks

Quang-Vinh Dang and **Tan-Loc Nguyen**

Abstract The popularity of WiFi technology opens many new attack opportunities for attackers. It is a common practice to deploy an intrusion detection system to mitigate these attacks. In recent years, a few research studies have used different machine learning techniques to empower the intrusion detection system, hence improving the detection performance. However, most of the published methods do not consider the relationship between network traffic, so these methods consider the incoming traffic flows as independent traffic. In this paper, we employ graph neural networks to learn the relation between incoming network flow. The experimental results show that we can improve the performance of intrusion detection systems.

Keywords Cyber-security · Classification · Intrusion detection

1 Introduction

It is hard to deny the importance of WiFi networks in modern life. We have recently observed a trend of switching from wired to wireless networks. It is widespread for home users and office users not to use any wired connection at all.

However, it also opens new doors to attackers. As the nature of wireless networks, anyone in the range of the radar signal can see the signal and somehow get access.

Intrusion detection is an important research problem in the security community. There are many different research studies focusing on detecting intrusion in computer networks, in general, and in WiFi networks specifically.

Q.-V. Dang (✉)
Industrial University of Ho Chi Minh City, Ho Chi Minh City, Vietnam
e-mail: dangquangvinh@iuh.edu.vn

T.-L. Nguyen
FPT University, Ho Chi Minh City, Vietnam
e-mail: locntse160366@fpt.edu.vn
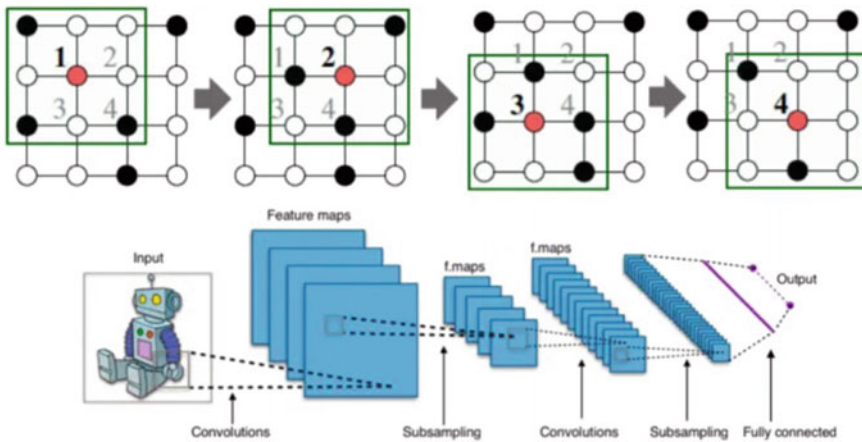
Fig. 1 Graph neural networks [19]

The intrusion detection system (IDS) plays the role of a gatekeeper of a local network. An IDS will determine which packet can go through and which packet should be stopped. There are two main approaches to implementing an IDS [14]: anomaly-based detection and signature-based detection. In the first approach, a malicious package is considered an outlier [4], i.e., a package which is much different from other packages. In the second family of the implementation strategy, the researchers usually implement a classification model to classify malicious data [8, 9].

Different classification models have been presented in published research studies [13, 22]. However, they usually consider packages as independent instances. It is a common practice for classification methods such as xgboost [6] or reinforcement learning [5]. However, they do not consider the relationship between packages. Researchers showed that it is rare for the attack to happen alone, but usually in a series of attacks [23].

Graph neural networks (GNN) [24] attracted much attention in recent years. Graph neural networks can learn the relationship between attacks, such as the attacks aiming at the same host. By that, a GNN can learn some information that is skipped by other supervised machine learning techniques. The core idea of GNN is presented in Fig. 1.

In this paper, we implement a GNN to deal with the problem of the intrusion detection system in WiFi networks. We evaluate our proposal using an open dataset.

2   Related Works

Intrusion detection has a long history in the security research community. In recent years, many researchers focus on using machine learning techniques to improve the performance of the intrusion detection system (IDS). We refer the readers to some

recent reviews for a comprehensive overview of machine learning techniques used for intrusion detection [12].

In the work of Dang [6], the authors studied many different supervised machine learning algorithms to serve as the core of IDS. The authors considered the IDS as a binary classification problem: given a network flow with some pre-defined features, a model needs to classify the flow to either the benign or malicious class.

The work of Dang [6] has been extended in the following works. The authors of [18] benchmarked different algorithms using the CICIDS2017 dataset [21]. The algorithms used by Maseer et al. [18] are visualized in Fig. 2.

A few research works study reinforcement learning techniques [1, 10, 11]. In reinforcement learning, a model does not need explicit labels like in supervised learning methods, but only the feedback of the environment. For instance, a model can let a package go through but learn the reaction of the system such as the package turns out to be a malicious package. The paradigm of reinforcement learning is presented in Fig. 3.
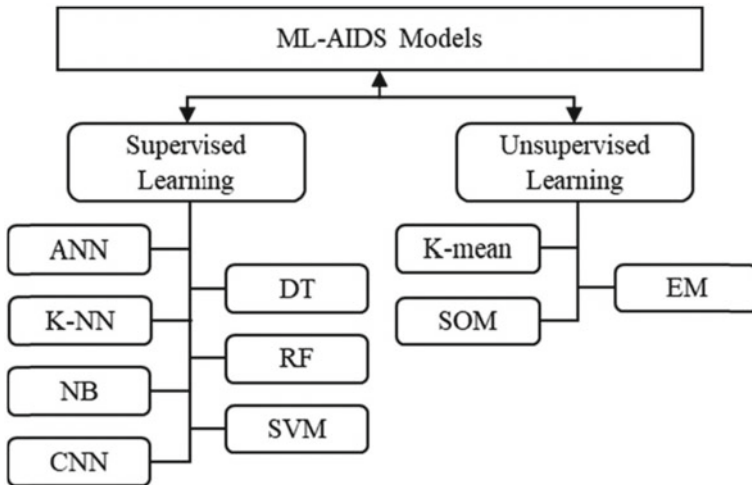
Fig. 2 Machine learning algorithms to be benchmarked in the work of Maseer et al. [18]
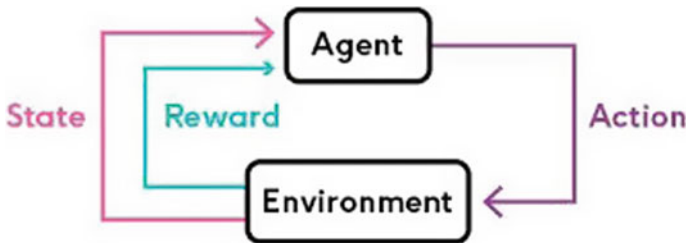
Fig. 3 Reinforcement learning
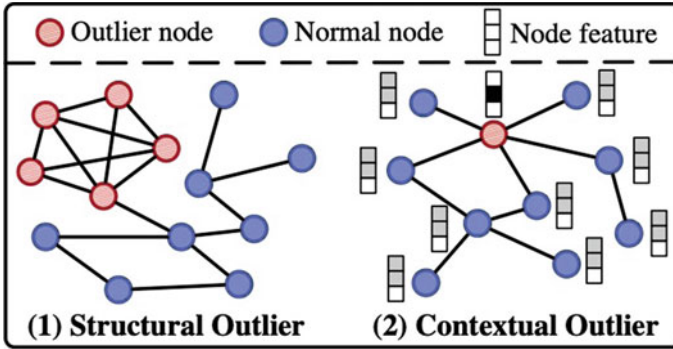
Fig. 4 Outlier detection on a graph [15]

Fuzzy methods have been studied to apply to the intrusion detection problem [7, 17]. Instead of assigning a fixed class (benign or malicious), fuzzy methods considered that a class assignment can be blurred, i.e., a network flow can belong to both classes simultaneously.

Another branch of detecting the intrusion is considering intrusion as an outlier in the network [4, 15] as visualized in Fig. 4.

3   Graph Neural Networks

Graph neural network is a neural network that can be applied to graph [16], similar to the idea of applying convolution neural networks to image data.

Similar to the convolutional neural networks, the core idea of GNN is to aggregate information of neighbor nodes to make a new representation of the current node. The process can be extended to the extreme when the entire graph is covered.

It is not easy to represent intrusion detection datasets as a graph as they are usually presented in the tabular mode [20, 21]. In tabular data, each row is considered independent data. However, we can generate a graph from the dataset by considering the host (determined by IP address) as an edge in a graph, and the connections between them are the package sent from the source to the destination.

The node embedding method can be performed iteratively. At the kth iteration, the nodes at k-distance are considered as follows.

$$h_{N(v)}^k = \text{AGG}_k\big(h_u^{k-1}, \forall v \in N\big) \tag{1}$$

The process is visualized in Fig. 5 [3].

However, the problem is that we need to classify edge rather than node. We simply apply a graph reverse transformation to convert nodes to edges and edges to nodes [2]. The idea of the conversion is visualized in Fig. 6.
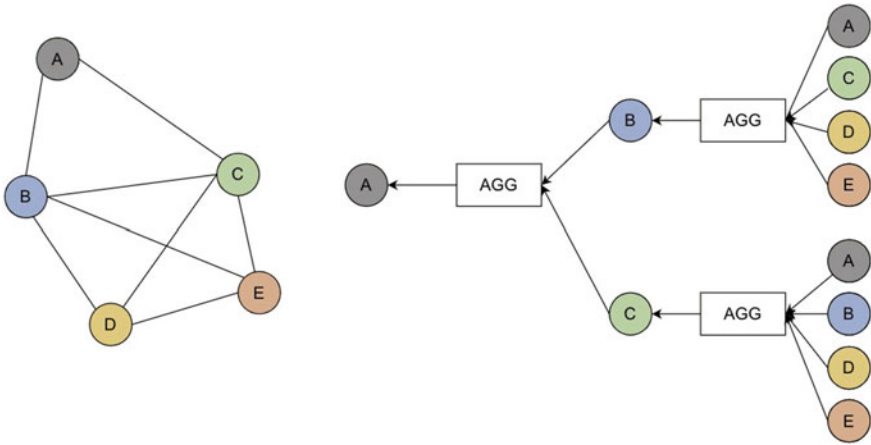
Fig. 5 Node embedding [3]
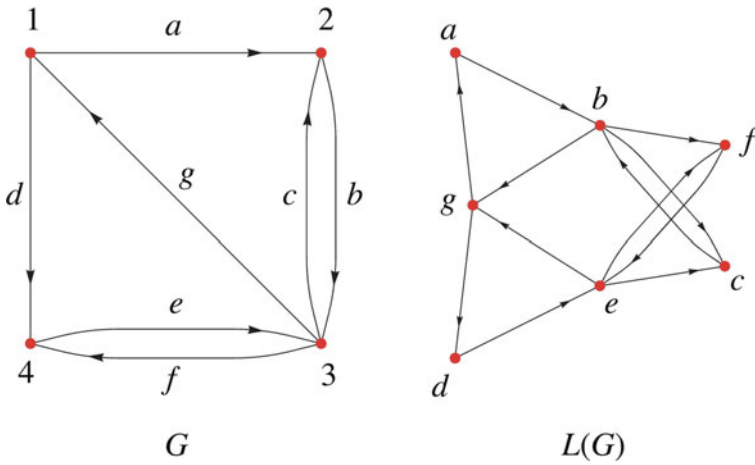
Fig. 6 Line graph

After the conversion, we have the embedding of the edge which represents the network traffic. We feed them to xgboost for classification.
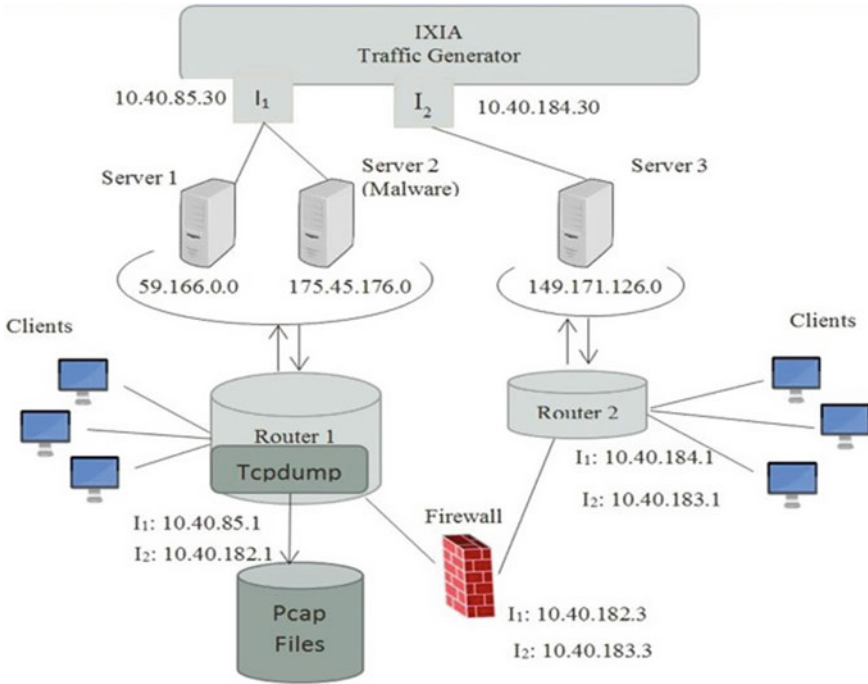
Fig. 7 Collection of data for UNSW-NB15 dataset

4 Experimental Results

4.1 Dataset

We use the dataset UNSW-NB15 [20]. The dataset is collected by the process visualized in Fig. 7. The number of malicious packages consumes about 7% of the total data.

The authors [20] have calculated some features for the dataset. The list of features is presented in Table 1.

4.2 Results

We compare the results of the graph neural networks with xgboost. xgboost is considered one of the most powerful models in detecting intrusion [6].

We use the ROC-AUC metric as the main metric. ROC-AUC score considers the entire range of thresholds rather than a single one, hence providing a better overview picture of the performance of the models.

Table 1 Features of UNSW-NB15 dataset

	No. name	Type	Description
0	1 srcip	Nominal	Source IP address
1	2 sport	Integer	Source port number
2	3 dstip	Nominal	Destination IP address
3	4 dsport	Integer	Destination port number
4	5 proto	Nominal	Transaction protocol
5	6 state	Nominal	Indicates to the state and its dependent proto…
6	7 dur	Float	Record total duration
7	8 sbytes	Integer	Source to destination transaction bytes
8	9 dbytes	Integer	Destination to source transaction bytes
9	10 sttl	Integer	Source to destination time to live value
10	11 dttl	Integer	Destination to source time to live value
11	12 sloss	Integer	Source packets retransmitted or dropped
12	13 dloss	Integer	Destination packets retransmitted or dropped
13	14 service	Nominal	http, ftp, smtp, ssh, dns, ftp-data,irc and…
14	15 Sload	Float	Source bits per second
15	16 Dload	Float	Destination bits per second
16	17 Spkts	Integer	Source to destination packet count
17	18 Dpkts	Integer	Destination to source packet count
18	19 swin	Integer	Source TCP window advertisement value
19	20 dwin	Integer	Destination TCP window advertisement value
20	21 stcpb	Integer	Source TCP base sequence number
21	22 dtcpb	Integer	Destination TCP base sequence number
22	23 smeansz	Integer	Mean of the ?ow packet size transmitted by the…
23	24 dmeansz	Integer	Mean of the ?ow packet size transmitted by the…
24	25 trans_depth	Integer	Represents the pipelined depth into the connec…
25	26 res_bdy_len	Integer	Actual uncompressed content size of the data t…
26	27 Sjit	Float	Source jitter (mSec)
27	28 Djit	Float	Destination jitter (mSec)
28	29 Stime	Timestamp	Record start time
29	30 Ltime	Timestamp	Record last time
30	31 Sintpkt	Float	Source interpacket arrival time (mSec)
31	32 Dintpkt	Float	Destination interpacket arrival time (mSec)
32	33 tcprtt	Float	TCP connection setup round-trip time, the sum…
33	34 synack	Float	TCP connection setup time, the time between th…
34	35 ackdat	Float	TCP connection setup time, the time between th…
35	36 is_sm_ips_ports	Binary	If source (1) and destination (3) IP addresses…

(continued)

Table 1 (continued)

	No. name	Type	Description
36	37 ct_state_ttl	Integer	No. for each state (6) according to specific r…
37	38 ct.flw_hhtp_mthd	Integer	No. of flows that has methods such as Get and…
38	39 is_ftp_login	Binary	If the ftp session is accessed by user and pas…
39	40 ct_ftp_cmd	Integer	No of flows that has a command in ftp session
40	41 ct_srv_src	Integer	No. of connections that contain the same servi…
41	42 ct_srv_dst	Integer	No. of connections that contain the same servi…
42	43 ct_dst_ltm	Integer	No. of connections of the same destination add…
43	44 ct_src_ ltm	Integer	No. of connections of the same source address
44	45 ct_src_dport.ltm	Integer	No of connections of the same source address (…
45	46 ct_dst_sport.ltm	Integer	No of connections of the same destination addr…
46	47 ct_dst_src.ltm	Integer	No of connections of the same source (1) and t…
47	48 attack_cat	Nominal	The name of each attack category. In this data…
48	49 Label	Binary	0 for normal and 1 for attack records

Some long texts are truncated

Table 2 ROC-AUC score of different models

Model	AUC score
Random Forest	0.932
xgboost	0.991
GNN	0.993

Table 3 F1-score of different models

Model	F1-score
Random forest	0.88
xgboost	0.92
GNN	0.93

The performance of each model in terms of the ROC-AUC score is displayed in Table 2. Similarly, the F1-score are presented in Table 3.

5 Conclusions

In this paper, we describe a method to apply graph neural networks to employ intrusion detection systems. We evaluate our proposal using a popular intrusion dataset. We showed that our method gain some improvement compared to previous methods. In the future, we will study other graph neural network methods to improve the model further such as embedding the features of edges and nodes.

References

1. Badr Y (2022) Enabling intrusion detection systems with dueling double deep q-learning. Digit Transform Soc (ahead-of-print)
2. Beineke LW (1970) Characterizations of derived graphs. J Comb Theory 9(2):129–135
3. Caville E, Lo WW, Layeghy S, Portmann M (2022) Anomal-e: a self-supervised network intrusion detection system based on graph neural networks. arXiv:2207.06819
4. Dang QV (2018) Outlier detection in network flow analysis. arXiv:1808.02024
5. Dang QV (2019) Reinforcement learning in stock trading. In: International conference on computer science, applied mathematics and applications. Springer, pp 311–322
6. Dang QV (2019) Studying machine learning techniques for intrusion detection systems. In: FDSE. Lecture notes in computer science, vol 11814. Springer, pp 411–426
7. Dang QV (2021) Studying the fuzzy clustering algorithm for intrusion detection on the attacks to the domain name system. In: WorldS4. IEEE
8. Dang QV (2022) Machine learning for intrusion detection systems: recent developments and future challenges. In: Real-time applications of machine learning in cyber-physical systems. pp 93–118
9. Dang QV (2022) Using machine learning for intrusion detection systems. Comput Inform 41(1):12–33
10. Dang QV, Vo TH (2021) Reinforcement learning for the problem of detecting intrusion in a computer system. In: Proceedings of ICICT
11. Dang QV, Vo TH (2021) Studying the reinforcement learning techniques for the problem of intrusion detection. In: ICAIBD. IEEE
12. Habeeb MS, Babu TR (2022) Network intrusion detection system: a survey on artificial intelligence-based techniques. Expert Syst e13066
13. Li Y, Qin T, Huang Y, Lan J, Liang Z, Geng T (2022) Hdfef: a hierarchical and dynamic feature extraction framework for intrusion detection systems. Comput Secur 102842
14. Lin YD, Wang ZY, Lin PC, Nguyen VL, Hwang RH, Lai YC (2022) Multidatasource machine learning in intrusion detection: packet flows, system logs and host statistics. J Inf Secur Appl 68:103248
15. Liu K, Dou Y, Zhao Y, Ding X, Hu X, Zhang R, Ding K, Chen C, Peng H, Shu K et al (2022) Benchmarking node outlier detection on graphs. arXiv:2206.10071
16. Lo WW, Layeghy S, Sarhan M, Gallagher M, Portmann M (2022) E-graphsage: a graph neural network based intrusion detection system for IOT. In: NOMS IEEE/IFIP network operations and management symposium. IEEE, pp 1–9
17. Masdari M, Khezri H (2020) A survey and taxonomy of the fuzzy signature-based intrusion detection systems. Appl Soft Comput
18. Maseer ZK, Yusof R, Bahaman N, Mostafa SA, Foozy CFM (2021) Benchmarking of machine learning for anomaly based intrusion detection systems in the CICIDS 2017 dataset. IEEE Access 9:22351–22370
19. Menzli A (2022) Graph neural network and some of GNN applications: everything you need to know
20. Moustafa N, Slay J (2015) Unsw-nb15: a comprehensive data set for network intrusion detection systems (unsw-nb15 network data set). In: Military communications and information systems conference (MilCIS). IEEE, pp 1–6
21. Sharafaldin I, Lashkari AH, Ghorbani AA (2018) Toward generating a new intrusion detection dataset and intrusion traffic characterization. In: ICISSP. pp 108–116
22. Umer MA, Junejo KN, Jilani MT, Mathur AP (2022) Machine learning for intrusion detection in industrial control systems: applications, challenges, and recommendations. Int J Crit Infrastruct Prot 100516
23. Wu Y, Wei D, Feng J (2020) Network attacks detection methods based on deep learning techniques: a survey. Secur Commun Networks 2020
24. Wu Z, Pan S, Chen F, Long G, Zhang C, Philip SY (2020) A comprehensive survey on graph neural networks. IEEE Trans Neural Networks Learn Syst 32(1):4–24

An IoT-Based System for Monitoring Power Failure in 22-KV Distribution Transformer Substations Using LoRa Communication

Nguyen Ngoc Hien, Luong Vinh Quoc Danh ⓘ**, Nguyen Thanh Phong, and Nguyen Thi Tram**

Abstract This paper presents the design and implementation of a power failure monitoring system for 22-kV transformer substations using the Internet of Things (IoT) technology and LoRa communication. The proposed system consists of 3 main components: Sensor nodes consist of voltage sensors and a LoRa transceiver module installed at the substation; Gateway station is composed of one LoRa transceiver module, one Wi-Fi module and one 3G/4G wireless module for transmitting data to Cloud server through internet connection and sending SMS alerts to users; and the ThingSpeak cloud server. The application of LoRa communication technology allows monitoring of grid voltage in real-time with lower operating costs than the methods of sending data over the internet and mobile phone networks. The research results can be applied to automate the monitoring and warning of power failures at the 22-kV distribution substations to help improve the stability of the power systems.

Keywords Distribution transformer · Internet of Things · LoRa · Voltage monitoring

1 Introduction

The 22/0.4-kV distribution substation is a type of substations commonly used in power distribution systems. Most of the power failure in the system occurs at the distribution substations. When there is a power failure at distribution substations or the area near the substations, the power supply agency cannot detect the problem immediately, but it needs to be informed by the customers. According to a study

N. N. Hien
Soc Trang Province Electricity Company, Soc Trang, Vietnam

L. V. Q. Danh (✉) · N. T. Tram
College of Engineering, Can Tho University, Can Tho, Vietnam
e-mail: lvqdanh@ctu.edu.vn

N. T. Phong
Mechatronic Engineer, Vinh Long Province, Vietnam

published in 2019, the normalized SAIFI (System Average Interruption Frequency Index) index of Vietnam ranked 8th out of 10 Southeast Asian countries, just above Cambodia and Myanmar [1]. Therefore, it is esential to monitor the operating status of distribution transformer substations. It will help to improve operational performance of transformers and maintain grid stability.

The SCADA technology has been widely applied to monitor and control the operation of power distribution systems [2, 3]. However, the adoption of this technology faces some challenges such as high installation, operation and periodic maintenance costs, and low compatibility of equipment provided by different vendors. In recent years, monitoring of distribution transformer substations based on Internet of Things (IoT) technology and wireless communications has also been proposed [4–13]. Specifically, in the studies [4–6], the data transmission between Sensor nodes at transformer substations and the Gateway station was done via GSM mobile phone network. Besides, the monitoring systems based on the IoT structure have also been introduced [7–9]. This approach allows the status information of the substations to be recorded in real time and stored for further analysis and evaluation purposes. However, the mentioned solutions require equipping each substation with an internet connection or a GSM/GPRS modem to transmit data to the server. This will lead to increased operating costs of the monitoring systems due to maintaining internet connections for a large number of distribution substations. In addition, in the studies [10–13], the data transmission method between Sensor nodes and Gateway station using the Zigbee standard and radio link has also been implemented although the transmission range is limited.

LoRa communication technology is considered as one of the suitable data transmission techniques for wireless sensor applications due to its ability to transmit data with the maximum transmission distance up to 5 km in urban area [14, 15]. In this work, the authors propose a method to apply the IoT technology and LoRa communication to monitor voltages at 22-kV transformer substations. The designed system consists of 3 main components: Sensor nodes installed at the transformer substations; Gateway station capable of connecting to cloud server and mobile phone networks; Cloud server for data storage and analysis. The proposed approach allows monitoring of grid voltage in real time without using internet or mobile connection at distribution substations.

2   System Design

The power failure monitoring and warning system consists of a Gateway station, the ThingSpeak Cloud Server [16] and Sensor nodes installed at the 22-kV distribution transformer substations, as shown in Fig. 1. In this study, the object to be monitored is the phase voltages of the 22-kV transformers at distribution substations. The Sensor node is designed to be powered by rechargeable batteries in the case of a power failure. Measurement data at the substation is transmitted to the Gateway station via the LoRa radio link.
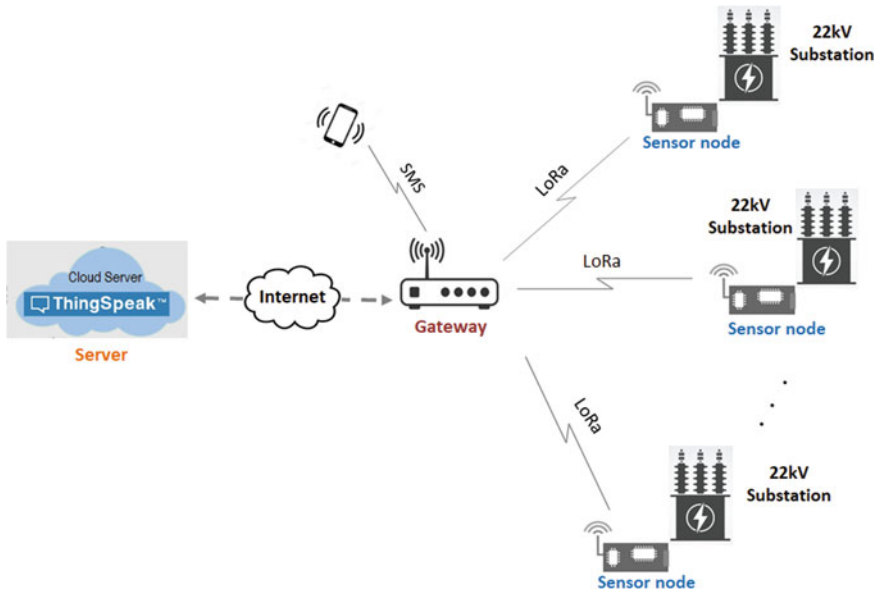
Fig. 1 Block diagram of the voltage monitoring system for the 22-kV distribution transformer substations

2.1 Sensor Nodes

The sensor node is composed of a microcontroller unit, 3 voltage sensors, one LoRa transceiver module, one LCD display, and one battery charger. Its block diagram is shown in Fig. 2.
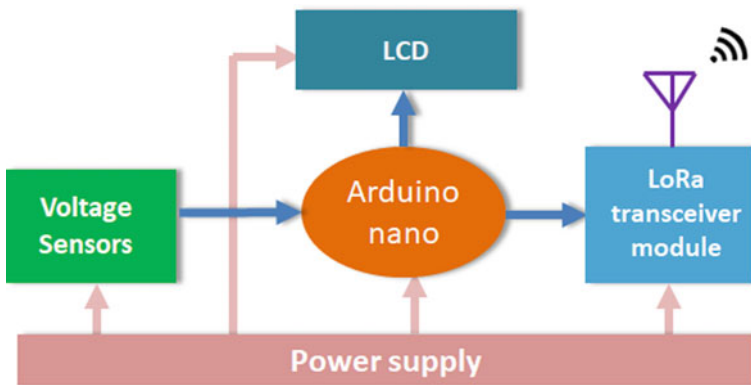
Fig. 2 The block diagram of the sensor nodes

- **Microcontroller unit**: An Arduino Nano kit [17] is used to control the operation of the Sensor nodes. The data measured by the voltage sensors will be transmitted to the Gateway station through the LoRa transceiver module.
- **Voltage sensor**: To measure voltage across three phases of the 22-kV distribution transformer substation, three ZMPT101B voltage sensor modules [18], capable of measuring voltage up to 250VAC, were used in this study. The output signal of the sensor is analog and varies in the range from 0 to 5VDC. These signals are fed to the ADC (analog-to-digital converter) inputs of the Arduino nano kit for further processing.
- **LoRa transceiver module**: A 433-MHz LoRa transceiver module [19] is used to transmit measurement data from Sensor nodes to the Gateway station.
- **LCD display**: A 1602 LCD display module [20] is used to display the measured voltage values and the Sensor node's operating status**.**
- **Battery charger**: To be able to operate in the case of a power outage, the Sensor node is equipped with one charging module [21] for two 3.7 V/2200 mAh 18,650-sized cell Li-ion rechargeable batteries. It helps to keep the sensor node working continuously for more than 12 h after power outage.

The flowchart of the operation control algorithm of the Sensor nodes is shown in Fig. 3. Accordingly, the voltage values of the phases are read at a frequency of 30 s/time. If a voltage failure is detected (phase voltage is low or higher than the preset threshold level), the control program will continue to check the voltage value for a period of $T = 15$ s. After this period, if the phase voltage still maintains at a higher/lower value than the threshold, the program will send data to the Gateway station.

2.2 Gateway Station

The block diagram of the Gateway station is shown in Fig. 4. It is composed of an Arduino nano kit, one 433-MHz LoRa transceiver module, one ESP32 NodeMCU Wi-Fi module [22], one 4G wireless module [23], one LCD, and one battery charger.

The flowchart of the control algorithm embedded in the Arduino nano kit is shown in Fig. 5. The Arduino nano gathers data from the Sensor nodes through the LoRa transceiver module. The collected data will be processed by the Arduino nano and then sent to the ESP32 NodeMCU module for uploading to the ThingSpeak server through Wi-Fi connection. The control algorithm of the ESP32 NodeMCU Wi-Fi module is presented in Fig. 6. In this experiment, data are uploaded to the ThingSpeak server every 5 min. On detecting a power outage at the substation, the Arduino nano generates an external interrupt signal to the ESP32 NodeMCU module. The ESP32 NodeMCU module will then execute an interrupt subroutine to send SMS alerts to users via the 4G wireless module.
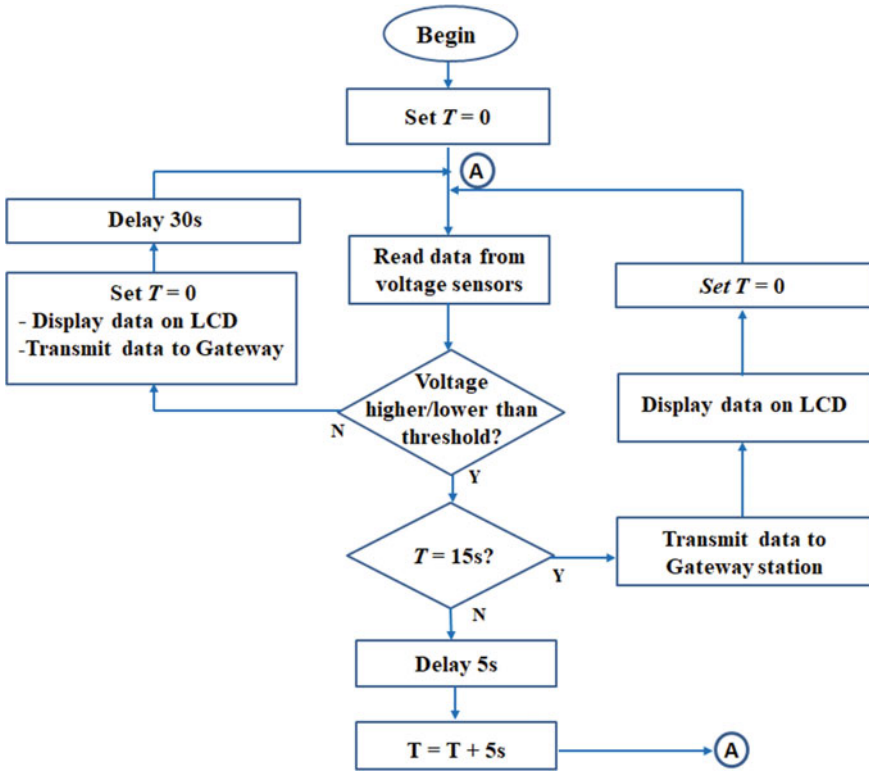
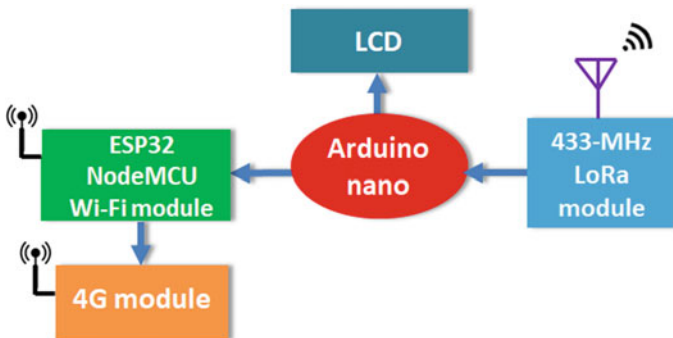**Fig. 3** Control algorithm of the sensor nodes
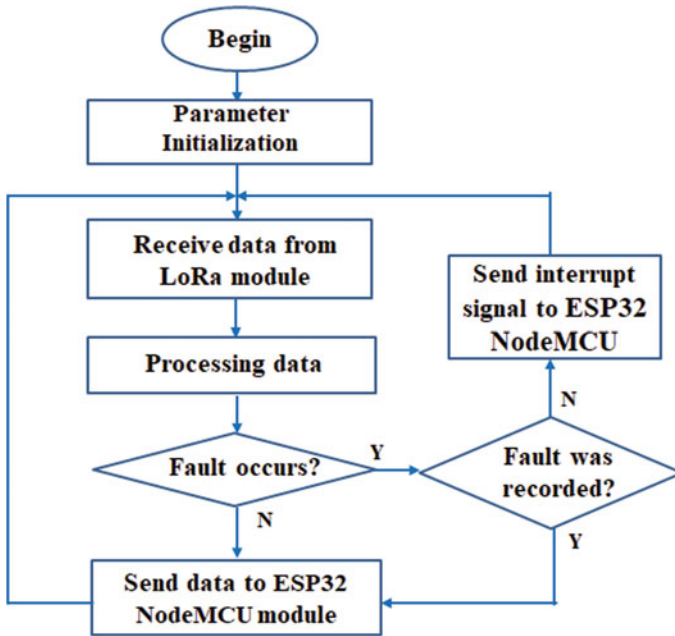

Fig. 4 Block diagram of the Gateway station

Fig. 5 Control algorithm of the Arduino nano kit at the Gateway station
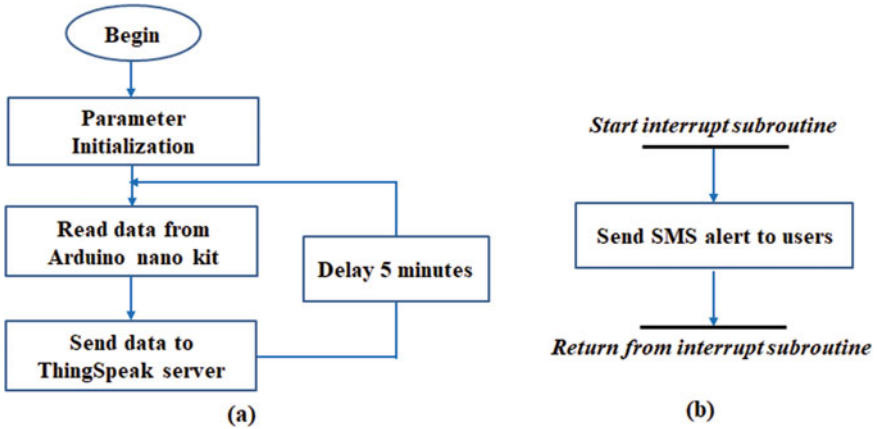

Fig. 6 Control algorithm for the ESP32 NodeMCU module: **a** main program; **b** interrupt subroutine for sending SMS alerts

2.3 Cloud Server

In this work, the ThingSpeak cloud server is used to store phase voltage data of distribution transformer substations. It also provides the management staff the ability to monitor these voltage data on mobile devices (laptops, smartphones) by accessing to the registered data channel corresponding to the substation of interest.

3 Experimental Results

A power failure monitoring and warning system for the 22-kV distribution transformer substations including one Gateway station and three Sensor nodes was designed and tested. First, the phase voltage changes of the distribution substation were simulated to evaluate the system performance. The Sensor nodes were then installed for testing at three 22-kV distribution transformer substations in Soc Trang City, Vietnam.

The modulation parameters of the LoRa transceiver modules were established to the values shown in Table 1. The antenna of the Sensor node and the Gateway station was installed at a height of 1.5 m and 15 m, respectively. Figure 7 depicts the electronic boards of a Sensor node. The antenna of LoRa module is fitted outside the plastic box to ensure efficient radio transmission. The test results show that, in the case of terrain with few tall buildings, the transmission distance between the Sensor nodes and the Gateway station can reach 2.7 km; For terrain with many obstacles, the maximum transmission range is about 450 m. The transmission distance can be improved further by using high-gain antennas, increasing the transmit power of the LoRa module and installation height of antennas.

Measurement data at the 22-kV transformer substations is transmitted to the ThingSpeak cloud server for storage. Technical staff can monitor the phase voltage changes by installing the ThingViewer App [24] on his/her smartphone. Figure 8 presents the graph showing changing of a phase voltage in which the information was updated every 5 min.

Table 2 presents the coding symbols for possible fault cases on the voltage phases of the substation. This coding method allows administrators to quickly identify problems and helps reduce the amount of data that needs to be transferred between the Sensor nodes and the Gateway station. Figure 9 depicts the SMS alerts to warn of over-voltage faults on the phases of the substation where the Sensor node #2 is installed.

Table 1 Modulation parameters of the LoRa transceiver module

Antenna gain	Transmit power	Spreading factor	Coding rate	Modulation bandwidth
7 dBi	17 dBm	12	4/5	125 kHz

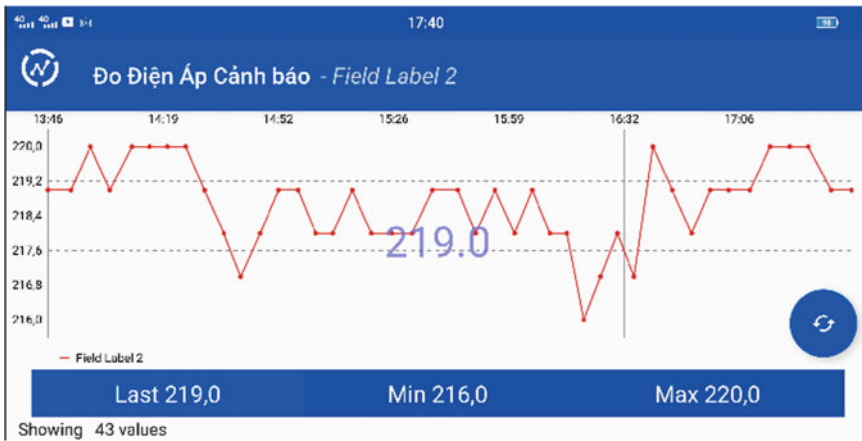**Fig. 7** Electronic circuits of the sensor nodes

Fig. 8 Graph of one phase voltage shown on smartphone screen

Figures 10, 11 and 12 show the installation of the Sensor nodes and Gateway station in the field. During the testing period from June 1 to July 15, 2022, the system recorded one unexpected power outage on July 8, 2022 and one planned power outage on July 11, 2022 exactly as it actually happened.

Table 2 Symbol codes of phase voltages at the distribution substations

Faults	Phases	Coding symbols		
		Sensor node #1	Sensor node #2	Sensor node #3
Outage/low voltage	Phase A	V1E01T	V2E01T	V3E01T
	Phase B	V1E02T	V2E02T	V3E02T
	Phase C	V1E03T	V2E03T	V3E03T
	Phases A–B	V1E12T	V2E12T	V3E12T
	Phases A–C	V1E13T	V2E13T	V3E13T
	Phases B–C	V1E23T	V2E23T	V3E23T
	Phases A–B–C	V1E3PT	V2E3PT	V3E3PT
Over-voltage	Phase A	V1E01C	V2E01C	V3E01C
	Phase B	V1E02C	V2E02C	V3E02C
	Phase C	V1E03C	V2E03C	V3E03C
	Phases A–B	V1E12C	V2E12C	V3E12C
	Phases A–C	V1E13C	V2E13C	V3E13C
	Phases B–C	V1E23C	V2E23C	V3E23C
	Phases A–B–C	V1E3PC	V2E3PC	V3E3PC

Fig. 9 SMS messages to warn of over-voltage faults at the sensor node #2

Fig. 10 Sensor node #2 installed at a 22-kV distribution substation

4 Conclusions

A power failure monitoring and warning system for the 22-kV distribution transformer substations was designed and tested. The combination of IoT technology and LoRa communication in the designed monitoring system helps reduce operating costs since it does not require maintaining internet and mobile connections at distribution substations as in previous works. The research results could be a potential alternative for monitoring the operational status of distribution substations, helping to improve the stability of the power systems. In the future, the authors will work on system expansion to meet the requirements of applications having a large number of sensor nodes.
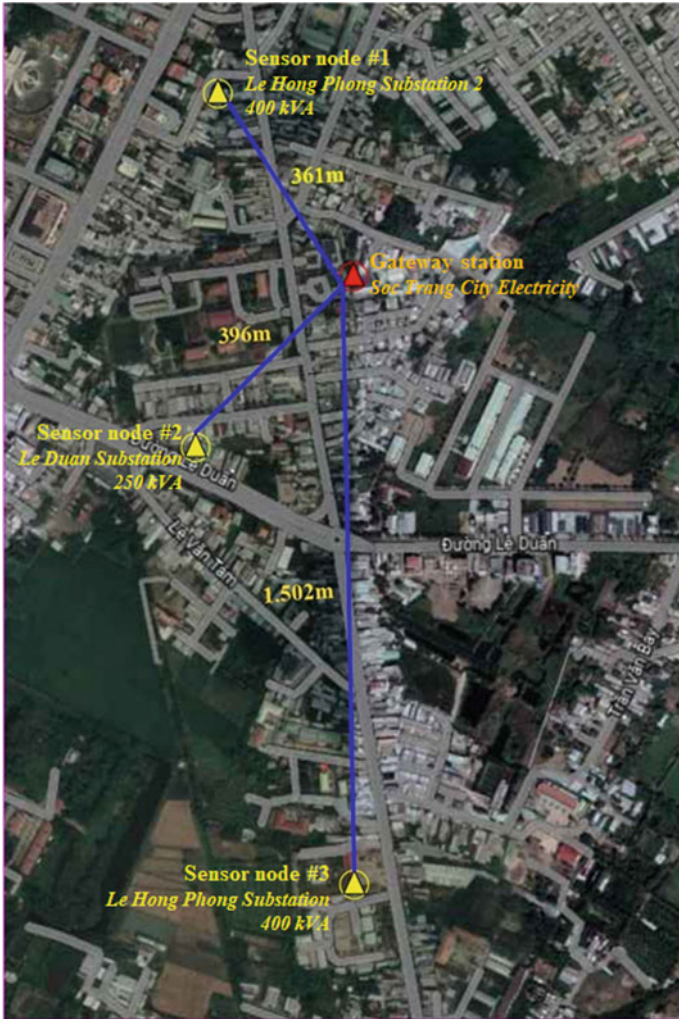
Fig. 11 Installation location of sensor nodes and Gateway station in Soc Trang City

Fig. 12 Installation of Gateway station

References

1. Huang YW, Kittner N, Kammen DM (2019) ASEAN grid flexibility: preparedness for grid integration of renewable energy. Energy Policy 128:711–726
2. Enescu FM, Bizon N (2017) SCADA applications for electric power system. In: Mahdavi Tabatabaei N, Jafari Aghbolaghi A, Bizon N, Blaabjerg F (eds) Reactive power control in AC power systems. Springer, Cham

3. Muruganandhan AD, Muthunagai R, Rajkumar S, Mohamed Vasif J (2020) Remote monitoring of distribution transformer with power theft detection using PLC & SCADA. In: International conference on system, computation, automation and networking (ICSCAN), pp 1–4

4. Hayati MAEAE, Babiker SF (2016) Design and implementation of low-cost SMS based monitoring system of distribution transformers. In: Conference of basic sciences and engineering studies (SGCAC), pp 152–157

5. Venkatakrishnan GR, Rengaraj R, Veluman A (2021) An experimental setup for monitoring distribution transformer health. Distrib Gener Altern Energy J 353:195–208

6. Ojo TP, Akinwumi AO, Ehiagwina FO, Ambali JM, Olatinwo IS (2022) Design and implementation of a GSM-based monitoring system for a distribution transformer. Eur J Eng Technol Res 7(2):22–28

7. Parihar AR, Khule SS (2019) Condition monitoring of distribution transformer using Internet of Things (IoT). Int J Sci Res (IJSR) 8(7):435–438

8. Yamuna R, Geetha R, Gowdhamkumar S, Jambulingam S (2019) Smart distribution transformer monitoring and controlling using IoT. Int Res J Multi 1(2):111–115

9. Gopiya Naik S, Subramanya Y, Raghu M (2020) IoT-based monitoring and control of faults in power distribution transformers. SSRG Int J Electr Electron Eng 7(12):37–41

10. Dharappanavar AR, Jolad S, Machakanur S, Beeraldinni S (2018) Smart metering and health monitoring of distribution transformers using RF technology. J Emerg Technol Innovative Res 5(9):757–761

11. Faria RAP (2012) Wireless sensor network for electrical secondary substations. In 9th European radar conference, pp 602–605

12. Shinge V, Shukla O, Panday P, Chaple M (2016) Wireless transformer parameter monitoring system using RF module. Int J Innovative Res Electr Electron Instrum Control Eng 4(4):341–344

13. Mahmood MH, Makki SA (2021) Power distribution transformers monitoring based on zigbee and sensors technology. In: 7th ınternational engineering conference "Research and Innovation amid Global Pandemic" (IEC), pp 112–117

14. Semtech—LoRa. https://www.semtech.com/lora

15. Wang H, Fapojuwo AO (2017) A survey of enabling technologies of low power and long range machine-to-machine communications. In: IEEE Commun Surv Tutorials 19(4):2621–2639

16. ThingSpeak. https://thingspeak.com/

17. Arduino nano. https://docs.arduino.cc/hardware/nano

18. ZMPT101B datasheet. https://datasheetspdf.com/pdf-file/1031464/ETC/ZMPT101B/1

19. Ra-02 LoRa module. https://docs.ai-thinker.com/en/lora/man

20. LCD 16x2 characters. https://www.seeedstudio.com/LCD-16x2-Characters-White-Text-Blue-Background-p-1612.html

21. J5019 Battery Charger. https://mekatroniks.com/product/7030/

22. ESP32 modules. https://www.espressif.com/en/products/modules

23. 4G A7670C module. https://www.simcom.com/product/A7670X.html

24. ThingViewer App. https://play.google.com/store/apps/details?id=dev.stol.thingviewer&hl=en&gl=US

Effects of Proton Irradiation on Optocouplers with Bipolar and MOSFET Technologies, a Comparison of In-Situ and Ex-Situ Results

Heinz-Christoph Neitzert, Luigi Palma, Andrea Denker, Juergen Bundesmann, Alina Hanna Dittwald, and Felix Lang

Abstract The properties of two different types of optocouplers, a conventional bipolar one with phototransistor output stage and a photorelay with power MOS output stage, have been determined before, during, and after irradiation with 68 meV protons with a fluence of up to 1e12 protons/cm^2. In-situ measurements of the radiation-induced current of the input LEDs and in the case of the bipolar optocoupler also of the current-transfer-ratio of the device enabled a separate evaluation of input and output device degradation. A moderate degradation of the LED performance is observed for both devices, but in the case of the MOS-based photorelay, the most important overall device parameters are still within the specifications even for the highest irradiation level, while for the coupler with bipolar phototransistor a more than one order of magnitude decrease of the current-transfer-ratio is already observed for moderate fluences. This strong degradation is mainly due to the strong loss of photo-generated charge carriers with increasing fluence.

Keywords Optocoupler · Technologies · Photorelay · Proton irradiation

H.-C. Neitzert (✉) · L. Palma
Department of Industrial Engineering (DIIN), Salerno University, Fisciano, Italy
e-mail: neitzert@unisa.it

L. Palma
e-mail: l.palma11@studenti.unisa.it

A. Denker · J. Bundesmann · A. H. Dittwald
Protons for Therapy, Helmholtz Zentrum Berlin (HZB), Berlin, Germany
e-mail: denker@helmholtz-berlin.de

J. Bundesmann
e-mail: bundesmann@helmholtz-berlin.de

A. H. Dittwald
e-mail: alina.dittwald@helmholtz-berlin.de

F. Lang
Institute of Physics and Astronomy, University of Potsdam, Potsdam, Germany
e-mail: lang1@uni-potsdam.de

1   Introduction

The optocoupler is an important component for space electronics, separating the sensitive control electronics from the high power part of the satellite or space-ship and contributing in this way to increase the system reliability. But at the same time, it is one of the most sensitive components with respect to high energy radiation, which is besides extreme temperature cycles one of the main concerns of electronic component stability in space. One of the reasons is the fact that the minority charge carrier lifetime, which is crucial for most optoelectronic components, is strongly influenced by radiation, and in this respect Crystalline Silicon is one of the most sensitive materials. Crystalline Silicon is so far the only material used in commercial optocoupler photoreceivers, even if recently more radiation-hard materials, such as perovskite have been proposed also for the realization of optocouplers [1]. There have been already a series of comprehensive reports on the radiation hardness of optocouplers mainly focused on the traditional type, that combines an IR-LED with a Silicon phototransistor [2–4] but also devices with dual photodiodes as receivers have been investigated, that permit to compensate in a differential scheme the inevitable Silicon photoreceiver degradation under irradiation. In the present study, we compare state-of-the-art photorelays that means optocouplers with a combination of a photodiode array with some threshold electronics and a high power MOS-transistor output for the receiving parts, with a traditional type optocoupler with phototransistor output regarding their radiation hardness.

2   Experimental

2.1   Investigated Devices

The first-investigated device type (CNY75C from VISHAY) is a conventional opto-coupler with an IR-LED as emitter and high gain Silicon phototransistor with separate connectable base as receiver. This particular type has a high current-transfer-ratio (CTR) [5], specified to exceed a value of 150% for a LED input current of 10 mA [6]. During operation the base contact has not necessarily been contacted, even if appropriate additional biasing can optimize system performance, but in our case the separate base contact of the device under test was very useful, because charge carrier photo-generation properties and transistor gain and the influence of irradiation on these parameters can be checked independently. The second type is a TOSHIBA TLP3542 photorelay. This latter type has also an IR-LED as emitter and a receiver, composed of a photodiode array, a decision circuit and output power MOSFETs with a maximum output current of 2.5 A and a very low ON-state resistance of 100 mΩ that is specified to be achieved for LED input currents above 3 mA [7].
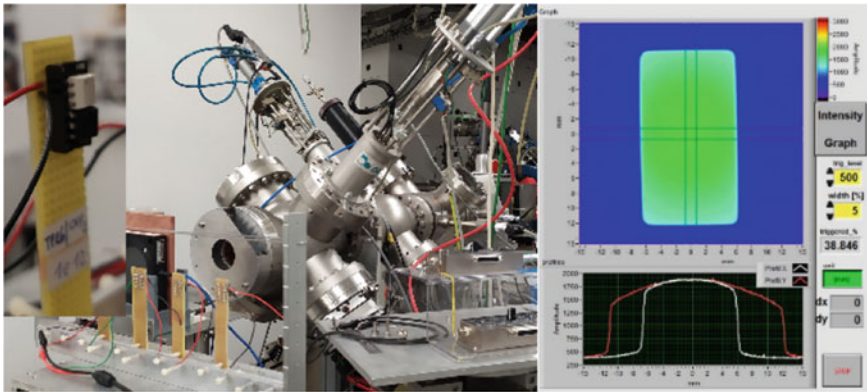
Fig. 1 **a** Intensity (x–y) plot and x-axis and y-axis intensity distributions of the proton beam with an approximated area of 10×20 mm and **b** irradiation setup with mounted samples (see photo on the left side)

2.2 Proton Irradiation Setup and Conditions

The irradiation has been done at the Helmholtz-Zentrum Berlin (HZB) cyclotron with a proton energy of 68 MeV. At this high energy, a homogeneous irradiation of the devices under test in the z-direction is given. For the calculation of the generated defect profile along the z-direction the SRIM-code [8], a Monte Carlo-based simulation tool has been used. The initial proton beam has been widened and, using an appropriate mask, a 10×20 mm wide area has been irradiated.

This allowed us to contemporarily irradiate both type of optocouplers in a single run. The irradiation spot and the mounted devices are shown in Fig. 1. Three different values of the proton fluence of 1e11, 3e11, and 1e12 protons/cm^2, respectively, have been used.

3 Results and Discussion

3.1 Optocoupler In-Situ LED Degradation Monitoring

Because it is impossible to measure the output power of the input LED independently, we monitored in-situ during irradiation the current induced by the irradiating beam in the LED. This radiation-induced current is larger than the beam current itself, because each particle creates an elevated number of electron–hole pairs in the active layer of the LED that can then be measured at the contacts as a short circuit current. Because it is known, that emission and photovoltaic properties of optoelectronic devices are often related [9, 10], this characterization can give a first indication of

Fig. 2 Comparison of the
normalized current, induced
by the proton irradiation in
the LED diodes of the two
types of optocouplers
(bipolar type: black full trace
and MOS type: blue dotted
line) as a function of the
proton fluence
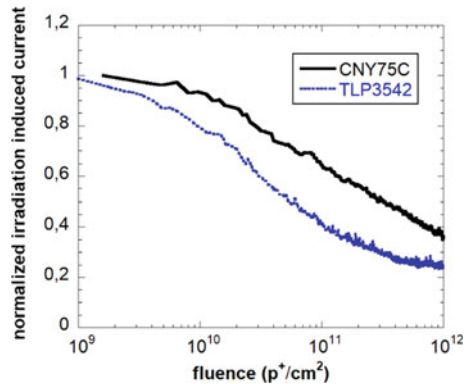
the degradation of the LED emission as well. Degradation of the GaAs layer in a triple junction solar cell with a GaAs middle junction, irradiated with protons of the same energy (68 MeV), as used for the present experiment, has been recently reported [11].

Comparing the change of the radiation-induced current for the both types of devices (see Fig. 2), we observe an initial stronger decrease for the TLP3542 type, that however, tends to saturate for higher fluence values.

At a fluence of 1e12 protons/cm^2 still a slightly higher decrease to about 24% of the initial value has been observed and a decrease to 36% of the original value for the CNY75C device.

3.2 Bipolar Optocoupler Stability Under Radiation

Also regarding the output characteristics of the bipolar optocoupler degradation, we performed an in-situ experiment, which is shown in Fig. 3. In the inset, the measurement configuration has been sketched: The input LED has been powered by a 9 V battery and a 470 Ω series resistance. The resulting output current values normalized to the LED input current is also a measure of a kind of current-transfer-ratio, but utilizing one of the transistor junctions as photodiode type receiver. This operation type is made possible because the base contact of the phototransistor can be separately contacted. The disadvantage of the photodiode type receiver configuration is of course the much lower current-transfer-ratio (CTR) value, but on the other hand this type of operation permits to operate at higher frequencies.

Before and after irradiation, the bipolar optocouplers devices have been characterized in detail. In particular current–voltage characteristics of the input LED and of the base-emitter and base–collector diodes, the latter with and without LED irradiation with different current values have been done. As an example, we show in Fig. 4 the base–emitter diode dark I–V characteristics of the CNY75C with and without irradiation (with a fluence value of 1e12 protons/cm^2). After irradiation, we observe
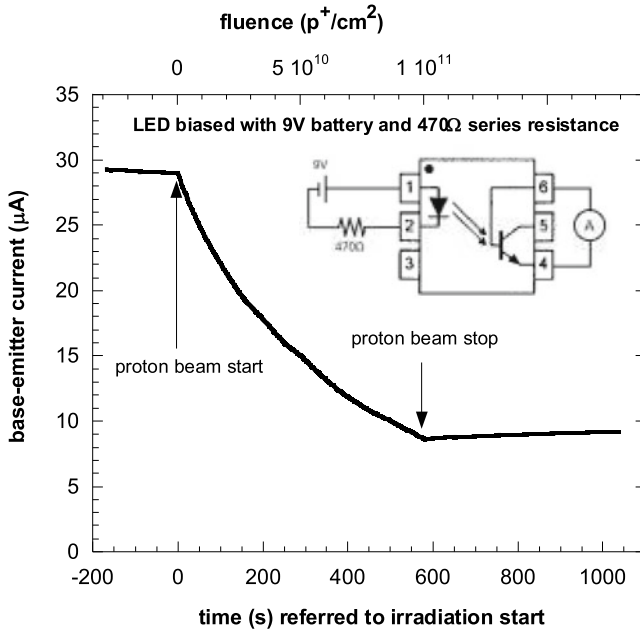
Fig. 3 Monitoring of the phototransistor base-emitter photocurrent of a CNY75C type optocoupler before, during and after proton irradiation. The input LED is biased with a 9 V battery and a 470 Ω series resistance (as shown in the inset)

clearly changes in the low and high voltage ranges. At low voltage, an increase of the saturation current and of the ideality factor due to an increase of recombination and in the high current regime, a decrease of the dark current due to the increase of the diode series resistance (in the demonstrated case, for example, from a value of 6.71 Ω to a value after irradiation of 8.32 Ω). Similar behavior has been reported in the literature [12]. As can be seen, we do observe a constant photocurrent value of 0.029 A before irradiation that decreases during irradiation by about a factor of 3. After the end of the irradiation (fluence value of 1e11 protons/cm^2), the monitored current starts again to increase slightly, indicating the beginning of an annealing process of radiation-induced defects. This has also been reported after the irradiation of amorphous Silicon [13] solar cells.

It should be mentioned that the increased recombination rate due to proton irradiation has also been confirmed by junction reverse-recovery experiments that due to the limited space will not be shown here.

As an example of the optocoupler overall performance before and after the different irradiation levels, the measurement of the collector current, with a source measurement unit as a function of the applied collector emitter voltage up to a value of 10 V, for a constant LED input current of 10 mA, is shown in Fig. 5. A monotonic and strong decrease of the collector current with irradiation, and hence of the CTR

Fig. 4 Comparison of the current–voltage characteristics of the phototransistor base-emitter junction of an CNY75C optocoupler with (dotted line) and without (full line) proton irradiation (1e12 protons/cm^2)
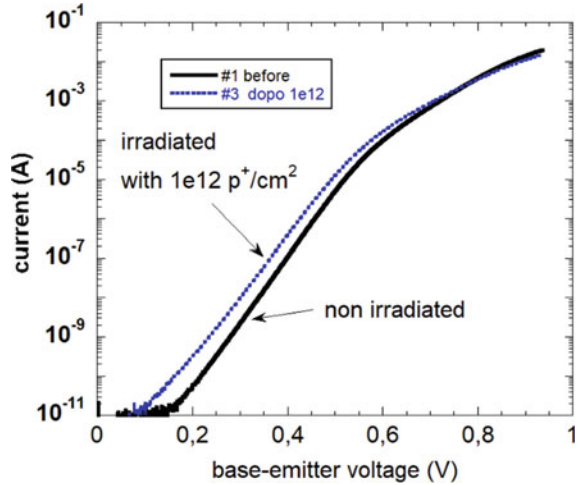
value, can be observed with a more than three orders of magnitude decrease in case of the highest fluence.

In order to determine the contribution of the different effects on the overall performance degradation in Table 1, the remaining factors of key measurement parameters are listed for the different irradiation levels. The initial values before degradation are the following: A base-emitter junction photocurrent ($I_{\text{ph be}}$) for a 10 mA LED current of 17.6 μA, a CTR value at $I_{\text{LED}} = 10$ mA and $V_{\text{CE}} = 2$ V of 200, 8% and a very high common emitter current gain (β), measured for a constant base-current (I_{b}) of 20 μA, with a value of 734. It can be clearly seen that the main contribution decrease of the CTR value with increasing irradiation level is due to the responsivity changes of the photosensitive part of the phototransistor and that the decrease of the LED

Fig. 5 Comparison of the collect current of the CNY75C characteristics of the phototransistor of an CNY75C optocoupler for a constant LED current value of 10 mA without and with different levels of proton irradiation (between 1e11 and 1e12 protons/cm^2)
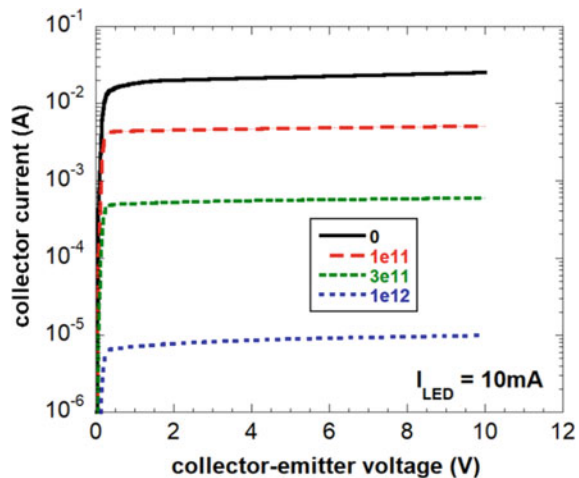
Table 1 Remaining factors of CNY75C optocoupler parameters measured for devices that have been irradiated with 3 different proton fluence values

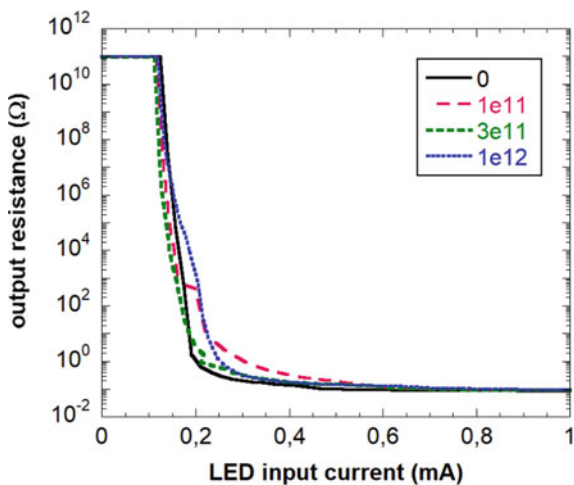| Fluence (p^+cm^{-2})	Normalized LED radiation-induced current	I_{ph} be for $I_{LED} = 10$ mA	β for $I_b = 20\,\mu A$	CTR for $I_{LED} = 10$ mA and $V_{CE} = 2$ V
1e11		0.2560	0.812	0.25,500
3e11		0.0355	0.622	0.00,259
1e12	0.361	0.00,107	0.345	0.00,039

efficiency and of the transistor gain gives only a minor contribution to the overall degradation of this type of optocoupler.

3.3 MOS Photorelay Stability Under Irradiation

Regarding the test of the photorelay, even if this optocoupler has a more complex receiver circuit, only few key parameters are accessible for testing. The most important characterization is the measurement of the device output resistance as a function of the input LED current. Such a characterization is shown in Fig. 6, for a non-irradiated device and devices, irradiated with 3 different irradiation levels.

These values, together with the normalized RIC change, measured during the in-situ characterization of the input LED of the second type of optocoupler, are plotted in Table 2, as a function of the irradiation level. It can be observed that only the RIC shows a significant degradation with increased irradiation level, while only minor increases of the threshold current for a given output resistance and of the output resistance for a given input current can be observed. Even after the proton fluence of

Fig. 6 Optorelay output resistance as a function of the LED current for non-irradiated [black full line] and with different fluences up to 1e12 protons/cm^2 irradiated devices (colored dotted lines)

Table 2 Normalized LED recombination induced current, LED threshold current at an output resistance (R_{out}) value of 1 Ω and optocoupler output resistance (R_{out}) at a fixed I_{LED} value of 1 mA for the TLP3542, for different proton fluences

Proton fluence (p^+cm^{-2})	Normalized LED radiation-induced current	$I_{threshold\ LED}$ (mA) for $R_{out} = 1\ \Omega$	R_{out} (mΩ) for $I_{LED} = 1$ mA
0	1	0.196	84.4
1e11	0.466	0.302	89.9
3e11	0.271	0.232	91.3
1e12	0.221	0.244	93.5

1e12 protons/cm^2, the output resistance is lower than the maximum value, specified in the datasheet, of 100 mΩ. This means that this type of optocoupler is much more tolerant to higher irradiation levels than the classical type.

Important parameters that can be obtained from this characteristics are the threshold LED current, necessary to obtain a low output resistance value (e.g., a value of 1 Ω), and on the other hand the output resistance value for a given constant LED current of 1 mA.

3.4 Optocoupler Switching Time Changes Due to Irradiation

Besides the static characterization measured before and after irradiation. These measurements comprised reverse-recovery measurements of the input LEDs and in the case of the bipolar optocouplers also of the base-emitter and base–collector junctions. It can be stated that only for the LED of the CNY75C type optocoupler and of the base-emitter and base–collector junctions of the phototransistor, charge carrier storage during reverse-recovery experiments has been observed that has been successively lowered by proton irradiation due to the increased charge carrier recombination rates.

The comparison of the influence of the proton irradiation on the switching times of both types of optocouplers is summarized in Fig. 7.

It can be seen that before irradiation faster switching is obtained with the bipolar coupler, with increasing proton fluence the switch-off times slightly decrease. This is probably due to the reduced storage time in the neutral diode region. The switch-on times for both types of devices, however, increase with increasing proton fluence. In particular, the bipolar optocoupler switch-on times increases for more than one order of magnitude as compared to the non-irradiated reference device. It should be mentioned that an earlier study on power MOSFET-based optocouplers under high energy radiation showed an influence of radiation on the switching speed also for this type of optocouplers [14]. This could not be confirmed in the present study on new commercial power MOSFET devices. While it has been proposed to utilize eventually a completely different scheme for radiation-hard optocouplers by replacing, for

Fig. 7 Influence of the
proton fluence on the
switching times of bipolar
type (CNY75C) and
photorelay type (TLP3542)
optocouplers. The lines are
exponential fits to the data
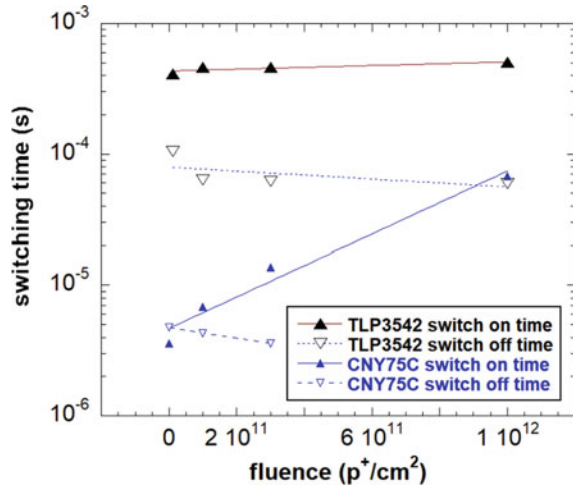
example, the input LED by a Vertical Cavity Surface Emitting Lasers (VCSELs) [15], here it has been shown that also the utilization of a different output stage can result in a rather radiation tolerant optocoupler, maintaining the conventional IR-LED as emitter in the input stage of the device.

4   Conclusions

The ability of optocouplers either with conventional phototransistor output or with a more complex receiver configuration with a photodiode array, a decision circuit and high power output MOS transistors has been tested to withstand high energy particle irradiation. In order to understand the overall performance and also to determine the weakest part of the devices that can cause failure under space conditions, a series of in-situ and ex-situ characterization techniques have been applied. It has been found that the more complex MOS-based "photorelay" can withstand high particle fluences up to $1e12$ protons/cm^2 with static and dynamic parameters still within the specifications. The bipolar technology-based conventional optocoupler shows serious degradation already for fluences below $3e11$ protons/cm^2. In particular, it could be demonstrated that this degradation is mainly caused by the photoreceiver properties of the phototransistor and only to a minor content due to the LED efficiency degradation and to the current gain loss of the phototransistor. Besides the degradation of the static characteristics, in the case of the optocoupler with bipolar output phototransistor, also an important increase of the switch-on time with increasing proton fluence has been observed.

References

1. Li D, Dong G, Li W, Wang L (2015) High performance organic-inorganic perovskite-optocoupler based on low-voltage and fast response perovskite compound photodetector. Sci Rep 5:7902
2. Reed RA, Marshall PW, Johnston AH, Barth JL, Marshall CJ, LaBel KA, D'Ordine M, Kim HS, Carts MA (1998) Emerging optocoupler issues with energetic particle-induced transients and permanent radiation degradation. IEEE Trans Nucl Sci 45:2833–2841
3. Gorelick JL, Ladbury R (2004) Proton, neutron, and gamma degradation of optocouplers. IEEE Trans Nucl Sci 51:3730–3735
4. Miyahira TF, Johnston AH (2007) Trends in optocoupler radiation degradation. IEEE Trans Nucl Sci 49:1104–1109
5. RENESAS: Current Transfer Ratio (CTR) and response time of photocouplers/optocouplers. https://www.renesas.com/us/en/products/interface-connectivity/optoelectronics/current-transfer-ratio-ctr-and-response-time-photocouplers-optocouplers
6. VISHAY: Datasheet CNY 75C (1999). https://www.vishay.com/docs/83536/83536.pdf
7. TOSHIBA: Datasheet TLP3542 (2019). https://toshiba.semicon-storage.com/eu/semiconductor/product/isolators-solid-state-relays/photorelay-mosfet-output/detail.TLP3542.html
8. Ziegler JF, Ziegler MD, Biersack JP (2010) The stopping and range of ions in matter. Nucl Instrum Methods Phys Res B 268:1818–1823
9. Neitzert HC, Ferrara M, Kunst M, Denker A, Kertesz Z, Limata B, Gialanella L, Romano M (2008) Electroluminescence efficiency degradation of crystalline silicon solar cells after irradiation with protons in the energy range between 0.8 MeV and 65 MeV. Phys Stat Sol (b) 245:1877–1883
10. Mchedlidze T, Mahabubul Alam M, Herguth A, Weber J (2021) In situ observation of the degradation in multi-crystalline Si solar cells by electroluminescence. Phys Stat Sol A 216:1800918
11. Lang F, Eperon GE, Frohna K, Tennyson EM, Al-Ashouri A, Kourkafas G, Bundesmann J, Denker A, West KG, Hirst LC, Neitzert HC, Stranks SD (2021) Proton-radiation tolerant all-perovskite multijunction solar cells. Adv Energy Mat 11:2102246
12. Sujatha R, Damle R, Kumar D (2020) Electron beam induced degradation in electrical characteristics of optocoupler. IEEE Trans Device AMD Mater Reliab 20:737–741
13. Neitzert HC, Landi G, Lang F, Bundesmann J, Denker A (2021) In situ stability test of a small amorphous silicon energy harvesting array under space conditions. In: Di Francia G, Di Natale C (eds) Sensors and microsystems, proceedings of the AISEM 2020 Regional workshop, lecture notes in electrical engineering, vol 753. Springer, Berlin, pp 131–138
14. Johnston AH, Miyahira TF (2007) Radiation damage in power MOSFET optocouplers. IEEE Trans Nucl Sci 54:1104–1109
15. Gilard O, Del Vecchio P, Moglia R, Béchou L, Quadri G (2012) Hardening principles and characterization of an optocoupler including a vertical cavity surface emitting laser. IEEE Trans Nucl Sci 59:1717–1721

Infant Crying Patterns' Analysis Using Machine Learning

Viktoria-Nikoleta Tsakalidou, Eleni Vrochidou, and George A. Papakostas

Abstract Communication is the most important process for a living organism. Autism is a complex developmental disorder that causes communication problems. The only way to communicate for babies is through crying, so screening analysis is an attractive approach to early diagnosis of autism to improve recovery. The aim of this paper is to explore the potential of machine learning (ML) in babies' crying decoding toward autism diagnosis, pain identification, baby needs, etc. An extended literature review on the subject has been made to provide sensible comparisons between recently introduced ML approaches. Research findings reveal that ML can facilitate infant needs decoding and early diagnosis through crying pattern analysis; however, available infant crying datasets are scarce.

Keywords Autism diagnosis · Machine learning · Pattern recognition · Baby cry · Sound analysis · Artificial intelligence · Human–computer interface · Review

1 Introduction

Every year, 100 million children are delivered globally. The proper and conscious care of newborns is challenging for new parents. Reading baby books or discussing with other parents who already have children is not enough to understand the needs of a newborn regarding its health and mental state. The latter is difficult since during the growing period senses are not fully formed. Babies mainly communicate by crying; they cannot speak and don't have full control of their bodies. New parents are getting

V.-N. Tsakalidou · E. Vrochidou · G. A. Papakostas (✉)
MLV Research Group, Department of Computer Science, International Hellenic University, Kavala, Greece
e-mail: gpapak@cs.ihu.gr

V.-N. Tsakalidou
e-mail: vitaaka@cs.ihu.gr

E. Vrochidou
e-mail: evrochid@cs.ihu.gr

distressed and face difficulties to calm down their newborns since all crying sounds seem identical. Accurately, decoding infants' cry sounds could facilitate new parents taking proper care of the newborns.

Analysis of babies' cries was introduced in the Nineteen Sixties once Wasz-Hockert identified four kinds of crying (pain, hunger, birth cry, and pleasure), using the expert knowledge of well-trained nurses [1]. Earlier research has shown that alternative types of screams can be discriminated acoustically by experienced listeners; yet, it is maybe more difficult to train a human to discriminate children crying, compared to train machine learning models. According to a study conducted by Mukhopadhyay [2], when a group of adults was trained to distinguish screaming sounds, the optimal reported accuracy of correct recognition was 33.09%. Machine learning algorithms that rely on prosodic and spectral features were able to discriminate the same data set and reached an 80.56% of correct classification rate. Developing intelligent tools able to decode infant crying would help young parents to understand the infants' daily needs, as well as provide insights toward early disease prediction, which is another crucial issue in infant crying research.
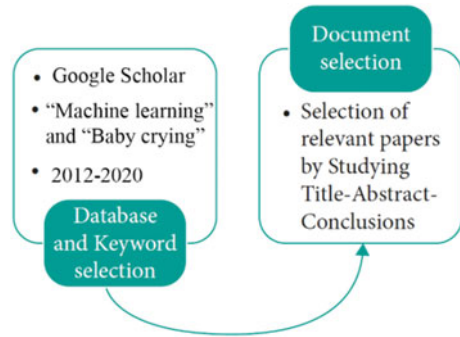
Researchers would be able to decide whether a baby is healthy or not, by studying and decoding the crying signals of unhealthy babies. This is due to the fact that unhealthy babies crying signals have different characteristics from that of healthy ones. Therefore, researchers would be able to understand if the child is autistic, has asphyxia, etc. Infant crying analysis presupposes crying data collection, data processing, feature extraction, feature selection, and classification.

Since infant crying data are considered sensitive data, it has been challenging for scientists to accumulate the required data for their research. Most commonly, researchers have to self-record baby crying or they need to acquire permission for datasets recorded from different research teams. The majority of the reported datasets are captured in hospitals, newborn intensive care units (NICU), clinics, homes, etc. The crying signal is captured in random short-time periods or electronic recording devices are placed on babies' beds for an extended time-period to record infant crying more systematically [3].

Specifically, for children who may be autistic, the process of diagnosis begins in infancy through symptoms related to the developmental disorder and interpersonal communication disorder [4, 5]. Autism is a disorder that affects more and more people around the world. Even experienced physicians still base their results on the study of independent individual behavioral patterns and on their experience, aided by certain quantitative indicators. Based on a survey by the National Center for Health Statistics reported autism in children of ages 3–17 in the United States is 2.2%, while in China it is about 1% [6]. Toward standardized early diagnosis, the Autism Diagnostic Observation Schedule (ADOS) program was established. ADOS is an observation scale developed to distinguish social behavior and communication in children and adults who are examined as possible patients of autism spectrum disorder [7]. Initially, the program was available as a tool for researchers and later, in 2001, was distributed publicly through Western Psychological Services [8]. Since then, it has been widely used in schools, communities, research settings, and clinics. ADOS is commonly used along with Autism Diagnostic Interview-Revised [9]. At

the same time, research studies started to investigate the prognostic value of behavioral and neurobiological measures in autism spectrum disorder (ASD) in order to enable a future diagnosis tool aided by a computer. This kind of research usually applies classification methods based on machine learning algorithms toward the prediction or classification of people into certain groups. Machine learning indicates all processes that involve the training of an algorithm to identify patterns in data, called an 'attribute' that can be subsequently used to predict new topics. Learning techniques based on, e.g., support vector machines (SVM) [10] are in need of a well-defined data set in order to derive the classification algorithm that best separates distinct classes. In the majority of the research works, pattern classification methods have been applied to neuroanatomical data measured by structural magnetic resonance imaging [11, 12], diffusion tensor imaging [13–15] or data analysis for automated voice analysis which has reported promising results [16].

This paper aims to review the applications of machine learning in baby crying decoding. Many research papers on the subject are available. The contribution of this work is the revision of the most up-to-date methodologies, along with the used features. Moreover, all available datasets on infant crying are collected and presented, highlighting the lack of public datasets on this particular problem. All referenced literature was collected through "Google scholar", regarding literature published between 2012 and 2020. The keywords used were machine learning along with baby crying. The conceptual illustration of the proposed work is presented in Fig. 1.

The structure of this paper is as follows. Section 2 presents related work regarding machine learning applications based on baby crying. In Sect. 3, a discussion and a comparison of the data used in the referenced research articles take place. Section 4 discusses the features and models that are used. Finally, Sect. 5 concludes the paper.

2 Related Work

In recent years, many researchers used alternative classification models for infant crying processing. Their effort is on improving the classification accuracy of infant

crying, involving differentiation between pathological and normal cries and, thus, understanding the significance of crying. In this section, indicative-related work in the field of children crying patterns processing is presented, including crying decoding in general, i.e., autism diagnosis, pain identification, baby needs, etc.

In [17] the authors tried to automatically recognize, if a baby's crying was triggered by pain. The dataset that was used was the iCOPE (pain vs. no pain). The features that were used were Mel Scale (MS), Constant-Q Chromagram (CQC), MFCC, Local Binary Pattern (LBP), Robust Local Binary Pattern (RLBP), and Local Phase Quantization (LPQ). The machine learning model that was used was an SVM. The reported performance was 71.68%. Results revealed that data augmentation could not result in significant improvement in the accuracy due to the fact that the limited data were not able to describe the range of alterations in infant crying signals.

In [18], a baby communication algorithm based on the Gaussian Mixture Model was presented. The dataset that was used was called "Donate A Cry", which is available online [19]. The results were promising with 81.27% accuracy on a dataset of 714 baby cries and for different types of crying.

The researchers in [20] proposed an application of a convolutional neural network (CNN), where the CNN recognized the so-called Dunstan baby language that consisted of five "words" or phonemes used by babies of age under 3 months to communicate their needs before they start crying. The used dataset was the Dunstan Baby Database [21], including needs such as hunger, pain, discomfort, etc., while the used features were spectrograms. The proposed architecture was trained for a set of 250 small-duration recordings and was tested for other 65 recordings with a recognition rate of 89% for the length of all audio files being less than one second. The recordings were extracted from certified Dunstan language recordings.

The research reported in [22] proposed a method for the timely diagnosis of children with autism, in which acoustic features were used for crying sounds. Research on autism prediction based on crying is limited; autism is commonly predicted through functional magnetic resonance imaging (fMRI) [23] or electroencephalography [24]. The used datasets in [22] were self-recorded. The feature extraction methods included wavelet decomposition coefficient, Mel Frequency Cepstral Coefficients (MFCC) with Discrete Wavelet Transform (DWT-MFCC), MFCC and Linear Prediction Cepstrum coefficient (LPCC). The authors used two machine learning models, SVM and CNN. From their results, it was revealed that MFCC features with SVM and CNN reported the optimal correct classification rate, while DWT-MFCC demonstrated the most stable performance in five distinct signal-to-noise ratios (SNRs).

The goal of the authors in [25] was the comparison of the performance of the Daubechies wavelet family in baby crying classification. They used a Probabilistic Neural Network (PNN) and a General Regression Neural Network (GRNN) toward the classification of baby crying signals. The dataset they used was called "Baby Chillanto" [26], belonging to the Instituto Nacional de Astrofísica Optica y Electronica (INAQE)—CONACYT, in Mexico [27]. The used features were the Wavelet and the Packet Transform. The proposed methodology reported 99% performance accuracy.

In [28], a machine learning system, called Ubenwa, was introduced, to enable the diagnosis of asphyxia through automated analysis of the infant's cry. The method was deployed via a smartphone and wearable technology. The used dataset was called "Baby Chillanto". The used features were the MFCC, while the achieved accuracy was 85% with an SVM model.

The authors in [29] presented a method to recognize if the baby had asphyxia or not (normal case) through the baby crying analysis. The used dataset was again the "Baby Chilllanto" for asphyxia and a self-recorded dataset for the normal case. MFCC and SVM were used as the features and the classification model. Results indicated that SVM with RBF kernel could lead to a good performance with an accuracy of 95.86%.

The goal of the authors in [30] was to recognize through infant crying whether a child was autistic or not. The features that they used were logarithmic energy, Audio power, SONE, Total loudness, First MFCC coefficient, Zero-Crossing Rate (ZCR). All features were applied to MFCC and Spectral flatness. The authors proposed an SVM model. The dataset was self-recording with autism spectrum disorder (ASD) and typically developed (TD) boys. The corresponding results were in terms of sensitivity 85.71%, specificity 100%, and precision of the proposed approach for boys 92.85%. The same measures for girls were, respectively, 71.42%, 100%, and 85.71%.

The authors in [31] tried to find potential signs of early ASD appearance in a group of high-risk patients, evaluated against a control group, relying on the fundamental and the vocal tract resonance frequencies. The used dataset was self-recorded and captured by BioVoice, a custom software. The results revealed that high-risk newborns could be discriminated against the healthy ones.

In [32], the goal was to investigate if autistic infants from an early age show differences in vocal production. The features that were used were the $F0$ frequency and the phonation (voicing). The data were self-recorded according to the Autism Diagnostic Observation Schedule—Generic (ADOS-G) [7].

The research in [33] determined if a regular movement of the upper-limb could be used to classify with accuracy low-functioning children with ASD of ages between 2 and 4. The authors used the ADOS [7] software. The proposed learning model was an SVM and the used data were self-recorded from the authors' institute by utilizing the Griffiths Mental Development Scales [34]. Results reported an accuracy of 96.7%.

Table 1 summarizes the above-mentioned-related work by pointing out some useful characteristics.

3   Datasets

Baby crying datasets are scarce. As it can be observed in Table 2, the data that researchers used to identify either autism or other classes are limited. Table 2 includes all datasets found in the literature and is not limited to the datasets used in the referenced related work. The lack of adequate datasets is attributed to the sensitivity of

Table 1 Related work for diagnosis via baby crying pattern analysis

Ref.	Features	Classifier	Performance	Dataset
[17]	MS MFCC CQC LBP LPQ RLBP	SVM	71.68	iCOPE
[18]	Mean frequency and standard deviation	K-means clustering	81.27	Donate A Cry
[20]	Spectrogram	CNN	89	Dunstan Baby Database
[22]	MFCC	SVM and CNN	Up to 92.33	Self-recorded
[25]	Wavelet packet transform	PNN, GRNN	99	Baby Chillanto
[28]	MFCC	SVM	85	Baby Chillanto
[29]	MFCC	SVM	95.86	Baby Chilllanto asphyxia and self recorded
[30]	MFCC SONE ZCR	SVM	85.71	Self-recorded
[31]	Fundamental frequency $F0$	Using BioVoice, a custom software	Up to 100	Self-recorded
[33]	FDR	SVM	96.7	Self-recorded

the data collection process for the baby's crying and the sensitivity around babies in general. Additionally, data collection and labeling are time-consuming and require experts' knowledge. It is observed that most researchers collected the data themselves either from clinics that work with or asked permission to receive data from other researchers. In all cases, researchers have to deal with the bureaucracy related to ethics, to wait for their research to be approved in order to proceed with data collection. However, there is a small number of datasets publicly available, as it can be seen in Table 2. Yet, most datasets are with limited samples.

Some of the available datasets are extracted from the Donate A Cry campaign [19], and the Dunstan Baby Database which is on payment. The available data related to autism are even less. The data on babies' needs, e.g., if the baby is hungry or in pain or drowsy, etc., are more common compared to the available data on autism. Having data available on autism, which is considered an important and complex issue, could offer opportunities for efficient results of early diagnostic systems and for timely treatment. Moreover, as a general observation, due to the lack of datasets, it is hard to directly compare the performance of different methodologies that are tested on different datasets. The classes with respect to infant crying a mainly related to current needs, such as hungry, pain, discomfort, tiredness, lonely, scared, etc., or to an underlying issue, such as autism, asphyxia, etc.

Table 2 Available infant cry datasets

Ref.	Total data	Classes	Type of dataset
[17]	113	42 pain 71 no pain	Self-recorded named iCOPEaudio
[18]	714	9 Groups (hungry, needs burping, belly pain, discomfort, tired, lonely, cold/hot, scared, don't know)	Donate A Cry [19]
[20]	315	65 train and 50 pain 50 hunger 50 discomfort 50 need to burp 50 belly pain	Dunstan Baby Database [21]
[22]	28	18 typically developed and 10 with ASD	Self-recorded at Hospital of Anhui medical university
[25]	1.726	507 normal 879 deaf signals and 340 asphyxia	Baby Chillanto [26], Instituto Nacional de Astrofisica Optica y Electronica (INAQE)—CONACYT, Mexico
[28]	69	Normal asphyxiating and deaf infants	Baby Chillanto [26]
[29]	338	169 normal and 169 asphyxias	Baby Chilllanto [26] asphyxia and self recorded
[30]	62	31 ASD and 31 typically developed	Self-recorded
[31]	24	17 control cases and 7 high-risk	Self-recorded from parents and Istituto Superiore di Sanita, IRCCS Fondazione Stella Maris, and IRCCS Pediatric Hospital Bambino Gesu
[33]	30	15 ASD and 15 typically developing children	Self-recorded from their institute by utilizing the Griffiths Mental Development Scales

4 Discussion

According to Table 1, one can notice that most researchers collect their own data with parental or clinical approval. This is due to data sensitivity, where are restrictions and regulations in certain countries putting barriers in combining multiple sources. In addition, depending on the applied research different characteristics of the baby crying need to be extracted. The most commonly used feature is the Mel Frequency Cepstral Coefficients (MFCC), which is a finite set of features (including about 10–20 values) that concisely defines the entire shape of a spectral envelope. It is usually used to describe timbre. Additionally as shown in Table 1 different learning models are employed. However, the most common is Support Vector Machines (SVM). This is because SVMs can handle a large number of features effectively and report high performance when categorizing objects between two categories. As it can be observed from the results summarized in Table 1, the success rates range from 80% up to 100%. However, for their results, each researcher used a different dataset, therefore the methods cannot be directly compared. It would be a great success in

the future, if researchers in the field could use the same data for comparative reasons, so as to conclude with the most valid methodology.

5   Conclusions

Computer innovation progress has supported the collection and processing of high-resolution images and voice recordings. These improvements have revolutionized the fields of medical imaging and machine learning. In this work, the most critical aspects of machine learning in infant cry analysis are reviewed. Research findings revealed that machine learning could provide accurate predictions, reaching high classification accuracies, especially by using the SVM model. The emerging potentials of machine learning are multiple, as it could have a great impact on medicine, e.g., in infant autism diagnosis. However, publicly available datasets are scarce in the literature and researchers have to collect data themselves either in collaboration with a clinic, or from schools, etc. Future work should focus on collecting data and on creating a publicly available large dataset, on the extraction of effective features and the investigation of novel model machine learning architectures toward enhanced classification performances.

References

1. Wasz-Höckert O, Partanen TJ, Vuorenkoski V, Michelsson K, Valanne E (1964) The identification of some specific meanings in infant vocalization. Experientia 20:154–154. https://doi.org/10.1007/BF02150709
2. Mukhopadhyay J, Saha B, Majumdar B, Majumdar AK, Gorain S, Arya BK, Bhattacharya SD, Singh A (2013) An evaluation of human perception for neonatal cry using a database of cry and underlying cause. In: Indian conference on medical informatics and telemedicine (ICMIT). IEEE, pp 64–67. https://doi.org/10.1109/IndianCMIT.2013.6529410
3. Ji C, Mudiyanselage TB, Gao Y, Pan Y (2021) A review of infant cry analysis and classification. EURASIP J Audio Speech Music Proc 8(2021). https://doi.org/10.1186/s13636-021-00197-5
4. Werling DM, Geschwind DH (2013) Sex differences in autism spectrum disorders. Curr Opin Neurol 26:146–153. https://doi.org/10.1097/WCO.0b013e32835ee548
5. Bremer E, Balogh R, Lloyd M (2015) Effectiveness of a fundamental motor skill intervention for 4-year-old children with autism spectrum disorder: a pilot study. Autism 19:980–991. https://doi.org/10.1177/1362361314557548
6. Zablotsky B, Black LI, Maenner MJ, Schieve LA, Danielson ML, Bitsko RH, Blumberg SJ, Kogan MD, Boyle CA (2019) Prevalence and trends of developmental disabilities among children in the United States: 2009–2017. Pediatrics 144. https://doi.org/10.1542/peds.2019-0811

7. Lord C, Risi S, Lambrecht L, Cook EH, Leventhal BL, Dilavore PC, Pickles A, Rutter M (2000) The autism diagnostic observation schedule-generic: a standard measure of social and communication deficits associated with the spectrum of autism. J Autism Dev Disord 30:205–223. https://doi.org/10.1023/A:1005592401947

8. Lord C, Rutter M, Goode S, Heemsbergen J, Jordan H, Mawhood L, Schopler E (1989) Austism diagnostic observation schedule: a standardized observation of communicative and social behavior. J Autism Dev Disord 19:185–212. https://doi.org/10.1007/BF02211841

9. Le Couteur A, Lord C, Rutter M (2003) The autism diagnostic interview- revised

10. Vapkin NV (1995) The nature of statistical learning theory

11. Ecker C, Marquand A, Mourao-Miranda J, Johnston P, Daly EM, Brammer MJ, Maltezos S, Murphy CM, Robertson D, Williams SC, Murphy DGM (2010) Describing the brain in autism in five dimensions-magnetic resonance imaging-assisted diagnosis of autism spectrum disorder using a multiparameter classification approach. J Neurosci 30:10612–10623. https://doi.org/10.1523/JNEUROSCI.5413-09.2010

12. Ecker C, Rocha-Rego V, Johnston P, Mourao-Miranda J, Marquand A, Daly EM, Brammer MJ, Murphy C, Murphy DG (2010) Investigating the predictive value of whole-brain structural MR scans in autism: a pattern classification approach. Neuroimage 49:44–56. https://doi.org/10.1016/j.neuroimage.2009.08.024

13. Lange N, DuBray MB, Lee JE, Froimowitz MP, Froehlich A, Adluru N, Wright B, Ravichandran C, Fletcher PT, Bigler ED, Alexander AL, Lainhart JE (2010) A typical diffusion tensor hemispheric asymmetry in autism. Autism Res 3:350–358. https://doi.org/10.1002/aur.162

14. Ingalhalikar M, Parker D, Bloy L, Roberts TPL, Verma R (2011) Diffusion based abnormality markers of pathology: toward learned diagnostic prediction of ASD. Neuroimage 57:918–927. https://doi.org/10.1016/j.neuroimage.2011.05.023

15. Deshpande G, Libero LE, Sreenivasan KR, Deshpande HD, Kana RK (2013) Identification of neural connectivity signatures of autism using machine learning. Front Hum Neurosci 7:670. https://doi.org/10.3389/fnhum.2013.00670

16. Oller DK, Niyogi P, Gray S, Richards JA, Gilkerson J, Xu D, Yapanel U, Warren SF (2010) Automated vocal analysis of naturalistic recordings from children with autism, language delay, and typical development. Proc Natl Acad Sci 107:13354–13359. https://doi.org/10.1073/pnas.1003882107

17. Felipe GZ, Aguiar RL, Costa YMG, Silla CN, Brahnam S, Nanni L, McMurtrey S (2019) Identification of infants' cry motivation using spectrograms. In: International conference on systems, signals and image processing (IWSSIP). IEEE, pp 181–186. https://doi.org/10.1109/IWSSIP.2019.8787318

18. Sharma K, Gupta C, Gupta S (2019) Infant weeping calls decoder using statistical feature extraction and Gaussian mixture models. In: 10th international conference on computing, communication and networking technologies (ICCCNT). IEEE, pp 1–6. https://doi.org/10.1109/ICCCNT45670.2019.8944527

19. Gveres: Donate a Cry—Corpus. https://github.com/gveres/donateacry-corpus

20. Franti E, Ispas I, Dascalu M (2018) Testing the universal baby language hypothesis—automatic infant speech recognition with CNNs. In: 41st international conference on telecommunications and signal processing (TSP). IEEE, pp 1–4. https://doi.org/10.1109/TSP.2018.8441412

21. Smith J (2013) Calm the crying: using the Dunstan baby language, the secret baby language that reveals the hidden meaning behind an infant's cry. Libr J 240

22. Wu K, Zhang C, Wu X, Wu D, Niu X (2019) Research on acoustic feature extraction of crying for early screening of children with autism. In: 34rd youth academic annual conference of Chinese association of automation (YAC). IEEE, pp 290–295. https://doi.org/10.1109/YAC.2019.8787725

23. Karunakaran P, Hamdan YB, Sathish (2020) Early prediction of autism spectrum disorder by computational approaches to fMRI analysis with early learning technique. J Artif Intell Capsul Networks 2:207–216. https://doi.org/10.36548/jaicn.2020.4.003

24. O'Neill M, Shear T (2018) EEG for diagnosis of autism spectrum disorder. Pediatr Neurol Briefs 32:13. https://doi.org/10.15844/pedneurbriefs-32-13

25. Saraswathy J, Hariharan M, Vijean V, Yaacob S, Khairunizam W (2012) Performance comparison of Daubechies wavelet family in infant cry classification. In: IEEE 8th international colloquium on signal processing and its applications. IEEE, pp 451–455. https://doi.org/10.1109/CSPA.2012.6194767

26. Instituto Nacional de Astrofisica Optica y Electronica (INAQE). Baby Chillanto Database of infant cry. http://ingenieria.uatx.mx/orionfrg/cry/

27. Reyes-Galaviz OF, Cano-Ortiz SD, Reyes-García CA (2008) Evolutionary-neural system to classify infant cry units for pathologies identification in recently born babies. In: Seventh Mexican international conference on artificial intelligence. IEEE, pp 330–335. https://doi.org/10.1109/MICAI.2008.73

28. Onu CC, Udeogu I, Ndiomu E, Kengni U, Precup D, Sant'Anna GM, Alikor E, Opara P (2017) Ubenwa: cry-based diagnosis of birth asphyxia. 1711

29. Sahak R, Mansor W, Lee YK, Yassin AIM, Zabidi A (2010) Performance of combined support vector machine and principal component analysis in recognizing infant cry with asphyxia. In: Annual international conference of the IEEE engineering in medicine and biology. IEEE, pp 6292–6295. https://doi.org/10.1109/IEMBS.2010.5628084

30. Khozaei A, Moradi H, Hosseini R, Pouretemad H, Eskandari B (2020) Early screening of autism spectrum disorder using cry features. PLoS ONE 15:e0241690. https://doi.org/10.1371/journal.pone.0241690

31. Orlandi S, Manfredi C, Bocchi L, Scattoni ML (2012) Automatic newborn cry analysis: a non-invasive tool to help autism early diagnosis. In: Annual international conference of the IEEE engineering in medicine and biology society. IEEE, pp 2953–2956. https://doi.org/10.1109/EMBC.2012.6346583

32. Sheinkopf SJ, Iverson JM, Rinaldi ML, Lester BM (2012) A typical cry acoustics in 6-month-old infants at risk for autism spectrum disorder. Autism Res 5:331–339. https://doi.org/10.1002/aur.1244

33. Crippa A, Salvatore C, Perego P, Forti S, Nobile M, Molteni M, Castiglioni I (2015) Use of machine learning to identify children with autism and their motor abnormalities. J Autism Dev Disord 45:2146–2156. https://doi.org/10.1007/s10803-015-2379-8

34. Griffiths R (1970) The abilities of young children. A study in mental measurement

A Performance Evaluation Study to Optimize Encryption as a Service (EaaS)

Ahmed Y. A. Al-Tamimi, Mohammad Abu Snober, and Qasem Abu Al-Haija

Abstract Cloud computing is becoming adopted increasingly by organizations all around the world. This is because the cloud is proven more dependable, affordable, elastic, and secure than traditional storage. However, this rapid and huge growth has opened the door for a great number of threats against the data in the cloud. Therefore, EaaS "Encryption as a service" was proposed to protect the data at all times. In this paper, we study, evaluate, and analyze the performance of three cryptographic algorithms, 3DES, AES, and Blowfish in terms of encryption time, decryption time, and memory consumption (Throughput). The aim is to provide more insights into the implementation of each and determine which provides more security with lower memory cost and execution time to be used in the EaaS solution that depends on crypto-algorithms to secure data and privacy in a cloud environment.

Keywords Cloud computing · Encryption as a service (EaaS) · Cryptography · Advanced encryption standard (AES) · Triple data encryption algorithm (3DES) · Blowfish · Twofish · Asymmetric key algorithms · Symmetric-key algorithms · Encryption · Decryption · ECB

1 Introduction

Cloud computing is growing in a way that makes it more valuable for attackers to study and improve mechanisms to breach into cloud data, either while the data is at rest or in transit [1]. Therefore, a service called Encryption as a Service (EaaS) has been proposed to minimize the risks that could affect the data in the cloud using cryptography and to improve the cyber defense against several active and passive cyber-attacks [2].

A. Y. A. Al-Tamimi · M. A. Snober · Q. A. Al-Haija (✉)
Department of Computer Science/Cybersecurity, Princess Sumaya University for Technology (PSUT), Amman, Jordan
e-mail: q.abualahaija@psut.edu.jo

681

Cryptography could be referred to as a way to hide and protect data so that only authorized parties can access specific data. Cryptography is divided into encryption and decryption [3]. Encryption is converting the plain text into a different text called the cipher text, using different algorithms and a specific key. In contrast, decryption converts the cipher text back into plain text using the same algorithm used in encryption and a specific key. These algorithms could be asymmetric or symmetric key algorithms [4].

This paper examines and investigates the performance evaluation of three common cryptographic algorithms: AES, 3DES, and Blowfish in terms of encryption time, decryption time, memory consumption, and throughput. The aim is to provide more insights into the implementation of each and determine which provides more security with lower memory cost and execution time to be used in the EaaS solution that depends on crypto-algorithms to secure data and privacy in a cloud environment.

The leftover parts of this manuscript are structured as follows: Sect. 2 provides an essential theoretical background to fulfill the important knowledge required throughout this paper. Section 3 provides the details of the proposed model, including feature selection, machine learning modeling, the dataset, and cross-validation. Section 4 discusses the experimental results and Sect. 5 concludes the finding of this research paper.

2 Cryptographic Algorithms Overview

In this section, we provide a short systematic review to discuss the crypto-algorithms and the ones that were used to conduct the investigation study in this research.

2.1 Asymmetric Key Algorithms

These cryptographic algorithms use a unique key to encrypt data and a different one to decrypt it. So, the sender will encrypt the data he will send by using the receiver's public key, which might be publicly known. Then when the data arrives, only the intended receiver can get the original data by decrypting the cipher text using his private key [5]. Figure 1 illustrates the main processes in the asymmetric cryptographic systems.

One of the most known asymmetric key algorithms is RSA. RSA is considered one of the popular asymmetric key algorithms, and it is based on block cipher cryptography. RSA generates its' public and private keys using prime numbers. Typical key sizes in RSA are 1024, 2048, and 4096, where these keys will be used to encrypt and decrypt the data. Encryption uses the public key; and decryption uses the private key [6]. Usually, lightweight public cryptography is used to secure cloud and IoT systems [7, 8].
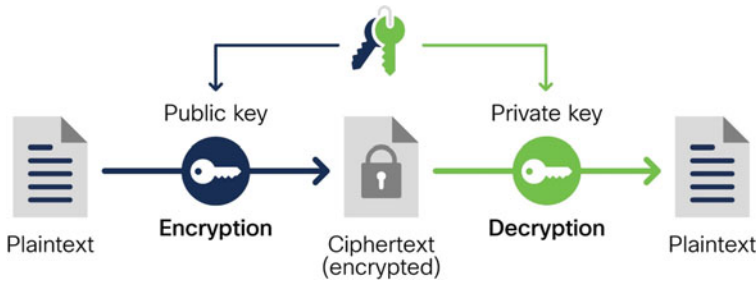
Fig. 1 General process of asymmetric encryption

2.2 Symmetric Key Algorithms

These cryptographic algorithms also called the "Secret key algorithm" use only one shared key for encryption and decryption. So, the sender will encrypt the data he will send by using the shared key, which shall not be publicly known. Then, when the data arrives, the receiver can get the original data by decrypting the cipher text using the same shared key [9]. Figure 2 illustrates the main processes in symmetric cryptographic systems.

One of the famous symmetric key algorithms which Bruce Schneier found in 1993. Blowfish constantly proved the advantages in processing time, power consumption, and throughput compared to other algorithms. The key size could be between 32 and 448 bits. This algorithm is applied through a 16-round Feistel network, where every round has a key permutation and a data substitution operation [10].

The standard encryption algorithm and AES stands for Advanced Encryption Standard; in 2001, NIST announced this algorithm as a standard, which meant it replaced DES as the encryption standard. The only type of attack that was proved to affect AES was the brute force attack [11]. AES has three key sizes 128, 192, and 256 bits. It also has a round where the number of these rounds is affected by the key size where a 128-bit key encrypts in 10 rounds, a 192-bit key in 12 rounds, and a
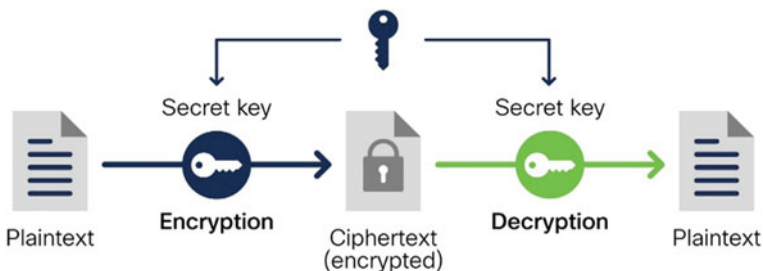
Fig. 2 General process of symmetric encryption

256-bit key in 14 rounds. AES is considered fast, flexible, and reliable; that is why it is currently widely used in cryptography [12].

Another famous example of a symmetric key algorithm is the Triple Data Encryption Algorithm (TDES, 3DES); a block cipher that applies the Data Encryption Standard (DES) three times to each data block of 64-bits and has a key size of 112, 168 bits [8].

Twofish is another famous symmetric key block cipher, it was founded in 1998 by Bruce Schneier, an open-source algorithm that has a block size of 128 bits, uses key sizes of 128, 192, and 256 bits and consists of a 16-round Feistel network.

2.3 Algorithmic Comparison

This subsection compares different aspects of each algorithm used in this experiment. Table 1 summarizes the comparison between the investigated algorithms 3DES, AES, Blowfish, and Twofish in terms of the year found, security, throughput, Block sizes, key sizes, and the number of rounds.

3 Experimental Modeling and Evaluation

Three of the four algorithms mentioned above have been chosen because they are the most known symmetric key algorithms currently used and the point of the experiment is to decide which of them will be the most suitable to be used in an Encryption as a Service solution in terms of time, memory consumption, and throughput.

Implemented and compared in this research using Java programming language. By employing the NetBeans IDE and Java security libraries to develop the key generation, encryption, and decryption phases. Besides, we have used ten files of

Table 1 Basic comparison between used algorithms [13, 14]

Algorithm/aspects	3DES	AES	Blowfish	Twofish
Year founded	1998	2000	1993	1998
Security	Low/moderate security	High security	High security	High security
Throughput	High	High	High	High
Block sizes	64 bits	128 bits	64 bits	128 bits
Key sizes	112, 168 bits	128, 192, 256 bits	32–448 bits	128, 192, 256 bits
Number of rounds	48 DES-equivalent rounds	10, 12, and 14 rounds (depends on the key size)	16 rounds	16 rounds

different types divided as follows: three text files of sizes 140 KB, 2.1 MB, and 25 MB, two image files of sizes 1.15 MB and 3.1 MB, two pdf files of sizes 13.6 MB and 36 MB, and three video files of sizes 158.5 MB, 226 MB, and 351 MB. We used a 6-core CPU Ryzen 5 5600× @ 4.6 GHz and 16 GB of ram for this experiment. These files were used to validate all the algorithms and calculate the encryption/decryption times, memory consumption, and throughput.

Electronic codebook (ECB) was the block cipher mode for operation in these experiments. Finally, the evaluation of the stated algorithms was conducted using four key performance indicators: encryption time, decryption time, memory consumption, and throughput in simple terms **Throughput = file size/encryption OR decryption time**. Differences were made clear between the algorithms in these categories showing different strengths and weaknesses.

3.1 Analyzing Encryption Time

Table 2 and Fig. 3 compare the encryption time (in milliseconds) required by the 3DES, the AES, and the Blowfish algorithms to encrypt a file. The comparison in the table considers the running time using ten files, each with different sizes and types.

According to the results presented in Table 2 and Fig. 3, the empirical evaluation showed that 3DES requires the most time to encrypt the files, and Blowfish and AES had almost the same results with smaller files. In contrast, AES had almost the same time of Encryption for the different files but was getting faster than Blowfish as the file size grew and the reason behind this is that CPUs have AES instructions support and acceleration which boosts the performance of the AES compared to any other cryptographic algorithm.

Table 2 Encryption times in milliseconds

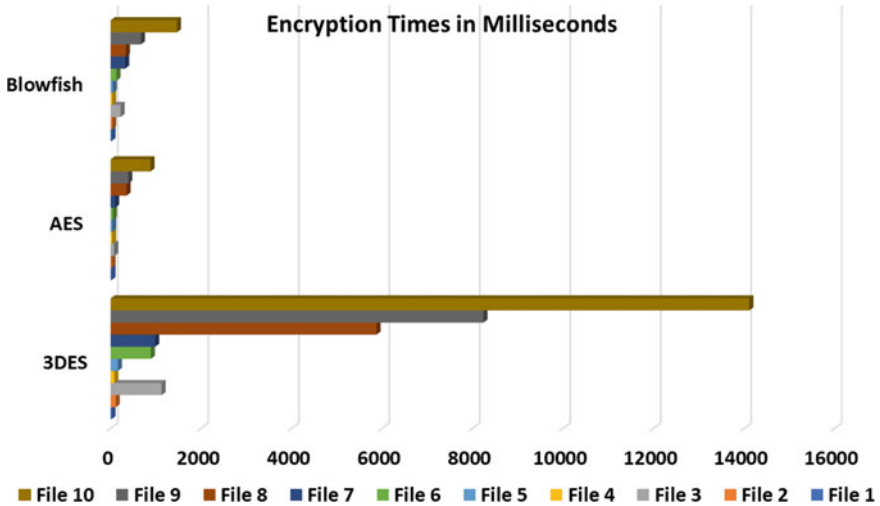| File	File type	File size (MB)	3DES	AES	Blowfish
File 1	text1	0.15	16	16.5	16
File 2	text2	2.1	112	16	32
File 3	text3	25	1125	78	219
File 4	image1	1.15	79.7	31	31
File 5	image2	3.1	159	32	47
File 6	pdf1	13.6	888	47.6	127
File 7	pdf2	36	983	95	318
File 8	vid1	158.5	5874	350	336
File 9	vid2	226	8240	388	667
File 10	vid3	351	14,116	880	1464

Fig. 3 Analyzing encryption time (ms)

3.2 Analyzing Decryption Time

Table 3 and Fig. 4 compare the decryption time (in milliseconds) required by the 3DES, the AES, and the Blowfish algorithms to decrypt an encrypted file and return it to the plain form. The comparison in the table considers the running time using three files, each with different sizes and types.

According to the results presented in Table 3 and Fig. 4, the empirical evaluation showed that it took a bit longer to decrypt the cipher files overall, and TDES took the most time to decrypt. At the same time, AES was faster than Blowfish as the file size

Table 3 Decryption times in milliseconds

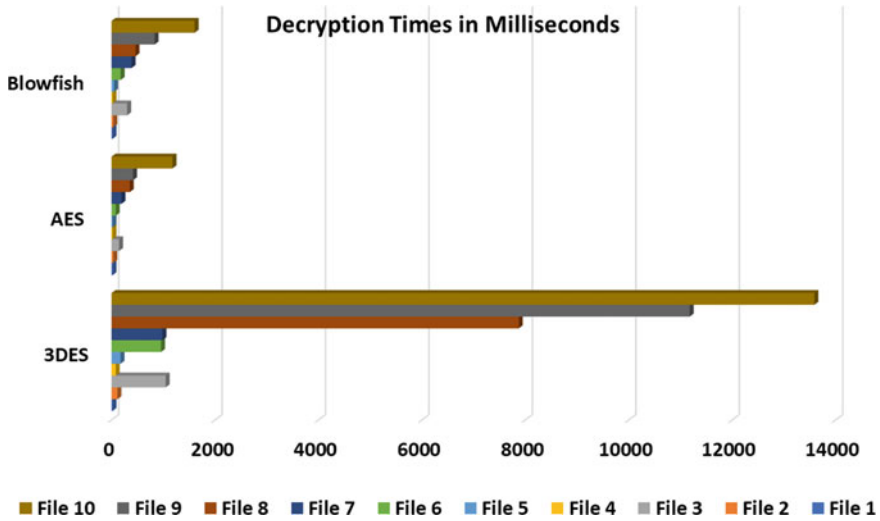| File	File type	File size (MB)	3DES	AES	Blowfish
File 1	text1	0.15	16	15.5	16
File 2	text2	2.1	112	32	32
File 3	text3	25	1045	143	300
File 4	image1	1.15	79.4	15	16
File 5	image2	3.1	172	16	48
File 6	pdf1	13.6	955	80	176
File 7	pdf2	36	982	190	384
File 8	vid1	158.5	7871	352	461
File 9	vid2	226	11,177	414	831
File 10	vid3	351	13,587	1176	1605

Fig. 4 Analyzing decryption time

Table 4 Average memory consumption (MB)

Algorithm	3DES	AES	Blowfish
Average memory consumption	48.7 MB	39.15 MB	37.44 MB

got bigger based on the same reason that CPUs now offer AES instructions support and AES acceleration.

3.3 Analyzing Memory Consumption

Table 4 and Fig. 5 compare the memory consumption required by the 3DES, the AES, and the Blowfish algorithms This is regarding the cost to the system at the run time of the program, and on average it has been shown in the results that the TDES is the costliest to implement, whereas Blowfish was the least memory demanding.

3.4 Analyzing Throughput

Table 5 compares the throughput calculated for each algorithm based on the file sizes and the time each algorithm needs for the encryption and decryption of these files. According to the results, AES yielded the highest throughput with 263.7 MB/sec on encryption and 217.7 MB/sec on decryption and it has a higher throughput than
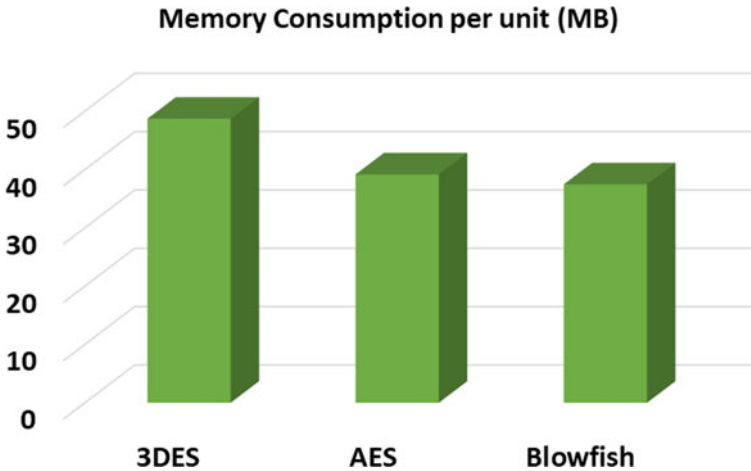
Fig. 5 Analyzing memory consumption

Blowfish because of the AES acceleration and instructions optimization supported on the CPU. On the other hand, 3DES has shown very slow encryption/decryption times as well as a very low throughput which shows inefficiency. Throughput (File size (MB)/ENC & DEC times (Sec) is shown in Fig. 6.

Table 5 Throughput [file size (MB)/ENC & DEC times (Sec)]

| File	File type	File size (MB)	3DES		AES		Blowfish	
			ENC (ms)	DEC (ms)	ENC (ms)	DEC (ms)	ENC (ms)	DEC (ms)
File 1	text1	0.15	16	16	16.5	15.5	16	16
File 2	text2	2.1	112	112	16	32	32	32
File 3	text3	25	1125	1045	78	143	219	300
File 4	image1	1.15	79.7	79.4	31	15	31	16
File 5	image2	3.1	159	172	32	16	47	48
File 6	pdf1	13.6	888	955	47.6	80	127	176
File 7	pdf2	36	983	982	95	190	318	384
File 8	vid1	158.5	5874	7871	350	352	336	461
File 9	vid2	226	8240	11,177	388	414	667	831
File 10	vid3	351	14,116	13,587	1037	1176	1464	1605
Average time			3159.2	3599.6	209.1	243.35	325.7	387
Throughput			21.5	20.2	263.7	217.7	156.4	130.1
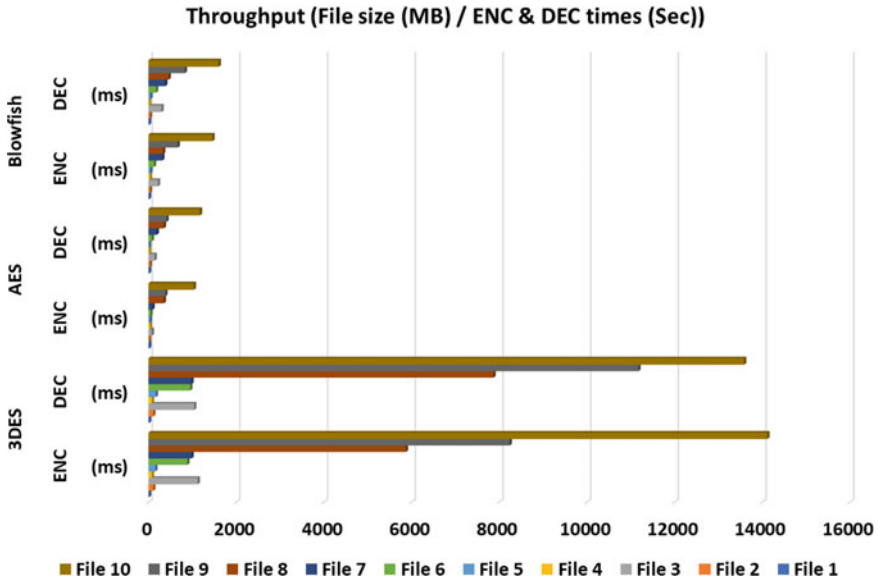
Fig. 6 Throughput [file size (MB)/ENC & DEC times (Sec)]

4 Challenges and Limitations

Since Encryption as a Service (EaaS) will be based on cryptographic algorithms it will still have the same weaknesses that these algorithms have and since we discussed symmetrical algorithms in this paper and the main challenges related to them are as follows:

1. The issues that concern the secret key such as:

   - Key sharing: Exchanging keys between two parties which could be more secured using asymmetrical algorithms.
   - Key length: The higher the length the more diffusion and randomness it yields into the encrypted file/data.
   - Randomness: The key should be related to something totally random such as a time, temperature, or something that is constantly being updated.

2. Endurability of the algorithm against known attacks.
3. Making sure that there are no flaws or back doors implemented in the solution that could affect the whole service which is meant to help protect the cloud and the data stored on it.

5   Conclusion and Future Work

Cloud computing environments usually involve the generation of huge amounts of big data. The performance and security of big data analysis and processing is an issue in cloud computing environments. Therefore EaaS "Encryption as a service" was proposed to protect the data at all times. In this paper, we have investigated the performance of three cryptographic algorithms, 3DES, AES, and Blowfish, in terms of encryption time, decryption time, memory consumption, and throughput. Our empirical results showed that every algorithm has its strengths and weaknesses. However, since we started our goal to acquire the best algorithm to secure data in a cloud in terms of security, time, and cost, therefore, according to the experimental results, we can conclude that AES was superior and has obtained better overall results than 3DES and Blowfish. Thus, we recommend AES be used to secure data in a cloud computing system.

Future work would be implementing, testing, and comparing more cryptographic algorithms, conducting more tests, and trying some hybrid solutions that consist of two or more cryptographic algorithms in order to obtain optimal results which would lead to choosing the best combination of algorithms to secure a cloud environment and its' data.

References

1. Al-Haija QA (2021) On the security of cyber-physical systems against stochastic cyber-attacks models. In: IEEE international IoT, electronics and mechatronics conference (IEMTRONICS), pp 1–6.https://doi.org/10.1109/IEMTRONICS52119.2021.9422623
2. Al-Haija QA, Ishtaiwia A (2021) Machine learning based model to identify firewall decisions to improve cyber-defense. Int J Adv Sci Eng Inf Technol 11(4):1688–1695
3. Ahmad A, AbuHour Y, Younisse R, Alslman Y, Alnagi E, Abu Al-Haija Q (2022) MID-crypt: a cryptographic algorithm for advanced medical images protection. J Sens Actuator Netw 11:24. https://doi.org/10.3390/jsan11020024
4. Stallings W (2005) Cryptography and network security (4th ed)
5. Shetty A, Shravya K, Krithika K (2014) A review on asymmetric cryptography—RSA and ElGamal algorithm. Int J Innovative Res Comput Commun Eng 2(5)
6. Singh G, Kinder S (2013) Integrating AES, DES, and 3-DES encryption algorithm for enhanced data security. Int J Sci Eng Res 4(7)
7. Al-Haija QA, Marouf I, Asad MM, Al Nasr K (2019) Implementing a lightweight Schmidt-Samoa cryptosystem (SSC) for sensory communications. Int J Smart Sens Intell Syst 12(1):1–9
8. Barker E, Mouha N (2017) NIST special publication 800-67 revision 2 "recommendation for the triple data encryption algorithm (TDEA) block cipher"
9. Anand Kumar M, Karthikeyan S (2012) Investigating the efficiency of blowfish and Rejindael (AES) algorithms. I J Comput Network Inf Secur 2:22–28 (2012). Published Online March 2012 in MECS. https://doi.org/10.5815/ijcnis.2012.02.04, Copyright © 2012 MECS
10. Sanchez-Avila C, Sanchez-Reillol R (2001) The Rijndael block cipher (AES proposal): a comparison with DES. In: Published in proceedings IEEE 35th annual 2001 international Carnahan conference on security technology (Cat. No.01CH37186)
11. Singh G, Singla A, Sandha KS (2011) Cryptography algorithm compassion for security enhancement in wireless intrusion detection system. Int J Multi Res 1(4)

12. Al-Haija QA, Al Tarayrah M, Al-Qadeeb H, Al-Lwaimi A (2014) A tiny RSA cryptosystem based on Arduino microcontroller useful for small scale networks. Procedia Comput Sci 34:639–646
13. Jeeva AL, Palanisamy V, Kanagaram K Comparative analysis of performance efficiency and security measures of some encryption algorithms. ISSN: 2248-9622
14. Santoso K, Muin M, Mahmudi M (2020) Implementation of AES cryptography and Twofish hybrid algorithms for cloud. J Phys Conf Ser 1517(1):012099. https://doi.org/10.1088/1742-6596/1517/1/012099

Experimental Investigations on Turbine-Generator Shaft Under Subsynchronous Resonance

P Manikandan, G. Sushanth, and K. M. Haneesh

Abstract Energy exchange takes place between turbine and generator in the power system during subsynchronous resonance (SSR) which leads to torsional interaction between the shafts. Resonance in the power system is caused by the series capacitors connected to the transmission line. This paper aims to present an electromechanical approach to analyse and interpret subsynchronous resonance using the Finite element method. Subsynchronous resonance is introduced in two test rigs consisting of turbine, generator, shaft, and coupler with capacitors. Experiments and simulations (torque analysis and frequency response analysis) are conducted in test rigs and ANSYS workbench 16.0. Moreover, a spring damper is modelled to improve the stability of the shaft. From the results, it is clear that mechanical stress is increased when capacitors are connected to the test rig. A spring damper is installed at the point where the deformation is high. The damper reduced the stress and the vibration.

Keywords Finite element method · Damper · Turbo-generator shaft · Subsynchronous resonance · Modal analysis · Rotor dynamics

1 Introduction

Torsional interactions occur in the power system when flexible alternating current transmission (FACTS) devices are connected to it [1]. High power capacitors are connected in series to improve the reactive power. The addition of series capacitors in the system leads to subsynchronous resonance which causes differences in speed

P Manikandan (✉) · K. M. Haneesh
Department of EEE, CHRIST (Deemed to be University), Bengaluru, India
e-mail: manikandan.p@christuniversity.in

K. M. Haneesh
e-mail: haneesh.km@christuniversity.in

G. Sushanth
Department of ECE, CHRIST (Deemed to be University), Bengaluru, India
e-mail: sushanth.g@christuniversity.in

and frequency of the turbine and generator [2]. This is currently a topic for many researchers [3–12]. Apart from resonance, there are several other reasons where torsional oscillations occur. They are short circuits near generator terminals, instability in turbogenerator shaft bearings, mal-synchronization, and non-uniform electric field. In HVDC links dampers are installed to overcome the vibrations created by subsynchronous resonance [8, 9]. Dampers based on inertia and coupling are currently used in practise to dampen the oscillations [13]. The finite element method and rotor dynamics are used to study the dynamics of rotating structures. The experimental modal analysis of static and dynamic structures has gained numerous applications in industry as well as in research [14]. Modal analysis technique can be used to decide the dynamic behaviour of structures in terms of modal factors such as natural frequency, mode shapes, and damping.

Experimental modal analysis can be accomplished using sensors and dampers which contribute to the detection and controlling vibration of the rotating structure [15–17]. Traditionally, subsynchronous resonance is detected and damped using Eigenvalue analysis, digital time simulation techniques, and frequency scanning methods. These traditional methods do not consider the geometry of the shaft and its dynamics. Therefore, an experimental and comprehensive analysis should be performed using the finite element method to study the dynamics of the shaft caused by subsynchronous resonance in the power system [3–5]. The analysis presented in this paper is devoted to the calculation of total deformation, equivalent stress, equivalent strain and strain energy of the shaft which is subjected to subsynchronous resonance. Accuracy in the finite element method depends on the size and shape of the mesh [18, 19]. The paper contains both simulation and experiment results, as well as their detailed analysis and discussion.

2   Theoretıcal Approach of Shaft Model

The turbine generator is of a solid cylindrical shaft, hollow cylindrical shaft, and solid tapered shaft. The solid cylindrical shaft which connects the turbine and generator is most common in practise. Mass/moment of inertia and stiffness matrix equations for a solid cylindrical shaft is normally derived from the rotational element using the finite element method [6, 7].

$$\left[I^e \right] = \int_{l^e}^{I} \rho J_x \begin{pmatrix} M_1^2 & M_1 M_2 \\ M_1 M_2 & M_2^2 \end{pmatrix} \tag{1}$$

$$\left[K^{(e)} \right] = \int_{0}^{1} G J_x \begin{pmatrix} \left(\frac{dM_1}{dx} \right)^2 & \left(\frac{dM_1}{dx} \frac{dM_2}{dx} \right) \\ \left(\frac{dM_1}{dx} \frac{dM_2}{dx} \right) & \left(\frac{dM}{dx} \right)^2 \end{pmatrix} \tag{2}$$

where $M1$ and $M2$ are shape functions, J is the moment of inertia, and G is the stiffness coefficient of the shaft considered. ρ is the poissons ratio, I is the inertia constant, and K is the constant.

The life of a turbine generator shaft depends on the load it handles and the total time of operation [1]. When the capacitors are connected for the purpose of compensating reactive power compensation, it results in a subsynchronous resonance condition that affects the shaft and blades of the turbine [9, 10]. The subsynchronous resonance is detected using Eigenvalue analysis, frequency scanning technique, and time domain simulation method [11, 12]. These techniques are used to detect electrical parameters like three-phase voltage and current, fault current, and voltage across series capacitors. Mechanical stress, strain and the deformation of the shaft are not extensively studied using Eigenvalue analysis, frequency scanning technique, and time domain simulation method [12, 13]. Dampers are connected to the shaft based on rotational vibrations. Installation of these dampers is not based on subsynchronous resonance which is a threat to the turbine generator shaft system. This threat becomes serious when the electrical signals fail to report the resonance in the system. Therefore, a more experimental and comprehensive analysis must be performed by considering electrical and mechanical parameters making it an electromechanical approach to interpreting subsynchronous resonance. An approach to such an analysis is given in the following section.

3 Proposed Approach

In the proposed approach, the turbine generator shaft is modelled and it is subjected to Torque analysis, Modal analysis, and Frequency response analysis. Inputs to the analysis are extracted from the experiments conducted on the test rig. Subsynchronous resonance is introduced in the test rigs by connecting capacitors. Torque analysis is performed for the shaft used in the first test rig. Stress, strain and deformation of the shaft are measured. Modal analysis and Frequency response analysis is performed for the shaft used in the second test rig. The vibration pattern of the shaft is studied in both cases. A spring damper is attached to the shaft model where the stress amplitude is high and its stability is improved. In the proposed approach, Test Rig I consists of two rotating masses connected by a shaft with a coupler. The Test Rig II consists of a Hydro turbine and generator connected by a belt. A damper is modelled for the shaft in the second experimental setup. Modelling a damper for the first experimental setup is ignored due to the fact of the presence of a coupler. Finite element method is used to analyse the stability of the shaft which connects the generator and shaft.
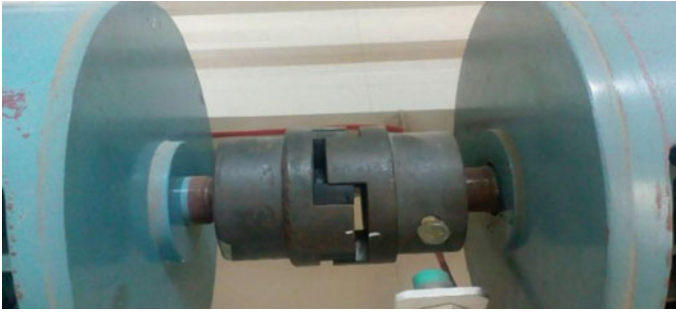
Fig. 1 Test rig I

4 Test Rıg I and Its Operatıon

Test Rig I consists of two rotating masses shown in Fig. 1. One acting as a prime mover (left-hand side blue) and the other acting as a generator (right-hand side blue). The generator is connected to both resistive and capacitive loads. Ferrous materials like stainless steel for the shaft and galvanized iron for coupler are used in the setup. The insulation class of the two rotating masses is 'F' which can handle temperatures up to 155 °C. In Fig. 1 Coupler is shown which connects the shaft of two rotating masses.

The speed of the two masses is controlled by a drive circuit. DCP3P20 module is used as a drive circuit. The machine is operated to its rated speed of 1500 RPM. Resistive loads (lamps) are connected to it. As the load increases, the speed of the machine reduces. At this condition, capacitors are connected to the system step by step to improve the reactive power. The speed and its corresponding torque during each percentage of compensation. When the capacitors are connected to the system, heavy vibration in the chassis and sparks in the prime mover is observed due to resonance.

5 Test Rıg II and Its Operatıon

The modal analysis and frequency response analysis are executed using Ansys. The major reason for selecting the test rig II is to overcome the difficulties faced in the test rig I. The Test Rig II consists of a reaction turbine (Francis turbine) and it is connected to the single-phase generator with a belt which was not similar in the case of first test rig. Francis turbines are the most commonly used type of hydro turbine because of their turbine efficiency and machine performance. The diameter and the mass of the shaft of the turbine are calculated before the installation of the entire setup. The torsional stiffness is calculated from the Rigidity modulus, a form factor that defines the geometry and length of the shaft [1]. Turbine and generator specification is given

in Table 1. The generator is connected with resistive loads (lamps) and it is operated to its rated 1500 RPM. The speed of the shaft reduces when the load current increases. Test Rig II is shown in Fig. 2. Capacitors are connected to the system to improve the reactive power. The change in speed due to the connection of capacitors is noted. It is observed that the intensity of lamp illumination changes when the capacitors are connected to the system.

Table 1 Technical specifications of test rig II

Turbine		
Component	Description	Dimensions [mm]
Venturimeter	Water flow measurement	Inlet diameter: 100 Throat diameter: 60
Shaft length	Solid shaft	Length: 380 Diameter: 55
Generator		
Component	Description	Rating
Capacitor	Aluminium electrolytic capacitors	15 μF
Generator	Single phase	3 A, 1500 RPM, 3 kVA

Fig. 2 Test rig II

6   Results and Analysis

The 3D model of the Test Rig 1 is modelled in the Design modeller in ANSYS 16.0 workbench. Materials used for the shaft is stainless steel and galvanized iron for the coupler. The torque analysis is carried out for Test Rig I. The analysis is performed for 10–50% compensation values obtained in the experiment. Equivalent stress, Equivalent elastic strain, Total deformation and Strain energy are found out using ANSYS workbench 16.0. The finite element method (FEM) is applied in ANSYS to perform torque analysis. The size of mesh for the 3D model in FEM is decided based on the level of accuracy and computation time. In this research paper, three different mesh size is selected and the changes in the results are shown in Fig. 3.

The amplitude of vibrations is measured. Based on the stress pattern of the shaft, a spring damper is modelled and again the frequency response of the shaft is obtained. Damping ratio is improved and again the frequency response is calculated. The results are tabulated in Table 2.
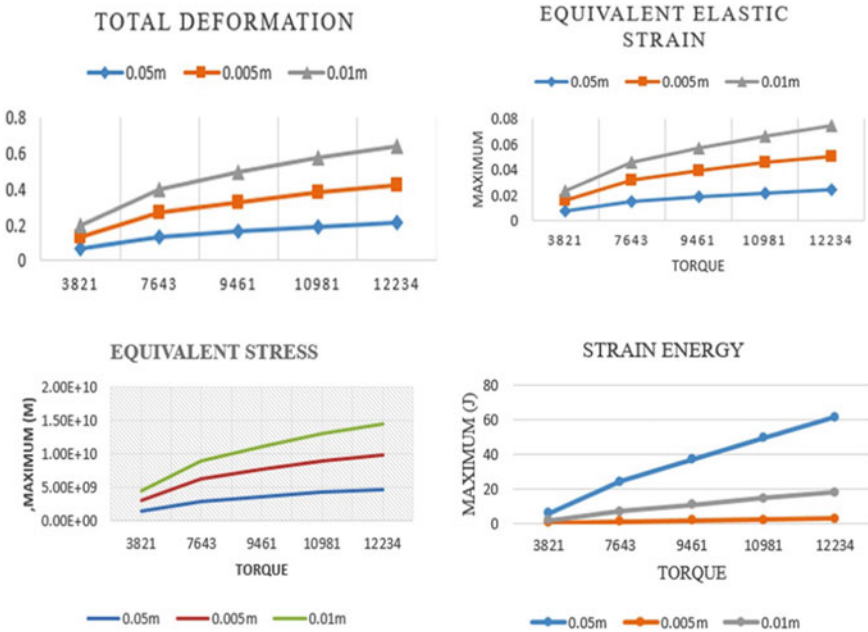

Fig. 3   Results of three different mesh size

Table 2 Frequency response amplitude for different damping ratio

Damping ratio	Without damper	With damper
0	2.1e14	9.6e7
0.1	2.7e−2	6.5e−9
0.2	1.7e−2	2.6e−9
0.3	1.7e−2	1.5e−9

7 Analysis of Results

Results of torque analysis and frequency response analysis are discussed in Sect. 6. The finite element method is used to solve the 3D model in ANSYS 16.0. The shaft of both Test Rig I and II is modelled and analysed for its mechanical characteristics like equivalent stress, equivalent strain, strain energy, and total deformation due to subsynchronous resonance (Table 3).

In Test Rig I, the galvanized iron coupler can be observed in Fig. 1. The 3D model of Test Rig I consists of a shaft, rotating mass, and the coupler. Since the amplitude of stress distribution in the shaft is less, a spring damper is not required for Test Rig I shaft. The 3D model is subjected to torque analysis for five different torques obtained from the experiment results. They are 3821, 7643, 9461, 10,981, and 12,234 Nm.

The torque increases when the compensation increases which can be seen in Table 2. The two rotating masses are connected to the shaft with bearings. At 30% of compensation, severe sparks were observed in the prime mover mass which is primarily due to the electrical as well as mechanical stress. IEEE First benchmark model (FBM) and Second benchmark model (SBM) on subsynchronous resonance do not consider the stress and strain of the shaft and therefore an experimental and comprehensive analysis is performed to determine the stress and strain distribution of the shaft.

The accuracy of the finite element method is based on the selection of an appropriate mesh size [3]. Three different mesh sizes are selected and applied to the torque analysis. Results of total deformation, equivalent elastic strain, and equivalent stress and strain energy shows the relativity between the results. The output of three different mesh sizes did not change exponentially. The changes are less than 10%. However, the deviation in strain energy is more when compared to the other three parameters. The reason for the large deviation is due to the material property of galvanized iron and stainless steel.

Table 3 Modal analysis results of shaft in test rig II

Parameter (shaft at 1573 RPM)	Magnitude
Total deformation	5.935e−7/mm
Equivalent stress	0.11157/mm
Equivalent elastic strain	5.5787e−7/mm
Strain energy	6.720e−6/mJ

In Test rig II, a real hydro turbine generator is used. The belt which connects the turbine shaft and generator shaft is ignored for the frequency response analysis and it is assumed that shafts of both turbine and generator are connected together without a coupler. The length and diameter of the turbine and generator shaft are measured more precisely. The stress distribution is more near the generator shaft terminal which is shown in Fig. 4 which is primarily due to subsynchronous resonance. The 50% compensation improves the reactive power and also induces resonance in the system. A spring damper is modelled near the generator terminal which is shown in Fig. 5 reduced the stress. The vibration amplitude shown in Table 2 decreases when the damper is installed in the shaft and also for the increased damping ratio to recapitulate, the behaviour of the shaft which connects the turbine and generator changes when capacitors are connected in series. The test rig II consists of a turbine and generator connected. The capacitors are connected to the system which creates a resonance in the shaft. Due to the resonance, the vibration of the shaft increases which is analysed using frequency response of the shaft. A spring damper effectively reduces the vibration and the electromechanical stress in the power system as in Fig. 6.

At the outset, the stability of the shaft is improved when a damper is connected at the highest point of stress. The frequency response analysis clearly indicate the stability improvement when damper is connected.
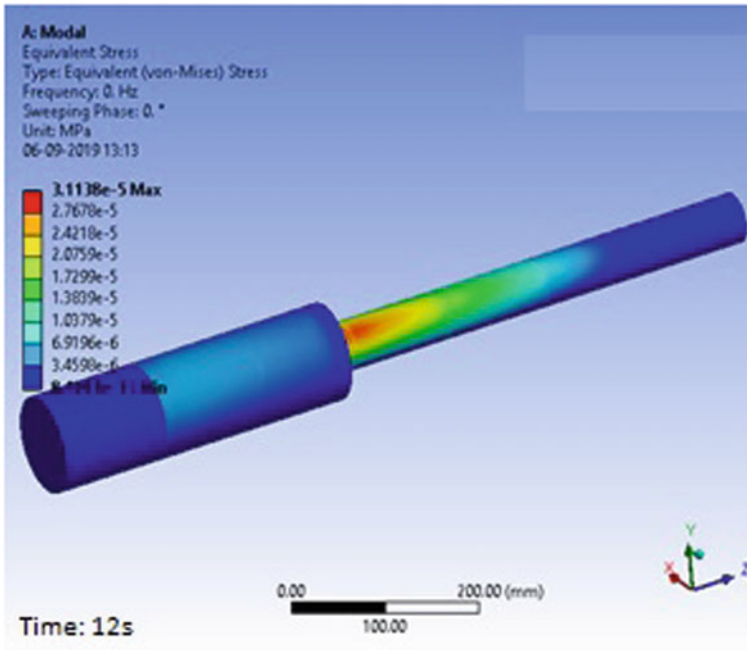

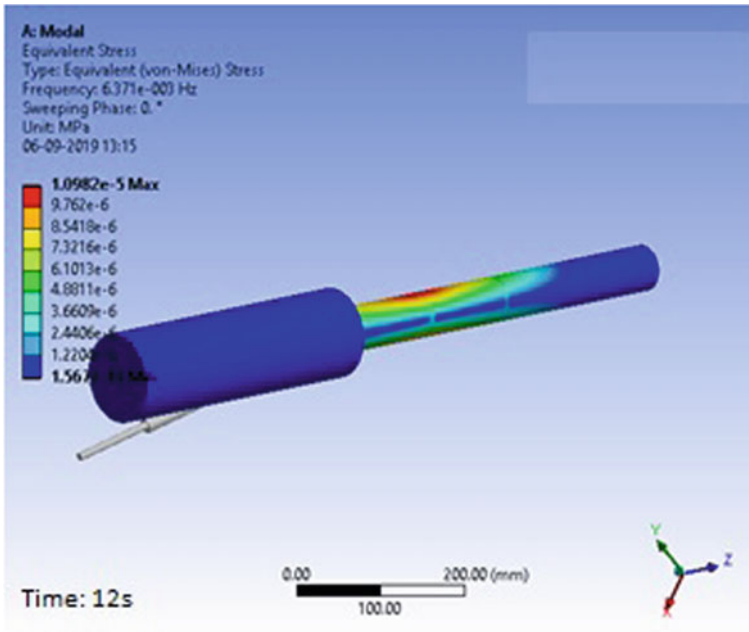**Fig. 4** Equivalent stress of the shaft in test rig II—without damper

Fig. 5 Equivalent stress of the shaft in test rig II—with damper

8 Conclusion

Determination of mechanical characteristics (equivalent stress, equivalent elastic strain, strain energy and total deformation) due to subsynchronous resonance lead to better design and production of the shaft. Torque analysis and frequency response analysis is an electromechanical approach to conduct non-destructive testing of the shaft. Dampers are installed based on the total deformation pattern which decreases the vibrations and improves the stability of the shaft during subsynchronous resonance. This paper presents an experimental and comprehensive analysis to study the subsynchronous resonance using two test rigs. The analysis is based on the deviation of the shaft from its rated speed due to the resonance introduced into the system by capacitors. The analysis and discussion of all the results are briefed in the paper. Galvanized iron couplers are less influenced by the effect of subsynchronous resonance whereas stainless steel shafts are more stressed due to the resonance. It has been found that the installation of a damper near the generator terminal based on the equivalent stress improved the stability of the shaft and reduced the vibrations. The presented analysis supports the idea of modelling a damper considering equivalent stress and strain due to subsynchronous resonance.
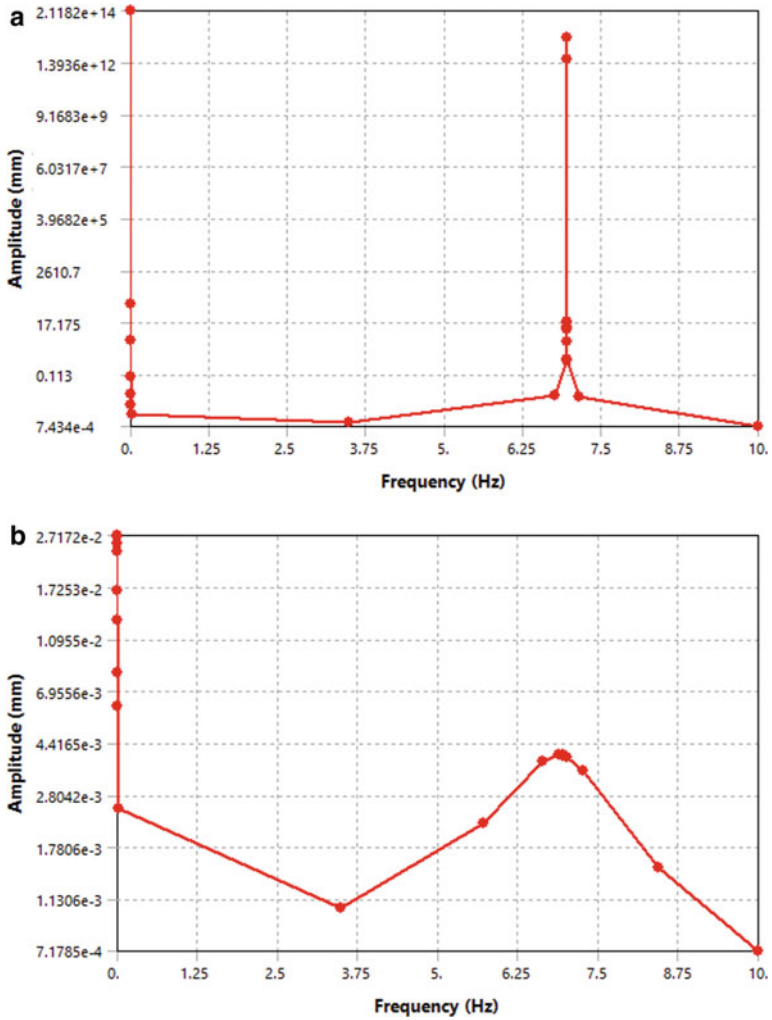
Fig. 6 **a** Frequency response of the shaft in test rig II (damping ratio—0-without damper). **b** Frequency response of the shaft in test rig II (damping ratio—0-with damper)

References

1. Manikandan P, Khan FA (2021) Rotor dynamics of turbine–generator shaft with dampers during subsynchronous resonance generated by series capacitors lecture notes in mechanical engineering, pp 191–202
2. Liang CC (1993) Torsional response of rotor system in steam turbine-generator. Taipower Eng J 538(6):35–52
3. Saxena A, Pareya A, Chouksey M (2016) Study of modal characteristics of a geared rotor system. Procedia Technol 23:225–231
4. Kirchg B (2016) Finite elements in rotor dynamics. Procedia Eng 144:736–750
5. Gawrylczky KM, Kugler M (2004) Sensitivity analysis of electromagnetic quantities in time domain by means of FEM. Serb J Electr Eng 1(2):167–174
6. Zlatko K, Lidija P (2005) Determination of a synchronous generator characteristics via finite element analysis. Serb J Electr Eng 2(2):157–162
7. Karlberg M (2010) Approximated stiffness coefficients in rotor systems supported by bearings with clearance. Int J Rotating Mach
8. Hernandez M, Guardado JL, Venegas V, Melgoza E, Rodriguez L (2008) Analysis of the torsional modes of the turbine-synchronous generator group. In: IEEE/PES transmission and distribution conference and exposition. Latin America, Bogota, pp 1–7
9. Tsai J (2007) A new damper scheme to restrict torsional torques on the turbine generator shafts and blades near a HVDC link. Electr Eng 89:377–387
10. Tsai JI, Lin CH, Tsao TP (2003) Long-term fatigue life loss of turbine blades owing to non-characteristic harmonic currents in asynchronous HVDC links. J Electr Power Syst Res 65(2):135–147
11. Xie X, Zhang C, Liu H, Liu C, Jiang D, Zhou B (2016) Continuous mass model based mechanical and electrical co-simulation of SSR and its application to a practical shaft failure event. IEEE Trans Power Syst 31(6):5172–5180
12. IEEE Sub Synchronous Resonance Working Group (1992) Readers guide to sub synchronous resonance oscillations. IEEE Trans Power Appar Syst 7:150–157
13. IEEE Sub Synchronous Resonance Working Group (1985) Terms, definitions and symbols for sub synchronous resonance oscillations. IEEE Trans Power Appar Syst PAS-104(6):1326–1334
14. IEEE Sub Synchronous Resonance Working Group (1998) Second benchmark model for computer simulation of sub synchronous resonance. IEEE Trans Power Appar Syst 104(5):1057–1066
15. Lambrecht D, Kulig T (1982) Torsional performance of turbine generator shafts especially under resonant excitation. IEEE Trans Power Appar Syst 101:3689–3697
16. Jackson MC (1979) Turbine generator shaft torques and fatigue: part I-simulation methods and fatigue analysis. IEEE Trans Power Appar Syst 98(6)
17. Mankowski O, Wang Q (2013) Real-time monitoring of wind turbine generator shaft alignment using laser measurement. Procedia CIRP 11(1):291–295
18. Bai B, Zhang LX, Guo T, Liu CQ (2012) Analysis of dynamic characteristics of the main shaft system in a hydro-turbine based on ANSYS. Procedia Eng 31:654–658
19. Elhefny A, Guozhu L (2012) Stress analysis of rotating disc with non-uniform thickness using finite element modeling. In: International conference on engineering and technology, Cairo, Egypt

Advantages of Using IP Network Modeling Platforms in the Study of Power Electronic Devices

Ivan Nedyalkov and Georgi Georgiev

Abstract In the present work, the possibility of studying power electronic devices using platforms for modeling IP networks is considered. This research attempts to confirm or deny the hypothesis that power electronic devices generate very little traffic and connecting them to a working IP network would not lead to any change in the working performance of an IP network. Different scenarios with different topologies of modeled IP network are created to test the hypothesis. For the purpose of the study, the GNS3 IP network modeling platform and various IP network monitoring tools are used.

Keywords GNS3 · IP networks · Modeling of IP networks · Network monitoring · Power electronic devices · Traffic characterization

1 Introduction

Technologies are developing constantly and quickly—new methods of data transfer, new communication networks, new services for users and many more directions in which there are developments. These innovations do not pass the power electronics, in particular, the power electronic devices (PED). In addition to research and development in the direction of new circuit solutions, increasing the efficiency of power converters, new voltage equalization circuits for energy storage systems [1–4], PEDs are also developing in the direction of improving, and some PEDs in the expansion of the already available communication possibilities. Now, the equipment of almost every PED includes the ability to connect to some kind of communication network. Whether it will be to the hegemon of communication networks, current IP network or to some derivative of the IP network, such as an IoT network, the PED must be able to be managed or monitored remotely, through a communication network, providing convenience to the personnel who uses it. Because of these new communication

I. Nedyalkov (✉) · G. Georgiev
South-West University "Neofit Rilski", Blagoevgrad, Bulgaria
e-mail: i.nedqlkov@swu.bg

possibilities and the conveniences they provide, it is recommended, even mandatory, for each PED to characterize the communication traffic generated by it.

Traffic characterization [5–7] can be achieved by creating an experimental communication network (in 99% of cases it is an experimental IP network) to which the PED will be connected. This experimental network can be composed of "n" number of network devices, in order to maximally recreate the physical IP network to which the studied PED would be connected. Such a network would require the investment of a lot of funds to purchase the relevant communication equipment. Not every scientific or development organization can afford this. To solve the problem of the lack of sufficient funds to purchase the necessary communication equipment, IP network modeling platforms can be used [8, 9].

The present work examines the advantage of using IP network modeling platforms in characterizing the communication traffic generated by PED. Several working models of IP networks are presented. Through these models, different variants of possible future use of the PED are studied and whether the communication traffic generated by the PED would have any impact on the performance of the IP network to which it is connected is determined.

2 Platform for Modeling, Monitoring Tools and Technology

2.1 Platform Used for Modeling

In the present work, the GNS 3 IP network modeling platform is used. This platform has been chosen due to many advantages and possibilities it offers, such as:

- GNS3 offers the ability to work with disk images of real operating systems of various global manufacturers of network equipment. In the platform, this process is called network device emulation. Through this functionality, experimental models of IP networks built from emulated network devices running operating systems of such real devices can be created. In this way, the created models of IP networks will come as close as possible to real IP networks.
- GNS 3 offers the possibility of connecting the modeled IP network to a real IP network or another communication network. Through this functionality, research opportunities are further increased. Thanks to this functionality, it is possible to test what would be the reaction of the modeled network when connecting to the Internet—is there going to be some change in the performance, will latency be observed in the modeled network and many other test scenarios.
- GNS3 offers integration with IP network monitoring tools. Thanks to this, the studies of the modeled networks can be carried out much more easily and the obtained monitoring data will be more comprehensive. For example, all nodes in the modeled network can be monitored in order to obtain the maximum possible

monitoring data. This possibility is used in this study, observing the exchange of packets in all nodes of the network using the Wireshark.

- Finally, GNS3 is free, unlike other similar platforms where some of the functionalities are paid for.

2.2 Monitoring Tools and Monitoring Technology Used

For the purposes of this work, several additional tools in the monitoring of IP networks are also used. It is about network analyzer and network protocol analyzer [10, 11]. The network analyzer used is Capsa 11 Free. This tool monitors various network parameters such as: generated traffic, used protocols, generated traffic by protocols, generated traffic by ports and many other parameters. The network protocol analyzer used is Wireshark. It monitors and collects the packets that are exchanged between all the nodes in the created IP network models. Once the monitoring is completed, the data collected by Wireshark is analyzed. The tool can be used to check whether the information exchange is secure or not, as it is done in the present work.

Additionally, mathematical distributions [12] for packet size are used. The distributions are obtained based on the captured packets by Wireshark and post-processing by a specialized program for obtaining mathematical distributions. The resulting distributions will be used to further visualize what is the distribution of the packets generated by the studied PED by size in the modeled IP network.

Finally, the monitoring technology used is passive monitoring. The passive monitoring method is chosen because it is easy to implement, and the modeled IP networks are small to use in the active monitoring method. The obtained data from the passive method are sufficient to characterize the traffic generated by one PED.

3 Models of IP Networks Used for Studying PED

3.1 Model of an IP Network Used for Characterizing the Generated Traffic from the PED

Figure 1 presents the topology of an IP network model designed to be used for characterizing the traffic generated by the PED. The studied PED is a Power Distribution Unit (PDU). This module is used for remotely managing the power supply of various network devices. The Internet Service Providers (ISPs) use it to remotely manage the power supply of their network devices, such as switches or routers. The device also offers functions for monitoring the temperature in the room where the network equipment is located, monitoring the value of the supplying voltage, as well as monitoring the absence of the supplying voltage. The characterization of the generated
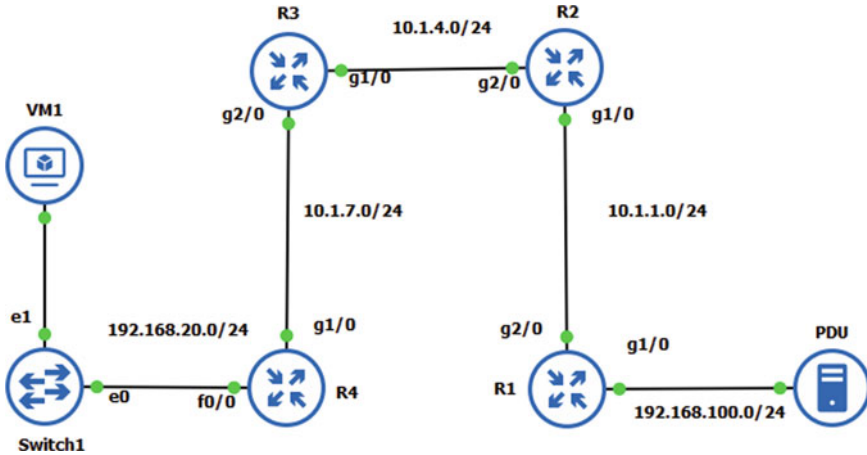
Fig. 1 Topology of the modeled network

traffic is recommended to be done for each device that is intended to be connected
to some working IP network [13, 14].

The modeled network is composed of four routers (R1–R4) and one switch
(Switch1). Such a topology is chosen so that the capabilities of the platform used for
studying PEDs could be demonstrated. For example, several more workstations can
be connected to the switch, through which the PDU can be managed, and through the
four routers. An example of a real IP network is modeled. VM1 is a virtual machine
through which the studied PDU is accessed, monitored and managed. The purpose of
this scenario is to present the capability of the platform for modeling of IP networks
to be used for characterizing the communication traffic generated by the PDU. The
network analyzer Capsa 11 monitors the traffic that is exchanged at the input/output
(PDU network interface card), and Wireshark is used for monitoring and capturing
the packets that are exchanged between the routers.

Figure 2 presents the generated (exchanged) traffic, which is monitored on the
PDU's network interface card by using Capsa 11. Figure 2a shows the traffic that
is measured by Capsa 11. The sample interval is set to 1 s, for the most accurate
measurement. Figure 2b shows the whole traffic that is exchanged during the entire
period of the study. As it can be seen from the results, especially from Fig. 2a, the
exchanged traffic is very small, than expected. Moments with no traffic are due to the
fact that the PDU is only accessible through a browser and when it is not accessible,
no traffic is exchanged/generated.

Figure 3 shows which protocol generates the most traffic, and it is the HTTP
protocol, because the PDU is accessible only through a browser. The traffic generated
by the other protocols is used for maintaining the connection between the PDU and
the VM1.
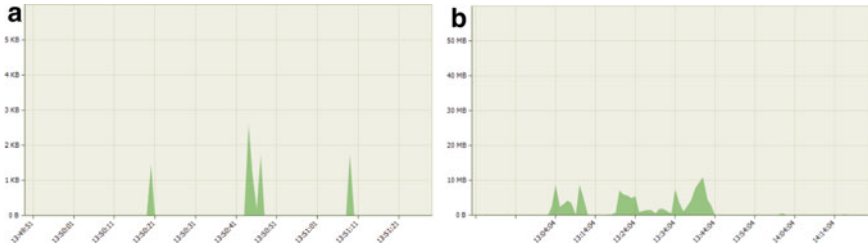
Fig. 2 Total generated traffic. **a** is the traffic measured very 1 s and **b** is the traffic generated/measured for the whole period of the study
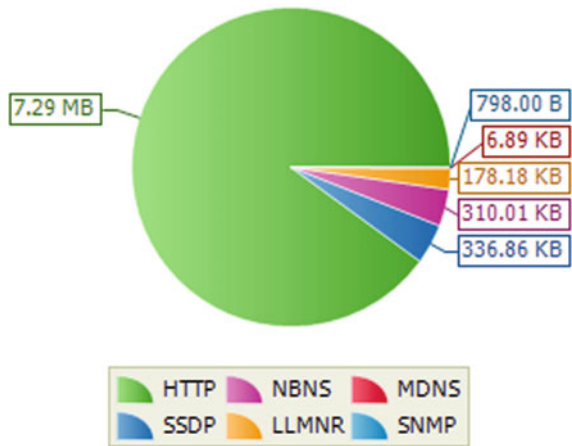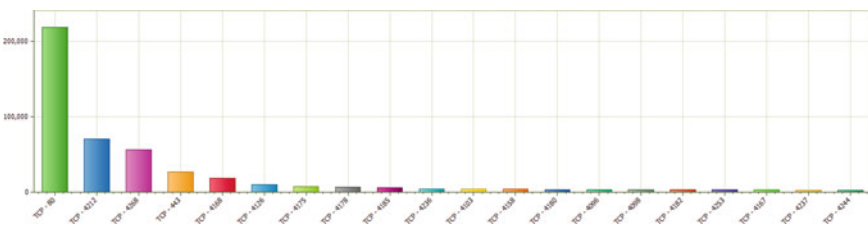
Fig. 3 Top application protocols by bytes

Figure 4 shows which ports generate the most traffic, and it is port 80, due to the use of the HTTP protocol. This information is useful to be known so that the network can be secured and unnecessary ports can be closed.
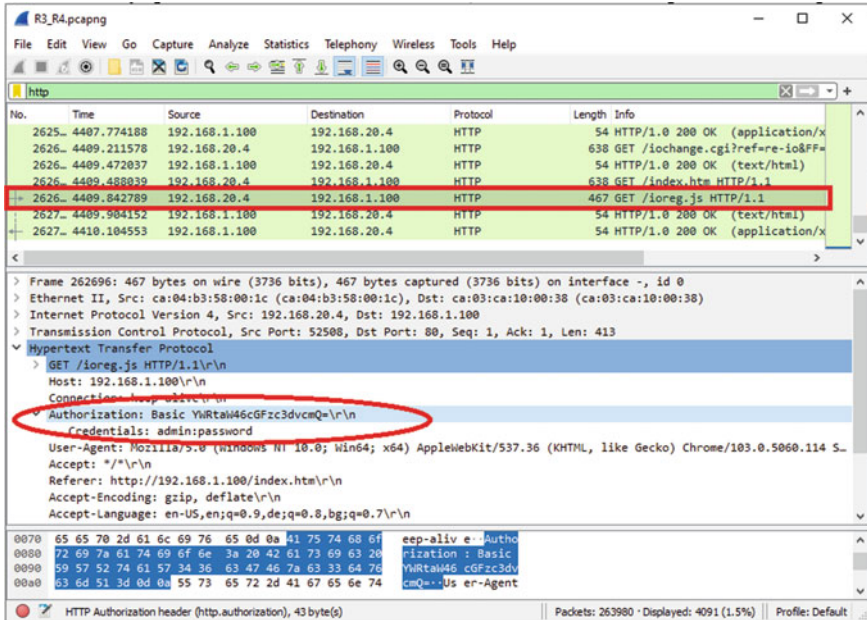

Fig. 4 Top port by total traffic

Fig. 5 Security checking

Figure 5 presents the result of using Wireshark to check whether the exchanged information is secure or not. It is clear from the figure that the exchanged information is not secure—the username and password to access the device are transmitted in plain text. This is inadmissible, because the PDU can easily be manipulated in this way. So, when the PDU is hacked the devices that are power supplied from it can easily be manipulated by turning them on/off.

Figure 6 presents the mathematical distribution by packet size with the Couchy approximation. For all connections between the devices, the distribution is the same. These are mainly the TCP and HTTP packets. As can be seen, packets of size 1000 bytes are few compared to all captured packets, which is a favorable option. This means that the PDU is not in danger of overloading the network with large-sized packets. The largest number are packets up to 60 bytes in size and packets with a size of 600 bytes.

In summary, the following can be concluded: the traffic generated/exchanged by/with the PDU is negligible, and at times when the device is not accessible, the traffic is zero. The generated packets are of relatively "normal" size. A disadvantage of the studied PDU is the insecurity of the data exchange, i.e., transmission of important data in plain text.
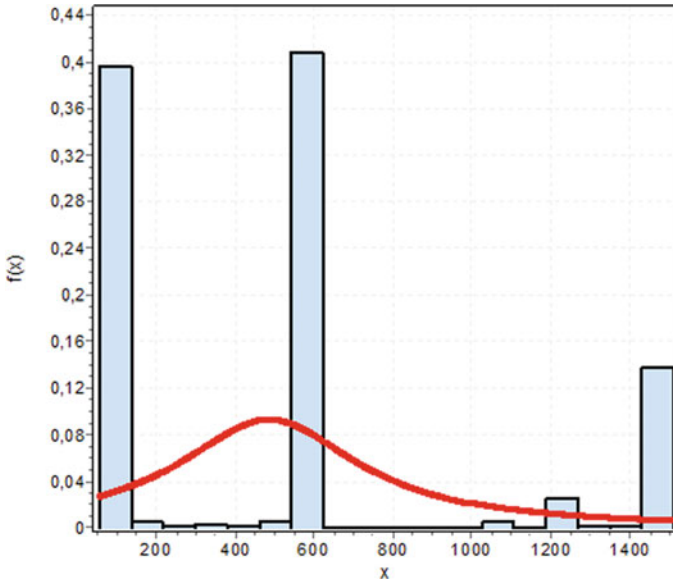
Fig. 6 Mathematical distribution

3.2 Model of an IP Network Used to Study the Impact of the Studied PED Over the Performance of the IP Network When It Is Connected to It

Figure 7 presents the topology of another modeled IP network through which the impact of the PED connectivity on network performance is studied. The special feature of this model is the connectivity of the modeled IP network to a real network—the Internet. The virtual machines (VM1 to VM3) access various resources on the Internet, as well as the tested PDU. Router_Firewall is a firewall through which the modeled network is connected to the Internet. A portion of the obtained results before and after adding the studied PDU is compared.

Figure 8a shows the measured traffic with the Internet on every single second, without the PDU connected to the network, and Fig. 8b with the PDU connected. As it can be seen from the results, they are almost the same, and the added PDU does not lead to a change in the amount of generated traffic.

Figure 9a shows the measured traffic with the Internet, for the entire period of the study, without the PDU connected to the network, and Fig. 9b with connected PDU. Again, the results are almost identical.

Figure 10 shows which protocol generates the most traffic. Figure 10a is for the period of study when the PDU is not connected to the modeled network and Fig. 10b shows the results when the PDU is connected to the network. As it can be seen from the results for SSL both are almost the same. The difference is in the volume of
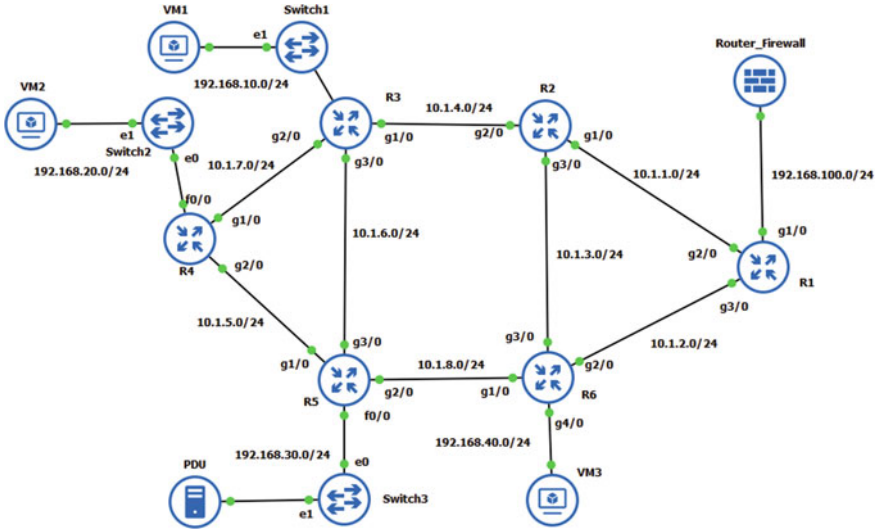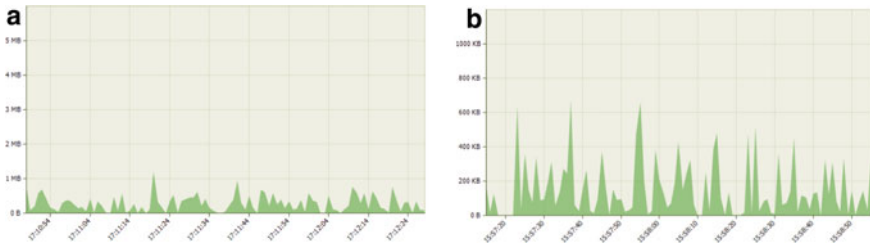
Fig. 7 Topology of the modeled network

Fig. 8 Generated traffic—**a** is the traffic measured every second without the PDU and **b** is the traffic generated with connected PDU
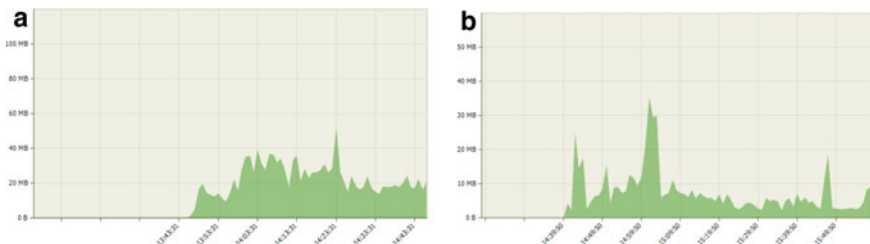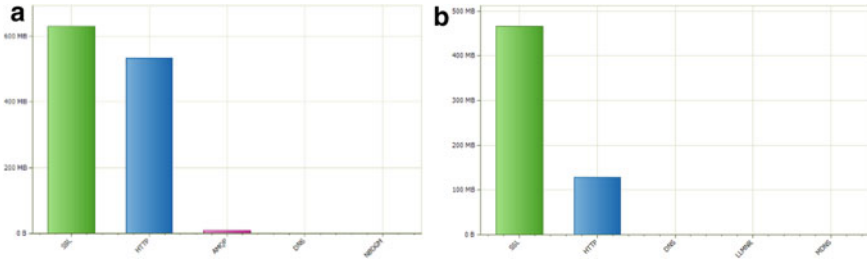

Fig. 9 Total generated traffic—**a** is the total traffic measured for the whole period of the study without the PDU and **b** is the total traffic with connected PDU

Fig. 10 Top application protocols by bytes—**a** without connected PDU and **b** with connected PDU

HTTP traffic, which is much smaller when connected to PDU. When connected to the PDU, the virtual machines mainly generate HTTP traffic to the PDU.

Figure 11 shows from which port the most traffic is generated in the modeled network without the connected PDU, and Fig. 12 shows the same information, but when the PDU is connected. As it can be seen, there is a difference in which port generates the most traffic. In the absence of the PDU, most traffic is generated from port 80, because during the measurement, the main traffic is generated by a 4 K IP camera, which is accessed through a browser on port 80. When the PDU is added to the network, the VMs mainly accessed different YouTube channels, the studied PDU, various Internet pages and the IP camera but less often. Therefore, when connecting the PDU to the modeled network, most traffic is generated from port 443—HTTPS, (YouTube channels and Internet pages) and less from port 80 (the PDU and the 4 K IP camera).
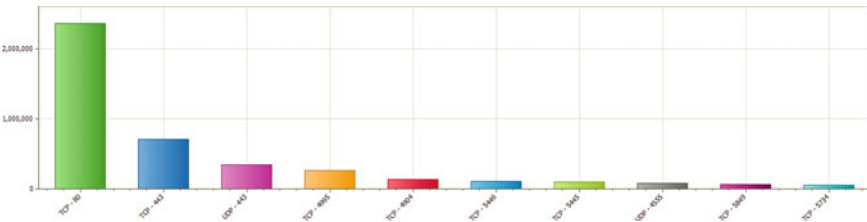
Fig. 11 Top port by total traffic without the PDU
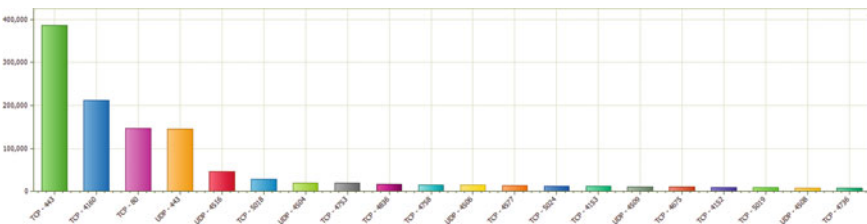
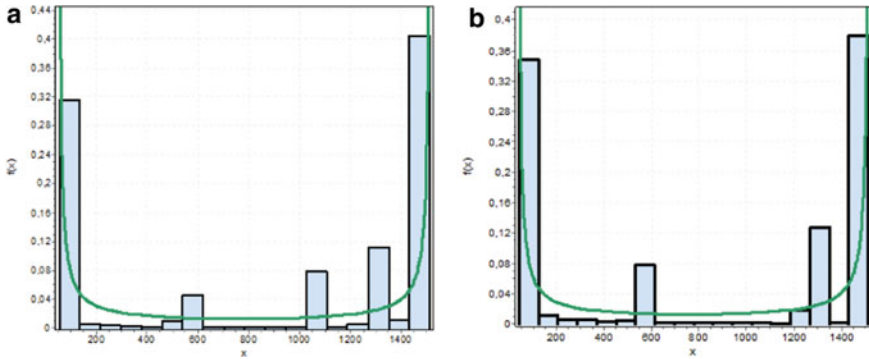Fig. 12 Top port by total traffic with connected PDU

Fig. 13 Mathematical distribution—**a** without the studied PDU and **b** with connected PDU

Figure 13a shows the mathematical distribution of packet size with Beta approximation in the network without the PDU, and Fig. 13b shows the same distribution but with the PDU connected. As it can be seen, there is almost no difference in the size of the generated packets before and after connecting the PDU. A slight increase in the number of 100-byte and 600-byte packets is observed when connecting the studied PDU, because the packets of this size are mainly generated by the studied PDU. When the PDU is connected, packets of large size (over 1000 bytes) decrease because, the IP camera is not accessed as often as in the period before the PDU was connected. The results of the mathematical distributions prove and confirm the expectation that the connection of the PED would not lead to any substantial and significant changes in the distribution of the packets by size.

In summary, the following can be stated: the obtained results of the study confirm the hypothesis that when the studied PED is connected to a working IP network, it does not affect the network's performance. Thanks to the platform GNS3 for IP network modeling, it is possible to create a model of a small experimental IP network through which the hypothesis could be verified. The realization of such a physical experimental network would require significant financial investments in the purchase of the relevant network equipment.

3.3 Model of an IP Network Supplying a Secure Data Exchange

Figure 14 presents the topology of a modeled IP network that demonstrates secure data exchange between the PDU and a workstation. The security of the data exchange is realized by means of a VPN. What is special about this scenario is the creation of a VPN tunnel between R4 and R1. Thus, all the traffic that is generated by the PDU will be transmitted in an encrypted form through R4, R3, R2 and R1. The idea of this scenario is to model a network where the traffic from the PDU is secured and the
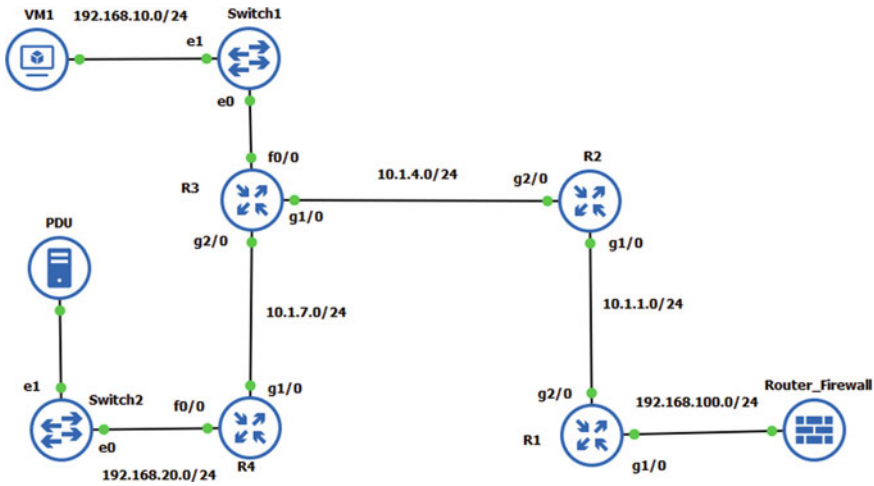
Fig. 14 Topology of the modeled network

PDU cannot be compromised. The network of Fig. 14 is connected to the Internet and VM1 access it. The workstation through which the PDU is accessed is not a virtual machine, but a physical workstation. Verification of secure data exchange between the PDU and the workstation is done using Wireshark. Of course, there are other methods for ensuring secure data exchange described in [15–18].

Figure 15 represents the result of the monitored/captured traffic between R2 and R3. As it can be seen from the Wireshark output, the tunnel is working (10.1.7.2 is the address of R4's g1/0 interface and 10.1.1.1 is the IP address of R1's g2/0 interface), and the exchanged traffic is encrypted. In parallel with the encrypted traffic, the traffic between VM1 and the Internet also flows. In this VPN tunnel, except the traffic between the PDU and the monitoring and control workstation, any other source of traffic cannot be connected to this tunnel. This eliminates the problem of the studied PDU, i.e., insecure data exchange, which is identified in point 3.1.

In summary, the following can be stated: this scenario demonstrates one of the possible ways to secure the traffic exchange between the PDU and the monitoring station. Thanks to the GNS3 platform, it is very easy and fast to create such scenarios and to test other PEDs.

4 Conclusion

Models of working IP networks have been created. The performance of these models has been tested and proved. Thanks to these models, different scenarios of PEDs operation have been studied. The selected IP network modeling platform offers many
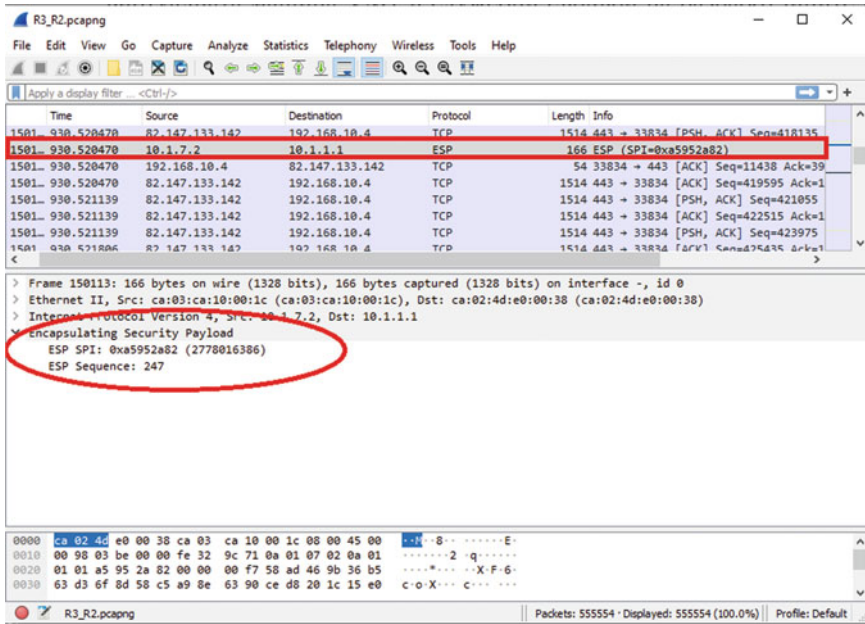
Fig. 15 Security checking

capabilities and functionalities such as running and emulating disk images of operating systems of real network devices, the ability to connect to real IP networks, integration with IP network monitoring tools and more. The platforms for modeling IP network can be used to characterize the communication traffic generated by any PED. Additionally, it can be checked whether the information exchanged between the PED and the command-and-control workstation are secure or not. If it is not, various technologies and techniques can be applied to test if the data exchange is secure. All this can be done by using platforms for modeling IP networks. Traffic characterization and verification for secure information exchange, through the use of platforms for modeling IP networks can also be applied to the study of any devices that have the ability to connect and work with IP networks. Through the platforms for modeling IP networks, various scenarios can be created to explore any possible operating situations in which the PEDs could operate. Thanks to the platforms for modeling IP networks, the hypotheses that PEDs generate extremely little traffic and connecting a PED to an existing working IP network does not lead to any, if not almost no significant changes in network performance, are confirmed by this study.

The main drawback of the platform used for modeling IP networks, and for all other such platforms, is the serious requirement for the computing capabilities of the workstation that will be used for modeling IP networks. The higher these computational capabilities are the larger and more complex IP network models can be modeled.

References

1. Tashev TD, Alexandrov AK, Arnaudov DD, Tasheva RP (2022) Large-scale computer simulation of the performance of the generalized nets model of the LPF-algorithm. In: Lirkov I, Margenov S (eds) Large-scale scientific computing. LSSC 2021. Lecture notes in computer science, vol 13127. Springer, Cham. https://doi.org/10.1007/978-3-030-97549-4_55
2. Peng J, Michael G, Kimmig A, Marinov MB, Wang J, Ovtcharova J (2020) An advanced IoT platform and its implementations focused on modern information technology generation. XI Nat Conf Int Participation (Electronica) 2020:1–4. https://doi.org/10.1109/ELECTRONICA50406.2020.9305135
3. Prathik A, Ahiraj S, Harsha Y, Prince K (2022) IoT based smart power extender with timer feature controlled through a mobile app. J Inform Technol 4(2):61–73
4. Shetty N (2021) A comprehensive review on power efficient fault tolerance models in high performance computation systems. J Soft Comput Paradigm 3(3):135–148
5. Sapundzhi, Popstoilov M (2019) C # implementation of the maximum flow problem. In: 2019 27th national conference with international participation (TELECOM), pp 62–65
6. Cherneva GP (2019) Control of the chaotic processes in chaos shift keying communication system. In: 2019 27th national conference with international participation (TELECOM), pp 1–3
7. Mirtchev ST (2020) Investigation of queueing systems with a polya arrival process. In: 2020 28th national conference with international participation (TELECOM), pp 29–32
8. Tashev TD, Marinov MB, Tasheva RP, Alexandrov AK (2021) Generalized nets model of the LPF-algorithm of the crossbar switch node for determining LPF-execution time complexity. AIP Conf Proc 2333:090039. https://doi.org/10.1063/5.0042856
9. Tashev TD, Monov VV, Tasheva RP (2017) High performance computations for study the stability of a numerical procedure for crossbar switch node. In: Dimov I, Faragó I, Vulkov L (eds) Numerical analysis and its applications. NAA 2016. Lecture notes in computer science, vol 10187. Springer, Cham. https://doi.org/10.1007/978-3-319-57099-0_76
10. Navabud P, Chen C-L (2018) Analyzing the web mail using wireshark. In: 2018 14th international conference on natural computation, fuzzy systems and knowledge discovery (ICNC-FSKD), pp 1237–1239
11. Majidha Fathima KM, Santhiyakumari N (2021) A survey on network packet inspection and ARP poisoning using wireshark and Ettercap. In: 2021 international conference on artificial intelligence and smart systems (ICAIS), pp 1136–1141
12. Marinov MB, Nikolov N, Dimitrov S, Todorov T, Stoyanova Y, Nikolov GT (2022) Linear interval approximation for smart sensors and IoT devices. Sensors 22:949. https://doi.org/10.3390/s22030949
13. Mirtchev ST (2018) Packet-level link capacity evaluation for IP networks. Cybern Inform Technol 18(1):30–40
14. Sapundzhi FI, Popstoilov MS (2018) Optimization algorithms for finding the shortest paths. Bulgarian Chem Commun 50, no. Special Issue B, pp 115–120
15. Dimitrov W, Jekov B, Kovatcheva E, Petkova L (2020) An analysis of the new challenges facing cyber security expertise. In: EDULEARN20 proceedings, pp 2978–2986
16. Dimitrov W (2020) The impact of the advanced technologies over the cyber attacks surface. In: Silhavy R (eds) Artificial intelligence and bioinspired computational methods, CSOC 2020. Advances in intelligent systems and computing, vol 1225. Springer, Cham.
17. Hristov P, Dimitrov W (2019) The blockchain as a backbone of GDPR compliant frameworks. Qual Access Success 20:305–310
18. Popov G (2019) A Discrete model of multi-agent intrusion detection system. II International conference on high technology for sustainable development (HiTech) 2019:1–5

Predicting Online Job Recruitment Fraudulent Using Machine Learning

Ishrat Jahan Mouri, Biman Barua, M. Mesbahuddin Sarker, Alistair Barros, and Md Whaiduzzaman

Abstract Employing individuals via the Internet has been a boon for businesses in the modern day. It is much simpler and more convenient than traditional recruitment methods. However, several scammers are abusing this platform, which may result in financial and privacy loss for job seekers and damage to the reputable organisation's name. In this research, we proposed a technique for detecting Online Recruitment Fraud (ORF). This model uses a publicly available dataset containing 17,780 job postings. We apply the four classification models to determine which classification model performs best for our suggested model. In this model, we use decision trees, random forests, Naive Bayes and logistic regression methods. We have estimated and evaluated the accuracy of several prediction systems. The random forest classifier provides the greatest accuracy, 97.16%, on our dataset. We have endeavoured to develop a method for detecting bogus recruiting postings.

Keywords Online recruitment fraud · Machine learning · Classification model · Natural language processing

I. J. Mouri · B. Barua (✉) · M. Mesbahuddin Sarker · Md Whaiduzzaman
Institute of Information Technology, Jahangirnagar University, Dhaka 1342, Bangladesh
e-mail: biman@buft.edu.bd

A. Barros · Md Whaiduzzaman
School of Information Systems, Queensland University of Technology, Brisbane, Australia

B. Barua
Department of CSE, BGMEA University of Fashion and Technology, Nishatnagar, Turag, Dhaka 1230, Bangladesh

1 Introduction

Online banking, online classes, e-commerce, online recruitment, etc., are now virtu-alised in the current period, which has seen the virtualisation of every industry that was once managed traditionally. The Internet has become the most popular platform for information searching, sharing, learning and research [1]. Globally, recruitment is currently conducted through job portals. On these platforms, organisations of varying backgrounds post job advertisements and vacancy lists containing the needed skills and experiences. In accordance with their preferences, job seekers from all cate-gories can post their resumes and academic credentials to these portals and apply for their preferred positions. Most firms use ATS software to recruit and hire employees [2]. Application Tracking System is software that allows recruiters to monitor appli-cants throughout the recruiting process. From placing advertisements to reviewing resumes and finding the ideal personnel, a substantial amount of time and effort is required. However, ATS software makes it simple and suitable to perform these vital tasks. Previously, small- and medium-sized businesses were unfamiliar with this software. However, small businesses are currently adopting this service due to its efficacy. According to one article, there were about 5 million job openings in the United States in 2015, most of which were posted online [3]. Scammers have taken notice of the widespread use of ATS software around the world. ORF is a new type of fraudulent activity. Very little research has been conducted on detecting online employment fraud. But ORF is a contemporary and significant subject that requires a great deal of attention and worry. This research proposes a machine learning-based methodology to identify fraudulent and legal job postings. This model was applied to a dataset of 17,880 job postings made available to the public. The pre-processing of data was crucial to this investigation. Text mining, lexical analysis, tokenisation and semantic analysis have been utilised as pre-processing procedures. After extracting the dataset's key attributes, it has been divided into two sections: the training and testing datasets. The training dataset was used to train the model, while the testing dataset was used to predict the model's final output. Four distinct classifi-cation methods, including random forest, decision tree classifier, NB (Naive Bayes) and LR (Logistic regression), were utilised in this research, which is described in detail later in this paper.

2 Literature Review

The authors of a research publication [4] established a technique for detecting Online Recruitment Fraud. Their proposed paradigm includes three primary phases of inves-tigation. To apply their model, they utilised a cost-free online dataset known as EMSCAD. The initial phase involved data preparation. In this step, noise and non-informative symbols and words were eliminated so that they would not interfere with the general alignment of the text. The second step required the selection of features.

A Support Vector Machine (SVM) was used to identify and extract features from labelled data. The final phase was classification, and random forest ensemble classifiers were employed to recognise phoney job postings from fake data. In recent research on models and algorithms, the random forest classifier has been deemed the most appropriate and effective technique. This model achieved a 97.4% detection rate for bogus jobs.

In a separate study [5], they investigated many characteristics of Online Recruitment Fraud (ORF) and, more crucially, employment fraud, including its intensity and other characteristics. In this work, they also clarified the use of ATS. On a publicly accessible dataset titled Employment Scam Aegean Dataset, they applied six WEKA classifiers: random forest classifier, naive Bayes, j48, oneR, zeroR and logistic regression (EMSCAD). They have picked four fields for identifying bogus job postings: String, HTML fragment, Binary and Nominal. The random forest classifier demonstrated the highest classification accuracy, 89.5%, but Logistic regression did quite poorly on the sample. They evaluated that job scams share similarities with well-known issues such as cyberbullying, phishing, Wikipedia vandalism, review fraud and e-mail spam, all of which require blended solutions.

In a different research work [6], the authors proposed a decision support system approach for preventing employment recruitment fraud. They applied their model using a profile matching method, and it is a model that compares the candidates' abilities to the job requirements and assigns a value. Moreover, in a previous study [7], the authors exhibited a deeper comprehension of the most recent advancements in machine learning classifiers for spam filtering. They explored strategies linked to both text and images.

Nowadays, online reviews play a crucial role in the purchasing process. A positive review is essential for growing a product's sales, while a negative review is sufficient for diminishing a product's popularity. As with phoney job postings, there is now an abundance of fake negative reviews. An article [8] proposes several ways and techniques for resolving review spam imprisonment. Their study article classified a number of review spam detection systems and launched a category of review spam detection methods. After data pre-processing, feature selection is regarded as the essential approach.

E-mail spam is regarded as the most common sort of spam. Every day, we receive an abundance of promotional, advertising and phishing e-mails. In the realm of spam filtering, several machine learning algorithms and their application were examined [9]. This study discusses numerous academic attempts to solve the spam problem using machine learning techniques. Support Vector Machine has been utilised in another suggested system [10] to distinguish between spam and ham e-mails. Utilising feature selection to implement Ant Colony Optimization yielded more precise and promising results.

In [1], the authors discussed online employment systems' significance for job searchers and employers. They introduced a model based on ensemble learning called ORF detector to detect bogus job postings. The ORF detector model was developed with the aid of 3 base classifiers termed j48, logistic regression (LR), random forest (RF) and three ensemble approach. The characteristics were categorised as linguistic,

contextual and metadata. They utilised six distinct measures to estimate the performance of the ORF detector: accuracy, precision, recall, $f1$ measure, sensitivity and specificity. The base classifiers have an average accuracy of 95.4%. Their end results demonstrated that ensemble basis approaches are highly advantageous for improving baseline classifier performance. The ORF detector model awarded $f1$ a score of 94%.

Seventy-five per cent of Fortune 500 businesses use an applicant tracking system (ATS) to assess and monitor all applications [2]. They studied a dataset of 17,000 job postings and determined that 95% are authentic and 5% are fraudulent. In addition, they mentioned that natural language processing (NLP) and machine learning are utilised to classify textual, structural and contextual aspects to distinguish between authentic and false job advertisements.

Another work is implementing supervised machine learning algorithms for spam e-mail filtering [11]. This model employs the C 4.5 Decision tree classifier, multilayer perceptron and Naive Bayes classifier. In a different study [12], they examined content-based filtering. Radial Basis Function Neural Networks (RBFNN) is regarded as one of the essential types of ANN used in research [13]. In [14, 15], they combined Genetic Algorithm (GA) and Support Vector Machine (SVM) to determine whether or not an e-mail is a spam. The GA approach has been implemented for picking SVM classifiers' preferred features. They launched a novel technique for filtering spam messages comprising seven distinct components in [16, 17]. This methodology relies on a user-specific history of past e-mails and spam e-mails. This model identified 98.17% of spam.

For spam filtering, a strategy utilising an Artificial Neural Network and the perceptron learning rule was suggested. In [18], authors proposed a technique for recognising the employment activities of violent groups on social media. They utilised a dataset generated by the Dark Web Project at the University of Arizona. Under the curve (AUC), the SVM classifier earned 89%, whereas the Naive Bayes classifier achieved 63%. Several machine learning techniques have been implemented to design numerous prediction models in the industry.

3 Methodology

3.1 Process

The primary objective of a machine learning study or activity is to collect data. The validity of the dataset is the most critical consideration for subsequent research and work. The model's output will be completely useless if the dataset is illegitimate. We utilised a publicly accessible dataset from Kaggle titled 'fake job postings' containing 17,780 job listings which is widely known as an online community platform for people who have an interest in data science and machine learning. Specialised workers manually interpreted all data. The process of explanation refers to the quality assurance of procedures. Following data collection, the next phase is

data processing. The collected dataset is understandable by humans but is not suitable for use in algorithms. Consequently, as explained in the next section, the dataset has been pre-processed to produce more accurate algorithms and output.

The third phase involves identifying the primary characteristics of the entire dataset. The primary characteristics have a significant impact on the value of the output. The dataset has been filtered because irrelevant information may interfere with the research. For data filtering, the techniques of the imputation of missing data, visualisation techniques for handling outliers and data scaling have been utilised.

After extracting the dataset's key features, it has been divided into two sections: the training dataset and the testing dataset. The machine learning algorithm utilises the training dataset to teach the model. After learning the model, the testing dataset forecasts the model's final output. Various machine learning algorithms and classifiers, such as random forest, decision tree classifier, NB (Naive Bayes) and LR (logistic regression), have been applied throughout this entire procedure. Each algorithm's precision has been scrutinised. It has been determined which classifiers have a higher accuracy percentage and which classifiers performed poorly on the dataset.

Figure 1 shows the proposed system model which visualises the working sequence of this research work.

3.2 Dataset Description

There are two separate groups which are real and fake jobs. The fraudulent feature indicates whether a job is legitimate or not. We have looked for some selective parameters for each job such which are Title, Location, Company profile, Job Description, Requirement, Benefits and Fraudulent. There are several categories of job posts in the dataset such as Marketing, HR, Medical, General Services, Engineering, Business Development and Finance so that the work would not be limited for some specific job.

3.3 Feature Analysis

There were 17,780 job posts in the dataset on which we have implemented the model. Among them, 865 jobs are fake and the rest are legitimate. The dataset was imbalanced in nature. There were a total of 18 feature variables in the dataset from where we have considered 5 feature variables and 1 target variable. All of these feature variables are text-based data. To proceed further with these textual data, we have applied NLP mechanism to transform these textual data into numeric values. After pre-processing the dataset, it has been split into two parts. 80% of the dataset was utilised for learning the model, and the rest 20% was utilised for implementing the model.
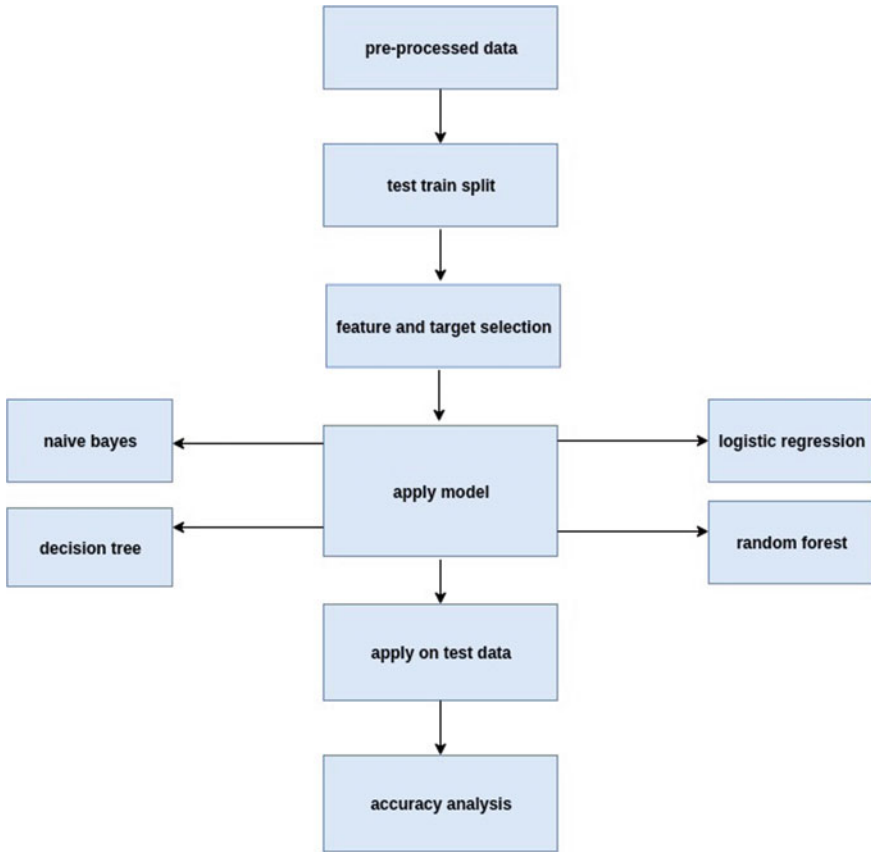
Fig. 1 Proposed system model

3.3.1 Graphical Analysis

After analysing the dataset in the initial stage, we have got some significant information which has been represented through some graphical analysis in Figs. 2 and 3.

3.3.2 Data Pre-processing

Text mining or text analytics is an artificial intelligence technology that uses natural language processing (NLP) to transform unstructured text in databases and documents into structured, normalised data suitable for exploration or driving machine learning (ML) algorithms. In this study, both lexical analysis and semantic analysis were utilised in Fig. 4.
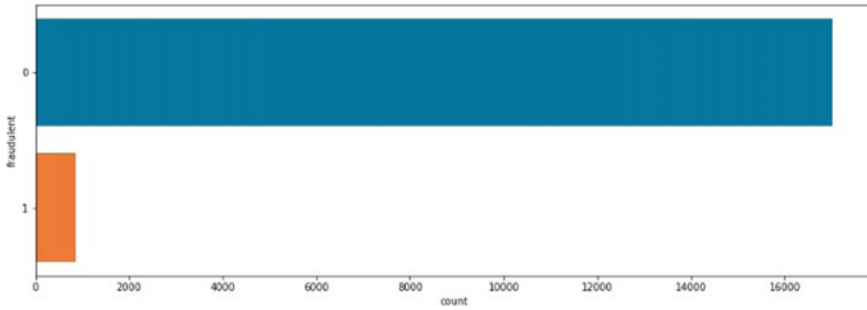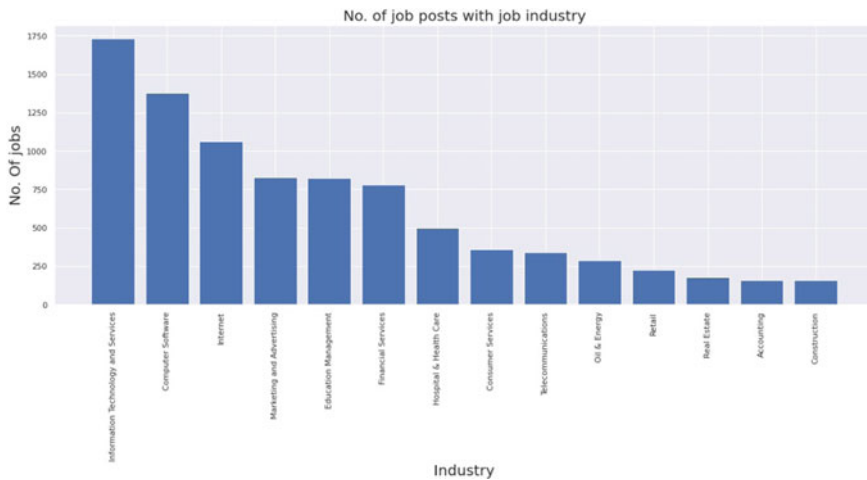
Fig. 2 Real and fake job comparison on bar chart

Fig. 3 Types of department and job number

Lexical analysis or tokenisation identifies and examines the structure of words. A language's word and phrase collection is called its lexicon, and the entire text is broken down in lexical analysis into words, phrases and paragraphs. Lemmatisation is a lexical analysis technique that has been employed here to reduce a few words to their dictionary or base form. This text processing technique also handles duplicate records as it always looks for the root form of duplicate words and eliminates the rest. It evaluates aspects such as the meaning of each word in the context of the phrase, the word's grammatical structure and its usage in adjacent sentences.

Firstly, we replaced null values with empty space (' ') and then removed the rows from the dataset that have significant empty values. After tokenisation, URLs and any non-essential characters (Numbers and Punctuation) are removed from the text. Then, every character was transformed to lowercase. We then eliminated stop words from the data. This is the NLP pre-processing step used most commonly. After removing stop words from the data, another natural language processing technique,
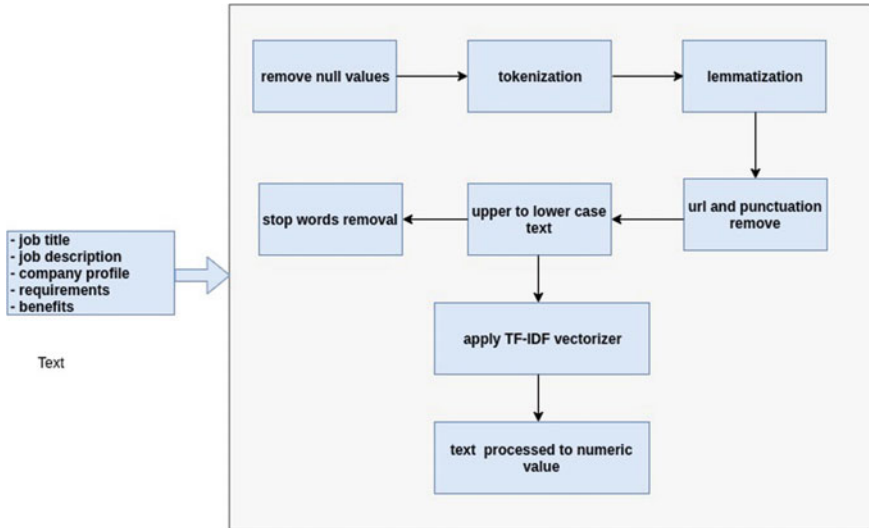
Fig. 4 Data pre-processing on text data

TF-IDF (Term Frequency-Inverse Document Frequency), was used to analyses the data. TF-IDF is used to determine the significance of a word within a corpus of texts. TF can be found by counting the number of occurrences of a given word in a document, and IDF determines the importance of each word in the manuscript. The TF-IDF values are counted now that both TF and IDF values are present. Null values identified with heatmap are shown in Fig. 5.

4 Algorithm Implementation and Analysis

4.1 Algorithms

The key processes of algorithms that are applied to our data are briefly described here so that we can understand how it operates to predict actual results in our dataset. The justification for using these algorithms are as follows:

 (i) As we have worked with numerical datasets, decision tree classifier works best for this type of dataset.
 (ii) For Naïve Bayes, feature variables of the dataset are independent and the extracted feature variables are equally contributed to the outcome.
(iii) Since in our dataset we have considered two classes: fraud job = 1 and real job = 0, in this case logistic regression significantly fits well with this type of dataset.
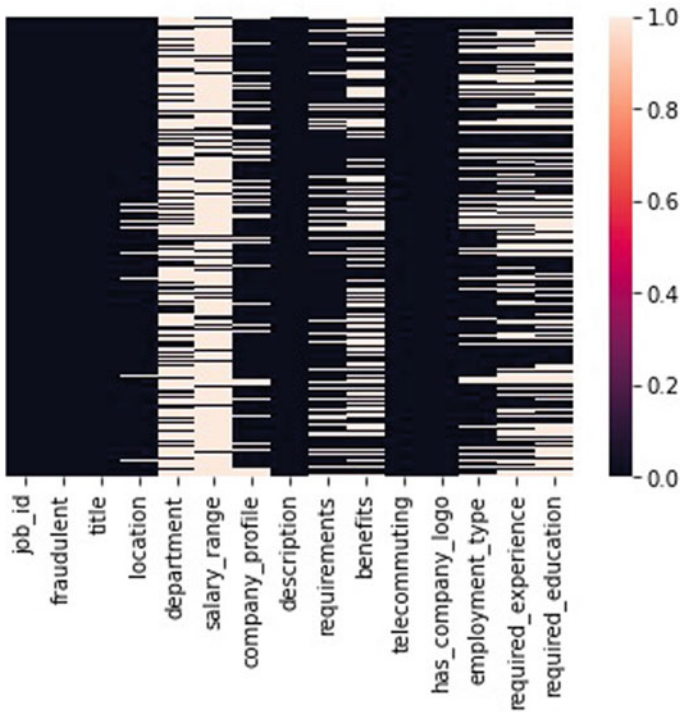
Fig. 5 Null values identify with heatmap

(iv) The significant reason for considering random forest is it performs well with both regression and classification problems with a high accuracy rate.

4.1.1 Decision Tree Classifier

In our dataset, the process of constructing a decision tree is completed through some specific steps. Gini impurity is one of the key processes that detects whether a selected feature will be wrong classification or not.

$$\text{Gini} = 1 - \sum_{i=1}^{n} (pi)^2$$

Here, if we consider total 10 data from our dataset where 4 of them are fake and 6 are real job then Gini equation splits the attributes as 6/10 for 0 and 4/10 for 1 where 1 is for fake jobs and 0 is for real job in our dataset. So, the Gini index is

$$1 - \left((4/10)^2 + (6/10)^2\right) = 0.48 \tag{1}$$

If we consider a feature variable from our dataset is 'about' where 4 of them are fake job with frequency less than 0.5 and 6 of them are real job with frequency greater than 0.5, then the Gini index is

$$1 - \left((0.45/4)^2 + (0.6/4)^2\right) = 0.96 \tag{2}$$

so if we merge the Gini index then we get

$$4/10 * 0.48 + 6/10 * 0.96 = 0.76 \tag{3}$$

So accordingly, the Gini index features with less than 0.76 will be considered to split the data in next level.

4.2 Naïve Bayes Algorithm

Bayes theorem produces a technique for calculating the posterior probability, $P(Y/X)$ from $P(Y)$, $P(X)$ and $P(Y/X)$.

$$P(a|b) = P(b|a) * P(a)/P(b) \tag{4}$$

Multinomial Naïve Bayes has been implemented in this model. In our dataset, there are one hundred feature variables. For example, a random feature variable like 'about' is considered. Now, according to the Naive Bayes theorem, the prior probability of this feature variable is

$$P(\text{about}) = 6/15 = 0.40 \tag{5}$$

Next, we calculate the probability of the job being fraud for each target variable. $P(1) = 9/15 = 0.60$ (4.6). Then, we calculate posterior probabilities.

$$P(\text{about}|1) = 6/9 = 0.66 \tag{6}$$

Now, we put these values in Eq. 4.

$$P(1|\text{about}) = 0.66 * 0.60/0.40 = 0.99(\text{Higher}) \tag{7}$$

The output is 0.99 which means the probability is higher. Naive Bayes classifier has worked in our dataset in this same way.

4.3 Logistic Regression

The hypothesis of the logistic function

$$h\theta(x) = g(\theta^{T}x) \tag{8}$$

For solving the classification problem, logistic regression is used. A 'S'-shaped curve that predicts two maximum values (0 or 1) is fitted in logistic regression. It is called Sigmoid function or logistic function $g(z)$. The logistic function is expressed as follows:

$$g(z) = 1/1 + e^{-z} \tag{9}$$

Now, we get the final output of the logistic regression hypothesis as

$$h\theta(x) = 1/1 + e^{-}\theta x \tag{10}$$

As the number of feature variable is not more than one hundred in our dataset, the hypothesis of logistic regression becomes

$$h\theta(x) = g(\theta 0 + \theta 1 \times 1 + \ldots \theta 100 \times 100) \tag{11}$$

Now, the classifier will predict the job 'fraud' if

$$g(\theta 0 + \theta 1 \times 1 + \ldots \theta 100 \times 100) \geq 0 \tag{12}$$

4.4 Random Forest Algorithm

Random forest generates a primary learner's model using row sampling with replacement and feature sampling with replacement. Initially, RF constructs N training sets from the initial database. This technique is also known as bagging or bootstrap aggregation. It is a frequently used ensemble learning method for decreasing variance within a noisy dataset. Row sampling and feature sampling are performed as a replacement for creating N decision trees, meaning that independent data points can be selected many times. The decision tree is regarded as the foundation of the random forest algorithm. Multiple decision trees alter the conditions of RF's decision-making. There will be distinct precision for each individual tree, and the final precision will be the mean of each individual tree's precision. Multiple decision trees are utilised to address the issue of missing labels or titles.
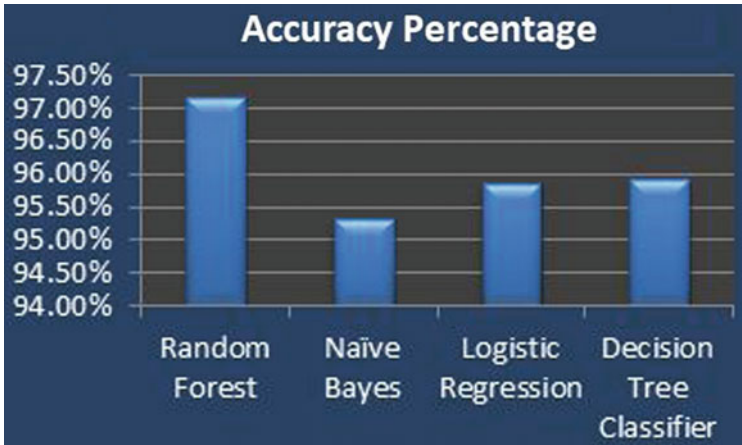
Fig. 6 Accuracy observation graph

5　Result and Discussion

5.1　Accuracy Prediction

Four classification algorithms have been evaluated to see which provides the most precise results on a dataset. The random forest, Naive Bayes, logistic regression and decision tree classifier machine learning algorithms have been implemented. Initially, to compare their precision, accuracy measurements were employed. The accuracy metric is used to evaluate classification models and calculate the overall number of predictions to the total number of predictions. It is evident from the results that there is no significant variation in accuracy between the classifiers. The random forest classifier achieved the best level of accuracy on the dataset, 97.16%. The entire accuracy range lies between 95 and 97% as in Fig. 6.

5.2　Performance Comparison with Evaluation Metrics

For measuring the performance of a model, it is essential to employ several metric explanations. The different performance metrics are shown in Figs. 7, 8, 9 and 10. Figure 7 conceptualises the performance measure metrics of three parameters which are precision, recall and $f1$ score of logistic regression. Only measuring precision is insufficient. Several measures, including precision, recall and $f1$ score, have been considered to determine the most effective method for addressing problems. Precision is the ratio of expected positive values to the total predicted positive values. The recall is the ratio of correct positive values to predictions that are all positive inside a dataset.
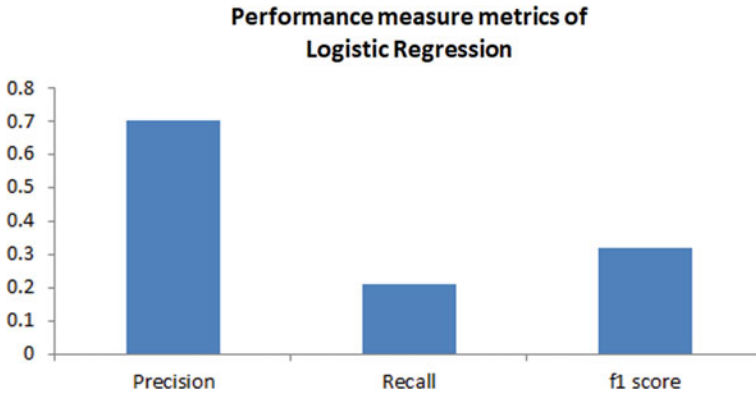
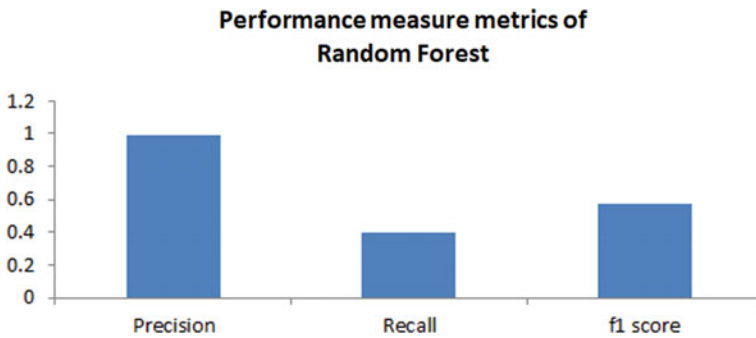**Fig. 7** Performance metrics of logistic regression

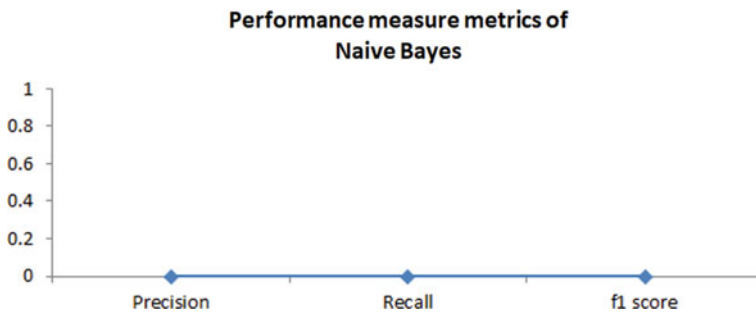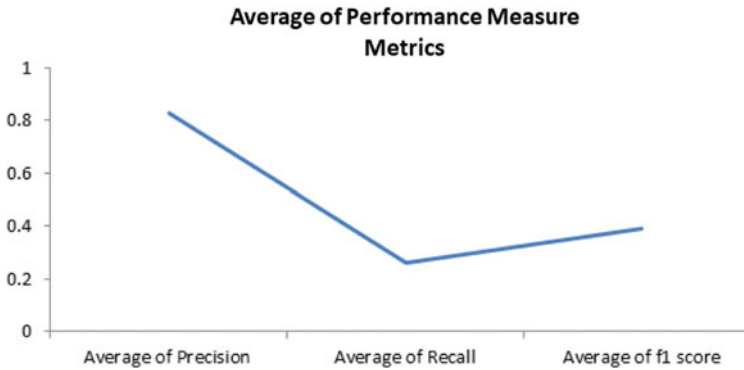**Fig. 8** Performance metrics of random forest

Fig. 9 Performance metrics of Naïve Bayes

Fig. 10 Average performance metrics

The harmonic mean of precision and recall is examined for a classifier's $f1$ score. In Fig. 10, we have calculated the average value of precision, recall and $f1$ score of random forest, decision tree, Naïve Bayes and logistic regression and summarised it in a graph format.

6 Conclusion and Future Work

6.1 Conclusion

We have taken around three months for literature review, revising the technologies and proceeding through the error and trial method in Python. We have faced remarkable complexities because of finding out a proper dataset, processing the dataset, implementing new modules of machine learning and finally analysing the output.

In this research, we have compared the performance of different supervised classification algorithms. We have implemented this model on a dataset containing 17,780 job posts. After implementing the model, random forest classifier performed the best among all other classifiers. The random forest classifier gave the highest accuracy percentage which is 97.16%. The accuracy range of all the classifiers is between 95 and 97%. This model can assist job seekers to identify fake and real jobs and save themselves from fraudsters.

6.2 Future Work

The accuracy of a machine learning model is contingent on the dataset. In future, we would like to work on this model with a larger dataset to increase the result's

accuracy range. To use this concept in the real world, we would like to develop a system for using it in a job portal. This concept can be implemented into the systems of various job portals to avoid fraudulent recruitment postings.

References

1. Lal S, Jiaswal R, Sardana N, Verma A, Kaur A, Mourya R (2019) ORFDetector: ensemble learning based online recruitment fraud detection. In: 2019 twelfth international conference on contemporary computing (IC3). IEEE, pp 1–5
2. Vidros S, Kolias C, Kambourakis G (2016) Online recruitment services: another playground for fraudsters. Comput Fraud Secur 2016(3):8–13
3. Alghamdi B, Alharby F (2019) An intelligent model for online recruitment fraud detection. J Inf Secur 10(03):155
4. Vidros S, Kolias C, Kambourakis G, Akoglu L (2017) Automatic detection of online recruitment frauds: characteristics, methods, and a public dataset. Future Internet 9(1):6
5. Suryanto T, Rahim R, Ahmar AS (2018) Employee recruitment fraud prevention with the implementation of decision support system. In: Journal of physics: conference series, vol 1028, no. 1. IOP Publishing, p 012055
6. Guzella TS, Caminhas WM (2009) A review of machine learning approaches to spam filtering. Expert Syst Appl 36(7):10206–10222
7. Hussain N, Turab Mirza H, Rasool G, Hussain I, Kaleem M (2019) Spam review detection techniques: a systematic literature review. Appl Sci 9(5):987
8. Dada EG, Bassi JS, Chiroma H, Adetunmbi AO, Ajibuwa OE (2019) Machine learning for email spam filtering: review, approaches and open research problems. Heliyon 5(6):e01802
9. Karthika R, Visalakshi PJWTC (2015) A hybrid ACO based feature selection method for email spam classification. WSEAS Trans Comput 14(2015):171–177
10. Christina V, Karpagavalli S, Suganya G (2010) Email spam filtering using supervised machine learning techniques. Int J Comput Sci Eng (IJCSE) 2(09):3126–3129
11. Sculley D, Wachman GM (2007) Relaxed online SVMs for spam filtering. In: Proceedings of the 30th annual international ACM SIGIR conference on research and development in information retrieval, pp 415–422
12. Cao Y, Liao X, Li Y (2004) An e-mail filtering approach using neural network. In: International symposium on neural networks. Springer, Berlin, pp 688–694
13. Wang HB, Yu Y, Liu Z (2005) SVM classifier incorporating feature selection using GA for spam detection. In: International conference on embedded and ubiquitous computing. Springer, Berlin, pp 1147–1154
14. Tak GK, Tapaswi S (2010) Query based approach towards spam attacks using artificial neural network. Int J Artif Intell Appl 1(4):82–99
15. Kufandirimbwa O, Gotora R (2012) Spam detection using artificial neural networks (perceptron learning rule). Online J Phys Environ Sci Res 1(2):22–29
16. Scanlon JR, Gerber MS (2014) Automatic detection of cyber-recruitment by violent extremists. Secur Inf 3(1):1–10
17. Candanedo IS, Nieves EH, González SR, Martín M, Briones AG (2018) Machine learning predictive model for industry 4.0. In: International conference on knowledge management in organizations. Springer, Cham, pp 501–510
18. Valanarasu MR (2021) Comparative analysis for personality prediction by digital footprints in social media. J Inf Technol 3(02):77–91

Delay-Efficient Vedic Multiplier Design Using 4:3 Counter for Complex Multiplication

M. Venkata Subbaiah and G. Umamaheswara Reddy

Abstract Multiplier is one of the functional blocks in the Arithmetic and Logic Unit. Designing a delay-optimized multiplier is always a challenging task at the system design level. In this paper, a 4:3 counter is proposed based on 2-bit reordering circuit. The Wallace tree multiplier (WTM) is designed using 4:3 counter and other adder circuits such as 6:3 counter, Full Adder (FA), as well as Half Adder (HA). The designed WTM is utilized in the design of Urdhva Tiryagbhyam (UT) sutra-based multiplier. In addition, the complex multiplier is designed using the proposed Vedic multiplier (VM). The designed complex multiplier's functionality is verified by Xilinx Vivado 2017.2 and also synthesized the circuits by targeting 'xc7s50fgga-484-1' device of Spartan-7 family. Furthermore, the performance of complex multiplier designed with proposed VM is compared based on the parameters such as Critical path delay (CPD) and LUT count with the existing multipliers.

Keywords Wallace tree multiplier · 4:3 counter · 2-bit reordering circuit · Urdhva Tiryagbhyam sutra · Complex multiplier

1 Introduction

Multiplier is one of the critical data path elements of the processor and is crucial in many circuits that are used for signal/image processing. Since it requires huge hardware and exerts more power there is always a need for the design of an efficient multiplier in respect of area, power, and delay. Vedic mathematics [1] is an ancient method used for doing computations that allows us to perform the computations in less time manually. The sutras or mathematical formulae came into availability with the great effort from Swami Bharati Krsna Tirthaji. There are many sutras and sub-sutras such as Nikhilam sutra, Anurupyena sutra, Ekadhikena purvena sutra, and many others for

M. Venkata Subbaiah (✉) · G. Umamaheswara Reddy
Department of E.C.E., S. V. U. College of Engineering, Sri Venkateswara University, Tirupati, Andhra Pradesh, India
e-mail: venkatmadaka@gmail.com

735

multiplication in which UT sutra is popular and applied to all numbers. In the literature, there are many works based on the UT sutra for multiplication for achieving better performance. A few of them are listed as follows.

VM is implemented with different adder structures such as Ripple Carry Adder (RCA) [2, 3], RCA with multiplexer based FA [4], Carry Look-ahead Adder (CLA) [2, 5], modified Carry Select Adder (CSLA) [6], Kogge-Stone Adder (KSA) [2, 6, 7], Han-Carlson Adder (HCA) [8], and Common Boolean Logic Adder (CBLA) [9]. The multiplier designed in [2–5] employed three adders of different size that performs the addition on the intermediate results concurrently to achieve the final result. For example, a 16-bit VM requires two 24-bit adders and one 16-bit adder in this case. The multipliers designed in [3, 6–9] employed three adders of same size that performs the addition on the intermediate results sequentially to achieve the final result. For example, a 16-bit VM requires three 16-bit adders and one HA in this case. The multipliers designed with Parallel Prefix Adders (PPAs) such as KSA and HCA offers less delay than conventional adder circuits. However, the circuit complexity increases as well as consumes huge power.

Rajasekhar and Satya Sai Ram [10] designed the VM and it is used along with CLA in the implementation of real Fast Fourier Transform. Kodali et al. [11] proposed UT sutra-based IEEE 754 format single precision (SP) and double precision (DP) floating point multiplier (FPM) that exhibits better performance when compared to Karatsuba algorithm-based single and double precision FPMs. Ramya and Seshasayanan [12] proposed SP FPM for binary coded decimal format, in which the 23-bit mantissa multiplication is carried out using VM. The circuit offers less delay and consumes less power. Pooja et al. [13] proposed VM using Quantum dot-cellular automata (QCA). Since the circuit is designed with QCA, the circuit is compact and consumes less power. Christilda and Milton [14] proposed predictor logic-based 2-bit VM. The predictor logic is useful in predicting the outputs of the circuit based on the Partial Product (PP) bits. Then that 2-bit VM is used for the implementation of higher bit VM. It is designed for the implementation of 2D FIR filter. In [15–17], VM based on reversible logic gates were designed. In [18], Baugh-Wooley multiplier is designed by employing CMOS domino logic-based modified FA that consumes less power and provides less delay.

The speed of the higher bit VM can be enhanced either by employing efficient lower bit multiplier or by employing the efficient adder circuits. Many of the previous works followed the second approach to enhance the speed of the VM. Such approaches improved the speed and the circuit area as well. In this paper, an attempt is made to improve the speed of VM by following the first approach that is a lower bit WTM [19] is employed. In this paper, a 4:3 counter is proposed using 2-bit reordering circuit. The proposed 4:3 counter is used along with 6:3 counter, FA, and HA in the design of 8-bit WTM. Then it is used along with 16-bit RCA in the design of 16-bit VM. The proposed VM is used in the implementation of complex multiplier, which is a prominent operation in the Discrete Fourier Transform (DFT) and Fast Fourier Transform (FFT).

The remaining parts of the paper is composed as follows. The multiplication method based on the UT sutra is described in Sect. 2 while in Sect. 3 the details of the proposed 4:3 counter, the methodology of the proposed 8-bit WTM, the 16-bit VM design using WTM and RCA, and the architecture of complex multiplier are presented. The simulation and synthesis results are presented in Sect. 4. Finally, Sect. 5 presents the conclusion.
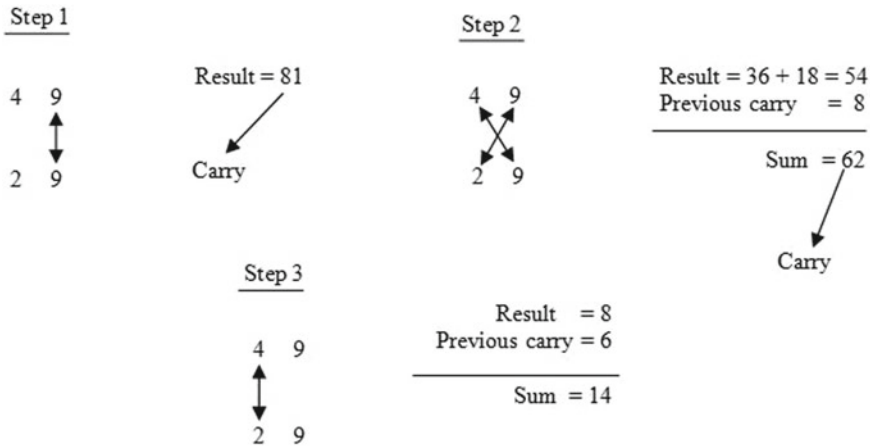
2 Multiplication Using Urdhva Tiryagbhyam Sutra

In the sutra, Urdhva and Tiryagbhyam words denote the vertical and crosswise operations, respectively. The working method of multiplication using UT sutra is explained as follows. For example, let us consider two 2-digit numbers 49 and 29. In step 1, the Least Significant Digits (LSDs) of two numbers that is nines are multiplied. If the result is a single digit number that is the required value. Otherwise, the LSD is the required value and the Most Significant Digit (MSD) is the carry that is to be added with the result generated in step 2. In step 2, the two digits of two numbers are crosswise multiplied that is 4 and 9 as well as 2 and 9 are multiplied and added together. The result should be added with the carry generated in step 1 to get the actual result. Here also, if the result has two digits the LSD is taken as actual value and MSD is the carry which is to be added with the result produced in step 3. In step 3, the MSDs that are 4 and 2 are multiplied and the result is added with the carry that is produced in step 2. Finally, the result is obtained by collecting the digits obtained in step 3, step 2, and step 1 in the order. The same is depicted in Fig. 1.

The procedure that is specified is also applicable to binary multiplication since it is same as decimal multiplication. If the two numbers have more than 2-bits then the multiplication is carried out directly by following the previously stated procedure or divide the bits of two numbers equally into two parts and apply the procedure, that is, a 4-bit multiplication can be carried out by first dividing 4-bit numbers into two equal parts then the procedure is applied. Hence, a 4-bit multiplier is designed with four 2-bit multipliers and a few adders. An 8-bit multiplier is designed with four 4-bit multipliers and a few adders. Similarly, an N-bit multiplier can be designed with four (N/2)-bit multipliers and a few adders.

3 Proposed Vedic Multiplier

This part brings the information of proposed 4:3 counter as well as the methodology of proposed 8-bit WTM and 16-bit VM design.

Step 1

4   9

2   9

Step 2

Result = 81

Carry

4   9

2   9

Result = 36 + 18 = 54
Previous carry   = 8
_____
Sum = 62

Carry

Step 3

4   9

2   9

Result   = 8
Previous carry = 6
_____
Sum = 14

Hence, the final result of the product is 1421

Fig. 1 Steps involved in UT sutra based multiplication

3.1 Proposed 4:3 Counter

The 4:3 counter is a circuit that is used to count the 1's present in four bits, designated as X_4, X_3, X_2, and X_1, taken from a specific bit-location and it generates three bits, designated as $Cout_2$, $Cout_1$, and S, at the output. Equation 1 [20] relates the 4:3 counter's inputs and outputs.

$$X_4 + X_3 + X_2 + X_1 = 2^2 \cdot Cout_2 + 2^1 \cdot Cout_1 + 2^0 \cdot S \tag{1}$$

The bit S is applied into same bit-location whereas the outputs $Cout_2$ and $Cout_1$ are fed into the immediate next two bit-locations of a specific bit-location from where the inputs are taken. On the input side, the 4:3 counter utilizes a 2-bit reordering circuit [21]. The 2-bit reordering circuit consists of 2 inputs represented by A_2, A_1, and 2 outputs represented by B_2 and B_1. The circuit regroups its input bits and keeps aside all 1's on the left side followed by all 0's in the order at the output. Table 1 gives the relation among its input as well as output bits.

The B_2 and B_1 are expressed in terms of A_2 and A_1 as given by Eqs. 2 and 3, respectively.

$$B_2 = A_2 + A_1 \tag{2}$$

$$B_1 = A_2 A_1 \tag{3}$$

Table 1 Truth table of 2-bit reordering circuit

Inputs		Outputs	
A_2	A_1	B_2	B_1
0	0	0	0
0	1	1	0
1	0	1	0
1	1	1	1

The 2-bit reordering circuits output can be expressed in the following Boolean expressions $v_4 = X_4 + X_3$, $v_3 = X_2 + X_1$, $v_2 = X_4 X_3$, and $v_1 = X_2 X_1$, which reduce the 16 binary input combinations into nine binary combinations at its output. Table 2 shows the functional table of first stage 2-bit reordering circuits. These nine combinations are reduced into six combinations by passing them again through the 2-bit reordering circuit. The Boolean functions for $Cout_2$, $Cout_1$, and S are given by Eqs. 4, 5, and 6, respectively, and its logic diagram is depicted in Fig. 2.

$$Cout_2 = w_1 \tag{4}$$

$$Cout_1 = w_1^1(u_4 u_3 + u_4 u_2 + u_4 u_3 u_2) \tag{5}$$

$$S = w_1^1 \left(u_4 u_3 u_2 + u_4 u_3^1 u_2^1 \right) \tag{6}$$

where w_1, u_2, u_3, and u_4 are given by Eqs. 7, 8, 9, and 10, respectively.

$$w_1 = v_2 v_1 \tag{7}$$

$$u_2 = v_4 v_3 \tag{8}$$

$$u_3 = v_2 + v_1 \tag{9}$$

$$u_4 = v_4 + v_3 \tag{10}$$

3.2 Proposed 8-Bit Wallace Tree Multiplier

In a multiplier, the two sets of bits are multiplied in three sequences of steps. The PP bits are evaluated in step 1 whereas in step 2 accumulated the PP bits hence it is called as PP Accumulation (PPA) stage. The final result is attained in step 3. In PPA

Table 2 Functional table of first stage 2-bit reordering circuits

Inputs				Outputs			
X_4	X_3	X_2	X_1	v_4	v_3	v_2	v_1
0	0	0	0	0	0	0	0
0	0	0	1	0	1	0	0
0	0	1	0	0	1	0	0
0	0	1	1	0	1	0	1
0	1	0	0	1	0	0	0
0	1	0	1	1	1	0	0
0	1	1	0	1	1	0	0
0	1	1	1	1	1	0	1
1	0	0	0	1	0	0	0
1	0	0	1	1	1	0	0
1	0	1	0	1	1	0	0
1	0	1	1	1	1	0	1
1	1	0	0	1	0	1	0
1	1	0	1	1	1	1	0
1	1	1	0	1	1	1	0
1	1	1	1	1	1	1	1
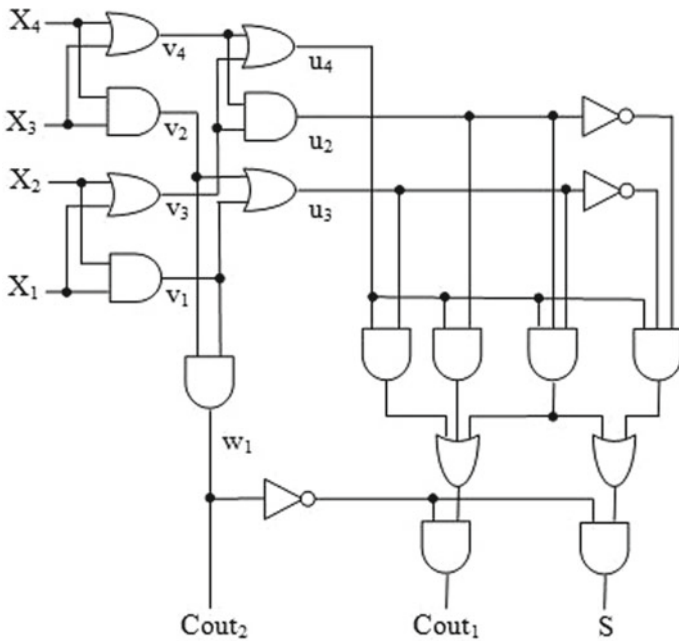
Fig. 2 Logic diagram of proposed 4:3 counter

stage, 4:3, 5:3, 6:3, and other higher bit counters are used together with FA and HA instead of only FA and HA for reducing the number of logic levels in computation. The 8-bit WTM [19] design is shown in Fig. 3 which uses a 4:3 counter together with a 6:3 counter, FA, as well as HA. Every dot in the figure indicates a binary bit. The circuit consists of a depth of four stages, with stage-1 computation employs seven 4:3 counters, eight FAs as well as one HA. In stage-1, the FA at third column takes three bits and produces two bits Cout and S at output. As Cout is fed into the fourth column, the S is fed into the same column. Similar to this, the 4:3 counter in the fifth column uses four input bits to generate the outputs $Cout_2$, $Cout_1$, and S. The S is applied in to the same column and $Cout_1$, $Cout_2$ are applied in to the sixth and seventh columns, respectively. The computation will be carried out similarly by the circuits used in the remaining columns. In stage-2 computation, seven FAs, two 4:3 counters, two 6:3 counters as well as one HA are employed while eight FAs and four HAs are used in the stage-3 computation. The two rows of binary bits have resulted after the stage-3 computation. These two rows of bits are summed together to obtain the resultant product. In order to reduce the number of computation steps, a circuit is chosen and employed in each column of the multiplier stage.
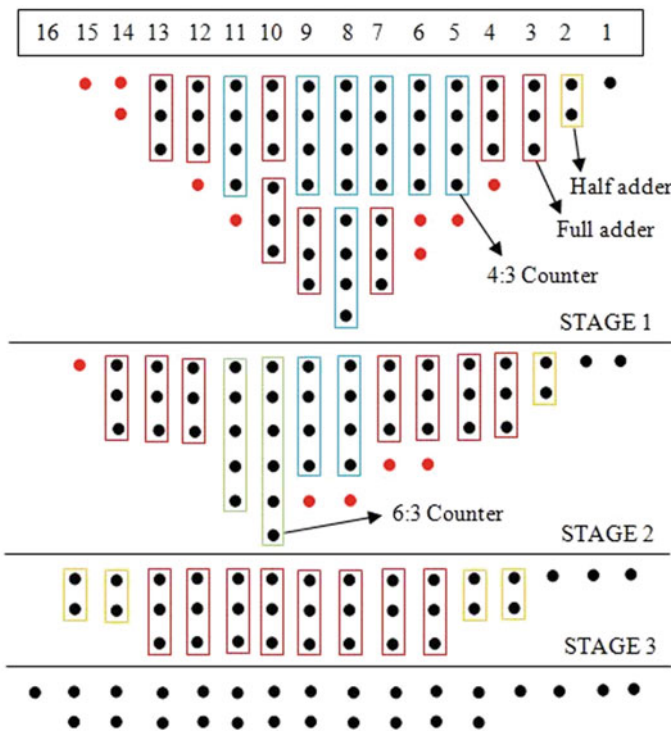

Fig. 3 8-bit WTM utilizing proposed 4:3 counter and other adder circuits

At every stage, the rightmost black colored dots indicate the resultant product bits while the bits shown with red colored dots are not included for computation.

3.3   Proposed 16-Bit Vedic Multiplier

Figure 4 depicts the block diagram of the 16-bit VM. It is used to multiply two numbers x and y of 16 bits. As stated earlier, the multiplication is carried out by dividing x and y equally into two parts as $x[15:8]$, $x[7:0]$ and $y[15:8]$, $y[7:0]$. The 8-bit numbers are multiplied using four 8-bit WTMs. To attain the final result, the results obtained from multiplier blocks are summed up with one HA and three 16-bit RCAs. Thus, the multiplier circuit consists of four 8-bit WTMs, three 16-bit RCAs and one HA.
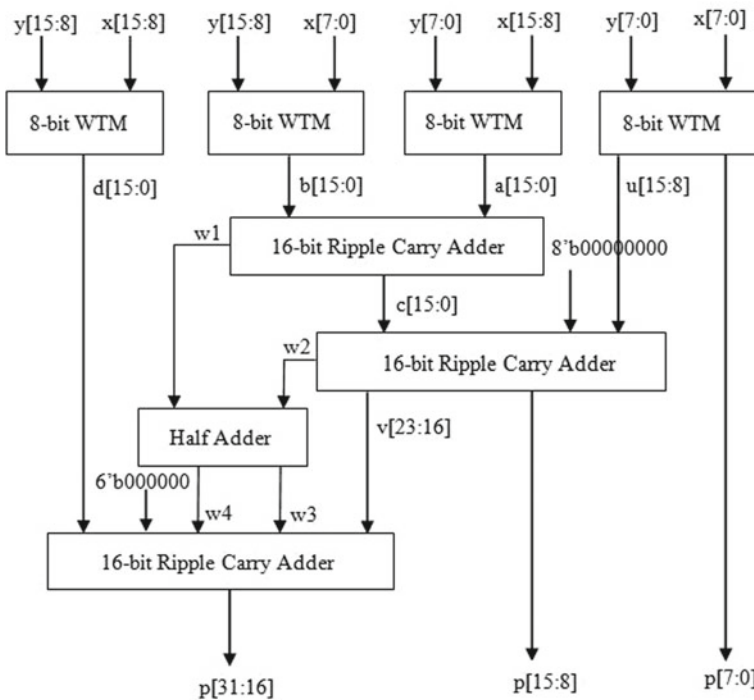

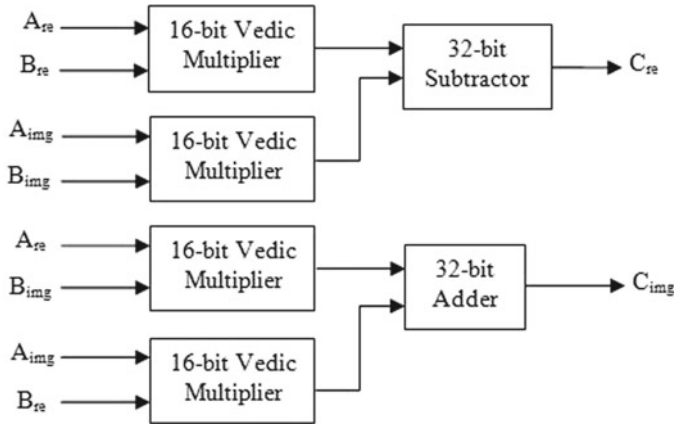**Fig. 4** Block diagram of 16-bit VM

Fig. 5 Block diagram of complex multiplier [8]

3.4 Architecture of Complex Multiplier

The performance of the digital signal processing operations such as DFT and FFT depends majorly on the performance of complex multiplier [8] block that is used in its implementation. The block diagram of complex multiplier is depicted in Fig. 5. In Fig. 5, A and B are the complex inputs and C is the complex output. The real and imaginary parts of inputs A and B are represented as A_{re} and A_{img} as well as B_{re} and B_{img}, respectively. Similarly, C_{re} and C_{img} are the real and imaginary parts of output C of the complex multiplier.

4 Results and Discussions

In Verilog HDL, the complex multiplier designed with both proposed and existing multiplier designs are coded using gate-level modeling and their functionality is validated using a test bench having a few specific input vectors. Figures 6 and 7 depict the simulation result of the 16-bit proposed VM and complex multiplier, respectively. Using Xilinx Vivado 2017.2, the designed multipliers were synthesized by targeting 'xc7s50fgga484-1' device of Spartan-7 family.

The performance of the designed circuits is validated based on LUT count and CPD in 'ns'. The area that the circuit occupies on the device is indicated by the LUT count, while the CPD specifies the delay of the circuit's longest path. Table 3 shows the performance comparison of proposed multiplier with existing multiplier designs. It is observed from Table 3 that the LUT count of the proposed 16-bit VM using WTM is reduced by 26.83%, 20.18%, 2.66%, 24.31%, and 13.58% as compared to 16-bit Array Multiplier (AM) [22], Conventional Carry Save Multiplier (CSM) [23], VM using RCA, VM using KSA, and VM using predictor logic, respectively. The
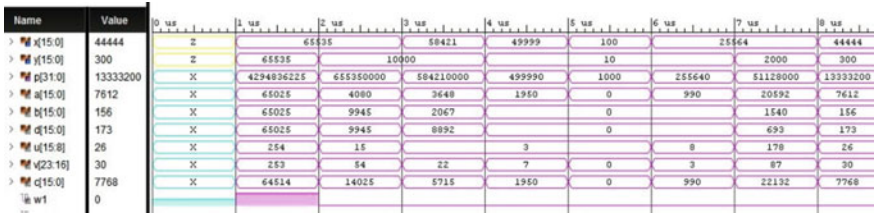
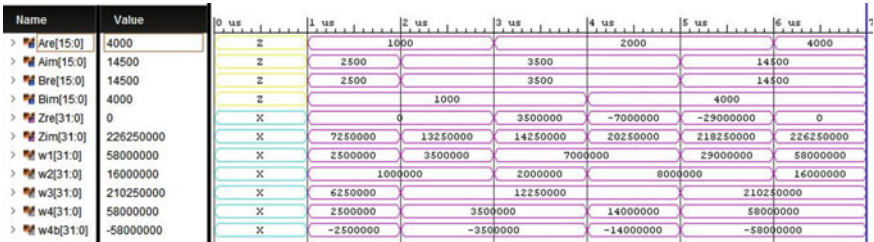**Fig. 6** Simulation result of 16-bit proposed VM

Fig. 7 Simulation result of complex multiplier

proposed 16-bit VM's CPD is decreased by 36.47%, 16.19%, 10.57%, and 8.10% as well as increased by 0.13% as compared to 16-bit AM, Conventional CSM, VM using RCA, VM using predictor logic, and VM using KSA, respectively.

Table 4 shows the performance comparison of complex multiplier designed using proposed multiplier with existing multiplier designs. It is observed from Table 4 that the LUT count of the complex multiplier designed with the proposed 16-bit VM using WTM is reduced by 24.11%, 11.87%, 2.74%, 20.78%, and 13.05% as compared to complex multiplier designed with 16-bit AM, Conventional CSM, VM using RCA, VM using KSA, and VM using predictor logic, respectively. The CPD of complex multiplier designed with proposed 16-bit VM is decreased by 29.64%, 12.41%, 4.88%, 1.83%, and 3.94% as compared to complex multiplier designed with 16-bit AM, Conventional CSM, VM using RCA, VM using KSA, and VM using predictor logic, respectively.

Table 3 Comparison of proposed multiplier's performance with existing multiplier designs

Type of the multiplier	Number of LUTs	Critical path delay (ns)
16-bit AM [22]	600	36.08
16-bit Conventional CSM [23]	550	27.35
16-bit VM using RCA [2]	451	25.63
16-bit VM using KSA [6]	580	22.89
16-bit VM using Predictor Logic [14]	508	24.94
Proposed 16-bit VM using WTM	439	22.92

Table 4 Performance comparison of complex multiplier using proposed and existing multiplier designs

Type of the multiplier used	Number of LUTs	Critical path delay (ns)
16-bit AM [22]	2476	44.03
16-bit Conventional CSM [23]	2132	35.37
16-bit VM using RCA [2]	1932	32.57
16-bit VM using KSA [6]	2372	31.56
16-bit VM using Predictor Logic [14]	2161	32.25
Proposed 16-bit VM using WTM	1879	30.98

5   Conclusion

A 4:3 counter circuit is designed, in this paper, using 2-bit reordering circuit. The 4:3 proposed counter and other adder circuits are used in the implementation of 8-bit WTM. The designed 8-bit WTM is utilized in the implementation of the 16-bit multiplier and it is used in the design of a complex multiplier. The designed circuits are programmed in Verilog HDL and their functional behavior is validated by Xilinx Vivado 2017.2 and also synthesized the circuits by targeting the FPGA device 'xc7s50fgga484-1' of the Spartan-7 family. From the results, it is observed that the proposed 16-bit VM outperforms the 16-bit AM, Conventional CSM, VM using RCA, and VM using predictor logic in terms of CPD. However, the CPD of the proposed multiplier has increased by 0.13% and occupies 24.31% less area as compared to VM using KSA. Further, it is observed that the complex multiplier designed with proposed 16-bit VM outperforms the complex multiplier designed with other existing multiplier designs in terms of CPD and LUT count.

References

1. Tirthaji JSSBK (1986) Vedic mathematics or sixteen simple mathematical formulae from the Vedas. Motilal Banarsidas, Varanasi-India
2. Bhavani M, Siva Kumar M, Srinivas Rao K (2016) Delay comparison for 16X16 Vedic multiplier using RCA and CLA. Int J Electr Comput Eng 6(3):1205–1212. https://doi.org/10.11591/ijece.v6i3.9457
3. Nagaraju N, Ramesh SM (2019) Implementation of high speed and area efficient MAC unit for industrial applications. Cluster Comput 22:4511–4517. https://doi.org/10.1007/-s10586-018-2060-z
4. Udaya Kumar N, Bala Sindhuri K, Subbalakshmi U, Kiranmayi P (2019) Performance evaluation of Vedic multiplier using multiplexer-based adders. In: Panda G, Satapathy S, Biswal B, Bansal R (eds) Microelectronics, electromagnetics and telecommunications. Lecture notes in electrical engineering, vol 521. Springer, Singapore, pp 349–356. https://doi.org/10.1007/978-981-13-1906-8_36
5. Singh AK, Nandi A (2017) Design of radix 2 butterfly structure using Vedic multiplier and CLA on Xilinx. In: 2017 Conference on emerging devices and smart systems (ICEDSS), pp. 120–123. https://doi.org/10.1109/ICEDSS.2017.8073670

6. Gulati P, Yadav H, Taleja MK (2016) Implementation of an efficient multiplier using the Vedic multiplication algorithm. In: 2016 international conference on computing, communication and automation (ICCCA), pp 1440–1443. https://doi.org/10.1109/CCAA.2016.781-3946

7. Satyendra T, Bharat M (2018) Discrete Wavelet transform using Vedic multiplier for image compression. In: 2018 IEEE international students' conference on electrical, electronics and computer science (SCEECS), pp 1–5. https://doi.org/10.1109/SCEECS.2018.8546873

8. Gupta T, Sharma JB (2018) Han–Carlson adder based high-speed Vedic multiplier for complex multiplication. Microsyst Technol 24:3901–3906. https://doi.org/10.1007/s00542-018-3872-8

9. Thakur AS, Tiwari V (2018) Design high speed FIR filter based on complex Vedic multiplier using CBL adder. In: 2018 international conference on recent innovations in electrical, electronics & communication engineering (ICRIEECE), pp 559–563. https://doi.org/10.1109/ICRIEECE44171.2018.9008438

10. Rajasekhar T, Satya Sai Ram M (2019) Low power VLSI implementation of real fast Fourier transform with DRAM-VM-CLA. Microprocess Microsyst 69:92–100. https://doi.org/10.1016/j.micpro.2019.05.016

11. Kodali RK, Boppana L, Yenamachintala SS (2015) FPGA implementation of Vedic floating point multiplier. In: 2015 IEEE international conference on signal processing, informatics, communication and energy systems (SPICES), pp 1–4. https://doi.org/10.1109/SPICES.2015.7091534

12. Ramya V, Seshasayanan R (2019) Low power single precision BCD floating-point Vedic multiplier. Microprocess Microsyst 72:102930. https://doi.org/10.1016/j.micpro.2019.102930

13. Pooja VG, Premananda BS, Ramesh GS (2018) Design of compact Vedic multiplier for high performance circuits. In: 2018 3rd IEEE international conference on recent trends in electronics, information & communication technology (RTEICT), pp 1168–1172. https://doi.org/10.1109/RTEICT42901.2018.9012654

14. Christilda VD, Milton A (2021) Speed, power and area efficient 2D FIR digital filter using Vedic multiplier with predictor and reusable logic. Analog Integr Circ Sig Process 108:323–333. https://doi.org/10.1007/s10470-021-01853-8

15. Ariafar Z, Mosleh M (2019) Effective Designs of Reversible Vedic Multiplier. Int J Theor Phys 58:2556–2574. https://doi.org/10.1007/s107-73-019-04145-0

16. Karthikeyan S, Jagadeeswari M (2021) Performance improvement of elliptic curve cryptography system using low power, high speed 16×16 Vedic multiplier based on reversible logic. J Ambient Intell Humanized Comput 12:4161–4170. https://doi.org/10.1007/s12652-020-01795-5

17. Rashno M, Haghparast M, Mosleh M (2021) Designing of parity preserving reversible Vedic multiplier. Int J Theor Phys 60:3024–3040. https://doi.org/10.1007/s10773-021-04903-z

18. Karuppusamy P (2019) Design and analysis of low-power. High-speed Baugh Wooley multiplier. J Electron Inform 01(02):60–70. https://doi.org/10.36548/jei.2019.2.001

19. Wallace CS (1964) A suggestion for a fast multiplier. IEEE Trans Electron Comput EC-13(1):14–17. https://doi.org/10.1109/PGEC.1964.263830

20. Krishna LH, Neeharika M, Viswanath J, Sreehari V, Mahammad SN (2021) Efficient design of 15:4 counter using a novel 5:3 counter for high-speed multiplication. IET Comput Digit Tech 15(1):12–19. https://doi.org/10.1049/cdt2.12002

21. Guo W, Li S (2021) Fast binary counters and compressors generated by sorting network. IEEE Transactions on very large scale integration (VLSI) systems, vol 29, no 6, pp 1220–1230. https://doi.org/10.1109/TVLSI.2021.3067010

22. Ram GC, Rani DS, Balasaikesava R, Sindhuri KB (2016) Design of delay efficient modified 16 bit Wallace multiplier. In: 2016 IEEE international conference on recent trends in electronics, information & communication technology (RTEICT), pp 1887–1891. https://doi.org/10.1109/RTEICT.2016.7808163

23. Suman S, Ngangbam PS, Selvakumar R, Harshit S (2021) Design of 32-bit cell based carry-save combinational multiplier with reduced area and propagation delay. J Phys Conf Series 1804, pp 1–8

Improved Logistic Map and DNA-Based Video Encryption

Sweta Kumari and Mohit Dua

Abstract In the recent era, data security is important for multimedia communication such as image and video. Secured communication and confidentiality of data play an important role in many online services like authentication, video conferencing, online classes, etc. In this paper, a video encryption technique using improved logistic map and DNA sequencing has been proposed to encrypt the video. The proposed video encryption technique has mainly three phases, firstly key is generated using SHA-256. Second, permutation of the video frame is completed using improved logistic map and SHA-256. In the third step, diffusion on permuted video frame is performed using SHA-256 key and DNA sequencing. Efficiency of the encryption technique is measured through PSNR, entropy, correlation coefficients and NPCR. The presented encryption technique is resistant to the brute force and statistical attack.

Keywords Encryption · Improved logistic map · PSNR · NPCR · Entropy

S. Kumari · M. Dua (✉)
Department of Computer Engineering, National Institute of Technology, Kurukshetra, Haryana, India
e-mail: er.mohitdua@nitkkr.ac.in

1   Introduction

Transfer of data, in the wireless communication field, has evolved with many challenges. People frequently share digital data such as images and videos, in abundance through social networks because of advancement in the technologies. This raise the issue of data security and privacy. Unencrypted data is more vulnerable to cyber-attacks. Therefore, there is need for the data to be transmitted securely through any network and the method is called Encryption [1–3]. Video data are large, thus, the classical encryption techniques like Data Encryption Standard (DES) [4–6] and Rivest, Shamir, Aldeman (RSA) [7, 8] are not efficient to encrypt the video. [9, 10] Advanced Encryption Standard (AES) is also popular for encrypting video, but it consumes more processing time. Therefore, to encrypt the video chaos-based encryption has gain popularity as it is more efficient and less time-consuming as compared to classical encryption technique. In this work, a video encryption, using improved logistic map and DNA sequencing, is proposed to encrypt the video.

The proposed video encryption is divided into six steps. In the first step, key is generated using SHA-256 [11, 12]. Secondly, the video is divided into N ($N =$ Frame Per Second (FPS) * Length of the video) frames. In the third step, each frame is selected and converted into three RGB components. In the fourth step, permutation on the frame is performed using improved logistic map and SHA-256 generated key. In the fifth step, diffusion of the permuted frames is performed using SHA-256 and DNA sequencing to obtain the encrypted video. In the final step, video is joined to obtain encrypted video. To decrypt the video, reverse process is followed on the video frames, first diffusion is performed on the video frames using the SHA-256 key and DNA sequencing and then permutation on the diffused frame using the same SHA-256 key and improved logistic map.

This paper is organized in the following ways: Sect. 2 describes the related theories of the proposed work. Section 3 describes the detail architecture of the proposed work. Section 4 describes the experimental result of the proposed work. Section 5 describes the conclusion of the proposed approach and future work.
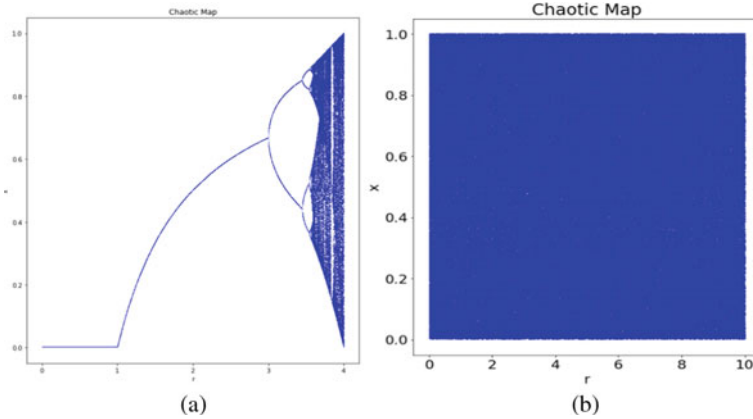
2   Analysis of the Related Theory

2.1   Logistic Map

Chaotic maps are the mathematical relation that shows major changes when there is little change in the initial conditions and it is commonly known as Butterfly effect. Logistic maps [13, 14] are the most common and simple chaotic map. The equation of the logistic map is represented in Eq. 1.

$$Xn + 1 = r * Xn * (1 - Xn) \tag{1}$$

Fig. 1 Bifurcation diagram **a** logistic map and **b** improved logistic map

Logistic map has limitations of stable and blank windows and its range lies in [0,4]. To overcome its limitation, improved logistic map [15] has been used in the proposed approach. The range of the improved logistic map is [0,10]. The equation of the improved logistic map is represented in Eq. 2.

$$Xn + 1 = \mod(r * Xn * (1 - Xn) - (4 - r) * Xn * (1 - Xn)) * 2^K, 1) \quad (2)$$

where 'Xn' is the output of chaotic sequence, obtained by looping the chaotic map, 'r' $\in (0,10]$ and 'K' $\in [9, 16]$, these parameters are initial values for generating the chaotic sequence.

The chaotic map shows a multiple behaviour, and it has transitions between these behaviours due to change in parameter 'r'. The dynamical representation of transitions is called bifurcation diagram. The bifurcation diagram of the logistic and improved logistic map is shown in Fig. 1. Lyapunov exponent is a measure for the predictability of a dynamic system. It characterizes the rate of separations of infinitesimally close trajectories. It also describes the average rate of predictability of lost. The Lyapunov exponent of logistic and improved logistic map is shown in Fig. 2.

2.2 DNA Sequencing and Its Rules

Deoxyribonucleic acid (DNA) sequencing plays an important role in the biological research. DNA sequence has four nucleic acid such as A(adenine), C(cytosine), T(Thymine) and G(Guanine) [7, 16–18]. These nucleic acids are paired with each other to get new DNA pattern. The rule of the DNA sequencing given in Table 1.
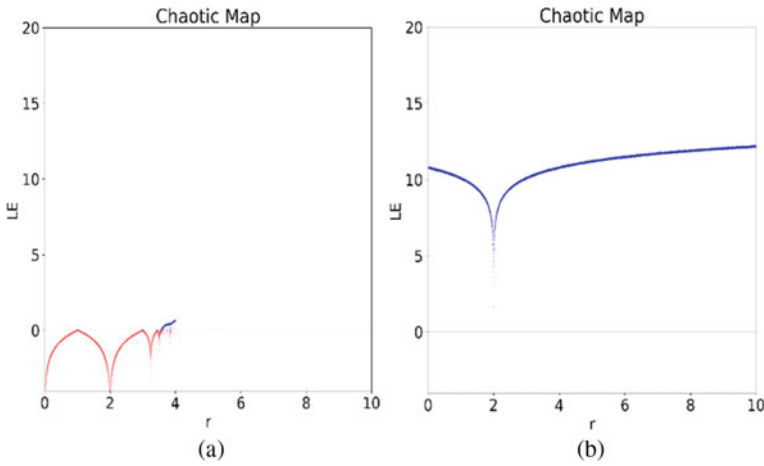
Fig. 2 Lyapunov exponent **a** logistic map, **b** improved logistic map

Table 1 Rule of the DNA

	R1	R2	R3	R4	R5	R6	R7	R8
T	00	00	11	11	10	01	10	01
A	11	11	00	00	01	10	01	10
G	10	01	10	01	00	00	11	11
C	01	10	01	10	11	11	00	00

3 Proposed Video Encryption Approach

This section describes the proposed video encryption technique based on the improved logistic map and DNA sequencing. Figure 3 depicts the detailed architecture of the proposed video encryption. Steps for encryption of the video encryption are discussed below:

(i) Generate key using SHA-256.
(ii) Split video into N (N = Frame per second * duration of the video in seconds).
(iii) Each frame is selected and split into RGB components.
(iv) Permutation is performed on each frame using SHA-256 key and improved logistic map to obtain permuted image.
(v) Diffusion is performed on the permuted image using SHA-256 key and DNA sequencing to obtain encrypted video frame.
(vi) Repeat steps (iii)–(v), all encrypted frames are joined to get encrypted image.

To decrypt the video, reverse process of the encryption is followed to get decrypted video. While decrypting the video, firstly encrypted video is split into 'N' encrypted
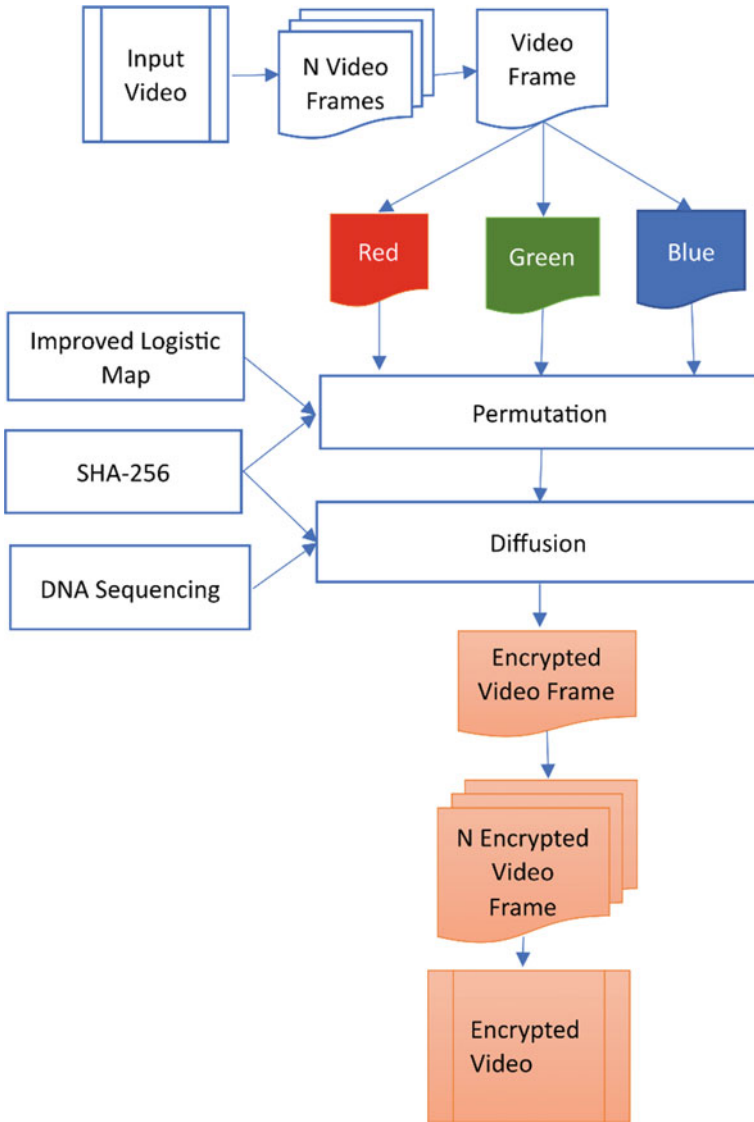
Fig. 3 Detailed architecture of the video encryption

frames, then each encrypted frame is selected, and diffusion is performed after diffusion permutation on the encrypted video frame to get the final decrypted frame. All decrypted frames are shuffled and arranged according to the sequence to obtain the decrypted frame.

4   Results

4.1   *Experimental Setup*

For experimentation, video of Rhino.mp4 [19] of 15 FPS and 114 frames, Train.mp4
[19] with 25 FPSs and 262 frames is taken. Python has been used to implement the
proposed video encryption scheme on a Windows 10 computer running an Intel Core
i5 2370 M CPU with 8 GB of RAM and a 1 TB Hard disk storage. Python libraries
like numpy, openCv, skimage, pillow, imageio and matplotlib are used to perform
the experiments.
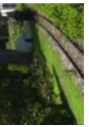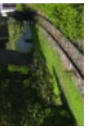
4.2   *Observation*

To perform the analysis, random frames of video Rhino.mp4 and Train.mp4 are
used. Entropy, Correlation Coefficients (CC), Peak Signal to Noise Ratio (PSNR)
and NPCR values are calculated and analysed. Table 2 represents the analysis of the
proposed video encryption technique. CC_h represents the correlation coefficients in
the horizontal directions. CC_v represents the correlation in the vertical direction and
CC_d depicts the correlation in the diagonal direction.

5   Conclusion and Future Works

In this research work, a novel video encryption technique has been proposed using
improved logistic map and DNA sequencing. Permutation and diffusion are the main
phases in the encryption. SHA-256 key and improved logistic map are used for scram-
bling, and for random substitution, SHA-256 key DNA sequencing are used**.** The
experimental results are good, entropy achieved, in the proposed video encryption,
is 7.9989 that is nearly equal to 8 that shows encrypted frame has high randomness.
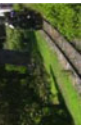Additionally, it attains correlation coefficients in horizontal, vertical and diagonal
as 0.0003, − 0.002 and 0.001, respectively, that shows encrypted frames has low
correlation among the neighbouring pixels. The value of the peak signal noise ratio
obtain is 38.006 that shows encrypted video frame is of high quality. This encryption
technique is resistant to brute force attack and plan text attack. The presented video
encryption technique works on video without sound. The future aspects of this work
to enhance it with audio and to improve the quality of the video.

Table 2 Analysis of proposed video encryption scheme

Original video frame	Decrypted video frame	Entropy	CC			PSNR	NPCR
			CC_h	CC_v	CC_d		
		7.9989	− 0.001	0.001	0.001	38.006	99.59
		7.9989	− 0.001	− 0.005	0.003	37.959	99.68
		7.9980	− 0.006	− 0.005	− 0.003	38.02	99.59
		7.9975	0.0003	0.005	0.002	38.040	99.58
		7.9972	− 0.002	− 0.002	0.004	37.91	99.70
		7.9981	0.002	0.007	− 0.003	38.005	99.61

References

1. Yasser I, Mohamed MA, Samra AS, Khalifa F (2020) A chaotic-based encryption/decryption framework for secure multimedia communications. Entropy 22(11):1253
2. Sethi J, Bhaumik J, Chowdhury AS (2022) Chaos-based uncompressed frame level video encryption. In: Proceedings of the seventh international conference on mathematics and computing. Springer, Singapore, pp 201–217
3. Maazouz M, Toubal A, Bengherbia B, Houhou O, Batel N (2022) FPGA implementation of a chaos-based image encryption algorithm. J King Saud Univ Comput Inform Sci
4. Dinkar A, Sahana B (2021) AES-based android video encryption and decryption app. In: Proceeding of fifth international conference on microelectronics, computing and communication systems. Springer, Singapore, pp 327–339
5. Raja SP (2018) Secured medical image compression using DES encryption technique in Bandelet multiscale transform. Int J Wavelets Multiresolut Inf Process 16(04):1850028
6. Sharma S, Kumar K (2018) GUESS: genetic uses in video encryption with secret sharing. In: Proceedings of 2nd international conference on computer vision & image processing. Springer, Singapore, pp 51–62
7. Mumthas S, Lijiya A (2017) Transform domain video steganography using RSA, random DNA encryption and Huffman encoding. Procedia Comput Sci 115:660–666
8. Yousif SF (2018) Encryption and decryption of audio signal based on Rsa algorithn. Int J Eng Technol Manag Res 5(7):57–64
9. Panwar K, Purwar RK, Srivastava G (2021) A fast encryption scheme suitable for video surveillance applications using SHA-256 hash function and 1D sine–sine chaotic map. Int J Image Graph 21(02):2150022
10. Dua M, Makhija D, Manasa PYL, Mishra P (2022) 3D chaotic map-cosine transformation based approach to video encryption and decryption. Open Comput Sci 12(1):37–56
11. Hafsa A, Fradi M, Sghaier A, Malek J, Machhout M (2022) Real-time video security system using chaos-improved advanced encryption standard (IAES). Multimedia Tools Appl 81(2):2275–2298
12. Batinga J, Valladolid LM, Peradilla M, Selective-packet encryption scheme with authentication for real-time video streaming session using AES-256-GCM
13. Elrefaey A, Sarhan A, El-Shennawy NM (2021) Parallel approaches to improve the speed of chaotic-maps-based encryption using GPU. J Real-Time Image Process, 1–10
14. Babaei A, Motameni H, Enayatifar R (2020) A new permutation-diffusion-based image encryption technique using cellular automata and DNA sequence. Optik 203:164000
15. Dou Y, Li M (2021) An image encryption algorithm based on a novel 1D chaotic map and compressive sensing. Multimedia Tools Appl 80(16):24437–24454
16. Akkasaligar PT, Biradar S (2020) Selective medical image encryption using DNA cryptography. Inf Secur J A Global Perspect 29(2):91–101
17. Arthi G, Thanikaiselvan V, Amirtharajan R (2022) 4D Hyperchaotic map and DNA encoding combined image encryption for secure communication. Multimedia Tools Appl 81(11):15859–15878
18. Farri E, Ayubi P (2022) A robust digital video watermarking based on CT-SVD domain and chaotic DNA sequences for copyright protection. J Ambient Intell Human Comput, 1–25
19. Valli D, Ganesan K (2017) Chaos based video encryption using maps and Ikeda time delay system. Eur Phys J Plus 132:542. https://doi.org/10.1140/epjp/i2017-1

Interval Type-2 Fuzzy Logic Controller Development for Coreless DC Micromotor Speed Control Applications

Yannis L. Karnavas and Nikolaos V. Chatzipapas

Abstract The objective of this work is to design, develop and demonstrate optimized fuzzy controllers for processes presenting nonlinearities such as coreless DC micromotors speed control problems, in order to improve the overall control system performance. One type-1 fuzzy logic controller (FLC) and one type-2 FLC (both Tagashi-Sugeno based) were designed and implemented in real time to improve motor speed control performance. For this purpose, a high-end microcontroller was used in which the developed controllers where embedded. The parameters of the input and the output membership functions of the proposed FLCs were optimally tuned using a well-known optimization algorithm, i.e., the particle swarm optimizer (PSO). A comparison of type-1 and type-2 Tagashi-Sugeno fuzzy control architectures is performed in different experimental scenarios and the relevant results are discussed and analyzed. The results demonstrate that type-2 FLC exhibits very satisfactory motor driving capability, providing zero overshoot, faster rise time and low settling time.

Keywords DC motors · Coreless micromotor · Speed control · Microcontroller · Embedded systems · Controller design · Interval type-2 fuzzy logic · Industrial applications · Electronic systems

Y. L. Karnavas (✉) · N. V. Chatzipapas
Electrical Machines Laboratory, Department of Electrical and Computer Engineering, Democritus University of Thrace, 671 00 Xanthi, Greece
e-mail: karnavas@ee.duth.gr

N. V. Chatzipapas
e-mail: nikochat13@ee.duth.gr

1 Introduction

There are many industrial applications that often use DC coreless micromotors (CMM). Compared to conventional—with laminated core—DC motors of the same volume, CMMs present relatively better power density (W/gr) and higher efficiency. Additional desirable characteristics (by comparison to their iron-core counterparts), include [1–3]: (a) operation without "cogging" phenomena and smoother rotation due to their coreless rotor, (b) faster acceleration due to their rotor which has low inertia, (c) lower weight, (d) lower generation of heat, longer power supply (battery) life and higher efficiency due to zero rotor iron losses, (e) more precise speed control, exhibiting very low torque ripple and zero cogging torque, (f) precise low speed operation and low levels of starting voltage (e.g., 0.3 V), (g) commutator life and brushes life are prolonged due to their low inductance and (h) sharper response leading to low time constant (e.g., 10 ms typically).

The aforementioned properties make CMMs an excellent choice for a variety of applications, for example [4–6]: (a) medical equipment (stirrers and shakers, centrifugal CPAP blowers, infusion pumps in ambulances, gear and peristaltic dialysis pumps, positioning drive systems, e.g., for X-ray screens, centrifuged in laboratories), (b) office automation and banking machines (coin sorters/counters, ATMs, card readers) and (c) other (turn-table motors for high-end audio, tape recorders for authorities, e.g., police, dispensing/printing of tickets, entrance doors' automatic drives, drives for systems of laser leveling, airplane entertainment systems, e.g., LCD screens positioners, surveillance cameras pan and tilt drives.

However, the nonlinearity of this type of motor makes them difficult to use in automatic speed control. Indeed, in several cases, approaches of classical control fail to tackle these problems. Therefore, the biggest challenge in controlling CMMs is to overcome their nonlinear behavior [7–9].

In 1965, fuzzy sets (more specifically, type-1 fuzzy sets) were initially introduced by Zadeh [10]. Type-1 fuzzy sets (T1FS) are used for the design of type-1 fuzzy logic controllers (T1-FLC) [11], where the successful application of T1-FLCs has been reported in many research papers. Among them, two T1-FLCs were applied for current and speed control of DC motors [12]. Despite the obvious advantages of T1FS, they have been shown to be unable to fully deal with the effects of uncertainty (e.g., [13]). This is justified by the fact that in a T1FS, the membership degrees are characterized by crisp values. Zadeh also introduced (as extension of T1FSs) type-2 fuzzy sets (T2FS). T1FSs characterized by membership functions which are definite, while the membership functions of T2FSs are themselves fuzzy. At the same time, the type-1 membership functions have membership degree as crisp numbers, while the type-2 membership functions have membership degree which may belong as any subset in the [0,1] interval; this is named primary membership function (PMF). Additionally, a value called secondary membership function (SMF) exists for each

PMF, which defines PMFs' probability. Since the computational cost is increased due to this improvement, interval type-2 fuzzy logic controllers (IT2-FLCs) have been developed where the SMFs are zero or one [14].

IT2-FLCs are widely used because of their reasonable computations. Among others, in [15], a type-2 FLC is developed for level control of fluid. In [16], an optimal type-2 FLC is implemented for DC motor speed control using a genetic algorithm. In [17], IT2 fractional PID controllers have been designed and tested on unmanned aerial vehicle flight tests. To reduce the effects of uncertainty associated, a T2-FLC was designed in [18] to control a DC-DC buck converter.

In the above context, this paper demonstrates an IT2-FLC design along with its microcontroller implementation for the real-time CMM speed control. The IT2-FLC performance is compared with the corresponding one of its type-1 counterpart. The paper is organized as follows: In Sect. 2, the relevant theory of CMM control representation is given. In Sect. 3, the design of the IT2-FLC structure developed is shown. In Sect. 4, experimental results and discussion are reported whereas Sect. 5 concludes the work.

2　Coreless DC Micromotor Theory and Problem Statement

CMMs differ from conventional DC motors in many ways. The rotor winding is the primary distinction. The coil is a thin hollow cylinder as opposed to coils twisted around a stack of iron lamination sheets. The stator, which fits into the hollow core of the winding and generates the magnetic field flow, contains permanent magnets (PM). The outer motor housing is permanently attached to it, completing the magnetic circuit. The rotor revolves around the magnetic core while being supported by bearings. CMMs are typically small (i.e., 6–75 mm) in diameter. Because they are constructed of precious metals, CMM's commutators and brushes are often small (platinum, silver, gold or palladium). A smaller motor is also made possible by a smaller commutator, which also has less wear and a lower peripheral speed.

The typical equivalent circuit is depicted in Fig. 1a. Winding resistance (R_a) and inductance (L_a) characterize the armature winding, in which the source voltage (V_s) is applied. Electromotive force (E_a) is developed by induction, while the winding is fed by the armature current (i_a). This force is proportional to the magnetic flux (Φ), to the rate of change in shaft position (θ) or equivalently to the rotational speed (ω_m). The back-emf coefficient (k_e) expresses this proportionality, taking into consideration that, due to the motor's design, its range of operation is linked to the linear portion of stator's ferromagnetic material's magnetization curve. Hence, the following equations are derived:
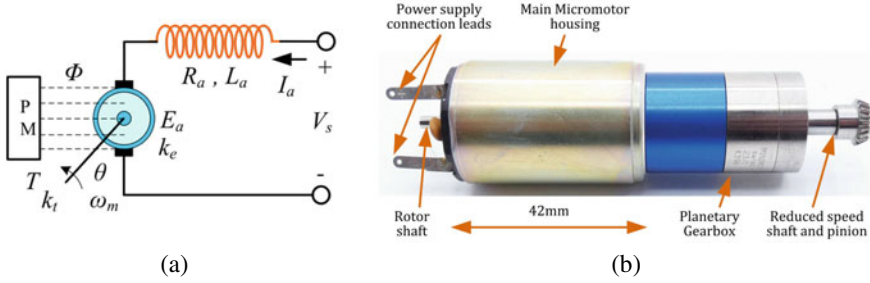
Fig. 1 Coreless DC micromotor, **a** equivalent circuit and **b** view of micromotor under study

$$V_s = E_a + i_a R_a + L_a \frac{di_a}{dt} \tag{1}$$

where

$$E_a = k_e \omega_m, \quad k_e = K_e \Phi, \quad \omega_m = \frac{d\theta}{dt} \tag{2}$$

The back-emf represents the conversion from the electrical to the mechanical power. The magnetic flux is proportional to the coefficient k_t and the developed torque T_{em} is proportional to the armature current. Considering that J_m is the rotational inertia, B_m is the viscous friction coefficient and T_L is the load torque, the equations regarding the motor's mechanical part can be described as:

$$T_{em} = k_t i_a = T_{out} + T_L + T_f \tag{3}$$

where

$$k_t = K_t \Phi, \quad T_{out} = J_m \frac{d\omega_m}{dt}, \quad T_f = B_m \omega_m \tag{4}$$

With the combination of (1), (2) and (3), (4) the following differential equations are obtained:

$$L_a \frac{d}{dt} i_a(t) + R_a i_a(t) = V_s(t) - k_e \left(\frac{d}{dt} \theta(t) \right) \tag{5}$$

$$J_m \left(\frac{d^2}{dt^2} \theta(t) \right) + J_L \left(\frac{d^2}{dt^2} \theta(t) \right) + B_m \left(\frac{d}{dt} \theta(t) \right) = k_t i_a(t) \tag{6}$$

Finally, by applying the Laplace transform to Eqs. (5) and (6), the following transfer function is derived:
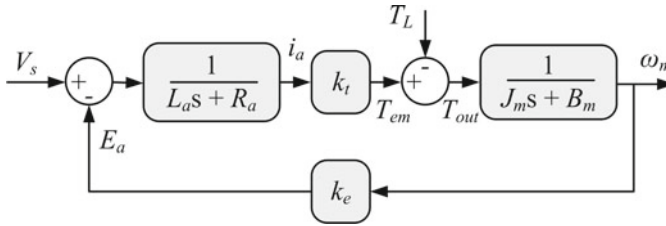
Fig. 2 Closed-loop speed control block diagram of a coreless DC micromotor

$$\frac{\theta(s)}{V(s)} = \frac{k_t}{J_m L_a s^3 + (J_m R_a + L_a B_m)s^3 + (k_e k_t + R_a B_m)s} \tag{7}$$

This transfer function is represented in block diagram form as shown in Fig. 2. The supply voltage is the only input, and the rotor position or its derivative (i.e., the speed) is the only output for the CMM, as it can be noticed. For the motor's model identification, the six parameters (R_a, L_a, k_e, k_t, J_m, B_m) have to be known. The CMM used in this work is depicted in Fig. 1b, while the corresponding parameters are shown in Table 1. Thus, the purpose of the designed controller is to acquire at each time instant the actual motor speed, calculate the error with respect to the desirable (reference) speed, i.e., error $= \omega_m^{actual} - \omega_m^{ref}$, perform calculations according to its strategy and provide appropriate output signal to the motor driver in order to recover the speed to the reference one. Here, a PWM voltage is used according to the motor driver characteristics, as in (8),

$$\text{PWM}_{signal} = \frac{1}{a}|\text{error}| + \delta, \quad a = 19, \delta = 108 \tag{8}$$

3 Interval Type-2 Fuzzy Logic Controller Development

A general representation of interval type-2 fuzzy logic system (IT2-FLS) controller is depicted in Fig. 3. It is known that, one major difference between Tagashi-Sugeno and Mamdani architectures approach is that the former provides singleton membership functions (MFs) for the output variable [19]. This is a quite desirable characteristic because the computational burden is reduced for the microcontroller which executes the fuzzy strategy and thus is suitable in real-time applications.

Another feature of type-2 MFs is the kind of uncertainty involved. In Fig. 4, type-2 MF with uncertainty in the mean (and common standard deviation) and with uncertainty in the standard deviation σ (and common mean) are shown. In this work,

Table 1 Technical characteristics of the micromotor under study (mfg. Faulhaber)

Quantity	Symbol	Value	Unit
Output power	$P_{2(max)}$	6.53	W
Efficiency	η_{max}	74	%
Nominal voltage	V_N	18	V
Terminal resistance	R_a	12.07	Ω
Rotor inductance	L_a	1487.1	μH
Back-EMF constant	k_e	3.53	mV/rpm
Torque constant	k_t	4.733	oz-in/A
Rotor inertia	J	1.983×10^{-4}	oz-in-s^2
Mechanical time constant	τ_m	15	ms
No-load current	I_o	0.033	A
Current constant	k_I	0.214	A/oz-in
Friction torque	T_R	0.156	oz-in
Stall torque	T_H	7.193	oz-in
No-load speed	n_o	5,100	rpm
Speed constant	k_n	283	rpm/V
Slope of n-T curve	$\Delta n/\Delta T$	690	rpm/oz-in
Angular acceleration	a_{max}	36	$\times 10^3$ rad/s^2
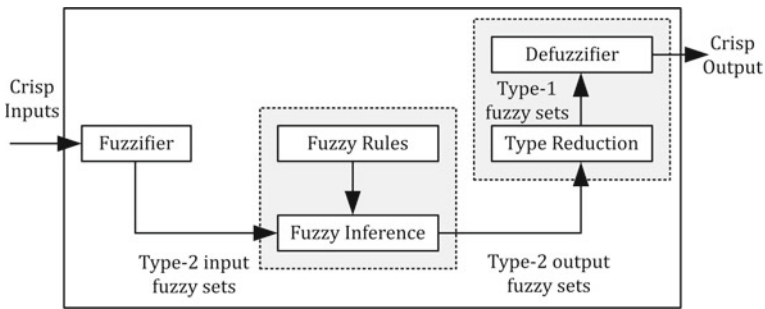
Fig. 3 General structure of IT2-FLS

it has been found by experiments that the former is more suitable for our application. Consequently, if the mean for each MF is denoted as μ, and another variable δ_μ is considered also as the corresponding uncertainty value, the centers of each MF can be expressed as:

$$c_1, c_2 = \mu \pm \delta_\mu \quad (\text{with } \sigma_1 = \sigma_2 = \sigma) \tag{9}$$
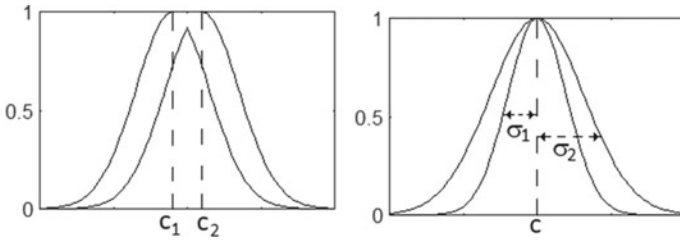
Fig. 4 Type-2 MF with uncertainty in the mean (left) and with uncertainty in the standard deviation (right)

The following apply for the parameters tuning of the fuzzy controllers: Because the output of a type-1 FLS can be described as a closed-form mathematical expression, tuning its parameters is both feasible and simple. For this, numerous optimization techniques have been thoroughly investigated (e.g., [15]). Unfortunately, the output of a type-2 FLS cannot be expressed by a closed-form mathematical formula; as a result, changing its parameters involves an additional level of complexity. On the other hand, to date, there are several optimization methods available to be used for such problems. Among them, population-based algorithms like genetic algorithms, particle swarm optimization (PSO) algorithms or even meta-heuristic bio-inspired optimization techniques may be used.

The number of total parameters for optimization relies on the number of MFs for these inputs and outputs, which are the error e and its derivative de/dt in our type-2 fuzzy controller and the control signal u as its sole output. Based on the above, five MFs have been chosen for the inputs and six MFs for the output (considering -1, 0, 1 as to be used by default). Thus, based on Fig. 4, the total number of the parameters to be optimized by the utilized algorithm can be chosen as 13, i.e.,:

$$\mu_{11}, \mu_{12}, (\mu_{13} = 0), \mu_{14}, \mu_{15} \quad \text{(for input 1, i.e. error)}$$
$$\mu_{21}, \mu_{22}, (\mu_{23} = 0), \mu_{24}, \mu_{25} \quad \text{(for input 2, i.e. change in error)}$$
$$\delta_{\mu} \quad \text{(common to all MFs)}$$
$$\sigma \quad \text{(common to all MFs)}$$
$$(-s_4 = -1), -s_3, -s_2, -s_1, (s_0 = 0), s_1, s_2, s_3, (s_4 = 1) \quad \text{(for output, i.e. PWM)}$$
$$(10)$$

PSO was implemented and executed off-line in order for the above parameters to be determined. Figure 5 depicts the final input and output MFs of the developed interval type-2 fuzzy controller, as obtained from the PSO optimization. Specifically, in Fig. 5a the normalized speed error MF is shown which corresponds to the range [− 500 rpm, 500 rpm], in Fig. 5b the normalized change in speed error MF is shown

which corresponds to the range [− 140 rpm, 140 rpm], while in Fig. 5c the singleton MFs of the controller output values are shown which account for the motor driver PWM signal adjustment, i.e., this value is being multiplied with the PWM function as per Eq. (8). Also, the corresponding rule base (fuzzy association matrix, FAM) is shown in Table 2.

The above procedure completes the design of the type-2 fuzzy controller proposed here. Due to space limitations the underlying theoretical aspects are not presented here. The reader may refer to [20–23] for further details on type-2 fuzzy logic systems and the corresponding theory in order to completely understand the design phase.

4   Experimental Results and Discussion

To analyze the performance of the developed two fuzzy controllers (IT2-FLC compared to the corresponding T1-FLC), an experimental apparatus was set up as shown in Fig. 6. STM32F407VET6 development board was utilized owing an ARM® Cortex®-M4 microcontroller, with a clock frequency of 180 MHz. A dual H-bridge driver board (BBTS7960) was also used to drive the coreless DC micromotor. The latter is selected since it can produce PWM signals with a frequency up to 25 kHz, it can handle the range of voltages for this application and can rotate the motor in both directions (if needed). An OMRON E6A2-CW5C, producing 200 pulses/revolution rotary incremental encoder with was attached to the motor's shaft for measuring speed. For the acquisition of the measured (calculated through the encoder) speed, a digital to analog converter is also necessary and, here, the 10-bit MCP4725 DAC is selected. Finally, an ACS712 current sensor is used for measuring the micromotor's current, having a sensitivity of 185 mV/A.

For demonstration purposes, the scenarios (cases) examined were three step input responses in different references speeds (e.g., low, medium, high). Initially, in all cases, the micromotor was in idle state and at time $t = 0$, the disturbance occurred. Figure 7, present the experimental results recorded for the motor speed, both for type-1 FLC and type-2 FLC. From this figure, it can be clearly seen that the type-1 fuzzy controller exhibits an overshoot and some oscillations before reaching the steady-state, whereas the type-2 fuzzy controller presents no overshoot at all, exhibits a faster rise time and consequently has a lower settling time. These observations are summarized in Table 3, while in Table 4 the values of well-known metrics such as mean square error (MSE), integral square error (ISE), integral absolute error (IAE) and integral in time of absolute error (ITAE) are presented. From the above results it can be easily seen that the designed IT2-FLC's performance is superior compared to the corresponding one of a well-tuned type-1 fuzzy logic controller.
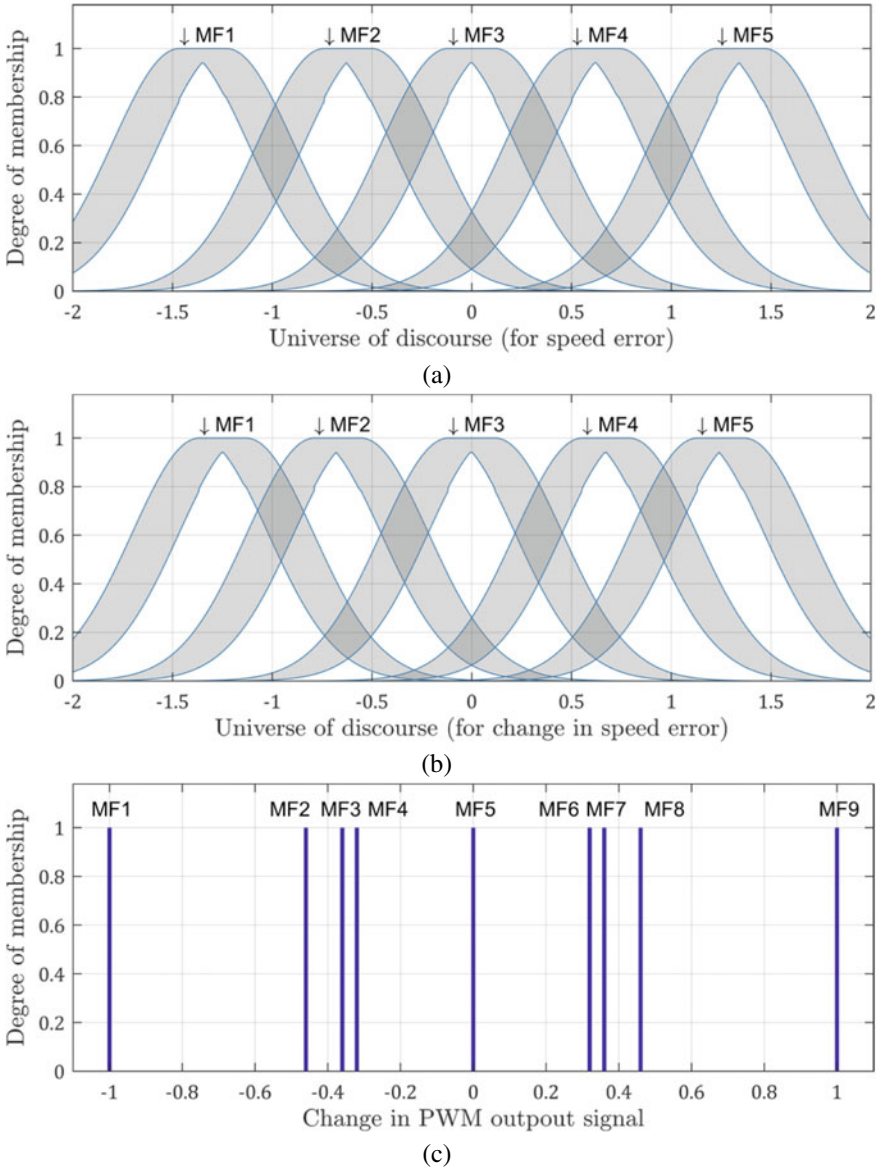
Fig. 5 Membership functions (MFs) of the developed interval Type-2 fuzzy controller, **a** for normalized speed error, **b** for normalized change in speed error and **c** for controller output

Table 2 Fuzzy association matrix (rule base) of the developed IT2-FLC

	Error				
	MF1	MF2	MF3	MF4	MF5
Change in error					
MF1	1.00	0.46	0.36	0.32	0.00
MF2	0.46	0.36	0.32	0.00	− 0.32
MF3	0.36	0.32	0.00	− 0.32	0.36
MF4	0.32	0.00	− 0.32	− 0.36	− 0.46
MF5	0.00	− 0.32	− 0.36	− 0.46	− 1.00
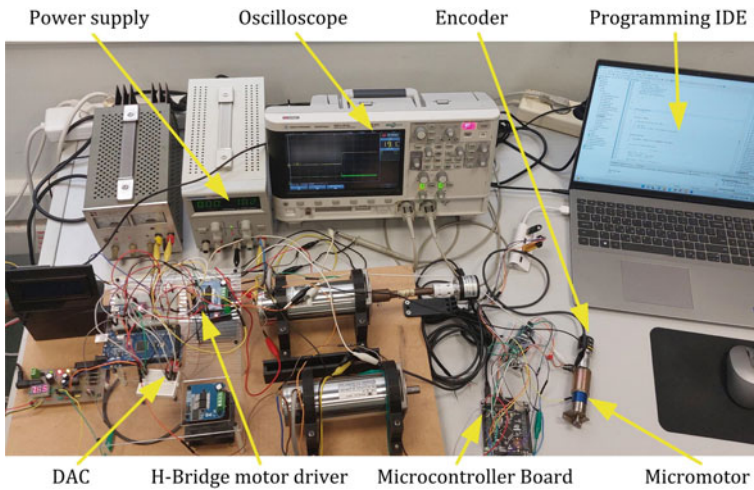
Fig. 6 Experimental apparatus for the coreless micromotor IT2 fuzzy speed controller development and testing

5 Conclusions

In this paper, T1-FLC and IT2-FLC were developed and implemented in a microcontroller platform for real-time coreless DC micromotor speed control problem. Both T1-FLC and IT2-FLC were optimized using the PSO algorithm. In order to evaluate the performance of the controllers, various motor speed disturbances were considered, despite the fact that the controllers were optimized for best performance in a single operating point. Results showed that IT2-FLC outperformed the T1-FLC, in a wide region of disturbances. As future work, an IT2-FLC with fewer membership functions (both for input and output variables) could be designed and also, for the optimization of the controllers other meta-heuristic bio-inspired algorithms may be applied.
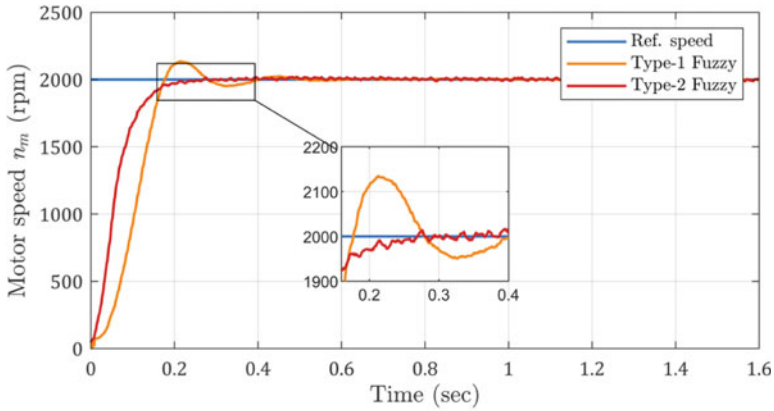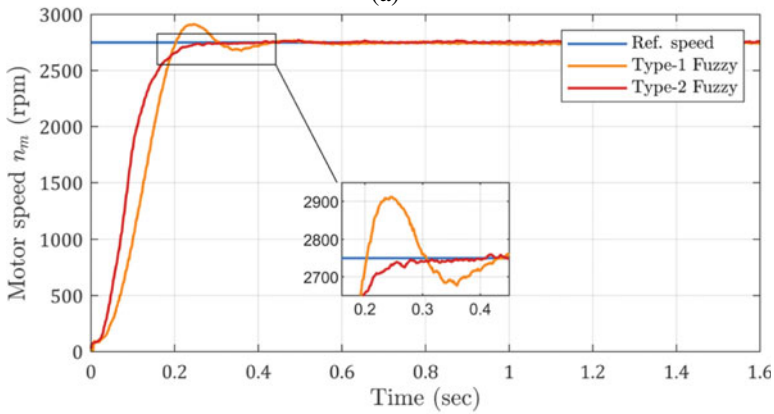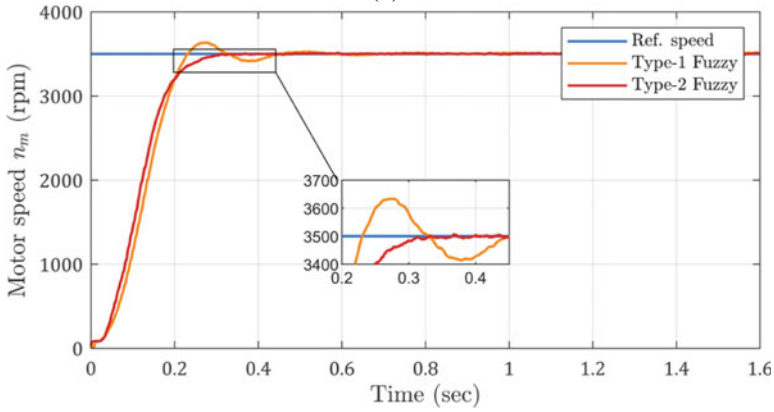
Fig. 7 Experimental speed responses of the micromotor under study with type-1 and type-2 fuzzy controllers, in reference speeds of **a** 2000 rpm, **b** 2750 rpm, **c** 3500 rpm

Table 3 Performance of the examined fuzzy controllers (time-response characteristics)

Case	Fuzzy controller	Rise time (ms)	Settling time (ms)	Overshoot (%)
Ref. speed 2000 rpm	Type-1	112	482	6.92
	Type-2	105	226	–
Ref. speed 2750 rpm	Type-1	128	501	5.87
	Type-2	119	241	–
Ref. speed 3500 rpm	Type-1	141	543	3.80
	Type-2	137	286	–

Table 4 Performance of the examined fuzzy controllers (metrics values)

Case	Fuzzy controller	MSE ($\times 10^5$)	IAE	ISE ($\times 10^5$)	ITAE
Ref. speed 2000 rpm	T1-FLC	1.56	223.2	3.117	22.79
	IT2-FLC	0.79	135.4	1.581	16.76
Ref. speed 2750 rpm	T1-FLC	3.39	348.2	6.779	39.74
	IT2-FLC	2.43	258.2	4.851	24.28
Ref. speed 3500 rpm	T1-FLC	5.85	462.3	11.670	47.88
	IT2-FLC	5.22	419.2	10.430	40.12

References

1. Gieras JF, Gieras IA (2002) Performance analysis of a coreless permanent magnet brushless motor. In: Proceedings of 37th IAS annual meeting, IEEE industry applications conference, vol 4. Pittsbutgh, USA, 13–18 Oct 2002, pp 2477–2482
2. Pastorino R, Naya MA, Pérez JA, Cuadrado J (2011) Geared PM coreless motor modeling for driver's force feedback in steer-by-wire systems. Mechatronics 21:1043–1054
3. Karnavas YL, Chasiotis ID (2016) PMDC coreless micro-motor parameters estimation through Grey Wolf optimizer. In: Proceedings of the XXII international conference on electrical machines (ICEM), Lausanne, Switzerland, 4–7 Sept 2016, pp 865–870
4. Gieras JF (2008) Electric motors for medical and clinical applications. In: Proceedings of the international conference on electrical machines and systems (ICEMS), 17–20 Oct, Wuhan, China
5. Chung SU, Hwang GY, Hwang SM, Kang BS, Kim H (2002) Development of brushless and sensorless vibration motor used for mobile phone. IEEE Trans Magn 38(5):3000–3002
6. Karnavas YL, Chasiotis ID, Peponakis EL (2016) Optimization of standard PMDC motors used in automotive applications for higher power density. In: Proceedings of 3rd international conference on mathematics and computers in sciences and industry (MCSI), Chania, Crete, Greece, 27–29 Aug 2016, paper ref. no. 034, pp 7–13
7. Ravaud AR, Lemarquand G, Lemarquand V (2009) Ironless permanent magnet motors: three-dimensional analytical calculation. In: Proceedings IEEE electric machines and drives conference (IEMDC), Miami, FL, USA, 3–6 May 2009, pp 947–952
8. Karnavas YL, Paschaloglou TP, Mouroutsos SG, Chasiotis ID, Drakaki M, Boutalis YS (2019) Application of Salp Swarm algorithm for DC motor parameter estimation in an industry 4.0 control systems IoT framework. In: Proceedings of the 12th international conference on developments in eSystems engineering (DeSE), Kazan, Russia, 7–10 Oct 2019, pp 778–783

9. Karnavas YL (2020) Application of recent nature-inspired meta-heuristic optimization techniques to small permanent magnet DC motor parameters identification problem. IET-J Eng 2020(10):877–888
10. Zadeh LA (1965) Fuzzy sets. Inf Control 8(3):338–353
11. Mamdani EH, Assilian S (1975) An experiment in linguistic synthesis with a fuzzy logic controller. Int J Man Mach Stud 7(1):1–13
12. Yousef HA, Khalil HM (1995) A fuzzy logic-based control of series DC motor drives. In: Proceedings of the IEEE international symposium on industrial electronics, vol 2, pp 517–522
13. Hagras AH (2007) Type-2 FLCs: A new generation of fuzzy controllers. IEEE Comput Intell Mag 2(1):30–43
14. Liang Q, Mendel M (2000) Interval type-2 fuzzy logic systems: theory and design. IEEE Trans Fuzzy Syst 8(5):535–550
15. Wu, Tan WW (2004) A type-2 fuzzy logic controller for the liquid-level process. In: Proceedings of IEEE international conference on fuzzy systems, vol 2, pp 953–958
16. Maldonado Y, Castillo O (2012) Genetic design of an interval type-2 fuzzy controller for velocity regulation in a DC motor. Int J Adv Rob Syst 9(5):204
17. Sarabakha A, Fu C, Kayacan E, Kumbasar T (2018) Type-2 fuzzy logic controllers made even simpler: from design to deployment for UAVs. IEEE Trans Industr Electron 65(6):5069–5077
18. Lin P-Z, Hsu C-F, Lee T-T (2005) Type-2 fuzzy logic controller design for Buck DC-DC converters. In: Proceedings of the 14th IEEE international conference on fuzzy systems, pp 365–370
19. Mendel JM, Mouzouris GC (1997) Designing fuzzy logic systems. IEEE transactions on circuits and systems II: analog and digital signal processing 44(11):885–895
20. Wu D, Mendel JM (2014) Designing practical interval type-2 fuzzy logic systems made simple. In: Proceedings of the IEEE international conference on fuzzy systems, pp 800–807
21. Bojan-Dragos C-A, Precup R-E, Preitl S, Roman R-C, Hedrea E-L, Szedlak-Stinean A-I (2021) GWO-based optimal tuning of type-1 and type-2 fuzzy controllers for electromagnetic actuated clutch systems. IFAC-PapersOnLine 54(4):189–194
22. Hassani H, Zarei J (2015) Interval type-2 fuzzy logic controller design for the speed control of DC motors. Syst Sci Control Eng 3(1):266–273
23. Mendel JM, Hagras H, Tan W-W, Melek WW, Ying H (2014) Introduction to type-2 fuzzy logic control: theory and applications. IEEE Press, Wiley, New Jersey, USA

Performance of a Low-Power 6T-SRAM Cell for Energy-Efficient Leakage Reduction Using DTMOS Technique

G. Nibhasya, Kakarla Hari Kishore, Fazal Noorbasha, and Udari Gnaneshwara Chary

Abstract Leakage current consumes the majority of the active mode energy in the high-performance integrated circuits of today. In particular, in high microprocessor and system-on-chip architectures, the SRAM cell array is the primary source of leakage current. So low-leakage SRAM design is essential. Today's VLSI designs are all about cutting down on power dissipation, supply voltage, leakage currents, and chip area. However, raising these parameters increases sub-threshold leakage currents and power dissipation, reducing design performance. Increasing the cell area reduces leakage power dissipation in standby mode. To solve these problems, it is best to cut down on effective leakage currents and dynamic power dissipation. For low voltage and energy constraints, the power dissipation, area, and delay performance of the low-power design of the 6T-SRAM cell with the DTMOS technique for a proposed low-power SRAM will be implemented in the Tanner EDA tool in 22 nm technology. The power of both types of SRAM cells will be compared using low-power techniques and a power analysis.

Keywords 6T SRAM · Low power · Leakages · Sleep transistors · Power dissipation

G. Nibhasya · K. H. Kishore (✉) · F. Noorbasha
Department of ECE, Koneru Lakshmaiah Education Foundation, Vaddeswaram, Guntur, Andhra Pradesh, India
e-mail: kakarla.harikishore@kluniversity.in

F. Noorbasha
e-mail: fazalnoorbasha@kluniversity.in

U. G. Chary
Department of ECE, B V Raju Institute of Technology, Narsapur, Telangana, India

1   Introduction

The leakage current of a CMOS gate depends on the input combinations. This paper describes a method for minimizing leakage in VLSI circuits. It is possible to reduce leakage by 25% with almost no delay [1]. High leakage current contributes to CMOS circuit power dissipation. Estimating and reducing leakage power requires identifying and modeling leakage components. Leakage mechanisms incorporated into the MOSFET are discussed in this study, including drain-induced barrier lowering, gate-induced drain leakage, and gate oxide tunneling [2]. The ice's threshold voltage depends on its gate voltage, so as the gate voltage increases, the leakage current decreases [3]. Nanometer design issues arise due to device scaling [4]. SRAM cells are designed with stability in mind. Memory stability is affected by the MOSFET aspect ratio and operating conditions. Memory stability allows it to run properly. It is the SRAM cell's stability metric (SNM) from the SRAM cell's voltage transfer properties [5]. Memory is a data storage device. Each memory cell is an IC chip with MOS transistors. It is called semiconductor memory. Semiconductor memory is classified as volatile or non-volatile. These are non-volatile memories. Random access memory (RAM) is a type of volatile memory. The two types of random-access memory are dynamic RAM for primary storage and static random-access memory (SRAM) for cache. This paper is concentrated more on SRAM. A single-bit SRAM consists of only CMOS transistors and no other additional circuitry. A multi-bit SRAM needs multiplexing and de-multiplexing circuitry to access the data and address lines for reading and writing the information. Due to the evolution of process technology, i.e., the decrease in channel length, increased the number of transistors that are integrated per chip, resulting in high leakage currents, power dissipation, reliability problems, costs for cooling techniques, etc. So, to reduce the consumption of power the circuit need for low-power circuits aroused. In digital CMOS circuits, power consumption is primarily associated with 2 components, i.e., dynamic power for the switching activity for the charge and discharge of the load capacitance, and static power for the leakage currents. The total power utilization of a digital device is the combination of its static, dynamic, and short circuit power given a

$$P_{\text{total}} = P_{\text{dynamic}} + P_{\text{static}} + P_{\text{short - circuit}} \tag{1}$$

$$\text{Dynamic} = \alpha C_L V_{\text{dd}}^2 f \tag{2}$$

$$\text{Static} = V_{\text{dd}} * I_{\text{leak}} \tag{3}$$

Here α is the switching activity, C_L is the load capacitances, V_{dd} is the voltage supply, f is the operating frequency, and I_{leak} is the combination of all leakage currents.

Dynamic power dissipation can be minimized by scaling the supply voltages. As for the static power elements the aim is to maintain the leakage current as minimum as possible. As the technology is evolved, leakage power is exponentially increased

and gradually it becomes the main source of power. Therefore, in current digital devices, low-power approaches, particularly those for static power reduction, are required at practically every design stage. To change the state of SRAM, use SNM [6]. During reading from SRAM, the stored value should not change, but during writing, it should allow new data [7]. SRAM dissipates power both dynamically and statically. During read and write activities, dynamic power is used, while standby power is used [8]. This paper's main goal is to design and analyze 6T-SRAM cells in different types of CMOS. In this study, PTM model cards are used to measure cell performance in different ways. It generates accurate and compatible model files for a variety of processes [9, 10]. The Cadence Virtuoso Analog Design Environment is used for the designs. Device (W/L) ratios shrink and VT drops, which makes leakage an issue because it depends on the (W/L) ratio, VDD, and VT. The CMOS inverter's gate leakage, sub-threshold leakage, and reverse bias PN junction leakage all played a role in the leakage currents, as did the gate leakage. Leakage power is comparable to dynamic power at lower (< 90-nm) technologies. Leakage power reduction techniques such as VTCMOS, MTCMOS, and DTMOS are all well-known. This paper is an attempt to summarize the low-power approaches used to decrease the static power, i.e., leakages in the circuit. It sheds light on various techniques and the respective standby average power of the circuit. The larger goal is to use this single-bit SRAM cell in low-power applications. The paper following described Sect. 2 describes how to save energy by using 1-WL and 2-BLs instead of a 6T-SRAM cell. Section 3 shows the cell's leakage reduction power and energy, as well as its low-voltage stability. Section 5 simulation results with the exaltation of power, a discussion and compared results analysis part, and finally, a conclusion.

2   6T-SRAM Cell Design and Stability

2.1   *Standard Model of a 6T-SRAM Cell*

SRAM's topology has undergone numerous iterations throughout the years. Compared to other SRAM cell types, the noise tolerance of 6T SRAM caught people's attention. Two access transistors and a handful of cross-coupled CMOS (DTMOS) inverters make up the 6T-SRAM cell design. Input and output ports are connected via high-loading bit lines. These bit lines are responsible for the entire process of browsing and writing, and we'll be able to observe how they are managed.

DTMOS is represented by connecting the gate to the body of a simple MOS transistor, the threshold voltage of the derived DTMOS is reduced upon forward body biasing. Basic model of 6T-SRAM cell is shown in Fig. 1.

A. **Read-Operation**:

   Always charge the bit lines to VDD before initiating the browsing process. When a word line (WL) is enabled, it discharges a bit line connected to cell node 0 via the NMOS semiconductor. This tells us that the node contains 0 and 1 in it. By
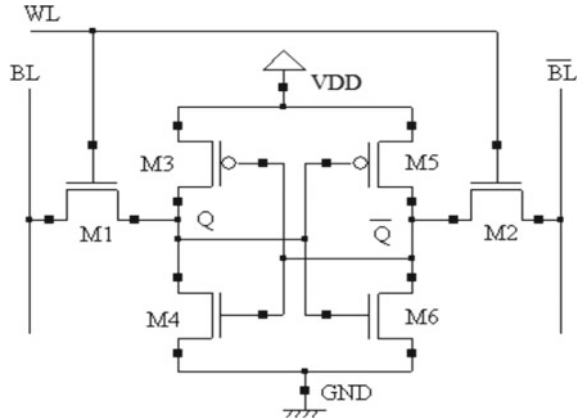
detecting the bit lines, we will find the node has 1/0.The bit line carrying "1" is
connected to the node containing "1".

B. **Writing Operation**:

   1/0 requires always giving information to the bit line (BL) in relation to the bit
   line bar (BL). Once enabled, the data is written into several nodes.

3 Low-Power Leakage Techniques

Every SRAM subcircuit's power leakage is measured as a function of operation
(read/write/idle). The static power loss arises from the leakage from the power source.
Channel punch-through, drain-induced barrier lowering (DIBL), sub-threshold leak,
gate oxide tunnel, hot carrier effect, reverse bias *p-n* junctions, and gate-induced
drain leak are some of the characteristics that lead to leakage current. Sub-threshold
leak, which is arisen from the sub-threshold Id and tunneling current, is the essential
parameter to keep an eye on.

The Ids is below the threshold drain current (ID) in the weak inversion area (when
VGS < VTH). The tunnel current is the current that runs through the oxide layer as
it becomes thinner.

$$I_{\text{Leakage}} = I_0 e^{\frac{(V_{\text{gs}} - V_{\text{th}})}{n V_{\text{T}}}} \tag{4}$$

where $I_0 = \mu_0 C_{0x} V_{\text{T}}^2 e^{1.8}$, V_{T} is the thermal voltage, from the above equation, it is
a proof that current is proportional to voltage (VGs-VTH). By raising the V_{th}, this
leakage may be reduced to a minimum. The VTH is the most significant parameter
in circuit design (threshold voltage). Low VTH is favored in active mode due to
the elevated performance, whereas higher VTH is favored in sleep mode leading to
decreased leakage power. There is a variety of VLSI approaches for lowering leakage
power. Every strategy cost-effectively reduces leakage power.

Fig. 2 DTMOS inverter
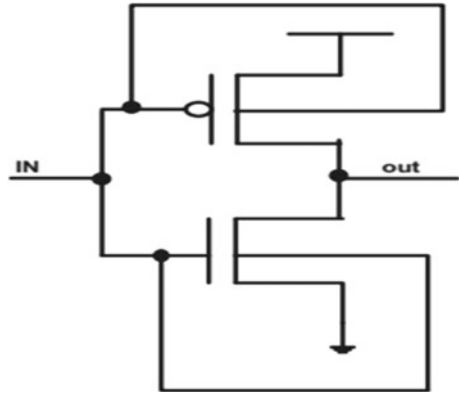
3.1 DTMOS

Figure 2 indicates a dynamic threshold MOS (DTMOS) circuit, which comprises NMOS and PMOS transistors with their body and gate terminal connected. The body voltage in DTMOS modifies with the gate voltage (V_g). DTMOS can dynamically adjust the MOSFET's threshold voltage V_t for high ON current in active phase and low OFF current in standby phase. As a result, it aids the designer in achieving great system performance while consuming minimal power. The substrate-source junction in active mode is forward biased, while in standby state it is reverse biased. DTMOS is a prominent approach for dynamically changing V_t in bulk CMOS. The body voltage follows the V_g when the DTMOS transistor is turned on. However, as the devices are scaled down, both resistance and capacitance of substrate are increased, resulting in a rise in the RC time constant. This prevents the substrate from fast switching which is the DTMOS's fundamental flaw.

3.2 SRAM Cell Using DTMOS Approach

Aggressive device scaling is driven by performance and density gains. That increased sensitivity to PVT changes and standby leakage is more noticeable in small circuits like SRAM that use low level devices. This work tries to solve these problems in a traditional 6T-SRAM cell while keeping its fully differential architecture, which is what this work is about. Proposes a fully differential DTMOS-6T SRAM bit cell. As shown in Fig. 3, it also uses differential operation, which means that pull-down NFETs and pull-up PFETs can be swapped out for each other with WL (world line) and WLB (word line bar). The proposed design loses only a small amount of area due to the extra control WLB. As any read or write operation of the SRAM cell can happen by switching on the access transistor. Hence to ensure a correct logic the WLB should be low before the WL goes high and WLB should go high after

Fig. 3 Purposed 6T SRAM with DTMOS inverter (unconventionally)

MN1, MN2: W/L = 66 nm / 22 nm
MP1, MP2, MN3, and MN4: W/L = 44 nm / 22 nm
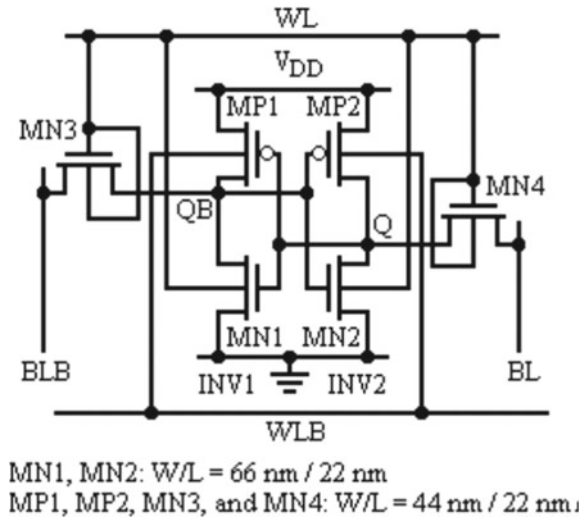
WL goes low. This can be done by choosing WL and WLB two non-overlapping signals. Access FETs use DTMOS. When the proposed cell is in standby mode, these new techniques put it in a similar state to CON6T. Because the proposed bit cell has the same hold state as the DTMOS when it is in hold mode, the standby leakage is the same. These techniques reduce V_{ts} dynamically. Using these unique biasing schemes, we get better results in terms of read/write delay and spread at the cost of complexity and overhead. They (DTMOS) use forward biasing schemes to access the cell, increasing drive currents. When the supply voltage is above 0.6 V, these biasing schemes can cause large currents through the PN junction between the p-well and n-well. As reported in the parasitic bipolar transistor's hFE is less than unity. In the burn-in mode of 65 nm CMOS, hFE is greater than unity. The proposed SRAM operates at sub-threshold (VDD = 400 mV), so the forward biasing current is irrelevant. However, the proposed design requires a triple-well process.

3.3 Power Gating

This method is utilized in IC design to curtail the utilization of power, by turning off the current to circuit blocks that are not in use. Power Gating, unlike Clock Gating, which saves dynamic power, saves leakage power. As we progress from sub-micron to deep sub-micron technologies, leakage power dissipation becomes more important than dynamic power dissipation. Because a direct route exists among the power supply VDD and the ground GND in any CMOS digital logic circuit with pull-up and pull-down networks, the device will continue to dissipate power leak. When the device is not in use, the power and ground terminals can be gated out. So, sleep transistors are introduced here, i.e., a PMOS and NMOS transistors are inserted whose

gate terminals are inverse to each other. The PMOS and NMOS sleep transistors are both ON, during normal operation, i.e., when Sleep = 0, virtual power and virtual ground nodes are created to ensure that the circuit operates normally. When Sleep = 1, the circuit has low activity, i.e., it is in standby state. So, the sleep transistors are turned OFF. And because the pull-up and pull-down networks break the direct route from the power terminal to the ground, no leakage power is dissipated. Because the sleep transistors are still ON during normal operation, they contribute to some extra leakage power. In comparison with that of the pull-up and pull-down networks, though the leakage power from these two additional transistors is negligible, they are specially fabricated with a high threshold voltage V_t to eliminate any surplus leakage power during normal operation [11]. Figure 5 shows the power gating techniques.

4 Implementation

A typical SRAM cell is comprised of 6 MOSFETs. In an SRAM, every bit is saved on 2 cross-coupled inverters made up of 4 transistors. There are two stable states in this storage cell, which are denoted by the numbers 0 and 1. Throughout the read and write function, 2 extra access transistors are introduced to govern the access to a storage cell. There are three modes in which an SRAM cell can operate: standby read and write mode. The circuit is in standby state, i.e., the same state is retained, whenever the word line WL = 0. Both the bit lines BL′ and BL are pre-charged to high voltage, i.e., logic 1, at the start of the read cycle. When the word line WL is raised to logic 1, both the pass transistors are enabled, causing a voltage drop on one of the bit lines BL. Then there will be a minor voltage difference among the BL and BL′ lines. A sensing amplifier will detect which line has the greater voltage and consequently decide whether one or zero was saved [7, 12, 13]. The write phase starts by having the value to be stored in the bit line. If the value 0 need to be written, a zero is given to the bit line, i.e., by configuring BL' to one and BL to zero. This standard SRAM cell is implemented along with low-power SRAM cells. Various SRAM configurations are implemented in the Tanner EDA tool in 22 nm technology. The schematics of all these circuits implemented in *s*-edit are shown in Fig. 4. DTMOS technique is applied as shown in Fig. 4 and the respective power is calculated accordingly. The power gating technique is applied with sleep transistor as depicted in Fig. 4. The sleep transistor approach can be applied to only pull-down network of the circuit. This methodology is shown in Fig. 4. Another power gating technique is applied as in Fig. 4. The PMOS and NMOS are exchanged from a typical sleep transistor technique and it is implemented as shown in Fig. 3. Another power gating technique is introduced in Fig. 4 in which PMOS and NMOS are linked in parallel to each other and implanted in both pull-down and pull-up networks. Another method used to minimize leakage power is transistor stacking. This is shown in Fig. 3 in which transistors are stacked both in pull-up and pull-down networks whereas in Fig. 4 additional transistors are present only in pull-down network. The suggested SRAM

Fig. 4 Purposed 6T SRAM with DTMOS inverter (conventionally)

MN1, MN2: W/L = 66 nm / 22 nm
MP1, MP2, MN3, and MN4: W/L = 44 nm / 22 nm
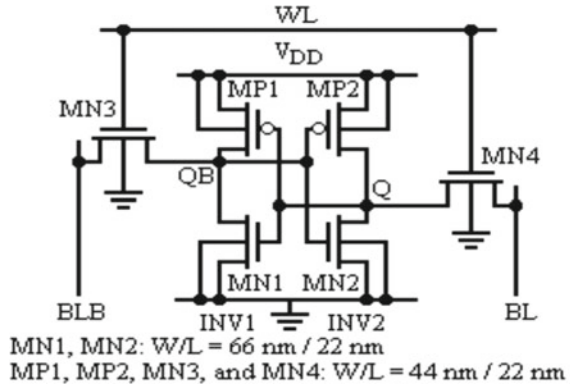
Fig. 5 Power gating technique
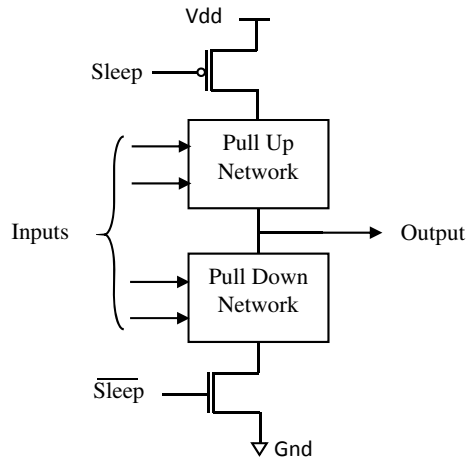
cell is depicted in Fig. 4. The layouts of conventional and suggested SRAM cells are illustrated in Fig. 5.

4.1 6T-SRAM Cell

Figure 6 shows a schematic design of a conventional 6T-SRAM cell. The 2 pull-up transistors (*P*0, *P*1), 2 pull-down transistors (*N*0, *N*1), and 2 pass transistors make up the 6T-SRAM cell (*N*2, *N*3). The word line inputs regulate the gate of pass transistors (*w*l). The BL and BLB are linked to the cell whenever the word line is set high, allowing the cell to be read out or written into from the bit line. Dynamic power dissipation is the power assessed in this condition owing to output switching activity. When the *w*l is set to zero, the cell does not execute any read or write operations,
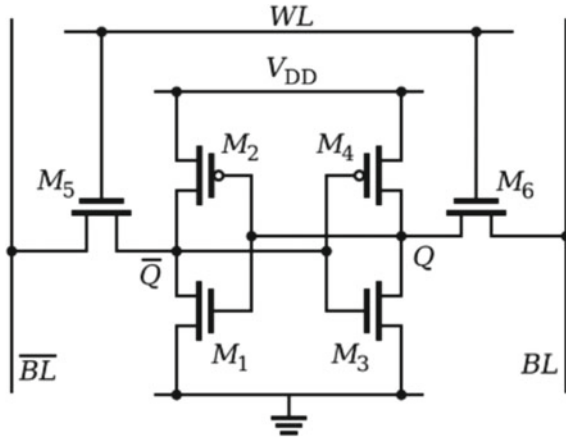
hence it is in the holding phase. Static or leaky power dissipation is the term for the power assessed in this condition. A write driver that checks the existence of information and permits the information to be written into the cells is required for effective cell writing. This write driver is a basic AND gate with write enable and data as inputs. The write enables of the write drivers is turned off while reading is to be done. It is critical that the BL and BLB be pre-charged to a specified amount of voltage prior to reading begins, ensuring that both bit lines have a similar voltage. The pre-charge circuit is accountable for this pre-charge. Following pre-charge the capacitor at one end drains owing to voltage difference among node of accessing transistor, based on the value held at the output (q, qb) of the SRAM cell. A sense amplifier is a differential amplifier that detects and amplifies the difference among the voltages in BL and BLB. While reading, the output lines BL and BLB are used.

4.2 Conventional 6T-SRAM Cell

Cell array, address decoders, column multiplexer; sense amplifier, I/O, and control circuitries are all parts of a conventional SRAM. A single SRAM memory cell's circuit generally consists of 4 transistors organized as 2 cross-linked inverters. The circuit has 2 stable states in this manner, which correspond to the logical "0" and "1" values. The 2 extra transistors are needed in addition to the 4 transistors to regulate memory cell accessibility throughout read and write function. A memory cell with 6 transistors is referred to as a 6T memory cell. The cell is attached to a V_{dd}, the bit values stored in it are kept. The 2 inverters are linked back-to-back by transistor $P1$, $N1$, and $P2$, $N2$. The pass transistors are constructed by the transistors of $N3$ and $N4$. The bit line and its complement are represented by BL and BLbar. Further peripheral circuits, including the precharge circuit, write circuit, and sensing amplifiers, are coupled to these. The word line signals (WL) are utilized to trigger read

and write functions. Based on the value being written, the write function comprises pre-charging the two-bit lines to VDD and drawing one of the bit lines to the ground. After the pre-charge cycle, the word line WL is active, and the logic value on BL and BLbar are transmitted to T and F, respectively. There are two steps to the read operation as well. The word line WL is enabled once both bit lines have been pre-charged to VDD. The bit line to the node that stores the logic value 0 is pushed down. This change in voltage at the bit line is detected by the sense amplifiers, which amplify it to CMOS logic levels. The read route in an SRAM cell contains the pull-down NMOS and the pass transistor. The write route, on the other hand, includes the pull-up PMOS and the pass transistors. Transistors $P1$, $N1$, and $P2$, $N2$ must be considered weak, while pass transistors $N3$ and $N4$ must be built stronger, to improve writing ability. When it comes to reading, the opposite is preferred. The pull-down transistor is built tougher than the pass transistor to ensure excellent read stability. The information in the SRAM cell should not be destroyed during the read operation. As a result, more powerful inverter and weak pass transistors are preferred. While utilizing powerful PMOS transistors increases read consistency, it reduces write margin. To establish an acceptable, write margin, pass transistors must be properly sized.

4.2.1   Leakage Component in an SRAM Cell

Dynamic and static power loss is the 2 basic components of power loss in CMOS circuit. Switch transient current loading and unloading of load capacitance (CL) cause dynamic dissipation. I_{leak} have continually taken from the power source cause static dissipation. Sub-threshold leak, an inadequately source of leakage, can be anything from reverse-biased PN junctions to drain-induced barrier lowering (DIBL) to gate, punch-through, or oxide tunneling leakage.

Junction Tunneling Leakage

The two primary elements of reverse-biased p–n junction leak are minority carrier diffusion toward the edge of the depletion zone and electron–hole pairs production in the reverse-biased junction depletion region. The junction tunneling current is proportional to the amount of doping in the junction and the reverse bias voltage applied across it.

$$I_D = I_S\big[(\exp V_D/V_T) - 1\big] \tag{5}$$

Researchers do not seek to minimize junction tunneling current in an SRAM since it is a little contribution to overall leakage current; nonetheless, it should be figured out that junction tunneling current may be lowered by applying forward substrate biasing.

Sub-threshold Leakage

The Ids of a transistor when the V_{gs} is much less than V_{th} is known as a sub-threshold leak. When the transistor is working in the weak inversion area, a sub-threshold leak occurs. In short channel circuits, the sub-threshold current I_S is proportional to the V_{th}, resulting in a significant I_S.

$$I_{Dsub} = I_S\left[1 - e^{\frac{-V_{ds}}{V_t}}\right]\left[e^{\frac{V_{gs}-V_T-V_{off}}{nV_t}}\right] \tag{6}$$

The V_{th} of every part of the transistor in an SRAM cell may be raised to decrease sub-threshold leakage. The disadvantage of this strategy is that it causes the cell's read/write latency to rise. The write delay rises when the V_{th} of the pull-up PMOS transistor is raised, but the impact on the read delay is insignificant. The rise in the V_{th} of the pull-down NMOS transistors, on either hand, raises the read latency while having just a little influence on the writing latency. The read and write latency both rise when the V_{th} of the pass transistors is raised. The writing latency of an SRAM cell is often less than its reading latency due to the late sensing amplifier and output buffers in the read channel. As a result, lowering the V_{th} of PMOS transistors to minimize sub-threshold leak is a viable option as long as the writing latency is smaller than the reading latency. Schematics of Various SRAM configurations are shown in Fig. 7.

5 Simulation and Results

The circuit design is built using 22 nm CMOS technology files. All designs are completed, and simulation is carried out in tanner EDA. As the working of the SRAM cell does not change, the output remains same for all the circuits. Figure 8 shows the simulation outcome of the SRAM cell.

The average power loss is assessed using the Tanner EDA tool. The power dissipation is measured throughout the standby mode of operation, for the power gating technique where sleep transistors are used. The comparison table of average power for various low-power SRAM configurations is shown in Table 1.

As shown in this table, using DTMOS technique, the average power increased instead of decreasing. By using the power gating technique, i.e., sleep transistors, during standby mode, there is a significant decrease in the average power but there will be an increase in the area. By using only pull-down sleep transistor, power is decreased in comparison with traditional SRAM, but the area increase will be less compared to the previous configuration. The remaining configurations also show a significant decrease in power but on a large scale, i.e., for multi-bit SRAM, using 10 transistors will cause a massive increase in the area which is not ideal. Transistor stacking also decreases the average power of the SRAM cell. Similarly, stacking with 10T gives a prominent power reduction but the area is increased significantly. There is
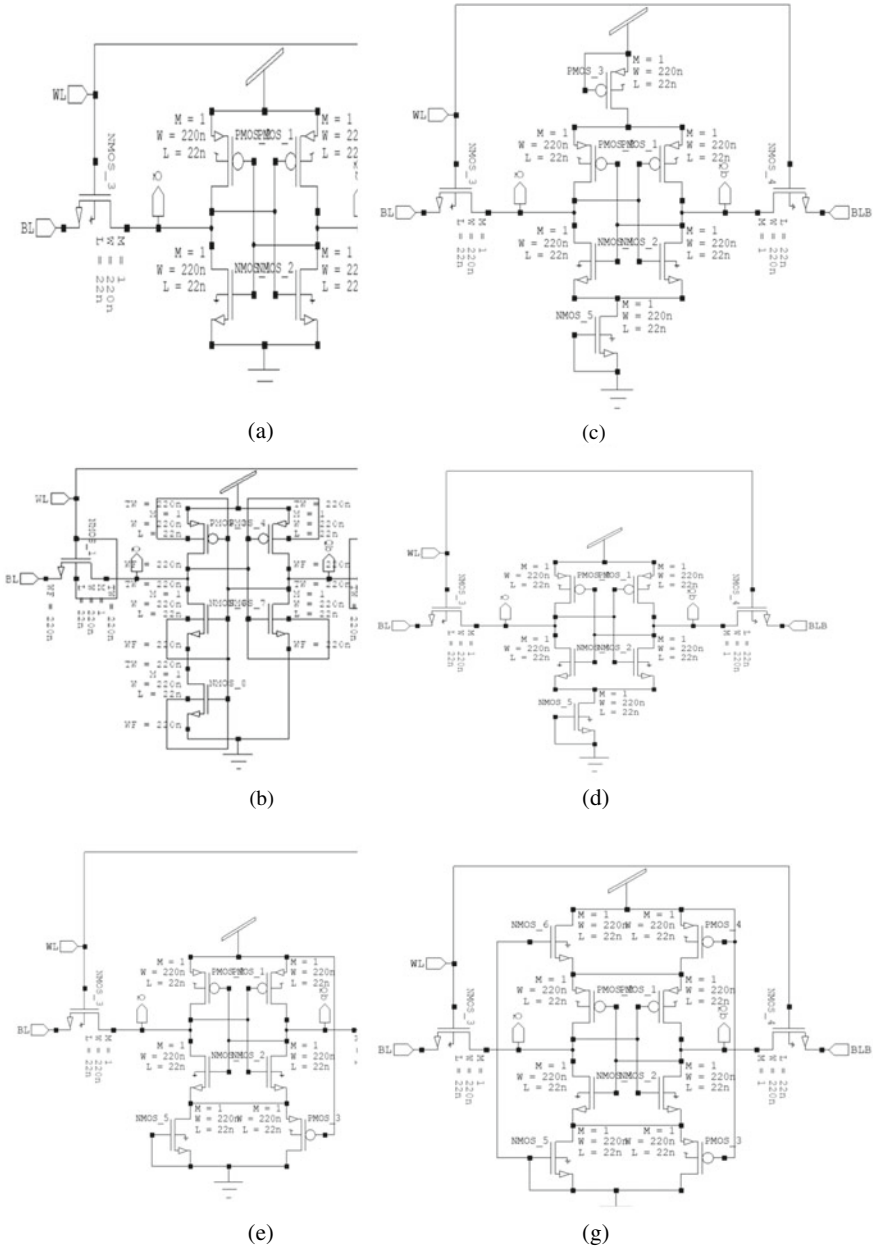
Fig. 7 a–h Schematics of various SRAM configurations

(f)

(h)

Fig. 7 (continued)

(a)

(b)
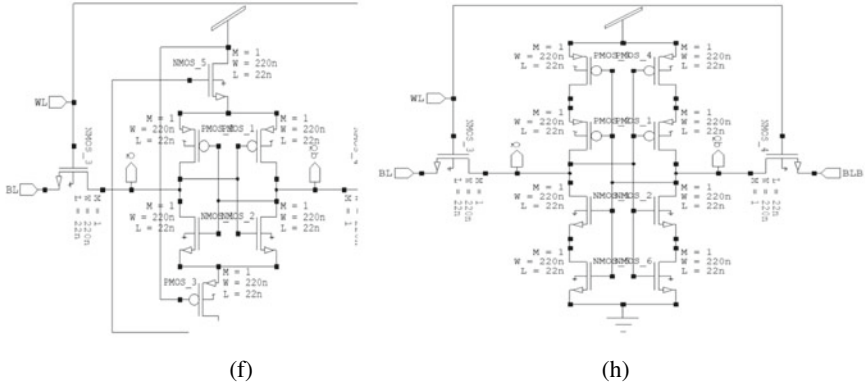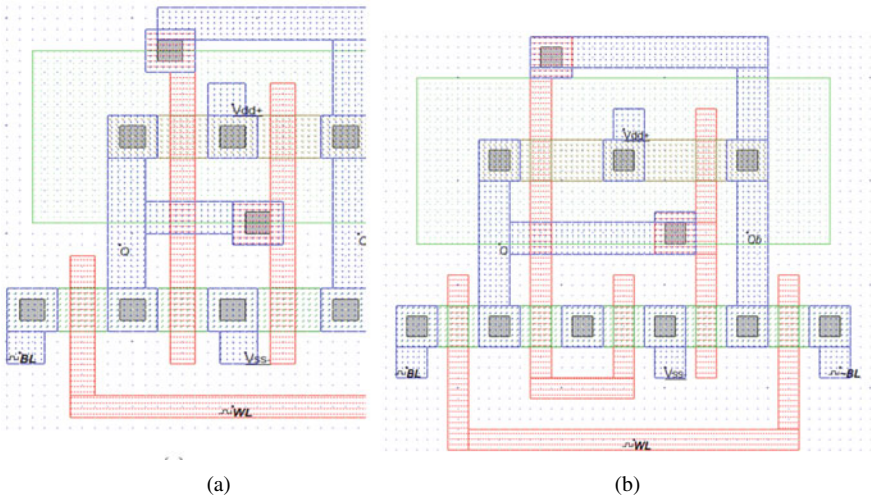
Fig. 8 a Layouts of 6T, b 7T SRAM cell

a decrease in power by using only 7 transistors. Such configuration is compared with conventional SRAM and respective average power is shown in Fig. 9. Comparison of Power is shown in Fig. 10.

A. *Static Power Dissipation*

Power dissipation takes the form of leakage current when the gadget is powered off or in sleep phase. This kind of power dissipation is caused by transistor switching activity. Static power dissipation is caused by the transistor's junction leak.

Table 1 Comparison of average power of various SRAM configurations

S.No.	SRAM	Average power (22 nm) (W)
1	Conventional 6T-SRAM cell	3.577930e−007
2	Using DTMOS-7T	3.205362e−005
3	Using sleep transistors-8T	1.243758e−009
4	Sleep transistors (only pull down)-7T	1.945668e−007
5	Power gating-8T	1.973538e−007
6	Sleep transistors (PD and PU exchanged)-8T	5.099474e−009
7	State retention-10T	6.060973e−009
8	Stacking-10T	9.461887e−008
9	Stacking (only pull down)-8T	2.261524e−007
10	Stacking-7T	2.710774e−007
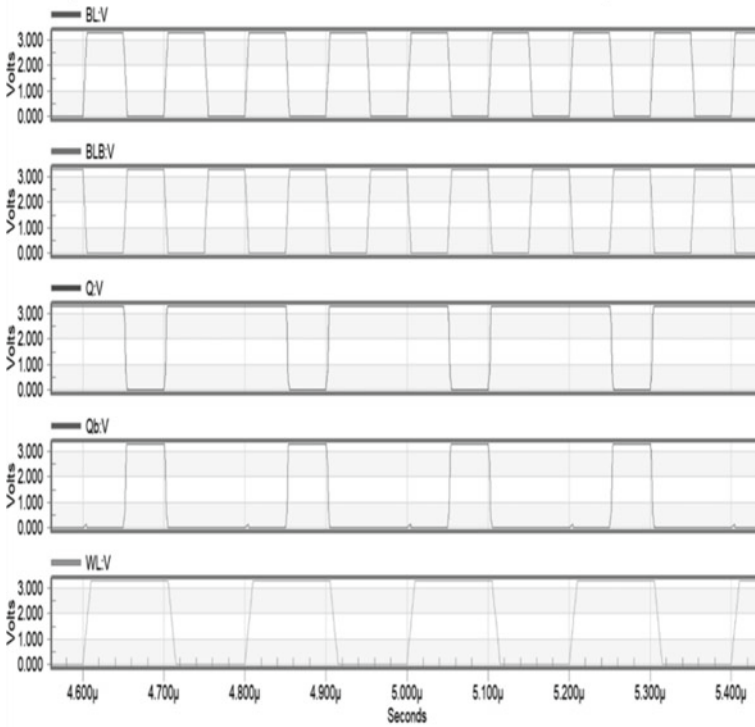
Fig. 9 Simulation outcome of SRAM cell

Fig. 10 Comparison of power

AVERAGE POWER

■ Average Power

3.58E-07

2.71E-07

EXISTING CELL   PROPOSED CELL
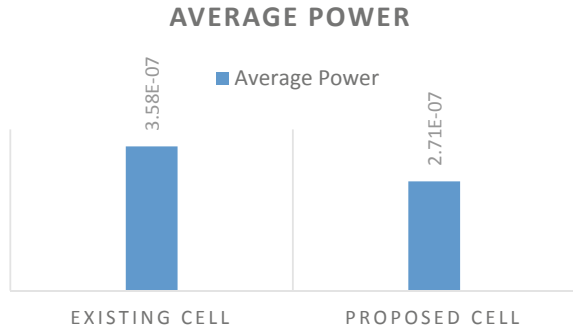
Figure 11 depicts the static power dissipation of an SRAM cell. In comparison with other standard approaches, the suggested low-power SRAM in tanner EDA has lower static power loss.

B. *Dynamic Power Dissipation*

Dynamic power dissipation is the power supply used throughout write and read activities. Dynamic power dissipation occurs when switching transients.

Figure 12 illustrates the dynamic power dissipation of a configured SRAM cell. In comparison with other current approaches, the suggested low-power SRAM in tanner EDA has the lowest dynamic power dissipation.

C. *Power Delay Product (PDP)*

By multiplying the average power use and the delay time, the PDP is obtained.

Figure 13 depicts the PDP of an SRAM cell. When compared to the recommended approaches, the traditional procedures have a higher power delay product.
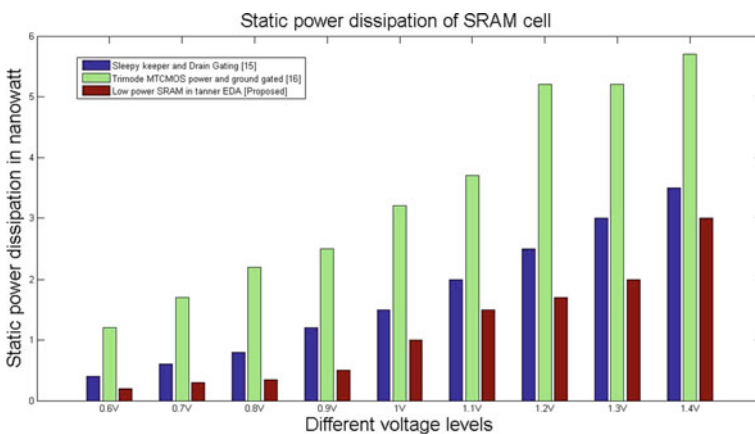
Fig. 11 Power dissipation in a static SRAM cell
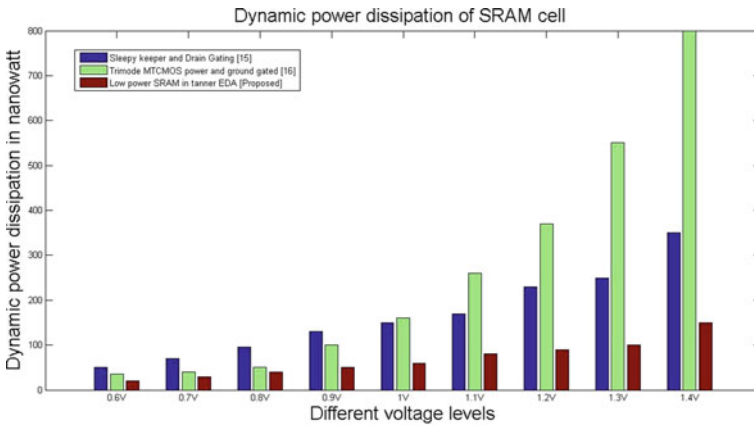
Fig. 12 Power dissipation in a dynamic SRAM cell
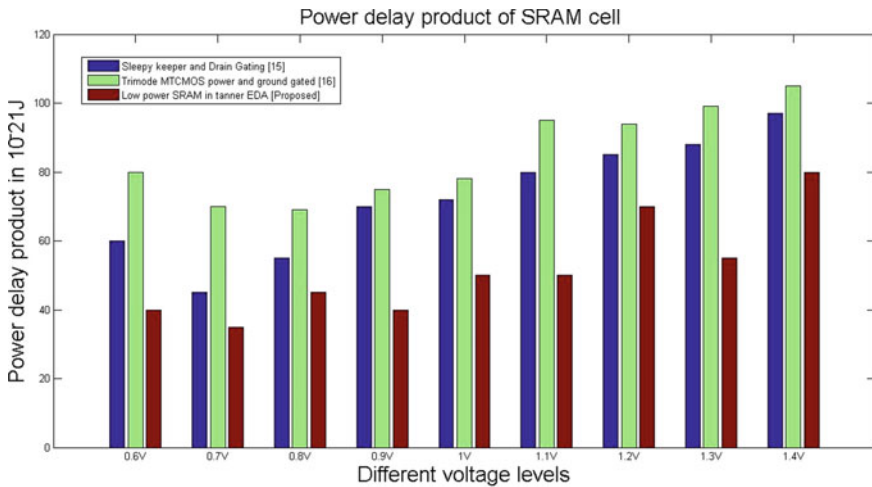
Fig. 13 Power delay product SRAM cell

6 Conclusion

In this paper, all the low-power SRAM circuits are implemented in 22 nm technology in the Tanner EDA tool. Power consumption is an important factor in IC chips. As the technology nodes are decreased, more emphasis should be given to the power. So, here dynamic power dissipation is decreased by minimizing the V_{dd}. In all the implemented circuits, the V_{dd} applied is 1 V to minimize the switching power. Various low-power approaches are implemented to the SRAM cell and the average power is calculated. But static I_{leak} are more significant in comparison with

dynamic power as feature sizes become smaller. So, in this paper, various low-power techniques are mentioned to achieve a prominent reduction of leakage power. Power gating techniques using sleep transistors and transistor stacking are introduced. So conventional SRAM is implemented along with low-power SRAM cells in S-Edit and their corresponding average power is calculated and they are compared. There is a lowering in the average power and the power delay product of the suggested SRAM in comparison with typical SRAM. The static and dynamic power dissipation of the SRAM that was built is lower than the power dissipation of other methods. This power discrepancy is particularly apparent in SRAMs with several bits of data.

References

1. Abdollahi FF, Pedram M (2004) Leakage current reduction in CMOS VLSI circuits by input vector control. IEEE Trans Very Large Scale Integr Syst 12:140–154
2. Roy K, Mukhopadhyay S, Mahmoodi-Meimand H (2003) Leakage current mechanisms and leakage reduction techniques in deep submicrometer CMOS circuits. In: Proceedings of the IEEE, vol 91, no 2
3. Assaderaghi F, Sinitsky D, Parke SA, Bokor J, Ko PK, Hu C (1997) Dynamic threshold-voltage MOSFET (DTMOS) for ultra-low voltage VLSI. In: IEEE Trans Electr Dev 44(3):414–422
4. Mutoh S, Douseki T, Matsuya Y, Aoki T, Shigematsu S, Yamada J (1995) 1-V power supply high-speed digital circuit technology with multithreshold-voltage CMOS. IEEE J Solid-State Circuits 30(8):847–854
5. Kim S, Kosonocky SV, Knebel DR, Stawiasz K (2004) Experimental measurement of a novel power gating structure with intermediate power saving mode. In: Proceedings of the 2004 international symposium on low power electronics and design (IEEE Cat. No.04TH8758), pp 20–25
6. Giterman R, Vicentowski M, Levi I, Weizman Y, Keren O, Fish A (2018) Leakage power attack-resilient symmetrical 8T SRAM cell. IEEE Trans Very Large-Scale Integr (VLSI) Syst 26(10):2180–2184
7. Roy K, Mukhopadhyay S, Mahmoodi-Meimand H (2003) Leakage current mechanisms and leakage reduction techniques in deep-submicrometer CMOS circuits. Proc IEEE 91(2):305–327
8. Chang IJ et al (2009) A 32 kb 10T sub-threshold SRAM array with bit-interleaving and differential read scheme in 90 nm CMOS. IEEE J Solid State Circuits 44.2:650–658
9. Anjana R, Kumar Somkuwar A (2013) Analysis of sub threshold leakage reduction techniques in deep sub-micron regime for CMOS VLSI circuits. In: International conference on emerging trends in VLSI, embedded system, nano electronics and telecommunication system. IEEE
10. Prasad G, Anand A (2015) Statistical analysis of low-power SRAM cell structure. Analog Integr Circ Sig Process 82:349–358
11. Chen YG, Shi Y, Geng H (2014) Multibit retention registers for power gated design. IEEE Trans Comput Aided Des 33:507–518
12. Khandal B, Roy B (2013) Design and simulation of low power 6TSRAM and control its leakage current using sleepy keeper approach in different topology. Int J Modern Eng Res 3(3):1475–1481
13. Gavaskar K, Ragupathy US, Malini V (2019) Design of novel SRAM cell using hybrid VLSI techniques for low leakage and high speed in embedded memories. Wireless Pers Commun 108(4):2311–2339

Tuning XGBoost by Planet Optimization Algorithm: An Application for Diabetes Classification

Luka Jovanovic⬤, Marko Djuric⬤, Miodrag Zivkovic⬤, Dijana Jovanovic⬤,
Ivana Strumberger⬤, Milos Antonijevic⬤, Nebojsa Budimirovic⬤,
and Nebojsa Bacanin⬤

Abstract Recent years have seen an increase in instances of diabetes mellitus, a metabolic condition that if left untreated can severely decrease the quality of life, and even cause the death of those affected. Early diagnostics and treatment are vital for improving the outcome of treatment. This work proposes a novel artificial intelligence-based (AI) approach to diabetes classification. Due to the ability to process large amounts of data at a relatively quick rate with admirable performance, the XGBoost approach is used. However, despite many advantages, the large number of control parameters presented by this algorithm makes the process of tuning delicate and complex. To this end, the planet optimization algorithm (POA) is tasked with selecting the optimal XGBoost hyperparameters so as to achieve the best possible classification outcomes. In order to demonstrate the improvements achieved, a comparative analysis is given that presents the proposed

L. Jovanovic · M. Djuric · M. Zivkovic · I. Strumberger · M. Antonijevic · N. Budimirovic ·
N. Bacanin (✉)
Singidunum University, Danijelova 32, 11000 Belgrade, Serbia
e-mail: nbacanin@singidunum.ac.rs

L. Jovanovic
e-mail: luka.jovanovic.191@singimail.rs

M. Djuric
e-mail: marko.djuric.19@singimail.rs

M. Zivkovic
e-mail: mzivkovic@singidunum.ac.rs

I. Strumberger
e-mail: istrumberger@singidunum.ac.rs

M. Antonijevic
e-mail: mantonijevic@singidunum.ac.rs

N. Budimirovic
e-mail: nebojsa.budimirovic.20@singimail.rs

D. Jovanovic
College of Academic Studies "Dositej", 11000 Belgrade, Serbia
e-mail: dijana.jovanovic@akademijadositej.edu.rs

approach alongside other contemporary algorithms addressing the same classification task. The attained results clearly demonstrate the superiority of the proposed approach.

Keywords Optimization · Diagnostics · Machine learning · Swarm intelligence · Planet optimization algorithm

1   Introduction

Diabetes mellitus refers to a category of metabolic conditions defined by persistent hyperglycemia ensuing due to problems with insulin secretion, cell insulin response, and in some cases both. Metabolic anomalies in carbohydrates, lipids, and proteins are some of the consequences of these defects as insulin is an important anabolic hormone. When an individual's insulin level is not high enough to produce an adequate response in order to better protect, primarily, the muscle and fatty tissues, as well as liver, and the signal transduction system, effector enzymes or sometimes genes can be responsible for said abnormalities. The harshness of the symptoms can vary depending on the type of diabetes and how long it was present. It is not uncommon for the patients to exhibit no symptoms in the early stages of the disease, notably if they have type 2 diabetes. On the other hand, individuals with pronounced hyperglycemia and children that have complete insulin deficiency exhibit symptoms of weight loss, blurred vision, polyphagia, and polydipsia. Diabetes that is not adequately controlled can in some cases end up in a stupor, coma, and in extreme cases death if not it is not treated properly [18].

Left untreated diabetes can harm the kidneys, eyes, nerves, as well as the cardiovascular system of those affected. Adult people that have diabetes are two or even three times as likely to have a heart attack or a stroke. There are three types of diabetes: type 1, results from and autoimmune response preventing the body from producing insulin, thus requiring daily administration. Type 2 diabetes is the most prevalent type accounting for nearly 95% of the diagnosed cases. It results from reduced cellular sensitivity to the hormone. Gestational diabetes is the third type of diabetes that develops in pregnant women. It tends to self-resolve after childbirth. However, it may make the mother more susceptible to type 2 diabetes later in life [30].

Artificial intelligence (AI) is a science that utilizes computers in order to mimic human behavior, by teaching them to make decisions, learn from them, and judge which action is best to take. In order to mimic human intellectual activities, AI uses knowledge as an object, interprets and studies its expression methods, and uses these techniques in order to gather more knowledge. AI is a collection of various sciences and disciplines such as computer science, biology, philosophy, logic, and psychology among others [33]. It has accomplished much in the fields of robotics [27], speech recognition [20], and image processing [17]. AI and, especially, machine learning (ML) had a rapid development in the field of data analysis, and in general when it comes to computing that can allow our applications to behave intelligently. Being

one of if not the most popular newest technology of the fourth industrial revolution ML can give systems the ability to constantly learn and enhance without the need for specific programming. ML models are often used for classification with great success. ML classification can be regarded as a learning method that is supervised; it also tackles predictive modeling problems, where we have a class label that is predicted for the example that was given. On a mathematical level, function (f) is mapped from input (X) giving (Y) output that represents targets, categories, or labels. The class prediction can be exacted on structured as well as unstructured data. An example of using ML classification is detecting whether an email is considered spam or not [25].

One of the biggest challenges in ML is tuning the model to a specific problem. More often than not ML will have the need for hyperparameter tuning. Hyperparameters are what determine the efficiency that the selected model training process will have, as well as the quality that results from said training. ML algorithms can be considered black boxes when it comes to hyperparameter tuning. Hyperparameters can be viewed as external controls which affect the way the model operates and are under the full control of the user. It is challenging to determine the optimal settings empirically, but previous experience with the specific model and data used can be beneficial. Usually, hyperparameter tuning is done automatically, as the selection of optimal values can be tedious and slow, costing excessive resources [19].

The hyperparameters of XGBoost, a tree-based ensemble ML model, have been selected and optimized by the proposed approach in order to better classify diabetes. The motivation for this research is twofold. Firstly, planet optimization algorithm (POA) is a new approach that is not yet fully examined on practically NP-heavy problems [24]. Secondly, as the XGBoost has archived admirable results applied to similar complex problems, it is a promising candidate for further improving results when addressing this specific task. However, XGboost has to be adapted for every individual problem, and there is always room for improvement.

The main contributions of this work may be outlined as the following:

- A proposition for an innovative application of the POA to the optimization of XGboost hyperparameters.
- Demonstrating the superior performance of the described application in comparison to contemporary algorithms through a comparative analysis.

The rest of this work is arranged according to the following: Sect. 2 puts forth a literature review of preceding works, as well as an in-depth view of XGBoost. Section 3 covers the POA in detail. The experimental procedure and attained results are covered in Sect. 4. Finally, the work is concluded in Sect. 5 followed by future works in the field.

2 Background and Related Works

The term swarm intelligence is used to describe both natural and artificial collective attitudes of decentralized and self-governing systems. They are usually composed

of a collective of simple individuals collaborating and interacting with their habitat. This group of algorithms was inspired by nature, notably biological systems. The individual agents are following basic rules, and even though there is no universal control system that dictates in what way those individual agents should operate, there are local, and to some extent, random interactions among said agents that lead to evolution of behaviors on a global scale that agents at an individual level are unaware of. There are numerous examples of swarm intelligence in nature including bird flocking, bacterial growth, animal herding, fish schooling, ant colonies, and bee hives. Inquiry into swarm intelligence began at the end of the 1980s. Aside from its application in solving optimization problems, it can also be applied to communications, dynamic control, tracking of moving objects, library materials acquisition, planning and developing of heating systems, prediction, and medical dataset classification. Swarm intelligence can be used efficiently in a many contemporary fields, including engineering [2, 3] social sciences [7], health care [6], security [38], finance [8], and various other industries [34], MRI classification tuning [9], estimation of COVID-19 infections [35, 37], artificial neural network tuning and hyperparameters' optimization [5], cloud applications and task scheduling issues [4, 10], wireless sensor networks [36], and so on.

Nowadays, the field of medicine and science, in general, is becoming more and more digital. Being able to analyze the vast amounts of data provided by medical research is key to offering better treatment to patients. When it comes to diabetes, swarm intelligence has found its use in classification.

Al-Tashi et al. presented a hybrid version of the dynamic ant colony algorithm, consisting of three levels of correcting, including wavelets transform, alongside single variable decomposition by incorporating a support vector machine. This allows for optimal features to be selected and finds the minimal subdivision of features in order to determine a suitable diagnosis, while maintaining best possible accuracy and sensitivity. UCI repository diabetes datasets were chosen for the experiment. Decision tree and Naive Bayes achieved an accuracy of 79.5652%, deep learning, and extreme learning machine achieved an accuracy of 82.29%, CART, AdaBoost, Logiboost, and grading learning algorithms achieved an accuracy of 78.64%, 77.86%, 77.47%, 66.40% [1].

Li et al. have analyzed the data of patients diagnosed with diabetes in Urumqi, Xinjiang region of China utilizing an assortment of data mining techniques like an integrated learning model, decision tree, and support vector machine. The collected data were initially examined by using SMOTE algorithm which tends to be one of the better algorithms when it comes to feature selection coupled with feature selection with an non-equivalent method that determines features including glucose level, age, BMI. Chosen features are then refined by a data mining classifier that can recognize if features are normal or abnormal. This SMOTE-based recognition system has a ROC value of 0.9817 and an accuracy of 94.65% [21].

Joshi et al. propose a recognition approach that is focused on a backpropagation neural network. This method collects data from patients with diabetes and processes it, extracting features from the information collected. There are 8 features used as input for the initial layer, and the computed result is then transmitted to a hidden

layer that is comprised of 10 concealed neurons. The analysis of features in the hidden layer is effective, which yields great results when it comes to the classification process. Ultimately, the system is implemented using MATLAB tool, and it achieved a classification accuracy of 81% [15].

2.1 The XGBoost Algorithm

The XGBoost algorithm makes use of an additive training approach, so as to optimize an objective evaluation function. Accordingly, each subsequent step of the optimization is reliant on the results of the previous. The t-th objective function for the XGBoost model is shown in Eq. (1)

$$F_o{}^i = \sum_{k=1}^{n} l\left(y_k, \hat{y}_k^{i-1} + f_i\left(x_k\right)\right) + R(f_i) + C,\tag{1}$$

in which loss term is denoted as l for the t-th iteration, the constant term is shown as C, and R determines the regularization parameter of the model. R can be computed according to:

$$R(f_i) = \gamma T_i + \frac{\lambda}{2}\sum_{j=1}^{T} w_j^2\tag{2}$$

Generally, assigning larger values for parameters γ and λ results in simpler tree structure. The values od g and h are derivatives of the model and can be calculated according to the following equations:

$$g_j = \partial_{\hat{y}_k^{i-1}} l\left(y_j, \hat{y}_k^{i-1}\right)\tag{3}$$

$$h_j = \partial_{\hat{y}_k^{i-1}}^2 l\left(y_j, \hat{y}_k^{i-1}\right)\tag{4}$$

The solution can be obtained from the next formulas:

$$w_j^* = -\frac{\sum g_t}{\sum h_t + \lambda}\tag{5}$$

$$F_o{}^* = -\frac{1}{2}\sum_{j=1}^{T} \frac{\left(\sum g\right)^2}{\sum h + \lambda} + \gamma T,\tag{6}$$

in which $F_o{}^*$ stands for the loss function score and w_j^* represents solution weights.

3 The Planet Optimization Algorithm (POA)

The original POA is inspired by universal laws governing the motion of objects affected by gravity. On a fundamental level, this algorithm simulates a planetary system obeying Newton's gravitational laws [24]. The fundamental equation for this algorithm is shown in Eq. (7)

$$|\overrightarrow{F}| = G \times \frac{m_1 \times m_2}{R^2} \tag{7}$$

with $\overrightarrow{F}$ being the gravitational force between planets at R distance, G represents the gravitational constant, m_1 and m_2 represents the mass of the planets.

While Eq. (7) models the gravitational pull between planets, the force equation gives less efficient results. To adjust for this, the planetary optimization algorithm makes use of moment(M) as a search parameter during the optimization process as shown in Eq. (8).

$$|\overrightarrow{M}| = |\overrightarrow{F}| \times R \tag{8}$$

The POA makes use of a simulation of the universe, as a boundless space, inhabited by various astrophysical bodies. To aid visualization, the solar system will be used as an example.

The example system is comprised of the Sun, the Earth, and Earth's Moon, with the Sun exerting a gravitational pull on the Earth keeping it in a stable orbit. Likewise, the Earth exerts its own pull on the Moon, keeping it in orbit, despite the Sun's mass being 330,000 times that of the Earth. With this in mind, it can be deduced that the two primary factors that influence orbits are mass and distance. The algorithm for simulating these principles can therefore be formulated as in the following:

- The Sun represents the optimal solution. Accordingly, within a given search space, it will pose the higher mass and exert the greatest gravitational moment on objects around it.
- Other objects in the system experience a gravitation moment between each other. In practice, despite the Sun possessing the greatest mass in the system, the effect on distant objects is negligible. Additionally, this mechanism aids in avoiding getting stuck in local optima.

During the i-th repetition, the planet assigned the highest mass represents the Sun. The planets closest to it will move toward it, due to the influence of the gravitational moment (M_p^t) between the Sun other planetary bodies. However, if the largest planet in the t-th repetition does not represent the best solution and should all the objects move toward it, the algorithm would get stuck in sub-optimal conditions. A smaller planet at a potential location further away is far less affected by the lower gravitational momentum (M_b^t) due to the distance. The second solution is, therefore, free to explore for a better location in upcoming iterations.

The basis of the algorithms is centered around the stated two principles. The current largest object does not need to necessarily be the true optima in a certain search space. Furthermore, the location of this optima does not need to be known exactly. In practice, the current best-known solution would possess a higher mass and therefore act as the Sun.

The algorithm is implemented according to the following.

3.1 Stage 1: Optimal Start

In theory, the outcomes of a good algorithm that provide an optimal solution should not be affected by initial positioning. However, in practice, the opposite is true for many stochastic algorithms. Should a promising region of the search space be located in a remote minor area, the initial locations of agents play an important role. If the initial population starts without agents initialized within the area, the probability of locating true optima in later iterations greatly reduces.

Nevertheless, when initial solutions exist around the global optima, the convergence probability toward a true optimum is highly likely. Accordingly, an efficient initialization should make use of the critical sampling method. However, this requires that the algorithm has awareness of the specific problem, and that is not easy to achieve with most algorithms.

Likewise, selecting the optimal solution from the initial population to act as the Sun is crucial. This decision defines convergence rates, together with the algorithm's future accuracy.

With this in mind, the initial step for the algorithm is to find a sufficient solution so as to maximize the accuracy and rate of convergence in the first repetition.

3.2 Stage 2: M Factor

With the momentum factor defined according to Eq. (9)

$$M = |\overrightarrow{F}|R_{ij} = G\frac{m_i m_j}{R_{ij}^2} \times R_{ij} \qquad (9)$$

accordingly, the following parameters may be defined. The mass of the planets according to Eq. (10)

$$m_i, m_j = \frac{1}{a^{\text{obj}_{i,j}/\alpha}} \qquad (10)$$

in which the constant value of a equals 2, likewise $a = |\max(\text{obj}) - \text{obj}_{\text{sun}}|$. By doing so, should the objective function value for a given planet be lower its mass will be large. Objective function values $\text{obj}_{i,j}$, $\max(\text{obj})$, obj_{sum} represent the values of i-th and j-th planet, being the least optimal solution and Sun respectively.

Celestial body distances may be determined as Cartesian distance as shown in Eq. (11)

$$R_{ij} = ||X_i^t - X_j^t|| = \sqrt{\sum_{k=1}^{\text{Dim}} (x_i^t + x^t + j)^t} \tag{11}$$

where Dim represents the number of dimensions.

Finally, G defines a parameter equal to the unity of the algorithm.

3.3 Stage 3: Global Search

Using the principles defined above, an equation for simulating global search may be defined according to Eq. (12)

$$\overrightarrow{X_i^{t+1}} = \overrightarrow{X_i^t} + b \times \beta \times r_1 \times (\overrightarrow{X_{\text{Sum}}^t} - \overrightarrow{X_i^t}) \tag{12}$$

On the left side of the equation $\overrightarrow{X_i^{t+1}}$ denotes the location for a given celestial body in the $t + 1$ repetition. On the right equations side $\overrightarrow{X_i^t}$ denotes the current position of a planet, $\beta = M_i^t / M_{\text{Max}}^t$, $r1 = \text{rand}(0, 1)$, b representing a constant. Additionally, $\overrightarrow{X_{\text{Sum}}^t}$ describes the current position of the optimal solution.

3.4 Stage 4: Local Search

Ascertaining an optimal solution depends on the difficulty of a problem being addressed. In many instances, only, approximate location of true optima can be determined. In terms of the POA, this means that the true location of the Sun in search space is yet to be located.

In cases where the span between the Sun and other celestial bodies is short, a local search will be performed. The planet that currently possesses the highest mass will act as the Sun, and the planets nearest to it will move toward it. The main goal for the specific approach is improving accuracy in smaller search spaces. The local search process can be formulated as shown in Eq. (13)

$$\overrightarrow{X_i^{t+1}} = \overrightarrow{X_i^t} + c \times r_1 \times (r_2 \times \overrightarrow{X_{\text{Sum}}^t} - \overrightarrow{X_i^t}) \tag{13}$$

in which $= c_0 - t/T$, t for the t-th repetition, with T being the maximum allowed amount of repetitions and $c_0 = 2$. Finally, r_2 is the Gaussian distribution function given in Eq. (14)

$$f(x, \mu, \sigma) = \frac{1}{\sigma\sqrt{2\pi}} exp(-\frac{(x-\sigma)^2}{2\sigma^2}) \tag{14}$$

The Gaussian distribution is a popular option for stochastic algorithms that model physical processes. For parameter r_2, the distribution mean is given as $\mu = 0.5$; finally, the standard divination is $\sigma = 0.2$. This effectively results in the movement around the Sun not ignoring potential solutions during a local search.

Exploitation focuses on obtaining new solutions better than existing ones. Having a mechanism focus excessively on local solutions leads to a strong convergence rate, and algorithms often get stuck in local mode.

As opposed to exploitation, the task of exploration is to locate new potential solutions from the global search space. This mechanism helps prevent the algorithm from getting stuck around sub-optimal local solutions. However, one notable disadvantage of exploration is its slow convergence.

With all this in mind, the pseudo-code for the PSO algorithm is given in Fig. 3.4. The parameter R_{min} governs exploration and exploitation. The algorithm performs both local and global searches concurrently, increasing accuracy.

The R_{min} variable needs to satisfy the following:

- When R_{min} is large, the focus is shifted on exploitation
- When R_{min} is small, the focus is on exploration

$$R_{min} = \left(\sum_{1}^{Dim} (up_i - low_i)^2 \right) / R_0 \tag{15}$$

The implementation used in this research selects R_{min} based on Eq. (15) by diving the search with $R_0 = 1000$ in to 1000 sub-areas. Additionally, low and high represent
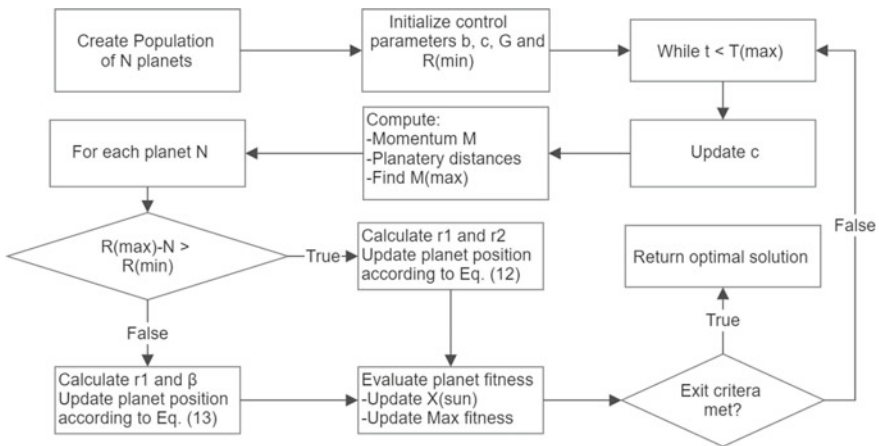
Fig. 1 POA block diagram

the lower and higher thresholds for a specific problem. A block diagram for the POA is given in Fig. 1.

Algorithm 1 PSO Algorithm

Generate starting population of N planets
Initialize parameters b, c, G, R_{min}
Assess fitness of planets in population
Set best planet as X_{Sun}
Determine $max(fintess)$
while $t < Maxiterations$ **do**
  Refresh value of c parameter
  Determine moment force (M) for all planets
  Determine Cartesian distance between planets and Sun
  Determine planet masses
  Locate M_{max}
  for $i = 0; i < N ; N$ **do**
    if $R_{Sun-planet(i)} > R_{min}$ **then**
      Compute $r_1; \beta$
      Compute $\overrightarrow{X_i^{t+1}} = \overrightarrow{X_i^t} + b \times \beta \times r_1 \times (\overrightarrow{X_{Sun}^t} - \overrightarrow{X_i^t})$
    else
      Compute $r_1; r_2$
      Compute $\overrightarrow{X_i^{t+1}} = \overrightarrow{X_i^t} + c \times r_1 \times (r_2 \times \overrightarrow{X_{Sun}^t} - \overrightarrow{X_i^t})$
    end if
    Refresh value of X_{Sum}
    Compute planet fitness
    Update $max(fitness)$
  end for
end while
return Optimal Solution

---

4 Experiments and Discussion

The experimental setup used for the conducted research has been inspired by the work presented in [11]. This section first briefly describes the utilized dataset, followed by providing the experimental setup and the metrics which were used. Finally, a comparative analysis of obtained performance outcomes of the proposed algorithm along with other cutting-edge methods is provided.

4.1 Dataset Description

This research makes use of the PIMA Indian diabetes (PID) dataset, originally acquired from the National Institute of Diabetes and Digestive and Kidney Diseases. The main purpose behind this dataset is the construction of an intelligent model that

Table 1 Diabetes dataset details

Attributes	Description	Mean	Std. deviation	Range
Pregnancies	No. of pregnancies	3.85	3.37	0–17
Glucose	2 h of oral glucose tolerance plasma glucose concentration test	121	32	0–199
Blood pressure	Systolic pressure in mm Hg	69.1	19.3	0–122
Skin thickness	Triceps skin-fold thickness (mm)	20.5	15.9	0–99
Insulin	Two hours of serum insulin (mu U/ml)	79.8	115	0–846
BMI	Body mass index (weight in kg/(height in m)^2)	32	7.88	0–67
Diabetes pedigree function	Hereditary factors used in diabetes prediction	0.47	0.33	0.078–2.4
Age	Age (years)	33.2	11.8	21–81
Outcome	Class variable (0 or 1)	0.35	0.48	Y/N

is capable of leveraging available data in order to determine if a person is healthy of affected by diabetes.

The dataset provides eight medical predictor variables along with one target variable. Diabetes classification can be considered a problem of binary classification. Parameter details are available in Table 1.

The dataset is comprised of a total of 768 records of both healthy and individuals affected by diabetes. All of which are females older than twenty-one. The dataset consists of 268 individuals affected with diabetes and 500 healthy individuals.

4.2 Experimental Setup and Metrics

During experimentation, the optimization algorithm has been used on the following XGBoost hyperparameters (Table 2).

The remaining XGBoost parameters remain default with a fixed value.

To ensure a fair comparison, due to the randomness inherent in stochastic algorithms, all approaches are executed in multiple independent runs, with the worst, mean average, median accuracy being recorded as well as standard deviation. The formula for accuracy is shown in Eq. (16)

$$\text{Accuracy} = \frac{\text{TN} + \text{TP}}{\text{FP} + \text{FN} + \text{TP} + \text{TN}} \tag{16}$$

in which TN and TP represent true negative and positive, while FN and FP represent false negatives and false positives.

Table 2 The XGBoost hyper-parameters that were optimized

Paramater name	Boundaries	Paramater type	Details
Learning rate (η)	[0.1, 0.9]	Continuous	Reduces weight each step
Min_child_weight	[0, 10]	Continuous	Larger value help prevent local optimization
Subsample	[0.01, 1]	Continuous	Governs random sampling to prevent overfitting
Collsample_bytree	[0.01, 1]	Continuous	Controls feature sampling proportion
Max_depth	[3, 10]	Integer	Larger values give more specific and local samples
Gamma	[0, 0.5]	Continuous	Dictates loss function

4.3 Comparative Analysis

In the performed simulations, the results of the XGBoost tuned by the POA meta-heuristics were evaluated against the results achieved by other cutting-edge swarm intelligence methods applied to the XGBoost model withing the exact same context.

The metaheuristics used for the comparative analysis were firefly algorithm (FA) [31], bat algorithm (BA) [32], artificial bee colony (ABC) [16], sine cosine algorithm (SCA) [22], monarch butterfly optimizer (MBO) [29], Harris hawks optimizer (HHO) [14], elephant herding algorithm (EHO) [28], whale optimization algorithm (WOA) [23], and social network search (SNS) [26]. Every competitor metaheuristic method was implemented independently by the authors for the purpose of this research, by utilizing the recommended control parameters' values suggested by the original publications.

All metaheuristics methods and the XGBoost tuning framework were developed from the scratch in Python by using standard and ML libraries: numpy, scipy, pandas, matplotlib, seaborn, and scikitlearn.

The experiments were conducted with 16 solutions per population ($N = 16$) and 10 iterations for every algorithms' run ($T = 10$). Since the utilized dataset is slightly imbalanced, to tackle the class imbalance additional steps need to be taken. While other methods for addressing dataset imbalance exist [12], the utilization of the synthetic minority over-sampling technique (SMOTE) [13] is suggested. In the first set of experiments, SMOTE technique was not applied, while the second set of experiments utilizes SMOTE to generate novel entries of the observed minority class by data point connection with K-nearest neighbors. This allows adding synthetic generated entries without the need for direct replication from the minority classes, effectively allowing avoidance of the overfitting problem during training. The simulation framework was developed in Python, and the experiments were executed on the Intel® Core™ i9-11900 K Processor with 64 GB of RAM, and Windows 11 O.S.

Table 3 XGBoost diabetes diagnostics NO SMOTE—general metrics

Metrics	XGBoost-POA	XGBoost-FA	XGBoost-BA	XGBoost-ABC	XGBoost-SCA	XGBoost-MBO	XGBoost-HHO	XGBoost-EHO	XGBoost-WOA	XGBoost-SNS
Best (%)	**93.5603**	92.7652	92.9855	93.2147	93.3778	92.6415	92.9796	93.0543	92.9804	93.0241
Worst (%)	**93.5568**	92.7613	92.9801	93.2096	93.3717	92.6372	92.9734	93.0505	92.9729	93.0178
Mean (%)	**93.5584**	92.7631	92.9828	93.2123	93.3744	92.6436	92.9769	93.0523	92.9764	93.0192
Median (%)	**93.5586**	92.7633	92.9831	93.2124	93.3746	92.6437	92.9771	93.0523	92.9765	93.0194
Std	0.000009	0.000022	0.000025	0.000018	0.000009	0.000019	0.000009	0.000025	0.000023	0.000011

Table 4 XGBoost diabetes diagnostics with SMOTE—general metrics

Metrics	XGBoost-POA	XGBoost-FA	XGBoost-BA	XGBoost-ABC	XGBoost-SCA	XGBoost-MBO	XGBoost-HHO	XGBoost-EHO	XGBoost-WOA	XGBoost-SNS
Best (%)	**93.8852**	92.7964	93.0142	93.4259	93.5276	92.8389	93.1173	93.2035	93.0094	93.2762
Worst (%)	**93.8849**	92.7925	93.0097	93.4218	93.5242	92.8352	93.1148	93.1983	93.0056	93.2731
Mean (%)	**93.8851**	92.7946	93.0124	93.4238	93.5253	92.8367	93.1161	93.2014	93.0073	93.2749
Median (%)	**93.8851**	92.7947	93.0124	93.4239	93.5264	92.8367	93.1162	93.2015	93.0074	93.2750
Std	**0.000001**	0.000016	0.000045	0.000025	0.000037	0.000065	0.000044	0.000045	0.000052	0.000102

Additionally, as all observed methods are stochastic by nature, they were executed in 30 independent runs, while the best, worst, mean, and median accuracy were noted, as well as the standard deviation. A comparative analysis is presented between the proposed approach and other popular contemporary approaches applied to the same task. The results without SMOTE are shown in Tables 3 and 4 show results with SMOTE, where the best obtained results are given in bold text. The outcomes of both experiments indicate that the proposed XGBoost-POA method established firm first place for all observed metrics, achieving the average accuracy of around 93.56% without SMOTE employed, outperforming the XGBoost-SCA on the second place by around 0.2% on average. The average accuracy of XGBoost-POA is leveraged to approximately 93.88% when SMOTE method is applied, while the second best approach is again XGBoost-SCA, trailing by around 0.3% in this case.

5 Conclusion

This research proposed recent POA algorithm as the optimizer used to tune the XGBoost hyperparameters' values. This particular task is very important in the machine learning area, as each model needs to be optimized for a particular dataset.

This hybrid model was evaluated on a diabetes dataset that is a slightly disproportional dataset, containing minority classes that could pose a challenge to be correctly classified. The results were compared to the performances of other implemented cutting-edge metaheuristics approaches that included FA, BA, ABC, SCA, MBO, HHO, EHO, WOA, and SNS algorithms used in the same experimental setup. The simulations were separated into two parts. First part utilized the original imbalanced dataset, while the second part of experiments utilized synthetic dataset that was generated with the help of SMOTE method. SMOTE is used for generating additional minority class entries to address the disparity between the classes of the dataset. The final experimental conclusions suggest superior accuracy achieved by the proposed XGBoost-POA model for this particular dataset. This research also shown that the XGBoost model may be additionally optimized through the use of swarm intelligence algorithms to achieve very promising level of performance for a hard and important task of diabetes classification.

References

1. Al-Tashi Q, Rais H, Abdulkadir SJ (2018) Hybrid swarm intelligence algorithms with ensemble machine learning for medical diagnosis. In: 2018 4th international conference on computer and information sciences (ICCOINS), pp 1–6. https://doi.org/10.1109/ICCOINS.2018.8510615
2. Bacanin N, Antonijevic M, Bezdan T, Zivkovic M, Rashid TA (2022) Wireless sensor networks localization by improved whale optimization algorithm. In: Mathur G, Bundele M, Lalwani M, Paprzycki M (eds) Proceedings of 2nd international conference on artificial intelligence: advances and applications. Springer Nature Singapore, Singapore, pp 769–783

3. Bacanin N, Antonijevic M, Bezdan T, Zivkovic M, Venkatachalam K, Malebary S (2022) Energy efficient offloading mechanism using particle swarm optimization in 5g enabled edge nodes. Cluster Comput. https://doi.org/10.1007/s10586-022-03609-z

4. Bacanin N, Bezdan T, Tuba E, Strumberger I, Tuba M, Zivkovic M (2019) Task scheduling in cloud computing environment by grey wolf optimizer. In: 2019 27th telecommunications forum (TELFOR). IEEE, pp 1–4

5. Bacanin N, Bezdan T, Venkatachalam K, Zivkovic M, Strumberger I, Abouhawwash M, Ahmed A (2021) Artificial neural networks hidden unit and weight connection optimization by quasi-refection-based learning artificial bee colony algorithm. IEEE Access

6. Bacanin N, Sarac M, Budimirovic N, Zivkovic M, AlZubi AA, Bashir AK (2022) Smart wireless health care system using graph LSTM pollution prediction and dragonfly node localization. Sustain Comput Inform Syst 35:100711

7. Bacanin N, Zivkovic M, Bezdan T, Venkatachalam K, Abouhawwash M (2022) Modified firefly algorithm for workflow scheduling in cloud-edge environment. Neural Comput Appl 34(11):9043–9068. https://doi.org/10.1007/s00521-022-06925-y

8. Bacanin N, Zivkovic M, Jovanovic L, Ivanovic M, Rashid TA (2022) Training a multilayer perception for modeling stock price index predictions using modified whale optimization algorithm. In: Smys S, Tavares JMRS, Balas VE (eds) Computational vision and bio-inspired computing. Springer Singapore, Singapore, pp 415–430

9. Bezdan T, Zivkovic M, Tuba E, Strumberger I, Bacanin N, Tuba M (2020) Glioma brain tumor grade classification from MRI using convolutional neural networks designed by modified FA. In: International conference on intelligent and fuzzy systems. Springer, pp 955–963

10. Bezdan T, Zivkovic M, Tuba E, Strumberger I, Bacanin N, Tuba M (2020) Multi-objective task scheduling in cloud computing environment by hybridized bat algorithm. In: International conference on intelligent and fuzzy systems. Springer, pp 718–725

11. Butt UM, Letchmunan S, Ali M, Hassan FH, Baqir A, Sherazi HHR (2021) Machine learning based diabetes classification and prediction for healthcare applications. J Healthc Eng

12. Chakrabarty N, Biswas S (2020) Navo minority over-sampling technique (NMOTE): a consistent performance booster on imbalanced datasets. J Electron 2(02):96–136

13. Elreedy D, Atiya AF (2019) A comprehensive analysis of synthetic minority oversampling technique (smote) for handling class imbalance. Inform Sci 505:32–64

14. Heidari AA, Mirjalili S, Faris H, Aljarah I, Mafarja M, Chen H (2019) Harris hawks optimization: algorithm and applications. Future Gen Comput Syst 97:849–872

15. Joshi S, Borse M (2016) Detection and prediction of diabetes mellitus using back-propagation neural network, pp 110–113. https://doi.org/10.1109/ICMETE.2016.11

16. Karaboga D, Basturk B (2008) On the performance of artificial bee colony (ABC) algorithm. Appl Soft Comput 8(1):687–697

17. Kaur C, Garg U (2021) Artificial intelligence techniques for cancer detection in medical image processing: a review. Mater Today Proc

18. Kharroubi AT, Darwish HM (2015) Diabetes mellitus: the epidemic of the century. World J Diabetes 6(6):850–867

19. Koch P, Golovidov O, Gardner S, Wujek B, Griffin J, Xu Y (2018) Autotune: a derivative-free optimization framework for hyperparameter tuning

20. Lee W, Seong JJ, Ozlu B, Shim BS, Marakhimov A, Lee S (2021) Biosignal sensors and deep learning-based speech recognition: a review. Sensors 21(4). https://doi.org/10.3390/s21041399, https://www.mdpi.com/1424-8220/21/4/1399

21. Li Y, Li H, Yao H (2018) Analysis and study of diabetes follow-up data using a data-mining-based approach in new urban area of Urumqi, Xinjiang, China, 2016–2017. Comput Math Methods Med 2018:7207151. https://doi.org/10.1155/2018/7207151

22. Mirjalili S (2016) SCA: a sine cosine algorithm for solving optimization problems. Knowl Based Syst 96:120–133

23. Mirjalili S, Lewis A (2016) The whale optimization algorithm. Adv Eng Softw 95:51–67

24. Sang-To T, Hoang-Le M, Wahab MA, Cuong-Le T (2022) An efficient planet optimization algorithm for solving engineering problems. Sci Rep 12(1):1–18

25. Sarker IH (2021) Machine learning: algorithms, real-world applications and research directions. SN Comput Sci 2(3):160. https://doi.org/10.1007/s42979-021-00592-x
26. Talatahari S, Bayzidi H, Saraee M (2021) Social network search for global optimization. IEEE Access 9:92815–92863. https://doi.org/10.1109/ACCESS.2021.3091495
27. Vrontis D, Christofi M, Pereira V, Tarba S, Makrides A, Trichina E (2022) Artificial intelligence, robotics, advanced technologies and human resource management: a systematic review. Int J Human Resour Manage 33(6):1237–1266. https://doi.org/10.1080/09585192.2020.1871398
28. Wang GG, Deb S, Coelho LDS (2015) Elephant herding optimization. In: 2015 3rd international symposium on computational and business intelligence (ISCBI), pp 1–5. https://doi.org/10.1109/ISCBI.2015.8
29. Wang GG, Deb S, Cui Z (2019) Monarch butterfly optimization. Neural Comput Appl 31(7):1995–2014
30. World Health Organization AL (2021) Diabetes. https://www.who.int/news-room/fact-sheets/detail/diabetes
31. Yang XS (2009) Firefly algorithms for multimodal optimization. In: Watanabe O, Zeugmann T (eds) Stochastic algorithms: foundations and applications. Springer, Berlin, pp 169–178
32. Yang XS (2011) Bat algorithm for multi-objective optimisation. Int J Bio-Inspired Comput 3(5):267–274
33. Zhang C, Lu Y (2021) Study on artificial intelligence: the state of the art and future prospects. J Ind Inf Integr 23:100224
34. Zhang Y, Agarwal P, Bhatnagar V, Balochian S, Yan J (2013) Swarm intelligence and its applications. Sci World J 2013:528069. https://doi.org/10.1155/2013/528069
35. Zivkovic M, Bacanin N, Djordjevic A, Antonijevic M, Strumberger I, Rashid TA, et al (2021) Hybrid genetic algorithm and machine learning method for covid-19 cases prediction. In: Proceedings of international conference on sustainable expert systems. Springer, pp 169–184
36. Zivkovic M, Bacanin N, Tuba E, Strumberger I, Bezdan T, Tuba M (2020) Wireless sensor networks life time optimization based on the improved firefly algorithm. In: 2020 international wireless communications and mobile computing (IWCMC). IEEE, pp 1176–1181
37. Zivkovic M, Bacanin N, Venkatachalam K, Nayyar A, Djordjevic A, Strumberger I, Al-Turjman F (2021) COVID-19 cases prediction by using hybrid machine learning and beetle antennae search approach. Sustain Cities Soc 66:102669
38. Zivkovic M, Tair MKV, Bacanin N, Hubálovský Š, Trojovský P (2022) Novel hybrid firefly algorithm: an application to enhance XGBoost tuning for intrusion detection classification. PeerJ Comput Sci 8:e956

A Survey on Image Processing Techniques for Detection of Cavities in Dental X-ray Images

V. Geethasree, Ch. Sai Swapna Sri, V. Sravani, K. Bhaskari, and Praveena Manne

Abstract A dental X-ray vividly exposes all of the features of the mouth that cannot be seen physically, such as hidden dental structures and bone loss. Cavities in teeth may be detected individually from X-ray pictures because a change in brightness correlates to a change in depth, surface orientation, material quality, and difference in scene illumination. The quality of a cavity differs from those of a healthy tooth. The X-rays must be processed using the appropriate image processing techniques. Most X-ray scans include noise initially, which degrades image quality. As a result, several image processing techniques are employed in the detection of dental cavities utilizing dental X-ray images. A literature review was undertaken on image enhancement, image segmentation, and feature extraction techniques for automating the procedure of dental cavity detection.

Keywords Image enhancement · Image segmentation · Feature extraction · Dental X-ray

1 Introduction

Dentin, pulp, and enamel make up the structure of a human tooth. Various kinds of bacteria often found in the mouth cause infection in human teeth. Dental caries is the common name for these illnesses. Caries cause lasting damage to the teeth, resulting in a cavity. It is a fairly prevalent condition across the world, with dental cavities affecting 60–90% of schoolchildren and practically all adults. The dental cavity impacts teeth's daily tasks by reducing biting capacity, increasing sensitivity, causing pain, and so on.

Dentists frequently treat caries patients by obtaining radiographs (X-rays) of their teeth and examining the X-ray with their naked eyes to detect cavities. This might result in a few cavities being missed at an early stage or not being detected adequately.

V. Geethasree · Ch. Sai Swapna Sri · V. Sravani · K. Bhaskari · P. Manne (✉)
ECE Department, BVRIT Hyderabad College of Engineering for Women, Hyderabad, Telangana, India
e-mail: atluri.praveena@gmail.com

As a result, automation is required for a variety of reasons, including a dearth of dental professionals, varying degrees of experience among dentists, and the fact that a second view is always beneficial in verifying decisions. The procedure for dental cavity detection includes the steps shown in Fig. 1.

2 Literature Survey

2.1 Image Enhancement

Image enhancement is a technique for increasing visualization and information understanding.

Contrast stretching increases the image intensity variation to the appropriate level and emphasizes hidden information visible in the X-ray image's black-and-white regions [1]. The pixel range between lower and higher thresholds is transmitted when this approach is applied. When a new pixel range is specified, the new lower stretch value will linearly stretch the higher number of pixels while compressing the remaining pixels [2].

Histogram equalization considers the entire image, it may increase noise [3]. To tackle this issue, adaptive histogram equalization (AHE) was developed, which emphasizes local contrast rather than total contrast. However, AHE has a washout effect [4] and causes artifacts as well as a loss of image detail [5]. CLAHE is inevitably introduced, lowering the local histogram's height. CLAHE is a preferred contrast enhancement method due to its ease of use and rapidity [6, 7]. Low contrast in medical images can be effectively increased using the CLAHE approach and gamma adjustment [8, 9]. AHE and CLAHE are paired with other algorithms to address their flaws. A MAHE is proposed, which combines AHE with a median filter to minimize noise.

Combining CLAHE and a sharpening filter, which employs a Laplacian filter, a SLAHE process is presented. When compared to AHE and MAHE, the RMSE for CLAHE and SLAHE is smaller [10]. Gamma Correction (GC) was developed, which is a nonlinear method that improves localization and features by performing direct operations on individual pixels [11, 12].

An approach for multiscale morphology was proposed in [13]. This approach improves local contrast by separating bright and dark portions from the original image.

The Laplacian filter, as demonstrated in [14, 15], improves the image's edges while eliminating the low-frequency components. The anisotropic filter is used to minimize the noise [1]. In [16], the Butterworth High Pass filter is employed to boost the image's contrast. In [17], a guided filter is introduced that conserves edges by removing artifacts. A TV-homomorphic filter was used in [18] to balance the brightness and improve the information. A homomorphic wavelet filter is used to eliminate noise

Fig. 1 Procedure for dental cavity detection
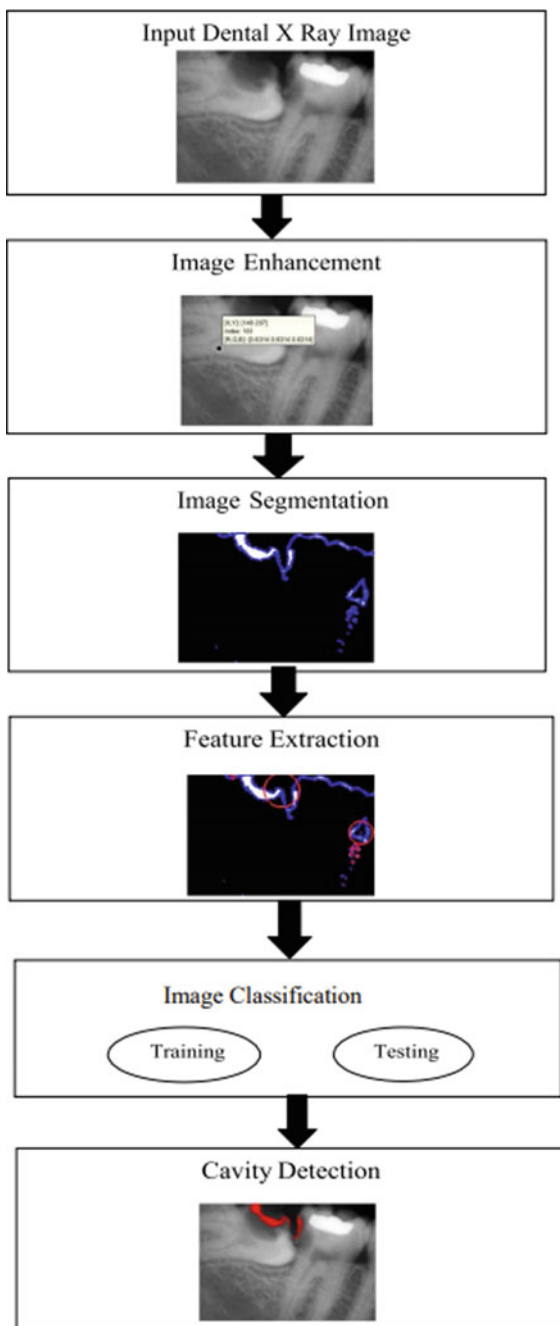
and non-uniformity in the brightness dispensation of X-ray images [19]. Using a sharpening filter improves diagnostic performance, according to [20, 21].

2.2 Image Segmentation

Image segmentation is an essential step in extracting the Region of Interest (An image's region of interest (ROI) is a segment that can be filtered or edited) from an image, which is subsequently used for additional processing such as recognition and description. An ROI can be represented as a binary mask image. In the mask image, pixels inside the ROI are marked 1, while those outside the ROI are marked 0.

An automatic morphological filtering wavelet-based technique for teeth segmentation in X-ray images was presented in [22]. Because of its multi-resolution property, wavelet-based segmentation was required to catch the tiny edges between various teeth, even with low-quality X-ray images that morphological filters couldn't discriminate.

It is difficult to separate the infected area when employing usual standard thresholding, i.e., global thresholding, and it will not help for image processing in the future. To get over these restrictions, a local gray-level distribution-based adaptive thresholding technique has been created [23]. For dental caries, adaptive thresholding provides a greater performance value [15]. Otsu's approach is a methodology for global thresholding. The image's histogram is used in the threshold search process. The image processing technique of Otsu thresholding can be utilized to enhance dental diagnosis based on X-ray reading. The test results showed that images of healthy teeth had a lower threshold value than images of uncomfortable teeth under all circumstances, regardless of whether the image had image enhancement or not [24].

The Canny edge detection technique utilizes hysteresis thresholding, which contributes to its high performance. To execute hysteresis thresholding, high and low thresholds must be generated based on the whole image data. This step increases the computing complexity of the Canny Edge Detector when compared to other edge detection techniques. The Canny method is rarely used in real-time applications since it is more difficult to implement directly and results in significant latency. One of the advantages of the Canny edge detection approach is its capacity to determine edges with a low error rate. Tania et al. [25] discusses the techniques of Canny edge detection and Sobel edge detection. According to research, the Canny edge detection method surpasses the Sobel edge detection methodology.

It is unusual to identify an edge detector that operates much faster than the Canny edge detector only if the necessary conditions are favorable. When given in a combined form, the Sobel edge detection approach can detect both horizontal and vertical edges independently, making the calculation reasonably cost-effective. In both horizontal and vertical directions, a particular gradient magnitude operation is applied. A Sobel edge detection operator is made up of two convolution kernels. With one kernel for each perpendicular orientation, these kernels are made to react

optimally to edges that run vertically and horizontally in relation to the pixel grid. In the improved image, the Sobel method achieved superior edge detection, and its thresholding (based on maximum entropy) displays a more representative portion of the image [26].

The level-set approach cannot be effectively employed in dental situations because of its high computing cost, complex parameterization, and sensitivity to the positioning of starting contours. As a consequence, even though the entity is composed of several unconnected elements, an object from an image may be recovered [27]. Cystic lesion segmentation and extraction using active contour-based segmentation is proposed in [28], to analyze cyst development behavior. For nonlinear backgrounds, low contrast, and noisy images, the segmentation approach yields positive results. This method does not work well with images with inhomogeneous intensities. The level-set technique, which combines active contour models (snake model) with geometric models, is an improvement over the snake model. The images are scaled to lessen the Level Set Active Contour method's time complexity and flaws. The larger the image, the longer it takes for the contours to extend beyond the image's limits. The temporal complexity of an image lowers as its size decreases [29].

A K-Means clustering approach was presented in [30], and it works as an unsupervised method for segmenting input images. The mean square error is reduced using a K-Means clustering approach, which results in excellent accuracy without losing execution speed [2]. Fuzzy clustering techniques, such as the K-Means algorithm, are better suited to exclusive clustering tasks. Fuzzy clustering techniques, such as FCM, on the other hand, are well suited to overlapping clustering tasks. The K-Means technique is found to require less time to compute than the FCM approach for the Iris dataset. As a consequence, [31] demonstrates that the K-Means outperforms the FCM in terms of computation time. A fuzzy clustering method's processing time increases as it combines additional fuzzy logic-based procedures. K-Means clustering is a basic and uncomplicated method. FCM, KFCM, and KFCM K-Means are used for non-mapping clustering while FCM is utilized for multiple clustering. Furthermore, KFCM solves the flaws of the FCM method. A subtractive clustering approach is presented in [2]. The subtractive clustering approach and the traditional K-Means algorithm are compared in terms of RMSE and PSNR, and the suggested method is found to perform better.

The medical images often contain unknown uncertainties and noise, FCM is commonly used in image segmentation. Utilizing conditional spatial Fuzzy C-means clustering (csFCM), [32] extracted pulp, enamel, dentin, and neighboring dental tissues. As a result, when compared to commonly utilized FCM techniques, the performance increased. This clustering technique has issues with cluster center movement and susceptibility to overlapping intensity distributions between classes. Gaussian kernel-based conditional spatial Fuzzy CMeans (GK-csFCM) were developed to address this flaw [9]. This algorithm can categorize dental components better than the csFCM and FCM approaches. GK-csFCM has high accuracy, sensitivity, and specificity percentage in quantitative analysis. The Hyperbolic Tangent Gaussian kernel fuzzy C-Means clustering Otsu (HTGkFCM-Otsu) in the proposed [17] work offers advantages over FCM in terms of processing speed and simplicity. This method

employs a Gaussian kernel and a Hyperbolic Tangent function for Euclidean distance for dental image segmentation with spatial information to give reduced noise. Thus, this approach offers more effectiveness and reliability. Similarly, HTGkFCM is a byproduct of improved results by using an FCM with a pre-defined membership matrix.

The Watershed algorithm is built on the idea of extracting specific background and foreground, followed by the use of markers to run a watershed and identify the precise limits. Regarding markers, it can be user-specified, such as manually clicking and obtaining marker coordinates, or it can be defined by utilizing established techniques such as thresholding or other morphological processes. We cannot use watershed algorithms directly because of the noise. This algorithm is a prominent segmentation algorithm that separates overlapping images and is used for region segmentation. The segmented part of interest is obtained using this approach [33]. This method has the benefit of being basic, instinctual information that can be parallelized. The method's primary problem is over-segmentation induced by the presence of many local minima. Marker-controlled watershed improvements were developed to mitigate the effects of excessive over-segmentation. The various segmentation techniques were examined, and it was discovered that marker-based segmentation is the best in most circumstances since it marks and then separates the sections. The accuracy is 89.78%, and the average execution time is 324.45 ms, according to the trials. Experimentation, on the other hand, identifies limitations in the low-resolution dental X-ray image. In this case, the introduced method failed to distinguish the correct dental region from the uneven background. To address this issue, the combination of the marker-based watershed segmentation method with a hybrid median filter increases the performance of the proposed approach [34].

2.3 Feature Extraction

Feature extraction aids in the reduction of redundant data in data collection. Principal Component Analysis (PCA) and Kernel Principal Component Analysis (kPCA) are used to analyze the collected features, and the modified feature space is then submitted to a linear regression model for diagnosing the TB illness. When the accuracy of PCA using the wrapper technique (96.07%) was compared to the accuracy of kPCA (62.50%), it was discovered that PCA using the wrapper approach performed better. The accuracy rating improves after the Principal Component Analysis (PCA) for a 99% variance coverage, indicating the relevance of the PCA's attribute selection [35]. Modified Principal Component Analysis (MPCA) is used to extract features from processed images [36, 37].

Gabor filters have high frequency and spatial localization, making them ideal for texture/surface mapping applications. These are the kinds of bandpass filters that accept frequencies within a given range while rejecting frequencies outside of that range. The Gabor filter offers the advantages of high extraction, precision, and a complete and exact border. For the extraction of information from residential

structures, the Gabor filter approach produces a quick and accurate output. The Gabor filter takes the least amount of time to compute. The Gabor filter is time-efficient [38]. Gabor filtering may be used to create stable low-level features, allowing for the development of robust applications based on Gabor features [39].

To smooth out the fine features and match templates, Fourier descriptors are employed. To characterize the texture of the removed tooth, the suggested technique for numerous features employs Fourier descriptors for shape analysis and Gray Level Co-occurrence Matrix (GLCM) for attributes such as energy, contrast, correlation, and homogeneity. As a result, both form and texture analysis of the removed tooth are studied as features in this method [14, 27, 30, 40–42]. The mean square error is compared for all the techniques. Among the other approaches, the suggested algorithm yields the lowest mean square value [43].

Local Binary Pattern (LBP) as a feature extraction descriptor has the advantage of being simple, impervious to grayscale fluctuations, and effectual in illumination [44].

Blob detection on dental radiographs has obtained superior accuracy and provides a more robust and automated means to identify caries on dental radiographs [45].

3   Conclusion

This work has conducted a detailed study of several methodologies proposed by various researchers over the previous years. This research looked at a variety of image enhancement, image segmentation, and feature extraction approaches used in dental X-ray imaging. Because of its simplicity and speed, CLAHE is commonly used for image enhancement. Furthermore, the RMSE is lower. To reduce the noise impact, a variety of filters and image-enhancing techniques are applied. Clustering is mostly used for segmentation. Various clustering algorithms have been developed. According to the literature, the Hyperbolic Tangent Gaussian kernel fuzzy C-Means clustering Otsu (HTGkFCM-Otsu) provides benefits over FCM in terms of processing speed and simplicity. To achieve the intended region of interest, a mixture of image segmentation algorithms is utilized. One of the most often utilized feature extraction techniques is GLCM. This approach has the best performance on medical images, based on properties like energy, contrast, correlation, and homogeneity.

References

1. Leo M, Kalpalatha Reddy T (2012) Layerwise segmentation of dental X-ray images. In: 2012 2nd world conference on innovation and computer sciences, vol 2. http://doi.org/10.13140/2.1.2109.5361
2. Dhanachandra N, Manglem K, Chanu YJ (2015) Image segmentation using K-means clustering algorithm and subtractive clustering algorithm. Procedia Comput Sci 54:764–771. http://doi.org/10.1016/j.procs.2015.06.090

3. Poulist MAJ (2012, 17th May 2012) Contrast Limited Adaptive Histogram Equalization (CLAHE) [Online]. Available: http://radonc.ucsf.edu/research_group/jpouliot/Tutorial/HU/Lesson7.htm

4. Zhiming W, Jianhua T (2006) A fast implementation of adaptive histogram equalization. Presented at the 8th international conference on signal processing (ICSP)

5. Jen T, Wang S (2006) Generalized histogram equalization based on local characteristics. Presented at 2006, IEEE international conference on image processing

6. Al-Ameen Z, Sulong G, Rehman A, Al-Dhelaan A, Saba T, Al-Rodhaan M (2015) An innovative technique for contrast enhancement of computed tomography images using normalized gamma-corrected contrast-limited adaptive histogram equalization. EURASIP J Adv Signal Process 32:1–12

7. Rui W, Guoyu W (2017) Medical X-ray image enhancement method based on TV-homomorphic filter. In: 2017 2nd international conference on image, vision, and computing (ICIVC). IEEE, pp 315–318

8. Sudhakar MS, Bagan KB (2011) A novel approach for retrieval of medical images in bit plane domain. In: 2011 IEEE international conference on signal and image processing applications (ICSIPA), pp 478–483. http://doi.org/10.1109/ICSIPA.2011.6144075

9. Fariza A, Arifin AZ, Astuti ER, Kurita T (2019) Segmenting tooth components in dental X-ray images using Gaussian kernel based conditional spatial fuzzy C-means clustering algorithm. Int J Intell Eng Syst 12(3):108–117. http://doi.org/10.22266/ijies2019.0630.12

10. Ahmad SA, Taib MN, Khalid NEA, Taib H (2012) An analysis of image enhancement techniques for dental X-ray image interpretation. Int J Mach Learn Comput 2(3)

11. Mustapha A, Hussain A, Samad SA (2011) A new approach for noise reduction in spine radiograph images using a non-linear contrast adjustment scheme based adaptive factor. Sci Res Essays 6(20):4246–4258

12. Ikhsan IAM, Hussain A, Zulkifley MA, Tahir NM, Mustapha A (2014) An analysis of X-ray image enhancement methods for vertebral bone segmentation. In: 2014 IEEE 10th international colloquium on signal processing and its applications, pp 208–211. http://doi.org/10.1109/CSPA.2014.6805749

13. Zheng W, Yang H, Sun H, Fan H (2007) X-ray image enhancement based on multi-scale morphology. In: 2007 1st international conference on bioinformatics and biomedical engineering, pp 702–705. http://doi.org/10.1109/ICBBE.2007.183

14. Geetha V, Aprameya KS (2019) Analysis of image segmentation techniques for diagnosis of dental caries in X-ray images. Int J Comput Inf Eng 13(2)

15. Geetha V, Aprameya KS, Hinduja DM (2020) Dental caries diagnosis in digital radiographs using back-propagation neural network. Health Inf Sci Syst 8(1):8. http://doi.org/10.1007/s13755-019-0096-y. PMID: 31949895; PMCID: PMC6942116

16. Salimzadeh S, Kandulu S (2020) Teeth segmentation of bitewing X-ray images using wavelet transform. Informatica (Slovenia) 44. http://doi.org/10.31449/inf.v44i4.2774

17. Kumar A, Bhadauria HS, Singh A (2019) Semi-supervised OTSU based hyperbolic tangent Gaussian kernel fuzzy C-mean clustering for dental radiographs segmentation. Multimedia Tools Appl. http://doi.org/10.1007/s11042-019-08268-8

18. Kushol R, Nishat Raihan Md, Sirajus Salekin Md, Ashikur Rahman ABM (2019) Contrast enhancement of medical X-ray image using morphological operators with optimal structuring element, vol 1. In: Conference on computer vision and pattern matching

19. Manuella DFB, Glaucia MBA, Cinthia PMT, Rivea IFS, Francisco HN (2013) Performance of digital radiography with enhancement filters for the diagnosis of proximal caries. Oral Radiol Braz Oral Res 27(3):245–251

20. Georgieva VM, Mihaylova AD, Petrov PP (2017) An application of dental X-ray image enhancement. In: Proceedings of the 2017 13th international conference on advanced technologies, systems and services in telecommunications (TELSIKS), Nis, Serbia, 18–20 October 2017

21. Virupaiaha G, Sathyanarayana AK (2020) Analysis of image enhancement techniques for dental caries detection using texture analysis and support vector machine. Int J Appl Sci Eng 17(1):75–86

22. Said E, Fahmy GF, Nassar D, Ammar H, Jain AK, Ratha NK (2004) Biometric technology for human identification—"Dental X-ray image segmentation". In: SPIE proceedings. SPIE Defense and Security, Orlando, FL, 12 April 2004, vol 5404, pp 409–417. http://doi.org/10.1117/12.541658

23. Joe-Air J, Chang H-Y, Wu K-H, Ouyang C-S, Yang M-M, Yang E-C, Chen T-W, Lin T-T (2008) An adaptive image segmentation algorithm for X-ray quarantine inspection of selected fruits. 60(2):190–200. http://doi.org/10.1016/j.compag.2007.08.006

24. Setianingrum AH, Rini AS, Hakiem N (2017) Image segmentation using the Otsu method in dental X-rays. In: 2017 second international conference on informatics and computing (ICIC), pp 1–6. http://doi.org/10.1109/IAC.2017.8280611

25. Tania UT, Motakabber SMA, Ibrahimy MI (2013) Edge detection techniques for iris recognition system. IOP Conf Ser Mater Sci Eng 53:012041. http://doi.org/10.1088/1757-899X/53/1/012041

26. Román JCM, Fretes VR, Adorno CG, Silva RG, Noguera JLV, Legal-Ayala H, Mello-Román JD, Torres RDE, Facon J (2021) Panoramic dental radiography image enhancement using multiscale mathematical morphology. Sensors 21. http://doi.org/10.3390/s21093110

27. Rad AE, Rahim MSM, Norouzi A (2013) Digital dental X-ray image segmentation and feature extraction. TELKOMNIKA Indonesian J Electr Eng 11(6):3109–3114

28. Veena Divya K, Jatti A, Revan Joshi P (2016) Appending active contour model on digital panoramic dental X-rays images for segmentation of maxillofacial region. In: 2016 IEEE EMBS conference on biomedical engineering and sciences (IECBES), Kaula Lumpur, Malaysia. IEEE, Piscataway, pp 4–8

29. Kaushik A, Mathpal PC, Sharma V (2014) Edge detection and level set active contour model for the segmentation of cavity present in dental X-ray images. Int J Comput Appl 96:24–29. http://doi.org/10.5120/16822-6576

30. Rad AE, Rahim MSM, Kumoi R, Norouzi A (2013) Dental X-ray image segmentation and multiple feature extraction. Glob J Technol 2

31. Bora DJ, Gupta AK (2014) A comparative study between fuzzy clustering algorithm and hard clustering algorithm. Int J Comput Trends Technol (IJCTT) 10(2):108–113. ISSN: 2231-2803

32. Fariza A, Arifin AZ, Astuti ER, Kurita T (2019) Segmenting tooth components in dental X-ray images using Gaussian kernel-based conditional spatial fuzzy C-means clustering algorithm. Int J Intell Eng Syst 12(3):108–117. https://doi.org/10.22266/ijies2019.0630.12

33. Vani Kumari S, Usha Rani K (2020) Analysis on various feature extraction methods for medical image classification. http://doi.org/10.1007/978-3-030-46943-6_3

34. Kaur A, Verma A (2013) The marker-based watershed segmentation—a review. IJEIT 3(3):171–174

35. Oliveira J, Proença H (2010) Caries detection in panoramic dental X-ray images. Comput Vis Med Image Process 175–190. https://doi.org/10.1007/978-94-007-0011-6_10

36. Roopa H, Asha T (2018) Feature extraction of chest X-ray images and analysis using PCA and kPCA. Int J Electr Comput Eng 8:3392–3398. https://doi.org/10.11591/ijece.v8i5.pp3392-3398

37. Patil S, Kulkarni V, Bhise A (2019) Algorithmic analysis for dental caries detection using an adaptive neural network architecture. Heliyon 5(5):e01579. http://doi.org/10.1016/j.heliyon.2019.e01579

38. Munawar HS, Aggarwal R, Qadir Z, Khan SI, Kouzani AZ, Mahmud MAP (2021) A Gabor filter-based protocol for automated image-based building detection. Buildings 11(7):302. http://doi.org/10.3390/buildings11070302

39. Kamarainen JK, Kyrki V, Kalviainen H (2002) Robustness of Gabor feature parameter selection. In: Proceedings of the IAPR conference on machine vision applications (IAPR MVA 2002), December 11–13, 2002

40. Veena Divya K, Jatti A, Joshi R, Deepu Krishna S (2017) Characterization of dental pathologies using digital panoramic X-ray images based on texture analysis. In: 2017 39th annual international conference of the IEEE Engineering in Medicine and Biology Society (EMBC), pp 592–595. http://doi.org/10.1109/EMBC.2017.8036894

41. Verma D, Puri S, Prabhu S, Smriti K (2020) Anomaly detection in panoramic dental X-rays using a hybrid deep learning and machine learning approach. In: 2020 IEEE region 10 conference (TENCON), pp 263–268. http://doi.org/10.1109/TENCON50793.2020.929376
42. Croock MS (2017) Edge detection and features extraction for dental X-ray
43. Raju J, Modi CK (2011) A proposed feature extraction technique for dental X-ray images based on multiple features. In: 2011 international conference on communication systems and network technologies, pp 545–549. http://doi.org/10.1109/CSNT.2011.116
44. Benrachou DE, dos Santos FN, Boulebtateche B, Bensaoula S (2015) Online vision-based eye detection: LBP/SVM vs LBP/LSTM-RNN. In: CONTROLO'2014—proceedings of the 11th Portuguese conference on automatic control, pp 659–668. http://doi.org/10.1007/978-3-319-10380-8_63
45. Majanga V, Viriri S (2021) Automatic blob detection for dental caries. Appl Sci 11(19):9232. http://doi.org/10.3390/app11199232

Polar Decoder-Based Full Adders: Implementation and Comparative Analysis Using 180 nm and 90 nm Technologies in Cadence

T. Vijayalakshmi and J. Selvakumar

Abstract In the case of digital applications, addition is the most often utilized mathematical operation. Because they impact floating-point and arithmetic logic units, as well as cache/memory address computations, the stability of FA cells is considered to be critical. Full adders are critical elements in applications like DSP systems and microprocessors. The design of polar decoder-based full adders is crucial since the polar decoder architecture is extensively used in majority of the digital systems including processors. As a result, adder design is important in digital design. This study looks into Cadence implementations of polar decoder-based full adders in 180 nm and 90 nm technologies, with consideration of delays and power consumption.

Keywords Polar decoder · Full adder · Comparative analysis · Implementation · 90 nm technology · Cadence · 180 nm technology

1 Introduction

Many digital circuits that execute addition or subtraction use a full adder circuit [1]. It contains three inputs and two outputs [2]. Polar codes have been confirmed as one among the channel coding strategies for 5G uplink control channels, which has sparked a lot of interest in high-performance but reduced decoding algorithms [3]. When contrasted to LDPC or turbo codes, the original SC decoding method limited from significant BER degradation for small block lengths due to its inherent error propagation inadequacy [4]. The SCL and SCS polar decoders were designed to mitigate this performance decrease by using the depth-first and breadth-first search strategies, accordingly. In addition, polar decoders on the basis of sphere decoding have

T. Vijayalakshmi (✉) · J. Selvakumar
Department of ECE, SRMIST, Kattankulathur, Tamil Nadu, India
e-mail: vt1586@srmist.edu.in

J. Selvakumar
e-mail: selvakuj@srmist.edu.in

been developed for achieving near maximum-likelihood performance with minimal decoding complexity [5].

Handling the LLR-oriented SCL or SCS decoding of polar codes, which created hard bit choices on the basis of their LLR inputs, has been researched in order to enable the use of polar decoders depending on logarithmic domain [6]. Soft-output decoders, like the BP and SCAN polar decoders, have been suggested for enabling IDD [7]. The difficulty of BP decoding can be further decreased by employing early-stopping techniques. Soft-output polar decoders with higher complexity have been examined [8]. A BPL decoder is suggested, which provides equivalent BER performance [9] by creating permuted polar code factor graphs for producing a list of codewords and conducting BP decoding. Likewise, the SCANL decoding approach of [10] achieved somewhat higher BER performance. Soft-output associated with the SCL decoder has just been accomplished [11].

Polar codes are a significant advancement in encoding [12]. Subsequently, a novel SC-list decoding technique for polar codes was described, which outperforms the basic SC decoder and is nearly as good as the ideal ML decoding at high SNR [13]. The combination of polar codes using simple CRC was developed to increase the short minimum distance of polar codes [14]. Here, it points out that when CRC is concatenated, the list size necessary to approximate ML is substantially bigger than when it is not concatenated. For such enormous list sizes, the intricacy of the above SC-List decoder would be prohibitive. In certain contexts, average complexity, rather than worst-case complexity, defines a useful statistic [15]. Low processing energy consumption suggests low average complexity, which is useful in a cell phone, for instance. Low average complexity to decode every user at a BS when numerous users are concurrently decoded signifies the capacity to economically and effectively distribute the operations of the users [16]. Likewise, distinct decoding blocks' execution might be shared across time.

The paper contribution is

- To implement the polar decoder-based full adders in Cadence.
- To analyze polar decoder-based Full Adders implementations in 180 nm, and 90 nm, technologies in Cadence.
- To estimate the polar decoder-based full adders in terms of power consumption as well as delays.

The paper organization is: Sect. 1 is the introduction of polar decoder-based full adder. Section 2 is literature survey. The full adder description for the comparative analysis in Cadence is Sect. 3. Section 4 is polar decoder implementation in Cadence. Section 5 is results. Section 6 is conclusion.

2 Literature Survey

2.1 Related Works

In 2020, Shen et al. [17] the low-latency software polar decoder has been investigated. The SLP algorithm and the MDS algorithm were two new algorithms suggested to improve the latency of SCL decoding. Furthermore, as differentiated with traditional segmentation algorithms, the suggested SLP algorithm enhanced decoding performance. The decoder was about 20% quicker than the conventional flexible software polar list decoder with respect to software implementation.

In 2021, Zhang et al. [18] have presented a way to enhance the BP decoder's BLER performance for polar codes such that it was similar to the SCL decoder. The suggested decoder, in contrast to BPF decoding, concentrated on previous knowledge of the code bits in the factor graph. To create the corrective set, two ways have been presented. The simulation outcomes revealed that the BPC decoder has a BLER identical to that of the BPF decoder, but with half the complexity and latency. Furthermore, in low as well as medium SNR areas, the BLER associated with the BPC decoder could approximate that of the CA-SCL decoder.

In 2020, Cao et al. [19] for MU-MIMO systems, researchers have developed a polar decoder. The decoding architecture has been completely unfurled to optimize hardware parallelism, and the round-trip scheduling data path has been decoupled to permit concurrent execution of several code words. In addition, to decrease hardware complexity, a hybrid decoding data path was proposed, which proposed complementary decoding units having mixed data models. When 36 users were handled concurrently, a decoding throughput of 100.6 Gbps was reached for (1024, 512) polar codes, with a latency of 0.43 µs.

In 2020, Fang et al. [20] for lowering the decoding delay, the NSC decoder with tanh-based improved LLR has been developed. Thanks to the recursive feature of the polar sequence's dependability ranking supplied in the 5G standard. The BER performance over turbulent channel was nearer to that of the traditional SC decoder for practical-length polar codes, as verified by simulation. In terms of turbulence-stability, the NSC decoder has steady behavior in a broader variety of turbulence settings after being trained in mild and intense turbulence.

In 2021, Xiang et al. [21] have suggested a SSCS polar decoder that combined the benefits of the stack decoder's depth-first search with the belief propagation decoder's soft information output. In turbo-style receivers, this contained the significant advantage of allowing SISO decoding and smooth iterative information interchange. The simulation findings demonstrated that the suggested SSCS decoder could beat traditional SISO polar decoders at moderate to high SNRs, albeit needing less complexity.

In 2019, Song et al. [22] have suggested two enhanced decoders in both low and high SNR zones to minimize space and time complexity. The Adaptive SCS (ASCS) decoder, on the other hand, contained searching width flexibility and stack depth. A channel condition estimator was also presented for choosing acceptable selection

criteria for various SNR circumstances. Two upgraded SCS decoders outperformed the classic SCS decoder for the polar code, according to the findings. Over BI-AWGNCs, the presented method might attain higher values. The SCS polar decoder's effective parallel hardware design was initially suggested and built using 90- and 65-nm technologies. The benefits it has over the existing have been proven by the results.

In 2012, Li et al. [23] for polar codes having CRC, they presented an adaptive SC-List decoder. Simulations demonstrated that it reduced complexity significantly. We further showed that a polar code decoded by the introduced method having a very large maximum list size showed better FER.

In 2020, Zhou et al. [24], initially, an ESSD on the basis of synchronous determination has been developed. The latency and complexity of the suggested ESSD were comparable to other methods at high SNRs on the shown codes. The suggested ESSD, when implemented in C++, lowered latency by 44.77% when compared with other methods.

In 2021, Ivanov et al. [25] have described a new method for decoding polar codes using SCL-Flip. On the basis of the route metric of SCL decoding, a new bit-selection measure for crucial group was proposed. The enhanced SCL technique on the basis of SN decoders was created using the suggested measure. GSCLF would be the abbreviation for this decoder. The suggested decoder's major idea was to combine two strategies: the first was fast decoding representations of polar codes and the second was subjecting extra decoding attempts. When these two techniques were used together, they result in a considerable decrease in both spatial complexity and the amount of calculations needed for decoding while maintaining outstanding performance. Based on the simulation findings reported in this research, we could infer that the computational complexity was lower.

In 2019, Ardakani et al. [26] have shown how to implement the SCL and SCF decoders quickly. We offered in a polar code's decoding tree, which reduced decoding latency dramatically. In addition, we described new fast SCF decoders that decoded specific particular nodes in a polar code's decoding tree without serially calculating bit LLRs. In comparison with the original SCF decoder, we noticed an enhancement of up to 81% utilizing the suggested fast parallel SCF decoders. The code's BER performance did not suffer as a result of the large reduction in decoding time.

3 Full Adder Description for the Comparative Analysis in Cadence

A FA is a digital logic circuit that combines three binary values together. It is often utilized in ALU and data processing units [10] in processor chips to accomplish logical as well as arithmetic functions. The bits to be involved in the Single bit Full Adder are defined by the three inputs C, D, and E_{in} [27]. The sum and carry functions are the adder's outputs. The following is the output-to-input association:

$$\text{sum}(u) = C \oplus D \oplus E_{\text{in}} \text{ And} \tag{1}$$

$$\text{Carry}(E_{\text{out}}) = C D + (D \oplus C) E_{\text{in}} \tag{2}$$

Typical FA implementation approaches involve $28T$, $14T$, $20T$, and $10T$ [27], in which T signifies the total count of transistors in the FA architecture. As scaling gets approaching nanoscale, power dissipation becomes more significant. Even though there exists a substantial degree of power loss even in sleep mode due to leakage power, battery life is shortened [28]. To address the aforementioned issue, the method employs transistors with multiple and changeable threshold voltages. For applications with more operational speed, minimum threshold voltage transistors are employed in the modeling. Longer delays are seen in transistors having a high threshold voltage [29]. A few of the contemporary Full adder designs, as well as their designs, are also reviewed.

$28T$ FA implementation: In this full adder design, the addition is accomplished utilizing 28 [30] transistors. Since it sort of design has more transistors, power dissipation [31], including the space employed, will be greater, and the input load will be more.

$20T$ FA: The count of transistors is lowered to 20 in this generation. In spite of the general lesser transistor count employed in this circuit, the battery consumption and latency are lowered when compared to the $28T$ [27] FA.

$14T$ FA circuit: A $14T$ full adder design was devised to lower the transistor count, resulting in reduced latency and power consumption than a variant having a higher transistor count.

$10T$ FA circuit: In the design of a $10T$ FA, there exist just transistors. There are very few transistors than in the $28T$ transistor modeling. A concept must be clarified or a dictionary must be provided when it is first introduced. The power dissipation lowers as the count of transistors rises. The propagation latency [10] lowers as a consequence.

4   Polar Decoder Implementation in Cadence

In this part, we go through the fundamentals of polar coding. Assume the system depicted in Fig. 1, which employs a polar code. The system's input/output signals are all vectors of length O, in which O shows the polar code length that are being employed.

The encoder input vector $v \in G_2^O$ is made up of two parts: a data part v_B and a frozen part v_{B^d}, in which B is determined using the polar code design methods described in [32]. In this investigation, we set the frozen component v_{B^d} to zero. We describe a frozen-bit indication vector b as b shows a 0–1 vector of length O having
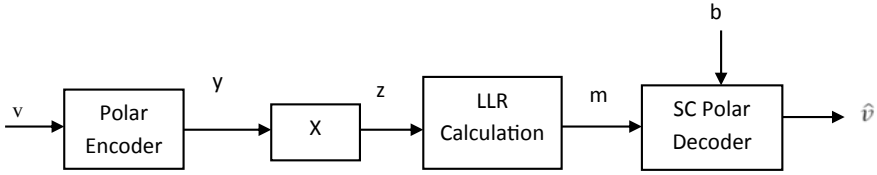
Fig. 1 Communication strategy using polar decoding

the following properties:

$$b_j = \begin{cases} 0, & \text{if } j \in B^d \\ 1, & \text{if } j \in B \end{cases} \tag{3}$$

The system's decoder gets access to the frozen-bit indication vector. The system's channel X describes a discrete memoryless channel having input alphabet $Y = \{0, 1\}$ and output alphabet Z, as well as transition probabilities $\{X(z|y) : y \in Y, z \in Z\}$. A codeword $y \in G_2^O$ is communicated and a channel output vector $z \in Z^O$ is received for every usage of the system. A Log-Likelihood Ratio (LLR) vector $m = (m_1, \ldots, m_O)$ is calculated by the receiver. This is fed to the Successive Cancellation (SC) decoder.

$$m_j = \ln\left(\frac{P(z_j|y_j = 0)}{P(z_j|y_j = 1)}\right) \tag{4}$$

The system's decoder describes a SC decoder, as explained in [32] that receives the frozen-bit and channel LLRs indication vector as inputs and derives an approximation $\hat{v} \in G_2^O$ associated with the data vector v. The SC algorithm generates bit decisions in natural index order, one at a time, with every bit decision relying on previous bit decisions.

Algorithm 1 defines a precise formulation of the SC algorithm, with the functions $g_{O/2}$ and $h_{O/2}$ specified as

$$g_{O/2}(m) = (g(m_0, m_1), \ldots, g(m_{O-1}, m_{O-1})) \tag{5}$$

$$h_{O/2}(m, w) = \left(h(m_0, m_1, w_0), \ldots, h(m_{O-1}, m_{O-1}, w_{O/2-1})\right) \tag{6}$$

This include the following,

$$g(m_1, m_2) = 2 \tanh^{-1}(\tanh(m_1/2) \tanh(m_2/2)) \tag{7}$$

$$h(m_1, m_2, w) = m_1(-1)^w + m_2 \tag{8}$$

The function g is estimated utilizing the min-sum formula in the actual implementations presented in this work.

$$g(m_1, m_2) \approx (1 - 2t(m_1)) \cdot (1 - 2t(m_2)) \cdot \min\{|m_1|, |m_2|\}. \tag{9}$$

Here, h is achieved in a different (precise) way.

$$h(m_1, m_2, w) = m_2 + (1 - 2w) \cdot m_1 \tag{10}$$

The recursive structure of the SC decoding method allows for low-complexity implementations, since a decoding occurrence of block length O is split down into two decoding occurrences of lengths $O/2$ each for the decoder.

Algorithm 1 $\hat{v} = \text{DECODE}(m, b)$

$O = length(m)$
If $O == 2$ then

$\hat{v}_0 \leftarrow t(g(m_0, m_1)) \cdot b_0$
$\hat{v}_1 \leftarrow t(h(m_0, m_1, \hat{v}_0)) \cdot b_1$
Return $\hat{v} \leftarrow (\hat{v}_0, \hat{v}_1)$

else

$m' \leftarrow g_{O/2}(m)$
$b' \leftarrow (b_0, \ldots, b_{O/2-1})$
$\hat{v}' \leftarrow \text{DECODE}(m', b')$
$w \leftarrow \text{ENCODE}(\hat{v}')$
$m'' \leftarrow h_{O/2}(m, w)$
$b'' \leftarrow (b_{O/2}, \ldots, b_{O-1})$
$\hat{v}'' \leftarrow \text{DECODE}(m'', b'')$
Return $\hat{v} \leftarrow (\hat{v}', \hat{v}'')$

end

---

5 Results

5.1 Cadence Virtuoso Implemented Model

Full adder circuits have been introduced to the newest Virtuoso GPDK Tool. It is constructed and validated in the 180 nm platform once the threshold voltage, pulse width, and supply voltage are chosen. The latency within the input, as well as output,
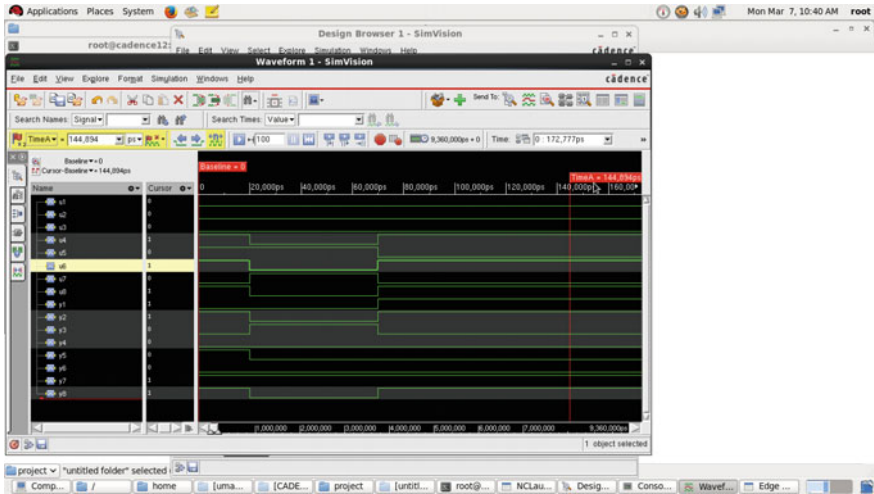
Fig. 2 Simulation for polar decoder in cadence

and also power consumption together with waveforms have all been examined in
180 nm and 90 nm technologies.

5.2 Analysis on Performance and Simulation Outcomes in Cadence

The present FA circuits are modeled employing the Cadence Virtuoso circuit
modeling tool on 180 nm and 90 nm platforms. The supply voltage is 1.2 V across all
three platforms, with threshold voltages of 0.9 and 0.6 V for distinct technologies,
and also battery consumption and delay within the input and output. These are the
simulation findings for a standard $28T$ full adder using 180 nm and 90 nm technology.
Simulation for polar decoder in Cadence is shown in Fig. 2.

5.3 Comparative Analysis of Simulation Outcomes

Current FA implementations, like $28T$, $10T$, $14T$, and $20T$, have been employed in
180 nm and 90 nm technologies for power consumption and latency. In 180 nm tech-
nology, a $28T$ design uses 0.000006, but the identical transistor in 90 nm requires
0.000004. Based on the information, it can be determined that the 90 nm tech-
nology uses the least amount of electricity. The Power Gating Procedure can also
be employed to lower leakage current with this technique. Comparative analysis of
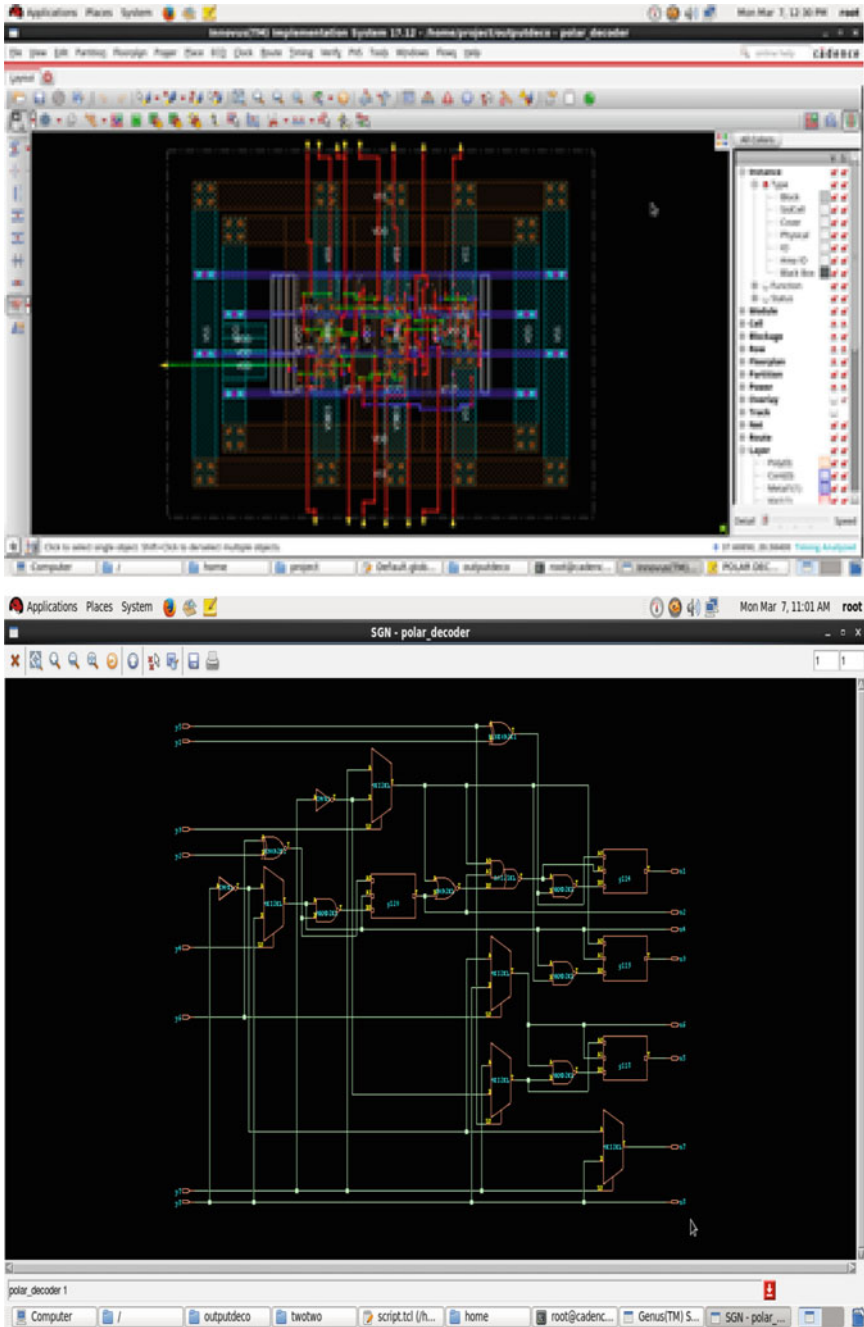90 nm technology for polar decoder in Cadence is shown in Fig. 3 (Fig. 4).

Fig. 3 Comparative analysis of 90 nm technology for polar decoder in cadence
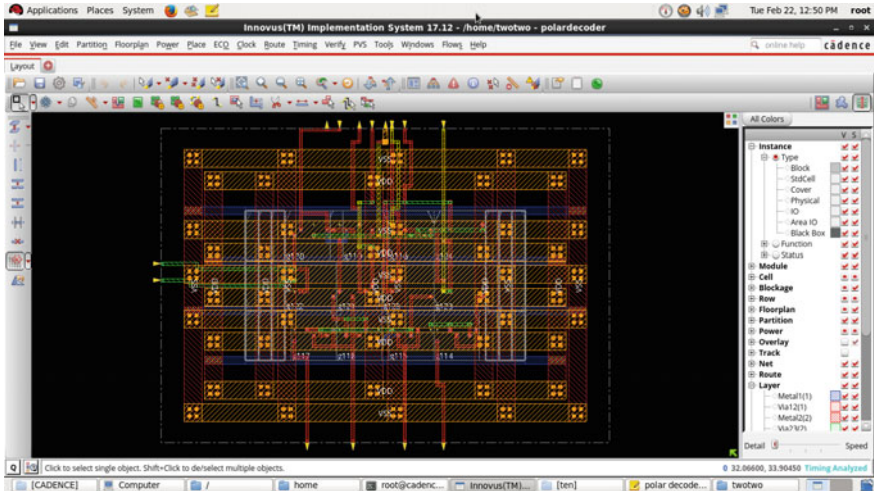
Fig. 4 Comparative analysis of 180 nm technology for polar decoder in cadence

6 Conclusion

The most commonly used mathematical operation in digital applications was addition. The stability of FA cells was regarded crucial since they affect floating-point and arithmetic logic units, as well as cache/memory address computations. In applications such as DSP systems and microprocessors, full adders were essential. Because the polar decoder architecture was widely employed in most digital systems, including CPUs, the design of polar decoder-based full adders was critical. As a result, in digital design, adder design was critical. Cadence implementations of polar decoder-based FAs in 180 nm and 90 nm technologies were investigated in this work, with delays and power consumption taken into account.

References

1. Cammerer S, Gruber T, Hoydis J, Ten Brink S (2017) Scaling deep learning-based decoding of polar codes via partitioning. In: Proceedings of IEEE global communications conference, pp 1–6
2. Fang J et al (2020) Neural network decoder of polar codes with tanh-based modified LLR over FSO turbulence channel. Opt Express 28(2):1679–1689
3. Arikan E (2009) Channel polarization: a method for constructing capacity-achieving codes for symmetric binary-input memoryless channels. IEEE Trans Inf Theory 55(7):3051–3073
4. Doan N, Hashemi SA, Gross WJ (2018) Neural successive cancellation decoding of polar codes. In: Proceedings of IEEE 19th international workshop on signal processing advances in wireless communications, pp 1–5
5. Arıkan E (2009) Channel polarization: a method for constructing capacity achieving codes for symmetric binary-input memoryless channels. IEEE Trans Inf Theory 55(7):3051–3073

6. Babar Z, Egilmez ZBK, Xiang L, Chandra D, Maunder RG, Ng SX, Hanzo L (2019) Polar codes and their quantum-domain counterparts. IEEE Commun Surv Tutorials 22(1):123–155
7. Tal I, Vardy A (2015) List decoding of polar codes. IEEE Trans Inf Theory 61(5):2213–2226
8. Dai J, Niu K, Si Z, Dong C, Lin J (2017) Polar-coded non-orthogonal multiple access. IEEE Trans Signal Process 66(5):1374–1389
9. Balatsoukas-Stimming A, Parizi MB, Burg A (2015) LLR-based successive cancellation list decoding of polar codes. IEEE Trans Signal Process 63(19):5165–5179
10. Manjunath KM, Abdul Lateef Haroon PS, Pagi A, Ulaganathan J (2015) Analysis of various full-adder circuits in cadence. In: International conference on emerging research in electronics, computer science and technology
11. Aurora H, Condo C, Gross WJ (2018) Low-complexity software stack decoding of polar codes. In: 2018 IEEE international symposium on circuits and systems (ISCAS). IEEE, pp 1–5
12. Xiang L, Egilmez ZBK, Maunder RG, Hanzo L (2019) CRC-aided logarithmic stack decoding of polar codes for ultra reliable low latency communication in 3GPP new radio. IEEE Access 7:28559–28573
13. Arıkan E (2010) Polar codes: a pipelined implementation. In: Proceedings of 4th international symposium on broadband communications, ISBC 2010, pp 11–14
14. Yuan B, Parhi KK (2014) Early stopping criteria for energy-efficient low-latency belief-propagation polar code decoders. IEEE Trans Signal Process 62(24):6496–6506
15. Pillet C, Condo C, Bioglio V (2020) SCAN list decoding of polar codes. In: ICC 2020—2020 IEEE international conference on communications (ICC). IEEE, pp 1–6
16. Xiang L, Liu Y, Egilmez ZBK, Maunder RG, Yang L-L, Hanzo L (2020) Soft list decoding of polar codes. IEEE Trans Veh Technol 69(11):13921–13926
17. Shen Y et al (2020) Low-latency segmented list-pruning software polar list decoder. IEEE Trans Veh Technol 69(4):3575–3589
18. Zhang M, Li Z, Xing L (2021) An enhanced belief propagation decoder for polar codes. IEEE Commun Lett 25(10):3161–3165
19. Cao S, Zheng H, Lin T, Zhang S, Xu S (2020) An unfolded pipelined polar decoder with hybrid number representations for multi-user MIMO systems. IEEE Trans Circuits Syst II Express Briefs 67(11):2472–2476
20. Fang J et al (2020) Neural successive cancellation polar decoder with tanh-based modified LLR over FSO turbulence channel. IEEE Photonics J 12(6):1–10
21. Xiang L, Liu Y, Maunder RG, Yang L-L, Hanzo L (2021) Soft-output successive cancellation stack polar decoder. IEEE Trans Veh Technol 70(6):6238–6243
22. Song W et al (2019) Efficient successive cancellation stack decoder for polar codes. IEEE Trans Very Large Scale Integr (VLSI) Syst 27(11):2608–2619
23. Li B, Shen H, Tse D (2012) An adaptive successive cancellation list decoder for polar codes with cyclic redundancy check. IEEE Commun Lett 16(12):2044–2047
24. Zhou H, Song W, Gross WJ, Zhang Z, You X, Zhang C (2020) An efficient software stack sphere decoder for polar codes. IEEE Trans Veh Technol 69(2):1257–1266
25. Ivanov F, Morishnik V, Krouk E (2021) Improved generalized successive cancellation list flip decoder of polar codes with fast decoding of special nodes. J Commun Netw 23(6):417–432
26. Ardakani MH, Hanif M, Ardakani M, Tellambura C (2019) Fast successive-cancellation-based decoders of polar codes. IEEE Trans Commun 67(7):4562–4574
27. Irfan Khan PA, Mishra RS, Dhariwal S (2016) Comparative analysis of different types of full adders using 180 nm and 90 nm technology. In: International conference on advances in emerging technology
28. Gupta R, Pandey SP, Akashe S, Vidyarthi A (2013) Analysis and optimisation of active power and delay of 10T full adder using power gating technique at 45 nm technology. IOSR J VLSI Sig Process 2(1):51–57
29. Varadharajan SK, Nallasamy V (2017) Low power VLSI circuits design strategies and methodologies: a literature review. In: IEEE conference on emerging devices and smart systems (ICDSS 2017), 3–4 March 2017

30. Damle MB, Limaye SS, Sonwani MG (2013) Comparative analysis of different types of full adder circuits. IOSR J Comput Eng 11(3):01–09
31. Saradindu Panda A, Banerjee BM, Mukhopadyay AK (2012) Power and delay comparison in between different types of full adder circuits. Int J Adv Res Electr Electron Instrum Eng 1(3)
32. Dumer I, Shabunov K (2006) Soft-decision decoding of Reed-Muller codes: recursive lists. IEEE Trans Inform Theory 52(3):1260–1266

LFSR Schema Using CMOS VLSI Technologies—Design, Implementation and Comparative Analysis

P. Umamaheswari and J. Selvakumar

Abstract Linear Feedback Shift Register (LFSR) is fundamentally a shift register capable of generating random sequences. It is a Pseudo-Random Number Generator (PRNG) whose randomness is driven through the linear feedback function governed by the primitive polynomial. LFSR has many real-time use cases but is not limited to cryptographic keys, NONCE, fast digital counters, data whitening, ATSC digital broadcasting standards, Intelsat business service, CDMA cellular telephony, Ethernet scrambles, etc. Due to the enormous growth in the VLSI industry, optimised LFSR designs were constructed to fit inside the chip's silicon substrate to perform the indented tasks. The Complementary Metal Oxide Semiconductor (CMOS) technique is largely adopted over the globe for the design and implementation. This work investigates the effect of LFSR design over two different CMOS technologies, namely 90 nm and 180 nm, through the pre-layout and post-layout simulations. Further, the results have been compared among themselves. Fascinatingly, LFSR using 90 nm occupies a very less area footprint of 90.07 μm^2 and 0.04371049 W of power consumption in a Cadence Virtuoso environment. The area occupancy of 90 nm LFSR is 29.43% less than the 180 nm LFSR, which shows the impact of technology mapping. In addition, the proposed LFSR design is compared with the existing LFSR designs of various technologies, and the results ensure the consistency of the CMOS-based LFSR.

Keywords Linear feedback shift register (LFSR) · Substrate · Primitive polynomial · Area footprint

P. Umamaheswari (✉) · J. Selvakumar
Department of ECE, SRMIST, Kattankulathur, Tamil Nadu, India
e-mail: up6772@srmist.edu.in

J. Selvakumar
e-mail: selvakuj@srmist.edu.in

827

1 Introduction

Recent trends in the digital era demand the industries for high-density Integrated Circuits (ICs). Hence, the design optimisations and technology libraries are very important to accomplish the task [1, 2]. The deep-submicrometer (DSM) technology has been equipped the Very Large-Scale Integration (VLSI) industry to adapt more Intellectual Property (IP) cores on a single silicon substrate to make it as System on Chip (SoC) designs [3, 4]. The design of SoC appeals two major prerequisites. Since the chip occupies more IPs, it becomes complex, thus increasing the quantity of test data to test the SoC design. On the other hand, it is recommended for an SoC design to undergo a secure data transmission when it's connected to the communication peripherals. These two aspects can be viewed as self-testing of SoC before the time to market and establishing data privacy on the internal to external communications of SoC designs [5, 6].

Automatic Test Equipment (ATE) serves as a test vector providing agent to accomplish the self-testing. However, it requires a high volume of channel capacity for Inputs and Outputs. Moreover, speed and memory limitations have become stringent constraints to adapt for testing the system. Hence, a crucial demand has been created for the Built-in Self-Test (BIST). Test-decompression is a renowned methodology that can effectively support the BIST [7].

Similarly, to achieve data privacy, ciphering schemes have been suggested in which the lightweight cryptosystems were compelling solutions. Moreover, lightweight cryptosystems are well-suited privacy preservation mechanisms that fit any SoC design without compromising the speed and area requirements [8]. Though these two requisites are different from the point of design and testing, a single solution can be provided to address these two with the help of LFSR. Moreover, LFSR is an integral part of many modern applications but is not limited to scan designs [9], Rapid Single Flux Quantum (RSFQ) circuits [10], delay path test vectors [11], etc.

In general, LFSR is a Serial In Parallel Out (SIPO) shift register with a linear feedback condition whose output is the function of its previous state value. The shift register will have an initial value, technically called a seed, to drive the operations. The fundamental operation is shifting that happens by the operating clock. The linear function in the feedback loop brings randomness to the LFSR design, which could be utilised for BIST and lightweight cryptosystems [12]. LFSR design comprises 'n' number of flip-flops where the 'n' denotes the number of random bits required from LFSR. The primitive polynomial is a driving factor for any LFSR design through which the design can be constructed.

Further, the linear function is designed with the help of Ex-OR or Ex-NOR logic operations in which the present state value of the flip-flops was operated. The choice of Ex-OR or Ex-NOR is purely based on the designer. The maximal length of the LFSR is determined as $2n - 1$.

On analysing the sequences, Ex-OR-based LFSR will not produce the value of all zeros, whereas the Ex-NOR-based LFSR will not produce the value of all ones due to the exclusive nature of the logic operations. Therefore, an Ex-OR function has been

preferred for VLSI implementations since the Ex-NOR-based LFSR occupies more transistors, thus increasing the design's area requirement. The proposed work focuses on the comparative analysis of a Fibonacci LFSR design with two different CMOS technology libraries, namely 90 nm and 180 nm. The performance was analysed through speed, area and power parameters, in which the prime focus of this work is to reduce the area requirement by adopting the CMOS technique.

2   Related Works

Mahaboob et al. presented a 4-bit LFSR counter which generates random sequences for cryptographic applications. The implementation was implemented using the sub-micron layout tools with CMOS 120 nm and 90 nm technology libraries. The characteristic polynomial of $X^4 + X^3 + 1$ was chosen to yield the maximum length sequence. Flip-flops have been constructed using various methodologies such as NAND gates, transmission gates and pass transistors. Further, Ex-OR was utilised in the feedback loop to achieve a random behaviour. The LFSR design was made using the DSCH3 tool and the parametric analyses were carried out through Microwind software after generating the layout. To accomplish an LFSR using NAND gate-based flip-flops, 148 transistors were required which consumes 169 μW of power in terms of 90 nm technology [13]. Sundararaman et al. discussed the design of diffused bit generator using LFSR with the primitive polynomial of $X^8 + X^7 + X^3 + X^2 + 1$ using CMOS 45 nm technology. Master–Slave D flip-flop configuration was adopted to design the shift registers whereas XOR was being used to generate the feedback input. This design was designed and simulated in Cadence Virtuoso environment and the average power consumption was estimated as 5 μW with the supply voltage of 1.2 V [14].

Daniel et al. proposed a multi-stage CMOS LFSR counter using 130 nm technology in which the single-stage LFSR performance was effectively achieved by adapting a decoding logic. The design consumes 747.9 μW of power when its subjected to post-layout simulations [15]. Radhika Sharma and Balwinder Singh have proposed LFSR architecture with a modified CMOS logic named Gate Diffusion Input (GDI). This technique predominantly uses a fewer number of transistors which effectively reduces the power consumption of the design. Through the GDI technique, XOR gate was designed with four transistors, much less than the traditional CMOS-based XOR gate. Further, the power consumption of the proposed GDI-based LFSR was determined as 34.73 μW on 90 nm technology with the silicon occupancy of 817.95 μm². On analysing the results, it was observed that the proposed LFSR has the power reduction of 45.4% and the area reduction of 20% than the traditional CMOS-based LFSR design [16].

Similarly, Kiruthiga et al. experimented the LFSR design with two different logic styles, namely GDI technique and Conditional Discharge Flip-Flop (CDFF). The D flip-flop was designed using the CDFF technique, in which the flip-flop requires 8 transistors and 4 inverters to accomplish the task. Also, 4 transistors are required to

design the XOR gate for the GDI technique. Hence, this proposed LFSR demands 20 transistors to have a flip-flop, XOR gate pair which can be increased per the characteristic polynomial. The implementation was carried out in the Tanner tool through which the proposed design consumes the power, which is 33% lesser than the traditional CMOS LFSR [17]. Roshini et al. analysed the effect of logic styles on the performance comparison of LFSR design through four different techniques: traditional CMOS, GDI, modified GDI (mGDI) and Multi Threshold CMOS (MTCMOS). All these designs were made using CMOS 180 nm technology on Cadence Virtuoso platform. On analysing the results, the mGDI technique outperforms all other logic styles thus yielding a reduction of 30%, 39% and 40% in power, propagation delay and area footprint of traditional CMOS LFSR. On the other hand, mGDI LFSR has 6% of low power and 14% of minimised delay than the GDI LFSR [18].

Abubaker et al. proposed a memristor-based 4-bit LFSR design in which 16 memristors were used to construct a Master–Slave D flip-flop. Hence, 64 memristor were used to design a 4-bit shift register. Memristor Ratioed Logic (MRL) scheme was adopted to build the LFSR design. TSMC 65 nm technology was adopted to design and simulate the LFSR in Cadence Virtuoso environment. This proposed design consumed 94.15 μW of power which was 66% less than the traditional CMOS LFSR design [19]. Suresh Babu and Anand have proposed a Modified Dynamic MOS Current Mode Logic (MDMCML)-based LFSR which eradicates the issues in traditional MCML technique. CMOS 65 nm technology was chosen as a library to design and simulate the LFSR in which the design requires 87.19 μW of power to produce the random sequences. The power consumption was compared against different CMOS logic variants, such as traditional CMOS, MCML, transmission gate and transistor stack methods. The power reduction through MDMCML technique ensures the low power capability of the design and it is well-suited for the battery powered systems [20].

On observing the existing design methodologies of LFSR, the primary concern was given to the power consumption. To achieve this, GDI, mGDI, CDFF, MCML, MDMCML and memristor techniques were adopted. Though many logic styles have been proposed, the fundamental elements are PMOS and NMOS, which are the core items of CMOS logic style. In the real-world scenario, 90% of the chips are made up of traditional CMOS logic, a well-established and articulated concept. On analysing the existing works, the following observations were made.

- In most of the works, post-layout verification has not been presented with which the effect of technology mapping has not been studied
- Transistor optimisations have been validated with only one technological library which is not sufficient
- Though less number of transistors were used in few designs, the change in the W/L ratio effects in high power consumption
- Most of the low power techniques will have degradation in the output voltage when more number of flip-flops were cascaded to design a 'n' bit LFSR

- Drain and Source in the techniques like GDI/mGDI are driven through inputs rather than the Supply and Ground terminals which causes voltage swing in cascaded designs
- Very few works have reported the area consumption which is a crucial parameter in the back-end process of the IC design.

Considering all the limitations of existing works, the proposed work aims to investigate the 4-bit LFSR design against two different CMOS technologies, namely 90 nm and 180 nm, using the Cadence Virtuoso platform. This work illustrates the effect of change of technology map and the corresponding performance analysis in terms of speed, area and power requirements.

3   Proposed Methodology

The Fibonacci LFSR design is being adopted to investigate the effect of technology libraries. The characteristic polynomial which was chosen for the LFSR construction is $X^4 + X^3 + 1$. The maximum length of the proposed LFSR design is calculated as $2^m - 1$ where 'm' is the number of bits used in the LFSR design. Since this LFSR uses 4 bits, the maximum length is determined as 15. The Fibonacci structure is said to be a 'shift and operate' design in which the shifting process takes place initially and the linear function will be executed at the end. This work uses XOR as a linear function to bring randomness to the circuit.

3.1   Building Blocks of LFSR

In general, LFSR will be constructed using the flip-flops and linear function. Hence, D flip-flop has been used in this work to design a shift register. D flip-flop has several types of realisations in which Master Slave (MS) D flip-flop ensures the values at exact triggering and serves as a good buffer element that avoids setup and holds timing issues when cascaded. The LFSR construction has three consecutive phases, such as 1. design of shift register, 2. converting to ring register and 3. adding a linear function to feedback. Figures 1, 2 and 3 depict the process of above-mentioned phases. The 3-bit LFSR has been taken to explain the LFSR construction procedure.

The fundamental design of LFSR is driven from the construction of SIPO shift register whose structure is presented in Fig. 3. Upon allying a synchronous clock, shift register will get an input from the Serial In port and the output is the concatenation of the results of flip-flops. During the second phase, feedback is introduced between the first and last flip-flops though the shift registers are converted as ring register. Hence, the value of the shifting is circling around 3 bits based on the seed value. Seed value is the important requirement to be provided for the design since the Serial
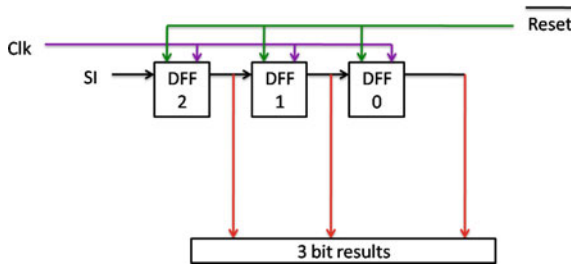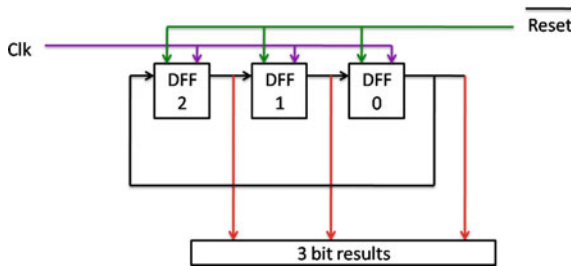
Fig. 1 Design of shift register using D flip-flop

Fig. 2 Converting shift register into ring register
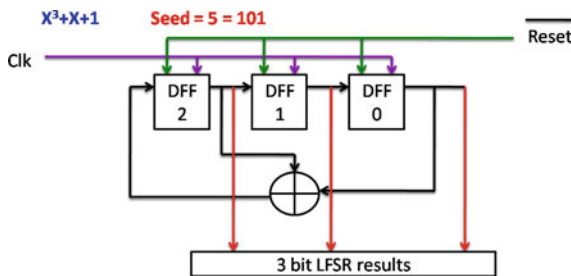

Fig. 3 LFSR architecture using D flip-flops and XOR gate

In port is directly connected to the output of the last flip-flop to create the feedback. Figure 4 illustrates the design of ring register.

On the final phase of LFSR construction, linear function is added to the feedback. XOR is used as a linear function in which the number of inputs to be XORed is based on the primitive polynomial of the LFSR. It is performed in such a way that where and all the polynomial is having power value, those bits of the sequences are XORed to create a feedback which brings the randomness to the LFSR. The final LFSR architecture is shown in Fig. 5.

The 4-bit Fibonacci-based LFSR design is constructed using Cadence Virtuoso environment with 90 nm and 180 nm technologies and the 90 nm design is shown
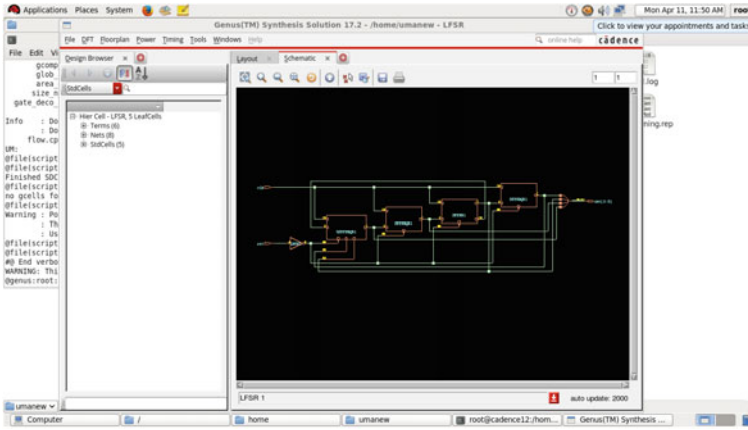
Fig. 4 LFSR design using 90 nm technology—Cadence Virtuoso platform
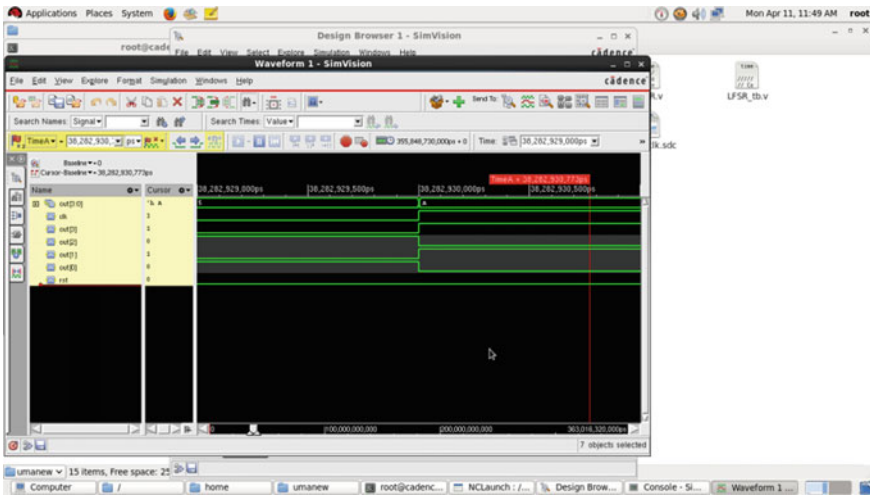
Fig. 5 Functional simulation of the proposed LFSR

in Fig. 4. Further, the random sequences generated from the LFSR are illustrated in Table 1 which was verified through the functional simulation performed through the 'spectre' simulation tool of Cadence Virtuoso environment (Fig. 5). On analysing Table 1, it is impressively producing 15 random data except all zeros. This is due to the adoption of XOR operation in the linear function. Since the XOR gate requires fewer transistors than XNOR, it has been chosen as the linear function.

Table 1 Random sequences generated through the proposed LFSR

| No. of iteration	LFSR value	No. of iteration	LFSR value
0	0101	8	0001
1	1011	9	0011
2	0110	10	0111
3	1100	11	1111
4	1001	12	1110
5	0010	13	1101
6	0100	14	1010
7	1000	For 4–bit LFSR, number of random data = 15 (0 to 14)	

3.2 Results and Discussion

The proposed LFSR is validated by analysing the delay, area and power components with respect to transistor length such as 90 nm and 180 nm. The analyses were made upon generating a design layout in Cadence tool presented in Fig. 6a, b. No local and global constraints were given for the layout generation. Hence, the EDA tool generated the layout for both the technology libraries by its own. To analyse the effect of timing, two critical parameters were considered: Worst Negative Path (WNP) and Total Negative Slack (TNS).

Similarly, the calculation includes internal, switching and leakage power. Pre-layout and post-payout analyses were carried out and the results of post-layout analyses were presented in the subsequent section. Tables 2 and 3 show the delay, area and power analysis.

On observing Table 3, it has been identified that the leakage power is high for a lower nm, and for a higher nm, the leakage power is low. However, internal power and switching power consumptions were contrary with the leakage power consumption. This is due to the technology library change witnessed using the analysis. Further, to investigate the impact of traditional CMOS technique with the new techniques mentioned in Sect. 2, a comparative analysis has been made and presented in Table 4.

From the comparative analysis, though the designs have attained good results in speed and power consumption, the area requirement is high when compared to the standard CMOS architectures. This study reveals that the traditional CMOS technique is a good fit for designing the LFSR architecture. The observations of the works are presented below:

- Two different technology libraries have been used for validation
- It has been found that traditional CMOS technique is free from the problem of contention during switching when the circuit is cascaded
- Leakage power will be very less for the 180 nm LFSR than the 90 nm LFSR due to the high range of transistor length.
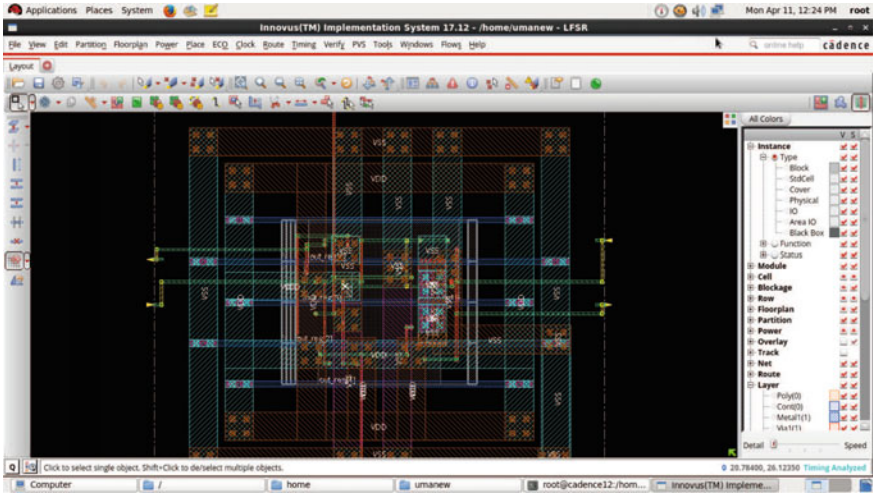
(a)
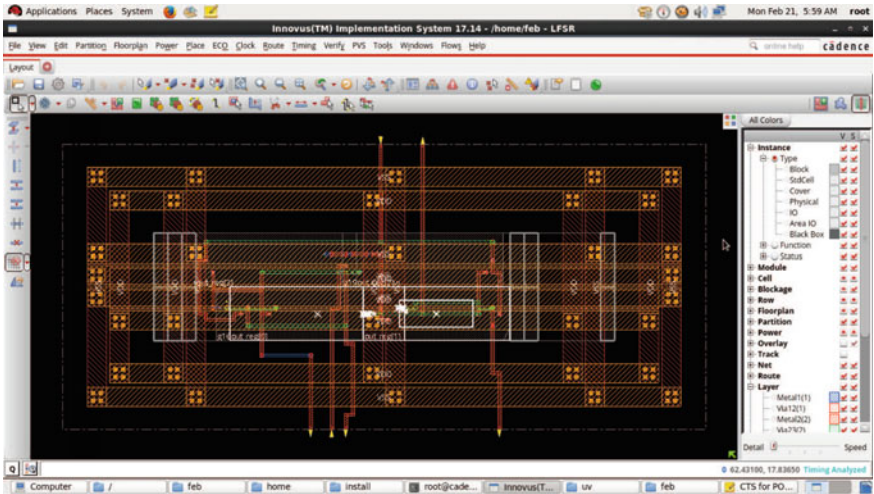
(b)

Fig. 6 **a** LFSR layout for 90 nm and **b** LFSR layout for 180 nm

- Transistor optimisation techniques such as GDI will not meet out the full voltage swing since the technique will not have a proper supply and ground connections.

Table 2 Results of area and delay analysis

Technology library for LFSR	Parameters for validation	Obtained value
90	Area	90.0711 μm^2
	WNP	0.226 ns
	TNS	0.000 ns
180	Area	306.028 μm^2
	WNP	0.533 ns
	TNS	0.000 ns

Table 3 Results of power analysis

Power components	90 nm LFSR	180 nm LFSR
Internal power (W)	0.04140649	0.15428854
Switching power (W)	0.00181596	0.00687226
Leakage power (W)	0.00048804	0.00000932
Total power (W)	0.04371049	0.16117011

Table 4 Comparative analysis of proposed LFSR with existing designs

References	Technique used	Area (μm^2)
Ref. [13]	Transmission gates	270
	Pass transistors	321
Ref. [16]	GDI	103.5
This work	CMOS	90.0711

4 Conclusion

This work aims to analyse the LFSR architecture with two different transistor libraries namely 90 nm and 180 nm. The design was made on Cadence Virtuoso environment by adopting the Fibonacci structure. MS D flip-flops and XOR gates have been used as building blocks of the LFR construction and their phases of operations were explained. Comparing the results of 90 nm and 180 nm LFSR deigns, the area occupancy of 90 nm LFSR is approximately 30% less than the area occupancy of 180 nm LFSR. In contrast, leakage power of 180 nm LFSR is 1.9% less than the 90 nm LFSR. It has been identified that if the transistor length is high, power consumption will be high and vice versa. Hence, the effect of technology map has been effectively studied. Also, the proposed work has been compared with the existing techniques such as transmission gate, pass transistor and GDI. Though the designs yield low power, the area occupancy is higher than the traditional CMOS technique, which evidences the consistency of the CMOS logic style. As a continuation, the future work will be on developing a LFSR-driven cryptosystem for confidentiality preservation.

References

1. Murugan K, Baulkani S (2019) VLSI implementation of ultra power optimised adiabatic logic based full adder cell. Microprocess Microsyst 70:15–20
2. Kim H-S, Kim Y, Kang S (2003) Test-decompression mechanism using a variable-length multiple-polynomial LFSR. IEEE Trans Very Large Scale Integr Syst 11(4):687–690
3. Xing J, Wang H, Yang S (2006) Constructing IP cores' transparency paths for SoC test access using greedy search. Microelectron Reliab 46(7):1199–1208
4. Hu Y, Zhou C (2010) Integration and verification case of IP-core based system on chip design J Shanghai Univ 14(5):349–353
5. Oveis-Gharan M, Khan GN (2020) Reconfigurable on-chip interconnection networks for high performance embedded SoC design. J Syst Archit 106:101711
6. Chen K, Sun L, Deng Q (2022) Hardware and software co-verification from security perspective in SoC platforms. J Syst Archit 122:102355
7. Lala PK (2009) An introduction to logic testing, vol 59
8. Sravani MM, Ananiah Durai S (2021) Attacks on cryptosystems implemented via VLSI: a review. J Inf Secur Appl 60:102861
9. Yuan H, Zhou C, Sun X, Zhang K, Zheng T, Liu C, Wang X (2018) LFSR reseeding-oriented low-power test-compression architecture for scan designs. J Electron Test Theory Appl 34(6):685–695
10. Chen L, Li S, Ying L, Niu M, Liu H, Zhang H, Zhang X, Gao X, Ren J, Peng W, Wang Z (2022) A new LFSR based high-frequency test method for RSFQ circuit. Superconductivity 2:100011
11. Pomeranz I (2019) LFSR-based test generation for path delay faults. IEEE Trans Comput Des Integr Circuits Syst 38(2):345–353
12. van Tilborg HCA, Jajodia S (2011) LFSR. In: van Tilborg HCA, Jajodia S (eds) Encyclopedia of cryptography and security. Springer, Boston, p 720
13. Basha MM, Fairooz T, Hundewale N, Reddy KV, Pradeep B (2012) Implementation of LFSR counter using CMOS VLSI technology. Lecture notes of the institute for computer sciences, social informatics and telecommunications engineering, LNICST, vol 62, pp 275–281
14. Rajagopalan S, Rethinam S, Lakshmi G, Mounika P, Vani R, Chandana D (2017) Diffused bit generator model for TRNG application at CMOS 45 nm technology. In: 2017 International conference on microelectronic devices, circuits and systems, ICMDCS 2017, vol 2017, pp 1–5
15. Morrison D, Delic D, Yuce MR, Redoute JM (2019) Multistage linear feedback shift register counters with reduced decoding logic in 130-nm CMOS for large-scale array applications. IEEE Trans Very Large Scale Integr Syst 27(1):103–115
16. Sharma R, Singh B (2016) Design and analysis of linear feedback shift technique. IEEE, pp 8–12
17. Kiruthiga S, Shangeeth M, Rajesh Kumar SP, Sowndarya R (2020) LFSR using CDFF and GDI. In: 2020 6th international conference on advanced computing and communication systems, ICACCS 2020, pp 595–598
18. Oommen R, George MK, Joseph S (2018) Study and analysis of various LFSR architectures. In: 2018 international conference on circuits and systems in digital enterprise technology, ICCSDET 2018, pp 1–6
19. Sasi A, Amirsoleimani A, Ahmadi A, Ahmadi M (2018) Hybrid memristor-CMOS based linear feedback shift register design. In: ICECS 2017—24th IEEE international conference on electronics, circuits and systems, vol 2018, pp 62–65
20. Babu AS, Anand B (2020) Modified dynamic current mode logic based LFSR for low power applications. Microprocess Microsyst 72:102945

A Review on Image Denoising Algorithms for Various Applications

Gali Rama Lakshmi, G. Divya, D. Bhavya, Ch. Sai Jahnavi, and B. Akila

Abstract Image is well-known word in various fields like medical, engineering, and arts. A literature review is conducted on image qualities, and the need to improve the quality of image for various applications are identified. Numerous noises are added to an image both internally and externally in different stages which results in the poor quality of image. At few points, the noise in the image leads to loss of critical information and creates a lot of damage in that area. Purpose of this review is to gain knowledge about the image denoising and give details about denoising filter algorithms used for noise removal from images. Various techniques exist to overcome noise in any image. Multiple filters and combinations of filters have been designed to remove noise, and those are summarised in this paper for better understanding.

Keywords Image processing · Denoising techniques · Filters · Image quality · Mean · Median

1   Introduction

Image processing is a process of performing certain operations on an image so as to improve the image quality in terms of enhancement, smoothing, sharping, etc., and also to extract required information from images [1]. Image processing can be done using two methods: (i) Analog Image Processing (AIP) and (ii) Digital Image Processing (DIP). Printouts and photographs are related to AIP. In DIP, there are many digital image processing procedures which help in management of the digital images by using Software systems. Among all those techniques, denoising techniques have been considered in this paper. Better quality of images without noise can be obtained by using different hybrid filtering techniques on the images.

G. Rama Lakshmi (✉) · G. Divya · D. Bhavya · Ch. Sai Jahnavi · B. Akila
BVRIT Hyderabad College of Engineering for Women, Hyderabad, India
e-mail: ramalakshmi.g@bvrithyderabad.edu.in

Denoising is a method of image processing which is used for noise reduction. It is a challenging part in the image processing which helps in image segmentation, restoration, visual tracking, and classification where finding the original image is critical for strong recital. In image processing, there are different techniques for denoising an image. The main area of denoising is to suppress the noise and estimate original image from a noisy image. Redundancy is also a type of noise in an image which needs to be removed to get a better quality of image for processing. Utilising micro-images, the current light field approach is implemented. However, the full potential of light field pictures' inherent redundancy is not yet thoroughly examined [2].

Noises added in image may be caused due to different intrinsic and extrinsic conditions which cannot be avoided in practical situations, among which, few are electricity, heat, sensor illumination levels, environmental issues, etc. Such noises are named based on their properties and/or reasons behind noise induction. Most popular noises among defined noises are Poisson, Gaussian, Salt and Pepper (S&P), and Speckle noise.

Gaussian noise is one of the additive noises whose probability density function is same as that of the normal frequency distribution [1]. It is one of the utmost commonly used noises in image processing as it has uniform distribution throughout the signal. It arises during high temperature and/or transmission and by poor illumination which is termed as Sensor noise [3].

Speckle noise is a multiplicative noise caused due to the influence of environment on image sensor during acquisition. Medical photos, active Radar images, and SAR images are the most common sources of speckle noise [4].

Unlike Gaussian and Speckle noises, Poisson noise is neither additive nor multiplicative. It is noted in gamma rays, visible light, and X-rays where the Electromagnetic (EM) waves have some statistical nature. To be more precise these sources emit photons having random fluctuations resulting in the randomness in images, which is treated as noise. As photons play major role, this noise is also called as Quantum (Photon) noise or Shot noise.

Salt and Pepper noise or Impulse noise is caused due to sharp and sudden changes in the image. Few of such disturbances include ACD converter error, errors during data transmission and/or failure in memory cell. They are generally reflected as white or black spots in the image.

2   Literature Survey

In order to remove the noises mentioned above multiple filter algorithms are adopted and they are classified based on different categories. One such set of classification is linear and nonlinear type of filtering algorithms. Linear filtering is the method for filtering in which the output pixel value is the linear combination of the neighbouring input pixels. It involves convolution and/or transform analysis, whereas Convolution or Fourier multiplication cannot be used to perform nonlinear filtering.

2.1 Median Filter

The elegant approach of linear filters (convolution and/or transform analysis) is not applicable to the median filter because it is nonlinear [5]. A new method of characterising median was introduced using matrix operator. New parameter called 'column sum' it is the added value of each column of median matrix that characterises the input signal and appears at the median filter output along with the trend of a signal extracted from median matrix, that helps in predicting features of signal like trends (maximum/minimum) monotonic behaviour and periodicity.

2.2 Adaptive Median Filter (AMF)

To obtain better quality denoised images, a combination of AMF and weighting mean filter was used. In the case of keeping the image edge as much as probable, this latest method can efficiently remove S&P noise of various densities, as well as Gauss noise. Gauss noise is also well restricted by this method, as the new algorithm uses a mean filter algorithm. Since the adaptive median filter has a good capability for S&P denoising, and the enhanced weighting mean filter has a great effect for Gauss denoising, it is recommended that they are combined and then applied to image denoising pre-process to achieve better images [6].

2.3 Mean Filter (MF)

MF is basically a linear filter. It has the benefit of removing random noise and impulse interference, and also retains image edge information to a larger extent. The idea behind mean filtering is to take a specific type of window and move it around the image, replacing the pixel grey value in the window's centre with the mean values of the pixel grey value in a window. If there are noise lumps in an image or a great amount of noise points in the filter window, the compression extremum method must be used in the filter window. Mean filtering can significantly suppress additive noise, but it also destroys image details and causes the image to blur; therefore, it needs to be improved. When an image is more complex, a better pre-processing can be done by combining it with block average filtering method under the window structure of automatic recognition [7].

2.4 Iterative Mean Filter (IMF)

Further improvements were made in mean filter, which helped in designing Iterative Mean filter. A fixed-size window was considered from which means of a noise-free grey pixels is calculated and used for IMF. PSNR, SSIM, Image Enhancement Factor, Visual Information Fidelity, and Multiscale Structure Similarity are few parameters based on which the quality of the image was accessed [8]. Unlike median filter in which median is calculated and replaced as centre pixel value, in this filter a fixed-size window of 3×3 pixels is considered whose constrained mean is calculated for centre pixel. An iterative process was also introduced in order to remove high-density noise. After experimentation, it was concluded that using IMF, noise is reduced to decent level, and the structure of the image, edges, and details are well preserved hence concluding that IMF outperforms rest of the state-of-the-art denoising methods.

2.5 Recursive Mean Filter

Recursive mean is another type of mean filtering algorithm which is a denoising method to remove noise from an image. In [9] S&P noise was the main focus, and for the purpose of observing the performance of the filter recursive mean filter, it was compared with similar methods, such as DBA, MDBUTMF, and NAFSMF. The quality of the denoised image was verified using PSNR and SSIM. This algorithm was applied on 15 512×512 sized natural images of the MATLAB library. All these images were stored in greyscale mode. To assess the denoising quality, 10, 30, 50, 70, and 90% noise densities were considered. According to the results produced, RMF shows better performance when compared with the known filters whose performance can show further success when the window size is made adaptive.

2.6 Distance-Based Mean Filter (DBMF)

To reduce the S&P noise, a distance-based mean filter was also proposed. To identify noise, adaptive conditions were applied. The DBMF concentrates on pixel similarity based on distance and ignores pixels with noise while determining a new grey value. The DBMF outperformed the adaptive median filter. Experiments were carried out on 20 images from the MATLAB library, each with a different level of noise [10]. The PSNR and SSIM were used to compare various denoising outcomes of DBMF with those of other parallel denoising algorithms (AMF, MDBUTMF, BPDF). It was discovered that DBMF outperforms other approaches in removing noise at various levels.

2.7 Non-local Means (NLM) Filter

The NLM filter [11] was created to remove Gaussian noise; however, it has been updated to reduce speckle noise. A non-local means-based filter is produced by combining a measure of neighbourhood similarity with an optimal weight kernel and neighbourhood reclassification in the filtering process. The NLM algorithm compares the geometrical configuration of an entire neighbourhood. In ultrasound imaging, the NLM filter reduces speckle noise with maximum likelihood estimator. It results in improved noise reduction and edge enhancement. It is best for photographs with tricky structures. The Person distance is introduced as a meaningful measure for patch comparison in the Bayesian non-local means-based filter. This filter beats the SRAD and SBF filters. The median NLM filter suppresses noise while preserving low contrast features.

2.8 Probabilistic Non-local Means (PNLM) Filter

PNLM technique for picture denoising was presented where (1) flaw in the classic NLM's weight function were pointed; (2) all the statistics related to patch-wise differences that are theoretical were derived for Gaussian noise; and (3) this information was used to formulate new weight function for PNLM which reflects the similarities between noisy patches. When NLM weights are substituted with the PNLM weights in the evaluated NLM variations, encouraging results can be seen. The major advantage of this framework is that the denoising process is connected to the type of the noise present in the image, making it useful for denoising a variety of noise kinds. A universal denoising framework for many sorts of noises can be constructed in this way. The PNLM filtering technique also includes a theoretical foundation for quantifying patch similarities, particularly crucial values of D such that $\Pr(D* - \alpha \leq D \leq D* + \alpha \,|fl, k) = \alpha$, which can be utilised as early terminations and thresholds for the rejection or acceptance of similar patch.

2.9 Bilateral Filter (BF)

Bilateral filtering is a local and noniterative method which smooths images while keeping edges using nonlinear combination of nearby data present in the image. It combines the pixels based on their geometric and photometric similarities in which it considers the values that are near rather than the distant ones. Generally, few filters act separately on three bands' colour images. Unlike such filters, bilateral filter contemplates perceptual matric based on CIE-Lab colour space [12]. Bilateral filtering has a generality similar to classical filtering, which is referred to as domain filtering in this chapter. By explicitly enforcing a photometric distance in the range

component of a bilateral filter, it is possible to process colour images in a visually appropriate manner. In reality, just as the parameters of domain filters are determined by the picture qualities and the desired result, the parameters of bilateral filters are determined by the image properties and the desired result. There are multiple types of domain filters among which, one is oriented filters, and these filters can be coupled with range filters.

2.10 Guided Image Filtering

The guided filter is one of the local filters which is linear in nature which now has become one of the fastest edge-preserving filters. Guided filter uses a reference image called guided image whose content is used to compute the filtered output [13]. Beyond smoothing, the guided filter can transfer the structures of the guidance image to the filtering output, allowing for novel filtering applications such as dehazing and guided feathering. Experiments demonstrate that the guided filter works well in a wide range of computer vision and computer graphics applications. Few of such applications are edge-aware smoothing, detail improvement, HDR compression, picture matting/feathering, dehazing, joint upsampling, and so on. Firstly, they create a new filter that has the good edge-preserving smoothing property while still being efficient and non-approximate to compute. Local linear model is a learning model that is unsupervised; hence, more models can be designed using guided filter with advanced performance. This is something that is left to future research.

2.11 Guided Bilateral Filter (GBF)

The BF, as well as its variants just like joint/cross BF, are famous edge-preserving image smoothing methods. Robust estimate is known to be linked to the bilateral filter. A new method was presented for obtaining the joint/cross bilateral filter as an example of a general filter, which is called the guided bilateral filter [14]. This novel filtering technique is generic, iterative, and employs a guide image. It inherits the robustness qualities of the robust bilateral filter. The GBF can handle non-Gaussian noise on picture to be filtered with this methodology using a scheme which converges local minimum level when the cost function is nonconvex. A probabilistic elucidation of the weights might be utilised to merge the filter derivation. This filter takes two photos as inputs: the image to be handled and the guiding image. If the guide is of good quality, the GBF only requires four input parameters; otherwise, it requires five. Depending on input data, the insights and commendations for setting these parameters were given to it. From the viewpoint of robust statistics, derivation of the bilateral filter was examined. It has been demonstrated experimentally that the only IRLS implementation (named Robust Bilateral Filter) completely assures robustness in the existence of noise and outliers. In terms of PSNR, the GBF surpasses three

other filters that use a guide picture in experiments. Outliers in the picture to be processed are robust to the proposed filter, but not the outliers of the guide image. To get around this constraint, re-processing the guide using something like the Robust Bilateral Filter is recommended.

2.12   Unsharp Mask Guided Filtering

A new and simplified guided filter was presented with an argument that estimating two or more coefficients at the same time is inefficient, resulting in halo artefacts and inconsistencies in the structure. Through the study of unsharp masking, better guided filter is introduced that requires only single coefficient. Considering the improved formulation of guided filter, successive guided filtering network was introduced. In order to create a path for the improvement in efficiency and accuracy, alternative filtering outcomes can be selected during interphase. According to the results, it was observed that the projected filtering method sanctuaries sharp and thin edges. It was also shown that the proposed approach works for a variety of applications, including up sampling, denoising, and cross-modal filtering.

2.13   Weiner

The elimination of noise from medical images is critical, and the Wiener filter is employed to do it effectively. The main purpose of the Wiener filter is to lower image noise by comparing it to the original image. Because of its simplicity and speed, this filter is commonly used [15]. It is simple because it calculates a set of ideal filter weights using a system of linear equations, lowering the noise level of a received signal. According to the findings, Wiener is effective in de-blurring and noise reduction in images.

2.14   Collaborative Weiner Filter and Explicit Guided Filter for Denoising—A Hybrid Approach

A new image denoising filter algorithm was designed using explicit guided filter and collaborative Wiener filter in which edge-preserving properties of guided filter and de-blurring properties of Wiener filter were used. The major goal of this filter was to minimise the blurring of the image and reduce the loss of useful information. During pre-processing, the structure of reference image used in guided image transfers its structure to the output, i.e. pre-processed image. The Wiener filter is used to process the noisy input image, and this pre-processed output image is also used for

collaborative filtering. When compared to the guided filter, the results shown by this strategy are capable of achieving greater denoising performance regardless of the image format. It can be used for picture restoration, smoothing, HDR compression, dehazing, enhancement, and joint upsampling. After the experimentation [16], it was observed that not only fine features and edges of the image were preserved using this hybrid approach, but also the blurring was condensed to a decent level. As a result, the Wiener filter enhances the outcomes. This method produces good outcomes in a reasonable amount of time and money.

3   Conclusion

It is evident from the results of several filtering techniques, that the median filter is adequate for Salt and Pepper (S&P) noise. It detects the centre pixel value by employing column sum in a matrix, and if the window size is larger, it takes more time depending on the size of the window. The main benefit of using a Mean filter is that it removes random noise and impulse interference while also retaining more image edge information. It can also considerably reduce additive noise. Gaussian noise and S&P noise can be removed with the use of an Adaptive Mean filter. When this filter is combined with Gauss denoising, better results are obtained. Non-local Mean filters are superior at reducing speckle and Gaussian noises, and they're employed for noise reduction and edge enhancement. The Probabilistic Non-Local Means denoising technique is dependent on the type of noise in the image, making it suitable for all known and unknown noises. Not only does the Bilateral filter improve denoising outcomes, it also integrates numerous types of domain filters to create a diverse collection of denoising algorithms. Guided filter provides smoothening effect, and it can also be used for transforming structures from guided image to output image. Hence, it is used for a wide range of computer vision and graphic applications which include edge-aware smoothing, detail improvement, HDR compression, picture matting/feathering, dehazing, joint upsampling, and so on. The Wiener filter is particularly known for its simplicity and quickness, but it can also be used to de-blur images and reduce noise.

References

1. https://au.element14.com/gaussian-noise-definition
2. Sathesh A (2020) Light field image coding with image prediction in redundancy. J Soft Comput Paradigm 2(3):160–167
3. https://en.wikipedia.org/wiki/Gaussian_noise
4. Maity A, Pattanaik A, Sagnika S, Pani S (2015) A comparative study on approaches to speckle noise reduction in images. In: 2015 international conference on computational intelligence and networks, pp 148–155. https://doi.org/10.1109/CINE.2015.36

5. Devarajan G, Aatre VK, Sridhar CS (1990) Analysis of median filter. In: ACE'90. Proceedings of [XVI annual convention and exhibition of the IEEE in India], pp 274–276. https://doi.org/10.1109/ACE.1990.762694

6. Sun H, Zhang L, Jin X (2012) An image denoising method which combines adaptive median filter with weighting mean filter. In: Proceedings of 2012 international conference on measurement, information and control, pp 392–396. https://doi.org/10.1109/MIC.2012.6273278

7. Weizheng X, Chenqi X, Zhengru J, Yueping H (2020) Digital image denoising method based on mean filter. In: 2020 international conference on computer engineering and application (ICCEA), pp 857–859. https://doi.org/10.1109/ICCEA50009.2020.00188

8. Erkan U, Thanh DNH, Hieu LM, Engínoğlu S (2019) An iterative mean filter for image denoising. IEEE Access 7:167847–167859. https://doi.org/10.1109/ACCESS.2019.2953924

9. Erkan U, Engınoğlu S, Thanh DNH (2019) A recursive mean filter for image denoising. In: 2019 international artificial intelligence and data processing symposium (IDAP), pp 1–5. https://doi.org/10.1109/IDAP.2019.8875957

10. https://doi.org/10.1145/3380688.3380704

11. Wilson B, Dhas JPM (2013) A survey of non-local means based filters for image denoising. Int J Eng Res Technol (IJERT) 02(10)

12. Tomasi C, Manduchi R (1998) Bilateral filtering for gray and color images. In: Sixth international conference on computer vision. IEEE Cat. No. 98CH36271, pp 839–846. https://doi.org/10.1109/ICCV.1998.710815

13. He K, Sun J, Tang X (2013) Guided image filtering. IEEE Trans Pattern Anal Mach Intell 35(6):1397–1409. https://doi.org/10.1109/TPAMI.2012.213

14. Caraffa L, Tarel J-P, Charbonnier P (2015) The guided bilateral filter: when the joint/cross bilateral filter becomes robust. IEEE Trans Image Process 24(4):1199–1208. https://doi.org/10.1109/TIP.2015.2389617

15. Sailaja V, Sunitha P, Vasantha Lakshmi B, Prasanth V (2019) Wiener filtering in frequency domain to enhance speech corrupted by colored noise. Int J Rec Technol Eng 8(2S11)

16. Parihar AS, Garg Y, Bisht S (2020) A hybrid approach for image denoising using explicit guided filter and collaborative wiener filter. In: 2020 2nd international conference on advances in computing, communication control and networking (ICACCCN), pp 1040–1045. https://doi.org/10.1109/ICACCCN51052.2020.9362732

An Analysis of Codebook Optimization for Image Compression: Modified Genetic Algorithm and Particle Swarm Optimization Algorithm

Pratibha Chavan, B. Sheela Rani, M. Murugan, Pramod Chavan, and M. Kulkarni

Abstract Billions of images are uploaded daily, and it requires a large storage space. Utilization of better storage capacity and to improve uploading/downloading time, researchers have designed an image compression model. Many researchers have implemented various approaches to improve the image compression ratio of an image. This paper presents an analysis of various optimization algorithms based on vector quantization (VQ). The first algorithm is a modified genetic algorithm. It is based on Darwin's principle which is natural characteristics. Those who are fit can survive and use it to optimize the codebook. A second algorithm for optimization of the codebook is particle swarm optimization (PSO). PSO algorithm is superior to finding the codeword vectors of codebook from the training image samples for image compression. In the PSO algorithm, the selection approach plays an important role to select the particle based on the fitness of the population. Training images from the standard image database are used for the design of the codebook. The input image set is 4×4 or 8×8 blocks and is represented as vectors. They are referred to as codewords in the codebook, and it is a component of a code. The codebook size is measured by codewords. The block size is decided by the length of the codeword. These codewords generate the codebook by entering the vector value. Compression is done with the help of sending indices to the decoder. Likewise, analysis of quality measures is presented to the modified GA and PSO algorithms based on mean square

P. Chavan · B. Sheela Rani (✉)
Sathyabama Institute of Science and Technology (Deemed to be University), Jeppiaar Nagar, Rajiv Gandhi Salai, Chennai, Tamil Nadu 600 119, India
e-mail: sheelarani@sathyabama.ac.in

P. Chavan · M. Kulkarni
Department of E&TC Engineering, Trinity College of Engineering and Research, Pisoli, Pune, Maharashtra 411048, India

M. Murugan
SRM Valliammai Engineering College, Kattankulathur, Chengalpattu District, Tamil Nadu 603203, India

P. Chavan
Department of E&TC Engineering, K J College of Engineering and Management Research, Pisoli, Pune, Maharashtra 411048, India

© The Author(s), under exclusive license to Springer Nature Singapore Pte Ltd. 2023   849

error, peak signal-to-noise ratio, structural similarity index, and average difference. In this work, we have calculated bits per pixel (BPP), the compression ratio (CR), and the % compression ratio. The experimental results are validated.

Keywords Codebook · Modified genetic algorithm · Particle swarm optimization · Vector quantization

1 Introduction

Image compression [1–3] is essential because the education system is using the online platform for teaching, and demand increases for digital notes to be shared with students all over the world. As doctors are doing research on placid trail for patients of COVID-19, the same numerous data storage of patient increases. It improves the transmission speed of information to be transmitted or received in hybrid communication channel and furthermore modern applications [4, 5]. Image compression is classified into a lossy image compression [6] and lossless image compression. These techniques are challenging that to achieve a good compression ratio [7, 8]. Due to small information loss, quality of restoration is poor in lossy method [9, 10]. Lossless image compression technique is having negligible loss [11, 12]. Therefore, the data of the encoder and decoder are closely similar, and the restoration quality is good. Depending on application, researchers can select lossy or lossless image compression [13–15].

Research flow is as follows:

1. This research work is based on vector quantization.
2. The input image is divided into 4 by 4 blocks, and that input vectors are represented by 16-bit codeword.
3. Modified GA and PSO are codebook optimization algorithms, and they are used to improve compression ratio.
4. To achieve good compression ratio, error must be minimum.
5. In the end, the analysis of the BPP and CR is compared.

The work is prepared in following sections. Section 2 scrutinizes the literature survey. Section 3 presents vector quantization method, and Sect. 4 exposes modified GA and PSO. Section 5 presents the experiments, and research work is concluded in Sect. 6.

2   Literature Review

2.1   *Contribution by Researchers*

In 2020, Shakya, Subarna, and Lalitpur, Nepal Pulchowk introduced a novel bi-velocity particle swarm optimization scheme for multicast routing problem. Dhaya R. and R. Kanthavel introduced comprehensively meld code clone identifier for replicated source code identification in diverse web browsers. Daniela Sánchez, Patricia Melin, and Oscar Castillo have investigated the firefly algorithm (FF) [6]. Blinking characteristics of fireflies are used in this model. One important feature is that regardless of their sex, fireflies are attracted to one another. Brighter the control attractiveness, brighter the firefly attracts the less bright firefly, else move by chance. Proficient codebook is designed using firefly algorithm [16]; the challenge is less availability of brighter fireflies in exploring.

In 2019, Panda and Das [17] have introduced a gray wolf optimizer (GWO). The gray wolves have hunting behavior and leadership hierarchy. This algorithm is character-motivated algorithm and used for optimization [18]. Neighboring region is supported for the primary elucidation of every progression to produce the best outcome. If termination criteria are not fulfilled, then step will be continued [19].

In 2018, Cui, Z., Li, F. and Zhang, W. have introduced VQ-based bat algorithm (BA). BA is used for image compression. BA technique improves the result. The codebook is designed efficiently by varying all possible parameters.

In 2016, Mirjalili and Lewis [20] have presented whale optimization algorithm. WOA follows the group performance. This algorithm is encouraged through the bubble-net track approach. This is a popular optimization algorithm when it is evaluated with conventional methods [21]. Hence, all these features are considered in this research work along with the challenges faced by these optimization algorithms. This paper is enlightening the performance of image compression models by GA and PSO algorithms.

2.2   *Problem Definition*

New era of internet is demanding for compressed image for the same need to design an optimal codebook with better compression rate and minimum error at reconstructing image [1]. Researchers have proposed optimization techniques for codebook generation because the performance of VQ depends on codebook. Image compression model using modified genetic algorithm was presented in [2] that provides minimized error at reconstructing the image. Selection, crossover, and mutation operators are used for codebook design. Outcomes were satisfactory appropriate to its unique chromosome feature use in the codebook design. Limitation of modified GA is that it undergoes more execution time when population size is large. The researcher has proposed another optimization technique called particle swarm optimization (PSO)

[3]. It offers a superior efficiency and better compression ratio. It initializes the swarm size and calculates the fitness value. Those who are best fit swarm, that position is updated by replacing previous swarm. The steps are repeated until it fulfills the criteria. If the position of the swarm is not varied or the termination criteria are satisfied, then stop. The best position of the particles is updated. For the maximum particle velocity, instability occurs in the particles. It is necessary for analyzing these optimization models to get better image compression results.

2.3 Motivation

Optimization algorithms, specialization, and problem face for image compression are described in Table 1. At first, the modified genetic algorithm has been implemented [2] which reduces artifact impacts and simplifies the design of the codebook. Modified GA is based on natural characteristics, so there would be no chances of duplications and gives better results. Modified GA has challenge to produce optimal outcomes. Likewise, second algorithm has explored a novel approach by vector quantization for image compression using particle swarm optimization (PSO) algorithm, which is a superior model. PSO is high quality and better than other optimization model. Therefore PSO model could outperform the other image compression standards. Analysis of these optimization models is to be presented in this paper.

Table 1 Characteristics and problems face in various image compression models

Algorithm	Characteristics	Problem face
Modified genetic algorithm	Reduced artifact impacts	The challenge to produce optimal outcomes
PSO algorithm	Superior compression ratio	For the high particle velocity challenge is stability
Firefly algorithm	Generate an efficient codebook	Shortage of brighter fireflies
Bat algorithm	Provide high PSNR as compared to the LBG	No significance difference in PSO

3 Novel Idea of the Proposed Technique Andmodels

3.1 A. Vector Quantization and Codebook Optimization Method

VQ process is superior to scalar quantization techniques. VQ can reduce the distortion with the number of reconstruction levels in keeping constant. Scalar quantization quantizes every value individually.

Figure 1 shows scalar quantization. Vector quantization is complex method and quantizes several values jointly. VQ is usual a lossy image compression technique and presents good compression ratio as shown in Fig. 2.

Vector quantization is a conventional methodology for image compression. As a main contribution, codebook is optimized in such a way that it minimizes error in the reconstructed image. A few images from the database are used for the codebook generation. Set of blocks is presented as vectors. The encoder sends their indices to achieve a compression through a channel. Output file reconstructs the image by placing correct vectors on the image with the help of decoder. The codebook is optimized using optimization algorithms, i.e., GA and PSO, and we could get

Fig. 1 Scalar quantization
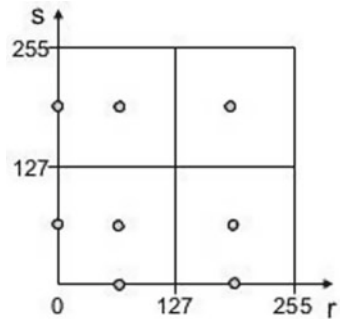
Fig. 2 Vector quantization
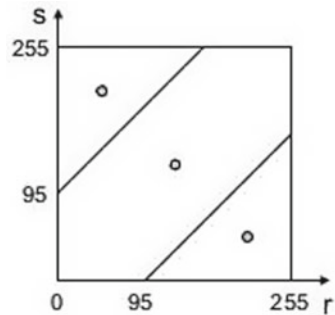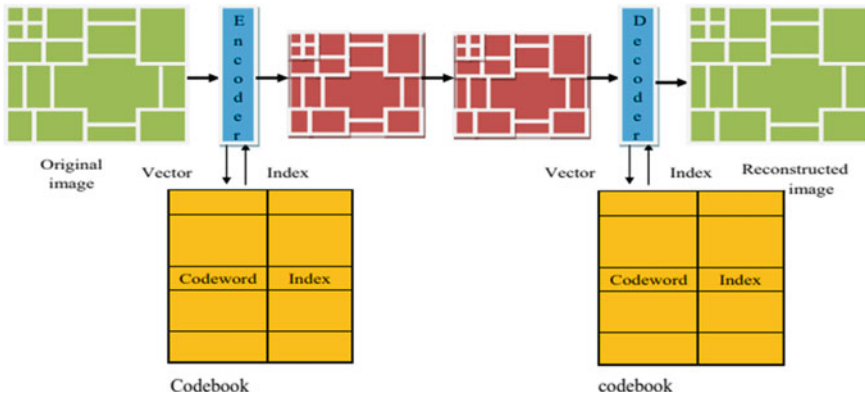
Fig. 3 Architecture of the vector quantization

better results. In this paper, we are presenting the analysis using these optimization algorithms. The architecture of the vector quantization is demonstrated in Fig. 3.

3.2 Codebook Structure and Fitness Function

The codewords cd1 are stored in the codebook cb1. The size of the codebook can be changed depending upon the size of the input image. Codebook cb1 consists of 256 codewords, i.e., cd1 (1, 1), cd1 (1, 2) … cd1 (1, 256). These codewords are divided further in three parts, viz. the code of codebook (cbook1), indices/positions of codebook (imgind1), and their corresponding image value/pixel (imgcd1). Figure 4 shows the structure of the codebook. A set of chromosomes is stored in cbook1 of cd1 (1, 1) by the process of chromosome selection, and then crossover and mutation are performed on these stored chromosomes. The selection of chromosome, crossover, and mutation take place on a random basis. Then again a new set of chromosomes is selected for cd1 (1, 2), and the entire process is repeated again up to cd1 (1, 256). 0– 255 blocks can be designed in the codebook, and up to 256 codewords are presented for distribution [1]. To design the codebook in such a way that it minimizes the image compression effect.

The tradeoff between the number of codeword selected and the extent to which distortion in the image is bearable must be decided [11]. The traditional vector quantization techniques failed to cope up with this requirement to some extent. Thus, for designing an optimal codebook design, the principles of clustering are applied to the traditional vector quantization algorithm. Image is initially divided into $n \times n$ non-overlapping subdivisions. The similar data vectors are then identified from these subdivisions (blocks) and placed into similar groups. Codebook is generated with the reference input vectors, and then we apply a quantization process. Now, instead of selecting a separate codeword for each of the vectors, the same codeword

Fig. 4 Structure of codebook
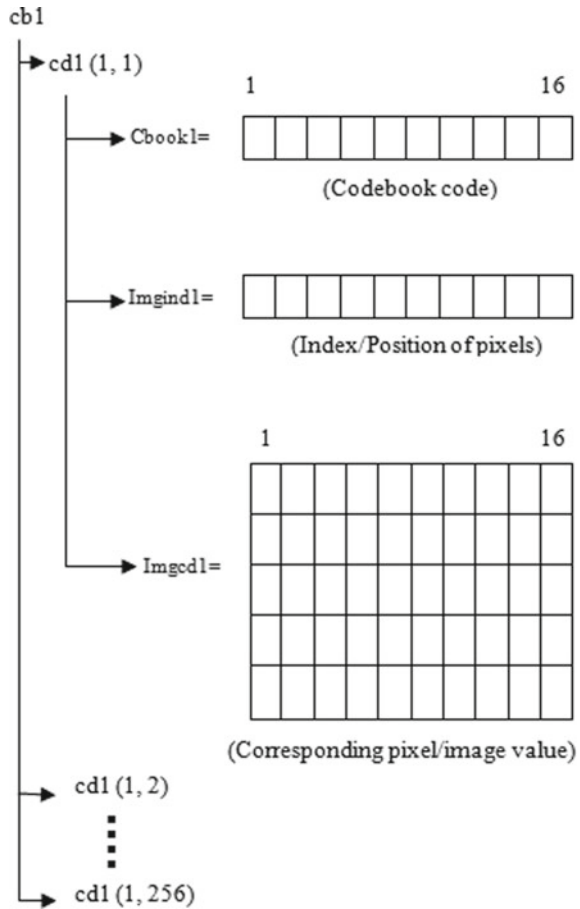
is selected for all the vectors that are placed in the same group and the process of vector quantization is carried out for generation of an optimal codebook. Thus, clustering reduces the number of codewords to be used in the codebook design [3]. The lesser the number of codewords used the higher is the compression ratio achieved and lesser is the image distortion. The identical index of this codeword is transmitted at output file. Figure 5 shows the image division into 4×4 non-overlapping blocks and the initial codebook generated using vector quantization.

Efficiency of genetic algorithm depends on fitness, and it is used for the selection of chromosomes. Fitness is calculated with the help of MSE.
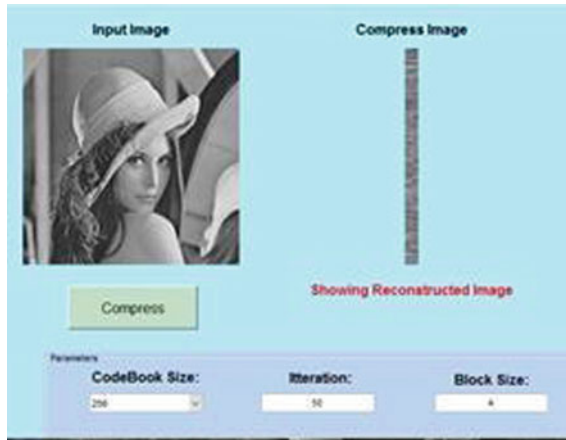
Fig. 5 Image division into 4 × 4 non-overlapping block and codebook generated using vector quantization

3.3 Algorithm for Initial Codebook Generation is Given as Follows

Algorithm for initial codebook generation
Step 1: Input image as training set
Step 2: The input image is converted into appropriate structure by dividing it into non-overlapping blocks
Step 3: The blocks of image to be selected for a codeword are picked up on the basis of the code in MATLAB
Step 4: Calculate fitness of all solutions
Step 5: Evaluate the best fitness function
for I = 1: n hpsnr = 0
for j = 1: q level if tpsnr > hpsnr
hpsnr = tpsnr;
best_unit = j;
end
next j
next i
end

Number of blocks that belong to the codebook (best-unit) + 1; allocate the block position to the blocks that belong to the best unit in the array of codebook; here, *n* is the number of blocks in the input image, and *q* level corresponds to the quantization level used.

3.4   Quality Measures Are as Follows

3.4.1   Peak Signal-to-Noise Ratios (PSNR)

In image compression, PSNR measures appearance the quality of the image to a detrimental level. PSNR equation is as follows (1),

$$PSNR = 10 \log 10 \left(255 \times \frac{255}{MSE} \right) \tag{1}$$

$$PSNR = 10 \cdot \log_{10} \left(\frac{MAX_I^2}{MSE} \right)$$

$$= 20 \cdot \log_{10} \left(\frac{MAX_I}{\sqrt{MSE}} \right)$$

$$= 20 \cdot \log_{10}(MAX_I) - 10 \cdot \log_{10}(MSE)$$

Here, MAX_I is the maximum possible pixel value of the image. Let us consider pixels are 8 bits per sample, then it is 255. In the absence of noise, images I and K are same and thus the MSE is zero. Practically, PSNR is around 30 dB.

3.4.2   Mean Square Error (MSE)

Calculate variations among the actual and reference pixel, and its average is represented by mean squared error. MSE is measured as (2).

$$MSE = \frac{1}{mn} \sum_{i=0}^{m-1} \sum_{j=0}^{n-1} [I(i, j) - K(i, j)]^2 \tag{2}$$

3.4.3   Structural Similarity (SSIM) Index

It is a quality measure, and its score is represented by an Eq. (3)

$$SSIM(x, y) = [l(x, y)]^\alpha \cdot [c(x, y)]^\beta \cdot [s(x, y)]^\gamma \tag{3}$$

SSIM is concerned with quality measurement method to local region using a sliding window approach. Size of $B \times B$ moves horizontally and vertically from top-left corner to bottom-right corner, all over the image. Accuracy of SSIM is great but acquires more computational cost.

3.4.4 Average Difference (AD)

The difference between the input image and output image in image compression is represented as (4)

$$AD = \frac{1}{MN} \sum_{i=1}^{M} \sum_{j=1}^{N} (x(i, j) - y(i, j)) \tag{4}$$

where $x(i, j)$ represents the input (reference) image and $y(I, j)$ represents output image.

4 Codebook Optimization Models

4.1 Modified Genetic Algorithm

Modified genetic algorithm is used as a natural characteristic for optimization of codebook design in vector quantization for image compression.

Modified GA steps are as follows:

Procedure: Modified Genetic Algorithm

Generation of initial chromosomes
While, iterations $\tau < \tau_{off}$
for $\tau = 1\ to100$
Step 3: Calculate the fitness of all solutions
Step 4: Evaluate the best fitness function

Step 5: Selection operator: Select the best fit parent chromosome
Step 6: Crossover operator: Select the best fit children chromosomes
Step 7: Mutation operator: Mutate other children chromosome than the best fitting one
Step 8: Find best fitness solutions
Step 9: Update the best fitness chromosome
Step 10: Termination: if the criterions are satisfied
Step 11: If not then Return step 2
Step 12: $\tau = \tau + 1$
 end for end while
End

Quality of codebook depends on fitness, and fitness is better for minimum error in reconstructed image. Clustering is used to cluster similar data into same block. Genetic operators are selection, crossover, and mutation.

Selection of the best fit children chromosome:

(1) Generate random population of n chromosomes.

(2) Calculate the fitness of each chromosome in the population.
(3) Select two parent chromosomes those who are best fit.
(4) Crossover the parents to generate a children.
(5) Apply mutation probability.
(6) Place best fit children in a new population.

4.2 Particle Swarm Optimization Algorithm

This method is for optimizing the codebook through the significance of each particle and exploit pbest and best to focus the automatic clustering. Clustering reduces the computational complexity, while the stochastic search method of PSO algorithm helps in obtaining an optimal solution [3, 6]. PSO is a multi-agent approach based on the bird flocking and used for optimization. It is starting with a random particle solution. They move to search for optima by renewing iterations and each particle by two "best" values. The best solution (fitness) it has reached and referred as pbest. Another "best" value in the population is a global best and referred as gbest. In this model, xi is particle position and vi is velocity. The best position in the vector is pbest. Updated velocity is found with the help of Eqs. (5) and (6).

$$Vid' = w * vid + c1 * r1 * (pbest - xid) + c2 * r2 * (gbest - xid) \quad (5)$$

$$Xid' = xid + Vid' \quad (6)$$

Inertia weight is represented by w, random numbers are $r1$ and $r2$, coefficient of the self-recognition component is $c1$, social component is $c2$, and both are positive constant. Based on the best position, particle leads effectively in the search space. The development of PSO [3] is based on a particle's position toward a target location.

Steps of PSO:

Procedure: Particle swarm optimization
Step 1: Selection of particle
Step 2: Calculate fitness
Step 3: Update pbest
Step 4: Select gbest
Step 5: Particle velocity calculation
Step 6: Renew position of the particle
Step 7: Steps are repeated till termination criteria are achieved

Velocity and position of each particle are randomly initialized. Particle maintains its pbest (local best position) and gbest (global best position). To renew the position of given particle, current position of these particles should be better than the previous one.

5   Experimental Results

The PSO and GA were tested in MATLAB. In this database included category 1, 2, 3, and 5 images were downloaded from standard database and for category 4 were manually collected.

The analysis of the compression ratio and BPP is demonstrated in Table 2. Results are compared with other algorithms [17–21]. The original image is shown in following Fig. 6, and decompressed by modifying GA is shown in Fig. 7, and Fig. 8 shows decompressed by PSO. CR analysis of optimization algorithms is shown Fig. 9.

We are also demonstrating results on gray-level image. The parameter used in the experimentation is population size: 50 and 100. We continue this uniformity testing. We have set different iterations: 10 and 50. In the experimentation, we divide the image into 4×4 and 8×8 blocks to encode. We have designed a codebooks using optimization algorithms. In the output file, send indexes to represent every codeword. Initial population is selected with best fitness chromosomes. It has been observed [1, 2] that if the initial chromosomes are fit, then the solution of clustering would be best

Table 2 Types of images and sets

Type of image	Total images in each set
Texture images (category 1)	50 images
Nature image set (category 2)	30 images
Medical image set (category 3)	30 images
Satellite image set (category 4)	10 images
Miscellaneous set (category 5)	50 images
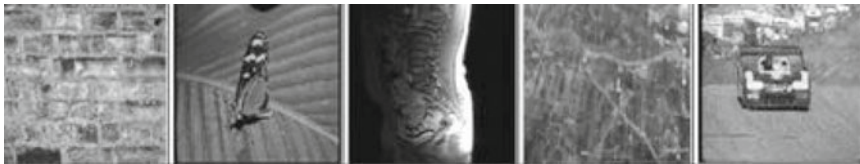
Fig. 6 Original image: **a** texture image, **b** nature image, **c** medical image, **d** satellite image, and **e** miscellaneous image

Fig. 7 Decompressed image by modifying GA: **a** texture image, **b** nature image, **c** medical image, **d** satellite image, and **e** miscellaneous image
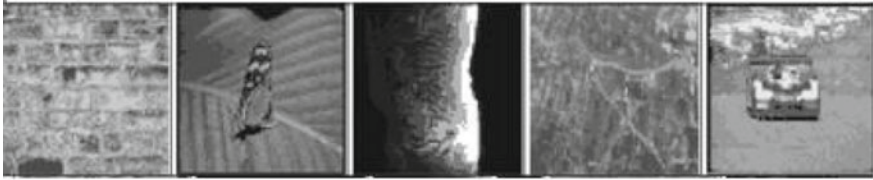
Fig. 8 Decompressed image by PSO: **a** texture image, **b** nature image, **c** medical image, **d** satellite image, and **e** miscellaneous image
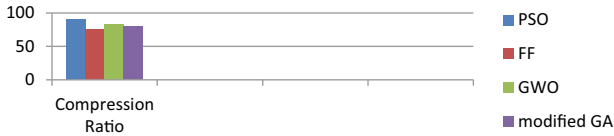
Fig. 9 CR analysis of optimization algorithms

as it has much depends on them. The result shows that quality measure parameters are achieved by PSO which is greater than the modified genetic algorithm. Training sets (Fig. 10) are taken with size 512X512, and reconstructed image is shown in Fig. 11. Performance analysis of optimization algorithms are shown in Figs. 12, 13, 14, 15, 16, 17, 18 and 19. Comparison of quality measures is shown in Tables 3 and 4.

Fig. 10 Training image of Leena (512 × 512)

Fig. 11 Reconstructed image of Leena
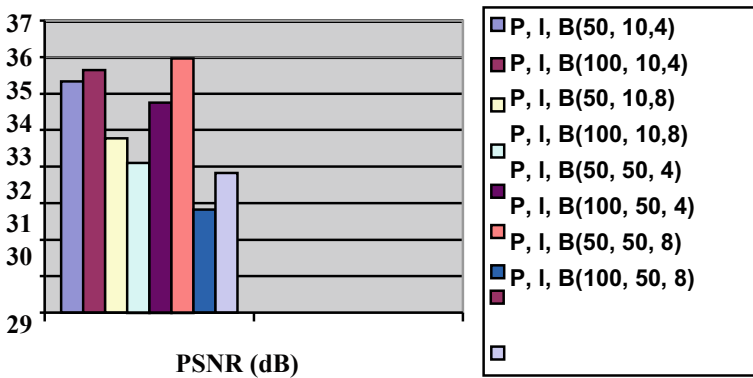
Fig. 12 PSNR analysis of optimization algorithms
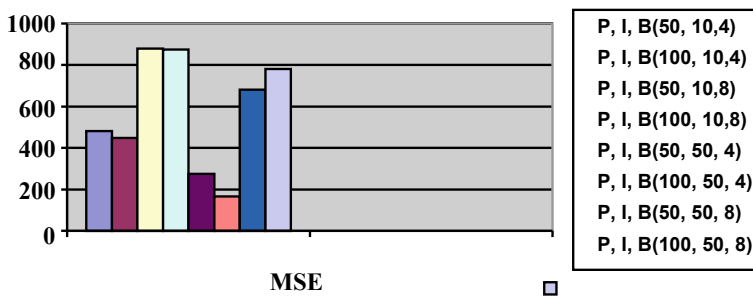
Fig. 13 MSE analysis of optimization algorithms

6 Conclusion

Analysis of image compression has been simulated in MATLAB, and the experimentations have been carried out. The performance of the PSO algorithm is to be compared with a modified GA algorithm in terms of analysis on error measures
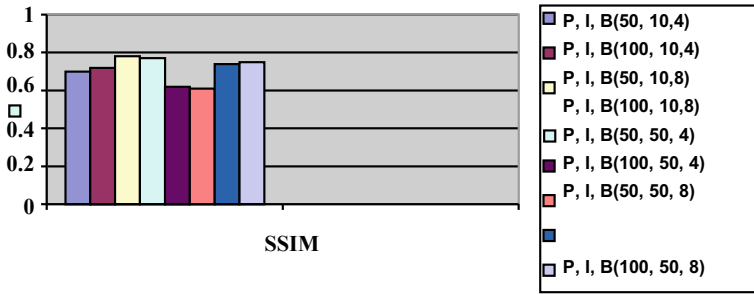
Fig. 14 SSIM analysis of optimization algorithms
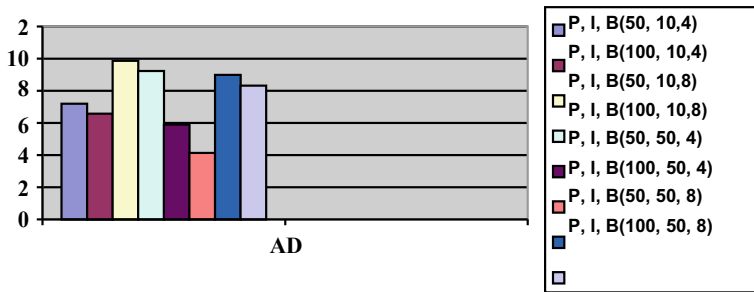
Fig. 15 AD analysis of optimization algorithms
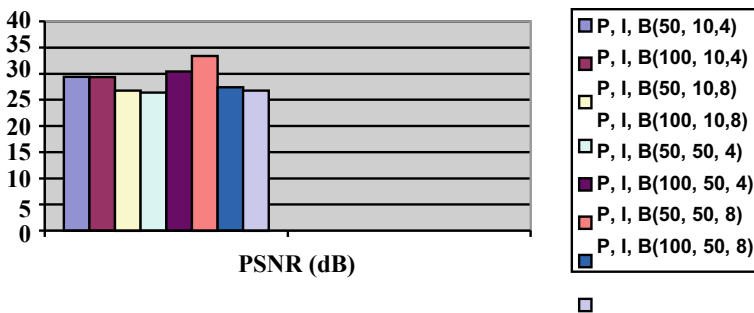
Fig. 16 PSNR analysis of optimization algorithms

like PSNR, MSE, SSIM, and AD. Experimental results show that the PSO is better than the modified genetic algorithm. We have shown that PSO outperforms the image compression standard. A bitrate, BPP, is 8. The compression ratio for PSO is 90.90%, for FF it is 75%, GWO it is 83.33%, and 80% of modified GA. The experimental results indicate clear superiority of PSO over the existing techniques. From result, we have proved that the % of the CR of PSO model is best among other models.
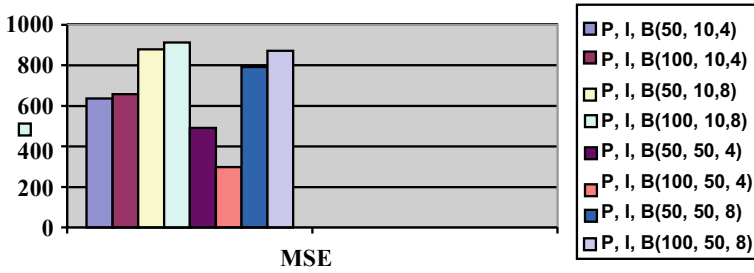
Fig. 17 MSE analysis of optimization algorithms
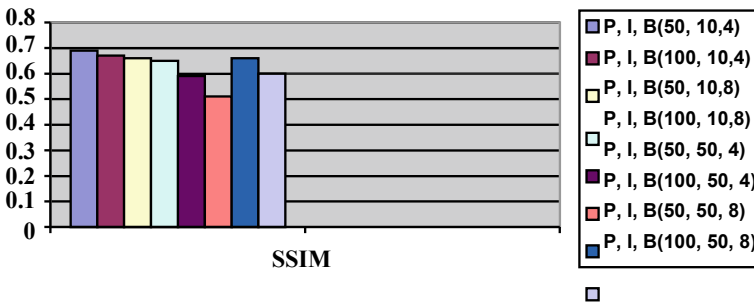
Fig. 18 SSIM analysis of optimization algorithms
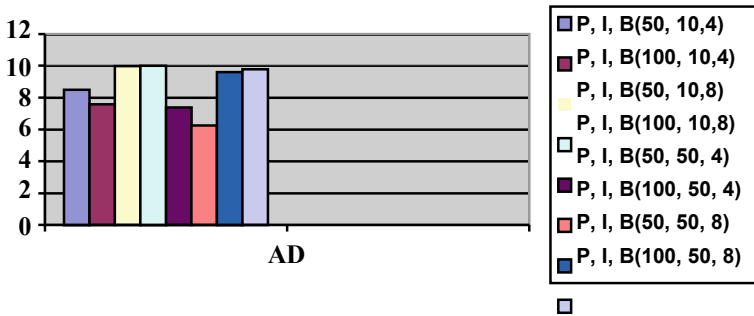
Fig. 19 AD analysis of optimization algorithms

Table 3 Comparison of quality measures block size of 4 × 4 and 8 × 8, iteration 10 and 50, population size 50 and 100 using the PSO algorithm on grayscale image 512 × 512 and codebook size = 256

Population size (P)	Iteration (I)	Block size (B)	PSNR (dB)	MSE	SSIM	Average difference
50	10	4	35.34	480.82	0.70	7.19
100	10	4	35.64	448.29	0.72	6.58
50	10	8	33.77	878.73	0.78	9.87
100	10	8	33.10	875.11	0.77	9.23
50	50	4	34.76	275.37	0.62	5.90
100	50	4	35.96	166.13	0.61	4.13
50	50	8	31.83	680.87	0.74	8.99
100	50	8	32.83	780.87	0.75	8.33

Table 4 Comparison of quality measures with block size of 4 × 4 and 8 × 8, Iteration 10 and 50, Population size 50 and 100 using modified GA algorithm on grayscale image 512 × 512 and codebook size = 256

Population size (P)	Iteration (I)	Block size (B)	PSNR (dB)	MSE	SSIM	Average difference
50	10	4	29.41	636.49	0.69	8.51
100	10	4	29.36	658.37	0.67	7.68
50	10	8	26.77	874.44	0.66	9.99
100	10	8	26.36	913.17	0.65	10.00
50	50	4	30.44	491.36	0.59	7.38
100	50	4	33.41	298.24	0.51	6.26
50	50	8	27.40	791.83	0.66	9.62
100	50	8	26.79	871.46	0.60	9.79

References

1. Rajkumar S, Malathi G (2016) A comparative analysis on image quality assessment for real time satellite images. Indian J Sci Technol 9(34). https://doi.org/10.17485/ijst/2016/v9i34/96766. ISSN (Print): 0974-6846
2. Sánchez D, Melin P, Castillo O (2020) Modular granular neural network optimization using the firefly algorithm applied to time series prediction. In: Yang X-S (ed) Nature-inspired computation and swarm intelligence. Academic Press, pp 199–216 (Chapter12). https://www.sciencedirect.com/science/article/pii/B9780128197141000233
3. Panda M, Das B (2019) Grey wolf optimizer and its applications: a survey. In: Nath V, Mandal J (eds) Proceedings of the third international conference on microelectronics, computing and communication systems. Lecture notes in electrical engineering, vol 556. Springer, Singapore. https://doi.org/10.1007/978-981-13-7091-5_17
4. Mirjalili S, Lewis A (2016) The whale optimization algorithm. In: Advances in engineering software, vol 95, pp 51–67. ISSN 0965-9978. https://doi.org/10.1016/j.advengsoft.2016.01.008. https://www.sciencedirect.com/science/article/pii/S0965997816300163

5. Cui Z, Li F, Zhang W (2019) Bat algorithm with principal component analysis. Int J Mach Learn Cyber 10:603–622. https://doi.org/10.1007/s13042-018-0888-4

6. Pang C-Y, Zhou R-G, Hu B-Q, Hu WW, El-Rafei A (2019) Signal and image compression using quantum discrete cosine transform. Inf Sci 473:121–141

7. Ernawan F, Kabir N, Zamli KZ (2017) An efficient image compression technique using Tchebichefbit allocation. Opt Int J Light Electron Opt 148:106–119

8. Roy SK, Kumar S, Chanda B, Chaudhuri BB, Banerjee S (2018) Fractal image compression using upper bound on scaling parameter. Chaos Solitons Fractals 106:16–22

9. Brahimi T, Laouir F, Boubchir L, Ali-Chérif A (2017) An improved wavelet-based image coder for embedded greyscale and colour image compression. AEU-Int J Electron Commun 73:183–192

10. Xiao B, Lu G, Zhang Y, Li W, Wang G (2016) Lossless image compression based on integer discrete Tchebichef transform. Neuro Comput 214:587–593

11. Turcza P, Duplaga M (2017) Near-lossless energy-efficient image compression algorithm for wireless capsule endoscopy. Biomed Sig Process Control 38:1–8

12. Zuo Z, Lan X, Deng L, Yao S, Wang X (2015) An improved medical image compression technique with lossless region of interest. Opt Int J Light Electron Opt 126(21):2825–2831

13. Chaurasia VS, Chaurasia V (2016) Statistical feature extraction based technique for fast fractal image compression. J Vis Commun Image Represent 41:87–95

14. Hussain AJ, Al-Fayadh A, Radi N (2018) Image compression techniques: a survey in lossless and lossy algorithms. Neuro Comput 300:44–69

15. Fu C, Yi Y, Luo F (2018) Hyperspectral image compression based on simultaneous sparse representation and general-pixels. Pattern Recogn Lett 116:65–71

16. Ji XX, Zhang G (2017) An adaptive SAR image compression method. Comput Electr Eng 62:473–484

17. Skorsetz M, Artal P, Bueno JM (2018) Improved multiphoton imaging in biological samples by using variable pulse compression and wavefront assessment. Opt Commun 422:44–51

18. Rashid F, Miri A, Woungang I (2016) Secure image deduplication through image compression. J Inf Secur Appl 27–28:54–64

19. Huang H, He X, Xiang Y, Wen W, Zhang Y (2018) A compression-diffusion-permutation strategy for securing image. Sig Process 150:183–190

20. Shakya S, Pulchowk LN (2020) A novel bi-velocity particle swarm optimization scheme for multicast routing problem. IRO J Sustain Wireless Syst 2:50–58

21. Dhaya R, Kanthavel R (2020) Comprehensively meld code clone identifier for replicated source code identification in diverse web browsers. J Trends Comput Sci Smart Technol (TCSST) 2(02):109–119

Design and Simulation of GaAs/InP and Si/SiC Heterojunction Solar Cells

A. Garg and R. K. Ratnesh

Abstract This paper represents a comparative simulation study of I–V characteristics of GaAs/InP and Si/SiC heterojunction solar cells. The design and simulation of device is done with COMSOL at 300 K. The calculated fill-factor of GaAs/InP and Si/Sic is 0.75 and 0.85, respectively. Moreover, open-circuit voltage (V_{oc}) of the GaAs/InP heterojunction solar cell is 0.4 V with efficiency of approx. 10%, whereas that of Si/SiC is 0.52 V with efficiency of approx. 14%. The effect of the material properties on the device with I–V and J–V curve is very well demonstrated.

Keywords Solar cell · Heterojunction · Fill-factor · Dark current

1 Introduction

The solar energy is the best alternative option for electricity generation which is based on photovoltaic effect. It converts the solar energy into electrical energy [1]. There is a systematic development of solar cell, namely first generation, second generation and third generation [2]. The solar cell performance depends on various parameters like materials, temperature, fill-factor, open-circuit voltage as well as short-circuit current. As we know, silicon is the most abundant material on the earth [3, 4]. The silicon-based solar cells are the most efficient and reliable solar cells [5]. Among the various solar cell materials, GaAs/InP and Si/SiC have drawn a great attention toward the research community due to its unique properties. Recently, we noticed that the heterojunction solar cell is more efficient over the conventional silicon solar cells [6]. The "heterojunction" is an interface between two layers. Both the layers of heterojunction are made up of different semiconductor materials and have unequal bandgap. The different materials help to improve the characteristics of heterojunction as compare to the conventional homojunction solar cells. The combination of numerous heterojunctions is known as heterostructures. These solar cells are made up

A. Garg · R. K. Ratnesh (✉)
Department of Electronics and Communication Engineering, Meerut Institute of Engineering and Technology, Meerut, Uttar Pradesh 250005, India
e-mail: ratnes123@gmail.com; ratneshwar.ratnesh@miet.ac.in

of *p–n* junction between high bandgap and low bandgap semiconductor [7]. Hetero-junction solar cells are also known as heterojunction intrinsic thin layer (HIT) solar cell. These solar cells have gained more attention as compare from conventional solar cells [8–10]. Heterojunction structure consists of two materials, out of which one is absorber and the second may be an absorber or any window material having wide bandgap. Both the materials can be organic, inorganic or mixed semiconductor materials. There are two types of structure of heterojunction: planar heterojunction and bulk heterojunction solar cell [11]. The efficiency of silicon heterojunction solar cell achieved is about 21% [8]. Other than silicon, there are more materials which can prove to be advantageous. Such materials are gallium arsenide (GaAs) and indium phosphide (InP). They are the materials of III-V semiconductor groups. These mate-rials are highly beneficial than silicon due to their high electron mobility and direct bandgap [12]. Whereas, other than silicon, there is other material also named as silicon carbide (SiC). The main advantage of SiC is the large tunable bandgap from 1.8 to 2.3 eV [13, 14].

This paper we simulate and analyze the heterojunction solar cell and the effect of various parameters have been demonstrated. We make a comparative study of different materials that are GaAs/InP and Si/SiC at 300 K temperature. The *I–V* characteristics, *P–V* curve, *J–V* curve and the various parameters are calculated and explained below in our study.

2 Tools and Techniques

The proposed heterojunction solar cell is simulated by using the software, i.e., COMSOL Multiphysics. This simulation software is very convenient and used by scientists and engineers both. It is helpful in designing and processing the devices in various fields of research and development. All types of solar cells can be analyzed like homojunction, amorphous, cadmium telluride (CdTe), copper indium gallium arsenide (CIGS) in different dimensions like 1D, 2D or 3D. We simulate the hetero-junction solar cell by adding two different materials such as GaAs/InP and Si/SiC and study their electrical characteristics.

3 Working of Solar Cell

During simulation process in COMSOL Multiphysics, there are necessary steps which are required to be followed. Defining the geometry and interval of the solar cell structure is the first step. Furthermore, solar cell structure is simulated in 1D. The geometry and interval can be varying according to the requirement. In this research work, we select a heterojunction solar cell, which is varying between two intervals, i.e., one from −10 to 0 and another is 0 to 10. After selecting the length in micrometer (µm) scale and intervals, our required geometry of structure is built.

Second, selecting the material on different domains. Then, doping plays the most important role. The adding of impurities to vary the electrical and optical properties of a material is said to be doping. The analytical and geometric doping is done on all the domains of the device. After doping, the process of recombination of electrons and holes is performed. The trap-assisted recombination model also known as Shockley-read-hole-model is used for electron and hole recombination. Then the last step is metal contact is done on both the terminals. From this simulation, we are able to find the *I–V*, *P–V* and *J–V* curve of GaAs/InP and Si/SiC heterojunction solar cell.

4 Results and Discussions

The mechanism of solar cell simulation can be observed from Fig. 1. The parameters of heterojunction solar cell have been evaluated based on different materials that are gallium arsenide (GaAs), indium phosphide (InP), silicon (Si) and silicon carbide (SiC). One material is of lower bandgap and other is of higher bandgap. The COMSOL software is used to determine the various parameters like open-circuit voltage (V_{OC}), short-circuit current (I_{SC}), fill-factor (*FF*), efficiency (η) and maximum power point, i.e., V_{mp} and I_{mp} of the device [2, 15–18]. The nonlinear *V–I* relationship is illustrated as:

$$I = I_{sc} - I_0\left(\exp\frac{qV}{kT} - 1\right) \tag{1}$$

where I_{SC} = reverse saturation current, $q = 1.6 \times 10^{-19}$ is the charge, $k = 1.38 \times 10^{-23}$ is Boltzmann constant and *T* is temperature.

Now, after plotting the *V–I* curve, we can find out certain values like V_{oc}, I_{sc}, V_{mp}, I_{mp} and P_{max}. Using these values, the fill-factor is calculated as shown in Eq. (2). It is the ratio of maximum output power to the product of short-circuit current I_{SC} and open-circuit voltage V_{OC}.

Fig. 1 Schematic structure of heterojunction solar cell **a** GaAs/InP **b** Si/SiC
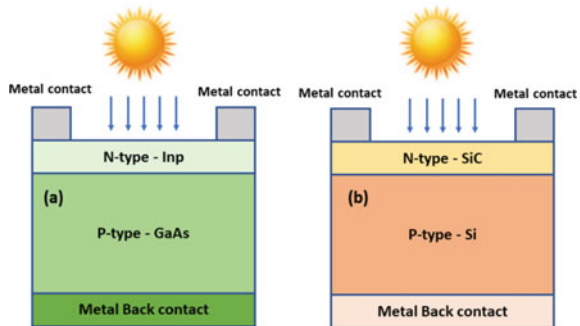
$$FF = \frac{V_{mp} \times I_{mp}}{V_{OC} \times I_{SC}} \tag{2}$$

The area of cell is formulated as shown in Eq. (3). It can be observed from the V–I and P–V curve of solar cell, the maximum voltage on x-axis is the open-circuit voltage (V_{OC}) when the current is zero. And the current on y-axis, when voltage is zero, is the short-circuit current. The point at which power is maximum at V_{mp} and I_{mp}. Therefore, the area of solar cell is defined as the product of V_{mp} and I_{mp}.

$$\text{Area} = V_{mp} \times I_{mp} \tag{3}$$

The efficiency is known as the ratio of maximum power to the input power given as shown in Eq. (4).

$$\eta = \frac{P_{\max}}{P_{\text{in}}} = \frac{V_{OC} \times I_{SC} \times FF}{P_{\text{in}}} \tag{4}$$

In Fig. 1a, p-type substrate is gallium arsenide (GaAs) and n-type is indium phosphide (InP) that is diffused over p-type. The bandgap of GaAs is 1.424 eV and InP is 1.344 eV given in Table 1. Both of the semiconductor material is of III–V group.

The GaAs is more advantageous over silicon due to its various properties like direct bandgap as well as good carrier mobility. Moreover, InP is considered to be environment friendly. Indium phosphide is advantageous due to the high radiation resistance than GaAs and Si and also have better efficiency. The electron and hole mobility of gallium arsenide are 8500 (cm²/Vs) and 400 (cm²/Vs), respectively. The I–V curve of GaAs/InP is simulated in COMSOL as shown in Fig. 2. The simulated I–V curve of GaAs/InP we calculate $V_{oc} = 0.4$ V, $I_{sc} = 3.35$ mA, $V_{mp} = 0.32$ V, I_{mp} = 3.15 mA and $P_{\max} = 1.01$mW, respectively.

Now, our second study is on different materials named as silicon (Si) and 3C silicon carbide (SiC). Silicon carbide has various electrical and optical properties which makes it an attractive choice in today's research industry. In Fig. 1b, it is shown that the p-type is silicon (Si) and n-type is silicon carbide (SiC). The n-type is deposited over p-type. The bandgap of Si is 1.12 eV and SiC is 2.36 eV given

Table 1 Parameters of various materials

Material parameters	(GaAs)	(InP)	(Si)	(SiC)
Energy gap (eV)	1.42	1.344	1.12	2.36
Electron affinity (eV)	4.07	4.38	4.05	3.83
Relative permittivity	12.9	12.5	11.7	9.72
Electron mobility (cm²/Vs)	8500	5400	1450	900
Hole mobility (cm²/Vs)	400	200	500	380
Electron lifetime (s)	10^{-8}	10^{-8}	10^{-8}	10^{-8}
Hole lifetime (s)	10^{-8}	10^{-8}	10^{-8}	10^{-8}

Fig. 2 *I–V* and *P–V* characteristics of GaAs/InP heterojunction solar cell
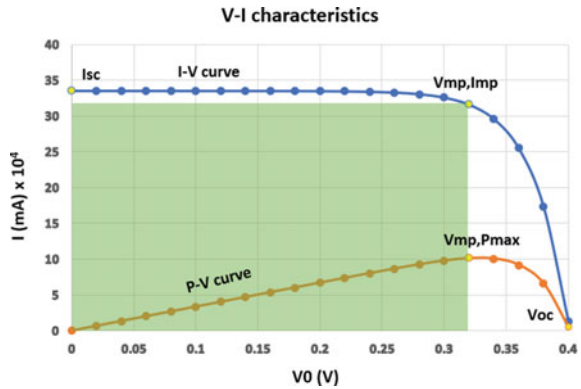
in Table 1. Both the materials have different bandgaps. The SiC exists in different crystal structures like 3C (cubic), 4H and 6H (Hexagonal) and many more. The electron and hole mobility of silicon carbide are 900 (cm^2/Vs) and 380 (cm^2/Vs), respectively. After simulation, we are able to find the *I–V*, *P–V* and *J–V* curve of Si/SiC heterojunction solar cell. The *I–V* and *P–V* curve of Si/SiC are simulated in COMSOL as shown in Fig. 3a, b. The simulated *I–V* curve of Si/SiC we calculate $V_{oc} = 0.52$ V, $I_{sc} = 3.04$ mA, $V_{mp} = 0.5$ V, $I_{mp} = 2.70$ mA and $P_{max} = 1.35$ mW.

Fig. 3 **a** *I–V* **b** *P–V* characteristics of Si/SiC heterojunction solar cells
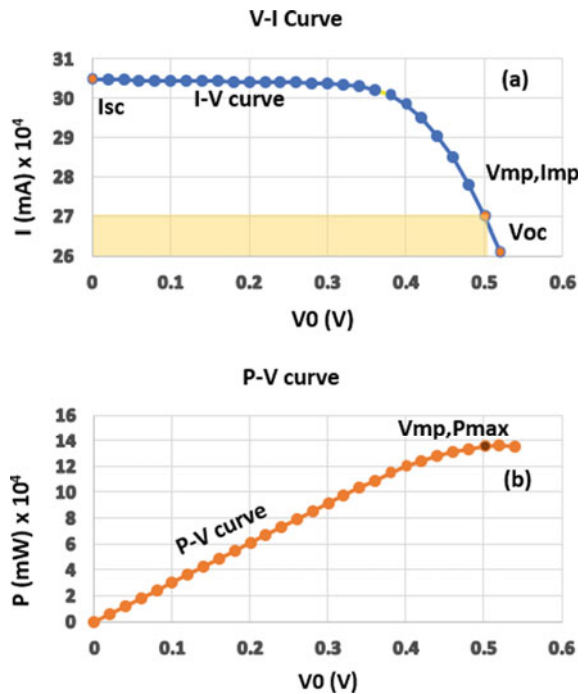
Another important curve simulated is J–V curve. The J–V curve of GaAs/InP and Si/SiC is simulated as shown below in Figs. 4 and 5, respectively. The value of J_{SC} and V_{OC} can be calculated from the given curve. Moreover, the influence of arc length on energy of GaAs/InP and Si/SiC solar cell is also shown. Here, one important concept is of dark current. When there is no illumination, certain voltage is applied on the device. Due to which the potential difference is developed across the terminals. The current is generated in the opposite direction due to the potential difference. This reverse current is said to be the dark current (J_{dark}) as shown in Eq. (5) [11].

$$J_{dark} = J_0 \left(e^{\frac{qV}{kT}} - 1 \right) \tag{5}$$

where J_0 is constant and k is Boltzmann's constant and T is temperature in kelvin.

The J–V curve shown in Figs. 4 and 5 is same as I–V curve. The difference between them is only on Y-axis. In Figs. 4 and 5, it can be seen that at $I = 0$, we can get the value of short-circuit current density, i.e., J_{SC}. The value of J_{SC} of GaAs/InP and Si/SiC is 3.35 mA/m^2 and 3.04 mA/m^2, respectively.

Under dark current, the structure of basic solar cell consists of donor and acceptor component, cathode and anode that behaves like a diode. The dark current curve is similar to I–V curve. There is negligible amount of current in reverse biased and high
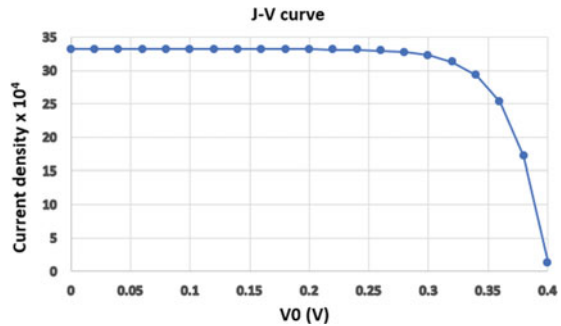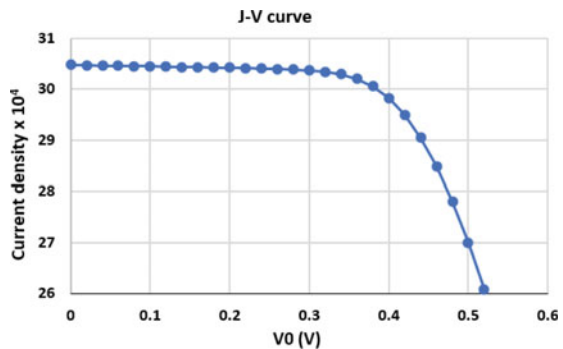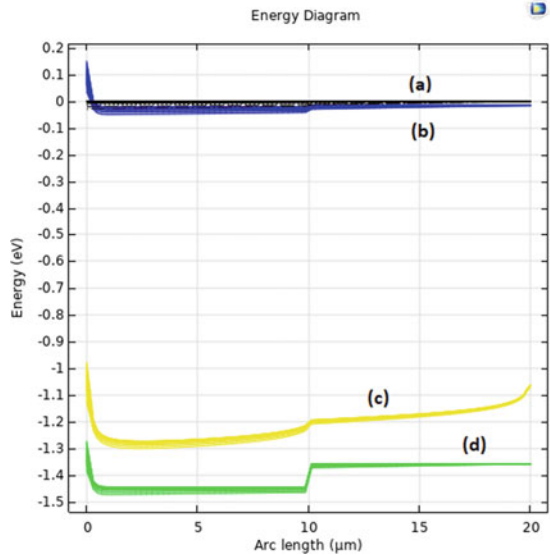
Fig. 4 J–V curve of GaAs/InP

Fig. 5 J–V curve of Si/SiC

amount of current in forward biased. And under the illumination condition, there is a flow of electrons toward cathode and flow of holes toward, resulting in the generation of the reverse current also known as photocurrent [11].

Moreover, the energy diagram of GaAs/InP and Si/SiC is shown in Figs. 6 and 7, respectively. The energy diagram shows the influence of arc length on energy. The conduction band, valence band and electrons-hole fermi energy levels of both the materials are shown.

The flow of electrons and holes from *n*-region to *p*-region and *p*-region to *n*-region in GaAs/InP and Si/SiC results in generation of electric field in the direction opposite to the current. The conduction and valence bands are in bend shape due to the generation of electric field.

When there is no illumination, the solar cell is in the equilibrium state and resulting in the value of fermi level to be constant. But, when the cell is illuminated, photons excite the electrons from valence band to conduction band due to which a pair of electron and hole is generated. This whole process is illustrating by the above two Figs. 6 and 7, respectively.

5 Conclusions

A comparative study of GaAs/InP and Si/SiC heterojunction solar cell can be summarized with the simulation of characteristics and various parameters using COMSOL Multiphysics. The resulted parameters of GaAs/InP are as follows: $V_{oc} = 0.4$ V, $I_{sc} = 3.35$ mA, $V_{mp} = 0.32$ V, $I_{mp} = 3.15$ mA, $J_{SC} = 3.35$ mA/m^2 and $P_{max} = 1.01$ mW.

Fig. 7 Schematic energy diagram. **a** Conduction band energy level. **b** Electron quasi-fermi energy level. **c** Hole quasi-fermi energy level. **d** Valence band energy level
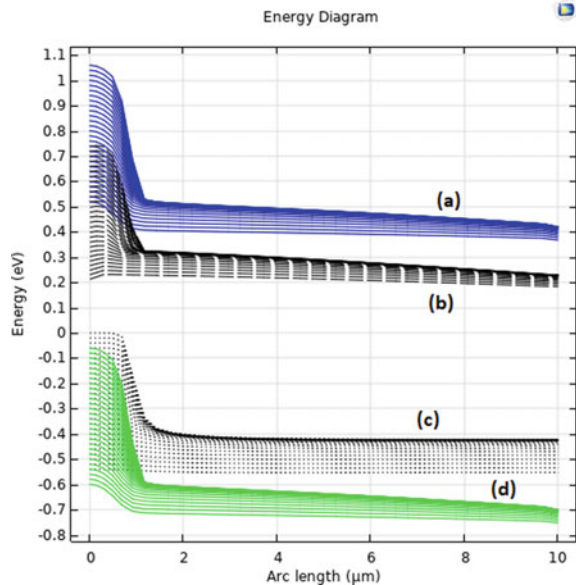
With these parameters, *FF* is 0.75 and efficiency is approx. 9.9%. Whereas, the parameters of Si/SiC are as follows: V_{oc} = 0.52 V, I_{sc} = 3.04 mA, V_{mp} = 0.5 V, I_{mp} = 2.70 mA, J_{SC} = 3.04 mA/m^2 and P_{max} = 1.35 mW. With these parameters, *FF* is 0.85 and efficiency is approx. 13.4%. The aim of the designing of device and simulation is to enhance the performance of heterojunction solar cells.

Compliance with Ethical Standards Conflict of Interest The authors declare that they have no conflict of interest.

Code Availability Not applicable.

Author Contributions *Ananya Garg:* main author, developed most of the theory presented in the paper, conducted experiment and wrote the paper. *Ratneshwar Kumar Ratnesh* has also considered as main author, developed most of the theory presented in the paper, conducted experiments, analyzed the data, and wrote the paper.

Ethics Approval Not applicable.

Consent to Participate Not applicable.

Consent for Publication Not applicable.

References

1. Chu Y, Meisen P (2011) Review and comparison of different solar energy technologies. Report of Global Energy Network Institute (GENI), Diego
2. Bagher AM, Abadi Vahid MM, Mohsen M (2015) Types of solar cells and application. Am J Opt Photon 3:94–113. https://doi.org/10.11648/j.ajop.20150305.17
3. Kamali AR, Prasanna Moorthy V (2022) Design of solar and battery hybrid electric vehicle charging station. J Trends Comput Sci Smart Technol 4:30–37. https://doi.org/10.36548/jtcsst.2022.1.005
4. Kumar NM (2019) Energy and power efficient system on chip with nanosheet fet. J Electr Inf 01:52–59. https://doi.org/10.36548/jei.2019.1.006
5. Fauzi IF, Shahimin MM, Mazalan M (2010) Simulation of cadmium telluride solar cells structure. In: Proceedings of 2010 IEEE student conference on research and development. https://doi.org/10.1109/SCORED.2010.5704029
6. Ma W, Saida T, Lim CC, Aoyama S, Okamoto H, Hamakawa Y (1994) The utilization of microcrystalline Si and SiC for the efficiency improvement in a-Si solar cells. In: Proceedings of 1994 IEEE 1st world conference on photovoltaic energy conversion, vol 1, pp 417–420. https://doi.org/10.1109/WCPEC.1994.519987
7. Marti A (2019) Limiting efficiency of heterojunction solar cells. IEEE J Photovolt 9:1590–1595. https://doi.org/10.1109/JPHOTOV.2019.2932626
8. Chien YJ, Chen MY, Chang J, Liu JSQ, Chang YL, Huang MY, Yang PC (2013) Metallization optimization for high efficiency silicon heterojunction solar cells using low-temperature paste screen printing. In: IEEE 39th photovoltaic specialists conference, pp 2187–2190. https://doi.org/10.1109/PVSC.2013.6744909
9. Ratnesh RK, Singh M, Pathak S, Dakulagi V (2020) Reactive magnetron sputtered-assisted deposition of nanocomposite thin films with tunable magnetic, electrical and interfacial properties. J Nanopart Res 22:290. https://doi.org/10.1007/s11051-020-05017-z
10. Yadav OP, Varshney A, Kumar A, Ratnesh RK, Mehata MS (2018) A2B corroles: fluorescence signaling systems for sensing fluoride ions. Spectrochim Acta Part A Mol Biomol Spectrosc 202:207–213. https://doi.org/10.1016/j.saa.2018.05.051
11. Fonash SJ (2009) Solar cell device physics. Academic Press, New York
12. Ansari ZA, Singh TJ, Islam SM, Singh S, Mahala P, Khan A, Singh KJ (2019) Photovoltaic solar cells based on graphene/gallium arsenide Schottky junction. Optik 182:500–506. https://doi.org/10.1016/j.ijleo.2019.01.078
13. Perny M, Saly V, Vary M, Mikolasek M, Huran J (2015) Electrical characterization of a-SiC/c-Si solar cell structures. In: 38th international spring seminar on electronics technology, pp 16–20. https://doi.org/10.1109/ISSE.2015.7247953
14. Chandan, Ratnesh RK, Kumar A (2021) A compact dual rectangular slot monopole antenna for WLAN /WiMAX applications. In: Innovations in cyber physical systems. LNEE, vol 788, pp 699–705. https://doi.org/10.1007/978-981-16-4149-7_63
15. Dincer F, Meral ME (2010) Critical factors that affecting efficiency of solar cells. Smart Grid Renew Energy 1:47–50. https://doi.org/10.4236/sgre.2010.11007
16. Dobrzanski LA, Szczęsna M, Szindler M, Drygala A (2013) Electrical properties mono- and polycrystalline silicon solar cells. J Achiev Mater Manuf Eng 59
17. Ratnesh RK, Goel A, Kaushik G, Garg H, Chandan, Singh M, Prasad B (2021) Advancement and challenges in MOSFET scaling. Mater Sci Semicond Proc 134:106002. https://doi.org/10.1016/j.mssp.2021.106002
18. Suman, Sharma P, Goyal P (2020) Evolution of PV technology from conventional to nano-materials. Mater Today Proc 28. https://doi.org/10.1016/j.matpr.2020.04.846

Exploration Metrics Based on Scientific Mapping in the Use of Social Networks and Politics 2.0

Carlos Mejía-Vayas ⬤, Leonardo Ballesteros-López ⬤,
Cristina Páez-Quinde ⬤, and Alexandra López-Paredes ⬤

Abstract The data exploration metrics through scientific mapping aim to find out the level of interest in social networks and politics 2.0 within the scientific community worldwide; the development of literary production in times of pandemic to which research is limited; the creation of both research and review articles sectioned by countries, authors, and keywords within the search carried out in the Scopus database. In the first instance, an analysis of the scientific literature is carried out in the primary citation index that is used worldwide to measure high-impact scientific production, such as Scopus; a total of 139,710 jobs were obtained, which were filtered only in the years of the COVID-19 pandemic, resulting in several jobs of 17,049. The results that could be analyzed through scientific mapping showed that scientific production increased in the keyword social networks (online) with several authors who mostly belong to developed and English-speaking countries; Mexico is the only country in Latin America within the results obtained through the maps. Finally, the analysis of the clusters relates keywords such as social networks, machine learning, and big data; within the systematic review, there are still no studies related to politics 2.0; therefore, it is concluded that the political keyword 2.0 still has no connection in terms of high-impact scientific production.

Keywords Exploration metrics · Scientific mapping · Scientometrics · Social networks · Politics 2.0

C. Mejía-Vayas (✉) · L. Ballesteros-López · A. López-Paredes
Facultad de Ciencias Administrativas, Grupo de Investigación Marketing C.S., Universidad
Técnica de Ambato, Ambato, Ecuador
e-mail: carlosvmejia@uta.edu.ec

L. Ballesteros-López
e-mail: lg.ballesteros@uta.edu.ec

A. López-Paredes
e-mail: ma.lopez@uta.edu.ec

C. Páez-Quinde
Centro de Capacitación y Desarrollo Soportes Educativos, Grupo de Investigación Marketing C.S,
Universidad Técnica de Ambato, Ambato, Ecuador
e-mail: mc.paez@uta.edu.ec

1   Introduction

To [1] mentions that the emergence of Web 2.0 has transformed the ways of carrying out a campaign around the world, traditional political meetings have lost attractiveness mainly to young people, for this reason now political campaigns last less time, they are more independent and punctual. Many political parties have expanded their IT offer from having simple web pages where bilateral communication was null to user profiles on social networks that allow greater interaction with the public; and to use these platforms, experts are hired for the creation of textual, image, sound or video content under professional standards.

Social networks have become the most used means of communication in recent years and therefore are an essential part of people's lives. With the emergence of Web 2.0, social media is the tool that political figures use the most to spread their ideologies and gain more followers since these platforms allow bilateral interaction between the content creator and other users.

In Ecuador, according to [2] 59.2% of the population has access to the internet, which is why all political parties use these sites to generate political campaigns since it facilitates a closer relationship with voters. In this way, political marketing investigates, plans, and designs campaigns with valuable information in which citizens can learn about the profile and proposals of a candidate.

Several authors in the world have reviewed in research the use of social networks in politics 2.0, to make an exhaustive analysis of these academic articles, techniques, such as bibliometrics, web metrics, and scientometrics, among others, are used; that allow measuring the scientific potential of an author, institution, or country. For this, there is specialized software such as VOSviewer or SciMAT that use algorithms that incorporate modules and perform a mapping between keywords.

The purpose of this research is to know the impact of exploration metrics on the use of social networks in politics 2.0, so the "VOSviewer" program will be used to carry out a scientific mapping of the metrics "social networks" and "political 2.0".

In Ecuador, the use of social networks in politics has become more popular in recent campaigns, the authors [3] in their article track the political campaigns of the candidates for the presidency of Ecuador in 2021 on their Facebook pages to evaluate the 2.0 communication processes, especially to analyze the linguistic elements of the publications and determine the digital political agenda with all the issues they addressed.

The authors highlight tools such as metrics that facilitate the use of social networks such as Facebook; these metrics are reflected in the number of followers, likes, and comments, among other aspects. These KPIs (Key Performance Indicators) allow you to evaluate the results of a digital campaign. By way of conclusion, they point out that the participation of voters toward a political account is related to the activity since if the number of publications is low, the same will be the interaction, it should also be emphasized that it is not only about the number of publications per day but also on the quality of content and political discourse.

In the article by [4], they carry out a comparative analysis of the networks as a resource in politics 2.0 in the sectional elections of Tungurahua based on the problem that the political parties do not have a content plan in the social media and run it empirically. To carry out the study, tools such as Fanpage Karma and Foller Me were used to monitor the level of interaction on each fan page of the candidates and the commitment of the voters to them.

As a result, it was obtained that political marketing in the sectional elections of Tungurahua was marked by the lack of an effective digital marketing plan, many of the candidates who contended for the positions of mayor, councilors, and prefects began their campaigns without a defined strategy. In social networks and in the course of the campaign, they improvised with content on Facebook and Twitter. Local political parties need to complement their work teams with experts in digital marketing and conversational marketing to manage social networks before, during, and after the campaign, since thanks to the results of the investigation it is concluded who had the greatest digital presence. They were elected to various positions.

2   State of the Art

The study by [5] entitled "Scientometric and bibliometric study as an instrument for analyzing trends in higher education. Case of industrial engineering and related programs" carry out a worldwide analysis of scientific production in the field of Industrial Engineering through keywords and Boolean operators to determine the most relevant topics and identify lines of research to improve missionary productive processes in Colombian universities.

As a result of the study, it is discovered that the keywords lose their number of mentions in the publications, which implies that the research interests shift to other areas and that a database with sub-themes should be built to improve the dispersion of themes to develop from the correlation, thus resulting in content synthesis to strengthen the investigation. Finally, the scientometric analysis confirmed through the keywords that industry 4.0 is based on research from versatile information systems to be used in manufacturing and process logistics.

In the article by [6] "Use of data science in digital marketing: framework, methods and performance metrics" he mentions that the metrics are used to calculate the efficiency of each of the digital marketing actions. These metrics are developed by web companies and try to store from different sources some aspects such as the type of data collected from different online sites, purchases made by users, their digital habits and behaviors that facilitate segmentation through artificial intelligence.

In his article, he concludes that companies are involved in data classification, specifically, it has been reported that many businesses spend a lot of time organizing, cleaning, and structuring their users' and customers' databases. In this context, the use of relevant performance indicators and metrics will help companies, marketers, and non-technical researchers in the marketing field to manage better searches and

be more efficient in the number of hours they spend in the analysis and distribution of data.

According to [7] in his article "Cybermedia and social networks audience analysis and metrics for journalistic content" he talks about the digital transition of printed newspapers given that more than half of internet users search for current news on social media. Now publishers have found a new way to distribute information, but a counterpart to these digital media is the loss of control over content distribution due to unpredictable algorithms.

As the methodology of the scientific article, exploratory research was used in which data analysis applications were used in the ten most important media profiles in Spain to collect metrics and measure the level of engagement of each of these sites. To obtain the results, the IAB technique was used, where a percentage of the division between the followers is obtained, divided by the number of interactions, which allows homogenization of metrics. It is concluded that the number of followers should be comparable to the number of interactions, based on the metrics obtained from comments, likes, and shares, which helps to calculate the degree of loyalty that users have toward digital information channels.

The authors [8] in their article on the use of metrics in the financial system carry out an analysis of the behavior of those involved who are investors, analysts, and lenders; with the objective of identifying how metrics have become a reference framework for financial marketing, mainly for the collection of data and analytics related to stakeholders (customers, employees, investors), and their influence on the decisions of this group toward a financial institution.

What the authors discovered in their research is that social media is a strong predictor of the stock market and the stock market, all thanks to online gauges that identify data such as web searches and potential interests. Mainly in social networks that have metrics that allow an analysis of how content influences the attitude of financial customers, where customer satisfaction increases toward the brand through loyalty motivators in the form of direct interaction or rewards for loyalty to the entity.

According to [9] in their analysis of the accounts of presidents of Latin America on the social network, Twitter clarifies that the fact of having an account or web page does not mean having a digital presence, since that it is required to integrate the online with the offline through effective communication strategies. Although social networks have control over the masses, good communication will make the difference between getting closer to your followers and moving away from your opponents.

This research work tries to calculate the rise of the Twitter social network, highlighting it as a tool that helps measure the impact of publications through interaction with retweets, replies, and mentions, since it allows users to become spokespersons for government entities. In addition, it highlights Ecuador as the country where organizations prioritize communication on social media, which is why the presidential account is one of the most followed accounts in the country with around 1 million followers compared to other accounts. Presidential elections in other countries such as Chile, Paraguay, and Brazil in which the number of people on Twitter is higher, but there is little interest in political profiles on the internet.

The 2.0 policy is not only about the web media that is used but also about the content that is uploaded to them; the authors [10] in their article "To understand digital politics—principles and actions" carry out a theoretical study of trends in digital resources where the "celebrification" of political personalities stands out, the use of memes (images with a humorous tint), and finally the hashtags whose function is to direct the conversation toward a specific topic.

For [11] scientometrics is based on the research of Eugene Garfield and Derek J. de Solla Price and is the study of scientific production to quantify and analyze it. Among the most relevant topics to investigate is the measurement of impact, the understanding of scientific citations, the sets of reference articles to investigate the impact of journals and institutes, the production of indicators, and the mapping of scientific fields for use in political and institutional contexts. Scientometrics is also used in academia to quantify everything from the number of graduates to the number of computers and hours spent in the classroom.

Bibliometrics is a part of scientometrics, [12] it is a branch of sociology that uses mathematical and statistical methods to analyze the course of scientific literature, such as research journal articles, and obtain guidelines for the development of a study and the conduct of the authors who produce it. Bibliometrics seeks to quantify scientific activity by applying treatments to the properties of written discourse and its typical behaviors. For this, bibliometric laws based on statistical behavior are used. The tools to measure these aspects are bibliometric indicators, which provide information on the results of scientific activity in any of its forms.

According to [13] the great scientific diversity in the world has led to the need to establish systems for measuring, and evaluating, comparing, and qualifying the quality of scientific results. For this, there are scales or indicators to quantify the impact of scientific publications.

In Ecuador, politics 2.0 has come to support a lot of participation, in the article by [14] where he analyzes Instagram in the political campaign of the candidates for president in 2021, mentions that all the candidates are they were forced to move their political campaigns to social networks due to the COVID-19 pandemic, so they had to present their proposals through platforms, but it is not only enough to have a digital presence, but also to know how each of these works and to what kind of audience are you targeting? Instagram is a social network used by young people, which means creating content completely focused on this segment.

The research seeks to identify the relationship between content marketing and political communication by candidates on Instagram, a study of the 4 applicants with the most votes in the first round was carried out: Andrés Arauz, Guillermo Lasso, Yaku Pérez, and Xavier Hervas; where three aspects were analyzed: type of content, level of activity, and engagement. It is concluded that there was an average of 15 daily publications for each candidate; the most published content was the political, followed by the citizen and finally the personal. Finally, the highest level of engagement was achieved by the applicant who best understood the Instagram social network, who was Xavier Hervas, with a reach of 6.6% compared to 2.6 and 1.4% of his opponents [15] (Tables 1 and 2).

Table 1 Scientific Activity Indicators

Indicators	Feature
Scientific productivity indicators	• Productivity by author, institution, country, and year • Most relevant authors by discipline or branch • Language used in the publication
Results indicators	• Quantify the technological activity of a sector, company, country, and opening of new markets • Evaluate results of research programs • Keyword analysis or co-authoring
Research indicators	• Documents (original articles, under review, papers, reports, books, among others) • Theoretical, experimental, or methodological character • Basic character or applied to the study

Table 2 Impact Indicator

| Indicators	Feature
Influence indicators	• Impact on article by number of times cited • Impact of sources used, according to their visibility in databases and libraries • Impact by journals used according to country or institution
Utility indicators	• Measure the growth of any discipline • Evidence cooperation between researchers in institutions or independent • Contrast the chronology of scientific production • Evaluate the expiration of scientific fields
Database indicators	• Determine omissions in different scientific fields • Generate documentary diversity in scientific journals and books • Confirm errors in the analysis and classification of a scientific nature

3 Methodology

The theoretical research in this research was carried out with the aim of collecting information and increasing the understanding of the concept's "metrics", "social networks," and "politics 2.0". Consequently, it was based primarily on the processes of abstraction, analysis, synthesis, induction, and deduction of these words to have a better understanding and proceed to carry out the practical part.

The research approach is qualitative in nature, it was based on the extraction and interpretation of data obtained from the Scopus base, with this approach concepts and understandings were developed from data patterns instead of collecting information to test models, hypotheses, or preconceived theories. Qualitative research was used as a flexible exploration design that allowed the elaboration of a map of each variable.

Through the exploratory research, it was possible to inquire about the exploration metrics and study indicators on social networks and politics 2.0 and that they are analyzed and studied separately in a bibliometric analysis, in turn, the research is
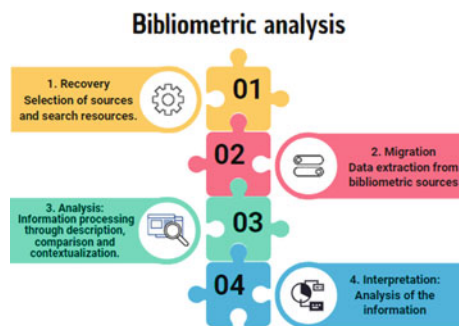
of a descriptive type since through from the download of Scopus data on the afore-mentioned keywords and the development of bibliometric maps in VOSviewer, it was possible to demonstrate the use of these keywords through aspects, such as the number of citations, authors of scientific articles, keywords, countries with the largest number of articles referring to keywords.

In the present study to collect the information, four aspects were taken into account that allows the generation of qualitative analysis as shown Fig. 1.

Recovery: In this first step, the Scopus repository was entered, and the following reference years were taken to obtain the database: the year 2002 for the variable "social networks", and the years 2019 to 2022 for "politics 2.0".

Migration: Once the data was segmented, the data was downloaded, which was in a "RIS" format compatible with VOSviewer that did not contain any type of filters so that it can later comply with the analysis.

Analysis: The use of the VOSviewer program was continued to collect biblio-metric indicators of the keywords.

Interpretation: The data was interpreted through a scientific mapping taking into account characteristics related to the study variables.

4 Results

Figure 2 shows the first search carried out in the Scopus database, in which there is no type of specific search filter; therefore, a total of 139,710 documents were obtained from the result of the keyword "social network".

To obtain a more secure result and by the intention of the investigation, Fig. 3 shows the filter performed in the search, which focuses on the years of publication from 2019 to 2022, since it is the range where more use was made of social networks due to the COVID-19 pandemic situation; the result of the search was 17,049 articles in the Scopus database.

Once the results of the scientific articles from which the respective analysis was carried out, they are downloaded by exporting a.RIS file Fig. 4; for later mapping in VoSviewer; finally, all the fields of the database are extracted.
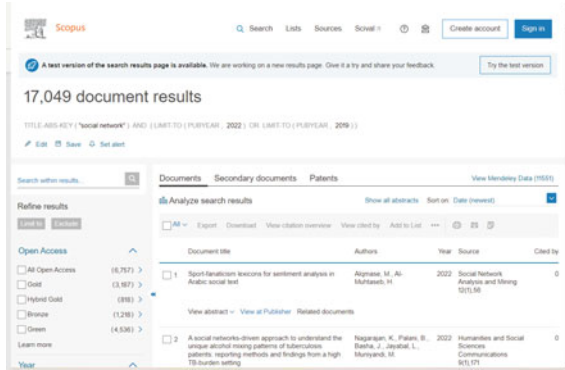
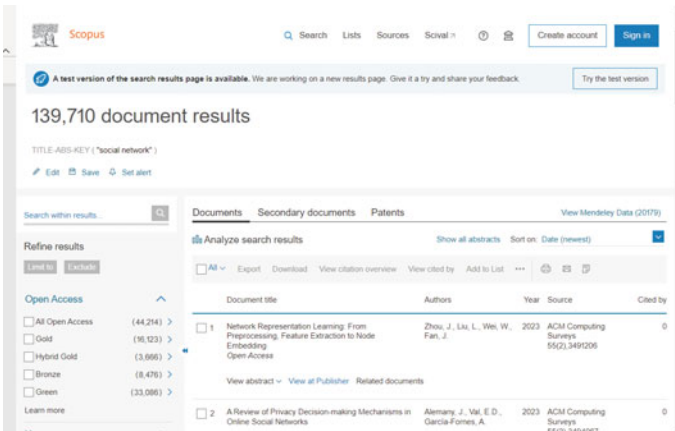**Fig. 2** Scopus data. *Source* Scopus web site

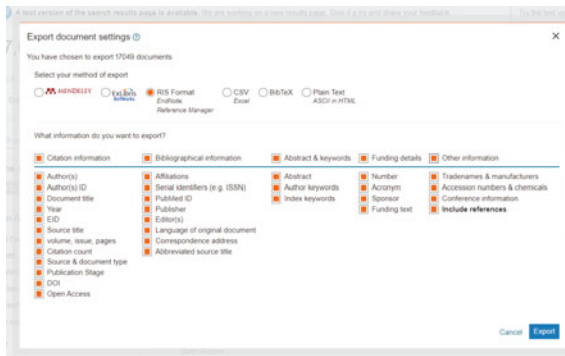**Fig. 3** Filter data. *Source* Scopus web site

Fig. 4 Data for mapping. *Source* Scopus web site

Figure 5 shows the network of all the authors who have articles referring to the keyword "social network"; the author with the most scientific production is Zhang, Y., as shown in Fig. 6, who in turn forms a main network of authors who cite this author. It is worth mentioning that the revised manuscripts are only from the years 2019–2022 where there was more use of social networks.

The network is made up of 11 clusters with a total of 116 authors of manuscripts indexed in Scopus, within-cluster one a total of 17 authors are shown who are referenced and put together a network based on keywords such as politics 2.0, social networks, Web 2.0; cluster 2, in the same way, is identified by 17 authors who form a network with the second most cited author and with the largest number of scientific articles Wang, X., as shown in Fig. 7.

Figure 7 shows that the author Wang, X., has a relationship with several work clusters, making a total of 8 clusters in which a multidisciplinary network is formed focused on keywords, documents, and citations that the authors have in their scientific papers.
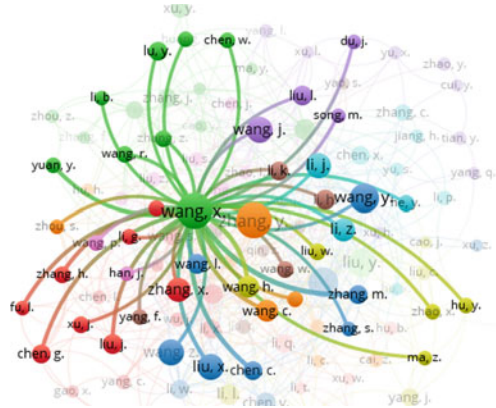

Fig. 5 Network for authors. *Source* VOSviewer software
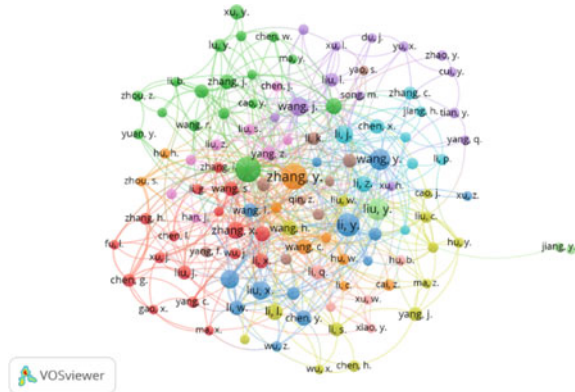
Fig. 6 Number clusters. *Source* VOSviewer software
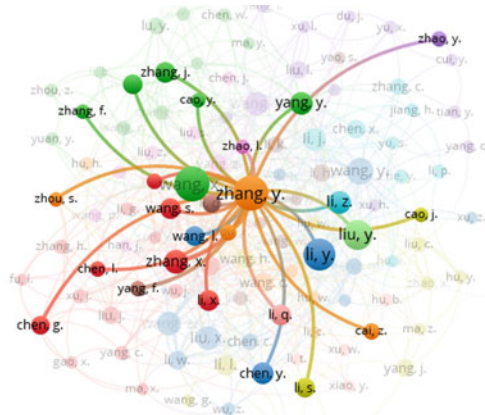
**Fig. 7** Author with more citations. *Source* VoSviewer software

Next, two density maps are considered, which have as a response the total number of documents written by the author and the total number of links that had the greatest interest by all the authors downloaded in the Scopus metadata.

In Fig. 8, according to the greater number of links made or references in the 17,049 articles from which the bibliometric analysis was carried out, the answer is that the most referenced authors are: Wang, X.; Zhang, X.; Liu, Y.; Wang, H.; Li, Y.; having a total of eight clusters as a network.

Regarding Fig. 9 in the density map, the authors with the largest number of scientific documents that they have since the year 2019–2020 period of the COVID-19 pandemic worldwide can be evidenced, where it was obtained that the author with the most scientific production is Zhang, Y.; Wang, Y.; Li, Y.; Yang, Z.; Liu, X.; Zhang, X.; Wang, J.; and in the same way; it is shown that Jiang, Y.; is an author with the first production within Scopus data.

Finally, the bibliometric analysis of the keywords of the research is carried out; During the years 2019 to 2022, when the use of social networks was most demanded by all network users, it is identified that a greater number of scientific articles were carried out based on social networks with a total number of 690 occurrences; followed

Fig. 8 Total link strength. *Source* VoSviewer software
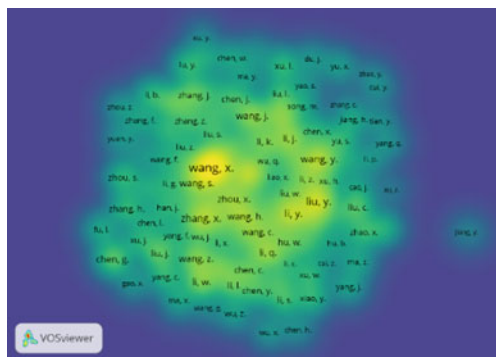
Fig. 9 Documents. *Source* VoSviewer software
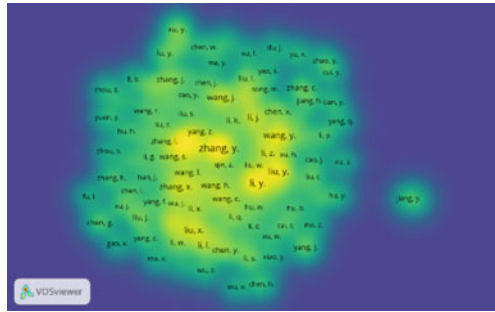
Fig. 10 Analysis keywords. *Source* VoSviewer software

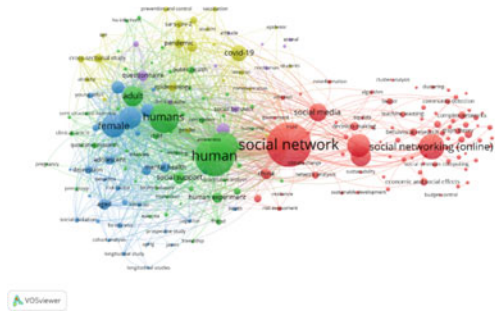by human with 573; social networking (online) with 306 occurrences as shown in Fig. 10; the same one that forms a scientific mapping of 8472 keywords that were described in scientific documents in times of the COVID-19 pandemic.

5 Conclusion

The use of bibliometric indicators for the evaluation of science allows an in-depth analysis from the quantitative and qualitative points of view of the behavior of science through its scientific production.

The evaluation of the behavior of the theme related to innovation and management projects through a bibliometric study of the publications in the Scopus database in the period 2019–2022 has shown the evolution achieved by this discipline to date and the tendency to continue developing in the coming years. It also provides a work tool for researchers in this field, taking into account that no references to similar studies applied to politics 2.0 were found.

The study confirms that the world leaders in this area are held by developed countries led by the United States, United Kingdom, and Germany; followed by other European and Asian countries, while poor and developing countries have a low level of representativeness expressed through their scarce scientific production, which

could be related to the possibility that some of the research and production activities of knowledge in most developing countries appear in "grey literature publications".

A language bias with a strong influence on English must also be recognized and it must be accepted that not all scientific production has the same opportunities for publication and not all publications have the same possibilities of integrating existing databases, among other elements that affect the low scientific production of underdeveloped countries.

Considering that this study constitutes a first approach to the bibliometric studies related to the subject, as well as the limitations identified in its realization, it is recommended as future lines of research to develop bibliometric studies of the subject covering a greater interval of time and bibliometric indicators, and carry out bibliometric studies on this subject in other databases and directories.

References

1. Gerl K (2018) Política 2.0 Internet y el trabajo de los partidos. Mayo. [En línea]. Available: https://nuso.org/articulo/politica-20/
2. INEC (2020) Indicadores de tecnología de la información y comunicación. [En línea]. Available: https://www.ecuadorencifras.gob.ec/tecnologias-de-la-informacion-y-comunicacion-tic/
3. Altamirano-Benitez V, Ruíz-Aguirre P, Baquerizo-Neira G (2022) Política 2.0 en Ecuador. Análisis del discurso y la comunicación política en Facebook. Rev Lat Comun Soc 80:201–223
4. Lozada-Nuñez MS, Herrera JBH (2020) Redes sociales una herramienta de marketing político en elecciones seccionales en Ecuador. 593 Digital Publisher CEIT 5(5):131–145
5. Fonnegra GM, Cuervo JE, Gallo SÁ (2020) Estudio cienciométrico y bibliométrico como instrumento de análisis de tendencias en educación superior. Caso ingeniería industrial y programas affines. Rev Esp 41(28):85–99
6. Saura JR (2021) Using data sciences in digital marketing: framework, methods, and performance metrics. J Innov Knowl 6(2):96–102
7. Cea N, De Vicente A (2019) Cibermedios y redes sociales: análisis de audiencias y métricas para los contenidos periodísticos. In: XI Congreso Internacional de Ciberperiodismo, pp 24–36
8. Edeling A, Srinivasan S, Hanssens D (2021) The marketing-finance interface: a new integrative review of metrics methods, and finding and an agenda for future research. Int J Res Market 38(4):857–876
9. Puertas-Hidalgo R, Jiménez LC, Suing A (2019) Comunicación política y redes sociales. Twitter: análisis comparativo de las Presidencias de la República de Latinoamérica. CISTI. Coimbra
10. Piñeiro-Otero T, Martínez Rolan X (2020) Para comprender la política digital—principios y acciones. Vivat Academia. Rev Comun 19–48
11. Millán JD, Polanco F, Ossa JC, Béria JS, Cudina JN (2017) La cienciometría, su método y su filosofía: reflexiones epistémicas de sus alcances en el siglo XXI. Rev Guillermo Ockham 15(2):17–27

12. Escorcia Otalora TA (2008) El análisis bibliométrico como herramienta para el seguimiento de publicaciones científicas, tesis y trabajos de grado [Tesis]. [En línea]. Available: https://repository.javeriana.edu.co/bitstream/handle/10554/8212/tesis209.pdf
13. Llerena Paz MA, Arévalo Avecillas ME, Ávila Bailón JA (2021) Indicadores bibliométricos: origen, definición y aplicaciones científicas en el Ecuador. Espíritu Emprendedor TES 5(1):130–153
14. Rocillo-Alba LE, Moscoso-Parra AE (2021) Marketing de contenido en la comunicación política de los candidatos presidenciales del Ecuador en Instagram 2021–2024. 593 Digital Publisher CEIT 6(3):131–145
15. Guzman LB, Escorcia YC, Ochoa GV (2017) Análisis Tendencial de las Investigaciones de Eficiencia Energética en Sistemas de Refrigeración durante los años 2013 a 2017. Reva Esp 38(54):12

Artificial Intelligence and Replacement of Human Talent: Case Study of Higher Education in Times of Pandemic

César A. Guerrero-Velástegui , **Santiago Peñaherrera-Zambrano** ,
Leonardo Ballesteros-López , **and Sonia López-Pérez**

Abstract The use of technology has invaded unprecedented professional areas that we could never have imagined, such as medicine, engineering, among others. The employ of robots has spread throughout the world mainly in manufacturing companies where they have reduced production times and costs and are guaranteeing greater production and quality in products. The objective of this research is to identify new challenges for organizations to visualize the harmony between technological growth and human talent. In addition, it is showing that the arrival of the new industrial revolution brings with it dramatic changes in job profiles. This research was carried out using data mining with the development of decision trees that allowed us to address the current problems of artificial intelligence and the replacement of human talent as a higher education case study. Applying this prediction and data segmentation technique, information was obtained that was analyzed for future decision-making in the field of education and the application of artificial intelligence in the study population. In addition, a structured questionnaire validated by experts was designed for data collection and reliability was measured with Cronbach's Alpha coefficient. Subsequently, the instrument was applied to teachers and students of higher education in the province of Tungurahua, with 100 informant agents. As a result, companies must seek a balance between machine and man. In addition to replacing humans, robots could be incorporated responsibly into work environments.

C. A. Guerrero-Velástegui (✉) · S. Peñaherrera-Zambrano · L. Ballesteros-López
Facultad de Ciencias Administrativas, Grupo de Investigación Marketing C.S., Universidad
Técnica de Ambato, Ambato, Ecuador
e-mail: ca.guerrero@uta.edu.ec

S. Peñaherrera-Zambrano
e-mail: spenaherrera@uta.edu.ec

L. Ballesteros-López
e-mail: lg.ballesteros@uta.edu.ec

S. López-Pérez
Centro de Idiomas, Universidad Técnica de Ambato, Ambato, Ecuador
e-mail: sda.lopez@uta.edu.ec

1   Introduction

The current pandemic scenario has forced several areas such as medicine, engi-
neering, higher education, among others, to use more and more diverse technologies
that have occasionally emerged. In fact, the particular case of artificial intelligence
(AI) that has found a lot of acceptance due to the implicit offer means changing the
way of living and working [1].

The present study aims to carry out an experimentation based on the development
of decision trees. It is focused on decision-making in the management of human
talent in higher education where AI can contribute to the continuous improvement
of the processes of higher education institutions, which have had to overcome all the
inconveniences that have arisen as a consequence of COVID-19 pandemic, in some
cases, reinventing itself to maintain operational continuity [2].

In addition, an important aspect that should not be overlooked is the fact that
higher education institutions are considered a priority for governments and even
more; so during this pandemic, in addition, in some cases, they have not experienced
any discontinuity during this COVID-19 outbreak, which has affected more than
190 countries and almost 1.6 billion students worldwide. At this point, the initia-
tives applied by governments and institutions included offering educational models
considered highly flexible, online, and open hybrids. In this context, AI contributes to
promoting learning environments at more adaptive, inclusive, flexible, personalized,
affective, and motivating levels, integrating the use of technology and knowledge
[3].

In the Ecuadorian case, concerning the university context, the strategic manage-
ment of human talent as a contribution to organizational development is essential for
achieving more excellent quality and adaptation of the processes carried out by insti-
tutions. In changing times where these values evolve rapidly and resources become
scarce, it is increasingly necessary to understand what influences the performance
and satisfaction of people at work. Therefore, in the labor area, public institutions,
as well as private ones, must carry out activities to satisfy the needs of internal and
external clients, with high standards of efficiency and quality in their services, as
expressed by [4].

Additionally, the use of Information and Communication Technologies (ICT), at
the academic and administrative level by the staff, is strategic, because the automation
of processes and the paradigm changes that have been used for a long time for virtual
education are necessary as competitive tools, especially at present when the pandemic
caused by COVID-19 has generated the implementation of teleworking and distance
academic activities online as mandatory in all countries [5].

In this way, it can be affirmed that in this work, technological factors will be understood as technical advances in line with David (2013) that speed up the pace of technological change that arrives, make the processes more efficient, and generate broad effects in society, such as Genetic engineering, the popularization of the Internet, and changes in communication technologies. They include activities and institutions that intervene in the creation of new knowledge and the control of the use of technology; an example of this is R&D consortia, university-sponsored technology incubators, patent and copyright laws, and government control over the Internet. Technological change can foster new industries, such as those based on nanotechnology, and disrupt others, such as the record label [6].

Technology also attempts to balance human sociopsychological needs with organizational goals. In this regard, it states that organic production is developed through the optimization of social and technical systems, and there is a constant exchange between the work system and the environment in general. Gutiérrez Cortes and Rivera Tovar [7] indicates that it is about the social aspects of people and the community and the technical aspects of the organizational structure and processes; what organizations must assume as the interrelation of social and technical aspects of an organization or society.

For [5], technologies are discovering a new conception of knowledge acquisition, so what is important in this new context is knowing how to formulate and asking the right questions about these data, shaping creative thinking, combining different perspectives and approaches to a subject, knowing how to work with information, learning to discern between what is valid and what is not.

Furthermore, it is important to mention that the processes within a higher education institution involve making decisions, so if they have to do with aspects related to human talent and become new challenges, which one's demand information that allows the human interaction with information and communication technologies. AI can be the basis for the improvement of several of the systems of a higher education unit, starting from the personnel who must be ready to make a qualitative leap to properly use artificial intelligence [8].

2 State of the Art

It is the ability of machines to use their algorithms. For example, learning from data and applying what they have learned to make decisions just as humans would, however, the difference is that devices do not need a break to be able to analyze large amounts of information [9].

According to Devang et al. (2019), who mention that artificial intelligence is the simulation of human intelligence through machines. It encompasses capabilities such as speech recognition, decision-making, semantic search, and learning tactics (p. 28) [4].

While for Nurock (2020), who considers that artificial intelligence is a set of technologies that are related to the information and communication sciences and that have in common the automation of intellectual functions p. 218.

Data Processing

It consists of extracting patterns and models with a high level of utility in the databases, which must have a high degree of durability in terms of information. Certainly, the level of data must be adequate so that it is associated with specific topics and maintains a high degree of permanence [10].

Meanwhile for [11], they define that data mining is the process of identifying the most outstanding information from large amounts of data since it aims to find patterns for later use in decisions.

The great flow of data that the new business contexts and the dynamism of the markets have brought with them. They have made companies need credible tools that allow, in a clear and concrete way, to collect, systematize, and analyze this data to improve decision-making. Thus, [12] defines data mining as a technology and a mathematical modeling strategy that tries to help understand the content of a database in a generalized way. Where the data is the raw material, now in which the user attributes some special meaning to them, as a result they become information.

Decision Trees

It is a tool that helps us to visualize the possible results of a series of interrelated decisions. Trees generally start with a single node and split as derived decisions occur. Finally, the shape that remains is a tree from which the name decision trees come [13].

On the other hand, [6] defines that it is one of the most practical tools in decision-making and easy to use because they are established as possible decision branches within a continuous scenario of events. Define two types of nodes, decision points that have alternatives and random points that represent randomness. After relating the two points, it will obtain a result for each of the final branches that will help it define the best course of action.

In the same line is [14], who states that it is a tool that helps decision-making because graphically represent a sequential decision process. It makes a decision and illustrates the way in which the problems and the sequence can be broken down of the decision process. The tree is created from left to right; however, its evaluation is done from right to left.

Industry 4.0

It is considered as the Fourth Industrial Revolution, which redefines business models and generates a global perspective that integrates the organizational environment, so that the manufacturing industry presents changes and digital transformations that are revolutionizing the sector and allow companies to exploit data and improve their systems [15].

Industry 4.0 revolutionizes manufacturing because it increases flexibility, mass customization, quality, and productivity. Currently, it is manufacturing, and maintenance is one of the most critical issues, so that, the companies are approaching their digital transformation from a technological and management perspective [16].

It represents the digitization and automation of manufacturing processes. It proposes the implementation of intelligent, widely interconnected, automatic, robotized, and systematized work environments at a high level. These changes with respect to the traditional industry will demand new skills and competencies of the workers or they will be replaced [17].

Human Talent Management

According to [7], the management of human talent is a structural issue, which in organizations must be operationalized in the different processes that comprise it. Being a set of necessary policies and practices that are in charge of directing the managerial positions that are related to people or resources that lead to the practice of the recruitment, selection, training, and performance evaluation processes [18].

Human Talent Management is one of the areas that has undergone changes in recent years. It has been a set of integrated decisions on labor relations that have a great influence on the effectiveness of the employees of each organization. It is considered at the same time as the function that allows people to contribute effectively to the achievement of organizational objectives and individual depending on, so that the culture, characteristics, and technology in the processes [19].

When it comes to the management of human talent, it is about the processes that develop or incorporate new members. In addition, it is retaining collaborators within the company, focusing on highlighting high potential people who have a focus on human resources management, and they are expected to perform better in their functions [20].

3 Methodology

For this research, decision trees were created using the data mining technique to collect data from administrative staff, teachers, and students of the marketing career of the Faculty of Administrative Sciences.

The study was divided into three phases. In the first place, data collection consists of collecting the available information by selecting the set of indicators that can help determine it, for which a structured questionnaire of 24 questions was applied. In fact, 4 of them were of sociodemographic information and the 20 indicator questions that allowed to identify the perceptions that the population has about artificial intelligence and the replacement of human talent in education.

The instrument had an instrument validation process. Cronbach's alpha statistic was used, which shows the following results (Table 1).

It has a value of 0.865 which is considered a reliable instrument for the development of research. The second stage called preprocessing is executed, the data is

Table 1 Reliability statistics

Cronbach's alpha	No. of elements
0.865	20

Fig. 1 Tools and meaningful learning
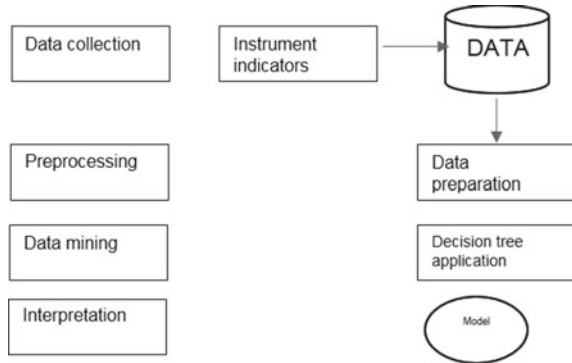
prepared to which the selected technique will later be applied, and this stage involves tasks such as cleaning data and transforming variables.

The values obtained in this phase will be interpreted for later presentation. In this way, it is sought that the results achieved allow the detection of the use of artificial intelligence through decision trees to replace human talent and serve as support in decision-making. For more details on these stages, they are provided in the following sections: Fig. 1 shows the method used to predict levels of competitiveness.

In this research, it worked with the design of our own database according to the research indicators. It is based on this; the data generation has been considered to contain relevant data. Similarly, different verification queries were run on the available data to obtain the dataset for analysis.

Regarding the DATA, it was taken from the study population that is the human resource of the Technical University of Ambato, from whom it was possible to obtain information for the processing of the data in the investigation.

Data preprocessing can be considered one of the longest steps in a typical data mining project. Generally, it has to do with the transformation of the data read to a more suitable form that allows the application of analysis tools. So, it may involve doing a data cleanup (sometimes also known as data rocking or data contention). It is transforming the data (for example, and it is making changes to the scale of variables), or it is even creating new ones.

The next step in this research is to determine the data mining technique to use. Data mining techniques can be descriptive and predictive (Jiawei Han 2012), but its work focuses only on the latter. However, as a first step, only decision trees will be considered, unlike other options that use it, for example: regression.

It was decided to use the decision tree technique taking into consideration its advantages and fields of application. Decision trees are a mining technique that allows

the analyzed data to be represented graphically. Thus, they help in the search for solutions to classification, prediction, and segmentation problems from a probabilistic point of view (Berry and Linoff 2011).

4 Results

As a starting point, the results presented in the tables give a descriptive analysis of the decision tree model based on the CHAID growth method. The dependent variable artificial intelligence in education is considered and the independent variables, age, sex. Artificial intelligence is considered within the hiring process and the use of artificial intelligence in the substitution of human talent, all within the scope of higher education (Table 2).

The independent variable is included in the decision tree. It is the use of artificial intelligence in the replacement of human talent. Therefore, the results obtained are the creation of three number of nodes, 2 number of terminal nodes, and the depth of the tree is one.

The figure can be identified through the indicated artificial intelligence applied to the field of education. It is considered that 90 people among service personnel, teachers, and students agree that AI strategies are applied. Thus, the related independent variable is the use of artificial intelligence in the substitution of human talent, where in Node 1, the application of this technique is considered adequate for an efficient development of activities as in Fig. 2.

The dependent variable IA in education, it is considered applicable based on the relationship with the variable in IA, and the generation of autonomy in fact, both in node 1 and in node 2, can be identified that they agree that the application of artificial

Table 2 Model summary

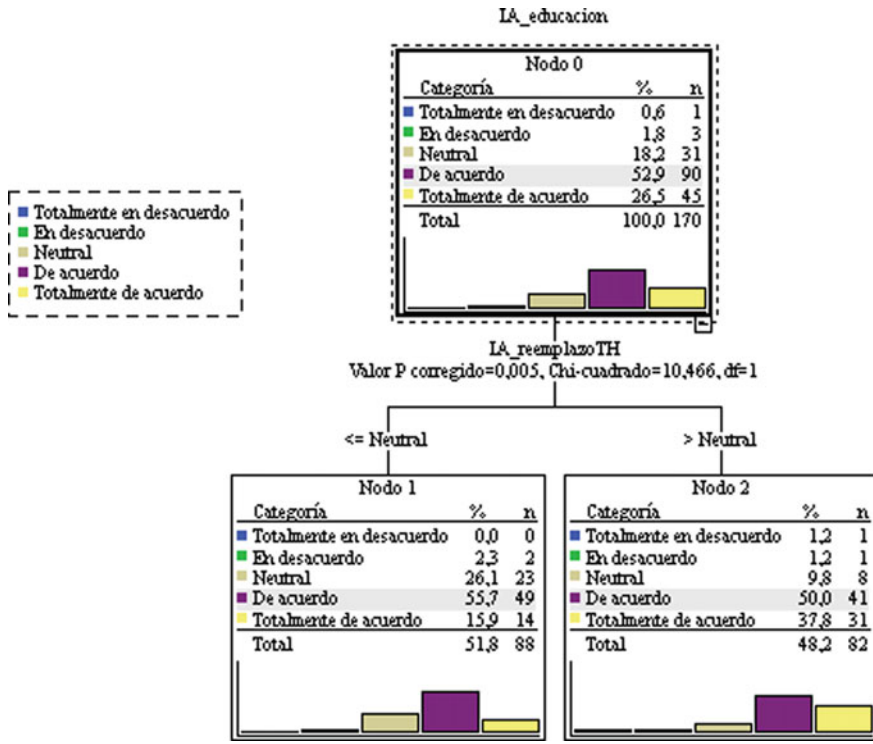| Specifications	Growth method	CHAID
Results	Dependent variable	IA_ education
	Independent variables	Age, Sex, IA_hiring, IA_replacementTH
	Validation	None
	Maximum tree depth	3
	Minimum of cases in a branch node	100
	Minimum of cases in a parental node	50
	Independent variables included	IA_replacementTH
	Number of nodes	3
	Number of terminal nodes	2
	Depth	1

Fig. 2 Human talent replacement

intelligence promotes autonomy in the processes and there is an improvement in their performance. Human talent and education criteria are shown in Fig. 3.

Surely, it is taking into account the AI indicator in the replacement of human talent. The independent variable analyzed is sex. Node 1 female considers that it is neutral against the fact that artificial intelligence can replace personnel. Node 2 male agrees that AI improves processes and replaces human talent. Human talent and gender criteria are shown in Fig. 4.

Each of the models analyzed in the research allows obtaining data that will improve the processes within each of the Directorates and Departments of the Technical University of Ambato, as well as allowing continuous improvement in terms of quality of service and teaching; allows decision-making with better opportunities.
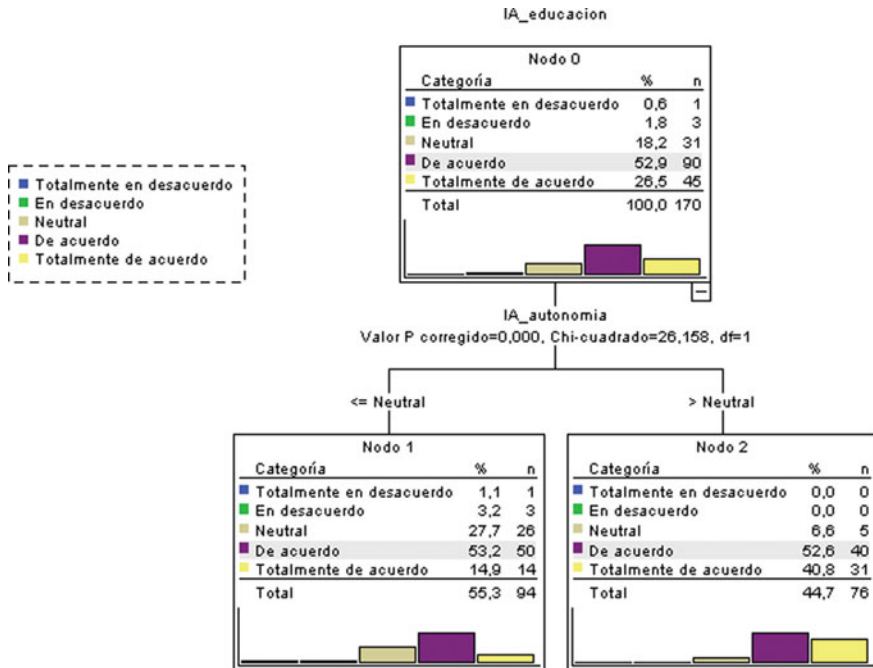
Fig. 3 Human talent and education criteria

5 Conclusions

It is taking into consideration the large amount of data generated by organizations in different fields. This research has sought to identify the use of artificial intelligence in the replacement of human talent through the application of data mining techniques. The research led to typical steps of the knowledge extraction process.

As a starting point, competitiveness indicators were selected from related works, so that, AI in education, age, sex, AI in the execution of hiring, AI and the replacement of human talent.

For this data mining research, it is very important to find the appropriate model for decision-making regarding the location of the ideal human resource in the processes that are carried out, in order to have a productive work in the directions of the Technical University of Ambato.

The decision tree technique was successfully applied to the dataset to analyze the replacement of human talent. The process carried out allows it to know how the artificial intelligence indicators have been growing or decreasing in the educational environment in terms of time in order to observe how the performance of human talent has been taking place based on the indicators.
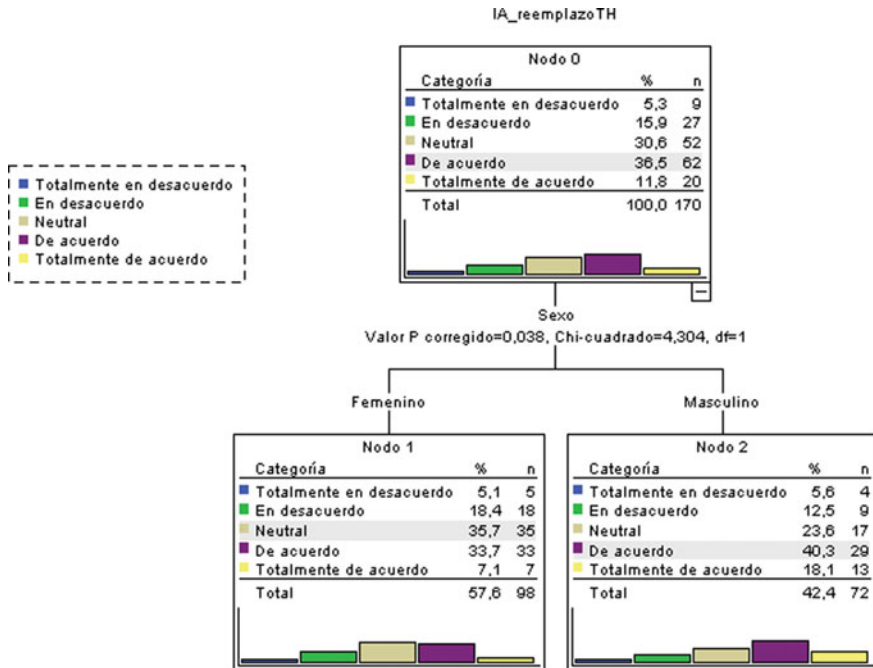
Fig. 4 Human talent and gender criteria

For that reason, these results can be inferred that this technique can help in decision-making. It is from a probabilistic point of view, in order to choose the most convenient options in the field of education.

References

1. Tripathi A, Kaur P, Suresh S (2021) AI in fighting Covid-19: pandemic management. Proc Comput Sci 185:380–386
2. Shamman A, Hadi A, Ramul A, Abdul Zahra M, Gheni H (2021) The artificial intelligence (AI) role for tackling against COVID-19 pandemic. Mater Today Proc (in press)
3. Vaishya R, Javaid M, Khan IH, Haleem A (2020) Artificial intelligence (AI) applications for COVID-19 pandemic. Diabetes Metabc Syndr Clin Res Rev 14(4):337–339
4. Gopinath N (2021) Artificial intelligence: potential tool to subside SARS-CoV-2 pandemic. Process Biochem 110:94–99
5. Armás-Arias S, Páez-Quinde C, Ballesteros-Lopez L, López-Pérez S (2021) Decision trees for the analysis of digital marketing in the tourism industry: Tungurahua case study. In: Multidisciplinary international congress on science and technology. CIT 2021, Quito

6. Ashraf A, Imran W, Véchot L (2022) Analysis of the impact of a pandemic on the control of the process safety risk in major hazards industries using a fault tree analysis approach. J Loss Prev Process Ind 74:104649

7. Gutiérrez Cortes W, Rivera Tovar C (2021) Human talent in geriatrics in Colombia and its relevance for the management of COVID-19. Lancet Healthy Longevity 2(3):e123–e124

8. Wang B, Yang Z, Xuan J, Jiao K (2020) Crises and opportunities in terms of energy and AI technologies during the COVID-19 pandemic. Energy AI 1:100013

9. Xu Z, Su C, Xiao Y, Wang F (2021) Artificial intelligence for COVID-19: battling the pandemic with computational intelligence. Intell Med (in press)

10. Radanliev P, De Roure D, Walton R (2020) Data mining and analysis of scientific research data records on Covid-19 mortality, immunity, and vaccine development—in the first wave of the Covid-19 pandemic. Diabetes Metab Syndr Clin Res Rev 14(5):1121–1132

11. Muhammad Shah A, Yan X, Qayyum A, Ali Naqvi R, Jamal S (2021) Mining topic and sentiment dynamics in physician rating websites during the early wave of the COVID-19 pandemic: machine learning approach. Int J Med Inform 149:104434

12. Khan M, Mehran M, Haq Z, Ullah Z, Naqvi S (2021) Applications of artificial intelligence in COVID-19 pandemic: a comprehensive review. Exp Syst Appl 185(15):115695

13. Guerrero M, Vanderloo L, Rhodes R, Faulkner G, Moore S, Tremblay M (2020) Canadian children's and youth's adherence to the 24-h movement guidelines during the COVID-19 pandemic: a decision tree analysis. J Sport Health Sci 9(4):313–321

14. Karl M, Kock F, Ritchie B, Gauss J (2021) Affective forecasting and travel decision-making: an investigation in times of a pandemic. Ann Tourism Res 87:103139

15. Moosavi J, Bakhshi J, Martek I (2021) The application of industry 4.0 technologies in pandemic management: literature review and case study. Healthc Analyt 1:100008

16. Spieske A, Birkel H (2021) Improving supply chain resilience through industry 4.0: a systematic literature review under the impressions of the COVID-19 pandemic. Comput Ind Eng 158:107452

17. Javaid M, Haleem A, Vaishy R, Bahl S, Suman R, Vaish A (2020) Industry 4.0 technologies and their applications in fighting COVID-19 pandemic. Diab Metab Syndr Clin Res Rev 14(4):419–422

18. Connell C, Lemyze C, McGill W (2021) The persistent link between growing talent and growing the top line: lessons from fast-growing firms in the COVID-19 recession. Organ Dyn 50(4):100807

19. Li W, Huang Z, Tan B, Chen G, Li X, Xiong K, Zhu R, Li R, Li S, Ye H, Liang Z, Dong X, Zhou S, Chen S, Xi H, Cheng H, Xu R, Tu S (2021) General recommendation for assessment and management on the risk of glucocorticoid-induced osteonecrosis in patients with COVID-19. J Orthop Transl 31:1–9

20. Bhaskara G, Filimonau V (2021) The COVID-19 pandemic and organisational learning for disaster planning and management: A perspective of tourism businesses from a destination prone to consecutive disasters. J Hosp Tourism Manage 46:364–375

A Proposed Approach to Detect Incident and Violation Through CCTV Using Convolutional Neural Network

Md. Mazbaur Rashid, Shariar Kabir Nayeem, and Md. Fahad Hossain

Abstract It is very challenging to predict a crime scene only by machine without human intervention. This research has tried to make that possible. Convolutional neural network (CNN) has been used to detect 4 objects which are handgun, fire, knife, and accidents. By detecting these objects easily with the help of CCTV cameras, the machine can predict the crime scene. Machines will be able to identify crimes swiftly and intervene based on situations like accidents or violence. This research has adopted a variety of techniques to reach the pinnacle of implementation and success. The model used here has been built with the help of CNN, and there are 4 objects to classify which are mentioned earlier. This research has succeeded in predicting crime scenes through CCTV cameras which may bring prosperity to the country and the nation.

Keywords Violation · Incidents · Convolutional neural network · Computer vision · Image classification

1 Introduction

In today's world, crime is one of the most troubling issues. Incident has been added to it, which is becoming more and more terrible day by day. Acting against the law by any person is basically a crime. Crime includes murder, rape, snatching, theft, and fighting. We also face all sorts of unpleasant incidents that destroy the peace of our society. Notable among these are car accidents, kidnapping, fire, etc.

Md. M. Rashid (✉) · S. K. Nayeem · Md. F. Hossain
Department of CSE, Daffodil International University, Dhaka, Bangladesh
e-mail: mazbaur15-2837@diu.edu.bd

S. K. Nayeem
e-mail: shariar15-2854@diu.edu.bd

Md. F. Hossain
e-mail: fahad.cse0365@diu.edu.bd

Our recent research found that Bangladesh crime rate and statistics was 2.37 for 2018 and 6.79% increased from 2017. Then we can see that in 2017, the crime rate and statistics was 2.22 and 2.23% decreased from 2016. In 2016, the crime rate and statistics was 2.27 and 11.97% which decreased from 2015. On the other hand, the crime rate and statistics was 2.58 for 2015 and 11.61% decreased from 2014 [1].

Moreover, if we focus on the recent crime index, it is very horrendous. Bangladesh ranks 17th among the top rated crime countries, and the crime index is 63.9 in 2022. Venezuela and Papua New Guinea occupy the first and second places in the crime index, respectively [2].

To prevent these complications, this research will help. The main purpose is to send a warning signal to the nearest police station or security personnel in case of any crime or incident of any kind it may detect through a CCTV camera.

CCTV means close circuit TV camera. CCTV is a small circuit camera whose job is always to capture video. In a word, a small circuit camera is called a CC or close circuit camera. Although the use of CCTV camera technology started in our country eight to ten years ago, it has been used in western countries much earlier. As it is not so expensive to use CCTV cameras, its demand and use are increasing manifold day by day.

We are living in an age where there is a possibility of having a CCTV camera at every street corner. We want to take advantage of them. We are thinking about making something that will help to catch incidents and violations in the CCTV cameras and send alerts to the nearest police station for taking necessary steps by the authorities and to save people's lives. We are starting with classification of 4 objects that are detection of handgun, fire, knife, and accidents. That means if any of these can be found on any scene in CCTV cameras, it will send a warning signal. Then the police will reach the destination and take action.

In this research, we have proposed a model based on convolutional neural network (CNN) to detect crime based on the detection of the objects mentioned earlier. According to a brief definition, convolutional neural network (CNN) is a sort of artificial neural network (ANN) which is used in image processing or recognition. It is especially built to analyze pixel data of images. The most advantageous feature of CNNs are that it reduces the number of parameters in ANNs [3].

2   Literature Review

There has not been much research done on this topic. This research discovered a few works. From them, some authors worked with four objects: blood, semen, saliva, urine [4]. Their study examines the methods of detection utilizing forensic light sources (FLS), as well as a quick summary of the many types of FLS available and the implications of biological evidence on various surfaces on detection. From their paper, it has been known that work will be done when everything happens which means crime has already happened. But our goal is to detect crime scenes before something unpleasant happens. Thus, there will be the possibility of saving lives.

Miyahara et al. [5] mainly focused on detecting kidnapping cases using skeleton analysis. They employed a digital camera mounted at a height of roughly 6 m above the ground, comparable to a public security camera. They worked with video where the resolution is 320×240 pixels and a frame rate of 25 frames per second. For each instance, 20 abduction recordings and another 20 non-criminal films were recorded, totaling 40 videos. Each video stream contained between 150 and 300 frames. When they employed the sum of skeletal analysis as the feature vector, they received the best results, with detection rates of 100.0% and 80.0% for abduction and normal instances, respectively. Though they are implementing it as a security camera by processing video, their aim is limited to one which is kidnapping.

Researcher reflected 3 objects like blood, gun, and knife in a study also. They have used CNN. They utilized ImageNet datasets that included 394 blood samples, 396 knife photos, 426 machine gun images, 482 revolver images, 406 shotgun images, and 302 gun in hand images. They claim an accuracy rate of 90–95%, albeit the precise figure may fluctuate from run to run due to the unpredictability of the training process [6].

Some authors mentioned about detecting objects for the purpose of detecting crime scenes [7]. They worked by detecting bed, book, bottle, chair, cup, etc. They described a system based on the faster R-CNN algorithm for object detection. The VGG-16 network and the region proposal network design details are presented first, followed by a brief description of the method which is RPN. They worked with 12 different classes and came up with an average accuracy of 74.33%. Although they have more classes, their accuracy is substantially lower than ours.

Little bit of transfer learning has been reflected by Ying et al. [8] Main goal here was to classify images for crime scene investigation. They used transfer learning to train the CNN. After extraction of all layers, they got higher CSI image classification performance. Their accuracy in S–fine-tuned model (96.35%) and lowest in VGG-s model (90.09%).

The use of active millimeter wave radar shown by O'Reilly et al. [9] for processing signals to detect concealed weapons. Authors basically preprocessed signals using ANN. The ANN's training, which requires the network to be trained on each weapon subclass type, is a flaw in this technique, resulting in a decline in the classifier's performance. Their ANN had an 80% true positive rate or detection rate, but the false positive rate or false alarm rate was just 6%. The results suggest that an ANN evaluated with the third knife test set would have a detection rate of 80% but a false alarm rate of 329%, indicating a considerable drop in performance. Mentioned a possible solution though they did not try.

Active appearance model is mentioned by Glowacz et al. [10] in detecting just one object which is knife. It is comparable to the techniques used in face segmentation and medical image analysis to detect a known object in an image, as well as an interest point typical of knives–to see if a knife is present in the image. They might also be used in baggage scanning systems.

Grega et al. [11] classified only two objects which are firearms and knives; they have mentioned that their algorithm will be able to alert people when these two objects

are found in the camera. They have also come up with a version of a weapon detection system that produces almost no false alarms. Haar cascade, OpenCV, pattern recognition, fuzzy classifier, and feature descriptor were all employed in this research.

In another research, author described a comprehensive system for detecting fingerprints at crime scenes using deep machine learning and convolutional neural networks (CNNs). Precision photography and sophisticated physical and chemical processing procedures are used to gather and store images from crime scenes as databases. Basically, they use fingerprint samples to detect criminals, not crime. And finally, they achieved 80% accuracy where our accuracy is much better [12].

Also a study used CCTV surveillance to monitor traffic and unprecedented violence in synchronization mode [13]. They used a motion detection algorithm and contour filtering. Also, to prove their accuracy, they compared it with the existing algorithm Lucas-Kanade's and showed that theirs is better.

It is important to detect the crime scene before an unanticipated situation occurs. This paper motivates in this case.

3 Methodology

Our first goal is to classify datasets. As we are working with 4 types of objects, we will do classification of all the object's datasets. With the classified datasets, the machine will be trained so that it can detect objects based on the datasets. Figure 1 depicts the entire workflow for identifying crimes and issuing alerts.

The camera will record the video and each of the frame generated from the video will be tested with this model so that it can detect any incidents and violations. We only have constructed the model in this research. The overall process of detecting incidents or violations from frames through the model is depicted in Fig. 2.

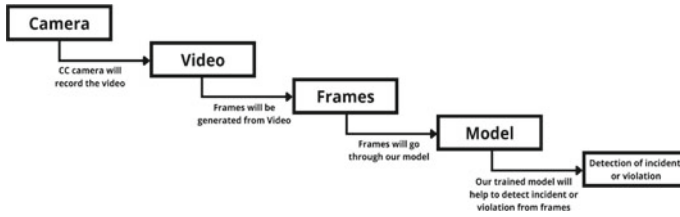**Fig. 1** Method of detecting crime and sending signals

Fig. 2 Process of detecting incidents or violations from frames through the model

3.1 Dataset

In this paper, we collected all the data from different sources from the Internet which are mentioned in the reference section. Then we processed our data to ensure accuracy across the board. After preprocessing, we basically will extract the features from, create a list of objects as directory names, and lastly train our algorithm so that it can detect object's classes. Figure 3 shows the workflow diagram. Data (images) counts for all the mentioned classes given in Table 1.

Handgun: Crime scene may happen and can be detected by CCTV camera. Criminals can also use weapons like pistols. So, this dataset is used where several types of handguns are there. This dataset [14] contains a variety of pistol-in-hand sample images. It includes 1249 images.

Fire: Fire also included in one of the objects to be detected. Basically, used for scenes where fire in a car accident or by blasting something. This dataset [15] is divided
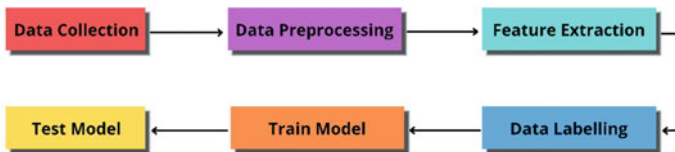

Fig. 3 Workflow diagram

Table 1 Data (images) counts for all the mentioned classes (4)

Name	Types	Amount	Total
Handgun	Pistol	1249	1249
Fire	Fire	999	999
Knife	Knife in hand	500	500
Accident	Car	592	2301
	Truck	576	
	Bike	568	
	Accidents in night	565	

Fig. 4 Dataset

into two parts where one includes fire images and another includes non-fire images. Fire image has about 755 images of fire, whereas the non-fire image's part includes 244 images and in total, it has 999 images.

Knife: For committing crime, criminals may also use a knife also. Thinking about that, the machine also trained with images of this knife dataset. Numerous pictures of knives in hands are here in this dataset. This dataset [16] includes 500 images.

Accident: This dataset is used for detecting accidents. Three types of vehicle car, trucks, and bike accident images are here. This dataset [17] includes 592 images of car accidents, 576 images of truck accidents, and 568 images of bike accidents. Lastly, 565 images are there for accidents that happened at night. Finally, it includes 2301 images in total (Fig. 4).

Each of the dataset is classified using CNN. The reason is, deep learning has emerged as a powerful machine learning technique that incorporates several layers of features or data representation and yields cutting-edge results. Deep learning applications have demonstrated outstanding performance across a range of application domains, but notably in the classification, segmentation, and object recognition of images. The performance of fine-grained image classification, which tries to differentiate subordinate-level categories, has recently improved [18]. Convolutional neural network is a part of the deep learning branch of machine learning. Deep learning algorithms analyze information in the same manner that the human brain does, albeit on a much smaller scale due to our brain's complexity as our brain has around 86 billion neurons. Extracting characteristics or features from images in order to find patterns in a dataset is known as image classification. Convolution is the process of multiplying two functions pointwise to create a third function where the image pixel matrix is one function, and filter is another. Using an ANN for image classification would be extremely computationally costly because of the vast size of the trainable parameters. So, choosing CNN will be a good move and we did it. We also used TensorFlow in CNN implementation which is a free and open-source framework for numerical computation and machine learning on a large scale.

Table 2 Objects information

SL	Object names
1	Handgun
2	Fire
3	Knife
4	Accidents

3.2 Data Preprocessing

As we already have given an idea about all 4 types or classes of datasets which are handgun, fire, knife, accident earlier, we have stored all the images in separate directories which were used as classes later. Because of collecting datasets from different sources. The resolution or size of images was not similar and messy. Thus, all classes had different sizes of images. So, we have resized the whole dataset's images into 256×256 pixels. Finally, all the 5049 images were resized to 256×256 to make the machine easy to learn.

3.3 Dealing with Objects

We have previously given a general notion of the objects. Handguns, fire, knives, and accidents will be the objects here to be detected. In the system, each image is organized into a directory, and the name of the directory is used to identify each object. A list of related items that were automatically derived from the directory names has been prepared to detect them (objects) as in Table 2.

3.4 Splitting the Dataset

This dataset contains 5049 images including all 4 classes. We have divided the complete dataset into batches where each batch has 32 images. After splitting as batches, we got 158 batches for the whole dataset. About 80% of the dataset is taken for training, 10% for validation, and 10% is for testing of the rest data. So, the measurement after splitting the dataset for training dataset is 126.4 batches where we have taken integer numbers, so 126 batches are taken for training. Similarly, 17 batches are taken to test the dataset and rest 15 batches for validation. Dataset is shuffled several times for better evaluation.

3.5 Data Normalization

Images inside the datasets are resized and rescaled by dividing each pixel by 255 for easier measurement. In a brief, the pixel values might be anything between 0 and 255. A color code is represented by each digit. The computation of large numeric values may get more difficult when utilizing the picture as is and sending it through a deep neural network. We may lessen this by normalizing the numbers to a range of 0–1.

3.6 Data Augmentation

Data augmentation is a term used in data analysis which describes methods and helps in enhancing the amount of data there by adding slight modification with copies of existing data or developing new synthetic data from existing data. It functions as a regularizer and aids in the reduction of overfitting during the training of a machine learning model. It has a close link to oversampling in data analysis. In a conclusion, we have chosen the following methods.

We used random flip to flip the dataset images horizontally and vertically. Besides, we have used random rotation in a scale 0.2 for augmentation. As a result, it was possible to consume a good accuracy. So, we can conclude the procedures like below,

- Training images are flipped horizontally.
- Training images are flipped vertically.
- Training images are rotated negative 90°.
- Training images are rotated positive 90°.

3.7 Model

We used the CNN deep learning methodology to train our model after our most recent deep learning study found that CNN is the best method for computer vision (CV). Various convolutional neural networks or CNN multilayers are utilized to train the dataset. The best performing network has six convolutional layers, a flatten layer, and two dense layers like Fig. 5.

(3×3) kernel size was varied in each convolutional layer. On separate levels, we utilized various filters. We started with 32 filters on the first layer, then 64 filters on the second layer and in all the subsequent layers, we have used the same filter size (64). We employed a maxpooling layer after each convolutional layer, with a pool size of (2×2). Model architecture summary is given in Table 3.

The dimension of data was changed from the convolutional layer where we have used a flatten layer and by this, we feed them into dense layer. We have used a single dense layer which had 64 hidden units and the activation function was "ReLU" as
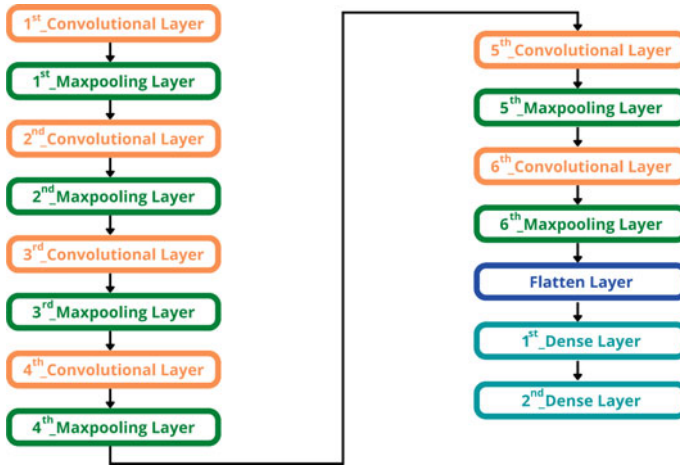
Fig. 5 Model architecture

Table 3 Model architecture summary

Layer no (type)	Output shape	Parameter
(Input layer)	64, 256, 256, 3	0
1 (Conv2D)	64, 254, 254, 32	896
2 (MaxPooling2D)	64, 127, 127, 32	0
3 (Conv2D)	64, 125, 125, 64	18,496
4 (MaxPooling2D)	64, 62, 62, 64	0
5 (Conv2D)	64, 60, 60, 64	36,928
6 (MaxPooling2D)	64, 30, 30, 64	0
7 (Conv2D)	64, 28, 28, 128	73,856
8 (MaxPooling2D)	64, 14, 14, 128	0
9 (Conv2D)	64, 12, 12, 128	147,584
10 (MaxPooling2D)	64, 6, 6, 128	0
11 (Conv2D)	64, 4, 4, 64	73,792
12 (MaxPooling2D)	64, 2, 2, 64	0
13 (Flatten)	64, 256	0
14 (Dense)	64, 32	8224
15 (Dense)	64, 4	132

Total parameters: 359,908
Trainable parameters: 359,908
Non-trainable parameters: 0

before. The equation for ReLU function is (1),

$$\text{ReLU}(X) = \text{MAX}(0, X) \tag{1}$$

The rectifier linear activation function (ReLU) is substantially more effective computationally. Here, if the input is negative, return 0; else, leave the input as it is.

A dense layer was also used to simulate the output layer, with four hidden units. In this layer, we employed the activation function "softmax" (2). Convolutional neural network (CNN), a subtype of deep neural networks (DNNs), is one that we have utilized in this instance because of its superior accuracy. DNNs, or deep neural networks, are employed often. The most significant nonlinear function in DNNs is the softmax function. Therefore, softmax is utilized as a result [19].

$$\sigma(z)_j = \frac{e^{zj}}{\sum_{k=1}^{K} e^{zk}} \quad \text{for } j = 1, \dots, k \tag{2}$$

The parameters used here are, σ which denotes softmax, z which is the input vector, K is the number of classes, the standard exponential function for the input vector is used as e^{zj} and e^{zk} means the standard exponential function for the output vector.

For optimization, the "adam" (3) optimizer was utilized. Because the Adam optimizer gives better results, takes less time to compute, and requires fewer tuning parameters than other optimization algorithms [20]. As a result of all of this, Adam is recommended as the default optimizer for most applications.

$$\theta_{t+1} = \theta_t - \frac{\eta}{\sqrt{\hat{v}_t} + \varepsilon} \hat{m}_t \tag{3}$$

$\theta_{(t+1)}$ and θ_t define weights at time $t + 1$ and t, respectively. ε here is a tiny positive constant to prevent the "division by 0" error. η defines step size parameter/learning rate (lr). m_t is combined gradients at time t, current (initially it is 0, $m_t = 0$). v_t defines squared sum of the previous gradients. (initially, V_t also stays at 0). The bias-corrected weight parameters $(\hat{m})t$ and $(\hat{v})t$ have been utilized in place of the standard weight parameters (m_t and v_t).

We allowed the optimizer to dynamically generate learning rate. So, it adopts the optimal pace of learning rate on its own.

To compute the particular loss, we utilized cross-entropy (4) loss function. As a loss function, the mentioned technique employed categorical cross-entropy (4). It outperforms all other loss functions, according to our study.

$$L_i = -\sum_j t_{i,j} \log(p_{i,j}) \tag{4}$$

Parameters are, L_i is known as loss, $\log(p_{i,j})$ is the scalar value in model output and finally, $t_{i,j}$ denotes the target value.

4 Model Evaluation

From the dataset, we have utilized 80% of the images for training, 10% for validation, and the rest 10% for the test set. So, 126 batches where there are 4032 images or 80% were taken for training, 15 batches with 480 images or 10% for validation, and the rest 17 batches with 537 images or 10% were taken for the test set. All the images are not evenly divided by the number of batches as it is not a multiple of the all number of images, 5049 by 32.

4.1 Learning Curve

In machine learning, the optimal value of a model's loss function for a training set is compared to the same loss function assessed on a validation dataset with the same parameters as the ideal function through a learning curve which is also known as training curve. Learning curves may be plotted after each update during training. The model is evaluated using a training dataset and a holdout validation dataset. The learning curve based on train test accuracy and loss is shown in Fig. 6.

Based on this learning curve, we can see that our model has neither underfitting nor overfitting concerns. The model stabilized over time, improving in accuracy.
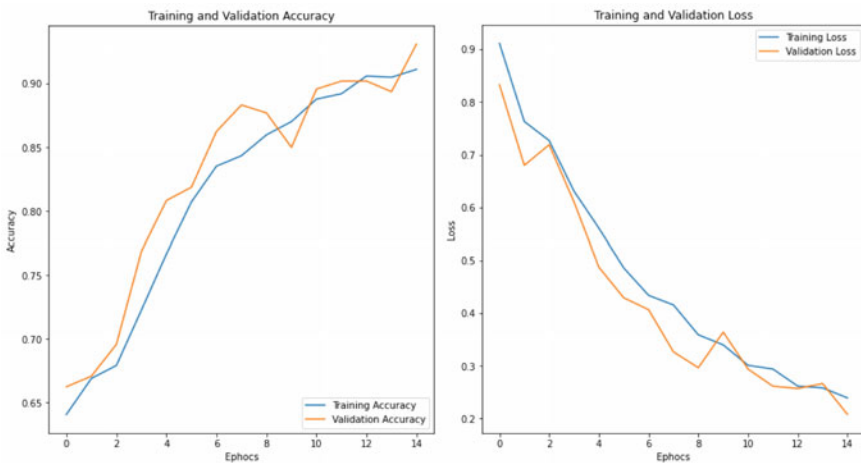

Fig. 6 Learning curve

4.2 Accuracy and Loss

We have tried with 20 epochs initially and noticed that after 15 rounds, the accuracy remains constant which is 92%. So, we reduced the epochs to 15 and finally got an accuracy of 92.10% on the test dataset and 21.38% loss. For the validation dataset, the accuracy was 93.12% and loss was 20.79%.

4.3 Prediction

We have tested the model with some random images to check whether it can predict the class accurately or not. 9 images were taken to test as input and the machine could predict all the images correctly. So, the actual label and predicted label were the same in the result as in Fig. 7. The confidence level also mentioned in the figure.

5 Conclusion

In this paper, violations and incidents have been shown to be very easily eliminated. By violations and incidents, we meant accident, fire, murder, stealing, and many more other crimes. The main goal is to detect such crimes by CCTV cameras. After detecting any crime activities, the machine will be able to send a warning message with required information like location, video, sound. With the help of this, it is possible to solve many hidden crimes that may happen out of the people's eye, authority, government, etc. Basically, 4 types of classification which are handgun, fire, knife, accidents separately done initially where each of them used to train machines by the help of CNN. We achieved 92.10% test accuracy. There may be some drawbacks like detecting mentioned objects in low light. Our goal is to solve as many of the drawbacks as possible. Thus, the system can be used and be one of the reasons for moving forward in the modern era. In the future, we will add a real-time detection facility based on processing videos. Build a reliable system reducing drawbacks and train machines such that it can detect required objects in low light as maximum crimes are committed at night. Will also work with optimization of the systems so that it can work smoothly. Future world is not limited to these 4 types of crimes we have currently working for. We will find all types of incidents and violations as many as possible.

Fig. 7 Prediction result

References

1. Bangladesh crime rate and statistics 2000–2022. MacroTrends [Online]. Available: https://www.macrotrends.net/countries/BGD/bangladesh/crime-rate-statistics. Accessed: 31 Jul 2022
2. Crime rate by country 2022 [Online]. Available: https://worldpopulationreview.com/country-rankings/crime-rate-by-country. Accessed: 06 Aug 2022
3. Albawi S, Mohammed TA, Al-Zawi S (2017) Understanding of a convolutional neural network. In: 2017 international conference on engineering and technology (ICET), pp 1–6. https://doi.org/10.1109/ICEngTechnol.2017.8308186
4. Lee WC, Khoo BE (2010) Forensic light sources for detection of biological evidences in crime scene investigation: a review
5. Miyahara A, Shimabukuro K, Nagayama I (2014) A study on intelligent security camera for crime scene detection. In: Proceedings of the ISCIE international symposium on stochastic systems theory and its applications, pp 34–40. https://doi.org/10.5687/sss.2014.34

6. Nakib M, Khan RT, Hasan MS, Uddin J (2018) Crime scene prediction by detecting threatening objects using convolutional neural network. In: 2018 international conference on computer, communication, chemical, material and electronic engineering (IC4ME2), pp 1–4

7. Saikia S, Fidalgo E, Alegre E, Fernández-Robles L (2017) Object detection for crime scene evidence analysis using deep learning, pp 14–24. https://doi.org/10.1007/978-3-319-68548-9_2

8. Ying L, Qian Nan Z, Fu Ping W, Tuan Kiang C, Keng Pang L, Heng Chang Z, Lu C, Jun LG, Nam L (2021) Adaptive weights learning in CNN feature fusion for crime scene investigation image classification. Connect Sci 33:719–734

9. O'Reilly DB, Bowring NJ, Harmer S (2012) Signal processing techniques for concealed weapon detection by use of neural networks. In: 2012 IEEE 27th convention of electrical and electronics engineers in Israel, pp 1–4

10. Glowacz A, Kmieć M, Dziech A (2013) Visual detection of knives in security applications using active appearance models. Multimed Tools Appl 74. https://doi.org/10.1007/s11042-013-1537-2

11. Grega M, Matiolanski A, Guzik P, Leszczuk M (2016) Automated detection of firearms and knives in a CCTV image. Sensors (Basel, Switz) 16

12. Pavithra R, Suresh KV (2019) Fingerprint image identification for crime detection. 0797-0800. https://doi.org/10.1109/ICCSP.2019.8698014

13. Dhaya R (2020) CCTV surveillance for unprecedented violence and traffic monitoring. J Innov Image Process 2:25–34. https://doi.org/10.36548/jiip.2020.1.003

14. University of Granada (2020) Pistols object detection dataset—resize-416 × 416. Roboflow, 16 Feb 2020 [Online]. Available: https://public.roboflow.com/object-detection/pistols/1. Accessed: 31 Jul 2022

15. Saied A (2020) Fire dataset. Kaggle, 25 Feb 2020 [Online]. Available: https://www.kaggle.com/phylake1337/fire-dataset. Accessed: 31 Jul 2022

16. Shekhar S (2020) Knife dataset. Kaggle, 02 Mar 2020 [Online]. Available: https://www.kaggle.com/shank885/knife-dataset. Accessed: 31 Jul 2022

17. Mghatee, Mghatee/accident-images-analysis-dataset: this data-set includes 10480 images including three folders namely accident—detection, vehicles-in-accidents and accident-severity. The number of classes are 2,3 and 3 for the these folders. GitHub [Online]. Available: https://github.com/mghatee/Accident-Images-Analysis-Dataset. Accessed: 31 Jul 2022

18. Dhillon A, Verma G (2019) Convolutional neural network: a review of models, methodologies and applications to object detection. Progr Artif Intell 9. https://doi.org/10.1007/s13748-019-00203-0

19. Gao Y, Liu W, Lombardi F (2020) Design and implementation of an approximate Softmax layer for deep neural networks. In: 2020 IEEE international symposium on circuits and systems (ISCAS), 2020, pp 1–5. https://doi.org/10.1109/ISCAS45731.2020.9180870

20. Rabby AKMSA, Sadeka H, Abujar S, Hossain S (2018) EkushNet: using convolutional neural network for Bangla handwritten recognition. Proc Comput Sci 143:603–610. https://doi.org/10.1016/j.procs.2018.10.437

Fiber Bragg Grating Strain Sensors in Smart Factories: Review of Opportunities and Challenges

Paul Stone Macheso and **Mohssin Zekriti**

Abstract Physical parameter monitors are necessary for the conversion of conventional factories to smart factories. The creation of new sensors for monitoring physical parameters in difficult-to-access areas is necessary for this move. In this line, a large number of optical sensors based on integrated optical wave guides or optical fibers have been designed and manufactured over the previous ten years. As a potent tool for real-time monitoring of physical parameters like temperature, pressure, strain, and humidity. Fiber Bragg Grating (FBG)-based sensors have attracted a lot of attention. The main reasons for using FBG sensors in smart factories are immunity to electromagnetic interference and radio frequency; compact in size and offer multiple sensing to different physical parameters; permit remote sensing and are not prone to corrosion. In this paper, a review of FBG-based sensors for strain parameter monitoring and their application in the smart factories is presented. An overview of the historical background is followed by an explanation of the fundamentals of FBG sensing and a discussion of the electromagnetic theory of waveguide modes in optical fibers. Then give a review of current research in FBG strain sensor development. A review of the challenges and applications of FBG strain sensors specifically in smart manufacturing follows.

Keywords Fiber Bragg grating · Optical fiber sensors · Strain · Smart factories · Bragg wavelength · Photo-sensitivity

P. S. Macheso (✉) · M. Zekriti
Euromed Research Center, Euro-Mediterranean University of Fes, Fes, Morocco
e-mail: p.macheso@ueuromed.org

1 Introduction

1.1 A Historical Context of Fiber Bragg Gratings

The discovery of photosensitivity in optical fibers has led to the development of numerous devices for a range of purposes [1]. This finding significantly influenced the advancement of sensor and communication systems. The basis for a fiber Bragg grating is often the photosensitivity feature of silica fiber doped with germanium (FBG). When exposed to ultraviolet (UV) radiation, some doped glasses exhibit photosensitivity, which results in a higher refractive index. As a result, when a fiber is exposed to UV radiation, its refractive index changes permanently, with the shape and characteristics of the UV exposure beam having an impact [2].

When a side of fiber is exposed to UV light by the interference of two crossing beams, an FBG with a user-defined central wavelength that is independent of the wavelength of the writing beam is produced. With lengths ranging from millimeters to centimeters, this UV treatment will permanently etch a regular form with a periodicity half the necessary Bragg wavelength into the fiber core. Because the FBGs may be generated with such freedom, Bragg wavelengths that are much beyond the telecommunications wavelength of 1550 nm can be written [3].

2 Literature Survey

Fiber Bragg grating (FBG) strain sensors are a well-established research topic and are also growing their market share because of their high sensitivity and affordable price. Rao et al. [4] looked at a review of FBG strain sensors with an emphasis on the physical principles, interrogation methods, and read-out procedures.

Newly developed high performance single head FBG,categories are highlighted in particular, and to which FBG strain sensors belong. A number of alternative sensing methods are mentioned, such as mode-locked FBG strain sensors splitting. Their operational theory and performance are recorded, and they and those of classic architectures are contrasted [5]. To sum up, certain innovative applications and substantial market sectors for fiber-optic strain sensors are predicted, in addition to the key market players active in this sector.

Fiber-optic sensing is now a practical option for evaluating the effectiveness of civil infrastructure due to substantial advancements in the field [6]. Their unique qualities make them an important choice for civil engineers and a reliable option alternative to conventional sensors [7]. These features include small size, high resolution, great long-distance signal transmission, immunity to electromagnetic and radio frequency fields interference, and the capacity to multiplex a number of probed sensors.

Due to its small size, as stated in [8], the fiber Bragg grating sensor is compactly or superficially connected to a range of materials, including concrete, reinforcing steel, steel sheets, fiber-reinforced polymer (FRP) strips, and others.There has been a lot of recent study on the use of fiber Bragg gratings (FBGs) as optical sensors to monitor structural performance [8]. The foundation of many of these studies is the ability of fiber optic sensors to track the internal strain of structures.

The method for designing wide-range FBG strain sensors described in this study [9] can be used to find extra-large strain in unusual structures. For accurate measurement, the elastic modulus, and adhesive layer thickness are investigated in the wide-range FBG strain sensor's strain transmission rate distribution. The wide-range FBG strain sensor, which is the subject of this study, has been proposed, and its capable of simultaneously experiencing and quantifying the extra-large strain experienced by the unique structure [9]. Although this sensor has potential uses for tracking the structural health of unusual structures, one drawback was that it wasn't used in smart factories.

Zhang et al. [10] examined the design and calibration of a small, multi-component force sensor based on an elastic transducing body and eight multiplexed fiber Bragg gratings. They provided construction instructions for multiplexed multi-component force sensors based on FBG strain sensors. Zhang et al. [10] suggested that due to their multiplexing abilities and immunity to electromagnetic interference, multi-component force sensors may be preferable to fiber Bragg grating (FBG) strain sensors for carrying out these local strain measurements in the control of robots in electromagnetically noisy environments. Despite strides in strain monitoring, the technique not applied in a sophisticated industrial setting.

In [11] they suggested additional research on the application of optical Fiber Bragg Grating (FBG) strain sensors for gear diagnostics. Although it can be extremely useful, the development, justification, and experimental validation of a novel diagnostic approach based on FBG strain sensors for both gear types under various operating conditions, such as speed and load, as well as for local problems of various severity levels, is not yet implemented in smart factory settings.

A number of fiber-reinforced polymer (FRP) packaged optical fiber Bragg grating strain sensors were suggested by [12] in order to fully address the requirements of difficult civil engineering infrastructures. Experimental research is done to examine how well these sensors operate in both common and difficult conditions. Experimentally and conceptually, it has been shown that FRP-packaged FBG strain sensors have significantly higher durability in harsh environments while maintaining the same exceptional sensing performance as the bare FBG sensor. However, this work suffered greatly because these sensors were not used in smart factory settings.

A fiber-optic Bragg Grating (FBG) strain sensor for uniaxial rock compression testing was discussed in [13]. For the cylinder-shaped rock samples, the optical FBG sensors were made by hand and put together. A compression test on a hard rock sample was conducted after a calibration procedure was completed to ensure the mechanical performance of the FBG package. The strain was then measured using both the conventional Bragg grating sensor and the compression sensor. The FBG

strain sensor prototype offered potential uses in structural health monitoring but was not used in a smart industrial environment.

The use of a fiber Bragg grating (FBG) strain sensor for oil and gas derrick health monitoring was suggested by the authors of [14]. The system was composed of the optical interrogator, monitoring program, and FBG strain sensors. When the sensors were fastened to a derrick, the system's performance was evaluated. The outcomes demonstrated the viability of the field application. The work exploited significant electromagnetic radiation immunity benefits of optical sensors, but it had a limitation in that it was not applied in a smart factory environment, which is consistent with the industrial 4.0 characteristics.

In [15] they propose for sustainable industrialization using IoT and big data analysis with machine learning to pave the way for industrial processes that are resource and energy efficient conservation, product development that satisfies both current and future demands, and safe and skill-enhancing employment with low waste generation, execution speed, and cost. Through sustainable practices enabled by the processing and analysis of industrial data using big data and IoT, the verified model is effective in terms of power consumption, latency, and execution time, resulting in a decrease in the creation of industrial waste and an increase in production rate. The study's strengths made use of cross disciplinary technologies like machine learning and the Internet of Things (IoT), but not fiber Bragg grating sensing technique.

A novel, extremely accurate strain measurement technique based on a fiber Bragg grating sensor was also reported in the Moreover Ref. [16]. The sensor is more sensitive than a fiber Bragg grating sensor alone because it combines a fiber Bragg grating with a sensitivity-boosting technique. The suggested strain sensor's ability to detect battery strain has been shown in a test comparing it to bare fiber Bragg grating sensors. This FBG method is essential for extended use in smart factories since it offers battery management systems information on the load placed on power batteries.

In this paper there a review of opportunities and challenges of using Fiber Bragg Strain Sensors in smart factories which are inline with the industrial 4.0 is presented which has more advantages by blending the inherent advantages of FBG sensors and the technological aspect of smart factories having automation and connectivity as its central backbone.

3   Theory of Fiber Bragg Grating Sensors (FBG's)

The essential idea behind an FBG-based sensor is the wavelength change of the perturbed Bragg signal as a result of measurement factors including strain, temperature, and force. Relevant factors are the material's refractive index and grating pitch [15].These gratings work in sensor systems by absorbing light from a Bragg wavelength portion of the spectrum.

FBGs are systems that use the diffraction grating theory and are created by periodically modulating the longitudinal index of refraction of the fiber core [16] The
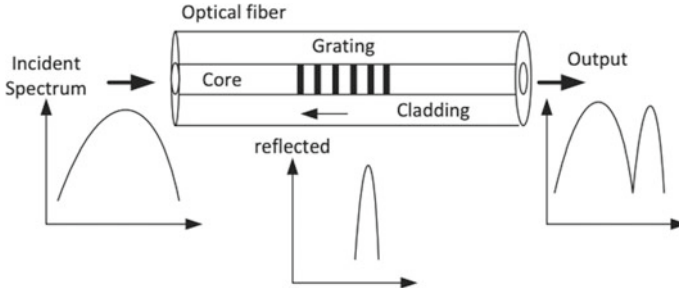
Fig. 1 Structure of fiber Bragg grating [7]

core's refractive index is supposed to vary on a regular basis thanks to the grating. The grating lets light through as The structure's gratings all reflect some light back (Fig. 1).

The refractive index of the optical fiber core (n_{eff}) with respect to the grating length and the period of the grating microstructure (Λ) effectively define the Bragg wavelength (λ_B).

$$\lambda_B = 2n_{\text{eff}}\Lambda \tag{1}$$

The shift in Bragg grating wavelength can be calculated by expanding Eq. (1) in terms of partial derivatives with respect to the temperature, wavelength, and length.

$$\Delta\lambda_B = 2\left(\Lambda\frac{\delta n_{\text{eff}}}{\delta L} + n_{\text{eff}}\frac{\delta\Lambda}{\delta L}\right)\Delta L + 2\left(\Lambda\frac{\delta n_{\text{eff}}}{\delta T} + n_{\text{eff}}\frac{\delta\Lambda}{\delta T}\right)\Delta T$$
$$+ 2\left(\Lambda\frac{\delta n_{\text{eff}}}{\delta\lambda} + n_{\text{eff}}\frac{\delta\Lambda}{\delta\lambda}\right)\Delta\lambda \tag{2}$$
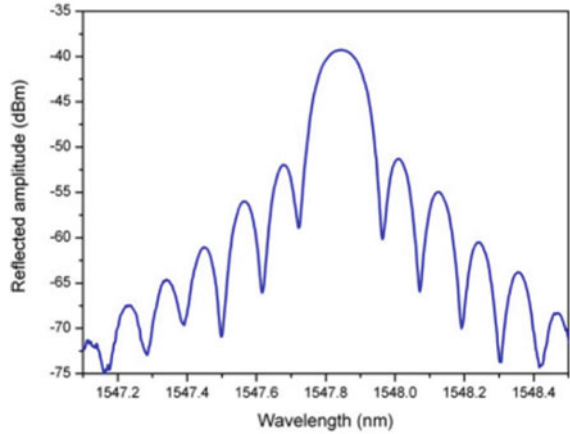
where ΔL is the change in physical length of the grating due to the temperature applied, ΔT is the change in Temperature and $\Delta\lambda$ is the change in wavelength.

As shown in Fig. 2 for a 1 cm long FBG, a uniform FBG acts as a selective mirror in the wavelength region close to the Bragg wavelength to produce a pass-band reflected amplitude spectrum. In reality, a faint Fresnel reflection is produced for each change in the refractive index along the fiber axis. At the Bragg wavelength, they increase phase, creating a broad reflection band bordered by side lobes. The highest peak reflected amplitude is -40 dBm, with a wavelength range of 1547.2–1548.4 nm.

4 Strain Optical Response

Bragg grating is impacted by the strain in two different ways. First, the Bragg wavelength will change due to the alteration in the physical distance between succeeding index modulations. Second, the strain-optic effect will cause a change in refractive

Fig. 2 Spectrum of reflected amplitude of a 1 cm long uniform FBG

index, which will cause the Bragg wavelength to shift [17]. The central wavelength of the Bragg grating varies as a function of strain as follows:

$$\Delta\lambda_B = 2\left(\Lambda\frac{\delta n_{\text{eff}}}{\delta L} + n_{\text{eff}}\frac{\delta\Lambda}{\delta L}\right)\Delta L \tag{3}$$

where ΔL denotes the change in physical length caused by the applied strain on the grating. Provided that the integrated path of the longitudinal strain is given by $\varepsilon_z = \frac{\Delta L}{L}$. Equation (3) can be rewritten as:

$$\Delta\lambda_B = 2\Lambda\frac{\delta n_{\text{eff}}}{\delta L}\Delta L + 2n_{\text{eff}}\frac{\delta\Lambda}{\delta L}\varepsilon_z L \tag{4}$$

Defining

$$\Delta n_{\text{eff}} = \frac{\delta n_{\text{eff}}}{\delta L}L \tag{5}$$

And

$$\Delta\left(\frac{1}{n_{\text{eff}}^2}\right) = \frac{2\Delta n_{\text{eff}}}{n_{\text{eff}}^3} \tag{6}$$

By Substituting Eqs. (5) and (6), Eq. (4) can be written as

$$\Delta\lambda_B = 2\left[\frac{-n_{\text{eff}}^3}{2}.\Delta\left(\frac{1}{n_{\text{eff}}^2}\right)\right] + 2n_{\text{eff}}\varepsilon_z L \tag{7}$$

Having a grating with a particular center wavelength ,λ_B, the shift in the center wavelength is denoted as

$$\frac{\Delta\lambda_B}{\lambda_B} = (1 - p_e)\,\varepsilon_z \tag{8}$$

where P_e is 0.213 for germanosilicate optical fiber and ε_z is the applied strain. Equation (8) can be rearranged and simplified as follows:

$$\Delta\lambda_B = \lambda_B \left(1 - p_e\right)\varepsilon_z \tag{9}$$

When the Fiber Bragg Grating is strained, its central wavelength λ_B drifts. Equation (9) is a way to express wavelength shift where p_e is the photo-elastic constant, and ε_Z is the strain applied.

4.1 Calibration of FBG Strain Sensors

Calibration for temperature-dependent strain readings is described in [17] using a four point bending test and might be used for this study. Electrical strain gauges are employed for calibration, and a finite element model is provided for comparison. It was presented in a way to calibrate FBG sensors over a wide-range of positive and negative strain values utilizing the four point bending test. It is crucial to know if the strain in that area is constant because electrical or FBG sensors assess an average strain along the gauge length.

5 FBG Strain Sensor Opportunities in Smart Factories

Optical sensors are becoming one of the most important components in a number of industrial sectors, including the manufacturing, civil and energy, medical, automotive, and aerospace industries [18]. The increasing installation of items using optics technology is the main factor driving the global market for distributed optic temperature sensing. In smart factories, fiber Bragg gratings are widely utilized for strain sensing, particularly in hard environments with high temperatures, severe electromagnetic interference (EMI), or highly corrosive environments. During the development and testing of a prototype, strain monitoring is essential. Strain measurements guarantee that parts function as intended and that the apparatus is robust and reliable [18, 19].

When inspecting complicated structures like aircraft and turbines in smart manufacturing, it's crucial to pay particular attention to strain monitoring. Although there are various ways to measure stress, the FBG sensors are the most effective overall for measuring strain [20]. It is possible to assess the dynamic strain in a variety of transportation systems, including automobiles, trains, and airplanes. Dynamic strain testing and vibration stress testing with fiber Bragg gratings have numerous more applications than construction projects and automobiles. Industrial machinery can be equipped with FBG sensors to measure the frequency and amplitude of stress vibrations.

Utilizing some extremely tiny FBG sensors, which can be used in smart electronic sectors, it is possible to monitor the stress in electric circuit boards and other constrained areas. Residual stress monitoring, which is crucial in smart factories, is the measurement of stress during casting, welding, and forming activities. For this use, FBG strain sensors are widely employed. They can also be used to monitor stress during rapid drilling operations in smart manufacturing.

6   Challenges of FBG Strain Sensors

The handling of the FBG strain sensors is difficult due to their fragility, wavelength cross sensitivity, and bulky interrogation devices. Because FBG strain sensors are constructed of fragile optical fiber cables that cannot endure process conditions, they are challenging to install in smart manufacturing environments [21]. Along with these difficulties, using pricey, intricate industrial equipment like oscilloscopes and optical spectrum necessitates a high level of deployment and maintenance skill [22].

Additionally, since both temperature and strain cause a Bragg wavelength shift, temperature strain discrimination is another difficulty that cannot be overcome by a single FBG [23]. The above-mentioned issue, demodulation of amplitude spectrum throughout the curing cycle process, is resolved in practice using two FBGs with different temperatures and/or strain sensitivities [24].

7   Conclusion and Future Scope

The usage of Fiber Bragg strain sensors in smart factories was studied in this paper, which began with a historical review of FBGs before conducting an extensive literature review of FBG-based strain sensors. The physics underpinning fiber Bragg grating optical sensors is also well covered, as is the optical response of FBG strain sensors. These FBG strain sensors are used in smart factories for cars and transportation systems and have applications in harsh environments. However, they are expensive to implement and call for specialist equipment like optical spectrum analyzers and interrogators.

Due to their inherent advantages, more intelligent FBG sensors are predicted to be released onto the market in the near future. To connect these sensors, diagnostic tools, and other associated equipment, optical communication will also be used. Manufacturing will use an increasing number of optical sensors based on FBG to monitor physical characteristics, including strain measurements. The sensing system would also be hooked to a central network, allowing devices to function remotely, gather data, and perform fundamental computer operations. Additionally, future plans must take into account the use of portable, affordable interrogators to improve the demodulation of sensor data.

Fabrication of strain FBG sensors employing phase mask technology and their deployment in a smart manufacturing environment should be implemented in future scope. The simulation in ANSYS Lumerical FDTD and COMSOL software will be implemented.

References

1. Hill KO, Fujii Y, Johnson DC, Kawasaki BS (1978) Photosensitivity in optical fiber waveguides: application to reflection filter fabrication. Appl Phys Lett 32:647–649
2. Othonos A, Kalli K (1999) Fiber Bragg gratings-fundamentals and applications in telecommunications and sensing. Artech House, Boston
3. Kashyap R (2009) Fiber Bragg gratings. Academic Press
4. Rao YJ, Webb DJ, Jackson DA, Zhang L, Bennion I (1997) In-fiber Bragg-grating temperature sensor system for medical applications. J Lightw Technol 15(5):779–785
5. Jung J, Nam H, Lee B, Byun JO, Kim NS (1999) Fiber Bragg grating temperature sensor with controllable sensitivity. Appl Opt 38(13):2752–2754
6. Zhang B, Kahrizi M (2007) High-temperature resistance fiber Bragg grating temperature sensor fabrication. IEEE Sens J 7(4):586–591. https://doi.org/10.1109/JSEN.2007.891941
7. Mihailov Stephen J (2012) Fiber Bragg grating sensors for harsh environments. Sensors 12(2):1898–1918
8. Daud S, Ali J (2018) Fibre Bragg grating and no-core fibre sensors. Springer, New York
9. Daud S, Aziz MSA, Chaudhary KT, Bahadoran M, Ali J (2016) Sensitivity measurement of fibre Bragg grating sensor. J Teknol 78(3)
10. Zhang D, Wang J, Wang Y, Dai X (2014) A fast response temperature sensor based on fiber Bragg grating. Measur Sci Technol 25(7):075105
11. Pinet E, Hamel C (2007) True challenges of disposable optical fiber sensors for clinical environment. In: Third European workshop on optical fibre sensors, vol 6619. International Society for Optics and Photonics, p 66191Q
12. Liao CR, Wang DN (2013) Review of femtosecond laser fabricated fiber Bragg gratings for high temperature sensing. Photon Sens 3(2):97–101
13. Lee CH, Lee J, Kim MK, Kim KT (2011) Characteristics of a fiber Bragg grating temperature sensor using the thermal strain of an external tube
14. Cheng Y, Lu X, Gong Y, Wu Y, Rao Y (2013) Derrick safety monitoring system based on fiber Bragg grating strain sensors. Photon Sens 3(3):237–240
15. Suma V (2019) Towards sustainable industrialization using big data and internet of things. J ISMAC 1(01):24–37
16. Zhu P, Wu J, Huang M, Feng X, Deng H, Xie H, Soto MA (2019) Alternating strain response of fibre Bragg grating sensors embedded into carbon fibre composites for wind blade health monitoring. In: Seventh European workshop on optical fibre sensors, vol 11199. SPIE, pp 81–84
17. Prussak R, Stefaniak D, Kappel E, Hühne C, Sinapius M (2019) Smart cure cycles for fiber metal laminates using embedded fiber Bragg grating sensors. Compos Struct 213:252–260
18. Kreuzer M (2006) Strain measurement with fiber Bragg grating sensors. HBM, Darmstadt, S2338-1.0 e, 12
19. Sahota Jasjot K, Gupta Neena, Dhawan Divya (2020) Fiber Bragg grating sensors for monitoring of physical parameters: a comprehensive review. Opt Eng 59(6):060901

20. Grouve WJB, Warnet L, de Boer A, Akkerman R, Vlekken J (2008) Delamination detection with fibre Bragg gratings based on dynamic behaviour. Compos Sci Technol 68(12):2418–2424
21. Sorensen L, Gmür T, Botsis J (2006) Residual strain development in an AS4/PPS thermoplastic composite measured using fibre Bragg grating sensors. Compos Part A Appl Sci Manuf 37(2):270–281
22. Rao YJ (1997) In-fibre Bragg grating sensors. Measur Sci Technol 8(4):355
23. Qiu Y, Wang QB, Zhao HT, Chen JA, Wang YY (2013) Review on composite structural health monitoring based on fiber Bragg grating sensing principle. J Shanghai Jiaotong Univ Sci 18(2):129–139
24. Sundaram BA, Kesavan K, Parivallal S, Ahmed AF, Ravisankar K (2011) Monitoring of FRP strengthened concrete structures using FBG sensors. Proc Eng 14:1549–1556

Development of Converged Contents Applications Using Beacon with Bluetooth v4.0

Kil Hong Joo and Nam Hun Park

Abstract Recently, the commercialization of various convenience services using beacon on the Bluetooth low energy technology is on the rise as one of the results of technological innovation by the information communication technology, which rapidly develops with the coming of the fourth industrial revolution. In addition, due to expansion of the scope of information communication infrastructure and things such as "smart city", a large-scale convergence contents platform based on the IoT becomes one of the major issues in the IT industry. However, the technical measure concerning the management and processing of data collected by wireless sensor devices such as beacons is still unclear, and the concrete solutions to this problem are currently needed. Therefore, this study suggests one basic point about the technique to analyze and manage the large data collected by the beacon. It also efficiently provide the converged contents service using the user information data stored in the server. The development of this application enhances the social utilization value of beacon service in the future.

Keywords Beacon · Bluetooth · Bluetooth low energy · Internet of things (IoT) · Convergence contents

1 Introduction

IT infrastructure, which shows phenomenal growth figures worldwide every year, is gradually taking root in our lives today thanks to innovative technological developments not only quantitatively but also qualitatively. Thanks to such influence, the

K. H. Joo
Department of Computer Education, Gyeongin National University of Education, 155, Sammak-ro, Manan-gu, Anyang-si, Gyeonggi-do, Republic of Korea
e-mail: khjoo@ginue.ac.kr

N. H. Park (✉)
Department of AI Convergence, Anynag University, 22, Samdeok-ro 37beon-gil, Manan-gu, Anyang-si, Gyeonggi-do, Republic of Korea
e-mail: nmhnpark@anyang.ac.kr

demand for related contents through media such as web and application increases exponentially throughout society such as humanities, engineering, art, education, physical education, and medicine. have. Accordingly, various contents utilizing information and communication technology have been improved in quality technology, and contents services useful in our real life such as location-based information contents are being provided in the form of web or applications like an explosion. In addition, as the popularization of mobile devices such as smartphones and tablet PCs has become a catalyst, various mobile services using short-range wireless communication technologies such as RFID, NFC, Bluetooth, and beacon are being provided. As one of the national strategic projects recently announced by the government, research and development on "smart city" technology, which integrates and builds the entire city's infrastructure into one, and manages the data using IoT technology, is being actively conducted. Nevertheless, the current address of short-distance wireless communication technology shows that the service that can be actually applied is limited due to the technical limitations of the region where the service is provided and the data storage space, and that it provides only low-capacity basic data information. In the current era of preparing for the 4th Industrial Revolution, in a situation where more efficient measures for management, operation, and maintenance of large data such as big data are urgently needed, the technical limitations of data transmission are due to the expansion of mobile services, where demand is continuously skyrocketing. It can cause serious disability [1, 2]. In addition, in business marketing where service speed is important, the provision of innovative mobile content that satisfies the client's requirements and the absence of a management system for it can become a stumbling block against the flow of the information age to be led in the future [3, 4]. Therefore, in order to plan and effectively supply contents that play a key role in the business marketing of these mobile services, a new concept of customer-oriented convergence that actively reflects the needs of clients, consumers, by combining various cutting-edge IT technologies including short-distance wireless communication technology. The development of technology is absolutely necessary [5, 6]. Accordingly, in this study, using Bluetooth low energy (BLE)-based beacons, customized integrated content services covering life, culture, and medical categories are provided through client-friendly applications, and an app content management system that stores client information as the main server, collects this stored data, and puts statistically analyzed figures on the dashboard through the content management system (CMS) to analyze customer tendencies or patterns in an easy-to-understand manner for managers who are content providers. We want to present a model, and by applying beacon technology to the existing content and giving variety of content types in terms of quality, we contribute to the commercialization of next-generation urban smart integrated content service that can realize one-to-one business marketing through the analysis of collected data [7–9].

Fig. 1 Beacon service

2 Related Works

2.1 Beacon Service

Beacon is one of short-distance wireless communication technologies such as NFC and is a representative beacon device as shown in Fig. 1. It provides various services centered on low-power Bluetooth-based beacons with relatively low battery consumption, such as Apple's iBeacon. This beacon is usually linked with Bluetooth to send a signal to a mobile device, and when the mobile device that received this signal transmits an ID value to the cloud of a dedicated server, it receives the data value through authentication and verification [10–12]. In addition, since beacons can provide an active location information service linked with GPS, users are increasingly expected to use them in terms of ease of use.

2.2 Comparison of Beacon and NFC

Until recently, in the mobile service market, NFC was mostly established in various services centered on payment services such as T-money, concert tickets, and mobile payment, but now, the position is gradually replaced by beacons combined with low-power Bluetooth [13]. Since the communication range of NFC is only 10 cm or less, the service is possible only when the terminal or payment device is in close contact, so the safety is high in terms of security [14, 15]. On the other hand, beacon has the advantage of a wide communication range (based on Bluetooth v4.0) of up to 50 m or more, and because service is provided through an app installed on a smartphone, short-distance contact is unnecessary. It has a very advantageous advantage in terms of popularity because it is not only inexpensive, but also has a low maintenance cost. Comparison of Beacon and NFC is given in Table 1.

Table 1 Comparison of beacon and NFC

	Beacon	NFC
Transmitting/receiving range	Up to 50 m	10 cm or less
Base technology	Bluetooth	RFID
Power consumption	Up to 2 years	No battery required
Main features	1:n services Various SW app Bluetooth executional and related SW Active service	1:1 services Strong security Passive service

3 Development Details

3.1 Test Environment for Beacon App

In this study, Odroid-C2 compatible with Ubuntu 16.04 on Kernel 3.14 and Android 5.1 × on Kernel 3.14 was used for smooth testing of beacon-only applications. The specifications of the Bluetooth module are high speed v3.0 and low energy v4.0, and the beacon adopts Onyx Beacon One, a basic type of Onyx Beacon with iBeacon technology, and in the case of a coin battery, the lifespan is 1 year, and the range of application can be recognized up to 40 m. Odroid-C2 (L) and Onyx Beacon One (R) used for app. function test is shown in Fig. 2.

Fig. 2 Odroid-C2 (L) and Onyx Beacon One (R) used for app. function test

3.2 Development Configurations

Android Studio was used for the development of this beacon app, and after planning and designing the activities and UI for each part using this development tool, the function test of the developed app was repeatedly performed in the Odroid-C2 environment through the coding process.

3.3 Beacon App Setting

In this app, the initial user goes through the login process through the e mail account registration process, and if the account is not registered, the app service cannot be used. Various numerical analysis of pattern analysis and app performance evaluation for each user is possible on the dashboard within Firebase. Application's Account Registration and Login Activity are shown in Fig. 3.

In this study, focusing on the fact that the marketing service through the issuance of electronic coupons randomly distributes electronic coupons in a random manner without understanding the user's store visit pattern in detail, a follow-up method to actively induce users to revisit. As a part of business marketing, the best convergence content service with reference to major domestic and foreign cases to implement life, culture, and medical content functions applicable to various environments that meet the requirements of this beacon app as an app, and utilize them in actual business

Fig. 3 Application's account registration and login activity

Table 2 Activity design of convergence content functions

Life contents	Cultural contents	Medical contents
Production information	Reservation information	Hospital information
Discount information	Stadium information	Medical staff information
Store GPS	Cultural locations	Hospital locations

Table 3 Codes related to coupon transfer function

* Sending coupons
1 onyxBeaconManager.setCouponEnabled(true); //Redeem coupons linked to nearby beacons//
2 "main_package.content" //Coupon listener – broadcasting new actions//
//When the application is in the background, a manifest is registered in a subclass of BroadcastReceiver to receive coupons//
4 <receiver android:name="packageName.ContentReceiver">
5 <intent-filter>
6 <actionandroid:name="packageName.content/>
7 </intent-filter>
8 </receiver>

sites function was applied. Activity design of convergence content functions is given in Table 2.

In case of notification message of this app, it is processed as two events, action filtering and scanning event part. In case of action filtering, package setting is defined as "app.package.name.scan" and scanning event setting is defined as "BeaconApplication.SCAN_EVENT" did. The related codes for these two items are "beacon scanning event" and "invalid RSSI identification", and the beacon scanning event is coded to work when the app's Bluetooth scanner cannot scan a beacon within the transmission/reception range for a certain period of time did. Also, invalid RSSI identification works when multiple scanned beacons receive an RSSI value, which is displayed on the app screen by "BeaconApplication.INVALID_RSSI" as an error event of the Bluetooth stack. The coupon sending function of this app consists of the codes given in Table 3.

4 Experiments and Evaluations

After running this app for the first time, it goes through the login process of entering an email address and password through a registered email account, and then moves to the main menu where you can use the contents. The activity layout of the main menu is divided into three parts: a content delivery part, a beacon scanning part, and a user menu part. For the experimental evaluation of the app developed in this study,

Fig. 4 Beacon scanning activity's major/minor numbering value

the process of interworking with a Bluetooth v4.0-based beacon and the functional test of the convergence content service was set as the experimental evaluation goals.

4.1 Beacon and App Integration Test

In this experiment, a scanning function for a plurality of beacons and an interworking test with an app in a building where actual beacons are installed was performed. A beacon basically has a unique identification code for each device, and in this identification code, unique numbering of major and minor values is written for each beacon device. Based on this numbering, as a result of scanning, 10 beacons spaced at intervals of about 5 m within a radius of 40 m, which is the maximum transmission/reception range based on this numbering, all beacons were scanned on the app screen in Fig. 4. It was confirmed that normal reception sensitivity was maintained.

4.2 Converged Contents Service Test

In this experiment, a test was performed by running an app installed on a Bluetooth-enabled smartphone. First, the coupon transmission function was tested, and the product information and GPS location information functions were evaluated. Figure 5 shows the screen in which the program proceeds normally as a result of performing a simulation in which coupons are transmitted to the smartphone.

When an app user enters a store with a smartphone, it receives a signal from a beacon installed at the entrance and sends an ID from the server operated by the store manager to receive product or sale information, as shown in Fig. 6.
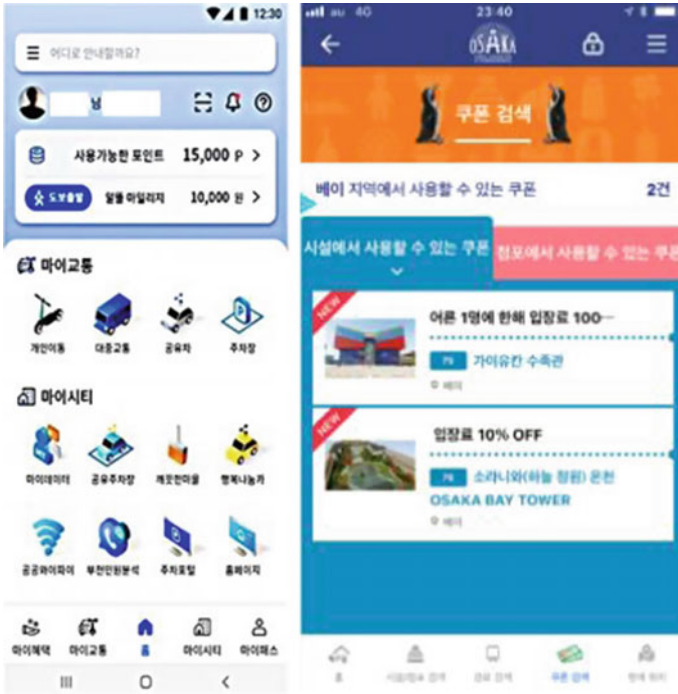
Fig. 5 Lifestyle contents coupon delivery activity
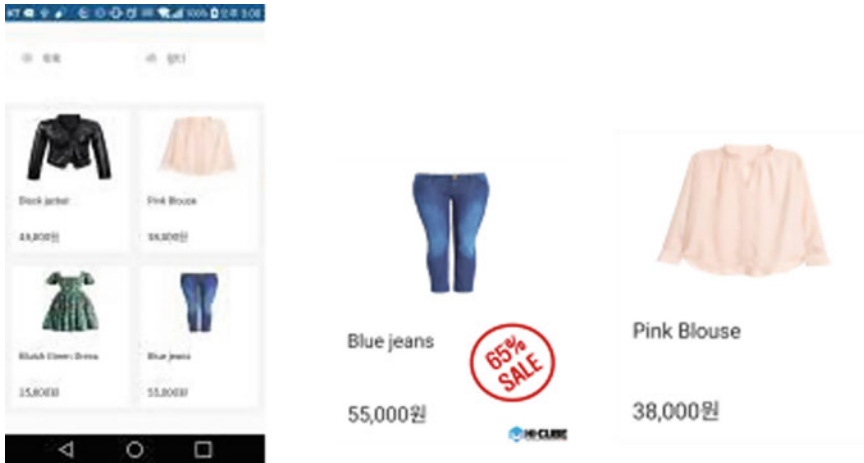
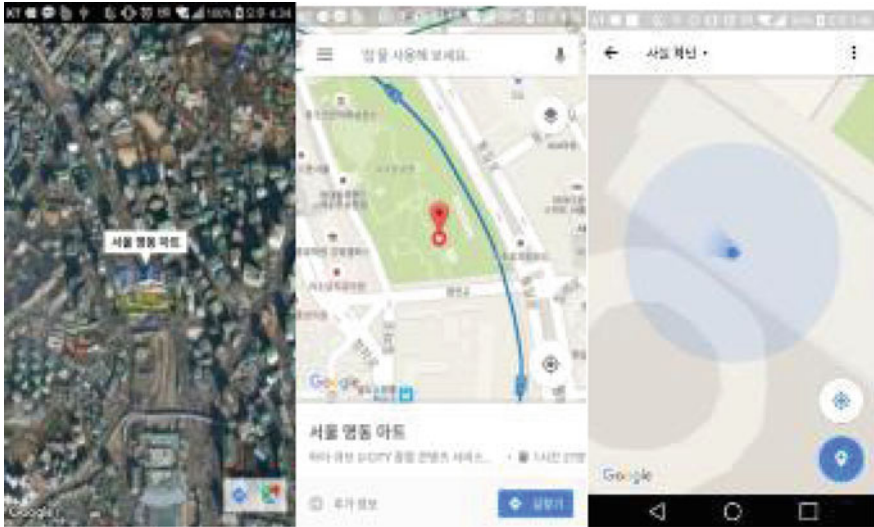**Fig. 6** Lifestyle contents services

Fig. 7　Lifestyle contents GPS location service

Real-time geographic information service is provided to users based on Google Earth, and the markup of stores where beacon service is available is shown on the map, and store location, shortest route, transportation, and location information away from the store are displayed as shown in Fig. 7.

In the case of cultural contents, content services for spectator seating information, game information, and GPS location information are provided, and the function implementation screen for each content as shown in Fig. 8.

In the case of medical content, hospital information, hospital promotion, and GPS location information content services are provided, and the function implementation screen for each content for this content as in Fig. 9.

4.3　Performance Evaluation

Repeated tests were performed to evaluate the performance of this developed app, and a total of three areas of living content, cultural content, and medical content were selected as evaluation targets. In the case of, we measured the response time when sending a ticket and, in the case of medical content, when sending a message. As a result of the measurement, a result value higher than the standard value was derived, and an error was detected about 1 or 2 times, but the error code was checked through debugging the cause of the error. It can be seen that errors occur more frequently as the beacon transmission/reception range is large, and data delay decreases as the distance between the beacon and the mobile device is closer. Therefore, in this experimental evaluation, as shown in Fig. 10, it was numerically proved that the
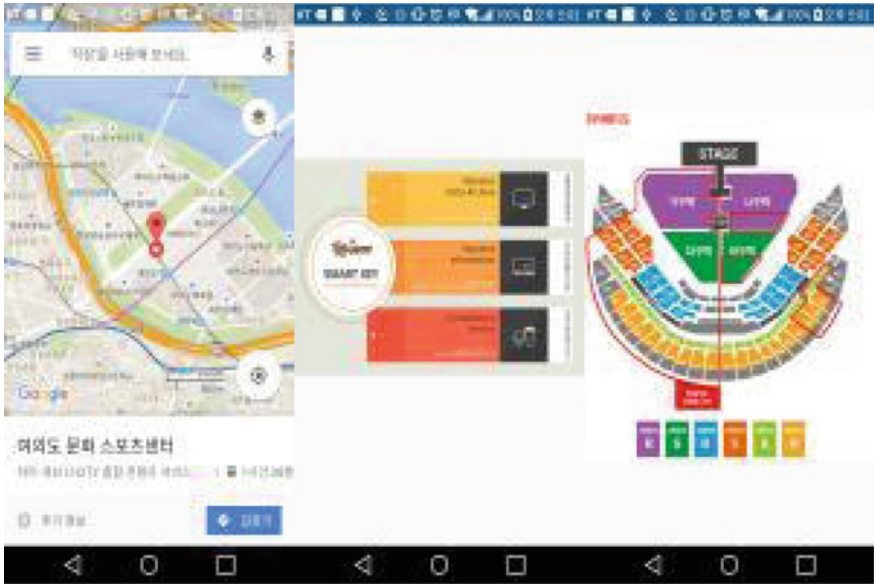
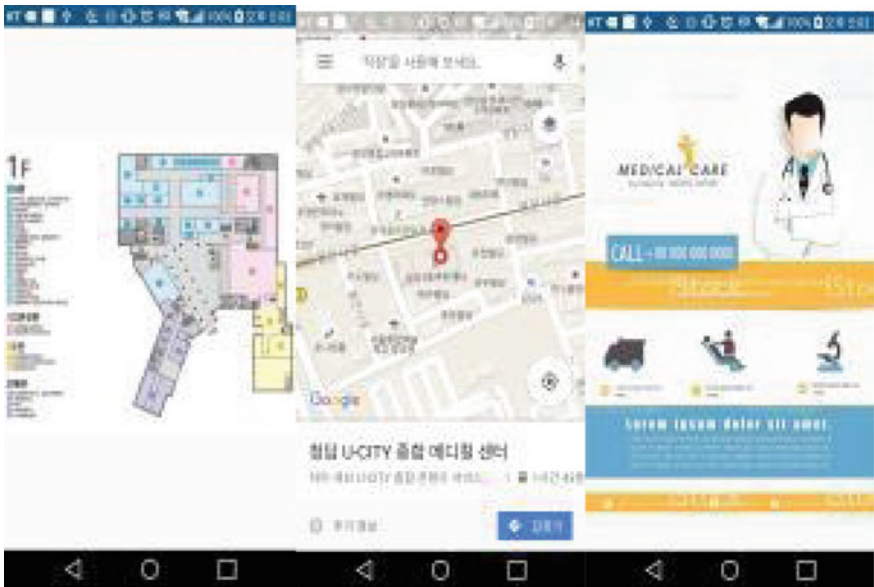**Fig. 8** Cultural contents service

Fig. 9 Medical contents service

accuracy of app data transmission normally shows a value above the standard value from the 1st to 5th tests.

In addition, it was possible to derive the result that more effective marketing is possible by providing information by deriving user visit count, access rate, accumulation rate, time series status, etc., through interworking with beacons and content management system through the developed app. Response time and payload are shown in Fig. 11.
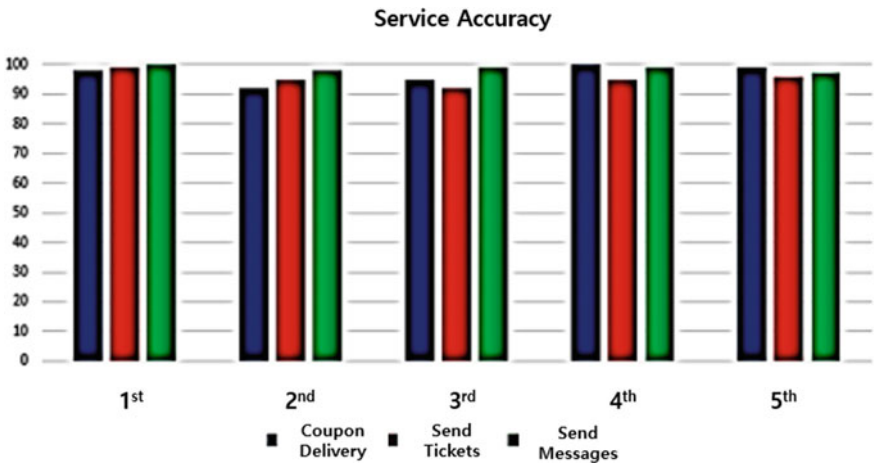
Fig. 10 Service accuracy
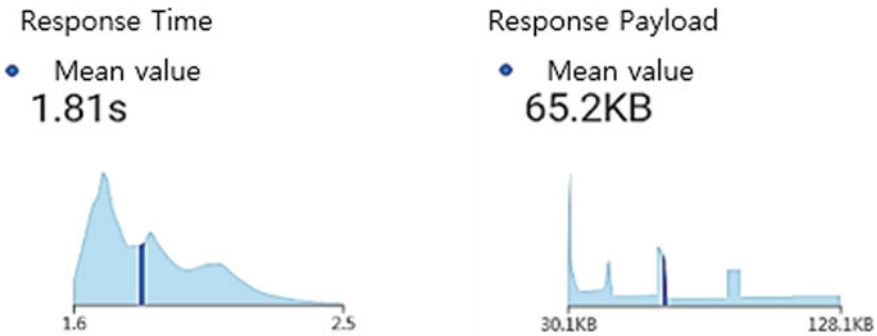
Fig. 11 Response time and payload

5   Conclusion

In this study, based on the converged content service function that enables app users to enjoy various services in various business marketing environments using Bluetooth v4.0-based beacons, and the collected data transmitted from the first beacon through the content management system platform connected to the server. We developed an app that can perform customer pattern analysis. Currently, various beacon services are in progress, but only simplified passive services are being made, and a system that can apply valuable data for collected user information data through an analysis process is not universal. In the future, through the results of this study, it is expected that it will be possible to provide more convenient convergence content services to users in the upcoming 4th Industrial Revolution era, and to expand the related service infrastructure according to the expansion of beacon services.

References

1. Seo JH (2014) The BLE based Super high speed and low power protocol for indoor localization between mobile and fixed device. Korea Computer Congress Paper
2. Griffiths S et al (2019) Exploring bluetooth beacon use cases in teaching and learning: increasing the sustainability of physical learning spaces. Sustainability 11(15):4005
3. Subedi S, Kwon G-R, Shin S, Hwang S-S, Pyun J-Y (2016) Beacon based indoor positioning system using weighted centroid localization approach. Information and Communication Engineering, Chosun University
4. Blasio D, Salvatore G et al (2019) Beacon-related parameters of bluetooth low energy: development of a semi-automatic system to study their impact on indoor positioning systems. Sensors 19(14):3087
5. Faragher R, Harle R (2015) Location fingerprinting with bluetooth low energy beacons. IEEE J Sel Areas Commun 33(11)
6. Liao J et al (2020) The use of bluetooth low energy Beacon systems to estimate indirect personal exposure to household air pollution. J Exposure Sci Environ Epidemiol 30(6):990–1000
7. Wang Y, Yang Q, Zhang G, Zhang P (2016) Indoor positioning system using Euclidian distance correction algorithm with bluetooth low energy beacon. In: International conference on Internet of things and applications, pp 243–247
8. Namgung H, Lim IK, Lee JW (2015) Using iBeacon positioning system location estimation techniques. J Korea Inst Inf Commun Sci 19(4)
9. Yao Y, Huang Y, Wang Y (2019) Unpacking people's understandings of bluetooth beacon systems—a location-based IoT technology. In: Proceedings of the 52nd Hawaii international conference on system sciences
10. Bouchard K, Ramezani R, Arjun A (2016) Naeim: evaluation of bluetooth beacons behaviour. In: IEEE 7th annual ubiquitious computing, electronics and mobile. Communication conference, pp. 1–3
11. Deepesh PC, Rath R, Tiwary A, Rao VN, Kanakalata N (2016) Experiences with using iBeacons for indoor positioning. In: Proceedings of the 9th India software engineering conference
12. Vivekanandam B (2021) Design an adaptive hybrid approach for genetic algorithm to detect effective Malware detection in android division. J Ubiquit Comput Commun Technol 3(2):135–149
13. Dickinson P, Cielniak G, Szymanezyk O (2016) Indoor positioning of shoppers using a network of bluetooth low energy beacons. In: International conference on indoor positioning and indoor navigation, pp 1–8

14. Golestanian M, Poellabauer C (2016) Indoor localization using multi-range beaconing poster. In: Mobile hoc'16 proceedings of the 17th ACM international symposium on mobile ad hoc networking and computing, pp 397–398
15. Asokan R, Vijayakumar T (2021) Design of Whatsapp image folder categorization using CNN method in the android domain. J Ubiquit Comput Commun Technol (UCCT) 3(03):180–195

A CNN-Based Underage Driver Detection System

Roshini Mohanan , **Jisha Jacob** , **and G. R. Gnana King**

Abstract The road accidents caused by driving of young and inexperienced drivers have been increasing day by day. Due to the rise in catastrophic accidents, there have been several serious injuries and damages. Therefore, age detection utilizing deep learning is established here in order to alert and stop these massive calamities. In this system, the CNN model is used to predict the age from a face image, and the age classifications task is developed as a classification problem. By predicting the age from the faces and barring the children from driving, the proposed method aids in keeping our children safe. Here first detect faces from the input video stream, then extract the face Region of Interest. Then, in order to estimate the age of a person, an age detector algorithm is employed here. In this system for face detection, Open CV's DNN module and DNN face detector are used. In this proposed system, the face is detected from the real-time video frames via a web camera. Then predict the age of the person from the face. If minor aged person is detected, then car cannot be started by that person and the system alert the guardians by alarm. If the detected person's age is above underage, then the car will start automatically. The system will also send an alerting SMS to the guardians using GSM module. The proposed system is intended to identify underage drivers and stop them from operating a vehicle.

Keywords Convolutional neural network · Deep neural network · Face detection · GSM · Open CV · SMS

1 Introduction

There are many fields that use age prediction, including smart human–machine interface growth, the artificial intelligence, health and electronic commerce. Accurately predicting the age of person is a major challenge. A number of applications now require automatic age and gender detection as a result of the growth of social networks and social media. Numerous technologies are currently available that can determine

R. Mohanan (✉) · J. Jacob · G. R. G. King
Sahrdaya College of Engineering and Technology, Kodakara, Thrissur, Kerala, India
e-mail: roshinivmohanan03@gmail.com

gender and age. The technologies include those used in retail, cosmetology, forensics, entertainment and more. Age prediction is important in crime investigation since it makes it easier to track down a specific criminal using that person's age. Nowadays, the field of computer vision began to take facial analysis seriously. A person's identity, age, gender, emotions and ethnicity can all be inferred from their face features. Age estimates from unfiltered faces in real time still need to be improved in order to satisfy the needs of real world applications. As a result, the community of computer vision continues to experiment with novel techniques and methods for ongoing improvement. The task of categorizing ages is developed in this case as a classification problem. The age can be determined from a face image using the CNN model. The eyebrows, mouth, nose and eyes are the fundamental facial features. The age can be determined from a face image using the CNN model.

Motor vehicle accidents are the primary cause of teen fatality. Among teenagers between the ages of 13 and 19 years, about 41% of fatalities are occurred. According to [1], the motor vehicle accidents are responsible for 57.9% of unintentional injury deaths in people aged 10 to 14 and 72.3% of unintentional injury deaths in people aged 15 to 19. With the lack of driving experience and despite the increasing accidents, teens are still taking the car. The youth gets into trouble because they are prone to sensation seeking, impulsive behavior and risk-taking. Sometime, young children also starts the car by mistakenly while playing. In order to prevent minors from operating a vehicle, this study proposes and experimentally tests an automatic system that can determine a person's age from face photos.

2 Related Works

The challenge of automatically extracting age-related features from facial images has drawn more and more attention in recent years. Many new approaches have been proposed recently. Dibyajyoti Sharma suggests various approaches and techniques in [2], including PCA, LBP, SVM, VIOLA-JONES and HOG. These techniques are used in a variety of situations to identify human emotion, gender and age through a webcam. According to Afroz [3], their project's main focus could be that a child wouldn't be able to turn on the stove. Therefore, [3] proposes an intelligent stove that may try to ensure safety and will detect age from real-time video streaming. The stove can also offer safety by emitting a gas detection alarm. The system is executed using CNN and the Haar Cascade object detection technique from machine learning.

Wanga [4] frequently emphasizes how convolutional neural networks can be used to train feature representations, leading to a significant improvement in age and gender prediction task performance. Here, a MATLAB image classifier is created. In this instance of deep learning, the CNN effectively creates abstract features from the training data. And it could otherwise need to be handcrafted in conventional machine learning approach. To train this deep network, a lot of processing power and time are required.

In [5], Sadia Mahjabin puts out a convolutional neural network-based age esti- mator that can almost precisely predict age from facial photos while using less training data than previous studies in the field. Low mean absolute error is main- tained here. Here, a model that performs age estimation as a regression problem is created on top of the 50-layer residual network. In order to improve age and gender prediction, a deep CNN is proposed in [6] and a significant improvement may be shown in a variety of tasks, including face recognition. In order to clearly advance, this topic using current techniques, a straightforward CNN architecture is presented in [6, 7]. The Paul Viola and Michael Jones' efficient method of using HAAR feature- based cascade classifiers to train a deep CNN model is effective. The cascade function is trained utilising a large number of positive and negative images in this machine learning-based process. The unfiltered faces that predict age and gender categorise unrestricted real-world facial photos into specified ages and genders [7, 8].

3 Proposed System

The proposed system is a child lock system that protects the children by preventing them from driving. Here, input image frames are get through the real-time video when the camera is on. Then face is detected from the frames using Open CV's DNN module and it supported the pre-trained face detector model. The input video frames are given to the pre-trained face detection model and face of the person is detected. And a bounding box is created across the face. Then the cropped face image is used as input image for age and gender estimation. Here, age and gender are detected using the CNN algorithm. For age detection, the input image is given to the trained model (saved model) created using the CNN model. Then the age of the person is predicted. After that, the predicted age output is given as input to the Arduino through USART. If the predicted age is above 18, then the car starts automatically. The car consists of 4 DC motors and it is controlled using a L293D motor driver IC. If the predicted age below 18, then a buzzer will be ON for alerting the parents. If the predicted age is near underage (19–21), then the system will send alerting SMS to the guardians using GSM. This alert message helps parents to know that whether their unlicensed children takes the car. Block diagram of the proposed system is shown in Fig. 1.

3.1 Software Implementation

Face Detection. Here, the faces are detected from the input video stream via web camera. Here, face detection is performed using the Open CV's DNN module. Caffe, TensorFlow and Torch/PyTorch are just a few of the deep learning frameworks that this module supports. This module supports DNN face detector. It utilizes ResNet- 10 architecture as its backbone. It supported the single-shot-multibox detector. The
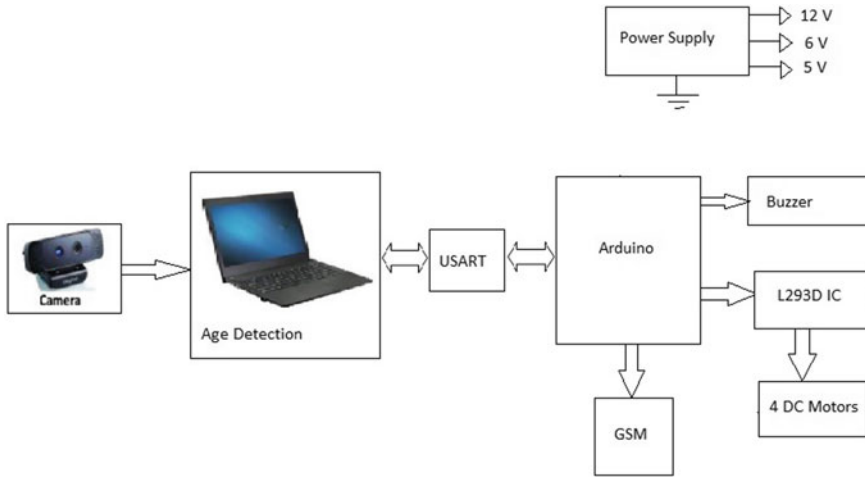
Fig. 1 Proposed system

Open CV provided pre-trained model of this face detector is used here and it is a quantized TensorFlow model. Here, there are two sets of files are used—.pb file and .pbtxt file. The .pb file is a protobuf file (protocol buffer) and it holds the graph definition and the trained weights of the model. The .pb file holds the protobuf in binary format and the .pbtxt file holds it in text format. For the face detection, the input video frames are passed to the pre-trained model and a bounding box is created across the face.

Age Detection. Here, extract the face Region of Interest after the face detection. It is given as input for age prediction. Then an age detector algorithm is applied for the prediction. Here, Caffe model is used for detecting the age. Two sets of files are utilized in the Caffe model. They are .prototxt file and .caffemodel file. The model architecture is described in the .prototxt file, and the weights for the actual layers are contained in the .caffemodel file. Here, UTKFace—age, gender and ethnicity (face data) csv dataset is used for training. The total age ranges are divided into 10 age groups. The 10 input classes are (0–5), (6–10), (11–15), (16–18), (19–21), (22–30), (31–41), (42–60), (61–80), (80–100).

CNN Model. Convolutional neural network is a deep neural network architecture used in computer vision. CNN is frequently utilized in a number of fields, including object detection, picture categorization, face recognition and image identification. In the CNN, the image classification takes place in several steps. First, it takes the input image data and processes the input data. Then classifies the data under certain categories. Then each input image is sent through a sequence of layers to train and test CNN models. The layers are convolution layers with filters or Kernels, pooling layer and fully connected layer. A softmax function is then used to categorize an image using probabilistic values between 0 and 1. And [9] has an example of categorize an
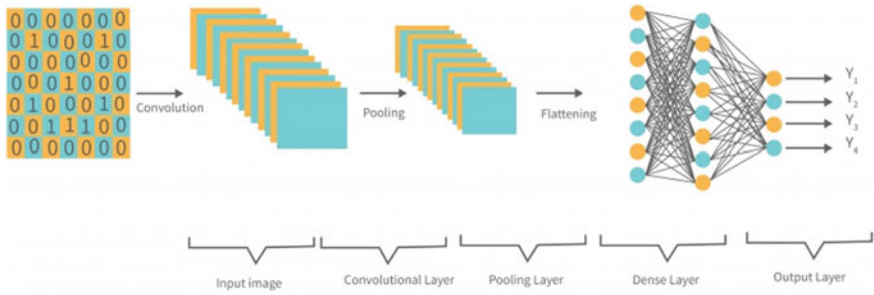
Fig. 2 CNN architecture. *Source* Google [13]

image of an object using softmax layer. A vector of *K* real numbers is transformed into a distribution of *K* potential outcomes using the softmax function. To normalize output to a probability distribution over expected output classes, the softmax function is typically used as the neural network's final activation function. Figure 2 shows the fundamental architecture of CNN [10–12]. Convolution procedure in the convolution layer retrieves features from the input images and feature map is the output of this process.

Reduce the feature map without removing the important features is the purpose of the pooling layer. The purpose of a classification unit is to produce output based on input data and it includes FC layers. The flattened input used by the fully connected layer means that each input is tied to each neuron. If FC layers are present, they are often located near the end of CNN architecture.

Caffe. A deep learning framework called Caffe was created by Berkeley AI Research and volunteers from the community. One NVIDIA K40 GPU can process more than 60 M pictures per day with Caffe. Application and creativity are encouraged by its expressive architecture. It is possible to switch between CPU and GPU by setting one flag to train on a GPU computer. Caffe is ideal for use in industry deployment and research trials due to its speed. For age estimation using the convolution neural network, gathering a large dataset for training the algorithm may be a monotonous and time consuming job. The dataset must be well labeled and from social image database which has the private information of the subjects.

Network Architecture. The proposed network architecture is used for both age and gender classification. By the network, all three color channels are processed directly. The input image size is 128×128. The network consists of 6 convolution layers.

Layer 1: Here, 8 filters and kernal size of 3×3 are convoluted with stride 1, padding 0 and activation-relu, which results in output of size $128 \times 128 \times 8$.

Layer 2: 16 filters and kernal size of 3×3 are convoluted with stride 1, padding 0 and activation-relu, which results in output of size $128 \times 128 \times 16$ which is followed by maximum pooling which reduce the size and dropout layer.

Layer 3: 16 filters and kernal size of 3 × 3 are convoluted with stride 1, padding 0 and activation-relu, which results in output of size 64 × 64 × 16.

Layer 4: 32 filters and kernal size of 3 × 3 are convoluted with stride 1, padding 0 and activation-relu, which results in output of size 64 × 64 × 32 which is followed by maximum pooling which reduce the size and dropout layer.

Layer 5: 32 filters and kernal size of 3 × 3 are convoluted with stride 1, padding 0 and activation-relu, which results in output of size 32 × 32 × 32.

Layer 6: 64 filters and kernal size of 3 × 3 are convoluted with stride 1, padding 0 and activation-relu, which results in output of size 32 × 32 × 64 which is then followed by maximum pooling which reduce the size and dropout layer get an output of size 16 × 16 × 64.

The convolutional layer is then followed by a flatten layer which reshapes the tensor to own a shape that is adequate to the quantity of elements contained within the tensor. This is the identical thing as making a 1d-array of elements. The flatten layer is then followed by a dense layer with 10 nodes. A softmax activation function is used in the dense layer. It assigns a probability for every class. Then predict the class which has the maximum probability for the given test image is taken as output of prediction.

UTKFace Dataset. The UTKFace dataset has large-scale face images. It has an age range from 0 to 116. This dataset has different annotations such as age, gender and ethnicity. The photos in the dataset vary greatly in resolution, occlusion, facial expression, illumination, position, etc. Some sample images of UTKFace dataset are shown in Fig. 3. The age, gender and ethnicity (face data) csv dataset [14] from kaggle are used here. This dataset consists of a CSV of facial images. The dataset consists a total of 23,705 images.

Fig. 3 Sample images of UTKFace dataset. *Source* Google, UTKFace dataset [15]
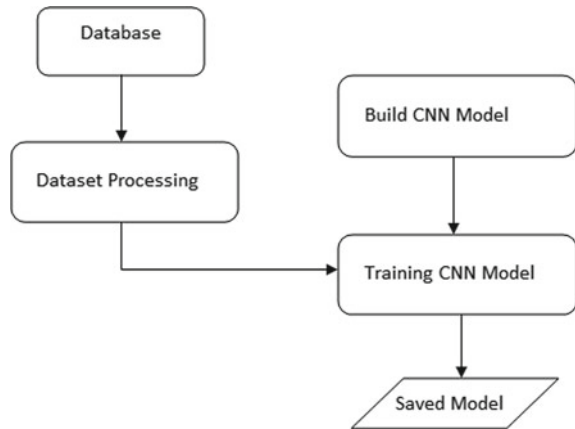
Flowchart The steps for training are depicted in Fig. 4. In the training phase, first the dataset is processed and CNN model is created. After that, the CNN model is trained using the processed dataset. And in the last step, the model is saved for future use.

The steps for testing are depicted in Fig. 5. After the completion of training, the model is used for predicting the age and gender. In the real-time testing phase, first read the input images from the camera. Then this image is passed in to the pre-trained face detection model and the face is detected. Then cropped the image by creating a blob from image. It resizes and crops image from center, subtract mean values, scales values by a scale factor of 1.0 and convert the image from BGR to RGB format and finally given it as input to our trained model. The predicted age and gender are then displayed on the screen continuously.

3.2   Hardware Implementation

Figure 6 shows the hardware implementation of the proposed system. The predicted output from the PC is fed to the Arduino via serial communication. The Arduino Uno is used here for controlling other hardware outputs (buzzer, GSM, L293D IC) according to the input conditions. The Arduino Uno is an open-source microcontroller board developed by Arduino.cc. The Microchip ATmega328P microprocessor is used in the Arduino Uno. GSM module is used for sending SMS to the guardians. GSM module is a device that gives a wireless data link to a network by using GSM mobile telephone technology. For network identification, the GSM module employs SIMs to identify the device and send SMS. When a person with age above 18 is detected, then the car starts automatically. Here, four DC motors are used for starting the car. A DC motor converts the direct current electrical energy into mechanical energy. The most popular types of DC motor are those that rely on magnetic field forces. A L293D

Fig. 5 Testing phase
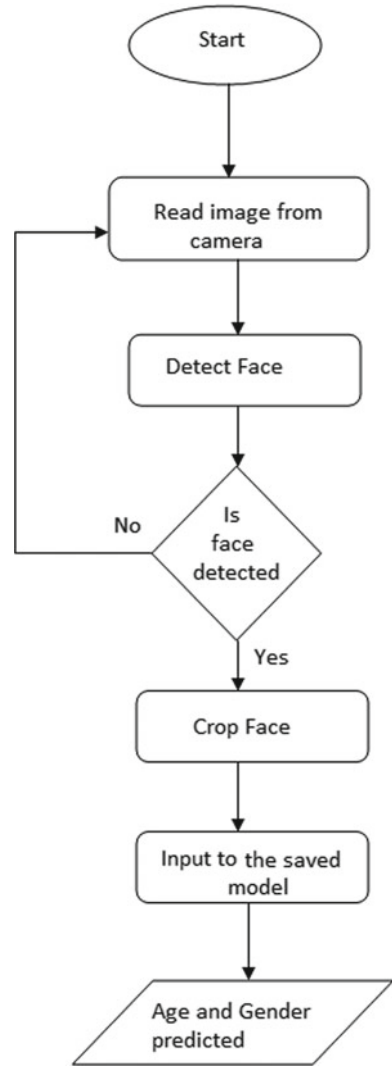
motor driver IC is used for controlling the DC motors. Piezoelectric buzzer is used for generating alarm for alerting the guardians. A 5v piezo buzzer is used for producing alarms when any under aged person is detected. A buzzer is an audio signaling device. Buzzer can be any of type mechanical, electromechanical, or piezoelectric. The circuit diagram of the hardware implantation is shown in Fig. 7.

The components required for the hardware implementation are listed below:

Arduino Uno: Microcontroller-ATmega328P, Operating voltage–5 V. Here, Arduino Uno is utilized to generate the outputs as displayed in Table.1 in response to the input conditions.
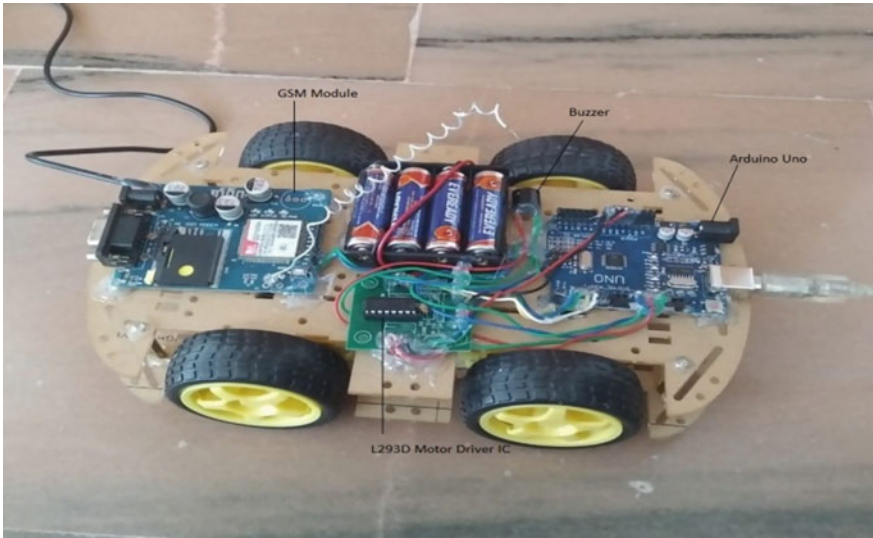
Fig. 6 Hardware implementation
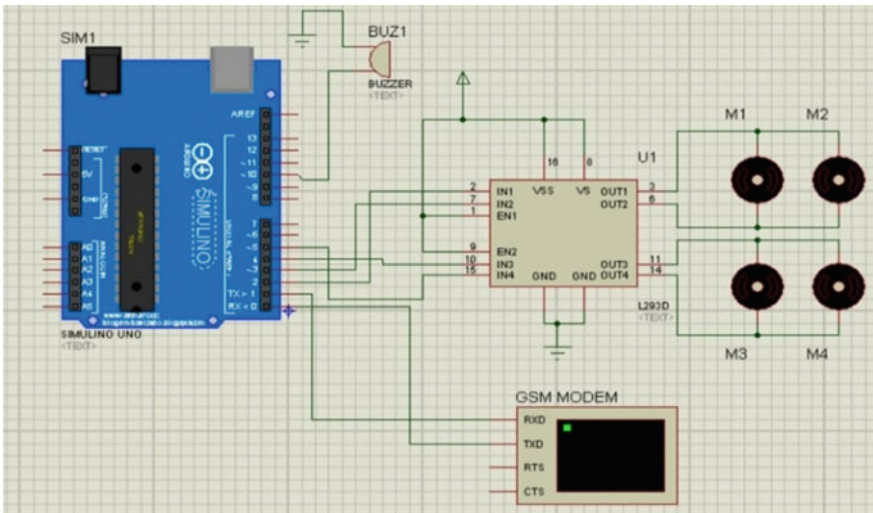
Fig. 7 Circuit diagram

Table 1 Test condition for proposed system

S. No.	Condition	Output
1	A = Age (19–21)	Car starts and SMS send
2	B = Age ≤ 18	Buzzer ON
3	C = Age > 18	Car starts

Buzzer: 5 V buzzer.

L293D motor driver IC: Motor output voltage—(4.5 V–36 V), Logic input voltage—5 V, Output Current per channel—600 mA. L293D IC is used to control the DC motors.

DC motor: 6 V, 100 RPM DC motor.

GSM Module: 12 V, SIM800.

4 Experimental Setup and Results

This section explains the experimental setup first and then the results. The work is implemented using Tensorflow, Keras and Python. The hardware requirements of the system are Arduino Uno, DC motor, GSM module, Piezoelectric buzzer. Software requirements are Pycharm-community, Python programming, Arduino IDE.

The proposed system is tested on some people of age below 18 and above 18. After getting the image through the real-time video using the web camera attached with the PC. In this system, the face is detected from the video frames using the pre-trained DNN face detection model. Then a bounding box is created across the face and the cropped face image is used as input image for age and gender estimation. And the class of image is predicted using our trained model of CNN. Finally, predict the age and gender of person in real time. A sample image of real-time age prediction is depicted in Fig. 8.
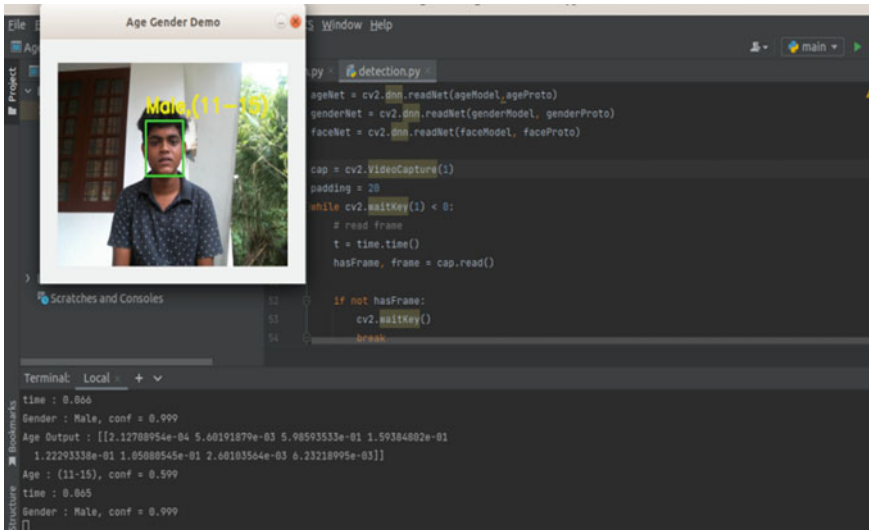
Fig. 8 Real-time age prediction output

After that, the predicted age output is given as input to the Arduino through USART. When the predicted age is above 18, the car is started automatically by starting the motors. When the predicted age is below 18, an alarm is produced using buzzer for alerting the parents. When the predicted age is near underage (19–21), the system send an alerting SMS to the guardians as shown in Fig. 9. The testing accuracy of the model is found to be 95%. The split ratio between training and testing dataset is 4:1. The training is done with 50 epoch. And an Adam optimizer is used here. Adam is an optimization algorithm that can be used to iteratively update network weights depending on training data. The accuracy graph of the training is depicted in Fig. 10. The proposed system successfully controlled the motor and detected the under aged people.

In the proposed system for serial communication, we assign some values to the respective age categories are given in Table 1. The value *A* is assigned for the age between 19 and 21, *B* is assigned for the age 18 and below 18 and *C* is assigned for the age above 18, and the respective output is shown in Fig. 11.

The proposed model is trained on Adience dataset and achieved a testing accuracy of 86%. In the existing work, [16] achieved an accuracy of 48.59% and used a dataset of Wiki, UTKFace and Adience datasets have been merged into one containing
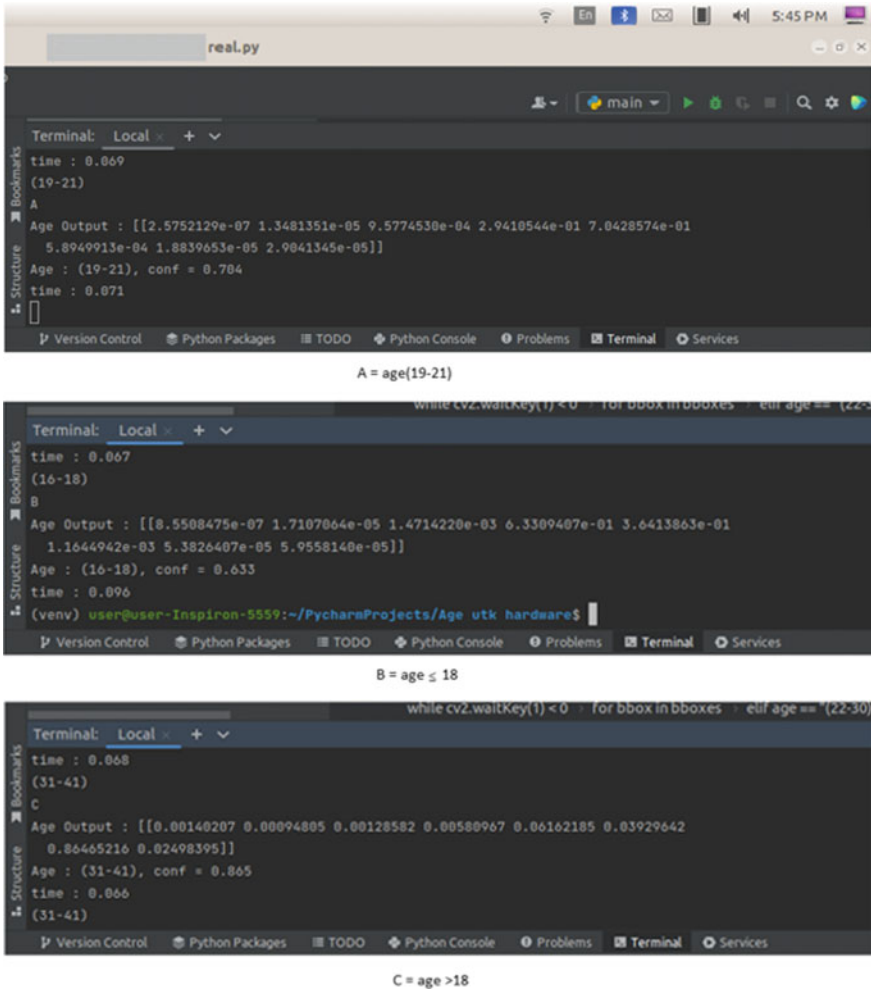
Fig. 9 SMS received

Fig. 10 Accuracy plot
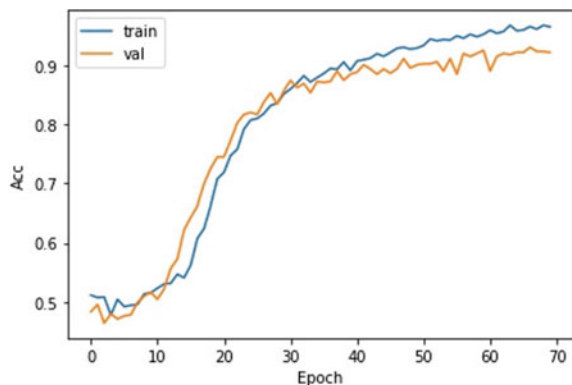
Fig. 11 Outputs for *A*, *B* and *C*

18,728 images. In this work, the proposed model with UTKFace dataset achieved an accuracy of 95% and the proposed system outperforms the existing work.

Table 2 gives the age detection results where the actual age of the person and respective predicted ages are depicted here. In the proposed system, a child of age 15 is detected in age group of 11–15. Similarly, all the ages in the table are successfully predicted in this study.

Table 2 Age detection results

Real age	Predicted age
8	6–10
15	11–15
20	19–21
26	22–30
53	42–60

5 Conclusion

Since there are many elements that determine how old anybody seems, it is difficult to infer the age of a person from their face. A person's genetics, make up, lifestyle, job, habits are the challenging elements for the age prediction. A prototype of proposed system is successfully developed. The suggested technology is intended to identify and stop underage drivers from operating a vehicle. The CNN model utilized to estimate the age from a facial image in this age classification task, which is built as a classification problem. In this proposed system, the face is detected from the real-time video frames using web camera. Then predicted the age of the person from the face. When minor aged person detected, then the car cannot be started by that person and the system alert the guardians by alarm. Otherwise, the car will start automatically and the system also send SMS to the guardians. The proposed system successfully controlled the car and the buzzer. Finally, the proposed child lock system is developed and tested successfully. The age prediction in this system can be used in other applications such as autonomous system, robotics and mobile app, etc., and the accuracy may be increased by including more images into the dataset.

References

1. Sleet DA, Ballesteros MF, Borse NN (2010) A review of unintentional injuries in adolescents. Ann Rev Public Health 31(1):195–212. https://doi.org/10.1146/annurev.publhealth.012 809.103616
2. Sharma D, Dutta S, Bora D (2020) REGA: real-time emotion, gender, age detection using CNN—a review. In: Conference paper, Jan 2020. https://doi.org/10.15439/2020KM18. https://www.researchgate.net/publication/348637154
3. Afroz M, Hasan N, Arefin Hossain MI (2021) IoT based two way safety enabled intelligent stove with age verification using machine learning. In: 2021 international conference on computer communication and informatics (ICCCI-2021). Coimbatore, India, 27–29 Jan 2021
4. Wanga G, Davies SR (2019) Deep machine learning for age and gender prediction. ICTACT J Soft Comput 09(04)
5. Mahjabin S, Alam MM, Talukder KH (2019) Age estimation from facial image using convolutional neural network (CNN). In: International conference on computer, communication, chemical, materials and electronic engineering (IC4ME2), 11–12 July 2019
6. Rafique I, Hamid A, Naseer S (2019) Age and gender prediction using deep convolutional neural networks. In: 2019 international conference on innovative computing (ICIC)

7. Agbo-Ajala O, Viriri S (2020) Deeply learned classifiers for age and gender predictions of unfiltered faces. Hindawi Sci World J 2020. Article ID 1289408. https://doi.org/10.1155/2020/1289408

8. Lee J-H, Chan Y-M, Chen T-Y, Chen C-S (2018) Joint estimation of age and gender from unconstrained face images using lightweight multi-task CNN for mobile applications. In: 2018 IEEE conference on multimedia information processing and retrieval (MIPR). IEEE, pp 162–165

9. https://towardsdatascience.com/softmax-activation-function-how-it-actually-works-d292d335bd78

10. Simon J, Naveen Kumar A (2021) A novel signal processing based driver drowsiness detection system. J IoT Soc Mob Anal Cloud 3(3):176–190

11. Deng Y, Fei L, Teng S, Zhang W, Liu D, Hou Y (2021) Towards efficient age estimation by embedding potential gender features. In: 2021 IEEE international conference on acoustics, speech and signal processing (ICASSP). IEEE ©2021. 978-1-7281-7605-5/20/$31.00

12. Bao H-TQ, Chung S-T (2020) A light-weight gender/age estimation model based on multi-taking deep learning for an embedded system. In: Proceedings of the Korea information processing society conference. Korea Information Processing Society, pp 483–486

13. https://www.interviewbit.com/blog/cnn-architecture/

14. https://www.kaggle.com/datasets/nipunarora8/age-gender-and-ethnicity-face-data-csv

15. https://susanqq.github.io/UTKFace/

16. Opu MNI, Koly TK, Das A, Dey A (2020) A lightweight deep convolutional neural network model for real-time age and gender prediction. In: 2020 third international conference on advances in electronics, computers and communications (ICAECC). IEEE ©2020. 978-1-7281-9183-6/20. https://doi.org/10.1109/ICAECC50550.2020.9339503

EC-MAC Protocol for Energy Harvesting Wireless Sensor Networks

BA. Anandh and D. Antony Pradeesh

Abstract The duty cycle MAC technique has been deployed in wireless sensor networks to decrease sensor node energy utilization. EC-MAC, or Energy-conservation Medium Access Control, is used to reduce energy consumption. The primary goal is to improve sleep latency while also balancing energy usage across sensor nodes. The suggested EC-MAC is compared to the RI-MAC and the outcome is shown. The simulation is done in NS-2. The presented method produces better results in terms of packet delivery ratio, overall energy, duty cycle, and leftover energy, according to the experimental results.

Keywords Energy consumption · Medium access control · Wireless sensor network · Duty cycle · Packet delivery ratio

1 Introduction

Wireless sensor networks, an emerging topic, integrate sensing, processing, and networking into a single compact device. Due to the enhanced mesh network protocols, these gadgets create a connection that reaches beyond cyberspace in the real world. The mesh networking connection can look for and utilize any conceivable communication link by hopping data across the network in quest of its destinations. The capabilities of any individual gadget are extremely limited, but the combination of many devices opens up innovative technological options. The capacity to gather energy from the environment allows WSN nodes to function as Energy Harvesting-based Wireless Sensor Networks (EHWSNs). A WSN must be self-sustaining, durable, and almost maintenance-free. In the light of this, energy harvesting could be

_____

BA. Anandh
Department of Electronics, PSG College of Arts & Science, Coimbatore, India

D. A. Pradeesh (✉)
Department of ECS, KG College of Arts and Science, Coimbatore, India
e-mail: antony.pradeesh@gmail.com

defined as a method for producing energy out of a network's environmental circumstances to maintain a steady power supply for a particular sensor node and the entire WSN.

In the field of wireless sensor networks, there is a substantial study on the introduction of unique algorithms for data collection [1], distributed signal processing [2], and ad hoc routing [3, 4]. A low-power, effective, and adaptable hardware platform is required to enable the algorithms and protocols being developed for wireless sensor networks [5]. To enable nodes to function at low duty cycles in retaining network-level connection, modern network protocols including Zigbee [6], T-MAC [7], and S-MAC [7, 8] are introduced.

The duty cycle, which indicates how much time a node spends in the listening period, is determined by the ratio of the monitoring period to the wake-up period. To prevent overhearing and idle listening, a node with a low duty cycle is in sleep mode most of the time and, to prevent higher latency and increased transient energy due to initial beginning cost, a stable duty cycle size should be attained.

Various lower duty cycle protocols that differ in synchronization and the types of channels that are required, such as a transmitter or receiver-initiated operation, are proposed for WSNs [9]. Low-duty protocols are classified into asynchronous and synchronous types. The asynchronous schemes employ transmitter initiation and receiver initiation. Synchronous type is defined by the notion of wireless sensor and network data sharing [10].

In the transmitter-initiation, method a node forwards preface, control, or data frequently till one of its "hits" the monitoring time of the target node [11]. But in the receiver initiation method, a node sends preface, control, or acknowledgement frequently to notify the adjacent nodes about the desire to accept packets [12].

2   Existing System

The most significant systems of the twenty-first century are typically considered to be wireless sensor networks. WSN was made possible by developments in micro-electromechanical systems (MEMS), which typically feature communication and signal processing abilities [13–16]. This approach resulted in the creation of power-limited, inexpensive, and tiny sensor nodes [17]. These incredibly tiny sensor nodes can understand, communicate with, and interact with a remote user via a sink-like gateway. WSN makes calculations easier everywhere, which is another step in the growth of the personal computer [18]. However, while being excellent, the functions are still restricted by energy limitations.

The priority placed on the development of WSNs is shown in the extensive research that is establishing and revising energy-effective MAC protocols. The most common classifications used in the reviews [19–21] seem to be schedule-based and contention-based MAC protocols.

Single-hop broadcast could be easily done in synchronous multichannel MAC systems because of synchronization. The packet is simply broadcast to the neighbouring node via the nodes in MuChMAC [22], Y-MAC, and MC-LMAC [23]. Without the need for a broadcast channel, MC-LMAC offers single-hop transmission.

The Medium Access Control protocol (MAC), which aids sensor nodes in energy conservation, is crucial. The EC-MAC protocol specifies who may broadcast when and mediates the use of the radio network over multiple nodes. MAC protocols typically have several other objectives in addition to energy conservation. Every node must have an equal chance to communicate with several nodes under a fair protocol. High bandwidth consumption should be supported by the protocol to avoid wasting radio channel time [24].

3   EC-MAC Design

The EC-MAC node that has a comparatively higher amount of residual energy awakens more frequently and contributes more to the network. The energy consumption rate of every node will be achieved by distributing the data traffic load during the network lifetime approximately equally to each node. Enhanced sensing coverage or QoS is also a result of this, which largely depends on the number of active sensor nodes still present. It is assumed that the network is organized and that sensing actions happen at a low frequency when creating the EC-MAC protocol.

3.1   Overview of the Protocol

The periodic listen/sleep device is used by EC-MAC. Figure 1 represents a duty cycle suggestion with three nodes. The Superframe is a single sleep cycle that includes a listening session. This consists of a listening period and a sleeping phase. In Fig. 2, the listen period is divided into RTS/CTS and SYNC time slots. The work cycle merely depends on how much time you spend sleeping because the amount of the listening period is corrected within EC-MAC. SYNC data and RTS/CTS packets are often exchanged during the listening time. Both the sender and the receiver should awaken from their slumber phase after establishing RTS/CTS communication effectively and start sending and receiving data.

The node initially sets up a special listen/sleep schedule and periodically broadcasts the concept within the SYNC communication. Due to this synchronization information, one other node pays special attention. Similar to S-MAC, the node adopts the new schedule, and it has received from another node as its own when it does so. Recognize that each node only employs this followed schedule initially. Within the first synchronization time, such kind of self-organization action will be finished.
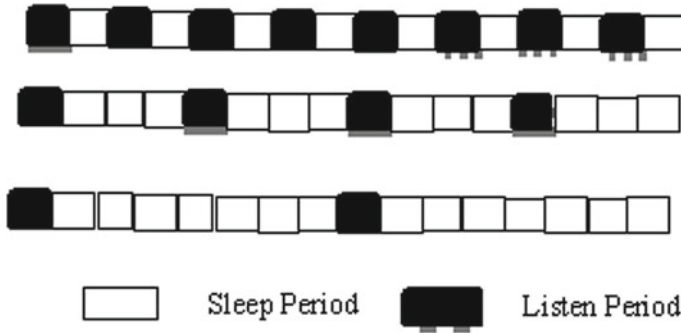
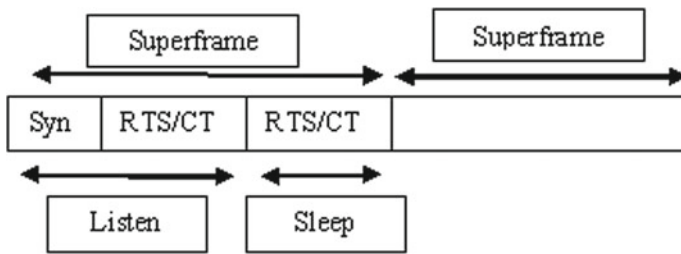Fig. 1 Distribution of duty cycle

Fig. 2 Superframe of EC-MAC

The system function phase starts after the self-organization phase. A new node adjusts the duty period in this phase based on the remaining power. The source address, the time until the next wake-up, and the listen/sleep cycle are the three key fields that make up SYNC message data. The address upon that node providing the SYNC packet would be the address of the source. The next listen/sleep and the wake-up time plan are presented to indicate whether or not the node will be energetically active at all times as well as how frequently the active time will occur.

Each node manages the one-hop neighbour scheduling in this fashion. If packets need to be sent to a particular node, each node awakens during the neighbour schedule. The sensor nodes in S-MAC establish a virtual cluster with the same schedule, and the border nodes adhere to both clusters' schedules. In contrast, nodes rarely form virtual clusters in EC-MAC since every node adjusts dynamically its plan based on the rate of energy consumption. Therefore, it is important to maintain one-hop neighbours' schedules.

Figure 3 depicts a data transfer to the sink (E) from source (A). The duty cycle is indicated as a percentage next to the node ID; for instance, a node with a duty cycle of 25% will have a listen period that is 3 times of sleep period. Every node essentially has its individual listen/sleep plan. Suppose a node needs to send a packet, it awakens during the listening time of the next hop, exchanges RTS and CTS, and then sends
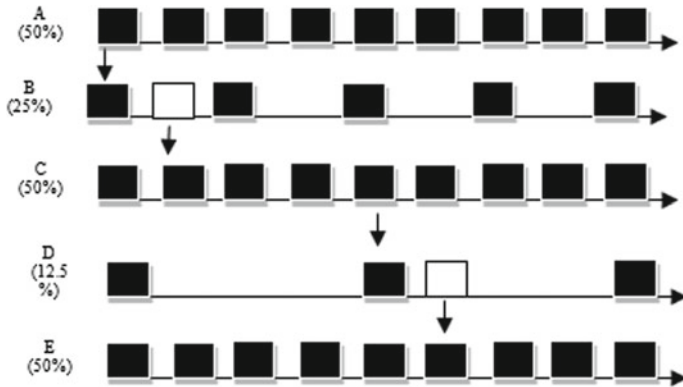
Fig. 3 Data transmission sample in EC-MAC

the data to the next hop node and finally, it reaches the sink. The node doesn't wake up during the neighbour's listen period; however, if it has no packets to send.

The time and flow of EC-MAC communications are shown in Fig. 4. A sender waits (*L*) for a probe (*P*) from a receiver before auto-acknowledging (*A*) precisely 192 s later. After an arbitrary delay, possibly on a different channel, the sender sends a data frame (DATA). Before sleep mode, the receiver validates in the second probe and listens for the auto-acknowledgement.

Figure 5 displays pending traffic between a sender (Node 1) and a recipient (Node 2). The sender activates hardware auto-acks, switches on its radio, assigns its address to 0×8002, and starts to listen. The receiver awakens at a later time and transmits a probe with 0×8002 as the destination address and 0×0002 as the source address along with a request for an acknowledgement. The sender's radio produces an auto-ack when it gets the probing frame. The receiver determines that an incoming auto-acknowledgement frame might be present when it detects the start of the auto-ack, so it keeps listening for a minimum of 352 s (or perhaps a lesser time if the data seem jumbled) prior to switch-off the radio. If a genuine auto-acknowledgement is
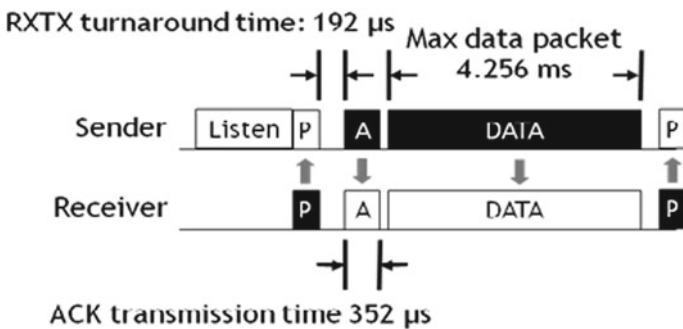
Fig. 4 802.15.4 initiated link layer of EC-MAC
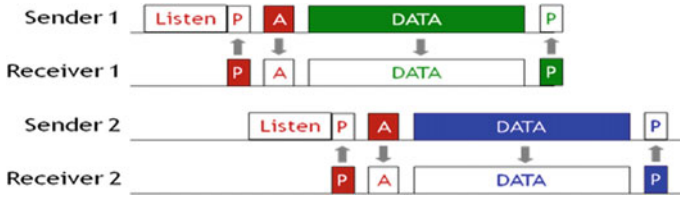
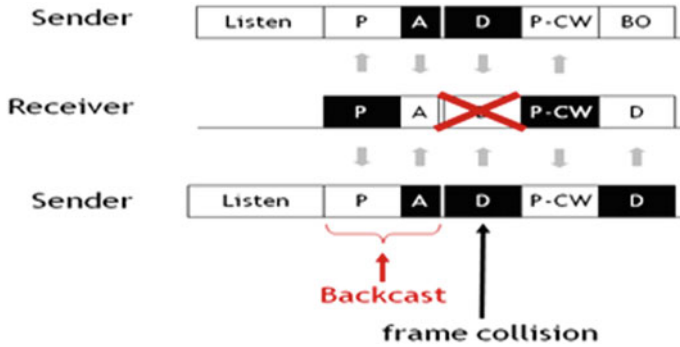**Fig. 5** EC-MAC multichannel parallel data transfers

Fig. 6 EC-MAC contention mechanism

obtained, the receiver deduces the awaiting traffic and keeps itself alert in anticipation of this information.

The first method is depicted in Fig. 6. In this diagram, all nodes stop communicating periodically, such as directing beacons, and rather run at an extremely low duty cycle. The node alone awake occasionally, possibly every ten seconds or once per minute, to send a query to the broadcast address to see whether any of their neighbours require them to stay up. By setting its radio to acknowledge all frames, Node 1 starts an asynchronous network wake-up. Node 2 eventually sends a probe. Node 2 sleeps while Node 1 automatically acks this probe.

4 Experimental Results and Discussion

This research runs simulations, changes the network settings, and compares the outcomes to those of RI-MAC to assess the performance of the proposed system. Query-based communication is used in the WSN for this system. Average energy, delay, balance factor, and remaining energy are considered for the performance of the proposed EC-MAC and the current RI-MAC and Network Simulator 2 (NS-2) are used to run the simulations [25]. The mobile sink inserts a query packet and is then routed to the target region. The appropriate response packet is then sent back
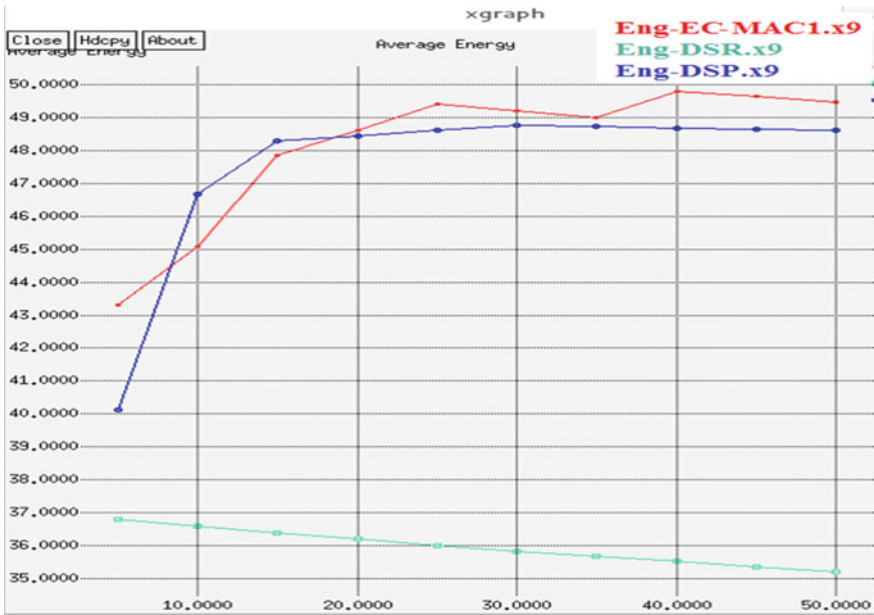
Fig. 7 Comparison of average energy

to the portable sink by multi-hop networking. These sink nodes are used to collect data from sensors. The internal function GraphComputation'SinkVertexList is used to get the sink vertices and then use FindPath to get the paths.

Figure 7 displays the average energy ratio between the existing RI-MAC and the proposed EC-MAC. It is evident from the simulation results that the suggested strategy provides greater average energy.

Figure 8 shows a comparison of the planned EC-MAC with the current RI-MAC using NS-2. From the simulation results, it is obvious that the suggested solution outperforms the current RI-MAC while adding additional latency to their workflow. Figures 9 and 10 show that the proposed EC-MAC method produces the best results.

The packet delivery ratios for the suggested EC-MAC and the present RI-MAC for four senders are given in Table 1. When compared with the receiver-triggered MAC protocol, the adaptive medium access control offers some advantages. Four senders make up the RI-MAC, and 90.7% of packets are delivered on average. The average packet delivery ratio is found as 98.5% while employing adaptive medium access control protocol. Table 1 clearly gives that the proposed MAC outperforms the existing RI-MAC.

The wake-up timings of 59 terminals in a multi-hop test platform are shown in Fig. 11 for a variety of sampling/probing intervals. In comparison with the Tiny OS LPL default, EC-MAC awakes the network around 38% quicker in this waste wake-up demonstration. Fewer packets demonstrate that EC-MAC has significantly higher channel efficiency because it sends far fewer packets to accomplish this.
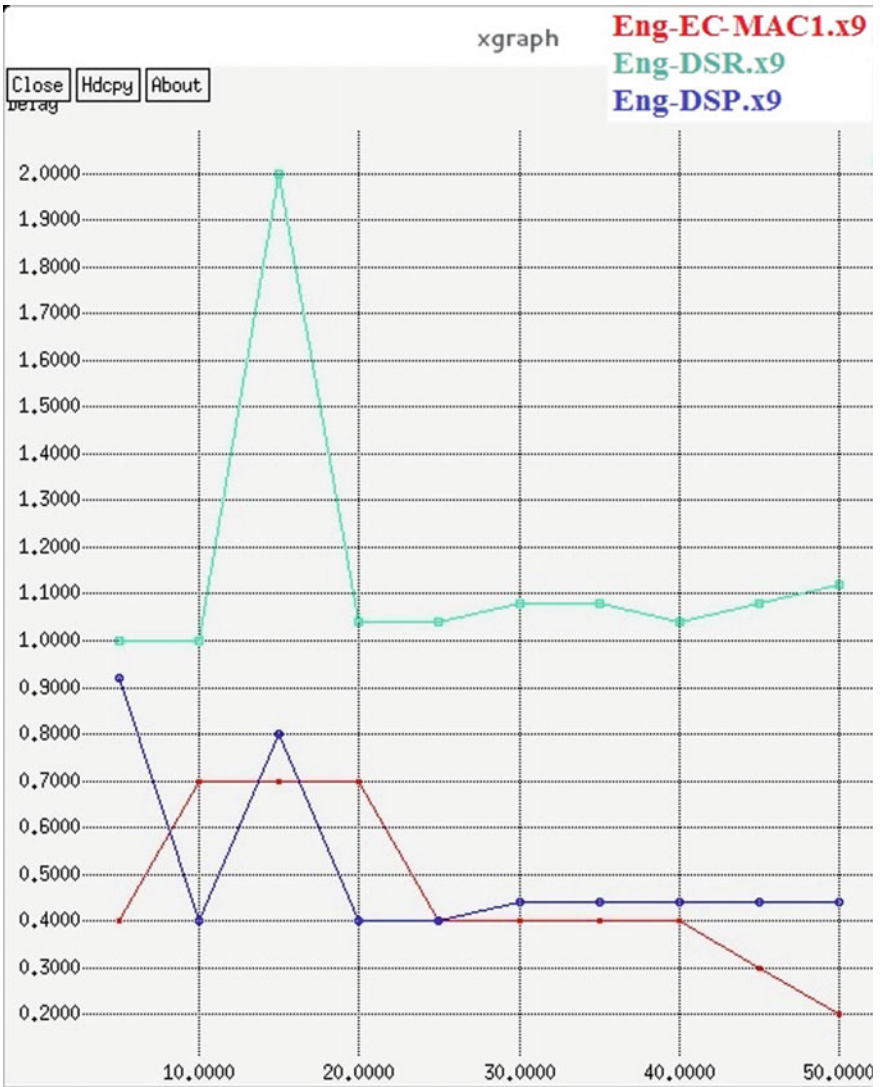
Fig. 8 Comparison of delay

Cumulative distribution function (CDF) is used here to determine the probability wherein a continuous random variable would occur within any measurable subset of a certain range. The CDF of wake-up latency is displayed in Fig. 12. It may seem counterintuitive, but larger probe intervals perform better overall because there is less chance of a node sending a probe whenever an adjacent is otherwise engaged as the probe interim period increases.
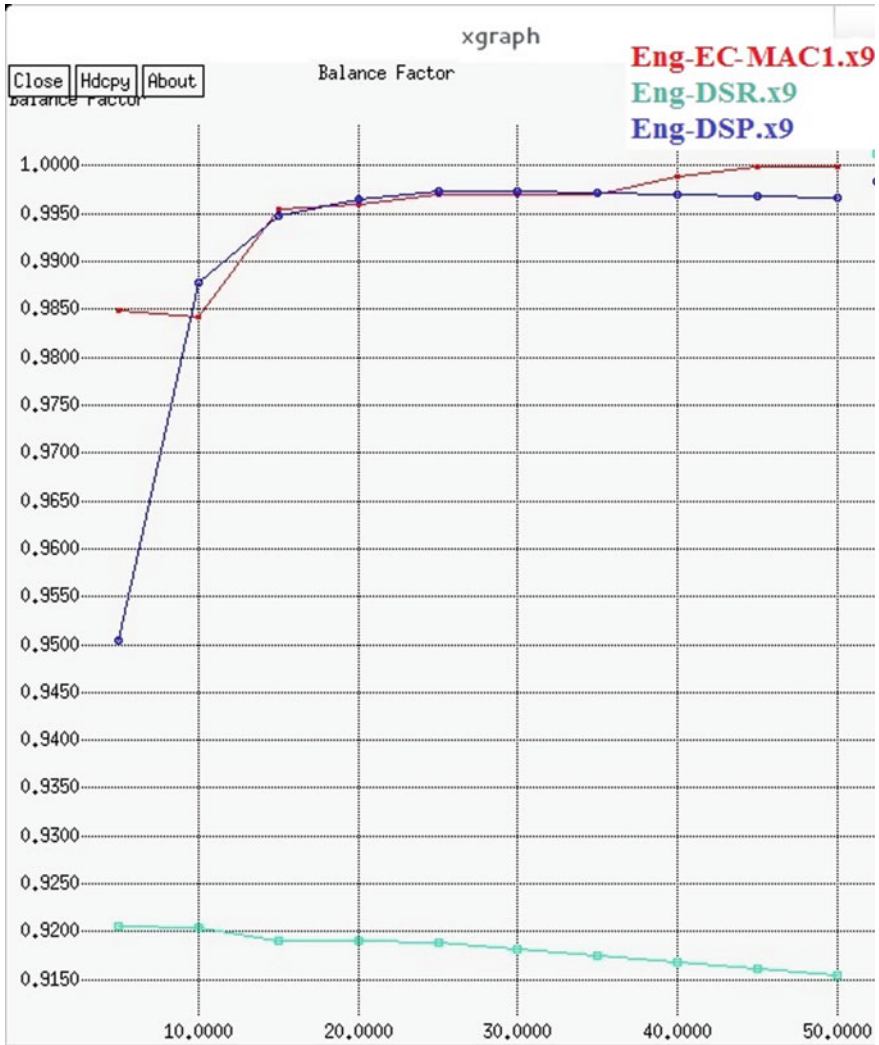
Fig. 9 Comparison of balance factor

5 Conclusion

The suggested techniques enable sensor nodes to modify their duty cycle by their remaining energy to decrease sleep delay and balance energy consumption across nodes. According to NS-2 simulations, compared to RI-static MAC's duty cycle scheduling method, DSR and DSP both exhibit reduced end-to-end delays and higher packet delivery ratios. They can also help balance the energy use across sensor nodes at the same time. While compared with the receiver-initiated MAC, the adaptive MAC
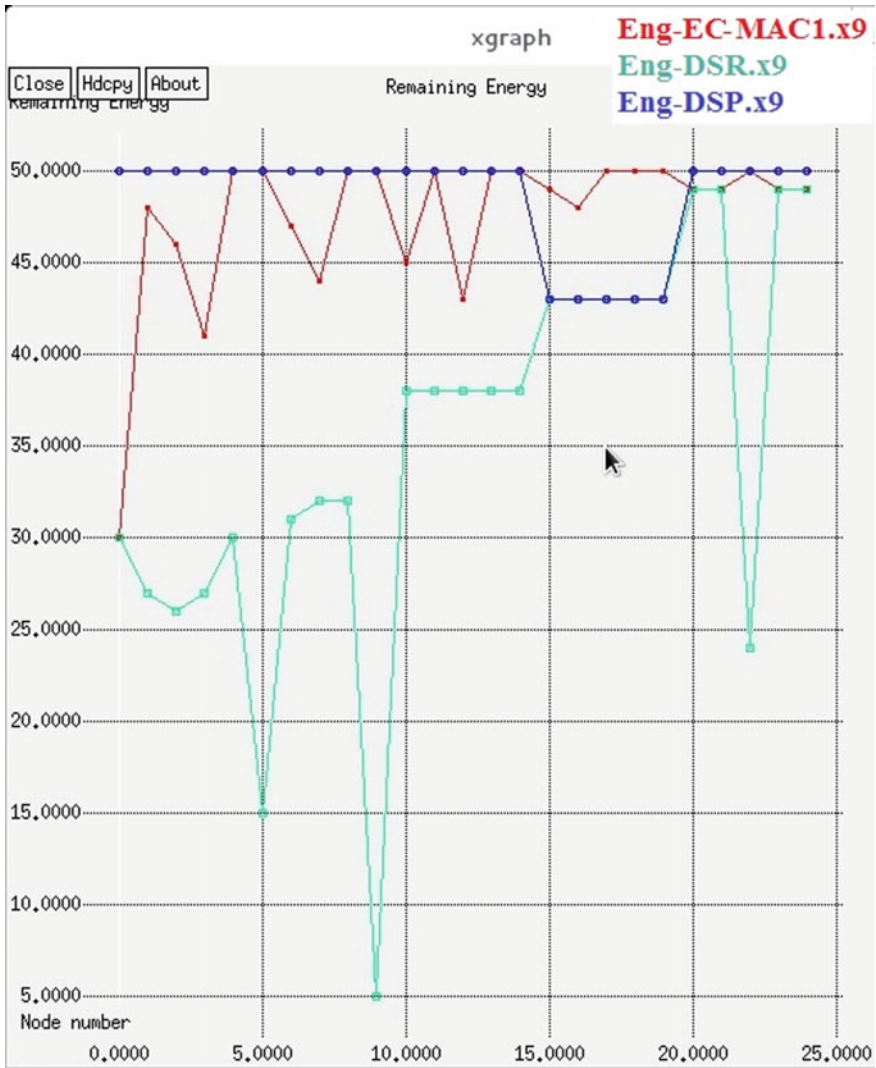
Fig. 10 Comparison of remaining energy

Table 1 Packet delivery ratios of RI-MAC and EC-MAC in percentage

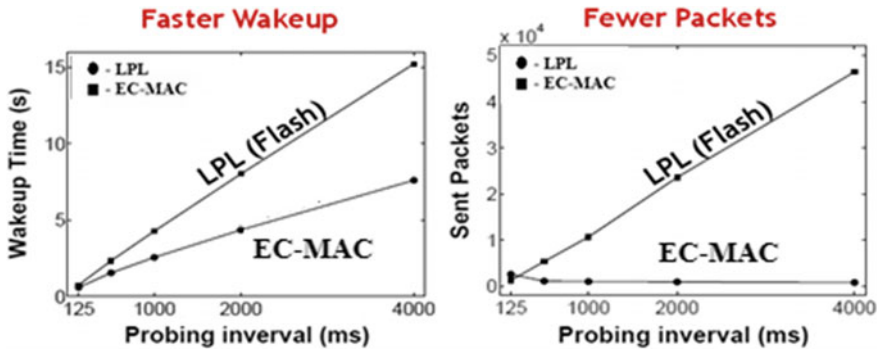|	RI-MAC				EC-MAC			
	Number of senders							
	1	2	3	4	1	2	3	4
Average	99.90	97.50	95.60	90.70	99.90	99.30	99.30	98.5
Minimum	–	97.30	95.00	90.30	–	98.20	98.30	96.70
Maximum	–	97.70	96.80	90.90	–	100	99.50	99.50

Fig. 11 Comparison of wake-up time
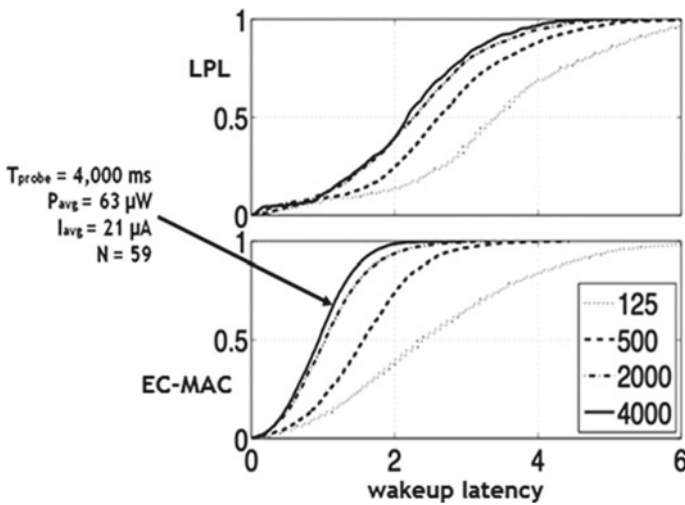
Fig. 12 EC-MAC wake-up at the low duty cycle

protocol performs better and also compared with the RI-MAC protocol, the EC-MAC has many benefits. In comparison with RI-MAC, EC-MAC wakes up the network more quickly and effectively. A quicker wake-up indicates a reduced baseline power consumption. Low incast (inside an area) performance of high packet delivery is provided by EC-MAC. Low-duty cycles are ideal for EC-MAC wake-up. The EC-MAC 802.15.4 protocol standards are used in the NS-2 simulation. Because it uses less energy, there is a lot of energy left over. The experimental results show that the suggested EC-MAC performs better than the current RI-MAC. In future works, S-MAC can be employed since it employs a number of unique methodologies to save energy and enable self-configuration. It facilitates multi-hop system operations at low duty cycles.

References

1. Bhattacharyya D, Kim T, Pal S (2010) A comparative study of wireless sensor networks and their routing protocols. Sensors 10:10506–10523
2. Tunca C, Isik S, Donmez MY, Ersoy C (2014) Distributed mobile sink routing for wireless sensor networks: a survey. IEEE Commun Surv Tutorials 16:877–897
3. Ullah Z (2020) A survey on hybrid, energy efficient and distributed (HEED) based energy efficient clustering protocols for wireless sensor networks. Wirel Pers Commun 112:2685–2713
4. Djedouboum A, Abba Ari A, Gueroui A, Mohamadou A, Aliouat Z (2018) Big data collection in large-scale wireless sensor networks. Sensors 18:4474
5. Aledhari M, Razzak R, Parizi RM, Saeed F (2020) Federated learning: a survey on enabling technologies, protocols, and applications. IEEE Access 8:140699–140725
6. Vidhya SS, Mathi S (2022) Investigations on power-aware solutions in low power sensor networks. In: Ranganathan G, Fernando X, Shi F (eds) Inventive communication and computational technologies. Lecture notes in networks and systems, vol 311. Springer, Singapore. https://doi.org/10.1007/978-981-16-5529-6_69
7. Diniesh VC, Murugesan G (2022) Review on mobility aware MAC protocol using mobile internet of things. Multimed Tools Appl. https://doi.org/10.1007/s11042-022-13131-4
8. Fotohi R, Firoozi Bari S, Yusefi M (2020) Securing wireless sensor networks against denial-of-sleep attacks using RSA cryptography algorithm and interlock protocol. Int J Commun Syst 33. https://doi.org/10.1002/dac.4234
9. Maulidin, Mahmuddin M (2019) An enhanced energy efficient hybrid asynchronous duty cycle MAC in wireless sensor. In: Joint conference on green engineering technology and applied computing, IOP conference series: materials science and engineering, vol 551
10. Cheng L, Niu J, Luo C, Shu L, Kong L, Zhao Z, Gu Y (2018) Towards minimum-delay and energy-efficient flooding in low-duty-cycle wireless sensor networks. Comput Netw 134:66–77
11. Lin E-YA, Rabaey JM, Wolisz A (2004) Power-efficient rendez-vous schemes for dense wireless sensor networks. In: 2004 IEEE International conference on communications (IEEE Cat. No.04CH37577), vol 7, pp 3769–3776. https://doi.org/10.1109/ICC.2004.1313259
12. Yaqub MA, Khan MTR, Ahmed SH, Kim D (2018) Receiver-initiated dynamic duty cycle scheduling schemes for underwater wireless sensor networks. In: 2018 15th IEEE Annual consumer communications and networking conference (CCNC), IEEE, pp 1–6
13. Majumder K, Ray S, Sarkar SK (2010) A novel energy efficient chain based hierarchical routing protocol for wireless sensor networks. In: International conference on emerging trends in robotics and communication technologies, IEEE, pp 339–344
14. Gürses E, Akan ÖB (2005) Multimedia communication in wireless sensor networks. Ann Télécommun 60:872–900. https://doi.org/10.1007/BF03219952
15. Kalsoom T, Ramzan N, Ahmed S, Ur-Rehman M (2020) Advances in sensor technologies in the era of smart factory and industry 4.0. Sensors 20:6783
16. Tan WL, Lau WC, Yue O (2012) Performance analysis of an adaptive, energy-efficient MAC protocol for wireless sensor networks. J Parallel Distrib Comput 72:504–514
17. Simplício MA, Barreto PSLM, Margi CB, Carvalho TCMB (2010) A survey on key management mechanisms for distributed wireless sensor networks. Comput Netw 54:2591–2612
18. Srisooksai T, Keamarungsi K, Lamsrichan P, Araki K (2012) Practical data compression in wireless sensor networks: a survey. J Netw Comput Appl 35:37–59
19. Ngo V, Anpalagan A (2009) A detailed review of energy-efficient medium access control protocols for mobile sensor networks. Comput Electr Eng 36:383–396
20. Gopalan SA, Kim DH, Nah JW, Park JT (2010) A survey on power-efficient MAC protocols for wireless body area networks. In: 3rd IEEE International conference on broadband network and multimedia technology, IEEE, pp 1230–1234
21. Bazan O, Jaseemuddin M (2012) A survey on MAC protocols for wireless adhoc networks with beamforming antennas. IEEE Commun Surv Tutorials 14:216–239

22. Fan X, Ao T, Xia Z (2018) Address allocation scheme based on local MAC address. In: Sun X, Pan Z, Bertino E (eds) Cloud computing and security, ICCCS 2018. Lecture notes in computer science, vol 11063. Springer, Cham. https://doi.org/10.1007/978-3-030-00006-6_23
23. Lee J, Kim S (2020) EnRI-MAC: an enhanced receiver-initiated MAC protocol for various traffic types in wireless sensor networks. Wirel Netw 26:1193–1202
24. Huang C, Huang G, Liu W, Wang R, Xie M (2021) A parallel joint optimized relay selection protocol for wake-up radio enabled WSNs. Phys Commun 47:101320
25. Network simulator. http://www.isi.edu/nsnam/ns

Prediction of Brain Diseases Using Machine Learning Models: A Survey

Zaina Pasha, Saravanan Parthasarathy, Vaishnavi Jayaraman, and Arun Raj Lakshminarayan

Abstract According to the American Cancer Society, cancers related to the brain and nervous system are ranked as the tenth leading cause of mortality in humans. In addition to this, the World Health Organization (WHO) reports that low-income nations are experiencing a lack of neurologists, who play an essential part in the functioning of the healthcare sector. There is currently no method that is reliable enough to permit the classification of brain illnesses into multiple classes. The multi-class classification of clinical brain images was made possible by our machine learning approach, which we proposed. The classification of brain disorders, including Alzheimer's disease, dementia, brain cancer, epilepsy, stroke, and Parkinson's disease, would be accomplished using a deep learning-based convolutional neural network (CNN). The Visual Geometry Group-16 (VGG-16) architecture was taken into consideration throughout the feature selection process, and the Adam optimizer was used to perfect the model. The proposed CNN model would be beneficial in alleviating the arduous labor of neurologists.

Keywords Machine learning · Predictive modeling · Classification · Brain diseases · CNN · VGG-16

Z. Pasha (✉) · S. Parthasarathy · V. Jayaraman · A. R. Lakshminarayan
B. S. Abdur Rahman Crescent Institute of Science and Technology, Chennai, India
e-mail: zaina.bint.pasha@gmail.com

S. Parthasarathy
e-mail: saravanan_cse_2019@crescent.education

V. Jayaraman
e-mail: vaishnavij_cse@crescent.education

A. R. Lakshminarayan
e-mail: arunraj@crescent.education

1 Introduction

A productive control center is a necessity for every system if that system is to achieve its potential for output. When it comes to the human system, the brain is the organ that serves as the command-and-control hub. The human brain is a complex and wondrous organ that can regulate not just our memories and feelings but also our actions, as well as our breathing, digesting, and elimination processes, which are all essential to our continued existence. It is an organ that frequently has the tendency to be disregarded, and as a result, a great deal of complexity results from ignorance. Encephalopathy is a term that is used to describe a wide variety of brain illnesses [1]. It is a health problem that someone must be concerned about in its early beginnings and ignoring it can have some major implications on the person's well-being if it is allowed to progress further. When doing a patient evaluation, a physician needs to be aware of different diseases that can affect the brain and take them into consideration. From Parkinson's disease and brain tumors to Alzheimer's and other forms of dementia, epilepsy, and multiple sclerosis [2]. Despite this, there are still many others that have not been interpreted. It has been discovered that tumors, which can either be benign or malignant, are the most dangerous types. In the process of dividing and reproducing themselves, cancerous tumors are one of the primary contributors to a person's risk of developing the disease, which then spreads to other areas of the body via the blood. The victim may have to deal with symptoms such as impaired eyesight and hearing, a change in behavior, a loss of cognitive capabilities, having frequent headaches, feeling nauseous, loss of motor abilities, and a long list of other issues.

Certain imaging techniques were utilized to detect various symptoms associated with brain diseases, such as tumors, hemorrhage, clogged blood vessels, injuries, strokes, and abnormal growths [3]. Magnetic resonance imaging (MRI) works by combining radio waves and magnetic fields to produce detailed images of the tissue of interest. Computerized Tomography, or CT scans, on the other hand, make use of X-rays to produce images of the organ, bones, and tissue in a two-dimensional format. Imaging methods such as positron emission tomography (PET), functional magnetic resonance imaging (MRI), and single-photon emission computed tomography (SPECT) are some of the others that are frequently utilized. After the images have been obtained using imaging techniques, the physicians will need to extract useful information from the images in order to determine which disease the patient may be suffering from. When all aspects of the situation are considered, it is extremely unlikely that a doctor will be able to identify all the diseases that a patient may be experiencing at the same time as they seek treatment for one condition. When this happens, technology such as image classification can play a significant part in helping with laborious chores like classifying the many symptoms a person might have and being able to further connect them with the condition that causes them. There are numerous classification techniques, including neural networks, fuzzy logic, evolutionary algorithms, and support vector machines [4].

The phrase "machine learning" was initially used by Arthur Samuel, a computer scientist at IBM who was also one of the first people to explore the fields of artificial intelligence and computer games [5]. He was also one of the first people to try their hand at playing video games on a computer. He came up with a software that could be used to play the game of checkers, and when it was used more and more, it gained experience and grew able to make more accurate predictions applying algorithms each time it was used. It is crucial for the field of medicine to be able to discover ailments in patients before it is too late for them to be cured. This is because the Dutch philosopher Desiderius Erasmus asserted that "prevention is better than treatment." Since quite some time ago, artificial intelligence has been assisting medical personnel in more promptly diagnosing diseases with the potential to cause fatalities. In addition to this, it assists the doctors by completing organizational tasks that don't require any kind of human intervention on their part. Because of this, the doctors could devote more of their time to their patients [6].

The remaining paper is arranged as follows: Sect. 2 specifies the existing research accomplishments relating to ML-based brain image classification techniques. Section 3 reveals the characteristics of the proposed model. In Sect. 4, the paper concludes with the forthcoming research direction.

2 Literature Review

All illnesses and impairments that negatively influence the brain are considered brain disorders. Memory loss, altered sensations, and even changes in personality are all possible outcomes of these illnesses. Researchers are very interested in building novel prediction models for the early diagnosis of brain illnesses. Parkinson's disease (PD) is one of the most challenging illnesses for radiologists to diagnose. Salvatore et al. [7] created an ML algorithm to diagnose PD and Progressive Supranuclear Palsy (PSP). The images were pre-processed with skull-stripping and normalizing by Brain Extraction Tool (BET-tool). PCA was applied to extract features. The SVM model was employed to classify unidentified photos, which would be accomplished using the maximal marginal distance hyperplane. The Leave One Out approach and selecting N/2 individuals for training and N/2 subjects for testing were used for validation. To obtain biomarkers, image maps of voxel-based distribution patterns were constructed. For each of the three binary labels, the accuracy, specificity, and sensitivity were greater than 80%. Payan and Montana [8] used sparse autoencoders and 3D neural networks to classify the brain's MRI. The extracted patches were implemented for training, validation, and testing. Applying 3D convolutions to an input map and a filter map yielded a $64 \times 91 \times 75$ feature map. Max-pooling was performed on 150 hidden units to generate $12 \times 18 \times 15$ feature maps. The sigmoid function was used to select a hidden layer, and the SoftMax function was used to obtain an output layer. Finally, 486,000 ($150 \times 12 \times 18 \times 15$) outputs were obtained and used as inputs for the neural network. The difficulty in employing an overcomplete autoencoder was that it could only learn the identity function.

Veeramuthu et al. [9] used the Probabilistic Neural Network-Radial Basis Function (PNN-RBF) method to train and classify brain MRIs. The proposed method uses discrete wavelet transform to break down the signal in order to obtain a better image, feature extraction using GLCM to convert RGB to grayscale, PNN-RBF for classification, and morphological filters to segment the images by comparing the region of interest (RIO) with the adjacent pixels. The proposed method has a 98% rate of accuracy. This aids in the early detection of the tumor. Mathur et al. [10] implemented the preprocessing techniques of Fourier Transform and wavelet transform for feature extraction. Principal Component Analysis (PCA) was used for feature reduction. MATLAB 2011b's biostatistical toolbox was applied to develop an algorithm for the Support Vector Machines (SVM) preparation. For the classification of normal and abnormal brain MRI images, an open SVM toolbox was downloaded, extended to Kernel SVM, and applied to the MRI data. The difficulties encountered during feature classification consisted of enhancing the classification quality, which was accomplished through wavelet transform. The DWT + PCA + KSVM + GRB kernel obtained better results in classification. The model hopes to reduce computation time, test new kernels, and do multi-classification in the future.

Islam and Zhang [11] have developed a CNN capable of detecting and classifying Alzheimer's disease using MRI data. The images were pre-processed and routed via a stem layer, multiple other inceptions, and reduction layers with varying combinations of convolution, max-pooling, and filter expansion layers, an average pooling layer, a dropout layer, and a SoftMax layer with four distinct outputs. Backpropagation and ground truth were applied to assess the outcomes. Utilized were the hyper-parameters of the Inception-V4 model. The neural network was required to learn from a limited data set. Utilizing RMSProp helped optimize the network. The achieved accuracy was 73.75%. Hebli and Gupta [12] developed a rapid approach for identifying the tumor as malignant or benign via image processing and machine learning. Images undergo preprocessing and morphological treatments. Multiplying the output image by the input image yields the tumor region. Discrete Wavelet Transform (DWT) was used for feature extraction to obtain coefficients, which were then given to PCA for feature reduction, which speeds up the operation. K-Fold cross-validation was performed to improve the classification's overall accuracy. In training and evaluating the database, the RBF kernel-based model obtained the highest accuracy.

The primary objective of Mohsen et al. [13] was to distinguish between normal MRIs and MRIs of various types of brain tumors. Data acquisition, image classification with Fuzzy C-Means, feature extraction with DWT, feature reduction with PCA, and classification with deep learning networks (DNN) were the methodologies used. Reducing hardware specifications, shortening the time required to process large images, and improving classification accuracy were the obstacles encountered. In the future, they plan to combine the DWT and the CNN model, as the DNN proved successful in MRI classification. Selvapandian and Manivannan [14] identified the tumor using a Gradient Boosting Machine Learning (GBML) classifier. The procedure includes image preprocessing, feature extraction, classification, and segmentation. In the preprocessing step, a Gabor kernel was employed. In the feature extraction step, intensity features, Gray-Level Co-occurrence Matrix (GLCM), and Gray-Level

Run-Length Matrix (GLRLM) were used. To segment the images, morphological operations such as erosion and dilation were performed. The proposed model has a mean accuracy rate of 98.3%. GBML classification was used to overcome the difficulty of large training data.

Hemanth et al. [15] employed a CNN model within the MATLAB environment that efficiently classifies brain tumor images. In addition to preprocessing, normalization, and aggregation, the image was average filtered to further reduce noise. A pixel was assigned a 3×3 matrix, and pixel sorting was performed to determine the normal. The standard value was then assigned to the pixel, and the process was repeated until the image was free of noise. CNN was used for feature extraction and pixel-based segmentation (LinkNet). ReLu was employed to shorten the duration of training, resulting in a 91% of accuracy. Afshar et al. [16] employed CapsNet to address these challenges. The pooling layers were replaced by a "Routing Agreement Process" in which the capsule beneath the parent capsule predicts its conclusion. It comprises a layer that functions as a decoder and attempts to extract features. A tumor's coarse boundary was leveraged to sharpen the architecture's focus. The proposed model achieved a 90.89% accuracy by drastically reducing background variations.

Das et al. proposed a CNN model capable of classifying three types of tumors [17]. MATLAB was used to format the used data set. First, the images were resized, then filtered with Gaussian filters, and the contrast was enhanced with histogram equalization. The CNN consists of three layers: convolutional, subsampling, and dropout. ReLu was employed as the activation function, while SoftMax was used in the output layer. The neural network was trained using the Adam optimizer, which was used to compile the model. Since the number of parameters exceeded the amount of data, overfitting was a concern. The model's mean precision was 93.33%. Swati et al. [18] used transfer learning and block-wise fine-tuning to classify Contrast Enhanced-MRIs of brain malignancies with greater accuracy for a small data set. First, images were preprocessed, then the CNN was trained using a feed-forward and back-propagation technique. The VGG-19 architecture was implemented using a block-based approach. The performance was evaluated using five-fold cross-validation. The model effectively decreased overfitting and boosted convergence speed. In the earliest layers, the model learns low-level features from the MRI, and in subsequent layers, it learns domain-specific features from the low-level features. The focus was on 2D MRI rather than 3D MRI, and the model achieved an accuracy of 94.82%.

Sultan et al. [19] proposed a deep learning algorithm that uses CNN to classify the brain tumor as meningioma, glioma, or pituitary. The method includes preprocessing in which the images were shrunk and enlarged. The method under consideration does not involve segmentation. CNN's architecture consists of sixteen layers, including input, convolutional, activation, dropout, normalization-pooling, fully connected, a soft-max, and classification layers. The difficulty was preventing overfitting, and it cannot be applied to small data sets. The proposed model had an accuracy of 96.13 and 98.7% for the two employed data sets. Abiwinanda et al. [20] proposed and compared five distinct CNN architectures for the classification of brain tumors. The

Adam optimizer was used to achieve optimal values for the hyper-parameters. Architecture 2 had decreasing validation loss with each successive epoch. It contained two convolutional layers, a max-pooling layer, a flattening layer, a fully connected layer, and an output layer whose activation function was SoftMax. In order to overcome the problem of computational costs, the image size was shrunk. Validation accuracy was 84.19% and training accuracy was 98.51%.

The conventional approaches for classifying tumor images were inefficient and indistinguishable. Hence, Shrot et al. [21] suggested a semi-automated ML technique that uses DTI and perfusion imaging to maximize categorization. It requires DTI and perfusion analysis, sequence normalization, feature extraction, and SVM for feature selection and binary classification. Using a binary hierarchical tree, the tumors were classified as glioblastoma, metastasis, meningioma, and PCNSL. The classification was evaluated using leave-one-out cross-validation. Except for PCNSL, the overall classification error was 14.2%, and both specificity and sensitivity were greater than 90%. Due to the spatial averaging of the features, the model cannot recognize tiny deviations. Anaraki et al. [22] suggested a method for classifying different grades of gliomas based on CNN and the genetic algorithm. To prevent overfitting, the method begins with preprocessing and normalization, followed by data augmentation. The convolutional layer has been used to reduce the number of parameters. An efficient architecture was selected with the help of a genetic algorithm (GA), and the loss function was optimized down with the use of stochastic gradient optimizers. For model averaging, a bagging algorithm was used to overcome the difficulty of satisfying the unobserved data sets, thereby increasing the overall accuracy. This approach does not require a lengthy feature extraction process. The overall categorization accuracy was determined to be 93.1%. Geometric procedures and two-stage wavelet decomposition were used to process and improve the images.

Shakeel et al. [23] employed Multi-layer Block Propagation Neural Network (MLBPNN) and infrared technologies to classify images of brain tumors. As classifiers, GLCM, PCA, the fractal dimension method, segmentation by multifractal detection approach, MLBPNN, and Adaboost were employed for feature extraction. MLBPNN was superior to the latter since it aids in the early diagnosis of cancer. To remotely access the brain images, infrared sensors were combined with the WSN for image sensing. Classes were saved in accordance with the size of the tumor. Utilizing hole filling to highlight the malignancy. Using MLBPNN, the challenge of overcoming network loss of motion and balancing weights was addressed. Huang et al. [24] created a Convolution Neural Network Based on Complex Network model using a graph generated at random. After acquiring the model parameters, they generated random graphs using the Erdos–Renyi (ER), Watts–Strogatz (WS), and Barabasi–Albert (BA) algorithms, which were then converted to a directed acyclic graph (DAG), and node and edge operations were performed to obtain the output module. The activation functions Gaussian Error Linear Unit (GELU) and Rectified Linear Units (ReLu) were employed for enhancement. During network generation, the channels were restricted due to aggregation, and the input and output nodes

were not explicitly defined. They needed to reduce test loss and training time while increasing accuracy. The modified CNNBCN model was able to classify images of brain tumors and overcome obstacles.

Ismael et al. [25] applied residual networks to classify the brain tumor. Data gathering, visualization, image processing, data augmentation, model training, and evaluation were conducted. The data was separated using a patient-level and image-level technique. Multiple augmentation approaches were used, resulting in a 4% improvement. ResNet50 was implemented for the classification of brain imaging data sets. The method involves skipping several layers. A collection of 3064 brain MRI pictures served as a baseline. For the evaluation, precision, recall, $F1$-score, and balanced accuracy were used. The attained accuracy was 99% at the image level and 97% at the patient level. CNNs were potent designs, but they also have their drawbacks. Since the method developed by Ahuja et al. [26] was based on transfer learning, training on large-scale data was unnecessary. DarkNet-19 and DarkNet-53 were pre-trained networks used for the classification of tumors, and DarkNet-53 has been determined to be superior. The tumor's location was determined with the aid of feature maps. K-means clustering was used to group pixels of similar color. The tumor was represented by neon pink, while the background was represented by neon green. Using the super-pixel approach, the MRI was segmented. The experimental results showed an accuracy of 98.54%, although the method was only applicable to 2D images and required a format conversion to Portable Network Graphics (png). Key findings and interpretation are given in the Table 1.

3   Research Gap and Proposed Work

All the proposed models in [7–26] involve binary classification of the medical images and meant only for a particular brain disorder. Our scope further widens and aims at classifying multiple brain diseases and being able to find if any new abnormalities were to be found.

A deep learning-based framework for identifying brain diseases was outlined in Fig. 1. VGG-16, a pre-trained model, could be employed to detect brain diseases. VGG-16 is a convolution neural net (CNN) is regarded as one of the most effective vision model architectures. Instead of having many hyper-parameters, VGG-16 focuses on convolution layers of 3×3 filters with a stride of 1 and always uses the same padding and max-pool layers of 2×2 filters with a stride of 2. This configuration of convolution and max-pool layers is maintained throughout the entire architecture. It concludes with fully connected layers and a Soft Max output. The number 16 in VGG-16 indicates that it has 16 layers with weights. All hidden layers employ ReLu as their activation function. ReLu is more computationally efficient because it accelerates learning and reduces the probability of the vanishing gradient problem. The activation function gives the neural network nonlinearity. Since the sigmoid and tanh functions are unsuitable for multi-class classification, we recommend the SoftMax activation function to determine the relative probabilities.

Table 1 Key findings and interpretation

S. No.	Author(s)	Methodologies used	Advantages	Disadvantages
1	Salvatore et al. [7]	BET-tool, normalization, principal component analysis, support vector machine, leave one out, FDR, voxel-based distribution pattern	Morphological biomarkers obtained, precise classification, improved efficiency	Precise voxels only for PD, large data used
2	Payan and Montana [8]	Sparse autoencoders, 3D neural networks, sigmoid function, SoftMax function, statistical parametric mapping (SPM)	Patient status is known, 3D slices obtained, self-learning, efficient feature extraction	Learns only identity function, difficulty in interpretation of the result
3	Veeramuthu et al. [9]	PNN-RBF, GLCM, discrete wavelet transforms, Fisher Discriminant Ratio, morphological filters	Early-stage detection, minimized training time, high accuracy	Filters were only pixel-based, complex, and perplexing
4	Mathur et al. [10]	Fourier transform, wavelet transform, MATLAB 2011b, kernel SVM	High accuracy	Low quality classification, excess computational time, not meant for multi-classification
5	Islam and Zhang [11]	Preprocessing, inception and reduction layers, Inception-V4 hyper-parameters, RMSProp optimizer, TensorFlow, python	Improved feature detection, time efficient, overfitting rectified, one step analysis	Small data set was employed
6	Hebli and Gupta [12]	Discrete wavelet transform, principal component analysis, K-Fold cross-validation, support vector machine	RBF kernel has an adjustable parameter and high accuracy	Can't classify the stages, can't locate the tumor
7	Mohsena et al. [13]	Data acquisition, Fuzzy C-Means, discrete wavelet transform (DWT), principal component analysis (PCA), deep learning networks (DNN), linear discriminant analysis (LDA)	High accuracy, low hardware specifications	Time consuming and expensive methodology

Table 1 (continued)

S. No.	Author(s)	Methodologies used	Advantages	Disadvantages
8	Selvapandian and Manivannan [14]	Preprocessing, Feature extraction, segmentation, GBML classifier, GCLM, GBRLM, regression trees	Manages large data sets, alternative for radiologists, high accuracy	Format transformation required and lack of weights
9	Hemanth et al. [15]	Preprocessing, normalization, aggregation, average filtering, feature extraction, pixel-based segmentation, CNN (LinkNet)	Reduced noise, precise feature extraction, swift training, and desirable outputs	Additional filters required to remove noises
10	Afshar et al. [16]	CapsNet architecture, segmentation, convolutional and capsule layer, python, Keras library	Spatial relations were preserved, high accuracy, focuses on ROI, aids in medical decision making	Highly sensitive to unknown background, time-consuming, works only on segmented images, a lot of concatenation
11	Das et al. [17]	Gaussian filters, histogram equalization, ReLu, SoftMax, Adam optimizer, MATLAB format, dropout	Reduced parameters, reduced training time, efficient feature extraction	Overfitting issues, multiple layers, high precision only for 1 class
12	Swati et al. [18]	Preprocessing, CNN, Transfer learning, fine-tuning, block-wise strategy, VGG-19 architecture, five-fold cross-validation	High accuracy, small data set, reduced overfitting, increased speed of convergence	Only meant for 2D images, convergence depends on initial learning rate, normal brain MRIs weren't included
13	Sultan et al. [19]	Preprocessing, ReLu, K-Convolutional filters, data normalization, dropout layer, stochastic gradient descent	Swift training phase prevents overfitting, segmentation not required, good prediction	Padding of images is required; large-scale testing and fine-tuning is required
14	Abiwinanda et al. [20]	Adam optimizer, convolutional layers, a max-pooling layer, a flattening layer, a fully connected layer, SoftMax, ReLu, Cross-entropy	Minimized validation loss, manages disturbances efficiently, will aid medical professionals	High computational costs, image dimensions had to be reduced, increasing filters don't have an effect

Table 1 (continued)

S. No.	Author(s)	Methodologies used	Advantages	Disadvantages
15	Shrot et al. [21]	Diffusion tensor imaging, perfusion imaging, feature extraction, support vector machine, normalization, binary hierarchical tree, arterial input function	Microstructures can be understood, automated classification	Minor deviations were ignored, chances of error in classifier nodes, sensitivity low for PCNSL
16	Anaraki et al. [22]	Convolutional neural network, geometric algorithm, stochastic gradient optimizers, bagging algorithm	Suitable architecture, computational costs reduced, work with unseen data, loss function reduced, feature extraction not required	Must be tried out with larger data sets, data augmentation due to limited data
17	Shakeel et al. [23]	Fractal dimension algorithm, multi-fractal detection technique, PCA, GLCM, hole filling, clustering, infrared sensors	Comforting for elderly patients, early detection of tumors, tumors were highlighted	High memory usage, based on just 2D images, loss of geometric information
18	Huang et al. [24]	CNNBCN, Erdos–Renyi (ER) algorithm, Watts-Strogatz (WS) algorithm, Barabasi-Albert (BA) algorithm, ReLu, GeLu, Network Generators	Nodes were explicit, training time is minimized	Complex and confusing, networks need to be simplified
19	Ismael et al. [25]	Pareto principle, data augmentation, ResNet architecture	High accuracy, learns high level features, manages diversity and complexity	Only meant for MRI's, too many augmentation techniques
20	Ahuja et al. [26]	Wavelet decomposition, geometric operations, super-pixel technique, K-Means clustering	Large-scale data not required, ideal similarity coefficients, pruning technique not required	Works only on 2D images, conversion to png format
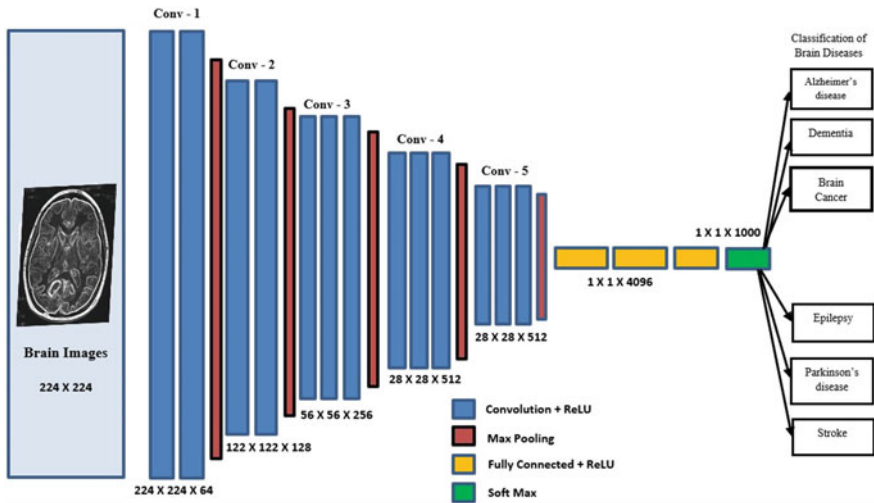
Fig. 1 VGG-16 model for multiple brain diseases classification

The proposed model would identify multiple brain diseases, including Alzheimer's disease, Dementia, Brain Cancer, Epilepsy, Parkinson's disease, and Stroke, using these features. The new system would assist physicians in identifying various brain diseases at an early stage, thereby increasing the survival rate.

4 Conclusion and Future Work

The proposed method classifies medical images of the brain into six distinct diseases. It will facilitate the efforts of medical professionals such as radiologists, neurologists, etc., and enable them to detect brain disease prior to its deterioration, thereby saving the life of the patient. In the future, we intend to classify all other brain diseases and propose any unclassified diseases discovered during the classification process. As a result, the system will be able to recognize any unusual changes in the DNA sequences linked to brain cells, revealing any anomalies. Consequently, it would save many lives in unexpected situations involving patients with multiple diseases. It will also allow commoners to examine themselves with limited testing, hence decreasing the time required for disease identification. We also aim to reduce the algorithm's time complexity in order to increase its efficacy, as robust algorithms are required to solve the problems in the healthcare industry.

References

1. https://www.webmd.com/brain/what-is-encephalopathy
2. https://www.americanbrainfoundation.org/diseases/
3. https://www.ninds.nih.gov/health-information/patient-caregiver-education/factsheets/neurol ogical-diagnostic-tests-and-procedures-fact-sheet
4. Gavali P, Banu JS (2019) Deep convolutional neural network for image classification on CUDA platform. In: Deep learning and parallel computing environment for bioengineering systems, Academic Press, pp 99–122
5. https://www.expert.ai/blog/machine-learning-definition/
6. Kumar Y, Koul A, Singla R, Ijaz MF (2022) Artificial intelligence in disease diagnosis: a systematic literature review, synthesizing framework and future research agenda. J Ambient Intell Humanized Comput 1–28
7. Salvatore C, Cerasa A, Castiglioni I, Gallivanone F, Augimeri A, Lopez M, Quattrone A (2014) Machine learning on brain MRI data for differential diagnosis of Parkinson's disease and progressive supranuclear palsy. J Neurosci Methods 222:230–237
8. Payan A, Montana G (2015) Predicting Alzheimer's disease: a neuroimaging study with 3D convolutional neural networks. arXiv preprint arXiv:1502.02506
9. Veeramuthu A, Meenakshi S, Darsini VP (2015) Brain image classification using learning machine approach and brain structure analysis. Proc Comput Sci 50:388–394
10. Mathur Y, Jain P, Singh U (2017, April) Foremost section study and kernel support vector machine through brain images classifier. In: 2017 International conference of electronics, communication and aerospace technology (ICECA), vol 2. IEEE, p 559562
11. Islam J, Zhang Y (2017, November) A novel deep learning based multi-class classification method for Alzheimer's disease detection using brain MRI data. In International conference on brain informatics, Springer, Cham, pp 213–222
12. Hebli A, Gupta S (2017, December) Brain tumor prediction and classification using support vector machine. In: 2017 International conference on advances in computing, communication and control (ICAC3), IEEE, pp 1–6
13. Mohsen H, El-Dahshan ESA, El-Horbaty ESM, Salem ABM (2018) Classification using deep learning neural networks for brain tumors. Future Comput Inf J 3(1):68–71
14. Selvapandian A, Manivannan K (2018) Performance analysis of meningioma brain tumor classifications based on gradient boosting classifier. Int J Imaging Syst Technol 28(4):295–301
15. Hemanth G, Janardhan M, Sujihelen L (2019, April) Design and implementing brain tumor detection using machine learning approach. In: 2019 3rd International conference on trends in electronics and informatics (ICOEI), IEEE, pp 1289–1294
16. Afshar P, Plataniotis KN, Mohammadi A (2019, May) Capsule networks for brain tumor classification based on MRI images and coarse tumor boundaries. In: ICASSP 2019–2019 IEEE International conference on acoustics, speech and signal processing (ICASSP), IEEE, pp 1368–1372
17. Das S, Aranya ORR, Labiba NN (2019, May) Brain tumor classification using convolutional neural network. In: 2019 1st International conference on advances in science, engineering and robotics technology (ICASERT), IEEE, pp 1–5
18. Swati ZNK, Zhao Q, Kabir M, Ali F, Ali Z, Ahmed S, Lu J (2019) Brain tumor classification for MR images using transfer learning and fine-tuning. Comput Med Imaging Graph 75:34–46
19. Sultan HH, Salem NM, Al-Atabany W (2019) Multi-classification of brain tumor images using deep neural network. IEEE Access 7:69215–69225
20. Abiwinanda N, Hanif M, Hesaputra ST, Handayani A, Mengko TR (2019) Brain tumor classification using convolutional neural network. In: World congress on medical physics and biomedical engineering 2018, Springer, Singapore, pp 183–189
21. Shrot S, Salhov M, Dvorski N, Konen E, Averbuch A, Hoffmann C (2019) Application of MR morphologic, diffusion tensor, and perfusion imaging in the classification of brain tumors using machine learning scheme. Neuroradiology 61(7):757765

22. Anaraki AK, Ayati M, Kazemi F (2019) Magnetic resonance imaging-based brain tumor grades classification and grading via convolutional neural networks and genetic algorithms. Biocybernetics Biomed Eng 39(1):63–74
23. Shakeel PM, Tobely TEE, Al-Feel H, Manogaran G, Baskar S (2019) Neural network based brain tumor detection using wireless infrared imaging sensor. IEEE Access 7:5577–5588
24. Huang Z, Du X, Chen L, Li Y, Liu M, Chou Y, Jin L (2020) Convolutional neural network based on complex networks for brain tumor image classification with a modified activation function. IEEE Access 8:89281–89290
25. Ismael SAA, Mohammed A, Hefny H (2020) An enhanced deep learning approach for brain cancer MRI images classification using residual networks. Artif Intell Med 102:101779
26. Ahuja S, Panigrahi BK, Gandhi TK (2022) Enhanced performance of DarkNets for brain tumor classification and segmentation using colormap-based superpixel techniques. Mach Learn Appl 7:100212

Cardiac Arrhythmia Detection and Prediction Using Deep Learning Technique

K. Nanthini, D. Sivabalaselvamani, K. Chitra, P. Aslam Mohideen, and R. David Raja

Abstract One of the fatal diseases in the world is heart disease. Every year, millions of people die of cardiovascular diseases. However, one can decrease the mortality rates if the heart disease was detected and treated early. Usually, people do an electrocardiogram (ECG) test to know about the well-being of their heart. Some kind of irregular functioning and illness in the heart can be found in an ECG test. When the heart malfunctions or if there is any improper beating of the heart, then it results in arrhythmia. There are several types of arrhythmia and some of them are fatal. The process to identify the correct type of arrhythmia is quite difficult and effort-taking process. Even the small changes in the ECG relate to another kind of arrhythmia. It takes experience and patience to recognize the type of arrhythmia accurately. Therefore, deep learning techniques should be employed to analyze the test. Machine learning that involves many levels of processing is known as deep learning. From computer vision to natural language processing, there's a lot to learn. It has been used in various applications. This method is receiving more popularity because of extreme accuracy, provided the numerous amount of data. The interesting feature is that it analyses the examples and distinguishes the classes and levels automatically. This study is regarding arrhythmia prediction in ECG and the attention it deserves in deep learning community. Providing CNN model, we are going to elaborate the process of detecting cardiac arrhythmia using ECG dataset in this study. The model is executed by rendering CNN with cardiac arrhythmia recognition database. *Purpose*: About one-third of the world's population is affected by arrhythmia. Hence, the development of new and successful methodologies is highly in demand in the field of arrhythmia prediction. Further, the need of a cost-effective wearable monitoring gadget to identify the condition of arrhythmia is highly recommended. It assures the

K. Nanthini · D. Sivabalaselvamani (✉) · K. Chitra · P. A. Mohideen · R. D. Raja
Department of Computer Applications, Kongu Engineering College, Perundurai, Erode, Tamil Nadu, India
e-mail: sivabalaselvamani@gmail.com

P. A. Mohideen
e-mail: aslammohideenp.20mca@kongu.edu

R. D. Raja
e-mail: davidrajar.20mca@kongu.edu

trouble-free environment for those who are affected. *Observations*: Various research papers that were written bases on arrhythmia prediction using machine learning techniques. Additionally, there are also new advancements all over Internet regarding deep learning-based strategies. These strategies can bring an immense change in cardiac arrhythmia prediction.

1 Introduction

As per the World Health Organization (WHO), 17.9 million deaths across the world are due to cardiovascular diseases (CVD) in 2016. This shows that 30% of the total deaths are because of CVD at that particular year. Moreover, WHO alerts that the fatality rate will increase up to 23.6 million by the year 2030. The important factor to avoid heart illness is to identify it early. By adopting healthy lifestyle and appropriate medicines, one can avoid the lifetime risk of cardiovascular disease. A person puts themselves in critical situation if the chronic disorders like CVD are not recognized early. Due to this, identifying the irregularities in the heart is significant. As we already see, cardiac diseases cause numerous deaths across the world. One-third of the deaths on the planet are because of cardiovascular diseases. Therefore, the prediction of cardiovascular disease is crucial. To find the condition and irregular beatings of heart, cardiologists and other specialists conduct ECG test. By attaching electrodes on the skin, cardiologists measure the electrical movements of the heart using an ECG. A time-series data will be employed to represent an ECG. Not so long ago, medical practitioners are bound to perform ECG test by hands. But this method has some disadvantages. For instance, this kind of analysis is likely to have errors. To come across the level of basic ones, machine learning has become more eminent method to run an ECG test. While running an ECG test, bio signals can be abnormal and non-linear. To avoid these situations, the ECG signal must be processed. Due to this method, noise suppresses the ECG signal as well as the ECG interval features. Another important thing about the machine learning methods, which were mentioned previously, is that it takes a cardiac specialist to identify the ECG signals and features accurately.

The crucial thing is that it does not has the features extracted automatically. It is more stable and trustworthy in accordance with accuracy and measure. The model can be trained once it has the feature representation of the dataset. As far as the deep learning technique is considered, it creates space for independent learning of features. Along with it, this technique allows the learning of the features that are important to the signal recognition tasks at hand. To train these models, deep learning method consists of numerous variables. And training consumes a lot of processing

power. Though it does not matter as cloud computing has minimum number of training-related issues due to the availability of high processing capacity.

1.1 The Human Heart

Heart is one of the vital organs in the body and it has two major features. And it pumps blood from the lungs to the body's tissues and pumps blood from the body's tissues to the lungs. On looking into the structure of the heart, it has four quartets that are separated by myocardium. And those four partitions can be divided into two parts. The two higher chambers are known as atria, while the two lower chambers are known as ventricles. Atria are primarily responsible for the collection of blood from parts of the body, whereas ventricles are responsible for pumping of the blood. Coming back to the subject of the work, which is arrhythmia, is one of the cardiovascular illnesses. To identify this illness, one should watch the beatings of the heart. And every heartbeat starts with the *P*-wave. This wave is created by the sinus node (natural cardiac pacemaker). *P*-wave, which is also known as positive or slow wave, is an initial electrical occurrence that happens throughout a heartbeat or one cardiac cycle with the modification of the atria. Schematic representation of normal ECG is shown in Fig. 1.

Important features of normal ECG is tabulated in Table 1. In case of ventricular septal depolarization, the *Q*-wave is generated. On the contrary to *P*-wave, *Q*-wave is known for its negative wave, rapid, and tiny. The *R*-wave is another kind of wave, known for powerful, quick, and +ve frequencies. It forms throughout the cardiac cycle whenever there is substantial ventricular depolarization. After the occurrence of the *R*-wave, there comes the *S*-wave. It is a negative wave that can move quickly. As the final one in the heartbeat, *T*-wave is the last wave. Further, ventricular repolarization is a slow-moving positive wave. As displayed in Fig. 2, the isoelectric line is a linear line that connects 2 waves. The connecting thing between any two waves is these lines that do not include both. A heartbeat consists of two parts and they are the PR segment and the ST segment. Additionally, the cardiac cycle includes another two segments that are PR and QT intervals. The mentioned segments are the time length between a segment and two waves. A healthy human heartbeat takes the time of 0.6 s to complete one cardiac cycle.

The most common interval in the view of ECG aspects that are frequently used for classification is the *R–R* intervals. The distance between one QRS complex's peak and the following QRS complex's peak is the *R–R* interval. The *R–R* properties, which are often employed, are the post-RR, average RR, pre-RR, and local RR. Each patient has waveforms that have different temporal and morphological qualities. And that is one of the most difficult aspects of computerized ECG signal classification. Sometimes, different patients with different cardiac cycles can have the same kind of ECG waveforms at different periods of time. On the contrary, the same patient may have different waveforms at different times. Along with the issue of ECG classification, heart rate variability is another issue to be considered. The parameters of ECG
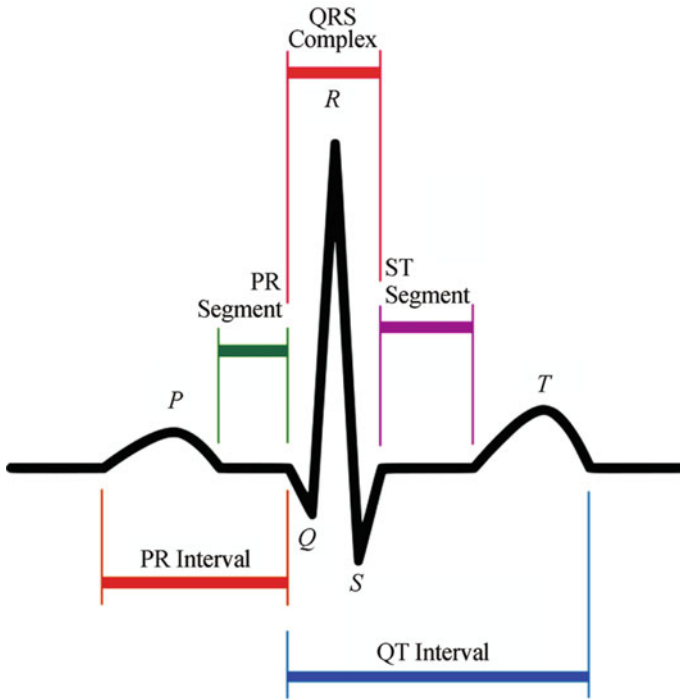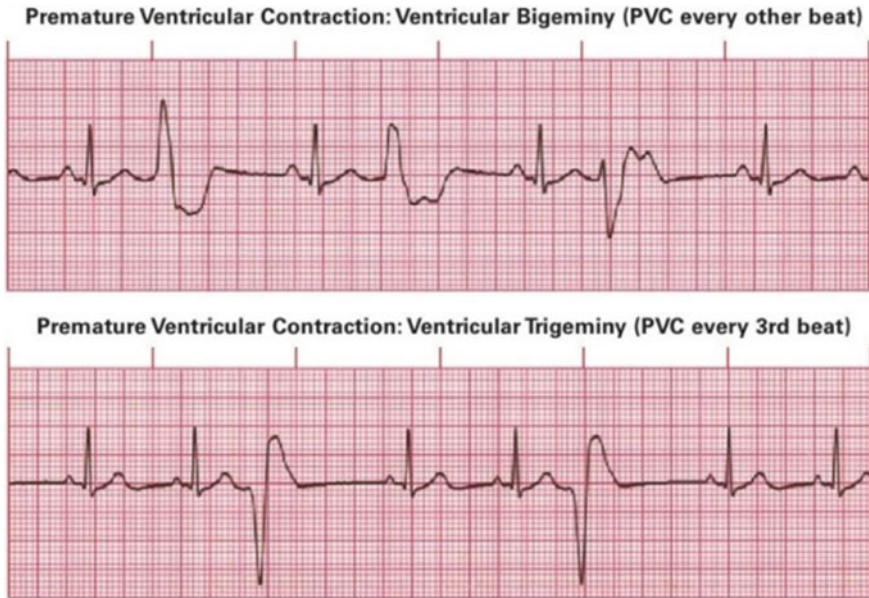
Fig. 1 Schematic representation of normal ECG

Table 1 Important features of normal ECG

ECG feature	Description
P wave	It represents atrial depolarization; amplitude: 0.1–0.12 mV; duration: 0.08–0.1 s
QRS complex	It represents ventricular depolarization; amplitude: 1 mV; duration: 0.08–0.12 s
T wave	It represents ventricular repolarization; amplitude: 0.1–0.3 mV; duration: 0.12–0.16 s
P-QRS-T	It indicates one mechanical heart beat; duration: 0.6–1 s
PR interval	It tracks the impulse from atria through A–V node; duration: 0.12–0.2 s
RR interval	It is the time elapsed between successive two R waves; duration: 0.6–1 s

that include RR interval and PR interval may change according to the psychological states such as enthusiasm, depression, workouts, other physical factors, and much more.

Premature Ventricular Contraction: Ventricular Bigeminy (PVC every other beat)

Premature Ventricular Contraction: Ventricular Trigeminy (PVC every 3rd beat)

Fig. 2 Premature ventricular contraction for ventricular bigeminy and trigeminy

1.2 Arrhythmias

Arrhythmia is known as the irregular heartbeats or the abnormal rhythm in the cardiac cycle. For instance, a healthy person with good a physique has a heart rate between 60 and 100 bpm. But the person who has arrhythmia has palpitation or even they can feel speeding, flickering, or skipping in their heartbeat.

The possible symptoms of arrhythmia are chest ache, fatigue, lightheadedness, inefficient breathing, or sometimes there may be no symptoms at all. There are three main categories of arrhythmia and they are bradycardia (slow), irregular or extra heartbeat, and tachycardia (rapid).When it comes to irregular or extra heartbeat, one may feel a frequent beat, a swift beat, a fluttering sensation, or a skipped beat. These abnormal heartbeats are the symptoms of irregular heartbeats. Two examples of abnormal heartbeats are APC and PVC. When the heart rate falls below the normal range of beats per minute, then it is classified into bradycardia. Some examples of bradycardia are AV heart clots (first, second, and third degrees), left and right bundle branch congestion, and tachy-brady syndrome. Atrial premature contraction is shown in Fig. 3.

When the heartbeat rate exceeds the normal range of 60–100 beats per minute, then it is tachycardia. Usually, the heartbeat range of tachycardia is between 100 and 350 beats per minute. Along with ventricular fibrillation, tachycardia is the type of arrhythmia that can be more fatal.

Fig. 3 Atrial premature contraction

1.3 Deep Learning Approach

One of the brand new features of machine learning within AI technology is deep learning. This method has shown successful results while used in several applications. Deep learning model is inspired by biological brain learning and learns immense data. The eminent driving forces behind deep learning are big data, processing power, and algorithms. Of all these bygone years, it has gained many names. And one of them is artificial neural networks. To get exact and accurate results, deep learning is utilized and yet it is hard to interpret it. The decision-making accuracy of deep network is amazing. However, one should understand why the model has come to such conclusions. Subsequently, evaluating the results brought by the deep learning model is an important thing.

Deep learning differs from regular machine learning in several ways. Here, they prepare the crucial steps such as extraction, selection, and classification of features. And these steps are necessary in machine learning algorithms whereas deep learning does not require them to be explicitly described. Deep learning model is designed to be a self-learning one that is processed with numerous sets of data. The time, frequency domain, and other built features, beat-to-beat interval, are included in deep learning. On the contrary, they are not included in machine learning algorithms. Those features are crucial for considering the raw QRS shape that is vital in diagnosing abnormalities.

2 Literature Review

Annam et al. [1] they have taken the MIT-BIH arrhythmia database hosted at PhysioNet and used various deep learning techniques to predict the cardiac arrhythmia. Accuracy for each algorithm is observed and compared with algorithms sensitivity.

Aslam and Jaisharma [2] Here a construction for formative resemblance using a hierarchical RF formation and NR design model precisely predicts CVD by 90.3%. Yuepeng et al. [3] observe the attributes that cause heart disease, and they constructed a forecast model focused on KNN, DNN, and LSTM. Rahul et al. [4] the research is able to provide quicker and various alternatives. Deep learning and gradient boosted trees are two algorithmic leaning used to obtain the predicted values.

Swapna [5] compared the performance using a various deep learning architectures of CNN, CNN-RNN, CNN-LSTM, and CNN-GRU and attained the high accuracy of 0.834. Kefaya et al. [6] team classified this critical gap by examining a DNN model that exactly analyzes arrhythmia relying on an individual raw ECG heartbeat. The contribution considerably develops current arrhythmia prediction methodology by obtaining an effective system to assess arrhythmia prediction assessments. The Cleveland heart disease data source and data mining methodologies are used by Kavitha et al. [7]. The test results show that the HDP model with the hybrid system has an accuracy of 88.7% when using Random Forest, DT, and HM (Hybrid of RF & DT). On the MIT-BIH arrhythmia database for heartbeat classification, Srinidhi et al. [8] conducted a thorough assessment of LSTM-based deep learning DL systems with many productivity measures. The BiLSTM DL design has 95% sensitivity and 98% specificity in categorizing heartbeats.

To overcome the drawbacks of existing approaches, Shadab et al. [9] proposed a novel DL structure based on a 1D CNN for categorization of healthy and non-healthy people. To avoid over-fitting, a variety of measures are employed. This network has a training accuracy of over 97% and a test accuracy of 96%. Decision Tree, Naive Bayes, Random Forest, SVM, KNN, and logistic regression techniques are employed by Sujatha and Mahalakshmi [10]. Random Forest is more precise for prediction, according to observational data, with an accuracy of 83.52%. Norma et al. [11] to predict cardiac illness, this team recommends HDPM for a CDSS that comprises DBSCAN, a hybrid SMOTE-ENN, and XGBoost. With NB, LR, MLP, SVM, DT, and RF, Statlog and Cleveland were used. With accuracy of 95.90 and 98.40% in each, our framework outperformed other approaches. Sarah et al. [12] the goal of this study was to create a predictive design for CAD diagnosis. RF and NB were used to prove the theory. With 13 characteristics, NB outscored RF by 83% in accuracy.

Mohamed et al. [13] contribute to HDP research that uses the LSTM approach. The main goal is to develop a smart algorithm that uses the LSTM approach to forecast cardiac disease. It is proved to be the most successful methodology when compared to the MLP method. Halima et al. [14] detected HD was proposed clinical support model. The results reveal that Nave Bayes outperforms both cross-validation and train-test split approaches, with accuracy of 82.17% and 84.28%, respectively, when utilizing the UCI data set. Sharma et al. [15] has used the Cleveland heart disease database to conduct deep neural network analysis. A few DNN methods have been created through research, every with completely different characteristics as compared to the others. The test set includes 147 instances, as well as the DNN achieves an accuracy of 82.7%, a misclassification possibility of 17.3%, a sensitivity of 81.03%, as well as a selectivity of 82.8%.

Toomula et al. [16] proposed an efficient fusion-based feature extraction with multikernel extreme learning machine (FFE-MKELM) for COVID-19 diagnosis using Internet of things (IoT) and wearables with increased sensitivity of 97.34%, specificity of 97.26%, accuracy of 97.14%, and F measure of 97.01%.

Adeen and Sondhi [17] the goal of analysis is to compare the productivity of numerous classification approaches in way to identify the most effective approach for estimating whether or not a patient will develop HD, which also compares the Nave Bayes, Help Vector Machine, Random Forest, as well as supervised learning models to find the most effective approach. Database has been categorized into training and testing data as well as designs have been equipped, or using Python, the precision has been mentioned. A comparison of the performance of the methodologies is shown below and the table provides their accuracy scores, recall, accuracy, and F1 score. Random Forest has been reported to have greater accuracy (95.08%), recall (0.91%), and $F1$ score (0.91%) than other methodologies.

Sayali et al. [18] because of the enormous volume of information expansion in the biomedical or healthcare fields, precise clinical data analysis has become advantageous for earlier disease detection as well as patient care. On the basis of the dataset, authors are continuing to work on predicting heart disease using the Nave Bayes and KNN algorithms and propose extending this work by predicting disease risk utilizing structured data. The CNN-UDRP approach has a forecasting accuracy of more than 65%. Nanthini [19] The LSTM model was proposed to predict the epilepsy using EEG signals with UCI dataset which gives 99% of training and testing accuracy.

Sivabalaselvamani [20, 21] in this journal, the coronary diseases are discussed and their related cardiovascular diseases ECG signals with CFS + PSO order was applied to arrange heart Diseases highlights into subgroups. Hemalatha [22] here a cross-breed frame work is discussed for the prediction of heart disease and route set techniques (SVMRS) with a accuracy rate of 98.3%. Sathesh [23] the paper focuses on the monitoring of fetal echo cardiology (FEC), for the detection of abnormalities in the heart rate of the child in the womb, where the early detection would allow the doctor to start with the treatment from the womb, or to be prepared for the complications on delivery, or with the treatment after the birth.

Shakya [24] here, leveraging fog computing and data from the BSNs, a data fusion technique was developed. Using a variety of sensors, daily actions are converted into data that is then combined to create high-quality data. In order to increase quality, categorization is done using a new kernel random data collector. An experimental investigation using a depth of around 10 and an estimate count of 45 with 7 features parameters shows a 96% accuracy.

Nanthini [25] the K-means algorithmic rule and KNN techniques are proposed to predict the cardiovascular discomforts and diseases using machine learning in Python and depicts accuracy in frequent intervals.
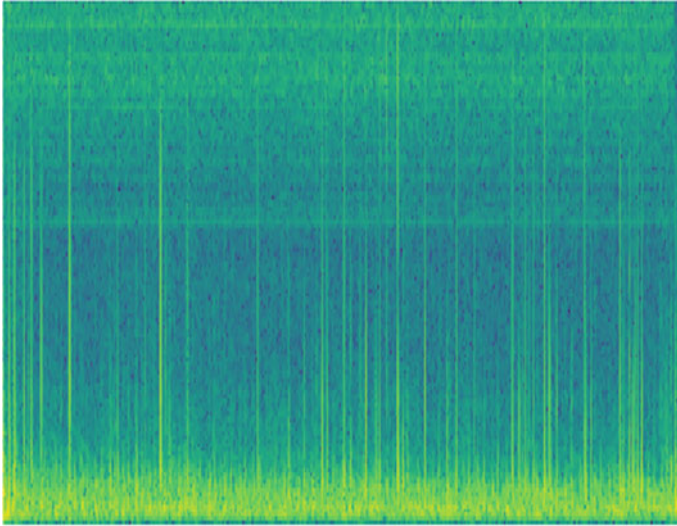
Fig. 4 Normal ECG signal

3 Materials and Methods

3.1 EEG Dataset

Datasets derived from the GitHub have been used for the implementation of proposed algorithm. Here the ECG images are taken for the arrhythmia processing. The database consists of ECG images of train and validation dataset, and validation dataset consist of normal and abnormal ECG images. The training dataset consist of 1000 ECG images which have 400 abnormal images and 600 normal ECG images, and the validation data consist of 225 ECG images in which 143 ECG images are normal signals and 83 are abnormal ECG signals. Normal ECG signal is shown in Fig. 4, and abnormal ECG signal is shown in Fig. 5.

3.2 Methodology

To analyze the dataset and find the cardiac arrhythmia, I employed CNN. It is a type of deep learning model for analyzing the data that has a grid pattern, such as pictures. It is to improve the inner features of 2D images. Convolutional neural network was chosen for this study because it proves to be prominent for any prediction problems partaking image data, and here to predict the arrhythmia, the CNN model was the right choice.
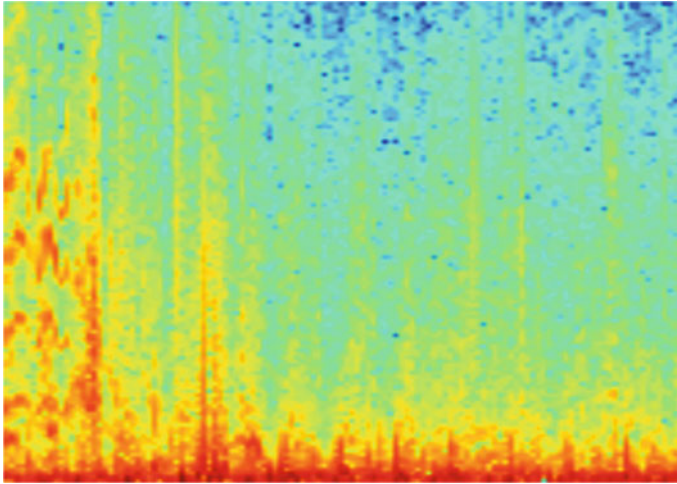
Fig. 5 Abnormal ECG signal

3.3 Convolution Neural Network

This research uses training and learning neural networks to identify diverse data categories. To categorize, classification models of CNN were employed in the current research. CNNs are made up of convolution and pooling phases that aid in extracting relevant features from image maps. A CNN model takes a three-dimensional tensor as input, which is an image with height and width information as well as RGB value. The neural network then goes to the steps of gradual processing with this input image. These are layers of the network. Convolution begins with the application of the kernel to a portion of the image. The initial pixels on the upper left part of the matrix fit the size of the kernel usually in this location. The pixel values of the kernel and image are multiplied together for a concluding value in the modified image map. Figure 6 depicts how to calculate the first pixel value in a Feature map using a 6 × 6 input image and a 3 × 3 kernel size as in Fig. 6. All values are determined in the same way as the value set's new feature.

$$F(1,1) = 3 \times 1 + 5 \times 1 + 5 \times 1 + 5 \times 0 + 5 \times 0 + 5 \times 0 + 5 \times (-1) + 5 \times (-1) + 2 \times (-1)$$
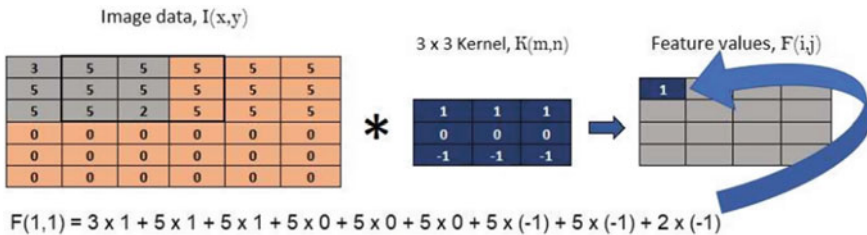
Fig. 6 Feature value extraction in CNN

This kernel is moved on image data from left to right in step increments, which of these step increments are called strides. The convolution F of a kernel and image data are represented by the following equation

$$F(i, j) = \sum_m \sum_n K(m, n).I(i - m, j - n)$$

The above equation represents the dimensions of the image i and j, the kernel size $m \times n$ is represented as K, and F, I, and j represent the convolution. The pooling layers, fully connected layers, activation layers, output dropout, and flatten are all present in most CNN models. All of the above-mentioned layers were present in various layouts in CNN models.

3.4 Activation Function

An activation function is frequently placed after each convolution layer in a CNN model. The ReLu (Rectified Linear Unit) function is a good choice on CNN models. The negative values of the input feature matrix are set to zero by ReLu. Because CNNs are primarily employed for real-world data processing, nonlinearity in the learning model is required, as convolution is a linear operation. ReLu is defined mathematically as

$$f(x) = \max(0, x)$$

For any $(-)$ve entries of input (x), preceding formula computes ReLu, $f(x)$, to generate zero output values and identity otherwise.

3.5 Pooling Layers

Pooling layers after convolution layers in CNN decrease the dimensions of feature maps, resulting in a matrix with fewer dimensions and more meaningful features. Figure 7 explains how to convert a 4×4 matrix to a 2×2 feature value set. Pooling layers help to limit the number of parameters in the model, which helps to avoid over-fitting issues.

In models of CNN, autocorrelation occurs when the network is trained in both native and noise input, resulting in a negative classification effect. Despite the fact that pooling layers lower the size of feature maps, they can maintain the most significant information for network data processing. The purpose of max pooling operation is used for pooling steps, and a 2×2 window is used in the same way as in Fig. 7. The highest of each set was chosen as features of input for the feature value pair in this case.
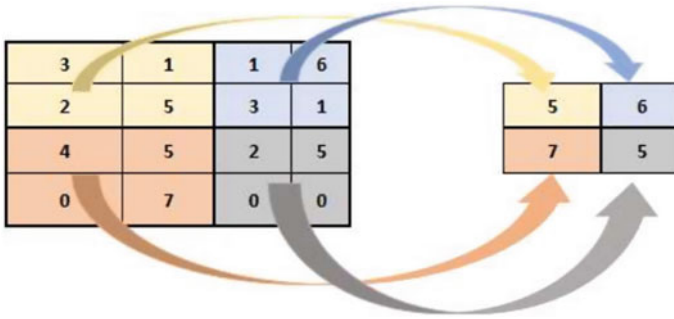
Fig. 7 Max pooling on convolution layer

3.6 Fully Connected Layer and Softmax Activation

In completely connected layers, each of the node in the following layer is linked to the neurons in upcoming levels by a feature map containing the most essential information received from the pooling and convolution layers. Dense layers are layers that are fully connected. Fully linked layers perform early categorization on input data using the retrieved characteristics from preceding layers. The fully linked and softmax layers of CNN's architecture is shown in Fig. 8. Finally, the training data classes are classified using the Softmax activation layer.

Flatten layers are executed prior to the output layer that transform vectorization of a multidimensional output, while dropout layers are used to neglect some data on a few neurons in the network to avoid over-fitting difficulties. This step is required to determine the output shape based on the number of learnt and projected classes. If a CNN training session's input data has two categories, the flatten layer would be needed to reduce the fully connected layer's result to a vector of two values, one for each of the categories. A larger vector is created at the output layer for category information classification.
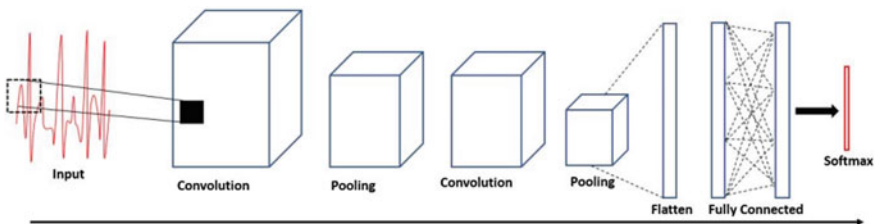
Fig. 8 A full sequence of a CNN with fully connected and softmax layers for output

3.7 Back Propagation and Gradient Descent

In theory, a CNN model takes picture data and propagates it through layers of convolution and fully linked layers. The training data classes' output values are calculated. Weights are assigned randomly on the initial iteration, therefore output values are also unpredictable. The error is computed and back propagated at this point by computing its gradients using weights from previous CNN layers. The CNN models' parameters are then adjusted via gradient descent. Technique for minimizing some of the function values by descending to the lowest value is known as gradient descent. When the input data is taught via neural network, predictions are made during the classification process. The accuracy of a predicted network can be represented in p, and the intended accuracy in y. As a result, if the network value of prediction is p and the desired target values are y, the error for S set of predictions can be calculated as E.

$$E = \frac{1}{2} \sum_{s} (y - p)^2$$

This error value is lowered through back propagation by altering the weights so that the values y and p are near to one another. This is achieved by back propagation by changing the weight values in relation to gradient descent algorithms. These methods are used to calculate partial weight (W) derivative with regard to error (E) values.

3.8 Transfer Learning with Deep Convolution Neural Network

Even though standard CNNs were employed in the first implementations of this research project, an ongoing approach termed transfer learning was also applied to compute classification accuracies. Traditionally, ML and DL models, as well as their corresponding validation and training datasets, have to be in the similar feature and has the similar distribution. A new technique known as "transfer learning" has presented a completely different perspective on learning. In the transfer learning method, knowledge from one dataset can be applied to a familiar dataset. This kind of model can be used in two ways. The first method is to fully apply the network which is trained to the latest data. The second method was to train some of the layers of the network that had already been trained and train the layers to reach the expected accuracy. ResNet, VGG-19, and VGG-16 are some of the most popular transfer learning models.
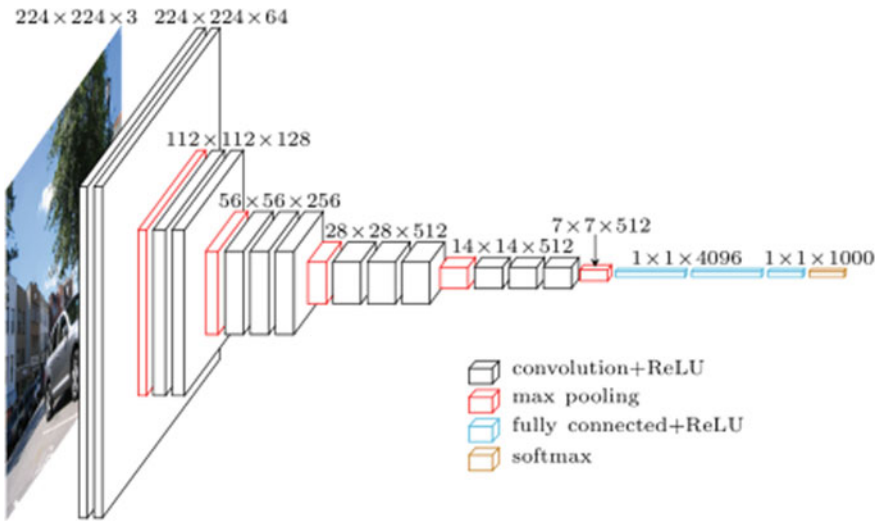
Fig. 9 Architecture of VGG16 model

3.9 VGG16 Model

In recent years, VGG16 is the most popular architecture of CNN as in Fig. 9. It comprises 16 layers. It is one of the categories of VGG model. Because of the uniformity, this category of VGG model is the most demanding one. It seems to be difficult in the beginning, but as time goes it will be more convenient. The challenging part in employing VGGNet is that it consists of 138 million parameters. For classification of images, this approach is the most preferred one.

3.9.1 VGG19 Model

VGG19 is a 19-layer variant of the VGG model as shown in Fig. 10. VGG-19 is a 19-layer convolutional neural network. Here ImageNet database to load a pre-trained version of the network has been trained on over a millions of images. The network can categorize photos into 1000 different categories. As a result, the network has a huge number of feature representations for a variety of images.

4 Implementation

The dataset includes two classes for comparing the arrhythmia predicted by the proposed algorithm to the arrhythmia identified by a qualified cardiologist. The first
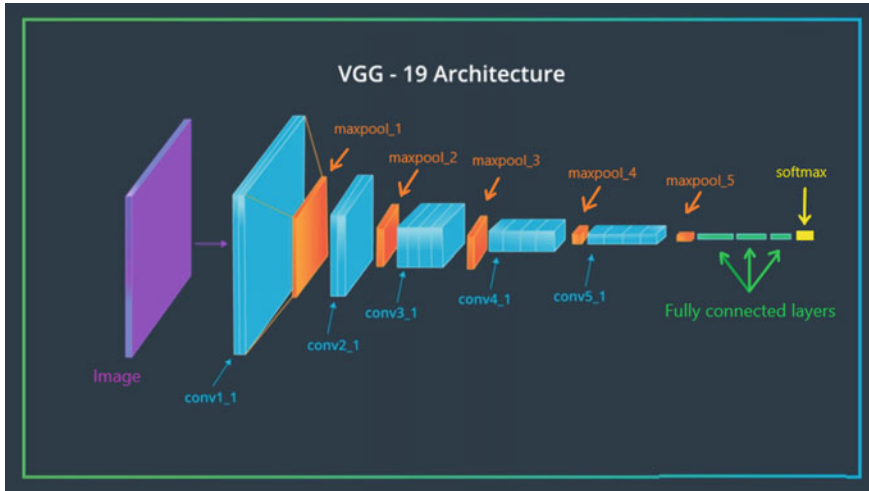
Fig. 10 Architecture of VGG19 model

one of the class represents normal and second class represents the abnormal signals (Fig. 11).

The *X* and *Y* columns of the dataset are divided into training and test datasets as *X*-Test, *Y*-Test and *X*-Train, *Y*-Train data. The test data has 1000 samples, and the training data has 255 samples for prediction. A bar graph was drawn on the data values to find the label variations. A bar graph regarding dataset is shown in Fig. 12. There are 600 normal samples and the count of 400 abnormal samples are employed in the prediction model, and the validation dataset consist of 255 samples which has 143 normal ECG and 83 abnormal ECG. To achieve better accuracy, fitting functions using data samples were used in the training data model. Adjust the weights according to the data value to improve accuracy. CNNs and densities were imported from TensorFlow Keras. First, we implement a deeper CNN layer to find the accuracy rate using the testing samples of the ECG signals and we predicted the accuracy rate in the responding model and then we train the same data with VGG16 and VGG19 a CNN model with 16 + 3 layers' deep model and predicted the arrhythmia rate.

5 Result

Arrhythmia is one of the leading cardiovascular diseases. Forecasting and prediction of cardiovascular disease are complicated process. ML as well as deep learning approach has been used in retrieving results and estimations in the field of healthcare. Our primary motive is to predict cardiac arrhythmia. The proposed work is about obtaining utmost accuracy by training and testing an existing database.

```
Number of samples in training set (normal): 600
Number of samples in validation set (normal): 143
Number of samples in training set (abnormal): 400
Number of samples in validation set (abnormal): 82
```
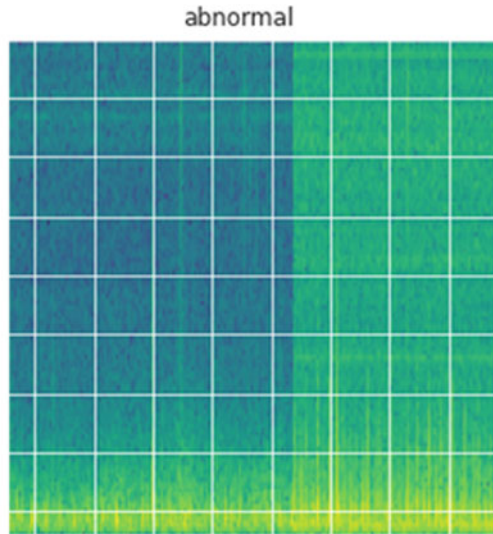

Fig. 11 Sample of the recorded data
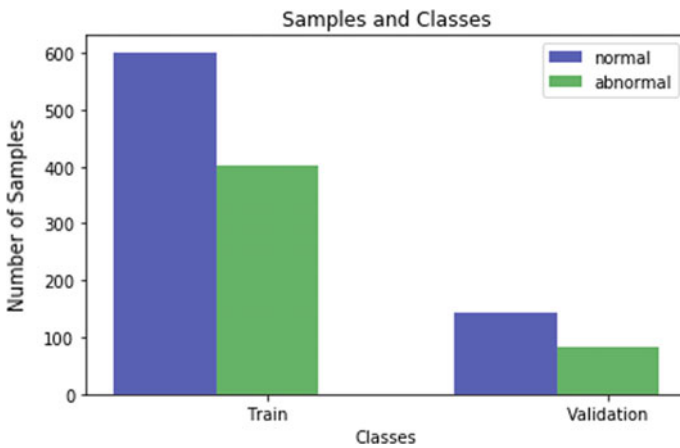
Fig. 12 Bar chart of label train and test data

Table 2 Accuracy obtained from the used mode

Model	Accuracy (%)
VGG16	96.86
VGG19	97.65

Here in the study, the employed CNN computes for extracting image classification and this leads to the prediction of arrhythmia. In the beginning, a few layers of CNN are used to predict the level of accuracy. Because of data inefficiency, the research is based on transfer learning approach. As a result, VGG16 and VGG19 models are executed to evaluate the process and to generate the results. In VGG16, the initial step is to train the model with 16 layers and those layers are pre-trained. Further, some more layers are added on top of VGG16 to obtain the highest level of accuracy. The extracted features from the model are then applied to train and test the data with the batch size of 16 and epoch value of 20. The next step is to fit the model and accuracy of train and test data, and loss of test and train data of the model will be acquired. Over-fitting happens when the accuracy rate of training dataset. To elaborate about fitting, first split the data as training and validation and import the required library. Hereafter, fitting function is used on training samples on features that are extracted from training data features, validation data, and its labels with respective batch size and epoch values. The process of both VGG16 and VGG19 models are the similar one. Finally, the accuracy of 96.86% is achieved in VGG16 model and 97.65% is obtained in VGG19 model. To increase the overall efficiency of the model, multiple models such as VGG-16 and VGG-19 are used as there are more layers and features extracted from it, which gives an overall increase in prediction. Table 2 shows the obtained results used by the models VGG16 and VGG19.

The Figs. 13 and 14 show the model accuracy and model loss of the VGG16 model, and Figs. 15 and 16 depict model accuracy and loss of the VGG19 model.

Fig. 13 VGG16 model accuracy
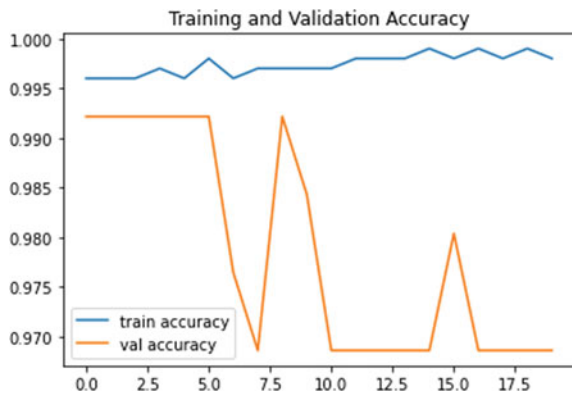
Fig. 14 VGG16 model loss
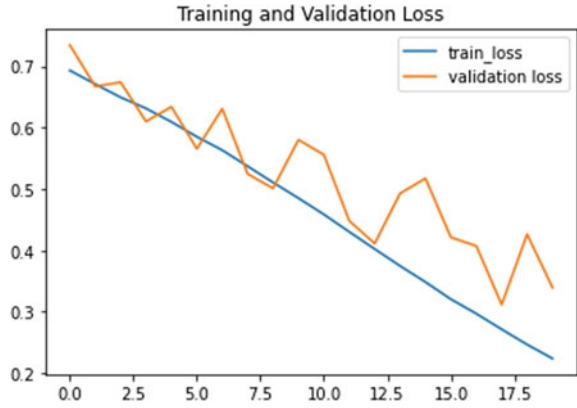
Fig. 15 VGG19 model accuracy
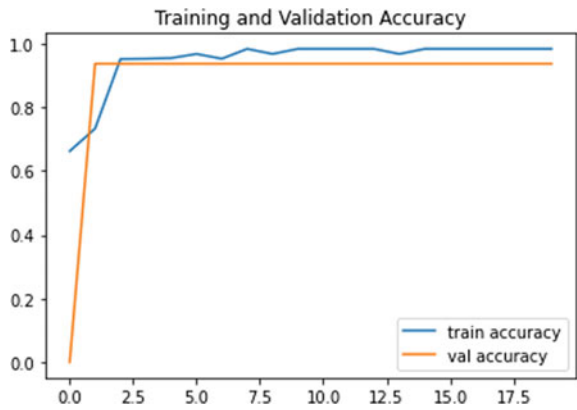
Fig. 16 VGG19 model loss
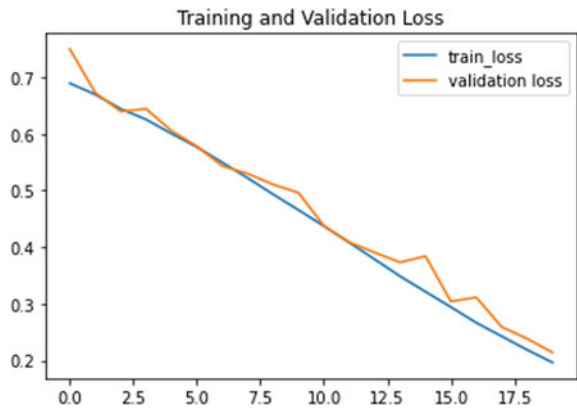
6 Conclusion

In past years, machine learning approaches were used to predict cardiac arrhythmia. However, deep learning is now being utilized to make arrhythmia prediction easier, as it reduces calculation time and increases the rate of learning. In case of machine learning, a large dataset is required with selected characteristics to train on. Though, ML is self-contained, it is a lengthy procedure when dealing with big amounts of data. On the contrary, deep learning performs both extraction and classification at the same time. In terms of medical picture analysis and disease prediction, deep learning plays a critical role.

7 Future Enhancement

In future, we prefer to use CNN to categorize several levels and stages given the dataset with a high level of accuracy rate. The focus of upcoming research in the coming times will be about the earlier detection of cardiac arrhythmias. It is advantageous for the persons who are in need of the treatment before the condition becomes severe. Concurrent cardiac arrhythmia detection has certain struggles regarding real-time monitoring, where the duration of monitoring and the play a crucial part. In order to get over this kind of obstacle, innovation is required in the design and the development of the product.

References

1. Annam JR et al. (2020) Classification of ECG heartbeat arrhythmia: a review. Proc Comput Sci
2. Aslam M, Jaisharma K (Jan 2021) Hierarchical random forest formation with nonlinear regression model for cardiovascular diseases prediction. In: International conference on computer communication and informatics (ICCCI)
3. Yuepeng L, Mengfei Z, Zezhong F, Yinghan C (Dec 2020) Heart disease prediction based on random forest and LSTM. In: 2nd international conference on information technology and computer application (ITCA)
4. Sah RD, patro SP, Padhy N, Salimath N (Mar 2021) Diabetics patients analysis using deep learning and gradient boosted trees. In: 8th International conference on computing for sustainable global development (INDIACom)
5. Swapna G et al. (2018) Automated detection of cardiac arrhythmia using deep learning techniques. In: International conference on computational intelligence and data science (ICCIDS)
6. Qaddoum K, Alazzam A, Al Azawi R (2020) A deep neural network heartbeat classification approach for arrhythmia detection. In: Seventh international conference on information technology trends (ITT)
7. Kavitha M, Gnaneswar G, Dinesh R, Rohith Sai Y, Sai Suraj R (Jan 2021) Heart disease prediction using hybrid machine learning model. In: 6th International conference on inventive computation technologies (ICICT)

8. Srinidhi H, S GM, Kiran MHM, Srinivasa KG (2021) A comparative study and analysis of LSTM deep neural networks for heartbeats classification. Health Technol 11:663–671. Djerioui M, Brik Y, Bilal A (Sep 2020) Heart disease prediction using MLP and LSTM models. In: International conference on electrical engineering (ICEE)
9. Shadab H, Susmith B, Shadab A, Suaib M (May 2021) Novel deep learning architecture for heart disease prediction using convolutional neural network. Mach Lear
10. Sujatha P, Mahalakshmi K (Oct 2020) Performance evaluation of supervised machine learning algorithms in prediction of heart disease. In: IEEE International conference for innovation in technology (INOCON)
11. Fitriyani NL, Muhammad S, Ganjar A, Rhee J (July 2020) HDPM: An effective heart disease prediction model for a clinical decision support system. IEEE Access 8:133034–133050
12. Sarah S, Yasmeen A, Alsahali S, Asalam N (2020) Automated prediction of coronary artery disease using random forest and naïve bayes. In: International conference on advanced computer science and information systems (ICACSIS)
13. Djerioui M, Brik Y, Bilal A (Sep 2020) Heart disease prediction using MLP and LSTM models. In: International conference on electrical engineering (ICEE), Pranav M, Ankita D, Suganya G, Premalatha M (2020) Cognitive approach for heart disease prediction using machine learning. In: International conference on emerging trends in information technology and engineering (ic-ETITE)
14. El H, Boujraf S, Chaoui NEH, Maaroufi M (Sept 2020) A clinical support system for prediction of heart disease using machine learning techniques. In: 5th International conference on advanced technologies for signal and image processing (ATSIP)
15. Sharma V, Rasool A, Hajela G (2020) Prediction of heart disease using DNN. In: Second international conference on inventive research in computing applications (ICIRCA)
16. Toomula S, Paulraj D, Bose J, Bikku T, Sivabalaselvamani D (2022) IoT and wearables for detection of COVID-19 diagnosis using fusion-based feature extraction with multikernel extreme learning machine. In Wearable Telemedicine Technology for the Healthcare Industry (pp. 137-152). Academic Press.
17. Adeen P, Sondhi (February 2021) Random forest based heart disease prediction. Int J Sci Res (IJSR) 10(2)
18. Ambekar S, Phalnikar R (2018) Disease risk prediction by using convolutional neural network. In: Fourth international conference on computing communication control and automation (ICCUBEA)
19. Nanthini K, Dr Tamilarasi A, Dr Pyingkodi M, Dishanthi M, Kaviya SM, Aslam Mohideen P (2022) Epileptic seizure detection and prediction using deep learning technique, International Conference on Computer Communication and Informatics (ICCCI)
20. Sivabalaselvamani D, Selvakarthi D, Rahunathan L, Eswari SN, Pavithraa M, Sridhar M (2021 January) Investigation on heart disease using machine learning algorithms. In 2021 International Conference on Computer Communication and Informatics (ICCCI) (pp 1–6). IEEE
21. Sivabalaselvamani D, Selvakarthi D, Rahunathan L, Gayathri G, Baskar MM (2021 December) Survey on improving health care system by implementing an air ambulance system with the support of drones. In 2021 5th International Conference on Electronics, Communication and Aerospace Technology (ICECA) (pp 878–883). IEEE
22. Hemalatha S, Tamilarasi A, Kavitha T, Sivabalaselvamani D, Raj MK (2022 January) A crossbreed framework for heart disease prediction using SVM and rough set techniques. In 2022 International Conference on Computer Communication and Informatics (ICCCI) (pp 1–5). IEEE
23. Sathesh A (2019) Performance analysis of granular computing model in soft computing paradigm for monitoring of fetal echocardiography. J Soft Comput Paradigm (JSCP) 1(01):14–23

24. Shakya S, Joby PP (2021) Heart disease prediction using fog computing based wireless body sensor networks (WSNs). IRO J Sustain Wirel Syst 3(1):49–58
25. Nanthini K, Preethi S, Venkateshwaran S (2020) Heart disease prediction using machine learning algorithms. Int J Adv Sci Technol

Hardware Prototype Model of Conventional Gas Stove Automation System—Application of Random Forest Regression Algorithm

R. R. Lekshmi, D. Annirudh, R. Surya, S. Kousik Harish, and S. Srilekha

Abstract   The society's convenience food intake practice has made culinary science one of the blazed areas of food industries. Higher quality food standards and convenience require good knowledge on culinary science. Unlike chefs, consumers are not much aware of the culinary skills. Moreover, working adults are coped with time pressures, often forget to supervise food under process. This leads to time and fuel wastage. This paper involves development of gas stove automation system that controls flame intensity to allow cooking under pressure cooking, boiling, and hybrid modes. The model employs parameters like whistle count, food surface temperature and cooking time, fed through touch display. The temperature module evaluates food surface temperature using a contactless sensor while employing random forest regression model. The gas knob is adjusted using stepper motor. The proposed model is expected to reduce lead cooking time and fuel consumption, improve dish quality and prevents any possible fire accidents.

Keywords   Automation · Graphical user interface · Random forest regression · Raspberry Pi · Sensor · Stepper motor

1   Introduction

India has a rich and highly diverse cuisine that involves many prolonged processing stages. The various diets are strongly related to cultural factors, religion, social identity, availability of food and local agricultural practices. Economic development in India has fostered urbanization that has brought notable changes in many aspects of well-being, including the diet pattern [1]. India has accorded to a shift in consumer preferences from traditional home food to "away" and packaged convenience food. This shift has led to the food choice improvement with new aroma, tastes and textures and new food product technology development. On a per calorie basis, "away" food

R. R. Lekshmi (✉) · D. Annirudh · R. Surya · S. Kousik Harish · S. Srilekha
Department of Electrical and Electronics Engineering, Amrita School of Engineering,
Coimbatore, Amrita Vishwa Vidyapeetham, Coimbatore, India
e-mail: rr_lekshmi@cb.amrita.edu

contributes to significantly higher total fat, higher saturated fat, less dietary fibre, less calcium, less proteins and less iron than home food. "Away" foods are subjected to adulteration, improper use of food additives and microbial contamination, thus pose a high risk of gastrointestinal disorder. It has been pointed out that convenience food that saves food preparation time, lacks nutrients and thus poses a degraded diet quality. This has a major impact on public health. Healthier diet quality is assured through traditional home food preparation with greater amount of time. Researches point out limited time availability and lack of culinary skills as barriers to healthy diet preparation. Lack of time prevailed among working adults and parents has led them to lean on convenience food. Working parents are coped with time pressures and often forget to supervise the food under process. This yields to undercooked or overcooked food with decreased food value.

A smart food system provides a solution to working adults and busy parents by assisting them in culinary skills. Research works have been intensely carried out for the development of such automated food processors. Frizziero [2] has presented the design of a coffee machine. An automatic pasta machine conceived for coffee shop that can cook "geared spaghetti" in less than a minute has been presented in [3]. Solanki [4] has designed and developed an automated fast food machine for large food industry. The design of high-tech vending machine that can vend about fifteen products is proposed in [5]. Svosve and Gudukeya [6] has presented design and development of an automatic electric cooking stove that checks for vessels on the heating plate to switch on and has the function to prevent burning of food. Castro [7] has developed a low-cost gas stove control incorporating temperature and humidity sensors to monitor the cooking process. The development of a smart gas controller on a reconfigurable hardware to allow remote control of the gas knob via bluetooth technology has been implemented in [8]. Refs. [9, 10] have developed an Internet of Things (IoT)-based smart cooking system. An automatic cooking robot that incorporates a novel feeding system to perform basic Chinese culinary is developed in [11]. Yalmar [12] has designed an automation system that turns off the conventional gas stove in the absence of personal or after a prescribed time. Huq [13] has implemented a simple electromechanical system to switch off the gas under the absence of vessel in the stove. Jahan [14] has developed a stove to harvest energy from the heat generated from the cooking process. The system is incorporated with MQ2 sensor to detect gas leakage and provides notification with the help of IoT.

Major research works focus on the design of smart system that switches off the gas stove when a prescribed condition is met. It is observed that designs presented in literatures require a greater understanding on the working of the system, and hence are not apt for a normal consumer to easily operate. Indian cuisine involves diverse cooking stages with distinct flame intensity and cooking modes like pressure, boiling, or sautéing down the cooking stages. There exists no research work that deals with the design of automatic system to perform multi-culinary modes suitable for Indian cuisine. In this paper, an attempt is made to fill the identified research gap through the development of a system that controls the existing conventional gas stove to assist in Indian cuisine cooking.

This paper involves design and development of a control model that automates conventional gas stove to perform multi-culinary skills that includes pressure cooking and boiling modes. The model incorporates auto ignition, contactless temperature determination, whistle count, humidity sensor, flame intensity adjustment, LPG gas leakage detection modules and a Graphical User Interface (GUI). The GUI provides a user-friendly environment to control and monitor the cooking process in a conventional LPG gas stove. All decision making and functional execution are done by Raspberry Pi, coded using Python Language. Each culinary skill is executed based on the user entry provided through the GUI. The GUI is developed with the help of Hyper Text Markup Language (HTML), Cascading Style Sheets (CSS) and JavaScript. The proposed system initiates cooking through auto ignition module and controls the flame intensity, based on the cooking parameters that include temperature of the food, humidity at the cooker nozzle, cooking time and the whistle count. The proposed system also ensures security against gas leakage through gas leakage detection module. The efficiency of the proposed system in saving significant time and fuel, while delivering perfectly cooked dish is also verified.

The paper is organized as follows:

Section 2 presents an overview of the proposed automation system. The hardware implementation of the automation system is explained in Sect. 3. The experimental results under different cooking modes are presented in Sect. 4. Finally, conclusions are made in Sect. 5.

2   Proposed Gas Automation System

The proposed gas automation system employs Raspberry Pi, coded using Python. The touch screen display serves as the communication gateway between the user and the microcontroller. These inputs include surface temperature, humidity, whistle count and cooking time. The controller executes various cooking procedures based on the set and current cooking parameter values. The parameters are tracked based on the cooking mode, which includes pressure cooking mode and boiling mode. The functional diagram of the proposed gas stove automation system is shown in Fig. 1.

The controller execution ensues when the cooking parameter entries are made by the user through the GUI. At the outset, the controller initiates the gas knob control mechanism to uttermost flame position. Meanwhile, auto ignition module is activated to set the flame. Subsequent to this stage, the controller starts to track the cooking parameters to decide the gas knob position at each cooking stages.

Under the pressure cooking mode, the whistle count and the humidity are tracked to decide the gas knob position, while, under the boiling mode, the temperature of food and cooking time is tracked. Tracking of cooking parameters requires distinct modules that include whistle count sensor, humidity sensor, and temperature module. The whistle count module incorporates a sound sensor to detect the whistle. Each whistle detection increments the controller timer. The process is terminated when the count reaches the set value. However, the module is designed to take no action
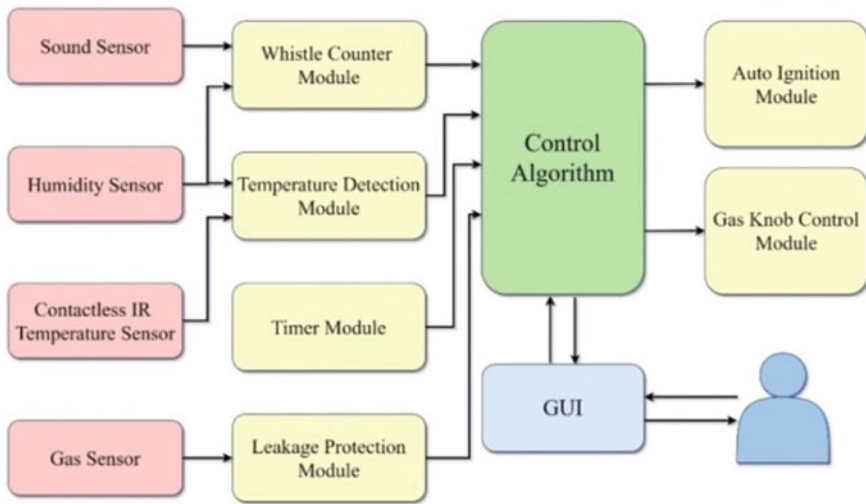
Fig. 1 Functional diagram of the proposed gas stove automation system

for fortuitous sounds other than whistle. It is well known that during the pressure release, whistle is accompanied with the moisture level rise at the cooker nozzle. A humidity sensor is employed to detect the rise in humidity. Thus, the whistle count module incorporates sound and humidity sensors, to guarantee a robust performance. This is clearly presented in Fig. 1. The process is terminated when the number of whistles is completes the set value given by the user.

Temperature is a crucial cooking parameter that prevents food from overcooking and undercooking while preserving the food nutrient values as per science-based cooking. Thus, determination of temperature is an inevitable aspect under boiling mode. The temperature measurement of food is done using a temperature sensor. Probe type temperature sensors are not preferred or recommended while cooking. This calls for a contactless temperature sensor as exhibited in Fig. 1, to measure the surface temperature of the food. The module employs random forest regression (RFR) model to determine the actual temperature based on the value sensed by the contactless sensor.

The proposed system adjusts flame intensity based on cooking parameters corresponding to cooking mode. As shown in Fig. 1, the intensity of flame is adjusted by turning the gas knob, which is controlled by a hybrid synchronous stepper motor. Time is one of the vital elements to ensure a healthy and quality diet. The distinct preparation levels are built with sufficient cooking time. This demands a timer module of the microcontroller. To evade fire accidents due to gas leakage, the automation system accommodates a gas sensor module as presented in Fig. 1. This module is incorporated with an air quality sensor that tracks for any gas leakage. In the event of a gas leakage, the automation system immediately turns OFF the gas knob, meanwhile, alerts the user.

3 Hardware Implementation of the Proposed Gas Stove Automation System

This session presents the hardware implementation of the gas stove automation system that incorporates various modules presented in Sect. 2. The sensors are incorporated into a structure that has the provision to adjust height to match with the vessels of any height. Figure 2 shows the structure of the proposed automation system.

The temperature, humidity and whistle sensors are incorporated in a horizontal plank held in inverted fashion to face the vessel. The gas sensor is positioned near the burner to detect any gas leakages. The gas knob control module is mounted on the knob. This is clearly shown in Fig. 2. Raspberry Pi 3b+ (1 GB, 32 bits) [15] is chosen as the control engine of the proposed model. The controller is coded to initiate the process execution through gas knob control module, start the auto ignition module, fetch the set values of cooking parameters fed by the user, acquisition of current cooking parameters from various modules, determination of surface temperature adopting RFR model.

3.1 Knob Control Model

The gas knob control, to adjust the flame, is achieved with the help of a stepper motor. The hybrid stepper motor (17HD34008—2 phase, 1.8° step angle) has a remarkable holding torque and a low power requirement, with no compromise on the precision of step angle. These characteristics make the motor suitable to perform the knob control. The motor is operated under open-loop control mode. It is important to track the knob position while controlling the gas stove knob. A normally open reed switches are diploid to limit the working angle of the stepper motor. The switches are placed in the flame OFF, HIGH and SIM positions. The positioning of these switches

Fig. 2 Structure of the proposed gas stove automating system
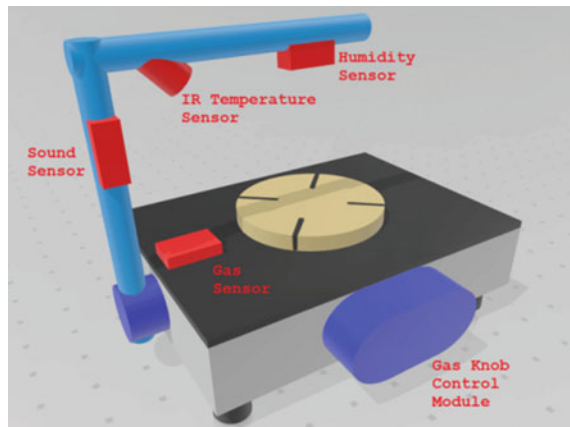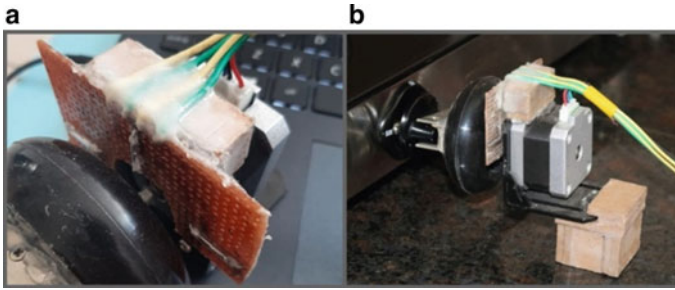
Fig. 3 Knob control module: **a** positioning of reed switches and **b** mounting

and mounting of the knob control module is shown in Fig. 3. The assembly presented in Fig. 3 is interfaced with the step motor and is plugged in to the gas knob. The operation of the unit is supervised by the controller. The knob control under pressure cooking mode is based on the whistle count and humidity rise status. A digital sound sensor (LM393) is employed to perform the dedicated function of whistle count. To avoid un-designed sensor function, the controller accounts for the whistle count only when high decibel sound occurs for at least 5 s.

The pressure release is accompanied with rise in humidity level near the nozzle. Thus a digital humidity sensor (DHT22) is also included in the whistle count module to confirm the occurrence of whistle. This adds robustness to the whistle count module. The controller is coded to count the whistle when the sound sensor activates, while there is a rise in humidity level near the nozzle.

The knob control under boiling mode depends on the surface temperature of the food and the cooking time. The probe or dip type temperature sensor is not preferred and recommended. Hence, a contactless temperature sensor (MLX90614) is deployed in the proposed model. The sensor is placed above the vessel such that it is not affected by the steam during the cooking process. The contactless IR sensor is interfaced with the controller through the I2C communication protocol. However, a significant difference is found in the temperature sensed by the IR sensor and the probe type sensor. The deviation is significant at higher temperatures when the liquid starts to boil. The variation in the contactless sensor reading is due to the increased molecular vibrations of water molecules at higher temperature. It is now required to determine the actual temperature while employing the contactless sensor. This is done using RFR algorithm, one of the supervised machine learning techniques that guarantees to produce accurate results in many applications [16–20]. The model requires supervised training using input set and the target. The contactless sensor temperature and the humidity value are the input set, while, the actual temperature obtained from the probe (DS18B20) is the target. The training process calls for a database that includes input set and target. The humidity and surface temperature values are obtained from humidity sensor, contactless temperature sensor and temperature probe, respectively. The controller is coded to record the corresponding parameters for an interval of 5 s and create a database which is saved as.csv file. Table

Table 1 Sample database for RFR model training

S. No.	Entry no.	Time (s)	Probe temperature (°C)	IR temperature (°C)	Humidity (%)
1	1	7.17	30.17	30.4	63.6
2	22	205.57	40.96	42.35	65.82
3	37	355.81	50.42	49.15	64.54
4	56	525.01	60.06	56.39	63.78
5	77	728.42	70.7	64.97	63.82
6	105	974.85	80.14	72.45	83.3
7	141	1316.21	90.2	79.46	97.68
8	167	1585.73	96.14	85.6	99.9

1 gives the sample database taken from a total of 173 entries recorded in.csv file. The parameters corresponding to columns 5 and 6 form the input set, and column 4 forms the target used to train the RFR model. The dataset is split into training and test data matrix of features and labels, in the ratio of 80:20.

The trained model is then tested with the 20% data. The performance of RFR model is validated using mean absolute error and R^2 values and are found to be 0.936 and 0.996697, respectively. The values confirm the excellent performance of temperature module.

The digital gas sensor (MQ2, Chemiresistor), incorporated in the gas leakage sensor module, monitors the air quality for any trace of gas leakage. The customers consistently prefer automation system that employs a user-friendly GUI.

3.2 GUI Development

The gas automation system incorporates a touch graphical interface for the user to enter cooking parameters such as number of whistles, cooking time and food surface temperature, as well as to monitor the status of the cooking process. The GUI is a webpage-based application, which is developed using JavaScript, HTML5 and CSS3. HTML provides the basic structure of sites, which is modified and enhanced by JavaScript and CSS. The CSS sets the presentation, formatting and layout of the webpage. The JavaScript helps to control the behaviour of different elements. The homepage of the developed webpage is shown in Fig. 4.

The home page shown in Fig. 4 allows the user to choose pre-set cooking for various dishes and instantaneous knob control. The "Dishes" option allows navigation to pre-set dish list page. Each pre-set dish navigates to the process page of the corresponding dish. The process page allows the user to select different cooking parameters that include whistle count, food surface temperature, flame intensity and cooking time. The parameters are selected from the drop down list. The values of these parameters are entered in the control page.
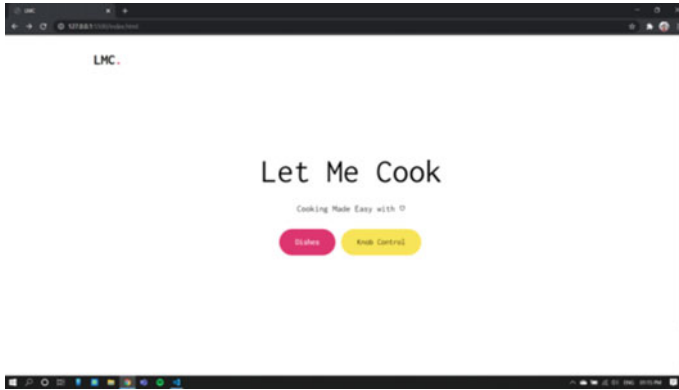
Fig. 4 GUI home page

4 Testing of Hardware Prototype

An effective performance of the proposed automation system is guaranteed through a well programmed microcontroller, interfaced with the sensors presented in Sect. 2. The modules listed in Sect. 2 that includes knob control module, whistle count module and temperature determination module are tested. The modules are then interfaced with the touch screen display, which is installed with web-based application. The developed gas automation system is tested for its performance under pressure cooking mode. Figure 5a shows the experimental setup of the developed gas automation system under pressure cooking mode.

The cooking process under pressure cooker mode is initiated by feeding the cooking parameters which include flame intensity and whistle count. The process page for dish preparation under pressure cooking mode is shown in Fig. 6.

Figure 6 illustrates that post auto ignition; the system maintains maximum flame until the occurrence of the first whistle. The flame is reduced to 20% thereafter. The system then waits for 3 whistles before the termination of the process. The
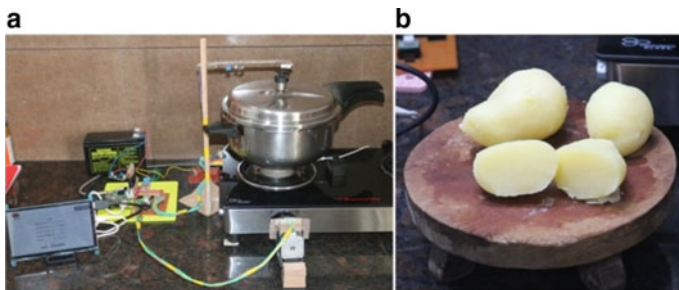
Fig. 5 Pressure cooking mode: **a** experimental setup **b** end product—perfectly cooked potatoes

Fig. 6 Process page—pressure cooking mode

status of each cooking stage is included in the front end. Figure 6 clearly shows that the first process stage of maintaining 100% flame intensity, second process stage of occurrence of first whistle and third process stage of reducing the flame intensity to 10% is executed. Figure 6 also shows the occurrence of first of three whistles. The automation system operating under pressure cooking mode, following the instructions showed in Fig. 6 yields well-cooked potatoes as shown in Fig. 5b.

The developed gas automation system is now tested for its performance under boiling mode. Figure 7a shows the experimental setup of the developed gas automation system under boiling mode.

The cooking process under boiling mode is initiated by entering the cooking parameters which includes flame intensity, temperature and cooking time.

Figure 8 shows the process page for dish preparation under boiling mode. The cooking stages include maintaining 100% flame intensity till the surface temperature
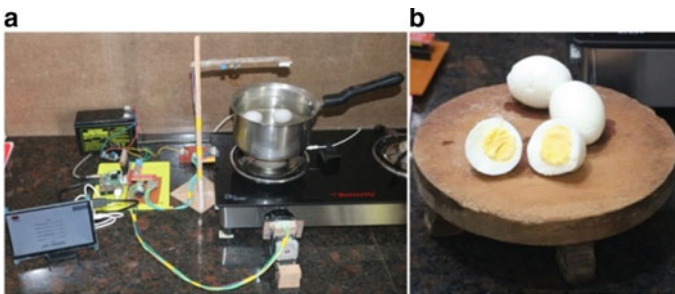
Fig. 7 Boiling mode: **a** experimental setup **b** end product—perfectly boiled eggs

reaches 100 °C. The cooking is then continued at 10% flame intensity for 7 min. Figure 8 illustrates that the dish is currently on 100% flame intensity, while the temperature has reached only 85.05 °C. The automation system operating under boiling mode, following the instructions as shown in Fig. 8 yields hard boiled eggs as shown in Fig. 7b. The automated gas automation system provides a safety feature that checks for any gas leakages. This is done with the help of gas leakage sensor, placed near to the burner. The developed gas automation system is tested for its effective operation during gas leakage.

Figure 9 shows the experimental setup to test the effectiveness of the gas leakage module.

The developed system is powered with the pulse ignition module being intentionally disconnected. This causes the gas knob to rotate in CCW direction to reach the high flame position. With the auto ignition module disconnected from the system, gas leakage occurs. Figure 9 shows the instruction set to bring the flame intensity to 70% and wait till temperature reaches 100 °C, followed by the reduction of flame to 30% and finally waits for 2 min. As the process is initiated with no auto ignition module, the gas sensor detects the leakage in less than 5 s and interrupts the microcontroller to terminate the process immediately. Meanwhile, an alert is displayed indicating the detection of gas leakage to the user. This is clearly displayed in Fig. 9. The developed gas automation system under pressure cooking, boiling and instantaneous control mode has proved to be successful in performing the dedicated cooking task. The results obtained from various experiment setup proves the effective operation of the proposed automated gas control system.

Fig. 8 Process page—boiling mode

Fig. 9 Experimental setup of gas automation module to test for gas leakage

5 Conclusions

The shift in society's food consumption habit from home cooked meals to convenient food is the current world wide accepted trend. The convenience food saves food preparation time, but results in a degraded diet quality. On the other way, the traditional home cooked food requires greater amount of preparation time, while it assures healthier diet. The work involves development of a gas stove automation system that adjusts the flame intensity based on the cooking parameters set by the user. These parameters include whistle count, food surface temperature and cooking time. The knob control module incorporated with a hybrid synchronous stepper motor under open-loop operation is found to be effective in controlling the flame intensity. The user-friendly GUI, developed with the help of HTML, CSS and JavaScript has provided a handy platform for the user to input cooking parameters and monitor the cooking process. The temperature being an inevitable factor during cooing is tracked with the help of contactless sensor. The module employs random forest regression model to log values similar to probe type sensor. The mean absolute error and R^2 values of 0.936 and 0.996697, respectively, confirm the excellent performance of temperature module.

The developed automation system is proved for its effective and efficient performance under pressure cooking and boiling modes. The automation system delivered a well-cooked dish under the two distinct cooking modes. The cooking stages and time are fed following science-based cooking. Thus, the design system consume no extra time or fuel, as in manual cooking, thus saving the fuel. An experiment is also conducted on the developed system while detaining the pulse ignition module inactive. The experiment proves the efficacious operation of the automaton system in protecting against gas leakage by terminating the process and switching off the gas

stove, at the event of gas leakage. The gas leakage protection feature of the system allows the user to be less concerned about the cooking process and engage themselves in other activities. The developed system proves to be a viable cooking assistant to perform Indian culinary which involves pressure and boiling mode. The developed gas stove automation system is considered as a promising aspect for conducting future research works.

References

1. Golait R, Pradhan NC (2006) Changing food consumption pattern in rural india: implication on food and nutrition security. Indian J Agric Econ 61:374–388
2. Frizziero L (2014) A Coffee machine design project through innovative methods: Qfd, value analysis and design for assembly. ARPN J Eng Appl Sci 9:1134–1139
3. Piancastelli L, Frizziero L (2014) Design, study and optimization of a semi automatic pasta cooker for coffee shops and the like. ARPN J Eng Appl Sci 9:2608–2617
4. Solanki AB, Solanki VR, Shah DN (2014) Design and development of automatic fast food machine. Int J Mech Eng Rob Res 3:145–148
5. Sibanda V, Munetsi L, Mpofu K, Murena E, Trimble J (2020) Design of high-tech vending machine. Procedia CIRP 91:678–683
6. Svosve C, Gudukeya L (2020) Design of a smart electric cooking stove. Proc Manufact 43:135–142
7. Castro JDV, Velasquez DFY, Calpa EAU (2019) Towards a low-cost gas stove control for domestic cooking. In: 4th IEEE Colombian conference on automatic control (CCAC), Medellin, Colombia
8. Sastry KRK (2020) Implementation of smart gas controller on a reconfigurable hardware. Int J Sci Technol Res 9:5779–5782
9. Perumal MG, Srivatsan K, Vijayakumar P, Krishnaprasanna R, Rajashree R (2018) IOT based smart kitchen system. Int J Civil Eng Technol 9:737–748
10. Garg S, Chatterjee JM, KumarAgrawal R (2018) Design of a simple gas knob: an application of IoT. In: International conference on research in intelligent and computing in engineering, San Salvador, El Salvador
11. Yan W, Guan E, Ma W, Fu Z, Zhao Y (2010) Automatic cooking robot with a novel feeding system. In: International conference on intelligent robotics and applications, Berlin, Heidelberg, pp 519–529
12. Yalmar A, Parihar M, Kadam V, Kharat K (2015) Implementation of automatic safety gas stove. In: Annual IEEE India conference (INDICON), New Delhi
13. Huq RM, Hoque MA, Chakraborty P, Jafar IB, Rahman KH (2012) Design and implementation of a simple electromechanical system to reduce domestic gas wastage and accidents in South-Asia. In: 6th International conference on sensing technology. Kolkata, India
14. Jahan S, Talukdar S, Islam MM, Azmir MM, Saleque AM (2019) Development of smart cooking stove: harvesting energy from the heat, gas leakage detection and IoT based notification system. In: IEEE International conference on robotics, electrical and signal processing techniques, Bangladesh, pp 117–120
15. Jayapriya M, Yadav S, Ram AR, Sathvik S, Lekshmi RR, Selva Kumar S (2017) Implementation of fuzzy based frequency stabilization control strategy in raspberry pi for a wind powered microgrid. Proc Comput Sci 115:151–158
16. Radhika N (2015) Prediction of tool condition during turning of aluminium/alumina/graphite hybrid metal matrix composites using machine learning approach. J Eng Sci Technol 10:1310–1325

17. Zimmerman N, Presto AA, Kumar SPN, Gu J, Hauryliuk A, Robinson ES, Robinson AL, Subramanian R (2018) A machine learning calibration model using random forests to improve sensor performance for lower-cost air quality monitoring. Atmos Meas Tech 11:291–313
18. Vijai P, Bhagavathi SP (2018) Performance comparison of techniques for water demand forecasting. Proc Comput Sci 143:258–266
19. Shanmuga PS, Abinaya M (2018) Feature selection using random forest technique for the prediction of pest attack in cotton crops. Int J Pure Appl Math 118:2899–2902
20. Wu S, Zhang JM, Wang R (2021) Machine learning method for CPTu based 3D stratification of New Zealand geotechnical database sites. Adv Eng Inf 50:1–19

A Review on the Impact of Cognitive Factors in Introductory Programming

Amanpreet Kaur and Kuljit Kaur Chahal

Abstract Understanding the cognitive factors that contribute to introductory programming students' abilities to learn to program is critical to helping computer educators create better opportunities for students to improve their programming performance. The goal of this research is to explore cognitive factors that have an influence on programming performance in introductory programming courses in particular. The study documents 17 factors from 25 empirical studies that analyzed the influence of these factors on programming performance. Our analysis shows a wide range of cognitive factors studied and interrelated groups of factors studied in literature focused on introductory programming courses. This is a valuable review of information regarding influencing cognitive factors to restructure aspects of future introductory programming course curricula to benefit students' ability to learn to program.

1 Introduction

In a recent study in 2019, Bennedsen and Caspersen [1] found 72% average passing rate in CS1 students in a replication study of their 2007 study where CS1 students' average passing rate was 67%. Students' programming performance is essential in introductory programming courses**.** There are many factors that contribute students' programming performance. Students with prior programming experience found to

A. Kaur (✉) · K. K. Chahal
Department of Computer Science, Guru Nanak Dev University, Amritsar 143005, India
e-mail: amanpreetcs.rsh@gndu.ac.in

K. K. Chahal
e-mail: kuljitchahal.cse@gndu.ac.in

have higher programming score than students without prior programming experience [2]. In another context, male students found to have higher grades and persistence to continue study in CS than female students [3]. In introductory programming education-related literature, work on identifying and assessing factors that contribute to programming performance has been done to understand the behavioral framework behind students' ability to learn to program [4–6]. More specifically, students' cognitive factors like memory, reasoning, and attention influence what they can achieve academically in introductory programming courses. Considering underlying cognitive and psychosocial factors, students' programming performance can be predicted more accurately and reliably. In view of this point, this review paper includes work on students' cognitive abilities, and experiences of learning to program in introductory programming courses. The review listed early identifiable cognitive factors that impact programming performance on novice programmers.

We distinguish between articles about introductory programming and those regarding other parts of computer education when selecting papers. We have limited our scope to the cognitive aspects of students. We excluded work on school-level students and on non-CS students.

There have been reviews with broader scope to include published work related to introductory programming courses [6, 7]. Our review investigates specifically on cognitive factors related to students' introductory programming success. With the identification of these factors, tools can be developed for the early detection of at-risk students in the course, eventually will help in the development of more informed and personalized interventions to foster students' programming learning abilities. Focusing more on interventions that the introductory programming education can adopt to enhance teaching is likely to bring better results.

2 Research Methodology

2.1 Research Questions

This review aims to explore the literature on introductory programming by identifying studies that are of interest to the computing community and the cognitive factors that these publications analyzed and identified. We explored the following research questions:

1. Which cognitive aspects of programming performance have been the focus of researchers in the introductory programming courses field?
2. What tools have been developed to measure cognitive abilities in the context of programming?
3. What developments have been made in the literature regarding the design of future interventions to boost students' cognitive abilities to learn to program?

2.2 Data Collection

For systematically reviewing the literature and answering research questions, an extensive search was conducted for relevant papers using guidelines proposed by [8]. The search phrase is as follows:

(Introductory programming OR CS1) AND (cognitive OR psychological OR psychology OR nomological) AND factor.

The search phrase is applied to the "title, abstract, and keyword" fields of Scopus, IEEE Xplore, and ACM Digital Library. The papers in the publication period till May 2022 were included. In the next stage, research papers were selected by examining the title and abstract of each paper for their relevance to the review objective. We eliminated irrelevant papers which did not include cognitive factors as predictors. The 25 papers were finalized to review.

3 Cognitive Factors

Cognitive factors modulate the learning process and performance of a person. These cognitive factors are listed in Tables 1 and 2. A wide range of cognitive factors has been identified in the literature to represent different cognitive processes of acquiring knowledge, storing it in the memory, and using it to solve real-life problems. The factors have been identified existing literature and other web sources in an attempt to list out all the related cognitive factors to learning. The Cattell–Horn–Carroll Theory of Cognitive Abilities and Bloom's Taxonomy, established theories in the psychology research field, have identified the cognitive factors for learning. The cognitive factors related to learning are given in Table 1 with the definition and source of the factor. The remaining cognitive factors are presented in Table 2 due to their relevance to introductory programming.

4 Cognitive Factors on Predicting Introductory Programming Performance

This section reports research that investigates the influence of students' cognitive abilities in introductory programming courses. The ability to learn to program has a broad definition including cognitive styles, verbal ability, decomposition, etc. There are advances toward more complex evaluations of assessments of students' ability to learn to program, while grades and standard assessments are still the most common ways for assessment. Some recent research has introduced machine learning predictive models to predict students' programming performance using cognitive features in introductory programming [2, 14, 15]. Table 2 lists all cognitive factors used as predictors to programming performance in introductory programming courses.

Table 1 Cognitive factors for learning

Factor	Description	Source
Knowledge	Information recall gained through experience and understanding	Bloom's taxonomy [9]
Comprehension	Ability to understand the meaning, translation, and interpretation of a situation and to state it in one's own words	Bloom's taxonomy [9]
Application	Ability to use knowledge in a new situation. Require a higher level of understanding of learned material	Bloom's taxonomy [9]
Analysis	Understanding of material and identification of relationships between sub-parts of material	Bloom's taxonomy [9]
Synthesis	Ability to creatively put sub-parts together to formulate new structures or patterns	Bloom's taxonomy [9]
Evaluation	Ability to purposefully judge the value of the material on predefined criteria	Bloom's taxonomy [9]
Meta-cognitive	Knowledge, understanding, and control of one's own cognitive processes	[10]
Field-dependent/field-independent	Ability to distinguish embedded parts of an organized visual field as independent fields from a given field	[11]
Convergent/divergent	Ability to find one well-defined solution to given problem/ to develop multiple solutions to given problem to reach the best solution	[11]
Perception	Cognitive process to generate and interpret a mental representation of the observed environment	[12]
Attention	Ability to focus other cognitive processes on a specific situation or material	[12]
Learning and memory	Ability to acquire new knowledge and modify existing to encode, and store in memory	[12]
Language	Ability to use words in a conventional way to communicate with others	[12]
Reasoning and problem-solving	Ability to use deductive, inductive, and abductive reasoning to solve problems	[12]

Table 1 (continued)

Factor	Description	Source
Social cognition	Ability to process and apply knowledge in social contexts and interpersonal relationships	[12]
Crystallized intelligence (Gc)	Domain of one's acquired knowledge and experience	[13]
Fluid intelligence (Gf)	Ability to apply previously acquired knowledge to a given problem	[13]
Short-term memory (Gsm)	Ability to hold information to use in immediate context	[13]
Visual perception (Gv)	Ability to perceive, analyzes, and use simulated mental imagery to visualize patterns in a given problem	[13]
Auditory perception (Ga)	Ability to analyze auditory stimuli patterns	[13]
Long-term retrieval (Glr)	Ability to store and retrieve information for the long term	[13]
Cognitive speediness (Gs)	Ability to perform intelligently and quickly	[13]
Reaction time/decision speed (Gt)	One's speed to react to a given situation or problem	[13]

Factors mentioned in above Table 2 have been used by research works individually or in combinations to predict programming performance in introductory programming courses. The detailed review of cognitive factors related to introductory programming research is as follows:

4.1 Cognitive Style

Earlier, in an attempt to understand to cognitive side of introductory programming students, Werth [16] aimed to predict students' grades at the beginning of the course using cognitive development and cognitive style (field-dependent/field-independent). Also, cognitive style diversity and cognitive intelligence have direct implications related to learning and performance of teams [42]. Another research work found that cognitive style and self-efficacy scores of students in web-based distance education environment had not significant influences on students' grade point average [43].

Table 2 Cognitive factors used in introductory programming performance prediction

Cognitive factor	Description	Papers
Cognitive development and style	Information processing, way of perceiving, and remembering	[16]
Problem-solving skills	Identifying and implementing solutions for problem	[2, 14, 17–21]
Decomposition skills	Breaking down a problem into subproblems	[22]
Study habits	Approaches to learning	[2, 23, 24]
Prior programming experience	Basic knowledge of programming constructs	[2, 14, 21, 25, 26]
Rainfall problem	A programming task	[27]
Performance and engagement patterns	Acquired habits that support occupational performance	[28, 29]
Practice	Rehearsing repeatedly to help learn	[30]
Class attitude	Feeling regarding class	[31–33]
Class experience	Formal and informal learning	[32, 34]
Self-assessment	Student's review of learning outcome	[32]
Programming self-efficacy	Positive/negative perceptions on programming	[35–38]
Persistence	Continuation of effort	[35, 36]
Self-beliefs	Students' belief in their ability	[37]
Implicit intelligence beliefs	Beliefs regarding the nature of intelligence	[15]
Constructive learning theories	Construction of knowledge by practical experience	[39]
Cognitive load	Load working memory can hold at a point of time	[40]
Spatial visualization	Thinking and understanding an object form three dimensions	[33]
Goal orientation	Reasons and patterns for individual's reaction and interpretation of tasks	[41]

4.2 Problem-Solving Skills and Prior Programming Experience

According to prior literature, cognitive tests such as instruments to assess problem-solving are suggested as the important predictors of novice programmers' programming skills [17–19]. Lishinski et al. [19] informed the associations of programming skills hierarchy with generic problem-solving abilities and the positive role of problem-solving skills in most complex programming practices. Similarly, Lishinski et al. [20] modeled the interactions of problem solving, self-efficacy, and personality factors of introductory programming students in the context of learning to program

process. Veerasamy et al. [14] also used problem-solving skills with prior programming experience and in-class formative assessment as predictors to predict students at-risk in programming. Similarly, Ahadi et al. [26] used past programming experience, gender, behavior in lectures and labs, and source code snapshots as predictors to identify high and low performing computer students. Prior programming experience had also been used in explaining students' study habits [2], in predicting programming performance by finding its interrelationship with the frequency of programming of topics revised [21] and in identifying students at-risk of failing where data taken from different sets of introductory programming courses [25].

4.3 Decomposition Skills

In CS1, novice programmers' ability to decompose problems into subproblems improves their programming experience. To decompose a problem, students are expected to break down the problem into subproblems and after solving subproblems independently, reunite to provide solution to original problem. From that perspective, Keen and Mammen [22] used software quality metrics to assess students' decomposition ability progression in the long-term projects assigned to them during their CS1 and compared the metrics to typical stand-alone project metrics.

4.4 Study Habits

Further in the framework of learning difficulties, Gomes et al. [23] found that students' study methods and attitudes toward learning to program strongly correlated to their programming performance and their perceptions of competence during introductory programming courses. Similarly, the learning styles and study habits of distance learners of online programming course elaborate significant relationships with their learning performance [24]. Liao et al. [2] analyzed and compared the study habits of high-performing and low-performing students from the CS1 population.

4.5 Rainfall Problem

To assess learners' ability to transfer knowledge across the exam questions and conceptual understanding of programming constructs, the Rainfall problem was used as an exam question by Lakanen et al. [27] on CS1 students. The Rainfall problem was given as the final written exam which students attempted with a pencil and paper. The authors of the study informed about students' difficulties with knowledge transfer and insufficient conceptual understanding.

4.6 Performance and Engagement Patterns

Advancements in technology reveal challenges of engaging diverse populations in programming education. In view of this point, Khosravi and cooper [28] used learning analytics to investigate groups of students with similarities in their patterns of performance and patterns of in-class and online class engagements and to provide appropriate appraisals to them to master their learning objectives of a programming course. Clusters were identified and analyzed to find the similarities in patterns of performance. Kanaparan et al. [29] also focused on the affects students' engagement can have on their programming performance in introductory programming performance.

4.7 Practice

According to Höök and Eckerd [30], students' ability to perform well in introductory programming course final exam had potential connections to the time amount that students spend practicing programming.

4.8 Class Attitude and Class Experience

Students' class attitudes have a significant impact on content understanding and learning outcomes in programming. In view of this factor, Dorn and Elliott [31] developed and formally validated Computing Attitudes Survey (CAS) to assess attitude development related to gained knowledge and problem-solving skills during CS1. Ishizue et al. [32] used students' objective and subjective class attitudes along with students' *self-assessment* based on *experiences* within class hours and outside class hours. A study by Cutts et al. [33] used study attitudes, abilities to articulate commonplace search strategies, and *spatial visualization* and reasoning to report on the factors that affect the articulation of search strategies eventually affecting programming performance. Lunn et al. [34] focused on students' experiences to predict their computing identity, where the experiences of students defined as recognition, interest, performance beliefs, and sense of belonging to their computing fields. The study has also found the relation of students' experience to performance of underrepresented student groups such as African American and Hispanic/Latinx in computing field.

4.9 Programming Self-efficacy

Brown [35] created and evaluated the collaborative self-modeling technique that used simulated personal experiences to increase programming performance and self-efficacy and *persistence*. Similarly, Kanaparan et al. [36] showed the positive relationship between students' programming self-efficacy beliefs and two behavioral engagement factors: effort and *persistence*. To further enrich cognitive domains of introductory programming, *self-beliefs* about programming aptitude and students' self-perception as programmers have profound influences on programming practice behavior and achievement. Also, students' *self-beliefs* in the introductory programming context include five constructs: programming interest, programming self-concept, debugging self-efficacy, programming aptitude mindset, and programming anxiety [37]. A study by Wiedenbeck et al. [38] showed that programming self-efficacy, software self-efficacy, and computer playfulness influence students' interest in programming which in turn influences their programming performance.

4.10 Implicit Intelligence Beliefs

A recent study by Flanigan et al. [15] claimed that implicit intelligence beliefs, incremental beliefs, and entity beliefs were not potentially influenced programming performance in CS, but as the students' progress through the course, their implicit intelligence beliefs revealed linear changes.

4.11 Constructive Learning Theories

To implement constructive alignment, Cain [39] used portfolio assessment to assist in teaching introductory programming and highlighted the factors such as pragmatic constructive learning theories with an aligned curriculum, formative feedback, and student motivation.

4.12 Cognitive Load

Toma and Vahrenhold [40] measured the cognitive load and emotional reaction of students regarding lab assignments. The author then framed these factors with self-efficacy, psychological traits, and help-seeking behavior of students to understand the influence on introductory programming performance.

4.13 Goal Orientation

Ishizue et al. [41] predicted placement and skill ranking of students pursuing introductory programming course. Psychological factors such as goal orientation, multidimensional competitiveness, self-efficacy, and intrinsic motivation was used as predictors. The study found that subscales of goal orientation (mastery orientation, performance approach and performance avoidance) have significant contribution in prediction process.

5 Results and Discussion

We have exclusively listed the papers that studied cognitive factors and programming performance of students specifically from introductory programming courses. The papers from the broad spectrum of computing education are not listed in the review, so this review does not include all the papers on introductory programming. The cognitive factors included in the studies reviewed are shown in the Venn diagram in Fig. 1. The diagram shows that some studies have used single factors to predict programming performance while others have used combinations of factors for prediction. It can be observed from the diagram that cognitive style, decomposition skills, implicit intelligence beliefs, performance and engagement patterns, Rainfall problem, constructive learning theory, and practice factors have been used individually in the literature by their respective studies to predict programming performance. The diagram also explains that study habits have been measured with prior programming performance, class attitude, and learning style, where class attitude with problem solving skills to find out their combined influences on programming performance in introductory programming courses. Similarly, programming self-efficacy has been studied with persistence, self-belief, and cognitive load for its impact on performance in the literature. The diagram gives a clear view of the independent and interconnected existence of cognitive factors in the existence of introductory programming.

In summary, the understanding of cognitive factors' influence on students' programming performance benefits educators majorly in the following points:

- Students' ability to perform in programming can be measured with more accuracy and reliability.
- Various forms of cognitive ability of students represented by student-generated data can inform teachers about students' future success in learning programming.
- Existence of various relationships between students' programming ability and cognitive abilities such as programming self-efficacy, class attitudes, intelligence beliefs, study habits, and patterns of engagement.
- Based on research, development of new interventions to help increase CS students' programming performance.

Fig. 1 Cognitive factors in introductory programming

6 Future Work

There remains scope for future research to identify significant and non-significant psychological factors in the context of introductory programming courses. The literature in this domain can be further explored by replicating previous studies that proposed validated assessment tools. Different cultures with international domains can be explored to assess the influence of cognitive factors in introductory programming. Further, different combinations of cognitive factors can be explored for their interrelations in the introductory programming context.

References

1. Bennedsen J, Caspersen ME (2019) Failure rates in introductory programming: 12 years later. ACM Inroads 10(2):30–36
2. Liao SN, Shah K, Griswold WG, Porter L (2021) A quantitative analysis of study habits among lower-and higher-performing students in CS1. In: Proceedings of the 26th ACM conference on innovation and technology in computer science education, vol 1. pp 366–372
3. Babes-Vroman M, Juniewicz I, Lucarelli B, Fox N, Nguyen T, Tjang A, Haldeman G, Mehta A, Chokshi R (2017) Exploring gender diversity in CS at a large public R1 research university. In: Proceedings of the 2017 ACM SIGCSE technical symposium on computer science education, pp 51–56
4. Nolan K, Bergin S (2016) The role of anxiety when learning to program: a systematic review of the literature. In: Proceedings of the 16th koli calling international conference on computing education research, pp 61–70
5. Medeiros RP, Ramalho GL, Falcão TP (2018) A systematic literature review on teaching and learning introductory programming in higher education. IEEE Trans Educ 62(2):77–90
6. Luxton-Reilly A, Albluwi I, Becker BA, Giannakos M, Kumar AN, Ott L, Paterson J, Scott MJ, Sheard J, Szabo C (2018) Introductory programming: a systematic literature review. In: Proceedings companion of the 23rd annual ACM conference on innovation and technology in computer science education, pp 55–106
7. Rountree N, Rountree J, Robins A (2002) Predictors of success and failure in a CS1 course. ACM SIGCSE Bull 34(4):121–124
8. Kitchenham B (2004) Procedures for performing systematic reviews. Keele UK Keele Univ 33:1–26
9. Krathwohl DR (2002) A revision of Bloom's taxonomy: an overview. Theory Pract 41(4):212–218
10. Flavell JH (1979) Metacognition and cognitive monitoring: a new area of cognitive–developmental inquiry. Am Psychol 34(10):906
11. Danili E, Reid N (2006) Cognitive factors that can potentially affect pupils' test performance. Chem Educ Res Pract 7(2):64–83
12. Cognitive and metacognitive definition. https://neurotray.com/cognitive-and-metacognitive-definition/
13. Schneider WJ, McGrew KS (2018) The Cattell–Horn–Carroll theory of cognitive abilities
14. Veerasamy AK, Laakso MJ, D'Souza D, Salakoski T (2021) Predictive models as early warning systems: a bayesian classification model to identify at-risk students of programming. In: Intelligent computing 2021, Springer, Cham, pp 174–195
15. Flanigan AE, Peteranetz MS, Shell DF, Soh LK (2022) Shifting beliefs in computer science: change in CS student mindsets. ACM Trans Comput Educ (TOCE) 22(2):1–24
16. Werth LH (1986) Predicting student performance in a beginning computer science class. ACM SIGCSE Bull 18(1):138–143
17. Porter L, Zingaro D, Lister R (2014) Predicting student success using fine grain clicker data. In: Proceedings of the tenth annual conference on International computing education research, pp 51–58
18. Venables A, Tan G, Lister R (2009) A closer look at tracing, explaining and code writing skills in the novice programmer. In: Proceedings of the fifth international workshop on computing education research workshop, pp 117–128
19. Lishinski A, Yadav A, Enbody R, Good J (2016) The influence of problem solving abilities on students' performance on different assessment tasks in CS1. In: Proceedings of the 47th ACM technical symposium on computing science education, pp 329–334
20. Lishinski A (2016) Cognitive, affective, and dispositional components of learning programming. In: Proceedings of the 2016 ACM conference on international computing education research, pp 261–262

21. Sharma R, Shen H (2018) The interplay of factors affecting learning of introductory programming: a comparative study of an Australian and an Indian university. In: 2018 13th International conference on computer science and education (ICCSE), IEEE, pp 1–6
22. Keen A, Mammen K (2015) Program decomposition and complexity in CS1. In: Proceedings of the 46th ACM technical symposium on computer science education. pp 48–53
23. Gomes AJ, Santos AN, Mendes AJ (2012) A study on students' behaviours and attitudes towards learning to program. In: Proceedings of the 17th ACM annual conference on innovation and technology in computer science education, pp 132–137
24. Çakıroğlu Ü (2014) Analyzing the effect of learning styles and study habits of distance learners on learning performances: a case of an introductory programming course. Int Rev Res Open Distrib Learn 15(4):161–185
25. Lagus J, Longi K, Klami A, Hellas A (2018) Transfer-learning methods in programming course outcome prediction. ACM Trans Comput Educ (TOCE) 18(4):1–8
26. Ahadi A, Lister R, Haapala H, Vihavainen A (Aug, 2015) Exploring machine learning methods to automatically identify students in need of assistance. In: Proceedings of the eleventh annual international conference on international computing education research, pp 121–130
27. Lakanen AJ, Lappalainen V, Isomöttönen V (2015) Revisiting rainfall to explore exam questions and performance on cs1. In: Proceedings of the 15th Koli calling conference on computing education research, pp 40–49
28. Khosravi H, Cooper KM (2017) Using learning analytics to investigate patterns of performance and engagement in large classes. In: Proceedings of the 2017 acm sigcse technical symposium on computer science education, pp. 309–314
29. Kanaparan G, Cullen R, Mason D (2013) Self-efficacy and engagement as predictors of student programming performance
30. Höök LJ, Eckerdal A (2015) On the bimodality in an introductory programming course: an analysis of student performance factors. In: 2015 International conference on learning and teaching in computing and engineering 2015 Apr 9, IEEE, pp 79–86
31. Dorn B, Elliott TA (2015) Empirical validation and application of the computing attitudes survey. Comput Sci Educ 25(1):1–36
32. Ishizue R, Sakamoto K, Washizaki H, Fukazawa Y (2013) Student placement and skill ranking predictors for programming classes using class attitude, psychological scales, and code metrics. Res Pract Technol Enhanc Learn 13(1):1–20
33. Cutts Q, Haden P, Sutton K, Box I, Hamer J, Lister R, Tolhurst D, Fincher S, Robins A, Baker B, de Raadt M (2006) The ability to articulate strategy as a predictor of programming skill. In: Conferences in research and practice in information technology series
34. Lunn S, Ross M, Hazari Z, Weiss MA, Georgiopoulos M, Christensen K (2021) How do educational experiences predict computing identity? ACM Trans Comput Educ (TOCE) 22(2):1–28
35. Brown J (2009) Investigating collaborative self-modeling and its impact on introductory programming self-efficacy. In: 2009 IEEE symposium on visual languages and human-centric computing (VL/HCC) 2009 Sep 20, IEEE, pp 244–245
36. Kanaparan G, Cullen R, Mason DD (2017) Self-efficacy and behavioural engagement in introductory programming courses
37. Scott MJ, Ghinea G (2014) Measuring enrichment: the assembly and validation of an instrument to assess student self-beliefs in CS1. In: Proceedings of the tenth annual conference on International computing education research, pp 123–130
38. Wiedenbeck S, Sun X, Chintakovid T (2007) Antecedents to end users' success in learning to program in an introductory programming course. In: IEEE Symposium on visual languages and human-centric computing (VL/HCC 2007) 2007 Sep 23, IEEE, pp 69–72
39. Cain A (2014) Factors influencing student learning in portfolio assessed introductory programming. In: 2014 IEEE International conference on teaching, assessment and learning for engineering (TALE) 2014 Dec 8, pp 55–62
40. Toma L, Vahrenhold J (2018) Self-efficacy, cognitive load, and emotional reactions in collaborative algorithms labs—a case study. In: Proceedings of the 2018 ACM conference on international computing education research 2018 Aug 8, pp 1–10

41. Ishizue R, Sakamoto K, Washizaki H, Fukazawa Y (2018) Student placement and skill ranking predictors for programming classes using class attitude, psychological scales, and code metrics. Res Pract Technol Enhanc Learn 13(1):1–20
42. Aggarwal I, Woolley AW, Chabris CF, Malone TW (2019) The impact of cognitive style diversity on implicit learning in teams. Front Psychol 10:112
43. DeTure M (2004) Cognitive style and self-efficacy: predicting student success in online distance education. Am J Distance Educ 18(1):21–38

Improving Robustness of Two Speed Serial Parallel Booth Multiplier Using Fault Detection Mechanism

Sreelakshmi R. Nair and J. P. Anita

Abstract When it comes to circuit design, digital elements have a pivotal and crucial impact. Input values given to these components can be degraded by internal and external disturbances, it can happen either by virtue of foreign factors, to the lack of efficiency in the sensors, or maybe due to unknown lags in the communication systems. Hence, it is vital when the output responses related to these devices stay as robust when slightest fluctuations occur. Layout of robust components has been reported as primary challenge in the implementation of electronic systems. Ways to improve the robustness of circuits have been dealt with but either by adding huge amount of extra logic, alter the circuit latency, or these are suitable only for such circuits like microprocessors. Also, they suffer limitations by capturing application particular information of the circuit. However, the proposed methodology requires only a small increment in the extra hardware, which only affects the timing characteristics of the circuit in a less considerable manner, and will spontaneously apply to any of the circuits which are arbitrary.

Keywords Activator · Application-specific knowledge · Booth multiplier · Comparator · Equivalence property · Fault detection mechanism · Robustness

1 Introduction

Robustness is a property which defines the ability of a system to respond and produce stable output to its input even in the presence of disturbances [1]. Currently, the technology is progressing so fast. The results of progress are miniaturization, reduction in the consumption of power, and enhancement of delay [2]. These progress effects the performance of systems. In this point, robustness is an important notion to consider. There are methods to increase the robustness and they are summarized as follows:

S. R. Nair · J. P. Anita (✉)

Department of Electronics and Communication Engineering, Amrita School of Engineering, Amrita Vishwa Vidyapeetham, Coimbatore, India
e-mail: jp_anita@cb.amrita.edu

1033

(1) Space-based approaches include extra logic structures to ensure repetition and increase resilience.
(2) Timing-based approaches: In this case, does affect timing of circuit behavior in question to verify FFs output values as correct.
(3) Application-particular approaches: This method purely addresses the circuit's devoted components for a robust solution has been specifically derived [3].

All of these approaches, however, have severe flaws: Space-based approaches add a lot of extra logic to the circuit. Timing-based techniques have the disadvantage of potentially increasing latency and, as a result, limiting the circuit's actual design. Application-specific methods are only useful to designated areas of circuit [4] at the same time they are inapplicable for other processing. Such flaws are addressed here by utilizing application-specific information from the circuits, such as the condition or status while they are performing the function which are similar in nature. This method introduces very less hardware overhead and affect negligibly on the timing [5, 3]. Proposed method of this work is applied in a serial and parallel arithmetic method of SQRT-based Booth multiplier at 8-bit, 16-bit, 32-bit, and 64-bit sizes related with critical pathways increase overall efficiency by decreasing logic sizes and increasing the robustness of multiplications [6]. The improved radix-4 serial Booth multiplier is location agnostic and removes over encoded all-zero or all-one processing. The multiplier is a primitive block that can be readily implemented into prevailing DSPs, CPUs, and GPUs because it takes two operands' values simultaneously. The multiplier improves computing performance significantly for specific input sets [7].

Section 2 gives a review of the literature, including background information and the principles of multiplication including radix-4 Booth algorithm and describes the robustness. Sections 3 and 4 give proposed work and the obtained results. Finally, the contribution is summarized in Sects. 5 and 6 discusses the future scope.

2 Literature Survey

In [3], an approach for improving circuit robustness is done by obtaining application-particular circuit information, such as, connections between FFs. This increases the robustness since we can make use of the partial redundancies that are present in the majority of circuits (even the ones that have been optimized). For accelerating digital filters, artificial neural networks and other machine learning algorithms, [6] presents a two-speed, radix-4, serial–parallel multiplier. Because the multiplier only adds Booth encodings that don't equal zero and bypass over null actions, the time depends regarding the multiplied amount. In order to analyze data dependencies and identify unnecessary logic processes, the logic operations utilized in conventional carry select adders (CSLA) and binary to excess-1 converter-based CSLA are investigated in [7]. In [1], they provide instructions on how to create a robust circuit.

A formal concept of robustness through graceful degradation for differentiated functional safety aspects was put forth in [2]. A minor error by the environment should only produce a minor error by the system when the error is quantified as part of the specification, such as the number of failures. If, given such a specification, a finite environment error only results in a finite system error, they deemed the system to be robust. The cornerstone of the robust design process outlined in [8] is the use of redundant data expression *L* across the full collection of logic units in the system. Tudevdagva et al. [9] discusses a measure theoretical method for assessing the robustness of complex systems. This idea enables a consistent evaluation of the robustness of embedded systems. A comprehensive soft-error-tolerant flip-flop topology that is impervious to both internal flip-flop SEUs and all transient pulses of combinatorial logic was proposed in [10]. Redundancy in time and space as well as the switch characteristics of MOS transistors are used to eliminate any potential soft errors. In [5], they offer a novel method for modeling robustness as well as novel techniques for measuring or observing the resilience of a system. To demonstrate the versatility of the suggested technique, it is tweaked and applied to several contexts. In [4], a PowerPC 603 flip-flop is simulated and tested for resistance to supply voltage and temperature variations. And the outcome shows that PowerPC can handle almost all variations. As a result, it is suitable for industrial use. Paper [11] provides a novel approach for scaling digital circuits, using unpredictable gate delays, to reduce performance variability and increase parametric yield [12–17].

3 Proposed Work

Transient failure is becoming more common in electronic circuits. Area reduction and the influence of external variables such as high-energy radiation, electrical noise, and other environmental disturbances are the main reasons for this [3, 11]. Hence, robustness is an important metric to be considered. There are various ways of methods already used for improving the robustness. But these methods along with enhancing the robustness they are introducing some negative effects like increasing the area overhead, changing the timing behavior [8, 10]. In this work, we offer a new technique that overcomes these limitations by finding application-specific circuit information. In a specific way, it collects information on the relationship between the flip flops, such as when they are of same value [3]. As a same way, proposed method of this work is applied in serial and parallel arithmetic method of SQRT-based Booth multiplier at 8-bit, 16-bit, 32-bit, and 64-bit sizes for improving overall performance and decrease logic sizes with critical paths and improves the robustness of the multiplications [6, 7]. Finally, this work is presented in Verilog HDL and synthesized in Xilinx FPGA and proved all the comparisons in terms of area, delay, and power. The two-speed, radix-4, serial–parallel multiplier is used to speed up digital filters, artificial neural networks, and other machine learning methods. The multiplier is a modified serial–parallel (SP) radix-4 Booth multiplier that only adds nonzero Booth encodings while skipping the zero operations. The modified serial Booth multiplier, which disregards computations

that are encoded as all-zero or all-one, regardless of location. Performance of large DSP applications is usually influenced by the important prime of multiplication. A form of mathematics is binary multiplication. Binary operations only use the bits "0" and "1," which are the only bits used. Using only the integers "0" and "1" instead of the old method's 10 values from 0 to 9 is how binary multiplication differs from conventional multiplication. Two binary values are multiplied using an array of full adders and half adders in a digital combinatorial circuit known as an array multiplier. Using this array, the several goods involved are added virtually simultaneously.

In order to give the most crucial bits of the result time to be produced, sequential bit interface computing adds between words, adds zero values to the incoming stream of input. By adding a coupled to a secondary output is a second shift memory, Booth multiplication produces the present product's smallest values while producing the most significant bits of the earlier product. The computation is effectively skipped, allowing the Booth multiplier to operate at efficiency levels above 100% and complete the multiplication sooner than expected.

The multiplier is created to be a simple block that is readily implemented into existing DSPs, CPUs, and GPUs. It takes both operands' integers concurrently. The multiplier significantly improves computational performance for specific input sets. The multiplier's essential component is that performance is enhanced by both input set sparsity and internal binary representation [9]. The outputs of the radix-4 Booth multiplier are provided as input to the entire Fault detection mechanism (FDM), which results in increment related to robustness of multiplications.

The circuit is divided into two paths by the radix-4 Booth multiplier; each having critical paths, τ and $K\tau$, respectively. This is a K-delay completely combinational design, and the multiplier is clocked at a frequency of $(1/\tau)$.

K, which is utilized in the multiplier's circuitry, is cycles made up of necessary for such addition to finished prior saving the outcome in it product memory. Figure 1 depicts it.

Fig. 1 Two speed serial parallel booth multiplier [6]
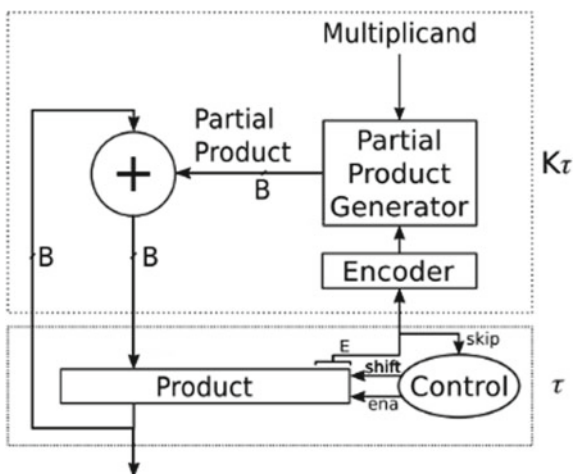
The triple LSBs of the combination are evaluated in encoding. In this multiplication before the addition is done, and a choice is made between two cases.

(1) Null encodings are ignored if $E = 0$, so just the arithmetic right shift function is done. The encoding and partial product are zero and 0x, respectively.
(2) If it is not a zero number, there are double cases can be differentiated by obtaining.

$$\text{skip} = \begin{cases} 1, & \text{if } P[2:0] \in \{000, 111\}0, \\ \text{otherwise.} & \qquad (10) \end{cases}$$

When the encoding is not a zero number (skip $==0$), the circuit has a time line of K count at when skip $= 1$, which leaves and allows to be carried out: right shift and cyclic count collection. This guarantees that the adder and partial product generator have enough propagation time, enabling the product register to adhere to its timing limitations.

Sensor data acquisition in electrical drives, transmission lines, and power management systems is typically used to identify flaws in manufacturing processes. A crucial part of diagnosis is being able to tell the difference between a malfunctioning condition and an usual operational one. How well faults are found in production systems depends on how well false positives are eliminated from obtained data. Fault detection and diagnosis in monitoring and supervision schemes describe high-efficiency and high-quality manufacturing systems.

All application-specific data that was generated using the Equivalence Property (EP), that is, every true divisions P_j with subsequent stage S that qualify EP. The development of an FDM has utilized this knowledge. A fault signal F must be established with every identified EP $(S, P_j)E$, which is given the value "1" when a loop exists the status of S (confirmed through activator), also the FFs in the group P_j will not receive the same value (verified by the comparator). A non-robust sequential circuit is depicted in Fig. 2.

Activator (A)—Signal A should be produced and set to "1" in each EP if and only if the circuit is in state S. (S, P_j). As previously stated, a BDD now contains every valid state S. As a result, each BDD node is modified to follow a MUX gate, allowing for the easy acquisition of relevant logic triggering signal A from the BDD. A's time needs to be changed appropriately as a result. When a system switches between two states, transient faults are believed to emerge. As a result, the states' S are gathered for state sl which results into the checking for those states must perform a state prior to comparing the validations of all flip-flops in P_j, i.e., the activator signal A must create a state prior to the validation to one another, which requires the buffering of signal A for a cycle, which performs by simply increasing an extra FF L-Act1. Although, because L-Act1 is susceptible to transitory errors, robustness can no longer be guaranteed. It leads to the familiarization of the next FF L-Act2, which acquires this signal's magnitude A. The results of the FF, L-Act1 with L-Act2 were compared after a cycle. An error is raised when the quantities do not match (by setting the fault signal F to "1").
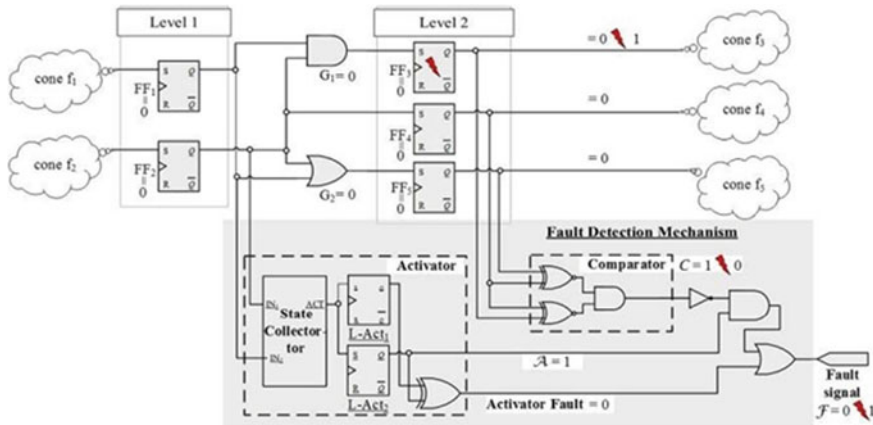
Fig. 2 Circuit of non-robust sequential circuit [3]

Comparator(C)—For each EP (S, P_j), signal C should form and assigned to "1" if and only if the FFs within a division P_j have values as same for both. It is simply accomplished by using XNOR gates to connect the respective FF outputs and comparing the results. When an extra fan-out is familiarized to the specific FF, the timing is somewhat altered, but this is readily mentioned by state-of-the-art power optimization methods and hence is insignificant.

Fault Signal F Generation—The fault signal F is created as a result of the eventual fusion of both signals into a single FDM. F is given the number "1" when a defect is found. The situation is the same (S, P_j), which is defined by $F = C$ A, and thus, a temporary defect can be easily understood in the following application. This occurs when the circuit merely exits a stage S (acquired inside two FFs, L Act1 with L Act2, that trigger this signal A) and each FFs of P1 were not the same for a given EP. The multiplication resilience is increased in terms of space, power, and latency when this FDM is used with 8-bit, 16-bit, 32-bit, and 64-bit data. All comparisons with regard to area, latency, and power were confirmed. The work was presented in Verilog HDL and produced in a Xilinx FPGA.

4 Results and Discussion

This portion portrays about implementation values of two speed serial parallel Booth multiplier using Fault Detection Mechanism. The multiplier is being compared in terms of area, power, and delay for 8-, 16-, 32-, and 64-bit versions.
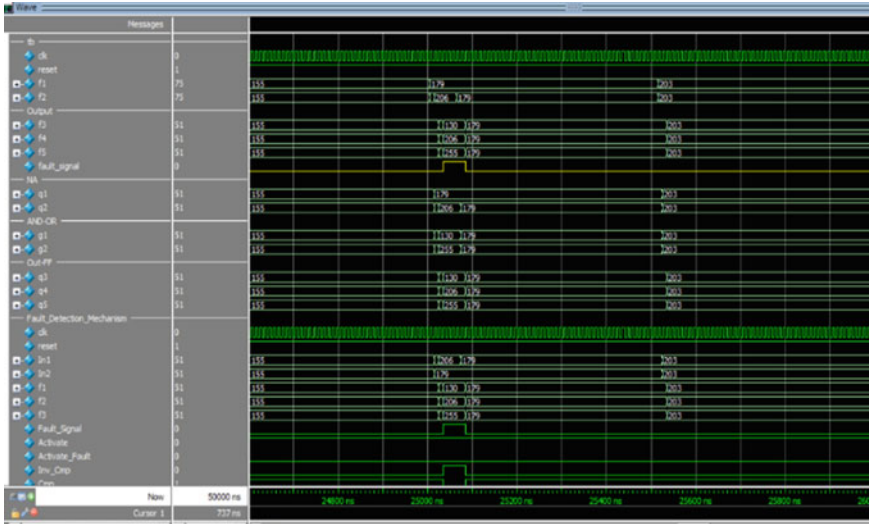
Fig. 3 Waveform simulation of N-bit FDM

4.1 Simulation Results

The waveforms depicted (Figs. 3, 4, 5, 6, and 7) are generated by executing Verilog HDL code in ModelSim-Altera 6.5b (Quartus II9.1) Starter Edition. In Fig. 3, the input $f1$ and $f2$ are given values through the testbench directly. It only shows the simulation result of N-FDM. Figures 4, 5, 6, and 7 are the simulation results for the Booth multiplier with FDM. Robustness is a notion that can be defined based on performance. Here, the input for the proposed FDM is given as the multiplier and multiplicand of radix-4 Booth Multiplier. Giving those input produced accurate outputs and shows that robustness is improved for the multiplications.

Figure 4 shows the simulation result of 8-bit Booth multiplier with FDM. Figure 5 shows the result of 16 bit and Fig. 6 shows the simulation result of 32 bit.

Figure 7 shows the simulation result of 64-bit booth multiplier with the FDM.

4.2 Multiplier Comparisons

By synthesizing on Xilinx FPGA, a two-speed radix-4 Booth multiplier with Fault Detection Mechanism is compared in terms of power, area, and latency. The findings are given in Table 1 as a comparison.

In order to increase overall performance and decrease logic sizes with critical path, the proposed approach of this work is used to the fault detection mechanism in serial and parallel arithmetic methods of SQRT-based Booth multipliers at 8-bit,
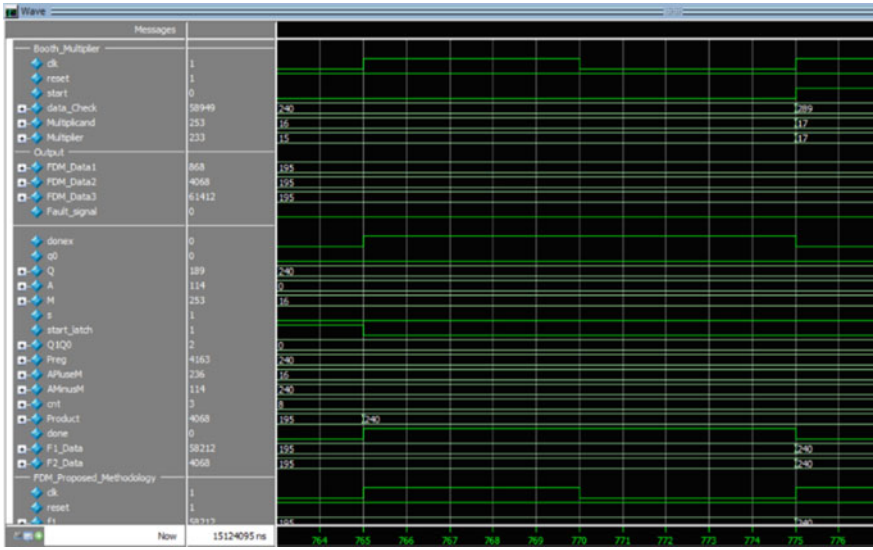
Fig. 4 Waveform simulation of 8-bit FDM
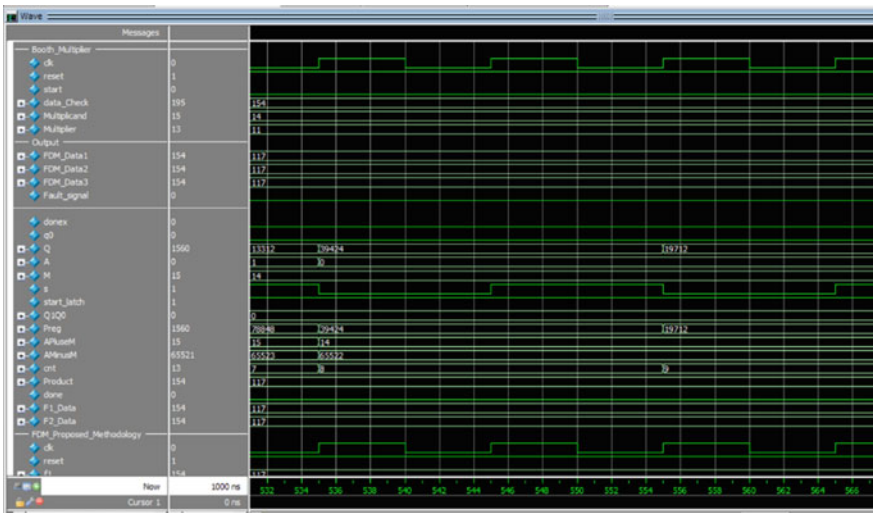
Fig. 5 Wave form simulation of 16-bit FDM

16-bit, 32-bit, and 64-bit sizes. The comparison in terms of area, power, and latency was carried out in Xilinx ISE Design Suit 14.5, and the Verilog HDL code of 8, 16, 32, and 64 bits is verified in ModelSim. It enables the code to be put together and provides an accurate timing analysis with all of the component data, including how much space each takes up in the design.
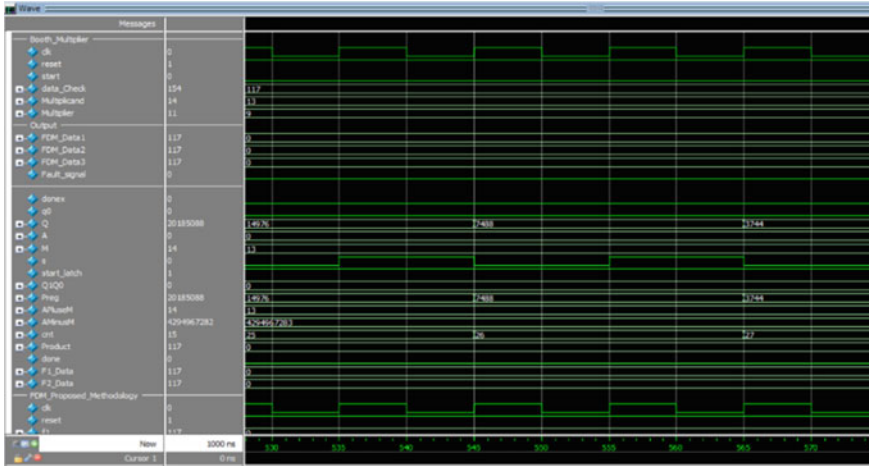
Fig. 6 Waveform simulation of 32-bit FDM
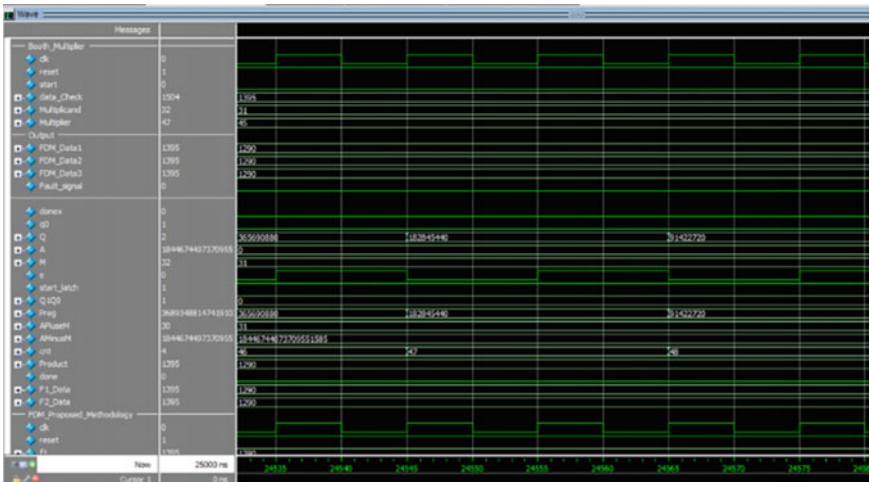
Fig. 7 Waveform simulation of 64-bit FDM

Table 1 and Fig. 8 make it clear that power and area are also growing as a result of the delay's increase in bit size. The elements of area in this case are Slice LUT, Occupied Slice, and Slice Register. The findings indicate that the 8-bit Two Speed Radix-4 booth. The best option is a multiplier because of its greater robustness, which is determined by performance. Area, power, and delay are the factors that influence performance and are therefore used to gauge resilience.

Table 1 Comparisons of calculating application particular knowledge for improving robustness of two speed radix-4 booth multiplier

Parameters	Results obtained for improving robustness of two speed radix-4 booth multiplier			
	8-bit	16-bit	32-bit	64-bit
Slice register	192	344	648	1256
Slice LUT	203	377	624	1167
Occupied slice	106	243	465	905
IOB	85	165	325	645
Delay (ns)	3.291	3.923	6.211	11.953
Power (W)	3.532	3.542	3.601	3.626
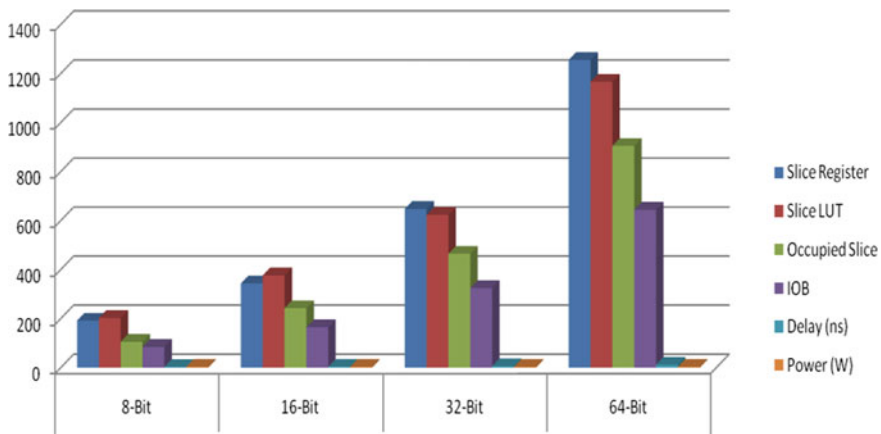
Fig. 8 Two speed radix-4 booth multiplier for 8, 16, 32, and 64 bits

5 Conclusion

In this work, a methodology is proposed for improving robustness by extracting application specific knowledge. The circuit has a lot of unnecessary logic added, which is one of the major problems with the current approaches. Timing-based approaches have the drawback of potentially increasing latency, which limits the actual design of the circuit. Application-specific techniques are not applicable to other processing and are only beneficial for certain circuit regions. In order to strengthen the resilience of the multiplications and improve overall performance, the proposed method is applied to serial and parallel arithmetic methods of SQRT-based Booth multipliers at 8-bit, 16-bit, 32-bit, and 64-bit sizes. Area, power, and delay characteristics of the FDM Booth multipliers are compared. The resulting technology can be applied automatically to any circuit and only slightly increases the amount of additional hardware required. It also has a negligible effect on the timing behavior of the circuit.

6 Future Scope

Robustness is an important notion to be considered in the circuit design. The proposed technique will be applied to huge datasets in the future (industrial-sized) circuits. Here, robustness of multiplication is improved and analyzed in terms of area, power, and delay. As bit size increases, the area, power, and delay also increases.

So, this can be overcome and thereby improving the quality of the circuit.

References

1. Doyen L, Henzinger TA, Legay A, Nickovic D (2010) Robustness of sequential circuits. In: Proceedings international conference on application of concurrency to system design ACSD, vol 77(no 4). https://doi.org/10.1109/ACSD.2010.26
2. Bloem R, Greimel K, Henzinger TA, Jobstmann B (2009) Synthesizing robust systems. Formal Methods Comput Aided Des 85(2). https://doi.org/10.1109/FMCAD.2009.5351139
3. Huhn S, Frehse S, Wille R, Drechsler R (2019) Determining application-specific knowledge for improving robustness of sequential circuits. In: IEEE Transactions on very large scale integration (VLSI) systems, vol 27(no 4). https://doi.org/10.1109/TVLSI.2018.2890601
4. Vinoth R, Jennifer P, Srinivasn R (2016) A robust flip-flop for industrial applications. ICTACT J Microelectr
5. Barke M et al. (2012) Robustness validation of integrated circuits and systems. In: 2012 4th Asia symposium on quality electronic design (ASQED), vol 55(no 4). https://doi.org/10.1109/ACQED.2012.6320491.27
6. Moss DJM, Boland D, Leong PHW (2019) A two-speed, radix-4, serial– parallel multiplier. In: IEEE transactions on very large scale integration (VLSI) systems, vol 27(no 5). https://doi.org/10.1109/TVLSI.2018.2883645
7. Mohanty BK, Patel SK (2014) Area–delay–power efficient carry-select adder. In: IEEE transactions on circuits and systems II: express briefs, vol 61(no 6). https://doi.org/10.1109/TCSII.2014.2319695
8. Garcia-Leyva L, Rivera-Dueñas J, Calomarde A, Moll F, Rubio A (2016) Robust sequential circuits design technique for low voltage and high noise scenarios. In: MATEC Web of Conferences, vol 44(no 3). https://doi.org/10.1051/matecconf/20164202003
9. Tudevdagva U, Heller A, Hardt W (2013) A model for robustness evaluation of embedded systems, vol 92(no 5). https://doi.org/10.1109/IFOST.2013.6616885
10. Chen M, Orailoglu A (2007) Improving circuit robustness with cost-effective soft-error-tolerant sequential elements. In: 16th Asian test symposium, vol 77(no 12). https://doi.org/10.1109/ATS.2007.51
11. Patil D, Yun S, Kim SJ, Cheung A, Horowitz M, Boyd S (2005) A new method for design of robust digital circuits. In: Proceedings International Symposiumon Quality Electronic Design (ISQED), vol 88(no.2). https://doi.org/10.21917/ijme.2016.0032
12. Prabhu E, Mangalam H, Karthick S (2016) Design of area and power efficient Radix-4 DIT FFT butterfly unit using floating point fused arithmetic. J Cent South Univ 23:1669–1681
13. Balakumaran R, Prabhu E (2016) Design of high speed multiplier using modified booth algorithm with hybrid carry look-ahead adder. In: International conference on circuit, power and computing technologies, pp 1–7
14. Sriram S, Simran K, Vinayakumar R, Akarsh S, Soman KP (2019) Towards evaluating the robustness of deep intrusion detection models in adversarial environment. Commun Comput Inf Sci 1208

15. Hemamithra KG, Lakshmi Priya S, Lakshmirajan K, Mohanraj R, Ramesh SR (2018) FPGA Implementation of power efficient approximate multipliers. In: International conference on recent trends in electronics, information and communication technology, pp 1281–1285
16. Shetty N (2021) A comprehensive review on power efficient fault tolerance models in high performance computation systems. J Soft Comput Paradigm 3(3):135–148
17. Bindhu V, Ranganathan G (2021) Effective automatic fault detection in transmission lines by hybrid model of authorization and distance calculation through impedance variation. J Electr 3(01):36–48

Development of a Categorized Alert Management Tool for the City of Madrid

Antonio Sarasa-Cabezuelo and **José Luis Sierra-Rodriguez**

Abstract In recent decades, there have been several key events in the field of access to information such as the emergence of open and linked data repositories, the expansion of social networks and the development of mobile and web technologies. In this way, the necessary infrastructure has been created to be able to access and exploit the information immediately and in real time. In this sense, the use of applications that implement value-added services processing information from repositories and networks has been extended. This article describes a system that combines a mobile application and a web application that exploit information retrieved from Twitter, the open data repository of the Madrid City Council and an online newspaper, with the aim of implementing an alert generation service categorized in real time on events that have occurred in the city of Madrid.

Keywords Android app · Web application · Twitter · Social networks · Open data repository · Alert generation system

1 Introduction

In recent decades, technological advances have facilitated access to information. In this sense, there are several elements that have been key. First, a large number of companies and institutions have published data and information about their activities in digital repositories in the form of open data [1] or linked [2] with the aim that anyone can analyze and exploit this information with different purposes. Likewise, the use of social networks of different types [3] has been massively extended, which has provided a means to disseminate information very quickly and in real time [4, 5]. And on the other hand, mobile and web technologies have been developed [6],

A. Sarasa-Cabezuelo (✉) · J. L. Sierra-Rodriguez
Universidad Complutense de Madrid, 28040 Madrid, Spain
e-mail: asarasa@ucm.es

J. L. Sierra-Rodriguez
e-mail: jlsierra@ucm.es

facilitating the creation of applications that allow easy access to information. In particular, many of these applications implement value-added services [7], which use data and information that they capture from repositories and other applications and exploit them to implement other uses than those they originally had [8]. In this way, the user has become accustomed to having applications that provide information and services in real time [9]. In particular, there is a demand for services that offer information in real time about events that occur and may affect us [10, 11]. For example, in recent years, there have been several drops in global services by Google, Facebook and other companies, and those affected went in masse to social networks such as Twitter to find out what was happening [9, 12]. This situation is repeated at the local level in other types of events [13] such as when the network or mobile connection services of telecommunications companies stop working [14].

This article describes a system that offers a real-time service for generating alerts on events that occur in the city of Madrid. Madrid is a large city with a large number of inhabitants and the number of events of different types that occur every day and affect the life of the citizen is enormous. There are several applications that use geolocation and real-time notification about the waiting time for buses and metro in the city of Madrid, such as "Mi Transporte Madrid-Metro-Bus-Cercanías" [15] or "Madrid Metro Cercanias Bus" [16]. Google Maps [17] provides real-time information on events that affect roads and communication routes. There are also applications that generate news alerts through user notifications such as "Feedly" [18], "Appy Geek" [19] or "Reddit" [20]. On the other hand, among the Android apps there are applications such as "Citizen. Safety and Awareness" [21] that generates alerts about crimes committed in New York City in real time (the application is in direct contact with the New York police, so that when one of its agents receives a warning from the central, Citizen collects the data and transmits it to its users), the SocialDrive application [22] that allows creating a community of drivers with the purpose of sharing information about traffic in real time, or the Madrid Urban application [23] that detects the geolocation of a person and offers an interactive map with all the interesting places that are around and when clicking on one, detailed information about it is displayed.

However, there is no tool that centralizes all the information so that a citizen can consult in real time the events that have occurred in a certain area of Madrid. On the contrary, the information is dispersed in different sources such as online newspapers, web pages, or information published by users on social networks. In this way, access to information is not effective, fast or consistent. In this sense, the objective of the developed system is to provide access to information on events that occur in a comprehensive, intuitive, visual, and real-time manner. To do this, the system acts as an aggregator that retrieves data from multiple information sources, consolidates the information extracted and synthesizes event alerts. The alerts generated are visually displayed on a map of Madrid, in which it is possible to interact to perform searches with different filters based on the district or the category of the alert, obtain statistics on the alerts produced or simply access the specific information of an event. To facilitate its use, a web version and a mobile version have been implemented that are related through a common database.

The structure of the paper is as follows: Sect. 2 describes the architecture and data model of the application. Section 3 describes the functionality of the web application and the implemented Android app. And finally, Sect. 4 proposes the conclusions and a set of lines of future work.

2 Architecture

2.1 Architecture

The system has been designed using a client–server architecture so that there are two types of clients: a web application and an Android-type mobile application. The server implements the services invoked from the clients and manages a MongoDB-type NoSQL database that stores all the data that is collected through the data collector.

A schematic of the system architecture is shown in Fig. 1. The clients share the same database so that any update of the stored information maintains consistency and also serves as a communication element between both applications. In the case of the Android application, a service API has been implemented that acts as an intermediary with the database, and is responsible for sending and receiving the corresponding data according to the requests of the Android user. On the other hand, the web application is used by the user to consult the alerts generated about the community of Madrid, the statistics obtained from the alerts, or the definition of new types of alerts for the application. All the information displayed on the web is obtained from the database, in which all the data retrieved by a component that acts as a data collector is stored.
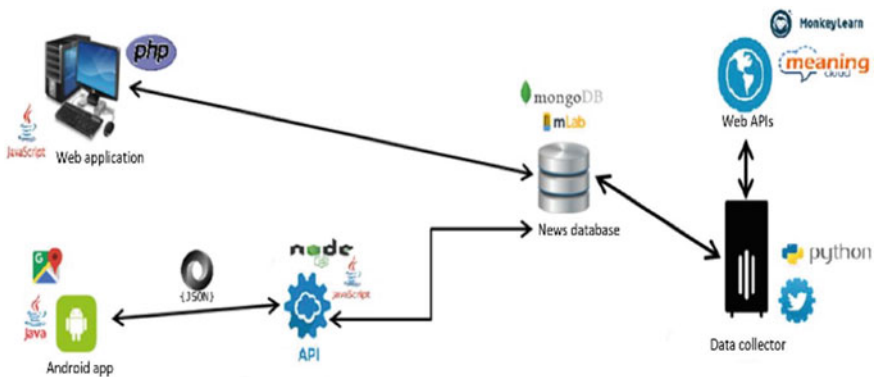
Fig. 1 Application architecture

2.2 Data Model

Information persistence has been implemented using a MongoDB-type documentary NoSQL database. For this, a database called "News" has been created that contains five collections:

- The alerts collection stores all the alerts collected from the social network Twitter and the "Madridiario" newspaper, as well as the alerts inserted by users from the web and mobile application.
- The statistics collection stores all the alerts that will be used to calculate general statistics and statistics by city districts. They are obtained from both the social network Twitter and the newspaper "Madridiario".
- The estDetenidos collection stores the statistics related to the arrests made by the Madrid Municipal Police in each district of Madrid.
- The estAccidentes collection stores statistics related to accidents (with and without injuries) in each district of Madrid.
- The estSeguridad collection stores statistics related to citizen security in each district of Madrid.

The system has a REST API that allows the Android application to interact with the database. The functionality that the API implements is the following:

- Alerts by district. Make a GET request that has to receive as a parameter the name of the district from which you want to search for alerts.
- Alerts by district and category. Make a GET request that receives by parameter the district or districts and the categories of the alerts that you want to collect.
- Number of alerts by district and/or categories. Make a GET request to obtain the number of alerts corresponding to the indicated categories in a district.
- Add alerts. Make a POST request and given the data of a user, the description of the alert, the category and the district, a new alert is added to the database.

The information stored in the database is drawn from several different data sources:

- The online newspaper Madridiario [24]. The news is retrieved from the events section of the newspaper, and its title, its text entry, its date, its URL and the district to which it belongs are taken from each event. This information is then stored in the database. To implement this functionality, the BeautifulSoup Python library has been used, which allows web scraping. In addition, each event must be categorized, and for this a classifier has been implemented that categorizes the news based on certain keywords that may appear in its title. In the event that the classifier assigns the category "Nothing," then that event is discarded. Finally, a Cron-type program has been developed that is responsible for executing the data recovery program every 5 min, verifying that the recovered events are within the current hour interval and 5 min earlier. In this way, if and only if it is within this range, it is inserted into the database and avoids storing repeated events.

- Twitter. The data generated by the social network Twitter is analyzed and collected from a program that is in continuous operation. Tweets generated by a set of accounts that publish events and news from Madrid are collected, and which are specified in the collection program. Every time a tweet is retrieved, the program applies a filter to avoid having unnecessary content, which consists of discarding retweets, a reply to another user or a mention by another user. If the tweet has passed the previous filter, it is assigned a category through the aforementioned classifier. If the assigned category is "Nothing," the tweet is discarded. Finally, a district is assigned by means of a zone classifier and the corresponding collections of the database are updated with the information of the new tweet, the category and district obtained. If no district is assigned to the tweet then it is discarded. To implement the collection program, the Twitter Tweepy API [24] has been used. In order to be able to obtain alerts in real time, the program is running continuously, and for this a Cron program has been implemented in charge of executing the Twitter data collector.
- Municipal Police of Madrid [25]. The Madrid City Council provides monthly information on the activity of the Municipal Police [26] for the previous month by means of an Excel document obtained from an open data repository. From the document is extracted to store in the database: statistics of detainees by district, accidents by district and related to safety by district. To execute this data collector, a Cron program has been implemented that is in charge of executing it on the 25th of each month.

Finally, two classifiers have been implemented:

- A classifier to get the district to which a Twitter alert belongs based on the text. For this, we have used a classifier called "MonkeyLearn" [27] that is in the cloud and is capable of analyzing text. In the classifier, a module called Districts ("Distritos") has been defined that contains the 21 districts of Madrid and an additional one called "General" (for alerts that are not only from a specific district).
- A classifier to obtain the categories to which an alert belongs. For this, a classifier called "MeaningCloud" has been used, which offers a web service to analyze text. Two models have been defined in the classifier: "news" and "tweets." Although both models use the same categories, however, the first is in charge of categorizing the alerts that come from the Madridiario newspaper while the second is in charge of categorizing those coming from Twitter. Eight categories have been defined: pollution, crime, disasters and accidents, events, terrorism, public transport, traffic, and nothing. In each model, categories are defined by sets of keywords that help classify each alert.

3 Functionality

Next, the functionalities of the Android app and the web application of the developed system will be described.

3.1 Web Application

The main functionality of the web application is to display in real-time information about the alerts generated in the districts of Madrid.

The main screen of the application is made up of a side menu on the left with various functionalities and an interactive map that allows to view alerts for Madrid's districts that have been generated in the last hours. Each district in which there is at least one alert is marked by an icon. At the top there is a button called "Update map" ("Actualizar mapa") (Fig. 2) which, when pressed, updates the alerts on the map. It is possible to move around the map using the mouse, as well as to select a specific district marker to view the information it contains. When a district marker is selected, the name of the district appears, the number of alerts it contains, and a blue button called "View alerts" ("Ver alertas") (Fig. 2) that shows the alerts for that district in descending order and in detail. If it is wanted to read the news in detail, see a photo, etc., then it must simply click on the title that appears in blue (it is a link to the news) and a new tab will automatically open with the page corresponding to news.

Likewise, at the bottom of the map there is a drop-down with all the districts and a set of icons that represent all the categories used to classify alerts. If it is selected a district and a set of categories in the drop-down menu, and click on the pink "Search" button, then the alerts for the district and selected categories will be displayed and sorted in descending order by their current status. The list of alerts can be updated using the blue "Update alerts" button that appears next to the district name. The update is carried out taking into account the selection of district and categories made.

Through the side menu the user can access four options (Fig. 3):

- Alerts. It contains a drop-down menu where it is selected a district, and by clicking on the "Show" button, the alerts for the selected district are listed in descending
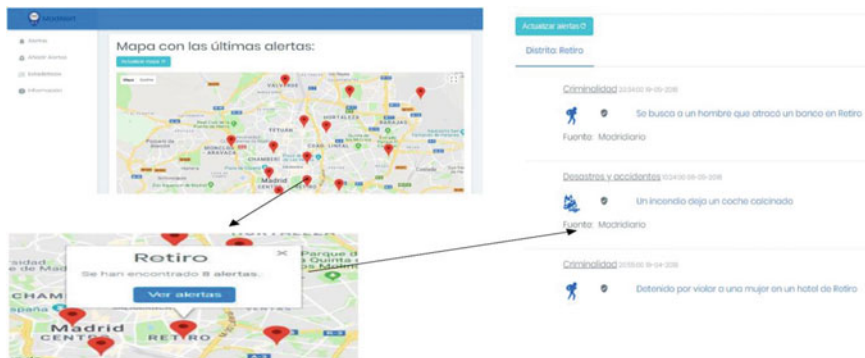
Fig. 2 Pipeline to search for alerts on the web application map

Fig. 3 Web application side menu options

order. The list of alerts can be updated using the blue "Update alerts" button that appears next to the district name.

- Add alerts. It allows adding a new alert by filling in the fields of a form (name, email, category, district, and content of the alarm) and clicking on the "Add alert" button.

- Statistics. It allows access to three types of statistics available:
  1. General statistics by categories. It contains a drop-down menu where it must select a category and then click on the "Search" button. Alert statistics for the selected category will be displayed. First the month before the current one and then the month before this one.
  2. Statistics by districts. It contains a drop-down menu where it must select a district and click on the "Show" button. Alert statistics for the selected district will be displayed. First the month before the current one and then the month before this one.
  3. Statistics of the data obtained from the Municipal Police of Madrid. It contains a drop-down menu where it must select a type of statistics and click on the "Show" button. The statistics of the selected type will then be displayed.
- Information. It contains a menu where it can be accessed information about support (terms and conditions, privacy policy …).

3.2 App Android

The main functionality of the Android application is to inform the user in real time of the alerts that occur in the Madrid districts, according to the user's preferences.

When the app is loaded, three tabs are displayed: "Alerts," "Map," and "Districts." By default, the application is located in the Alerts tab, where the alerts are displayed according to the configuration that the user has established. If there is no configuration or it is the first time the application is running, then a message is displayed to configure the application.

To configure the application (Fig. 4), access the menu (icon with three stripes in the upper left corner), which contains the following options: user configuration, contact, support, about us, and faq. Next, it is chosen the "configuration" option from the menu that allows to determine which alerts are shown in the "Alerts" tab and in the "Map" tab. To do this, the user sets the search radius kilometers (the distance is counted from the point of origin, and the radius must be between 0 and 25 km). Then, a list appears to select the categories of alerts (it is possible to select as many categories as you like). In particular, the "All" option represents that it is required to retrieve alerts from all the categories there are.

Finally, there is a switch that establishes whether the location is active or not. If the location is enabled the point of origin will be the exact location of the user and if it is disabled the point of origin will be the central marker of the district that the user can choose from a drop-down list that appears. In particular, the "All" ("Todos") option appears in the drop-down menu, which indicates that information is required for the 21 existing districts, and the "General" ("General") option that represents all the alerts that do not have a defined district.
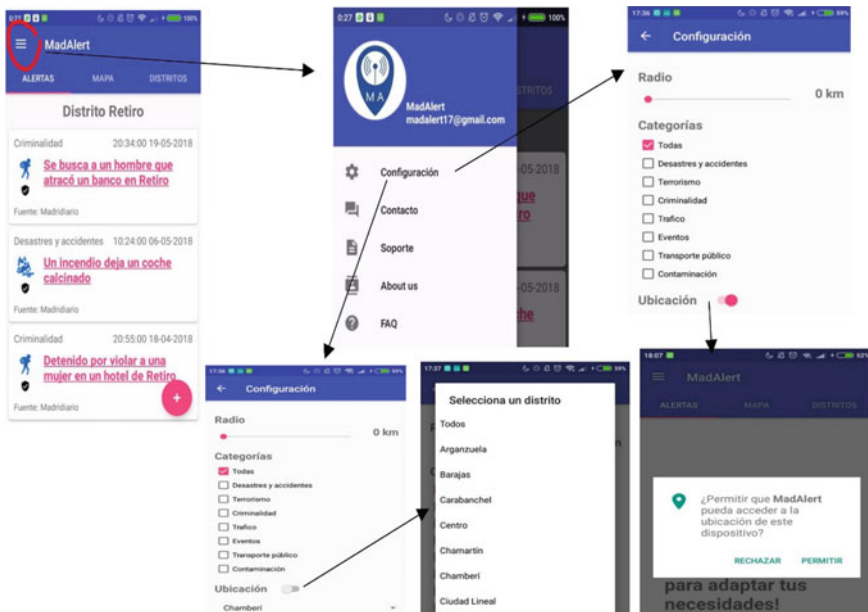
Fig. 4 Pipeline to configure the Android app

Fig. 5 **a** Alerts retrieved from a district, **b** message when there are no alerts

When all the information fields are filled in, they are automatically saved without the need to press any save button. In this way, when returning to the "ALERTS" ("Alertas") tab, the alerts corresponding to the established configuration appear. Next, the different configuration cases will be discussed:

- Radius 0 kms. In this case, only the alerts of the district corresponding to the user's location or the one chosen by the user in the configuration are shown (Fig. 5a). The category to which the alert belongs, the date, the source and if it is verified or not appears.
- Radius greater than 0 km. In this case, the alerts of the districts that are part of the circumference of the radius chosen by the user are searched. For this, it is taken into account that the center is the current location or the chosen district.

In the event that no alert is found using the corresponding configuration, a message will be displayed indicating it (Fig. 5b). To update the alerts tab, you can perform the gesture of moving the window down.

Finally, in this tab you can add an alert in real time by pressing the "+" button. In this way, a form is displayed in which the data must be completed to characterize the alert to be searched. Next, click on "Add" ("Añadir") (if any data is not complete, it is indicated by a small circle and if you click on it, then it informs about what remains to be added). For the alert to be added, the chosen category has to be consistent with the alert category. Otherwise, an error message will be displayed and the alert is not added.

The "MAP" ("MAPA") tab shows a map of the community of Madrid with alert markers corresponding to the districts of Madrid according to the configuration defined by the user. The marker appears when there are alerts in that district. When
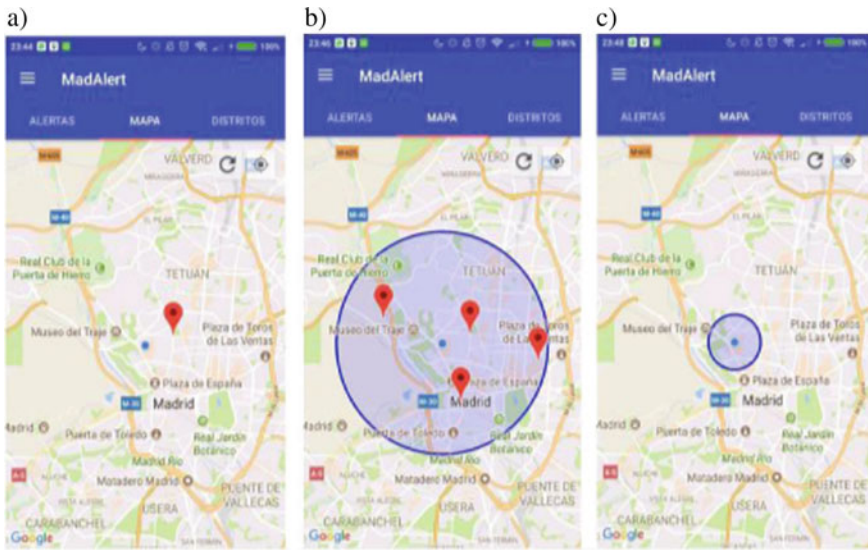
Fig. 6 **a** Search radius 0, **b** search radius greater than 0, and **c** search by district

clicking on a marker, it appears which district it is and the number of alerts with the specified configuration. The map view will be different according to the configuration established by the user:

- Radius 0 km and location activated (Fig. 6a). In this case, a blue point is displayed that corresponds to the current location of the user and a marker that corresponds to that district will be displayed whenever there are alerts according to the established configuration.
- Radius greater than 0 km and location activated (Fig. 6b). In this case, a circle appears on the map with the radius chosen by the user and within it the markers of the contained districts that have alerts. The center of this circle corresponds to the blue point that represents the user's location.
- Radius 0 km and district selection (Fig. 6c). In this case, when the user has the location deactivated, then the district from which he wants to obtain the alerts must be selected. In this way, the alerts for that district are searched and only the marker corresponding to the district will appear on the map if there are alerts. Otherwise, no marker will appear on the map.
- Radius greater than 0 km and district selection. In this case, a circle appears on the map with the radius chosen by the user and within it the markers of the contained districts that have alerts. The center of this circumference corresponds to the center point of the district chosen by the user.

If it is necessary to view the alerts of a district from the map, just click on the corresponding marker (the red icon), and then a window will open displaying the

name of the district and the number of alerts out there. And if it must be view them, just click on the corresponding alert.

To update the map, you can click on the button with the refresh icon in the upper right corner.

In the "DISTRICTS" ("Distritos") tab, a screen called "Select a district" ("Seleccionar distrito") is displayed with a drop-down to select a district and buttons to mark one or more categories. From this configuration, alerts will be searched if you click on the Show ("Mostrar") button. The district view will be different depending on whether or not there are alerts with those specifications:

- If no category is selected then a message is displayed indicating that at least one category must be selected.
- If a different district is selected from the "All" ("Todos") option and the "All" ("Todos") category then all alerts from the district are displayed regardless of the category.
- If a different district is selected from the option "All" ("Todos") and several categories then the alerts of the district with the selected categories are displayed. If there are no alerts for one of the categories but there are for others, then the ones you have are displayed.
- If the district "All" ("Todos") and any category is selected then the alerts of all the districts that have alerts with the selected categories are displayed. Each alert shows the district to which they belong.

In either case, if the district does not have alerts with the selected categories, then a message is displayed stating that there is nothing to display with that combination.

To update the district tab, it is able to perform the gesture of moving the window down when the alerts are displayed.

4 Conclusions and Future Work

This article has described a system that combines a web application and an Android app that exploit the information retrieved from the social network Twitter, the open data repository of the Madrid City Council and the online newspaper Madridiario. The system implements an added value service that consists of generating categorized alerts in real time of events that occur in the city of Madrid. In this way, the system becomes a tool that channels the information from the three indicated information sources to synthesize the consolidated information represented by the alerts. Some of the advantages of the system are immediate and real-time access to information on events that have occurred in Madrid, the functionalities offered by the system to access and manage alerts through different views, criteria and filters, the graphic representation of the alerts on a map showing the alerts distributed by districts as well as the possibility of accessing the information related to each displayed alert. Disadvantages include the dependence of the system on the information sources used to generate the alerts, the geographic limitation of the system since only alerts are

generated from the city of Madrid, or the number of information sources used to generate the alerts that it would be interesting to use more.

On the other hand, the current version of the system can be improved in various ways, having the following lines of future work:

- Expansion of the number of information sources used to process and generate alerts.
- Extend the functionality of the system to offer the service in other cities.
- Implement the possibility of offering the user interface in different languages in order to broaden the target audience.
- Offer a notification service so that the user can receive notifications about the publication of new alerts according to a configuration specified by the user.
- Develop a new functionality that allows generating statistical data about the use of the application or the most visited alerts and categories. Likewise, the possibility of downloading the statistics in formats such as pdf, json, and others could be offered.
- Implement a social network system between users, so that alerts found by users can be shared.
- Develop a version for IOs of the application in such a way as to add a new way of accessing information.
- Exploit the historical information about the alerts that have been generated to create a predictive system of events using machine learning algorithms and/or artificial intelligence.

References

1. Attard J, Orlandi F, Scerri S, Auer S (2015) A systematic review of open government data initiatives. Gov Inf Q 32(4):399–418
2. Haller A, Fernández JD, Kamdar MR, Polleres A (2020) What are links in linked open data? a characterization and evaluation of links between knowledge graphs on the Web. J Data Inf Qual 12(2):1–34
3. Althoff T, Jindal P, Leskovec J (2017) Online actions with offline impact: How online social networks influence online and offline user behavior. In: Proceedings of the tenth ACM international conference on web search and data mining, pp 537–546
4. Mora-Cantallops M, Sánchez-Alonso S, Visvizi A (2019) The influence of external political events on social networks: the case of the Brexit Twitter Network. J Ambient Intell Humanized Comput 1–13
5. Khan A, Bibi F, Dilshad M, Ahmed S, Ullah Z, Ali H (2018) Accident detection and smart rescue system using android smartphone with real-time location tracking. Int J Adv Comput Sci Appl 9(6):341–355
6. King DL (2021) The mobile revolution. Libr Technol Rep 57(2):5
7. Sarasa-Cabezuelo A (2021) Creation of value-added services by retrieving information from linked and open data portals. In: Advanced concepts, methods, and applications in semantic computing, IGI Global, pp 147–165
8. Sarasa-Cabezuelo A (2019) Exploitation of open data repositories for the creation of value-added services. In: Proceedings of the international symposium on distributed computing and artificial intelligence, Springer, Cham, pp 134–141

9. Mihunov VV, Lam NS, Zou L, Wang Z, Wang K (2020) Use of Twitter in disaster rescue: lessons learned from Hurricane Harvey. Int J Digit Earth 13(12):1454–1466
10. Jovanovic M, Babic I, Cabarkapa M, Misic J, Mijalkovic S, Nikolic V, Randjelovic D (2018) Soserbia: Android-based software platform for sending emergency messages. Complexity
11. Prawira M, Sukmana HT, Amrizal V, Rahardja U (2019) A prototype of android-based emergency management application. In: Proceedings of the 7th international conference on cyber and IT service management, vol 7. pp 1–6
12. Von Nordheim G, Boczek K, Koppers L (2018) Sourcing the sources: an analysis of the use of twitter and Facebook as a journalistic source over 10 years in The New York Times, the guardian, and Süddeutsche Zeitung. Digit J 6(7):807–828
13. Berbakov L, Tripi FN, Abad AC, Gómez JV, Pavković B (2017) Android application for collaborative mapping in emergency situations. In: Proceedings of the 25th telecommunication forum, pp 1–4
14. Hernández-Fuentes A, Monnier A (2020) Twitter as a source of information? Practices of Journalists Working for the French National Press. J Pract 1–18
15. GooglePlay: Mi Transporte Madrid-Metro-Bus-Cercanías. Available online: https://play.google.com/store/apps/details?id=com.movimad.transportemad&hl=en_US&gl=US. Accessed 5 July 2021
16. GooglePlay: Madrid Metro Bus Cercanías. Available online: https://play.google.com/store/apps/details?id=com.greenlionsoft.free.madrid&hl=es. Accessed 5 July 2021
17. Google Maps API: Objetos de mapas. Available online: https://developers.google.com/maps/documentation/android-api/map?hl=es-419. Accessed 5 July 2021
18. GooglePlay: Feedly. Available online: https://play.google.com/store/apps/details?id=com.devhd.feedly. Accessed 5 July 2021
19. GooglePlay: Appygeek Available online: https://play.google.com/store/apps/details?id=com.mobilesrepublic.appygeek. Accessed 5 July 2021
20. GooglePlay: Reddit. Available online: https://play.google.com/store/apps/details?id=com.reddit.frontpage&hl=es. Accessed 5 July 2021
21. GooglePlay: Citizen. Safety and Awareness. Available online: https://play.google.com/store/apps/details?id=sp0n.citizen&hl=es. Accessed 5 July 2021
22. GooglePlay: SocialDrive. Available online: https://play.google.com/store/apps/details?id=rge.tech.usuarios&hl=es. Accessed 5 July 2021
23. GooglePlay: Madrid Urban. Available online: https://play.google.com/store/apps/details?id=com.phonegap.madridUrbanAndroid&hl=en_US&gl=US. Accessed 5 July 2021
24. Martín-García N (2017) Conexiones en diseño y publicidad entre prensa gratuita y digital: análisis empíricos. El profesional de la información 26(6):1056–1064
25. Shelar A, Huang CY (2018) Sentiment analysis of twitter data. In: 2018 International conference on computational science and computational intelligence, pp 1301–1302
26. Criado JI, Pastor V, Villodre J (2017) Redes sociales digitales en los ayuntamientos espa-ñoles. Colección NovaGob Academia 2
27. Royo-Montañés S, Gómez AB (2019) Portales de datos abiertos. Metodología de análisis y aplicación a municipios españoles. El profesional de la información 28(6)
28. Zhuang Y (2019) Emotional analysis of sentences based on machine learning. In: Proceedings of international conference on big data analytics for cyber-physical-systems, Springer, Singapore, pp 813–820

Non-destructive Food Quality Monitoring System

E. Shanthini, V. Sangeetha, P. M. Anusha, A. Jayanthi, R. Mahendra Prakash, and N. Ram Prasanth

Abstract Food waste is one of the biggest costs of concern in all over the country. Research papers roughly say food wastage is about 1,300,000,000 tons. This paper provides a detailed view of predictive analytics of ML together comparing different strategies to separate different types of food. Non-destructive food quality is checked by based on the outer appearance of the given sample without destructing and sensed by the given sensors. This proposed system employed with PIC microcontroller which acts as a central processing unit, hygrometer, and temperature sensors together with three types of gas sensors which send the data sent to the cloud. For classifying the different types of foods like vegetables, fruits, and dairy qualities, the data is sensed with different types of grove gas sensors MQ9 (CO, Coal, Gas, Liquid Gas), MQ3 (Alcohol Vapor), and MQ2 (Combustible Gas, Smoke) furthermore with environmental sensors were acquired and sent that data to the Internet of Things. The novelty of this system is used to predict the quality of food under climatic conditions and also in traveling time with the help of IoT and their android application and the estimation of time that can preserve the different types of food in the storage.

E. Shanthini · V. Sangeetha
Faculty of Electronics and Communication Engineering, Sri Ramakrishna Engineering College, Coimbatore, Tamil Nadu, India
e-mail: Shanthini.e@srec.ac.in

V. Sangeetha
e-mail: Sangeetha.v@srec.ac.in

P. M. Anusha (✉) · A. Jayanthi · R. M. Prakash · N. R. Prasanth
Student of Electronics and Communication Engineering, Sri Ramakrishna Engineering College, Coimbatore, Tamil Nadu, India
e-mail: anusha.1802016@srec.ac.in

A. Jayanthi
e-mail: jayanthi.1802061@srec.ac.in

R. M. Prakash
e-mail: Mahrendraprakash.1902158@srec.ac.in

N. R. Prasanth
e-mail: Ramprasanth.1902153@srec.ac.in

1 Introduction

There are many problems in monitoring the food quality systems or technologies
namely not user friendly, non-portable, lack of accuracy plus non-predictable trav-
eling time. But this system proposed here is versatile, economical additionally can
monitor through mobile app, so it is easy to use and operate by the user. The Internet
of Things, machine learning, and easy-to-use android applications have been used
throughout the study. Where the sample namely fruits/vegetables/dairy products were
retained under a week for observation. Therefore, the sensor data graded into three
kinds of tags namely new garden as HIGH, semi-fresh as MEDIUM, and rotten as
LOW. Further, the learning algorithms of four different machines Random Forest,
Decision tree, XGBoost, logistic regression are the predictive analysis algorithms
developed based on the concept for categorizing and ranking the fruits or vegetables
through the details given by analyzation and also notify the user over the state of
environment for certain fruits and vegetables based on their conditions and features.
Development of program courseware found on the data which is available under the
environmental state neither it is favorable nor unfavorable. Hardware system PIC
microcontroller inbuilt wireless fidelity uploads the progressed data for the details
storage to the cloud computing. By this, the system notifies about environmental
change while travelling time (export or import). Android application pick up the data
from the Anaconda, operated with alerting message which is kept under observation
of monitoring fruits/vegetables storage.

2 Related Works

Jeer Hayes, Alexis Acquit, Karl Crowley, Kim Lau and Dermot Diamond proposed
a web-based color sensor to monitor the food quality. The low-cost colorimetric
sensor any change in the sample was recorded and captured in the WIFI camera
and then the data which is received was shifted to a Personal Computer which the
information uploaded next to the web. The software used here is color examination
and then scanning of the given sample was processed to data which is available.
The fresh method used here to monitor sea related flesh in bundle. Web-based color
details can be processed remote mode using advanced internal-based program that
exactly reflects the quality of the food. Color change shows change in the potential
of hydrogen space furthermore indicated for the food related to flesh product in
the starting stage. This proposed system decreased the requirement of staff in the
monitoring or observing of quality of products related to foods which can be judged
to every chemical engineers.

Atkore Prajwal, Patil Vaishali, zade payal, Dhapudkar Summit (2020) proposed Food Quality Assurance and Observing Program Project. People want healthy food to live healthy lives. There is a need for such a machine that guides us in terms of clean food. A sensor such as the pH sensor, the gas sensor, and the temperature sensor helps detect food intake. The proposed system provides information on the contaminant content present in food. This program is designed for people to be able to identify food quality. Sensors such as pH sensor, gas sensor, and temperature sensor are connected to the ATMEGA328P microcontroller, and the detected value is displayed on the LCD screen. It provides an easy way to find out the number of contaminants in food. Maintains and manages the diet plan.

3   Existing Method

The Arduino board connected to the different kinds of temperature and humidity sensors to detect the state of environmental conditions along with the sensor which detects alcohol-based release gas is MQ6 and also measures the light falling by using a photo resistor sensor. The Internet of Things developed here to send the data that can been transmitted and also retrieved the data any time which is connected to the Arduino Uno through which the WIFI module is connect. The sensor data is displayed on the LCD display. Then, the user can use the output through the speaker via voice.

The system is designed to filter and examine the given sample of foods. The machine algorithms used here to examine by the method for identifying the chemical composition in separation, tested through eight various ML algorithms and also predict the food decaying quality. This paper examines the result of accuracy of each and every ML algorithm used and analysis with the different set of data for the separate form of foods, namely fruits, vegetables, fish, dairy products, meat, etc. The accuracy for various food ranges from 80 to 90% with the image processing involved in eight ML algorithms. Overly, this proposed system shows analytic of the samples through processing image.

The system has developed a way to control the quality of remote food online by web-based color information that can be processed in remote mode. The low-cost colorimetric sensor any change in the sample was recorded and captured in the WIFI camera and then the data which is received was shifted to a Personal Comptroller change shows change in the potential of hydrogen space furthermore indicated for the food related to flesh product in the starting stage. This proposed system decreased the requirement of staff in the monitoring or observing of quality of products related to foods which can be judged to every chemoreceptor. The software used here is color examination and then scanning of the given sample was processed to data which is available. The fresh method used here to monitor sea related flesh in bundle.

4 Methodology

4.1 Hardware

In our proposed methodology, the main processing unit is a PIC microcontroller, temperature and humidity sensor, and data was sent to the clouds from the three gas sensors. The sensor data was collected and sent to the IoT to differentiate the vegetables/fruits quality. The data is then processed in the android application using a ML model to separate. What is different about the model is that it uses IoT to predict the quality and amount of time that can save different types of food in storage (Fig. 1).

4.1.1 Microcontroller

For this project, we used the PIC 16f877A microcontroller. The PIC has a different type series. It has 12 series, 16 series, 14 series, 24 series, 18 series, etc. In our project, we use an 18-series microcontroller. The very pin is an MCLR and the 5 V dc supply is given with a 10 K resistor. The same offer is also directly given to the 11th pin. Based on the tank circuit, the pin number 12 is planned. To the pin-13 and pin-14, 4 MHz crystal oscillator consists of a tank circuit and also the two 22pf capacitors are connected.
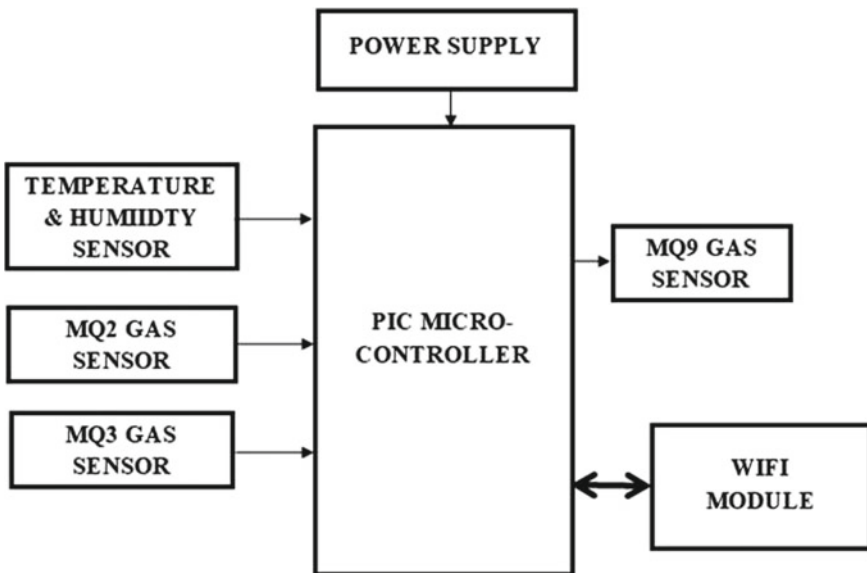
Fig. 1 Block diagram of the system

4.1.2 Gas Sensor

The sensor (MQ9, MQ3, and MQ2) is used here to detect the changes in smells. The analogue sensor output was used to digitize the data. While the data was digitized, the ADS1115 ADC was used. The PIC microcontroller was also connected to the I2C protocol, a visual sensor connector for humidity and temperature. (HTU21D (F)) was a digital humidity value with the temperature release applied to the proposed system.

4.1.3 Temperature and Humidity

The sensor is connected to the microcontroller through I2C communication. Interference diagram for this sense. Inside the open storage chamber, our sensor is stored (has no control area) with fresh apple and tomato for two week and after that the data was collected from the sensor and stored in a microcontroller. An additional Semi is new apples and rotten apples and tomatoes taken with data properly gathered. Collected data used Machine learning modeling for classification purposes explained in more detail in the software section.

4.2 Software

Importing packages in this project is for data processing. Arrays are works with NumPy and also for the data fragmentation the Scikit-learn is used, all our basic packages are used to build and test the models. Building and testing partition models. Let us bring all our basic packages to our Python site.

Data Processing

A precautionary measure will be used in this project to determine non-database values. The reason for the missing prices could be data corruption or failure to record data.

Data Classification

The data classification will be a process with the variables that will be defined as independent, dependent with the X, Y variables accordingly. The data which is derived as a variable used for testing the data set and also for the modeling. The testing data inserts into the training dataset after the testing data splatted. Train Test Split Algorithm is used for splitting the data in the Python. It's the easiest way to split the data.

Data Modelling

Data modeling is the process where the two different types of ML models can be separated to build and test the dataset. In these, various types of models can be separated the most useful for this project classification found to solve the problems. The Scikit-learn are the packages used here to classify the ML algorithm which is customized to give the solution.

4.2.1   Classification of Algorithm

Editing using Boost Classifier the accuracy and speed are affected because it's a powerful ML algorithm. The different parameters and its values will be specifically classified while using the Boost model, and the main goal of the boosting sequence is collecting. Guessing accuracy t is improved by covering the weak readers. The next fast result is predicted based on the previous fast results t-1. Finally, the prediction of the result is in less weight and the and those are subdivided and also have a higher weight (Fig. 2).

The four boxes shown above are the four dividers always split the + and again − same way as possible.
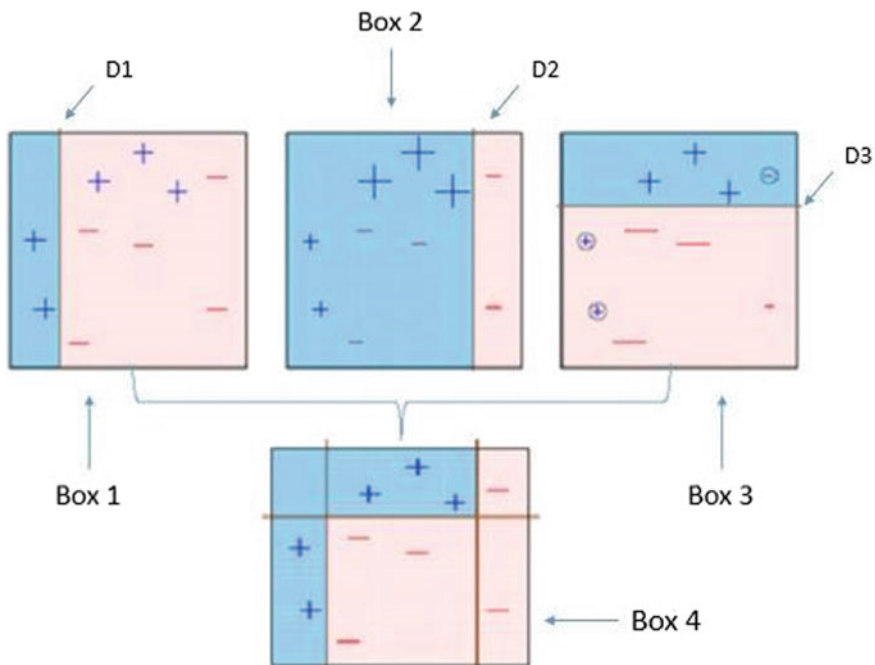
Fig. 2   Four dividers

1. **Box 1:** The 1st phase creates the split D1 in the left side. The D1 has separate three + points in the left side and it says everything to right side D1 and also intimates the left side D1 also. The prediction is based on one factor because the tree present here differs in one level.
2. **Box 2:** The 2nd phase gives three separates + points. It creates a vertical line D2. It says everything to the left + and also right − points. Here, the prediction makes a mistake while the three points misinterpreted.
3. **Box 3:** Also, the 3rd phase creates the horizontal line and divides incorrectly. The extra weight was given to the + points and the − points placed incorrectly in D3. However, this filter fails to place the points in a circle.
4. **Box 4:** This is a final and weighted combination of all the three weak sections as the fourth phase is divided correctly. This is the basis of developing the Boost algorithm and a good idea of classifying all the points. The importance of the various features and parameters used to conclude the strongest conclusion and it build the new model which is resolve the previous segmentation error. When now, let us get to Boost. The Boost readers base ensembles of trees and the tree assembly is the model; it is the set of trees for division receding (CART). Trees planted in succession and efforts to reduce the level of improper segregation are made with subsequent repetition.

5   Experimental Results

Main focus of our project is to monitor food spoilage with specific logical features. Pic microcontroller and environmental commercial sensors used and the additional data collected from the sensor during two weeks, detected in the PCA method and finally found, the data is not linear separated and therefore straightforward and linear there both methods are to classify the data and progress correctly (Figs. 3, 4, 5, 6, 7 and 8).

The best ML algorithms are used for android. In addition, the android app is designed to monitor the status of fruit/vegetables by using IoT in a specific remote area. IoT integrated cloud computing helps to analyze real-time data, lower operating costs, and the performance speed. This system was successfully designed and found to be the best in reliability, performance (Table 1).

6   Conclusion

The proposed system contains a PIC microcontroller as a central processing unit, temperature, and humidity sensor including three gas sensors like combustible gas, smoke, CO, coal gas, liquid gas, alcohol vapor, etc., as well as the receiving gas data being sent to the cloud computing. The received data is then worked and progressed
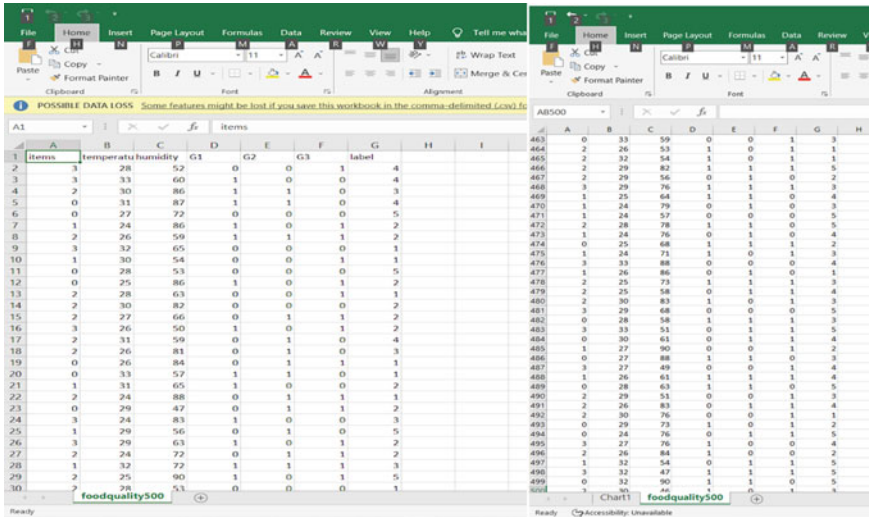
Fig. 3 Dataset
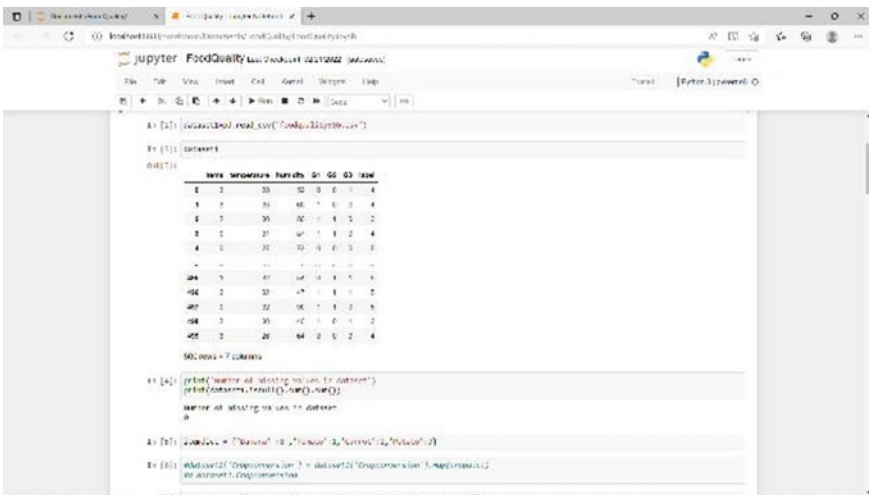
Fig. 4 Implementation of algorithms

in the android application using a machine learning model to separate the data. Here, ML is a retrospective, random forest, deciduous tree, XGBoost algorithms. The best XGBoost ML algorithms are included in the android application with the best accuracy and performance of about 98%. The newcomers to this app, it uses Internet of Things and its android app can be used to predict the quality of food during travel (import and export), a time limit that can keep different types of food in storage.
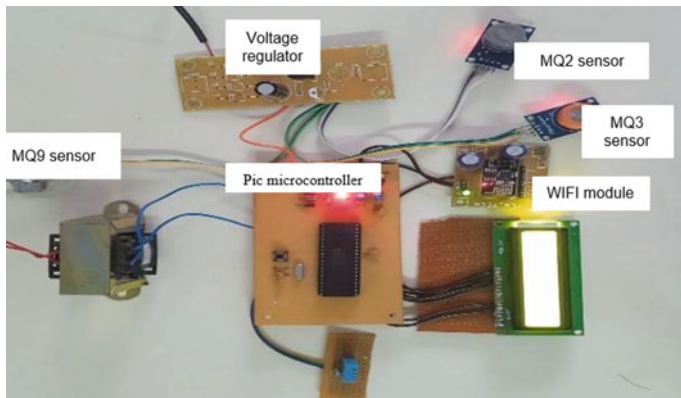
Fig. 5 Hardware interface

Fig. 6 Sensors result

And this is an expensive, modern, portable, and an easily accessible system that was developed and successfully tested.
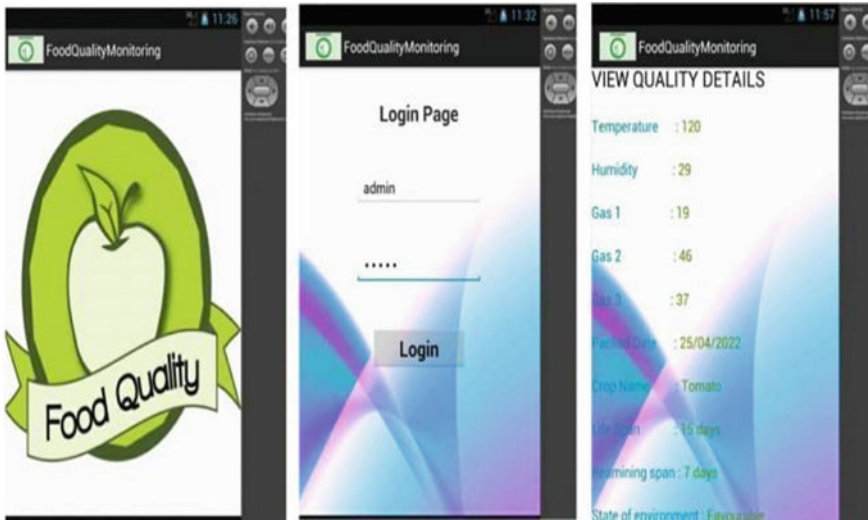
Fig. 7 Android applications
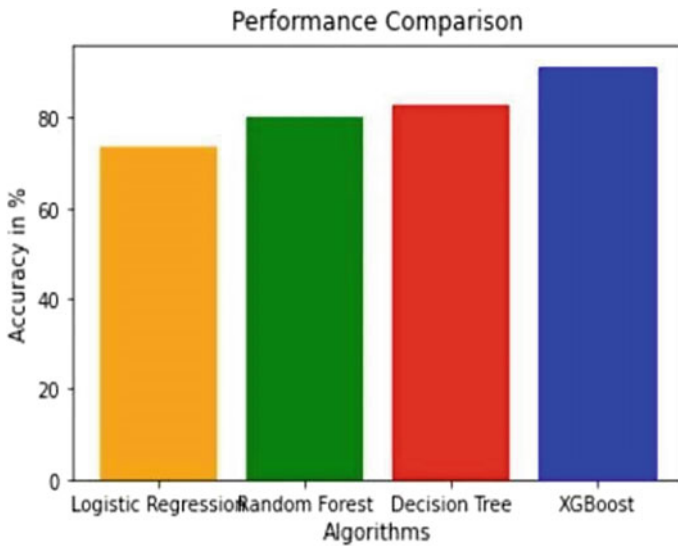
Fig. 8 Algorithms performance comparison

Table 1 Comparsion

S. No.	Name of the machine learning model	Training period	Testing time period	Accuracy	Verification occurance	Performance
1	XGBoost	0:00:21:718,250	0:00:00:0.11149	97	3	97
2	Logistic regression	0:00:03:026,312	0:00:00:0.01002	87.2	3	87.2
3	Random forest	0:00:03:893,352	0:00:00:0.31112	91.2	3	91.2
4	Decision tree	0:00:45:476,207	0:00:00:0.01804	88	3	88

References

1. Pandian DAP (2019) Image inpainting technique for high quality and resolution enhanced image creation. J Innovative Image Process 1(1):39–50
2. Kumar TS, Senthil T (2019) A novel method for HDR video encoding, compression and quality evaluation. J Innovative Image Process (JIIP) 1(02):71–80
3. Gustavsson J, Cederberg C, Sonesson U (2020) Global food losses and food waste. In: Swedish institute for food and biotechnology (SIK) Gothenburg, Sweden, Accessed 31 March 2020
4. Wu Y et al. (2019) Air quality monitoring for vulnerable groups in residential environments using a multiple hazard gas detector. Sensors 19(2):362
5. Tiwari A, Sadistap S, Mahajan SK (2018) Development of an environment monitoring system using the internet of things. In: Ambient communications and computer systems, Springer, Singapore, pp 403–412
6. Hassan N et al. (2018) The role of edge computing in the internet of things. IEEE Commun Mag 56(11):110–115
7. Sharma SK, Wang X (2017) Live data analytics with collaborative edge and cloud processing in wireless IoT networks. IEEE Access 5:4621–4635
8. Chongtham Phisut P, Seesaard T, Kerdcharoen TV (2015) Monitoring of microbial canned food spoilage and contamination based on e-nose for smart home. In: 12th International conference on electrical engineering/electronics, computer, telecommunications and information technology (ECTICON), IEEE
9. Kaur H, Sawhney BK, Jawandha SK (2018) Evaluation of plum fruit maturity by image processing techniques. J Food Sci Technol 55:3008–3015
10. Wijaya DR et al. (2017) Development of mobile electronic nose for beef quality monitoring. Proc Comput Sci 124:728–735
11. Alfian G et al. (2020) Improving efficiency of RFID-based traceability system for perishable food by utilizing IoT sensors and machine learning model. Food Control 110:107016
12. Ireri D, Belal E, Okinda C, Makange N, Ji C (2019) A computer vision system for defect discrimination and grading in tomatoes using machine learning and image processing. Artif Intell App 2:28–37
13. Zhang Z (2016) Missing data imputation: focusing on single imputation. Ann Transl Med 4(1)
14. Septiarini A, Hamdani H, Hatta HR, Kasim AA (2019) Image-based processing for ripeness classification of oil palm fruit. In: Proceedings of the 2019 5th international conference on science in information technology (ICSITech), Yogyakarta, Indonesia, pp. 23–26

15. Sahu B, Tiwari A, Raheja JL (2020) Development of machine learning and edge IoT based non-destructive food quality monitoring system using raspberry Pi 2020. In: IEEE International conference on computing, power and communication technologies (GUCON), Galgotias University, Greater Noida, UP, India
16. Nandi CS, Tudu B, Koley C (2016) A machine vision technique for grading Of harvested mangoes based on maturity and quality. IEEE Sens J 16:6387–6396
17. Géron A (2019) Hands-on machine learning with scikit-learn, keras, and tensorflow: concepts, tools, and techniques to build intelligent systems, O'Reilly Media

Author Index